

Lecture Notes in Civil Engineering

K. Murali  
V. Sriram  
Abdus Samad  
Nilanjan Saha *Editors*

# Proceedings of the Fourth International Conference in Ocean Engineering (ICOE2018)

Volume 1

 Springer

# Lecture Notes in Civil Engineering

Volume 22

## Series editors

Marco di Prisco, Politecnico di Milano, Milano, Italy

Sheng-Hong Chen, School of Water Resources and Hydropower Engineering,  
Wuhan University, Wuhan, China

Ioannis Vayas, National Technical University of Athens, Zografou Campus,  
Zografou, Greece

Sanjay Kumar Shukla, School of Engineering, Edith Cowan University, Joondalup,  
Perth, Australia

Giovanni Solari, University of Genoa, Genova, Italy

Anuj Sharma, Iowa State University, Ames, IA, USA

Nagesh Kumar, Department of Civil Engineering, Indian Institute of Science  
Bangalore, Bangalore, Karnataka, India

Chien Ming Wang, School of Civil Engineering, The University of Queensland,  
St Lucia, QLD, Australia

**Lecture Notes in Civil Engineering (LNCE)** publishes the latest developments in Civil Engineering - quickly, informally and in top quality. Though original research reported in proceedings and post-proceedings represents the core of LNCE, edited volumes of exceptionally high quality and interest may also be considered for publication. Volumes published in LNCE embrace all aspects and subfields of, as well as new challenges in, Civil Engineering. Topics in the series include:

- Construction and Structural Mechanics
- Building Materials
- Concrete, Steel and Timber Structures
- Geotechnical Engineering
- Earthquake Engineering
- Coastal Engineering
- Hydraulics, Hydrology and Water Resources Engineering
- Environmental Engineering and Sustainability
- Structural Health and Monitoring
- Surveying and Geographical Information Systems
- Heating, Ventilation and Air Conditioning (HVAC)
- Transportation and Traffic
- Risk Analysis
- Safety and Security

To submit a proposal or request further information, please contact the appropriate Springer Editor:

- Mr. Pierpaolo Riva at [pierpaolo.riva@springer.com](mailto:pierpaolo.riva@springer.com) (Europe and Americas);
- Ms. Swati Meherishi at [swati.meherishi@springer.com](mailto:swati.meherishi@springer.com) (India);
- Ms. Li Shen at [li.shen@springer.com](mailto:li.shen@springer.com) (China);
- Dr. Loyola D'Silva at [loyola.dsilva@springer.com](mailto:loyola.dsilva@springer.com) (Southeast Asia and Australia/NZ).

More information about this series at <https://link.springer.com/bookseries/15087>

K. Murali · V. Sriram · Abdus Samad  
Nilanjan Saha  
Editors

# Proceedings of the Fourth International Conference in Ocean Engineering (ICOE2018)

Volume 1

 Springer

*Editors*

K. Murali  
Department of Ocean Engineering  
Indian Institute of Technology Madras  
Chennai, Tamil Nadu, India

Abdus Samad  
Department of Ocean Engineering  
Indian Institute of Technology Madras  
Chennai, Tamil Nadu, India

V. Sriram  
Department of Ocean Engineering  
Indian Institute of Technology Madras  
Chennai, Tamil Nadu, India

Nilanjan Saha  
Department of Ocean Engineering  
Indian Institute of Technology Madras  
Chennai, Tamil Nadu, India

ISSN 2366-2557                      ISSN 2366-2565 (electronic)  
Lecture Notes in Civil Engineering  
ISBN 978-981-13-3118-3              ISBN 978-981-13-3119-0 (eBook)  
<https://doi.org/10.1007/978-981-13-3119-0>

Library of Congress Control Number: 2018960240

© Springer Nature Singapore Pte Ltd. 2019, corrected publication 2022

This work is subject to copyright. All rights are reserved by the Publisher, whether the whole or part of the material is concerned, specifically the rights of translation, reprinting, reuse of illustrations, recitation, broadcasting, reproduction on microfilms or in any other physical way, and transmission or information storage and retrieval, electronic adaptation, computer software, or by similar or dissimilar methodology now known or hereafter developed.

The use of general descriptive names, registered names, trademarks, service marks, etc. in this publication does not imply, even in the absence of a specific statement, that such names are exempt from the relevant protective laws and regulations and therefore free for general use.

The publisher, the authors and the editors are safe to assume that the advice and information in this book are believed to be true and accurate at the date of publication. Neither the publisher nor the authors or the editors give a warranty, express or implied, with respect to the material contained herein or for any errors or omissions that may have been made. The publisher remains neutral with regard to jurisdictional claims in published maps and institutional affiliations.

This Springer imprint is published by the registered company Springer Nature Singapore Pte Ltd. The registered company address is: 152 Beach Road, #21-01/04 Gateway East, Singapore 189721, Singapore

# **Organising Committee**

## **Advisory Committee**

B. Ramamurthi, Director, IITM Patron and Chairman  
The Head, Department of Ocean Engineering, IITM Vice Chairman  
Director, CWPRS Member  
Chairman, CWC Member  
Chairman, Chennai Port Trust Member  
Chairman, Ennore Port Limited Member  
Vice Chancellor, Indian Maritime University Member  
Director, INCOIS and NIOT Member  
Director, NIO Member  
CMD, DCI Member  
Organizing Secretary, ICOE2018, Convener

## **Scientific Committee**

Shinji Sato, Japan  
Tomoya Shibayama, Japan  
Hitoshi Tanaka, Japan  
Kyung-Duck Suh, Korea  
Holger Schüttrumpf, Germany  
Peter Fröhle, Germany  
Qingwei Ma, UK  
Perumal Nithiarasu, UK  
M. R. Dhanak, USA  
Krish Thiagarajan, USA  
Zhenhua Huang, USA

Felice Arena, Italy  
Roberto Tomasicchio, Italy  
P. Ferrant, France  
Ioan Nistor, Canada  
P. Lin, China  
Decheng Wan, China  
Adrian Law, Singapore  
Inigo-Losada, Spain  
T. E. Baldock, Australia  
Ron Cox, Australia  
Enrique Alvarez Del Rio, Mexico  
Janaka Wijetunga, Sri Lanka  
K. H. Kim, Korea  
Shin Hyung Rhee, Korea  
Richard Manasseh, Australia  
M. C. Deo, India  
R. Sundaravadivelu, India  
V. Sundar, India  
A. D. Rao, India  
P. K. Bhaskaran, India  
D. Sen, India  
Ira Didenkulova, Russia  
Efim Pelinovsky, Russia

## **Local Organizing Committee**

S. A. Sannasiraj, IITM, Chennai  
K. Murali, IITM, Chennai  
V. Sundar, IITM, Chennai  
R. Sundaravadivelu, IITM, Chennai  
V. Anantha Subramaniam, IITM, Chennai  
S. K. Bhattacharya, IITM, Chennai  
S. Nallayarasu, IITM, Chennai  
P. Ananthakrishnan, IITM, Chennai  
P. Krishnankutty, IITM, Chennai  
S. Surendran, IITM, Chennai  
R. Panneer Selvam, IITM, Chennai  
Srinivasan Chandrasekaran, IITM, Chennai  
G. Suresh Kumar, IITM, Chennai  
P. Shanmugam, IITM, Chennai  
Nilanjan Saha, IITM, Chennai  
Rajiv Sharma, IITM, Chennai

Jitendra Sangwai, IITM, Chennai  
Rajesh Nair, IITM, Chennai  
Abdus Samad, IITM, Chennai  
Deepak Kumar, IITM, Chennai  
V. Sriram, IITM, Chennai  
Tarun K. Chandrayadula, IITM, Chennai  
R. Vijayakumar, IITM, Chennai  
Suresh Rajendran, IITM, Chennai  
J. Purnima, NIOT, Chennai



# Preface

The fourth International Conference in Ocean Engineering (ICOE2018) is organized by the Department of Ocean Engineering, Indian Institute of Technology Madras (IITM). The Department of Ocean Engineering has achieved significant success with a dynamic profile in terms of training graduate and postgraduate professionals for careers across the globe. The department is a centre of excellence in disciplines spanning across the areas of ship design, coastal and harbour structures, deep-water technologies, marine geo-techniques, energy and areas in oil and gas. The department organized its flagship conference ICOE in 1996, 2001 and 2009. This conference is aimed at bringing experts in the field to interact with young researchers. The main theme of the conference is “Emerging Opportunities and Challenges in Ocean Engineering”. It is aimed at addressing the upstream challenges in ocean engineering. Thus, the fourth International Conference in Ocean Engineering 2018 (ICOE2018) offers an exciting platform for academicians, engineers from industry, policy makers and administrators from all over the globe to deliberate on various conference themes.

The technical programme of the conference has been carefully planned with 8 keynote addresses from experts from USA, UK, Norway, South Korea, India and Italy; 149 contributed papers; and special sessions in the modernization of ports, hydrodynamics, ocean energy and naval architecture with invited speakers. All the papers accepted in this conference have been reviewed by experts in the procedure of blind peer review and subsequently revised by the authors incorporating the remarks and suggestions of the reviewers, thus improving the quality of the contributions. These papers will be published as two volumes in Springer book series “Lectures Notes in Civil Engineering”. The present volume consists of 3 keynote papers and 70 papers in the areas of marine vehicles and floating systems, computational modelling, ocean modelling, marine foundations and petroleum engineering and technology.

We would like to thank the members of the Advisory Committee, International Steering Committee and Local Organizing Committee and the reviewers, who have greatly contributed to the improvement of the quality of papers, providing constructive critical comments, corrections and suggestions to the authors. Finally, we

wish to thank all the authors who submitted their papers, making this conference possible. It is the quality of their contributions and presentations that really has made this conference a success and come up as a book volume.

Chennai, India

Prof. K. Murali  
Dr. V. Sriram  
Dr. Nilanjan Saha  
Dr. Abdus Samad

# Contents

## Part I Keynotes

<b>Waiting on Suitable Weather to Perform Marine Operations</b> . . . . .	3
Ove T. Gudmestad	
<b>Wave Overtopping in the UK During the Winter of 2013/14</b> . . . . .	13
Dominic E Reeve	
<b>Modernization of Port</b> . . . . .	25
R. Sundaravadivelu	

## Part II Marine Vehicles and Floating systems

<b>Response Control of FPSO Using Multiple Tuned Liquid Dampers</b> . . . . .	43
Gurusamy Saravanan, Deepak Kumar and Ruchi Saraswat	
<b>High-Speed Simulation in Towing Tank for Dynamic Lifting Vessels</b> . . . . .	65
Nimmagadda Naga Venkata Rakesh, Polisetty Lokeswara Rao and V. Anantha Subramanian	
<b>Coupled Boundary Element Method (BEM) and Finite Element Method (FEM) for Hydroelastic Analysis of Floating Plate</b> . . . . .	81
Anoop I. Shirkol and T. Nasar	
<b>Hydroelasticity Analysis of a Container Ship Using a Semi-analytic Approach and Direct Coupling Method in Time Domain</b> . . . . .	103
Debasmit Sengupta, Sumit Kumar Pal, Ranadev Datta and Debabrata Sen	
<b>Numerical Study on the Influence of Head Wave on the Hydrodynamic Derivatives of a Container Ship</b> . . . . .	117
T. V. Rameesha and P. Krishnankutty	

<b>Retrofitting Integrated Wedge-Flap for Improvement of Resistance of High-Speed Displacement Vessel</b> .....	135
Lijo Joseph and V. Anantha Subramanian	
<b>Numerical Estimation of Underwater Radiated Noise of a Marine Propeller in Non-cavitating Regime</b> .....	149
Abhishek Kumar Tewari, Vijit Misra and R. Vijayakumar	
<b>Estimation of Hydrodynamic Derivatives from Sea Trial Data Using System Identification Technique</b> .....	169
K. O. S. R. RaviSekhar RadhaKrishna and R. Panneer Selvam	
<b>Effect of Forward Speed on Roll Damping of a Container Ship Using URANS Simulations</b> .....	187
Mohsin A. R. Irkal, S. Nallayarasu and S. K. Bhattacharyya	
<b>Design and Analysis of a Carbon Composite Propeller for Podded Propulsion</b> .....	203
Ashok Kumar, G. Lal Krishna and V. Anantha Subramanian	
<b>Passing Vessel Effect on Mooring System of a Berthed Ship—A Case Study at Jawahar Dweep Berth No: 5, Mumbai Port</b> .....	217
Keshav Sundar, V. Nandhini and S. Nallayarasu	
<b>Hydrodynamic Study on the Performance Evaluation of Flapping Foils in Open Water Condition</b> .....	259
Anties K. Martin, B. K. Alok, P. Krishnankutty and P. Ananthakrishnan	
<b>Numerical Study of Water Depth Effect on Sway Velocity and Rudder Derivatives of a Container Ship in Manoeuvring</b> .....	275
Akhil Balagopalan and P. Krishnankutty	
<b>Numerical Investigation of Influence of Microbubble Injection, Distribution, Void Fraction and Flow Speed on Frictional Drag Reduction</b> .....	293
Sudhir Sindagi, R. Vijayakumar, Somanath Nirali and B. K. Saxena	
<b>Hydroelastic Responses of a Pontoon-Type VLFS in Different Water Depths</b> .....	319
Sakthivel Somansundar and Rajamanickam Panneer Selvam	
<b>Effect of Slamming and Green Water on Short-Term Distribution of Vertical Bending Moment of a Containership in Abnormal Waves</b> .....	333
Suresh Rajendran and C. Guedes Soares	
<b>Vibration Control of Large Floating Offshore Structures by Means of Damping Plates: A Case Study</b> .....	347
Carlo Ruzzo, Felice Arena and Vallam Sundar	

<b>Experimental Investigation on Effect of Submerged Solid Baffle in a Barge Carrying Liquid Sloshing Tank</b> .....	365
T. Nasar and S. A. Sannasiraj	
<b>Design Approach for Reducing the Wave Added Resistance by Hull Form Optimisation</b> .....	385
M. Kumar Sanchana, R. Vijayakumar and V. V. S. Prasad	
<b>Hydrodynamic Aspects of Turret-Moored FPSOs</b> .....	401
Balakrishnan G. Nair, R. Vijayakumar and P. Ananthakrishnan	
<b>Duct Optimization and Performance Evaluation Using CFD for the Reefer Container Hold</b> .....	423
Elangovan Muniyandy, Ananth Kumar and Sunil Arora	
<b>Technological Trends for Ocean Research Vessels</b> .....	435
Nitin Agarwala	
<b>Feature Extraction of Underwater Images by Combining Fuzzy C-Means Color Clustering and LBP Texture Analysis Algorithm with Empirical Mode Decomposition</b> .....	453
M. Somasekar and S. Sakthivel Murugan	
<b>Embedded System Design for Autonomous Unmanned Surface Vehicles in Laboratory Environment</b> .....	465
Awanish C. Dubey, V. Anantha Subramanian and V. Jagadeesh Kumar	
<b>Design and Development of Unmanned Underwater and Aerial Vehicle</b> .....	479
A. Palaniappan, P. Ganesh, S. B. Pranesh, D. Sathianarayanan and G. A. Ramadass	
<b>Effect of Rudder and Roll Control Mechanism on Path Prediction of Autonomous Underwater Gliders</b> .....	491
R. V. Shashank Shankar and R. Vijayakumar	
<b>Development of Controller for Robotic Fish</b> .....	507
M. P. R. Prasad and A. M. R. B. Aminur	
<b>Part III Computational Modelling</b>	
<b>Multi-directional Irregular Wave Modelling with CFD</b> .....	521
Weizhi Wang, Hans Bihs, Arun Kamath and Øivind Asgeir Arntsen	
<b>Numerical Study of Superposition Principle for Surface Gravity Waves</b> .....	531
Vinay Kumar Gupta, Alok Khaware, Ashok Sivanandham and K. V. S. S. Srikanth	

<b>Numerical Modelling of Hydrodynamic Impact of Tsunami on Coastal Structures in the Presence of Curved Sea Wall</b> .....	547
Aditya Gupta, Manasa R. Behera and Amin Heidarpour	
<b>Numerical Study on Secondary Flow Characteristics After Dual Stepped Cylinder at Low Reynolds Number</b> .....	559
Junxian Wang, Qingwei Ma and Shiqiang Yan	
<b>Modelling Wave Interaction with Porous Structures Using Boussinesq Equations</b> .....	573
Shagun Agarwal, V. Sriram and K. Murali	
<b>Breaking Focused Waves Generated Using the Transient Wave Packet Method and the Breaking Impact Forces on a Vertical Cylinder</b> .....	585
Arun Kamath, Mayilvahanan Alagan Chella and Hans Bihs	
<b>Effect of Emerged Coastal Vegetation on Wave Attenuation Using Open Source CFD Tool: REEF3D</b> .....	591
H. S. Arunakumar, Praveen Suvarna, P. A. Abhijith, Ashwin S. Prabhu, U. Pruthviraj and Arun Kamath	
<b>CFD Study of Regular Waves on a Jacket Structure</b> .....	605
Ankit Aggarwal and Hans Bihs	
<b>Computational Study on the Hydrodynamic Effects of Interceptors Fitted to Transom of Planing Vessel</b> .....	613
Suneela Jangam, V. Anantha Subramanian and P. Krishnankutty	
<b>Numerical Modelling of Scour Around an Offshore Jacket Structure Using REEF3D</b> .....	627
Nadeem Ahmad, Hans Bihs, Arun Kamath and Øivind A. Arntsen	
<b>Numerical Modelling of Bed Shear Stress in OpenFOAM</b> .....	637
Nandakumar Visuvamithiran, V. Sriram and Jaya Kumar Seelam	
<b>Fully Coupled Aero-Hydrodynamic Simulation of Floating Offshore Wind Turbines with Overset Grid Technology</b> .....	647
Ping Cheng and Decheng Wan	
<b>A Parallelized Inflow-Boundary-Based Numerical Tank: Performance on Individual SMA Nodes</b> .....	663
Shaswat Saincher, Sagar Dave, Chetan Anghan and Jyotirmay Banerjee	
<b>Simulation of Floating Bodies in Waves and Mooring in a 3D Numerical Wave Tank Using REEF3D</b> .....	673
Tobias Martin, Hans Bihs, Arun Kamath and Øivind Asgeir Arntsen	

<b>Application of an Efficient Numerical Model for CO<sub>2</sub> Sequestration in Deep Saline Aquifers</b> .....	685
P. Dinesh, M. R. Behera, P. G. Ranjith and N. Muthu	
<b>Prediction of Motions and Wave-Induced Loads on a Container Ship Using Nonlinear 3D Time-Domain Panel Method</b> .....	709
Ranadev Datta and C. Guedes Soares	
<b>Part IV Ocean Modelling</b>	
<b>Estimation and Analysis of Extreme Maximum Wave Heights</b> .....	723
S. Satish, S. A. Sannasiraj and V. Sundar	
<b>Seasonal Variability of Circulation Along the North-East Coast of India Using Princeton Ocean Model</b> .....	733
P. S. Swathy Krishna and Hari V. Warrior	
<b>Water-Level Forecasting Using Neuro-wavelet Technique</b> .....	749
Pradnya Dixit and Shreenivas Londhe	
<b>Seasonal and Inter-Annual Variations in Wave Characteristics of Vizhinjam, South-West Coast of India</b> .....	761
Sisir Kumar Patra, Basanta Kumar Jena, V. Suseentharan and M. V. Ramanamurthy	
<b>Multidecadal Fluctuations of Storminess of Black Sea Due to Teleconnection Patterns on the Base of Modelling and Field Wave Data</b> .....	773
Yana Saprykina, Sergey Kuznetsov and Nikolay Valchev	
<b>Climate Change Impact on Design Waves Using Climate Models</b> .....	783
Pooja Jain and M. C. Deo	
<b>Assessment of Nonlinear Quadruplet Interactions for Measured Spectra in Deep Waters on the East Coast of India Through Gauss–Legendre Quadrature Method</b> .....	795
M. Kamalakannan, M. Kalyani, V. Prabhakar, Basanta Kumar Jena and R. Venkatesan	
<b>Sensitivity Study of Wind Drag Coefficient on Surge Modelling for Tropical Cyclone</b> .....	813
C. Gowri Shankar, Manasa Ranjan Behera and P. Vethamony	
<b>Tidal Circulation Studies Using Regional Model in the Bay of Bengal</b> .....	829
Saikat Pramanik, Samiran Mandal, Abhijit Shee, Subrota Halder and Sourav Sil	

## Part V Marine Foundations

<b>Vertical Pull-Out Capacity of Torpedo Anchors</b> . . . . .	839
S. Keerthi Raaj, R. Sundaravadivelu and Nilanjan Saha	
<b>Design of Piles for a Berthing Structure on Artificial Slope</b> . . . . .	855
S. V. Sivapriya, R. Sundaravadivelu and S. R. Gandhi	
<b>Numerical Study of the Behaviour of Pipe Sheet Pile Wall and Diaphragm Wall in Vertical Face Berthing Structure</b> . . . . .	867
P. Kavitha and R. Sundaravadivelu	
<b>Field and Numerical Study of Vibration on Existing Berthing Structure Due to Pile Driving</b> . . . . .	877
Jeena Mary John, R. Sundaravadivelu and Nilanjan Saha	
<b>Alternative Foundation Methods for Upgradation of Oil Jetty</b> . . . . .	889
R. Sundaravadivelu, S. Sakthivel, S. Srinivasalu, A. Chitra and J. Bharath Priyan	
<b>Influence of Grouser Geometrical Parameters of Deep-Sea Crawler Vehicle on Soft Clays</b> . . . . .	899
C. Janarthanan, K. Gopkumar, V. Sundaramoorthi, N. R. Ramesh and G. A. Ramadass	
<b>Testing of Soft Clays Using Bevameter for Deep-Sea Mining Machine</b> . . . . .	913
K. V. Reshma, C. Janarthanan, V. Sundaramoorthi, K. Jayanthi, B. O. Vishwanath, P. Muthuvel, K. Gopkumar and G. A. Ramadass	
<b>Part VI Petroleum Engineering &amp; Technology</b>	
<b>Estimating Belowground Free Phase Gas (FPG) in Tropical Peatlands of South-West Coast of India Using Ground Penetrating Radar (GPR)</b> . . . . .	931
Koravangatt Devi and Rajesh R. Nair	
<b>Integrating, Predicting and Preventing Flow Assurance Issues—A Review</b> . . . . .	941
Anchit Khanna and Samarth Patwardhan	
<b>Coupled Flow and Geomechanics Model for CO<sub>2</sub> Storage in Tight Gas Reservoir</b> . . . . .	955
Awez Hanegaonkar, Tapan Kidambi and G. Suresh Kumar	
<b>RETRACTED CHAPTER: Effect of Nanocellulose as an Additive in Cement</b> . . . . .	969
Vignesh Shenoy, Sanjay Joshi and Mikhil Dange	



**Analyzing the Physical and Chemical Properties of Water Column Nutrients and Sediments Along Southeast Coast of India** ..... 985  
 G. Annalakshmi and S. Sakthivel Murugan

**Modeling Investigations on Sorption of Petroleum Hydrocarbons to Clay Minerals in a Saturated Porous Aquifer** ..... 997  
 Renu Valsala and Suresh Kumar Govindarajan

**Experimental and Numerical Investigations on In Situ Chemical Oxidation Model for Groundwater Contaminated with Petroleum Hydrocarbons** ..... 1009  
 Natarajan Aarthi, Duraisamy Ashwin, Subbaiyan Gokulprasath, Mangottiri Vasudevan, Narayanan Natarajan and Govindarajan Suresh Kumar

**Numerical Modelling on Enhanced Mobility of Petroleum Hydrocarbon in Saturated Porous Media** ..... 1021  
 M. Berlin and G. Suresh Kumar

**Mathematical Modelling and Analysis of Nano-dust Explosion** ..... 1033  
 Adnan Deshmukh, Samarth Patwardhan, Nilesh Sakpal, Akshay Agwan and Sagar Wakale

**Environmental Challenges and Opportunities in Marine Engine Heavy Fuel Oil Combustion** ..... 1047  
 Abdul Gani Abdul Jameel, Abdulrahman Alkhateeb, Selvedin Telalović, Ayman M. Elbaz, William L. Roberts and S. Mani Sarathy

**Exergy Analysis of Auxiliary Boiler for Marine Application** ..... 1057  
 Jitendra Singh Pal, S. N. Sapali and T. R. Anil

**Retraction Note to: Effect of Nanocellulose as an Additive in Cement** ..... C1  
 Vignesh Shenoy, Sanjay Joshi and Mikhil Dange

# About the Editors

**Dr. K. Murali** is a professor in the Department of Ocean Engineering, IIT Madras. He has authored about 100 publications in international conferences and journals and is the recipient of the Endeavour Research Fellowship from the Australian Government. He received a major research grant from ISRO for developing coastal research models after the Indian Ocean tsunami. His field of research specialization is computational hydrodynamics. He has more than 20 years of consultancy experience in coastal and port engineering. He has completed 50 coastal protection design works in and around India.

**Dr. V. Sriram** is an associate professor in the Department of Ocean Engineering, IIT Madras. He received the prestigious Newton International Fellowship (from the Royal Society, UK) in 2009, Alexander von Humboldt Fellowship (from AvH foundation, Germany) in 2011, DST INSPIRE Faculty Award (from DST) and RJ Garde Research Award (from Indian Society of Hydraulics). He is a visiting researcher at City, University of London and a visiting professor at Leibniz Universität Hannover, Germany. He has published more than 60 papers in international journals and conferences. His research work focuses on computational hydrodynamics. He has developed state-of-the-art numerical models applied to ocean engineering, particularly coastal and offshore engineering.

**Dr. Abdus Samad** is an associate professor in the Department of Ocean Engineering, IIT Madras, working in the areas of marine energy, fluid mechanics and optimization. He has received several awards from various bodies, has published more than 100 articles in a number of journals and conferences and has filed several patents. He was a knowledge transfer associate in the UK from 2008 to 2010 and was a Brainpool invited scientist in South Korea during his sabbatical leave in 2016.

**Dr. Nilanjan Saha** is an associate professor in the Department of Ocean Engineering, IIT Madras. He has published 20 papers in international journals and is the recipient of the IEI Young Engineer Award—Marine 2013 from the Institution of Engineers, India; Young Researcher Award—2013 from the Ministry of Earth Sciences; and Hari Om Ashram Prerit Research Award. His area of interest includes stochastic analysis of marine structures. He is currently applying his knowledge in offshore renewable energy with an emphasis on extremes.

**Part I**  
**Keynotes**

# Waiting on Suitable Weather to Perform Marine Operations



Ove T. Gudmestad

**Abstract** The marine industry carries out a large number of marine operations worldwide. The operations are becoming more and more advanced and include deep-water installation activities and commercial transport through the Arctic ice. The probability of encountering an unwanted event during these operations is high in certain areas of the world, in particular, where reliable weather forecasts do not cover the complete duration of the operation. Det Norske Veritas (now DNVGL) has considered the statistics of the reliability of weather forecasts (performing a comparison of forecasted wave heights and actual measured waves) and suggests that the wave height criterion for starting the operation (using specific equipment) should be reduced by an “alpha factor”. The alpha factor depends on location, season of the year and duration of the operation. However, in certain areas, like in the Arctic, where the weather forecasts are particularly uncertain, no alpha factors for operations exceeding a short period have been suggested. The need to wait for a suitable weather forecast (WOW) exceeding the expected period of an operation puts a lot of strain on project management as WOW is costly for the party who shall pay for the waiting. Good project management takes this into account, prioritizing safe operations higher than taking the risk of encountering unwanted events with the possibility of substantial economic loss and also the potential for unsafe operations. Examples will be given from actual operations on the Norwegian shelf, and a discussion of operations in Arctic conditions will be provided.

**Keywords** Design versus operations

Weather limitations for temporary operations

Influence of wave height and wave period · Reliability of weather forecasts

Alpha factor · Waiting on weather

Requirement to decisions for initiating a marine operation

Management of marine projects · Specifics for the situations in the Arctic region

---

O. T. Gudmestad (✉)

University of Stavanger, Stavanger, Norway

e-mail: [otgudmestad@gmail.com](mailto:otgudmestad@gmail.com)

© Springer Nature Singapore Pte Ltd. 2019

K. Murali et al. (eds.), *Proceedings of the Fourth International Conference in Ocean Engineering (ICOE2018)*, Lecture Notes in Civil Engineering 22,

[https://doi.org/10.1007/978-981-13-3119-0\\_1](https://doi.org/10.1007/978-981-13-3119-0_1)

# 1 Introduction

## 1.1 *Design Aspects Versus Operational Activities*

International design standards are concerned with the safety of technical solutions. The load and resistance factor design method [1] specifies load and resistance factors to be applied to characteristic values for load and resistance in structural design. The ISO 19900 series of standards, for example, ensures safe design with an acceptable low probability of damage or collapse. Checking of the design for different limit states (serviceability, ultimate, fatigue and extreme) ensures that attention is paid to regular usage, continued operations in the defined ultimate condition, and avoidance of collapse in case of an extreme event situation. Damage caused by continued use is ensured through fatigue checks. It is recognized that safe operations shall be ensured for personnel, the environment and the asset. The characteristic values are normally specified in international standards; however, the ISO member countries are allowed to define “stricter” requirements, thereby reducing the probability of damage or collapse. For certain structures (like structures to be used in the oil and gas industry), high characteristic values are selected for loads. This is ensured through selecting values with low annual probability of exceedance for the load estimates. For other types of structures where damage will not have very large consequences (e.g. for structures supporting wind turbines), lesser values of the characteristic loads can be selected.

In the case of temporary activities, such as during construction work and during temporary marine activities, the owner/operator is freer to select criteria as long as they ensure safety during the specified operations. It may be prudent to wait for suitable weather conditions rather than to initiate activities under harsh conditions. It may, for example, represent large savings to hire construction vessels for well maintenance rather than to hire a large drilling rig. The reduced day rate of the construction vessel compared to that of a rig could more than compensate for periods of *waiting for suitable weather conditions to carry out the operation*. However, the equipment must be suitable for the season and be able to go on safe stand-by should harsh weather unexpectedly appear. In this paper, we will discuss aspects which shall be taken into account when making decisions regarding marine operations. A special discussion will be related to marine activities in cold climate regions.

## 1.2 *Weather Limitations for Temporary Operations*

Temporary operations are carried out as specialized operations and are not representative of day-to-day activities. Such operations could be part of construction, installation or maintenance activities. These activities should normally be performed during the good weather season, avoiding the harsh weather season when the probability of high winds or large waves is substantial. Historical weather data can normally

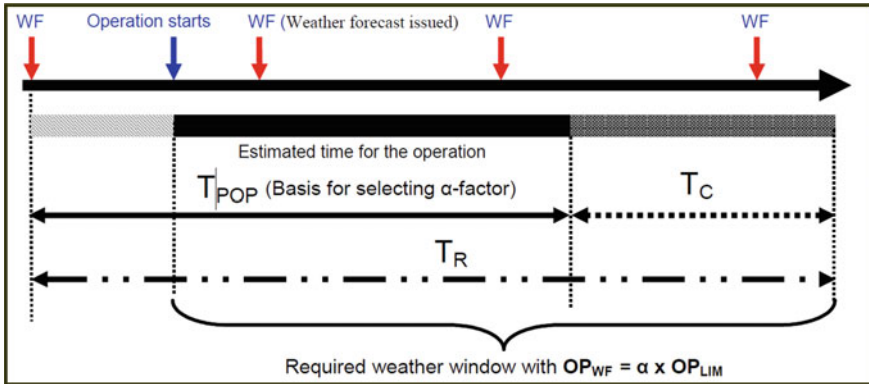


**Fig. 1** From DNV [2]: Marine operations with a reference period (TR) less than 96 h and a planned operation time (TPOP) less than 72 h may normally be defined as weather-restricted. However, in areas and/or seasons where a corresponding reliable weather forecast is not considered realistic, a shorter limiting TR shall be applied

be produced for a location, from which we can calculate the probability of finding the required weather window (with limited wave condition for the duration of the planned operation). Wave data are often hind-casted from past weather maps in case actual measurements are not available. Based on such data and information about equipment capability, we can find the probability of having the work done during different seasons of the year. We will also find the expected time we will have to wait for suitable weather to perform the actual operation.

On site, the actual weather condition and weather forecast will decide whether we will be in position to start the operation. Normally, *weather-restricted operations* are operations that can be carried out within a weather window of 72 h (3 days). For operations that need more time, the seasonal 10-year expected maximum weather could apply. However, in situations with long-term reliable weather forecasts (e.g. under constant high-pressure situations) when the operator is in close contacts with meteorological centres, longer weather-restricted periods exceeding the 72 h could be considered.

For a general view of operation planning, see Fig. 1 (from DNV [2]).

## 2 Requirements to Temporary Marine Operations

### 2.1 Vessel Response Due to Wind and Waves

Vessels are responding to wind loads, and certain operations, like crane operations, are very vulnerable to the wind conditions. Lifting operations may, therefore, not be conducted during strong winds. More important is the response to waves where any

vessel will respond in all six degrees of freedom. The response to waves varies very much from vessel to vessel; bilge keels will reduce heave and roll motions because of increased added mass and damping, while bulb bows will reduce the pitch motion because of increased bow buoyancy when the vessel pitches into waves. Furthermore, increased vessel size causes reduced heave motions, also because of the increased added mass. To design the most suitable vessel for certain operations is an art left for the naval architects.

The response amplitude operators (RAOs) are normally used to study the response to waves. The RAOs give the response to one-metre high waves with different periods and are found (from analysis or from wave tank experiments) for all six degrees of freedom of motions and for different angles of approach of the waves. At certain wave periods, a vessel gets into resonance with the waves and the values of the RAOs can be considerable (depending on vessel damping), amplifying the vessel's response. Resonances with large waves will thus produce considerable vessel motions. Also, resonances with long swell waves (periods typically of 15 s or more) could cause significant vessel motions and certain activities cannot be carried out during swell waves. Activities that may be halted are, for example, installation of "jackups" when heave due to swells could lead to mud-mat damage as mud-mats hit the bottom and during lifting when the crane's response be amplified by the response of the vessel; see, for example, DN [3]. In the cited case, a vessel that could not work in limited waves was contracted with the consequence that more than 75 M US \$ was wasted.

The requirement to an actual marine operation is determined by the motions which can be tolerated during the operation. Based on the vessel's RAOs, we can then decide on the limited wave height/period during which the operation can be carried out for any specific vessel. It is obvious that the information about vessel's RAO is important when judging the capability of a vessel to perform a task. Some vessels may be capable of working in Hs of 4.0 m for a specific marine operation, while a competing vessel may be limited to 2.5 m. Vessel owners do therefore treat information about their vessels' RAOs as confidential information. However, for the customer, it is of importance to know:

- The vessel's RAOs during bid evaluations to determine the likely operation time (including the expected downtime) for the vessels being considered for a marine operation.

## ***2.2 Influence of Wave Height and Wave Period***

As discussed above, statistics regarding wave heights (significant wave heights,  $H_s$ ) and wave periods (wave spectral shapes and spectral peak periods,  $T_p$ ) are important for selection of vessel to perform a marine operation. This information is used to determine the probability of successful operations during a certain season of the year. Weather forecasters will often give the wave height, while the wave period be much more uncertain. However, knowledge about the wave period is as least as important



as knowledge about the wave height. It might also be important to have information about swell waves under which the sea may appear as calm, while resonance with vessel motions may restrict the ability to work; see, for example, Olugbenga et al. [4]. Therefore, in order to select a suitable vessel for an operation, the customer provides the bidders with the following information:

- Wave height and wave period statistics for the actual season and for following months (in case of the necessity to extend a contract).
- Wave heights and swell periods during the season and following months.

Of another matter is the possibility that two wave conditions occur simultaneously: Wind waves coming from the prevailing wind direction and swell waves, potentially coming from another direction. The combination could result in severe roll motions even if the vessel is heading up against the wind waves [5]. Such situations have been recorded in the Norwegian Sea (at the Norne field at 66° north).

### ***2.3 Reliability of Weather Forecasts***

Weather conditions could deteriorate quickly and weather forecasts become more and more uncertain as time passes. A marine activity will get a “go” when the expected wave conditions during the preparation phase, the work phase and the end of work phase for an activity are within the limiting conditions for the activity. Time starts ticking when the preparation gets to a “no return to start” situation, for example, when the sea fastening is being cut during the preparation of an offshore lift operation. Normally in the North Sea area, we refer to a 72-h period as the period when weather-restricted operations can be executed. In case of stable high-pressure situations, however, the reliability of the forecasts can be very good, even exceeding the 72-h period set for weather-restricted operations. Other locations of the world would have longer periods of reliable weather forecasts, while the forecast uncertainty is even larger in the Barents Sea and in most Arctic Seas during long periods of the year.

Note that the needs to identify the uncertainty in the weather forecast do not only relate to the wave height, but also relate to the wave spectrum and in particular to the peak period of the wave spectrum. A comprehensive review of uncertainty in weather prediction is given by Bauer et al. [6].

### ***2.4 Alpha Factor***

In view of the limitations due to the weather conditions, it is of most importance to be able to estimate the uncertainty in the weather forecasts. DNV [2] has evaluated the uncertainty in the weather forecasts for certain offshore seas: “B 700–701: Uncertainty in both monitoring and forecasting of the environmental conditions shall

**Table 1** Alpha factor for North Sea conditions

Table 4-1 $\alpha$ -factor for waves, base case							
Operational Period [h]	Design Wave Height [m]						
	$H_z = 1$	$1 < H_z < 2$	$H_z = 2 = 2$	$2 < H_z < 4$	$H_z = 4$	$4 < H_z < 6$	$H_z \geq 6$
$T_{POP} \leq 12$	0.65	Linear Interpolation	0.76	Linear Interpolation	0.79	Linear Interpolation	0.80
$T_{POP} \leq 24$	0.63		0.73		0.76		0.78
$T_{POP} \leq 36$	0.62		0.71		0.73		0.76
$T_{POP} \leq 48$	0.60		0.68		0.71		0.74
$T_{POP} \leq 72$	0.55		0.63		0.68		0.72

be considered. It is recommended that this is done by defining a forecasted (and, if applicable, monitored at the operation start) operational criteria— $OP_{WF}$ , defined as:

$$OP_{WF} = \alpha \times OP_{LIM}$$

where  $OP_{LIM}$  is the limiting operational environmental criteria”.

Furthermore, it could be noted that a recommendation is given for operations that can be halted: “703: For operations that could be halted, see 506, the alpha-factor could normally be selected based on a TPOP defined as the time between weather forecasts (e.g. 12 h) plus the required time to safely cease the operation and bring the handled object into a safe condition”. Table 1 (Table 4.1 from DNV [2]) gives alpha factors for different wave heights and operational periods in the North Sea. See also DNV [2] for more details in case there is a meteorologist at site, etc.

Even if the alpha factors given by DNV provide guidance on recommended wave heights for initiating a marine operation, no guidance on wave periods is given except for a general statement: “706: Special considerations should be made regarding uncertainty in the wave periods. I.e. if the operation is particularly sensitive to some wave periods (e.g. swell), also uncertainty in the forecasted wave periods shall be considered”.

## 2.5 *Waiting on Suitable Weather (WOW) to Perform Marine Operations*

In case the weather condition is not suitable to initiate a marine operation, the captain of the vessel has to decide on putting the operation on hold, causing the complete marine spread to be put on hold. It shall be noted that the law of the sea gives the captain this responsibility when there is a danger to personnel, to the environment or to the ship (the asset). The costs of waiting on weather can be very large, in particular in oil- and gas-related projects where delays can lead to loss of production. The captain will be advised by his marine engineering staff as to the potential consequences of continuing the work. Furthermore, the client will normally employ a warranty surveyor to stay on board accepting any task that shall be covered by insurance.

Although the client could demand that the operations continue without insurance, the client cannot demand that the captain carries on if he decides it is unsafe to perform the task. Normally, the team of persons representing the client, the warranty surveyor and the captain will agree on when a task can be initiated and continued. An on-board meteorologist can in many situations be to good help to provide sound advice for decisions.

As most mariners have a careful attitude to work when the weather conditions deteriorate, a situation could develop where the decision to halt the work was not warranted; the weather did not deteriorate. In such situations, the client could be tempted to sue the marine operator for delaying the activity unnecessarily. Such a case is not optimal and could end up in court. However, the captain's decision is in general protected, in particular when safety to personnel, the environment and/or the vessel is in danger. A specific situation is the case when management of the operator getting involved in the decision. A high-reliability organization would not work like this. See, for example, [7]. She studied organizational processes necessary to operate safely technologically complex organizations that should not do great physical harm to themselves and their surrounding environments. There are, however, examples of near misses or actual misses in marine operation activities [8].

### 3 Specifics of Marine Operations in the Arctic Region

The design weather conditions in the Barents Sea are typical for the extreme conditions in the Arctic region. Orimolade et al. [9] have concluded that the estimated 100-year  $H_s$  for four locations in the Barents Sea show that the extreme wave heights in the Barents Sea in general are less harsh further north compared to the south. The general observation is in agreement with the expected spatial trends in the wave climate in the Barents Sea. Finally, a 57-year hind-cast dataset used in their study does not suggest any specific temporal trend in the historical significant wave heights at the selected Barents Sea locations.

On the other hand, the paper does not consider the weather conditions during typical marine operational conditions, although long periods of limited waves are present during the summer season, during which marine operations safely can be executed. During the fall season, however, the weather conditions become quite unpredictable as small-scale polar low pressures can develop at the ice edge. Here, cold air above the ice and warmer air above the open sea create an unstable situation that can lead to polar low pressures travelling south and eastwards (due to the Coriolis effect). For a review of polar lows, see Rasmussen and Turner [10], and see also Fig. 2.

The creation of polar lows is not well understood; however, meteorologists may give a forecasted probability of polar lows. The probability may be unrealistically high due to the uncertainty in the generating process. Furthermore, polar lows are cyclone-type weather conditions and the paths of the polar lows are very uncertain. During such conditions, there is a certain probability of a polar low, and marine operations which require several days of limited waves have to be put on hold. Even

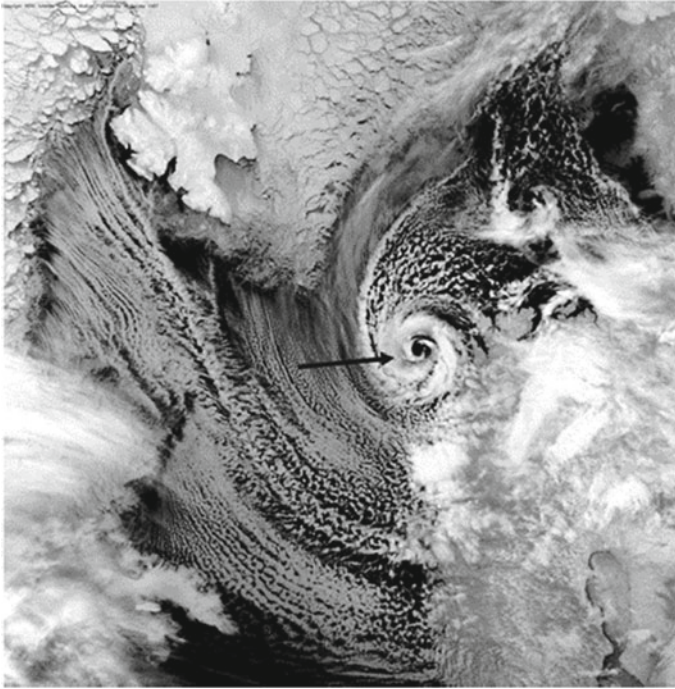


**Fig. 2** A satellite image of a fully developed polar low over the Barents Sea from 0418 UTC 27 February 1987 (Courtesy Neil Lonie: NERC Satellite Receiving Station, Dundee University, Scotland, <http://www.sat.dundee.ac.uk/>)

if the waves in polar lows may not reach design wave conditions, the waves will reach heights exceeding the requirements of safe marine operations. Furthermore, polar lows are followed (on the backside) by large accumulations of snow or hail. Wilcken [11] has concluded that it will not be possible to suggest alpha factors for seasons of the year when polar lows may be created reaching some location where marine operations be undertaken. Under such conditions, marine operations must be very carefully reviewed together with meteorologists prior to initiating activities that may be hampered in case of polar low occurrences.

Resent research [12] has also confirmed a model suggested by Dysthe and Harbitz [13] that polar lows travelling with the phase speed of the waves can be in resonance such that the effective fetch is sufficiently long to create very large waves within few hours. In such cases also the integrity of marine vessels may be endangered. Meteorologists suggest that this resonant situation should be forecasted to prepare seafarers for situations with very large wave buildup [14].

## 4 Conclusions

In this paper, we have discussed the requirements to carry out safe marine operations, criteria are reviewed, and we have emphasized on the needs for forecasting the uncertainty of wave heights and the wave periods [15] throughout the period of the marine operation. At present, main emphasis is on wave heights; however, resonances between vessel characteristics (vessel RAOs) and waves with periods matching the peaks of the vessels' RAOs could lead to large response of marine vessels with the potential of failed marine operations. Also, special attention should be on forecasting swell waves being in resonance with peak periods of the vessels' RAOs.

It is, furthermore, concluded that weather conditions in Arctic regions during seasons when polar low pressures can occur are particularly uncertain, and that marine operations cannot be conducted during forecasting of potential polar low pressures.

Finally, we present a conclusion that high-reliability companies are very aware of the potential of severe conditions during marine operations, respecting the advice of meteorologists and decisions of their captains.

**Acknowledgements** The author acknowledges the cooperation with former Ph.D. student A. P. Orimolade and with Professor B. Furevik of Norwegian Meteorological Office in Bergen, Norway, during the research leading to this publication.

## References

1. ISO (International Standard Organization) (2013) Petroleum and natural gas industries. General requirements for offshore structures. Geneva, Switzerland
2. DNV (Det Norske Veritas) (2011) Marine operations, general, DNV-OS-H101. Høvik, Norway
3. DN (2011) Dagens Næringsliv. Oslo 23.08.2011 (assessed 1st Feb 2018). <https://www.dn.no/nyheter/energi/2011/08/23/bestilte-skip-som-ikke-talte-sjo>
4. Olugbenga AA, Gudmestad OT, Agbakwuru J (2017) Swell description for Bonga offshore Nigeria location. *Ocean Syst Eng Int J* 20(4)
5. Kragtwijk HJ, Vestbostad TM, Vugts JH, Gudmestad OT (2002) On the sensitivity of the roll motion of an FPSO. In: 21st international conference on offshore mechanics and arctic engineering, vol 1, Oslo, Norway, June 23–28, 2002. ISBN: 0-7918-3611-8 | eISBN: 0-7918-3599-5
6. Bauer P, Thorpe A, Brunet G (2015 Sept) The quiet revolution of numerical weather prediction. *Nature* 525:47–55. <https://doi.org/10.1038/nature14956>
7. Roberts K (1990) Some characteristics of one type of high reliability organization. *Organ Sci* 1(2)
8. Gudmestad OT (2014 Mar) Influence of human and organizational factors, communication and management on risk in organizations and projects. *Saf Secur Eng* 4(1):54–63. ISSN: 2041-931
9. Orimolade AP, Furevik BR, Noer G, Gudmestad OT, Samelson RM (2016a) Waves in polar lows. *J Geophys Res Oceans* 121(8):6470–6481
10. Rasmussen EA, Turdner J (2003) Polar lows: mesoscale weather systems in the polar regions, p 612. Cambridge University Press, Cambridge. ISBN 0-521-62430-4.T
11. Wilcken S (2012) Alpha factors for the calculation of forecasted operational limits for marine operations in the Barents Sea. Master thesis. University of Stavanger, Norway

12. Orimolade PA, Haver S, Gudmestad OT (2016b) Estimation of extreme significant wave heights and the associated uncertainties: a case study using NORA10 hind-cast data for the Barents Sea. *Mar Struct* 49:1–17
13. Dysthe KB, Harbitz A (1987) Big waves from polar lows? *Tellus A* 39A:500–508
14. Noer G (2017) Personal communication between Orimolade and meteorologist Noer of Norwegian Met. Office in Tromsø, Norway
15. Natskår A, Moan T, Alvær PO (2015) Uncertainty in forecasted environmental conditions for reliability analyses of marine operations. *Ocean Eng* 108:636–647

# Wave Overtopping in the UK During the Winter of 2013/14



Dominic E Reeve 

**Abstract** The sequence of Atlantic storms experienced by the UK during the winter of 2013/14 was very unusual. They led to widespread flooding on the west and southern coastlines of the UK and caused damage to the mainline railway between Plymouth and London. In this paper, an investigation of the severity of the impacts of the storms is presented, based on reports and new computational modelling. The resulting hypothesis is that the extensive flooding and damage were due to an unusually high percentage of swell waves. The current overtopping design formulae are not best suited to bimodal seas and new research is required to provide better design guidance for such cases.

**Keywords** Wave overtopping · Computational modelling · Coastal flooding  
Bimodal seas · Extreme events

## 1 Introduction

Coastal flooding and erosion are the problems experienced across the globe. The causes can be inappropriate development in the coastal zone, poor design or construction and changes in physical conditions. The latter has become the focus of much recent research based on climate change predictions promulgated by the IPCC [1, 2]. If one takes the definition of climate to be the typical conditions experienced over a time window (often taken to be anything from 10 to 30 years), then the fact that climate changes over longer periods than the window is hardly surprising given our understanding of cycles of variation that have periods much greater than a few decades. It is the cause of the change and the rate of change that has exercised the IPCC, but these are not the focus of this paper. Records from many tide gauges demonstrate a rise in sea levels over the last decade or more. It is this, together with the potential for changes in the frequency and intensity of storms that represents a

---

D. E. Reeve (✉)  
Swansea University, Swansea, Wales, UK  
e-mail: [d.e.reeve@swansea.ac.uk](mailto:d.e.reeve@swansea.ac.uk)

© Springer Nature Singapore Pte Ltd. 2019  
K. Murali et al. (eds.), *Proceedings of the Fourth International Conference in Ocean Engineering (ICOE2018)*, Lecture Notes in Civil Engineering 22,  
[https://doi.org/10.1007/978-981-13-3119-0\\_2](https://doi.org/10.1007/978-981-13-3119-0_2)

major risk to coastal communities. In a review of the global socio-economic potential impacts of sea level rise and increased storminess, it has been argued that the projected increases in sea level could lead to a fivefold increase in the areas of coastal zones which are flooded during storms by the 2080s [3]. Indeed, recent UN research indicates that ~40% of the world's population lives within 100 km of the coast [4]. In the UK context, 40% of our manufacturing industry is situated at or close to the coast and almost 90% of our trade passes through seaports. Ensuring facilities such as ports and other infrastructure are adequately protected is crucial for ensuring continued economic prosperity and the safety of the population.

Coastal flooding occurs either because the still water level exceeds the defence crest level, or because a breach in the defence occurs that allows water to flow through a segment of the defence or because waves run up the front face of the structure and over the crest line (known as wave overtopping). Many coastal defences are designed to withstand some level of overtopping. However, under extreme conditions overtopping rates may lead to erosion of the back face leading to slumping and lowering of the crest; damage and erosion of the crest; removal of sediment and or armour units from the front face leading to slumping of the front face and/or erosion of the core and eventual breaching. Excessive wave overtopping is a major cause of breaching in coastal defences and so being able to predict overtopping rates under extreme conditions is an important design requirement. However, wave overtopping can lead to flooding, even if no damage occurs to the structure, if inadequate account has been taken of drainage capacity. In these cases, overtopping water gradually accumulates behind the structure, pooling, thus creating a flooding hazard. Water overtopping a defence will have appreciable momentum and often flow from an overtopping can penetrate 10s of metres inland.

Key elements of wave overtopping are illustrated in Fig. 1. The overtopping rate, measured in  $\text{m}^3/\text{s}/\text{m}$ -run of defence, is often denoted by ' $q$ '. The distance between the undisturbed water level and the crest of the defence is termed the freeboard,  $R_c$ .

Overtopping usually occurs under conditions where there is a combination of large waves and high water levels [6, 7]. Such conditions are common during mid-latitude storms in which low surface pressure and strong winds act to generate surge and waves. Empirical formulae for predicting wave overtopping under these conditions have been developed by a number of researchers [7–10]. Most of the formulae relate

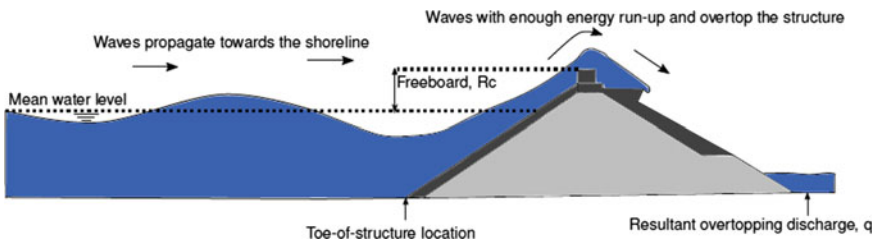


**Fig. 1** Illustration wave overtopping and key quantities (adapted from [5])



a non-dimensionalised overtopping rate to the freeboard through an exponential or power law. For example, Owen's formula reads [11]:

$$Q = ae^{-bR/r} \quad (1)$$

where  $Q = q/(gH_s T_m)$ ,  $R = (R_c/H_s)\sqrt{(s_m/2\pi)}$ ,  $H_s$  is the significant wave height at the toe of the sea wall,  $T_m$  is the mean zero crossing period at the toe of the sea wall,  $s_m$  is the notional wave steepness ( $H_s/\text{deep water wavelength}$ ),  $r$  is a roughness coefficient which varies from 0 to 1 depending on the material properties of the front face of the sea wall, and parameters  $a$  and  $b$  are empirically determined and vary with the geometry of the sea wall. Empirical formulae such as Eq. (1) are used in the design of coastal defences around the world and provide effective estimates under storm wave conditions.

However, the formulae are based on wave conditions best described as wind seas, with a unimodal frequency spectrum and relatively low peak wave period, and are not representative of conditions with a significant swell component. In an investigation of the applicability of empirical formulae to describe overtopping by swell waves [12], the formulae of Owens, Hedges and Reis and Van der Meer [7–9] were compared against physical modelling results of wave overtopping under bimodal wave conditions. Hawkes [12] found that Owen's formula over predicts the mean overtopping rate by a factor of as much as 5. As Owen's formula depends on wave period and was based on wind sea conditions only, this behaviour is perhaps not unsurprising. Both the Van der Meer and Hedges and Reis formulations account for the dependence of wave overtopping on wave breaker type, with separate formulae for plunging and surging waves, and were found to give better predictions than Owen's formula. However, over the range of foreshore slopes used by [12] the Van der Meer formula was found to give an underestimate of overtopping and it was concluded that none of the three formulae provided adequate predictions of overtopping under swell wave conditions.

In many places around the world, coastal storm wave conditions cannot always be described by unimodal, wind sea spectra, such as the Pierson–Moskowitz or JONSWAP spectra [13]. As will emerge in the following sections, when unusual meteorological conditions occur the presence of a significant swell component can alter the expected overtopping volumes and cast doubt on the efficaciousness of traditional overtopping formulae.

The structure of this paper is as follows. In Sect. 2, the meteorological conditions that affected the UK during the winter of 2013/2014 are described together with the features that made this an unusual season. Section 3 describes the computational model used to simulate wave overtopping. Section 4 presents a selection of results from the modelling, and the paper concludes with a brief discussion of the results and scope for future research.

## 2 The Winter of 2013/2014

From December 2013 to January 2014, the UK experienced a sequence of storms typical of the season. From late January to mid-February 2014, a succession of six major storms passed over the UK, separated by intervals of 2–3 days. The UK Met Office now names major storms, and in this period, there were four named storms. Taken individually, the first two storms were notable but not exceptional for the winter period. However, the later storms from early to mid-February were much more severe. Overall, the period from mid-December 2013 to mid-February 2014 saw at least 12 major winter storms, and when considered overall, this was the stormiest period of weather the UK has experienced for at least 20 years [14].

Storm Petra which hit the UK on 5 February 2014 caused considerable damage along the coast, particularly in mid-Wales, Devon and Cornwall. Estimating the severity of storms is not straightforward. Meteorological measurements tend to focus on surface pressure and wind speeds while operational flood agencies emphasise water level and wave height. Based on a comparison of measured and modelled wave heights, [15] argued that the wave conditions during this period were the most energetic for about 60 years. A slightly different perspective was provided by [14] who noted that although no individual storm could be regarded as exceptional, the clustering and persistence of the storms was highly unusual. Further, the tracks of the storms fell at uncharacteristically low latitude, leading to severe gales along the south and west coasts of the UK where the bulk of the ocean wave energy was directed. Peak wave periods were very long so individual waves contained more energy than normal storm waves and hence were able to inflict greater damage and flooding.

A summary of the damage experienced during the period around Storm Petra is given in Table 1. There was widespread flooding in Cornwall on 2 February 2014. Extensive damage to sea walls occurred along the south Devon coast on 4 February 2014, leading to the closure of the mainline London to Plymouth railway service for several days and severe restrictions on timetabled services for several months.

The total economic damage for England and Wales during the winter period was estimated to be between £1000 million and £1500 million, including the damage associated with fluvial and groundwater flooding [16]. Detailed meteorological analysis of the storms and their impacts can be found in [14].

## 3 Computational Model

To investigate what impacts a bimodal wave state might have on wave overtopping of coastal structures, we adopted the NEWRANS model [17], in which a ‘numerical flume’ can be created to simulate the fluid dynamical processes. Here, we provide a summary description of the model and the interested reader is referred to [17] for further details. The model solves the Reynolds-averaged Navier–Stokes equations on a fixed rectangular mesh. As a result, a set of equations are defined for the mean flow

**Table 1** Locations and extent of damage during Storm Petra

Date	Location	Observed damage	Cost estimate
2/2/14	Looe Bay	Flooding	N/A
	Perranporth	Flooding	N/A
	Bude	Flooding	N/A
	Portreath	Flooding	N/A
	Trevone, Padstow	Wall collapse	N/A
	Newquay	Sea wall damage/Road collapse	N/A
4/2/14	Dawlish	Sea wall collapse	£35 million
	Newton Abbott/Paignton	Sea wall collapse	N/A
	Newton Abbott/Plymouth	Sea wall collapse	N/A

containing contributions from the fluctuating turbulent flow. To describe the turbulent flow, the model is coupled with a second-order  $k-\varepsilon$  turbulence closure model, where  $k$  is the turbulent kinetic energy and  $\varepsilon$  is the turbulent dissipation. It incorporates a volume-of-fluid (VOF) surface capturing scheme to allow for accurate simulation of large surface deformations during wave breaking and overtopping. The model simulates a single liquid phase (water) and does not capture bubble formation. The model has been validated through a range of applications to wave breaking, run-up and overtopping [17–19].

A crucial element of the modelling is proper creation of the wave conditions. A bimodal wave condition represents a significant challenge because not only are the waves random but there is a widespread of wave periods. There are two established methods for generating waves: the wave paddle method which emulates the paddle movement in a laboratory wave tank; and the internal mass source. For the wave paddle method, waves are generated from the boundary of the domain and propagate away from the boundary in one direction. The velocity and free surface value are specified on the wave boundary. Reflected waves that reach the paddle position can degrade the wave generation signal due to re-reflection from the wave generation boundary. In addition, the method can introduce mass to the domain through Stokes' drift included in the boundary conditions. A scheme to avoid these problems was presented by [20]. The internal mass source function method, developed by [21], generates waves within the domain causing waves to propagate away from the generation area from either side. An important consideration when using the internal mass source method is the size and positioning of the internal mass source: if the source region is placed too deep below the surface, the wave will be too small; if placed too close to the surface, the waves generated will be too steep.

Both methods were tested. A key measure of the bimodality of the waves is the percentage of swell,  $P_{sc}$ , defined as the percentage of energy in the swell component

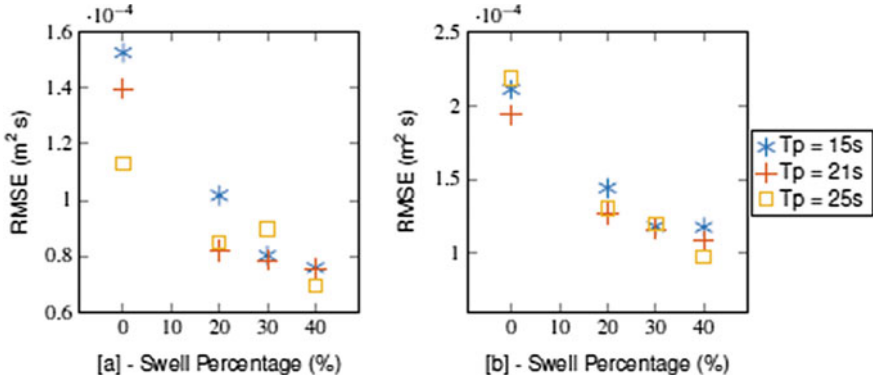


**Fig. 2** RMSE between observed and simulated  $S(f)$  for (left) wave paddle and (right) internal mass source (adapted from [5])

of the energy density spectrum,  $S(f)$ . To compare the accuracy of the two wave generation methods, the model wave distributions were compared against a sequence of experiments described in [22] for which bimodal conditions were created for a range of  $T_p$  and  $P_{sc}$ . The waves were predominately intermediate water waves ( $0:05 < d = L < 0:75$ ). The spectra from the simulations and experiments are compared at a point a short distance from the wave generator. The root mean square error (RMSE), between the simulated and experimental spectra (averaged over frequency), was calculated for both internal mass source and paddle methods. Results are shown in Fig. 2 which indicates that the paddle method produces a more accurate representation of the desired spectrum. The RMSE reduces for both methods as  $P_{sc}$  increases.

The wave paddle wave generation method was chosen for the main set of simulations. A more detailed discussion of the creation of bimodal wave conditions in the computational flume is given in [5, 23].

## 4 Results

In order to specify a bimodal spectrum that had the desired combination of wave characteristics (e.g.  $H_{m0}$ ,  $T_p$ ,  $T_{m-1,0}$ ,  $T_{m02}$ ), an iterative semi-automated procedure was developed to form the wave train. This was used, for example, to define a sequence of spectra which had constant energy and integrated wave period ( $T_{m-1,0}$ ), but varying percentages of swell such as shown in Fig. 3. The peak period,  $T_p$ , is defined as the period at which the spectrum attains its maximum value. This can vary quite rapidly and is hence not a reliable measure of the energy of the sea state, although it is used in some overtopping formulae.  $T_{m02}$  has an approximate equivalence to the mean zero up-crossing period familiar in time-domain analysis, while  $T_{m-1,0}$ , sometimes known as the mean energy period, is the mean wave period with respect

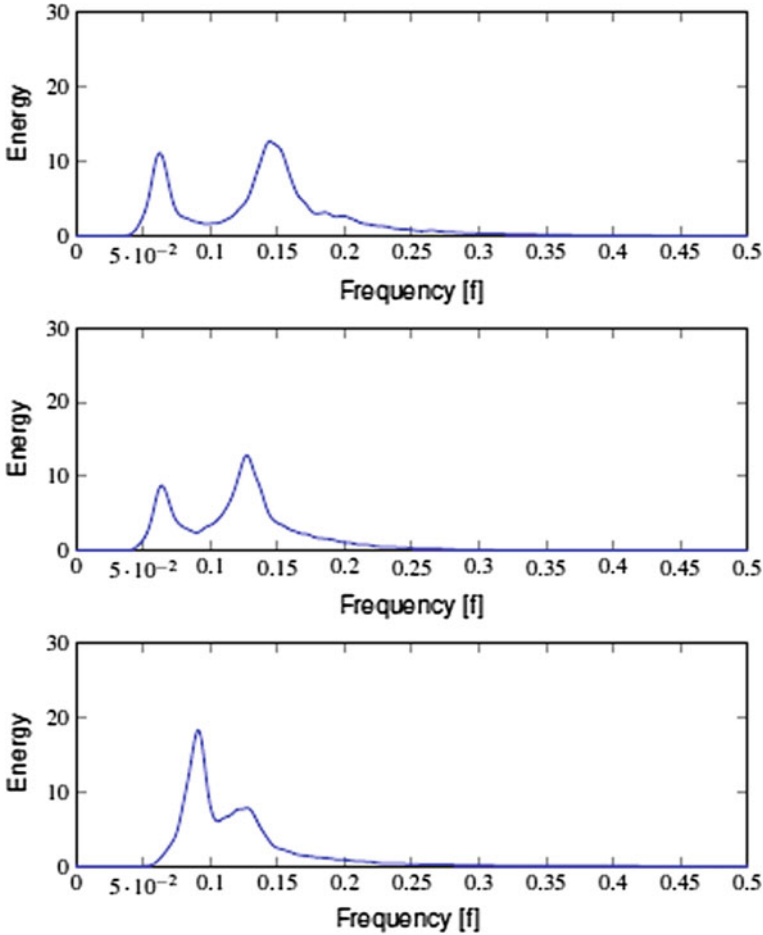


**Fig. 3** Example spectra for defined  $T_{m-1,0} = 12$  s for varying  $P_{sc}$  with a constant total energy content.  $P_{sc} = 20, 50$  and  $80\%$  from top panel to bottom panel (adapted from [5])

to the spectral distribution of energy and may be thought of as the period of the regular wave that has the same significant height and power density as the sea state under consideration. Both  $T_{m02}$  and  $T_{m-1,0}$  are used in recent overtopping formula, and [7] argues that  $T_{m-1,0}$  places more weight on energy at lower frequencies and is therefore more appropriate for describing overtopping due to bimodal sea states.

Experimental studies of overtopping under bimodal seas are scarce. However, results of some experiments can be found in [12, 24]. The bimodal sea conditions consisted of two superimposed JONSWAP spectra, with each spectrum defined by its significant wave height,  $H_s$ , and peak wave period,  $T_p$ . The model was validated against three experiments for which wave conditions had equal energy, with a wind sea peak period at 7 s coupled with swell at 11, 14 and 19 s. The computational

model was able to replicate the observed experimental overtopping discharges very well for Iribarren numbers above 2.2 [5]. However, the model under-predicted when little overtopping discharge was observed and when a low Iribarren number was observed. This is likely to be due to difficulties encountered by the volume-of-fluid method capturing small overtopping volumes, as well as the representation of the turbulent wave breaking processes for low Iribarren number.

An extensive set of computational experiments was devised in order to explore how mean overtopping rates varied with swell percentage, freeboard, and measures of wave period ( $T_p$ ,  $T_{m02}$  and  $T_{m-1,0}$ ). Some of the representative results are shown here. The wave conditions were defined by their total energy, swell percentage,  $P_{sc}$ , and mean wave period,  $T_{m02}$ . All wave conditions had equal energy, as defined by the integral of their spectra. The wave sequences for each case were derived with a high energy content, representative of conditions during the storms at Dawlish. Wave sequences were created that had equal energy but varying mean wave period and associated swell percentage.

Figure 4 shows the mean overtopping rate plotted against mean wave period for a range of swell percentages. Results from individual computations are shown as dots with the line of best fit showing the averages observed for the given swell percentage. Except in the cases with the largest percentage of swell, there is a clear increase in overtopping rate with mean period. Also clear is the reduction in the scatter of computed overtopping rates as the mean wave period increases. This suggests swell percentage has a greater effect on mean overtopping discharge in sea states for which  $T_{m02}$  is relatively small, representative of wind sea conditions.

Figure 4 also shows that for a fixed value of  $T_{m02}$ , overtopping rates increase with increasing swell percentage. Again, this sensitivity is strongest for conditions with relatively low swell percentage ( $P_{sc}$  between 10 and 30%), reducing as the swell percentage increases.

Figure 5 shows mean overtopping rates as a function of swell percentage for  $T_{m-1,0} = 4, 7$  and 10 s. There is a clear increase in overtopping rate with swell percentage,

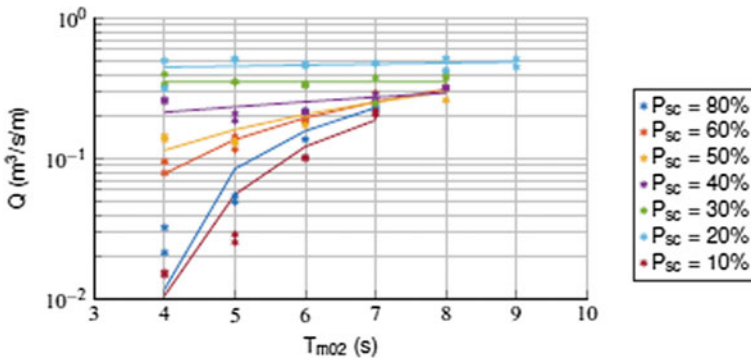
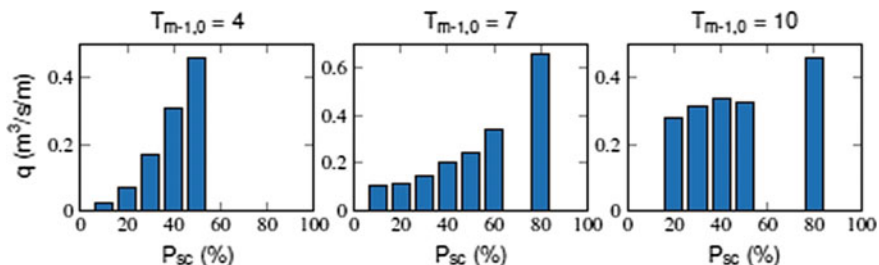


Fig. 4 Mean overtopping rate plotted against mean wave period ( $T_{m02}$ ), for varying  $P_{sc}$  with a constant total energy content (adapted from [5])



**Fig. 5** Mean overtopping rate plotted against swell percentage for  $T_{m-1,0} = 4, 7$  and  $10$  s (left, middle and right panels, respectively) (adapted from [5])

which is especially noticeable for the smaller periods; but influence of swell percentage is still observed for the higher mean wave periods. Potentially the most important swell percentage is 20–40% due to the increased rate in overtopping discharge associated with these swell percentages. The influence of swell percentage on  $T_{m-1,0}$  is an important finding as  $T_{m-1,0}$  is the recommended parameter used for overtopping discharge under bimodal conditions. The results in Fig. 5 demonstrate that for a fixed value of  $T_{m-1,0}$ , overtopping discharge can still vary with swell percentage.

## 5 Discussion and Conclusions

The storms of winter 2013/2014 experienced by the west coast of the UK led to extensive flooding and damage. Analyses of the storm conditions indicated that while individual storms were not exceptional, the clustering and storm tracks were unusual. In particular, wave spectra along the south and south-west UK coastline highlighted the increased frequency of bimodal conditions. Reliable methods for predicting wave overtopping under bimodal and swell conditions have been constrained by limitations of the empirical methods and by a lack of suitable data.

In this paper, we have described a computational investigation aimed at addressing some of these limitations. The study is based on an adaptation of a well-established RANS-VOF model to examine the influence of swell and bimodal wave conditions on overtopping.

The selection of results shown here demonstrates that the wave overtopping rate is strongly dependent on the swell content of the wave energy spectrum, with greatest sensitivity evident for swell percentages in the range 20–40%. Further, the overtopping rates show sensitivity to swell percentage when either  $T_{m02}$  or  $T_{m-1,0}$  is held constant. This suggests that the guidance provided in [7] regarding the applicability of empirical overtopping formulae to bimodal conditions is potentially overstated. This is further supported by a study of the impacts of these storms at a site in Wales [25], which illustrated how current overtopping formula underestimated wave overtopping rates.

Our study confirms the sensitivity of overtopping rates to the shape of the wave spectrum (not just its integral) and points to a requirement to include this factor in empirical formula. Our understanding of overtopping in bimodal sea states is incomplete and further research is required, given the damaging nature of their impacts.

**Acknowledgements** The author would like to acknowledge the contributions of Dr. Daniel Thompson, particularly for the figures.

## References

1. IPCC WG1 (2007) *Climate change 2007: the physical science basis*. Contribution of the Working Group I to the Fourth Assessment Report of the Intergovernmental Panel on Climate Change, Cambridge University Press, Cambridge, UK, 940 pp
2. IPCC WG2 (2007) *Climate change 2007: impacts, adaptation and vulnerability*. Contribution of the Working Group II to the Fourth Assessment Report of the Intergovernmental Panel on Climate Change. Cambridge University Press, Cambridge, UK, 1000 pp
3. Nicholls RJ, Cazenave A (2010) Sea level rise and its impact on coastal zones. *Science* 328(5985):1517–1520
4. SEDAC (2011) Percentage of total population living in coastal areas, Technical report, United Nations. URL: [http://sedac.ciesin.columbia.edu/es/papers/Coastal\\_Zone\\_Pop\\_Method.pdf](http://sedac.ciesin.columbia.edu/es/papers/Coastal_Zone_Pop_Method.pdf), (Accessed 4/1/18)
5. Thompson DA (2017) Computational investigation into the effects of bimodal seas on wave overtopping. Ph.D. thesis, Swansea University, 263 pp
6. Pugh D, Woodworth P (2014) *Sea-level science: understanding tides, surges, tsunamis and mean sea-level changes*. Cambridge University Press, Cambridge
7. Van der Meer J, Allsop N, Bruce T, De Rouck J, Kortenhaus A, Pullen T, Schüttrumpf H, Troch P, Zanuttigh B (2016) *EurOtop 2016: manual on wave overtopping of sea defences and related structures*. An overtopping manual largely based on European research, but for worldwide application. Technical report. URL: <http://www.overtopping-manual.com> (Accessed 4/1/18)
8. Owen MW (1980) Design of seawalls allowing for wave overtopping, HR Wallingford Report EX924, UK
9. Hedges T, Reis M (1998) Random wave overtopping of simple sea walls: a new regression model. *Proc Inst Civ Eng Water Marit Energy* 130:1–10
10. Steendam GJ, Van Der Meer JW, Verhaeghe H, Besley P, Franco L, Van Gent MR (2004) The international database on wave overtopping. In: *Coastal engineering 2004—proceedings of the 29th international conference*. World Scientific Publishing Co. Pte. Ltd., Singapore, pp 4301–4313. URL: [http://eproceedings.worldscinet.com/9789812701916/9789812701916\\_0347.html](http://eproceedings.worldscinet.com/9789812701916/9789812701916_0347.html) (Accessed 4/1/2018)
11. Environment Agency: Overtopping of Seawalls. R&D Project Record W5/006/5, 1999. 132p. [https://www.gov.uk/government/uploads/system/uploads/attachment\\_data/file/290227/sprw5-006-5-e-e.pdf](https://www.gov.uk/government/uploads/system/uploads/attachment_data/file/290227/sprw5-006-5-e-e.pdf) (accessed 4/1/2018)
12. Hawkes P (1999) Mean overtopping rate in swell and bimodal seas. *Proc Inst Civ Eng Water Marit Energy* 136:235–238
13. Reeve DE, Chadwick AJ, Fleming CA (2012) *Coastal engineering: processes, theory and design practice*, 2nd edn. Spon Press, 514 p
14. Masselink G, Castelle B, Scott T, Dodet G, Suanes S, Jackson D, Floc'h F (2016) Extreme wave activity during 2013/2014 winter and morphological impacts along the Atlantic coast of Europe. *Geophys Res Lett* 43:2135–2143. <https://doi.org/10.1002/2015gl067492>
15. UK Met Office/Centre for Ecology and Hydrology: The recent storms and floods in the UK, February 2014, 29 p. <http://nora.nerc.ac.uk/id/eprint/505192/1/N505192CR.pdf> (accessed 4/1/2018)



16. Environment Agency: The costs and impacts of the winter 2013 to 2014 floods. Report SC140025/R1, 2016, 275 p. [https://www.gov.uk/government/uploads/system/uploads/attachment\\_data/file/501784/The\\_costs\\_and\\_impacts\\_of\\_the\\_winter\\_2013\\_to\\_2014\\_floods\\_-\\_report.pdf](https://www.gov.uk/government/uploads/system/uploads/attachment_data/file/501784/The_costs_and_impacts_of_the_winter_2013_to_2014_floods_-_report.pdf) (accessed 4/1/18)
17. Lin P, Liu PL-F (1998) A numerical study of breaking waves in the surf zone. *J Fluid Mech* 359:239–264
18. Jones DK, Zou Q, Reeve DE (2013) Computational modelling of coastal flooding caused by combined surge overflow and wave overtopping on embankments. *J Flood Risk Manag* 6(2):70–84. <https://doi.org/10.1111/j.1753-318x.2012.01155.x>
19. Soliman A, Reeve DE (2003) Numerical study for small freeboard wave overtopping and overflow of sloping sea walls. In: *Proceedings of coastal structures 2003*, ASCE, Portland, USA, pp 643–655
20. Torres-Freyermuth A (2007) Estudio de la Hidrodinámica de la Zona de Rompientes mediante ecuaciones tipo RANS. Ph.D. thesis, Universidad de Cantabria, Santander
21. Lin P, Liu P (1999) Internal wave-maker for Navier-Stokes equations models. *J Waterw Port Coast Ocean Eng* 125(4):207–215
22. Polidoro A, Pullen T, Powell K (2016) Modelling shingle beaches in bimodal seas—development and application of Shingle-B. Technical Report December, HR Wallingford. URL: <http://www.channelcoast.org/shingleb/>
23. Thompson DA, Karunaratna H, Reeve DE (2016) Numerical simulation of bimodal seas: a comparison between wave generation methods. *Water Sci Eng* 9(1):p3–13
24. Coates TT, Jones RJ, Bona PFD (1998) Wind/swell seas and steep approach slopes: technical report on wave flume studies. Technical Report TR 24, HR. Wallingford
25. Thompson DA, Karunaratna H, Reeve DE (2017) Modelling extreme wave overtopping at Aberystwyth Promenade. *Water* 9:663–679. <https://doi.org/10.3390/w9090663>

# Modernization of Port



R. Sundaravadivelu

**Abstract** India has a coastline spanning of 7516.6 km, forming one of the biggest peninsulas in the world. Central and relevant ministries administer the 12 major ports and 200 minor and intermediate ports. The modernization of ports needs deepening of harbour basin, upgradation of mechanical handling system, use of new type of fenders, etc. The various case studies are explained in this keynote. Behaviour of berthing structure with pile sheet pile wall is analysed through numerical and experimental investigation. The suitable rehabilitation methods adopted for the structures which are damaged due to natural causes. Artificial submerged reef is to stabilize the shore from erosion and stability of these structures proven by physical model study.

**Keywords** Modernization of port · Deepening · Touch pile wall · Rehabilitation Artificial reef

## 1 Modernization of Ports

### 1.1 Introduction

India has a coastline spanning of 7516.6 km, forming one of the biggest peninsulas in the world. According to the Ministry of Shipping, around 95% of India's trading by volume and 70% by value are done through maritime transport. It is serviced by 12 major ports, 200 notified minor and intermediate ports. Central government's shipping ministry administers the major, the minor and intermediate ports which are administered by the relevant departments or ministries in the nine coastal states: Andhra Pradesh, Odisha, West Bengal, Tamil Nadu, Kerala, Karnataka, Goa, Maharashtra and Gujarat. All the major and minor ports visualized on India's map are

---

R. Sundaravadivelu (✉)

Department of Ocean Engineering, Indian Institute Technology Madras,  
Chennai 600042, Tamil Nadu, India  
e-mail: [rsun@iitm.ac.in](mailto:rsun@iitm.ac.in)

© Springer Nature Singapore Pte Ltd. 2019

K. Murali et al. (eds.), *Proceedings of the Fourth International Conference in Ocean Engineering (ICOE2018)*, Lecture Notes in Civil Engineering 22,  
[https://doi.org/10.1007/978-981-13-3119-0\\_3](https://doi.org/10.1007/978-981-13-3119-0_3)

shown in Fig. 1a, and the percentage of total commodity is compared in given pie chart Fig. 1b.

## ***1.2 Modernization***

Government of India plans to modernize these ports and has approved a project called Sagarmala. The ports and shipping industry in India play a vital role in sustaining growth in the country's trade and commerce. The Indian Government has allowed foreign direct investment (FDI) of up to 100% under the automatic route for port and harbour construction and maintenance projects. The government has also initiated National Maritime Development Programme (NMDP), an initiative to develop the maritime sector with a planned outlay of US\$11.8 billion.

## ***1.3 Needs for Modernization of Brown Field Port***

The following factors are considered as the need for modernization of brownfield port

- Existence for more than service life of 50 years
- The damages to port structures need to be retrofitted due to Bhuj earthquake on 26 January 2001, Indian Ocean, Tsunami on 26 December 2004 and storm surge and cyclone
  - Existing berths to be deepened while berthing operation.

# **2 Deepening of Port**

## ***2.1 General***

Dredging is the method for deepening of harbour basin. Dredging is the process by which underwater sediments and soils are removed using specialized equipment for the construction and maintenance of waterways, transportation infrastructures. Generally, dredging work in marine areas is carried out where the required draft for safe navigation of vessels is not available naturally and needs to be created artificial depth and/or to maintain already dredged depth to ensure safe movement of the vessels. Dredging during initial stage can be classified as capital dredging.

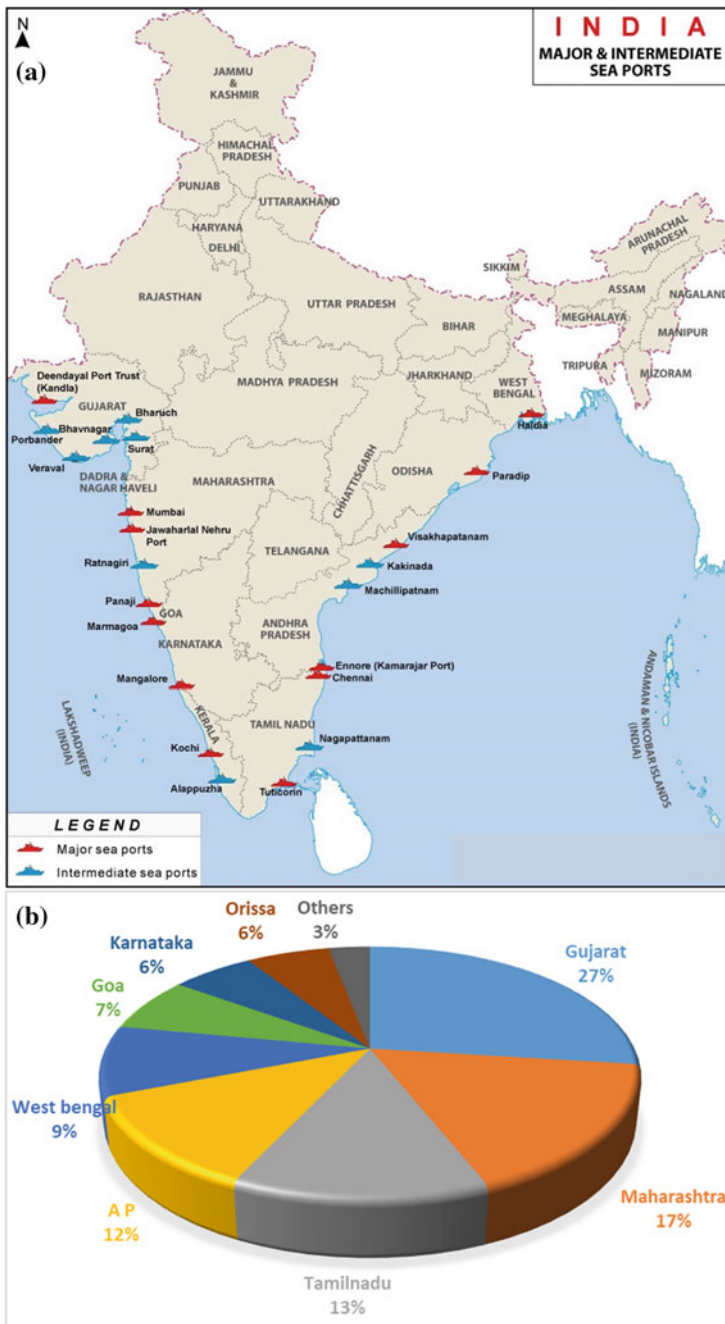


Fig. 1 Ports of India (a) and commodity handled in the various states (b)

## 2.2 Dredging Process

The dredging of harbour basin in Visakhapatnam Port (Fig. 2) and VOC Port (Fig. 3) is planned in such a way that the berths are in operation. The type of structural arrangement used is pile touch pile wall, rear berthing platform or pile sheet pile wall.

## 3 Berthing Structure with Touch Pile Wall

In order to understand the behaviour of this type of berthing structure, the model structure is created with scale ratio of 1 in 50. Aluminium pipes of 25 mm diameter with 1 mm thickness and 600 mm length are used as piles, and the aluminium pipes are welded together to act as touch pile wall. Piles are placed in two rows and three columns with a spacing of 0.12 m. Model of berthing structure is shown in Fig. 4.

The typical berthing structure with touch pile wall (Fig. 5a) is analysed by STAAD.Pro software, and the design is carried out as per IS4651. The cofferdam structure shown in Fig. 5b is analysed using STAAD.Pro and Plaxis. The influence of soil pressure among various loads can be applied on the pile via spring analysis in the STAAD.Pro, whereas interaction of soil with pile structure is directly applied by assigning the properties of soil in Plaxis analysis. The results of STAAD.Pro and Plaxis analysis are compared. The bending moment of pile in seaside and dockside is compared separately which is given in Fig. 6.

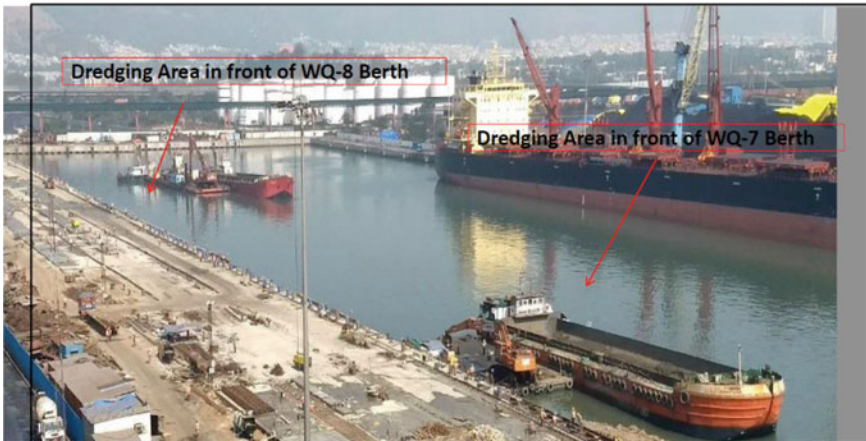


Fig. 2 Dredging work in Vizag Port

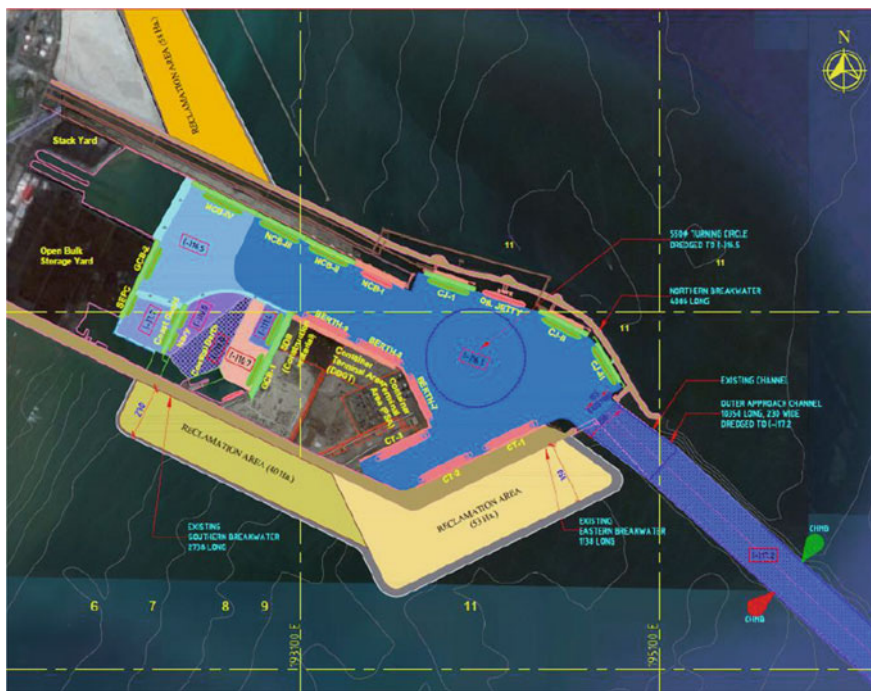
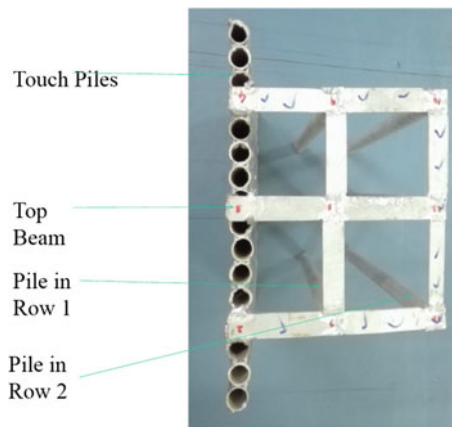


Fig. 3 Proposed dredging layout of VOC Port

Fig. 4 Top view of berthing structure model



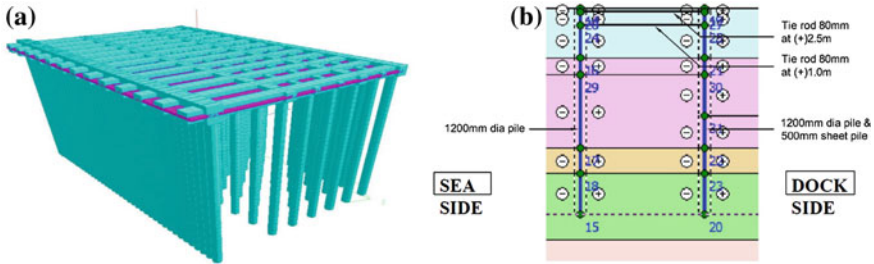


Fig. 5 Modelling of berthing structure in STAAD.Pro (a) and in Plaxis (b)

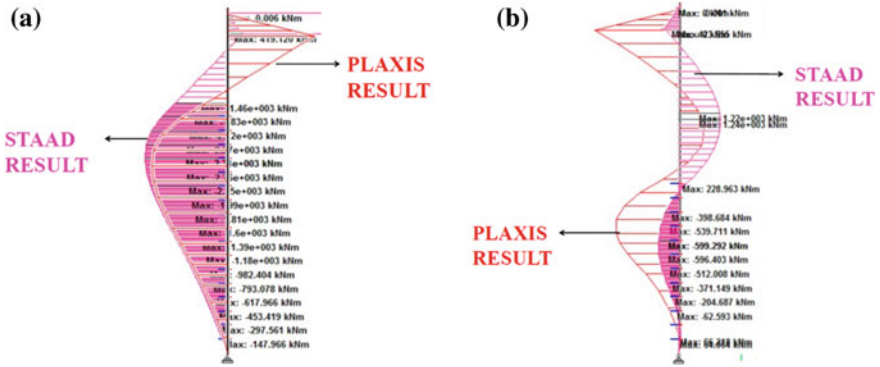


Fig. 6 Comparison of bending moment for seaside pile (a) and dockside sheet pile (b)

## 4 Damage Assessment and Rehabilitation of North Breakwater at Kamarajar Port

### 4.1 Introduction

Kamarajar Port Limited (KPL), the twelfth Major Port of India commissioned in 2001, is located about 11 nautical miles north of Chennai Port along with the Coromandel Coast in the State of Tamil Nadu at 13° 15.50' N and 80° 20.25' E. The northern breakwater is of length 3080 m, and the water depth at the head section is 11 m CD. The south breakwater is of length 1070 m. The primary armour at the head section is 6 m<sup>3</sup> Accropode for the northern breakwater. The initial design of breakwater is given in Table 1.

The breakwaters have been exposed to severe sea states like Fanoos, Nisha, Thane and Nilam cyclones. After the Thane and Nilam cyclones, the port authorities observed damages to the Accropode units as well as the armour layer has got dislodged at many sections. They felt the need to assess the health of the northern breakwater.

**Table 1** Design details as built-in section

Description	Trunk section as built at (-) 10.0 m CD	Head section as built at (-) 11.5 m CD
Water level (m CD)	(+) 1.68	(+) 1.68
Design wave height (Hs) (m)	6.1	6.6
Accropode size (T)	12	15
Crest level ( m CD)	(+) 5.55	(+) 5.75

## 4.2 Site Investigation

Based on the physical observation from the crest of the northern breakwater, it was found that the Accropode units have been dislodged and even some Accropods units had a severe structural damage. Significant movement of the armour units compared with the completion drawings of the breakwater was observed. There is a considerable gap between wave wall and armour units for a stretch of 15 m from the northern breakwater head section, and the under layer units were exposed. It may be noted that interlocking and gravity are governing the stability. The observed displacement and structural damage of the Accropods units were beyond the acceptable range.

The underwater survey using echo sounder was conducted to explore the damaged portion underwater. Based on the analyses of both profiles, it was inferred that the breakwater had undergone severe damages due to cyclones. The results also indicate that the crest level changes are in the range from 10 to 20 cm.

## 4.3 Mitigation Measures

The failure of the northern breakwater at Kamarajar Port Limited was mainly due to the inadequate crest elevation and hydraulic instability of Accropods during severe cyclones, namely Thane and Nilam. It is proposed to replace the existing dislodged and damaged Accropods units with Tetrapod units. It is envisaged to utilize two-layer armour units considering unequal settlement and requirement to increase the crest level. In this mitigation measure, the base width of the breakwater will change minimum only. So, it will not affect the clear width of the approach channel. The design details after the rehabilitation are given in Table 2.



**Table 2** Design details after rehabilitation

Head Section at (–) 11.0 m CD	Seaside	Harbour side
Crest level ( m CD)	(+) 9.0	(+) 9.0
Crest width (m)	22.0	22.0
Side slope	1:1.5	1:1.5
Toe mound	15 m top width, 5.9 m height, 2–4.5 T	15 m top width, 5.9 m height, 2–4.5 T
Armour layer	25 T tetrapod with thickness of 4.5 m (two layers)	25 T tetrapod with thickness of 4.5 m (two layers)
Under layer	1.5–2.5 T with a thickness of 1.4 m	1.5–2.5 T with a thickness of 1.4 m
Trunk Section (–) 10.4 m CD	Seaside	Harbour side
Crest elevation ( m CD)	(+) 9.00	(+) 4.35
Crest width (m)	9.0	9.0
Side slope	1:1.5	1:1.5
Toe mound	15 m top width, 5.85 m height, 2–4.5 T	4 m top width, 2.5 m height, 1–5 T
Armour layer	25 T tetrapod with thickness of 4.5 m (two layers)	7–13 T rock with thickness of 2.8 m (two layers)
Under layer	0.5–2.5 T with thickness of 1.35 m	0.5–2.5 T with thickness of 1.4 m

## 5 Berm Breakwater in Gopalpur Port

### 5.1 Introduction

Gopalpur port is located along the Bay of Bengal in Ganjam District, Odisha. The geographical coordinates of the port are 19°18'8" N, 84°57'56" E. The length of north breakwater is 435 m up to 7 m contours and 2170 m for south breakwater up to 13 m contour level. A berm breakwater is designed for south breakwater. The estimated total quantity of stone required for construction of berm breakwater is 6,688,563 MT. The quantity of stones dumped before cyclone is 3,429,036 MT.

The very severe cyclonic storm (VSCS), Phailin crossed Odisha and adjoining north Andhra Pradesh coast near Gopalpur in the evening of 12 October 2013. Due to this severe cyclonic storm, huge damage has been occurred on both north and south breakwater in the Gopalpur Port. The berm portion of the south breakwater including wave wall is slipped and flattened due to cyclonic waves. Due to Phailin cyclone, 705,930 MT of stones is washed out. Hence, 3,965,457 MT of stones is required to complete the construction. Also in North Breakwater which 360 m was built with root length of 25 m, the stones in the top (1 m layer) were washed out and the remaining length got flattened. Core layer and secondary armour on top and sides are flattened out due to cyclonic storm waves hitting the breakwater.

### 5.2 *Solution to Damage*

The section was flattened mostly along with harbour side due to cyclone. So, the centre line of the berm breakwater will be moved towards harbour side.

### 5.3 *Experimental Investigation*

A well-controlled experimental programme has been performed to ascertain the damage level for the breakwater section in 10 m water depth (Fig. 7).

#### 5.3.1 **Experimental Results**

For the stability tests that conducted on the section consists of Armour Layer (4–7 Ton)+ Under Layer+Core (model-A; 1:2 slope), and the results clearly demonstrate that the primary layer seems to be very stable as the percentage damage is zero for wave periods of 6 and 7.5 s. Damage level is insignificant for wave period of 9 s. In actual practice, the damage level up to 5% is allowed. Hence, the section adopted is safe and the seaward slope can be increased to 1:1.5. However, if the slope of 1:1.5 is to be adopted, it is recommended to use armour weights of 7–9 Ton. Similarly, model B (Under Layer+Core; 1:2 slope) and model C (Under Layer+Core; 1:1.5 slope) are stable as per the physical model study.



**Fig. 7** Photographs showing the model before and after testing

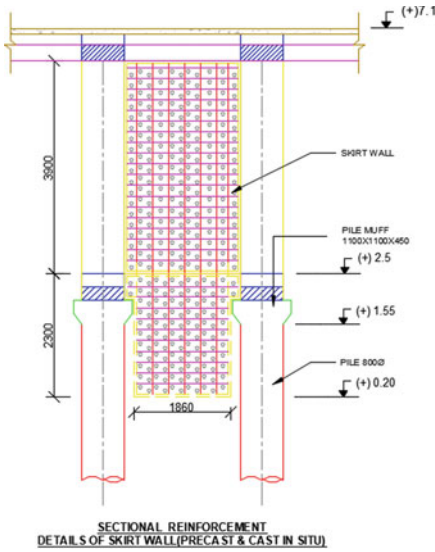


Fig. 8 Sectional view of landing jetty and site image

## 6 Jetty with Wave Breaker at JNPT

### 6.1 Introduction

Jawaharlal Nehru Port, also known as Nhava Sheva, is the largest container port in India, located east of Mumbai in Maharashtra, 18°57' N and 72°57' E. It is proposed coastal berth with landing jetty at JNPT.

The landing jetty has wave dissipater in seaside. It is facilitated to provide the tranquil zone since it will dissipate the wave energy by means of perforated panel. Landing jetty is used as ferry terminal at JNPT. Ferry service from India Gate to JNPT. JNPT is influenced by very heavy tidal variation. To eliminate the wave energy/dissipate, the wave energy skirt walls are provided. Figure 8 shows the sectional view and site image of the landing jetty with skirt wall as wave dissipater.

## 7 Rehabilitation and Retrofitting

### 7.1 General

The following steps to follow in rehabilitation and retrofitting projects.

- Zones of repair
- Investigation

- Repair methodology
- Case study
- Remaining life
- Post-repair monitoring.

## ***7.2 Causes of Damage***

- Wear and tear
- Extreme events like
  - Tsunami/Earthquake/Cyclonic wind, wave
  - Corrosion
  - Poor workmanship
  - Proper materials not used for construction.

## ***7.3 Rehabilitation of Offshore Transmission Tower at Port Blair***

Transmission tower from Suryachakra to Port Blair is present. It was damaged due to Tsunami in 2004. The significant damage was occurred on the junction between pile and pile cap. The pile cap has been dislocated from the original position. Figure 9 shows the offshore transmission tower and displacement of pile cap. The rehabilitation is carried out while the tower is being supported by the deck. The load from the deck is transferred to the pile by passing the damaged pile–pile cap joint. The retrofitting using additional reinforcement, micro-concrete and shear connectors is completed in three months.

## ***7.4 Rehabilitation of Offshore Tanker Terminal at Visakhapatnam Port***

The Offshore Tanker Terminal (OSTT) at Visakhapatnam port is built on the south side of the outer harbour basin and located at 140 m distance from the south breakwater. It was built having five mooring dolphins (MD-1–MD-5), two breasting dolphins (BD-1, BD-2) and a central unloading platform (CUP). The entire terminal is 407 m along with a maximum width of 31.3 m at the breasting dolphins. The depth around the terminal is approximately 19 m. Mooring dolphins MD-1, MD-2, MD-3 and breasting dolphin BD-1 are located west to the CUP, whereas BD-2, MD-4, MD-5 are located eastwards. The eastern side of the terminal suffered heavy damage during



Fig. 9 Displacement of pile cap in offshore transmission tower

Cyclone Hudhud witnessing complete submergence of MD-5 and partial submergence of MD-4 and BD-2. Figure 10 shows the aerial view of OSTT and satellite imagery of the terminal before and after the cyclone, respectively.

Hence, the rehabilitation is to bring the tilted caissons to original elevation by filling with new concrete duly anchoring with old RCC deck slab by inserting new reinforcement rods by drilling holes and grouting the same.

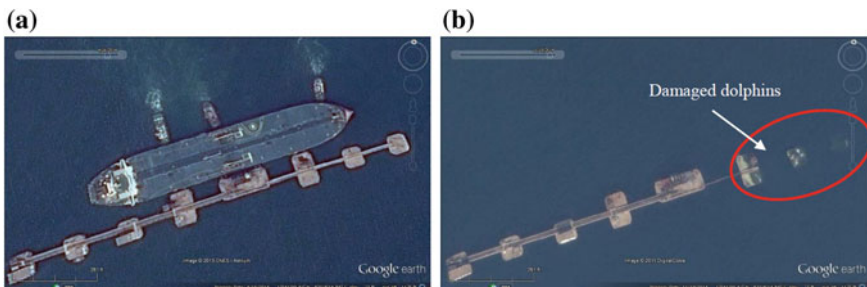


Fig. 10 Aerial view of OSTT before (a) and after cyclone (b)

### 7.4.1 Construction Methodology

- Dismantling and surface preparation on damaged dolphins
- Access working platform
- Drilling/installation of Rebar's
- Shuttering for micro-concrete wall
- Micro-concrete
- Mass concreting on BD and sand filling on MD'S
- Deck slab concrete and facia walls on south side of BD, MD'S
- Construction of facia beam and fixing of fenders on BD
- Fixing of marine fixtures, walkway bridge, foam tower on BD (Fig. 11).



**Fig. 11** View after completion of deck slab (top) walkway between berthing and mooring dolphin (bottom)

## **7.5 Repair Work on Berth Due to Bhuj Earthquake at Kandla Port**

Kandla, also known as the Deendayal Port Trust is a seaport in Kutch District of Gujarat State in western India, near the city of Gandhidham. Located on the Gulf of Kutch, it is one of major ports on west coast. Kandla Port has faced the severe damage due to the major earthquake. The **2001 Gujarat earthquake**, also known as the Bhuj earthquake, occurred on 26 January. The intraplate earthquake reached 7.7 on the moment magnitude scale and had a maximum felt intensity of X (*Extreme*) on the Mercalli intensity scale.

- As a consequence of Bhuj earthquake in 2001, cracks were noticed in 2000 precast hollow piles at a distance of 40 cm from the bracing beam bottom.
- All the racker piles suffered but collapse.
- IIT Madras proposed the repair methodology.
- Since time constraint as well as the tidal variation of 6 m during high and low tide, repair was restricted only to providing a micro-concrete reinforcement between 2001 and 2002 to get berth back into operation.

## **8 Wave Transformation on Submerged Reef**

### **8.1 Introduction**

Coastal areas are subjected to geomorphological changes due to natural and manmade activities. Artificial reef is considered an effective way in preventing coastal erosion due to its multipurpose benefits as compared to other shore protection methods. Artificial reefs are man-made underwater structure built to promote marine life, coastal protection, shoreline stabilization and recreational activities. Increased use of artificial reefs in coastal environment has led to study of the various design parameters of these reefs as the behaviour of waves and beach in the presence of these artificial reefs is not well established. Also, there is no fixed model or design of these reefs available; hence, various mechanisms of waves and beach in the presence of these reefs need to be studied as per the shape and size of the reef. Various construction materials like rock, concrete, geotextiles, steel can be used for construction of these reefs. Submerged wrecks are the most common form of artificial reef. Submerged reefs dissipate the incoming wave energy by forcing waves to break on top of the reef. Wave attenuation also occurs due to turbulence and nonlinear interaction between the reef and the incoming waves. Waves in the leeward side will be shorter and smaller and help in accumulation of sediments. These types of offshore reefs are custom-designed to trap sediment for each unique zone for different application.

The experimental investigation of wave transformation and breaking over the submerged reef with triangular steel wedge connected to shore is carried out. The

submerged reef was tested for regular and random wave at different water levels in Shallow Wave Basin at IIT Madras, India. The reef is designed for conditions of south-east coast of India. The reef makes an angle of  $13^\circ$  with respect to the shoreline and envisaged to trap the sediments from the longshore sediment transport. The submerged reef has a triangular wedge-shaped steel structure with armour stones and concrete cubes, the first of its kind in India. The main part of the submerged reef is triangular-shaped steel wedge weighing 900 t (in prototype scale) with dimensions  $60\text{ m} \times 50\text{ m} \times 2.5\text{ m}$  with slope on either side resting on stone bed. The model studies were carried out in 1:10 model scale for head sea condition with wave height 5–15 cm with wave period 1.9–3 s for three different still water levels, i.e. 50, 54 and 58 cm. The experimental study details of wave transformation and breaking over the submerged reef for regular wave and influence of water levels on these properties.

## 8.2 *Physical Model Study*

A submerged triangular reef was constructed using 25-mm-thick IS2062 grade steel sheets with base length 5 m and base height 6 m. The steel wedge consisted of top plate (horizontal crest) of 1 m length and 4.5 m height followed by slope of 1:0.8 on both the sides of the plate. The steel wedge has a height of 2.5 m and installed in the basin with the toe of the wedge 7.3 m from the wave maker. The horizontal crest of the steel wedge was at the water level for 50 cm water depth. At the opposite end of the wave generator in the basin, a beach with a 1:40 slope was made using 20 mm aggregate. Armour stone of size 10 cm was placed all around the steel wedge for a width of 1 m. Stones were placed for a depth of 10 cm to prevent toe scour. Additional concrete cubes of size 10 with 2 cm holes on all the six sides were placed all around the armour stone for a width of 0.5 m. Concrete cubes with holes were placed in random for a depth of 20 cm to dissipate the wave energy. The experimental set-up inside the shallow wave basin is shown in Fig. 12.

### 8.2.1 Results

- Intensity of wave breaking increases as the relative submergence of reef crest is reduced leading to higher air entrapment and energy dissipation.
- Breaker type is strongly influenced by the water level over the reef crest.
- Transmission coefficient increases with the submergence depth and with wave period.
- Transmission coefficient decreases with increasing wave height.
- When crest of reef is submerged, short period wave passes almost unhindered and longer wave propagates deeper and gets partially attenuated.
- Long waves lose their vertical symmetry and assume saw-toothed shape due to generation of primary secondary harmonics.
- Short waves do not develop tail wave as they grow in amplitude.



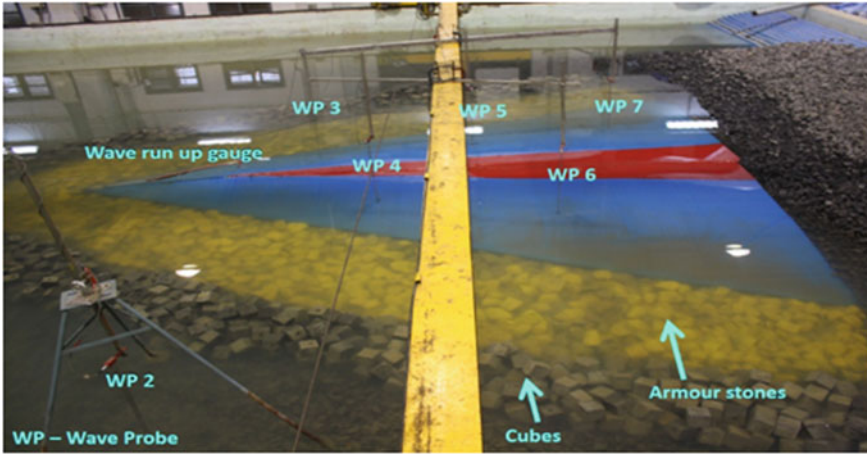


Fig. 12 Experimental set-up (1:10 scale) at shallow wave basin at IIT Madras

## 9 Summary

The modernization of ports needs deepening of harbour basin, upgradation of mechanical handling system, use of new type of fenders, etc. Both numerical and experimental investigations are carried out to understand the behaviour of new type of structures like touch pile wall and pile sheet pile wall. The techniques adopted for retrofitting of structures damaged by earthquake, tsunami and cyclone are explained by case studies. The details of new type of submerged reef which will restore the shoreline eroded by the breakwater constructed for a fishing harbour are also presented.

**Part II**  
**Marine Vehicles and Floating systems**

# Response Control of FPSO Using Multiple Tuned Liquid Dampers



Gurusamy Saravanan, Deepak Kumar and Ruchi Saraswat

**Abstract** The Floating Production Storage and Off-loading (FPSO) vessels are being used widely in offshore industries. The motion of FPSO subjected extreme sea condition needs to be controlled in order to maintain the station keeping of the vessel. The crude oil containers of an FPSO can be utilized as passive dampers for controlling the response of FPSO. These containers can act as Tuned Liquid Damper (TLD) if the natural frequency of the liquid oscillation in containers is tuned to the natural frequency of FPSO. FPSO container (tank) can be divided into several tanks (Multiple Tuned Liquid Damper, MTLTD) with different tank length and liquid depths. The natural frequencies of MTLTD can be intelligently distributed over a range around the natural frequency of FPSO or over a band of excitation wave frequencies. Each TLD can be modelled by using an equivalent Tuned Mass Damper (TMD) analogy. The present study attempts to comprehend the response control of FPSO under surge motion only, and the vessel is modelled as a single degree of freedom system subjected to random waves. Both time domain and frequency domain analyses have been carried out to verify the response control. From the present study, it has been found that MTLTD for FPSO will be effective if they are tuned to a range of wave excitation frequencies.

**Keywords** Floating production storage and Off-loading (FPSO)  
Tuned liquid damper (TLD) · Tuned mass damper (TMD)  
Multiple tuned liquid damper (MTLTD) and surge motion

---

G. Saravanan (✉) · D. Kumar  
Department of Ocean Engineering, Indian Institute of Technology Madras, Chennai, India  
e-mail: [gtsharavanan@gmail.com](mailto:gtsharavanan@gmail.com)

D. Kumar  
e-mail: [deepakkumar@iitm.ac.in](mailto:deepakkumar@iitm.ac.in)

R. Saraswat  
Department of Civil Engineering, JSS Academy of Technical Education, Noida, India  
e-mail: [rsaraswat@jssaten.ac.in](mailto:rsaraswat@jssaten.ac.in)

© Springer Nature Singapore Pte Ltd. 2019  
K. Murali et al. (eds.), *Proceedings of the Fourth International Conference in Ocean Engineering (ICOE2018)*, Lecture Notes in Civil Engineering 22,  
[https://doi.org/10.1007/978-981-13-3119-0\\_4](https://doi.org/10.1007/978-981-13-3119-0_4)

## 1 Introduction

Due to increasing demand for oil and gas, industries predominantly depend on ocean resources. For oil extraction and refinery processes, offshore industries rely on fixed structures such as concrete gravity platforms, steel jacket structures, complaint towers; and moored structures, namely spar platforms, tension leg platforms, semi-submersible production systems and FPSOs. In deep water oil fields where sub-sea pipelines are rarely possible, the FPSOs can be utilized for storing and processing the crude oil. Also, they have notable advantages: adaptability for water depth, early deployment in the production unit, self-contained, movable and re-locatable. It is worth to mention that there are 164 operating FPSOs worldwide (as of March 2015). Therefore, it is important to address the issues of safety, efficiency and motion control of FPSO systems under extreme sea state conditions. Wave loads on FPSO cause the interaction between FPSO and liquid in the cargo tanks; the liquid motion in the tanks affects the dynamics of FPSO badly. Excessive surge motion of the vessel could damage the riser system and so the whole production unit gets disrupted. Hence, the surge response control of FPSO is essential to investigate thoroughly. An easy way for structural control is to use passive dampers such as Tuned Mass Dampers (TMDs) and Tuned Liquid Dampers (TLDs) because of their quick installation, cost-effectiveness and minimal maintenance. Passive dampers do not require any external power sources. They impart forces that are developed due to the structural motion. In order to have robust and efficient damping devices, Multiple Tuned Mass Dampers (MTMDs) and Multiple Tuned Liquid Dampers (MTLDs) are preferred rather than single TMD/TLD.

Many researchers have explored the dynamics, efficiency and robustness of MTMD/MTLD. Clark [1] has designed a Multiple Tuned Mass Damper by extending the work of Den Hartog [2] from a single degree of freedom (SDOF) system to multiple degrees of freedom (MDOF) system. Igusa and Xu [3] have examined the effectiveness and robustness of MTMDs with natural frequencies uniformly distributed over a range. They have used the calculus of variations to optimize the design of the MTMDs with a constraint on the total mass. Kareem and Kline [4] have demonstrated the performance of MTMDs with frequencies uniformly and non-uniformly distributed within a specified interval. Moreover, it is observed that MTMDs with non-uniform frequency distribution do not meet any advantages or disadvantages over MTMDs with uniform frequency distribution. Fujino and Sun [5] have investigated extensively the implementation of MTLDs for SDOF systems by using both experimental and theoretical approaches. Lee and Reddy [6] have used cylindrical LTD to suppress the motion of fixed offshore platforms. Jin et al. [7] have done experimental and numerical study on TLDs for controlling earthquake response of jacket offshore platform. Sorkhabi et al. [8] have investigated the use of multiple shallow water tanks in response control of MDOF systems.

In FPSOs, the existing cargo tanks can be modelled as damping devices. Therefore, the present study applies the concept of MTLD for examining the FPSO's surge response control. Based on conventional approach, MTLDs are tuned to the surge

natural frequency of FPSO and the responses are obtained. Moreover, in case of deep-sea conditions, we may expect a band of wave frequencies to occur. Hence, an attempt is made to explore the effects on response control if MTLDs are tuned to a range of wave excitation frequencies. In addition, response control is also reviewed if MTLDs are tuned to the natural frequency of FPSO as well as to a range of excitation frequencies.

## 2 Theory of Tuned Liquid Dampers

Liquid in partially filled containers subjected to dynamic loads undergoes oscillatory motion known as sloshing, and it can be utilized as motion controlling device such as Tuned Liquid Dampers (TLDs). They are used to minimize the horizontal vibration of structures. The fundamental frequency of sloshing is tuned to a natural frequency of structure to suppress the structural vibration. The undesirable vibrational energy will be dissipated due to liquid motion. The frequency of TLD depends on tank length and liquid depth. Based on the ratio of the liquid depth to the tank length in the direction of the motion, the TLDs can be classified into two categories, i.e. shallow water TLDs and deep water TLDs. In the shallow water case, damping originates primarily from the action of wave breaking; whereas in deep water case, baffles and screens are needed to enhance the inherent damping.

If the amplitude of excitation is small, the dynamics of a TLD has similarities with the behaviour of TMD; hence, an easy way to understand the dynamics of rectangular TLDs is based on the equivalent TMD analogy. The equivalent model assumes that tank is rigid; fluid is homogeneous and incompressible; no sources and sinks are present in the liquid domain. The SDOF system with TLD and SDOF system with TMD are shown schematically in Fig. 1a, b. Upon using linear water wave theory, the equivalent mass and stiffness, corresponding to the fundamental mode of sloshing, can be derived as follows (Tait [9]).

The equivalent mass:

$$m_{eq} = \frac{8\rho bL^2}{\pi^3} \tanh\left(\frac{\pi h}{L}\right) \quad (1)$$

The equivalent stiffness:

$$k_{eq} = \frac{8\rho bLg}{\pi^2} \tanh^2\left(\frac{\pi h}{L}\right) \quad (2)$$

The fundamental sloshing frequency:

$$\omega_1^2 = \frac{\pi g}{L} \tanh\left(\frac{\pi h}{L}\right) \quad (3)$$

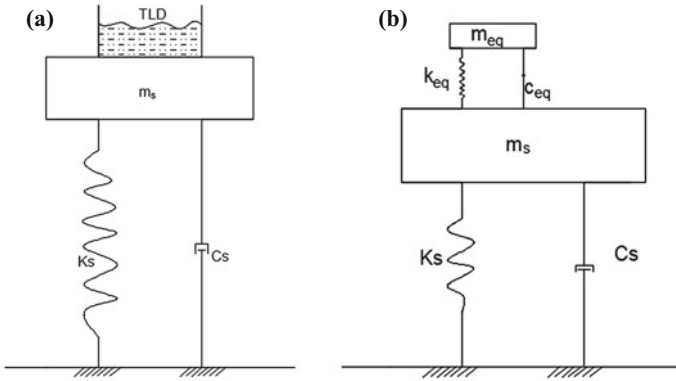


**Fig. 1** a SDOF system with TLD, b SDOF system with TMD

### 3 Problem Definition

The basic model for investigation is a moored FPSO vessel in deep water. In this study, the existing liquid cargo tanks are utilized to minimize the response of FPSO. The following configurations of FPSO with liquid tanks are considered for study:

*Configuration-1:* FPSO with empty tanks.

*Configuration-2:* FPSO with 5-identical rectangular liquid tanks. Natural frequency of each liquid tank is tuned to surge natural frequency of FPSO.

*Configuration-3:* FPSO with 6-identical rectangular liquid tanks. Natural frequency of each liquid tank is tuned to a wave excitation frequency.

*Configuration-4:* FPSO with 6-rectangular liquid tanks. Natural frequencies of them are distributed non-uniformly within a range of wave excitation frequencies.

*Configuration-5:* FPSO with 7-rectangular liquid tanks. Among them, one tank is tuned to natural frequency of FPSO, and frequencies of remaining tanks are distributed non-uniformly within a range of wave excitation frequencies.

The side view of configurations 2 through 5 has been viewed as sketched in Fig. 2a–d. The equivalent model for any configurations 2 through 5 can be viewed as an SDOF system with MTMDs as in Fig. 2e. The diagrams are not drawn in scale.

In order to compare the efficiency of MTLDs in different configurations, the total liquid mass in configuration-2 through configuration-5 is kept as constant. The details of length and liquid depth and natural frequency of tanks accommodated in all configurations are mentioned in Table 1.

#### 3.1 Wave Spectrum

In order to predict linear and nonlinear responses for design of offshore structures, ocean wave spectrum representing particular sea states is an essential factor. For

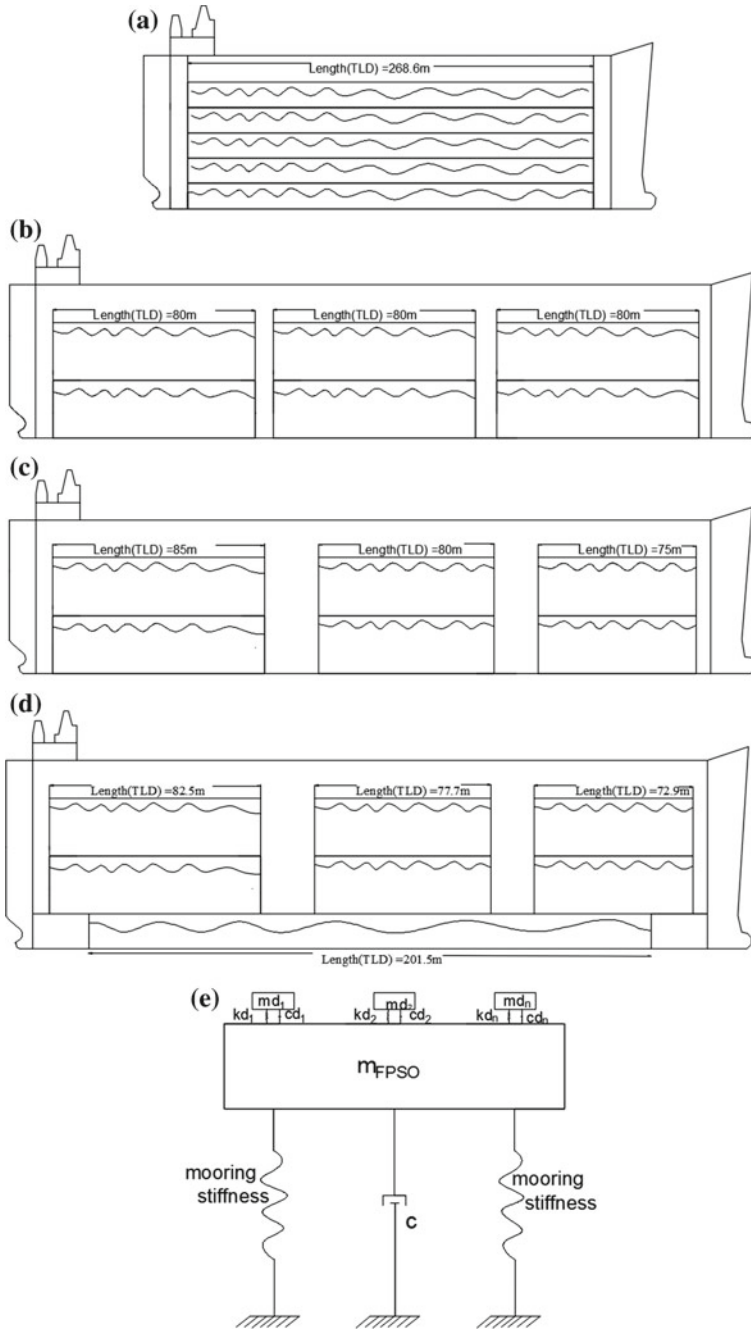


**Fig. 2** a FPSO with MTLDs: configuration-2, b FPSO with MTLDs: configuration-3, c FPSO with MTLDs: configuration-4, d FPSO with MTLDs: configuration-5, e Equivalent model for FPSO with MTLDs

**Table 1** Details of different configurations of FPSO with MTLDs

Cases	Number of TLDs	Particulars of TLDs		
		Tank length (m) $L_n$	Liquid depth (m) $h_n$	Sloshing frequency (rad/s)
Config-1	0	–	–	
Config-2	5	268.6 m (TLD <sub><i>n</i></sub> , <i>n</i> = 1, 2, 3,4, 5)	2.93	0.06269
Config-3	6	80 m (TLD <sub><i>n</i></sub> , <i>n</i> = 1, 2, 3,4, 5,6)	8.5	0.35216
Config-4	6	85 m (2-identical) TLD <sub>1</sub> , TLD <sub>2</sub>	8.5	0.33212
		80 m (2-identical) TLD <sub>3</sub> , TLD <sub>4</sub>	8.5	0.35216
		75 m (2-identical) TLD <sub>5</sub> , TLD <sub>6</sub>	8.5	0.37473
Config-5	7	201.5 m (TLD <sub>1</sub> )	1.65	0.06272
		82.5 m (2-identical) TLD <sub>2</sub> , TLD <sub>3</sub>	8	0.33227
		77.7 m (2-identical) TLD <sub>4</sub> , TLD <sub>5</sub>	8	0.35214
		72.9 m (2-identical) TLD <sub>6</sub> , TLD <sub>7</sub>	8	0.37448

design purposes, one can choose reasonably good wave spectrum which is expected in the ocean sites where the system can be operated safely. In the present study, Pierson–Moskowitz spectrum is used to represent the fully developed sea state with significant wave height,  $H_s = 16$  m. The one-sided power spectral density of wave height is given as in Eqs. (4) and (5), and the corresponding plot is shown in Fig. 3.

The modal frequency  $\omega_m$  exists at 0.3132 rad/s, and the dominant wave frequencies are distributed in the range between 0.28 and 0.38 rad/s.

$$S(\omega) = \frac{8.10}{10^3} \frac{g^2}{\omega^5} \exp(-(5/4)(\omega_m/\omega)^4) \tag{4}$$

$$\omega_m = 0.4\sqrt{g/H_s} \tag{5}$$



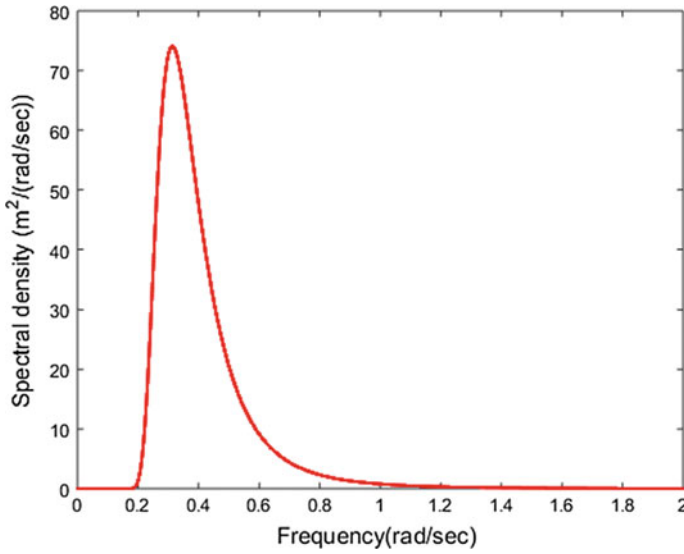


Fig. 3 Wave height spectral density function

### 3.2 Wave Load on FPSO

The ratio of draft of FPSO to the wavelength is less than 0.2 and so the slender body theory is applicable for FPSO; therefore, Morison's equation is applied to calculate wave loads on FPSO. One can write the horizontal hydrodynamic force on the FPSO as

$$f(t) = \frac{1}{2} \rho C_D B D |\dot{u} - \dot{x}| (\dot{u} - \dot{x}) + \rho C_M B D L \ddot{u} - (C_M - 1) \rho C_M B D L \ddot{x} \quad (6)$$

Here,  $\{C_D, C_M\}$  are the drag and inertia coefficients;  $\dot{u}$  and  $\ddot{u}$  are the ocean water particle velocity and acceleration, respectively; the set  $\{x, \dot{x}, \ddot{x}\}$  denotes the displacement, velocity and acceleration of FPSO, respectively;  $\{L, B, D\}$  represents the length, maximum beam and Draft of FPSO;  $\rho$  denotes the seawater density.

### 3.3 Mathematical Formulation

The equation of surge motion of FPSO is given as follows:

$$(m + a)\ddot{x} + (2\xi\omega m)\dot{x} + k_1x + k_2x^3 + k_5x^5 = f(t) \quad (7)$$

where  $f(t) = \frac{1}{2} \rho C_D B D |\dot{u} - \dot{x}| (\dot{u} - \dot{x}) + \rho C_M B D L \ddot{u} - (C_M - 1) \rho C_M B D L \ddot{x}$ .

The equation of motion of TLD<sub>*n*</sub> is given by:

$$m_n \ddot{x}_n + c_{dn}(\dot{x}_n - \dot{x}) + k_{dn}(x_n - x) = 0 \quad \text{for } n = 1, 2, 3 \dots \quad (8)$$

Here,  $\{m, \xi, \omega\}$  are the mass, damping ratio and surge natural frequency of the FPSO vessel; 'a' is the added mass due to surge motion of FPSO; the set  $\{x, \dot{x}, \ddot{x}\}$  denotes the displacement, velocity and acceleration of FPSO, respectively; the set  $\{x_n, \dot{x}_n, \ddot{x}_n\}$  denotes the displacement, velocity and acceleration of TLD<sub>*n*</sub> in the FPSO; the set  $\{m_{dn}, k_{dn}, c_{dn}, \omega_{dn}\}$  indicates the mass, stiffness, damping constant and natural frequency of the TLD<sub>*n*</sub>;  $k_1, k_2, k_3$  are the mooring coefficients obtained by catenary equations;  $\dot{u}$  and  $\ddot{u}$  are the ocean water particle velocity and acceleration, respectively; let  $\{L_n, h_n\}$  denote the length and liquid depth of TLD<sub>*n*</sub>. The following can also be noted.

Mass of TLD<sub>*n*</sub>:

$$m_{dn} = \frac{8\rho_n b L_n^2}{\pi^3} \tanh\left(\frac{\pi h_n}{L_n}\right) \quad (9)$$

Stiffness of TLD<sub>*n*</sub>:

$$k_{dn} = \frac{8\rho_n b L_n g}{\pi^2} \tanh^2\left(\frac{\pi h_n}{L_n}\right) \quad (10)$$

Damping constant of TLD<sub>*n*</sub>:

$$c_{dn} = 2\left(\sqrt{\frac{3\mu}{8(1+\mu)}}\right) m_{dn} \omega_{dn}; \quad \mu = \frac{m}{m_{dn}} \quad (11)$$

Natural frequency of TLD<sub>*n*</sub>:

$$\omega_{dn} = \sqrt{\frac{\pi g}{L_n} \tanh\left(\frac{\pi h_n}{L_n}\right)} \quad (12)$$

The equation of motion can be written in matrix form compactly:

$$[M]\{\ddot{X}\} + [C]\{\dot{X}\} + [K]\{X\} = \{F\} \quad (13)$$

where  $[M]$ ,  $[C]$ ,  $[K]$  are mass, damping and stiffness matrices;  $\{X\}$ ,  $\{\dot{X}\}$ ,  $\{\ddot{X}\}$  are displacement, velocity and acceleration vectors. For the configuration-2, one can have the following expressions.

$$\begin{aligned}
 M &= \begin{bmatrix} m+a & 0 & 0 & 0 & 0 & 0 \\ 0 & m_{d1} & 0 & 0 & 0 & 0 \\ 0 & 0 & m_{d2} & 0 & 0 & 0 \\ 0 & 0 & 0 & m_{d3} & 0 & 0 \\ 0 & 0 & 0 & 0 & m_{d4} & 0 \\ 0 & 0 & 0 & 0 & 0 & m_{d5} \end{bmatrix} \\
 C &= \begin{bmatrix} c + \sum_{i=1}^5 c_{di} & -c_{d1} & -c_{d2} & -c_{d3} & -c_{d4} & -c_{d5} \\ -c_{d1} & c_{d1} & 0 & 0 & 0 & 0 \\ -c_{d2} & 0 & c_{d2} & 0 & 0 & 0 \\ -c_{d3} & 0 & 0 & c_{d3} & 0 & 0 \\ -c_{d4} & 0 & 0 & 0 & c_{d4} & 0 \\ -c_{d5} & 0 & 0 & 0 & 0 & c_{d5} \end{bmatrix} \\
 K &= \begin{bmatrix} k_1 + \sum_{i=1}^5 k_{di} & -k_{d1} & -k_{d2} & -k_{d3} & -k_{d4} & -k_{d5} \\ -k_{d1} & k_{d1} & 0 & 0 & 0 & 0 \\ -k_{d2} & 0 & k_{d2} & 0 & 0 & 0 \\ -k_{d3} & 0 & 0 & k_{d3} & 0 & 0 \\ -k_{d4} & 0 & 0 & 0 & k_{d4} & 0 \\ -k_{d5} & 0 & 0 & 0 & 0 & k_{d5} \end{bmatrix} \\
 X &= \begin{Bmatrix} x \\ x_1 \\ x_2 \\ x_3 \\ x_4 \\ x_5 \end{Bmatrix} \quad \dot{X} = \begin{Bmatrix} \dot{x} \\ \dot{x}_1 \\ \dot{x}_2 \\ \dot{x}_3 \\ \dot{x}_4 \\ \dot{x}_5 \end{Bmatrix} \quad \ddot{X} = \begin{Bmatrix} \ddot{x} \\ \ddot{x}_1 \\ \ddot{x}_2 \\ \ddot{x}_3 \\ \ddot{x}_4 \\ \ddot{x}_5 \end{Bmatrix} \quad F = \begin{Bmatrix} p(t) \\ 0 \\ 0 \\ 0 \\ 0 \\ 0 \end{Bmatrix}
 \end{aligned}$$

$$p(t) = -A_1|\dot{u}|\dot{u} + A_2\ddot{u} + 2A_1|\dot{x}|\dot{u} - A_1|\dot{x}|\dot{x} - k_2x^3 - k_3x^5 \quad (14)$$

where  $A_1 = \frac{1}{2}\rho C_D B D$ ,  $A_2 = \rho C_M B D L$ ,  $a = (C_M - 1)\rho C_M B D L$ .

### 3.4 Parameters of FPSO–MTLD System

Mass ( $m$ ) = 136,004,663 (Kg)	Damping ratio, $\xi = 0.05$
Length ( $L$ ) = 312 (m)	$k_1 = 675,490$ (N/m), $k_2 = -110$ (N/m), $k_3 = 10$ (N/m)
Maximum beam ( $B$ ) = 45 (m)	Surge natural period of FPSO = 100.05 s
Draft ( $D$ ) = 10 (m)	Density of liquid in TLD, $\rho_n = 850$ kg/m <sup>3</sup>
Height ( $H$ ) = 30 (m)	$C_M = 1.25$ , $C_D = 0.7$

## 4 Solution Techniques

The nonlinear coupled Equations (7) and (8) can be solved in both time and frequency domains. The responses of FPSO are obtained by both ways; the root mean square values of responses are compared.

### 4.1 Time Domain Analysis

Newmark-beta's time marching algorithm is used to solve the systems (7) and (8).

At every time step, the following procedure is adopted:

1. Solve the linear system initially by considering the excitation force as:  $p(t) = -A_1|\dot{u}|\dot{u} + A_2\ddot{u}$ .
2. Get the linear responses and update the excitation function  $p(t) = -A_1|\dot{u}|\dot{u} + A_2\ddot{u} + 2A_1|\dot{x}|\dot{u} - A_1|\dot{x}|\dot{x} - k_2x^3 - k_3x^5$  using linear responses  $x, \dot{x}$ .
3. Obtain the system responses using updated  $p(t)$ .
4. Compare previous responses  $\{x, \dot{x}\}_{\text{previous}}$  with the updated responses  $\{x, \dot{x}\}_{\text{updated}}$  and check the tolerance of error. If the tolerance is met then store the responses.
5. If not so, again re-update the excitation function  $p(t) = -A_1|\dot{u}|\dot{u} + A_2\ddot{u} + 2A_1|\dot{x}|\dot{u} - A_1|\dot{x}|\dot{x} - k_2x^3 - k_3x^5$  by using  $\{x, \dot{x}\}_{\text{updated}}$  and get the system responses.
6. Repeat the steps 4 and 5 until convergent of responses.
7. Store the responses for every time step.

## 4.2 Frequency Domain Analysis

In the frequency domain approach, the nonlinear terms are simplified by stochastic linearization techniques and so the polynomials in the equation of motion (7) can be written as follows:

$$x^3 = \left(\frac{8}{\pi}\sigma_x^2\right)x \quad \text{and} \quad x^5 = \left(\left(\frac{8}{\pi}\right)^2\sigma_x^4\right)x$$

The following steps are used to solve the coupled system (13).

1. Get the Power Spectral Density Function (PSDF) for the excitation  $p(t) = -A_1|\dot{u}|\dot{u} + A_2\ddot{u}$ .
2. Obtain the frequency response function:  $H(\omega) = [-\omega^2[M] + i\omega[C] + [K]]^{-1}$  for linear part of equation of motion only.
3. Obtain response PSDF (displacement, velocity and acceleration) of linear part of equation.
4. Calculate the RMS values of  $x$  and  $\dot{x}$ . Rewrite the excitation function  $p(t) = -A_1|\dot{u}|\dot{u} + A_2\ddot{u} + 2A_1|\dot{x}|\dot{u} - A_1|\dot{x}|\dot{x} - k_2x^3 - k_3x^5$ .
5. Using terms  $A_1|\dot{x}|\dot{x}$  and  $k_2x^3 - k_3x^5$ , damping  $[C]$  and stiffness  $[K]$  matrices are modified.
6. Frequency response function for modified equation is obtained:  $\left\{H(\omega) = [-\omega^2[M] + i\omega[C] + [K]]^{-1}\right\}_{\text{updated}}$ .
7. Get the PSDF of updated  $p(t)$  in step 4.
8. Obtain the PSDF of displacement, velocity and acceleration using modified response function and modified excitation PSDF.
9. Compare the previous PSDFs (previous iteration) of responses with the updated PSDFs of responses and check the tolerance of error. If the tolerance is met, then store the PSDFs responses.
10. If tolerance error is high, go back to step 4 and continue till convergence is met.

## 5 Results and Discussions

An FPSO is analysed for its response in surge direction for its response control using its liquid in container as a passive control device (TLD). Several configurations are taken based on TLD tuning. In few configurations, TLDs are tuned to different frequencies to have robustness of response control. Details of different configurations are mentioned previously in text. The techniques used for obtaining the responses are time domain and frequency domain techniques. The time domain simulation is performed up to 3000 s to capture the transient and steady-state response of FPSO. The typical time histories of displacement responses of all configurations are plotted in Figs. 4, 5, 6, 7 and 8. The transient amplitude of configuration-1 is higher than

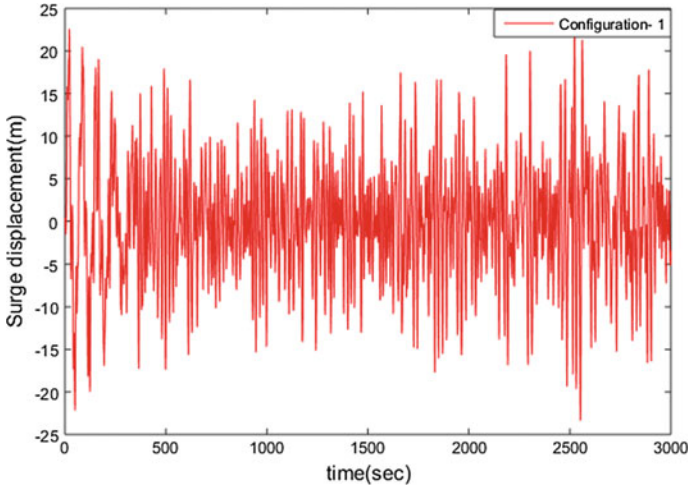


Fig. 4 Time history of displacement response of configuration-1

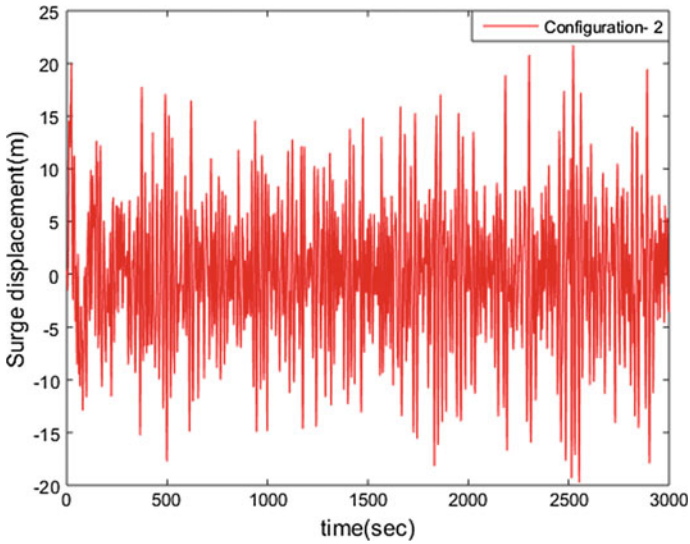
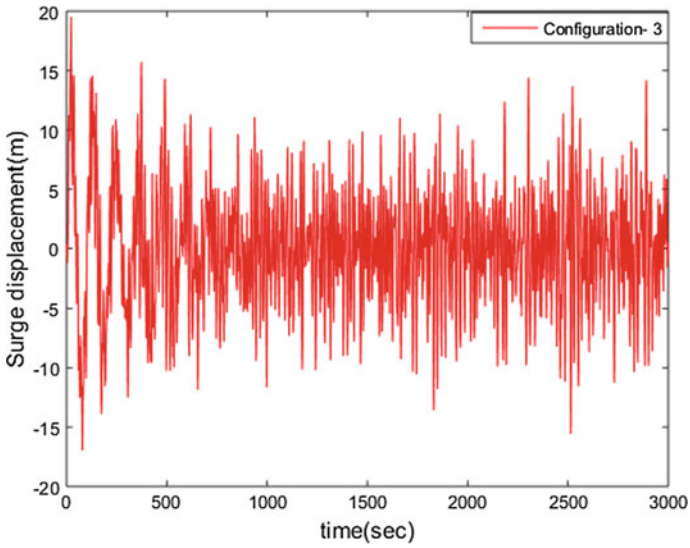
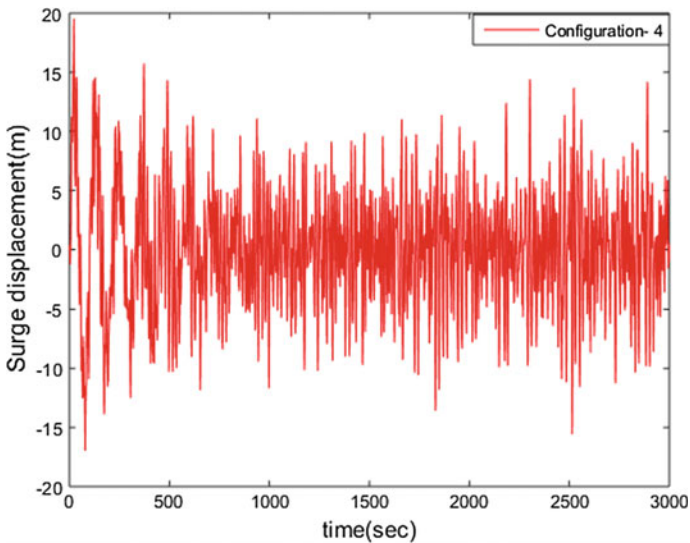


Fig. 5 Time history of displacement response of configuration-2

that of other configurations. This is because FPSO with empty tanks is highly flexible and so it undergoes large excursions. All configurations experience steady state approximately after 500 s, which is five times of the natural period of FPSO. The transient behaviour in configuration-2 differs qualitatively than the configurations 3, 4 and 5.



**Fig. 6** Time history of displacement response of configuration-3



**Fig. 7** Time history of displacement response of configuration-4

In Fig. 9, a short span of displacement time history of all configurations (shown in Figs. 4, 5, 6, 7 and 8) is highlighted to distinguish the performance of different configurations in response control. The configuration-2, which contains MTLDs tuned to structural frequency, yields minimal control than other configurations, because each TLD of 268.6 m length has lower sloshing frequency of 0.06269 (rad/s) and

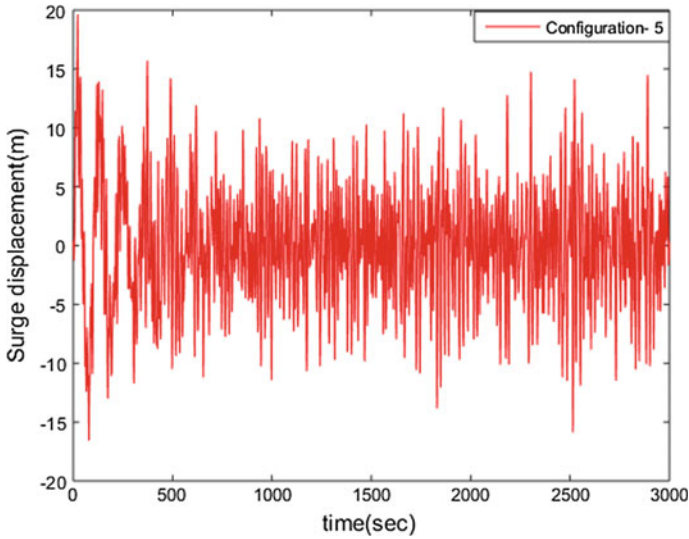


**Fig. 8** Time history of displacement response of configuration-5

so they develop less motion to counteract the FPSO motion. In the configuration-3, response reduces significantly; the possible reason is as FPSO is a moored structure, it is expected that the oscillation energy of FPSO is dominant in the excitation frequencies rather than at its own natural frequency. Similar control is noticed in configuration-4 too. Therefore, MTLDs with frequencies tuned to a wave excitation frequency and MTLDs with frequencies tuned to a band of excitation frequencies counteract FPSO motion effectively and so the response diminishes.

Having understood the dynamics of configurations 2, 3 and 4, in configuration-5, a single TLD tuned to the structural frequency and other remaining six TLDs with frequencies distributed over a range of excitation frequencies are used. The response control increases slightly in comparison to other configurations. From the given time history span in Fig. 10, it is visible that configurations 3, 4, 5 display similar trend in displacement response and so performance is almost the same. But configurations 4 and 5 are more robust because of its tuning to wide band of excitation and tuning to FPSO frequency too.

The frequency domain method is also used to justify the response control obtained in time domain analysis. The PSDFs of displacement of all configurations have been plotted in Fig. 11. The peaks of PSDF are present either at the natural frequency of the FPSO and or at the neighbourhood of the excitation frequencies. The RMS value of responses is calculated as the square root of the area under the PSDF curve. The PSDF curve of configuration-1 occupies larger area than other curves. In configuration-2, the peak value of PSDF at the natural frequency of FPSO reduces significantly, since all TLDs tuned to structural frequency and so they contribute in response reduction only at the structural frequency. Also, it is seen that configuration-2 has dominant



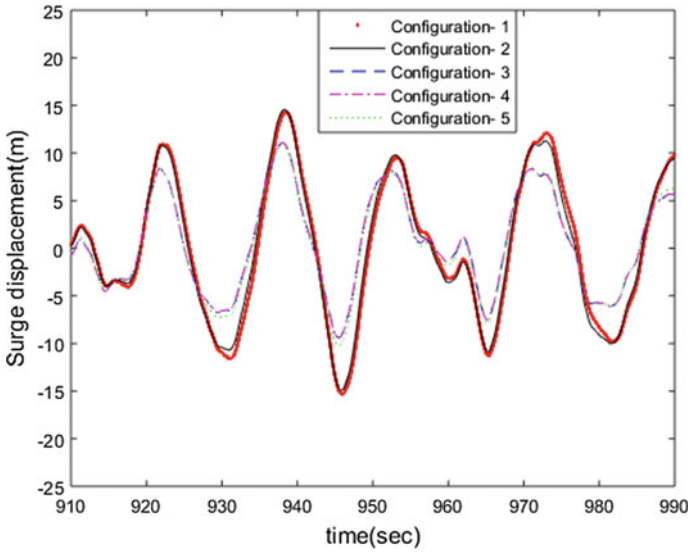


Fig. 9 Comparison of responses of all configurations

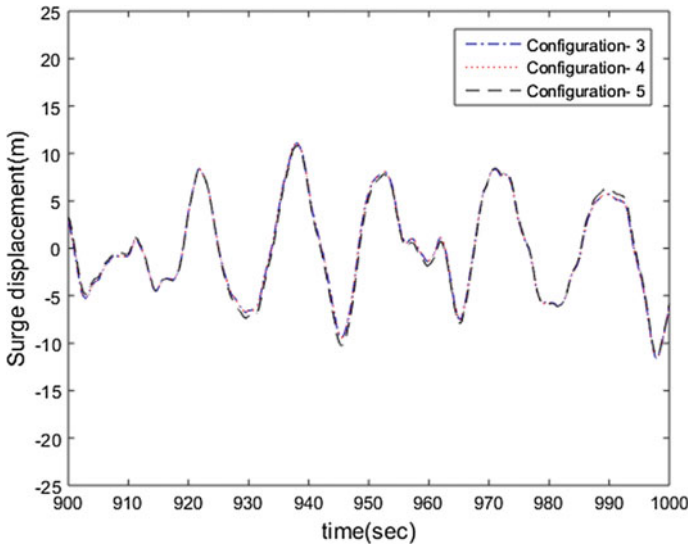
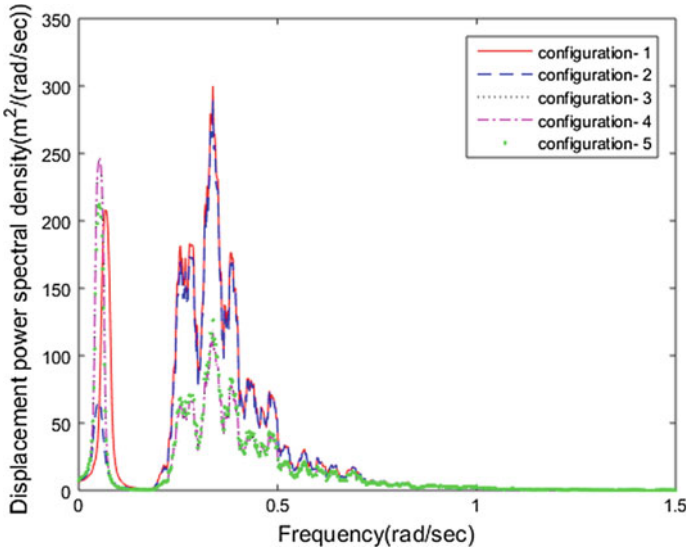


Fig. 10 Comparison of responses of configurations 3, 4 and 5

energy content in the band of excitation frequencies. The PSDF curves of configurations 3 and 4 have higher peak values at the natural frequency of system (FPSO). They have less energy density in the neighbourhood of excitation frequencies; this is because TLDs tuned to wave excitation frequencies damp the energy significantly.



**Fig. 11** Comparison of PSDF (time domain) of responses

In configuration-5, one can observe that the peak value of PSDF at the natural frequency of FPSO reduces marginally, because a TLD tuned to the FPSO's frequency contributes a little in response control.

Indeed, one can note that TLD tuned to the natural frequency of FPSO participates in energy reduction at the natural frequency of the system; whereas TLDs tuned to wave excitation frequencies reduce vibrational energy around the wave excitation frequencies. Being FPSO subjected to wave excitation, which has energy concentrated at approximately fixed band of frequencies, its response has large energy content in the region of wave excitation frequencies and so the MTLDs with frequencies tuned to wave frequencies are effective in response control.

The mass ratio for the configurations 2 through 5 is kept as constant so that tuning frequencies are the only responsible factors for control. Since total mass of dampers on FPSO plays a role in response control, one can vary the mass ratio depending on the volume of FPSO and may study the effects of mass ratio on control. However, the present study does not account the variability in mass ratio.

Having non-harmonic displacement time series, root mean square values of responses are obtained to quantify the response control. Table 2 shows the RMS values calculated in both time and frequency domains and percentage control in each configuration. The PSDFs of displacement of the configurations 3, 4 and 5 cover almost the same area, and it is seen from the RMS values in Table 3. The effectiveness of MTLDs on response control is assured by both time and frequency domain results.

From time domain results, the PSDFs of responses are also obtained. This will serve in qualitative comparison of the PSDF plots obtained from both time and fre-

**Table 2** RMS values of displacement responses and percentage control

Cases	RMS of displacement		Mass ratio	Percentage control (%)
	Time domain	Frequency domain		
Config-1	7.1034	6.8331	–	–
Config-2	6.4266	6.4328	0.4752	9.528
Config-3	5.007	5.0206	0.4753	29.513
Config-4	5.0111	5.0245	0.4753	29.455
Config-5	4.9964	5.0430	0.4754	29.662

**Table 3** RMS values of velocity/acceleration responses

Cases	RMS of velocity		RMS of acceleration	
	Time domain	Frequency domain	Time domain	Frequency domain
Config-1	2.7206	2.7107	3.3232	3.3243
Config-2	2.6733	2.6764	3.3179	3.3199
Config-3	2.0805	2.0859	3.2227	3.2246
Config-4	2.0815	2.0869	3.2228	3.2246
Config-5	2.1159	2.1220	3.2289	3.2308

quency domains. Figure 11 shows the PSDF of displacement response obtained using time domain analysis, and Fig. 12 shows the PSDF of displacement response obtained using frequency domain analysis. In the region of wave excitation frequencies, they have similar spectral shapes and peaks.

The energy transfer between FPSO and TLDs in different configurations can be viewed from Figs. 13, 14, 15 and 16. One can note that Fig. 13 indicates that desired frequencies for which TLDs can be tuned so that response control will be effective. The PSDF of FPSO displays the distribution of energy at natural frequency and at the wave excitation frequencies. FPSO being influenced by wave excitation frequencies, FPSO response has not been restrained effectively by the TLDs tuned to structural natural frequency.

Having reviewed the interaction between TLDs and FPSO in configuration-2, the other configurations are proposed to increase the response control. Figs. 14, 15 and 16 show the energy absorption capacity of MTLDs in configurations 3, 4 and 5, respectively. It is clearly visible that TLD response energy in configurations 3, 4 and 5 are high in the reason of FPSO response energy. So, expected control by configurations 3, 4 and 5 is higher in comparison to configuration-1. Configuration-5 has one additional TLD which is tuned to FPSO natural frequency. This gives little advantage in controlling the response over the configurations 3 and 4.

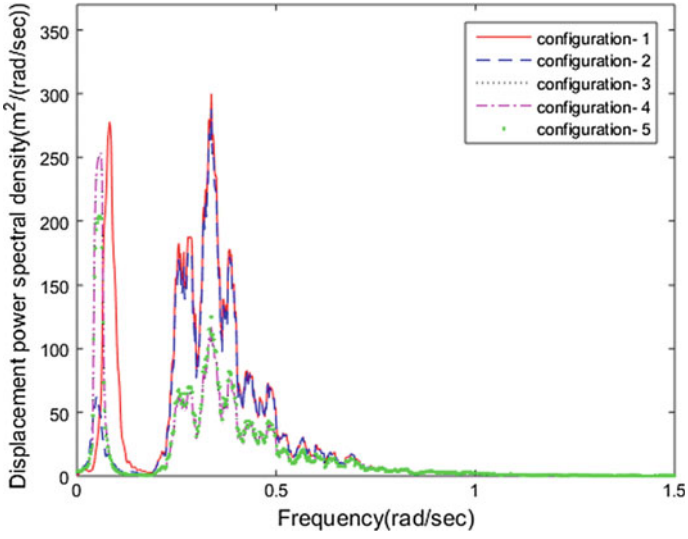


Fig. 12 PSDF (obtained from time domain) of responses

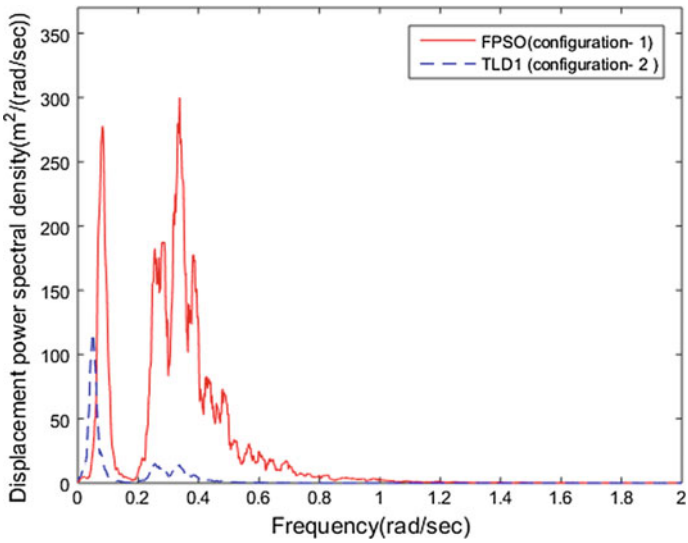


Fig. 13 PSDF of responses of FPSO (config-1) and TLD<sub>1</sub> (config-2)

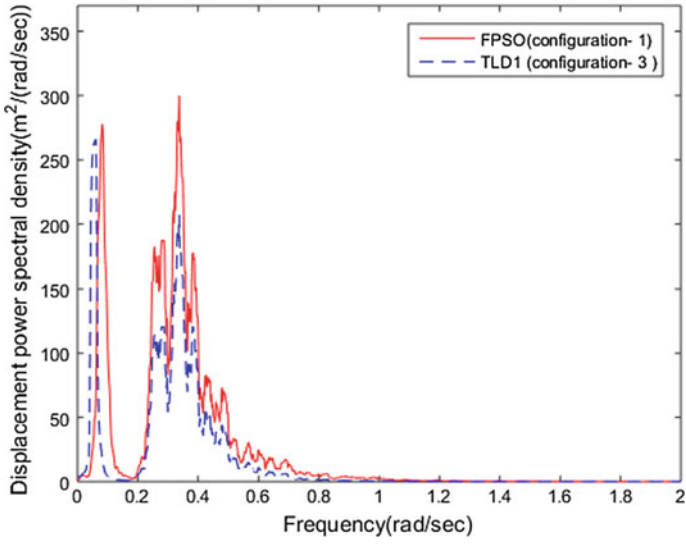


Fig. 14 PSDF of responses of FPSO (config-1) and TLD<sub>1</sub> (config-3)

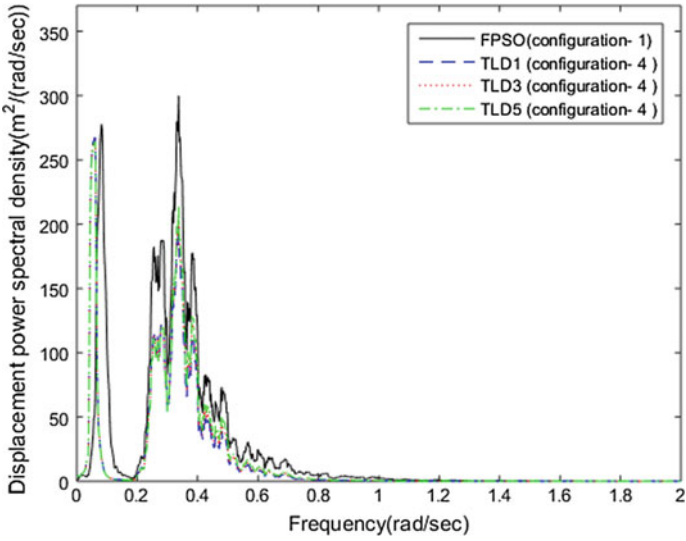


Fig. 15 PSDF of responses of FPSO (config-1) and TLDs (config-4)

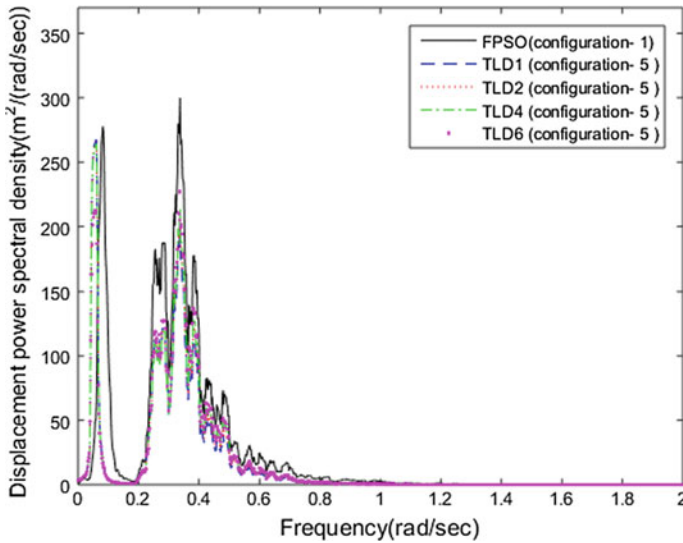


Fig. 16 PSDF of responses of FPSO (config-1) and TLDs (config-5)

## 6 Conclusions

The present study is intended to analyse the response control of FPSO using the concept of MTLDs. The available cargo containers in FPSO are modelled as liquid dampers. Both time domain and frequency domain methods are employed to prove the efficiency of MTLDs. Being FPSO is a flexible structure, the classical approach, where TLDs are tuned to structural frequency, provides very less control. In order to enhance the response control, TLDs are also tuned to wave excitation frequencies. Based on the analysis, the following salient remarks can be given:

1. MTLDs tuned to structural frequency exhibit about 9.528% response control.
2. A significant control of 29.513% is achieved by MTLDs tuned to a single wave excitation frequency.
3. MTLDs tuned to a range of wave excitation frequencies contribute response control of 29.455%.
4. A maximum control of 29.662% is gained by MTLDs tuned to structural frequency and wave excitation frequencies.
5. The performance of MTLDs tuned to a single excitation frequency, MTLDs tuned to a range of excitation frequencies, MTLDs tuned to structural frequency as well as a range of excitation frequencies does not differ significantly, but robustness of control can increase when TLDs are tuned to band of frequencies.
6. The present study reflects that for flexible structures, passive control devices are effective if they are tuned to wave excitation frequencies.

## References

1. Clark AJ (1988) Multiple passive tuned mass dampers for reducing earthquake induced building motion. In: Proceedings of ninth world conference on earthquake engineering
2. Den Hartog JP (1956) Mechanical vibrations, 4th edn. McGraw Hill, Inc., New York
3. Igusa T, Xu K (1994) Vibration control using multiple tuned mass dampers. *J Sound Vib* 175(4):491–503
4. Kareem A, Kline S (1995) Performance of multiple mass dampers under random loading. *J Struct Eng* 121(2):348–361
5. Fujino Y, Sun LM (1993) Vibrational control by multiple tuned liquid dampers. *J Struct Eng* 119(12):3482–3502
6. Lee SC, Reddy DV (1982) Frequency tuning of offshore platforms by liquid sloshing. *Appl Ocean Res* 4(4):226–230
7. Jin Q, Li X, Sun N, Zhou J, Guan J (2007) Experimental and numerical study on tuned liquid dampers for controlling earthquake response of jacket offshore platform. *Mar Struct* 20:238–254
8. Sorkhabi AA, Kristie J, Mercan O (2014) Investigations of the use of multiple tuned liquid dampers in vibration control. In: Proceedings of ASCE-structure congress
9. Tait MJ (2008) Modelling and preliminary design of a structure-TLD system. *Eng Struct* 30:2644–2655

# High-Speed Simulation in Towing Tank for Dynamic Lifting Vessels



Nimmagadda Naga Venkata Rakesh, Polisetty Lokeswara Rao  
and V. Anantha Subramanian

**Abstract** This paper presents a new testing technique developed for the simulation of high-speed dynamically lifted vessels. The complexity of the testing technique arises out of the need to test relatively small models in the towing tank in comparison with tests for normal displacement vessels. In order to simulate high Froude numbers much in excess of the threshold limit of 0.8 for planing, there are several challenges in designing the experiment. The challenges presented are due to small size model, necessity for giving the freedom to trim significantly and sink or emerge with reference to the static water level, lack of knowledge of the location of the point of trim, weight control of the model and delicate measurement system for the drag. Finally yet importantly, there is the caution that in the event of longitudinal plane instability there can be sometimes catastrophic damage and loss of transducers and even the model itself. The object of towing tank test for dynamically lifted crafts is to not only assess the drag and therefore power requirement, but also equally importantly verify that the hull form lifts clean at the transition-planing region, the bow wave formation and spray are not excessive, and there is no instability such as porpoising. Model tests also demonstrate the influence of loading, effect of centre of gravity location and the effect of chine lines and spray rails. Hence, model tests with dynamically lifting crafts are vital for verifying or improving the performance of the hull. This paper presents the development of a unique test set-up developed here to prepare and handle small-scale rapid-prototyped, precision models of high-speed planing hull forms. The new features incorporate an important counter-balancing mechanism, a sliding trim position control, vertical displacement guide system with delicate load cell-based data acquisition system. The newly developed system has been demonstrated in successfully simulating high speeds in the range of 25–30 knots with faithful capture of the entire kinematics, which include the trim, emergence and the wave pattern. This paper also presents some of the CFD simulation results for comparisons with the scenario recorded in the towing tank during experiments.

---

N. N. V. Rakesh (✉) · P. L. Rao · V. A. Subramanian  
Department of Ocean Engineering, Indian Institute of Technology Madras, Chennai, India  
e-mail: [rakesh.nnv@gmail.com](mailto:rakesh.nnv@gmail.com)

© Springer Nature Singapore Pte Ltd. 2019  
K. Murali et al. (eds.), *Proceedings of the Fourth International Conference in Ocean Engineering (ICOE2018)*, Lecture Notes in Civil Engineering 22,  
[https://doi.org/10.1007/978-981-13-3119-0\\_5](https://doi.org/10.1007/978-981-13-3119-0_5)



**Keywords** Planing · High-speed craft · Hydrodynamic model tests · Dynamic lift Porpoising · CFD simulation

## 1 Introduction

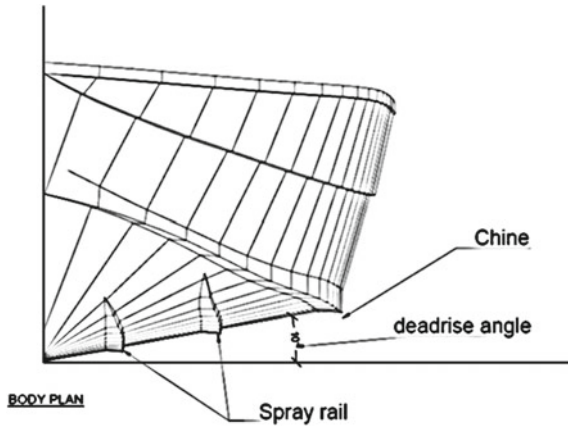
Hydrodynamic model tests are reliably used for assessing hull designs, especially for the high-speed planing crafts due to the complex and dynamic flow associated. High Froude number ( $Fn = V/\sqrt{Lg} > 1.0$ ) is characteristic to planing crafts and the vessel speed is large in relation to its length. Because of the nature of high dynamic lift, it is typical to associate a volumetric Froude number to non-dimensionalize the speed of the planing craft. The running trim of the vessel varies with speed due to the shift in location of centre of pressure relative to the centre of gravity. The planing craft performance is highly sensitive to the loading conditions, weight and the location of centre of gravity.

The present work describes the new experimental test set-up designed and fabricated for high-speed planing crafts in the towing tank facility at Department of Ocean Engineering, IIT Madras. The specialized set-up is used for small models (300–800 mm) at high speeds (up to 5 m/s) to measure resistance and running attitude. The development of the test set-up is described below.

Figure 1 shows different distinctive features of the planing hull forms. Many of these features determine the dynamic characteristics and therefore they need to be evaluated through tank tests. Some planing crafts are susceptible to dynamic instabilities in calm water due to the hull form, position of centre of gravity, speed and deadrise angle. The test set-up is used to predict the inception of porpoising and a feasible solution is found by investigating various remedies. Based on the test results, for stable operation at high speeds the critical parameters such as position and length of spray rails, loading conditions are prescribed along with the estimation of required engine power. In this context, three of the hulls, (namely Valeth, SHM and Timblo hulls) with varying dimensions and design features such as tunnels, spray rails are presented in the results section.

Day and Hagg [1] provided cable towed experiments of systematic test results concerning the porpoising stability limits of planing craft. Fridsma [2] conducted experiment for a series of hulls with different deadrise angle in Davidsons laboratory. The standard free to heave and trim resistance carriage was used based on the assumption that the thrust line is parallel to the smooth water surface. Thornhill et al. [3] investigated on porpoising instability phenomena for high-speed hulls. The model was fitted to the towing carriage by a gimbal and yaw restraint. The towing force was transmitted through a linear bearing to a load cell and the through a universal joint (free to pitch and roll) to the model. Kim et al. [4] studied on design of high-speed vessels for the improvement of resistance by three different hull forms of constant displacement. A new gimbal is developed so that the model ship is towed in inclined thrust direction when the model ship is trimmed while running and an anti-yaw guide is installed around bow of a model in order to prevent the yaw motion.

**Fig. 1** Geometric features of hard chine planing hull form



The brief literature review presented here shows on case-to-case basis; different researchers have developed customized methodologies to perform controlled tests on dynamically supported vessels.

## 2 Experiment Set-up

Three different planing hull forms are considered here to highlight the design development and performance of controlled tests in steady high-speed conditions. The hull forms and the principle dimensions are given below. Models were fabricated to high accuracy using rapid prototyping to standards prescribed by the ITTC recommended procedures 7.5-01-01-01 (Figure 2 and Table 1).

The towing tank at IIT Madras (Member ITTC) is 82.0 long 3.2 m wide and 2.6 m deep, with selectable speed up to 5 m/s equipped with precision speed control and high-speed data acquisition system. Based on the Froude scaling, the towing tank tests are performed using scaled models as per the ITTC recommended procedures 7.5-01-01-01.

A specialized resistance test set-up is designed and fabricated for high-speed planing crafts. The model is fixed to the set-up such that it is free to take its natural trim and heave attitude while the carriage tows the model along the centreline without any drift or sway. The test set-up consists of a precision linear guide system for friction free sinkage or emergence of the model, a pivot mechanism with block bearings for pitching of the model, a load cell for resistance measurement and a counterweight, connected to the guide rod, through a pulley to balance the excess weight of the components.

The dynamic force of the towed model is measured using a beam-type load cell. In this case, the thrust line is measured parallel to the free surface. During the experiment, the real-time force plot is displayed on the computer for monitoring and remedial measures (Figs. 3 and 4).

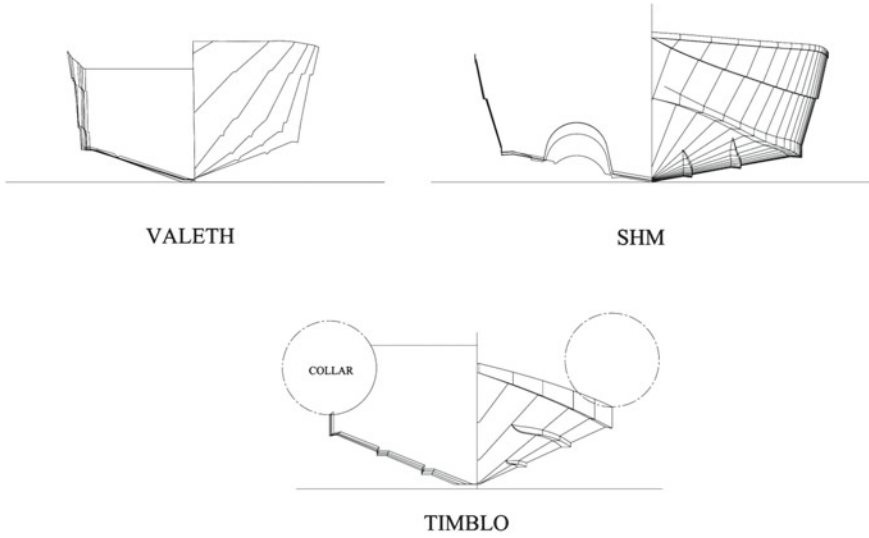


**Fig. 2** Body plans of three planing hulls

**Table 1** Principal dimensions of three different illustrative planing hulls

Quantity	VALETH		SHM		TIMBLO	
	Prototype	Model	Prototype	Model	Prototype	Model
Length overall	8.345 m	596.1 mm	11.285 m	684.3 mm	4.7 m	410.4 mm
Breadth	2.680 m	191.4 mm	3.700 m	224.3 mm	2.07 m	180.7 mm
Depth	1.420 m	101.4 mm	1.600 m	96.8 mm	0.90 m	78.6 mm
Draught	0.658 m	47.0 mm	0.677 m	42.4 mm	0.35 m	30.6 mm
Displacement (kg)	6900	2.45	12,541	2.72	884	0.572
Longitudinal C.O.G	3.108 m	222.0 mm	4.173 m	253.1 mm	1.328 m	116.0 mm
Deadrise angle ( $\beta$ ) ( $^\circ$ )	18.0	18.0	12.0	12.0	22.0	22.0
Design speed	25.0 knots	3.437 m/s	25.0 knots	3.167 m/s	25.0 knots	3.80 m/s
$L/\nabla^{1/3}$	4.42	4.42	5.45	5.45	4.94	4.94
Froude number	1.423	4.423	1.517	1.517	2.167	2.167
Model scale		14.000		16.492		11.453

### 3 Extrapolation Method

The recorded data of the measured force for each run is processed to obtain the average tow force value by selecting the data window for the constant speed duration from the time series plot corresponding to the particular speed. The dynamic wetted surface area is manually calculated from the video recorded above water showing

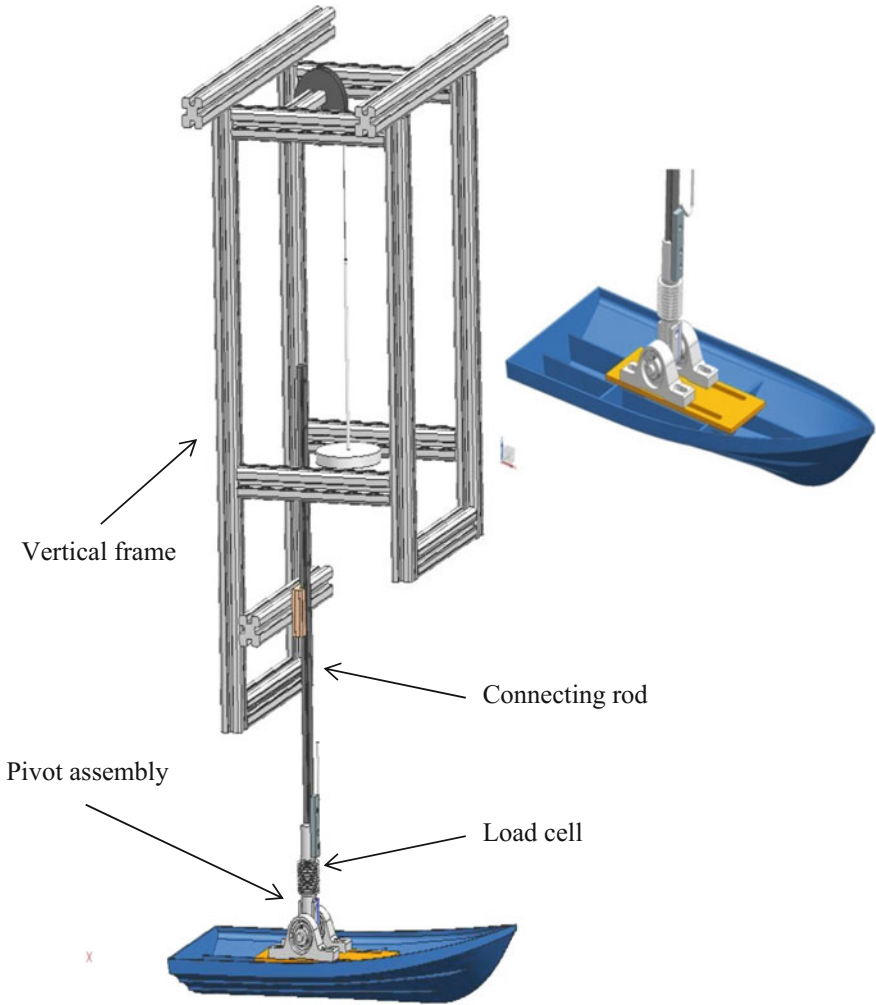


**Fig. 3** Experimental test set-up

the flow pattern and running attitude of the hull. The resistance of model measured at each speed is scaled to evaluate the prototype value based on Froude's method of extrapolation using ITTC 78 prediction method. The form factor  $(1+k)=1$  is assumed according to ITTC recommendations 7.5-02-05-01 for high-speed marine vehicles.

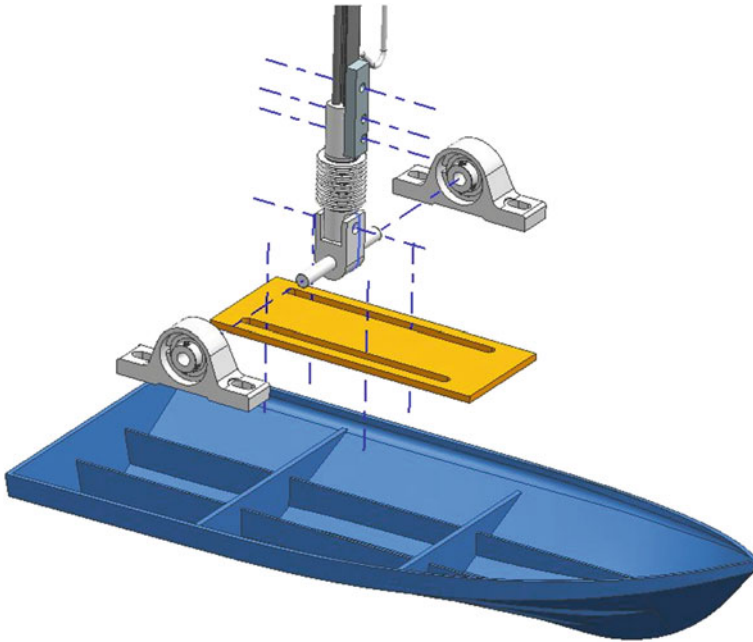


Fig. 4 Exploded view of the pivot mechanism

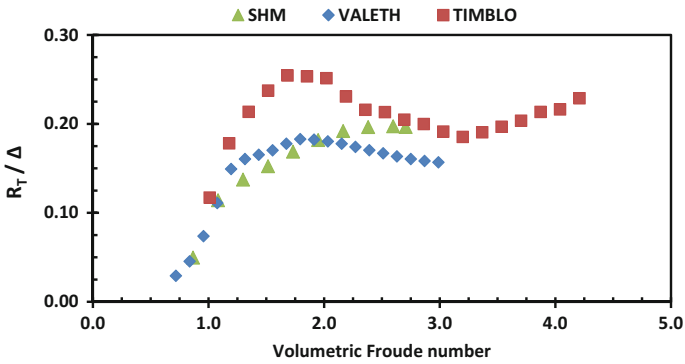


Fig. 5 Typical characteristic of resistance in the case of different planing hulls. Note the characteristic hump in resistance at the transition-planing speed

### 4 Results

The non-dimensional resistance  $R_T / \Delta$  value, dynamic waterline length and wetted surface area for the three different hulls are shown in Figs. 5, 6, 7 and 8.

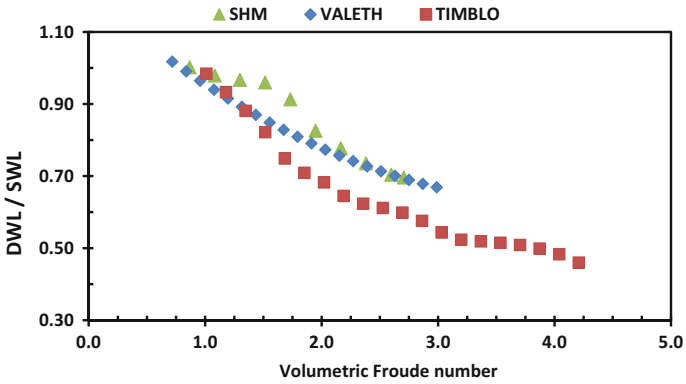


Fig. 6 Reduction of waterline length in increasing dynamic condition for different planing hulls

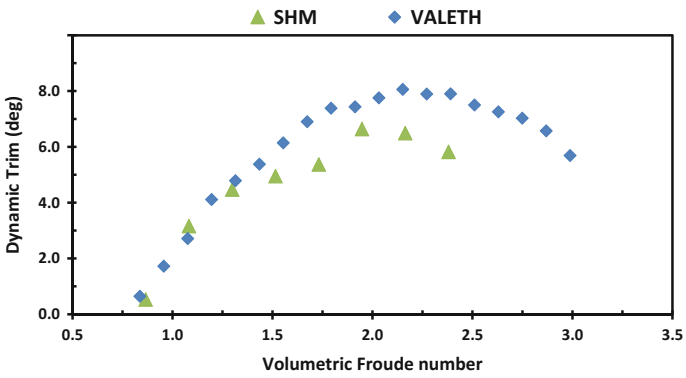


Fig. 7 Running trim as a function of speed

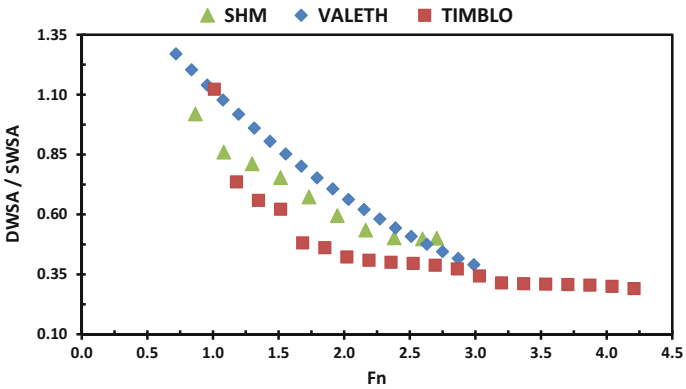
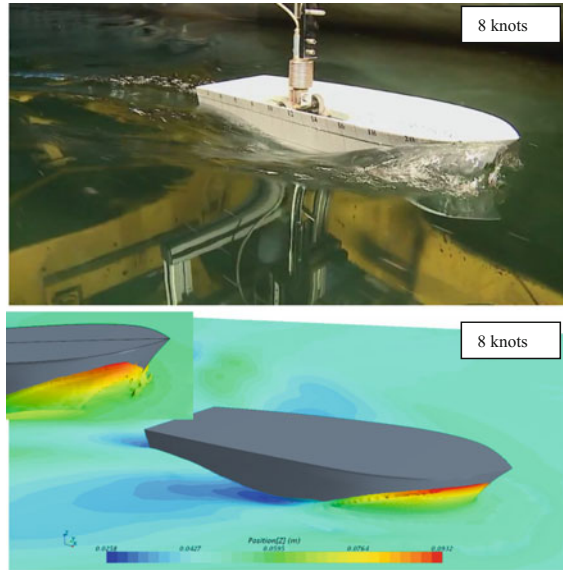


Fig. 8 Diminishing wetted surface area as a function of speed. The area may stabilize at very high speeds

**Fig. 9** Experiment and simulation free surface wave pattern of VALETH hull at pre-planing speed



## 5 Numerical Simulations

A commercial RANSE package STAR CCM+ is used for the simulation of planing vessels in calm water condition. The qualitative results in terms of wave pattern and the porpoising motions are presented here. In order to capture the flow phenomenon, the domain boundaries within which the computation grid is modelled is extended to  $2L$  (where  $L$  is length of the ship) in front of the bow,  $5L$  behind the transom and  $2L$  above the deck, below the keel and to the side of the hull. These dimensions are consistent with the minimum recommendations given in ITTC 7.5-03-02-03. Due to the centre-line symmetry of the ship as well as the flow, only half the hull is included in the domain. The analysis process considers the dynamic emergence and running trim based on 6-DOF motions. Wave pattern for the three different hulls at pre-planing and planing speed is compared with the CFD results. Figure 9 shows breaking of the bow wave for pre-planing speed 8.0 knots simulated in experiment and CFD for the Valeth hull. Figure 10 shows the full planing speed 25.0 knots, the formation of rooster-tail wave pattern is seen in the figures. Figure 11 shows the wave pattern at 10.0 knots for SHM vessel. Figure 12 shows the 25.0 knots speed and the wave pattern at the aft with double rooster tails merged further downstream; this pattern is due to the twin propeller tunnels. Similarly, Figs. 13 and 14 shows the pre-planing and planing speeds for Timblo hull.

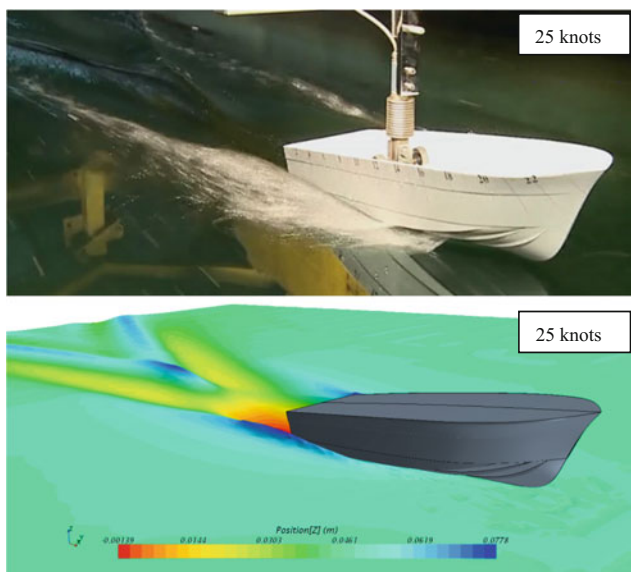


Fig. 10 Experiment and simulation free surface wave pattern of VALETH hull at planing speed

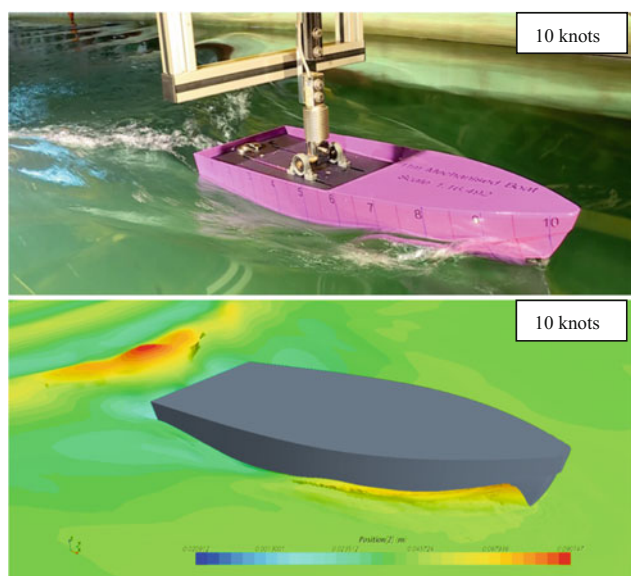


Fig. 11 Experiment and simulation free surface wave pattern of SHM vessel at pre-planing speed



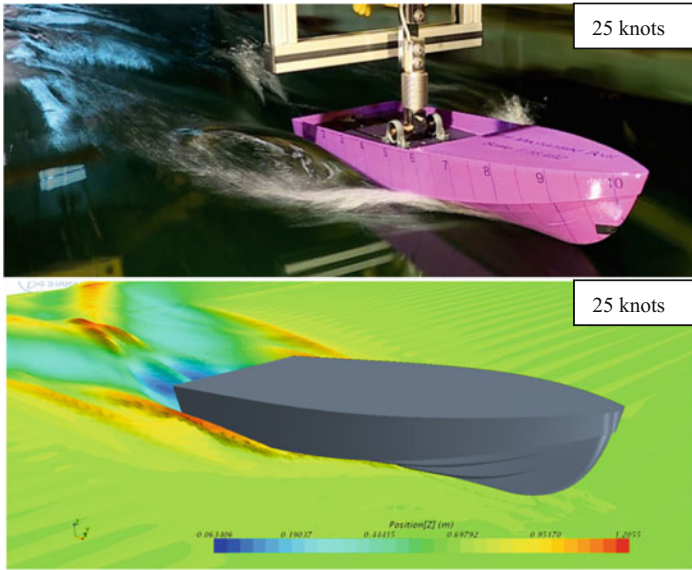


Fig. 12 Experiment and simulation free surface wave pattern of SHM vessel at design speed

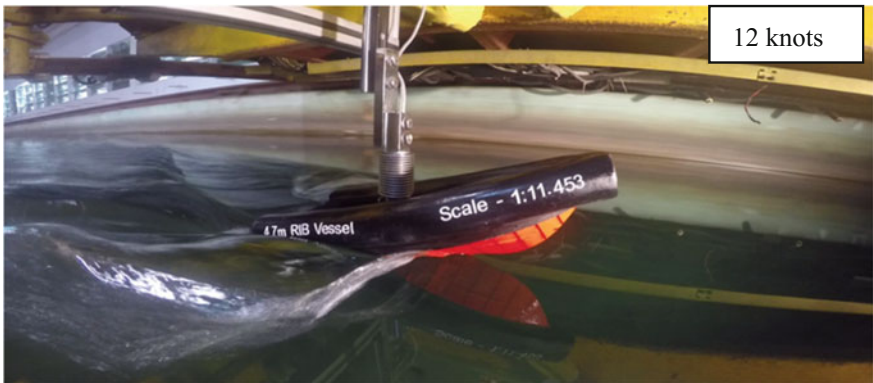


Fig. 13 Experiment and simulation of TIMBLO vessel at pre-planing speed

## 6 Simulation of Porpoising Phenomenon

Porpoising is an unstable coupled heave and pitch motions with diverging amplitudes in calm water. This dynamically unstable phenomenon is due to small perturbations of water, location of centre of gravity, deadrise angle and length of the beam. Figures 15, 16 and 17 show the porpoising motions of the TIMBLO vessel at 25.0 knots. Time series plots of sinkage and trim as obtained from CFD simulations are shown below in Fig. 16.



**Fig. 14** Experiment and simulation of TIMBLO vessel at planing speed

## 7 Conclusion

The paper reports in detail the development of an important test set-up for running tests on high-speed dynamically lifting vessels. This is a path-breaking development and exemplifies the use of a modest sized towing tank to realistically simulate measure and quantify the performance of high-speed planing hulls. Froude numbers in the range of up to four have been achieved with the test set-up. The development successfully demonstrates that with modern technology of model manufacture and sensitive electronic sensors for force measurements, miniaturization is a realizable goal. The tool combines effectively with CFD simulations to validate the dynamics and kinematics of high-speed planing hulls.



**Fig. 15** Snapshot showing porpoising motions of TIMBLO vessel at planing speed 25 knots

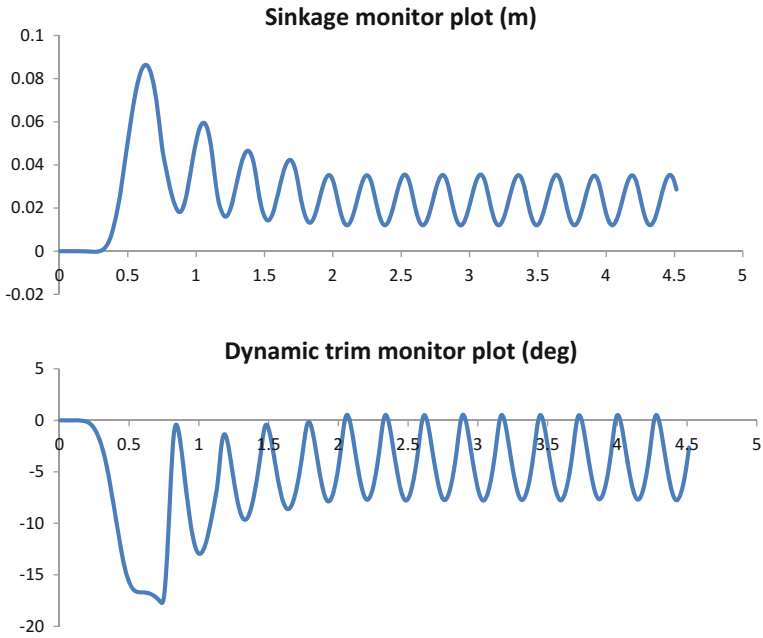


**Fig. 16** Unstable heave and pitch motions for TIMBLO at 25 knots

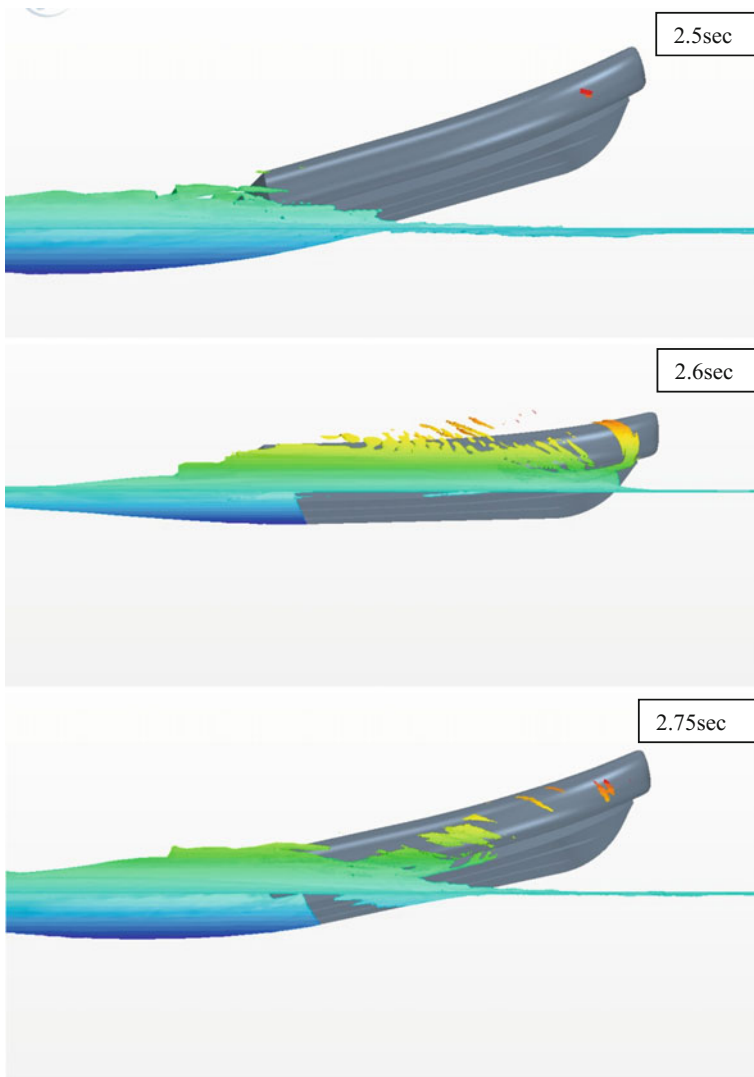


**Fig. 17** Snapshot of TIMBLO vessel at planing speed 25 knots

## References

1. Day JP, Hagg RJ (1952) Planing boat porpoising. Thesis submitted to web institute of Naval Architecture, Glen Gove, N.Y
2. Fridsma G (1969) A systematic study of the rough-water performance of planing boats (No. 1275). Stevens Institute of Technology, Hoboken, NJ, Davidson Lab
3. Thornhill E, Veitch B, Bose N (2000) Dynamic instability of a high-speed planing boat model. *Mar Technol SNAME News* 37(3):146
4. Kim DJ, Kim SY, You YJ, Rhee KP, Kim SH, Kim YG (2013) Design of high-speed planing hulls for the improvement of resistance and seakeeping performance. *Int. J. Naval Archit Ocean Eng* 5(1):161–177

# Coupled Boundary Element Method (BEM) and Finite Element Method (FEM) for Hydroelastic Analysis of Floating Plate



Anoop I. Shirkol  and T. Nasar

**Abstract** In the present study, a numerical model is developed to analyse equation of motion of the plate which is elastic in nature and has a shallow draft  $L/d \leq 1/20$  (small thickness). The platform may be of any shape (geometry) subjected to monochromatic waves. The developed numerical model is capable of investigating the VFLS of any geometry (arbitrary shape) at finite ( $0.05 \leq h/\lambda \leq 0.5$ ) depth. A hybrid numerical model is developed and used to solve fluid–structure interaction between the elastic thin plate and water wave. A Higher Order Boundary Element Method (HOBEM) has been adopted in order to maintain the same order, basis function and contains the same nodes between BEM and FEM. Two equations have been determined to build the connection between plate displacement and velocity potential. Displacement of the floating platform has been obtained by solving the plate equation of motion. To solve the plate equation of motion, FEM has been adopted. The equation which relates the plate displacement and water is solved by Boundary Integral Equation (BIE). A modified Green’s function which differs from the bygone Green’s function has been developed by using the Bessel, Hankel and Struve functions of order zero. Both the equations are solved simultaneously to get the displacement of floating elastic plate and velocity potential. The results obtained are validated with Wang (J. Fluids Struct. 19:557–572, 2004 [22]).

**Keywords** Fluid–structure interaction · Monochromatic · Bessel’s · Hankel

## 1 Introduction

Very Large Floating Structures (VLFSs) may serve the applications in the field of ocean engineering. Structures like floating bridges, floating oil containers, floating

---

A. I. Shirkol (✉) · T. Nasar  
National Institute of Technology Karnataka, Surathkal, Karnataka, India  
e-mail: [anoopshirkol@gmail.com](mailto:anoopshirkol@gmail.com)

T. Nasar  
e-mail: [t.nasar@gmail.com](mailto:t.nasar@gmail.com)

© Springer Nature Singapore Pte Ltd. 2019  
K. Murali et al. (eds.), *Proceedings of the Fourth International Conference in Ocean Engineering (ICOE2018)*, Lecture Notes in Civil Engineering 22,  
[https://doi.org/10.1007/978-981-13-3119-0\\_6](https://doi.org/10.1007/978-981-13-3119-0_6)

islands, floating airports are some of the applications of VLFSs. VLFSs are referred to as Very Large Floating Platform in some of the literature (VLFS/VLFP). VLFS are classified broadly into two categories [1], namely pontoon type and semi-submersible type of VLFS. In this article, we are mainly concentrating on pontoon type of VLFS. Hydroelasticity plays a major role in the design of VLFS. In order to check the elasticity of the VLFS, it is very necessary to predict the deflection precisely [1–16]. Many researchers and engineers have proposed interesting and attractive solutions to tackle the aforementioned problems and needs. The construction of VLFS is one of the suitable solutions to address the aforementioned problem. The large structure with small thickness floating on a sea is called as pontoon-type VLFS (the pontoon-type VLFS just floats on the sea surface). The pontoon-type VLFS is more flexible when compared with other kinds of offshore structures. Kashiwagi [17], Squire [18] and Watanabe [1] summarised the research on VLFSs in their review articles. Initially, VLFSs were analysed as a beam (2D) by considering Euler–Bernoulli’s beam theory. Researchers have analysed the VLFS as thick and thin plates. For the analysis of thin plate, they have considered classical thin plate theory and Mindlin’s theory for the analysis of thick plates. The study on hinge connections was carried out by [8–21]. Initially, equations are derived to relate the displacement of the plate and velocity potential. The first equation is derived from the equation of motion for the plate and is solved by Finite Element Method (FEM) to extract the displacement of the floating structure. By using BIE, the water wave theory has been solved and it relates to the elastic motions of floating plate and velocity potential [22]. Kashiwagi [2] described the modal expansion method, and he concluded to expand the plate modes as sum of the modal functions. Mode for free plate vibrations was derived by Meylan [23, 24]. By considering two-module hinged flexible structure, the dry natural oscillations were derived by [25]. In direct methods [26–29], the equations were solved directly without expanding them. Various authors [8, 14, 19–21] used the method of modal expansion to solve the hinged elastic floating plate. Generally, direct method is used to solve the complicated geometries, and to solve simple geometries, modal expansion method is adopted [13, 14]. In the literature available, it is concluded that the plate equation of motion is solved by Finite Element Method; whereas, the water wave equation is solved by Boundary Element Method or Higher Order Boundary Element Method. The hybrid model consisting of FEM–BEM has been developed by many researchers, for example [12–18, 30]. To reduce the deflection of the floating structure, vertical barriers were attached by the [31]. Skene [32] studied the overwash on the thin plate by using the nonlinear shallow water wave equation. However, it is learnt that two different modal functions have been used for FEM and BEM, and the order of FEM was higher than that of BEM. Wang [22] developed the HOBEM to overcome the difference in modal functions between FEM and BEM. Wang [22] used HOBEM especially for short wavelengths. The direct method has been employed in the present study as adopted by other researchers [4–8]. To discretise the elastic plate, FEM has been used, and to discretise the water wave, BEM has been adopted. A hybrid FEM–BEM model is developed to capture the vertical deflection. Kashiwagi [17] and Wang [22] used different basis functions in their developed hybrid FEM–BEM model. The proposed developed model has the



ability to analyse any random shapes (Cartesian coordinate system). The modified Green's function has been adopted in the present numerical model, and the obtained results are compared and validated with the results obtained by Wang [22]. Based on the number of panels per plate and integration points, the error has been calculated. The time taken to simulate the vertical deflection/elastic motions and convergence has been discussed in the present work.

## 2 Mathematical Formulation

This thesis deals with the analysis of hydroelastic behaviour of VLFS and its response to incident water waves. The primary objective of the study is to describe the motion of the plate and its response to the water waves. The behaviour of VLFS has been analysed by considering the frequency domain.

Figure 1 shows the rectangular geometry and coordinate system of the floating elastic plate. The plate occupies (covered) a certain part of the water surface which is denoted by  $S_B$ .  $S_F$ ,  $S_\infty$  and  $S_G$  to represent the open free surface, open free surface towards infinity and seabed, respectively. The vertical coordinate  $z$  points upwards with the water surface at zero and seafloor at  $z=0$ .  $x$  and  $y$  are the horizontal coordinates and are denoted by the vector  $X$ . The plate floats freely on the water surface with small draft and is continuously encountered by the incoming waves with different angles.

### 2.1 Equation of Motion for Elastic Plate

The parameters considered in the general problem are as follows: The floating plate which has the density  $\rho_i$  is considered to have the total length  $L$ , breadth  $B$  and thickness  $t$ , which freely floats on the water surface over a constant (flatbed) water depth  $h$ , wavelength  $\lambda$ , wave frequency  $\omega$  and density  $\rho_w$ . The structure is assumed to be elastic, homogeneous and isotropic in nature with  $D$  and  $\nu$  as flexural rigidity and Poisson's ratio, respectively. To satisfy the Laplace equation, fluid is assumed to be ideal, irrotational, inviscid, isotropic and homogeneous in nature. With angular frequency  $\omega$ , the incident wave is assumed to be coming continuously with an angle  $\theta$ . The equation of motion of elastic plate [Eq. (1)] can be solved with boundary conditions as mentioned in Eq. (2).

$$D\nabla^4 W + \rho_i h \frac{\partial^2 W}{\partial t^2} = P \quad (1)$$

with boundary conditions

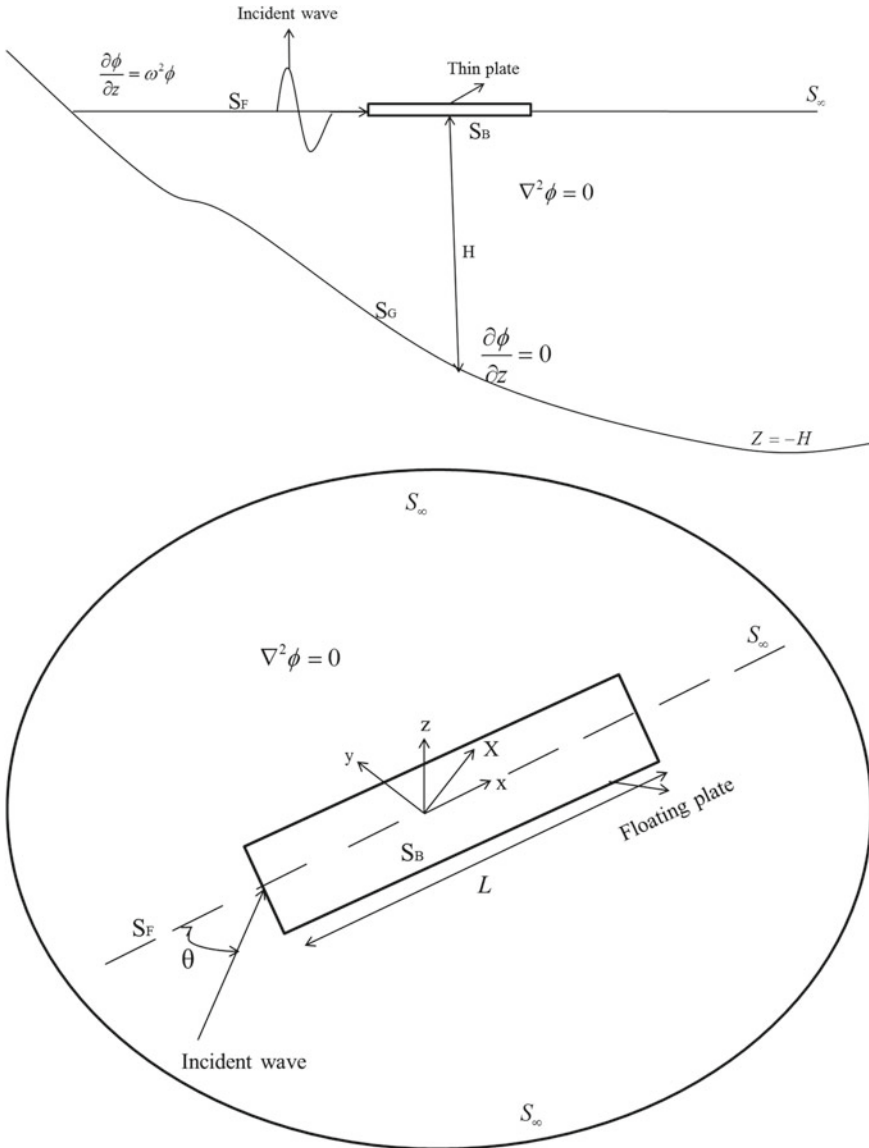


Fig. 1 Schematic diagram of floating structure

$$\frac{\partial^2 W}{\partial n^2} + \nu \frac{\partial^2 W}{\partial s^2} = 0 \quad \text{and} \quad \frac{\partial^3 W}{\partial n^3} + (2 - \nu) \frac{\partial^3 W}{\partial s^3} = 0 \quad (2)$$

Plate displacement is denoted by  $W(x, y, z)$ , pressure of the water surface following up on the plate is indicated by  $P$ , and  $n, s$  signify the normal and tangential directions individually.

$$P = -\rho g w - \rho \frac{\partial \phi}{\partial t} \Big|_{z=0} \quad (3)$$

Further, Eqs. (1) and (3) are equated to get the fluid plate interaction.

$$D\nabla^4 W + \rho_i h \frac{\partial^2 W}{\partial t^2} = -\rho \frac{\delta \phi}{\delta t} \Big|_{z=0} - \rho g W \quad (4)$$

$\phi(x, y, z, \lambda)$  denotes the velocity potential of water,  $\rho_w$  denotes density of the water,  $\lambda$  is the wavelength, and  $g$  is the gravitational acceleration constant. The variables are non-dimensionalised and are represented as follows,

$$\bar{x} = \frac{x}{L}, \quad \bar{y} = \frac{y}{L}, \quad \bar{z} = \frac{z}{L}, \quad \bar{w} = \frac{w}{L}, \quad \bar{t} = t\sqrt{\frac{y}{L}} \quad \text{and} \quad \phi = \frac{\phi}{L\sqrt{xy}}$$

where  $L$  is the longest dimension of the arbitrary shape. Substituting dimensionless variables in Eq. (4), it is modified as follows

$$\beta \nabla \bar{W} + \gamma \frac{\partial^2 \bar{W}}{\partial \bar{t}^2} = -\frac{\delta \bar{\phi}}{\delta \bar{t}} \Big|_{z=0} - \bar{W} \quad (5)$$

where the constants

$$\beta \text{ (Stiffness)} = \frac{D}{\rho L^4 g} \quad \text{and} \quad \gamma \text{ (Mass)} = \frac{\rho_i h}{\rho L}.$$

### 2.1.1 Equation of Motion for Fluid–Structure Interaction

The fluid–structure interaction problem can be considered at a single frequency which allows to represent the time dependence by  $\exp(i\omega t)$ , where  $i$  is the imaginary number and  $\omega$  is the angular frequency. Thus, the displacement and potential can be presented as the real parts of complex function as

$$\bar{W}(\bar{x}, \bar{y}, \bar{t}) = \text{Re}[w(\bar{x}, \bar{y})e^{-i\omega \bar{t}}]$$

$$\bar{\phi}(\bar{x}, \bar{y}, \bar{z}, \bar{t}) \Big|_{z=0} = \text{Re}[\phi(\bar{x}, \bar{y})e^{-i\omega \bar{t}}]$$

By substituting the above equations in Eq. (5) and omitting  $e^{i\omega t}$ , Eq. (5) becomes

$$\beta \nabla^4 w(\bar{x}, \bar{y}) - \omega^2 \gamma w(\bar{x}, \bar{y}) = i\omega \phi(\bar{x}, \bar{y}) - w(\bar{x}, \bar{y}) \quad (6)$$

Equation (6) is stated as the equation of motion for the plate.

The single frequency velocity potential of water must satisfy the Laplace equation.

$$\nabla^2 \phi = 0, \quad -\infty < x < 0 \quad (7a)$$

$$\frac{\partial \phi}{\partial z} = 0, \quad z = -H \quad \text{or} \quad z = -\infty \quad (7b)$$

$$\frac{\partial \phi}{\partial z} = -i\omega w, \quad z = 0, \quad X \in S_B \quad (7c)$$

$$\frac{\delta \phi}{\delta z} - \omega^2 \phi = 0, \quad z = 0, \quad X \in S_F \quad (7d)$$

The wave velocity potential must also satisfy the Sommerfeld radiation condition as  $|X| \rightarrow \infty$

$$\lim_{x \rightarrow 0} \sqrt{|x|} \left( \frac{\partial}{\partial |x|} - i\omega^2 \right) (\phi - \phi^{in}) = 0 \quad (8)$$

It is assumed that the incident velocity potential is a plane wave and is given by,

$$\phi^{in} = \frac{A}{\omega} e^{ik(x \cos \theta + y \sin \theta)e^{kz}}, \quad \text{for infinite depth} \quad (9)$$

$$\phi^{in} = \frac{A}{\omega} e^{ik(x \cos \theta + y \sin \theta)} \frac{\cosh k(z+H)}{\cosh kH}, \quad \text{for finite depth} \quad (10)$$

$$\frac{\omega^2}{g} = k \tanh kH$$

Relating Eqs. (7a-d) with Eq. (8) and transferring them into an integral equation using Green's function.

The free surface Green function  $G(X; \xi)$  satisfy

$$\nabla_X^2 G = 0$$

$$\frac{\partial G}{\partial z} - \omega^2 G = -\delta(X - \xi), \quad z = 0$$

$$\frac{\partial G}{\partial z} = 0, \quad z = -H \quad \text{or} \quad z = -\infty$$

where  $\xi = (\xi, \eta)$ . This gives us

$$\phi(x) = \phi^{in} + \int_{\Delta} G(X; \xi) (\omega^2 \phi(\xi) + i\omega w(\xi)) dS_{\xi} \quad (11)$$

The driving purpose for finite water depth was derived by John [33] as follows.

$$G(X, \xi) = \frac{-i}{2} \frac{\omega^4 - k^2}{(\omega^4 - k^2)H - \omega^2} \cosh^2(kH) H_0^{(1)}(k|X - \xi|) - \frac{1}{\pi} \sum_{m=1}^{\infty} \frac{k_m^2 + \omega^4}{(k_m^2 + \omega^4)H - \omega^2} \cos^2(k_m H) k_0(k_m |X - \xi|) \quad (12)$$

The Green's function which is modified is related to Meylan [24] and John [33] and is given below. Equation (13) is used in this numerical model.

$$G(X, \xi) = G(X, \xi) - \left[ \frac{H_0^{(1)}}{2\pi C} \right] (\cosh(kH)H)^2 \quad (13)$$

where,

$$C = \frac{H}{2} \left[ \frac{1 + (\sin(2\cosh(CH)H))}{2\cosh(CH)H} \right].$$

$J_0$  Bessel function with first kind and of order zero

$K_0$  Bessel function with second kind and of order zero

$H_0^{(1)}$  Hankel function with order zero

$\underline{H_0}$  Struve function with order zero

By expressing the integral operator

$$Gf(X) = \int_{\Delta} G(X, \xi) f(\xi) d\xi$$

in Eq. (11) and rewriting it as,

$$\phi(X) = \phi^{in}(X) + \omega^2 G\phi(X) + \lambda\omega G(X) \quad (14)$$

### 3 Discretisation of Plate (FEM)

Equation of motion (Eq. 6) for plate and water (Eq. 14) will be discretised using FEM and BEM. Plate equation of motion is discretised by FEM, and three degrees of freedom system have been adapted to each node; they are ( $w$ ) vertical displacement, ( $x$ ) rotational degree along  $x$  and ( $y$ ) rotational degree along  $y$ .

$$w(x) = N_d(X) \hat{w}_d, \quad X \in S_d \quad (15)$$

The basis vector is defined by

$$N_d(X) = [N_{11}N_{12}N_{13}N_{21}N_{22}N_{23}N_{31}N_{32}N_{33}N_{41}N_{42}N_{43}] \quad (16)$$

$$N_{j1} = N_{j1}(\hat{x}, \hat{y}), N_{j2} = N_{j2}(\hat{x}, \hat{y}), N_{j3} = N_{j3}(\hat{x}, \hat{y}), \\ (j = 1, 2, 3, 4)$$

and are given by

$$N_{j1}(\hat{x}, \hat{y}) = \frac{1}{8}(1 + \hat{x}_j\hat{x})(1 + \hat{y}_j\hat{y})(2 + \hat{x}_j\hat{x} + \hat{y}_j\hat{y} - \hat{x}^2 - \hat{y}^2) \\ N_{j2}(\hat{x}, \hat{y}) = \frac{a}{16}(1 + \hat{x}_j\hat{x})(\hat{y}_j + \hat{y})(\hat{y}^2 - 1) \\ N_{j3}(\hat{x}, \hat{y}) = -\frac{a}{16}(\hat{x}_j + \hat{x})(\hat{x}^2 - 1)(1 + \hat{y}_j\hat{y}) \quad (17)$$

The vector  $\hat{w}_d$  is a vector of elements, which is given by

$$\hat{w}_d = \left[ w_i^{(d)} \frac{\partial w_1^{(d)}}{\partial x} \frac{\partial w_1^{(d)}}{\partial y} w_i^{(d)} \frac{\partial w_2^{(d)}}{\partial x} \frac{\partial w_2^{(d)}}{\partial y} w_j^{(d)} \frac{\partial w_3^{(d)}}{\partial x} \frac{\partial w_3^{(d)}}{\partial y} w_4^{(d)} \frac{\partial w_4^{(d)}}{\partial x} \frac{\partial w_4^{(d)}}{\partial y} \right] \quad (18)$$

where,

$$w_j^{(d)} = w(x_j), \quad \frac{\partial w_j^{(d)}}{\partial x} = \frac{\partial}{\partial x} w(X_j) \quad \text{and} \quad \frac{\partial w_j^{(d)}}{\partial y} = \frac{\partial}{\partial y} w(X_j).$$

Now, both the basis vector  $N_d$  and constant vector  $\hat{w}_d$  are of dimensions  $1 \times 12$  and  $12 \times 1$ , respectively. This is of the manner  $|ZX|$ . We expand the potential in an identical manner to the displacement, i.e.

$$\phi(x) = N_d(X)\hat{\phi}_d, \quad X \in S_d \quad (19)$$

where  $\hat{\phi}_d$  is vector of constant and is given by,

$$\hat{\phi}_d = \left[ \phi_1^{(d)} \frac{\partial \phi_1^{(d)}}{\partial x} \frac{\partial \phi_1^{(d)}}{\partial y} \phi_2^{(d)} \frac{\partial \phi_2^{(d)}}{\partial x} \frac{\partial \phi_2^{(d)}}{\partial y} \phi_3^{(d)} \frac{\partial \phi_3^{(d)}}{\partial x} \frac{\partial \phi_3^{(d)}}{\partial y} \phi_4^{(d)} \frac{\partial \phi_4^{(d)}}{\partial x} \frac{\partial \phi_4^{(d)}}{\partial y} \right]$$

where,

$$\phi_j^{(d)} = \phi(x_j), \quad \frac{\partial \phi_j^{(d)}}{\partial x} = \frac{\partial}{\partial x} \phi(X_j) \quad \text{and} \quad \frac{\partial \phi_j^{(d)}}{\partial y} = \frac{\partial}{\partial y} \phi(X_j)$$

Likewise,  $\phi^{in}(X)$  can be written as

$$\phi^{in}(X) = N_d(X)\hat{\phi}_d^{in} \quad (20)$$

where

$$\hat{\phi}_d^{in} = \left[ \phi_1^{in} \frac{\partial \phi_1^{in}}{\partial x} \frac{\partial \phi_1^{in}}{\partial y} \quad \phi_2^{in} \frac{\partial \phi_2^{in}}{\partial x} \frac{\partial \phi_2^{in}}{\partial y} \quad \phi_3^{in} \frac{\partial \phi_3^{in}}{\partial x} \frac{\partial \phi_3^{in}}{\partial y} \quad \phi_4^{in} \frac{\partial \phi_4^{in}}{\partial x} \frac{\partial \phi_4^{in}}{\partial y} \right]^T$$

### 3.1 Plate Equation

Representing the potential and displacement in the finite element basis function, Eq. (6) will be solved. Further, Eq. (6) will be reduced to form the equivalent equation which will be applied to analyse the panels. Equations (16) and (19) are substituted in Eq. (6) to eliminate  $w(x)$  and  $\phi(x)$

$$\beta \nabla^4 (N_d \hat{w}_d) - \omega^2 \gamma (N_d \hat{w}_d) = i\omega (N_d \hat{\phi}_d) - (N_d \hat{w}_d).$$

$$\begin{aligned} & \int_{\Delta_d} \left\{ \beta \left[ \frac{\partial^2 N_d^T}{\partial x^2} \frac{\partial^2 N_d}{\partial x^2} + \frac{\partial^2 N_d^T}{\partial y^2} \frac{\partial^2 N_d}{\partial y^2} \right. \right. \\ & \left. \left. + 2(1-\nu) \frac{\partial^2 N_d^T}{\partial x \partial y} \frac{\partial^2 N_d}{\partial x \partial y} + 2\nu \frac{\partial^2 N_d}{\partial x^2} \frac{\partial^2 N_d}{\partial y^2} \right] \right\} dX^{(d)} \hat{w}_d \\ & - \int_{\Delta_d} (\omega^2 \gamma N_d^T N_d) dX^{(d)} \hat{w}_d = \int_{\Delta_d} [i\omega N_d^T N_d \hat{\phi}_d - N_d^T N_d \hat{w}_d] dX^{(d)} \quad (21) \end{aligned}$$

Now,

$$\langle N_d, N_d \rangle_{\Delta_d} = \int_{\Delta_d} N_d^T N_d dX^{(d)} \text{ is the mass matrix introduced by Meylan [24]}$$

$$\text{where, } \langle N_d, N_d \rangle_{\Delta_d} = [m]_d \quad (22)$$

$$\begin{aligned} & \int_{\Delta_d} \left[ \frac{\partial^2 N_d^T}{\partial x^2} \frac{\partial^2 N_d}{\partial x^2} + \frac{\partial^2 N_d^T}{\partial y^2} \frac{\partial^2 N_d}{\partial y^2} + 2(1-\nu) \frac{\partial^2 N_d^T}{\partial x \partial y} \frac{\partial^2 N_d}{\partial x \partial y} \right. \\ & \left. + 2\nu \frac{\partial^2 N_d}{\partial x^2} \frac{\partial^2 N_d}{\partial y^2} \right] dX^{(d)} = [k]_d \quad (23) \end{aligned}$$

where  $[k]_d$  is the stiffness matrix and  $[m]_d$  is the mass matrix. Equation (21) will be simplified by including mass and stiffness matrices.

$$\beta [k]_d \hat{w}_d - \omega^2 \gamma [m]_d \hat{w}_d = i\omega [m]_d \hat{\phi}_d - [m]_d \hat{w}_d \quad (24)$$

### 3.2 The Water Wave Equations

In HOBEM, the fluid potential is expressed as a function by using the nodal potentials. Substituting Eqs. (19) and (20) into Eq. (14), we obtain

$$N_d(X)\widehat{\phi}_d = N_d\widehat{\phi}_d^{in} + \omega^2 \sum_{x=1}^P (G_{de}N_e)\widehat{\phi}_e + i\omega \sum_{x=1}^P (G_{de}N_e)\widehat{w}_e \quad (25)$$

where

$$G_{de}N_e = \int_{\Delta_e} G(X; \xi)N_e(\xi)d\xi \quad (26)$$

Following Wang [22], we apply an inner product  $N_d$  to both sides of Eq. (25) resulting in,

$$\begin{aligned} \langle N_d, N_d \rangle_{\Delta_d} \widehat{\phi}_d &= \langle N_d, N_d \rangle_{\Delta_d} \widehat{\phi}_d^{in} + \omega^2 \sum_{e=1}^P \langle N_d, (G_{de}N_e) \rangle_{\Delta_d} \widehat{\phi}_e \\ &+ i\omega \sum_{e=1}^P \langle N_d, (G_{de}N_e) \rangle_{\Delta_d} \widehat{w}_e \end{aligned} \quad (27)$$

Analogous to the definitions of the mass and stiffness matrix, the Green's matrix  $[G]_{de}$  is defined as

$$[g]_{de} = \int_{\Delta_e} N_d^T(G_{de}N_e)dX^{(d)} \quad (28)$$

$$[m]_d \widehat{\phi}_d = [m]_d \widehat{\phi}_d^{in} + \omega^2 \sum_{e=1}^P [g]_{de} \widehat{\phi}_e + i\omega \sum_{e=1}^P [g]_{de} \widehat{w}_e, \quad (29)$$

Equation (29) is the solution for the waves with solitary panel. The answer to Green's matrix will be examined in Sect. 4.

## 4 Green's Matrix Solution

The calculation of  $[G]_{de}$  is separated into two cases, depending on whether  $d=e$  or not. This is because the free surface Green's function is singular at  $|X - \xi| = 0$ . Since  $X$  lies in element, the singularity only occurs when  $d=e$ . We also notice from Eq. (28) that Green's function occurs in the integral  $G_{de}N_e$  and therefore we only need to separate the solution  $G_{de}N_e$  into the singular and the non-singular cases.



By evaluating the integral  $G_{de}N_e$  using a numerical integration method, i.e. Gauss quadrature, we obtain

$$G_{de}N_e = \int_{\Delta_e} G(X; \xi) N_e(\xi) d\xi = \sum_{j=1}^M v_j G(X; \xi_j) N_e(\xi_j) \quad X \in \Delta_d, \quad \xi_j \in \Delta_e \quad (30)$$

where  $\xi_j$  and  $v_j$  are sets of  $M$  integration points and their corresponding weights. Note that  $\xi_j$  needs to be determined from the corresponding Gauss points  $r_j(r_j, s_j)$  by isoparametric coordinate transformation using basis function.

$$\int_{\Delta_d} N_d^T(G_{de}N_e) dX^{(d)} = \sum_{i=1}^N u_i N_d^T(X_i) (G_{de}N_e), \quad X_i \in \Delta_d \quad (31)$$

where  $x_j$  and  $u_j$  are sets of  $N$  integration points and their corresponding weights. By combining Eqs. (30) and (31), the numerical set of Green's matrix  $[G]_{de}$  is given by,

$$[g]_{de} = \sum_{i=1}^N u_i N_d^T(x_i) \sum_{j=1}^M v_j G^{(ij)} N_e(\xi_j) \quad (32)$$

where,

$$x_i \in \Delta_e, \quad \xi_j \in \Delta_e \text{ and } G^{(ij)} = G(X_i; \xi_j).$$

When  $X_i$  coincides  $\xi_j$  singularity occurs; thus to avoid this, Eq. (32) is solved. With the use of points like  $(x_i)$  and  $(\xi_j)$ , Eq. (32) can be solved. It is advisable to use more number of integration points when the model encounters singularity. Hamamoto [34] used the Coordinate Transformation Method to calculate the singular integral, and it is the most widely used method. Hence, in the present work, Coordinate Transformation Method has been adopted. The same set of integration points is used to overcome the singularity and to develop a non-singular Green's function.

Further, Eq. (32) is given as,

$$[g]_{de} = \begin{cases} N_1 G_1 N_2 & \text{if } d = e \\ N_1 G_2 N_1^T & \text{if } d \neq e \end{cases} \quad (33)$$

where  $G_j$  is  $N \times M$  rectangular matrix of the form

$$G_1 = \begin{bmatrix} G^{(11)} & G^{(12)} & \dots & G^{(1N)} \\ G^{(21)} & G^{(22)} & \dots & G^{(2N)} \\ \dots & \dots & \dots & \dots \\ G^{(N1)} & G^{(N2)} & \dots & G^{(NN)} \end{bmatrix} \quad (34)$$

$G_2$  is  $N \times N$  square matrix of the form

$$G_2 = \begin{bmatrix} G^{(11)} & G^{(12)} & \dots & G^{(1N)} \\ G^{(21)} & G^{(22)} & \dots & G^{(2N)} \\ \dots & \dots & \dots & \dots \\ G^{(N1)} & G^{(N2)} & \dots & G^{(NN)} \end{bmatrix} \quad (35)$$

$N_1$  is  $12 \times N$  matrix.

$$N_1 = \begin{bmatrix} u_1 N_d^{(1)T} & u_2 N_d^{(2)T} & \dots & u_N N_d^{(N)T} \end{bmatrix}$$

$N_2$  is  $M \times 12$  matrix

$$N_2 = \begin{bmatrix} v_1 N_d^{(1)T} \\ v_2 N_d^{(2)T} \\ \vdots \\ v_N N_d^{(N)T} \end{bmatrix} \quad (36)$$

## 5 Results and Discussions

The proposed model is capable of calculating the hydroelasticity of floating thin plate at any arbitrary depth and shape. Results of Wang [22] are used to validate and compare the proposed numerical model. Further, the modelling capacity is also demonstrated for finite and infinite water depths. The simulation time is expected to reduce, as the developed model consists of same basis functions in FEM and BEM. The accuracy of the proposed model is likely to be increased as the integration points and panels increase (Table 1).

Time period required to simulate the elastic motion of the floating thin plate has been noted. Initially, the model is analysed for 100 panels, and further it has been increased to 900 panels by considering  $N = M = 4$  as integration points.

**Table 1** Parameters

Length ( $L$ )	300 m
Breadth ( $B$ )	60 m
Height ( $H$ )	2 m
Draft ( $D$ )	0.5 m
Plate density ( $\rho_i$ )	922.5 kg/m <sup>3</sup>
Wavelength ( $\lambda$ )	2 m
Dimensionless rigidity of the plate ( $\beta$ )	$5.828 \times 10^{-3}$
Mass constant ( $\nu$ )	$1.507 \times 10^{-3}$

The reliance of the proposed numerical model is seen to be zero when the panel number reaches 900. Subsequently, the error is found to be nil as the number of panel reaches 900. Based on the dependency of the panels, the error is assessed. Error is calculated for the wave angle of  $\theta = 0$  and described in Table 2.

Figure 2a–d shows the vertical deflection for different number of panels with constant wave angle  $\theta = 0$ .

It has been observed that the time required for the simulation increases as the number of panels increases and the error in the elastic motions/deflection profile decreases.

Further, by keeping the integration point and panel numbers as constant, i.e.  $N = M = 4$  and 900, the simulation of vertical deflection has been captured and shown in Fig. 3a–d for different wave angles of attack ( $\theta = 0, \pi/2, \pi/4$  and  $\pi/6$ ). It can be observed that the vertical deflections along the corner of the plates are captured efficiently.

For different wave angles, the simulation time has been captured for number of panels varying from 100 to 900 and it has been presented in Tables 3, 4, 5 and 6.

Further, comparison between  $N=M=2$  and  $N=M=4$  has been carried out. The simulation time and error in the model for different wave angles ( $\theta = 0, \pi/2, \pi/4$  and  $\pi/6$ ) by varying panel numbers from 100 to 900 are shown in Tables 7, 8, 9 and 10. For  $N=M=2$ , the error obtained is slightly higher than that of  $N=M=4$ . However, the model simulation time is three times lesser for  $N=M=2$  (Fig. 4).

The analysis of the proposed numerical model at finite water depth is compared with the results of Wang [22], and the results are reported here.

The vertical deflections of the plate encountering different angles of waves are shown in Fig. 5 and are compared with Wang [22]. The corners of the plate are captured elegantly over Wang [22]. It is due to the use of modified Green’s function. According to the practical sense, the smooth surface profile can be observed in Fig. 5.

**Table 2** Error and convergence time of the model for angle of attack  $\theta = 0$

Panels	Time (s)	Error
100	66.144	0.3959
225	334.032	0.1013
400	1051.107	0.0216
625	2532.635	0.0111
900	5742.102	0.0010
1089	8932.165	0.0010

**Table 3** Error and convergence time of the model for angle of attack  $\theta = 0$

Panels	Time (s)	Error
100	66.144	0.4254
225	336.144	0.1365
400	1051.107	0.0498
625	2532.635	0.0131
900	5712.012	0

**Table 4** Error and convergence time of the model for angle of attack  $\theta = \pi/2$

Panels	Time (s)	Error
100	67.253	0.4125
225	326.757	0.1296
400	1011.846	0.0496
625	2537.883	0.0112
900	5687.23	0

**Table 5** Error and convergence time of the model for angle of attack  $\theta = \pi/4$

Panels	Time (s)	Error
100	65.46	0.4086
225	328.028	0.1340
400	1060.461	0.0442
625	2695.860	0.0127
900	5692.205	0

**Table 6** Error and convergence time of the model for angle of attack  $\theta = \pi/6$

Panels	Time (s)	Error
100	65.740	0.4108
225	326.054	0.1293
400	1050.88	0.0435
625	2640.409	0.0126
900	5385.264	0

**Table 7** Error and convergence time of the model for angle of attack  $\theta = 0$  and  $N, M=2$

Panels	Time (s)	Error
100	32.841	0.4191
225	113.355	0.1158
400	353.636	0.0316
625	907.434	0.0091
900	1989.565	0

**Table 8** Error and convergence time of the model for angle of attack  $\theta = \pi/2$  and  $N, M=2$

Panels	Time (s)	Error
100	20.182	0.3809
225	103.807	0.1328
400	362.531	0.0442
625	904.001	0.0126
900	1897.6193	0

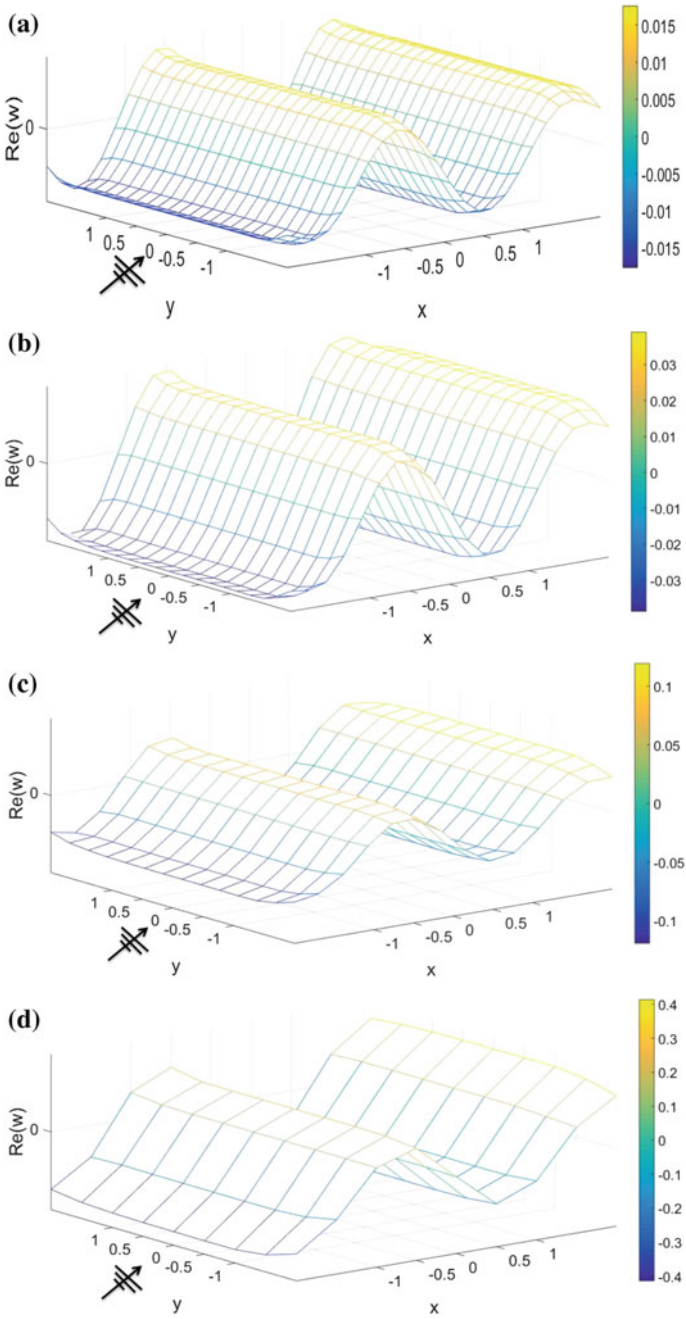
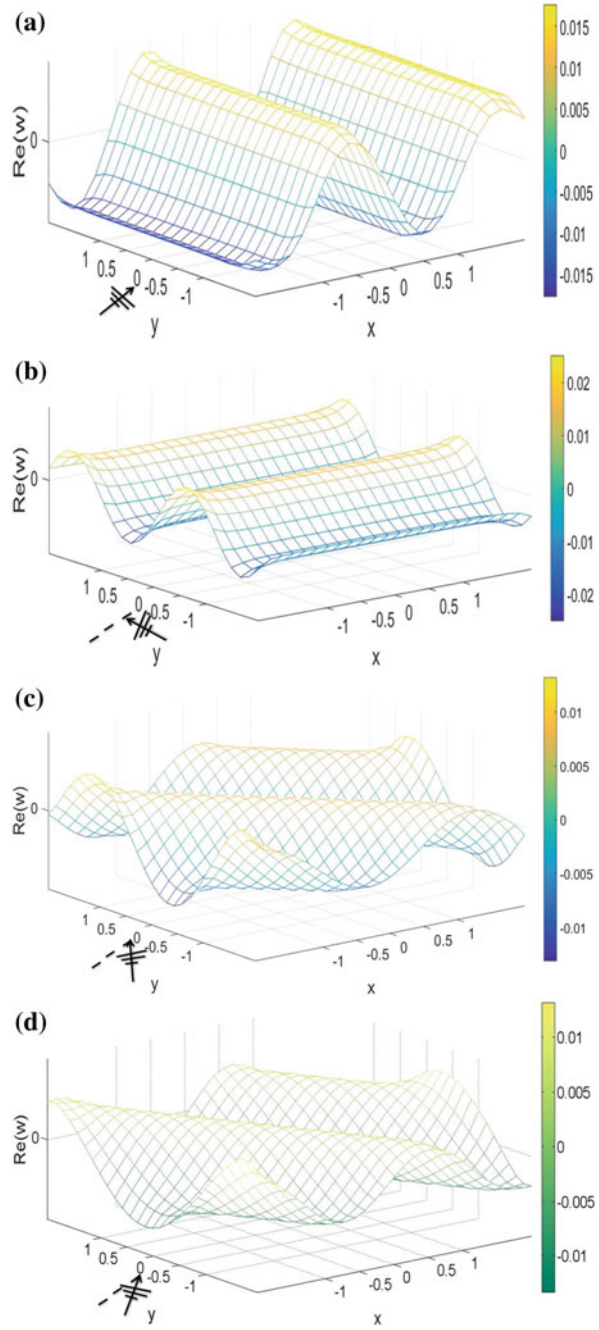


Fig. 2 Elastic motion for different panels: a 625, b 400, c 225 and d 100

**Fig. 3** Elastic motion for different wave angles: **a**  $-0$ , **b**  $-\pi/2$ , **c**  $-\pi/4$  and **d**  $-\pi/6$



**Table 9** Error and convergence time of the model for angle of attack  $\theta = \pi/4$  and  $N, M=2$

Panels	Time (s)	Error
100	21.214	0.4204
225	106.627	0.1386
400	345.691	0.0458
625	961.570	0.0132
900	1872.529	0

**Table 10** Error and convergence time of the model for angle of attack  $\theta = \pi/6$  and  $N, M=2$

Panels	Time (s)	Error
100	20.465	0.4214
225	103.9953	0.1338
400	332.914	0.0451
625	898.959	0.0131
900	1960.811	0

**Table 11** Error and convergence time of the model for angle of attack  $\theta = 0$  and  $N, M=2$

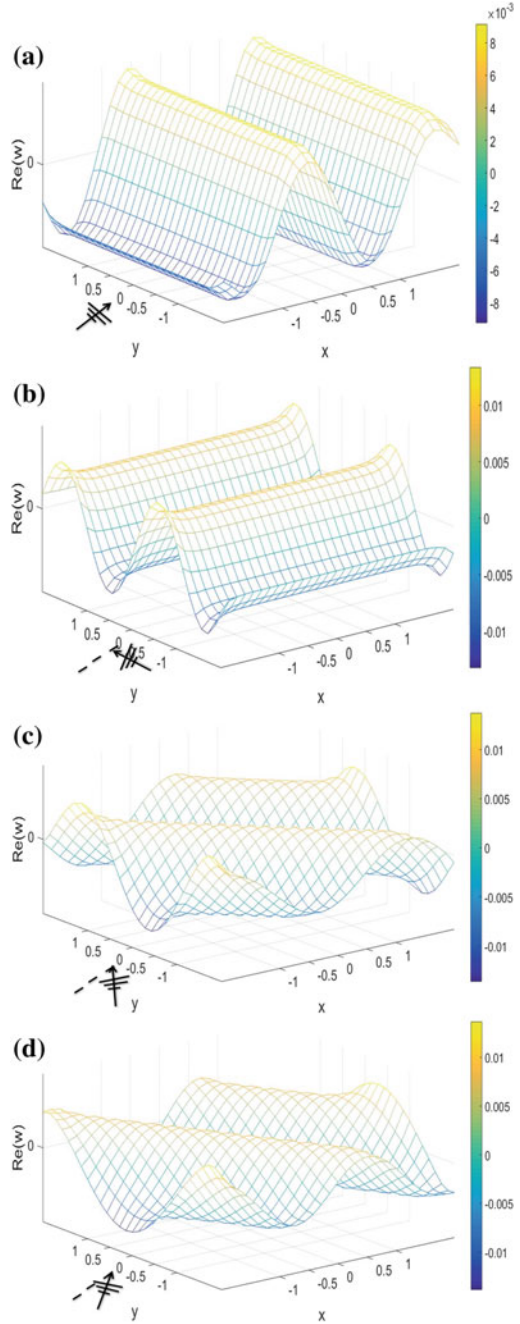
Panels	Present model time (s)	Error	Wang time (s)	Error
100	32.841	0.4191	21.775	0.2357
225	113.355	0.1158	113.354	0.0548
400	353.636	0.0316	369.544	0.0169
625	907.434	0.0091	925.887	0.0044
900	1989.565	0	2036.955	0

**Table 12** Error and convergence time of the model for angle of attack  $\theta = \pi/2$  and  $N, M=2$

Panels	Present model time (s)	Error	Wang time (s)	Error
100	20.182	0.3809	21.047	0.2233
225	103.807	0.1328	108.958	0.0579
400	362.531	0.0442	367.448	0.0803
625	904.001	0.0126	949.028	0.0454
100	1897.6193	0	2144.247	0

The comparison between the present model and Wang [22] for  $N=M=2$  is noted in Tables 11, 12, 13 and 14. It is witnessed in general that the present model takes less time to simulate than that of Wang [22]. There is a considerable saving of time when panels increase from 100 to 900.

**Fig. 4** Elastic motion for different wave angles: **a**  $-0$ , **b**  $-\pi/2$ , **c**  $-\pi/4$  and **d**  $-\pi/6$





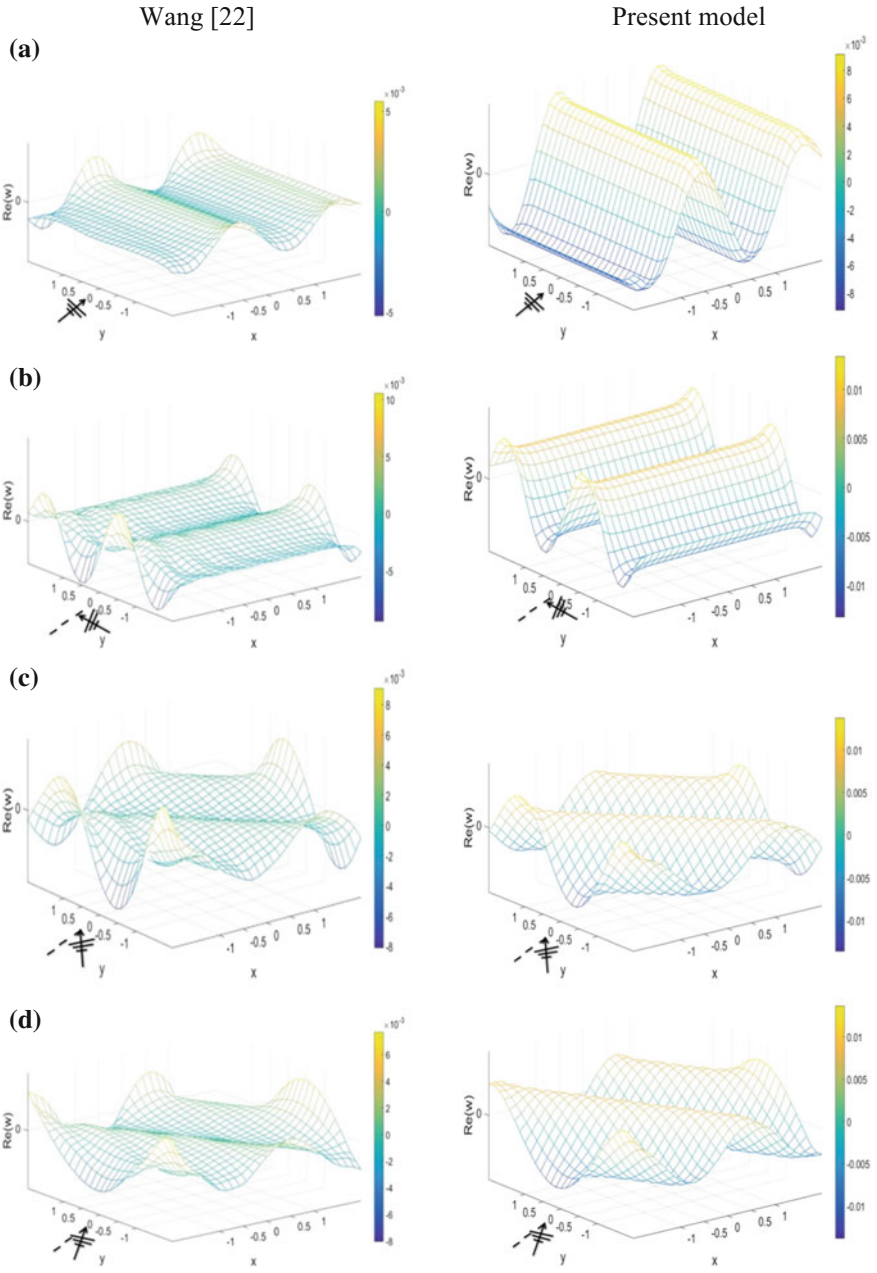


Fig. 5 Elastic motion for different wave angles: a  $-0$ , b  $-\pi/2$ , c  $-\pi/4$  and d  $-\pi/6$  and  $N, M=2$

**Table 13** Error and convergence time of the model for angle of attack  $\theta = \pi/4$  and  $N, M=2$

Panels	Present model time (s)	Error	Wang time (s)	Error
100	21.214	0.4204	20.545	0.2377
225	106.627	0.1386	106.521	0.0793
400	345.691	0.0458	359.234	0.0239
625	961.570	0.0132	945.527	0.0112
100	1872.529	0	2082.876	0

**Table 14** Error and convergence time of the model for angle of attack  $\theta = \pi/6$  and  $N, M=2$

Panels	Present model time (s)	Error	Wang time (s)	Error
100	20.465	0.4214	20.655	0.2357
225	103.9953	0.1338	110.216	0.0542
400	332.914	0.0451	380.003	0.0169
625	898.959	0.0131	978.376	0.0044
100	1960.811	0	2134.043	0

## 6 Conclusions

The developed numerical model has been analysed and validated with the available literature, and it shows good agreement. In the oblique wave structure interaction for finite water depth, the simulation time of the model for all the panels in the plate has been carried out for different integration points. As seen in the above section, the final number of panels for a plate is considered to be 900, because after 900 panels the error in the model will be negligible. It is seen that the integration points and number of panels depend inversely on the simulation time. It is also witnessed that as the integration points increase the error is reduced. For integration points  $N, M = 2$ , the error in the deflection is on the higher side as compared with  $N, M = 4$  and it is seen in the section above. From the Tables 3, 4, 5, 6, 7, 8, 9 and 10, it is seen how the model varies with respect to simulation time. Further, the model developed by Wang [22] has been used to compare the results with the developed model by considering the integration points as  $N, M = 2$ . The model developed by Wang is similar to the present developed model but it differs in the application of the Green’s function and is given in Eq. (13). Developed numerical model gives the better result in the case of finite water depth when compared with Wang [22]. In the present model, the error is without any fluctuations and decreases in the proper intervals.

Results obtained by Wang [22] are used to validate the developed numerical model. The present model shows better results at finite water depth when compared with Wang [22]. The error reduces in proper intervals without any fluctuation for the developed numerical model; whereas, for Wang [22] it fluctuates. The results

obtained by the proposed numerical model capture the better results at the corners of the plate.

## References

1. Watanabe E, Utsunomiya T, Wang CM (2004) Hydroelastic analysis of pontoon-type VLFS: a literature survey. *Eng Struct* 26(2):245–256. <https://doi.org/10.1016/j.engstruct.2003.10.001>
2. Kashiwagi M (1998) A B-spline Galerkin scheme for calculating the hydroelastic response of a very large floating structure in waves. *J Mar Sci Technol* 3(1):37–49. <https://doi.org/10.1007/BF01239805>
3. Wu C, Watanabe E, Utsunomiya T (1995) An eigenfunction expansion-matching method for analyzing the wave-induced responses of an elastic floating plate. *Appl Ocean Res* 17(5):301–310. [https://doi.org/10.1016/0141-1187\(95\)00023-2](https://doi.org/10.1016/0141-1187(95)00023-2)
4. Kim JG, Cho SP, Kim KT, Lee PS (2014) Hydroelastic design contour for the preliminary design of very large floating structures. *Ocean Eng* 78:112–123. <https://doi.org/10.1016/j.oceaneng.2013.11.006>
5. Kim KT, Lee PS, Park KC (2013) A direct coupling method for 3D hydroelastic analysis of floating structures. *Int J Numer Meth Eng* 96(13):842–866. <https://doi.org/10.1002/nme.4564>
6. Taylor RE (2007) Hydroelastic analysis of plates and some approximations. *J Eng Math* 58(1):267–278. <https://doi.org/10.1007/s10665-006-9121-7>
7. Shirkol AI, Nasar T, Karmakar D (2016) Wave interaction with Very Large Floating Structure (VLFS) using BEM approach—revisited. *Perspect Sci* 8:533–535. <https://doi.org/10.1016/j.pisc.2016.06.012>
8. Lee CH, Newman JN (2000) An assessment of hydroelasticity for very large hinged vessels. *J Fluids Struct* 14(7):957–970. <https://doi.org/10.1006/jfls.2000.0305>
9. Newman JN (2005) Efficient hydrodynamic analysis of very large floating structures. *Mar Struct* 18(2):169–180. <https://doi.org/10.1016/j.marstruc.2005.07.003>
10. Khabakhpasheva TI, Korobkin AA (2002) Hydroelastic behaviour of compound floating plate in waves. *J Eng Math* 44(1):21–40. <https://doi.org/10.1023/A:1020592414338>
11. Wang CM, Tay ZY, Takagi K, Utsunomiya T (2010) Literature review of methods for mitigating hydroelastic response of VLFS under wave action. *Appl Mech Rev* 63(3):030802. <https://doi.org/10.1115/1.4001690>
12. Riyansyah M, Wang CM, Choo YS (2010) Connection design for two-floating beam system for minimum hydroelastic response. *Mar Struct* 23(1):67–87. <https://doi.org/10.1016/j.marstruc.2010.01.001>
13. Fu S, Moan T, Chen X, Cui W (2007) Hydroelastic analysis of flexible floating interconnected structures. *Ocean Eng* 34(11):1516–1531. <https://doi.org/10.1016/j.oceaneng.2007.01.003>
14. Gao RP, Tay ZY, Wang CM, Koh CG (2011) Hydroelastic response of very large floating structure with a flexible line connection. *Ocean Eng* 38(17):1957–1966. <https://doi.org/10.1016/j.oceaneng.2011.09.021>
15. Kim BW, Kyoung JH, Hong SY, Cho SK (2005) Investigation of the effect of stiffness distribution and structure shape on hydroelastic responses of very large floating structures. In: *The fifteenth international offshore and polar engineering conference, International Society of Offshore and Polar Engineers*
16. Kim BW, Hong SY, Kyoung JH, Cho SK (2007) Evaluation of bending moments and shear forces at unit connections of very large floating structures using hydroelastic and rigid body analyses. *Ocean Eng* 34(11):1668–1679. <https://doi.org/10.1016/j.oceaneng.2006.10.018>
17. Kashiwagi M. (2000) Research on hydroelastic responses of VLFS: recent progress and future work. *Int J Offshore Polar Eng* 10(02). doi: ISOPE-00-10-2-081
18. Squire VA, Dugan JP, Wadhams P, Rottier PJ, Liu AK (1995) Of ocean waves and sea ice. *Annu Rev Fluid Mech* 27(1):115–168. <https://doi.org/10.1146/annurev.fl.27.010195.000555>

19. Loukogeorgaki E, Michailides C, Angelides DC (2012) Hydroelastic analysis of a flexible mat-shaped floating breakwater under oblique wave action. *J Fluids Struct* 31:103–124. <https://doi.org/10.1016/j.jfluidstructs.2012.02.011>
20. Michailides C, Angelides DC (2012) Modeling of energy extraction and behavior of a Flexible Floating Breakwater. *Appl Ocean Res* 35:77–94. <https://doi.org/10.1016/j.apor.2011.11.004>
21. Bathe KJ (1996) Finite element procedure. Prentice Hall, New York
22. Wang CD, Meylan MH (2004) A higher-order-coupled boundary element and finite element method for the wave forcing of a floating elastic plate. *J Fluids Struct* 19(4):557–572. <https://doi.org/10.1016/j.jfluidstructs.2004.02.006>
23. Meylan MH, Squire VA (1996) Response of a circular ice floe to ocean waves. *J Geophys Res-All Ser* 101:8869–8884. <https://doi.org/10.1029/95JC03706>
24. Meylan MH (2002) Wave response of an ice floe of arbitrary geometry. *J Geophys Res: Oceans* 107(C1). <https://doi.org/10.1029/2000jc000713>
25. Sun Y, Lu D, Xu J, Zhang X (2017) A study of hydroelastic behavior of hinged VLFS. *Int J Naval Archit Ocean Eng*. <https://doi.org/10.1016/j.ijnaoe.2017.05.002>
26. Meylan M, Squire VA (1994) The response of ice floes to ocean waves. *J Geophys Res-All Ser* 99:891–900. <https://doi.org/10.1029/93JC02695>
27. Hermans AJ (2000) A boundary element method for the interaction of free-surface waves with a very large floating flexible platform. *J Fluids Struct* 14(7):943–956. <https://doi.org/10.1006/jfls.2000.0313>
28. Yago K, Endo H (1996) Model experiment and numerical calculation of the hydroelastic behavior of matlike VLFS. *VLFS* 96:209–214
29. Pan Y, Sahoo PK, Lu L (2016) Numerical study of hydrodynamic response of mooring lines for large floating structure in South China Sea. *Ships Offshore Struct* 11(7):774–781. <https://doi.org/10.1080/17445302.2015.1066986>
30. Yoon JS, Cho SP, Jiwinangun RG, Lee PS (2014) Hydroelastic analysis of floating plates with multiple hinge connections in regular waves. *Mar Struct* 36:65–87. <https://doi.org/10.1016/j.marstruc.2014.02.002>
31. Yiew LJ, Bennetts LG, Meylan MH, French BJ, Thomas GA (2016) Hydrodynamic responses of a thin floating disk to regular waves. *Ocean Model* 97:52–64. <https://doi.org/10.1016/j.oceanmod.2015.11.008>
32. Skene DM, Bennetts LG, Meylan MH, Toffoli A (2015) Modelling water wave overwash of a thin floating plate. *J Fluid Mech* 777. <https://doi.org/10.1017/jfm.2015.378>
33. John F (1949) On the motion of floating bodies I. *Commun Pure Appl Math* 2(1):13–57. <https://onlinelibrary.wiley.com/doi/abs/10.1002/cpa.3160020102>
34. Hamamoto T, Suzuki A, Fujita KI (1997) Hybrid dynamic analysis of large tension leg floating structures using plate elements. In: The seventh international offshore and polar engineering conference, International Society of Offshore and Polar Engineers

# Hydroelasticity Analysis of a Container Ship Using a Semi-analytic Approach and Direct Coupling Method in Time Domain



Debasmit Sengupta, Sumit Kumar Pal, Ranadev Datta and Debabrata Sen

**Abstract** A three-dimensional semi-analytic method in time domain is used to predict the hydroelastic effects due to wave-induced loads on a container ship. A container ship with zero forward speed has been taken to perform the hydroelastic analysis. The pertinence of the proposed method is verified with the results obtained from the direct coupling between FEM and BEM in time domain. In both the approaches, the proposed structure has been modelled as an Euler–Bernoulli beam. However, in case of the semi-analytic approach, the container ship has been assumed as an equivalent rectangular barge with uniformly distributed mass. The hydrodynamic forces are obtained in time domain through impulse response function. The Duhamel integral is employed in order to get the structural deflections, velocity, etc. The hydrodynamic and structural part is then fully coupled in time domain through modal analysis to capture the proper phenomena. On the other hand, in case of the direct coupling, a 3D time domain lower order panel method is used for the solution of the hydrodynamic problem. Structural responses, shear forces and bending moments are calculated at different sections of the ship. The validation of the computed results is confirmed as satisfactory agreement is found between these two methods. It may be noted that the present semi-analytic technique appears to be time efficient, robust and could be a very useful tool in predicting the hydroelastic effects on a container ship in terms of shear force, bending moment, structural deflection at initial design stage.

**Keywords** Hydroelasticity · Container ship · Impulse response function  
Duhamel integral · BEM–FEM

---

D. Sengupta (✉) · S. K. Pal · R. Datta · D. Sen  
Indian Institute of Technology Kharagpur, Kharagpur, India  
e-mail: [debasmit.sg@iitkgp.ac.in](mailto:debasmit.sg@iitkgp.ac.in)

S. K. Pal  
e-mail: [sumitkpal@iitkgp.ac.in](mailto:sumitkpal@iitkgp.ac.in)

R. Datta  
e-mail: [ranadev@naval.iitkgp.ernet.in](mailto:ranadev@naval.iitkgp.ernet.in)

D. Sen  
e-mail: [deb@naval.iitkgp.ernet.in](mailto:deb@naval.iitkgp.ernet.in)

## 1 Introduction

The study of fluid-structure interaction problem, especially for large floating structures, has been of great importance since past few decades. Nowadays, ship-building and offshore industries are constructing larger structures to carry more cargo/passenger and to achieve more production benefit. Large offshore structures and ships are relatively more flexible and their natural frequencies can fall into the range of the encounter frequencies of commonly occurring sea spectrum. Hence, in this context the study of hydroelastic behaviour of ship like structures has been a key topic for research and development.

Since the progress of the classical hydroelastic tool to explore the fluid-structure interaction problem [1], scientific investigators have been contributed to the several aspects of this domain. Several numerical techniques have been proposed to investigate the hydroelastic analysis of floating bodies considering various aspects and challenges of this domain. The following are the few such examples of hydroelastic analysis of simplistic structures; the interaction of monochromatic incident waves with a horizontal porous flexible membrane has been investigated in the context of two-dimensional linear hydroelastic theory [2], a contemporary hydroelastic theory has been developed to describe how sea ice responds to an ocean wave field and those that relate to a very large floating structure (VLFS) experiencing comparable forcing [3], three methods have been proposed to determine the motion of a two-dimensional finite elastic plate floating on the water surface, allowing evolving freely [4].

However, it is seen from the literature that there is a need to develop a robust methodology to assess the hydroelastic analysis for complicated ship like structures more precisely. Few initial attempts were made to study the fluid-structure interaction problem for real ship shaped body [1]. Later, other noteworthy contributions in this area are as follows; a two- and three-dimensional hydroelasticity theory is developed to predict and compare the dynamic behaviour of a bulk carrier hull in waves [5], a hydroelasticity theory is used to analyse the response of barge and large container ship in waves [6], a fully coupled time domain ship hydroelasticity problem is investigated focusing on a springing phenomenon using a hybrid BEM–FEM scheme adopting a higher-order B-spline Rankine panel method [7] etc.

From the above discussion, it is interesting to note that either an analytical method is introduced to study the hydroelastic behaviour of very simplified two- or three-dimensional structures [8, 9] or rigorous numerical technique has been developed in order to deal with the fluid-structure interaction problem for ship shaped bodies [10, 11]. In this context, the present study is an attempt to inspect the hydroelastic behaviour of a container ship with zero speed and to evaluate the response assuming the ship as an equivalent rectangular barge with uniformly distributed mass. A robust and efficient semi-analytical approach in time domain [12] is used to obtain the structural deformation, bending moment, shear force, etc. which will be useful at the preliminary design stage. The hydrodynamic problem is solved using impulse response function [13, 14]. The structural part of the hydroelastic analysis has been solved using modal superposition approach of an Euler–Bernoulli beam. Finally,

the response of the structure is calculated semi-analytically by means of Duhamel integral. To check the robustness and efficiency of the present method, the obtained results for bending moments and shear forces are compared with a direct coupled BEM–FEM method in time domain and also with available published experimental results [15]. It is found out that the results obtained from the present study are showing satisfactory agreement with published results as well as the direct BEM–FEM coupling method. The main idea of the paper is to model a complicated ship like structure in a simplified way and to get the results good enough to predict the response accurately at initial design stage which can be further compared with sophisticated and computationally expensive methods.

## 2 Mathematical Formulation

In the present study, the fluid–structure interaction problem is solved in time domain. A one-dimensional beam model is taken into account to study the 3D barge structure. The structural deflection has been obtained using Duhamel integral, whereas the radiation forces are calculated using IRF in frequency domain. The coupling phenomena between the structural part and the hydrodynamic part are then fully investigated in order to execute the hydroelastic analysis more accurately.

### 2.1 Governing Equation

The deflection of the floating body is based on the foundation of an Euler–Bernoulli beam equation in the present study. The beam is free at both ends which means bending moment and shear force are zero at both the ends. The floating barge is considered as an equivalent beam on elastic foundation, and hence, the governing equations are obtained as,

$$\frac{\partial^2}{\partial x^2} \left( EI \frac{\partial^2 w}{\partial x^2} \right) + \rho A \frac{\partial^2 w}{\partial t^2} + k_f w = f(x, t) \quad (1)$$

where  $E$  is Young’s modulus,  $I$  is the vertical moment of inertia of the cross section,  $w$  is the elastic deflection of the body,  $\rho$  is the density of the material,  $A$  is the cross section area of the beam,  $k_f$  is the hydrostatic restoring coefficient and  $f(x, t)$  is the external wave force applied on the beam.

The above-mentioned differential equation is solved using modal superposition technique, i.e. the elastic deformation  $w(x, t)$  is assumed to be the summation of modeshape function  $W(x)$  and modal displacement  $q(t)$  as follows,

$$w(x, t) = \sum_{n=1}^{\infty} W_n(x) q_n(t) \quad (2)$$

As the beam is free-free at both the ends, the boundary conditions are as follows,

$$\frac{d^2 W(x)}{dx^2} = 0, \quad \frac{d^3 W(x)}{dx^3} = 0 \quad \text{at } x = 0 \text{ and } x = L \quad (3)$$

## 2.2 Hydrodynamic Solution

The hydrodynamic problem is solved using potential flow theory. The basic formulation has not been discussed here rigorously. Primary focus is given in the modelling of the hydrodynamic forces. The hydrodynamic forces comprise of wave excitation force  $F^{\text{exc}}$  and radiation force  $F^{\text{R}}$  as,

$$f(x, t) = F^{\text{R}}(x, t) + F^{\text{exc}}(x, t) \quad (4)$$

The radiation force is proportional to the velocity and acceleration of the body which not only varies over time but also with the length of the vessel. Hence, proper fluid-structure model is necessary to estimate the added mass and damping coefficient for elastic modes. The radiation forces are calculated using impulse response function theory in time domain. On the other hand, the wave exciting force is assumed as a periodic impulsive point load acting at the centre of gravity of the structure. The detailed modelling and the corresponding formulations of these forces can be found in [12].

## 2.3 Mode Functions

Deflection of the floating body has been represented by free-free beam modes. Six elastic modes have been taken for the convergence. Orthogonal property of the mode-shapes has been used in order to get the functions. Then, after few steps, the mode-shape functions for the Euler-Bernoulli beam are obtained as,

$$W_n(x) = (\cos(\alpha_n x) + \cosh(\alpha_n x)) - K_n(\sin(\alpha_n x) + \sinh(\alpha_n x)) \quad (5)$$

## 2.4 Coupling of Fluid-Structure

From the available literature [10], it is found out that the coupling phenomena are independent of the chosen hydrodynamic model. The coupling has been studied for the zero speed case of the container ship under head waves. While solving Eq. (1) by modal superposition approach, the following equation is obtained to get the corresponding modal deflection,



$$\ddot{q}_n(t) + \omega_n^2 q_n(t) = \frac{1}{\rho A} P_n(t) \tag{6}$$

The above differential equation has been solved by Duhamel integral technique as the generalized force,  $P_n(t) = \int f(x, t)W_n(x)dx$  does not fit to any known mathematical form. The deflection  $q_n(t)$  is thus obtained as,

$$q_n(t) = \frac{1}{\rho A \omega_n} \int_0^t P_n(\tau) \sin \omega_n(t - \tau) d\tau \tag{7}$$

Differentiating the deflection gives the normal velocity  $\dot{q}_n(t)$  of the concerned modeshape. Once the amplitude and velocity are obtained, the corresponding radiation force is also calculated for the next time step and thus the fluid-structure coupling is made in time domain.

## 2.5 Direct Coupling of BEM and FEM

The results in this paper are compared with numerical method based on direct coupling between BEM and FEM in time domain. Bending moment and shear force results for the container ship have been computed by this method. For the completeness of the paper, the method has been briefly discussed below.

### 2.5.1 Formulation of the Structural Problem

The ship hull is modelled as an Euler–Bernoulli beam floating in water. The governing differential equation of this beam is given by,

$$\rho A \frac{\partial^2 w}{\partial t^2} + EI \frac{\partial^4 w}{\partial x^4} + g B w = f \tag{8}$$

here  $E$  is the modulus of elasticity of the material,  $I$  is the moment of inertia, is the displacement along  $z$ -axis,  $\rho$  is the density of the material,  $A$  is the cross-sectional area of the beam,  $B$  is the width of the hull at the water plane,  $g$  is the acceleration due to gravity and  $f$  is the external force per unit length to the hull at  $x$ . The external force per unit length at  $x$  is obtained by integrating the total pressure on the hull surface at  $x$ .

The hull girder idealized as an Euler–Bernoulli beam has been discretized into a set of  $N$  finite elements. Each element has two nodes, each node having two degrees of freedom  $w$  and  $w_x$ . The subscript  $x$  denotes derivation with respect to  $x$ . In element  $e$ ,  $w$  at any point can be written in terms of the nodal degrees of freedom as,

$$w = \{N\}^{eT} \{d\}^e \quad (9)$$

here  $\{N\}^e = \{N_1^e \ N_2^e \ N_3^e \ N_4^e\}$  where  $N_i^e (i = 1, 4)$  are the Hermite shape functions and  $\{d^e\} = \{w_1^e \ w_{x1}^e, \ w_2^e \ w_{x2}^e\}$  is a vector of the degrees of freedom at the two nodes of element  $e$ .

Applying the Galerkin technique to Eq. (8) and using Eq. (9), the elemental finite element equation for element  $e$  can be written as,

$$[M^e]\{\ddot{d}^e\} + [K^e]\{d^e\} = \{F^e\} \quad (10)$$

Value of  $f$  comes from the hydrodynamic analysis explained in Subsect. 2.5.2. Equation (10) is a system of four linear simultaneous ordinary differential equations. Combining these elemental equations with consideration to the nodal connectivity of different elements, we get the global finite element equation. This is a set of  $2(N_e + 1)$  linear simultaneous ordinary differential equations. Adding a Rayleigh damping term, we get the following system of global finite element equations,

$$[M]\{\ddot{d}\} + [C]\{\dot{d}\} + [K]\{d\} = \{F\} \quad (11)$$

### 2.5.2 Hydrodynamic Analysis

The hydrodynamic problem is solved using 3D linear time domain panel code. The boundary value problem is solved using 3D transient free surface Green's function as can be seen in [16]. Detailed analysis of the numerical scheme used here is discussed in many sources [17–19] and hence not repeated here.

### 2.5.3 Numerical Integration

The global finite element Eq. (11) and the boundary element and pressure equations have been solved with the help of Newmark's time integration method. Solution of Eq. (11) gives the values of displacements, velocities and accelerations at the nodes. However, to solve the Euler–Bernoulli beam Eq. (11), force per unit length is required. The values of  $f$  in Eq. (11) at different locations can be obtained by solving the hydrodynamic problem.

According to Newmark's method, nodal displacement vector at any time instant  $t$  can be related to  $\{d\}$  at the previous time instant by the following equation,

$$\begin{aligned}
& \left( \frac{[M]}{\alpha \Delta t^2} + \frac{\delta}{\alpha \Delta t} [C] + [K] \right) \{d\}_t \\
& = \{F\}_t + [M] \left[ \frac{1}{\alpha \Delta t^2} \{d\}_{t-\Delta t} + \frac{1}{\alpha \Delta t} \{\dot{d}\}_{t-\Delta t} + \left( \frac{1}{2\alpha} - 1 \right) \{\ddot{d}\}_{t-\Delta t} \right] \\
& \quad + [C] \left[ \frac{1}{\alpha \Delta t} \{d\}_{t-\Delta t} + \left( \frac{\delta}{\alpha} - 1 \right) \{\dot{d}\}_{t-\Delta t} + \frac{\Delta t}{2} \left( \frac{\delta}{\alpha} - 2 \right) \{\ddot{d}\}_{t-\Delta t} \right] \quad (12)
\end{aligned}$$

After developing  $\{d\}$ , the velocities and acceleration vectors can be calculated using the following equations,

$$\{\ddot{d}\}_t = \frac{1}{\alpha \Delta t^2} (\{d\}_t - \{d\}_{t-\Delta t}) - \frac{1}{\alpha \Delta t} \{\dot{d}\}_{t-\Delta t} - \left( \frac{1}{2\alpha} - 1 \right) \{\ddot{d}\}_{t-\Delta t} \quad (13)$$

$$\{\dot{d}\}_t = \{\dot{d}\}_{t-\Delta t} + \Delta t [(1 - \delta)\{\ddot{d}\}_{t-\Delta t} + \delta\{\ddot{d}\}_t] \quad (14)$$

Using the velocities obtained from Eq. (14), force for the next time step can be calculated. Using this force and with the help of Eqs. (12)–(14), displacement, velocity and force vectors can be obtained for the next time step. In this way, the time marching is continued. The force on the hull is calculated from the boundary element equations, and the displacement, velocity and the acceleration vectors are calculated using the finite element equations at different time steps.

### 3 Results and Discussions

In the present study, a semi-analytic method in time domain is used to predict the hydroelastic response of a container ship modelled as a rectangular barge with uniformly distributed mass. The length of the barge is taken as 286.6 m which is same as of the container ship. The maximum breadth of the ship has been taken as the beam of the barge which is 40 m. And, the draft-to-length ratio is taken as 0.02. For the sake of simplicity, zero forward speed case of the ship has been considered for the present hydroelastic analysis.

Figure 1 demonstrates the geometry of the container ship and Fig. 2 shows the first four deformable modes of that ship which has been used in the coupled BEM–FEM method to get the wave-induced responses.

Six deformable modes have been considered to represent the elastic deflection of the floating body while analysing the fluid-structure interaction problem through the IRF method. Figure 3 shows the first four deformable modes of the vessel. The deflections are unscaled and only to demonstrate how the elastic deformation varies over the length at any instant  $t$ . The modes are numbered from 7 to 10 as the first six modes are the usual rigid body modes.

Figure 4 represents the radiation impulse response function obtained for the first six deformable modes. It can be seen from the figure that as the mode number increases the value of response function also gets decreased which indicates the fact

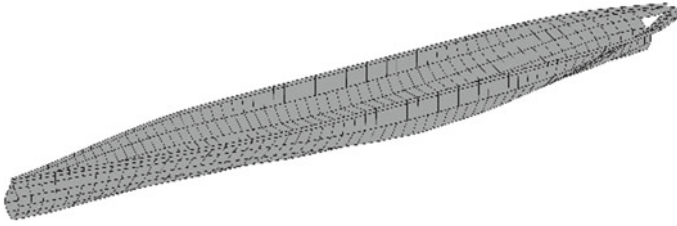


**Fig. 1** Geometry of discretized container ship

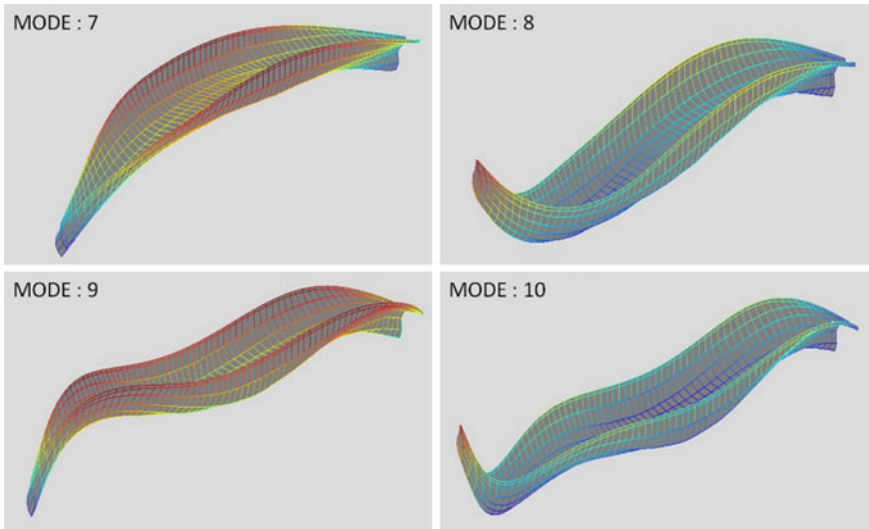


**Fig. 2** Deflection of the container ship for first four flexible modes

that higher modes have lesser contribution in total displacement and other responses due to wave induced loads.

For establishing the idea to estimate hydroelastic response of a container ship with a slender rectangular barge, the results for bending moments and shear forces have been compared with numerically enriched coupled BEM–FEM method. Results from the present methodology are termed as “IRF”, whereas the results obtained from the time domain panel method code are termed as “TD”. For better understanding and authenticity of the present formulation, the transfer function for bending moment is further compared with published experimental result [15]. In Fig. 5, the three results for bending moment RAOs have been plotted and compared with each other. The bending moments are non-dimensionalized by  $1/(\rho g A L^2 B)$  and have been plotted against non-dimensional wavelength  $\lambda/L$ . It is interesting to note that the result obtained from the present IRF method agrees well with the other two numerically expensive methodologies. Although there are slight differences between the bending moment values over all the frequency regions; however, it can be justified as the

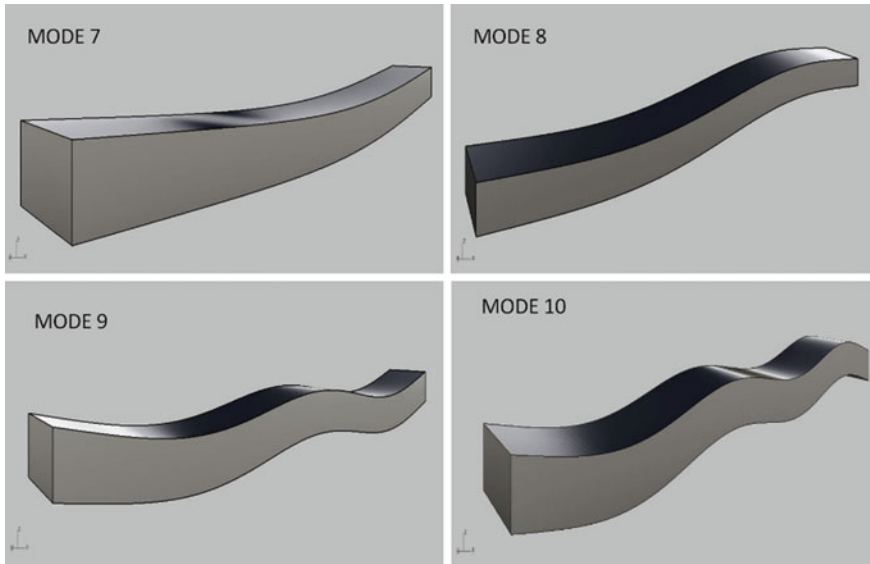


Fig. 3 Deflection of the barge for first four flexible modes

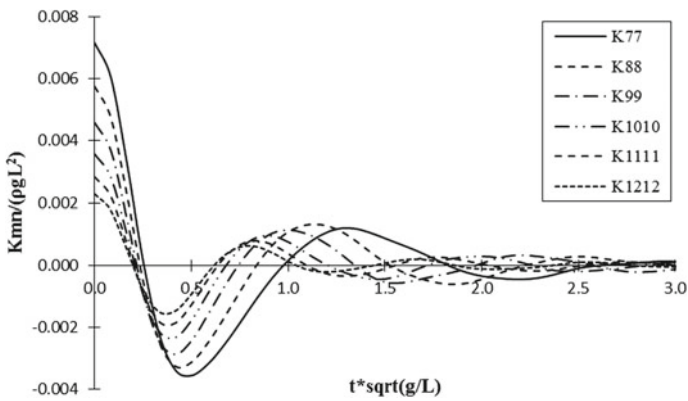
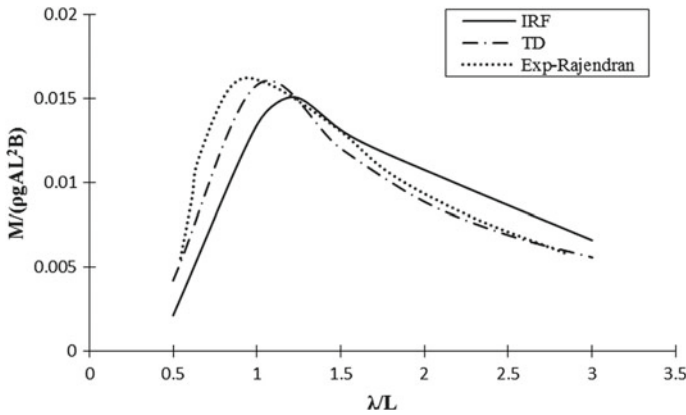
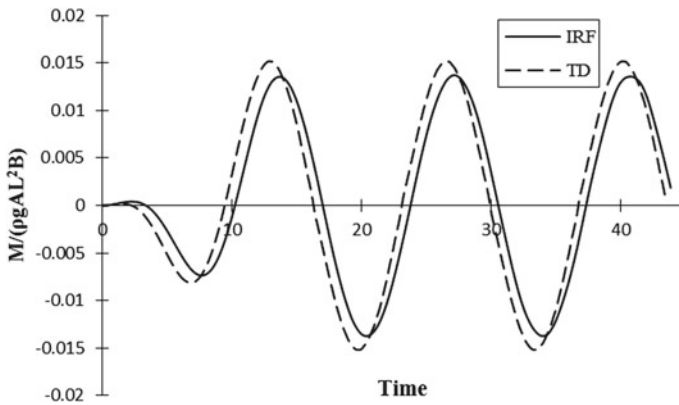


Fig. 4 Radiation impulse response function for first six deformable modes

present IRF method is a semi-analytic approach and the results are obtained considering the container ship to be a rectangular barge with uniformly distributed mass. Hence, it is practically not possible to match the data fully. However, the error is within 5% range of accuracy when compared to the other two methods and thus, could be useful at the initial design stage of such a container ship. Henceforth, it can be concluded that the idea which has been proposed as an alternative approach to estimate the response of a container ship is established. It also proves the robustness and efficiency of the present methodology.



**Fig. 5** Comparison of bending moment RAOs between IRF, coupled BEM–FEM and experimental results from Rajendran et al.



**Fig. 6** Comparison of time signals of bending moments between coupled BEM–FEM and the present IRF code

After establishing the authenticity of the present formulation, few more comparisons regarding shear force and bending moment results have been discussed for the sake of completeness of the present hydroelastic study. In Fig. 6, the time signal for bending moment at midship for  $\lambda/L = 1$ , i.e. when wavelength is close to the structural length, obtained from “IRF” and coupled BEM–FEM method have been compared. Figure 7 shows the comparison between bending moments along the length of the vessel obtained from these two methods. It is seen that the results match very well and thus it confirms the efficiency of the present analysis.

Shear force results have also been compared with the coupled BEM–FEM method for the completeness of the paper. In all the remaining figures, shear forces are non-dimensionalized by  $1/(\rho g A L B)$  and have been plotted against non-dimensional

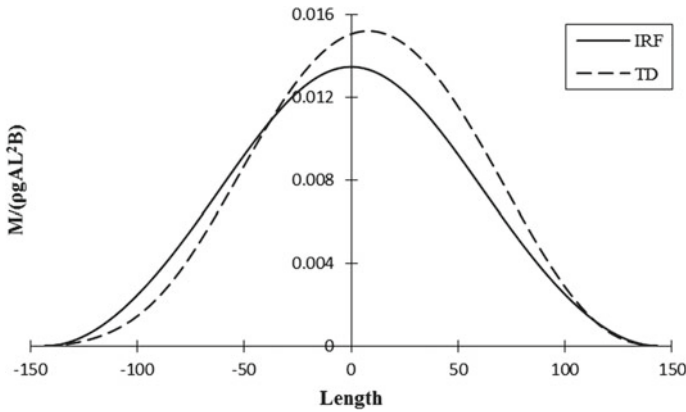


**Fig. 7** Comparison of bending moments along the length of the vessel between coupled BEM-FEM and the present IRF code

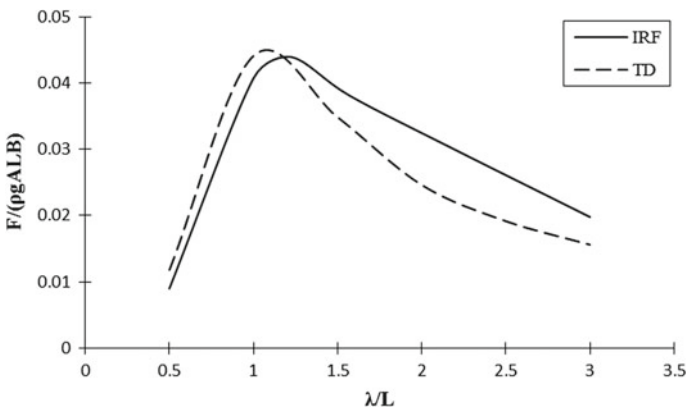


**Fig. 8** Comparison of shear forces between coupled BEM-FEM and the present IRF code

wavelength  $\lambda/L$ . Figure 8 shows the comparison between the shear force RAOs between coupled BEM-FEM and the present IRF code calculated at  $-L/4$  position of the vessel. From the figure, excellent agreement can be seen between these two methodologies. Keeping in mind the simplistic modelling of the structural problem, the slight differences over the lower frequency zone are justified in the range of engineering accuracy.

The study has been further progressed by showing the comparison between time signal of shear forces and shear forces along the length of the vessel between these two methods. In Fig. 9, the time signals have been plotted for  $\lambda/L = 1$ , i.e. when wavelength is equal to body length at  $-L/4$  positions. And Fig. 10 shows the comparison between shear forces along the length of the vessel obtained from these two methodologies. Excellent agreement can be seen from these two figures as well.

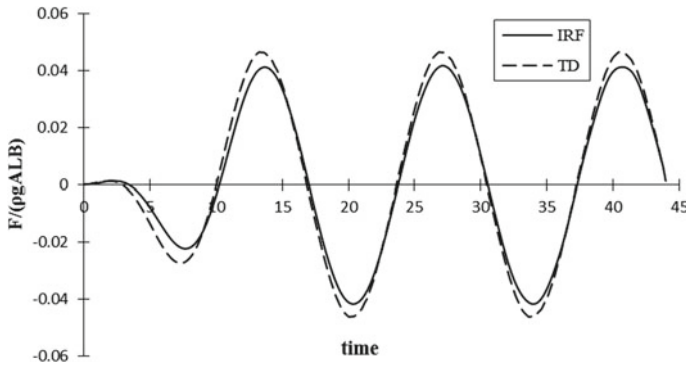


**Fig. 9** Comparison of time signals of shear forces between coupled BEM-FEM and the present IRF code

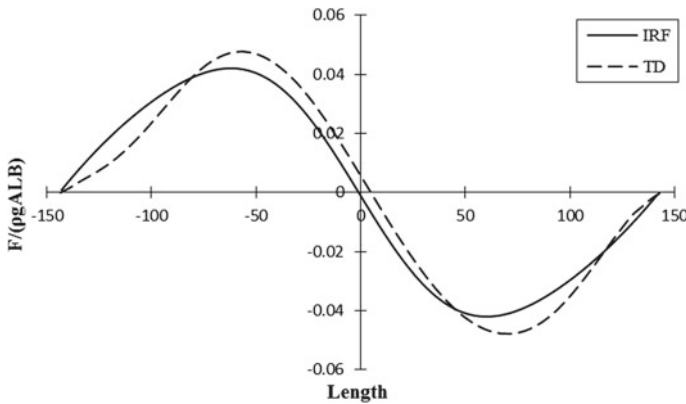


**Fig. 10** Comparison of shear forces along the length of the vessel between coupled BEM-FEM and the present IRF code

Therefore, as a conclusion, one can say that both the methods are representing the same phenomena although numerical approach and the structural modelling are different.

## 4 Conclusions and Future Scope

In the present paper, a semi-analytic three-dimensional time domain methodology has been delivered to estimate the hydroelastic response of a container ship with zero forward speed exposed to waves. An Euler-Bernoulli beam has been considered to model the rectangular barge with analytically defined modeshapes. The analysis has been carried out through impulse response function. Duhamel integral is employed in



order to get the structural response, bending moments and shear forces. The structural and hydrodynamic parts are then fully coupled in time domain for the solution of the hydroelastic problem in the present solution scheme.

Main focus is given in developing the idea of estimating the response of a container ship due to wave-induced loads with the help of a rectangular barge with uniformly distributed mass. The results for shear forces and bending moments RAOs obtained from this IRF method have been compared with the results obtained from the direct coupled BEM–FEM method. Time signals and along the length properties are also compared. Satisfactory agreement has been found between these two approaches which proves the robustness of the present concept. To establish the authenticity of the present work, the result for bending moment RAO at midship has been compared with the experimental results obtained from Rajendran et al. which once again proves the efficiency of the proposed state of the art.

For simplicity, a barge with uniformly distributed mass is studied in the present hydroelastic analysis. It is found out from the comparison results that despite simple assumptions, the results are good enough to fit in the range of engineering accuracy. The present methodology is more time efficient compared to the other two methods. Hence, the present concept can be used as an alternative procedure to guess the shear force, bending moment of a container ship at initial design stage.

As a future scope, the hydroelastic analysis can be carried forward by considering the coupled flexural and torsional vibrations. This methodology can be further extended to investigate the hydroelastic analysis of a container ship with forward speed where some nonlinearities such as nonlinear Froude–Krylov force, nonlinear hydrostatics, etc. can be incorporated. Horizontal bending of the ship can further be investigated to portray the fluid–structure interaction problem more accurately. This methodology is also able to study the response of a container ship arising due to local phenomena such as green water loading, slamming, etc. These forces could be obtained from rigorous CFD solver and then coupled with the present IRF method.

**Acknowledgements** This work was supported by Department of Science and Technology (DST), India through AORC program.

## References

1. Bishop RED, Price WD (1979) Hydroelasticity of ships. Cambridge University Press, Cambridge
2. Cho IH, Kim MH (1998) Interactions of a horizontal flexible membrane with oblique incident waves. *J Fluid Mech* 367:139–161. <https://doi.org/10.1017/S0022112098001499>
3. Squire VA (2008) Synergies between VLFS hydroelasticity and sea ice research. *Int J Offshore Polar Eng* 18(4):1–13
4. Meylan MH, Sturova IV (2009) Time-dependent motion of a two-dimensional floating elastic plate. *J Fluids Struct* 25:445–460. <https://doi.org/10.1016/j.jfluidstructs.2009.01.001>
5. Hirdaris SE, Price WD, Temarel P (2003) Two and three-dimensional hydroelastic modelling of a bulker in regular waves. *Mar Struct* 16:627–658. <https://doi.org/10.1016/j.marstruc.2004.01.005>

6. Senjanovic I, Malenica S, Tomasevic S (2008) Investigation of ship hydroelasticity. *Ocean Eng* 35:523–535. <https://doi.org/10.1016/j.oceaneng.2007.11.008>
7. Kim Y, Kim KH, Kim Y (2009) Analysis of hydroelasticity of floating ship like structure in time domain using a fully coupled hybrid BEM–FEM. *J Ship Res* 53(1):31–47
8. Karmakar D, Bhattacharjee J, Sahoo T (2009) Wave interaction with multiple articulated floating elastic plates. *J Fluids Struct* 25(6):1065–1078. <https://doi.org/10.1016/j.jfluidstructs.2009.03.005>
9. Sahoo T, Yip TL, Chwang AT (2001) Scattering of surface waves by a semi-infinite floating elastic plate. *Phys Fluids* 13(10):3215–3222. <https://doi.org/10.1063/1.1408294>
10. Senjanovic I, Malenica S, Tomasevic S (2009) Hydroelasticity of large container ships. *Mar Struct* 22:287–314. <https://doi.org/10.1016/j.marstruc.2008.04.002>
11. Zhang SX, Yang YQ, Wu XH (1996) The theoretical analysis and experimental study on ship's hydroelasticity. *J Hydrodyn* 11(1):65–72
12. Sengupta D, Pal SK, Datta R (2017) Hydroelasticity of a 3D floating body using a semi analytic approach in time domain. *J Fluids Struct* 71:96–115. <https://doi.org/10.1016/j.jfluidstructs.2017.03.007>
13. Cummins WE (1962) The impulse response function and ship motions. *Shiffstechnik* 9:101–109
14. Kara F (2015) Time domain prediction of hydroelasticity of floating bodies. *Appl Ocean Res* 51:1–13. <https://doi.org/10.1016/j.apor.2015.02.001>
15. Rajendran S, Soares CG (2016) Numerical investigation of the vertical response of a container ship in large amplitude waves. *Ocean Eng* 123:440–451. <https://doi.org/10.1016/j.oceaneng.2016.06.039>
16. Datta R, Sen D (2007) The simulation of ship motion using a B-spline based panel method in time domain. *J Ship Res* 51(3):267–284
17. Datta R, Rodrigues JM, Soares CG (2011) Study of the motions of a fishing vessel by a time domain panel method. *Ocean Eng* 38:782–792. <https://doi.org/10.1016/j.oceaneng.2011.02.002>
18. Datta R, Fonseca N, Soares CG (2013) Analysis of forward speed effects on the radiation forces on a fast ferry. *Ocean Eng* 60:136–148. <https://doi.org/10.1016/j.oceaneng.2012.11.010>
19. Sengupta D, Datta R, Sen D (2016) A simplified approach for computation of nonlinear ship loads and motions using a 3D time domain panel method. *Ocean Eng* 117:99–113. <https://doi.org/10.1016/j.oceaneng.2016.03.039>

# Numerical Study on the Influence of Head Wave on the Hydrodynamic Derivatives of a Container Ship



T. V. Rameesha and P. Krishnankutty

**Abstract** Traditionally, ship maneuvering performances are predicted in calm water condition to evaluate the directional stability and turning ability of the ship in the early design stages. Evaluation of maneuvering performance of a ship including wave effect is more realistic and important for the safety of ships at sea. Determination of hydrodynamic derivatives is the basic step in solving maneuvering equations of motion. Accurate estimation of hydrodynamic derivatives is necessary for the prediction of vessel trajectories. As the ship maneuvers through seaway, the effect of wave load will alter the maneuvering derivatives, consequently the vessel trajectory will be affected significantly. Hence, the influence of wave on hydrodynamic derivatives needs to be determined. For the present study, horizontal planar motion mechanism tests are numerically simulated for a container ship in head sea condition using RANS-based CFD solver. Obtained force/moment time series include both wave excitation forces/moment and hydrodynamic forces on the hull due to PMM motions. Fast Fourier transform (FFT) algorithm is used to filter the hydrodynamic forces/moment from the estimated total force/moment time series. The Fourier series expansion method is used to derive the hydrodynamic derivatives from the estimated force/moment time series. A comparison study is done with the wave-effected hydrodynamic derivatives and derivatives in still water condition.

**Keywords** Maneuvering · Planar motion mechanism · Captive model test

## 1 Introduction

Maneuvering predictions are often carried out in still water condition to investigate the maneuverability of the vessel in its early design stages. Practically, ship always

---

T. V. Rameesha (✉) · P. Krishnankutty  
Department of Ocean Engineering, Indian Institute of Technology Madras, Chennai, India  
e-mail: [tv.ramisha7@gmail.com](mailto:tv.ramisha7@gmail.com)

P. Krishnankutty  
e-mail: [pkrishnankutty@iitm.ac.in](mailto:pkrishnankutty@iitm.ac.in)

© Springer Nature Singapore Pte Ltd. 2019  
K. Murali et al. (eds.), *Proceedings of the Fourth International Conference in Ocean Engineering (ICOE2018)*, Lecture Notes in Civil Engineering 22,  
[https://doi.org/10.1007/978-981-13-3119-0\\_8](https://doi.org/10.1007/978-981-13-3119-0_8)

does sail in waves; hence for the safety of ship sailing, it is important to capture the wave effects on the maneuvering motion. Maneuvering predictions are usually done by solving maneuvering equations of motion. Estimation of hydrodynamic derivatives forms the basic step in the way of prediction. Hydrodynamic derivatives are derived from the resulting hydrodynamic forces/moments from the captive model tests of ship maneuvering. Several researchers conducted captive model tests experimentally [1–4] or numerically using computation fluid dynamics (CFD) [5–8]. Experiments are more reliable for the estimation of hydrodynamic derivatives. The test facilities for the captive model tests are rare, expensive, and time-consuming. Hence, numerical simulation of captive model tests using CFD techniques has gained importance. As ship sails through seaway, the effect of wave will alter the hydrodynamic forces acting on the hull, subsequently the hydrodynamic derivatives also have a considerable variation with the influence of wave. The quantitative estimation of the change of hydrodynamic derivatives with respect to wave will be more useful for the accurate prediction of maneuvering characteristics of vessel. Xu et al. [9] carried out planar motion mechanism tests in irregular waves to investigate the effects of varying wave drift forces on the ship steering characteristics, and the author concluded that significant value of the wave drift damping is induced during pure sway motion of ship in irregular waves. Yasukawa [10, 11] carried out direct maneuvering tests in both regular and irregular waves with container ship model. Model test in regular waves is carried out in head and beam waves, and long- and short-crested waves are selected for irregular wave study.

This paper presents the numerical studies conducted on a container ship in head sea condition to understand the effect of waves on the hydrodynamic derivatives using pure sway and pure yaw modes of planar motion mechanism simulated in a CFD environment.

## 2 Nomenclature

$B$	Beam (m)
$C_B$	Block coefficient
$D$	Depth (m)
$f_x$	Surge force amplitude (kN/m)
$f_y$	Sway force amplitude (kN/m)
$I_Z$	Moment of inertia in $z$ -direction
$L_{BP}$	Length between perpendiculars (m)
$m$	Mass of the ship (kg)
$m_z$	Yaw moment amplitude
$N_\delta$	Rudder deflection derivative in $z$ -direction
$N_{\dot{r}}$	Hydrodynamic coupled derivative of yaw moment with respect to yaw acceleration
$N_r$	Hydrodynamic linear coupled derivative of yaw moment with respect to yaw rate

$N_{rrr}$	Hydrodynamic third-order coupled derivative of yaw moment with respect to yaw rate
$N_{\dot{v}}$	Hydrodynamic coupled derivative of yaw moment with respect to sway acceleration
$N_v$	Hydrodynamic linear coupled derivative of yaw moment with respect to sway acceleration
$N_{vvv}$	Hydrodynamic third-order coupled derivative of yaw moment with respect to sway velocity
$N_{vvr}$	Hydrodynamic third-order cross-coupled derivative of yaw moment with respect to sway velocity and yaw rate
$N_{vrr}$	Hydrodynamic third-order cross-coupled derivative of yaw moment with respect to sway velocity and yaw rate
$r$	Yaw rate (rad/s)
$\dot{r}$	Yaw acceleration (rad/s <sup>2</sup> )
$t_r$	Thrust deduction factor
$T_p$	Propeller thrust
$T_a$	Draft at the aft end (m)
$T_m$	Mean draft (m)
$T_f$	Draft at the fore end (m)
$u$	Linear velocity in surge direction (m/s)
$\dot{u}$	Linear acceleration in surge direction (m/s <sup>2</sup> )
$v$	Linear velocity in sway direction (m/s)
$\dot{v}$	Linear acceleration in sway direction (m/s <sup>2</sup> )
$\nabla$	Displaced volume (m <sup>3</sup> )
$\delta$	Rudder angle (rad)
$X_\delta$	Rudder deflection derivative in $x$ -direction
$X_{rr}$	Hydrodynamic second-order coupled derivative of surge force with respect to yaw rate
$X_{\dot{u}}$	Hydrodynamic uncoupled derivative in surge with respect to surge acceleration
$X_{uu}$	Hydrodynamic second-order uncoupled derivative of surge with respect to surge velocity
$X_{vv}$	Hydrodynamic second-order coupled derivative of surge force with respect to sway velocity
$X_{vr}$	Hydrodynamic second-order cross-coupled derivative of surge force with respect to sway velocity and yaw rate
$Y_\delta$	Rudder deflection derivative in $y$ -direction
$Y_{\dot{r}}$	Hydrodynamic coupled derivative of sway force with respect to yaw acceleration
$Y_r$	Hydrodynamic linear coupled derivative of sway force with respect to yaw rate
$Y_{rrr}$	Hydrodynamic third-order coupled derivative of sway force with respect to yaw rate
$Y_{\dot{v}}$	Hydrodynamic coupled derivative of sway force with respect to sway acceleration

$Y_v$	Hydrodynamic linear coupled derivative of sway force with respect to sway velocity
$Y_{vvv}$	Hydrodynamic third-order coupled derivative of sway force with respect to sway velocity
$Y_{vvr}$	Hydrodynamic third-order cross-coupled derivative of sway force with respect to sway velocity and yaw rate
$d$	Distance between two oscillators (m)
$\omega_0$	Frequency of oscillation (rad/sec)
$\omega_e$	Encountering frequency (rad/s)
$U_m$	Model forward speed (m/s)
$Y_{vrr}$	Hydrodynamic third-order cross-coupled derivative of sway force with respect to sway velocity and yaw rate
$y_{0a}$	Amplitude of transverse oscillation (m)

### 3 Mathematical Model

Mathematical model of Son and Nomoto [3] representing maneuvering equations of motion in three degrees of freedom for a high-speed container ship is given by

$$(m - X_{\dot{u}})\dot{u} + (m - Y_{\dot{v}})vr = X \quad (1)$$

$$(m - Y_{\dot{v}})\dot{v} + (m - X_{\dot{u}})ur - Y_{\dot{r}}\dot{r} = Y \quad (2)$$

$$(I_Z - N_{\dot{r}})\dot{r} + N_{\dot{v}}\dot{v} = N \quad (3)$$

where  $X, Y, N$  are expressed as hull force/moment due to motion in the surge ( $x$ ) and sway ( $y$ ) directions and are given by

$$X = X(u) + (1 - t_r)T_P + X_{vr}vr + X_{vv}v^2 + X_{rr}r^2 + X_{\delta} \sin \delta + f_x \sin(\omega_e t + \varepsilon) \quad (4)$$

$$Y = Y_v v + Y_r r + Y_{vvv}v^3 + Y_{rrr}r^3 + Y_{vvr}v^2 r + Y_{vrr}vr^2 + Y_{\delta} \cos \delta + f_y \sin(\omega_e t + \varepsilon) \quad (5)$$

$$N = N_v v + N_r r + N_{vvv}v^3 + N_{rrr}r^3 + N_{vvr}v^2 r + N_{vrr}vr^2 + N_{\delta} \cos \delta + m_z \sin(\omega_e t + \varepsilon) \quad (6)$$

Wave excitation forces/moments are added in the right-hand side of equation of motion. These forces are calculated for the container ship using 2-D strip theory-based program, SEAWAY. Rudder and propeller derivatives in the right-hand side of equation of motion are independent terms, and these equations of motion are found out using empirical relations.

Two right-handed coordinate systems are used to represent the ship motion in the present study (Fig. 2), earth-fixed and ship coordinate systems, where  $x_{OG}, y_{OG}$  represent the position of center of gravity of the ship with respect to earth-fixed

**Table 1** Main particulars of the container ship and model

Particulars	Prototype	Model (1:36)
Length, $L_{BP}$ (m)	175	4.86
Beam, $B$ (m)	25.4	0.705
Draft at FP, $T_f$ (m)	8.0	0.22
Draft at AP, $T_a$ (m)	9.0	0.25
Draft at mid-ship, $T_m$ (m)	8.5	0.236
Depth, $D$ (m)	11.0	0.305
Displacement, $\nabla$ ( $m^3$ )	21.222	0.4548
Block coefficient, $C_B$	0.559	0.559

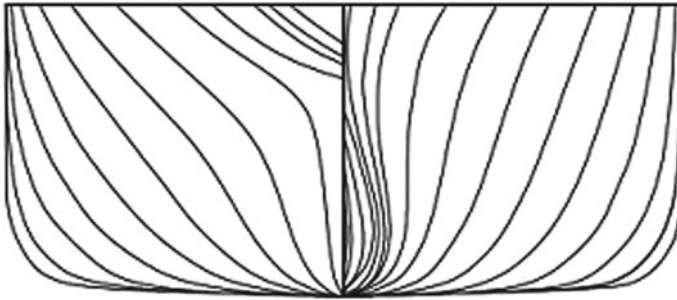


**Fig. 1** Body plan of S175 container ship

coordinate system and  $\psi$  is the heading or yaw angle which refers to the direction of the ship and  $\beta$  is the drift angle defined as the angle between resultant velocity in ship-fixed coordinate system and the longitudinal axes in earth-fixed coordinate system. A container ship (S175) has been used for the present study; the principal particulars of the ship are given in Table 1 and body plan in Fig. 1.

## 4 Numerical Simulation

### 4.1 PMM Tests

Planar motion mechanism (PMM) tests are experimental captive model tests conducted to determine acceleration and velocity-dependent derivatives appearing in the maneuvering equations of motion. PMM consists of two transverse oscillators, one at the bow and one at the stern position of the ship model, oscillated at prescribed motion amplitude  $y_{0a}$ , frequency  $\omega_0$ , and phase angle  $2\varepsilon$  while the model is towed at the speed  $U_0$ . Phase angle  $2\varepsilon$  between two oscillators determines the modes of operation of PMM. Total forces/moments acting on the hull are measured by the

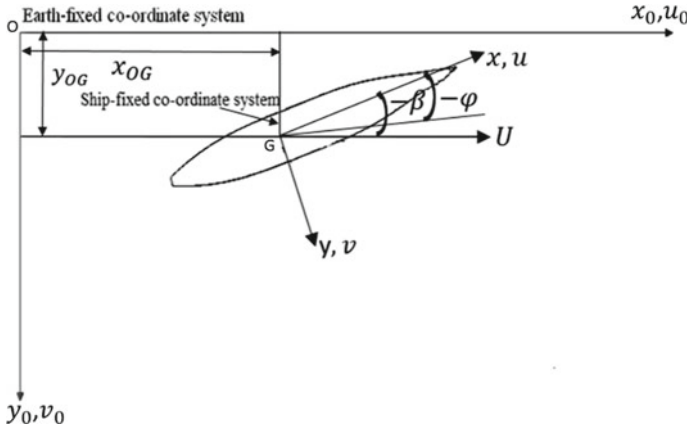


Fig. 2 Earth-fixed and ship-fixed coordinate systems

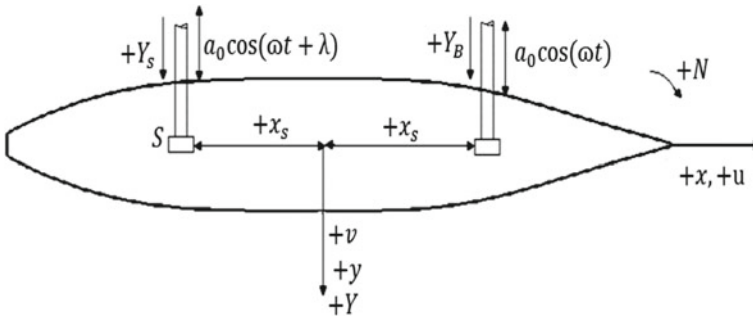


Fig. 3 Model setup in PMM test

dynamometer placed at the stern (*S*) and bow (*B*) of the model (Fig. 3). Present paper includes pure sway and pure yaw modes of simulation in head sea waves.

**Pure sway Test**

Pure sway test is used to determine sway-dependent velocity and acceleration derivatives appearing in the mathematical model. Phase angle  $2\varepsilon$  between the oscillators at the bow and stern of the model is made zero, so that ship undergoes translational motion in *y*-direction. Model kinematic parameters are represented as:

Transverse displacement,

$$y_0 = -y_{0a} \sin \omega_0 t \tag{7}$$

Transverse velocity,

$$\dot{y}_0 = -y_{0a} \omega_0 \cos \omega_0 t \tag{8}$$



Transverse acceleration,

$$\ddot{y}_0 = y_{0a}\omega_0^2 \sin \omega_0 t \quad (9)$$

### Pure Yaw Test

Pure yaw test is conducted to determine yaw-dependent velocity and acceleration derivatives appearing in the mathematical model. Phase angle between fore and aft oscillators  $2\varepsilon$  must satisfy the condition given by the expression,  $\tan \varepsilon = d\omega/2U_m$ . Model kinematic parameters are given by:

Yaw angle,

$$\varphi = -\varphi_a \cos \omega_0 t \quad (10)$$

Yaw rate,

$$\dot{\varphi} = -\varphi_a \omega_0 \sin \omega_0 t \quad (11)$$

Yaw acceleration,

$$\ddot{\varphi} = -\varphi_a \omega_0^2 \cos \omega_0 t \quad (12)$$

Numerical simulation of PMM experiments in head sea waves is carried out using RANS-based CFD software. Computational domain larger than International Towing Tank Conference (ITTC) [12] is selected for the numerical simulation of pure sway and pure yaw tests in waves due to the increased hydrodynamic disturbance in the presence of waves compared to still water condition. The fluid domain for dynamic simulation extends  $4 L_{PP}$  from the aft,  $2 L_{PP}$  from the bow,  $3 L_{PP}$  from each of port and starboard sides, and  $1 L_{PP}$  each from keel to bottom side, where  $L_{PP}$  is the length between perpendiculars (Fig. 4). Boundaries of a domain are composed of velocity inlet for inlet boundary, downstream pressure at outlet boundary, wall with no slip for the hull, and wall with slip for the ship.

An unstructured trimmed hexahedral cell with prismatic near-wall layers is selected to capture the flow properties around the hull surface. Rectangular volumetric block with high resolution is selected to resolve the free surface (Fig. 5). Around 40 grid points per wave length are used to capture the wave in longitudinal direction, and 20 grid points in the vertical direction are implemented to resolve the free surface (Fig. 6).

Transient finite volume simulations employed an implicit unsteady with a segregated (predictor–corrector) flow solver and semi-implicit method for pressure-linked equations (SIMPLE) solution algorithm. Second-order upwind spatial and first-order temporal discretization schemes are used. Based on the prior studies, SST (Menter)  $k-\omega$  turbulence model is implemented [7, 13]. The transient simulation is initialized at  $t = 0$ , and appropriate time step  $\Delta t$  is chosen based on the velocity of flow and

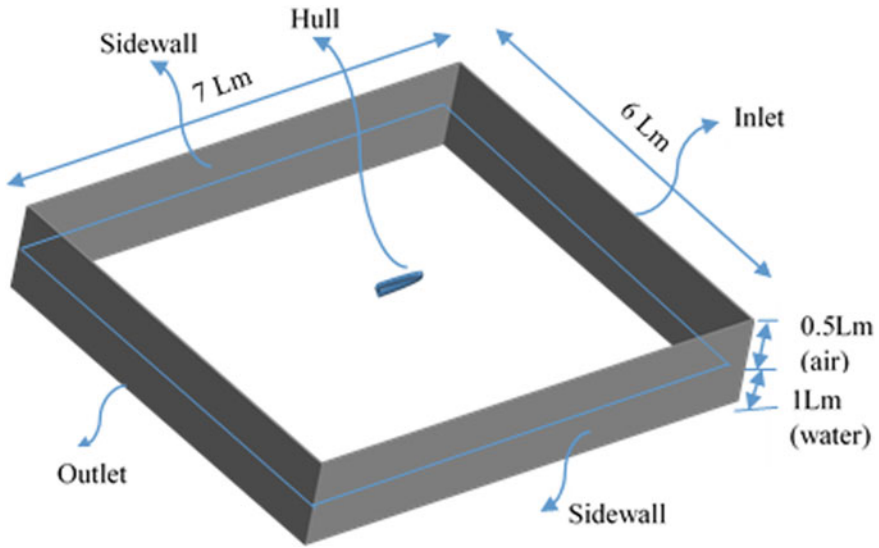


**Fig. 4** Computational domain for PMM test in waves

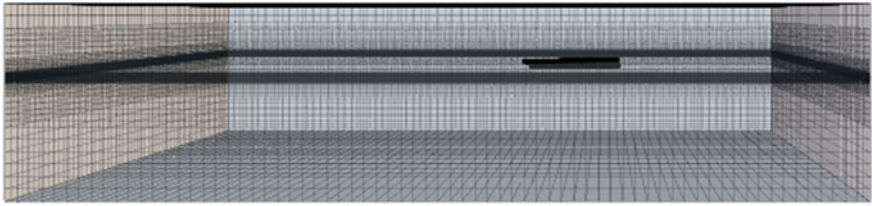


**Fig. 5** Mesh generated for pure sway test

also on grid size in the direction of flow. Grid independence study is carried out for the proper selection of grid size.

## 5 Analysis

Fourier series expansion method is used for deriving hydrodynamic derivatives from estimated hydrodynamic forces/moments. In this method, obtained hull forces/moments are numerically integrated over the full cycle using trapezoidal integration rule to express as sine and cosine terms and which are compared with the coefficients of the mathematical model of Son and Nomoto [3]. Hydrodynamic forces and moments on the ship hull can be expressed as

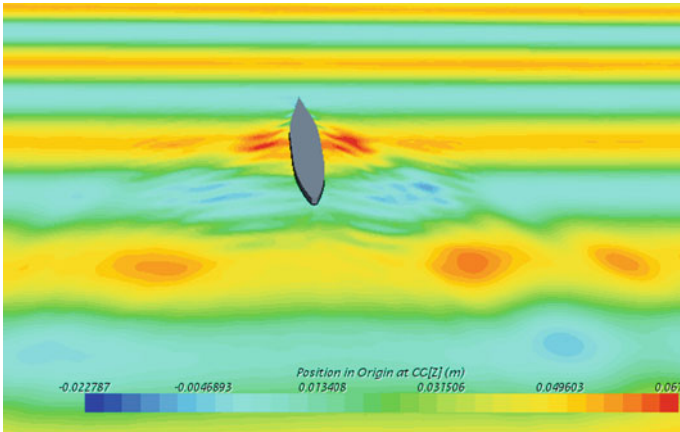


**Fig. 6** Water surface captured for pure sway test in head sea waves

$$f(t) = \sum_{m=0}^{\infty} (a_m \cos m\omega_0 t + b_m \sin m\omega_0 t) \tag{13}$$

$$a_0 = \frac{1}{T} \int_0^T f(t) dt \tag{14}$$

$$a_m = \frac{2}{T} \int_0^T f(t) \cos m\omega_0 t dt \tag{15}$$

$$b_m = \frac{2}{T} \int_0^T f(t) \sin m\omega_0 t dt \tag{16}$$

## 6 Results and Discussion

Pure sway and pure yaw modes of PMM are numerically simulated for a container ship in head sea condition with a model wave height of 0.056 m and model wave period of 2 s (Table 1 gives prototype and model details). Estimated total forces/moments from the pure sway mode of PMM tests include both hydrodynamic forces and wave forces (Figs. 7, 8 and 9). Hence, for deriving the hydrodynamic derivatives, hydrodynamic forces need to be filtered from the estimated total forces. Fast Fourier transform (FFT) technique is used to convert the obtained time series to frequency domain signal. From frequency plots (Figs. 10 and 11), lowest frequency peak corresponding to prescribed frequency of PMM oscillation is separated, and

**Fig. 7** Surge force in PMM pure sway mode in wave condition

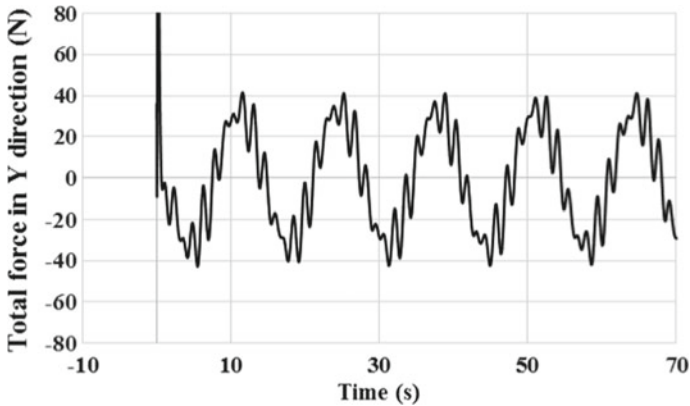
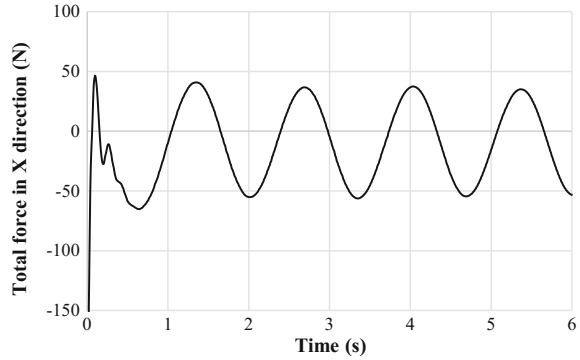


**Fig. 8** Sway force in PMM pure sway mode in wave condition

this lower frequency signal is converted to time domain (Figs. 12, 13 and 14) for deriving hydrodynamic derivatives.

Estimated forces and moments from the pure yaw mode of PMM simulation are shown in Figs. 15, 16 and 17. Forces/moment time signal contains noises, and it is filtered using FFT technique. Lower frequency peak in frequency domain plot (Figs. 18 and 19) is filtered and converted to time domain (Figs. 20, 21 and 22). Hydrodynamic derivatives are derived from the filtered time series using Fourier series expansion method and are compared with the calm water derivatives (Tables 2 and 3). Variation of turning parameters in waves is analyzed (Tables 3 and 4).

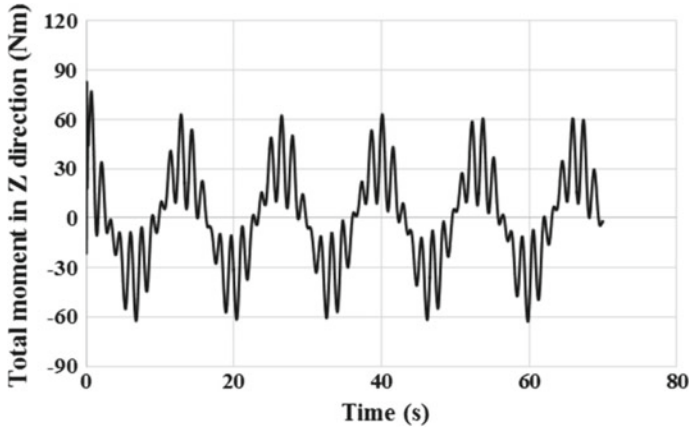
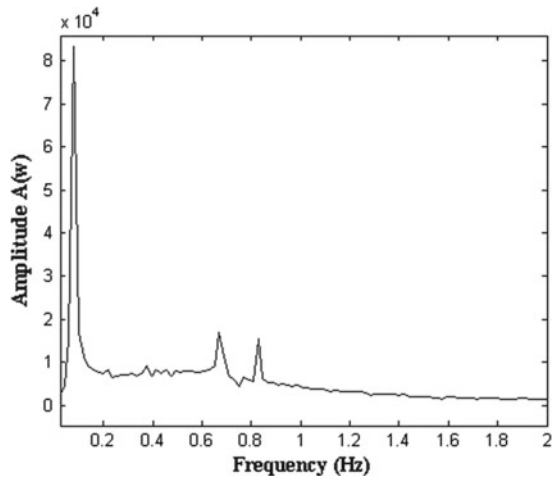
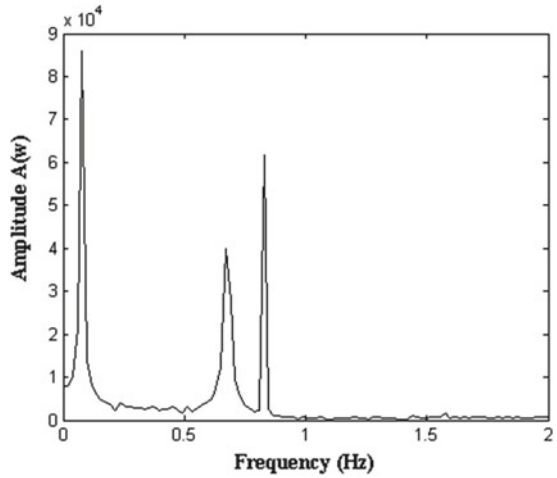


Fig. 9 Yaw moment in PMM pure yaw mode in wave condition

Fig. 10 Frequency domain representation of sway force in PMM pure sway mode



**Fig. 11** Frequency domain representation of yaw moment in PMM pure sway mode



**Fig. 12** Surge force in PMM pure sway mode (with and without wave effect)

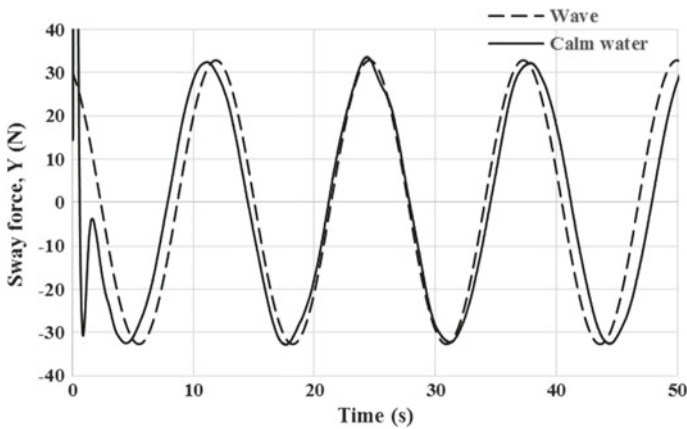
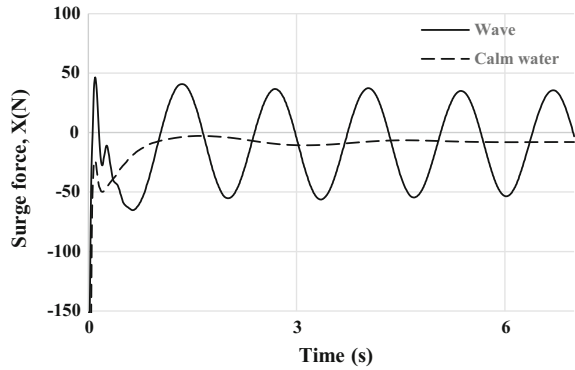


**Fig. 13** Sway force in PMM pure sway mode (with and without wave effect)

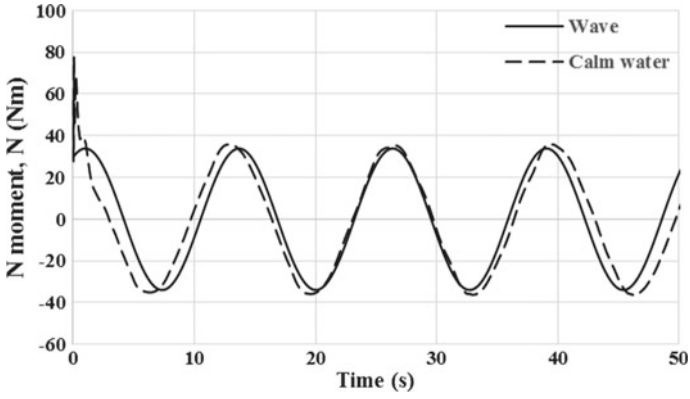


Fig. 14 Yaw moment in PMM pure sway mode (with and without wave effect)

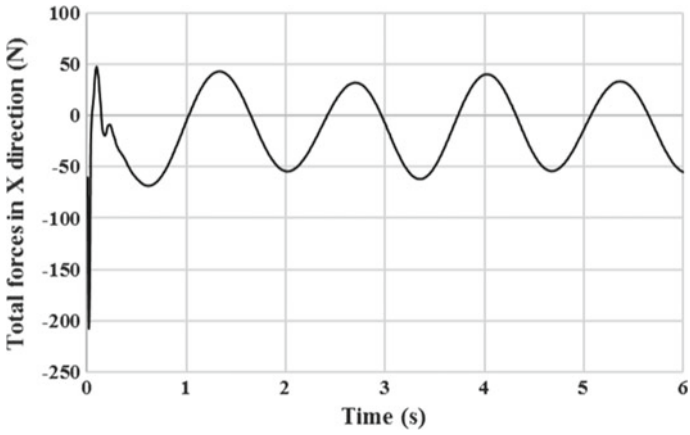


Fig. 15 Surge force in PMM pure yaw mode in wave condition

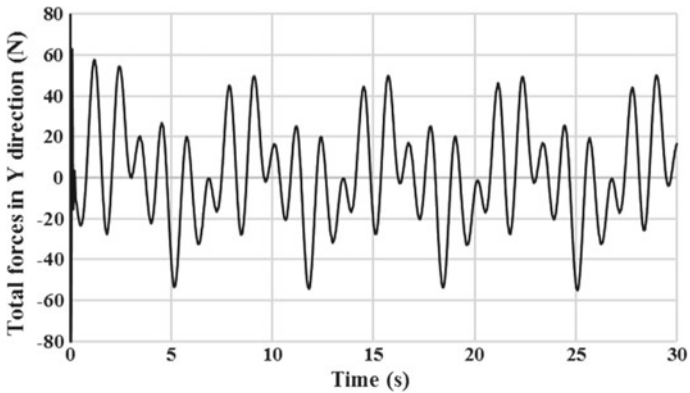
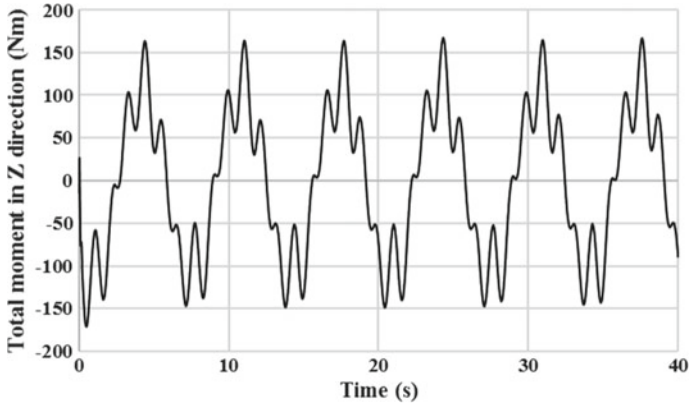
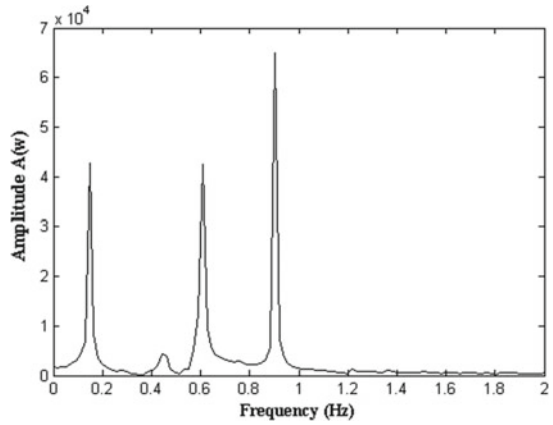


Fig. 16 Sway force in PMM pure yaw mode in wave condition

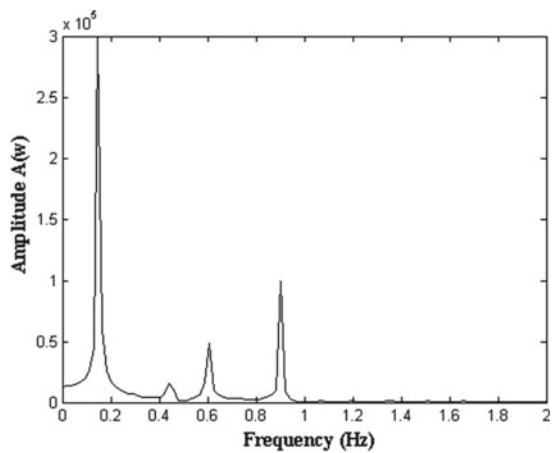


**Fig. 17** Yaw moment in PMM pure yaw mode in wave condition

**Fig. 18** Frequency domain representation of sway force in PMM pure yaw mode



**Fig. 19** Frequency domain representation of yaw moment in PMM pure yaw mode





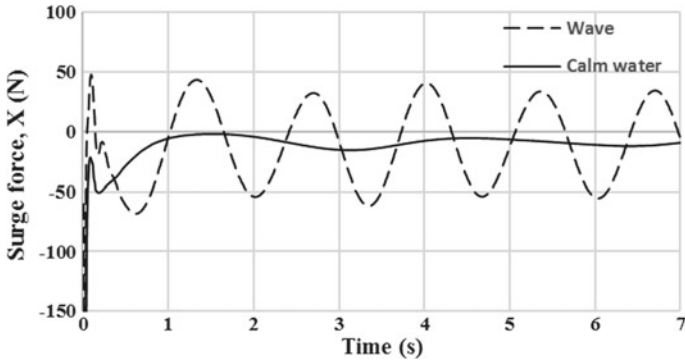


Fig. 20 Surge force in PMM pure yaw mode (with and without wave effect)

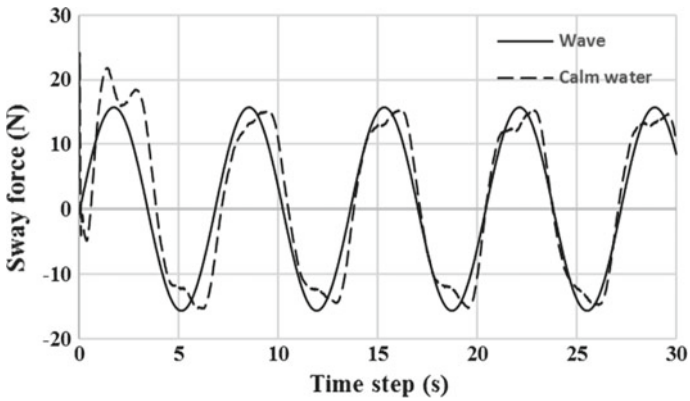


Fig. 21 Sway force in PMM pure yaw mode (with and without wave effect)

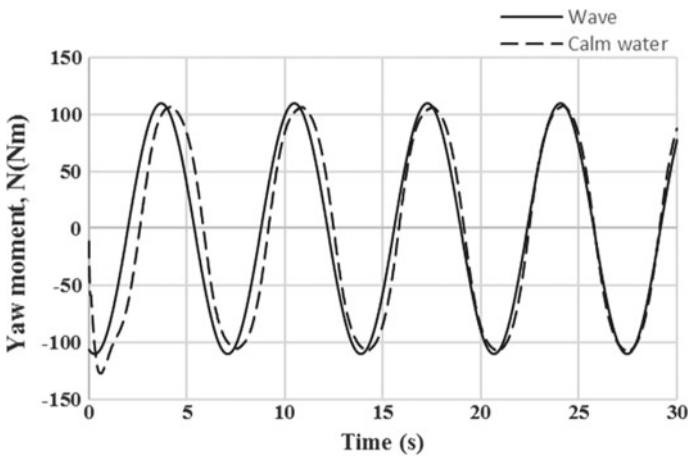


Fig. 22 Yaw moment in PMM pure yaw mode (with and without wave effect)

**Table 2** Wave effect on hydrodynamic derivatives (pure sway test)

Hydrodynamic derivative	Still water	Head wave	% change between calm water and head wave derivatives
$Y'_v$	-0.0097	-0.00786	-18.96
$Y'_b$	-0.0072	-0.00769	-6.8
$Y'_{vvv}$	-0.1432	0.0163	111.38
$N'_v$	-0.0038	-0.0042	-10.52
$N'_b$	-0.0002	-0.00051	-155
$N'_{vvv}$	-0.0191	-0.0216	-13.089
$X'_{uu}$	-0.00062	-0.001408	-127.096
$X'_{vv}$	-0.00014	-0.0021	-140

**Table 3** Wave effect on hydrodynamic derivatives (pure yaw test)

Hydrodynamic derivative	Still water	Head wave	% change between calm water and head wave derivatives
$Y'_r$	0.003	0.003534	-17.8011
$N'_r$	-0.0022	-0.00195	11.363
$X'_{rr}$	-0.00065	-0.0007	-7.69
$N'_f$	-0.00052	-0.000483	6.98
$Y'_f$	-0.0001	-0.0001159	-15.51
$N'_{rrr}$	-0.00393	-0.00284	27.565
$Y'_{rrr}$	-0.00644	-0.00135	79.02
$X'_{it}$	-0.0006309	-0.000538	14.57

**Table 4** Wave effect on turning parameters

Turning parameters	Still water	Head wave	% change between calm water and head wave
Steady turning radius (m)	286	240	16.08
Advance	277	209	24.55
Transfer	584	436	25.34
Tactical diameter	657	523	20.39

## 7 Conclusion

In the present study, pure sway and pure yaw tests of planar motion mechanism are carried out for container ship in head sea condition, and dependency of hydrodynamic derivatives on head waves is investigated. CFD analyses are performed, and it is observed that sway-dependent and yaw-dependent hydrodynamic derivatives appearing in the maneuvering equation of motion varied significantly in the presence of waves. First-order velocity-dependent derivatives obtained from pure sway test like  $Y'_v$  and  $N'_v$  show a variation up to 20% in the presence of waves. Sway-dependent third-order derivative  $Y'_{vvv}$  shows a higher variation up to 111.38% from still water condition to wave condition, but yaw-dependent third-order derivatives  $N'_{vvv}$  show a less variation of 13% for the same condition. Similarly, first-order derivatives obtained from pure yaw test like  $Y'_r$ ,  $N'_r$  show a variation up to 18% in the presence of head sea condition and acceleration derivatives like  $Y'_\dot{r}$ ,  $N'_\dot{r}$  show a variation of 16 and 7% respectively for the same. Third-order derivatives obtained from pure yaw tests like  $Y'_{rrr}$ ,  $N'_{rrr}$  show a higher variation of 27.5, 79.02% respectively in wave condition compared to calm water. The effect of these derivatives on turning circle maneuver is investigated. Turning circle radius and tactical diameter of the vessel are found to be reduced by 16.08, 20.39% respectively compared to calm water condition. Advance and transfer also have a considerable variation up to 25%, and the trajectory in waves is found to drift toward the direction of wave propagation. The results of simulation indicated that wave has a considerable influence on hydrodynamic derivatives and effects of wave on ship maneuverability cannot be neglected and this study can be extended by conducting the combined mode of PMM simulation in the same wave condition to simulate the maneuvering trajectory of ship in waves.

## References

1. Banerjee N, Rao CS, Raju MSP, Hughes P (2006) Determination of manoeuvrability of ship model using large amplitude horizontal planar motion mechanism. In: International conference in marine hydrodynamics, NSTL, Visakhapatnam, 5–7 Jan, pp 529–545
2. Gertler M (1959) The DTMB planar motion mechanism system. In: Symposium of towing tank facilities, Zagreb, Yugoslavia
3. Son KH, Nomoto K (1981) On the coupled motion of steering and rolling of a high speed container ship. *J Soc Nav Architect Jpn* 150:232–244
4. Kijima K, Yasuaki N, Yasuharu T, Masaka M (1990) Prediction method of ship manoeuvrability in deep and shallow waters. In: Proceedings of Marsim and ICSM, Tokyo, Japan
5. Sakamoto N, Carrica PM, Stern F (2012) URANS simulations of static and dynamic maneuvering for surface combatant: part 1. Verification and validation for forces, moment, and hydrodynamic derivatives. *J Mar Sci Technol* 17(4):422–445
6. Simonsen CD, Stern F (2008) RANS simulation of the flow around the KCS container ship in pure yaw. In: Proceedings of SIMMAN 2008 workshop on verification and validation of ship manoeuvring simulation methods, Lyngby, Denmark
7. Sheeja J (2010) Numerical estimation of hydrodynamic derivatives in surface ship manoeuvring. PhD thesis, Department of Ocean Engineering, IIT Madras, Chennai, India

8. Sulficker AN (2007) RANSE based estimation of hydrodynamic forces acting on ships in dynamic conditions. MS thesis, Department of Ocean Engineering, Indian Institute of Technology Madras, pp 27–54
9. Xu Y, Bao W, Kinoshita T, Itakura H (2007, Jan) A PMM experimental research on ship maneuverability in waves. In: ASME 2007 26th international conference on offshore mechanics and arctic engineering, pp 11–16. American Society of Mechanical Engineers
10. Yasukawa H (2006) Simulations of ship maneuvering in waves (1st report: turning motion). J Jpn Soc Nav Architect Ocean Eng 4:127–136
11. Yasukawa H, Nakayama Y (2009, Aug) 6-DOF motion simulations of a turning ship in regular waves. In: Proceedings of the international conference on marine simulation and ship manoeuvrability
12. ITTC recommended procedures (2011) Guidelines on use of RANS tools for maneuvering prediction. In: Proceedings of 26th ITTC
13. Sheno RR, Krishnankutty P, Panneer Selvam R (2016) Study of manoeuvrability of container ship by static and dynamic simulations using a RANSE-based solver. Ships Offshore Struct 11(3):316–334

# Retrofitting Integrated Wedge-Flap for Improvement of Resistance of High-Speed Displacement Vessel



Lijo Joseph and V. Anantha Subramanian

**Abstract** This paper reports the design for retrofitting of a high-speed displacement vessel for improving the speed because of deficiency in installed power for a 250-passenger ferry craft. The methodology is based on the evaluation of the integrated wedge-flap at the stern. High-speed displacement vessels operate at a steep region of the speed–resistance curve, and therefore, conservation of energy by drag reduction plays a major role in cost-effective operation of the vessel. The performance of the integrated wedge-flap at the stern is examined to recommend an appropriate design instead of an intuitive approach for the same. In a high-speed displacement vessel, various factors that lead to energy consumption are increased drag due to adverse dynamic trim, bow waves and unfavourable flow patterns in the stern region. The above-mentioned factors may also increase the wetted surface area of the hull, thereby increasing the overall drag and additional demand of power. The integrated wedge-flap is a combination of two appendages, namely wedge and stern flaps. The results from the study demonstrate that the integrated wedge-flap modifies the stern waves to flatter form, with reduction of the flow velocity below, resulting in increased dynamic pressure, improved trim and lift force with corresponding drag reduction. The numerical simulation of drag using commercial RANS code (Star-CCM+) shows the local influence of the energy saving appendage reinforced by validation with experiments. The study establishes a systematic method of introduction of the appendage to achieve significant drag reduction for the high-speed displacement hull form.

**Keywords** Integrated wedge-flap · Drag · Lift · Computational fluid dynamics · Dynamic trim · Dynamic pressure · RANS · Motion reference unit · Load cell · Dynamic fluid body interaction

---

L. Joseph (✉) · V. Anantha Subramanian  
Department of Ocean Engineering, Indian Institute of Technology Madras, Chennai, India  
e-mail: [lijojoseph022@gmail.com](mailto:lijojoseph022@gmail.com)

V. Anantha Subramanian  
e-mail: [subru@iitm.ac.in](mailto:subru@iitm.ac.in)

© Springer Nature Singapore Pte Ltd. 2019  
K. Murali et al. (eds.), *Proceedings of the Fourth International Conference in Ocean Engineering (ICOE2018)*, Lecture Notes in Civil Engineering 22,  
[https://doi.org/10.1007/978-981-13-3119-0\\_9](https://doi.org/10.1007/978-981-13-3119-0_9)

## Nomenclature

$C_b$	Block coefficient
DFBI	Dynamic fluid body interaction
LBP	Length between perpendiculars
LOA	Length overall
LWL	Length of waterline
MRU	Motion reference unit
RANS	Reynolds-averaged Navier–Stokes equation
VOF	Volume of fluid

## 1 Introduction

With increasing demand for fuel conservation and emission reduction, it is very important to improve the drag characteristic and therefore propulsive power in ships. Among the many adaptations, the introduction of specific appendages is one of the means of reducing drag and bringing down the power requirement. Some of the recent innovations are stern flap, wedges and interceptor in the case of vessels with higher speed in the displacement range or dynamic lift range vessels. There are situations where ships for changes in operational conditions do not achieve the design speed, or may not have the required power to achieve the guaranteed speed. Under such situations, properly designed energy saving device or appendages can be retrofitted to the hull with not only saving of penalty but also saving power. This study presents the use of combining a wedge and a flap and therefore resulting in the integrated wedge-flap to examine and improve the speed of a displacement hull. As the name implies, the integrated wedge-flap is a combination of otherwise single entities of wedge and stern flap used as power saving device.

Integrated wedge-flap can be, in principle, an extended appendage spanning the breadth of the hull, which extends from under the bottom of the hull to aft beyond the transom, making an angle with the buttock plane of the ship. Muller-Graf [1] carried out experimental investigation on the effectiveness of different types of spray rail system in semi-displacement hull and found that properly shaped and arranged spray rail system along with transom wedge is the most effective device to reduce the hull resistance of semi-displacement hull with round bilge keel. Karafiath et al. [2] reported greater power improvement in the case of integrated wedge-flap than the wedge acting alone or flap acting alone. They observed that at low speed, the integrated wedge-flap remains submerged fully, and thereby causing increased drag. At high speed, the flow detaches cleanly from the trailing edge of the integrated wedge-flap and slows down the flow velocity from the aft-most portion of the ship to the point forwards of the propeller. The decrease in flow velocity leads to increase in dynamic pressure, which results in a lift force that makes the integrated wedge-flap to come out from the submerged condition. Due to that, there will be a favourable trim,

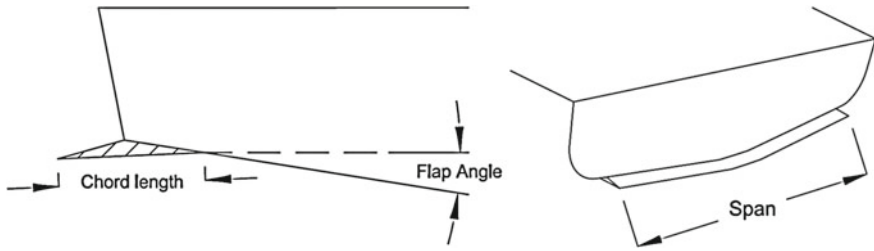


**Fig. 1** Integrated wedge-flap

**Table 1** Principal particulars of the vessel

Type of vessel	250-passenger ferry
LOA	47.50 m
LBP	44.12 m
Beam	10.00 m
Depth	4.30 m
Mean draft	2.10 m
Design speed	15 knots
Cb	0.544
Froude number	0.37
Model scale	15.95

decrease in wetted surface area, and these results in drag reduction. Later investigators experimented with the applicability of different hulls such as displacement, semi-displacement and planing hulls (Fig. 1).

Many researchers have reported the improvements due to wedge, spray rail or their combinations in the case of semi-displacement vessels [3] and high-speed vessels [4] and stern flaps Yaakob et al. [5]. Cumming et al. [6] reported that longer chord length results in improved resistance. Salas et al. [7] conducted numerically and experimentally the effect of individual appendages on the range of crafts from displacement, semi-displacement and planing hulls. These studies collectively touch upon different aspects of the influence of the appendages as drag reducing devices. This work reports the specific effect of the wedge-flap assessed through numerical simulation and validated from the experiments.

The principal particulars of the vessels are given in Table 1.

## 2 Parametric Study

As a specific case study, the approach here is to vary the chord length of the integrated wedge-flap through a range of distance, which is chosen from available literature guidelines. Firm guideline length is not available; however, a reasonable range can

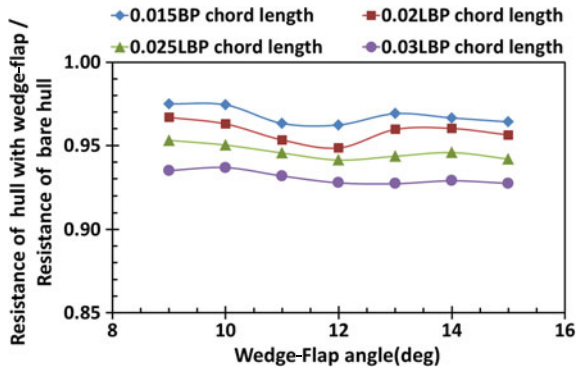


Fig. 2 Reduction of drag using different wedge-flap parameters

be selected from consideration of the fact that the flap length cannot be excessive since structurally it will require increased thickness to take the hydrodynamic load, and thereby adding its own drag. Other parameters are flap angle and flap span. On these considerations, the lengths have been chosen as 1.5, 2.0 and 3.0% of LBP. Wedge-flap angles are chosen in range from  $9.0^\circ$  to  $15.0^\circ$  with an increment of  $1.0^\circ$ . From the literature, it is found that the maximum reasonably possible span across the transom without impinging on the wake of the corners of transom and without requiring significant curvature of flap will give better performance [2]. The simulation has been performed for the Froude number ranging from 0.27 to 0.37.

Results of parametric study are given in Fig. 2; it is observed that at  $12.0^\circ$  flap angle, all the wedge-flaps with different chord length are giving higher reduction in resistance and also with increase in chord length the performance is getting better slightly. From the structural point of view, higher chord length is avoided. The more favourable wedge angle is  $12.0^\circ$  and chord length is 2.0% of LBP.

### 3 Computational Analysis

Computational analysis is performed by using commercial RANS code-based software, STAR-CCM+. Computational analysis is carried out by following the recommendations of ITTC 7.5-03-02-03 [8]. Taking advantage of symmetry, half of the model is used for analysis in order to bring down the convergence time. Analysis is carried out on model scale to facilitate direct comparison. The simulation has been performed for bare hull and hull with integrated wedge-flap (Fig. 3).

For mesh generation, unstructured meshes are used on the surface as well as for volume meshing. Surface remesher helps for generating surface mesh or remeshing the surface imported from the CAD software. Triangular meshes are formed on the surface by employing surface remesher as shown in Fig 4.



Trimmer mesh model is used to generate volume meshes, which forms hexagonal grids with minimum skewness and trimmer cells. To capture the boundary near the wall and to simulate turbulent velocity profile, prism layer mesh model is used along with volume mesh to generate orthogonal cells near the wall. Volume mesh used for the simulation with domain parameters is shown in Fig. 5. Boundary conditions are shown in Table 2.

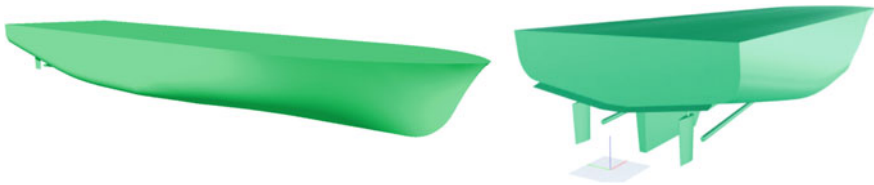


Fig. 3 Ship hull used for numerical analysis



Fig. 4 Surface meshed using surface remesher

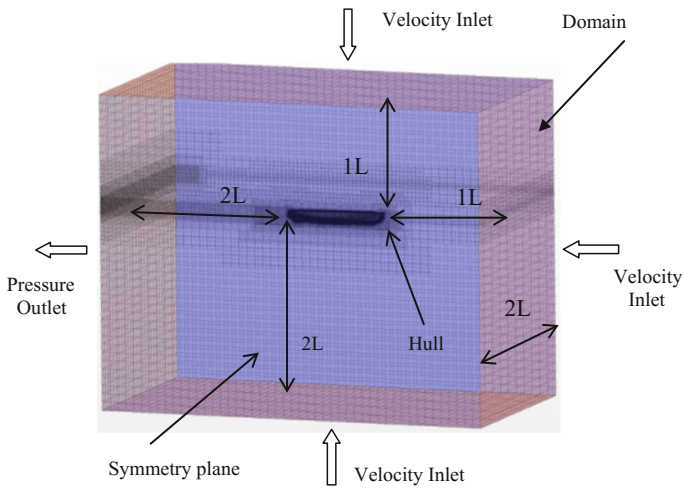


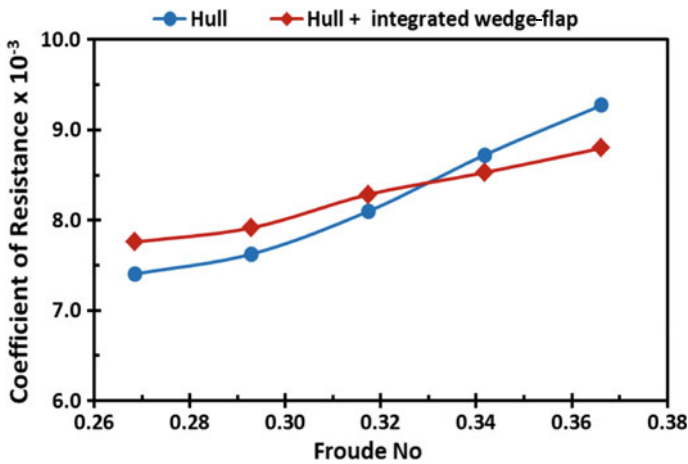
Fig. 5 Volume mesh used for the simulation

**Table 2** Boundary conditions

Faces	Physical boundary	Boundary condition
1	Domain inlet	Velocity inlet
2	Domain outlet	Pressure outlet
3	Domain top	Velocity inlet
4	Domain bottom	Velocity inlet
5	Domain side wall	Symmetric plane
6	Domain symmetry	Symmetric plane
7	Hull	Wall

Equation of motion of the body for the 6DOF is solved using Reynolds-averaged Navier–Stokes equation. Realizable  $K$ –epsilon turbulence model is used to solve the Reynolds stress in the Reynolds-averaged Navier–Stokes equation. The interaction between hull and fluid is captured using dynamic fluid body interaction (DFBI). Free surface is captured using VOF model. Two-layer All Y+ wall treatment is used along with  $k$ –epsilon turbulence model to solve viscous layer near wall. Segregated flow is used to solve flow equations. Implicit unsteady solver is used to control the update of the calculation at each physical time and controls the time step size.

As an observation, low-speed simulation shows that the wedge-flap gives adverse effect in reducing drag, and at higher speeds, there is drag reduction. The integrated wedge-flap improves the pressure distribution at the aft region at higher speed. Pressure contours are shown in Fig. 8. The pressure distribution along the length is shown in Fig. 9, and the influence of the wedge-flap is evident in the increased pressure at the stern region. The wedge-flap improves the dynamic trim at higher speed, see Fig. 7. Figure 6 shows the comparison of total drag.

**Fig. 6** Total resistance coefficient versus Froude number

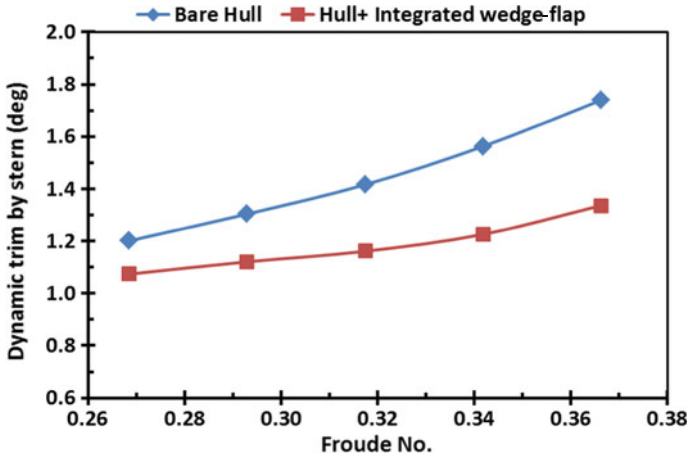


Fig. 7 Dynamic trim versus Froude number

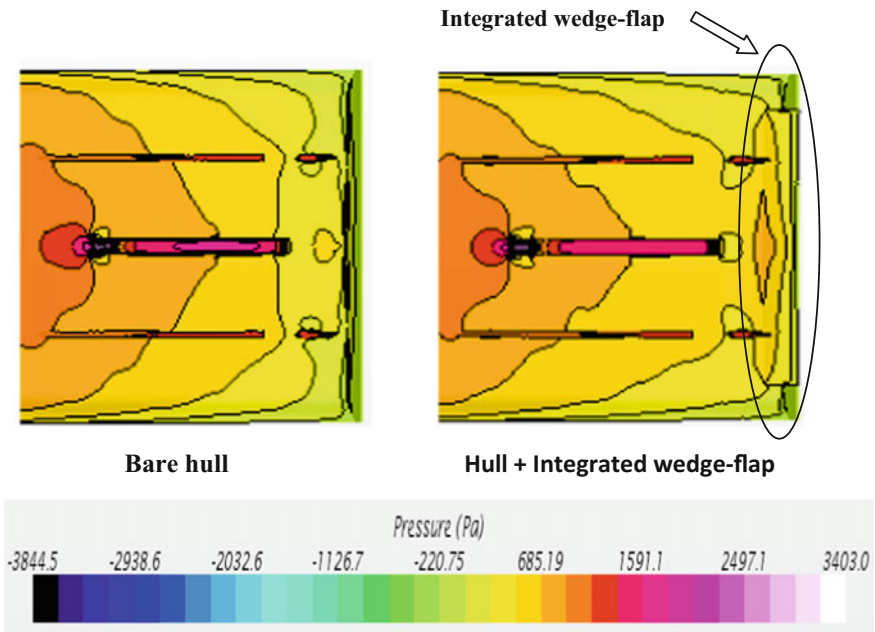
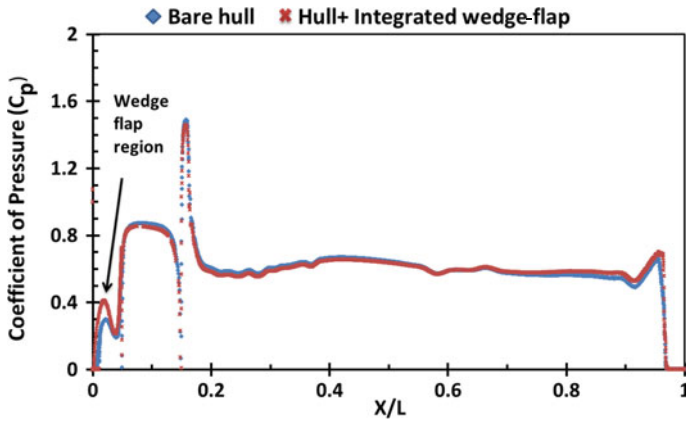
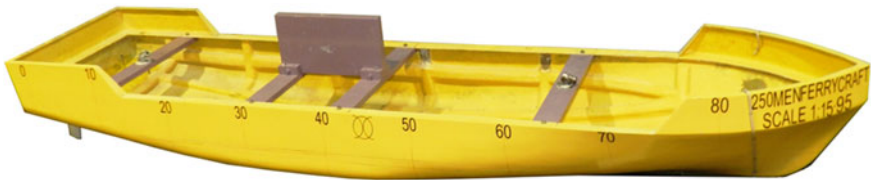


Fig. 8 Pressure distribution contours on the aft region of the hull



**Fig. 9** Pressure variation along length of ship from stern to bow



**Fig. 10** Hull used for the experiment



**Fig. 11** Integrated wedge-flap attached to the hull

### 4 Experiment and Validation

Experiments were conducted for validation and confirmation of the results. Tests were done as per *ITTC 7.5-02-02-01* [9]. The model scale is **1:15.95**. The tests measure both drag and trim. Comparison is shown in Fig. 12.

See Figs. 10, 11, 13, 14, 15 and 16; Table 3.

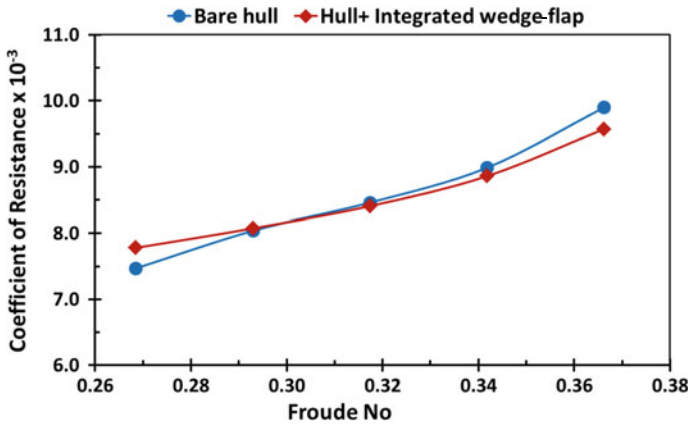


Fig. 12 Coefficient of resistance versus Froude number

Table 3 % Reduction in resistance by incorporating wedge-flap from CFD and EXPT

Sl. No.	Froude number	Coefficient of resistance				% Reduction in resistance with wedge-flap	
		Bare hull		Hull + wedge-flap		EXP	CFD
		EXP	CFD	EXP	CFD		
1	0.27	7.47E-03	7.41E-03	7.78E-03	7.76E-03	-4.16	-4.77
2	0.29	8.04E-03	7.63E-03	8.07E-03	7.92E-03	-0.46	-3.81
3	0.32	8.46E-03	8.10E-03	8.41E-03	8.28E-03	0.63	-2.31
4	0.34	8.99E-03	8.72E-03	8.86E-03	8.53E-03	1.41	2.25
5	0.37	9.90E-03	9.27E-03	9.57E-03	8.80E-03	3.30	5.12

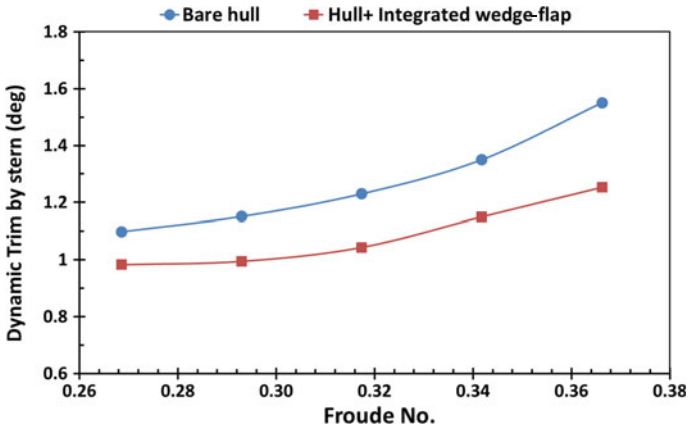


Fig. 13 Dynamic trim versus Froude number

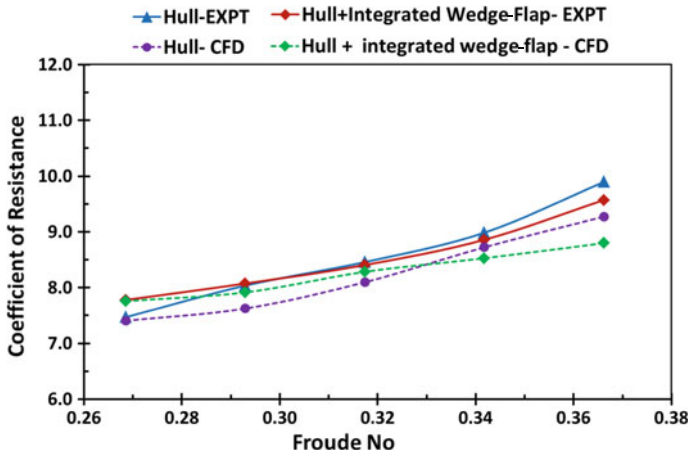


Fig. 14 CFD and experimental results comparison

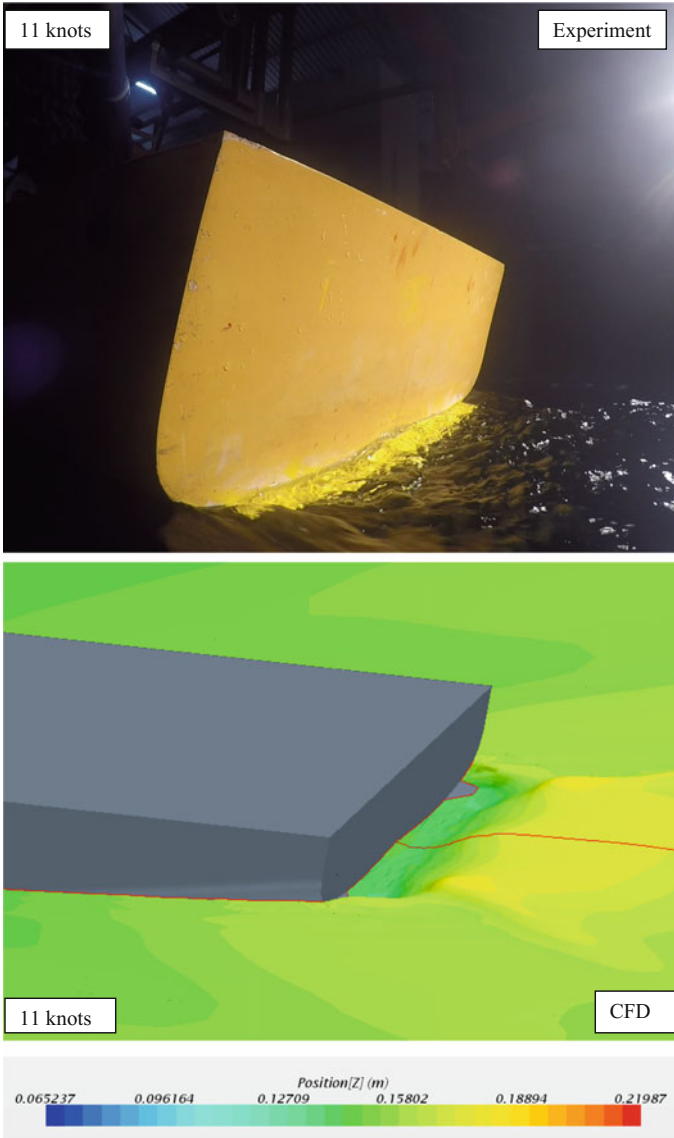


Fig. 15 At 10 knots speed, integrated wedge-flap is fully submerged

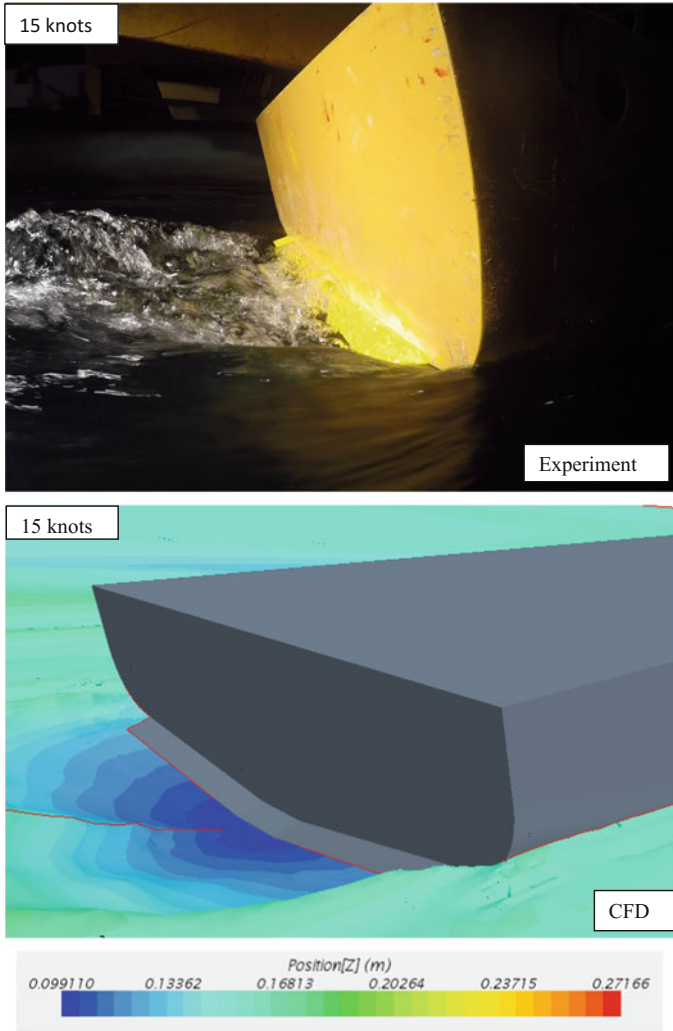


Fig. 16 Wedge-flap causes flow separation at 15 knots



## 5 Results and Conclusion

- Studies have been conducted on high-speed displacement vessel in a Froude range of 0.27–0.37.
- Hull attached with integrated wedge-flap provides adverse effect in reducing total drag at Froude number less than 0.32, but higher the Froude number its effect is being improved.
- Larger chord of integrated wedge-flap gives better performance compared to smaller ones.
- Experiment results from towing tank test show good agreement with CFD results.
- At design, Froude number of 0.37, integrated wedge-flap is reducing drag of 5.12% compared to bare hull.
- To reduce full-scale flap manufacturing cost and to simplify construction, flap ends can be rounded (radiused), with a radius equal to flap chord length.

In conclusion, the investigation provides a valuable tool and guideline for the design and retrofitting of an integrated wedge-flap. The retrofitting has resulted in the vessel achieving the guaranteed speed overcoming the earlier deficiency in engine power.

## References

1. Muller-Graf B (1991) The effect of an advanced spray rail system on resistance and development of spray of semi-displacement round bilge hulls. In: Proceeding fast sea transportation (FAST'91), Trondheim, vol 1, pp 125–142
2. Karafiath G, Cusanelli D, Lin CW (1999) Stern wedges and stern flaps for improved powering—U.S. navy experience. SNAME Trans 107
3. Bojovic P, Sahoo P (2000) Effect of stern wedges and advanced spray rail system on calm water resistance of high-speed displacement hull forms. In: Proceedings of Sea Australia 2000, Sydney, Australia
4. Cusanelli DS, Barry CD (2002) Stern flap performance on 110 ft patrol boat WPB1345 Staten Island. David Taylor Model Basin, Carderock Division, Naval surface warfare center, 9500 MacArthur Boulevard, West Bethesda, Maryland, Jan 2002
5. Yaakob O, Shamsuddin, King KK (2004) Stern flap for resistance reduction of planing hull craft: a case study with a fast crew boat model. J Technol 41(A): 43–52 (© Universiti Teknologi Malaysia)
6. Cumming D, Pollard R, Thornhill E, Hally D, Dervin M (2006) Hydrodynamic design of a stern flap appendage for the HALIFAX class frigates. MARI-TECH 2006, Halifax, NS, 14–16 June 2006
7. Salas M, Rosas J, Luco R (2004) Hydrodynamic analysis of the performance of stern flaps in a semi displacement hull. Latin American Applied research
8. ITTC-recommended procedures and guidelines—7.5-03-02-03 (2011) Practical guidelines for ship CFD applications
9. ITTC-recommended procedures and guidelines—7.5-02-02-01 (2002) Testing and extrapolation of resistance test

# Numerical Estimation of Underwater Radiated Noise of a Marine Propeller in Non-cavitating Regime



Abhishek Kumar Tewari, Vijit Misra and R. Vijayakumar

**Abstract** The underwater radiated noise levels (RNLs) emanating from surface and underwater marine platforms are becoming a topic of significant concern for all the nations in view of the global requirement to minimise the increasing adverse impact on marine life and maintain ecological balance in the so-called silent ocean environment. The studies have reported an increase in low-frequency ambient sea noise by an average rate of about 1/2 dB per year [Ross in *IEEE J Ocean Eng* 30(2):257–261, 2005 1] which is attributable to the growing fleet of ships. Marine propeller noise in both non-cavitating and cavitating regimes is an important component of the overall underwater radiated noise of a marine platform in addition to the machinery and flow noise. Merchant ships generally operate at low speeds, and hence, propeller noise in non-cavitating regime is an important area of concern. For military applications, design of low-noise propellers dictates the ships' survivability and operational performance. Hence, design and development of low-noise propulsion systems and, in particular, low-noise propellers is a relevant topic of current focus which is in line with the global need of the hour to design eco-friendly ships. In this respect, the main scope of this study is to numerically calculate the propeller noise in the non-cavitating regime for the uniform flow (no wake condition). Flow around the propeller is solved with a commercial CFD software STAR-CCM+, while hydro-acoustic analysis is performed using Ffowcs Williams–Hawkings (FWH) equation. The numerical closure was achieved using  $k-\epsilon$  Reynolds-averaged Navier–Stokes (RANS) model. The predicted hydrodynamic performance curves and radiated noise levels have been validated from the published experimental and numerical results.

**Keywords** Underwater radiated noise · Sound pressure level  
Hydrodynamic performance · Blade passage frequency · Cavitation

---

A. K. Tewari (✉) · V. Misra · R. Vijayakumar  
Indian Institute of Technology Madras, Chennai 600036, Tamil Nadu, India  
e-mail: [abhishek.navyguy@gmail.com](mailto:abhishek.navyguy@gmail.com)

© Springer Nature Singapore Pte Ltd. 2019  
K. Murali et al. (eds.), *Proceedings of the Fourth International Conference in Ocean Engineering (ICOE2018)*, Lecture Notes in Civil Engineering 22,  
[https://doi.org/10.1007/978-981-13-3119-0\\_10](https://doi.org/10.1007/978-981-13-3119-0_10)

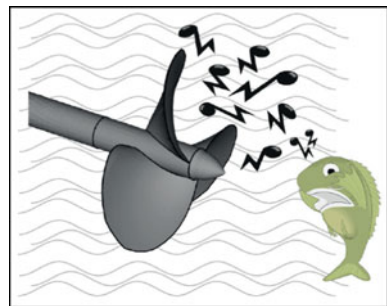
## 1 Introduction

The underwater radiated noise generated by a surface or underwater marine platform has gained significant global concern in recent times in view of the growing impetus on the analysis and minimisation of harmful effects of the increase in the ‘ambient noise’ on the marine ecosystem. The ocean is rightly called the ‘silent world’ where there is no room for any foreign noise/disturbance. Over the last few decades, the studies have reported an increase in low-frequency ambient sea noise by an average rate of about 1/2 dB per year which is attributable to the growing fleet of ships both commercial and military vessels. When we consider sources of ambient noise in deep water, the distance ship traffic is a dominant source of noise at frequencies around 100 Hz, and high ship-traffic activity is dominant source of noise in the frequencies from 50 to 500 Hz [2]. In case of military vessels, the radiated noise also effects the detectability, operability as well as survivability of the vessel.

Ships’ underwater radiated noise comprises the machinery noise, propeller noise and hydrodynamic flow noise. The propeller noise consists of both cavitating and non-cavitating noises. The merchant ships generally operate at low speeds (less than cavitation inception speed), and hence, the propeller noise in the non-cavitating region also becomes an important concern. Also, for deeply submerged vehicles, where cavitation does not occur, the non-cavitating noise becomes an important factor. The design intent is aimed at delaying the inception of propeller cavitation to speed greater than the normal operating/cruising speeds. Hence, it becomes important to study and quantify the propeller non-cavitating noise and identify and implement design steps to delay cavitation inception (Fig. 1).

Marine propellers operate in a highly three-dimensional turbulent wake field behind a ship, which makes it very complicated and difficult to resolve the flow-field variables. In order to perform the hydro-acoustic analysis and predict the noise generated by the propellers, it is first required to carry out the hydrodynamic analysis of the flow and estimate the flow parameters like velocities and pressure. This can be done either by experimental as well as numerical approaches. Several attempts have been made in the past by many researchers to estimate the propeller performance experimentally. Experimental works carried out by Amini and Steen [3], Liu et al.

**Fig. 1** DTMB 4119 propeller model *Source* Mousavi et al. [15]



[4] and Elghorab et al. [5] are relevant in this regard. But conducting the experiments requires complicated set-ups, and these are very expensive both in terms of time and cost. An alternative to this approach is conducting numerical simulations which have also been found very useful in undertaking these studies. These numerical methods have used both inviscid and viscous flow methods.

The noise which is detected in a fluid can be generated due to two reasons, namely due to the vibrations of the structure and due to the hydrodynamic fluid fluctuations. In the present study, only the noise generated by fluid fluctuations has been estimated.

Generally, to estimate the propeller-generated noise empirical, semi-empirical and Bernoulli-based methods have been used. But the generation of a method by aero-acousticians Ffowcs Williams–Hawkings (FWH) for calculation of noise generated by an arbitrary moving body in a fluid is considered as a novel development in this direction.

Seol et al. [6] investigated the non-cavitating propeller noise in non-uniform flow using potential-based panel method coupled with acoustic analogy (FWH equation) and boundary element method (BEM). Seol et al. [7] extended their work to estimation of propeller noise in the cavitating regime. The flow field was analysed with potential-based panel method, and the time-dependent pressure and sheet cavity volume data were used as the input for FWH formulation to predict the far-field acoustics.

In 2003, Salvatore and Ianniello [8] undertook numerical prediction of the acoustic pressure field induced by cavitating marine propellers using boundary integral formulations. A hydrodynamic model for transient sheet cavitation on propellers in non-uniform inviscid flow was coupled with a hydro-acoustic model based on the FWH equation. The study brought out splitting of the noise signature into thickness and loading term contributions. The predictions using the FWH equation were found to be close agreement with those obtained using Bernoulli equation model. Several attempts have been made in the recent years by many researchers to predict the non-cavitating propeller noise in uniform as well as non-uniform flow using various CFD codes coupled with either FWH equations or in-house built noise prediction codes.

In the present study, the underwater RNL of a DTMB 4119 model propeller has been predicted by a 3D numerical simulation of the flow around the propeller operating in the non-cavitating regime for the uniform flow (no wake) condition. For the near field, the RANS equations have been used for modelling the flow, and the  $k-\epsilon$  model has been used to simulate the turbulence. For the far-field acoustic, the FWH model has been applied. FWH steady and FWH-on-the-fly models have been used in the steady and transient analyses, respectively. Analysis of the radiated sound pressure level with respect to distance from the propeller has been carried out, and the results obtained have been discussed. The open water hydrodynamic characteristics obtained using numerical simulation have been validated with the published experimental results. The SPL predicted for the design advance coefficient ( $J$ ) of 0.833 has been compared with the available published numerical results. Further, the SPLs have been predicted for different advance coefficients, and the results obtained have been discussed.

## 2 Governing Equations

While performing the hydrodynamic analysis of fluid flow, the flow-field variables can be predicted by solution of the two basic equations, namely the continuity (Eq. 1) and momentum equations (Eq. 2).

$$\frac{\partial \rho}{\partial t} + \frac{\partial}{\partial x_i}(\rho u_i) = 0 \quad (1)$$

$$\frac{\partial}{\partial t}(\rho u_i) + \frac{\partial}{\partial x_j}(\rho u_i u_j) = \frac{\partial}{\partial x_j} \tau_{ij} - \frac{\partial p}{\partial x_i} + \rho g_i - \rho \bar{u}_i \bar{u}_j \quad (2)$$

where  $u_i$  is the velocity components of the fluid,  $\rho$  is the density,  $p$  is the pressure,  $\tau$  is the shear stress tensor,  $g$  is the acceleration due to gravity and  $\bar{u}_i \bar{u}_j$  is the Reynolds stress tensor. Equations (1) and (2) are coupled and should be solved simultaneously in an iterative manner.

The estimation of the distribution of Reynolds stress throughout the flow field has been the subject of numerous investigations. In this study, the k- $\epsilon$  model has been used to simulate the turbulence. This model has been used in many recent hydro-acoustic estimations like the studies undertaken by Ghassemi et al. in 2016 and 2017.

The first and most recognised work in the field of acoustic waves has been done by Lighthill (1952). The two basic governing equations of the continuity and momentum are employed to obtain overall sound production relationship by writing the continuity equation as follows:

$$\frac{D\rho}{Dt} + \text{div}(\rho \bar{u}) = \frac{\partial \rho}{\partial t} + \frac{\partial}{\partial x_i}(\rho u_i) = q \quad (3)$$

where  $q$  is the mass production rate per unit volume. The momentum equation is expressed as:

$$\frac{\partial}{\partial t}(\rho u_i) + \frac{\partial}{\partial x_j}(\rho u_i u_j) = -\frac{\partial p}{\partial x_i} - \frac{\rho g \partial \tau}{\partial x_i} + f_i \quad (4)$$

where  $f_i$  represents the body forces. From Eqs. (3) and (4), Eq. (5) is obtained as follows:

$$\frac{\partial^2 \rho}{\partial t^2} + c_0^2 \nabla^2 p = \partial^2(T_{ij})/\partial x_i \partial x_j \quad (5)$$

where  $c_0$  is the speed of sound and  $T_{ij}$  is the Lighthill stress tensor. It is expressed as

$$T_{ij} = \rho u_i u_j + \delta_{ij}(p - \rho c_0^2) + \tau_{ij} \quad (6)$$

The first term on the RHS of Eq. (6) is the turbulence velocity fluctuations (Reynolds stresses), the second term is due to change in pressure and density, and the third term is due to the shear stress tensor.

A generalisation of Lighthill’s theory to include aerodynamic surfaces in motion proposed by Ffowcs Williams–Hawkings (1969) has provided the basis for a significant amount of analysis of the noise produced by rotating blades, including helicopter rotors, propeller blades and fans. The FWH theory includes surface source terms in addition to the quadrapole-like sources introduced by Caridi (2007). The surface sources are generally referred to as thickness or monopole sources and loading or dipole sources. This equation is presented as follows (FWH 1969):

$$\frac{\partial^2 p'}{c_0^2 \partial t^2} - \nabla^2 p' = \frac{\partial^2}{\partial x_i \partial x_j} [T_{ij} H(f)] - \frac{\partial}{\partial x_i} ([P_{ij} n_j + \rho u_i (u_n - v_n)] \delta(f)) + \frac{\partial}{\partial t} ([\rho_0 v_n + \rho (u_n - v_n)] \delta(f)) \tag{7}$$

The terms at the RHS of Eq. (7) are named quadrapole, dipole and monopole sources, respectively,  $p'$  is the source pressure level at the far field ( $p' = p - p_0$ ),  $c_0$  is the far-field sound speed and  $T_{ij}$  is the Lighthill stress tensor defined in Eq. (6). Also,  $f$  is a function defined based on surface reference system where setting  $f = 0$  introduces a surface that embeds the external flow effect ( $f > 0$ ), and  $H(f)$  and  $\delta(f)$  are Heaviside and Dirac delta functions, respectively.

There are various ways to evaluate the FWH equation. Farassat proposed time-domain formulation that can predict arbitrary-shaped object in motion without the numerical differentiation of the observer time. The formulation of Farassat is very convenient in embodying the time-domain analysis of FWH equation. In the Farassat formulation, the pressure field is defined as:

$$P'(\vec{x}, t) = P'_T(\vec{x}, t) + P'_L(\vec{x}, t) \tag{8}$$

where  $P'$  is the acoustic pressure,  $P'_T$  and  $P'_L$  describe the acoustic pressure field resulting from thickness and loading, corresponding to the monopole and the dipole sources. In the present analysis, quadrapole noise has been neglected since the speed of rotation of the propeller is much less than the speed of sound in water.

By solving this equation, pressure variation and sound pressure level (SPL) measured in dB are calculated as follows:

$$\text{SPL} = 20 \log_{10} \left( \frac{P_{\text{rms}}}{P_{\text{ref}}} \right) \tag{9}$$

where  $P_{\text{rms}}$  is the root-mean-square sound pressure expressed in  $P_a$  and  $P_{\text{ref}}$  is the reference pressure of 1  $\mu\text{Pa}$ .

### 3 Numerical Modelling

The propeller model selected to undertake this analysis is the three-bladed DTMB4119 propeller which was originally designed by Denny. The data of this propeller was distributed to various research institutes by the ITTC propulsion committee for undertaking hydrodynamic research. Eight organisations including BEC France, HSVA Germany, HMRI Korea, SRI Japan, DERA UK, VTT Finland, University of Iowa USA and CSSRC China had conducted RANS calculations on the DTMB P4119 propeller and discussed the results during the workshop on Propulsion Committee held during 22nd ITTC [9]. Numerical modelling of the propeller and associated geometric parts has been undertaken using the commercial design software Rhino 3D. The solution of the flow around the propeller has been done using the commercial CFD code STAR-CCM+; the hydro-acoustic analysis has been performed using the in-built aero-acoustic analysis utility of STAR-CCM+. The details of the numerical modelling including propeller geometry, computational domain, boundary conditions and meshing have been discussed in subsequent paragraphs.

#### 3.1 Geometry

The geometry data of DTMB4119 propellers has been obtained from Brizzolara et al. [10], and the foil geometry has been obtained from the Report of the Propulsion Committee [11]. The details of this propeller are indicated in Table 1, and the front view of the propeller modelled for the present study using Rhino 3D software is shown in Fig. 2. The origin is located at the centre of the propeller, and the coordinate system has been selected such that positive  $x$ -axis is towards the upstream direction of the propeller, positive  $z$ -axis is upwards and positive  $y$ -axis is inwards into the plane.

**Fig. 2** DTMB 4119 propeller model

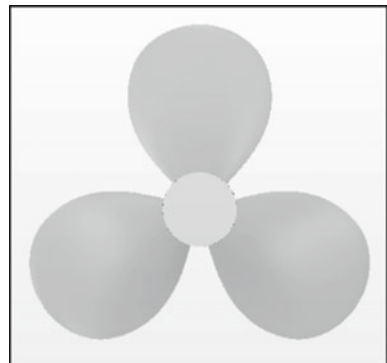


**Table 1** DTMB4119 propeller geometry data

(a) Propeller geometry data						
Prop	4119					
$r/R$	$c/D$	$rk/D$	$sk$ [°]	$P/D$	$t_{max}/c$	$f_{max}/c$
0.20	0.3200	0.00	0.00	1.1050	0.2055	0.0143
0.30	0.3635	0.00	0.00	1.1022	0.1553	0.0232
0.40	0.4048	0.00	0.00	1.0983	0.1180	0.0230
0.50	0.4392	0.00	0.00	1.0932	0.0902	0.0218
0.60	0.4610	0.00	0.00	1.0879	0.0696	0.0207
0.70	0.4622	0.00	0.00	1.0839	0.0542	0.0200
0.80	0.4347	0.00	0.00	1.0811	0.0421	0.0197
0.90	0.3613	0.00	0.0000	1.0785	0.0332	0.0182
0.95	0.2775	0.00	0.00	1.0770	0.0323	0.0163
0.98	0.2045	0.00	0.00	1.0761	0.0321	0.0145
1.00	0.0800	0.00	0.00	1.0750	0.0316	0.0118

(b) Hydrofoil geometry data			
Foil geometry at conventional stations NACA 66(Mod) and $a = 0.8$ camber			
Station	Thickness ordinate	Camber ordinate	Camber slope
$x$	$Y_T/t$	$Y_C/f$	$\frac{dY_C/f}{dx}$
0	0	0	–
0.005	0.0665	0.0423	7.149
0.0075	0.0812	0.0595	6.617
0.0125	0.1044	0.0907	5.944
0.025	0.1466	0.1586	5.023
0.05	0.2066	0.2712	4.083
0.075	0.2525	0.3657	3.515
0.1	0.2907	0.4482	3.100
0.15	0.3521	0.5869	2.488
0.2	0.4000	0.6993	2.023
0.25	0.4363	0.7905	1.635
0.3	0.4637	0.8635	1.292
0.35	0.4832	0.9202	0.933
0.4	0.4952	0.9615	0.678
0.45	0.5	0.9881	0.385
0.5	0.4962	1.0	0.091
0.55	0.4846	0.9971	–0.211
0.6	0.4653	0.9786	–0.532
0.65	0.4383	0.9434	–0.885
0.7	0.4035	0.8892	–1.295

(continued)



**Table 1** (continued)

(b) Hydrofoil geometry data			
Foil geometry at conventional stations NACA 66(Mod) and $a = 0.8$ camber			
Station	Thickness ordinate	Camber ordinate	Camber slope
0.75	0.3612	0.8121	-1.813
0.8	0.3110	0.7027	-2.712
0.85	0.2532	0.5425	-3.523
0.9	0.1877	0.3586	-3.768
0.95	0.1143	0.1713	-3.668
0.975	0.0748	0.0823	-3.441
1.0	0.0333	0	-3.003
(c) Model scale propeller details			
Type	DTMB4119		
Diameter ( $D$ )	305 mm		
Hub diameter ( $d$ )	60 mm		
No of blades ( $Z$ )	3		
Pitch ratio ( $P/D$ ) at 0.7R	1.084		
RPS	10		
Design $J$	0.833		
Design $V_A$	2.54 m/s		
Pitch	0°		
Skew	0°		
NACA section shape	66 (Mod)		
NACA meanline	0.8		

### 3.2 Domain

The computational domain along with all the parts and boundary conditions is shown in Fig. 3. It consists of an outer cylinder of length  $18D$  and diameter  $10D$  surrounding the propeller. A small cylinder of length  $0.385D$  and diameter  $1.1D$  is placed around the propeller. This cylinder represents the interface and is used to simulate the propeller rotation. The outer cylinder along with the shaft and the inner cylinder/interface constitutes the stationary part, and the propeller along with the hub and the inner cylinder/interface constitutes the rotating part. The open water condition has been applied to the inlet. The sizing of the domain is in accordance with the ITTC recommended guidelines for undertaking ship self-propulsion studies using CFD [12].

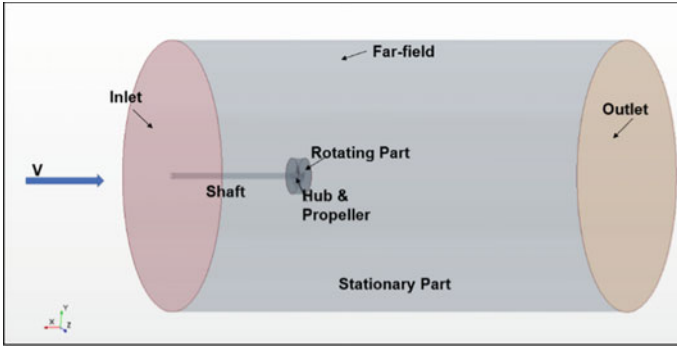


**Fig. 3** Computational domain

**Table 2** Boundary conditions

Region: stationary region	
Inlet	Velocity inlet
Outlet	Pressure outlet
Far field	Walls with slip condition

### 3.3 Boundary Conditions

The boundary conditions followed in the analysis are indicated in Table 2.

### 3.4 Meshing

An unstructured hybrid mesh was applied for grid generation. The meshing models selected for the present analysis are surface remesher, trimmer and prism layer mesher. Triangular cells have been used for meshing the blades and hub surfaces. Coarse grid has been used on the far field, and a finer grid has been used for near wall on the propeller blades, tip, interface to accurately capture the flow phenomenon in this region. The prism layer has been disabled from the inlet, outlet and far-field regions. All this have been done to reduce the computational time. A cylindrical volumetric mesh refinement has been applied around the rotating region to further refine the mesh in the region of interest. Three different base sizes, 30, 40 and 50 mm, has been used for the convergence study. The results of this have been discussed later in this paper. A cross section of the volume mesh on a vertical plane passing through the origin is shown in Fig. 4.

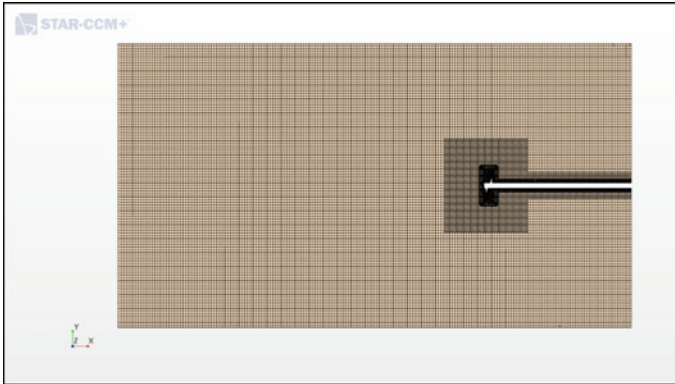


**Fig. 4** Meshed computational domain

### 3.5 Acoustic Analysis

The hydro-acoustic analysis has been carried out by suitable modification of the aero-acoustic utility of the CFD code. SPL has been estimated using the FWH equations for both steady and transient states. For the steady-state analysis, the propeller rotation has been modelled using moving reference frame (MRF) method. Moving reference frames (MRFs) are reference frames that can rotate and translate with respect to the laboratory reference frame. MRF models in STAR-CCM+ assume that the angular velocity of the body is constant and the mesh is rigid. For the transient analysis, the propeller rotation has been modelled using moving reference frame (MRF) as well as sliding mesh methods. In the sliding mesh method, the region containing the propeller geometry is meshed as a separate region, and a purely rotational motion is applied to the entire propeller mesh. This results in a transient calculation, which provides time-accurate results [13]. A quantitative comparison with respect to the two methods has been brought out. The position of the six FWH receivers (A1, A2, A3, B1, B2 and B3) with respect to the propeller is shown in Fig. 5.

## 4 Hydrodynamic Analysis and Findings

### 4.1 Convergence Analysis

The  $K_T$ ,  $10K_Q$  and  $\eta_O$  convergence analyses were examined for three base sizes, i.e. 20, 30 and 50 mm, leading to 6,710,447, 2,180,027 and 564,806 cells, respectively. A comparison of the  $K_T$ ,  $10K_Q$  and  $\eta_O$  values obtained for the design  $J$  of 0.833 for the three base sizes along with error analysis is shown in Table 3. From the analysis,

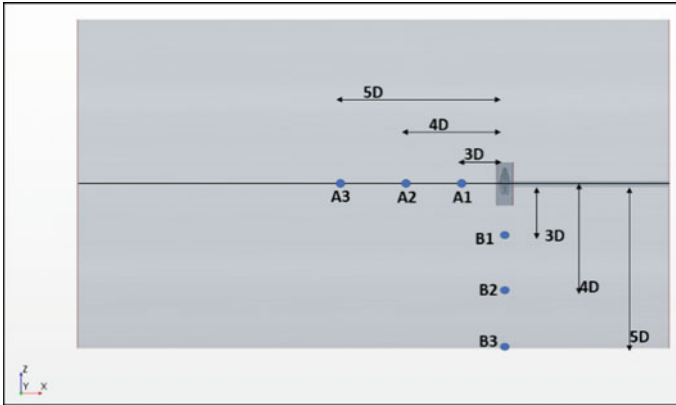


**Fig. 5** Location of the FWH receivers

**Table 3** Convergence analysis

Base size (mm)	$10K_Q$ -expt	$K_T$ -expt	$\eta_O$ -expt	$10K_Q$ -pred	$K_T$ -pred	$\eta_O$ -pred	$10K_Q$ -error	$K_T$ -error	$\eta_O$ -error
20	0.28	0.145	0.69	0.248	0.126	0.673	11.26	13.01	2.50
30	0.28	0.145	0.69	0.251	0.127	0.670	10.45	12.56	2.88
50	0.28	0.145	0.69	0.255	0.128	0.664	9.11	12.04	3.75

it was found that base size of 30 mm results in the least error, and hence, this base size was chosen for further analysis.

### 4.2 Open Water Characteristics

The open water characteristics of DTMB4119 model were estimated as a function of the advance coefficients for  $J$  values of 0.2, 0.4, 0.6, 0.8 and 1 using the steady-state analysis. From the convergence analysis, base size of 30 mm was selected for this simulation. Simulation for each value of  $J$  was executed for 550 iterations which took a physical time of about 10 h to complete the analysis and obtain the desired residuals. The processor used is Intel® Xenon® CPU E5-1620 v4 @ 3.50 GHz, and the installed memory is 16 GB. The variation of  $J$  was achieved by varying the value of advance velocity ( $V_A$ ) and keeping the propeller rotation rate constant.

The predicted open water characteristics were compared with the experimental results of Jessup et al. (1989) which have been obtained from the calculation results for the 22nd ITTC Propulsor Committee Workshop on Propeller RANS/PANEL Methods [14]. The comparison shows matching with an error of 2.88% in the open water efficiency at the design  $J$  of 0.833 (Fig. 6).

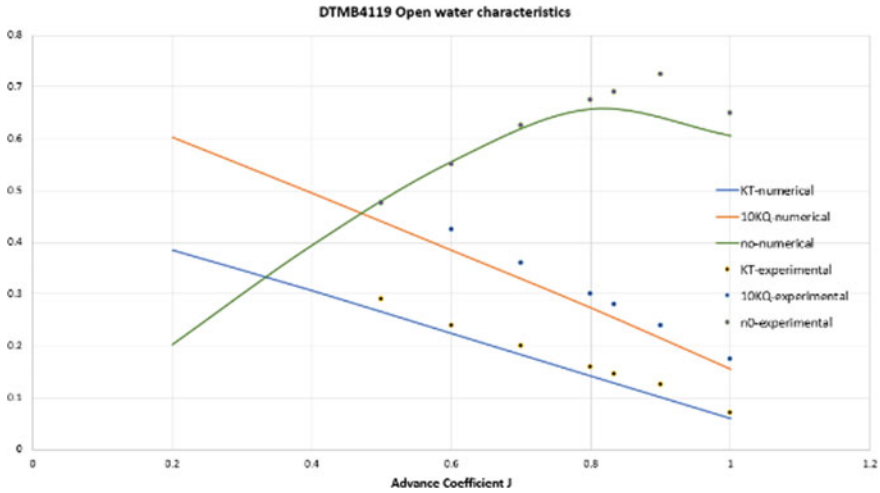


**Fig. 6** Comparison of numerical and experimental results of the open water characteristics of DTMB4119 model propeller

## 5 Acoustic Analysis and Findings

The hydro-acoustic analysis has been performed by suitable modification of the in-built aero-acoustics utility of the CFD software. The density and the speed of sound in the medium, i.e. water, were changed to  $1000 \text{ kg/m}^3$  and  $1500 \text{ m/s}$ , respectively. The propeller surface has been modelled as the impermeable FWH surface. The contribution from the hub has been neglected. Six receiver locations have been used in the analysis.

### 5.1 Steady-State Analysis

Initially steady-state analysis was carried out for  $J = 0.833$ , and the time series of acoustic pressures was obtained. Fourier transformation of this time series was undertaken to obtain the frequency distribution of the sound pressure levels. The pressure time history and frequency distribution of SPL are shown in Fig. 7.

Figure 7a shows the pressure-time history predicted for  $J = 0.833$  at the three receivers A1, A2 and A3 placed in line with the hub towards the downstream of the propeller. It can be seen that the acoustic pressure decreases from receiver A1 to A3 since the distance from the acoustic source/propeller increases in this direction. The SPL versus frequency distribution at receiver A1, A2 and A3 has been obtained using fast Fourier transformation (FFT) of the pressure-time histories predicted at these locations and shown in Fig. 7b. Two characteristic peaks/tonals are visible at 10 and 20 Hz in each of these SPL distributions. Pattern similar to Fig. 7a is also seen

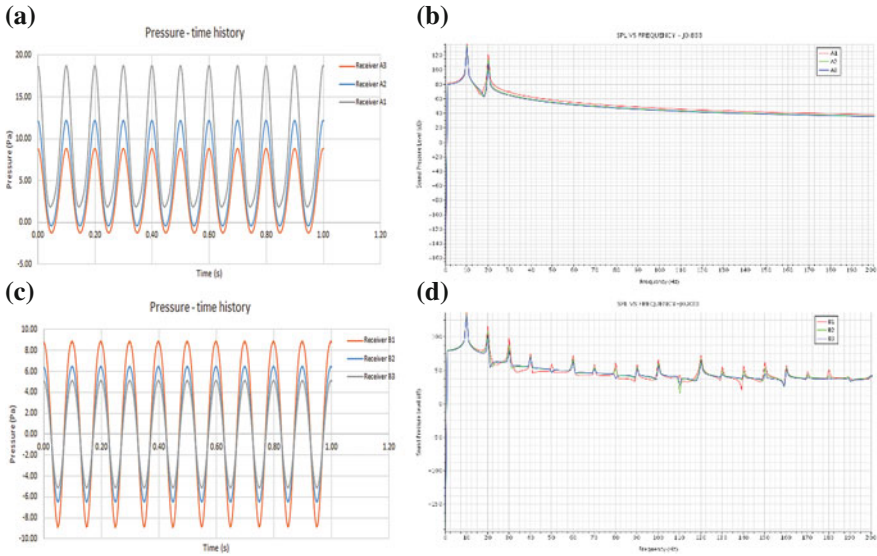


**Fig. 7** Pressure-time history and frequency distribution of SPL for  $J = 0.833$ . **a** Pressure-time history at receiver A1, A2 and A3. **b** SPL at receiver A1, A2 and A3. **c** Pressure-time history at receiver B1, B2 and B3. **d** SPL at receiver B1, B2 and B3

in Fig. 7c where the acoustic pressure reduces as we move from receiver B1 to B3 since the distance from the propeller increases in vertical direction. The SPL versus frequency distribution at receiver B1, B2 and B3 has been obtained using fast Fourier transformation (FFT) of the pressure-time histories predicted at these locations and shown in Fig. 7d. It exhibits two major peaks at 10 and 20 Hz.

### 5.2 Transient Analysis

Transient analysis was carried out for  $J = 0.833$  and a total time of 0.1 s which corresponds to the time taken by the propeller for one complete rotation. The time step was taken as the time required to rotate the propeller by  $2^\circ$  (in accordance with ITTC guidelines for ship self-propulsion using CFD [13]) and corresponds to  $5.56e-4$  s. Figure 8 shows that the SPL predicted by MRF, and sliding mesh methods for  $J = 0.833$  and  $rps = 10$  generally show similar results except at few frequencies.

Comparison of the sound pressure levels predicted by the numerical simulation (using sliding mesh method) with the numerical results of Seol et al. [6] for  $J = 0.833$ ,  $rps = 10$  and at a receiver location of 5D is undertaken and is shown in Fig. 9.

Deviations of about 5 dB in the SPL values are seen at frequencies between 12.5 and 25 Hz between the present study and numerical results of Seol et al. [6]. This may possibly be because the analysis by Seol et al. [6] was based on potential-based panel

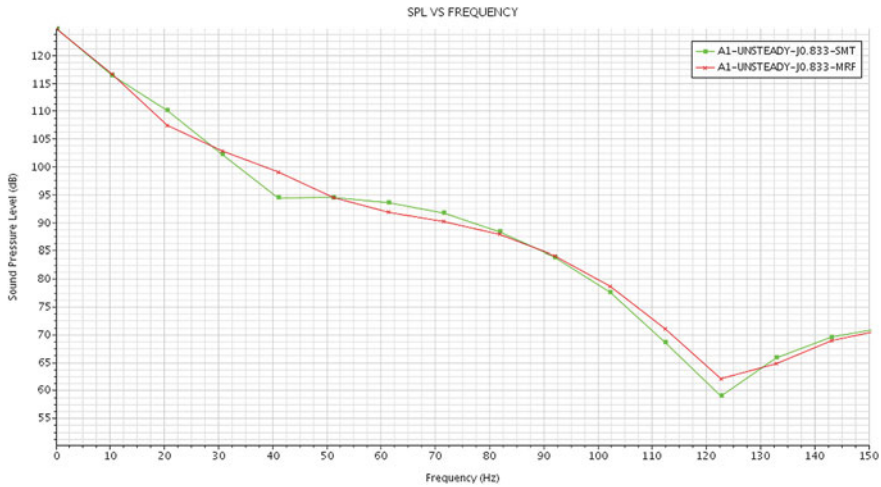


**Fig. 8** Comparison of SPL predicted for  $J = 0.833$  with MRF and sliding mesh methods

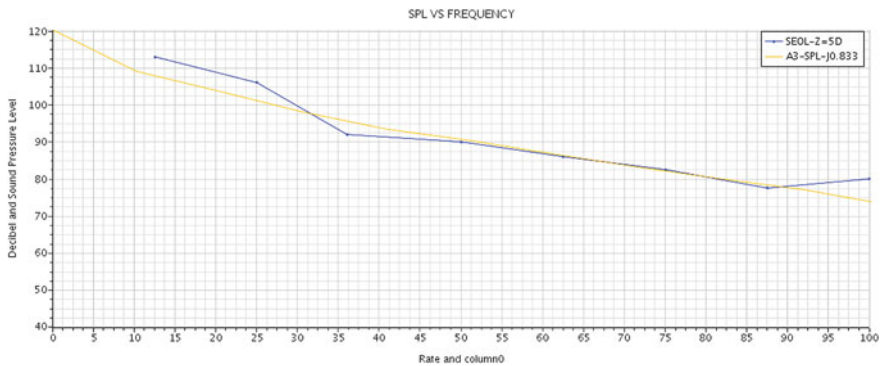


**Fig. 9** Comparison of predicted SPL with published numerical results

method coupled with time-domain acoustic analogy to predict the generated noise in non-uniform flow condition, and the present study has been carried out using RANS method for uniform flow condition. Sound pressure levels for  $J = 0.2, 0.4, 0.6, 0.8$  and  $1.0$  at the two receiver locations A1 and B1 using the sliding mesh method are shown in Figs. 10, 11, 12, 13 and 14, respectively.

The SPL obtained at two receiver locations A1 and B1 for different  $J$  values up to 500 Hz is shown in Figs. 9, 10, 11, 12 and 13. It is observed that SPL predicted at A1 reduces as advance coefficient increases. This observation is in line with the findings of Mousavi et al. [15] that decreasing the advance coefficients increases the acoustic pressure range of the noise recorded in the receiver.

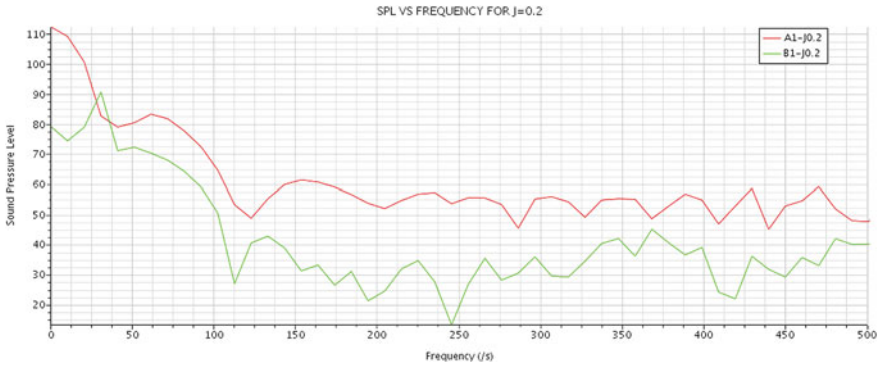


Fig. 10 SPL at receiver A1 and B1 at J = 0.2

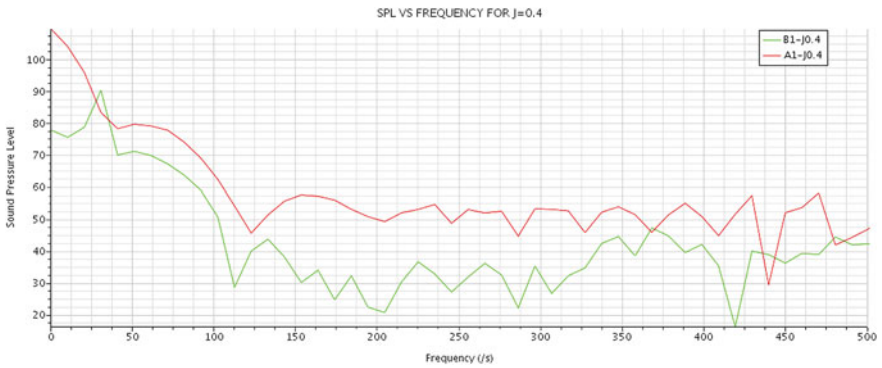


Fig. 11 SPL at receiver A1 and B1 at J = 0.4

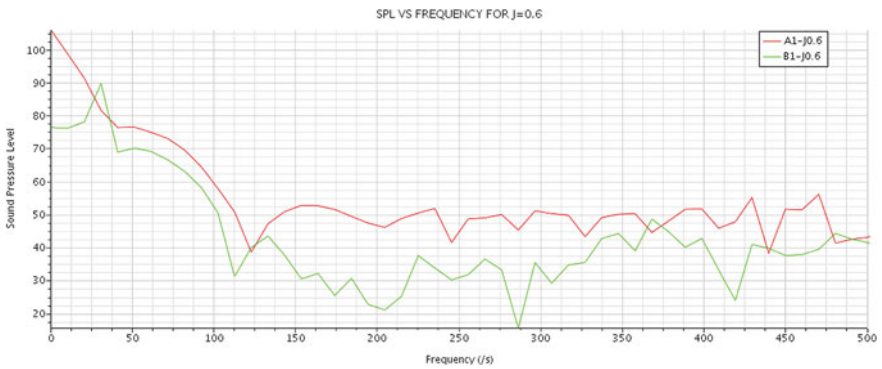


Fig. 12 SPL at receiver A1 and B1 at J = 0.6



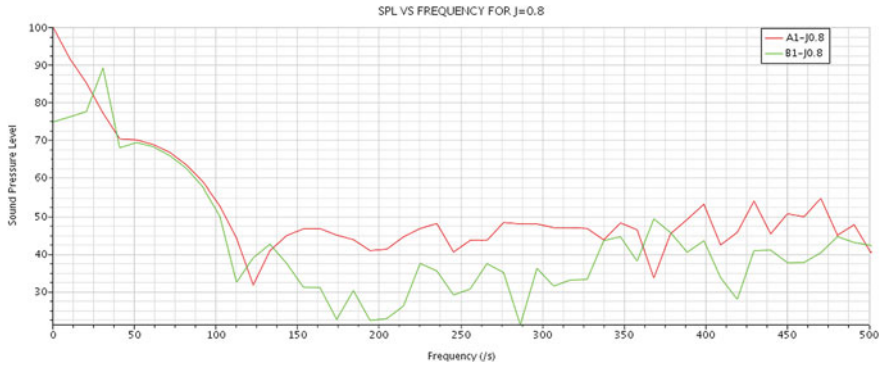


Fig. 13 SPL at receiver A1 and B1 at  $J = 0.8$



Fig. 14 SPL at receiver A1 and B1 at  $J = 1.0$

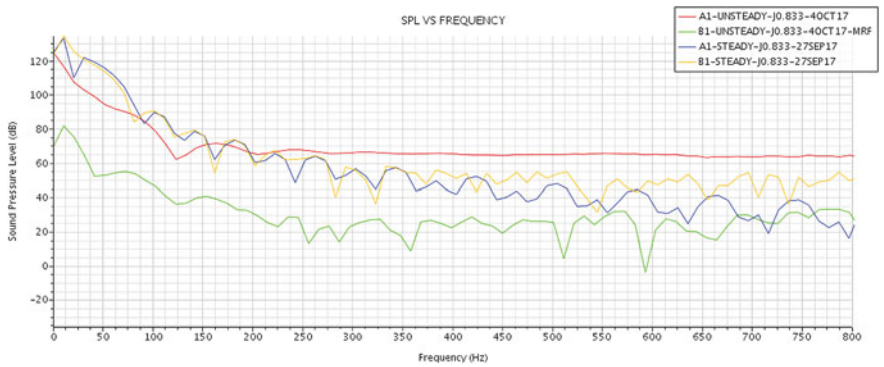


Fig. 15 Comparison of SPL obtained in steady and transient analyses for  $J = 0.833$

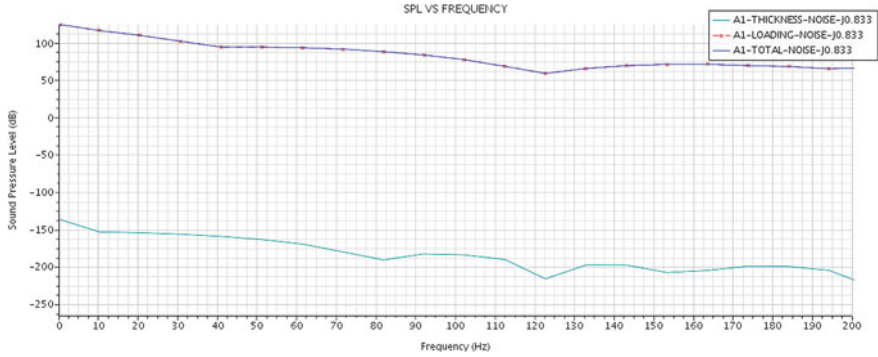


Fig. 16 Comparison of thickness and loading noise at receiver A1

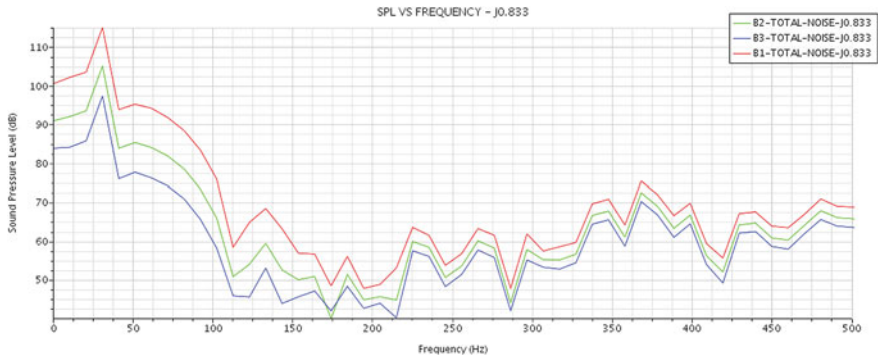


Fig. 17 Comparison of thickness and loading noise at receiver B1

A comparison of the SPL predicted for the steady and transient analyses for  $J = 0.833$  is shown in Fig. 15. The study shows that at the receiver location A1, up to 200 Hz, the SPL in the steady state is more than the SPL in transient state and beyond 200 Hz, the SPL in the transient state analysis stabilises to a value of about 70 dB, whereas SPL in the steady-state analysis keeps decreasing. At the receiver location B1, SPL in the transient analysis is always lower than that in the steady-state analysis.

A numerical simulation in order to analyse the contribution of the surface thickness and loading noise to the total surface noise was undertaken for  $J = 0.833$ . Figure 16 shows the thickness noise and loading noise at receiver A1. It shows that in the far field, the contribution of thickness noise is negligible in comparison to that of loading noise in the downstream direction of the propeller hub. Similar pattern has been seen at receiver locations A2 and A3. Similar observation was also brought out by Jang et al. [16] in 2014 wherein he observed that when the underwater radiated noise for the propeller is predicted in far field, the thickness noise is negligible compared to loading noise even though the advance coefficient is high.

In order to analyse the distribution pattern of loading and thickness noise corresponding to a value of  $J = 0.833$ , total surface noise components at receiver locations A1 and B1 were analysed. Figure 17 shows the thickness noise and loading noise at receiver B1. From Figs. 16 and 17 and also with the predicted thickness and loading noise values at receiver locations A2, A3, B2 and B3, it is observed that for a  $J = 0.833$ , loading noise is more dominant in the region on the hub axis (e.g. receiver location A1, A2 or A3) while the thickness noise is more dominant in the plane of blade rotation (e.g. receiver location B1, B2 or B3). This is in line with the acoustic findings of Seol et al. [6] wherein he observed that monopole thickness noise is known to radiate strongest towards the plane of blade rotation and the unsteady dipole loading noise has a strong radiation tendency towards the observer on the hub axis.

## 6 Conclusions

Numerical analysis to predict the underwater radiated noise of DTMB4119 model propeller operating in the non-cavitating regime in uniform flow (no wake condition) has been undertaken using the CFD code STAR-CCM+; the hydro-acoustic analysis has been undertaken using the FWH equations. The open water hydrodynamic characteristics and the SPL generated by the DTMB4119 model propeller for different advance coefficients have been predicted. Based on the analysis of numerical results, the following conclusions can be drawn:

- The numerical results and experimental data for the open water hydrodynamic characteristics of the model propeller show matching with an error of 2.88% in the open water efficiency at the design  $J$  of 0.833.
- The predicted SPL is compared with the numerical results of Seol et al. and shows matching. The deviations in the SPL from the numerical results of Seol et al. may be attributable to the difference in the methodologies adopted in the two studies.
- The SPL decreases as the distance of the observer/receiver from the propeller is increased.
- The moving reference frame and sliding mesh methods of modelling the propeller and its rotation in CFD show almost similar results in terms of SPL at very low rpms (rps = 10 in this study).
- Contribution of the thickness noise is negligible in comparison to that of loading noise at the receiver locations placed on the propeller hub axis for  $J = 0.833$ .
- Monopole thickness noise radiates strongest towards the plane of blade rotation, and the unsteady dipole loading noise has a strong radiation tendency towards the observer on the hub axis for  $J = 0.833$ .
- In the future scope of work, we can extend this study to analyse the effect of variation of geometrical parameters like rake angle, skew, section shape on the radiated noise levels of a marine propeller.

## References

1. Ross D (2005) Ship sources of ambient noise. *IEEE J Ocean Eng* 30(2):257–261
2. Acoustic measures and sonar principles (2017)
3. Amini H, Steen S (2011) Experimental and theoretical analysis of propeller shaft loads in oblique inflow. *J Sh Res* 55(4):1–21
4. Liu N, Wang S, Guo T, Li X, Yu Z (2011) Experimental research on the double-peak characteristic of underwater radiated noise in the near field on top of a submarine. *J Mar Sci Appl* 10:233–239
5. Elghorab MA, Aly AAE, Elwetedy AS, Kotb MA (2013) Experimental study of non-series marine experimental study of open water non-series marine propeller performance. In: World academy of science, engineering and technology, no. 78, pp 720–726
6. Seol H, Jung B, Suh JC, Lee S (2002) Prediction of non-cavitating underwater propeller noise. *J Sound Vib* 257(1):131–156
7. Seol H, Suh JC, Lee S (2005) Development of hybrid method for the prediction of underwater propeller noise. *J Sound Vib* 288(1–2):345–360
8. Salvatore F, Ianniello S (2003) Preliminary results on acoustic modelling of cavitating propellers. *Comput Mech* 32(4–6):291–300
9. The propulsion committee final report and recommendations to the 22nd ITTC
10. Brizzolara S, Diego V, Gaggero S (2008) A systematic comparison between RANS and panel methods for propeller analysis, Oct
11. Report of propeller committee ITTC 1978
12. ITTC (2014) ITTC—recommended procedures and guidelines—practical guidelines for ship self-propulsion CFD. 7.5-03-03-01 (Revision 00). p 9
13. Kellett P, Turan O, Incecik A (2013) A study of numerical ship underwater noise prediction. *Ocean Eng* 66:113–120
14. Brander P (2015) Calculation results for the 22nd ITTC propulsor committee workshop on propeller RANS/PANEL methods: steady panel method analysis of DTMB 4119 propeller, Jan
15. Mousavi B, Rahrovi A, Kheradmand S (2014) Numerical simulation of tonal and broadband hydrodynamic noises of non-cavitating underwater propeller. *Pol Marit Res* 21(83):46–53
16. Jang JS, Kim HT, Joo WH (2014) Numerical study on non-cavitating noise of marine propeller. *Internoise* 2014:3–8

# Estimation of Hydrodynamic Derivatives from Sea Trial Data Using System Identification Technique



K. O. S. R. RaviSekhar RadhaKrishna and R. Panneer Selvam

**Abstract** The aim of the paper is to demonstrate the application of system identification technique to estimate the hydrodynamic derivatives with the full-scale manoeuvring data of a ship. The application of such technique would be for design of autopilots, enhancement of manoeuvring characteristics of ships in service and validation of mathematical model for ship manoeuvring. The paper briefly describes the mathematical model for ship manoeuvring used for parameter identification of a bulk carrier using extended Kalman filter system identification technique. The standard manoeuvres conducted in line with the recommendations of International Maritime Organization (IMO) resolution 137 include turning circle trials and crash stop trial details are presented and using extended Kalman filter technique hydrodynamic derivatives are estimated. This paper includes also the full scale trial data of a inshore patrol vessel.

**Keywords** Sea trial · Extended Kalman filter · Hydrodynamic derivatives

## 1 Introduction

The inshore patrol vessel is a light-armed surface vessel primarily designed for patrol, search and rescue operations in shallow and coastal waters. The vessel is fitted with three waterjets. Waterjet propulsion is being fitted to the patrol vessels to improve the propulsive efficiency as well as the turning and stopping characteristics at high speeds which are quite important during patrol, search and rescue operations. The hull form is a double chine planing hull form with transom stern designed to facilitate fitment of waterjets. Knowledge of full-scale manoeuvring characteristics is an added advantage to the ship staff especially soon after the delivery of the ship. The data

---

K. O. S. R. RaviSekhar RadhaKrishna · R. Panneer Selvam (✉)  
Department of Ocean Engineering, Indian Institute of Technology Madras, Chennai 600036, India  
e-mail: [pselvam@iitm.ac.in](mailto:pselvam@iitm.ac.in)

K. O. S. R. RaviSekhar RadhaKrishna  
Hindustan Shipyard Limited, Visakhapatnam, India

© Springer Nature Singapore Pte Ltd. 2019  
K. Murali et al. (eds.), *Proceedings of the Fourth International Conference in Ocean Engineering (ICOE2018)*, Lecture Notes in Civil Engineering 22,  
[https://doi.org/10.1007/978-981-13-3119-0\\_11](https://doi.org/10.1007/978-981-13-3119-0_11)

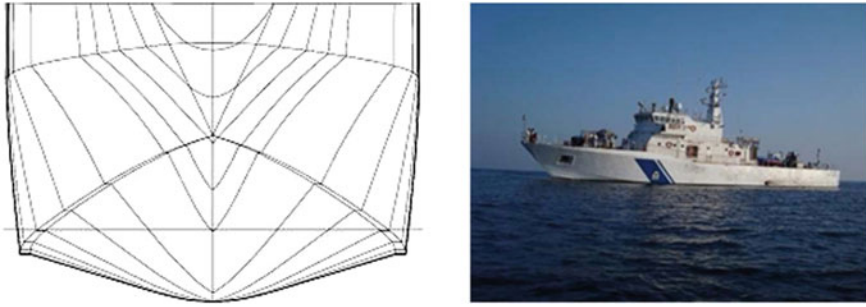


**Fig. 1** Body plan (left) and photograph (right) of inshore patrol vessel



**Fig. 2** Hull form (left) and photograph (right) of bulk carrier

was recorded during the sea trials of the vessel. The body plan and ship's photograph taken during the trials are shown in Fig. 1.

The bulk carrier presented in this paper is a 38,000 T displacement vessel with a service speed of about 14 knots. The vessel is propelled by a conventional single screw fixed pitch propeller driven by a four-stroke slow speed directly reversible marine diesel engine. The hull form is a typical high block merchant hull form. The full-scale sea trial data was recorded at the ballast draft. The ship's hull form and photograph are shown in Fig. 2.

### ***1.1 Main Particulars of the Inshore Patrol Vessel and Bulk Carrier***

The main particulars of the inshore patrol vessel and the bulk carrier are as given below:

In this paper, the results of turning circle trials and crash stop trial of the bulk carrier and the turning circle trials of the inshore patrol vessel conducted during full-scale sea trials are presented.

The data of the full-scale sea trials of bulk carrier is utilized to identify the hydrodynamic derivatives of the bulk carrier using extended Kalman filter technique.

	Inshore patrol vessel	Vessel bulk carrier
Length (LBP)	44.00 m	170 m
Breadth of the ship	8.36 m	28 m
Depth of the ship	4.50 m	14 m
Draft of the ship during trial	1.65 m	5 m
Displacement of the ship during trial	330 tonne	~19,000 tonne
Speed of the ship during trials	34 knots	15 knots
Main engines power	3 × 2720 kW	6500 kW
Propulsion	3 × waterjets	Single screw FPP

## 2 Full-Scale Sea Trials—Methodology and Results

In this section, the procedure for conducting each trial presented in this paper is described.

### 2.1 Turning Circle Trial

The turning circle trials are conducted to establish the turning characteristics of the vessel, namely the tactical diameter, advance and transfer of the ship. IMO specifies the criteria for turning characteristics of ships over 100 m in length. The same criteria are followed for this ship as well. A typical plot of ship’s track during turning circle manoeuvre is shown in Fig. 3. The step-by-step procedure for conduct of turning circle manoeuvre is as given below [1, 2]:

- (a) A suitable heading of the ship is chosen and maintained.
- (b) The engine RPM is set to a value not less than the RPM corresponding to 85% MCR.
- (c) The speed of the ship on GPS is observed and is maintained not less than 90% of speed corresponding to 85% MCR setting on the engine.
- (d) Once the desired speed and heading are achieved and are steady, the turning circle manoeuvre is initiated by ordering the rudder/waterjets 35/30° to port.
- (e) From the time, the order is executed, and the manoeuvre is deemed initiated; the following parameters are continuously recorded at regular intervals:

- Position—latitude and longitude
- Course
- Heading
- Speed
- Rudder/waterjet angle
- Wind speed and direction.

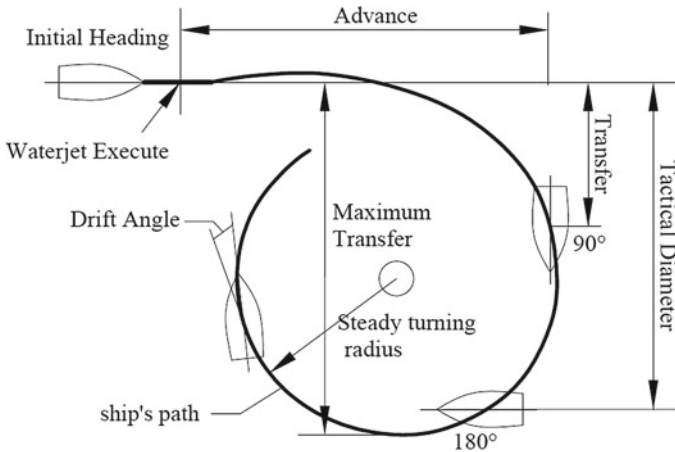


**Fig. 3** Typical plot of ship's track during turning circle manoeuvre

- (f) The rudder/waterjets are maintained at  $35^\circ/30^\circ$  until the ship completes one complete circle, i.e. the ship's heading reaches the initial steady heading.
- (g) After  $360^\circ$  change in heading, the rudder/waterjets are ordered amidships and the manoeuvre is complete.
- (h) From the observations, the track of the ship is plotted and the following are calculated and compared with the IMO criteria for compliance:
  - (i) The advance of the ship is measured as the distance travelled by the ship (in the direction of the initial heading) and by the time, ship's heading has changed by  $90^\circ$  from the initial heading.
  - (ii) The transfer of the ship is measured as the lateral distance travelled by the ship in the direction perpendicular to initial heading and by the time, the ship's heading has changed by  $90^\circ$ .
  - (iii) The tactical diameter is measured as the distance travelled by the ship in a direction perpendicular to the initial heading and by the time, the ship's heading has changed by  $180^\circ$ .

Port and starboard turning circle manoeuvres were conducted for inshore patrol vessel by deflecting the waterjets to  $30^\circ$  port and starboard, respectively. The turn was conducted at full-load displacement of 330 tonne. The initial conditions like the draft of the ship, sea and wind conditions during the trial are given in Table 1. The maximum angle of heel recorded during the turning circle trial was  $12^\circ$ . The tactical diameter, advance of the ship and transfer of the ship measured from the plotted track of the ship are compared with the IMO limiting values and presented in Table 1. The plot of ship's track during port and starboard turns is presented in Fig. 4.

Port and starboard turning circle manoeuvres were conducted for bulk carrier by deflecting the rudder to hard ( $35^\circ$ ) port and starboard, respectively. The turn was conducted at displacement of about 19,000 tonnes. The initial conditions like the



**Table 1** Initial conditions and results of turning circle manoeuvres port and starboard for inshore patrol vessel

Draughts of ship (in m)				Trial condition	
Draft marks Location	Port	STBD	Mean	Weather: strong breeze Sea state: 1–2 Wind: Beaufort 2–3	
Forward	1.62	1.62	1.62		
AFT	1.69	1.64	1.66		
Mid-ship	1.68	1.63	1.65		
Condition		Port		STBD	
Engine RPM: 2050	Speed (knots)	Time (s)	Angle of heel	Time (s)	Angle of heel
Waterjet angle: 30°	29	57	12°	56	12°
Parameter	IMO limit		Attained value		
			Port		STBD
Tactical diameter	5.0 L (220 m)		4.10 L	3.24 L	
Advance	4.5 L (198 m)		4.05 L	3.75 L	
Transfer	–		2.48 L	2.15 L	

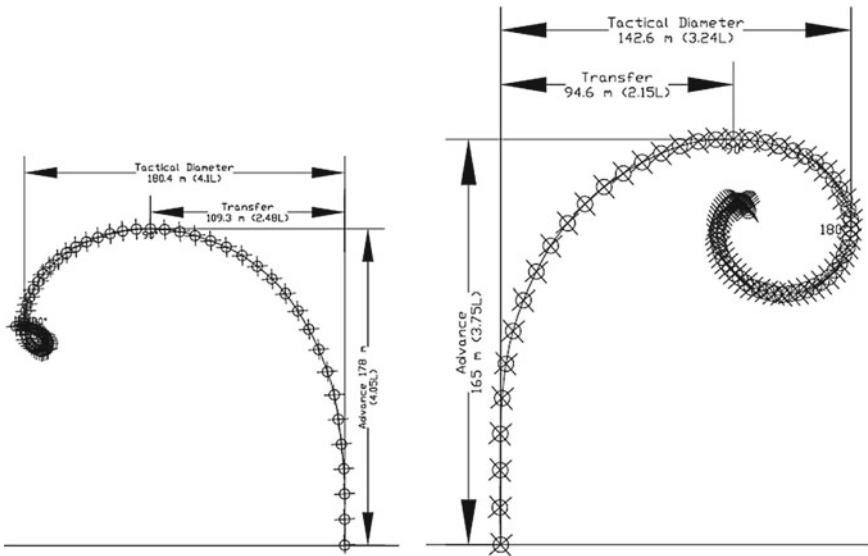


**Fig. 4** Plot of ship's track during port and starboard turning circle manoeuvres of inshore patrol vessel

**Table 2** Initial conditions and results of turning circle manoeuvres port and starboard for bulk carrier

Displacement	19,137 T	Parameter	IMO limit	Attained value	
				Port	STBD
TRIM	2.68 m				
Mean draft (m)	5.104	Advance	4.5 L (765 m)	3.61 L	3.62 L
Draught A.P (m)	6.55	Tactical diameter	5 L (850 m)	2.99 L	3.08 L
Draught F.P (m)	3.87	Transfer	–	0.74 L	0.85 L

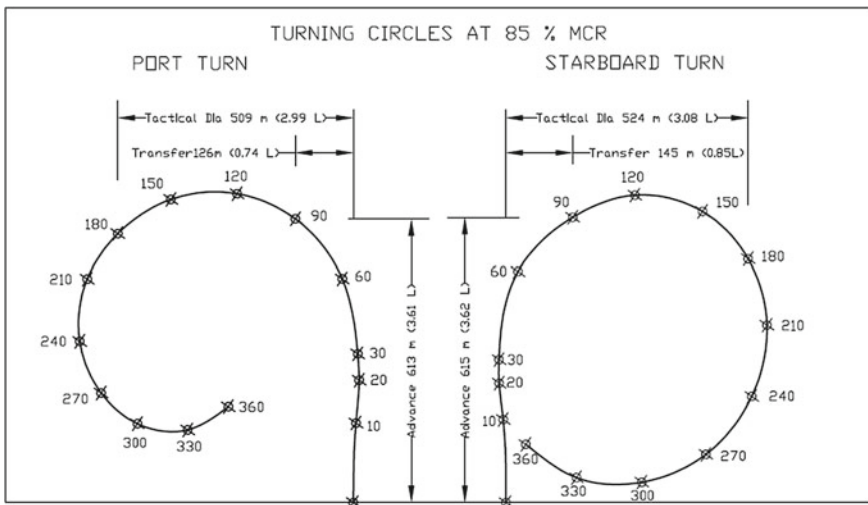


**Fig. 5** Plot of ship’s track during port and starboard turning circle manoeuvres of bulk carrier

draft of the ship, sea and wind conditions during the trial are given in Table 2. The tactical diameter, advance of the ship and transfer of the ship measured from the plotted track of the ship are compared with the IMO limiting values and presented in Table 2. The plot of ship’s track during port and starboard turns is presented in Fig. 5.

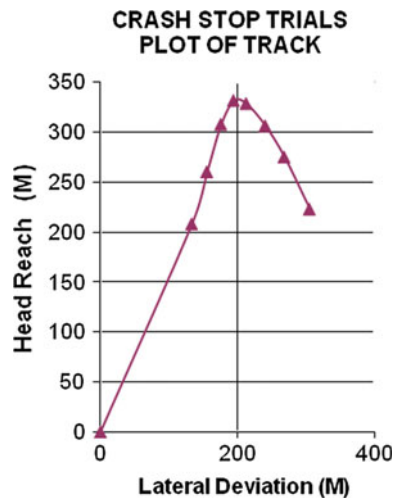
### 2.2 Crash Stop Trial

The crash stop trials are conducted to establish the minimum distance travelled by the ship before becoming dead in water. During an emergency, the vessel must be stopped at the shortest possible time and distance so as to avoid a collision. The stopping

distance, the time taken together with the environmental conditions recorded during sea trials will be a very useful guidance to the captain of a new ship. A typical plot of ship's track during crash stop manoeuvre is shown in Fig. 6. The step-by-step procedure for conduct of crash stop trial is as given below [1, 2]:

- (a) The ship's heading is maintained steady, and the engine RPM is set to achieve speed of the ship not less than 90% of the speed corresponding to 85% of MCR.
- (b) Once the ship attains steady heading and desired speed on the GPS, the crash stop manoeuvre is executed by reversing the waterjet direction by deploying the waterjet buckets in case of water jet propulsion for inshore patrol vessels or by reversing the engine and direction of rotation of propeller, thrust in case of bulk carrier.
- (c) The recording of data starts and the following parameters are recorded continuously:
  - Position—latitude and longitude.
  - Heading
  - Speed
  - Rudder/waterjet angle
  - Wind speed and direction.
- (d) The time taken for the ship to be dead in water is also recorded. In order to accurately determine the ship stop, it is recommended to carry out the trial in daylight even though the ship stop can be observed from the change in speed in the GPS.
- (e) From the observations, the track of the ship is plotted and the track length, head reach and the lateral deviation are measured and checked for compliance with the IMO criteria.

**Fig. 6** Typical plot of ship's track during crash stop trials



- (f) In general, the crash stop trials are conducted for both ahead to astern and astern to ahead directions.
- (g) The IMO limiting value for the length of the track before the ship is dead in water is 15 times the ship's length.

The crash stop trials were conducted at full-load displacement for inshore patrol vessel. The waterjet was reversed by deploying the buckets. The initial conditions and results of crash stop trial are as given below:

Ship speed	28.3 knots
Depth of water	50.0 m
Mean draft	1.65 m
Wind speed	13.5 knots
Time for ship stop	25.0 s
Distance travelled	209.0 m (4.75 L)
IMO limit	15 L

The crash stop trials were conducted at 19,000 T displacement for bulk carrier. The engine telegraph was ordered full astern from full ahead, and the thrust direction was reversed. The initial conditions and results of crash stop trial are as given below:

Ship speed	14.1 knots
Depth of water	50.0 m
Mean draft	5.1 m
Wind speed	10.0 knots
Time for ship stop	587 s
Distance travelled	2407 m (14.2 L)
IMO limit	15 L

### 3 Mathematical Model

The following equations with three degrees of freedom are written in a right-handed orthogonal coordinates system, moving with a ship, with the origin fixed at the mid-ship of a ship. The sign conventions are shown in Fig. 7.

$$\begin{aligned}
 m(\dot{u} - vr - x_G r^2) &= X_H + X_P + X_R \\
 m(\dot{v} + ur + x_G \dot{r}) &= Y_H + Y_P + Y_R \\
 I_Z \dot{r} + m x_G (\dot{v} + ur) &= N_H + N_P + N_R \\
 2\pi I_p \dot{n} &= Q_E + Q_P
 \end{aligned}$$

where the terms with subscripts  $H$ ,  $P$  and  $R$  represent the hull forces, the propeller forces and the rudder forces, respectively.  $Q_E$  and  $Q_P$  are the main engine torque and the propeller torque, respectively.

- (a) Hull Forces

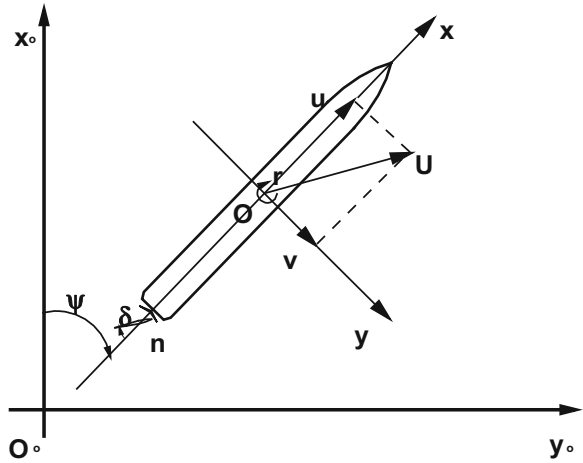
$$X_H = X_u \dot{u} + x_{vv} v^2 + X_{vr} vr + X_{rr} r^2 + X(u)$$

$$Y_H = Y_v \dot{v} + Y_r \dot{r} + Y_v v + Y_r r + Y_{v|v}|v||v| + Y_{r|r}|r||r| + Y_{vvr} v^2 r + Y_{vrr} vr^2$$

$$N_H = N_v \dot{v} + N_r \dot{r} + N_v v + N_r r + N_{v|v}|v||v| + N_{r|r}|r||r| + N_{vvr} v^2 r + N_{vrr} vr^2$$

where  $X(u)$  is obtained from the resistance test.

**Fig. 7** Co-ordinate system showing sign convention



During the crash stopping, the forward motion of the ship may become relatively small compared to the lateral motion of the ship, and the cross-flow drag component becomes dominant. In that case, the hull forces are represented as follows:

$$\begin{aligned}
 Y_H &= Y_* + Y_v \dot{v} + Y_r \dot{r} + (Y_v + Y_{v|v|}|v|)v \\
 &\quad - \frac{\rho}{2} dC_{D_0} \left\{ \int_{-\frac{L}{2}}^{\frac{L}{2}} |v + C_{rY}rx|(v + C_{rY}rx)dx - L|v|v \right\} \\
 N_H &= N_* + N_rur + N_v \dot{v} + N_r \dot{r} + N_v v - \frac{\rho}{2} dC_{D_0} \int_{-\frac{L}{2}}^{\frac{L}{2}} |v + C_{rN}rx|(v + C_{rN}rx)xdx
 \end{aligned}$$

(b) Propeller forces and engine torque

$$\begin{aligned}
 X_P &= (1 - t)\rho n^2 D^4 K_T(J_P) \\
 Y_P &= \begin{cases} 0 & \text{for } n > 0 \\ \frac{1}{2}\rho n^2 D^4 Y_P(J) & \text{for } n \leq 0 \end{cases} \\
 N_P &= \begin{cases} 0 & \text{for } n > 0 \\ \frac{1}{2}\rho n^2 D^4 N_P(J) & \text{for } n \leq 0 \end{cases} \\
 Q_P &= -2\pi J_{PP}\dot{n} - \rho n^2 D^5 K_Q(J_P)
 \end{aligned}$$

where

$$\begin{aligned}
 J_P &= u(1 - w_p)/(nD), \quad J = u/nP \\
 n &: \text{rps} \quad P : \text{pitch of propeller}
 \end{aligned}$$

In the above equation,  $Y_P$  and  $N_P$ , introduced to describe the propeller forces during the reverse rotation of the propeller, and can be considered as functions of  $J$ .

The thrust deduction factor,  $t$  and the effective propeller wake fraction,  $w_p$  are treated as functions of ship motion and operating condition.

For a diesel engine, the characteristics of main engine torque are as follows:

$$\begin{aligned}
 Q_E &= |Q_P| \quad \text{for } |Q_P| \leq Q_{EMAX} \\
 Q_E &= Q_{EMAX} \quad \text{for } |Q_P| > Q_{EMAX}
 \end{aligned}$$

(c) Rudder forces

$$X_R = -(1 - t_R)F_N \sin \delta$$

$$Y_R = (1 - a_H)F_N \cos \delta$$

$$N_R = (x_R + a_H)x_H \cos \delta$$

where

$$F_N = \frac{1}{2} \rho A_R U_R^2 f_a \sin a_R$$

$A_R$  = rudder area

$U_R$  = effective inflow velocity

$a_R$  = effective inflow angle

$$U_R = \sqrt{u_R^2 + v_R^2}$$

$$u_R = \varepsilon u_P \sqrt{\eta \left\{ 1 + \kappa \left( \sqrt{1 + \frac{8k_T}{\pi J^2}} - 1 \right) \right\}^2 + (1 - \eta)}$$

$$v_R = -\gamma(v + l_P r)$$

$$u_P = (1 - w_P)u$$

$$a_R = \delta - \delta_{0+} \tan^{-1} \frac{v_R}{u_R} \approx \delta - \delta_0 + \frac{v_R}{u_R}$$

$\eta$ : ratio of propeller diameter to rudder height

$\varepsilon, \kappa$ : coefficients representing propeller slip stream

$f_a$ : rudder normal force coefficient

$\delta_0$ : neutral rudder angle

$\gamma$ : flow straightening coefficient

$l_P$ :  $\approx 2x_R$

### Nomenclature used in Describing Mathematical Model and Geometry

Symbol	Definition
$B$	Maximum beam at design full-load waterline
$K$	Characteristic length; length between perpendiculars
$S$	Wetted surface area
$T$	Draft at design full-load condition
$\nabla$	Volume of displacement at design full-load condition
$C_B$	Block coefficient; $\nabla / LBT$
$A_T$	Total planform rudder area
$A_F$	Fixed rudder area
$A_R$	Movable rudder area
$\bar{b}$	Mean span of rudder
$c_r$	Root chord of rudder
$c_t$	Tip chord of rudder
$A$	Rudder aspect ratio; $\bar{b}^2 / A_T$
$C$	Propeller blade chord at 0.7 radius
$D$	Propeller diameter
$P$	Propeller pitch at 0.7 radius



### Hydrodynamic Coefficients

Symbol	Nondimensional form	Definition
$I'_z$	$I'_z = \frac{I_z}{\frac{1}{2}\rho L^5}$	Moment of inertia of ship about $z$ -axis
$J$	$J = \frac{u}{nD}$	Propeller advance coefficient based on ship speed $u$
$m$	$m' = \frac{m}{\frac{1}{2}\rho L^3}$	Mass of ship
$N$	$N' = \frac{N}{\frac{1}{2}\rho L^3 U^2}$	Hydrodynamic moment component about $z$ -axis (yawing moment)
$N_r$	$N'_r = \frac{N_r}{\frac{1}{2}\rho L^4 U}$	First-order coefficient used in representing $N$ as a function of $r$
$N_{r'}$	$N'_{r'} = \frac{N_r}{\frac{1}{2}\rho L^5}$	Coefficient used in representing $N$ as a function of $r$
$N_{r r }$	$N'_{r r } = \frac{N_{r r }}{\frac{1}{2}\rho L^5}$	Second-order coefficient used in representing $N$ as function of $r$
$N_v$	$N'_v = \frac{N_v}{\frac{1}{2}\rho L^3 U}$	First-order coefficient used in representing $N$ as a function of $r$
$N_{v'}$	$N'_{v'} = \frac{N'_v}{\frac{1}{2}\rho L^4}$	Coefficient used in representing $N$ as a function of $\dot{v}$
$N_{vrr}$	$N'_{vrr} = \frac{N_{vrr}}{\frac{1}{2}\rho L^5 U^{-1}}$	Coefficient used in representing $N_v$ as a function of $r^2$
$N_{v v }$	$N'_{v v } = \frac{N_{v v }}{\frac{1}{2}\rho L^3}$	Second-order coefficient used in Representing $N$ as a function of $v$
$N_{vvr}$	$N'_{vvr} = \frac{N_{vvr}}{\frac{1}{2}\rho L^4 U^{-1}}$	Coefficient used in representing $N_v$ as a function of the product $vr$
$n$		Propeller revolution rate

(continued)

(continued)

Symbol	Nondimensional form	Definition
$n_c$		Propeller revolution rate at steady command speed
$r$	$r' = \frac{rL}{U}$	Angular velocity component about $z$ -axis relative to fluid
$\dot{r}$	$\dot{r}' = \frac{\dot{r}L^2}{U^2}$	Angular acceleration component about $z$ -axis relative to fluid
$U$	$U' = \frac{U}{U}$	Linear velocity of origin of body axes relative to fluid
$u$	$\dot{u} = \frac{u}{U}$	Component of $U$ in direction of the $x$ -axis
$\dot{u}$	$\dot{u} = \frac{u'L}{U^2}$	Time rate of change of $u$ in direction of the $x$ -axis
$V$		Absolute speed in knots
$v$	$v' = \frac{v}{V}$	Component of $U$ in direction of the $y$ -axis
$\dot{v}$	$\dot{v}' = \frac{\dot{v}L}{U^2}$	Time rate of change of $v$ in direction of the $y$ -axis
$x$	$x' = \frac{x}{L}$	Longitudinal body axis; also the coordinate of a point relative to the origin of body axes
$x_G$	$x'_G = \frac{x_G}{L}$	The $x$ -coordinate of centre of gravity
$\beta$		Drift angle
$\delta$		Rudder angle
$\dot{\delta}$	$\dot{\delta}' = \frac{\dot{\delta}L}{U}$	Rudder deflection rate
$\eta$	$\eta = \frac{J_c}{J}$	Ship propulsion ratio
$y$	$y' = \frac{y}{L}$	Lateral body axis; also the coordinate of a point relative to the origin of body axes
$\psi$		Heading or yaw angle
$X_{u'}$	$X'_{u'} = \frac{X_{u'}}{\frac{1}{2}\rho L^3}$	Coefficient used in representing $X$ as a function of $\dot{u}$

(continued)

(continued)

Symbol	Nondimensional form	Definition
$X_{vr}$	$X'_{vr} = \frac{X_{vr}}{\frac{1}{2}\rho L^3}$	Coefficient used in representing $X$ as a function of the product $vr$
$X_{vv}$	$X'_{vv} = \frac{X_{vv}}{\frac{1}{2}\rho L^2}$	Second-order coefficient used in representing $X$ as function of $v$
$Y_v$	$Y'_v = \frac{Y_v}{\frac{1}{2}\rho L^2 U}$	First-order coefficient used in representing $Y$ as a function of $v$
$Y_{v'}$	$Y'_{v'} = \frac{Y_{v'}}{\frac{1}{2}\rho L^3}$	Coefficient used in representing $Y$ as a function of $\dot{v}$
$Y_{vrr}$	$Y'_{vrr} = \frac{Y_{vrr}}{\frac{1}{2}\rho L^4 U^{-1}}$	Coefficient used in representing $Y_v$ as a function of $r^2$
$Y_{vvr}$	$Y'_{vvr} = \frac{Y_{vvr}}{\frac{1}{2}\rho L^3 U^{-1}}$	Coefficient used in representing $Y_v$ as a function of the product $vr$
$Y_{v v }$	$Y'_{v v } = \frac{Y_{v v }}{\frac{1}{2}\rho L^2}$	Second-order coefficient used in representing $Y$ as a function of $v$
$Y$	$Y' = \frac{Y}{\frac{1}{2}\rho L^2}$	Hydrodynamic force component along y-axis
$Y_r$	$Y'_r = \frac{Y_r}{\frac{1}{2}\rho L^3 U}$	First-order coefficient used in representing $Y$ as a function of $r$
$Y_{r'}$	$Y'_{r'} = \frac{Y_{r'}}{\frac{1}{2}\rho L^4}$	Coefficient used in representing $Y$ as a function of $\dot{r}$
$Y_{r r }$	$Y'_{r r } = \frac{Y_{r r }}{\frac{1}{2}\rho L^4}$	Second-order coefficient used in representing $Y$ as a function of $r$

### 4 System Identification Technique Extended Kalman Filter

Mathematical model establishment is one of the important steps in the system identification technique. The parameters of the mathematical model of a system and its structure are established from the measured inputs and outputs of the system in system identification process. Identification of the system from inputs and outputs is relatively less costly in comparison with experimentation. Identification/establishment of ship manoeuvring hydrodynamic derivatives using experimental techniques like



**Fig. 8** Extended Kalman filter system identification technique process flow

PMM is expensive than the use of system identification technique to establish the ship manoeuvring hydrodynamic derivatives from standard full-scale manoeuvres conducted during the sea trials. The equations of motion of a ship in the horizontal plane contain the ship manoeuvring hydrodynamic derivatives as the parameters which are established using system identification. Continuous least squares technique, recursive least squares technique, Kalman filter technique, extended Kalman filter technique, neural networks, R-MISO method are some of the established identification techniques for identification of ship manoeuvring hydrodynamic derivatives

In this paper, the extended Kalman filter technique has been used to identify the manoeuvring hydrodynamic derivatives.

The process followed is depicted in Fig. 8.

With the rudder angle, heading angle, yaw rate and surge as the inputs for the mathematical model described in Sect. 3, the ship manoeuvring hydrodynamic derivatives have been identified and are presented in Sect. 5.

The extended Kalman filter system identification technique has been implemented in FORTRAN.

## 5 Results of System Identification Using Extended Kalman Filter Technique

The following hydrodynamic derivatives have been identified using extended Kalman filter system identification technique implemented in FORTRAN (Table 3).

**Table 3** Hydrodynamic derivatives identified using extended Kalman filter system identification technique

Hull coefficients					
X-equation	Value × 10 <sup>5</sup>	Y-equation	Value × 10 <sup>5</sup>	N-equation	Value × 10 <sup>5</sup>
$X'_{u'}$	-73.7	$Y'_{v'}$	-1219.0	$N'_{v'}$	-40.2
		$Y'_{r'}$	-92.8	$N'_{r'}$	-64.8
		$Y'_v$	-1369.8	$N'_v$	-725.0
		$Y'_r$	299.4	$N'_r$	-229.0

## 6 Conclusions

The salient conclusions and observations of the present study are given below:

Turning circle and crash stop trials: the manoeuvring characteristics are meeting the laid down IMO criteria as per IMO Res. MSC 137 (76).

The turning circle manoeuvre has been simulated using the identified hydrodynamic derivatives, and the percentage variation between the trial results and simulated values of tactical diameter and advance are 1.34 and 12.7%, respectively. The mathematical model described in the paper is most suitable for bulk carrier hull forms and can together be utilized for estimation of hydrodynamic derivatives using extended Kalman filter technique for typical high block bulk carrier hull forms.

**Acknowledgements** The authors acknowledge CMD of M/s Hindustan Shipyard Limited, Visakhapatnam, for allowing this work to be carried out during the sea trials.

## References

1. IMO (2002) Standards for ship manoeuvrability. Resolut MSC 137(76)
2. IMO (2002) Explanatory notes to the standards for ship manoeuvrability. MSC/Circ 1053

**K. O. S. R. RaviSekhar RadhaKrishna** holds the current position of Manager at Hindustan Shipyard Limited, Visakhapatnam, India, and is also Ph.D. scholar in the Ocean Engineering Department at Indian Institute of Technology Madras, India.

**Dr. R. Panneer Selvam** holds the current position of Professor in the Ocean Engineering Department at Indian Institute of Technology Madras, India

# Effect of Forward Speed on Roll Damping of a Container Ship Using URANS Simulations



Mohsin A. R. Irkal, S. Nallayarasu and S. K. Bhattacharyya

**Abstract** Ships are prone to large roll motions in beam and oblique seas at encounter frequencies near the design frequency of the vessel. The nonlinearity of roll damping and roll motion has been investigated in the past by various researchers. The prediction of roll damping and roll motion of ships becomes difficult by simplified approaches. Ship roll motion is highly influenced by viscous flow around the hull. Vortex formation and its shedding from the hull and appendages have larger contribution to roll damping. Therefore, the popular approach for prediction of roll damping and roll motion of ships is with the help of model experiments and more recently URANS (Unsteady Reynolds-averaged Navier–Stokes)-based simulations. Free roll decay experiments in calm water conditions give a good estimate of roll damping of ships at natural frequency. The flow characteristics around the hull may not be the same when the ship is moving at a forward speed. Hence, it is important to take into consideration the effect of forward speed on roll damping obtained from free roll decay of the ships. This paper addresses the effect of forward speed on roll damping of a 1:100 (Froude) scaled container ship model. The model is 2.88 m in length, 0.345 m in beam and was loaded to a draft of 0.12 m; free roll decay experiments at zero forward speed were carried out in a wave flume at Department of Ocean Engineering, IIT Madras. The wave flume is 4 m wide, 90 m long and has water depth of 2.5 m. The held-over free roll decay tests were carried out by subjecting the model to known initial heel and releasing it. The roll angle was measured using inclinometer via data acquisition CPU. The URANS-based simulations of the free roll decay experiments at zero forward speed were carried out in a commercial computational fluid dynamics (CFD) software and validated. The CFD model was then used to carry out the free roll decay simulations at two forward speeds of the ship model. The effect of forward speed on roll damping of the ship model was assessed from the results of CFD simulations.

**Keywords** Roll damping · Free roll decay · Container ship · Forward speed · CFD

---

M. A. R. Irkal (✉) · S. Nallayarasu · S. K. Bhattacharyya  
Department of Ocean Engineering, Indian Institute of Technology Madras,  
Chennai 600036, India  
e-mail: [irkal.mohsin@gmail.com](mailto:irkal.mohsin@gmail.com)

© Springer Nature Singapore Pte Ltd. 2019  
K. Murali et al. (eds.), *Proceedings of the Fourth International Conference in Ocean Engineering (ICOE2018)*, Lecture Notes in Civil Engineering 22,  
[https://doi.org/10.1007/978-981-13-3119-0\\_12](https://doi.org/10.1007/978-981-13-3119-0_12)

# 1 Introduction

A seagoing vessel is expected to have lower amplitude motions for smooth operation of shipboard tasks, better crew efficiency and passenger comfort. A stable vessel also improves the fuel efficiency. It is desirable to understand the modes of motion of a floating body and predict its stability at the design stage. The seagoing vessels are prone to many environmental and man-made catastrophes. Extreme weather can cause fatal wave and wind loads on a floating body causing it to collapse. Roll motion is one of the major causes of accidents in slender floating bodies like ships. The other modes of motion of a ship except roll motion have better stability. This is because roll motion in ships suffers from both insufficient damping and restoring forces and moments. Especially, for the wave loads near roll resonance the roll acceleration of ships becomes highly undesirable and unsafe. The subject of roll motion and roll damping of ships has been of importance for a long time. Roll motion being highly nonlinear due to the dependence on the viscous flow becomes difficult for prediction. The potential flow-based methods and solvers fail to explain the behaviour of ships in roll. Various approaches and methods have been used by naval architects and ocean engineers to predict and control roll motion of ships and ship-like floating vessels. The most popular method used for the prediction of roll motion and roll damping is through semi-empirical formulae, based on model tests and simplified theory related to flow dynamics around the hull and appendages of the ships [1–3]. The important outcome of this approach was the component-type roll damping where the total damping is divided into various components [4–6]. This approach experiences a setback due to various reasons, important one being drastic change in roll damping with slightest change in the ship design [7]. The hull shape or design and the location and orientation of the appendages like rudder, skeg, bilge keels and fins affect the flow dynamics around the hull significantly causing variations in the roll damping. The flow dynamics obviously changes with the ship moving at a forward speed and when subjected to waves. A few early attempts to measure and simulate the flow around hulls and sharp appendages like bilge keel and predict roll motion and damping can be found in [8–13]. Recently, a lot of work has been done in this field with the use of URANS simulations and the model experiments for validation purpose. Free and forced roll oscillation studies of ship models are presented in [14–18]. URANS-based simulations at design stage are proving to be a good option in understanding roll motion of ships since roll motion has a strong dependence on viscosity effects of the flow around the hull.

There are experimental and numerical studies which account for the effect of forward speed on roll damping as reported in [17, 19, 20]. The roll damping of ship changes with the change in forward speed. The overall roll damping improves with the increase in forward speed since the hull lift component contributes to damping [4, 20]. This paper presents the experimental and numerical study of free roll decay of a 1:100 scale container ship model. The experiments were carried out in calm water without forward speed for an initial heel angle of  $19^\circ$ . The measured data was then used to validate the URANS simulation of the free roll decay for same initial heel

and zero forward speed. Thereafter, the free roll decay simulations were carried out for two forward speeds of 0.734 m/s (7.34 m/s or 14 knots at full scale) and 1.276 m/s (12.76 m/s or 25 knots at full scale) corresponding to Froude number ( $Fr$ ) of 0.138 and 0.24 using the length between perpendiculars as reference. The validation of the URANS simulations and the simulation-based study on the effect of forward speed on roll damping are discussed.

## 2 Experimental Investigation

This section describes the facility, container ship model details and instruments used to carry out the free roll decay experiments in calm water.

### 2.1 Facility

The experiments of free roll decay of the container ship model were carried out in calm water condition in 4 m flume at the Department of Ocean Engineering, IIT Madras. The flume is 4 m wide, 90 m long and has a water depth of 2.5 m. It is capable of producing regular and irregular water waves with a flap type, hydraulic wave-maker. The opposite end has a beach made of rubble stones which minimises the wave reflection. Since no wave was used for free roll decay experiments, the model was placed midway between the wave-maker and beach. The model was subjected to initial heel of  $19^\circ$  and released to oscillate freely, and the roll motion was measured.

### 2.2 Container Ship Model

The container ship model has a length overall ( $L$ ) of 3.01 m and length between perpendiculars ( $L_p$ ) of 2.88 m. The beam ( $B$ ) of the model is 0.345 m and a depth ( $D$ ) of 0.24 m at the midship. The mass properties of the light hull were measured in laboratory using hanging experiments. The model was ballasted to a draft,  $d$  of 0.12 m using weights maintaining the roll radius of gyration,  $K_{xx}$  to be 36% of beam and pitch radius of gyration,  $K_{yy}$  to be 21% of length between perpendiculars. The vertical centre of gravity was calculated using hanging experiments of the light hull and position of the ballast weights. It was also confirmed with the help of inclining experiment in calm water. The hydrostatics from the CAD model was calculated and compared with the measurements as shown in Table 1. The centre of gravity and moment of inertia are reported in Table 2. Figure 1 shows the body plan of the container ship. Figure 2a shows the photographic view of the hanging experiment of



**Table 1** Hydrostatics and ship parameters from measurements and CAD

Particulars	Model (1:100)			Prototype
	Measured	CAD	Error %	
Length overall ( $L$ )	3.01 m	3.01 m	–	301 m
Length between perpendiculars ( $L_p$ )	2.88 m	2.88 m	–	288 m
Beam ( $B$ )	0.345 m	0.343 m	0.6%	34.5 m
Draft ( $d$ )	0.12 m	0.12 m	–	12 m
Depth ( $D$ )	0.24 m	0.24 m	–	24 m
$L_p/B$	8.397	8.397	–	8.397
$L/B$	8.725	8.725	–	8.725
Displacement, $W$	61.983 kg	62.951 kg	1.56%	61.983 tons
LCB (from forward perpendicular)	–	1.438 m	–	143.8 m
VCB ( $BG$ )	–	0.069 m	–	6.9 m
LCF (from forward perpendicular)	–	1.585 m	–	158.5 m
TCF	–	0 m	–	0 m
Block coefficient, $C_B$	–	0.531	–	0.531
Prismatic coefficient, $C_P$	–	0.599	–	0.599
$BM_T$	–	0.094 m	–	9.4 m
$BM_L$	–	5.388 m	–	538.8 m

**Table 2** Mass properties of container ship model

Draft, $d$ (m)	Displacement, $W$ (kg)	$KG$ (m)	$GM$ (m)	$I_{xx}$ (kg-m <sup>2</sup> )	$K_{xx}/B$	$I_{yy}$ (kg-m <sup>2</sup> )	$K_{yy}/L_p$
0.12	61.983	0.139	0.024	0.9806	0.3646	22.02	0.207

the ship, and Fig. 2b shows the CAD model of the ship which was used in the CFD simulations.

### 2.3 Instrumentation

The measurements were recorded in a CPU via a data acquisition instrument, *Spider8*. A dual-axis inclinometer was used to measure angular displacements of the

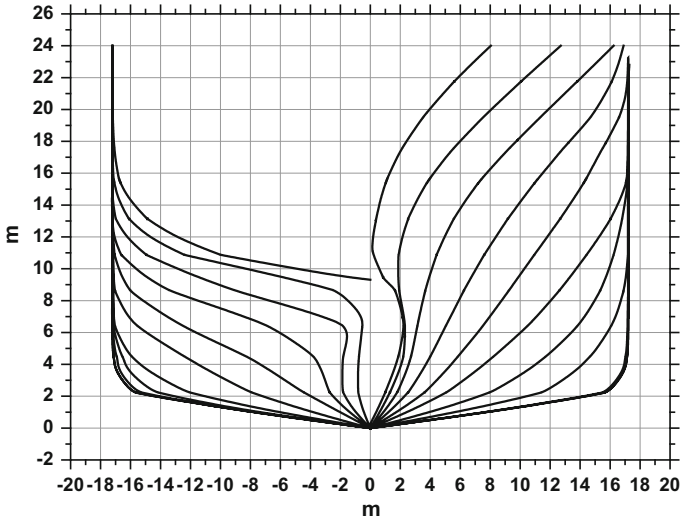


Fig. 1 Body plan of the container ship (full scale)

(a)



(b)



Fig. 2 a Photographic view of hanging experiment b CAD model of the container ship

container ship. The microelectromechanical system (MEMS)-based inclinometers have a sensor cell embedded in it. The sensor has a pair of electrodes: one is fixed and the other is free to move on springs. The relative motion of the moving electrode under gravity and the fixed electrode changes the capacitance between them. This change in capacitance is sensed by the sensor and converted into angular displacement. The inclinometer was calibrated in laboratory by inclining it to known angles using a simple tilt stand set-up and recording the voltage output from it. The calibration constant was found to be 25.2 mV/deg. It has a range of  $\pm 80^\circ$  with a resolution of  $0.01^\circ$ .

A resistive wave probe was used for measuring the elevation of the waves radiated from the model. The wave probe is 50 cm long and has two stainless steel rods which act as electrodes. The resistance of the wave probe changes with the depth of immersion of the probe which is reflected as change in voltage output. The wave probe was calibrated by immersing it in calm water through specified depth intervals and recording the corresponding output voltage. The voltage output so obtained was converted into wave elevation through the calibration constant. A wavemeter was used to amplify the signals from the wave probe before sending it to data acquisition system.

## 2.4 Free Roll Decay

The held-over free roll decay experiments were carried out by holding the model at a known initial heel of  $19^\circ$  and releasing it. The model was free to move in all degrees of freedom, and particular care was taken to minimise the coupling effect between the motions. The experiments were carried out in calm water and zero forward speed. The photographic view of the model installed in 4 m flume is shown in Fig. 3. The experiments were repeated to check the reproducibility of the measurements. The typical roll decay motion of the container ship model is shown in Fig. 4.



**Fig. 3** Container ship model installed in 4 m flume

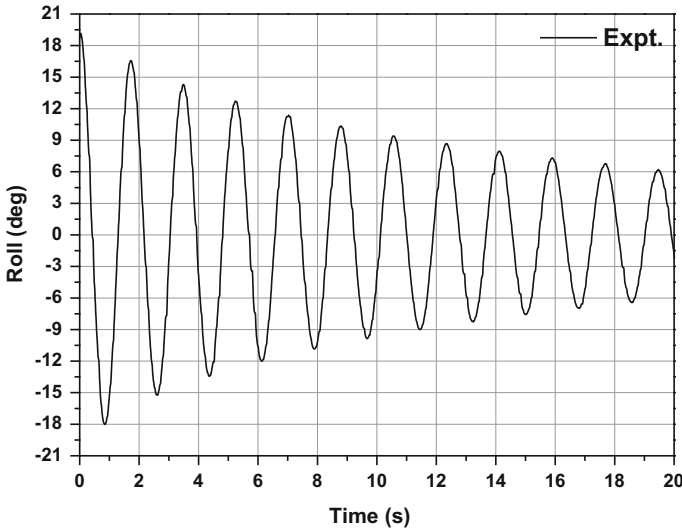


Fig. 4 Roll decay of the container ship ( $\varphi_0 = 19^\circ$ )

### 3 URANS Simulations

This section describes the computational domain, meshing and the solver details used to carry out the free roll decay simulations in calm water at zero speed and at two forward speeds as discussed earlier. The three-dimensional (3D) unsteady Reynolds-averaged Navier–Stokes (URANS) simulations of the six-degree of freedom, free roll decay were solved in a commercial software, STAR-CCM+ [21]. The averaged governing equations of continuity and momentum in tensor form for incompressible flow are given in Eqs. (1) and (2), respectively [22].

$$\frac{\partial(\rho \bar{u}_i)}{\partial x_i} = 0; \tag{1}$$

$$\frac{\partial(\rho \bar{u}_i)}{\partial t} + \frac{\partial}{\partial x_j}(\rho \bar{u}_i \bar{u}_j + \overline{\rho u'_i u'_j}) = -\frac{\partial \bar{p}}{\partial x_i} + \frac{\partial \bar{\tau}_{ij}}{\partial x_j} \tag{2}$$

where  $\overline{\rho u'_i u'_j}$  is the term representing Reynolds stresses, and  $\bar{\tau}_{ij}$  is mean viscous stress tensor. The simulations were solved using segregated flow solver with semi-implicit method for pressure linked equation (SIMPLE) technique for pressure and velocity coupling. Volume of fluid (VOF) method was used for multiphase flow with free surface between air and water as fluids. Implicit unsteady time-stepping with second-order upwind temporal discretization and a second-order upwind scheme for convection was used. A variable time-step scheme based on the Courant number (CFL number) was used with a minimum time-step size of  $1e-6$ . The mean CFL number of 0.5 and target maximum CFL number of 1 were used in the simula-

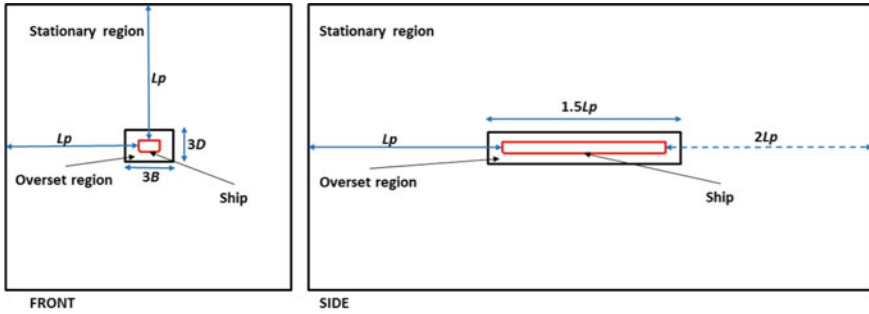
tion. The convergence limit of  $1e-4$  and below was achieved for all the continuity, momentum and turbulence variables with ten iterations per time step. The  $k-\omega$  SST model was used for turbulence modelling in all the simulations since it is suitable for separated flows from near wall. The linear discretized equations were solved using Gauss–Seidel iterative method in the algebraic multigrid (AMG) solver. The initial fluid depth was defined in the flat-wave properties of the VOF wave model, which is used to simulate surface gravity waves. The flat-wave model represents initial calm water condition which can be initialized with current and wind velocities. The coupled motion of the ship model under fluid forces and moments was simulated using dynamic fluid body interaction (DFBI) model allowing free motion in six degrees.

### 3.1 Computational Domain and Boundary Conditions

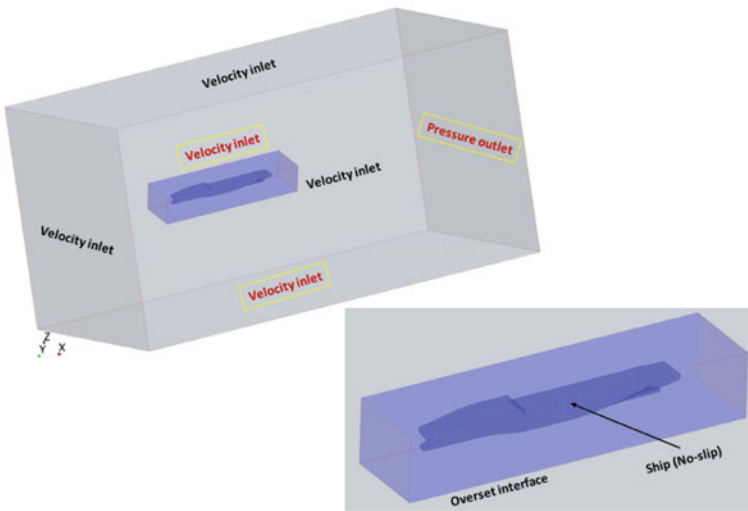
The computational domain has similar dimensions as recommended by the ITTC [23]. It extends one  $L_p$  on all four sides from the keel, deck, starboard and port at midship of the container as seen in front view of Fig. 5a. The domain extends up to one  $L_p$  ahead of forward perpendicular (FP) and up to  $2L_p$  behind aft perpendicular (AP) along the ship length as seen in side view in Fig. 5a. The whole domain was divided into two parts: inner moving region or overset region and outer stationary region. The dimensions of the overset regions are also shown in Fig. 5a. It is  $3B$  wide,  $3D$  deep and  $1.5L_p$  long. Figure 5b shows the boundary conditions set for the simulations. All the five sides of the cuboidal stationary domain are set as velocity inlet, and the boundary behind the container ship model is set as pressure outlet. The velocity of water or current can be specified as a vector in Cartesian coordinate system. For a free decay simulation with zero forward speed, the velocity components are set to zero and for simulations with forward speed the  $X$ -velocity of the current, i.e. velocity along the ship length is input with a finite value. The two regions are linked with an overset mesh boundary as shown in Fig. 5b. The ship model boundary was set as wall with no-slip. Overset meshes also known as overlapping or chimera mesh are used for a dynamic fluid body interaction (DFBI) simulations and have advantages over remeshing or deforming mesh techniques for high amplitude motions. The inner overset/moving region was given an initial heel along the  $X$ -axis at centre of gravity of the ship model before the simulation was started. Linear interpolation scheme was adopted for the connection between the overset and stationary regions which is more accurate but time-consuming.

### 3.2 Meshing

The meshing was carried out using the software's inbuilt meshing models. Three meshing models were chosen, viz. surface remesher, trimmer and prism layers. Surface remesher is used to retriangulate the existing surface to optimise it for the volume



(a) Domain dimensions



(b) Boundary conditions

Fig. 5 Computational domain

mesh being generated. It can be also used to alter the mesh size on a particular surface. The trimmer meshing model creates predominantly hexahedral cells in the domain, and it trims or cuts off the hexahedral cell according to the surface of the boundary in contact. The resulting mesh is hybrid composed of the structured hexahedral cells and polyhedral cells near the boundaries. The mesh was locally refined near free surface and bilge of the model using separate mesh blocks and surface remesher sizes. Prism layer mesher generates orthogonal prismatic cells near the boundaries used especially for walls with no-slip. It helps to simulate the near wall flow accurately and resolve the boundary layer and separated flow near the walls. The thickness of the prism layer and the number of cells is decided according to the wall  $y^+$  desired in the flow simulation. In the present simulations, the average wall  $y^+$  was maintained

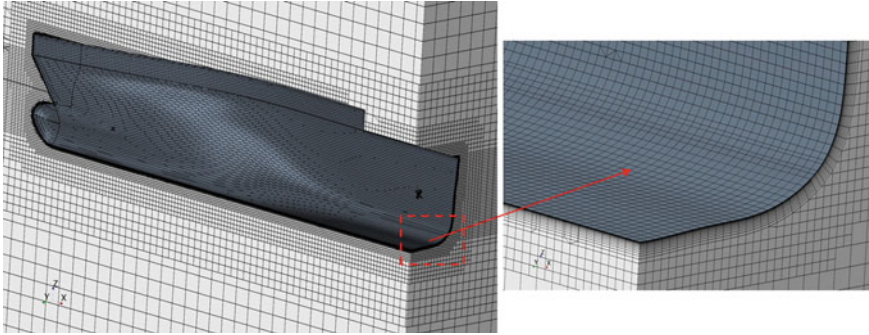


**Fig. 6** Computational mesh (fine mesh near free surface and near hull)

below 5 with the *All*  $y^+$  wall treatment (i.e. wall functions used for low as well as high wall  $y^+$  values), which is a good limit to resolve the near wall flow and separation.

Figure 6 shows the mesh at cut plane along  $X$ - $Z$  and  $Y$ - $Z$  plane for container ship model. The refinement of mesh can be seen near the ship model and free surface. The total cell count for the present simulations is around 2.96 million comprising of stationary region (0.54 million cells) and overset region (2.42 million cells).

## 4 Results and Discussions

The results from the experimental measurements and URANS simulations are discussed in this section. Initially, the simulation set-up was validated and compared with the experiments for roll decay at zero forward speed, i.e.  $Fr = 0$ . The simulation set-up was then used to simulate free roll decay at forward speeds of 0.734 and 1.276 m/s corresponding to  $Fr$  of 0.138 and 0.24, respectively. Froude number,  $Fr$ , is defined in Eq. (3), where  $V$  is the ship forward speed or the current speed in case of simulations and  $g$  is gravitational acceleration.

$$Fr = \frac{V}{\sqrt{gL_p}} \quad (3)$$

### 4.1 Validation of URANS with Experiments

The comparison of measured and simulated roll decay is shown in Fig. 7a for  $\varphi_0 = 19^\circ$  and  $Fr=0$ , i.e. in calm water with zero speed. The URANS simulations were carried out for a physical time of 20 s which covers at least ten roll cycles. The simulated roll motion replicates the experimental measurement closely up to seven cycles, and thereafter, there is slight decrease in motion as compared to experiment. Figure 7b

shows the comparison of measured and simulated damping ratio,  $\zeta$  plotted versus mean decay angle,  $\phi_m$  ( $(\phi_n + \phi_{n+1})/2$ ) obtained using logarithmic decrement method. Table 3 shows the values of experimental and simulated roll natural period,  $T_n$ ;  $\zeta$  and roll added mass,  $A$  averaged from first five  $\phi_m$ . The first half cycle of the decay motion was omitted in the calculation of values in Table 3. The roll natural period compares well with a difference of 0.453% and damping ratio with a difference of 4.762% with experiments taken as reference. It can be seen the comparison between experiments and simulations is reasonably good validating the simulation set-up; to be used for further investigation of the effect of forward speed on roll damping.

### 4.2 Effect of Forward Speed on Roll Damping Using URANS

The simulations of free roll decay with forward speed were carried out by giving the water current velocity in X-direction along the ship length. The ship model was constrained in surge, sway and yaw motions allowing pitch, roll and heave in the simulations with forward speed. The domain was initialised with the constant water current velocity, and the model was given the initial heel of  $19^\circ$  and allowed to roll freely. Figure 8a shows the roll motion obtained from the simulations at  $Fr = 0, 0.138$  and  $0.24$ . It can be seen that the ship model subjected to forward speed decays

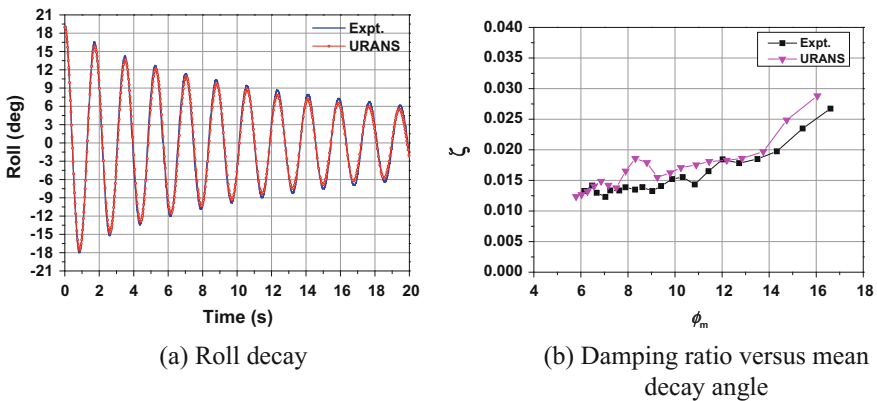


Fig. 7 Comparison from measurement and simulation ( $\phi_0 = 19^\circ, Fr=0$ )

Table 3 Validation of natural period, damping ratio and added mass obtained from initial five  $\phi_m$

	$T_n$ (s)	$\zeta$	$A$ (kg-m <sup>2</sup> )
Expt.	1.760	0.021	0.164
URANS	1.768	0.022	0.175
Difference %	-0.453	-4.762	-6.707



faster as opposed to the zero speed which is in confirmation with the results in [20]. The positive peak roll amplitude at the completion of third cycle is close to  $12^\circ$  for  $Fr = 0$ ,  $9^\circ$  for  $Fr = 0.138$  and  $5^\circ$  for  $Fr = 0.24$  as can be seen in Fig. 8a. The roll amplitude reduces to below  $1.5^\circ$  after sixth cycle for  $Fr = 0.24$ , which is indicative of improved roll damping with increasing ship speed. The variation of  $\zeta$  versus  $\phi_m$  is shown in Fig. 8b for three  $Fr$ . It can be clearly seen that roll damping increases with the increase in forward speed.

Table 4 shows the values of  $T_n$ ,  $\zeta$  and  $A$  averaged from first five  $\phi_m$  for three  $Fr$ . The roll damping increases by 81.82% for  $Fr$  of 0.138 compared with zero forward speed, whereas the damping increases by 65% for  $Fr = 0.24$  as compared with  $Fr = 0.138$ . The roll natural period behaves differently, it increases slightly by 1% for  $Fr = 0.138$  as compared with  $Fr = 0$ , and then, it reduces by 6.89% for  $Fr = 0.24$  as compared with  $Fr = 0.138$ . Similar is the behaviour of roll added mass as shown in Table 4.

Figure 9 shows the roll excitation moments at three  $Fr$ . It is observed that the roll excitation moment reduces with increasing forward speed, both at the pressure component (Fig. 9a) and shear component (Fig. 9b). Figure 10 shows the contours of velocity in water at the centre plane along ship length after completion of first roll cycle (see Fig. 8a). In the case of  $Fr = 0$ , the flow velocities are due to roll motion of the model, whereas in case of  $Fr = 0.138$  and 0.24, they are due to both the flow speed and motion of the model. The increased flow velocities for  $Fr = 0.138$  and 0.24

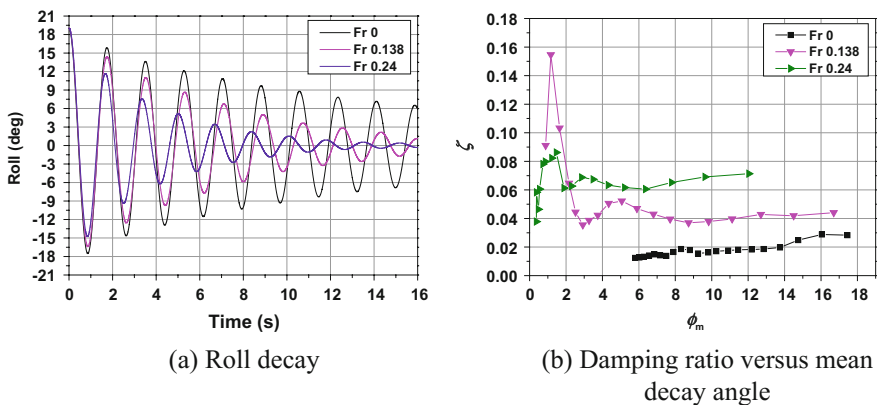


Fig. 8 Simulated free roll decay at three  $Fr$  ( $\phi_0 = 19^\circ$ )

Table 4 Comparison of natural period, damping ratio and added mass for three  $Fr$

$Fr$	$T_n$	$\zeta$	$A$
0	1.768	0.022	0.175
0.138	1.786	0.040	0.198
0.24	1.663	0.066	0.041

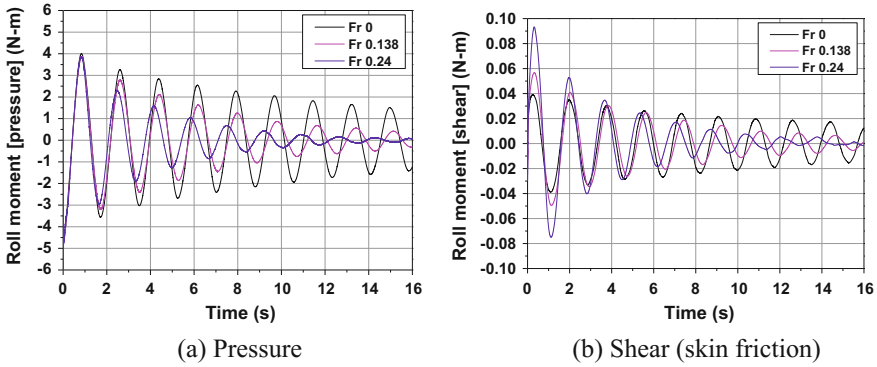


Fig. 9 Roll excitation moment at three  $Fr$  ( $\varphi_0 = 19^\circ$ )

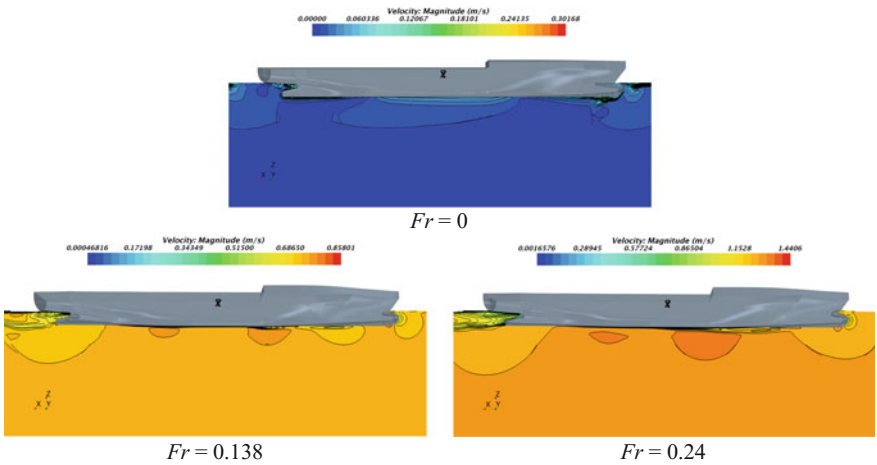


Fig. 10 Contours of water velocity at three  $Fr$  after first roll cycle i.e.  $t/T_n = 1$

cause lifting effect on the hull which contributes to both roll damping and restoring moment of the vessel which needs to be studied in detail.

## 5 Conclusions

Experiments of free roll decay of a container ship were carried out at zero speed, and the measured roll motion was used to validate the URANS-based numerical simulation set-up. The numerical set-up was then used to simulate free roll decay with two forward speeds. It was observed that the roll damping of the container ship increases with forward speed. This was also observed in the past literature, and

the main reason for increase in roll damping is the contribution from hull lift at forward speed. The roll natural period and added mass increase for a forward speed of 0.734 m/s as compared to zero forward speed, whereas roll natural period and added mass decrease for the forward speed of 1.276 m/s as compared to 0.734 m/s and zero forward speed.

Further, investigation on the variation of roll damping and roll natural period needs to be studied by subjecting the ship to various speeds. Experiments can also be conducted in towing tank for free or forced roll oscillation tests at forward speeds.

## References

- Ikeda Y, Himeno Y, Tanaka N (1977) On eddy making component of roll damping force on naked hull. *J Soc Nav Archit Jpn* 1977(142):54–64
- Ikeda Y, Komatsu K, Himeno Y, Tanaka N (1977) On roll damping force of ship-effect of hull surface pressure created by Bilge Keels. *J Kansai Soc Nav Archit Jpn* 165
- Schmitke RT (1978) Ship sway, roll, and yaw motions in oblique seas. *SNAME Trans* 86:26–46
- Ikeda Y, Himeno Y, Tanaka N (1978) Components of roll damping of ship at forward speed. *J Soc Nav Archit Jpn* 1978(143):113–125
- Himeno Y (1981) Prediction of ship roll damping-state of art. Michigan, USA
- Chakrabarti S (2001) Empirical calculation of roll damping for ships and barges. *Ocean Eng* 28(7):915–932
- Kawahara Y, Maekawa K, Ikeda Y (2012) A simple prediction formula of roll damping of conventional cargo ship on the basis of Ikeda's method and limitations. *J Shipp Ocean Eng* 2:201–210
- Downie MJ, Bearman PW, Graham JMR (1988) Effect of vortex shedding on the coupled roll response of bodies in waves. *J Fluid Mech* 189:243–264
- Lian W (1988) A numerical study of two-dimensional separated flow past bluff bodies at moderate KC-numbers. *Appl Ocean Res* 10(3):114–119
- Faltinsen OM, Sortland B (1987) Slow drift eddy making damping of a ship. *Appl Ocean Res* 9(1):37–46
- Sarpkaya T, O'Keefe JL (1996) Oscillating flow about two and three-dimensional bilge keels. *J Offshore Mech Arct Eng* 118(1):1
- Yeung RW, Liao SW, Roddier D (1998) Hydrodynamic coefficients of rolling rectangular cylinders. *Int J Offshore Polar Eng* 8:241–250
- Roddier D, Liao S, Yeung RW (2000) Wave-induced motion of floating cylinders fitted with bilge keels. *Int J Offshore Polar Eng* 10:241–248
- Yu Y-H, Kinnas SA (2009) Roll response of various hull sectional shapes using a navier-stokes solver. *Int J Offshore Polar Eng* 19:46–51
- Chun H, Chun S, Kim S (2001) Roll damping characteristics of a small fishing vessel with a central wing. *Ocean Eng* 28(12):1601–1619
- Paterson EG, Wilson RV, Stern F (2003 Nov) General-purpose parallel unsteady RANS ship hydrodynamics code: CFDSHIP-IOWA. IIHR
- Wilson RV, Carrica PM, Stern F (2006) Unsteady RANS method for ship motions with application to roll for a surface combatant. *Comput Fluids* 35(5):501–524
- Irkal MAR, Nallayarasu S, Bhattacharyya SK (2016) CFD approach to roll damping of ship with bilge keel with experimental validation. *Appl Ocean Res.* 55:1–17
- Taylan M (2004) Effect of forward speed on ship rolling and stability. *Math Comput Appl* 9(2):133–145
- Irvine M Jr, Longo J, Stern F (2013) Forward speed calm water roll decay for surface combatant 5415: global and local flow measurements. *J Ship Res* 57(4):202–219

21. CD-adapco (2016) STAR-CCM+® Documentation
22. Ferziger JH, Peric M (2002) Computational methods for fluid dynamics. Springer, Berlin
23. ITTC (2011) ITTC-recommended procedures and guidelines: practical guidelines for ship CFD applications. Rio de Janeiro

# Design and Analysis of a Carbon Composite Propeller for Podded Propulsion



Ashok Kumar, G. Lal Krishna and V. Anantha Subramanian

**Abstract** Though the bulk of marine propellers are almost exclusively manufactured in metal alloys, there has been a recent trend to look into composite materials for propellers. Carbon fibre because of its extremely high strength and favourable strength-to-weight ratio is therefore a strong candidate as an alternate material for propellers. This paper investigates the design, analysis and basic strength aspects of a carbon composite propeller for application as a podded propulsion unit. Propellers are roto-dynamic machines and are prone to fatigue, and therefore, this is one of the important considerations in the choice of the material. Therefore, long-term study in terms of not only strength, hydrodynamic performance, but also fatigue properties must be well established if carbon composite propellers are to be used as substitute for the conventional propellers. This study presents the design of a propeller based on favourable stacking orientation of the multiple layers using unidirectional carbon fibre and epoxy resin, technique of manufacture and test results for hydrodynamic performance. For this purpose, the propeller conforms to standard NACA profiles for high efficiency. The study reports the analysis for strength on the basis of modelling the layer sequence and assigning the directional properties for the carbon fibre. To validate the results, a segmented loading frame has been designed and the deflections measured in the radial direction. The results help to verify the deflections obtained and therefore to confirm the analytical approach to obtain the dynamic stresses and the deflections. The study lays the foundation for redesigning the propeller making full advantage of the strength-to-weight ratio of carbon composite to obtain high efficiency and to obtain the hydro-elasticity-based response characteristic.

---

A. Kumar (✉) · G. Lal Krishna · V. Anantha Subramanian  
Department of Ocean Engineering, Indian Institute of Technology Madras, Chennai 600036,  
Tamil Nadu, India  
e-mail: [s.ashokji@gmail.com](mailto:s.ashokji@gmail.com)

G. Lal Krishna  
e-mail: [lalkrishnarpn@gmail.com](mailto:lalkrishnarpn@gmail.com)

V. Anantha Subramanian  
e-mail: [subru@iitm.ac.in](mailto:subru@iitm.ac.in)

**Keywords** Pod propulsor · Composites · CFRP · Open water tests · CFD  
Static loading test · FEM

## Nomenclature

CFRP	Carbon fibre reinforced plastic
MRF	Moving reference frame
$\eta_0$	Open water efficiency
$K_T$	Thrust coefficient
$K_Q$	Torque coefficient
$n$	Propeller rpm
$V_A$	Speed of advance
$d$	Propeller diameter
$\rho$	Density of water
$T$	Thrust
$Q$	Torque

## 1 Introduction

Marine screw propellers are roto-dynamic machines which produce thrust from hydrodynamic action. They are subjected to high loading, pulsating forces as they rotate in the disc area, subjected to vibrations, centrifugal force, bending and axial-based thrust forces. They generally work in a heterogeneous flow environment due to the characteristic wake pattern behind a ship, and therefore, long-term stresses such as due to vibration, fatigue are also typical loading conditions. Therefore, choice of material is important and not only from the immediate thrust consideration. Conventional propeller materials include nickel aluminium bronze, manganese bronze, aluminium alloy and stainless cast steel alloy. Some common drawbacks of the conventional propeller materials are corrosion, cavitation, formation of galvanic cell and maintenance cost. Composite propellers may offer a solution. They are designed and constructed based on combinations of resins and reinforcement fibre. Composite materials are mainly known for the excellent strength properties, lightweight, improved fatigue properties, less corrosion, high thermal resistance and low maintenance cost. Material properties of carbon fibre, aluminium alloy, nickel aluminium bronze and manganese bronze are compared and listed in Table 1.

Carbon fibre reinforced plastic (CFRP) has polymer resin matrix material which binds together the reinforcing fibre. The resin and fibre may be made available separately and the laminate prepared to set at room temperature or cured in higher temperature controlled environment. Carbon fibre is also manufactured in the form of pre-preg material, which can be set and cured in an autoclave. The matrix polymer material is usually epoxy resin, and it binds the fibres together. The stacking sequence

**Table 1** Comparison between properties of carbon fiber, aluminium, NAB, manganese bronze

Material properties	Carbon fibre (unidirectional)	Aluminium alloy	Nickel aluminium bronze	Manganese bronze
Young's modulus (GPa)	120–220	68–72	122–130	110–120
Tensile strength (MPa)	800–1500	270–330	550–660	410–490
Density (g/cm <sup>3</sup> )	1.35–1.85	2.65	7.55	8.22
Thermal conductivity (W/m K)	20	117	42	80
Low coefficient of thermal expansion $\times 10^{-6}$ (Inch/inch degree Fahrenheit)	–1 to 8	7–13	9	12
Poisson's ratio	0.27	0.33	0.32	0.34

of the fibre significantly influences the structural properties of the composite. Carbon composite has high initial strength-to-weight ratio. Two important aspects that need investigation are the effect of absorption of moisture in marine condition and fatigue behaviour. Hence, a safe design approach is to have higher factor of safety for the CFRP material under cyclic loading conditions. Some other associated characteristics are less compression strength, complex manufacturing techniques, low fracture toughness and moisture absorption. Considering all the above-known characteristics and the unknown areas of long-term behaviour, it is important to make a first-hand beginning in the design, fabrication analysis of carbon composite propeller for marine application. This paper reports a systematic study which includes hydrodynamic performance analysis as well as strength and deflection under thrust loading.

## 2 Literature Survey

Izabella Krucinska [1] studied the bending method to evaluate the strength and failure strain of carbon fibre based on the mathematical framework of flexural theory. Gilchrist et al. [2] studied the static behaviour, fractographic observations, fatigue behaviour and finite element predictions of composite I-beams subjected to mechanical loads and also the failure under fatigue as well as impact on CFRP. Sun and Jun [3] brought out the effect of fibre misalignment and nonlinear behaviour of the matrix on fibre micro-buckling and the compressive strength of unidirectional fibre com-

posite. Young [4] studied the hydro-elastic behaviour of flexible composite propeller in wake flow. Young [5] also studied the flexible propellers with fully coupled BEM and FEM for subcavitating and cavitating flows and compared with experiments. Lin et al. [6] studied the effect of stacking sequence on a composite blade. The blade was analysed with different stacking sequences of composite lay-up. Blasques et al. [7] addressed the design and optimization of a flexible composite marine propeller by tailoring the laminate to control blade shape and consequently the developed thrust. Hara et al. [8] worked on the performance evaluation of composite marine propeller for a fishing boat by fluid–structure interaction analysis. Paik [9] made a comparative study of different composite propellers both numerically and experimentally. Das and Kapuria [10] studied the use of bend–twist coupling of a composite marine propeller for enhanced hydrodynamic properties. Because of the steadily widening application of carbon fibre composites, it is vital to initiate studies starting from application for small composite propellers and building up. Carbon composite propellers are also of strategic importance as non-metallic materials with high strength.

### 3 Design and Construction

The propeller geometry must suit direct connection to a submerged three-phase electrical motor prime mover characterized by a large hub to diameter ratio of 0.44, delivering 5 kW of input power. The CFRP propeller has been adapted from the standard Wageningen-B series data with sectional geometry from the same series. The design data gives the pitch, diameter, number of blades and the available thrust power. The blade sections chosen from the series give the most favourable blade sections, and primarily, these are intended for metal alloy propellers. The objective is to evaluate the hydrodynamic and strength characteristic of the carbon fibre propeller and modify the same in future to take advantage of the high strength of carbon fibre, also considering the long-term behaviour such as fatigue, moisture absorption effect etc. Table 2 provides the geometric properties of the propeller.

Negative form provides a monolithic propeller with hub and three blades. The propeller casting process involves hand lay-up process where the epoxy resin is bonded

**Table 2** Geometric properties of carbon fibre propeller

Diameter ( $D$ ) mm	450
Hub diameter ( $d$ ) mm	198
Pitch ratio ( $P/D$ )	1
Hub–diameter ratio ( $d/D$ )	0.44
Expanded area ratio ( $A_E/A_0$ )	0.35
Number of blades ( $Z$ )	3
Rotation	Left handed
RPM	748



with the carbon fibre layers in predetermined orientation. The reinforcement and matrix materials are to be laid within the split negative form. Due to the complexity in the split mould, the manufacturing of the propeller was carried out using hand lay-up process.

The design follows the optimum stacking sequence given by Lin et al. [11]. The propeller is designed with six layers of 300gsm carbon fibre stacked with the orientation sequence (0/-45/90/45/90/0) implying the angle in degrees in each layer. The matrix material is epoxy resin (LY556) mixed with the hardener HY951 in a ratio of 10:1. The manufacturing process has two options, viz. using pre-preg reinforcement carbon fibre with baking in an autoclave or hand lay-up. The manufacturing method adopted hand lay-up in view of the complexity of the multiple split mould required for the manufacture of a monolithic propeller with integral blades and hub. The lamination is a high-skill process. The matrix material permits room curing for 24 h. See Fig. 1 for the finished propeller.

First tests quantify the hydrodynamic characteristics as defined by the open water tests. The test set-up is shown in Fig. 2. The main propulsion motor was used as the prime mover in the open water test set-up, and the thrust and torque characteristics were obtained as a function of the forward speed, and these are plotted in Fig. 3. In the test set-up, the input power was measured using electrical input quantities and the output thrust was measured using a cantilever vertical beam and load cell at the upper end based on the principle of moments. The central shaft and plunger block shown in the figure act as the pivoting point in the cantilever arrangement for measuring the thrust.

An HBM 1t U1A-type load cell was used to measure the thrust produced by the pod propulsion unit. The load cell is enclosed with full-bridge connected strain gauges with temperature error compensation. The load cell is connected to HBM PMX which is a PC-based electronic measurement system to measure the thrust generated. The PMX is configured for the experiments using Catman software, which manages the settings and calibration data of the measuring instruments.

**Fig. 1** Carbon fibre propeller manufactured using hand lay-up process



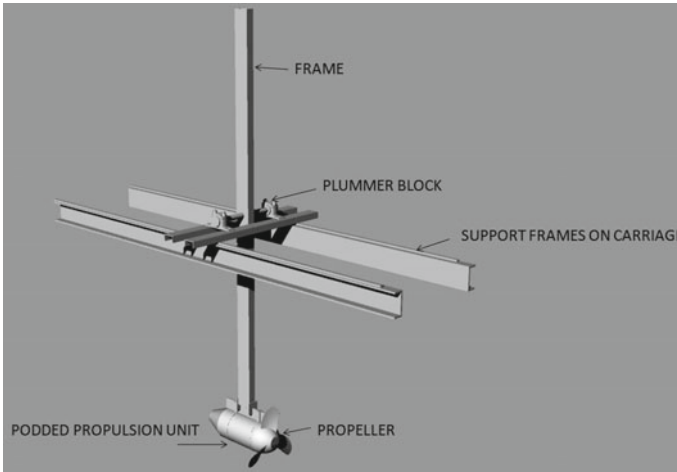


**Fig. 2** Test set-up to identify open water performance of carbon and Al propeller for a podded propulsion system

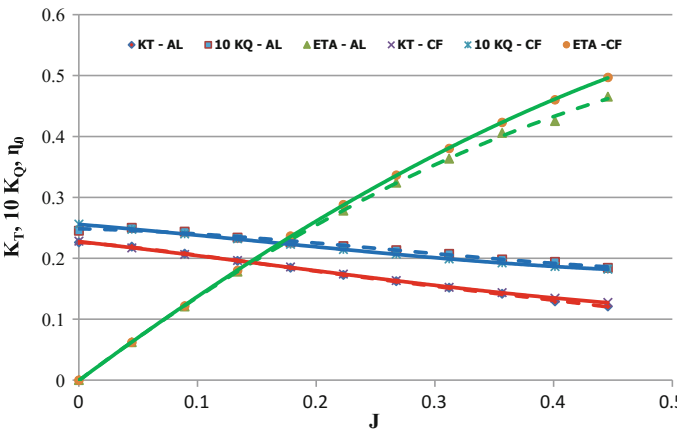


**Fig. 3** Open water characteristics of carbon fibre and aluminium propeller at 748 RPM

### 3.1 Towing Tank Experiments

The test procedure includes setting the towing carriage to a predetermined steady speed from zero which is also bollard condition to the cover maximum possible speed of the carriage for constant revolution of propeller; in this case, it is 748 RPM. This is the highest-rated rpm of the motor.

The speed of advance is non-dimensionalized as the usual advance coefficient  $J$ . The test results are plotted as non-dimensional thrust and torque values against  $J$ .

$$K_T = \frac{T}{\rho n^2 d^4} \quad (1)$$

$$K_Q = \frac{Q}{\rho n^2 d^5} \quad (2)$$

$$\eta_0 = \frac{K_T J}{K_Q 2\pi} \quad (3)$$

## 4 Numerical Modelling for Obtaining Pressure Distribution on the Propeller Blades

The numerical modelling gives the distribution of pressure and in turn provides the input for structural analysis of the propeller blade section under the bollard pull condition (maximum thrust condition).

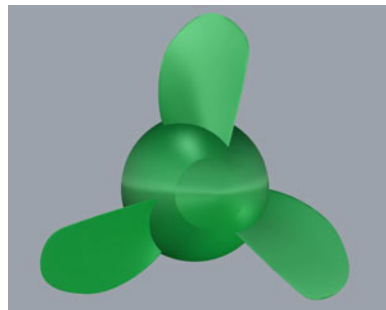
The geometry of the solid propeller is obtained using the 3D CAD modelling software Rhinoceros 5. The co-ordinates of the blade are imported, and the solid model is generated using loft technique; see Fig. 4. The data has been converted into .step file for further CFD studies.

A RANSE-based solver STAR-CCM+ was used. In this approach, an inertial frame of reference is attached to the outer domain and a moving reference frame fixed to the sub-domain. The rate of revolution is specified to the moving or rotating reference frame, and the flow is modelled as a steady problem with respect to the moving reference frame. Hence, at grid points in the sub-domain a rotational component according to the relative propeller rotations is added to the velocity. Figure 5 shows the domain developed in STAR-CCM+.

The propeller is modelled in a sub-domain as part of the outer domain with separate mesh generation for the sub-domain and outer domain and interfacing to connect the outer domain and sub-domain meshes, which are common for both regions. The grid uses a combination of structured and unstructured grids.

Hexahedral meshing is used for the volume mesh, and hexahedral cells trimmed to form polyhedral cells are used near the complex geometrical shape of the propeller

**Fig. 4** 3D-CAD model of the propeller



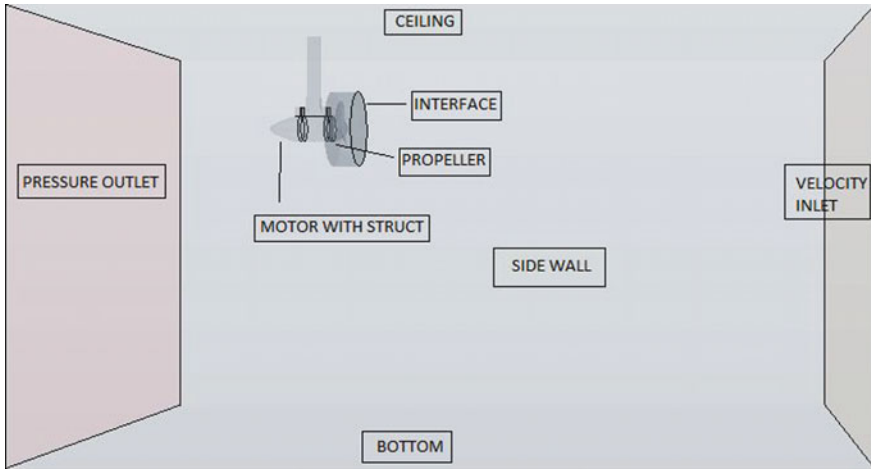


Fig. 5 CFD domain created in STAR-CCM+



Fig. 6 A view of generated mesh for CFD studies

body. To ensure proper calculation of forces and gradients on the propeller surface, it is necessary to have the mesh elements orthogonal to the propeller surface. Prism layer meshing is used in conjunction with the core volume mesh (Fig. 6). Mesh template growth rate is specified for a medium rate transition of mesh from inner fine mesh to the outer coarse mesh. The thrust distribution at bollard pull condition is given in Fig. 7. The total thrust from the computation is 1735 N, whereas from experiment the value is 1448 N. The thrust distribution is used as input for the structural analysis to obtain the deflections of the blade (Tables 3 and 4).

The RANSE-based solver STAR-CCM+ was used to compute the open water characteristics of podded propeller. From the above analysis, the thrust along the

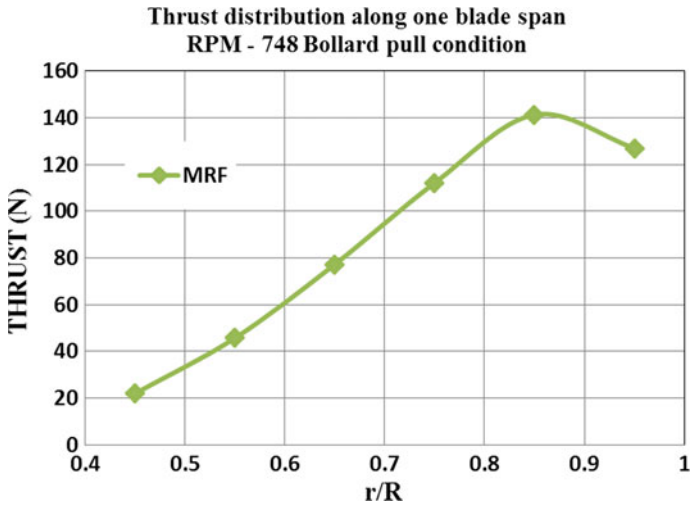


Fig. 7 Thrust distribution along the blade section in MRF method

Table 3 Solver parameters used in MRF method

Parameter	Settings
Solver	3D, steady
Turbulence model	K-Epsilon turbulence
Flow type	Segregated flow
Wall treatment	Two-layer all wall y+ treatment
Equation of state	Constant density
Fluid	Water

Table 4 Boundary condition incorporated for MRF method

Inlet	Velocity inlet
Outlet	Pressure outlet
Propeller blades	No slip
Side walls	Slip
Interfacial domain	Interface

blade sections from 0.4R to 1.0R is estimated for bollard condition and validated with the experimental results.

### 5 Static Loading Test

The load test was designed for basic understanding of the deflection behaviour of the material manufactured by the specific manual lay-up method. Loads as obtained from the CFD studies were applied at six sections ranging from 0.4R to 0.9R. Figures 8 and 9 shows the blade sections and segmental loading process. The deflections were measured using precision height gauge with 0.01 mm least count. Maximum tip deflection at full load was obtained as 5.2 mm. FEM-based analysis was carried out as described in Sect. 5.1. Table 5 shows the stiffness matrix incorporated for the analysis. The results were compared and are given in Table 6.

**Table 5** Stiffness matrix of composite propeller for FEM analysis

68.28	13.28	0.00	-1.25	-1.08	2.32	×10 <sup>9</sup>
13.28	68.28	0.00	-1.08	3.40	2.32	
0.00	0.00	16.75	2.32	2.32	-1.08	
-1.25	-1.08	2.32	13.55	0.88	-0.46	
-1.08	3.40	2.32	0.88	4.27	-0.46	
2.32	2.32	-1.08	-0.46	-0.46	1.29	



**Fig. 8** Blade sections with supporting structures



**Fig. 9** A view of segment loading for static load test

### ***5.1 Finite Element Analysis of Propeller Under Static Loading***

Static analysis of the propeller blade under thrust loading is carried out using a commercial finite element-based software ANSYS. The geometry of the propeller is imported to ANSYS APDL V15 in .iges format and is meshed. Tetrahedral mesh is used to capture the geometry. SOLID 185 elements are used for the finite element analysis of the propeller. The stacking sequence of the carbon fibre propeller is considered as designed, viz. 0/-45/90/45/90/0. In order to incorporate the effects of skewness and thickness variation in the finite element model, solid modelling is used. Composite lamina is orthotropic in nature. Material property of the laminate is modelled by the assembled  $6 \times 6$  global stiffness matrix considering the various fibre angles. The elements of the matrix are given in Table 5.

The mesh file which is generated in ANSYS has been exported to STAR CCM+, and the fluid boundary element pressures are mapped to the exterior surface of the ANSYS mesh. A load file is generated which applies the pressures developed on the propeller based on the nodal points. The boundary condition is used to simulate the actual conditions of the propeller. Translational degrees of freedoms at the shaft

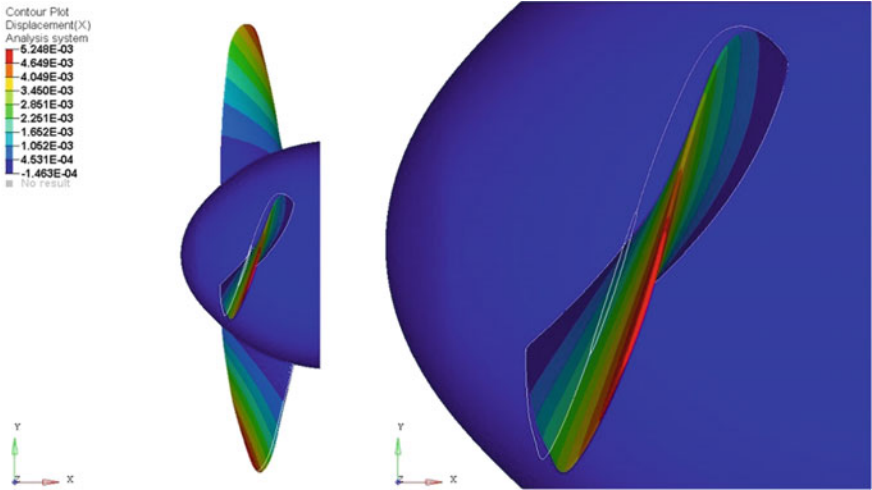


**Fig. 10** Propeller deflection using FEM-based software

**Table 6** Comparison of static deflection on a CFRP propeller in experiment and FEM analysis

Serial no.	Propeller radius	Load (kg)	Deflection based on experiments (mm)	Deflection using FEM-based software (mm)	Percentage of error
1	0–3R	0	0	0	0
2	0.4R–0.5R	2.06	0	0	0
3	0.5R–0.6R	4.28	0.5	0.69	0.38
4	0.6R–0.7R	7.24	1.18	1.48	0.254
5	0.7R–0.8R	10.51	2.14	2.49	0.164
6	0.8R–0.9R	13.25	3.44	3.54	0.0291
7	0.9R–1R	11.9	5.02	5.24	0.0438

and hub connection are arrested. From the solution of FEM analysis, the maximum deflection was found to be 5.248 mm and it is close match with the value obtained from experimental static loading test. Table 6 shows the comparison between experiments and FEM values. Figure 10 shows deflection of blade tip.

## 6 Conclusion

Carbon composite propeller has been designed, fabricated and tested for both hydrodynamic and structural properties. The carbon fibre propeller for podded propulsion has been successfully fabricated with characterization of its properties. The



study establishes the feasibility and practicality of manufacturing carbon composite propeller. High strength, lightweight, non-corrosion in marine environment are the important attributes. The deflection characteristics have been quantified and found to be within reasonable limits. The results encourage trial application for further understanding carbon composite propellers with long-term implications.

## References

1. Krucinska I (1991) Evaluation of the intrinsic mechanical properties of carbon fibres. *Compos Sci Technol* 41(3):287–301
2. Gilchrist MD, Kinloch AJ, Matthews FL (1996) Mechanical performance of carbon-fibre and glass-fibre-reinforced epoxy I-beams: II. Fractographic failure observations. *Compos Sci Technol* 56(9):1031–1045
3. Sun CT, Wanki Jun A (1994) Compressive strength of unidirectional fiber composites with matrix non-linearity. *Compos Sci Technol* 52(4):577–587
4. Young YL (2007) Hydroelastic behavior of flexible composite propellers in wake inflow. In: 16th international conference on composite materials, Kyoto, Japan
5. Young YL (2008) Fluid-structure interaction analysis of flexible composite marine propellers. *J Fluids Struct* 24:799–818
6. Lin HJ, Lai WM, Kuo YM (2010) Effects of stacking sequence on nonlinear hydroelastic behavior of composite propeller blade. *J Mech* 26(03):293–298
7. Blasques JP, Berggreen C, Andersen P (2010) Hydro-elastic analysis and optimization of a composite marine propeller. *Marine Struct* 23(1):22–38
8. Hara Y, Yamatogi T, Murayama H, Uzawa K, Kageyama K (2011) Performance evaluation of composite marine propeller for a fishing boat by fluid-structure interaction analysis. In: 18th international conference on composite materials, Jeju Island, Korea, pp 1–6
9. Paik BG, Kim GD, Kim KY, Seol HS, Hyun BS, Lee SG, Jung YR (2013) Investigation on the performance characteristics of the flexible propellers. *Ocean Eng* 73:139–148
10. Das HN, Kapuria S (2016) On the use of bend-twist coupling in full-scale composite marine propellers for improving hydrodynamic performance. *J Fluids Struct* 61:132–153. <https://doi.org/10.1016/j.jfluidstructs.2015.11.008>
11. Lin H, Lin JJ, Chuang TJ (2005) Strength evaluation of a composite marine propeller blade. *J Reinf Plast Compos* 24:1791–1807. <https://doi.org/10.1177/0731684405052199>

# Passing Vessel Effect on Mooring System of a Berthed Ship—A Case Study at Jawahar Dweep Berth No: 5, Mumbai Port



Keshav Sundar, V. Nandhini and S. Nallayarasu

**Abstract** The proposed new oil berth at Jawahar Dweep Island, Mumbai, is planned adjacent to the approach channel leading towards Pir Pau and Jawaharlal Nehru Port. The width of the channel is around 200 m and straight at the location. An existing berth J4 which is located adjacent to the new berth had in the past some incidences of breaking of mooring lines during monsoon season. The present study was done to study the effect of passing vessel effect and the environmental loading on a vessel berthed at that location. The study includes a complete simulation of mooring line forces due to wind, wave and current for the vessel ranges from 150,000 DWT to 250,000 DWT and arriving at the quick release mooring hook capacities. The passing vessel effect on the selected mooring hook capacities was reviewed by carrying out the combined effect of wind, wave and current together with the passing vessel effect. A critical review of the existing methods including OPTIMOOR simulation has been carried out to determine the suitable method for the present situation. The study indicated that the mooring hook capacities selected for the environmental loads shall be increased by 25% to cater for the combined effect of passing vessel. Several parametric studies have been carried out to include the distance between the passing vessel and the moored vessel, vessel speed, and vessel sizes, and the results are presented and discussed.

**Keywords** Mooring · Passing vessel · Berthed ship · Case study

---

K. Sundar  
Mumbai Port Trust, Mumbai 400001, India

V. Nandhini · S. Nallayarasu (✉)  
Department of Ocean Engineering, Indian Institute of Technology Madras, Chennai 600036, India  
e-mail: [nallay@iitm.ac.in](mailto:nallay@iitm.ac.in)

© Springer Nature Singapore Pte Ltd. 2019  
K. Murali et al. (eds.), *Proceedings of the Fourth International Conference in Ocean Engineering (ICOE2018)*, Lecture Notes in Civil Engineering 22,  
[https://doi.org/10.1007/978-981-13-3119-0\\_14](https://doi.org/10.1007/978-981-13-3119-0_14)

217

# 1 Introduction

The Mumbai Port is natural harbour sheltered between Mumbai island and mainland. Within the Mumbai harbour area, the ports handling liquid, solid and container cargo are located. The Mumbai harbour houses the Mumbai Port Trust (MbPT) Jetties located in Jawahar Dweep (JD) Island, Pir Pau Jetties and Jawaharlal Nehru Port Terminals on the east. The dock area located on the east coast of Mumbai island houses various naval docks. The map of Mumbai harbour is shown in Fig. 1.

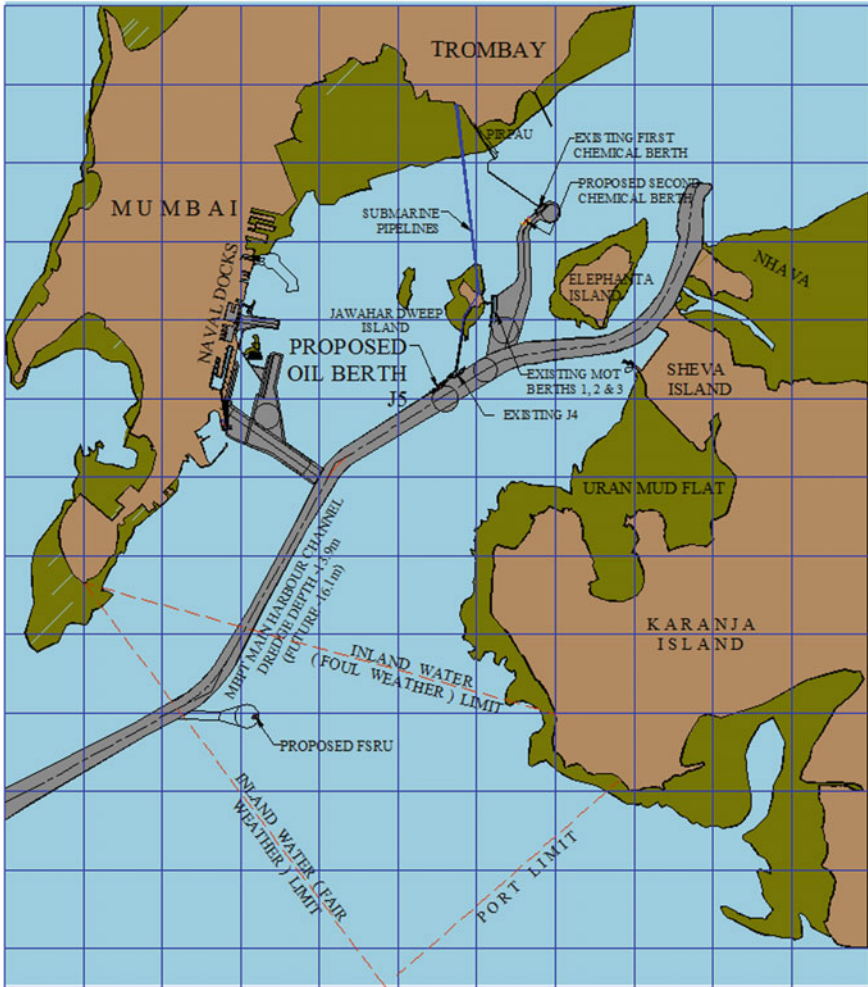


Fig. 1 Mumbai harbour area

Mumbai Port Trust (MbPT) is constructing a new oil jetty (J5) at Jawahar Dweep adjacent to the existing Jetty J4. The proposed jetty location is shown in Fig. 1, and the jetty is adjacent to the approach channel of width 200 m. A vessel berthed at such location would be subjected to motions in moored condition due to reasons as follows:

- (a) External environmental loads due to wave, wind and current.
- (b) Water movement associated with disturbances generated due to passing vessels in the vicinity of the moored ship.

The case study has been carried out to determine the effect of combining environmental loads together with the passing vessel effects on mooring loads of a ship berthed adjacent to the approach channel specifically for the proposed jetty at Jawahar Dweep (J5).

## 2 Literature Review

The passing vessel effect causes surge force (along the vessel length), sway force and yaw moment on the moored vessel. There are existing methods to calculate these forces and moment. They are mainly empirical equations based on some experimental data.

There are several methods available to determine hydrodynamic loads on moored vessel due to passing vessel. Some of the relevant methods are mentioned here. Wang [1] developed a slender body theory to derive forces on the moored ship due to the passing ship in infinite water depth. He also further developed shallow-water correction factors to account for under keel clearance into account. Seelig [2], developed shallow-water correction factors to Wang's equation in deep water. Flory [3] developed independent empirical equations using the model tests of various past researchers. Kriebel [4] developed correction factors for Wang deep-water equations as well as independent empirical equations for the calculation of forces on the moored vessel. Seelig's and Flory's work were based on experimental tests by Remery [5] and Muga [6], who studied the effect of several parameters on passing vessel forces and also the effect of type of mooring lines (in the form of spring constant) in resisting the passing vessel forces.

Methods based on Seelig [2] and Flory [3] are available in OPTIMOOR software, and the same is used for the present study.

The following points were observed from the literature study:

- The main parameters that influence the passing vessel forces are the passing vessel speed, the displacement ratio and the separation distance between the vessels.
- The empirical equations are based on experiments of specific parameters, and they can be used to estimate the passing vessel forces within those ranges of parameters.
- OPTIMOOR's dynamic analysis can be utilized for this study.

The objective of this case study is to analyse the increase in mooring line loads due to the passing vessel effect. The scope of the study is as follows:

- Optimum mooring layout development for vessels to be berthed at J5.
- Static mooring analysis using quasi-static methods for deriving mooring line loads from wind, wave and current.
- Passing vessel loads on the moored vessel by empirical methods described in the literature.
- Dynamic mooring analysis using OPTIMOOR software including the effect of passing vessel forces.
- Recommendations on channel widening, reduction of approach speed to MbPT
- Detailed mooring analysis report.

### 3 Jetty/Approach Channel Layout

#### 3.1 Jetty Layout

The mooring analysis is performed to determine the maximum possible loads on the mooring points considering all directions of wind, wave and current approach, on the existing orientation of the berth. The BS/OCIMF [7, 8] requirements were used for fender layout verification. The layout of fenders showing the spacing and position along the length of the berth is shown in Fig. 2. These structures shall be positioned and spaced based on guidelines of PIANC [9] and Oil Companies International Marine Forum (OCIMF).

The spring lines and bow/stern lines are arranged depending on the vessel bollard and winch locations. The proposed shore-based mooring points shall allow such variations and typical configurations are shown in Fig. 3 for 150,000 DWT vessels.

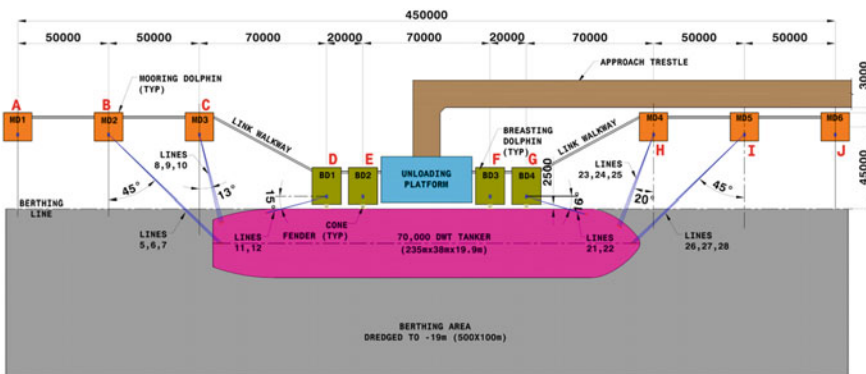


Fig. 2 Fender arrangements

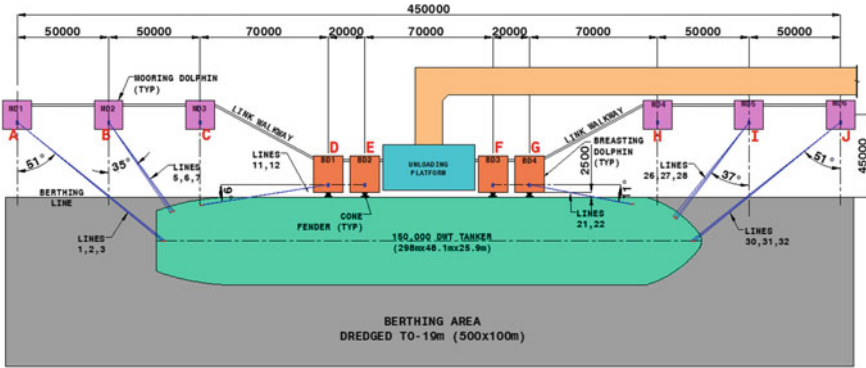


Fig. 3 Mooring layout for 150,000 DWT vessel

The mooring line angles are to follow the guidelines of OCIMF [7]. The mooring line loads are assessed using the mooring layout configuration shown in the figure.

### 3.2 Approach Channel Layout

The layout of the approach channel (width) greatly influences the passing vessel forces. The plan view of the approach channel and the location of the proposed jetty are shown in Fig. 4. Sectional view of the approach channel in front of J5 is shown in Fig. 5. The passing vessel effects on the moored vessel is considered for clear spacing of 75, 100, 150 and 200 m to determine the acceptable spacing and define conditions for the traffic during monsoon.

### 3.3 Moored Vessel Data

The oil companies (HPCL and BPCL) using the oil jetties at Jawahar Dweep, Mumbai, required that J5 be designed to handle fully laden Suez Max tankers for crude import to achieve economy in freight charges. The vessel sizes considered for the purpose of layout planning and structural design of the proposed jetty J5 are summarized in Table 1.

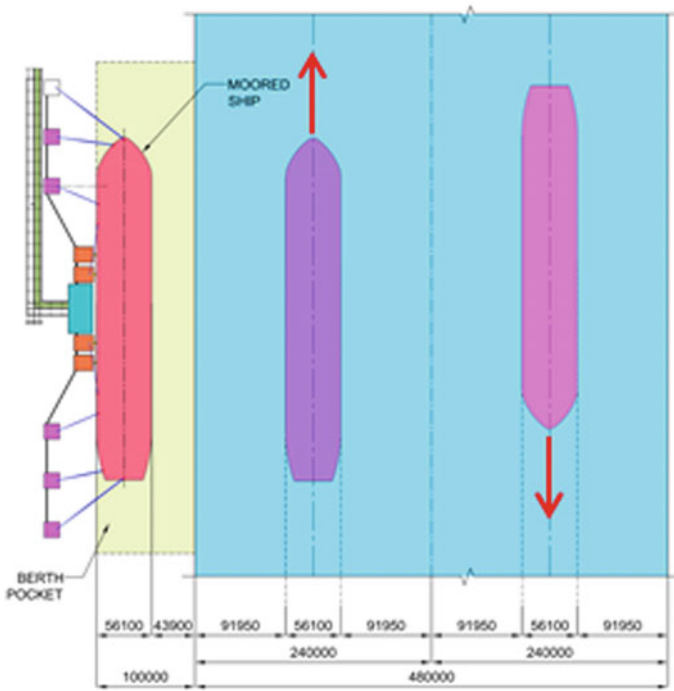


Fig. 4 Plan of approach channel

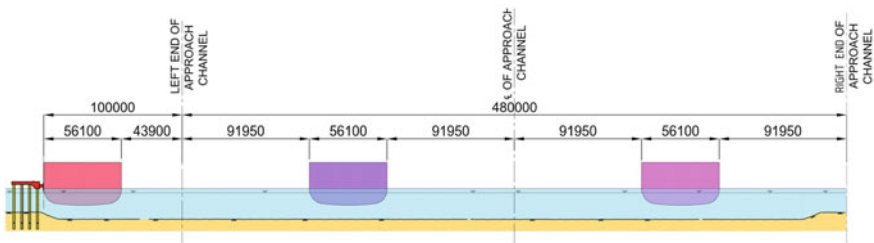


Fig. 5 Section of approach channel

### 3.4 Passing Vessel Data

The proposed J5 is located alongside of existing approach channel. The existing approach channel in front of J4 and J5 is widened from 370 to 480 m as shown in Fig. 4. The tankers primarily container vessels proposed to be moving along the channel are summarized in Table 2.

**Table 1** Design vessel sizes

Tanker	DWT	LOA (m)	Beam (m)	Fully loaded draft (m)	Maximum permissible loaded draft (m)	Laden draft (m)
VLCC	250,000	349	56.1	26.0	16.8 <sup>a</sup>	8.4
Suezmax	150,000	298	48.1	17.4	16.7 <sup>a</sup>	8.4
Aframax	100,000	263	42.5	15.4	15.4	7.7
Panamax	70,000	225	36.0	12.5	12.5	6.3

<sup>a</sup>Partially loaded to 140,000 parcel size

**Table 2** JNPT tankers moving alongside J5

Vessel type	Displacement (tonnes)	LOA (m)	Beam (m)	Fully loaded draft (m)	Cb
12000 TEU	200,000	366	50	15	0.7
14000 TEU <sup>a</sup>	240,000	400	55	15.5	0.7

<sup>a</sup>Not considered in the study at present as it is planned for future

## 4 Environmental Loads on Moored Ships

### 4.1 General

The environmental loads include the effect of wind, wave and current at the location. The environmental data for the concerned case study includes the wind, wave and current characteristics with reference to their predominant direction of occurrence.

### 4.2 Wind

The maximum wind speed is about 30 m/s with its percentage of occurrence less than 1%. For the purpose of determining the mooring loads, it is considered omnidirectional with a maximum wind speed of 30 m/s, in accordance with OCIMF [10] guidelines.

### 4.3 Wave

The predominant wave approach is from south-west not including the effect of local wind generated waves. The wave data extracted from the CWPRS report [11] is tabulated in Table 3.



**Table 3** Wave data extracted from CWPRS report

Description	223°	225°	223°
	WNW	W	WSW
Significant wave height (m)	0.2	0.44	0.6
Wave period (s)	10	10	10

Note WNW, W and WSW represent the offshore wave entry conditions

**Table 4** Design mooring load combination—dynamic mooring analysis

Description	N	NE	E	SE	S	SW	W	NW
	0°	55°	90°	135°	180°	225°	270°	315°
Wind <sup>1</sup> (m/s)	✓	✓	✓	✓	✓	✓	✓	✓
Wave <sup>3</sup>	–	–	–	–	–	✓	–	–
Current <sup>2</sup> (m/s)	–	✓ (0.71)	✓ (0.10)	–	–	✓ (1.05)	✓ (0.17)	–
Passing vessel	✓	✓	✓	✓	✓	✓	✓	✓

*Notes*

1. Wind speed of 30 m/s (58 knots) is used for all directions
2. Current speed is given for each direction
3. Wave height of 0.6 m with a period of 10 s is to be considered

### 4.4 Current

The flood current is towards north-east during flooding and south-west during ebb though some variations are noted.

Flood flow is from J5 to J4 and north, and ebb flow is from J4 towards J5. The flow during flood is higher than the ebb. The above directional current is used for the mooring analysis. For flood, average direction of 225° is used instead of three directions (220, 230 and 240).

### 4.5 Combinations of Wind, Wave and Current

The berth is oriented towards 57° from north towards east. The bearing of the berthing line is aligned south-west to north-east with a bearing angle of 57° towards east. The mooring analysis shall be carried out considering all critical directions of wind, wave and current combinations. Figure 6 shows the directions of the environmental loads considered for the analysis combining wind, wave and current.

The combination of wind, wave and current used for dynamic mooring analysis is given in Table 4. For static analysis, the passing vessel effect was not considered.

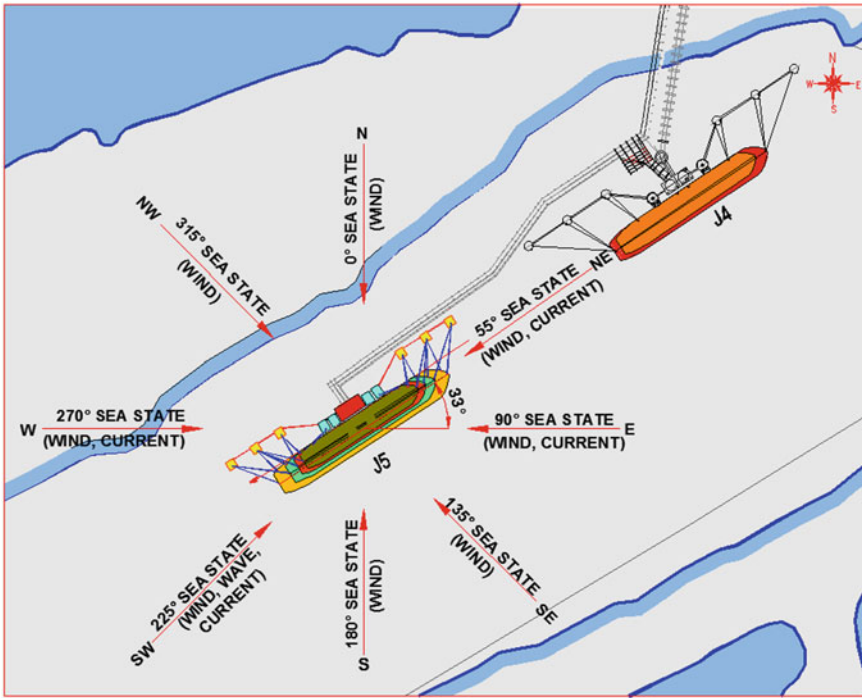


Fig. 6 Design mooring environments

### 4.6 Forces on Moored Vessel

The forces acting on a moored ship alongside a berth can be defined as shown in Fig. 7.

The equation for longitudinal wind force on the moored vessel can be calculated using the guidelines of OCIMF [10] as follows

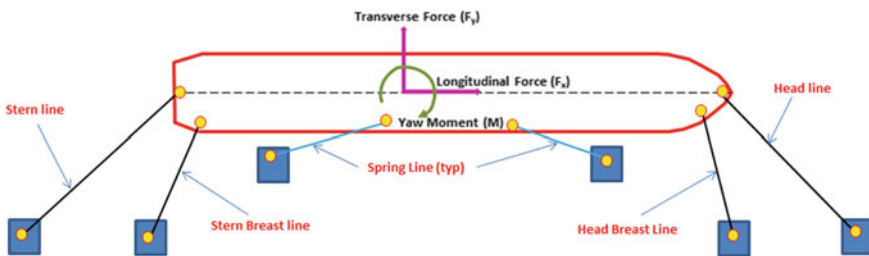


Fig. 7 Forces on a moored ship

$$F_{Xw} = \frac{1}{2} C_{Xw} \rho_a V_w^2 A_T \quad (1)$$

The equation for transverse wind force on the moored vessel can be calculated using

$$F_{Yw} = \frac{1}{2} C_{Yw} \rho_a V_w^2 A_L \quad (2)$$

The equation used within OPTIMOOR for the calculation of yaw moment is given by

$$M_{XYw} = F_{Yw} \left( \frac{X_w}{L_{\rho\rho}} \right) \quad (3)$$

The more traditional equation for yaw moment due to wind is given by

$$M_{XYw} = C_{XYw} \left( \frac{\rho_w}{7600} \right) V^2 A_L L_{BP} \quad (4)$$

Thus the yaw moment arm becomes

$$X_w = \left( \frac{C_{XYw}}{C_{Yw}} \right) L_{BP} \quad (5)$$

where

$A_L$	lateral wind area
$A_T$	transverse wind area
$C_{Xw}$	longitudinal wind force coefficient
$C_{Yw}$	lateral wind force coefficient
$C_{XYw}$	wind yaw moment coefficient
$F_{Xw}$	longitudinal wind force
$F_{Yw}$	lateral wind force
$L_{BP}$	length between perpendiculars
$M_{XYw}$	yaw moment due to wind
$V_w$	velocity of wind
$X_w$	moment arm at which lateral force is applied in producing moment
$\rho_a$	density of air

The value 7600 is a conversion factor of (tonne–metres)/(kilogram–knot–second).

The wind force coefficients are based on wind velocity at 10 m above the free surface. They are based on guidelines of OCIMF [10]. The following formula can be used to convert a wind velocity determined at some other elevation to that 10 m elevation:

$$V_{w10} = V_{wh} \left( \frac{10}{h} \right)^{1/7} \quad (6)$$

where

- $h$  elevation of known wind velocity
- $V_{w10}$  wind velocity at 10 m elevation
- $V_{wh}$  wind velocity at elevation  $h$ .

### 4.7 Current Loads

The general equation for longitudinal current force on moored vessel can be written as follows based on the guidelines of OCIMF [10]

$$F_{Xc} = \frac{1}{2} C_{Xc} \rho_w V_c^2 L_{BP} T \tag{7}$$

The general equation for lateral current force on moored vessel can be written as

$$F_{Yc} = \frac{1}{2} C_{Yc} \rho_w V_c^2 L_{BP} T \tag{8}$$

The general equation for yaw moment on moored vessel can be written as

$$M_{XYc} = \frac{1}{2} C_{XYc} \rho_w V_c^2 L_{BP}^2 T \tag{9}$$

The lateral moment arm  $X_c$  is obtained by:

$$X_c = \left( \frac{C_{XYc}}{C_{Yc}} \right) L_{BP} \tag{10}$$

Hence, the yaw moment can be calculated using

$$M_{XYw} = F_{Yw} \left( \frac{X_w}{L_{BP}} \right) \tag{11}$$

where

- $A_L$  lateral current area
- $A_T$  transverse current area
- $C_{xc}$  longitudinal current force coefficient
- $C_{yc}$  lateral current force coefficient
- $C_{xyc}$  current yaw moment coefficient
- $F_{xc}$  longitudinal force due to current
- $F_{yc}$  lateral wind force due to current
- $L_{BP}$  length between perpendiculars
- $M_{xyc}$  yaw moment due to current
- $V_c$  velocity of current

$X_c$	moment arm at which lateral force is applied
$\rho_w$	density of water
$T$	draft of vessel

The coefficients for longitudinal, lateral forces and yaw moment due to current are based on OCIMF guidelines [10].

## 4.8 Wave-Induced Loads

The forces generated by waves cannot be calculated using simplified formulation due to diffraction effect of large bodies and complex shape of the hull. Hence, the wave-induced loads and motions are calculated using the following approach.

- Response amplitude operators for six degrees of freedom for different shapes of the HULL are available from OPTIMOOR and can be purchased and included in the software. In this case, typical VLCC hull RAO has been included and selected for the present simulation.
- The software then uses these RAO to calculate the motion response in terms of surge, sway and heave for a given wave height and period by simple linear interpolation and apply to the equilibrium position of the tanker and obtain the forces induced on the mooring line.

## 5 Passing Vessel Loads on Moored Ships

### 5.1 Existing Guidelines

The passing vessel loads are caused due to the effect of a vessel crossing at the vicinity at some speed. Figure 8 shows an illustration of the passing vessel effect. When the ship 2 is moving, water gets displaced from bow towards the stern. At the bow, the water gets compressed and there develops a high-pressure field. Similarly, the displaced water converges at stern to form another high-pressure field. Along the sides of the same ship, due to the velocity of water, a low-pressure field is formed, due to Bernoulli's suction effect. The water slopes from high-pressure to low-pressure field. When a ship like ship 1 is present at this vicinity, it will be subjected to forces and moment due to this effect. This is called passing vessel effect.

The moored vessel subjected to forces due to this pressure gradient will undergo motions. The motion of moored ship alongside a berth can be in six degrees of freedom. These motions will induce loads on mooring lines attached to the jetty and the vessel. These forces need to be evaluated carefully to prevent the mooring lines from breaking thus avoiding the free movement or drift of the vessel away from the jetty. Such incidents could cause considerable damage to the ship-shore

connections such as loading arms and fluid connections and environmental damage due to pollution.

This paper is mainly concerned on how the addition of passing vessel loads to the mooring line analysis affects the determination of mooring hook capacity and the effects if they are ignored.

### 5.2 Estimation by Wang’s Method

Wang used slender body approach to determine passing vessel forces. The coordinate system considered for forces is shown in Fig. 9.

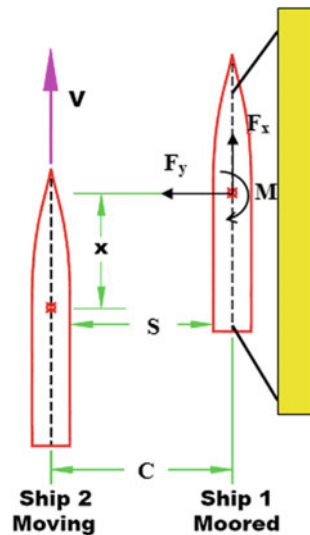
The longitudinal, transverse forces and yaw moment given by Wang [1] are Eqs. (12), (13) and (14), respectively.

$$F_{X\_WANG}(X, C) = \frac{\rho V^2}{2\pi} \int_{L_m} S'_1(x_1) \int_{L_p} \frac{S'_2(x_2)(x_2 - x_1 + X)dx_2}{[(x_2 - x_1 + X)^2 + C^2]^{3/2}} dx_1 \quad (12)$$

$$F_{Y\_WANG}(X, C) = \frac{\rho V^2 C}{\pi} \int_{L_m} S'_1(x_1) \int_{L_p} \frac{S'_2(x_2)dx_2}{[(x_2 - x_1 + X)^2 + C^2]^{3/2}} dx_1 \quad (13)$$

$$M_{z\_WANG}(X, C) = \frac{\rho U^2 C}{\pi} \int_{L_m} S'_1[(x_1)x_1 + S_1(x_1)] \int_{L_p} \frac{S'_2(x_2)dx_2}{[(x_2 - x_1 + X)^2 + C^2]^{3/2}} dx_1 \quad (14)$$

Fig. 8 Passing ship arrangements



Symbols used in Eqs. (12–14) are summarized below:

- $F_{X\_WANG}$  longitudinal force (surge) (N)
- $F_{Y\_WANG}$  lateral force (sway) (N)
- $M_{Z\_WANG}$  yaw moment (Nm)
- $X$  centre to centre longitudinal distance between the ships (m)
- $S$  lateral distance between the ships (m)
- $C$  centre to centre lateral distance between the ships (m)
- $\rho$  density of water (kg/m<sup>3</sup>)
- $V$  speed of the passing vessel (m/s)
- $L_m$  length of the moored ship (m)
- $B_m$  breadth of the moored ship (m)
- $L_p$  length of the passing ship (m)
- $B_p$  breadth of the passing ship (m)
- $S_{1(x_1)}$  parabolic sectional area distribution of moored ship
- $S_{2(x_2)}$  parabolic sectional area distribution of passing ship

The sectional area  $S_1(x_1)$  and its slope  $S'_1(x_1)$  are calculated using the following relationship for the moored ship

$$S_1(x_1) = S_1 \left( 1 - \left( \frac{-2x_1}{L_1} \right)^2 \right) \tag{15}$$

$$S'_1(x_1) = \frac{-8S_1x_1}{L_1^2} \tag{16}$$

where  $x_1$ ,  $L_1$  and  $S_1$  are the location of the section, length and the mid-ship area of moored ship, respectively.

The sectional area  $S_2(x_2)$  and its slope  $S'_2(x_2)$  are calculated using the following relationship for the moored ship.

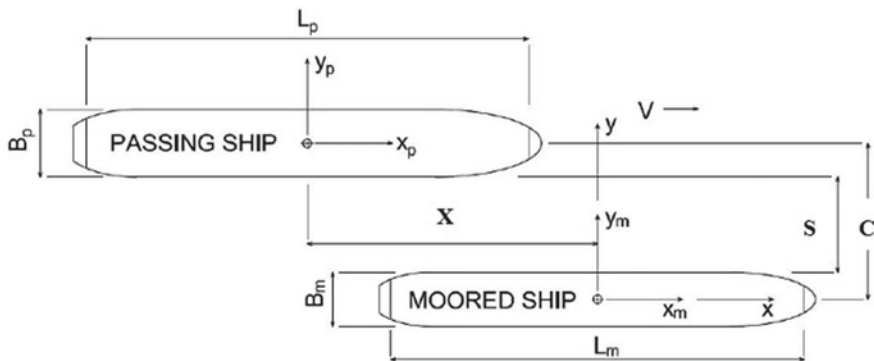


Fig. 9 Passing ship definitions of variables

$$S_2(x_2) = S_2 \left( 1 - \left( \frac{-2x_2}{L_2} \right)^2 \right) \tag{17}$$

$$S'_2(x_2) = \frac{-8S_2x_2}{L_2^2} \tag{18}$$

where  $x_2$ ,  $L_2$  and  $S_2$  are the location of the section, length and the mid-ship area of passing ship, respectively. The calculated normalized forces and moment for normalized distance with respect to the length of the ship are shown in Fig. 10. It can be observed that the forces, longitudinal and lateral do not occur at same time. But, longitudinal force and the moment occur at same time.

### 5.3 Estimation by Flory’s Method

Flory [3] developed empirical formulas based on various model test results and the theoretical results from Wang [1].

$$F_{X\_MAX\_FLORY} = 1.5 \times 10^{-5} L_m^2 e^{(0.0955 - \frac{0.6367d}{D})} V^2 [0.171 + 0.134 \ln(\Delta_D)] - \{0.71 + 0.28 \ln(\Delta_D)\} \ln(\Delta_S - 0.06) \tag{19}$$

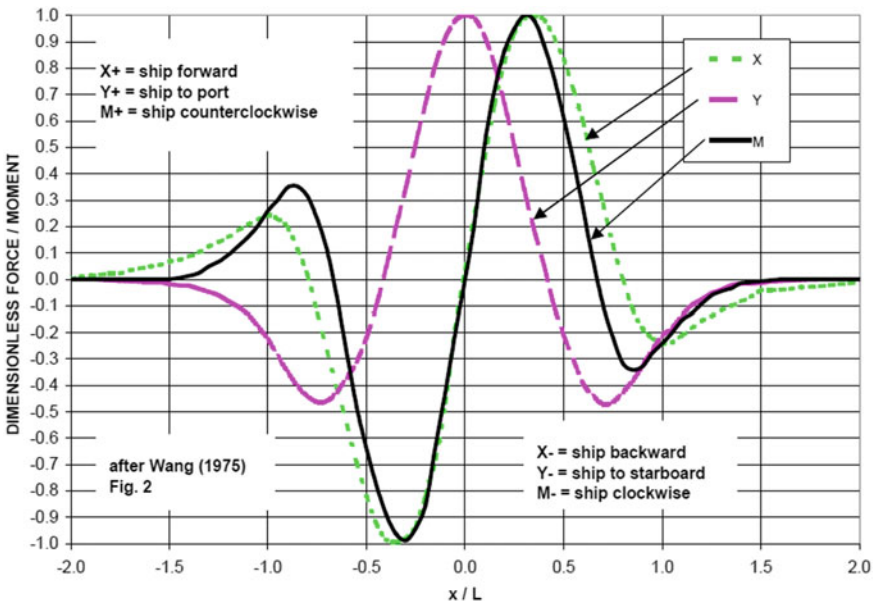


Fig. 10 Normalized forces and moment



$$F_{Y\_MAX\_FLORY} = 1.5 \times 10^{-5} L_m^2 e^{(0.5157 - \frac{3.348d}{D})} V^2 [e^{(1.168\Delta_R - 2.25)} - \{4.41 + 1.93 \ln(\Delta_R)\} \ln(\Delta_S)] \quad (20)$$

$$M_{z\_MAX\_FLORY} = 59 \times 10^{-9} L_m^3 e^{(0.343 - \frac{2.288d}{D})} V^2 [e^{(-0.47\Delta_D + 2.651)} - \{171.9 + 51.4 \ln(\Delta_D)\} \ln(\Delta_S - 0.06)] \quad (21)$$

Symbols used in Eqs. (19–21) are summarized below.

$F_{X\_MAX\_FLORY}$	surge force (N)
$F_{Y\_MAX\_FLORY}$	sway force (N)
$M_{Z\_MAX\_FLORY}$	yaw moment (Nm)
$D$	draft of the moored ship (m)
$V$	passing vessel speed (m/s)
$L_m$	length of the moored ship (m)
$d$	water depth (m)
$\Delta_D$	displacement ratio
$\Delta_S$	separation ratio

#### 5.4 Estimation by Seelig's Method

Seelig [2] based on existing experiments developed shallow-water correction factor for deep-water forces given by Wang [1]

$$CF_{X\_SEELIG} = 1 + 16 \left( \frac{D}{B_m} \right) e^{(-0.08 \left( \left( \frac{s}{B_m} \right) - 3.5 \right)^2)} \quad (22)$$

$$CF_{Y\_SEELIG} = CM_Z = 1 + 25 \left( \frac{D}{B_m} \right)^{-0.35} \left( \frac{D}{d} \right)^4 e^{(-0.08 \left( \left( \frac{s}{B_m} \right) - 3.3 \right)^2)} \quad (23)$$

Symbols used in Eqs. (22) and (23) are given below.

$CF_{X\_SEELIG}$	correction factor for surge force
$CF_{Y\_SEELIG}$	correction factor for Sway force
$CM_Z$	correction factor for yaw moment
$D$	draft of the moored ship (m)
$d$	water depth (m)
$B_m$	beam of the moored ship (m)
$S$	clear spacing between the moored and passing ship (m).

### 5.5 Estimation by David Kriebel's Method

Kriebel [4] developed empirical shallow-water correction factors to forces and moments calculated by deep-water theory by Wang [1] as an alternative to Seelig [3] correction factors.

$$CF_{X\_KRIEBEL} = 1 + 1.70e^{(2.94(\frac{D}{d}))} e^{\left(-0.08\left(\left(\frac{S}{B_m}\right)-3\right)^2\right)} \quad (24)$$

$$CF_{Y\_KRIEBEL} = 1 + 0.52e^{(4.33(\frac{D}{d}))} e^{\left(-0.08\left(\left(\frac{S}{B_m}\right)-2\right)^2\right)} \quad (25)$$

$$CM_{Z\_KRIEBEL} = 1 + 0.48e^{(3.87(\frac{D}{d}))} e^{\left(-0.08\left(\left(\frac{S}{B_m}\right)-2\right)^2\right)} \quad (26)$$

Symbols used in Eq.( 24–26) are given below.

$CF_{X\_KRIEBEL}$	correction factor for surge force
$CF_{Y\_KRIEBEL}$	correction factor for sway force
$CM_{Z\_KRIEBEL}$	correction factor for yaw moment
$D$	draft of the moored vessel (m)
$d$	water depth (m)
$B_m$	beam of the moored ship (m)
$S$	clear distance between the ships (m)

Kriebel [4] also developed empirical equations to calculate forces and moments on the moored ship due to passing ship using the latest experimental results

$$F_{X\_KRIEBEL} = \frac{1}{2}\rho DL_m V^2 \left\{ 0.0074\Delta_D e^{2.6(\frac{D}{d})} e^{-1.5(\Delta_s)} \right\} \quad (27)$$

$$F_{Y\_KRIEBEL} = \frac{1}{2}\rho DL_m V^2 \left\{ 0.0126\Delta_D e^{3.6(\frac{D}{d})} e^{-2.0(\Delta_s)} \right\} \quad (28)$$

$$M_{z\_KRIEBEL} = \frac{1}{2}\rho DL_m V^2 \left\{ 0.0044\Delta_D e^{3.2(\frac{D}{d})} e^{-3.4(\Delta_s)} \right\} \quad (29)$$

Symbols used in Eqs. (27–29) are given below.

$F_{X\_KRIEBEL}$	surge force (negative peak) (N)
$F_{Y\_KRIEBEL}$	sway force (maximum positive) (N)
$FM_{Z\_KRIEBEL}$	yaw force (maximum negative) (Nm)
$D$	draft of moored ship (m)
$d$	water depth (m)
$L_m$	length of the moored ship (m)
$V$	speed of passing ship
$\Delta_D$	displacement ratio
$\Delta_S$	separation ratio.

## 5.6 Parametric Evaluation

The effect of vessels passing through the neighbouring approach channel to JNPT has been assessed based on 200,000 tonnes displacement container vessels with 366 m LOA.

Longitudinal and transverse forces applied to the moored vessels due to passing vessel have been obtained using the **Flory method** for different passing speeds and spacing. The notation for the variables is shown in Fig. 11.

The maximum transverse force occurs when the passing vessel is crossing the centre of the moored vessel, while the longitudinal force occurs before and after crossing, and they are opposite in magnitude. This means that the longitudinal and transverse forces do not occur at the same time and require combining the forces in time domain. This can only be done in dynamic analysis unless if we decide to take the maximum longitudinal and transverse forces and combine them in a single static analysis conservatively. The calculation of forces and moment was done for different passing vessels, separation distances and vessel speed. The results are tabulated. Tables 5 and 6 give the forces longitudinal ( $F_x$ ) and transverse ( $F_y$ ) on 250,000 DWT vessels due to the passing vessel. The effect due to the separation distance and passing vessel speed is studied as illustrated here.

Figures 12, 13, 14, and 15 shows the variation of the longitudinal and transverse forces for four different passing vessel spacing of 75, 100, 125 and 150 m for different passing vessel speeds from 5 knots to 12 knots. Same data is represented in a different manner to show the effect of vessel speed and spacing in Figs. 16 and 17. It can be observed that the longitudinal and transverse forces reduce by 50% when the spacing is increased to 150 m. And the higher the passing vessel speed, higher would be the forces, and hence, the speed of the passing vessel should be restricted by some criteria. Figures 18 and 19 show the variation of the longitudinal and transverse forces for different passing vessel spacing and displacements of the moored vessel. From the figures, it can be noted that the main influencing factors are passing vessel's displacement, speed and the separation distance between the two vessels.

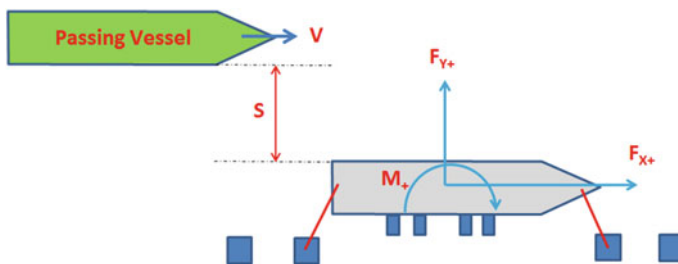


**Fig. 11** Notations used in the simulation (OPTIMOOR)

**Table 5** Calculated longitudinal and transverse force in tonnes (250,000 DWT)

Vessel speed (knots)	Passing vessel spacing (m)							
	75 m		100 m		125 m		150 m	
	$F_y$	$F_x$	$F_y$	$F_x$	$F_y$	$F_x$	$F_y$	$F_x$
5	98	39	81	32	68	27	57	23
6	142	56	117	46	97	39	81	33
7	193	77	159	63	132	53	111	45
8	252	100	208	82	173	69	145	58
9	319	126	263	103	219	87	183	74
10	394	156	324	128	270	107	226	91
11	477	189	392	155	327	130	274	110
12	567	225	467	184	389	154	326	131

**Table 6** Variation with spacing for different passing speeds

Spacing (S) (m)	Vessel speed (V) (knots)							
	5	6	7	8	9	10	11	12
<i>Transverse force <math>F_y</math> (tonnes)</i>								
75	98	142	193	252	319	394	477	567
100	81	117	159	208	263	324	392	467
125	68	97	132	173	219	270	327	389
150	57	81	111	145	183	226	274	326
<i>Longitudinal force <math>F_x</math> (tonnes)</i>								
75	39	56	77	100	126	156	189	225
100	32	46	63	82	103	128	155	184
125	27	39	53	69	87	107	130	154
150	23	33	45	58	74	91	110	131

## 6 Static Mooring Analysis

### 6.1 Mooring Wires

The characteristics of mooring wires used in the analysis are given in Table 7.

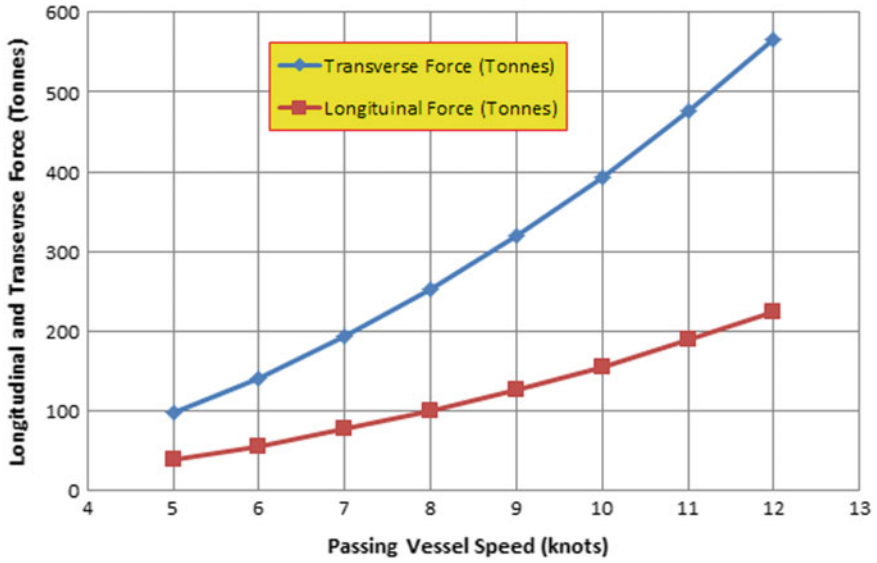


Fig. 12 Longitudinal and transverse force with speed of passing vessel (spacing = 75 m)

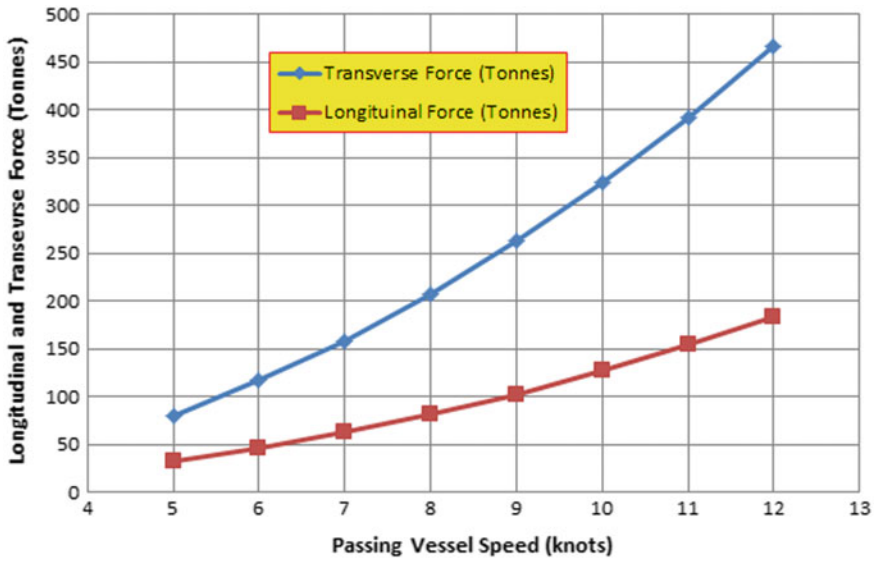


Fig. 13 Longitudinal and transverse force with speed of passing vessel (spacing = 100 m)

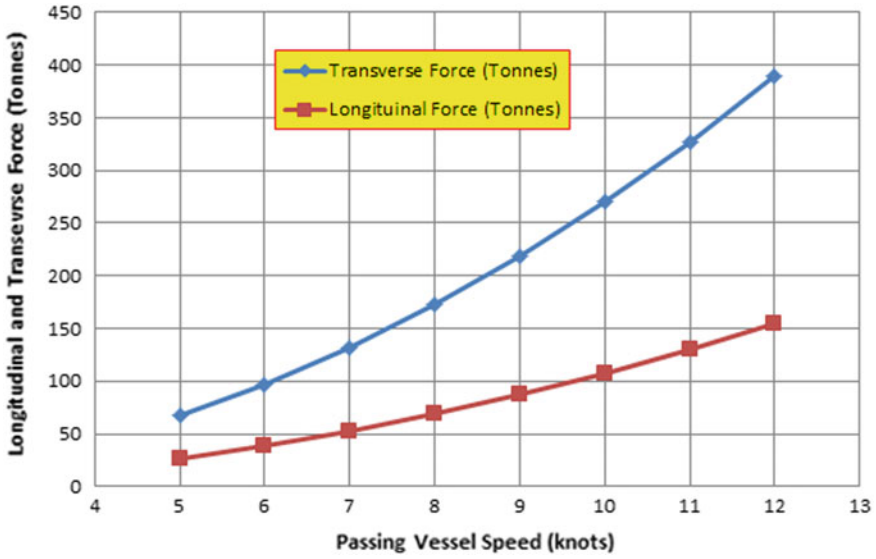


Fig. 14 Longitudinal and transverse force with speed of passing vessel (spacing = 125 m)

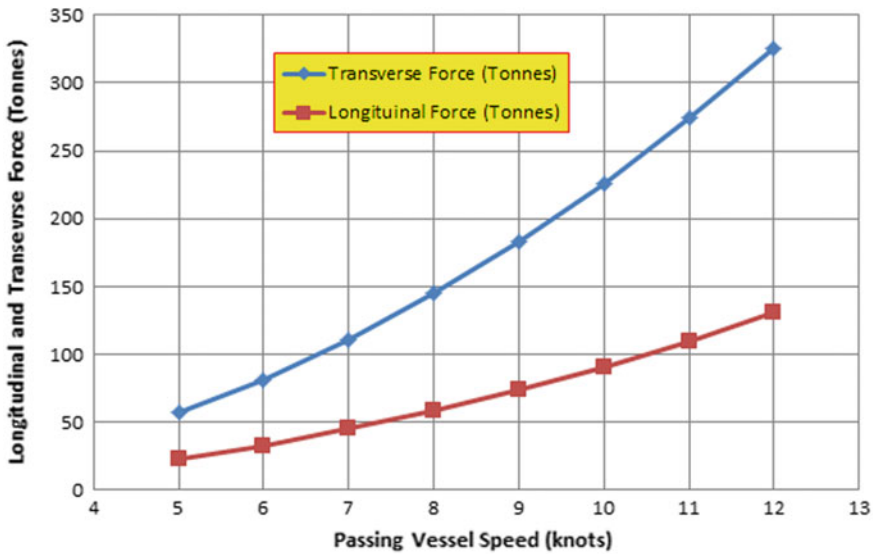


Fig. 15 Longitudinal and transverse force with speed of passing vessel (spacing = 150 m)

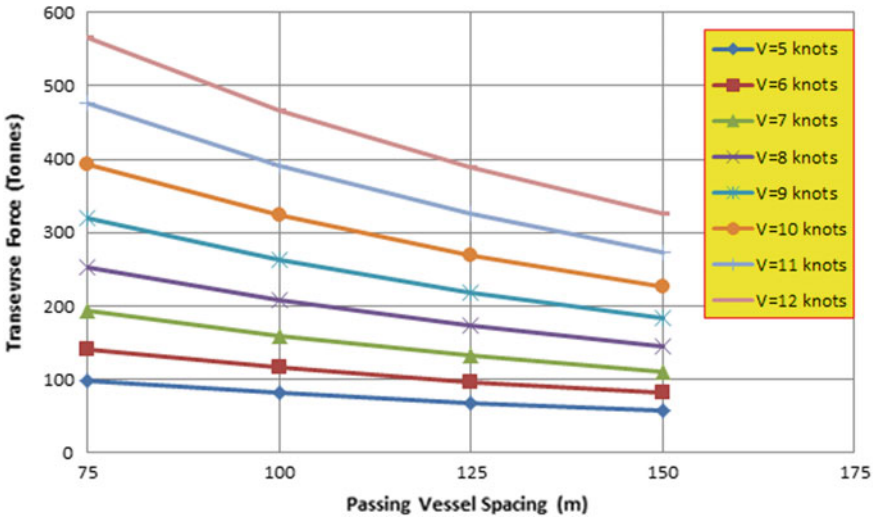


Fig. 16 Variation of transverse force with spacing of vessels

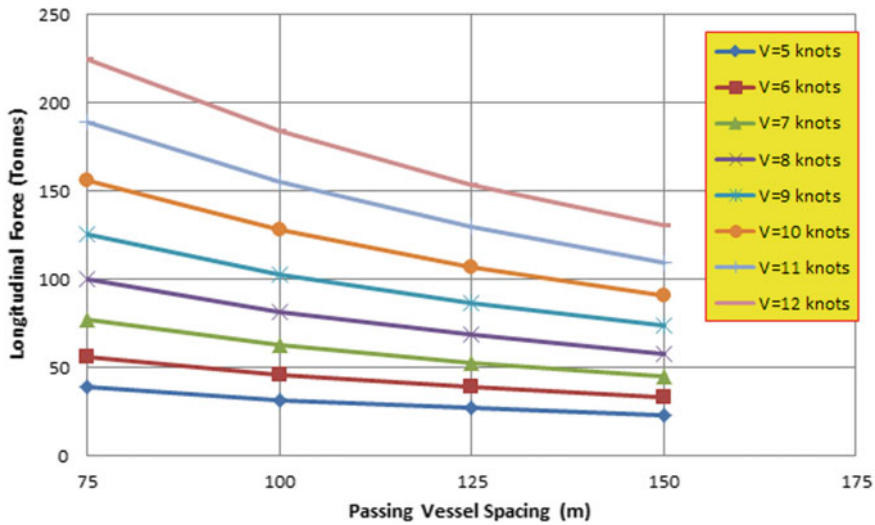


Fig. 17 Variation of longitudinal force with spacing of vessels

### 6.2 Mooring Design Criteria

The criteria given in Table 8 are meant for mooring lines that are properly maintained and inspected. Also, the mooring lines should have proper breaking hardware that has equivalent breaking strengths to that of mooring lines.

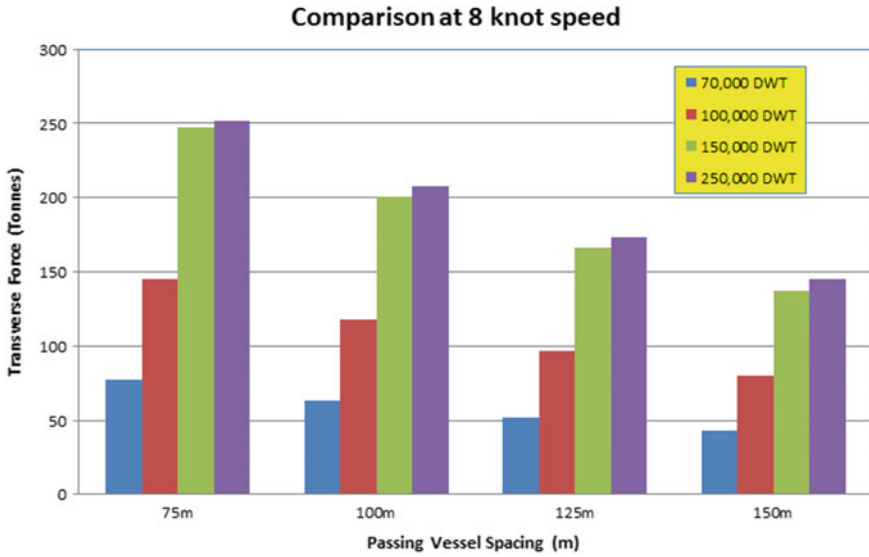


Fig. 18 Variation of transverse force with spacing of vessels

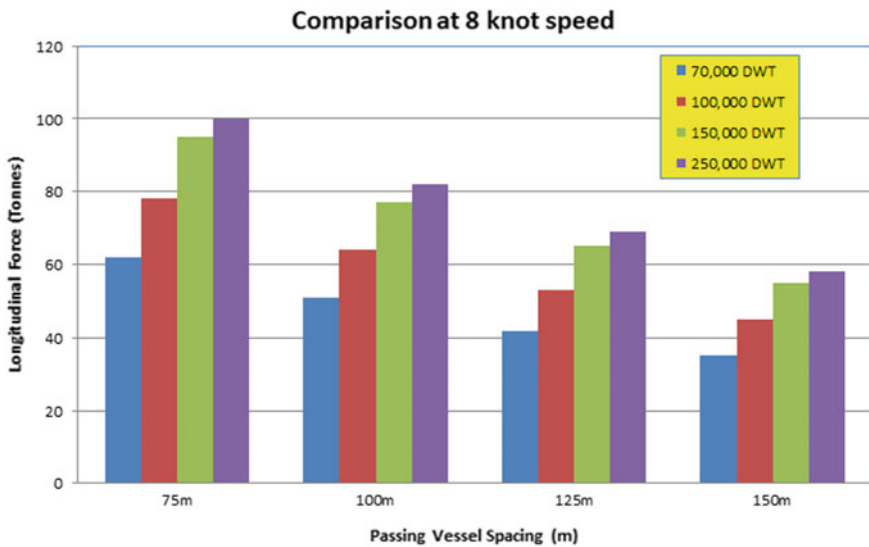


Fig. 19 Variation of longitudinal force with spacing of vessels

### 6.3 Modelling Fenders

The fenders are provided at breasting dolphins between the structure and the vessel. Hence, when the environmental loads are applied to the vessel, the fenders will



**Table 7** Tanker mooring equipment characteristics (typical)

	PANAMAX (70,000 DWT)	AFRAMAX (100,000 DWT)	SUEZMAX (150,000 DWT)	VLCC ( $\geq 250,000$ DWT)
Number of mooring wires	16 nos	16 nos	20 nos	20 nos
Type of mooring wire	6 × 36 IWRC Steel wire	6 × 36 IWRC Steel wire	6 × 36 IWRC Steel wire	6 × 36 IWRC Steel wire
Diameter of mooring wire (mm)	40	50	60	80
Wire minimum breaking load (MBL)	110 MT	168 MT	236 MT	410 MT
Safe working load (SWL)	60.5 MT	92.4 MT	129.8 MT	225.5 MT
Tail diameter (mm)	40	50	60	80
Minimum breaking load (MBL)	42T	64T	91MT	158MT

**Table 8** Mooring line tension criteria

	Analysis method	Tension Limit % MBL
Intact	Quasi-static	55
Intact	Dynamic	55

be compressed. The fenders are nonlinear compression elements and hence shall be modelled accordingly. Based on the design done by the detailed engineering consultant, the fender selected was SCN 2000 E3.0 with a rated maximum reaction of 4660 kN at 72% axial compression. Typical load–deflection relationship for a fender is shown in Fig. 20.

The load-axial deformation characteristics used in the simulation are shown Fig. 21.

## 6.4 Modelling Mooring Lines

The mooring lines are modelled as linear elastic tension cable element in OPTI-MOOR. The stiffness of the cable is calculated using its axial properties and its length provided as input. The length of mooring line is calculated by the program based on the geometry of the line from its fairlead point to the mooring hook.

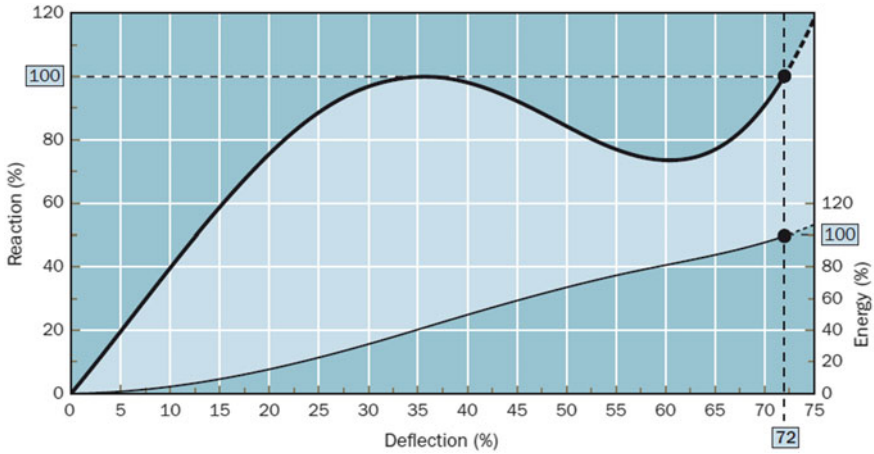


Fig. 20 Typical load–deflection relationship of rubber fender

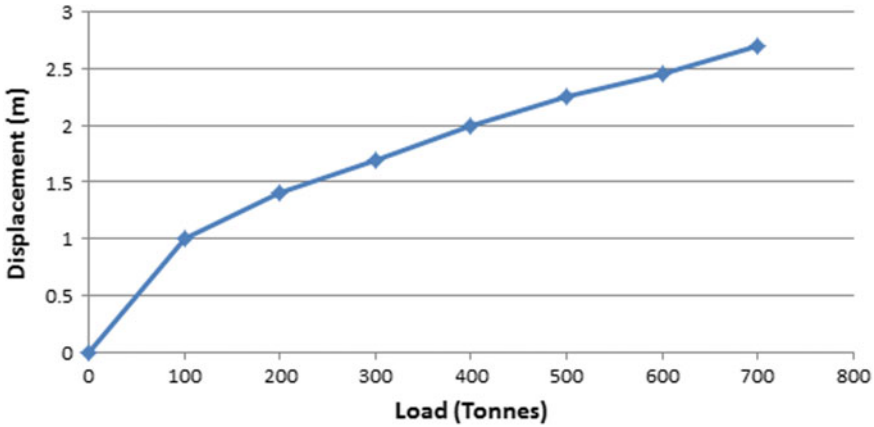


Fig. 21 Load–deflection relationship of rubber fender SCN2000 E3.0

The breasting and mooring dolphin structures are considered to be rigid and not moving when the mooring loads are applied.

### 6.5 Mooring Analysis Simulation

Environmental loads on the moored vessel are calculated using OCIMF [10] guidelines as discussed in Sect. 4. The static analysis is carried out to determine the mooring line tension using equilibrium of the vessel considering the mooring line elasticity and geometric restraint. Each time data is entered or altered on the mooring screen (or

arrangement screen), the OPTIMOOR computer program carries out a series of calculations to seek the vessel position which satisfies the force and moment equations for the system. This series of equations can be represented by the following:

$$\begin{aligned}\sum F_x + \sum P_x &= 0 && \text{Surge} \\ \sum F_y + \sum P_y &= 0 && \text{Sway} \\ \sum M_{xy} + \sum N_{xy} &= 0 && \text{Yaw}\end{aligned}\tag{30}$$

where

$F_x$  is the  $x$  vector component of an externally applied force, e.g. wind, current, or wave or effects from passing vessel.

$P_x$  is the  $x$  vector component of mooring line force (fenders exert no force in the  $x$  direction).

$F_y$  is the  $y$  vector component of an externally applied force, eg. wind, current, or wave or effects from passing vessel.

$P_x$  is the  $y$  vector component of mooring line force or fender force.

$M_{xy}$  is the moment in the  $x$ - $y$  plane produced by an externally applied force, e.g. wind current, or wave or effect from passing vessel.

$N_{xy}$  is the moment in the  $x$ - $y$  plane produced by an mooring line force or fender force.

The program seeks an equilibrium position which satisfies these equations by applying small iterations to the position of the moored vessel, first in the  $x$  (longitudinal) direction, then in the  $y$  (transverse) direction and then in the  $x$ - $y$  (rotation) direction. After each iteration in a particular direction, the program checks to see if the applicable equilibrium equation is satisfied. If the equation is under satisfied, the program then applies an iteration of the same magnitude in the same direction. If it is over satisfied, the program then applies a smaller iteration in the opposite direction. During each iteration step, the program recalculates the force in each mooring line and each fender for the iterated vessel position. The various mooring line force vectors are determined by the relative positions of the respective fairlead and bollard points. The fender vectors are applied perpendicular to the side of the vessel at the respective fender positions.

## 6.6 Environmental Loads

The mooring loads for the various approach of environmental loads are summarized in Table 9 for 70,000, 100,000, 150,000 and 250,000 DWT vessels. The variation of longitudinal and transverse forces for all tankers simulated is shown in Fig. 22. It can be observed that the largest forces occur for the 250,000 DWT tankers. The variation of the environmental loads in various directions is shown in Fig. 23.

**Table 9** Environmental loads on vessels for loaded draft (metric tonnes)

Direction	70000 DWT		100,000 DWT		150,000 DWT		250,000 DWT	
	$F_x$	$F_y$	$F_x$	$F_y$	$F_x$	$F_y$	$F_x$	$F_y$
North (0°)	15.2	-90.6	18.0	-111.4	21.6	-150.2	25.4	-265.2
North-east (55°)	46.3	0.2	54.7	0.1	67.1	0.5	91.8	0.3
East (90°)	26.7	60.9	31.7	74.7	38.2	101.5	48.2	182.1
South-east (135°)	3.0	107.1	3.5	131.7	4.3	177.5	5.7	311.5
South (180°)	-15.4	91.2	-18.2	112.5	-22.3	150.6	-31.1	252.6
South-west (225°)	-41.0	62.2	-48.9	81.1	-58.9	105	-80.3	118.5
West (270°)	-25.5	-70.1	-30.1	-86.8	-37.0	115.3	-50.9	-185.3
North-west (315°)	-5.3	-107.1	-6.3	-131.8	-7.6	-177.3	-9.3	-308.9

Note Negative  $F_y$  values moves the vessel towards the jetty inducing compression on the fenders

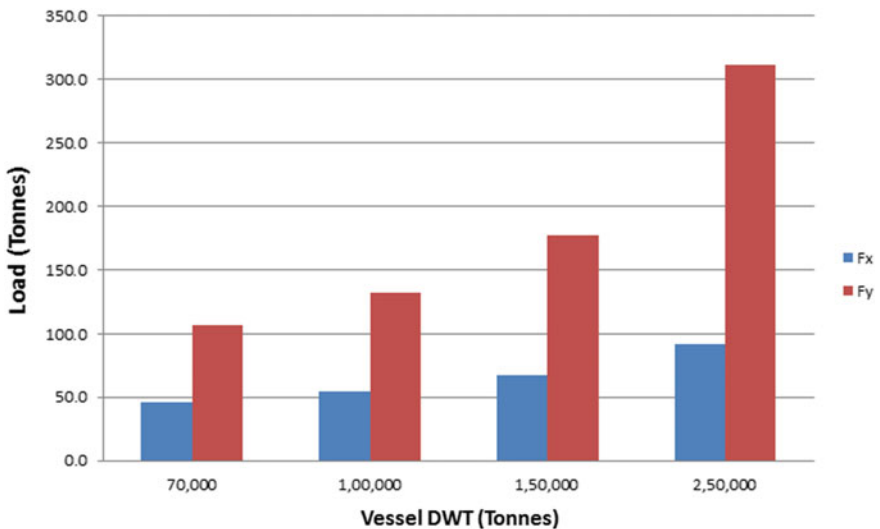


**Fig. 22** Variation of environmental loads on vessels (loaded draft)

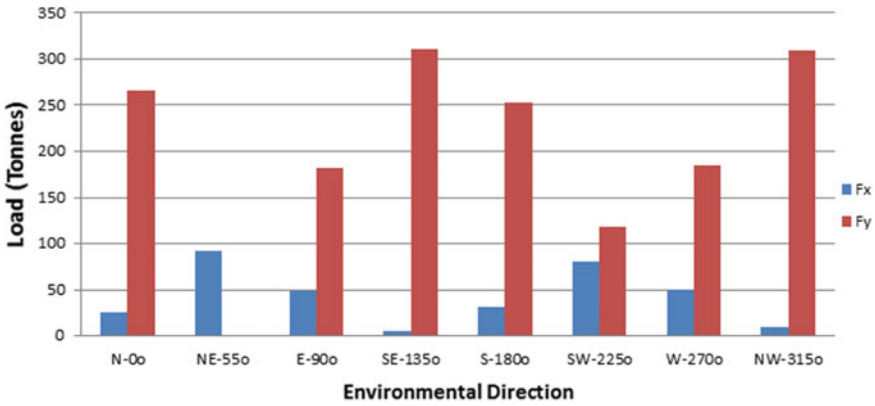


Fig. 23 Variation of environmental loads for 250,000 DWT tankers (loaded draft)

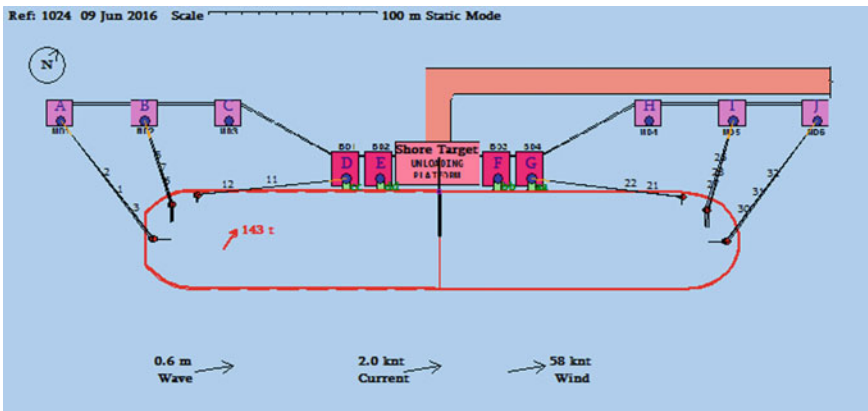


Fig. 24 Mooring loads for 250,000 DWT (loaded draft) (head = 3 lines, stern = 3 lines, breast = 3 + 3 lines, spring = 2 + 2 lines, total = 16 lines)

The mooring pattern and simulated environmental loads for 250,000 DWT tankers with loaded draft are shown in Fig. 24 as a typical example of simulation in OPTIMOOR.

A total of 16 lines are used for 70,000 DWT, 100,000 DWT, 150,000 DWT and 250,000 DWT tankers. The figure also represents the direction of loading of waves, wind and current.

**Table 10** Mooring line tensions for 250,000 DWT vessels (loaded draft)

Line no.	Mooring line tension (metric tonnes)							
	N-0°	NE-55°	E-90°	SE-135°	S-180°	SW-225°	W-270°	NW-315°
A-1	19.7	0.0	0.0	0.0	0.0	0.0	25.6	29.7
A-2	19.4	0.0	0.0	0.0	0.0	0.0	25.2	29.3
A-3	19.1	0.0	0.0	0.0	0.0	0.0	24.9	28.9
B-5	30.4	0.8	0.0	0.0	0.0	0.0	33.7	44.4
B-6	30.1	0.3	0.0	0.0	0.0	0.0	33.4	43.8
B-7	29.7	0.0	0.0	0.0	0.0	0.0	33.1	43.4
D-11	10.1	37.4	24.1	0.0	0.0	0.0	6.0	12.5
D-12	10.1	37.5	24.1	0.0	0.0	0.0	6.0	12.6
G-21	0.0	0.0	0.0	1.6	32.1	55.4	1.1	0.0
G-22	0.0	0.0	0.0	1.6	32.5	56.2	1.1	0.0
I-26	28.1	1.2	0.0	0.0	13.4	19.8	6.8	24.2
I-27	28.1	0.7	0.0	0.0	14.4	21.0	6.7	24.2
I-28	28.1	0.2	0.0	0.0	15.3	22.2	6.7	24.1
J-30	22.8	9.7	0.5	4.6	10.6	8.1	5.0	19.5
J-31	22.9	9.4	0.3	4.7	11.2	8.8	4.9	19.6
J-32	23.0	9.0	0.1	4.9	11.9	9.5	4.9	19.6

## 6.7 Results from Static Analysis

**Mooring line tension.** The mooring line tension for each type of moored vessel is presented here. Table 10 gives the line tension for each mooring line of 250,000 DWT vessels when subjected to loads from different directions. Figure 25 of the 250,000 DWT vessels in loaded and laden conditions. It can be seen that the line tensions are more for loading at south-west 225°. The mooring line tension for the other mooring vessels is compared and presented in Figs. 26 and 27 for loaded and laden draft.

**Mooring hook capacity.** The mooring hook capacity for different vessel lines was analysed, and the arrived mooring hook capacity is shown in Table 11.

## 7 Dynamic Mooring Analysis

### 7.1 Time-Domain Dynamic Analysis

The analysis must be carried out in the time domain to combine these forces with wind, wave and current. The result from the passing vessel is superimposed on the mooring loads due to wind, wave and current.

**Table 11** Mooring hook capacity

Mooring point	Mooring lines	Maximum mooring line tension (tonnes)		Utilization ratio		Mooring hook capacity provided (tonnes)
		Loaded draft	Laden draft	Loaded draft (%)	Laden draft (%)	
MD1	A-1, A-2, A-3, A-4	29.7	48.8	29.7	48.8	3 × 100
MD2	B-5, B-6, B-7	44.4	71.3	44.4	71.3	3 × 100
MD3	C-8, C-9, C-10	17.6	17.6	17.6	17.6	3 × 100
BD1	D-11, D-12, D-13	37.5	45.8	50.0	61.1	3 × 75
BD2	E-14, E-15, E-16	–	–	–	–	3 × 75
BD3	F-17, F-18, F-19	–	–	–	–	3 × 75
BD4	G-20, G-21, G-22	56.2	56.9	74.9	75.9	3 × 75
MD4	H-23, H-24, H-25	11.9	11.9	11.9	11.9	3 × 100
MD5	I-26, I-27, I-28	28.1	55.9	28.1	55.9	3 × 100
MD6	J-29, J-30, J-31, J-32	23.0	41.4	23.0	41.4	3 × 100

Note A-4, D-13, E-14, E-15, E-16, F-17, F-18, F-19, G-20 and J-29 are not used in the simulation

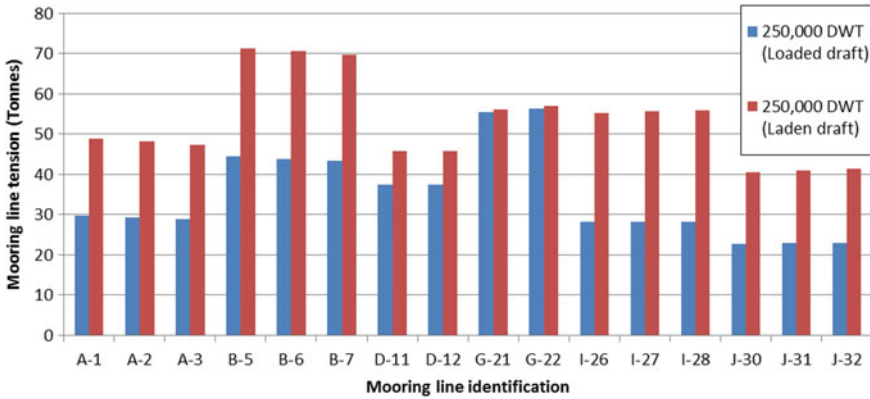


Fig. 25 Mooring line tension for 250,000 DWT

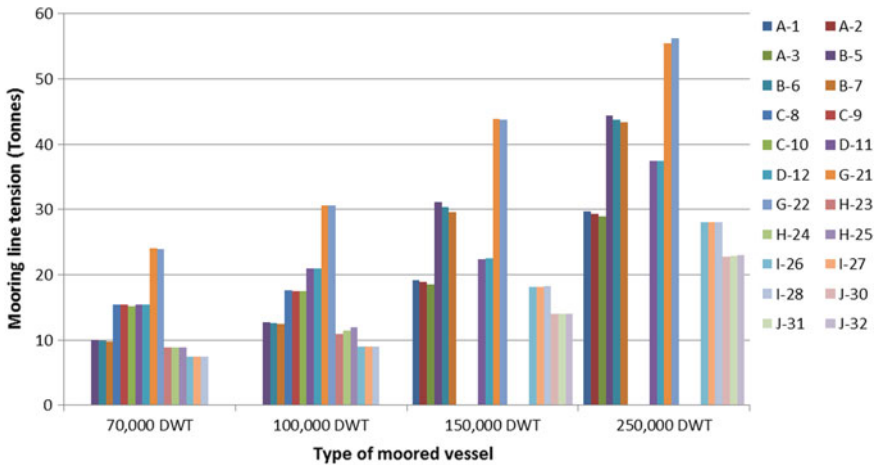


Fig. 26 Mooring line tension comparison (loaded draft)

### 7.2 Mooring Analysis Cases

Dynamic mooring analysis has been carried out for tankers with prevailing environmental conditions and passing vessel effects as summarized in Tables 12, 13, 14 and 15. The governing case results are presented for moored vessels 70,000 DWT and 100,000 DWT, and 150,000 DWT and 250,000 DWT tankers with passing vessel (200,000 DWT) for 75 m spacing and 300 m spacing with eight-knot speed, respectively. The load combinations are tabulated in Tables 12, 13, 14 and 15.



**Table 12** Dynamic mooring analysis for 70,000 DWT vessels

Environment	Wind + current + monsoon wave			
Spacing/speed (m)	Five knots	Six knots	Seven knots	Eight knots
75	✓	✓	✓	✓
100	✓	✓	✓	✓
150	✓	✓	✓	✓

**Table 13** Mooring failure 100,000 DWT vessels

Environment	Wind + current + monsoon wave			
Spacing/speed (m)	Five knots	Six knots	Seven knots	Eight knots
75	✓	✓	✓	✓
100	✓	✓	✓	✓
150	✓	✓	✓	✓

**Table 14** Mooring failure 150,000 DWT vessels

Environment	Wind + current + monsoon wave			
Spacing/speed (m)	Five knots	Six knots	Seven knots	Eight knots
150	✓	✓	X	X
200	✓	✓	✓	✓
300	✓	✓	✓	✓

X—Mooring line failure and hence mooring analysis discontinued

**Table 15** Mooring failure 250,000 DWT vessels

Environment	Wind + current (no monsoon wave)			
Spacing/speed (m)	Five knots	Six knots	Seven knots	Eight knots
150	✓	X	X	X
200	✓	✓	X	X
300	✓	✓	✓	✓

X—Mooring line failure and hence mooring analysis discontinued

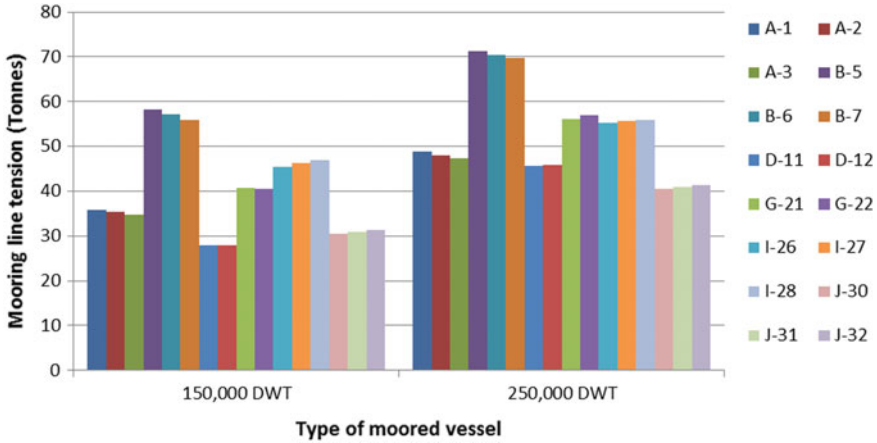


Fig. 27 Mooring line tension comparison (laden draft)

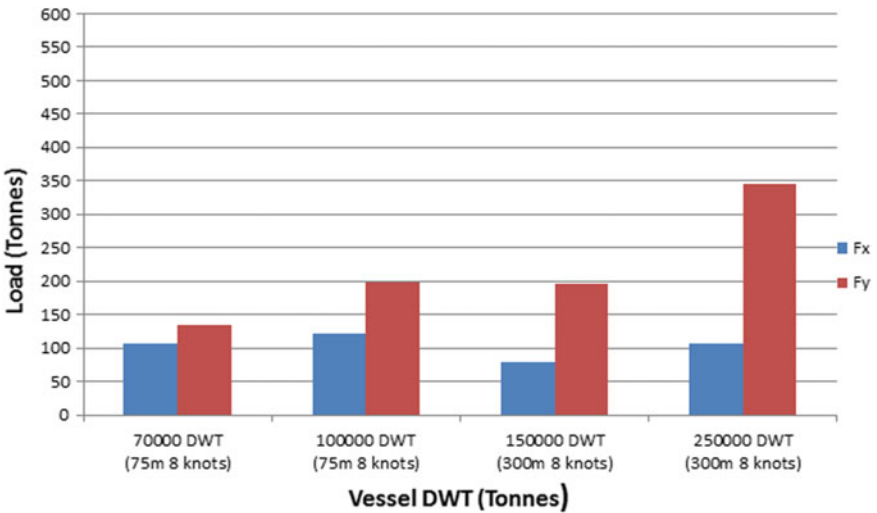


Fig. 28 Variation of passing vessel loads and environmental loads on moored vessels

### 7.3 Combined Passing Vessel Forces and Environmental Loads Acting Moored Vessel

The passing vessel loads with environmental loads are simulated in OPTIMOOR as shown in Fig. 30. The mooring loads for various environmental loading directions and passing vessel effects are summarized in Table 16 for 70,000, 100,000, 150,000 and 250,000 DWT vessels. Figure 28 shows a variation of loading for different passing vessel speeds, and Fig. 29 gives the variation with environmental load directions.

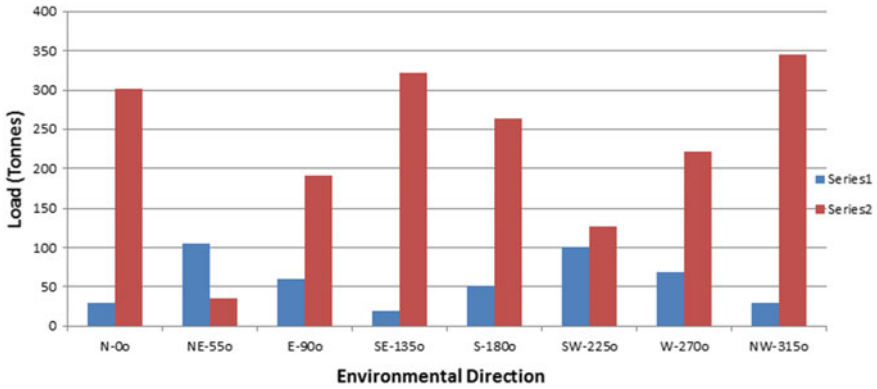


Fig. 29 Variation of passing vessel loads with environmental loads for 250,000 DWT tankers (300 m—eight knots)

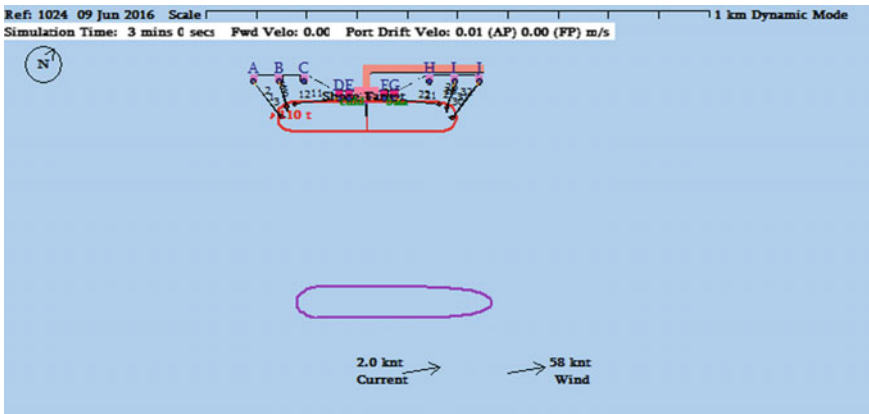


Fig. 30 Mooring loads for 250,000 DWT (300 m—eight knots)

A typical layout of OPTIMOOR simulation of passing vessel effects is shown in Fig. 34.

### 7.4 Spring Lines Configuration

Mooring analysis with 2 or 3 spring lines has been carried out, and the results indicate that the vessel gets detached due to large passing vessel loads combined with wave from south-west direction. The simulation with 2 and 3 spring lines is shown in Figs. 31 and 32.

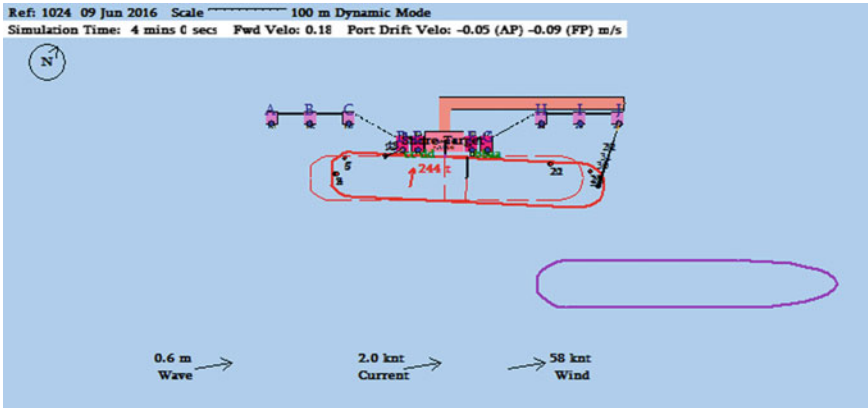


Fig. 31 Mooring arrangement with two spring lines

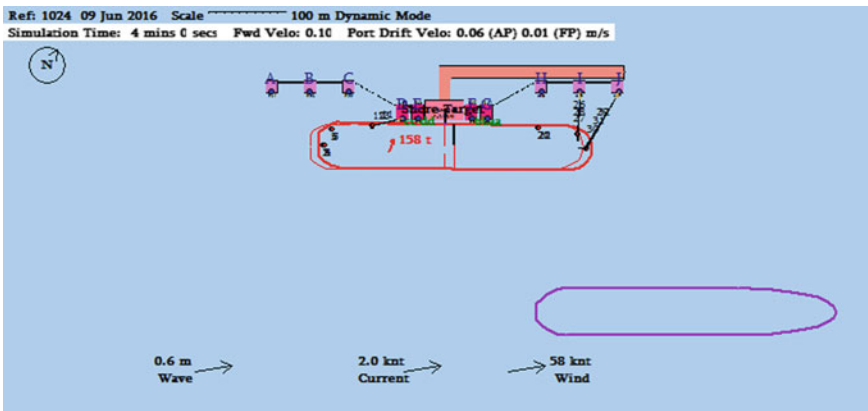


Fig. 32 Mooring arrangement with three spring lines

### 7.5 Results from Dynamic Mooring Analysis

**Mooring line tensions.** The line tension of mooring lines for the 250,000 DWT moored vessel is tabulated in Table 17, and the maximum tension in each mooring line is represented in Fig. 33. The increase in line load due to direction specific loads is mentioned in the table, and the same has been compared between different vessels in Fig. 34. The mooring line tension was compared for different moored vessels, and it has been found to be high for the 150,000 DWT vessels. Since, the wave loading was excluded for the 250,000 DWT vessels, the forces were found to be lesser.

**Mooring hook capacity.** The mooring line tension due to the effect of both the environmental loads with passing vessel effect is summarized in Table 18. It can be

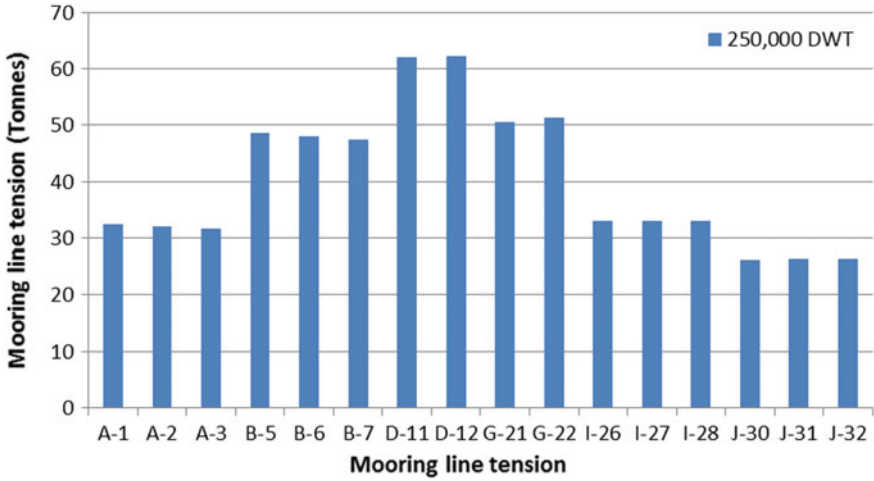


Fig. 33 Mooring line tension for 250,000 DWT

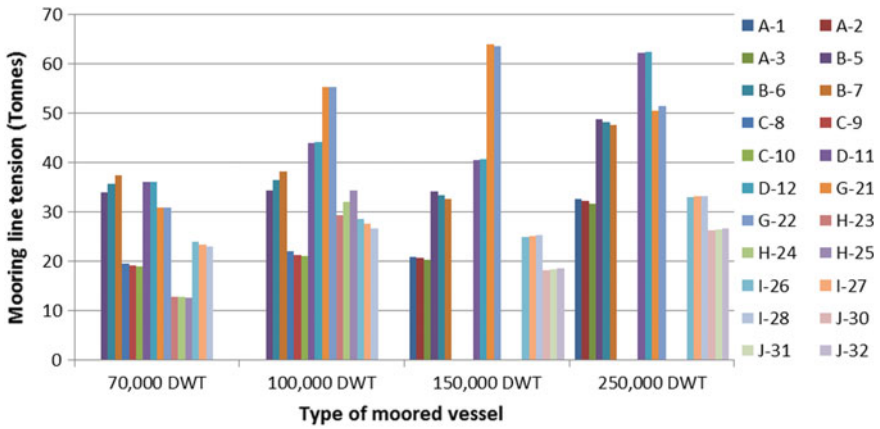


Fig. 34 Mooring line tension comparison between different moored vessels

observed that the maximum line tension exceeds 55% of MBL of mooring lines and the utilization ratio for mooring hooks is more than 0.8 for spring lines.

### 8 Comparison of Mooring Hook Capacity

A comparison of mooring hook capacities between the simulations with and without passing vessel forces is presented in Table 19. The comparison indicates that there is a considerable increase in line tension with the inclusion of passing vessel effects

**Table 16** Mooring loads on vessels due to passing vessel effect with environmental loads (metric tonnes)

Direction	70000 DWT (75 m—eight knots)		100,000 DWT (75 m—eight knots)		150,000 DWT (300 m—eight knots)		250,000 DWT (300 m—eight knots)	
	$F_x$	$F_y$	$F_x$	$F_y$	$F_y$	$F_y$	$F_x$	$F_y$
North (0°)	-38.7	-117.6	84.4	-177.3	32.8	-169.0	28.9	-300.9
North-east (55°)	107.0	24.9	120.9	-71.3	78.1	-19.6	105.6	-35.1
East (90°)	88.8	84.1	103.7	116.5	50.6	109.8	59.8	191.6
South-east (135°)	63.9	130.4	-71.8	172.3	15.5	185.9	19.5	322.5
South (180°)	-69.4	114.5	-93.5	153.3	-41.2	158.9	-51.0	263.5
South-west (225°)	-85.2	86.8	-116.7	124.7	-77.4	113.8	-100.4	127.4
West (270°)	-83.0	-96.6	-106.5	-165.7	-55.5	-137.6	-69.1	-221.8
North-west (315°)	-59.2	-134.2	-81.4	-197.7	-26.5	-196.1	-29.2	-344.6

and hence the utilization ratio. This indicated the need to increase the mooring hook capacity, and it has been revised as mentioned in the recommendations.

## 9 Summary and Recommendations

### 9.1 Summary

The following points summarize the salient details of the detailed mooring analysis carried out for the vessels moored at the J5 berth.

- Static mooring analysis has been carried out for 58-knot wind speed, 2-knot current and 0.6 m wave height as recommended in CWPRS report. The results indicate that the proposed mooring hooks have adequate capacity.
- An assessment of effect of vessels passing through the neighbouring approach channel to JNPT has been done based on 200,000 tonnes displacement container vessels with 366 m LOA.

**Table 17** Mooring line tensions for 250,000 DWT vessels (300 m—eight knots)

Line No.	Mooring line tension (metric tonnes)							
	N-0°	NE-55°	E-90°	SE-135°	S-180°	SW-225°	W-270°	NW-315°
A-1	32.5	22.5	0	0	0	0	0	29.5
A-2	32.1	22.2	0	0	0	0	0	29.2
A-3	31.6	21.9	0	0	0	0	0	28.8
B-5	48.6	34.5	2.8	0	0	0	0	38.9
B-6	48.1	34.1	2.2	0	0	0	0	38.6
B-7	47.5	33.8	1.7	0	0	0	0	38.3
D-11	62.1	18	62.1	27.5	0	0	0	10
D-12	62.3	18.1	62.3	27.6	0	0	0	10
G-21	50.5	2.5	0	0	1.8	32.3	50.5	5.2
G-22	51.3	2.5	0	0	1.8	32.8	51.3	5.2
I-26	33	33	3.5	0	2.3	15.2	12.8	12.4
I-27	33.1	33.1	3	0	2.4	16.2	13.8	12.4
I-28	33.1	33.1	2.3	0	2.6	17.2	14.9	12.3
J-30	26.2	26.2	15.6	3.9	7.1	11.7	3.6	8.1
J-31	26.4	26.4	15.1	3.7	7.2	12.4	4.1	8.2
J-32	26.5	26.5	14.6	3.5	7.3	13	4.5	8.2

**Table 18** Mooring hook capacity

Mooring point	Mooring lines	Maximum mooring line tension (tonnes)	Utilization ratio (%)	Mooring hook capacity provided (tonnes)
MD1	A-1, A-2, A-3,A-4	32.5	32.5	3 × 100
MD2	B-5, B-6, B-7	48.6	48.6	3 × 100
MD3	C-8, C-9, C-10	21.9	21.9	3 × 100
BD1	D-11, D-12,D-13	62.3	83.1	3 × 75
BD2	E-14,E-15,E-16	–	–	3 × 75
BD3	F-17,F-18,F-19	–	–	3 × 75
BD4	G-20, G-21, G-22	63.8	85.1	3 × 75
MD4	H-23, H-24, H-25	34.2	34.2	3 × 100
MD5	I-26, I-27, I-28	33.1	33.1	3 × 100
MD6	J-29, J-30, J-31, J-32	26.5	26.5	3 × 100

Note A-4, D-13, E-14, E-15, E-16, F-17, F-18, F-19, G-20 and J-29 are not used in the simulation

**Table 19** Comparison of mooring hook capacity with and without passing vessel forces

Mooring point	Mooring lines	Passing vessel loads + environmental loads		Environmental loads (loaded draft)		Environmental loads (laden draft)	
		Maximum mooring line tension (tonnes)	Utilization ratio (%)	Maximum mooring line tension (tonnes)	Utilization ratio (%)	Maximum mooring line tension (tonnes)	Utilization ratio (%)
MD1	A-1, A-2, A-3, A-4	32.5	32.5	29.7	29.7	48.8	48.8
MD2	B-5, B-6, B-7	48.6	48.6	44.4	44.4	71.3	71.3
MD3	C-8, C-9, C-10	21.9	21.9	17.6	17.6	17.6	17.6
BD1	D-11, D-12, D-13	62.3	83.1	37.5	50.0	45.8	61.1
BD2	E-14, E-15, E-16	–	–	–	–	–	–
BD3	F-17, F-18, F-19	–	–	–	–	–	–
BD4	G-20, G-21, G-22	63.8	85.1	56.2	74.9	56.9	75.9
MD4	H-23, H-24, H-25	34.2	34.2	11.9	11.9	11.9	11.9
MD5	I-26, I-27, I-28	33.1	33.1	28.1	28.1	55.9	55.9
MD6	J-29, J-30, J-31, J-32	26.5	26.5s	23.0	23.0	41.4	41.4

- Mooring pattern for the VLCC oil tankers (150,000 and 250,000 DWT) has been provided with 2 + 2 spring lines and 3 + 3 breast lines and 3 + 3 head and stern lines to limit the mooring line tension as discussed with the harbour master.
- The combined effect of passing vessel and the environmental loads has been investigated. The mooring load case with wave approaching from south-west direction is the most critical, and the vessel mooring lines break, and the vessel starts to drift. Hence during monsoon, the passing vessels shall be allowed in only one direction and away from the J5 berth by at least 300 m at a reduced speed of five knots. Considering the requirement of additional mooring lines, it is suggested to increase the longitudinal restraint capacity by increasing the mooring hook at breasting dolphins from  $3 \times 75$  to  $3 \times 100$  tonnes.



**Table 20** Recommended mooring hook capacity

Mooring point	Mooring hook capacity proposed (tonnes)	Remarks (tonnes)
MD1	3 × 125	Revised from 3 × 100
MD2	3 × 125	Revised from 3 × 100
MD3	3 × 125	Revised from 3 × 100
BD1	3 × 100	Revised from 3 × 75
BD2	3 × 100	Revised from 3 × 75
BD3	3 × 100	Revised from 3 × 75
BD4	3 × 100	Revised from 3 × 75
MD4	3 × 125	Revised from 3 × 100
MD5	3 × 125	Revised from 3 × 100
MD6	3 × 125	Revised from 3 × 100

- Similarly, the mooring line tension for the head and stern increases with combined effect, and hence, any variation to the predicted wind and current could overstress the line, and hence, it is suggested to increase the mooring hook capacity at mooring dolphins from 3 × 100 to 3 × 125 tonnes.
- The recommended mooring hook capacities are summarized in Table 20, and the same shall be adopted for the detail design of mooring structures.

## 9.2 Recommendation

Based on the points listed in Sect. 9.1, the proposed mooring hook capacities are summarized in Table 20. The analysis carried out indicates the significant increase in line loads due to passing vessel effects, when added to the environmental loads.

## References

1. Wang S (1975) Dynamic effects of ship passage on moored vessels. J Waterways Harb Coast Div ASCE
2. Seelig W (2001) Passing ship effects on moored ships. Technical Memorandum TM-6027-OCN, Facilities Engineering Service Center
3. Flory JF (2002) The effect of passing ships on moored ships. In: Prevention first 2002 symposium, California State Lands Commission, Long Beach, CA, Sept 10–22
4. Kriebel D (2005) Mooring loads due to parallel passing ships. Technical Report, TR-6056-OCN, Naval Facilities Engineering Service Center
5. Remery GFM (1974) Mooring forces induced by passing ships. In: Sixth annual offshore technology conference, Houston, May 6–8
6. Muga B, Fang S (1975) Passing ship effects—from theory and experiment. In: OTC 16719, Offshore technology conference, ASCE

7. OCIMF—guidelines and recommendations for the safe mooring of large ships at piers and sea islands
8. BS 6349—code of practise for maritime structures
9. PIANC—guidelines for the design of fender system (2002)
10. OCIMF guidelines for prediction of wind and current loads on VLCCs
11. CWPRS Central Water And Power Research Station report 4756

# Hydrodynamic Study on the Performance Evaluation of Flapping Foils in Open Water Condition



Anties K. Martin, B. K. Alok, P. Krishnankutty and P. Ananthakrishnan

**Abstract** The hydrodynamic performance of a rigid foil inspired from the thunniform kind of propulsion is analyzed numerically. The hydrofoil is allowed to oscillate in pure pitch, pure heave and combined motion by varying the Strouhal number from 0.1 to 0.4. Both 2D and 3D analyzed are done for the combined motion of oscillation. The NACA0012 foil of 0.7 m span and 0.141 m chord is selected for the study. Qualitative observations of the wake field and trailing water jet is studied and presented using average vorticity and velocity contours. The parameters such as thrust coefficient, power coefficient, and efficiency are plotted against the Strouhal number. It is found that the maximum efficiency is achieved in Strouhal number range of 0.15–0.3.

**Keywords** Biomimetic system · End effects · Fish swimming · Flapping foil

## 1 Introduction

The ability of fish swimming and bird's flight have enthused researchers to study the working of their natural propulsion and motivated the development of biomimetic propulsion for aquatic and aerial vehicles. Different types of bio-propulsion system are being studied by researchers to understand the application suitability in different vehicles. The biomimetic system could be a better alternative for the conventional propulsion system. Lighthill [1] suggested that the flapping foil will be the best

---

A. K. Martin (✉) · B. K. Alok · P. Krishnankutty · P. Ananthakrishnan  
Department of Ocean Engineering, Indian Institute of Technology Madras, Chennai, India  
e-mail: [antieskmartin@gmail.com](mailto:antieskmartin@gmail.com)

B. K. Alok  
e-mail: [alokbk987@gmail.com](mailto:alokbk987@gmail.com)

P. Krishnankutty  
e-mail: [prishnankutty@iitm.ac.in](mailto:prishnankutty@iitm.ac.in)

P. Ananthakrishnan  
e-mail: [anathakrishnan@iitm.ac.in](mailto:anathakrishnan@iitm.ac.in)

© Springer Nature Singapore Pte Ltd. 2019  
K. Murali et al. (eds.), *Proceedings of the Fourth International Conference in Ocean Engineering (ICOE2018)*, Lecture Notes in Civil Engineering 22,  
[https://doi.org/10.1007/978-981-13-3119-0\\_15](https://doi.org/10.1007/978-981-13-3119-0_15)

alternative for the conventional screw propeller system. The study of the flapping foil propulsion dates back to 19 the century itself. In 1895 Linden got the patent for converting the ocean wave energy into useful thrust force by placing a foil behind a model called Autonaut [2]. Rozhdestvensky and Ryzhov [3] developed the idea of using the flapping foil propulsion for underwater vehicles. In 1970, Lighthill [4] also shown that the thunniform propulsion is the best form for fast swimming. Flexible foils are more efficient than the rigid foil and compared to span wise flexibility, chord wise flexibility has a greater influence on the thrust production [5]. Too much flexibility will lead to flow separation and can cause less efficient propulsion [6]. The combined motion of heave and pitch gives more thrust and efficiency compared to that of the heave or pitch alone [7]. Anderson [8] investigated the influence of phase difference between heave and pitch motions and found that the maximum efficiency is achieved for a range of 90–100°. The studies show that the formation of reverse Karman vortex (counter-clockwise vortex) is the primary reason for the production of thrust and the clockwise vortex is the reason for the drag [9]. The application of foil propulsion system in marine vehicles is being actively researched by a few groups over the globe.

In this paper, 2D and 3D hydrodynamic analyse are carried out on a foil having a NACA0012 section where the hydrofoil is allowed to oscillate in heave, pitch and its combined motion for a Strouhal number range of 0.1–0.4.

## 2 Nomenclature

$A$	Surface area of the hydrofoil [m <sup>2</sup> ].
$A_0$	Double amplitude of the foil [m].
$C_L$	Lift coefficient.
$C_m$	Moment coefficient.
$F_x$	Drag force [N].
$F_z$	Lift force [N].
$M$	Moment about hinge point [Nm].
$St$	Strouhal number.
$U$	Inflow velocity [m/s].
$n$	No of cycles [n/s].
$T$	Torque [Nm]
$t$	Time period is seconds [s].
$Z_0$	Heave amplitude of oscillation of the foil [m].
$\rho$	Density of water [kg/m <sup>3</sup> ].
$\theta_0$	Amplitude of oscillation [rad].
$\omega$	Angular velocity [rad/s].

### 3 Numerical Methodology

All the numerical simulations are carried out in a CFD environment using the commercial software StarCCM++, where the flow over and around the hydrofoil is represented by the Reynolds Average Navier–Stokes (RANS) equation. The foil is placed at the transverse center of the domain, where the inlet is nearer to the foil and outlet is far away from the foil to capture the results effectively. The fluid domain is discretized using the unstructured grid. The pressure-velocity coupling is done by using the SIMPLE (Semi-Implicit Method for Pressure-Linked Equations) algorithm. Since second order upwind scheme is having better accuracy [10], it is used for the temporal discretization. The turbulence model K-Epsilon is chosen for the study as it gives better results for turbulent flows. The flow over the hydrofoil is analysed and plotted against the different Strouhal number. Table 1 shows the solver settings and the numerical parameters used in the study. The StarCCM++ overset mesh technic, which is also called chimera or overlapping mesh, is used for the analysis. In overset mesh, mesh containing the body is superimposed with the background mesh and data is interpolated between the two mesh regions. Figure 1 shows the 3D hydrofoil representation, where  $U$  is the inflow velocity and  $\theta$  is the angle of pitch.

**Table 1** Solver settings and parameters

Flow type	Segregated
Pressure-velocity coupling	Simple
Temporal discretization	Second order upwind
Time step	0.001 s
Total simulation time	50 s
Turbulence model	K-Epsilon

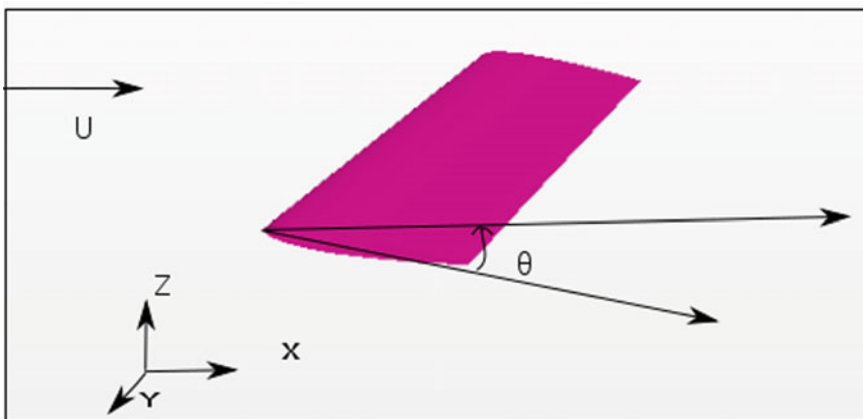
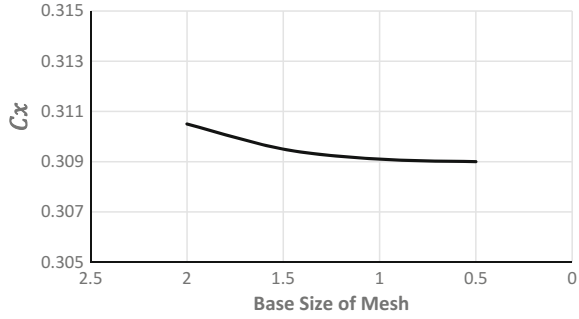


**Fig. 1** Definition sketch of the oscillating foil

**Fig. 2** Grid independence test



### 3.1 Grid Independence Study

The grid independence study is conducted to find out the best suitable mesh required for the study. The parameters chosen for the convergence is  $C_x$  for a Strouhal number 0.25. The base size of the mesh is varied from 2 to 0.5 by a factor of 0.5. Figure 2 shows the result of the study and parameter is converged up to 3 decimal points.

### 3.2 Boundary Condition

Figure 3 represent the complete view of the domain and the prism layers around the foil, where the foil is placed at the transverse center of the domain. The surface of the foil is assigned with no-slip condition where tangential velocity is zero. The inlet boundary condition is ‘velocity inlet’ and the outlet is ‘pressure outlet’. The other boundaries are assigned as slip walls where tangential velocity is considered. The foil is allowed to oscillate 10 complete cycles based on the frequency of oscillation (Table 2).

**Table 2** Boundary conditions

Boundary	Condition
Inlet	Velocity inlet
Outlet	Pressure outlet
Foil surface	No slip wall
Other boundaries	Slip wall

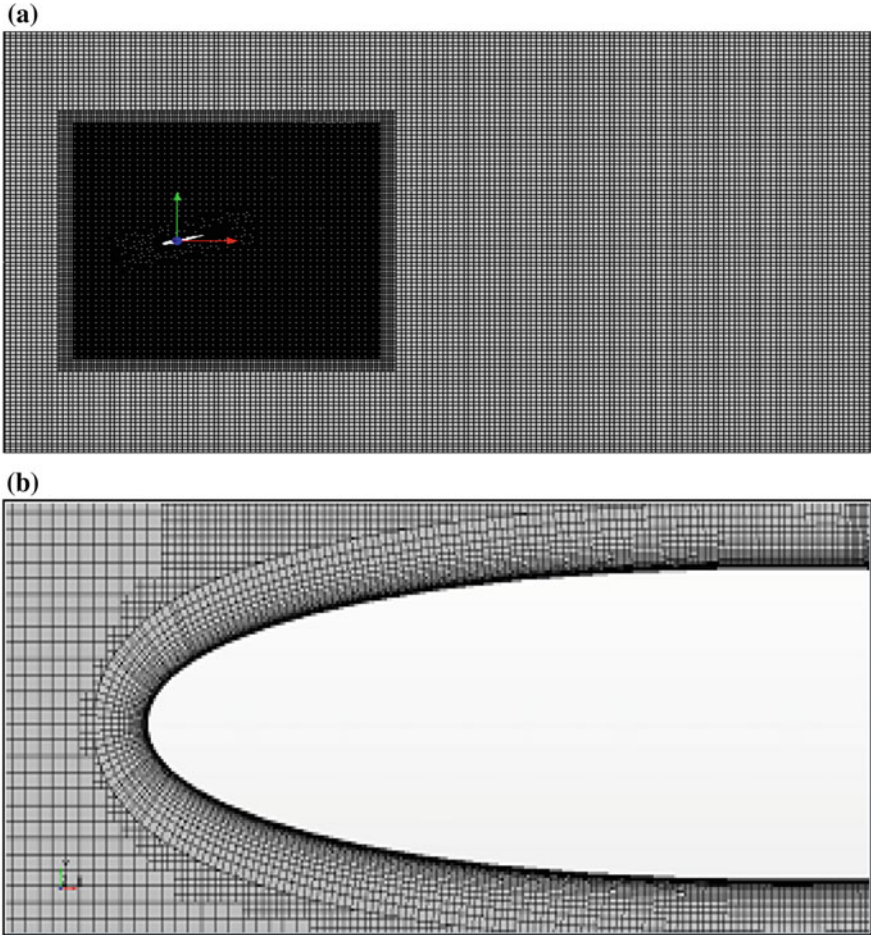


**Fig. 3** Mesh generated for the study **a** complete view of the domain, **b** detailed view of prism layers around the foil

### 3.3 Performance Parameters

The main objective of the study is to find out thrust and efficiency of the hydrofoil at the different operating conditions. Main outcomes are thrust coefficient ( $C_X$ ), Power coefficient ( $C_P$ ) and efficiency of the foil at different Strouhal numbers varying from 0.1 to 0.4.

Thrust and lift forces which acts, respectively in the direction of the ship axis and normal to inflow velocity. All the results obtained are represented against Strouhal number (Eq. 1)

$$St = \frac{f A_0}{U} \quad (1)$$

where  $f$  is the frequency of oscillation in Hz,  $A_0$  is the double amplitude of oscillation in m and  $U$  is the inflow velocity in m/s.

The heave motion of the foil is given by

$$Z = Z_0 \sin(\omega t) \quad (2)$$

where  $Z_0$  is the amplitude of oscillation in m and  $\omega$  is the frequency of oscillation in rad/s.

The rotational motion of the foil is given by

$$\theta = \theta_0 \sin(\omega t + \phi) \quad (3)$$

where  $\theta_0$  is the amplitude of rotation in radians.  $\phi$  is the phase difference between heave and the pitch motion of the fin where here we are taking that as  $90^\circ$ .

The average thrust force acting in the direction of motion of vehicle can be obtained by the equation

$$F_x = \frac{1}{nT} \oint f_x(t) dt \quad (4)$$

where  $n$  is the number of cycles per second (Hz),  $T$  is the period of oscillation in seconds.

Thrust coefficient of the hydrofoil is given by

$$C_x = \frac{F_x}{0.5\rho AU^2} \quad (5)$$

where  $A$  is the plan area of the foil in  $m^2$ ,  $\rho$  is the density of the water in  $kg/m^3$ .

The average lift force acting in the normal direction of the inflow velocity is

$$F_Z = \frac{1}{nT} \oint f_Z(t) dt \quad (6)$$

Lift coefficient is given by

$$C_Z = \frac{F_Z}{0.5\rho AU^2} \quad (7)$$

The average power required to oscillate the foil depend upon the torque produced by the system and the angular frequency of the motion, and for pitching is given as

$$P = T * \omega \quad (8)$$



where  $T$  is the torque required for the rotation in Nm and  $\omega$  is the angular velocity of pitch oscillation.

In combined motion of heave and pitch, the power is represented by

$$P = -fz \frac{dz}{dt} - Mt \frac{d\theta}{dt} \quad (9)$$

The average power coefficient is given by

$$C_p = \frac{P}{0.5\rho AU^3} \quad (10)$$

The efficiency of the oscillating foil is defined as the ratio of the output power to that of the input power and given as

$$\eta = \frac{F_x U}{P} = \frac{C_x}{C_p} \quad (11)$$

The thrust coefficient and efficiency are plotted against different Strouhal numbers in Figs. 11 and 13.

## 4 Validation of the CFD Results

The thrust coefficient  $C_x$  is chosen as validation parameter and it gives a good agreement with the experimental results of the Schouveiler et al. [11]. The slight variation of the results (Fig. 4) may be due to the presence of end plates at both edges of the foil where it can avoid the end losses to an extent, but in the numerical case, we are not considering the end effects.

## 5 Cases with Different Modes of Oscillation

The hydrofoil is allowed to oscillate in three different modes of oscillations. The first mode is pure rotation, where the foil is allowed to oscillate about its hinge point which is 1/3 of the chord length from the leading edge. In mode 2, the foil will undergo heave alone where only translation motion. In mode 3, the foil is allowed to oscillate in combined motion of heave and pitch.

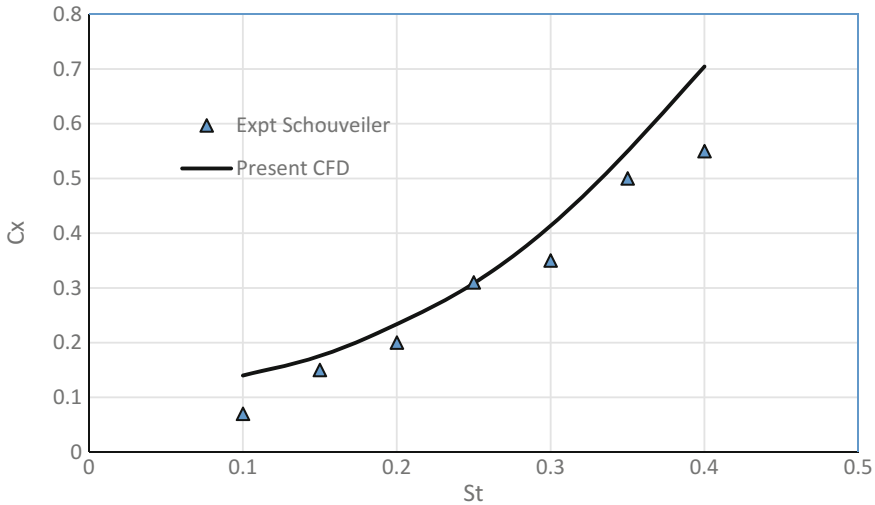


**Fig. 4** Thrust coefficient variation with Strouhal number

### 5.1 Pure Pitch

Equation (3) represents the pitch alone motion of the hydrofoil. All the simulations are carried out by keeping the amplitude of oscillation constant and varying its frequency.

Figure 5 represents the vortex shedding of the pure pitch motion. The counter-clockwise vortex which is the primary reason for the thrust force is clearly visible in the figure. Figure 6 shows the wake velocity of distribution in foil pitch mode at  $St = 0.2$ . It shows that the velocity of the flow is increasing behind the trailing edge which shows the formation of a water jet resulting in the thrust generation.

### 5.2 Pure Heave

Equation (2) represents the heave translation motion of the hydrofoil. The amplitude of oscillation is kept constant and the frequency of oscillation of the foil is varied to change the Strouhal number.

Figure 7 represent the vortex shed by the hydrofoil in heave oscillation. It is clear from the figure that the vortex formed at the leading edge is amalgamated with the vortex formed at the trailing edge and resulted in the formation of thrust force. Figure 8 represent the velocity contour around and behind the foil. The velocity behind the trailing edge is higher than that at the leading edge due to the formation of water jet at the trailing edge.

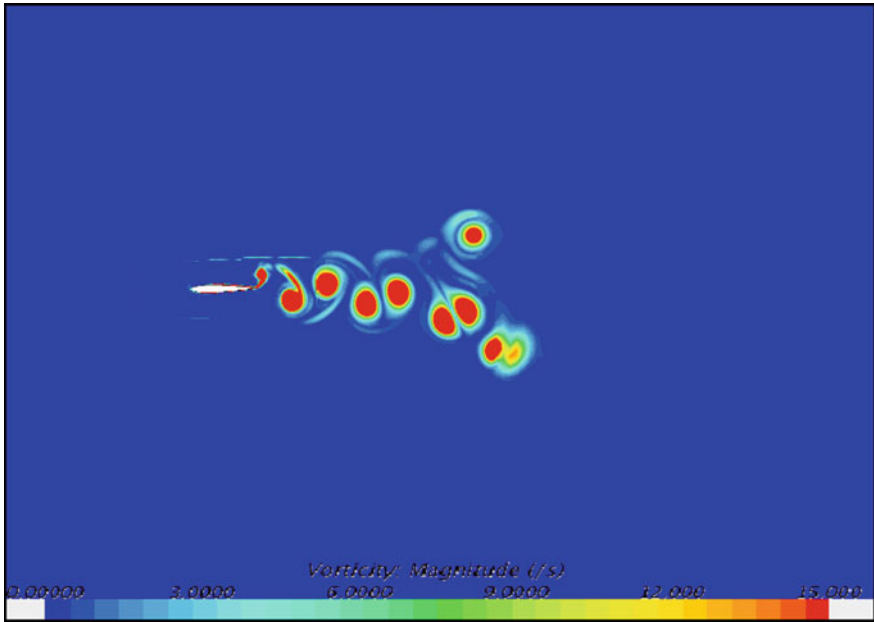


Fig. 5 Absolute vorticity in pitch mode at  $St = 0.2$

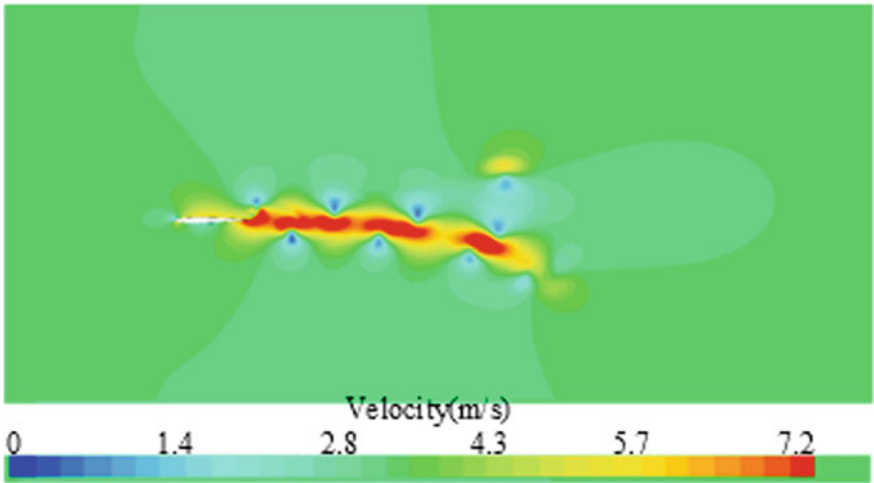


Fig. 6 Velocity contour behind the foil in pitch mode at  $St = 0.2$

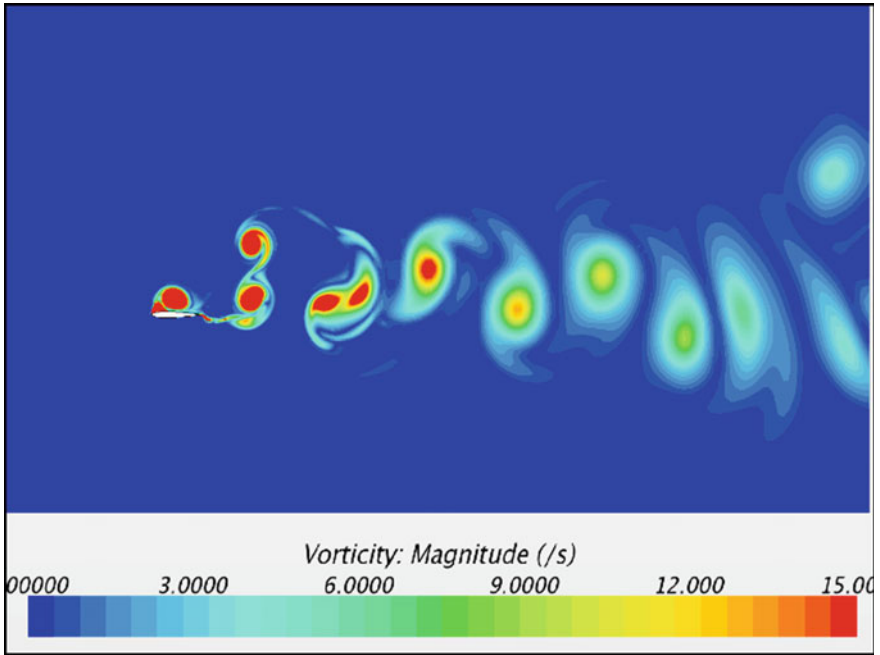


Fig. 7 Absolute vorticity in heave mode at  $St = 0.2$

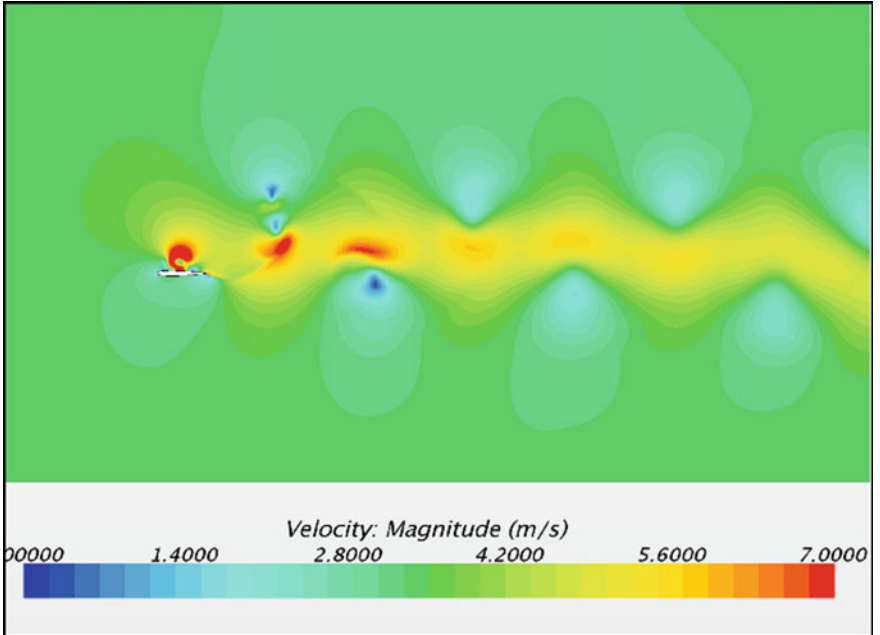
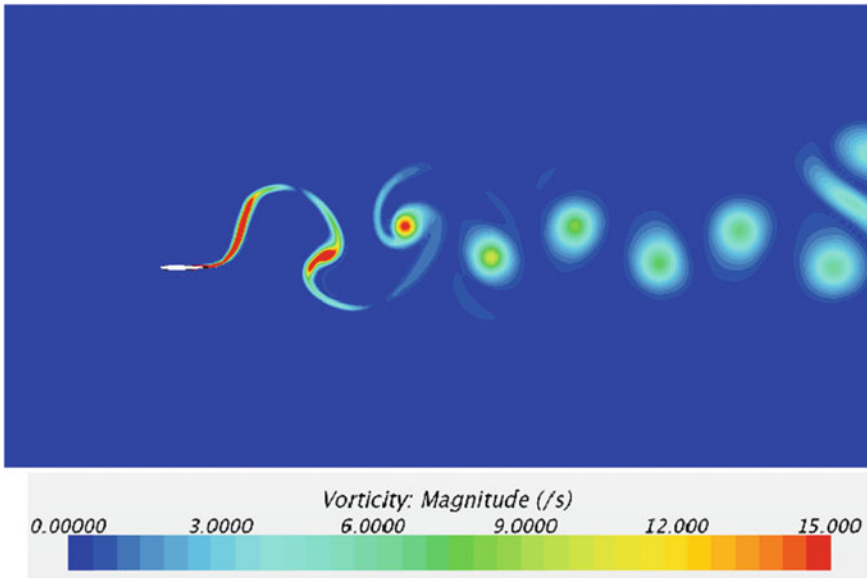


Fig. 8 Velocity contour behind the foil in heave mode at  $St = 0.2$



**Fig. 9** Absolute vorticity in combined motion at  $St = 0.2$

### 5.3 Combined Motion of Heave and Pitch

Equations (2) and (3) jointly give the combined heave and pitch motion of the fin. As the previous cases, the amplitude of oscillation is kept constant and the frequency of motion is varied. Here we considered both heave and pitch frequency as same.

Figure 9 shows the vortex shed by the foil in combined modes of the oscillation. The formation of reverse Karman vortex is clearly visible from the figure. The outward turning vortex causes the reactionary thrust force. This is produced by the downstream jet produced at the trailing edge. Strength of vorticity depends upon amplitude and frequency of the oscillation. Figure 10 shows the velocity of contour around the foil. The velocity at the trailing edge is higher than the velocity at the leading edge resulting in the formation of a water jet and the reactionary thrust.

## 6 Results and Discussion

The performance of the hydrofoil is analyzed and discussed for different modes of oscillation. Figures 11, 12 and 13 shows the performance comparison of the different modes of oscillation.

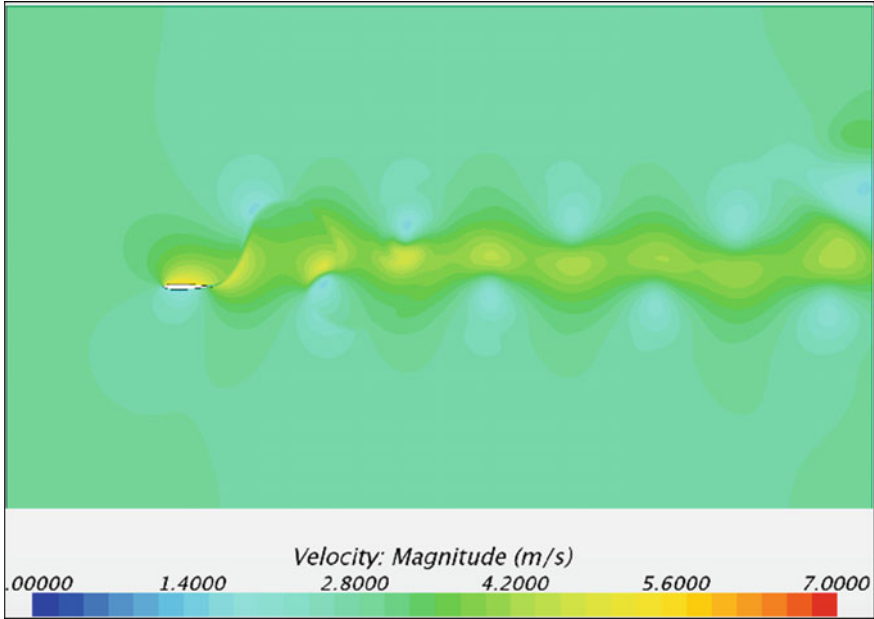


**Fig. 10** Velocity contour around the foil in the combined mode at  $St = 0.2$

**Fig. 11** Average thrust coefficient as a function of Strouhal number in different oscillation

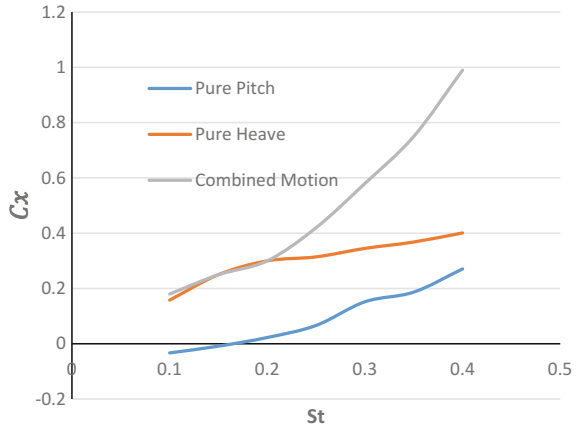
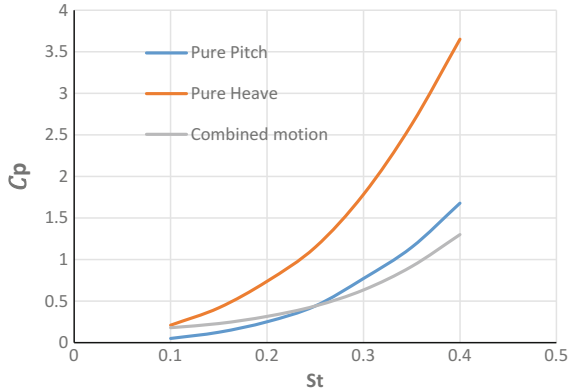


Figure 11 shows the thrust coefficient variation as a function of Strouhal number for different fin oscillation modes. It is clear that the thrust produced by the combined motion mode is higher than the independent heave and pitch mode. In pure pitch mode, for low Strouhal numbers, the drag force is dominating over the thrust force.

**Fig. 12** Average power coefficient as a function of Strouhal number



**Fig. 13** Propulsive efficiency of the foil at different operating modes

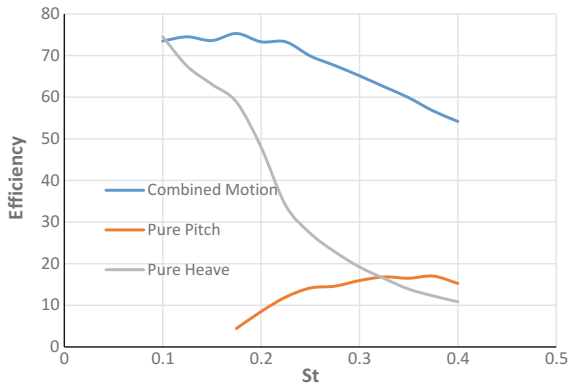
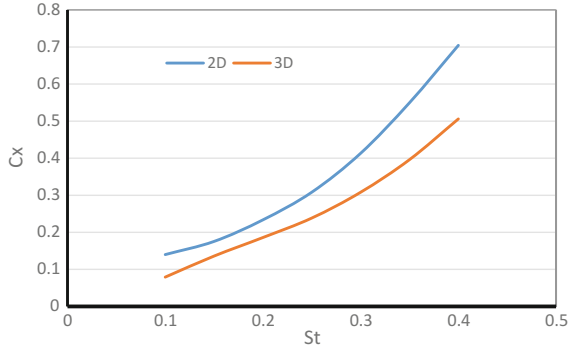


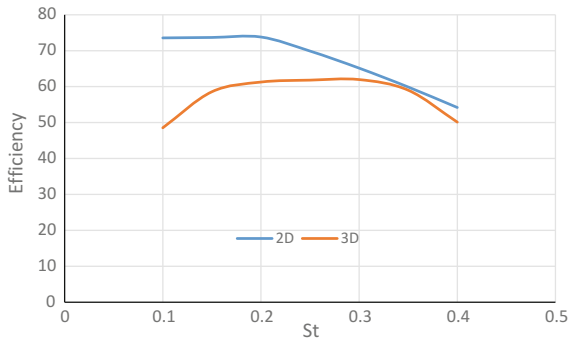
Figure 12 clearly shows that as the Strouhal number increases the power required for the oscillation also increases. Power required in pure heave mode is higher than in the other modes, where the combined mode motion requires less power over a wide range of Strouhal number. In the combined motion, the torque required to oscillate the foil is less which will result in less power consumption.

Figure 13 represents the efficiency of the foils at different conditions. It shows that the efficiency in combined mode is better than the other two cases. In pure pitching, the efficiency is less over a range of Strouhal number. This may be due to the flow separation developed because of the higher range of frequency and limitation of the angle of attack. The heave only case is showing an unusual curve for the efficiency. In heave motion, since the power required to oscillate the foil is proportional to the torque required and the angular oscillation. As the frequency of oscillation increases the torque also increases resulting in less efficiency for higher Strouhal number.

**Fig. 14** Average thrust coefficient obtained through 2D and 3D analysis



**Fig. 15** Efficiency of 2D and 3D foils



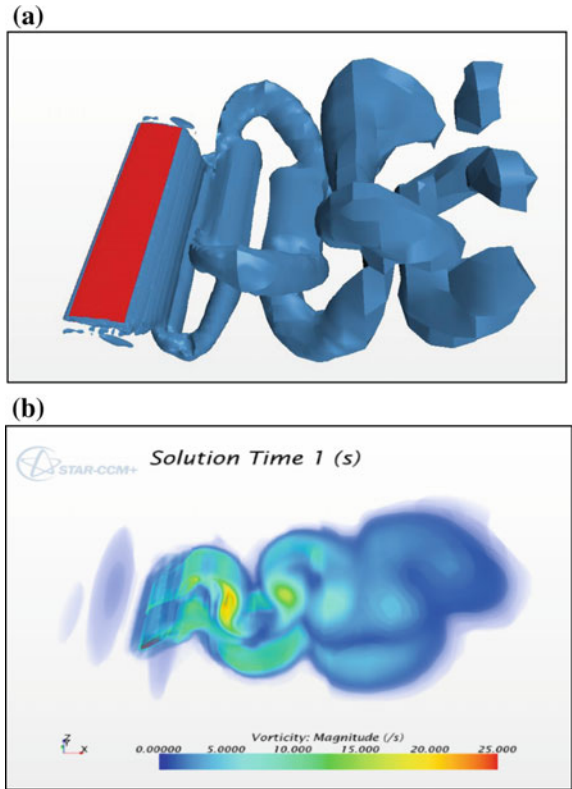
**Three Dimensional Fin Analysis**

The NACA0012 hydrofoil of 0.7 m span and 0.141 m chord length is used for the study. The fin is allowed to oscillate in the combined motion of heave and pitch. Figure 14 shows the variation of thrust coefficient as a function of Strouhal number for 2D and 3D cases. In 2D analysis, we assume span as infinite and hence the end effects are ignored, whereas the end effects are considered in the case of the 3D fin. The efficiency curves (Fig. 15) also justifies that the 2D efficiency is better than the 3D one. This is due to the end effects present in the case of the 3D fin.

Figure 16 shows the end effects and loses of the hydrofoil. Similar to the leading and trailing edges, the vortex is shed by the side edges of the foil also. There is a cross flow of the fluid over the foil to the side edge which is not present in the 2D case and resulted in less thrust generation and efficiency.



**Fig. 16** End effects and loses of the foil at the edges



## 7 Conclusion and Remarks

The hydrodynamic performance of a rigid foil oscillating in different modes such as pure pitch, pure heave and combined motion of heave and pitch are analysed for different Strouhal numbers ranging from 0.1 to 0.4. The numerical results are validated against the experimental one presented by Schouveiler et al. [11]. The performance parameters such as thrust coefficient, power coefficient, and efficiency are plotted against Strouhal number. It is found that the combined motion of heave and pitch gives better performance compared to that of the pitch or heave alone due to the less torque required for the oscillation. The maximum efficiency is noted in the Strouhal number range of 0.15–0.3. The hydrodynamic performance of 3D foil is inferior to 2D foil, as expected, due to the loses occurred from the end effects.

## References

1. Lighthill M (1969) Hydromechanics of aquatic animal propulsion. *Annu Rev Fluid Mech* 1(1):413–446
2. Linden H (1895) Improved combination with floating bodies, of fins adapted to effect their propulsion. U.K. Patent 14630
3. Rozhdestvensky KV, Ryzhov VA (2003) Aero-hydrodynamics of flapping-wing propulsors. *Prog Aerosp Sci* 39(8):585–633
4. Lighthill MJ (1970) Aquatic animal propulsion of high hydromechanical efficiency. *J Fluid Mech* 44:265–301
5. Simpson BJ, Hover FS, Triantafyllou MS (2008) Experiments in direct energy extraction through flapping foils. In: The eighteenth international offshore and polar engineering conference. International Society of Offshore and Polar Engineers
6. Martin AK, Krishnankutty P (2017 June) Study on the hydrodynamic efficiency of flexible foil at different operating parameters. In: ASME 2017 36th international conference on ocean, offshore and arctic engineering (pp. V07BT06A041-V07BT06A041). American Society of Mechanical Engineers
7. Jones KD, Dohring CM, Platzer MP (1996) Wake structures behind plunging airfoils: a comparison of numerical and experimental results. AIAA Paper No. 96-0078
8. Anderson JM, Streitlien K, Barrett DS, Triantafyllou MS (1998) Oscillating foils of high propulsive efficiency. *J Fluid Mech* 360:41–72
9. Triantafyllou MS, Triantafyllou GS (1995) An efficient swimming machine. *Sci Am* 272(3):64–71
10. STAR, CCM, and User Guide (2012) “6.02.” Available at the site of «Sarovskii Inzhenernyi Tsentr» [“Sarov Engineering Center”]: [http://www.saec.ru/STAR\\_CCM\\_userguide/](http://www.saec.ru/STAR_CCM_userguide/), accessed 21
11. Schouveiler L, Hover F, Triantafyllou M (2005) Performance of flapping foil propulsion. *J Fluids Struct* 20(7):949–959

# Numerical Study of Water Depth Effect on Sway Velocity and Rudder Derivatives of a Container Ship in Manoeuvring



Akhil Balagopalan and P. Krishnankutty

**Abstract** Correct prediction of the hydrodynamic derivatives is essential for the accurate determination of ships manoeuvring performance. Numerical and experimental methods are widely used for the determination of these derivatives. Even though experimental methods are more reliable, these facilities are rare and often prohibitively expensive. More viable option, primarily during the early stages of the ship design, is to determine these derivatives numerically. And also most of the ship manoeuvring studies and regulations are on deep water conditions, whereas the ship manoeuvring performance is much worse in shallow waters, and its controllability is difficult. An attempt is made in this paper to study the shallow water effects on the sway velocity-dependent derivatives and rudder derivatives numerically. KRISO container ship (KCS), a benchmark example used by different research groups, is taken for the present study. Straight line or static drift tests are performed in a numerical environment at different drift and different rudder angles using a commercial CFD package. These tests are conducted in both deep and shallow water conditions. Effects of water depth on the sway velocity-dependent hydrodynamic derivatives and rudder derivatives are evaluated, and the results are presented and analysed.

**Keywords** KCS · Manoeuvring · Straight line test · Hydrodynamic derivative CFD

## 1 Introduction

Manoeuvring quality assessment for seagoing vessels is essential for the navigational safety purpose. International Maritime Organization (IMO) has prescribed guidelines for the seagoing vessels to ensure its navigational safety as well as operational effi-

---

A. Balagopalan (✉) · P. Krishnankutty  
Department of Ocean Engineering, IIT Madras, Chennai, India  
e-mail: [bgakhil@gmail.com](mailto:bgakhil@gmail.com)

P. Krishnankutty  
e-mail: [pkrishnankutty@iitm.ac.in](mailto:pkrishnankutty@iitm.ac.in)

© Springer Nature Singapore Pte Ltd. 2019  
K. Murali et al. (eds.), *Proceedings of the Fourth International Conference in Ocean Engineering (ICOE2018)*, Lecture Notes in Civil Engineering 22,  
[https://doi.org/10.1007/978-981-13-3119-0\\_16](https://doi.org/10.1007/978-981-13-3119-0_16)

275

ciency during its voyage. Manoeuvring quality of a ship primarily depends on the hull geometry and is to be essentially determined in its initial stage of design. The surface ship manoeuvrability is governed by the equations of motions in surge, sway and yaw motions which are relevant motions in the horizontal plane. The directional stability and control characteristics of a ship are generally understood by solving these manoeuvring equations of motion for which the knowledge of hydrodynamic derivatives are important. Accurate prediction of hydrodynamic derivatives determines the quality of prediction of the manoeuvring characteristic of vessel such as turning ability and course keeping ability rudder effectiveness. Empirical relations given by researchers [1, 2] give a rough estimate of the hydrodynamic derivatives but fail to predict higher order and coupled non-linear derivatives. Numerical and experimental methods are widely used for the estimation of hydrodynamic derivatives. Even though experimental methods are more reliable, these facilities are rare and often prohibitively expensive. More viable option, primarily during the early stages of the ship design, is to determine these derivatives numerically.

In shallow water, the flow around the vessel modifies drastically and thus the hydrodynamic derivatives also. Ships operating in these regions become sluggish and behave poorly to the action of control surfaces. Hence, the correct estimation of hydrodynamic derivatives in shallow water is inevitable to predict the vessels manoeuvring behaviour when it is operating in water depth-restricted regions such as ports, harbours, inland waterways. Experimental facilities for shallow water manoeuvring studies are very rare all over the world. With the advancement of computational techniques, the application of computational fluid dynamic (CFD) is emerging as a powerful tool for the prediction of ship manoeuvring performance even for different water depth conditions. The manoeuvring performance results obtained from CFD are promising and are reliable when compared to the actual ships manoeuvring performance [3–5]. This paper presents the influence of water depth on the velocity derivatives  $Y_v, N_v, Y_{vv}, N_{vv}$  and rudder derivatives  $Y_\delta, N_\delta, Y_{\delta\delta}, N_{\delta\delta}$ . Stationary straight line tests with different drift angles and rudder angles were conducted using commercial CFD software STAR-CCM+. Numerical simulations were conducted for both deep water and shallow water conditions. Shallow water condition as  $H/T = 1.5$  is taken for the current study.

## 2 Nomenclature

$B$	Beam (m)
CB	Block coefficient
CM	Midship area coefficient
$D$	Depth (m)
$H$	Water height (m)
$L_{oa}$	Length overall (m)
$L_{pp}$	Length between perpendiculars (m)
$L_{wl}$	Load water line (m)

$N_v$	Hydrodynamic linear coupled derivative of yaw moment with respect to sway velocity
$N_{vvv}$	Hydrodynamic third-order coupled derivative of yaw moment with respect to sway velocity
$N_\delta$	Hydrodynamic linear coupled derivative of yaw moment with respect to rudder deflection
$N_{\delta\delta\delta}$	Hydrodynamic third-order coupled derivative of yaw moment with respect to rudder deflection
$T$	Draft (m)
$Y_v$	Hydrodynamic linear coupled derivative of sway force with respect to sway velocity
$Y_{vvv}$	Hydrodynamic third-order coupled derivative of sway force with respect to sway velocity
$Y_\delta$	Hydrodynamic linear coupled derivative of sway force with respect to rudder deflection
$Y_{\delta\delta\delta}$	Hydrodynamic third-order coupled derivative of sway force with respect to rudder deflection
$V$	Forward velocity of the ship (m/s)
$v$	Sway velocity (m/s)
$\beta$	Drift angle ( $^\circ$ )
$\delta$	Rudder angle ( $^\circ$ )

### 3 Straight Line Test

Sway velocity and rudder derivatives are found out by simulating the straight line test in CFD environment. Straight line tests are conducted for different drift angles ( $\beta = 3, 6, 9, 12, 15, 18$ ) to estimate the sway velocity derivatives  $Y_v$ ,  $Y_{vvv}$ ,  $N_v$  and  $N_{vvv}$ , (Fig. 1). Rudder derivatives  $Y_\delta$ ,  $Y_{\delta\delta\delta}$ ,  $N_\delta$  and  $N_{\delta\delta\delta}$  are estimated by giving different rudder angles ( $\delta = 5, 10, 15, 20, 25, 30, 35$ ) to the vessel with zero drift angle (Fig. 2). Numerical simulations are carried out for both deep water ( $H/T > 3$ ) and for shallow water ( $H/T = 1.5$ ) conditions.

### 4 Hull Geometry

The KRISO container ship (KCS) model, a benchmark model being used by different research groups worldwide, has been chosen for the present study. The main particulars of the vessel and model details are shown in Table 1.

**Fig. 1** Model with drift angle

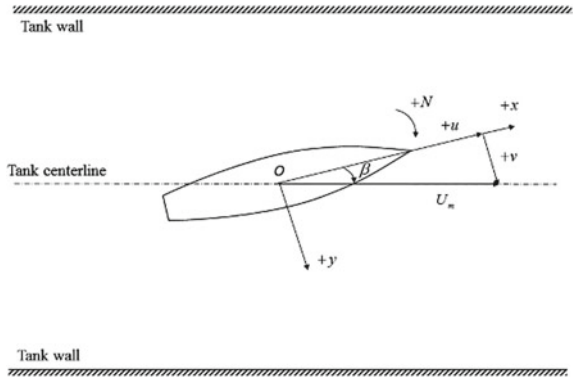


**Fig. 2** Model with rudder deflection

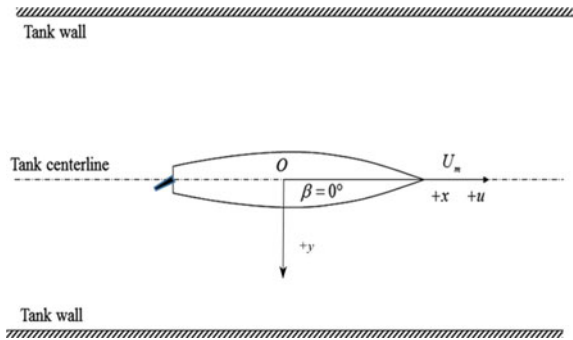


**Table 1** Particulars of the container ship

Main particulars	Full scale	Model (1:75.5)
$L_{pp}$ (m)	230.0	3.0464
$L_{wl}$ (m)	232.5	3.0791
$B_{wl}$ (m)	32.2	0.4265
$D$ (m)	19.0	0.2517
$T$ (m)	10.8	0.1430
Displacement ( $m^3$ )	52030	0.1209
$S$ w/o rudder ( $m^2$ )	9530	1.6719
CB	0.651	0.651
CM	0.985	0.98

## 5 Numerical Study

Commercial CFD package STAR-CCM+ is used for the present study. Solver settings for both deep and shallow water conditions are given in Table 2.

**Table 2** Computational parameters

Solver	3-D segregated implicit unsteady
Temporal discretization	Second order
Turbulence model	k-epsilon
Wall treatment	All wall y+
Free surface modelling	VOF method
Time step	0.01
Maximum physical time	50 s

**Table 3** Domain dimensions

Direction	Deep water ( $L_{oa}$ )	Shallow water ( $L_{oa}$ )
Forward	1.5	1.5
Aft	2.5	2.5
Side	2	2
Deck to top	1.5	1.5
Keel-bottom	1.5	0.022

**Table 4** Boundary conditions

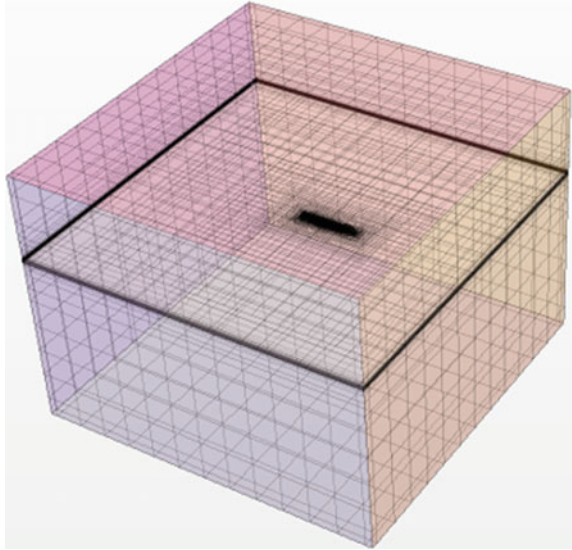
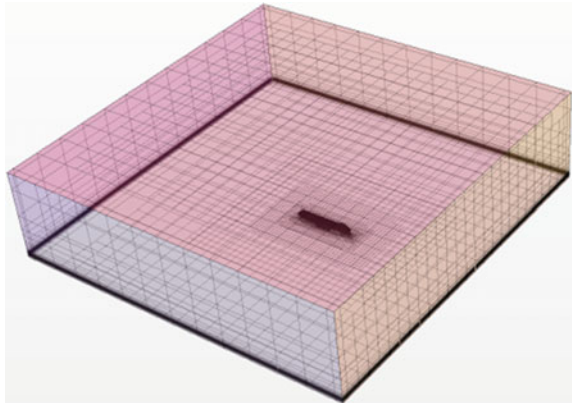
Inlet	Velocity inlet
Outlet	Pressure outlet
Top	Velocity inlet
Side	Wall with slip
Bottom	Wall with no slip
Hull	No slip wall

## 5.1 Computational Domain

Fluid domain (Table 3) is selected based on the ITTC Standards [6]. Two different computational domains are created based on deep water ( $H/T = 25$ ) (Fig. 3) and shallow water ( $H/T = 1.5$ ) (Fig. 4) conditions. The boundary conditions (Table 4) are applied to the computational domain for the analysis. Wave damping option is enabled at the side wall boundaries to avoid wave reflections.

## 5.2 Mesh Generation

Unstructured trimmed hexahedral mesh is generated with near wall prismatic layers using CFD tool (Figs. 5 and 6). Three separate volumetric blocks at bow, stern and free surface are created with refined mesh density. Separate meshes are generated for

**Fig. 3** Deep water domain**Fig. 4** Shallow water domain

different drift angles and for different rudder angles for each simulation trials. Mesh generated for  $9^\circ$  drift angle (Fig. 7) and  $20^\circ$  rudder angle (Fig. 8) is given below.

## 6 Grid Independence Study

Grid independence study is performed to ensure that the results are unaffected by the base size/number of cells. Four different grid sizes are selected to analyse the grid dependency. Inflow velocity of 1.1 m/s is given to the ship model, and the total resistance is estimated. It is observed that there is not much variation exists between



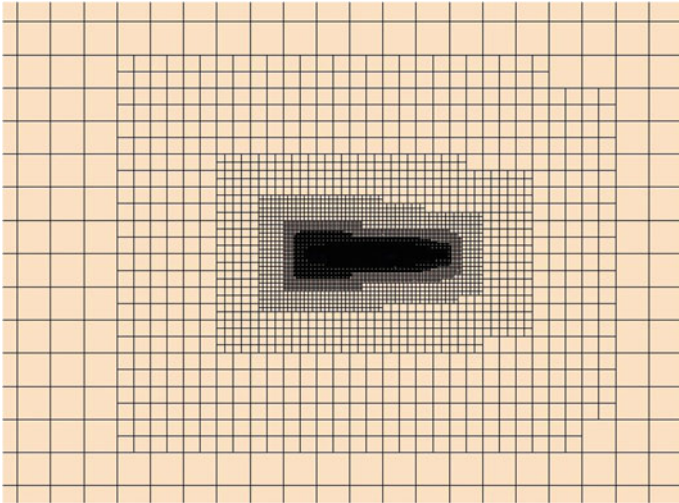


**Fig. 5** Generated mesh

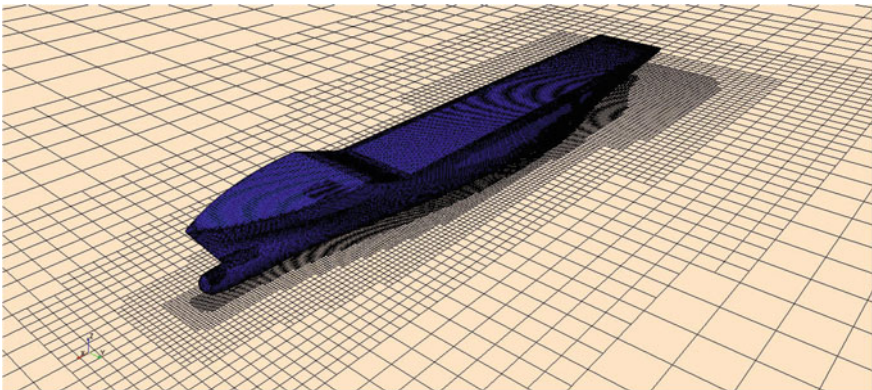


**Fig. 6** Mesh configuration around the vessel

the base sizes 0.1 and 0.085. Hence, the base size of 0.1 m with 1.7 million cells is selected. Grid independence test results are given in Table 5.

## 7 Grid Validation with CFD and Experimental Results

Numerical CFD resistance test for KCS model is conducted for different speeds with the same generated mesh condition, 0.1 m of base size and 1.7 million cells .

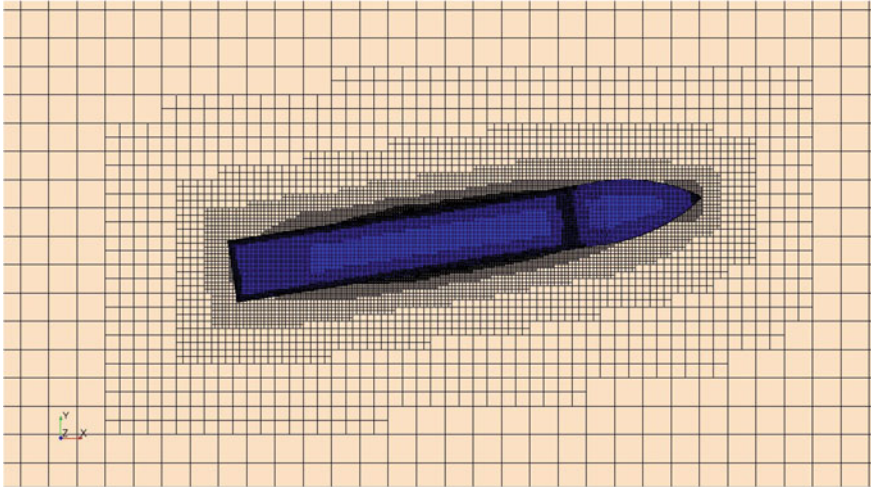


**Fig. 7** Ship at 9° drift angle

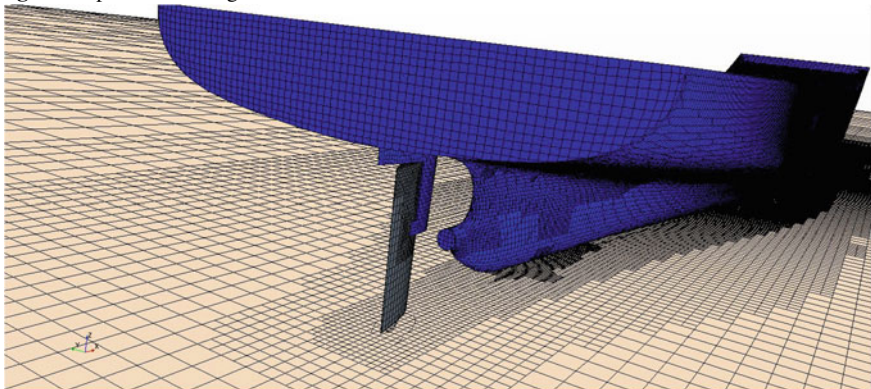


**Fig. 8** Ship at 20° rudder angle

Experimental resistance test (Fig. 9) is conducted at IIT Madras towing tank facility where the model is towed at different speeds, and the total resistance is measured at

**Table 5** Grid independence study results

No.	Base size (m)	Number of cells (millions)	Resistance (N)
1	0.15	1.1	4.78
2	0.1	1.7	4.541
3	0.085	2.2	4.533
4	0.07	2.9	4.17



**Fig. 9** KCS resistance test arrangement

**Table 6** CFD and experimental resistance test results

Model speed (m/s)	Resistance (N)	
	CFD	Experimental
0.7	2.182	–
0.77	2.461	2.71
0.829	2.801	2.67
0.888	3.17	2.95
0.947	3.56	3.36
1.066	4.24	4.27
1.1	4.54	4.44
1.125	4.722	4.66
1.184	5.129	5.07
1.243	5.608	5.56
1.302	6.195	6.01
1.362	6.865	6.66
1.421	7.696	7.51
1.48	9.032	8.81
1.539	10.605	10.65

its design displacement. CFD and experimental resistance test results are given in Table 6, and the same are compared in Fig. 10. The values closely match, and hence, the same grid is used for numerical analysis.

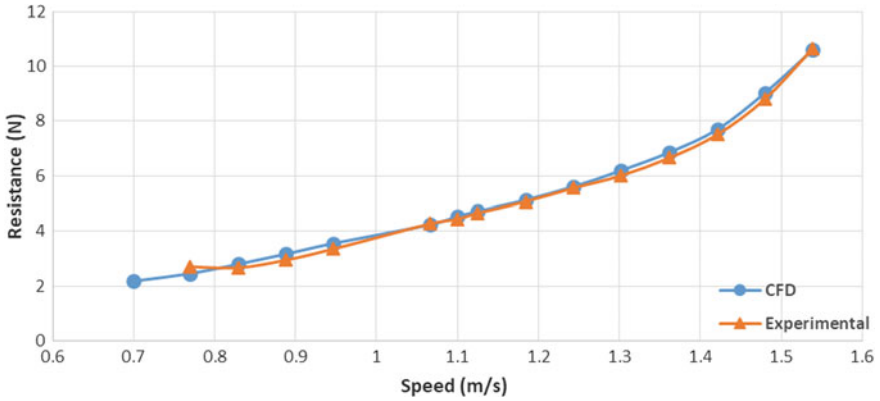


Fig. 10 CFD and experimental result comparison

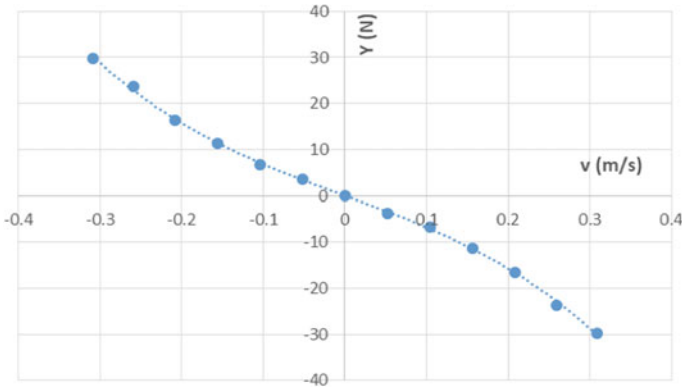


Fig. 11 Plot of sway force against sway velocity

## 8 Numerical Tests, Results and Discussions

Straight line tests are conducted for both deep water and shallow water conditions.

### 8.1 Deep Water Condition

#### 8.1.1 Sway Velocity Derivatives

Sway force and yaw moment acting on the vessel at its centre of gravity are estimated for different drift angles. These forces are plotted against the sway velocity  $v$  (Figs. 11 and 12). The sway velocity is given by

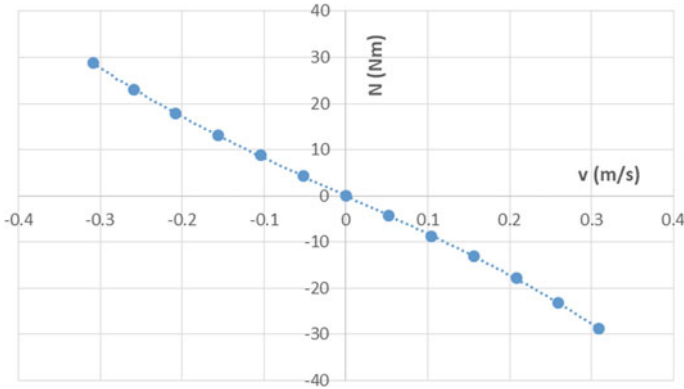


**Fig. 12** Plot of yaw moment against sway velocity

$$v = -V \sin \beta \tag{1}$$

The hydrodynamic derivatives are calculated by taking the slope of the curve at  $v = 0$ . Tests are conducted only to port side drift angle of the vessel, and values are mirrored by considering ship symmetry about its central longitudinal vertical plane.  $Y_v, N_v, Y_{vvv}, N_{vvv}$  are non-dimensionalised by using the following relations (Table 7).

$$Y'_v = \frac{Y_v}{0.5 \rho L w l^2 V} \tag{2}$$

$$N'_v = \frac{N_v}{0.5 \rho L w l^3 V} \tag{3}$$

$$Y'_{vvv} = \frac{Y_{vvv}}{(0.5 \rho L w l^2)/V} \tag{4}$$

$$N'_{vvv} = \frac{N_{vvv}}{(0.5 \rho L w l^3)/V} \tag{5}$$

**Table 7** Straight line test results

Drift angle (°)	Sway velocity $v$ (m/s)	$Y$ force (N)	$N$ moment (N m)
0	0.000	0	0
3	-0.052	3.673	4.297
6	-0.105	6.721	8.869
9	-0.156	11.285	13.073
12	-0.208	16.466	17.776
15	-0.259	23.621	23.089
18	-0.309	29.802	28.769

Third-order cubical curves are fitted on the above plots. Curves fitted with third-order polynomial in non-dimensional format are given below.

$$Y' = -0.0729712 v'^3 - 0.013726 v' + 7 \times 10^{-13} \quad (6)$$

$$N' = -0.0086672 v'^3 - 0.005556 v' - 8 \times 10^{-13} \quad (7)$$

Hydrodynamic derivatives are obtained by differentiating the above equation with respect to sway velocity,  $v$  at  $v = 0$  and equating the terms with that of Taylor series representation of force and moment. The order of differentiation depends on the order of derivatives to be estimated. Equating the likely terms with Taylor series will give the following relation for the hydrodynamic derivatives.

$$Y'_v = \left[ \frac{\partial Y'}{\partial v'} \right] \text{ at } v = 0 \quad (8)$$

$$Y'_{vvv} = \frac{1}{3!} \left[ \frac{\partial^3 Y'}{\partial v'^3} \right] \text{ at } v = 0 \quad (9)$$

$$N'_v = \left[ \frac{\partial N'}{\partial v'} \right] \text{ at } v = 0 \quad (10)$$

$$N'_{vvv} = \frac{1}{3!} \left[ \frac{\partial^3 N'}{\partial v'^3} \right] \text{ at } v = 0 \quad (11)$$

The non-dimensional hydrodynamic derivatives estimated are

$$Y'_v = -0.013726$$

$$Y'_{vvv} = -0.0729712$$

$$N'_v = -0.005556$$

$$N'_{vvv} = -0.0086672$$

### 8.1.2 Rudder Derivatives

Sway force and moment acting at the centre of gravity of the vessel for different rudder angles are estimated from the CFD analysis (Table 8). These are plotted against rudder angle (Figs. 13 and 14). The data is fitted with a third-order cubic polynomial curve and is represented in non-dimensional format as below.

$$Y' = -0.00121289 \delta'^3 + 0.00112811 \delta' - 5 \times 10^{-14} \quad (12)$$

$$N' = +0.00048225 \delta'^3 - 0.000466305 \delta' + 2 \times 10^{-12} \quad (13)$$

Rudder derivatives are non-dimensionalised by using the following relations.

$$Y'_\delta = \frac{Y_\delta}{0.5 \rho L w l^2 V} \quad (14)$$

**Table 8** Rudder forces and moments

Rudder angle $\delta$ ( $^\circ$ )	Y force (N)	N moment (N m)
0	0	0
5	0.536	-0.63
10	0.999	-1.274
15	1.339	-1.726
20	1.528	-1.97
25	1.799	-2.29
30	1.968	-2.562
35	1.98	-2.577

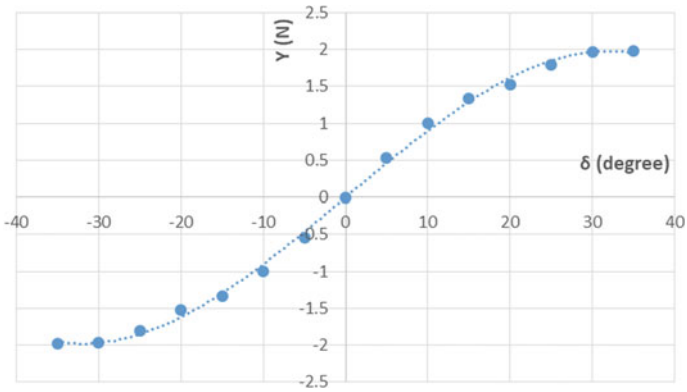


**Fig. 13** Sway force plotted against rudder angle

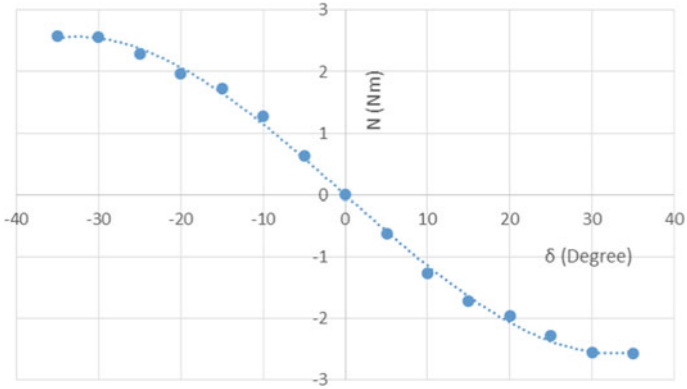


**Fig. 14** Yaw moment plotted against rudder angle

$$N'_\delta = \frac{N_\delta}{0.5\rho LwI^3 V} \tag{15}$$

$$Y'_{\delta\delta\delta} = \frac{Y_{\delta\delta\delta}}{(0.5\rho Lw^2)/V} \quad (16)$$

$$N'_{\delta\delta\delta} = \frac{N_{\delta\delta\delta}}{(0.5\rho Lw^3)/V} \quad (17)$$

Hydrodynamic rudder derivatives are obtained by differentiating the non-dimensional Eqs. 12 and 13 with respect to rudder angle,  $\delta$  at  $\delta = 0$  and equating the terms with that of Taylor series representation of force and moment. Order of differentiation depends on the order of requirement of derivatives. Expression for rudder derivatives is listed below.

$$Y'_\delta = \left[ \frac{\partial Y'}{\partial \delta'} \right] \text{ at } \delta = 0 \quad (18)$$

$$Y'_{\delta\delta\delta} = \frac{1}{3!} \left[ \frac{\partial^3 Y'}{\partial \delta'^3} \right] \text{ at } \delta = 0 \quad (19)$$

$$N'_\delta = \left[ \frac{\partial N'}{\partial \delta'} \right] \text{ at } \delta = 0 \quad (20)$$

$$N'_{\delta\delta\delta} = \frac{1}{3!} \left[ \frac{\partial^3 N'}{\partial \delta'^3} \right] \text{ at } \delta = 0 \quad (21)$$

Estimated non-dimensional rudder derivatives are given below.

$$\begin{aligned} Y'_\delta &= 0.00112811 \\ Y'_{\delta\delta\delta} &= -0.00121289 \\ N'_\delta &= -0.000466305 \\ N'_{\delta\delta\delta} &= +0.000482255 \end{aligned}$$

## 8.2 Shallow Water Condition

### 8.2.1 Sway Velocity Derivatives

Numerical simulations are repeated for shallow water condition with  $H/T = 1.5$ . Sway forces and yaw moments are estimated for different drift angles (Table 9). These values are plotted against sway velocity (Figs. 15 and 16). Third-order polynomial is fitted on the plot. This gives the cubic polynomial expression for sway force and yaw moment in non-dimensional format as

$$Y' = -0.483601 v'^3 - 0.02919 v' + 4 \times 10^{-12} \quad (22)$$

$$N' = -0.055701 v'^3 - 0.012297 v' - 3 \times 10^{-13} \quad (23)$$



**Table 9** Straight line test results

Drift angle (°)	Sway velocity $v$ (m/s)	$Y$ force (N)	$N$ moment (Nm)
0	0.000	0	0
3	-0.052	7.997	9.43
6	-0.105	15.748	19.239
9	-0.156	30.759	30.554
12	-0.208	47.585	45.031
15	-0.259	78.351	60.777
18	-0.309	108.798	78.832

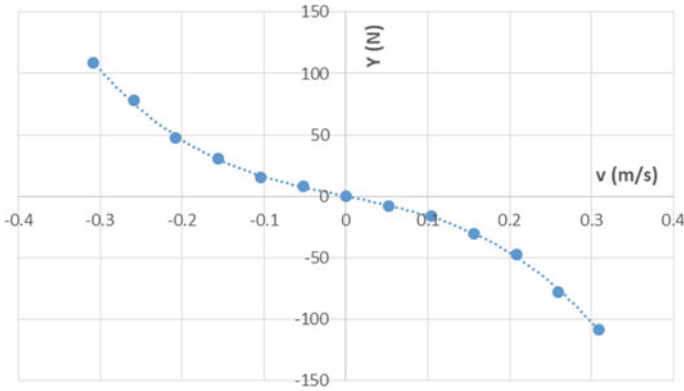


**Fig. 15** Plot of sway force against sway velocity

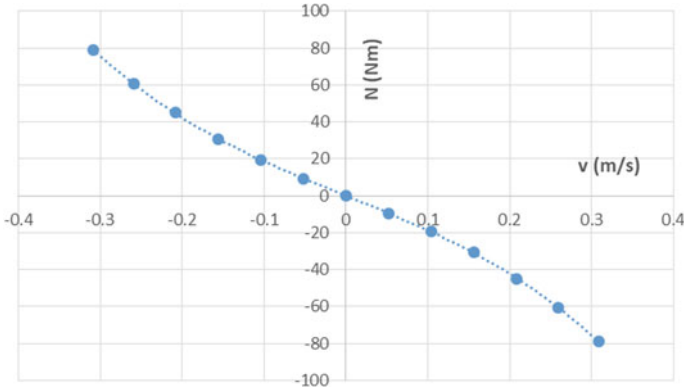


**Fig. 16** Plot of yaw moment against sway velocity

Hydrodynamic derivatives are estimated by using Eqs. 8, 9, 10 and 11. Estimated derivatives are given below.

$$Y'_v = -0.02919$$

**Table 10** Rudder forces and moments

Rudder angle $\delta$ ( $^{\circ}$ )	$Y$ force (N)	$N$ moment (N m)
0	0	0
5	0.365	-0.353
10	0.719	-0.681
15	0.999	-1.006
20	1.06	-1.153
25	1.273	-1.389
30	1.444	-1.631
35	1.499	-1.677

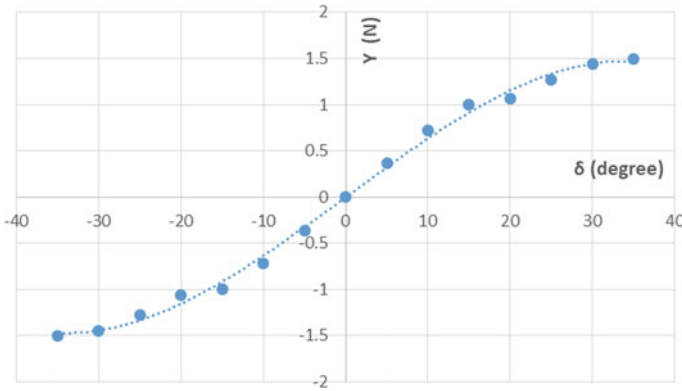


**Fig. 17** Sway force plotted against rudder deflections

$$Y'_{vvv} = -0.483601$$

$$N'_v = -0.012297$$

$$N'_{vvv} = -0.055701$$

### 8.2.2 Rudder Derivatives

Rudder derivatives are estimated by measuring the sway force and yaw moment acting at the centre of gravity of the vessel in shallow water condition (Table 10). These values are plotted against rudder angle (Figs. 17 and 18). Third-order polynomial curve is fitted on the graph and is represented in non-dimensional format as below.

$$Y' = -0.000758721 \delta'^3 + 0.00079154 \delta' - 4 \times 10^{-14} \tag{24}$$

$$N' = 0.000199038 \delta'^3 - 0.00026332 \delta' - 2 \times 10^{-12} \tag{25}$$

The derivatives are estimated by taking the slope of the curve at  $\delta = 0$  by using Eqs. 14, 15, 16 and 17. Rudder derivatives estimated are given below.

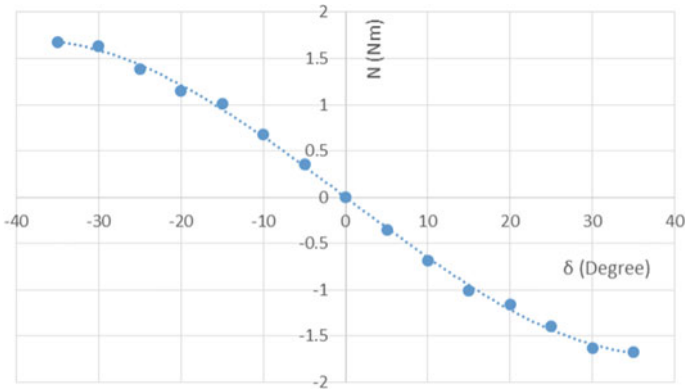


Fig. 18 Yaw moment plotted against rudder deflections

$$\begin{aligned}
 Y'_\delta &= 0.00079154 \\
 Y_{\delta\delta\delta} &= -0.000758721 \\
 N'_\delta &= -0.00026332 \\
 N'_{\delta\delta\delta} &= +0.000199038
 \end{aligned}$$

## 9 Summary and Conclusion

In the present study, straight line tests are conducted with different drift angles and rudder angles for both deep water and shallow water conditions. Numerical analysis clearly indicates the influence of water depth on these hydrodynamic derivatives. Sway velocity derivatives  $Y'_v$  and  $N'_v$  in shallow water show a variation of  $-112.65$  and  $-121.18\%$ , respectively, compared to that in deep water condition. Third-order derivatives  $Y'_{vvv}$  and  $N'_{vvv}$  show drastic variation of  $-562.73$  and  $-542.66\%$  from deep water to shallow water condition. Shallow water effect has a negative influence on the rudder performance too, as expected due to the inferior flow conditions.  $Y'_\delta$  and  $N'_\delta$  in shallow water are  $26.3$  and  $44.1\%$  higher than that in deep water.  $Y'_{\delta\delta\delta}$  and  $N'_{\delta\delta\delta}$  also follow the same trend and varies  $37.45$  and  $60.6\%$ , respectively, when water depth changes from deep to shallow. The numerical study clearly shows the effects of water depth on the manoeuvring performance of the container ship. This study can be further extended by estimating the acceleration derivatives and by simulating the turning trajectory of the vessel.

## References

1. Inoue S, Hirano M, Kijima K (1981) Hydrodynamic derivatives on ship maneuvering. *Int Ship Building Prog* 28(321):112–125
2. Kijima K, Nakari Y, Furukawa Y (2000) On prediction method for ship manoeuvrability. In: *Proceedings of international workshop on ship manoeuvrability at Hamburg ship model basin*, paper no. 7, Hamburg, Germany
3. Carrica PM, Ismail F, Hyman M, Bhushan S, Stern F (2013) Turn and zig-zag maneuvers of surface combatant using URANS approach with dynamic overset grids. *J Mar Sci Technol* 18:166–181
4. Cura-Hochbaum A (2011) On the numerical prediction of the ship's manoeuvring behaviour. *Ship Sci Technol* 5(9):27–39
5. Delefortrie G, Vantorre M (2007) Modeling the maneuvering behaviour of container carriers in shallow water. *J Ship Res* 51(4):287–296
6. ITTC recommended procedures (2011) Guidelines on use of RANS tools for ManeuverinPrediction. In: *Proceedings of 26th ITTC*

# Numerical Investigation of Influence of Microbubble Injection, Distribution, Void Fraction and Flow Speed on Frictional Drag Reduction



Sudhir Sindagi, R. Vijayakumar, Somanath Nirali and B. K. Saxena

**Abstract** The increase in fuel costs and looming restrictions on carbon dioxide emissions are driving the shipowner into reducing the ship's resistance and required installed power. It was earlier reported that, merchant vessels operating at lower speeds, the frictional drag accounts of almost 70–80% of the total drag; thus, there is a strong demand for the reduction in the fluid frictional drag, especially in the marine transportation business. The use of air as a lubricant, by injecting below the plate or the body, which is famously known as microbubble drag reduction (MBDR) in order to reduce that frictional drag is an active research topic. Latest developments in this field suggests that there is a potential reduction of 80% in frictional drag in case of flat plates and about 30% reduction in case of ships, which encourages researchers to investigate further. In this study, 3D numerical investigations into frictional drag reduction by microbubbles were carried out in Star CCM+ on a channel for different flow velocities, different void fractions and different cross sections of flow at the injection point. This study is the first of its kind in which variation of coefficient of friction both in longitudinal and transverse directions was studied along with actual localized variation of void fraction at these points. The numerical framework consists of the Reynolds-averaged Navier–Stokes (RANS) equations and the standard  $k-\varepsilon$  turbulence model with standard wall function treatment, which is validated in both conditions of with and without microbubbles with the existing experimental data. The design exploration study was carried out for various flow speeds, injector flow rates, cross sections of the channel/heights of channels and of

---

S. Sindagi (✉) · S. Nirali · B. K. Saxena  
Tolani Maritime Institute, Pune, India  
e-mail: [sindagi@gmail.com](mailto:sindagi@gmail.com)

S. Nirali  
e-mail: [somnathnirali@gmail.com](mailto:somnathnirali@gmail.com)

B. K. Saxena  
e-mail: [brjendras@tmi.tolani.edu](mailto:brjendras@tmi.tolani.edu)

R. Vijayakumar  
Indian Institute of Technology Madras, Chennai, India  
e-mail: [vijay2028@iitm.ac.in](mailto:vijay2028@iitm.ac.in)

course void fractions. Coefficient of friction and void fraction values are measured at 12 longitudinal positions, and at each longitudinal position, 11 in number transverse and 10 in number depthwise positions were studied. In all, for one simulation, data at more than 1000 positions were collected. More than 60 simulations were carried out to understand the effect. From the study, it is concluded that since it is a channel flow and as the flow is restricted in confined region, effect of air injection is limited to smaller area in transverse direction as bubbles were not escaping in transverse direction.

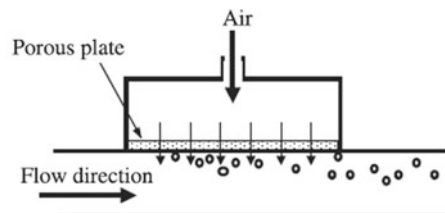
**Keywords** MBDR · Microbubbles · Frictional drag reduction

## 1 Introduction

Vehicles moving in water experience more frictional drag than vehicles on land or in the air, as the viscosity of water is higher than that of air. The increase in fuel costs and looming restrictions on emissions are driving the shipowner into reducing the ship's resistance and required installed power. It is reported that the fluid frictional drag accounts for as much as 60% of the total drag for cargo ship, and about 80% of that for a tanker; thus, there is a strong demand for the reduction in the fluid frictional drag. Numerous technologies [1], such as use of the micromorphology riblets, use of polymers, use of heating wall and vibrating the flexible wall, partial cavity creation, antifouling and coatings and super-hydrophobic surface and MBDR, have been studied and utilized to reduce the frictional drag of a surface. As shown in Fig. 1, MBDR effect is realized by injecting gas or air below the moving object (plate, ship, etc.).

This leads to two distinct drag-reducing phenomena: the bubble drag reduction and the air layer drag reduction. Experimental results of the air bubble drag reduction show that a significant drag reduction of greater than 25% could be made in the first few metres downstream of injection, and by gas layer formed on the underside of the flat plate, reduction of greater than 80% was measured. It is concluded that, MBDR has added advantages over other drag-reducing technologies, such as environmental-friendly, easy operation, low costs and high saving of energy. It is also reported that the MBDR is able to achieve 80% reduction in frictional drag, which can result in

**Fig. 1** Schematic drawing of a microbubble injecting system



a substantial fuel savings for both commercial and naval ships. The most significant contribution regarding microbubble drag reduction was presented McCormick and Bhattacharyya [2] by demonstrating hydrogen bubbles generated by electrolysis to reduce frictional drag on a fully submerged body of revolution. Experimental studies [3–7] on flat plate have been carried out to understand the effect of air lubrication on reduction of drag. Numerical simulation/numerical model of MBDR [4, 8–17] for the flat plate has been developed to understand the effect, while similar studies on the ship model [18–24] have been carried out. Numerical model employed in the investigation comprises of a microbubble laden flow, wherein two independent sets of Reynolds-averaged Navier–Stokes (RANS) transport equations were used to describe both phases of the flow. The shear stress transport (SST) turbulence model or a standard  $k-\omega$  turbulence model were used as the turbulent closure for the primary phase, and a zero-equation turbulence model is used for the microbubbles. Multiple-size group (MUSIG) based on population balance models, which resolves a wide range of bubble sizes taking into account the bubble break-up and coalescence, has been used [10] for the simulation.

In this study, numerical investigations into frictional drag reduction by microbubbles were carried out in a channel for different flow velocities, different void fractions and different cross sections of flow at the injection point. This study is the first of its kind in which variation of coefficient of friction both in longitudinal and transverse directions was studied along with actual localized variation of void fraction at these points. The numerical framework consists of the Reynolds-averaged Navier–Stokes (RANS) equations and the standard  $k-\varepsilon$  turbulence model with standard wall function treatment, which is validated in both conditions of with and without microbubbles by the existing experimental data. These simulations were aimed at understanding the mechanism of resistance reduction. Flow parameters were changed by changing the pressure and/or velocity of flow at the injector location by changing the depth of channel at the point of injection. The influence of bubble distribution near a wall, which directly controls the void fraction, was also investigated. The design exploration study was carried out for various flow speeds, injector flow rates, cross sections of the channel/heights of channels and of course void fractions.

## 2 Numerical Set-up and Validation with Experimental Results

### 2.1 *Enhancements Over Experimental Investigation Using CFD*

The experimental study was conducted by [25] using recirculating water channel shown in Fig. 2. The test section, which is 10 mm high, 100 mm wide and 2000 mm long, generates a fully developed turbulent flow. Compressed air was injected into the channel for different flow rates, and its effect was measured using shear stress

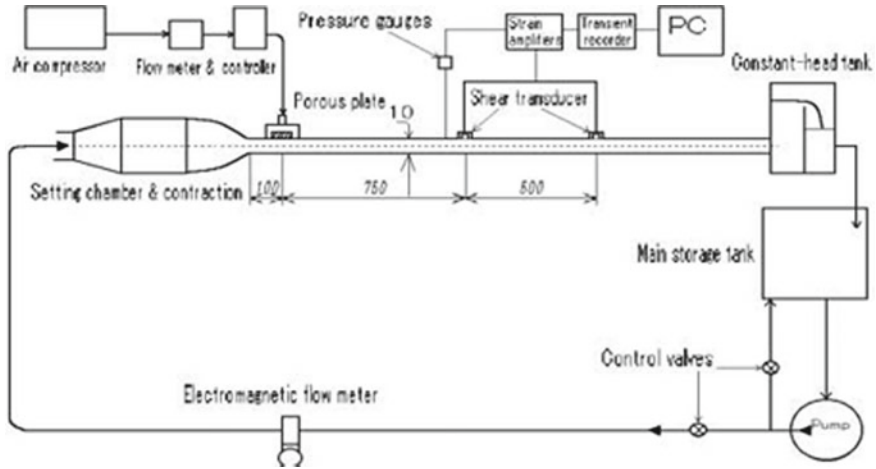


Fig. 2 Experimental set-up used for the investigation of MBRD by Moriguchi and Kato [25]

transducers placed at 750 and 1250 mm from the injection point. Similar set-up is used here to enhance the study using CFD technique. The experimental investigation was carried out at only two longitudinal locations, and no observation was made at spanwise locations, which is easily possible in CFD technique. In the numerical set-up, microbubbles were injected through series of holes of 1 mm in diameter in the test section at the upstream upper surface, generating air–liquid flow. Coefficient of friction and void fraction values were measured at 12 longitudinal positions, and at each longitudinal position, 11 in number transverse and depthwise positions were observed. In all, for one simulation, data at more than 1000 positions were collected. As shown in Table 1, simulations were performed at flow velocities ranging 4–7 m/s in the interval of 1 m/s, and at different airflow rates (12 values of void fraction). More than 60 simulations were carried out to study the effect of these flow parameters on coefficient of friction. Effect on  $C_F$  was also studied by changing the depth of channel at the injection point, which changes flow parameters. Here, as  $C_F$  values for different cases of injection of bubbles depend on the instance of time, they are normalized by averaging  $C_F$  values for time. In all,  $C_F$  value at one location is calculated by averaging their values for more than 1000 iterations, once the solution is converged.



**Table 1** Flow velocities and void fractions for which simulations carried out along with positions at which  $C_F$  being calculated

Flow speed of water	Void fraction	Longitudinal positions of $C_F$ being measured (mm)	Transverse positions of $C_F$ being measured (on one side of CL) (mm)	Distance from wall (mm)
4	0.015	100	0	0
5	0.03	200	1	1
6	0.045	350	2	2
7	0.06	400	3	3
	0.075	500	4	4
	0.09	600	5	5
	0.105	700	-1	6
	0.115	750	-2	7
	0.135	800	-3	8
	0.14	900	-4	9
		1000	-5	10
		1250		

## 2.2 Grid Independency Study and Numerical Set-up

The numerical and mesh set-up used for this exhaustive study is shown in Figs. 3 and 4. Grid independency study was also carried out to optimize and finalize the meshing. Initially, uniform mesh was generated throughout the channel, which, based on flow regime of air bubbles, is optimized for the further study. Dense meshing was generated for both with and without injection of air till no change in final result is obtained. Optimized mesh is shown in Fig. 4. For the simulation of three-dimensional, implicit unsteady segregated flow, volume of fluid (VOF) approach was used to solve Reynolds-averaged Navier–Stokes (RANS) equations and Eulerian multiphase equations of state with multiphase interactions based on density and surface tension of air and water. To account for the boundary layer effect, exact wall distance, two layer all  $y+$  wall treatment and realizable K-epsilon two-layer approaches were effectively utilized. For the simulation of turbulence, K-epsilon turbulence model was used. Velocity inlet boundary condition was used to set up the flow velocity of water at water inlet boundary. Similarly, for setting up of air inlet, mass flow rate boundary condition was used. At the outlet, pressure outlet boundary condition is used. For all other sides of channel, typical wall boundary condition with no slip condition was used.

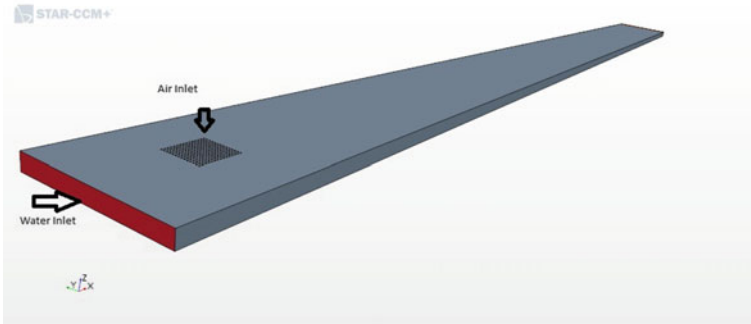


Fig. 3 Geometry used for simulations

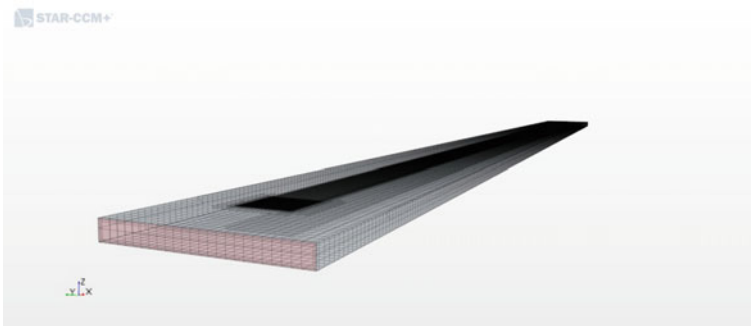


Fig. 4 Optimized mesh used for simulations

### 2.3 Validation of CFD Results with Experimental Results

Figure 5 shows the comparison of  $C_{F0}$  values with experiment without injection of air at a location of 750 mm from the injection point. Moreover, Figs. 6, 7 and 8 show the comparison of reduction in  $C_F$  values with experimental values, with and without injection of air at flow speed of 5, 6 and 7 m/s, respectively. Here,  $C_{F0}$  refers to the coefficient of friction without the injection of bubbles and  $C_F$  refers to coefficient of friction with the injection of bubbles. The value of  $C_F$  is calculated using

$$C_F = \frac{\tau_w}{\frac{1}{2}\rho_m U_m^2}$$

where  $\tau_w$ —shear stress,  $\rho_m$ —mean density of flow and  $U_m$ —mean flow velocity.

It is the general practice to show reduction in friction drag against the void fraction or volume fraction represented as

$$\text{Void Fraction or Volume Fraction (VF)} = \frac{Q_a}{Q_a + Q_w}$$

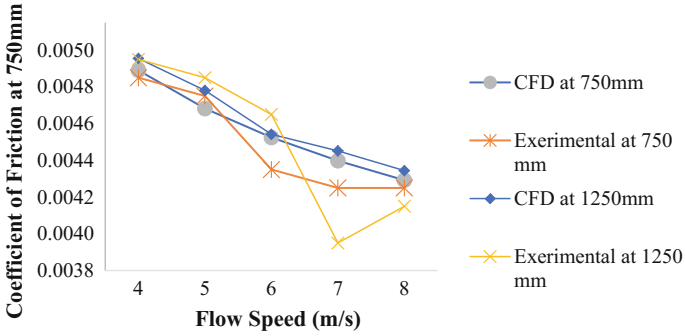


Fig. 5 Comparison of  $C_F$  values with experiment, without injection of air

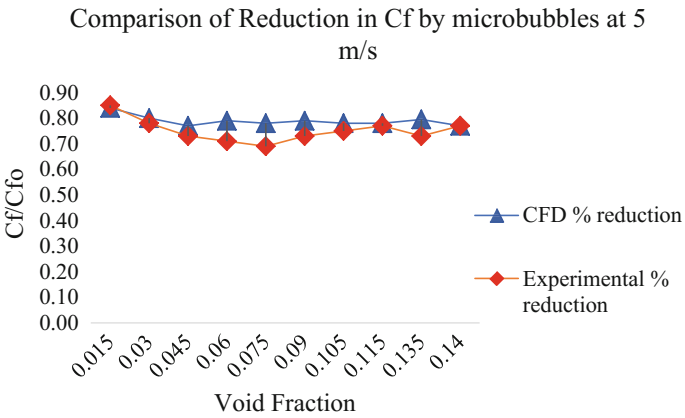


Fig. 6 Comparison of reduction in  $C_F$  with experiment, with and without injection of air at flow speed of 5 m/s

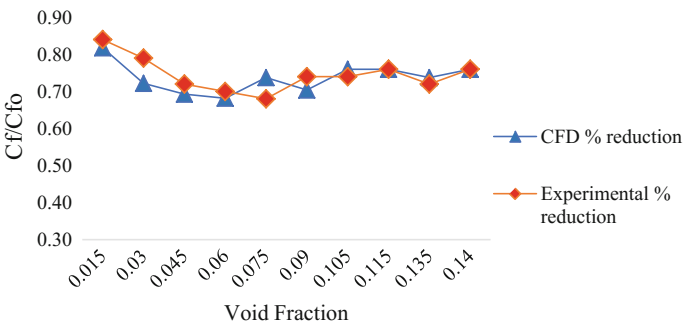
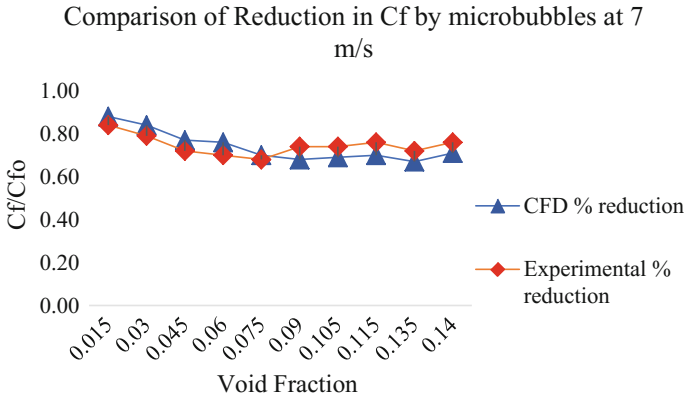


Fig. 7 Comparison of reduction in  $C_F$  with experiment, with and without injection of air at flow speed of 6 m/s



**Fig. 8** Comparison of reduction in  $C_F$  with experiment, with and without injection of air at flow speed of 7 m/s

where  $Q_a$ —air injection rate and  $Q_w$ —water flow rate.

From the comparison made, it can be seen that the simulation results obtained match closely with experimental results. Moreover, due injection of air below the plate causes reduction in the frictional drag. Reduction obtained depends on many factors such as void fraction, flow speed and location of point of analysis from the injection point. From these figures, it can be concluded that maximum reduction obtained due to injection of microbubbles is 33%, which also matches with experimental results.

### 3 Results and Discussion

#### 3.1 Investigation of Alteration of Flow Parameters Due to Injection of Microbubbles

Frictional drag of any body is given by the expression

$$R_F = C_F \frac{1}{2} \rho S V^2$$

From the above expression, it can be concluded that to reduce the frictional drag, one must reduce  $C_F$ , density of liquid ( $\rho$ ) flowing and the wetted surface area ( $S$ ). As seen from the previous experiments based on MBDR, it is clearly mentioned that combined effect of reduction in density and wetted surface area along with reduction in  $C_F$  due to alteration of flow properties and modification of turbulent momentum transport due to the presence of bubbles causes considerable reduction in frictional

drag. When air is injected into the boundary layer, an air–water mixture flow containing both air bubbles and water can be formed. If the amount of injected air increases, air bubbles begin to coalesce into patches that cover the surface continuously, and a transitional air layer is formed, where the patches coexist with air bubbles. If the flow rate of air is further increased, a continuous layer of air layer is formed, reducing the direct contact of water with the surface. Formation of continuous layer of air is the ultimate thing, reducing density of fluid from water to air. As observed from Fig. 9, the density variation is plotted against time at a location of 750 mm from the injection point. From Fig. 9, it can be concluded that the reduction in density is almost of the order of 45% which is causing the reduction in frictional drag. The shear stress developed due to viscosity of liquid can be estimated by using

$$\tau_w = \mu \frac{du}{dy} - \rho U' V'$$

However,  $U' V' = -q \Lambda \frac{\partial u}{\partial y}$

By substitution, we get

$$\tau = (\mu + \rho q \Lambda) \frac{\partial u}{\partial y}$$

where  $q \Lambda$  is eddy viscosity,  $q^2$  is turbulence energy, and  $\Lambda$  is energy containing turbulent scale. This shows that microbubble drag reduction is the result of three factors: reduction of density, increase of bubble suspension viscosity as the concentration approaches the packing limit and turbulence modification of the boundary layer. When air bubbles are present, the density of mixture decreases and accordingly shear stress is reduced. The second term in the above equation is known as Reynolds stress, which reduces as the density ( $\rho$ ) decreases. From Figs. 10 and 11, it can be concluded that the reduction in turbulent viscosity, dynamic viscosity at the

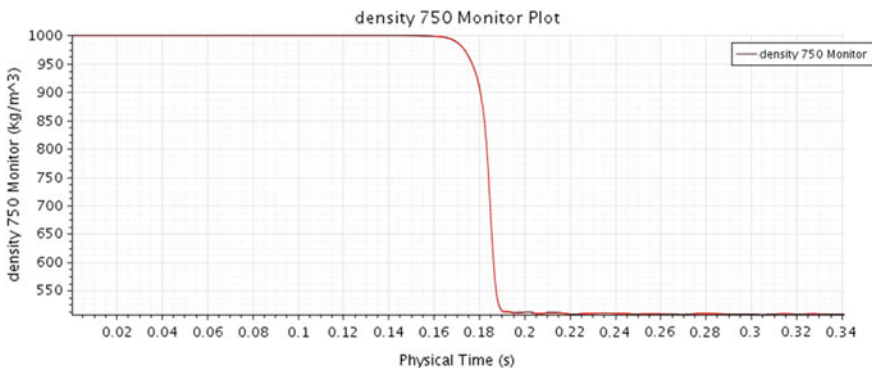


**Fig. 9** Variation of effective density of flow at 750 mm with respect to time at flow speed of 5 m/s and void fraction of 0.035

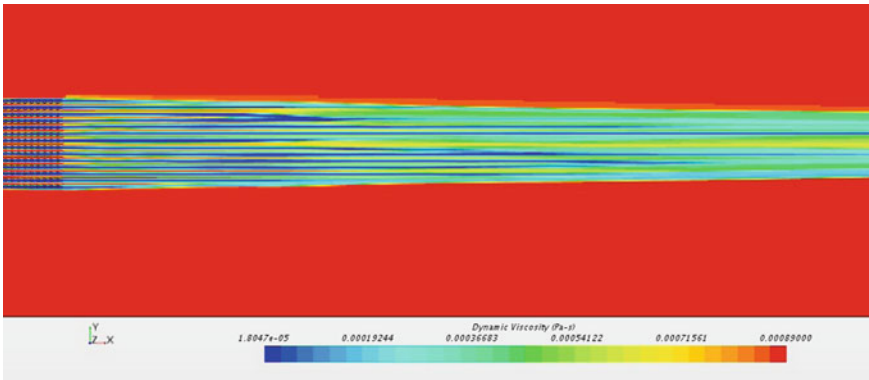


**Fig. 10** Variation of dynamic viscosity at flow speed of 6 m/s and void fraction of 0.105

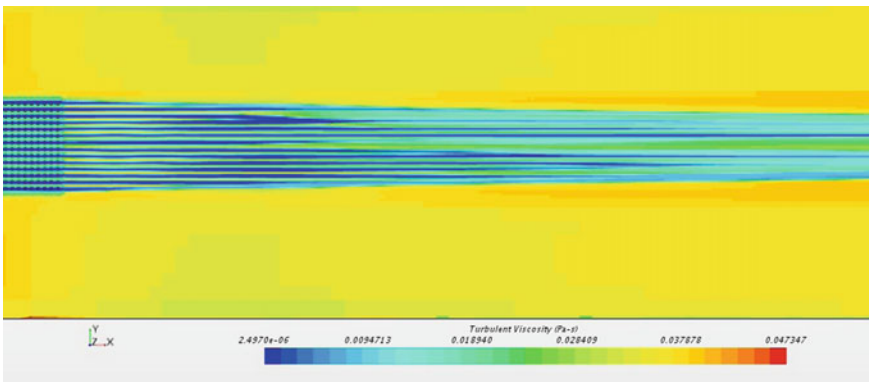


**Fig. 11** Variation of turbulent viscosity at flow speed of 6 m/s and void fraction of 0.105

localized area along with reduction in density due to injection of microbubbles, is causing reduction in  $C_F$  values.

Similarly, as presented in Figs. 12 and 13, other reasons for the reduction in the frictional drag are reduction in turbulent viscosity and increase in the turbulence dissipation rate due to the injection of bubbles. Reduction in density along with reduction in turbulent viscosity and increase in the turbulence dissipation rate are causing reduction in the frictional drag.

To conclude, MBDR effect is due to the alteration of local effective viscosity and density of the fluid along with the increase in turbulence dissipation rate reduces the Reynold's stress and in turn reduces the shear stress.

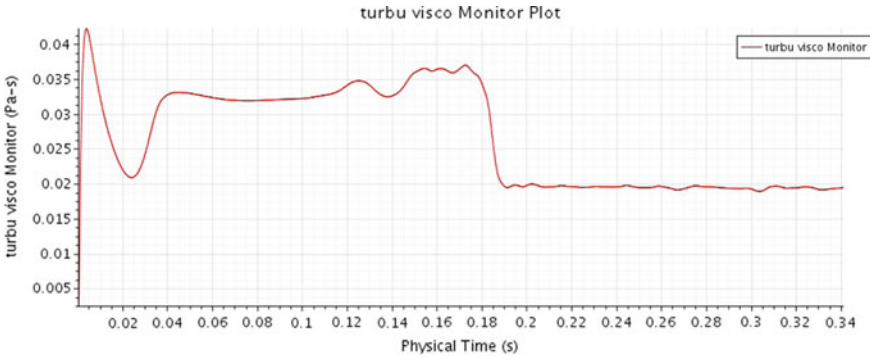


**Fig. 12** Variation of turbulent viscosity at 750 mm with respect to time at flow speed of 5 m/s and void fraction of 0.035

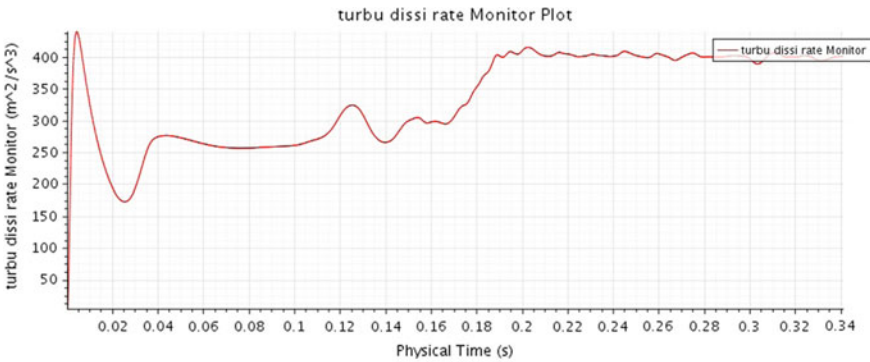


**Fig. 13** Variation of turbulence dissipation rate at 750 mm with respect to time at flow speed of 5 m/s and void fraction of 0.035

### 3.2 Study at Flow Speed of 6 m/s at Different Void Fractions

Figures 14 and 15 describe the variation of  $C_F$  values in longitudinal and transverse directions for two values of void fractions of 3 and 10.5%. From these figures, it can be concluded that with the increase in distance from the injection point in the longitudinal direction,  $C_F$  value increases, which is a general trend observed in many experiments. It means that the MBDR effect reduces with the increase in distance from the injection point. The transverse variation of MBDR effect is also observed very closely in the simulation. From these simulation results, it can be concluded that  $C_F$  value reduces with the increase in transverse distance from the centre line of channel. This reconfirms that MBDR effect reduces with the distance from the injection point both in longitudinal and transverse directions. Moreover, from Figs. 16 and 17, it can be seen that injected air converges to a smaller area in the transverse direction. This is in fact due the effect of boundary layer formation

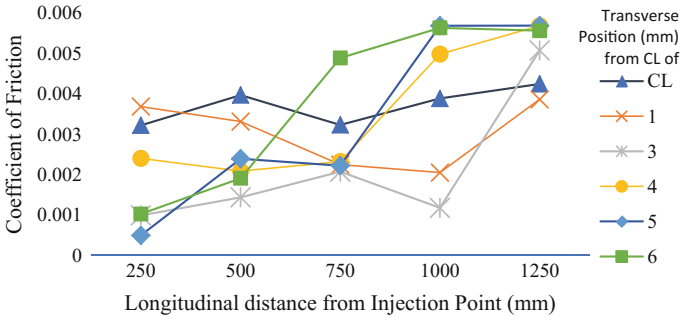


**Fig. 14** Variation of  $C_F$  for flow speed of 6 m/s and volume fraction of 0.03

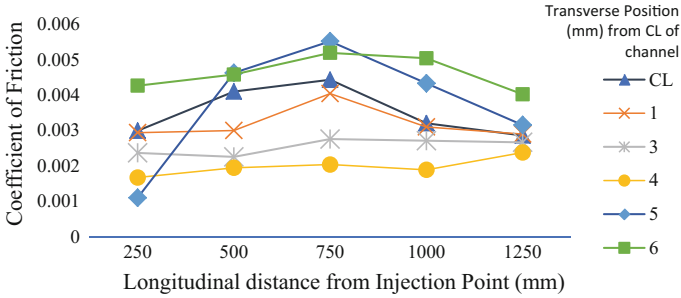
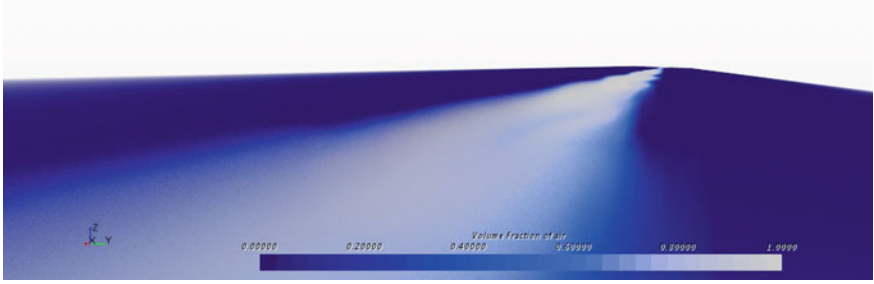


**Fig. 15** Variation of  $C_F$  for flow speed of 6 m/s and volume fraction of 0.105

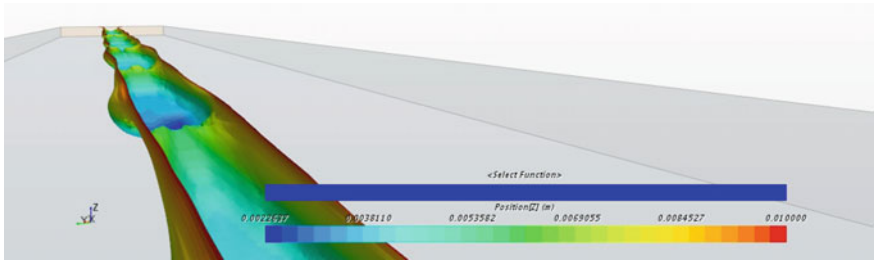
from side plates of channel. Hence, in case of rectangular channel, the MBDR effect is limited to smaller area in transverse direction. This clarifies that unlike in case of free flow to the sideways, wherein the bubbles escape in sideways, the bubbles are restricted to move in smaller area. Similar observation is made in Fig. 15, wherein  $C_F$  value increases with the distance from centre line of channel and it is maximum at a distance of 6 mm from the centre line. Interesting observation has been made from Fig. 15 that  $C_F$  value reduces after 750 mm from the injection point. This may be due to the fact that since bubbles are not escaping from the sides and as they are converging to smaller area of flow, possibly this concentration of bubbles is causing further reduction in  $C_F$  values. Similar conclusion can be made from Fig. 14.

Figure 17 also depicts that as the distance increases in the longitudinal direction, bubbles coalesce with each other and form air pockets. This is the major reason for variation in  $C_F$  values in longitudinal direction, as bubbles coalesce to form air pockets avoiding any contact of water with the surface and thus reducing the coefficient of friction. Figure 18 describes the longitudinal variation of  $C_F$  values for different values of void fraction. From Fig. 18, it can be concluded that  $C_F$  value decreases till void fraction is of 7.5%, beyond which these values start increasing. This may be due to the additional turbulence created by the injection of air bubbles.





**Fig. 16** Variation of volume fraction of air both in transverse and longitudinal directions



**Fig. 17** Variation of volume fraction of air both in all directions

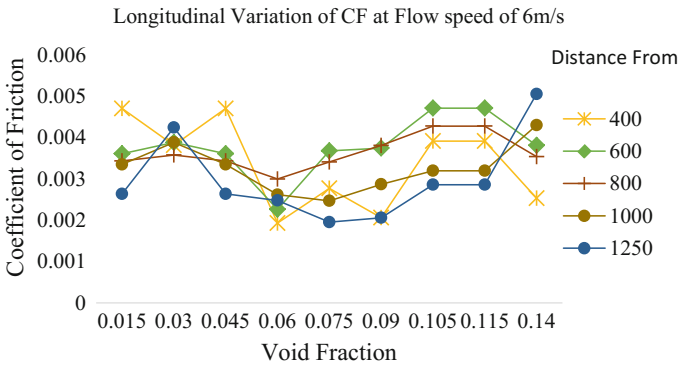


**Fig. 18** Longitudinal variation of  $C_F$  at flow speed of 6 m/s and different void fraction

To conclude, as the MBDR effect depends upon the presence of microbubbles,  $C_F$  values keep varying from point to point and do not follow any particular pattern.

Figure 19 describes variation of  $C_F$  values at different longitudinal and transverse locations for flow speed of 6 m/s and VF 11.5%, which clearly shows that  $C_F$  values increase with the increase in longitudinal and transverse distances from the air injection point. Moreover, it can be seen that there is a variation in  $C_F$  values in

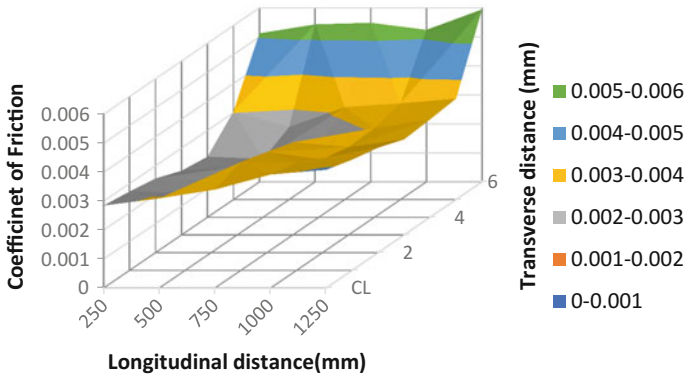


**Fig. 19** Variation of  $C_F$  at different longitudinal and transverse locations at flow speed of 6 m/s and VF 11.5%

longitudinal direction, which is mostly due to coalescence and breaking of bubbles with the distance from the injection point.

### 3.3 Study at Flow Speed of 5 m/s at Different Void Fractions

As mentioned earlier, investigation of MBDR effect was carried out at 5 m/s. From Fig. 20, it can be concluded that MBDR effect reduces with its distance from the injection point. Increase in effect at location 1250 mm from the injection point is due to the concentration of air bubbles at the location. As shown in Fig. 21 and similar to observation made at flow speed of 6 m/s, MBDR effect reduces with the increase in distance from the injection point in transverse direction. Investigation of MBDR effect in longitudinal direction along with variation of void fraction clarifies that for the void fraction value of 2%, where injection rate is very low, MBDR effect is low. With the increase in void fraction, MBDR effect increases, reaches to maximum and then further reduces. This may be due to the increase in turbulent viscosity caused due to the additional momentum created by injection of bubbles in the flow at higher rate.

To conclude, the distance from the injection point is the most important parameter in obtaining the reduction in frictional drag and that the boundary layer thickness of top plate has little effect on the skin friction reduction by microbubbles.

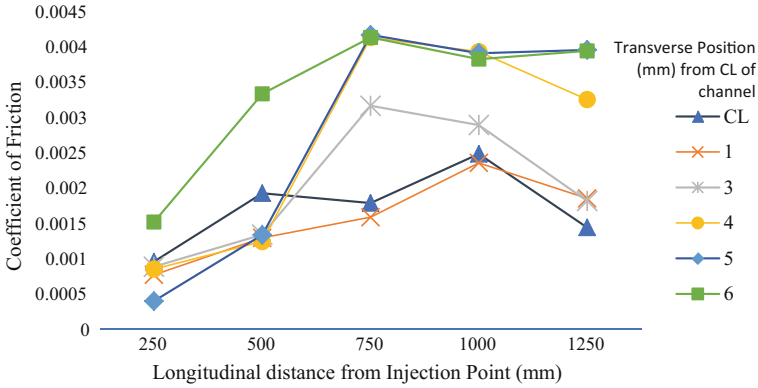


Fig. 20 Variation of  $C_F$  for flow speed of 5 m/s and volume fraction of 0.035

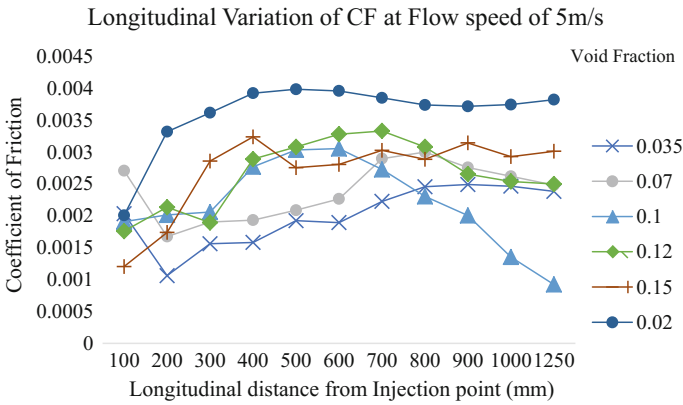


Fig. 21 Longitudinal variation of  $C_F$  at flow speed of 5 m/s and different void fraction

### 3.4 Study at Flow Speed of 7 m/s at Different Void Fractions

Figure 22 represents the variation of  $C_F$  values in longitudinal and transverse directions for flow speed of 7 m/s at void fraction of 9%. Interesting conclusion can be made from these results. Maximum MBDR effect occurs at a distance of 3 mm from the centre line and not at the centre line. Of course, the effect reduces with distance from the centre line. Figure 23 represents the variation of  $C_F$  values in longitudinal direction for flow speed of 7 m/s at different values of void fraction. From the figure, it can be concluded that MBDR effect is maximum at void fraction of 6%. The effect is minimum at void fraction of 3%, reaches to maximum value at 6% and again reduces at 9%. This implies that MBDR effect does not increase with the increase in airflow rate. At higher injection rate, it increases the turbulence of the flow, which alters the flow parameters increasing the frictional drag. In other words, to conclude,

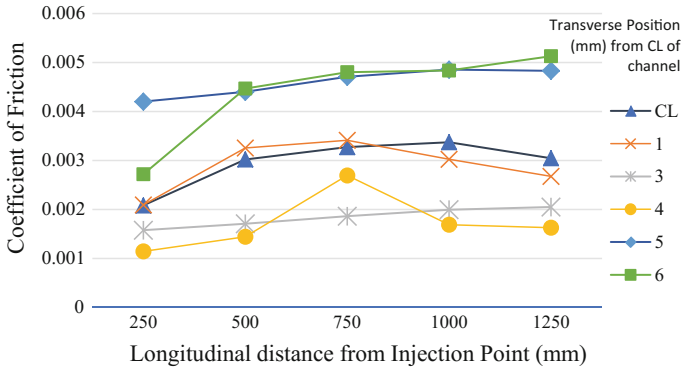


Fig. 22 Variation of  $C_F$  for flow speed of 7 m/s and volume fraction of 9%

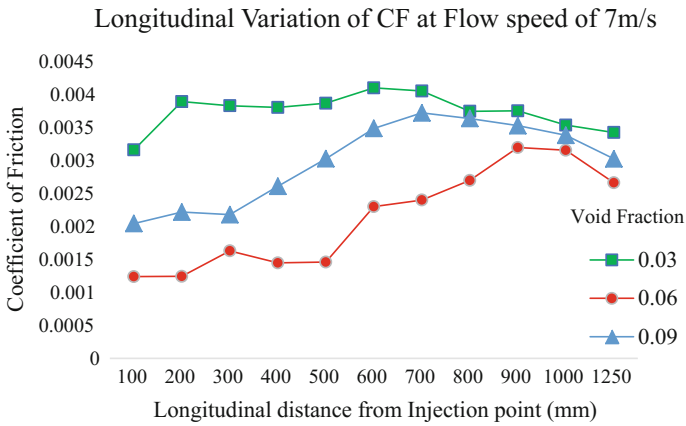


Fig. 23 Longitudinal variation of  $C_F$  at flow speed of 7 m/s and different void fraction

excessive microbubble injection destroys the favourable turbulent boundary layer and in doing so decreases the drag reduction effect.

### 3.5 Variation of $C_F$ Values in the Longitudinal Direction for Different Speeds and VF

Investigation on effect of flow speed on MBDR effect in longitudinal direction for different void fractions was carried out. From Figs. 24 and 26, it can be concluded that for void fraction values of 3 and 9%, in general, MBDR effect is more for a flow speed of 5 m/s giving lowest values of coefficient of friction. However, as shown in Fig. 25, in general, MBDR effect was found to be maximum at higher speed of

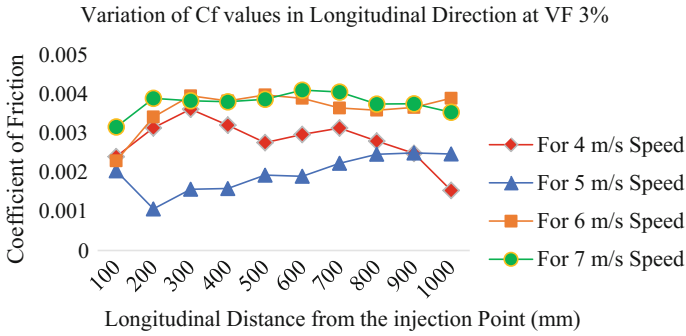


Fig. 24 Variation of  $C_F$  values in longitudinal direction for different flow speeds at VF of 3%

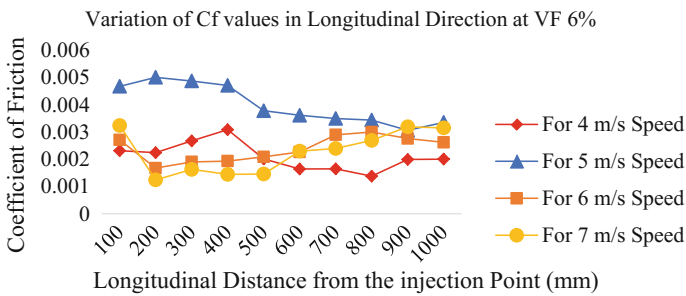


Fig. 25 Variation of  $C_F$  values in longitudinal direction for different flow speeds at VF of 6%

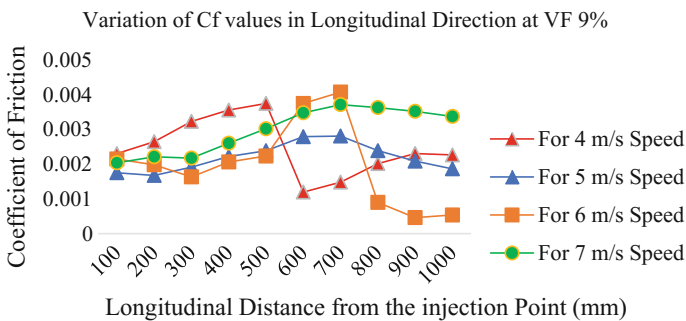


Fig. 26 Variation of  $C_F$  values in longitudinal direction for different flow speeds at VF of 9%

7 m/s at void friction of 6%. In most of the cases, MBDR effect reduced with the increase in distance from the injection point, except for few cases at void fraction of 9%, wherein MBDR effect increased from a point having distance 800 mm onwards for speed of 7 m/s and 600 mm onwards for 4 m/s.

To conclude, MBDR effect mostly depends on local void fraction than the injection void fraction. As mentioned previously, local void fraction depends on the coales-

cence and breaking of bubbles. Formation of air pockets increases the local void fraction and in turn reduces coefficient of fraction, which has been found in many cases, wherein MBDR effect was found to be more after certain distance from the injection point.

### 3.6 Variation of $C_F$ Values in Transverse Direction for Different Speeds and VF

Similar investigation on effect of flow speed on MBDR effect in transverse direction for different values of void fraction was carried out. From Figs. 28 and 29, it can be concluded that for void fraction values of 6 and 9%, MBDR effect reduced with the increase in distance from the injection point. For the case at void fraction of 3% (Fig. 27), similar observation was made for lower speeds of 4 and 5 m/s. However, at higher speeds, due to more turbulence created, air bubbles distributed more in spanwise direction, causing the increase in MBDR effect in spanwise direction. Moreover, MBDR effect is found to be more at lower speed of 4 m/s for VF 6%; however, for other cases of VF, similar trend could not be obtained, which implies that MBDR effect solely depends on local void fraction.

To conclude, MBDR effect quickly reduces in the streamwise direction at immediate downstream of injection and gradually decreases further downstream. In the spanwise direction, there is no constant reduction region and the reduction effect reduces linearly towards the side end.

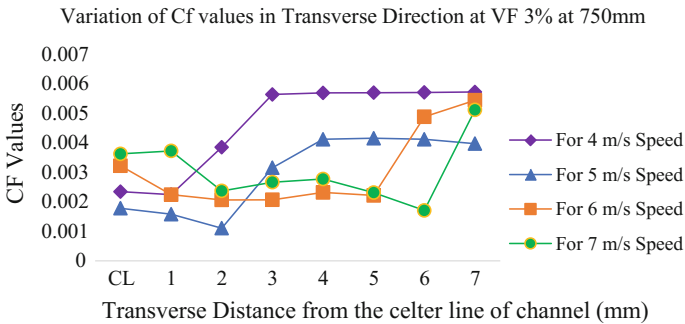


Fig. 27 Variation of  $C_F$  values in transverse direction for different flow speeds at VF of 3%

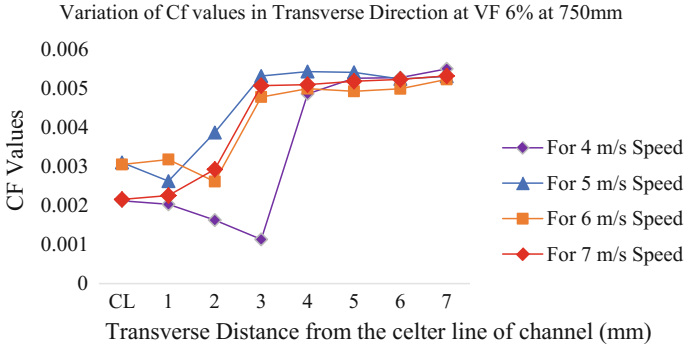


Fig. 28 Variation of  $C_F$  values in transverse direction for different flow speeds at VF of 6%

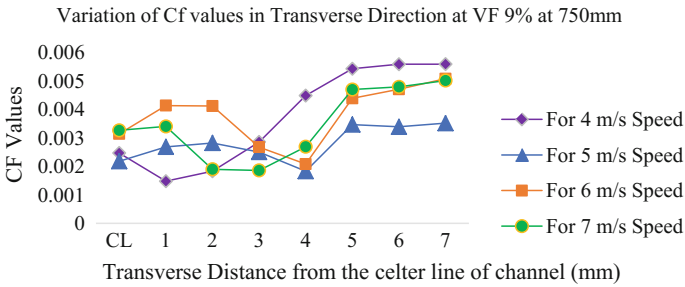


Fig. 29 Variation of  $C_F$  values in transverse direction for different flow speeds at VF of 9%

### 3.7 Investigation of Alteration of Flow Parameters and $C_F$ Values for Different Depths of Channel at the Injection Point

It is well-known fact that diameters of microbubbles generated depend on the flow parameters at the injection point. Hence, to investigate this effect, three different channels have been studied. All three channels have the same test section height of 10 mm throughout the length except at the injection point. Channel 1 has an air injection channel height of 10 mm at the injection point, Channel 2 has an air injection channel height of 5 mm at the injection point, and Channel 3 has an air injection channel height of 20 mm at the same point. Channels 2 and 3 are shown in Fig. 30 along with velocity distribution throughout the length. Investigation has been carried out to check the changes in MBDR effect due to this variation in flow parameters for three different speeds of 5, 6 and 7 m/s at constant volume fraction of 6%.

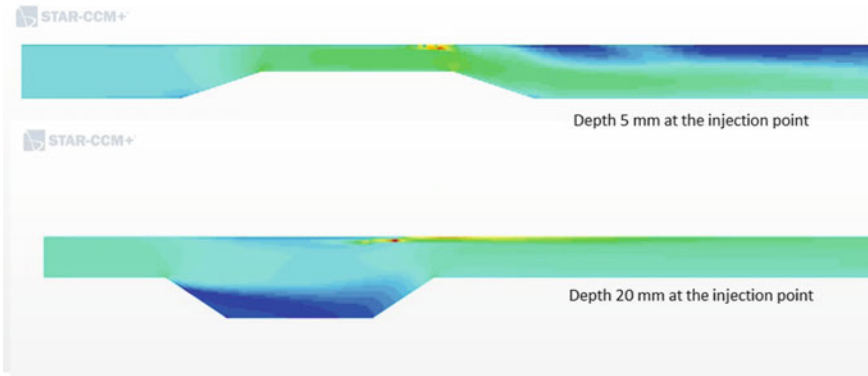


Fig. 30 Channels 2 and 3 with velocity distribution

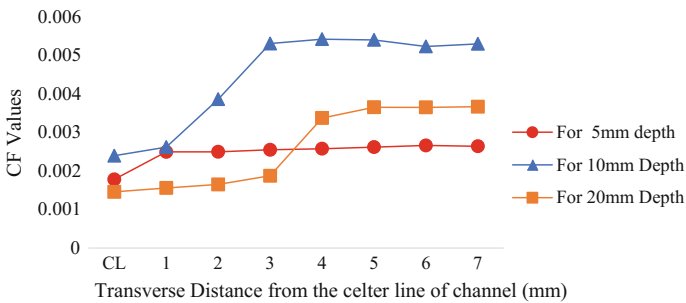
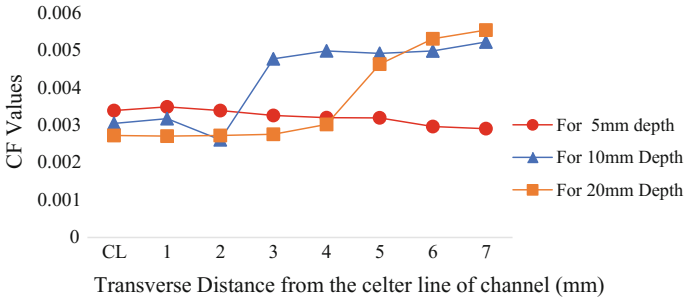


Fig. 31 Variation of  $C_F$  values in transverse direction at VF 6% at 750 mm and at flow speed of 5 m/s for different depths of channel

Figures 31, 32 and 33 show the variation of  $C_F$  values in transverse direction at 750 mm from the injection point and at constant value of volume fraction of 6% for different flow speeds of 5, 6 and 7 m/s, respectively, of course for different depths of channel. From these figures, it can be safely concluded that 5 mm depth at the injection point gives best results for the MBDR effect, attaining minimum values of coefficient of friction. Moreover, it can be seen that for 5 mm depth of channel, MBDR effect is almost equal in transverse direction. Also, it can be observed that MBDR effect is maximum for lower flow speed of 5 m/s as compared to other speeds. At higher flow speeds, additional turbulence created increases the turbulent viscosity and in turn the Reynolds stress.

Figures 34, 35 and 36 show the variation of  $C_F$  values at 750 mm in longitudinal direction at volume fraction of 6% and at flow speed of 5, 6 and 7 m/s, respectively, for different depths of channel. From these figures, it can be concluded that since bubbles are widely spreading in the transverse direction for 5 mm depth, MBDR effect in longitudinal direction reduces with the distance from the injection point. Moreover, the MBDR effect depends on both the flow speed and depth of channel at





**Fig. 32** Variation of  $C_F$  values in transverse direction at VF 6% at 750 mm and at flow speed of 6 m/s for different depths of channel

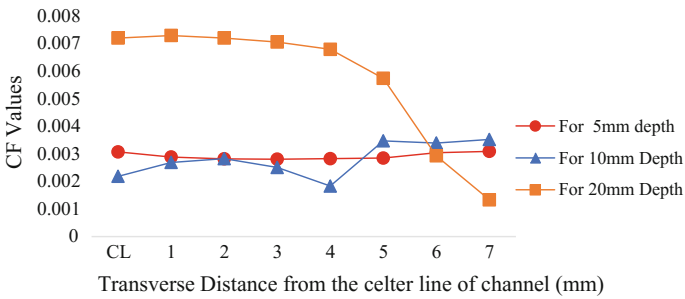


**Fig. 33** Variation of  $C_F$  values in transverse direction at VF 6% at 750 mm and at flow speed of 7 m/s for different depths of channel

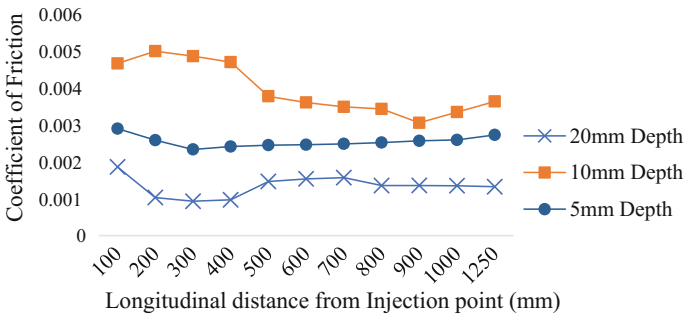


**Fig. 34** Variation of  $C_F$  values in longitudinal direction at VF 6% at 750 mm and at flow speed of 5 m/s for different depths of channel

the injection point. As seen from the figures, for flow speed of 5 m/s, 20 mm depth of channel at the injection point gives best result; however, for flow speed of 6 m/s, 10 mm depth gives best results. This once again implies that MBDR effect depends solely on distribution of bubbles which controls the local void fraction.

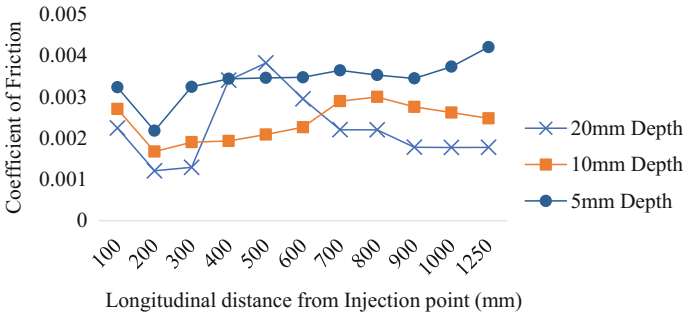


**Fig. 35** Variation of  $C_F$  values in longitudinal direction at VF 6% at 750 mm and at flow speed of 6 m/s for different depths of channel

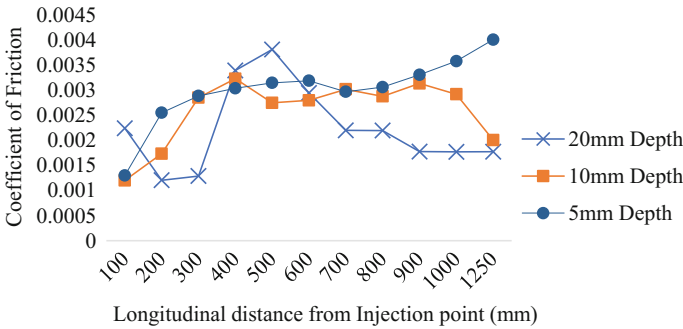


**Fig. 36** Variation of  $C_F$  values in longitudinal direction at VF 6% at 750 mm and at flow speed of 7 m/s for different depths of channel

Figure 37 shows the variation of void fraction and in turn distribution of microbubbles for different depths of channel at the injection point. As seen from the figure, for 5 mm depth of the channel, due to reduction of pressure at the injection point, flow velocity increases which in turn causes the increase in turbulence. This is forcing microbubbles to widely distribute in transverse direction and giving equal reduction in frictional drag in the transverse direction as well. Moreover, the flow rate in longitudinal direction decreases due to reduction in depth. To balance the mass flow rate, air volume fraction increases in spanwise direction. In case of depth of 10 mm or more, since velocity in longitudinal direction is less at the injection point as compared to 5 mm depth of channel, distribution of air bubbles in the spanwise direction is confined to smaller area.

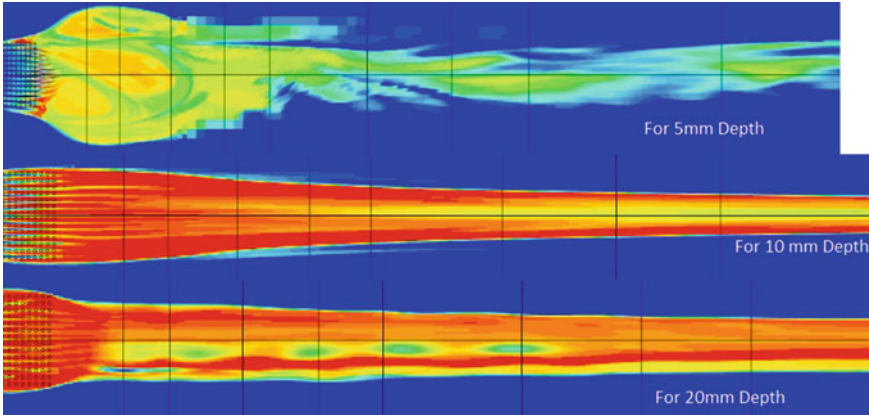


**Fig. 37** Variation of void fraction for different depths at the injection point

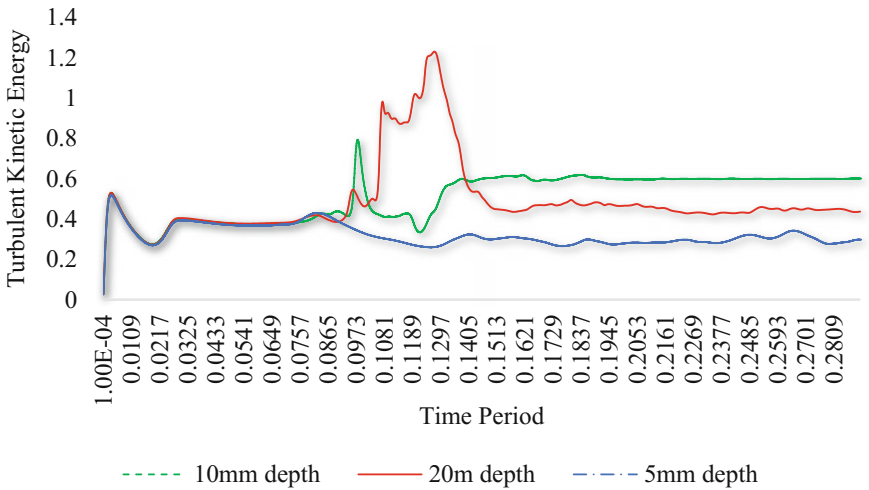


**Fig. 38** Variation of turbulent kinetic energy for different depths at 750 mm from the injection point

Figure 38 depicts the variation of turbulent kinetic energy for different depths at 750 mm from the injection point. From the distribution, it is confirmed that for 5 mm depth of channel, as more number of bubbles are distributed in spanwise direction, turbulent kinetic energy reduces, and for 20 mm depth of channel, the same is increased due to the injection of air. Moreover, from Fig. 38, it can be concluded that turbulent kinetic energy is lesser for 5 mm depth of channel. This implies that out of three channels tested, channel with depth of 5 mm gives the best results to reduce the frictional drag.

To conclude, it is found that the most important parameter in determining the fraction of drag reduction during gas injection is the effective void fraction, which is influenced by both—the injection rate and the static pressure under the test conditions.

## 4 Conclusions

The effect of microbubbles on frictional drag reduction was investigated in a 3D turbulent flow channel, with the main aim of investigating the effect of flow speed, void fraction and geometry at the injection point. Coefficient of friction and void fraction values are measured at 12 longitudinal positions, and at each longitudinal position, 11 in number transverse and 10 in number depthwise positions were studied. In all, for one simulation, data at more than 1000 positions were collected. More than 60 simulations were carried out to understand the effect. From the study, it is concluded that:

- The most important parameter in deciding the MBDR effect is the effective void fraction at the point of analysis, which is influenced by both—the injection rate and the static pressure under the test conditions. The reduction in the frictional drag is increased with the increasing mean void fraction.
- MBDR effect is due to the alteration of local effective viscosity and density of the fluid which reduces the Reynold's stress and in turn reduces the shear stress.
- Due to the restriction of flow in the spanwise direction, the MBDR effect reduces slowly in the streamwise direction and quickly reduces in the spanwise direction. The major reason for the same is distribution of air bubbles converging to smaller area in the spanwise direction as bubbles were not escaping sideways.
- The distance from the injection point is the most important parameter in obtaining the reduction in frictional drag, and the boundary layer thickness on the upper plate has little effect on the skin friction reduction by microbubbles.
- MBDR effect does not increase with the increase in airflow rate. At higher injection rate, excessive microbubble injection destroys the favourable turbulent boundary layer and in doing so decreases the drag reduction effect.
- MBDR effect depends on both the flow speed and depth of channel which decides the static pressure at the injection point.

**Acknowledgements** This research is well supported by SIEMENS Ltd. formerly known as CD ADAPCO. The authors express their sincere gratitude for their support. Moreover, the authors sincerely express their warm gratitude towards Mr. Sangmesh Biredar of CD ADAPCO for his invaluable inputs during the investigation using multiphase flow in Star CCM+.

## References

1. Sindagi S, Vijaykumar R, Saxena BK (2016) Frictional drag reduction: an EFD and CFD based review of mechanisms. In: International conference on EFD and CFD—MARHY 2016, IIT Madras, India
2. McCormick M, Bhattacharyya R (1973) Drag reduction of a submersible hull by electrolysis. *Naval Eng J* 85:11–16
3. Fontaine AA, Deutsch S (1992) The influence of the type of gas on the reduction of skin friction drag by microbubble injection. *Exp Fluids* 13:128–136
4. Kanokjaruvijit K, Martinez-botas RF (2005) Jet impingement on a dimpled surface with different crossflow schemes. *Int J Heat Mass Transf* 48:161–170
5. Sanders WC, Winkel ES, Dowling DR, Perlin M, Ceccio SL (2006) Bubble friction drag reduction in a high-reynolds-number flat-plate turbulent boundary layer. *J Fluid Mech* 552:353–380
6. Elbing BR, Winkel ES, Lay KA, Ceccio SL, Dowling DR, Perlin M (2008) Bubble-induced skin-friction drag reduction and the abrupt transition to air-layer drag reduction. *J Fluid Mech* 612:201–236
7. Tsai J-F, Chen C-C (2011) Boundary layer mixture model for a microbubble drag reduction technique. *ISRN Mech Eng* 2011:9 (Article ID 405701)
8. Kim S-Y (1995) The persistence of drag reduction following the injection of microbubbles into a turbulent boundary layer. *Int Commun Heat Mass Transfer* 22(3):353–357
9. Lu J, Fernández A, Tryggvason G (2005) The effect of bubbles on the wall drag in a turbulent channel flow. *Phys Fluids* 17:095102
10. Mohanarangam K, Cheung SCP, Tu JY, Chen L (2009) Numerical simulation of micro-bubble drag reduction using population balance model. *Ocean Eng* 36:863–872
11. Skudarnov PV, Lin CX (2006) Drag reduction by gas injection into turbulent boundary layer: density ratio effect. *Int J Heat Fluid Flow* 27:436–444
12. Kim D, Moin P (2010) Direct numerical study of air layer drag reduction phenomenon over a backward-facing step. Centre for Turbulence Research Annual Research Briefs
13. Rzehak R, Krepper E (2013) CFD modelling of bubble-induced turbulence. *Int J Multiph Flow* 55:138–155
14. Madavan K, Deutsch S, Merkle CL (1985) Numerical investigations into the mechanisms of microbubble drag reduction. *Trans ASME* 107:370–377
15. Legner HH (1984) A simple model for gas bubble drag reduction. *Phys Fluids* 27:2788
16. Kanai A, Miyata H (2001) Direct numerical simulation of wall turbulent flows with microbubbles. *Int J Numer Methods Fluids* 35:593–615
17. Ceccio SL (2010) Friction drag reduction of external flows with bubble and gas injection. *Ann Rev Fluid Mech* 42:183–203
18. Wu C-S, He S-L, Zhu D-X, Gu M (2006) Numerical simulation of microbubble flow around an axisymmetric body. In: Conference of global Chinese scholars on hydrodynamics
19. Kawabuchi M, Kawakita C, Mizokami S, Higasa S, Kodan Y, Takano S (2011) CFD predictions of bubbly flow around an energy-saving ship with Mitsubishi air lubrication system. *Mitsubishi Heavy Ind Tech Rev* 48(1)
20. Davenport J, Hughes RN, Shorten M, Larsen PS (2011) Drag reduction by air release promotes fast ascent in jumping emperor penguins- a novel hypothesis. *Mar Technol Prog Ser* 430:171–182
21. Shereena SG, Vengadesan S, Idichandy VG, Bhattacharyya SK (2013) CFD study of drag reduction in axisymmetric underwater vehicles using air jets. *Eng Appl Comput Fluid Mech* 7(2):193–209
22. Zverkhovskiy O, Kerkvliet M, Lampe A, Vaz G, van Terwisgab T Numerical study on air cavity flows. MARIN
23. Lyu X, Tang H, Sun J, Wu X, Chen X (2014) Simulation of microbubble resistance reduction on a suboff model. *Brodogradnja/Shipbuilding* 65(2)
24. Dogrul A, Arikan Y, Celik F (2010) A numerical investigation of air lubrication effect on ship resistance

25. Moriguchi Y, Kato H (2002) Influence of microbubble diameter and distribution on frictional resistance reduction. *J Mar Sci Technol* 7:79–85

# Hydroelastic Responses of a Pontoon-Type VLFS in Different Water Depths



Sakthivel Somansundar and Rajamanickam Panneer Selvam

**Abstract** Owing to the growth in human population, the land-scarce island countries and countries with long coastline are expanding their horizon to ocean environment through very large floating structures (VLFS) for different purposes as these are cost-effective, environment-friendly and can be manufactured easily. VLFS applications include floating airports, artificial islands, mobile offshore base and Mega-Float and are built using Pontoon-type or semi-submersible-type structures. In these types of structures, because of its large size, elastic deformations are more important than their rigid body motions. In this paper, hydroelastic behaviour of a barge Pontoon-type VLFS under various water depths is investigated. Analysis is based on three-dimensional linear hydroelastic theory to obtain the wave-induced hydroelastic response of the structures in the frequency domain. For solving this coupled fluid-structure interaction problem, the modal expansion method and the dry normal modes of vibration is commonly used for the floating structure. The structure is modelled using PATRAN [1], and the hydroelastic analysis is carried using HYDRAN-XR software. Responses in regular wave in the vertical mode at salient point along the length of the VLFS are presented for various wave headings and frequency. Vertical displacements at both edges of the structures and at the centre portion are found. Response for the six water depth conditions has been examined, and the observed results emphasize that vertical displacements are dominant in deep water conditions in relative to the shallow water conditions. Results also suggest that horizontal displacement is significantly higher in shallow water conditions.

**Keywords** Hydroelastic · Response amplitude operators · Added mass  
Damping coefficient · Mode shape · Displacements

---

S. Somansundar (✉) · R. Panneer Selvam  
Department of Ocean Engineering, Indian Institute of Technology Madras, Chennai 600036,  
Tamil Nadu, India  
e-mail: [somudce@gmail.com](mailto:somudce@gmail.com)

R. Panneer Selvam  
e-mail: [pselvam@iitm.ac.in](mailto:pselvam@iitm.ac.in)

© Springer Nature Singapore Pte Ltd. 2019  
K. Murali et al. (eds.), *Proceedings of the Fourth International Conference in Ocean Engineering (ICOE2018)*, Lecture Notes in Civil Engineering 22,  
[https://doi.org/10.1007/978-981-13-3119-0\\_18](https://doi.org/10.1007/978-981-13-3119-0_18)

## 1 Introduction

Recent developments of offshore industries lie in utilizing ocean space for different applications which include energy, food production, offshore storages, waste disposal facilities. This type of facilities requires more space and very large floating structures (VLFS) cater to the needs. VLFS are classified into two categories, one is Pontoon type and another is semi-submersible structures. Pontoon-type VLFS consist of box-type structures mainly designed for operation in calm water region. Semi-submersible-type VLFS platform consist of bottom hulls and top deck connected using vertical columns for open sea environment. Vertical deformation of the Pontoon-type VLFS is significantly higher than other floating bodies, and hence, investigating the hydroelastic effects due to the fluid–solid (elastic structure) interactions pertaining to the Pontoon-type VLFS is critically important.

In the past, many authors solved the hydroelastic problem based on analytical and numerical analyses. Aoki [2] examined an analytical formulation for wave radiation and diffraction problems on very large floating structures. This structure is modelled as one-dimensional thin beam placed on the water surface, and the eigenfunction expansion method is used for solving the boundary value problem. The hydrodynamic coefficients and wave exciting forces show significant shallow water effects, especially on added masses in the elastic deformation modes. Athanassoulis and Belibassakis [3, 4] developed a consistent coupled mode theory for the propagation of small amplitude water waves over variable bathymetry regions. The key feature of this method is by introducing an additional mode, the influence of the bottom slope can be studied. It turns out that the presence of the additional mode in the series representation of the potential makes it consistent with the bottom boundary condition and, at the same time, substantially accelerates the convergence. Ertekin and Kim [5] presented the hydroelastic behaviour of a rectangular airport or runway whose draft is small and which floats in a nearshore area based on linear, Level I Green-Naghdi theory. This method devised was proven to be very efficient in carrying out parametric study of the hydroelastic response of a mat-type floating runway in regular, oblique waves. The main parameters varied in the problem are the stiffness, length and beam of the mat. Tkacheva [6] studied that the spectral problem for a flexible platform (airport) floating on shallow water. The platform is modelled by a flexible plate of finite width and infinite length. A waveguide eigenmode is detected which propagates along the platform and attenuates exponentially away from it. The remaining eigenmodes are outgoing and growing exponentially away from the platform. All the eigenmodes can be excited only by external action on the platform. Zilman and Miloh [7] examined a circular buoyant elastic plate of homogeneous stiffness floating in shallow water. The edge of the plate is free of shear forces and bending moments. A closed form solution of the corresponding linearized problem is obtained. Numerical examples illustrating the analytic results for various physical parameters of the problem are presented. Hong et al. [8] investigated draft effects on hydroelastic response of Pontoon-type VLFS. A three-dimensional higher-order boundary element method (HOBEM) is extended to analyse elastic response



of structures. Main attention was paid to wave run-up along the waterline for various cases of draft scantling. Wang and Meylan [9] studied a solution for the linear wave forcing of a floating two-dimensional thin plate on water of variable depth. Meylan [10] investigated the modelling of floating runways using spectral theory in shallow water by considering it as hydroelastic systems.

Riggs et al. [11, 12] investigated the hydroelastic response of a Pontoon-type VLFS using three different hydroelastic computer codes. The code covered a mix of both fluid models and structural models to investigate the wave-induced response of very large floating structures. Two models are taken for comparison of rigid and elastic cases. It was expected that the benchmark problems herein will be of the value of both users and developers of hydroelastic codes. Sturova [13, 14] investigated the unsteady behaviour of a thin elastic Euler beam with heterogeneous structural properties, floating freely on the surface of an ideal incompressible liquid, is investigated using the linear theory and the unsteady behaviour of a thin elastic plate in the form of a strip of constant width and infinite length, floating on the surface of an ideal and incompressible liquid, within the limits of the linear shallow water theory. Karperaki et al. [15] examined the transient hydroelastic response of a floating, thin elastic plate, elastically connected to the seabed. Elastic connectors are approximated by a series of simple spring-dashpot systems positioned along the strip. A higher-order finite-element scheme is employed for the calculation of the hydroelastic response of the strip-connector configuration over the shallow bathymetry. Wang et al. [16] examined that mooring system significantly influences the motion response of the VLFS. Results concluded that numerical study has a good estimation of the motion response of the single module of a semi-submersible VLFS.

In this paper, hydroelastic behaviour of a barge Pontoon-type VLFS under various water depths is investigated. Analysis is based on three-dimensional linear hydroelastic theory to obtain the wave-induced hydroelastic response of the structures in the frequency domain.

## 2 Pontoon-Type VLFS

The Pontoon-type VLFS size is approximately  $100 \text{ m} \times 10 \text{ m} \times 2 \text{ m}$  with an operational draft of 1 m obtained from Riggs et al. [11]. The box consists of six flat plates: top deck and the bottom hull, the two sides, and the bow and stern plates. The elastic modulus is  $E = 15 \text{ GPa}$ , and Poisson's ratio is  $\nu = 0.3$ . The nominal plate thickness is 0.05 m and bending thickness 0.25 m. The mass density of the top deck is  $15,375 \text{ kg/m}^3$ , and the mass density of bottom hull is  $5125 \text{ kg/m}^3$ . The other plates are massless. These densities result in displacement of 1025 tonnes and a centre of gravity (CG) at 0.5 m above the still water line. The hydroelastic responses of Pontoon VLFS platform are carried out for water depths of 5, 10, 15, 20, 50 and 100 m for head sea and beam sea conditions. A schematic diagram of the Pontoon-type VLFS considered for analysis is shown in Fig. 1.

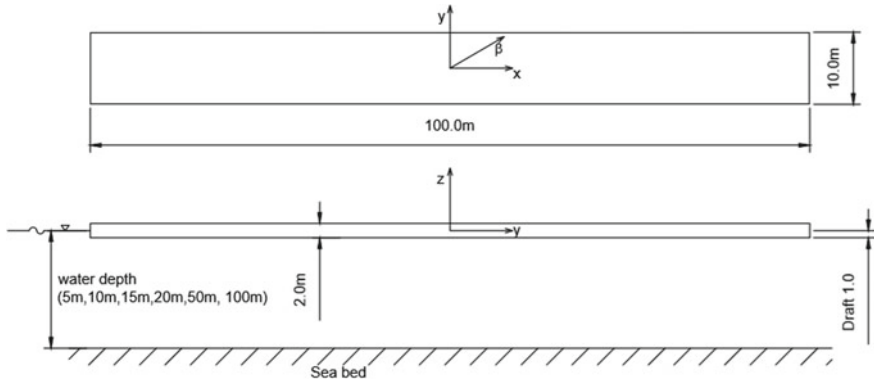


**Fig. 1** Top plan and front view of Pontoon-type VLFS

The description of degrees of freedom (DOF) for single Pontoon VLFS is shown in Fig. 1. The Pontoon VLFS platform consists of rectangular box-type structures. The coordinate system provided follows Pontoon VLFS coordinate system  $x_1 - x_2 - x_3$  ( $x, y, z$ ), where the origin of the coordinate system is located at the centre of gravity (CG). Axis  $x_3$  is directed vertically up, axis  $x_1$  is directed along longitudinal direction of the module, and  $x_2$  follows from right-hand rule. The wave heading angle is denoted by  $\beta$ . Hence, motions in  $x_1, x_2$  and  $x_3$  directions correspond to Pontoon VLFS surge, sway and heave motions, respectively.

### 3 Analysis Procedures

The structures are freely floating, analysed using HYDRAN-XR [17]. HYDRAN-XR is a computer program for the 3D hydroelastic response analysis of floating or fixed offshore structures and has been designed to analyse the wave-induced response of elastic structures. The numerical HYDRAN-XR procedure used the well-known frequency domain formulation of 3D linear hydroelasticity. The hydrodynamic motion response of a single rigid body and of multiple rigid bodies is treated as subsets of the more general formulation for flexible structures. HYDRAN-XR includes linear hydroelasticity (3D linear potential theory), linear structural dynamics and frequency domain solutions.

## 4 Numerical Models of Pontoon VLFS

The hydroelastic response of Pontoon VLFS platform is obtained for wave periods ranging from 2 to 32 s. Two different wave incidence angles are considered, namely  $0^\circ$  and  $90^\circ$ . The results are reported in terms of response amplitude operator (RAO), which is defined as the response for unit wave amplitude. A four node quadrilateral panels were used to model the Pontoon VLFS platform [8]. There are total 7150 panels and 7152 nodes for wet and dry surface of Pontoon VLFS with no symmetry option. The hydrodynamic panel mesh refers principally to the mesh of constant source panels that describe the wetted surface of the structure. The wetted surface of the structure is the surface with global coordinates  $x_3 \leq 0$  in the initial, static equilibrium position. Panels above the still water level are allowed, but they are not included in the hydrodynamic calculations.

## 5 Results and Discussions

The hydroelastic response of Pontoon VLFS platform is obtained for wave periods ranging from 2 to 32 s. Two different wave incidence angles are considered, namely  $0^\circ$  and  $90^\circ$ , and analysis is carried for six cases of water depths as mentioned in Sect. 2. From Fig. 2 it can be seen that the non-deformable modes such as surge, sway, heave, roll, pitch and yaw and deformable modes from the 7 to 18 modes respectively. Vertical bending modes are mode 7, mode 8, mode 10, mode 12, mode 14 (top deck), mode 16 (top deck), mode (top deck) 18. Horizontal bending modes are mode 9 and mode 15. Torsional modes are mode 11, mode 13, mode 17.

The significant results in terms of RAOs are presented for all the six cases considered; Fig. 3a shows the variation of Surge RAOs with respect to wave periods for head sea with varying water depth of the Pontoon VLFS. Surge RAOs increase as the wave periods increase, and it reduce as water depth increases. Figure 3b shows the variation of Heave RAOs with respect to wave periods for head sea for different water depths. Heave RAOs increase as the wave periods increase and also it increase as water depth increases unlike Surge RAOs. The peak values vary from 0.9 m/m in 100 m water depth to 0.65 m/m in 5 m water depth. Figure 3c shows the variation of Pitch RAOs with respect to wave periods for head sea for different water depths. Pitch RAOs increase as the wave periods increase and also it increase as water depth increases unlike Surge RAOs. The peak values vary from 1.4 %/m in both cases. But it is shifted from peak values from 10 to 21 s due to water depth variations.

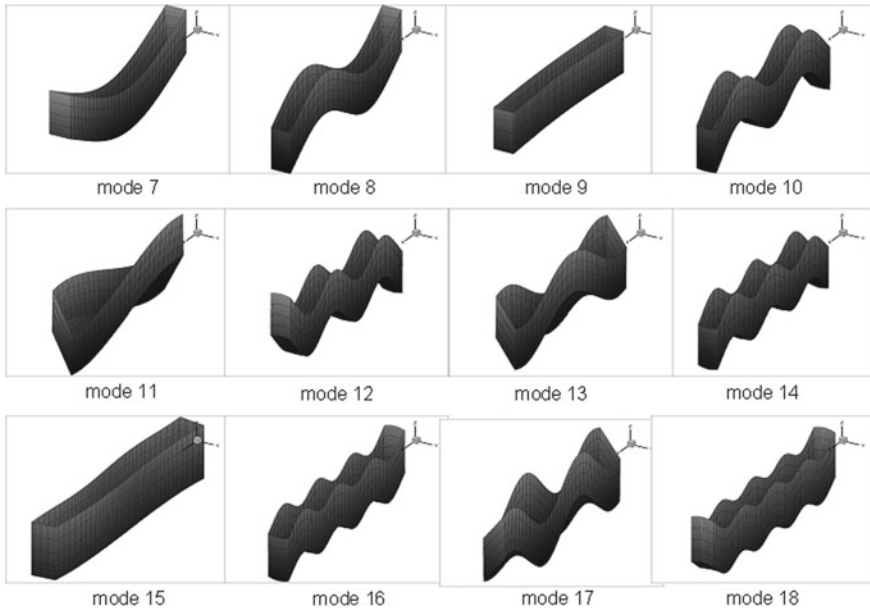


**Fig. 2** Deformable mode shape of Pontoon VLFS

Figure 4a shows the variation of added mass ( $a_{33}$ ) with respect to wave periods for varying water depth of the Pontoon VLFS. The values of 5 m water depth added mass significant variation compare to 100 m water depth from the periods 8 to 25 s. Figure 4b shows the variation of added mass ( $a_{11}$ ) marginal variation with respect to periods and water depth. Figure 4c shows the marginal variation of damping coefficient matrix ( $a_{11}$ ) with respect to wave periods for varying water depth of the Pontoon VLFS. Figure 4d shows the significant variation of damping coefficient matrix ( $a_{33}$ ) with respect to wave periods for varying water depth of the Pontoon VLFS. When there is increasing of wave period and water depth the damping coefficient matrix is significantly reduced. The peak values are  $6.5 \times 10^6$  to  $1.0 \times 10^6$  kg/s at 5 m and 100 m water depth respectively. It shows the fluid resistant reduces from 5 m water depth to 100 m water depth with changing the wave periods.

Figure 5a and b show the variation of added mass of mode 7 (bending) and mode 11 (torsional) with respect to wave periods for varying water depth of the Pontoon VLFS. Figure 5c and d show the variation of damping coefficient matrix of mode 7 (bending) and mode 11 (torsional) with respect to wave periods for varying water depth of the Pontoon VLFS. Figure 6a and b show the vertical nodal displacement at midsection of bow and stern for the Pontoon VLFS with respect to wave periods in head sea with varying water depth of the Pontoon. These plots show marginal variation for different water depths. Figure 6c shows the vertical nodal displacement at centre of top deck Pontoon VLFS with respect to wave periods for head sea with varying water depth. The peak values for six cases consider the marginal variation

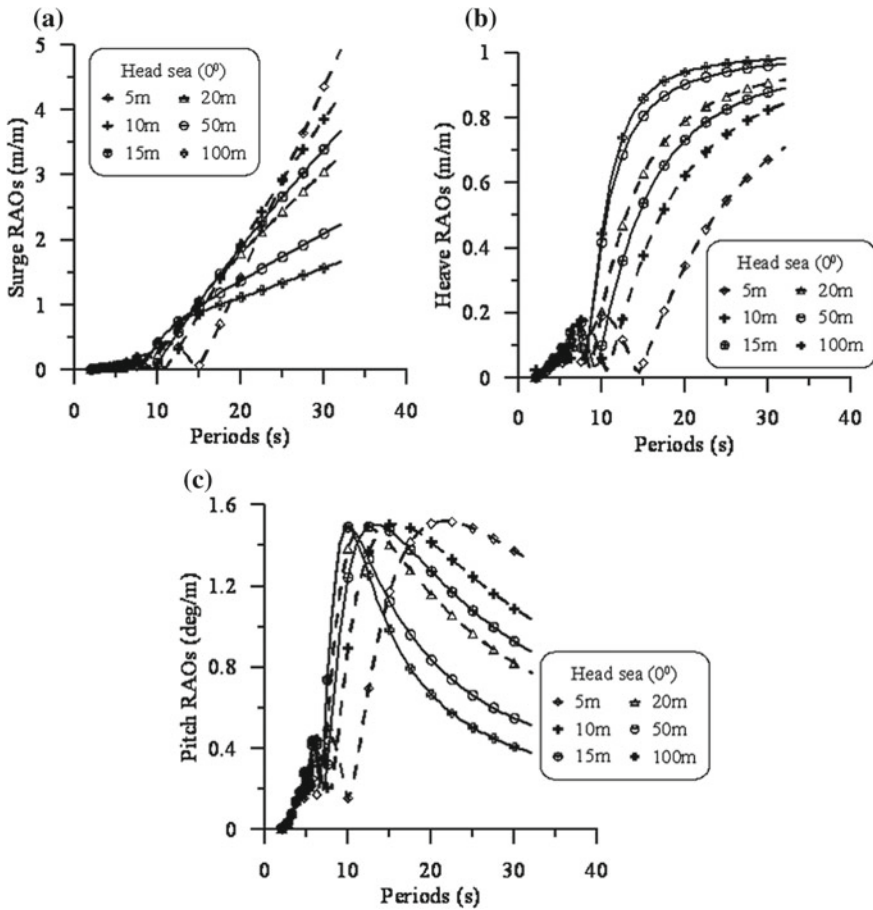


Fig. 3 Response amplitude operators of Pontoon VLFS

due to water depth variations. Figure 7a and b show horizontal nodal displacement at midsection of Pontoon VLFS with respect to wave periods for beam sea with varying water depth. The peak values for six cases exhibit significant variation due to water depth variations, varying from 1.2 to 7 m/m.

Figure 8a and b show the variation of rotation at both bow and stern of Pontoon VLFS with respect to wave periods for beam sea and for varying water depth. Figure 9a shows the significant variation of stresses at centre of top deck plate of Pontoon VLFS with respect to wave periods for head sea and for varying water depth. The peak values at 100 and 5 m water depth are  $2.5 \times 10^6$  and  $3.5 \times 10^6$  MPa/m, respectively. Figure 9b shows the significant variation of stresses at centre of bottom deck plate of Pontoon VLFS with respect to wave periods for head sea for varying water depth. The peak values at 100 and 5 m water depth are  $1.25 \times 10^6$  and  $1.8 \times 10^6$  MPa/m, respectively.

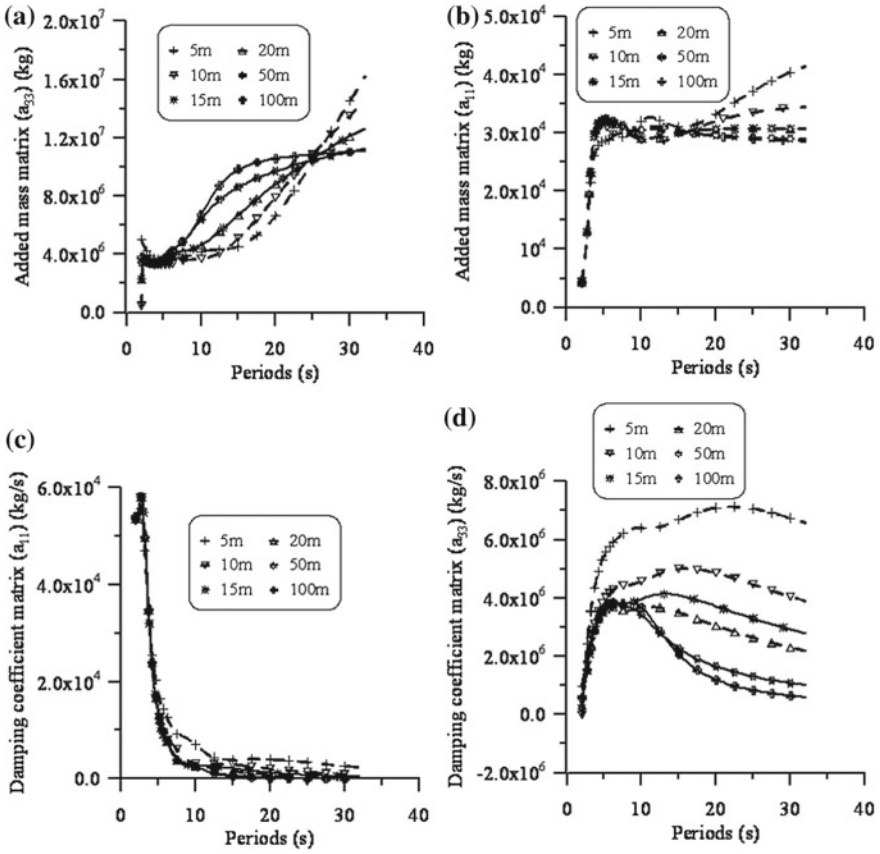


Fig. 4 Added mass and damping coefficient matrix of Pontoon VLFS

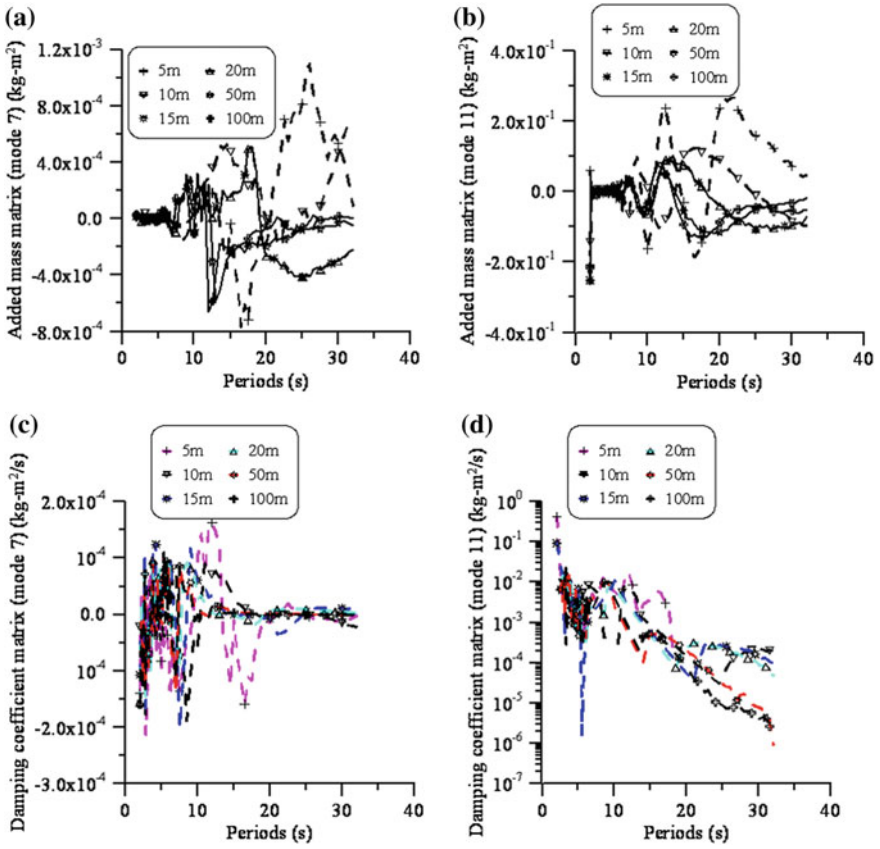


Fig. 5 Added mass and damping coefficient matrix of mode 7 and mode 11

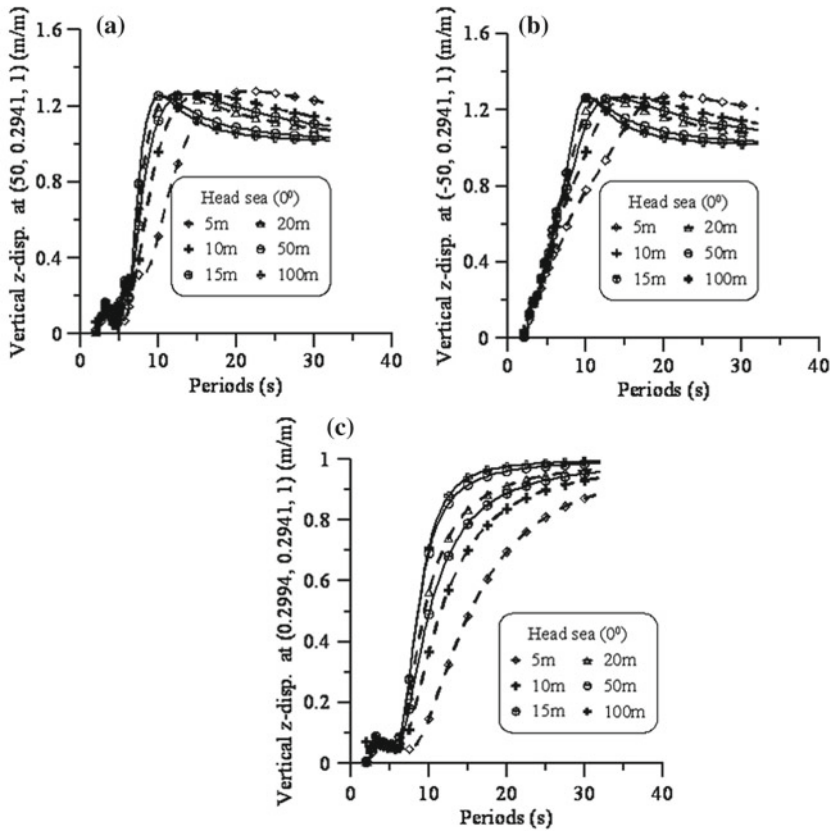


Fig. 6 Vertical nodal displacement of Pontoon VLFS

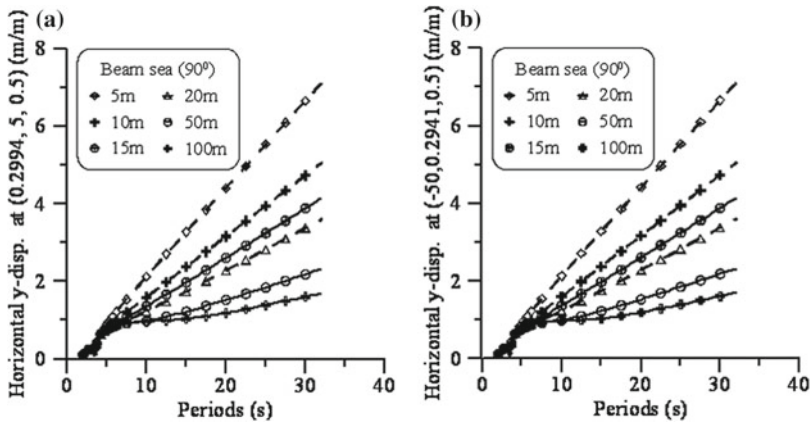


Fig. 7 Horizontal displacement of Pontoon VLFS



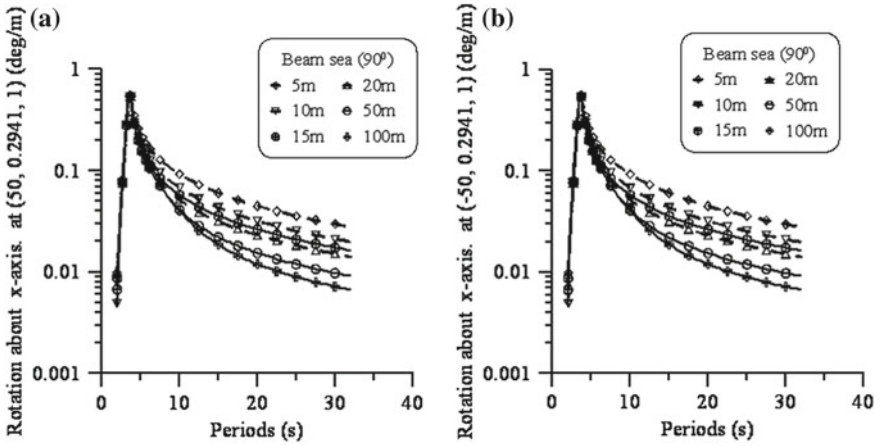


Fig. 8 Rotational at mid of bow and stern Pontoon VLFS

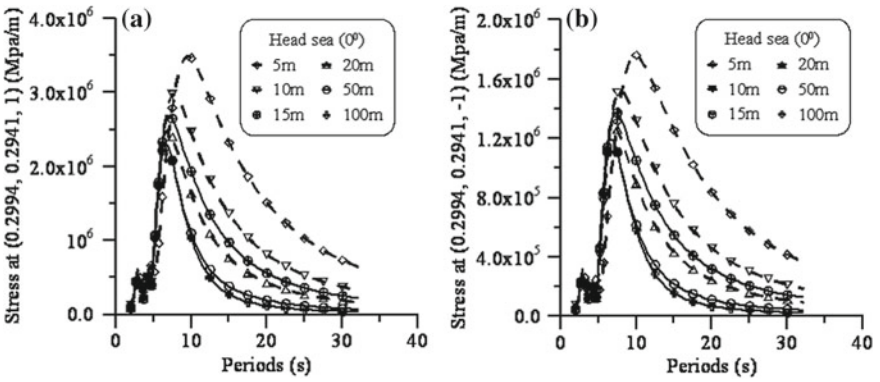


Fig. 9 Stress at top and bottom plate of Pontoon VLFS

## 6 Conclusions

The three-dimensional linear hydroelastic responses are carried out on a freely floating barge Pontoon VLFS for six different water depths numerically using HYDRAN-XR. Response amplitude operators (RAOs) for different modes, vertical and horizontal displacement and stresses at salient points for the barge Pontoon VLFS are presented. Results showed that effect of water depth is exhibited by the variations of RAOs for surge, heave and pitch DOF. Horizontal plane motions are dominant than the vertical plane motions. The added mass and damping coefficients are significantly varying with respect to the water depth. The study indicates that the water depth effects in the hydroelastic response of the barge Pontoon VLFS are more important and should be taken into account during design of the structures.

**Acknowledgements** The authors would like to acknowledge Prof. H. Ronald Riggs, University of Hawai'i at Manoa, for providing valuable insights into HYDRAN-XR procedure.

## References

1. MSC (2012) Patran reference manual [online]
2. Aoki SI (1997) Shallow water effect on hydrodynamic coefficients of very large floating structures. In: The seventh international offshore and polar engineering conference, Jan. International Society of Offshore and Polar Engineers
3. Athanassoulis GA, Belibassakis KA (1999) A consistent coupled-mode theory for the propagation of small-amplitude water waves over variable bathymetry regions. *J Fluid Mech* 389:275–301
4. Athanassoulis GA, Belibassakis KA (1998) Water-wave Green's function for a 3D uneven-bottom problem with different depths at  $x \rightarrow +\infty$  and  $x \rightarrow -\infty$ . In: IUTAM symposium on computational methods for unbounded domains. Springer, Netherlands, pp 21–32
5. Ertekin RC, Kim JW (1999) Hydroelastic response of a floating mat-type structure in oblique, shallow-water waves. *J Ship Res* 43(4):241–254
6. Tkacheva LA (2000) Eigenvibrations of a flexible platform floating on shallow water. *J Appl Mech Tech Phys* 41(1):159–166
7. Zilman G, Miloh T (2000) Hydroelastic buoyant circular plate in shallow water: a closed form solution. *Appl Ocean Res* 22(4):191–198
8. Hong SY, Choi YR, Hong SW (2001) Investigation of draft effects on analysis of hydroelastic responses of pontoon-type VLFS. In: The eleventh international offshore and polar engineering conference, Jan. International Society of Offshore and Polar Engineers
9. Wang CD, Meylan MH (2002) The linear wave response of a floating thin plate on water of variable depth. *Appl Ocean Res* 24(3):163–174
10. Meylan MH (2002) Spectral solution of time-dependent shallow water hydroelasticity. *J Fluid Mech* 454:387–402
11. Riggs HR, Niimi KM, Huang LL (2007) Two benchmark problems for three-dimensional, linear hydroelasticity. *J Offshore Mech Arct Eng* 129:149–157
12. Riggs HR, Hideyuki S, Ertekin RC, Jang WK, Iijima K (2008) Comparison of hydroelastic computer codes based on the ISSC VLFS benchmark. *J Ocean Eng* 35:589–597
13. Sturova IV (2008) Unsteady behaviour of a heterogeneous elastic beam floating on shallow water. *J Appl Math Mech* 72(6):704–714

14. Sturova IV (2008) Effect of bottom topography on the unsteady behaviour of an elastic plate floating on shallow water. *J Appl Math Mech* 72(4):417–426
15. Karperaki AE, Belibassakis KA, Papathanasiou TK (2016) Time-domain, shallow-water hydroelastic analysis of VLFS elastically connected to the seabed. *Mar Struct* 48:33–51
16. Wang Y, Wang X, Xu S, Ding A, Li J (2017) Motion response of a tension-leg-moored VLFS in shallow water. In: *The 27th international ocean and polar engineering conference*, July. International Society of Offshore and Polar Engineers
17. Riggs HR (2016) Hydrodynamic response analysis with integrated structural finite element analysis. HYDRAN-XR 16.3

# Effect of Slamming and Green Water on Short-Term Distribution of Vertical Bending Moment of a Containership in Abnormal Waves



Suresh Rajendran and C. Guedes Soares

**Abstract** The prediction of wave loads acting on a ship in small and moderate seas has almost become a matured technology in the field of naval architecture. However, shiploads in abnormal waves are rarely examined, both numerically and experimentally, because of the difficulty associated with the generation of the abnormal waves embedded in real deterministic waves. In this paper, a practical engineering numerical tool is used to analyse the effect of slamming and green water on the distribution of the vertical bending moment (VBM) peaks of a containership in abnormal waves. The experimental and the numerical simulations are conducted for two kinds of ship models. First one, with an extended bulwark for which no green water is observed and the second one without the extra bulwark for which severe green water shipping is observed. The numerical tool is based on a 2D time domain (TD) method, and the hydrostatic and hydrodynamic forces are calculated for instantaneous wetted surface. The radiation forces are represented by means of convolution integrals based on Cummins formulation. The hydrodynamic coefficients are also calculated for the exact wetted surface for each time instant. The ship is tested in the well-known abnormal wave ‘New Year wave’ and ‘North Alwyn wave’ for two ship speeds. The experimental results measured in the wave tank are compared with the numerical results. In order to compare the time series, the measured incident wave profile is used in the numerical simulation.

**Keywords** Vertical bending moment · Containership · Slamming  
Green water on deck · Short term distribution · Abnormal waves

---

S. Rajendran (✉)

Department of Ocean Engineering, IIT Madras, Chennai, India

e-mail: [sureshr@iitm.ac.in](mailto:sureshr@iitm.ac.in)

C. Guedes Soares

Centre for Marine Technology and Ocean Engineering (CENTEC), Instituto Superior Tecnico, University of Lisbon, Lisbon, Portugal

e-mail: [C.guedes.soares@centec.tecnico.ulisboa.pt](mailto:C.guedes.soares@centec.tecnico.ulisboa.pt)

© Springer Nature Singapore Pte Ltd. 2019

K. Murali et al. (eds.), *Proceedings of the Fourth International Conference in Ocean Engineering (ICOE2018)*, Lecture Notes in Civil Engineering 22,

[https://doi.org/10.1007/978-981-13-3119-0\\_19](https://doi.org/10.1007/978-981-13-3119-0_19)

## 1 Introduction

Slamming and shipping of green water are major concerns for ships from operational and structural point of view. Both phenomena can affect the attainable speed in service and can also damage the equipment and ship structures. Slamming is a complex phenomenon in which air compressibility, air bubbles, hydroelasticity, etc. may be relevant, Faltinsen et al. [1]. Since the pioneering work of Von Kármán [2], slamming has been extensively studied by many researchers using analytical, experimental and numerical methods. Wagner [3], Korobkin [4] and others conducted detailed investigation of the slamming problems based on analytical solutions. Slamming of complex shapes has also been studied numerically by many researchers, e.g. Zhao and Faltinsen [5], Sun and Faltinsen [6], Farsi and Ghadimi [7], etc. A recent detailed review of ship slamming can be found in Wang and Guedes Soares [8].

The phenomenon of green water loads on ships and offshore structures has been extensively studied during the last few decades. O'Dea and Walder [9], Lloyd et al. [10], Buchner [11], Fonseca and Guedes Soares [12, 13] investigated the problem of green water shipping by conducting model tests. Buchner [11] conducted a detailed experimental investigation on the behaviour of a FPSO model and identified the green water shipping phenomenon with 'dam breaking'. Dam breaking is associated with the relative motion between the ship bow and the water surface. When the bow plunges into the water or the pitch angle becomes maximum, an almost vertical wall of water appears in front of the bow and propagates towards the deck. Based on the studies conducted on a FPSO, Greco et al. [14] further categorized the problem based on the nature of the phenomenon. In addition to the dam breaking phenomenon, they identified plunging breaker in which the water hits the deck as a plunging breaker. Later on, when it flows into the deck, it follows the dam breaking pattern. Greco et al. [14] also identified 'hammer fist' method in which large mass of water rises above the deck collapses substantially over a large deck area.

Due to the complexity of the hydrodynamic problem and its close relevance to FPSOs, most of the studies have been limited to zero speed condition. Moreover, no studies have been conducted on the shipping of green water problem in abnormal waves, at least to the knowledge of the authors. Waves are classified as abnormal or freak waves when the ratio  $H_{\max}/H_s$  is larger than 2 where  $H_{\max}$  is the wave height of the single abnormal wave and  $H_s$  is the significant wave height of the deterministic waves in which the abnormal waves are embedded. The existence of abnormal, freak or rogue waves is an incontrovertible fact due to many reports on observations and accidents [15].

Previous researches on green water shipping have mainly focussed on the impact load that are highly important for assessing the local structural damages, like damage to deck structures. However, the effect of green water loads on ship motions and global loads have not been investigated by many researchers. Shin et al. [16] numerically calculated the effect of green water loads on the ship motions and on the midship wave bending moment using LAMP (large amplitude motion program). It was found that the green water loading had noticeable effect on the bending moment and the

presence of green water on deck reduces the sagging peaks. This was mainly due to the downward vertical force applied by the green water on deck which acts in opposition to the hydrostatic and wave forces acting on the bow. The vertical response and the effect of green water on the VBM acting amidship of a containership in abnormal waves was numerically analysed by Rajendran et al. [17]. A body nonlinear 2D TD method was used for the calculation in which the Froude–Krylov and hydrostatic forces were calculated for immersed surface. Similar to the findings of Shin et al. [16], reduction in the values of the sagging peaks were observed when the deck was wetted.

In this paper, the effect of slamming and green water load on the probability distribution of the VBM of a containership is numerically investigated, and the results are compared with the experimental results. The numerical simulation uses predefined wave traces that were reproduced in the experimental wave tank. The deterministic waves correspond to popular ‘New Year wave’, which occurred at Draupner platform in 1995 on the New Year day, and an abnormal wave measured at North Alwyn platform. Two models of the containership with and without bulwark were tested. The model without bulwark experiences severe green water on deck while the one with extended bulwark is devoid of any green water on deck. A 2D time domain (TD) nonlinear model proposed by Rajendran et al. [18] is used for calculation of the ship responses in abnormal waves. Due to the low block coefficient and pronounced bow flare, the responses of the containership in the severe sea states are highly nonlinear. Among the many sources of nonlinearity, body nonlinearity which is associated with the instantaneous change of the wetted geometry of the hull plays a major role. The TD method takes account of the body nonlinear radiation/diffraction, Froude–Krylov and hydrostatic forces. In order to facilitate faster computation, empirical method proposed by Buchner [11] is used for calculation of green water loads and Von Karman [2] approach is followed for calculation of slamming loads. The TD method is also used for generation of short-term distribution of loads in extreme sea condition.

## 2 Numerical Program

### 2.1 Equation of Motion

Numerical loads acting on the containership is calculated based on a 2D TD method proposed by Rajendran et al. [18]. For each time instant, the hydrodynamic and hydrostatic forces are calculated for the exact wetted surface. A computationally efficient method suitable for engineering applications is used for calculation of the radiation and diffraction forces for the instantaneous wetted surface. Radiation forces are calculated based on the convolution of the memory function and the fluid velocity and also includes the contribution from the infinite frequency added mass. The method facilitates the faster computation of short-term distribution of loads in severe seas. Surge is included in the equations of motions in a semi-empirical manner. The

final equations of motion are written as given by Eqs. (1)–(3). The equation of motion for surge, heave and pitch can be written as:

$$(M + A_{11}^{\infty})\ddot{\xi}_1(t) + \int_0^t K_{11}(t - \tau)\dot{\xi}_1(\tau)d\tau + C_{11}\xi_1(t) + (M \cdot Z_{cg} + A_{15}^{\infty})\ddot{\xi}_5 + \int_0^t K_{15}(t - \tau)\dot{\xi}_5(\tau)d\tau + C_{15}\xi_5(t) = F_1^E(t) \quad (1)$$

$$(M + A_{33}^{\infty})\ddot{\xi}_3(t) + \int_0^t K_{33}(t - \tau)\dot{\xi}_3(\tau)d\tau + C_{33}\xi_3(t) + A_{33}^{\infty}\ddot{\xi}_5 + \int_0^t K_{35}(t - \tau)\dot{\xi}_5(\tau)d\tau + C_{35}\xi_5(t) + F_3^H(t) - Mg = F_3^E(t) + F_3^G(t) + F_3^S(t) \quad (2)$$

$$(I_{55} + A_{55}^{\infty})\ddot{\xi}_5(t) + \int_0^t K_{55}(t - \tau)\dot{\xi}_5(\tau)d\tau + C_{55}\xi_5(t) + A_{53}^{\infty}\ddot{\xi}_3 + \int_0^t K_{53}(t - \tau)\dot{\xi}_3(\tau)d\tau + C_{53}\xi_3(t) + (M \cdot Z_{cg} + A_{51}^{\infty})\ddot{\xi}_1 + \int_0^t K_{51}(t - \tau)\dot{\xi}_1(\tau)d\tau + C_{51}\xi_1(t) + F_5^H(t) = F_5^E(t) + F_5^G(t) + F_5^S(t) \quad (3)$$

where surge, heave and pitch motions, respectively, are represented by  $\xi_1$ ,  $\xi_3$  and  $\xi_5$ .  $M$ ,  $g$ ,  $Z_{cg}$  and  $I_{55}$ , respectively, are the ship mass, acceleration of gravity, vertical centre of gravity of ship from MWL and the mass moment of inertia about the  $y$ -axis.  $F_3^H$  and  $F_5^H$  are the hydrostatic force and moment. The exciting forces due to the incoming waves,  $F_1^E$ ,  $F_3^E$  and  $F_5^E$ , are decomposed into a diffraction part,  $F_1^D$ ,  $F_3^D$  and  $F_5^D$ , and the Froude–Krylov part,  $F_1^K$ ,  $F_3^K$  and  $F_5^K$ .  $F_3^S$  and  $F_5^S$  represent the slamming force and moment and are calculated based on Eq. (4). Green water force and moment,  $F_3^G$  and  $F_5^G$ , are calculated based on Eq. (5). Infinite frequency added masses,  $A_{kj}^{\infty}$  ( $j, k = 1, 3, 5$ ), are calculated based on multi-parameter conformal mapping technique.  $K_{kj}$  is memory function and  $C_{kj}^m$  is radiation restoration coefficient. All the forces are calculated for the exact wetted surface.

### 2.1.1 Slamming and Green Water Forces

Slamming load is calculated, as given below, based on Von Karmen model where the water pile up is assumed to be zero. In this paper, slamming load is calculated

by means of rate of change of hydrodynamic momentum. Fonseca et al. [19] have shown that for ships with large bow flare, slamming force component due to rate of change of hydrodynamic momentum dominates over the initial impulse of the section.

$$\begin{aligned}
 F^{\text{slam}}(t) &= \int_L f^{\text{slam}} dx \\
 f^{\text{slam}}(x, t) &= \frac{\partial m^\infty(x)}{\partial t} \frac{Dv_{\text{rel}}}{Dt} - U \frac{\partial m^\infty(x)}{\partial x} \frac{Dv_{\text{rel}}}{Dt} \\
 &= \frac{\partial m^\infty(x)}{\partial T} \left( \frac{\partial v_{\text{rel}}}{\partial t} - U \frac{\partial v_{\text{rel}}}{\partial x} \right)^2 - U \frac{\partial m^\infty(x)}{\partial x} \frac{Dv_{\text{rel}}}{Dt} \quad (4)
 \end{aligned}$$

where  $m^\infty(x)$  is the sectional infinite frequency added mass,  $v_{\text{rel}}$  is the relative velocity between the section and the incident wave,  $T$  is the instantaneous draft of the section calculated based on the relative motion between the section and the wave elevation. Water exit problem is not considered in the numerical model. The second term is neglected assuming that the ship is slender and the variation of the added mass in the longitudinal direction is negligible.

The green water forces are calculated based on momentum theory, Buchner [11]. Vertical forces acting on the deck during the presence of green water is calculated based on momentum method [11]. The vertical force per unit length due to presence of green water is given by:

$$f^{gw}(x, t) = \left( \frac{\partial m_{gw}}{\partial t} \right) w + \left( g \cos \xi_5 + \frac{\partial w}{\partial t} \right) m_{gw} \quad (5)$$

where ‘ $w$ ’ is the velocity of deck and ‘ $m_{gw}$ ’ is the mass of the water on deck. The first term on the right-hand side denotes rate of change of mass of water over the deck. The mass of water on deck is calculated from the height of water above deck which is obtained from the vertical distance between relative motion and freeboard. The second term denotes the hydrostatic component and the third term denotes the acceleration of the deck.

## 2.2 Wave Loads

The wave-induced global structural loads acting at any cross section is calculated from the difference between the sum of inertia and hydrodynamic/hydrostatic moments up to that particular section (summing the forces acting on all the sections forward of that particular section).

$$M_j(t) = I_j(t) - R_j(t) - D_j(t) - K_j(t) - H_j(t) - G_j(t) \quad j = 3, 5 \quad (6)$$



where  $I_j$ ,  $R_j$ ,  $D_j$ ,  $K_j$ ,  $H_j$ , and  $G_j$ , respectively, are the inertia force, radiation, diffraction, Froude–Krylov, hydrostatic and green water loads acting forward of the cross section under investigation. In the partial body nonlinear method,  $R_j$ , and  $D_j$  are linear and other exciting forces are body nonlinear. For the fully body nonlinear method, all the exciting forces/moments are calculated for the immersed hull for each time step.

## 2.3 Irregular Waves

### 2.3.1 Wave Elevation

Based on Fourier transform technique, the measured incident irregular wave time series were reproduced in the numerical simulation. During the experiment, the incident waves were measured at the forward of the ship without the model. During the numerical simulation, the wave elevation is transferred to COG of the ship using Eq. (7). In head seas, the wave elevation at a fixed point is given by:

$$\zeta(t, x) = \sum_{n=1}^N \zeta_n^a \cos(\omega_n t + k_n x + \phi_n) \quad (7)$$

where  $\omega_n$ ,  $k_n$  and  $\phi_n$ , respectively, are the wave frequencies in rad/s, wave numbers and phase angles of the measured waves.

## 3 Experimental Set-up

The experiment was conducted by the Ocean Engineering Division of Technical University Berlin (TUB) as a part of the ‘Handling Waves’ project. The details of the experimental programme and the model description can be found in Clauss et al. [20] and Rajendran et al. [17, 18]. For the cases discussed in this paper, the test series were divided into two parts. The first series of tests were conducted on the model without the bulwark. The second model had an extra bulwark with an additional height of 9.94 m (in full scale). Both models were tested in the same sea state. The model was ballasted in both parts in such a way that the total weight and centre of gravity of the individual segments remains nearly same.

The containership models were tested in several deterministic irregular sea states in which the abnormal waves were embedded. In the present study, the tests conducted in irregular sea states with New Year (NYW) and North Alwyn waves are analysed. The model was tested with 0 and 0.13 Froude number in New Year wave and kept stationary in North Alwyn waves. The details of the experimental programme are given in Table 1 and the main particulars of the ship are given in Table 2. The abnormality

**Table 1** Description of the abnormal waves and the Froude number of the containership

No.	Type	Fn	$H_s$ (m)	$T_p$ (sec)	$H_{max}$ (m)	AI
1	New Year wave	0.0	11.91	16.3	24.5	2.06
2	North Alwyn	0.0	10.23	14.52	21.0	2.05
3	New Year wave	0.13	12.92	13.32	26.2	2.03

Fn—Froude number,  $H_s$ —significant wave height,  $T_p$ —Peak wave period,  $H_{max}$ —maximum wave height, AI—Abnormality index

**Table 2** Main particulars of the container ship

Length between perpendiculars (m), $L_{pp}$	117.6
Breadth (m), $B_{WL}$	20.2
Draught (m), $D$	8.1
Displacement ( $t$ )	12366.9
Block coefficient (-), $C_B$	0.65
LCG from aft (m), $X_{cg}$	59.02
VCG from baseline (m), $Z_{cg}$	7.35
Transversal metacentric height (m), $GM_T$	1.1
Scale of the model	1:70
Longitudinal inertia about centre of gravity ( $kg\ m^2$ )	8.4648e + 09

index (AI) is defined as  $H_{max}/H_s$  which is generally chosen by researchers to identify abnormal waves. An abnormality index above 2 represents abnormal wave, Guedes Soares et al. [21]. Figure 1 shows the containership models encountering New Year Wave for case 1. The model without extra bulwark experiences severe green water on deck, while the green water does not occur for the other model. However, severe bow flare slamming like phenomenon can be observed for the model with extra bulwark.

## 4 Results

The models were tested in deterministic sea states in the wave tank for 20–30 min in which the abnormal waves were embedded. Numerical simulations are carried out in the same deterministic sea states and short-term distribution of the load peaks are compared with the measured responses. For comparison of the short-term distribution of loads and to ensure statistically stationary process, sea states with longer duration (about 3 h) are desirable. However, the comparison of the available mea-

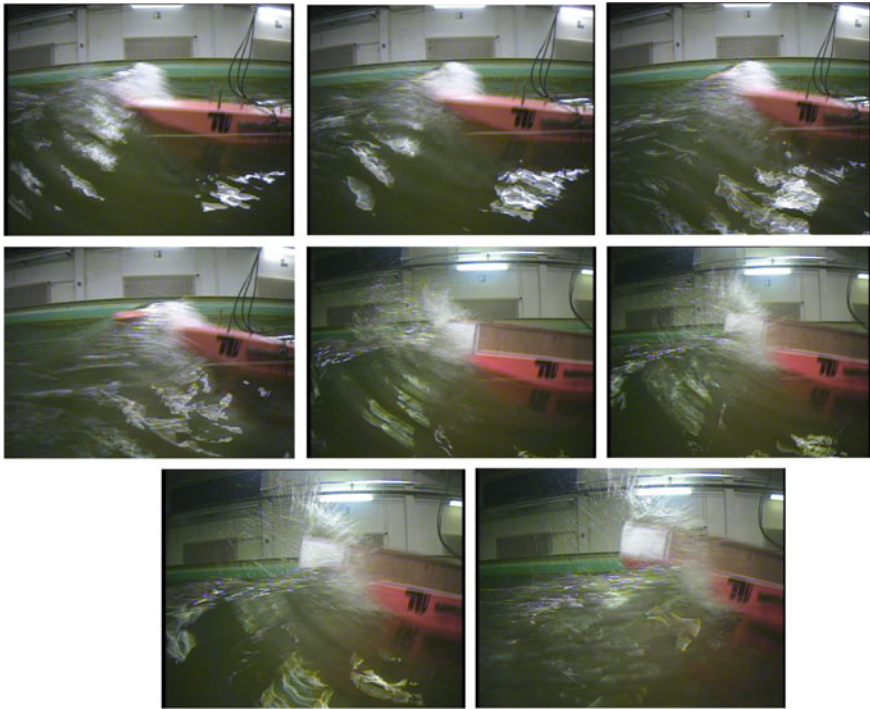


**Fig. 1** Containership model encountering New Year wave in the wave tank. The first four photographs show the model without extra bulwark and the next four pictures show the model with extra bulwark. Severe green water occurs for the model without extra bulwark

sured responses with the corresponding numerical simulation should give a fair idea about the influence of slamming and green water loads on vertical bending moment. In Fig. 2, the plot on top shows the time series of the deterministic sea state in which New Year Wave (NYW) is embedded (case 1). The plot on bottom compares the time series VBM measured at amidship for the models with and without extra bulwark. NYW crest occurs at the forward perpendicular of the ship at 260.5 s, as shown in Fig. 2, and the ship with extra bulwark experiences the largest sagging moment at that instant. As shown in Figs. 1 and 2, when the NYW crest is at the FP, the ship without extra bulwark experiences green water on deck, however, experiences lesser sagging moment compared to its counterpart. Green water on deck reduces the sagging moment and will be discussed in detail in the following section.

The probability of exceedance of the numerical and experimental vertical bending moment peaks at amidship is compared in Fig. 3. The numerical results consist of results with and without slamming and green water effects. The plot on the left shows the comparison between the experimental and numerical results for the ship without extra bulwark. The numerical results with slamming and green water effect are denoted by the acronym ‘NUM-WOBK’ and the ones without them are denoted

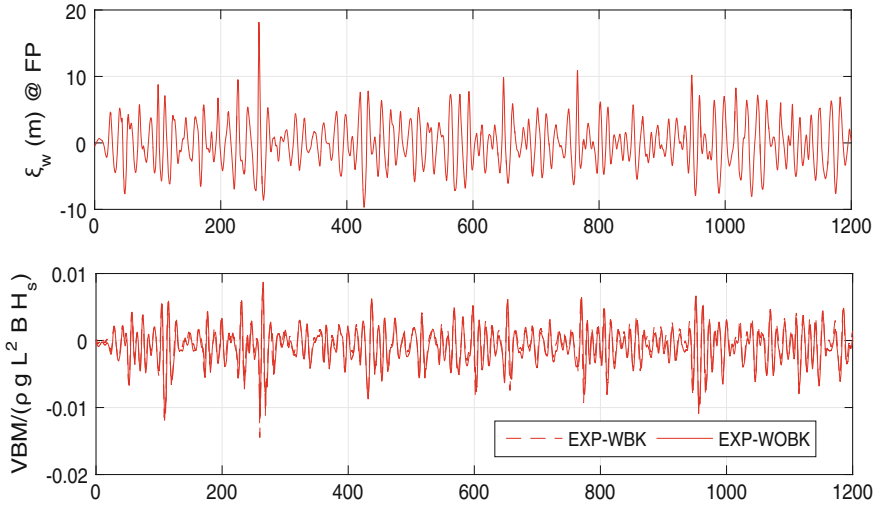


**Fig. 2** Top graph shows the time series of the irregular sea state in which NYW is embedded (case 1). Time series is measured at the forward perpendicular of the ship. The bottom plot compares the measured vertical bending moment at amidship for ship with and without extra bulwark

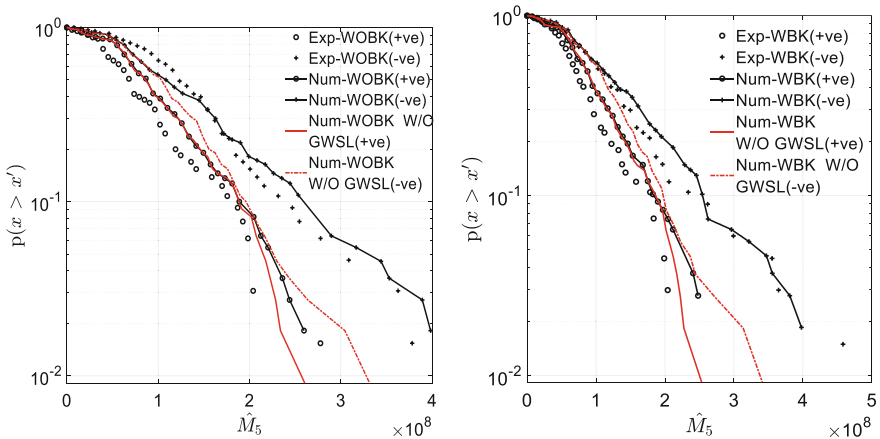


**Fig. 3** Probability of exceedance of the experimental and numerical vertical bending moment peaks at amidship for case 1

by ‘Num-WOBK W/O GWSL’. The hogging and sagging moment are considered as ‘+ve’ and ‘-ve’, respectively.

In general, the distribution of the peaks is asymmetric, which shows the non-linear nature of the bending moment time series. The sagging peaks are larger than the hogging peaks. The peaks from the numerical results without GWSL (Green Water and Slamming Loads) are less asymmetric. Inclusion of GWSL

increases the asymmetry in the distribution of the loads peaks. There is very good agreement between the experimental and the numerical results when these forces are considered. Here the slamming loads are calculated from the rate of the change of added mass, based on Eq. (4), which are generally not considered during the seakeeping calculation of the rigid hull. Instead, such loads are considered as impact loads and the transient response due to slamming, which is called as whipping, is calculated for the hydroelastic response of the hull. In this paper, no hydroelastic calculations are carried out and the slamming load is considered on the right-hand side of the equation of motion among other wave exciting loads and moments. Because of the pronounced bow flare of the containership and the large relative motion of the bow, the added mass changes significantly along the draft and results in a substantial load. As shown in Fig. 2, slamming loads results in almost 20% increase in the sagging peak values and also results in larger asymmetry in the distribution of the loads.

The plot on the right side of Fig. 3 shows the comparison between the experimental and the numerical results for the ship with extra bulwark. For this case, the ship does not experience any green water shipping. Regarding the comparison between the numerical results, inclusion of GWSL increases the sagging peak values, thus increases the asymmetry in the distribution of the load peaks. As observed before for the case without bulwark, the agreement between the numerical results with GWSL is really good, particularly for sagging peaks. From the comparison of the measured wave elevation and the bending moment time series, it is observed that the ship experiences the largest sagging peak value when the New Year Wave crest is at the bow as shown in Fig. 1. The largest sagging peak experienced by the model without extra bulwark is lesser than the other one. The model without extra bulwark experiences a maximum sagging load of 388 MNm, while the other model experiences 473 MNm. Shipping water reduces the sagging moment. This is mainly due to the downward green water forces acting on the bow, which acts opposite to the fluid forces acting upwards in the sagging position. There is no significant difference in the values of the largest of sagging peak between the numerical results. This may be due to the simplified model adopted to calculate the green water forces.

Similarly, Fig. 4 shows the comparisons between the experimental and the numerical simulations for case 2 mentioned in Table 1. In general, the agreement is good between the experimental and the numerical results. Inclusion of GWSL improves the prediction of the numerical results. It should be noted that the green water effects are only visible for the largest sagging peak values. However, the slamming effect, which increases the values of the sagging peaks, is clearly observable on comparison between the results from the two numerical methods.

The containership in transit condition (case 3) is depicted in Fig. 5. Here, the numerical model has used a linear radiation force instead of the body nonlinear radiation force along with GWSL. From the numerical analysis, it is found that the frequency of occurrence of green water on deck is higher than the zero speed condition for the ship without extra bulwark. The largest six sagging peaks are affected by the green water loads and the largest peak experienced by the ship without extra bulwark is reduced by 13%.

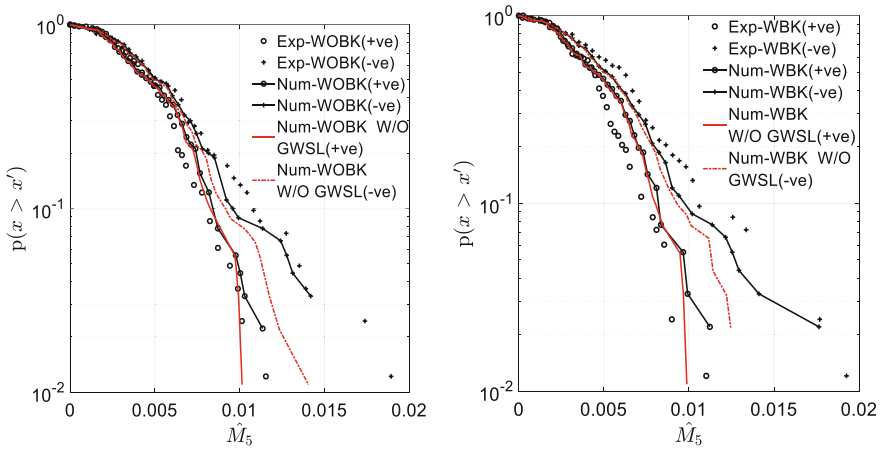


**Fig. 4** Probability of exceedance of the experimental and numerical vertical bending moment peaks at amidship for case 2

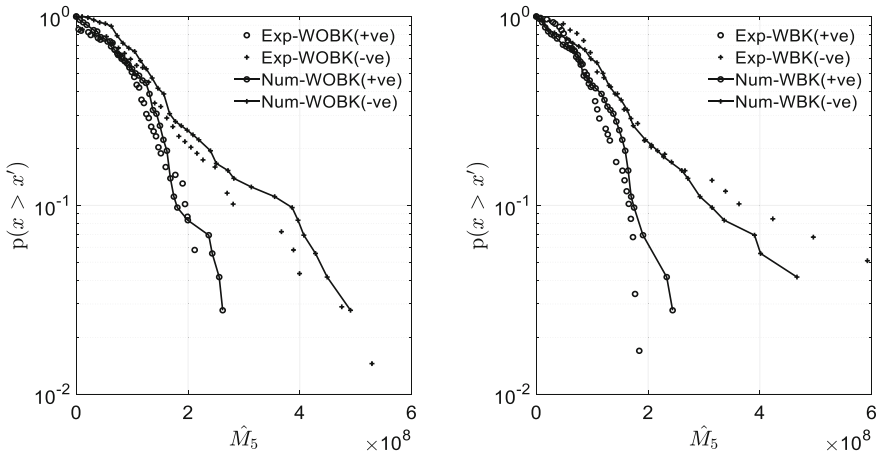


**Fig. 5** Probability of exceedance of the experimental and numerical vertical bending moment peaks at amidship for case 3

### 5 Conclusion

Effect of slamming and green water load on the short-term distribution of load is numerically investigated and compared with measured responses. A containership with and without an extra bulwark is used for the analysis. The effect of slamming is analysed by means of numerical simulations. Numerical simulations with and without slamming and green water loads are conducted. It was found that inclusion of slamming load in the equation of motion increases the asymmetry in the distribution

of vertical bending moment peaks. Slamming load significantly increases the sagging moment and an increase of up to 20% is observed for the largest numerical sagging peak value. The numerical results with the slamming loads and the measured responses are found to be in good agreement.

The effect of green water load on the sagging moment is mainly observed from the experimental results. The green water on deck reduces the sagging peaks at the midship, probably because of the down ward green water force acting in opposite to the fluid forces acting upwards during sagging condition. The frequency of the green water on deck is higher when the ship is in transit. The largest six sagging peaks are affected by the green water loads and the largest peak experienced by the ship without extra bulwark is reduced by 13%.

## References

1. Faltinsen OM, Landrini M, Greco M (2004) Slamming in marine applications. *J Eng Math* 48:187. <https://doi.org/10.1023/B:engi.0000018188.68304.ae>
2. Von Kármán T (1929) The impact on seaplane floats during landing. National advisory committee for aeronautics, Technical note no. 321, pp 309–313
3. Wagner H (1932) Uber Stossund Gleitverganke an der Oberflache von Flussigkeiten. *Zeitschrift fuer Angewandte Mathematik undMechanik* 12:193–215
4. Korobkin AA (2004) Analytical models of water impact. *Eur J Appl Math* 15:821–838
5. Zhao R, Faltinsen OM (1993) Water entry of two-dimensional bodies. *J Fluid Mech* 246:593–612
6. Sun H, Faltinsen OM (2006) Water impact of horizontal circular cylinders and cylindrical shells. *Appl Ocean Res* 28(5):299–311
7. Farsi M, Ghadimi P (2016) Effect of flat deck on catamaran water entry through smoothed particle hydrodynamics. *Proc Inst Mech Engi Part M J Eng Marit Environ* 230(2):267–280
8. Wang S, Guedes Soares C (2017) Review of ship slamming. *J Mar Sci. Appl* 16. Doi:<https://doi.org/10.1007/s11804-017-1437-3>
9. O'Dea JF, Walden DA (1984) Effect of bow shape and nonlinearities on the prediction of large amplitude motions and deck wetness. In: *Proceedings of 15th ONR symposium on naval hydrodynamics, Hamburg*
10. Lloyd RJM, Salsich JO, Zselezcky JJ (1985) The effect of bow shape on deck wetness in head seas. *Transactions Royal Institute of Naval Architects, London*, pp 9–28
11. Buchner B (1995) On the impact of green water loading on ship and offshore unit design. In: Kim H, Lee W (eds) *Proceedings 6th international symposium on practical design of ships and mobile units (PRADS'95)*, The Society of Naval Architects of Korea, vol 1, pp 430–443
12. Fonseca N, Guedes Soares C (2004) Green water effects on the bow of a containership advancing in regular and irregular waves. In: *The 9th international symposium on practical design of ships and mobile units (PRADS'04)*, Luebeck-Travemuende, Sept 2004, pp 412–419
13. Fonseca N, Guedes Soares C (2005) Experimental investigation of the shipping of water on the bow of a containership. *J Offshore Mech Arct Eng* 127(4):322–330
14. Greco M, Faltinsen O, Landrini M (2002) Water shipping on a vessel in head waves. In: *Proceedings of the 24th symposium on naval hydrodynamics*, vol 2, Fukuoka, 8–12 July, pp 40–52
15. Faulkner D, Buckley W (1997) Critical survival conditions for ship design. In: *Proceedings of the conference on design and operation for abnormal waves RINA*, London, United Kingdom
16. Shin YS, Belenky V, Lin WM, Weems KM, Engle AH (2004) Nonlinear time domain simulation technology for seakeeping and waveload analysis for modern ship design. *Transactions of the Society of Naval Architects and Marine Engineers*

17. Rajendran S, Fonseca N, Guedes Soares C (2011) Time domain comparison with experiments for ship motions and structural loads on a container ship in abnormal waves. In: Proceedings of the ASME 30th international conference on offshore mechanics and arctic engineering, OMAE 2011, Rotterdam, The Netherlands
18. Rajendran S, Fonseca N, Guedes Soares C (2015) Simplified body nonlinear time domain calculation of vertical ship motions and wave loads in large amplitude waves. *Ocean Engg.* 107:157–177
19. Fonseca N, Antunes E, Guedes Soares C (2006) Whipping response of vessels with large amplitude motions. In: Proceedings of the 25th international conference on offshore mechanics and arctic engineering, paper OMAE2006-92412
20. Clauss GF, Kauffeldt A, Klein M (2009) Systematic investigation of loads and motions of a bulk carrier in extreme seas. In: Proceeding of the ASME 2009 28th international conference on ocean, offshore and arctic engineering. OMAE 2009-79389
21. Guedes Soares C, Cherneva Z, Antão EM (2003) Characteristics of abnormal waves in North Sea storm sea states. *Appl Ocean Res* 25(6):337–344



# Vibration Control of Large Floating Offshore Structures by Means of Damping Plates: A Case Study



Carlo Ruzzo, Felice Arena and Vallam Sundar

**Abstract** Large floating multi-purpose platforms are interesting and emerging concepts in terms of envisaged future development in the offshore engineering. The investigation on the hydrodynamic behaviour of such structures plays an important role in their characterization. In particular, vibration control and motion reduction of the platform may be crucial for its operation since most of the renewable energy converters cannot cater to large support motions (e.g. wind turbines, photovoltaic plants and OWC wave energy converters). With this as the background, a small-scale open-sea experimental investigation on a barge structure has been carried out in the Natural Ocean Engineering Laboratory (NOEL) in Reggio Calabria, Italy. The barge was equipped with removable vertical plates in order to investigate their effects on the structure dynamics and their optimal configuration, in terms of its motion attenuation. In addition, a numerical model using the commercial software Ansys AQWA (v. 16.1) is used to investigate its dynamic effects for five different configurations of the plates both in the time and in the frequency domains.

**Keywords** Multi-purpose floating structures · Forces · Floating body dynamics  
Very large floating structures · Barge · Damping plates

## 1 Introduction

Offshore floating structures are currently widespread and are used for many purposes, within the variegated sub-fields of ocean engineering [1]. Among them, floating oil

---

C. Ruzzo (✉) · F. Arena  
DICEAM Department, Mediterranean University of Reggio Calabria, Reggio Calabria, Italy  
e-mail: [carlo.ruzzo@unirc.it](mailto:carlo.ruzzo@unirc.it)

F. Arena  
e-mail: [arena@unirc.it](mailto:arena@unirc.it)

V. Sundar  
Department of Ocean Engineering, Indian Institute of Technology, Madras, India  
e-mail: [vsundar@iitm.ac.in](mailto:vsundar@iitm.ac.in)

© Springer Nature Singapore Pte Ltd. 2019  
K. Murali et al. (eds.), *Proceedings of the Fourth International Conference in Ocean Engineering (ICOE2018)*, Lecture Notes in Civil Engineering 22,  
[https://doi.org/10.1007/978-981-13-3119-0\\_20](https://doi.org/10.1007/978-981-13-3119-0_20)

platforms have shown a rapid development since mid-1980s, leading to a variety of floating concepts, such as spar, semi-submersible and tension-leg platform [2]. Currently, the development of new concepts is towards renewable energy, fish farming, land increase, etc. In this context, large floating structures (LFS) and very large floating structures (VLFS) are envisaged to play a very important role in the near future [3, 4]. Such concepts have been proposed for multi-purpose floating platforms, dedicated to aquaculture, energy harvesting from wind, waves and currents, hydrogen generation, offshore desalinization, energy storage, etc. [5–7]. Furthermore, VLFS has been proposed also for floating airports, bridges, sub-sea tunnels and even floating cities. From technical point of view, the development of such concepts requires to face several challenges, e.g. regarding the connection of VLFS modules, the modelling of coupled hydro-elastic behaviour of the platforms and the motion reduction, which are crucial for most of their practical applications. Comprehensive reviews of the state of the art on these topics may be found in the literature [3, 4]. With regard to motion and stress reduction on VLFS, several strategies have been proposed. Some of the most relevant ones are the adoption of bottom-mounted [8] or floating [3] breakwaters to protect it from waves, the introduction of horizontal [9] or vertical damping plates [10] attached to their fore-end, and the absorption of wave energy via oscillating water column devices [11]. The effectiveness of these devices in real environmental conditions is still uncertain, and hence, the present on-sea experiments indicated as a priority by Wang and Tay [3] for the future development of VLFS are taken up.

The present study deals with the arrangement of an intermediate-scale open-sea experimental program on a floating barge model, equipped with removable vertical damping plates. Depending on the scale factor  $\lambda$  considered, the barge can be regarded as an intermediate-scale model of a LFS ( $\lambda = 10\text{--}20$ ) or a VLFS module ( $\lambda = 20\text{--}30$ ). The experiment was conducted in NOEL [12, 13] of Reggio Calabria, Italy, where, the local irregular wave conditions allow the scaled representation of full-scale wind-generated waves, typical of Mediterranean or ocean storms. The concept of intermediate-scale open-sea experiments as a low-cost alternative to the traditional small-scale activities in wave basins as proposed by Ruzzo et al. [14, 15] has also validated it through numerical and experimental studies on a spar floating support for offshore wind turbines. In this paper, the arrangement of the open-sea experiment is described in detail, with particular reference to the characteristics of the barge model, the installation site and the mooring system. Finally, a numerical analysis aimed to investigate the effects of the vertical damping plates on the dynamics of the structure has been carried out using the software Ansys AQWA [16, 17] and the results of which are presented. Such results provide precise information about the behaviour of the structure in presence of the vertical plates which can be validated against the experimental results.

## 2 Test Rig and Set-up

This section describes the arrangement of the field experimental test rigging. The characteristics of the barge model and the installation site are described in detail, as well as the considerations drawn in the design stage of the experiment on the mooring system and scaling issue. Along with quantitative information about the particular structure used in the present case study, this section reports also useful general information about the arrangement of field experiments on relatively LFS.

### 2.1 Description of the Model

The barge model taken into account in the present study is as shown in Fig. 1. It is basically a rectangular-shaped floating box, with its length and width significantly more than its height. Conventionally, the reference system adopted in this paper is such that  $x$ -axis and  $y$ -axis are along the longer and shorter sides of the barge, respectively. The  $z$ -axis originates from the still water level and is positive upwards.

The hull of the barge is made up of four steel pontoons, running along the barge edges and welded at the corners. The internal structure of the model is stiffened through steel beams in both the horizontal directions, interspersed by vertical stiffeners. The interior of the hull is filled with polystyrene and sealed with two steel laminas, at the top and bottom. Around the perimeter of the barge model, 22 vertical plates are deployed, which can move on vertical guides (Fig. 2), so as to work as external walls (if emerged) or damping plates (if submerged). At the barge centre, an aluminium tower is installed for the measurement of the rigid body motions in



**Fig. 1** Preliminary water test of the barge model at NOEL laboratory (18 vertical plates installed out of 22). *Source* [18]



**Fig. 2** Barge detail: vertical plates (in emerged position) and corresponding vertical guides

**Table 1** Characteristics of the barge model for field trials

	Symbol	Units	Value
Barge length	$L_x$	[m]	7.900
Barge width	$L_y$	[m]	2.385
Barge height	$H$	[m]	0.300
Vertical plate height	$h$	[m]	0.550
Draft	$D$	[m]	0.140
Total barge mass	$m$	[kg]	$2.714 \times 10^3$

waves, which will be achieved through a GPS antenna, able to measure the translational motions of the top section of the tower with respect to a fixed point onshore, coupled with an inertial platform for the measurement of the rotational motions of the barge. The tower is bolted at the bottom and secured via cables under tension to avoid local vibrations, which would otherwise alter the motion measurements. The most important characteristics of the model, excluding those depending on the mass distribution, are reported in Table 1.

The configuration chosen for the vertical plates affects the mass distribution of the barge, while it has negligible effects on the buoyancy, due to the small thickness (3 mm) of the plates. For this reason, the draft of the barge is the same, regardless of the configuration of the vertical plates. Quite contrary, other model characteristics change, due to the different mass distribution of the model. To take this into account, four cases have been considered in this study, as listed below.

- Case 1: all the vertical plates are emerged;
- Case 2: only the vertical plates along the longer sides of the barge (parallel to  $x$ -axis) are submerged;

**Table 2** Mass distribution characteristics of the barge model

Parameter	Symbol	Units	Case 1	Case 2	Case 3	Case 4
Centre of gravity position	$z_G$	[m]	0.068	0.015	0.051	-0.002
Moment of inertia about $x$	$I_{xx}$	[kg m <sup>2</sup> ]	$2.033 \times 10^3$	$2.002 \times 10^3$	$2.025 \times 10^3$	$1.989 \times 10^3$
Moment of inertia about $y$	$I_{yy}$	[kg m <sup>2</sup> ]	$1.622 \times 10^4$	$1.618 \times 10^4$	$1.621 \times 10^4$	$1.617 \times 10^4$
Moment of inertia about $z$	$I_{zz}$	[kg m <sup>2</sup> ]	$1.802 \times 10^4$	$1.802 \times 10^4$	$1.802 \times 10^4$	$1.802 \times 10^4$

- Case 3: only the vertical plates along the shorter sides of the barge (parallel to  $y$ -axis) are submerged;
- Case 4: all the vertical plates are submerged.

The characteristics of the barge model which depend on the mass distribution are reported in Table 2, with reference to the four cases defined above. In the table, all the mass moments of inertia are calculated with respect to the centre of gravity  $G$  of the model. As evident from Table 2, the submergence of the vertical plates has a small positive effect on the roll/pitch stiffness of the barge due to the lowering of the centre of gravity, while the variation of mass moments of inertia is out of scope of the present work.

## 2.2 Installation Site

The location of NOEL is shown in Fig. 3. The peculiarity of the site is that almost pure wind-generated waves of relatively small size ( $H_s = 0.20\text{--}0.40$  m) occur with a certain regularity, thanks to a combination of various environmental conditions, including the steadiness of the local wind, the small fetch and the coast profile. As observed by Boccotti [19], such a condition is crucial for the representativeness of the local sea-states as small-scale models of severe ocean storms under Froude laws (Table 3). This is because the scaling of wave spectra must be achieved not only for the wave surface elevation, but also for wave head of pressure at any depth. As a consequence, any swell component would alter the similitude in depth, due to its smaller attenuation with respect to the wind-generated component. However, Ruzzo et al. [20] observed that also local swells and mixed sea-states are precious for experimental studies on floating structures since they allow to identify the dynamic characteristics of the models over a wider frequency range, even though they are

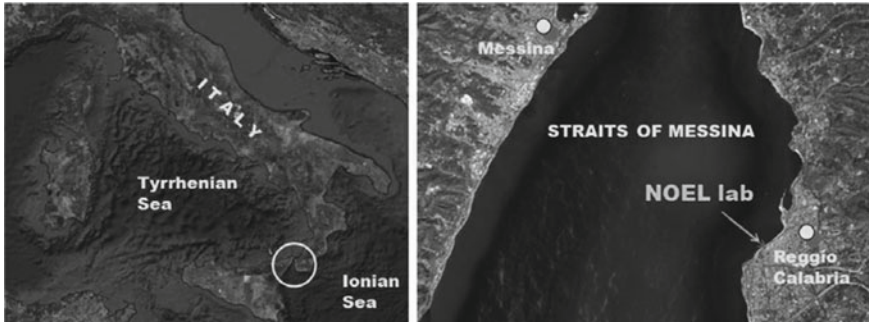


**Fig. 3** NOEL site. *Source* [14]

**Table 3** Froude scaling laws

Parameter	Units	Scale factor
Length	[m]	$\lambda$
Time	[s]	$\lambda^{0.5}$
Velocity	$[\text{m s}^{-1}]$	$\lambda^{0.5}$
Acceleration	$[\text{m s}^{-2}]$	$1$
Mass	[kg]	$\lambda^3$
Mass moment of inertia	$[\text{kg m}^2]$	$\lambda^5$
Force	[N]	$\lambda^3$

not representative of any realistic full-scale wave condition. The combination of all these properties makes the NOEL site particularly suitable for the installation of the barge model.

The design of the mooring system of the barge model is highly influenced by the local irregular bathymetry of NOEL site. The seabed, indeed, presents a significant slope (up to about 10%), which poses difficulties in the design of an appropriate symmetric mooring system. Further, the seaside mooring lines will be longer than the shoreward ones, due to the greater water depth at the anchor point. The steep variation in the water depth, however, has also its own advantages, since it facilitates testing of the barge model in different depths, both in shallow and deep waters. For the present study, a water depth,  $d$  of 8 m, has been chosen for the barge model and a four-point mooring system has been designed, using two different types of catenary line for the two each on shoreward and seaward sides. The characteristics of the resulting mooring system are reported in Table 4.

It should be noted that the horizontal tensions reported in Table 4 have been calculated using a quasi-static 2D model of each catenary line, under the hypothesis of horizontal seabed. In practice, the behaviour of the lines will be altered by the seabed slope in the proximity of the anchors; hence, the mooring system design should be adjusted immediately before the installation of the model, on the basis of

**Table 4** Characteristics of the mooring lines

Parameter	Units	Seaside mooring lines	Landside mooring lines
Anchor depth	[m]	-14.00	-4.000
Mass per unit length	[kg m <sup>-1</sup> ]	2.300	5.200
Unstretched length	[m]	20.20	14.20
Horizontal projection fairlead anchor (in the line direction)	[m]	12.27	12.27
Angle of the line direction with respect to <i>x</i> (in the horizontal plane)	[°]	45.85	134.2
Horizontal tension at equilibrium position	[N]	109.2	108.3

**Table 5** Examples of the characteristics of the full-scale structures represented by the model

Parameter	$\lambda = 1$ (model)	$\lambda = 10$ (LFS)	$\lambda = 30$ (VLFS module)
Barge sides	$L_x = 7.900$ m; $L_y = 2.385$ m; $H = 0.300$ m;	$L_x = 79.00$ m; $L_y = 23.85$ m; $H = 3.00$ m;	$L_x = 237.0$ m; $L_y = 71.55$ m; $H = 9.00$ m;
NOEL operational sea-state	$H_s = 0.300$ m; $T_p = 2.335$ s; mean-JONSWAP	$H_s = 3.00$ m; $T_p = 7.385$ s; mean-JONSWAP	$H_s = 9.00$ m; $T_p = 12.79$ s; mean-JONSWAP
NOEL ultimate sea-state	$H_s = 1.500$ m; $T_p = 5.222$ s; mean-JONSWAP	$H_s = 15.00$ m; $T_p = 16.51$ s; mean-JONSWAP	-

an updated bathymetry. Concerning the yaw stiffness of the mooring system, it will be enhanced through the delta connections of the mooring lines, whose side will be set equal to 10% of the corresponding line [21].

The design of any open-sea experiment must take into account at least two sea-states, corresponding to the ultimate local wave conditions (useful for checking the structural integrity of the model) and the characteristic wave conditions (useful for the representativeness of the results in scale) [14]. In the present case, the two sea-states considered for the design of the experiment are reported in Table 5, where two examples of scale factors are also shown, to highlight the versatility of the barge model, which is able to represent a scaled LFS (e.g.  $\lambda = 10$ ) or a scaled VLFS module (e.g.  $\lambda = 30$ ). Since the full-scale structure characteristics depend on the scale factor chosen, the results will be referred directly to the most general case of the 1:1 model that will be installed at NOEL. The same characteristics for any full-scale prototype can be then easily obtained by scaling up the desired results using Froude rules, as reported in Table 3.

### 3 Numerical Analysis and Effects of the Vertical Damping Plates

This section describes the results of the numerical analysis carried out to evaluate the effects of the presence and of the size of vertical plates on the dynamics of the barge model in the frequency and in the time domain. The results obtained are explained, and the implications on the adoption of vertical plates for vibration control of large floating structures are highlighted.

#### 3.1 Analysis of the Four Cases

The 1:1 barge model has been represented by a numerical model implemented using the software Ansys AQWA (v. 16.1) [16, 17]. The barge has been represented by a number of diffracting elements (variable for the four cases), whose maximum size is 0.1 m. The mooring system has been represented by four nonlinear catenaries, with their properties reported in Table 4. The fairleads have been located at the four bottom corners of the barge, i.e. at a depth  $z_F = -0.14$  m. It should be noted that the numerical model does not include the seabed slope and, particularly, the delta connection of the mooring lines. As a consequence, the resulting characteristics in yaw motion are not accurate. The Response Amplitude Operators (RAOs) of the barge have been obtained in absence and presence of the mooring lines, using an internal linearization algorithm to deal with their nonlinearity. The latter results for each of the four cases mentioned in Sect. 2.1 are shown in Figs. 4, 5, 6, 7, 8, and 9, where the 1:1 NOEL operational sea-state (Table 5) with a propagation direction of  $45^\circ$  has been used as the input wave condition for the linearization procedure of the software. It must be stated that such a wave direction has been used to excite all the degrees of freedom of the barge and to better highlight all of its dynamic properties. During its operational life, however, the model will be more commonly excited by sea-states propagating along  $x$ -axis, due to its orientation at the equilibrium position.

It should be noted that the presence of the vertical plates does not induce a reduction of the motion amplitude in any degree of freedom. Quite contrary, the amplitude of the motions increases while the natural frequency reduces. To better understand this behaviour, it is useful to consider in depth each of the results.

Surge RAOs of the four cases show two different natural frequencies. The higher one is related to Case 1 and Case 2, and the lower one is related to Case 3 and Case 4. The decrease of the natural frequency observed in the latter cases is due to an increase in the added mass in surge, induced by the vertical plates installed on the short side of the barge (Fig. 10). Similarly, the natural frequency in sway decreases for Case 2 and Case 4, when the vertical plates on the longer side of the barge are submerged, inducing an increase in the added mass in sway. Another effect due to the asymmetry in the mooring system is the coupling degrees of freedom between



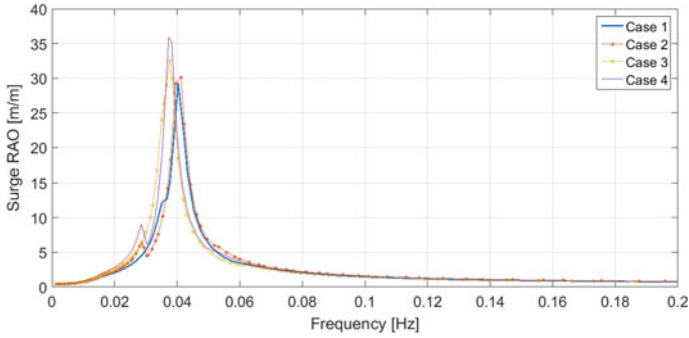


**Fig. 4** Surge RAOs of the barge model obtained in Ansys AQWA for the four cases

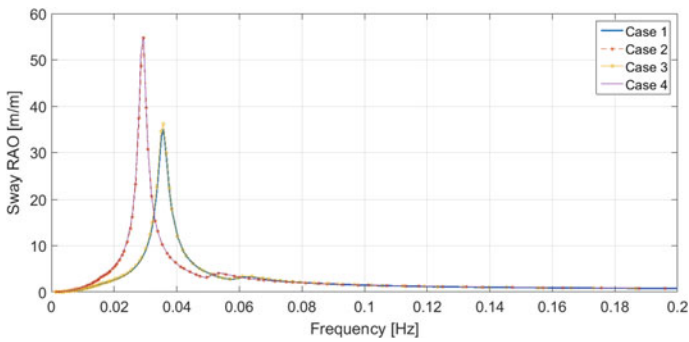


**Fig. 5** Sway RAOs of the barge model obtained in Ansys AQWA for the four cases

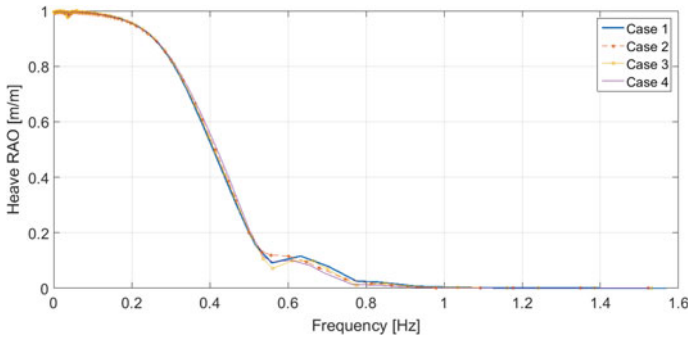


**Fig. 6** Heave RAOs of the barge model obtained in Ansys AQWA for the four cases

surge and sway. This effect is enhanced by the submerged plate in the longer barge side; hence, it is particularly evident in Case 2 and Case 4, where a small peak in the surge RAO can be observed at the sway natural frequency. It is interesting to note that this is a one-way coupling because barge motions in sway induce nonzero

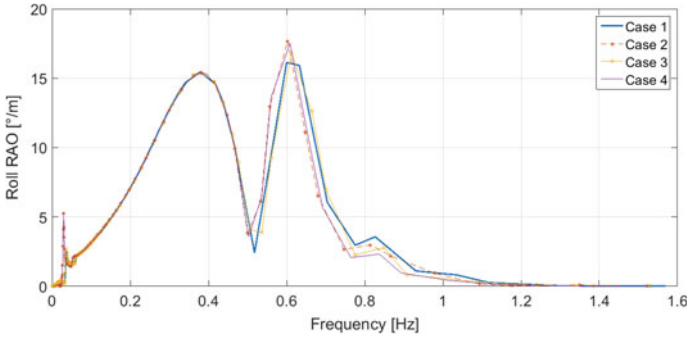


Fig. 7 Roll RAOs of the barge model obtained in Ansys AQWA for the four cases

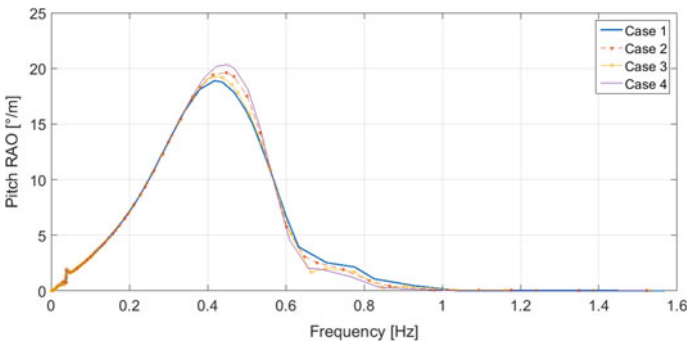


Fig. 8 Pitch RAOs of the barge model obtained in Ansys AQWA for the four cases

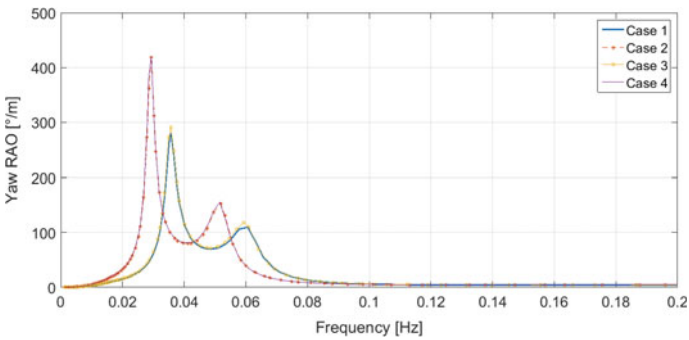
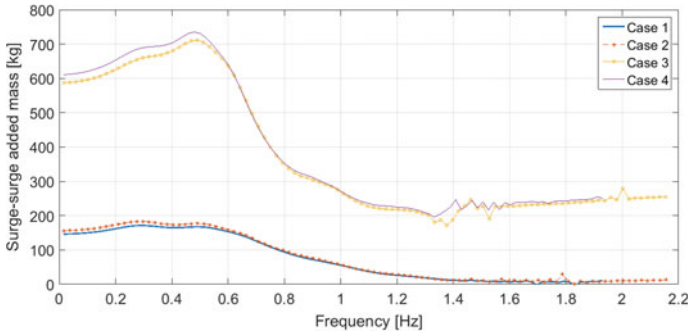
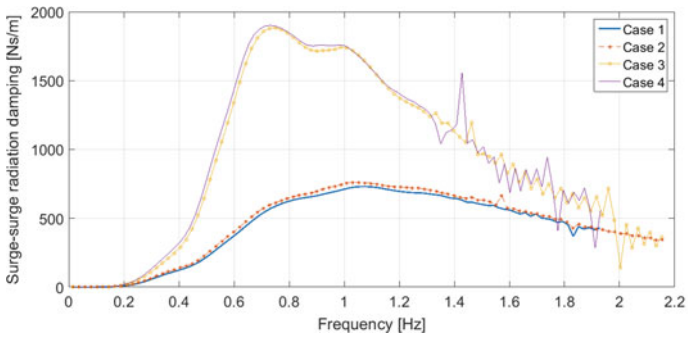


Fig. 9 Yaw RAOs of the barge model obtained in Ansys AQWA for the four cases

restoring forces in  $x$  direction from the mooring system, while motions in surge do not induce any restoring force in  $y$  direction. Concerning the amplitude of the motions, the introduction of the vertical plates results in two opposite effects:



**Fig. 10** Added mass (surge–surge) of the barge model obtained in Ansys AQWA for the four cases



**Fig. 11** Radiation damping (surge–surge) of the barge model obtained in Ansys AQWA for the four cases

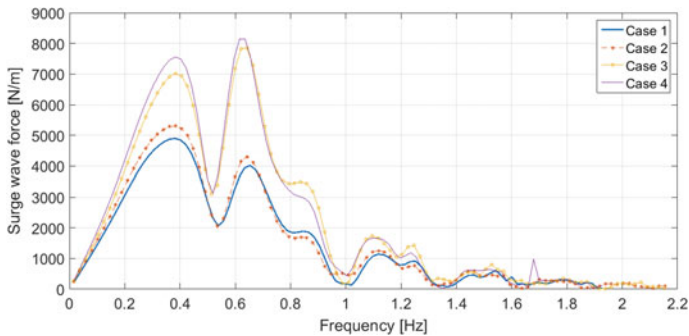


**Fig. 12** Surge force (diffraction+Froude–Krylov force components in  $x$  direction) of the barge model obtained in Ansys AQWA for the four cases (wave direction of  $45^\circ$ )

1. the radiation damping increases (Fig. 11), involving a reduction in motion amplitudes;
2. the wave force increases too (Fig. 12), involving an increase in motion amplitudes.

**Table 6** Examples of the characteristics of the full-scale structures represented by the model

Degree of freedom	Units	Case 1	Case 2	Case 3	Case 4
Surge	[m]	0.569	0.634	0.640	0.730
Sway	[m]	0.609	0.627	0.613	0.701
Heave	[m]	0.339	0.339	0.338	0.339
Roll	[°]	3.331	3.404	3.278	3.339
Pitch	[°]	3.205	3.159	3.219	3.282
Yaw	[°]	7.548	9.214	7.945	9.611

The second effect is stronger than the first, resulting in larger motions when the vertical plates are submerged.

Similar considerations may be done for roll and pitch, even if the increase in motion amplitude with respect to Case 1 is smaller. It is also interesting to highlight the qualitative behaviour of the yaw motion of the barge, since it is coupled to sway degree of freedom, again because of the asymmetry of the mooring system. For this reason, the yaw RAO is significantly affected by the presence of the submerged vertical plates on the longer side (Case 2 and Case 4), while the effects of the other vertical plates are practically negligible. Similarly, also roll and pitch are coupled with sway motion, as demonstrated by the small low-frequency peaks in the corresponding RAOs.

The time histories of the body motions have been obtained for both NOEL operational and ultimate sea-states (Table 5), using the fully nonlinear AQWA numerical model, and substantially confirm the above considerations. For sake of example, the results obtained in the time domain for the NOEL ultimate sea-state with a propagation direction of 45° are reported in Table 6. They are expressed in terms of standard deviations of the body motions in all the six degrees of freedom for each of the four structural configurations considered in this paper, using a single time history of duration  $\Delta t = 2000.0$  s and a time step  $dt = 0.1$  s.

### 3.2 Effect of the Vertical Plate Height

The results obtained as reported earlier discourage the adoption of vertical plates on the perimeter of large floating barges for the reduction of their motions since such motions actually increase. This effect is due to the combined increase of radiation damping and wave force in the frequency domain, in a way that the latter dominates among the former.

In this section, the effect of the vertical plate height is investigated, in order to check whether motion attenuation could be achieved by using deeper plates. In particular, Case 5 is introduced, which is similar to Case 4 except for the vertical plate height, which becomes equal to 1.10 m instead of 0.55 m, resulting in a significant

increase of the submerged area of the plate. All the other structural properties have been kept the same, including those depending on mass distribution, hypothesizing a corresponding design of the plates.

Similarly to the previous four cases, the RAOs have been calculated, using the same sea-state for the linearization process. The results obtained are shown in Figs. 13, 14, 15, 16, 17 and 18, where a comparison with Case 1 (no submerged plates) is also provided.

As evident from the results, the amplification of all the body motions is even more evident with respect to the previous cases, proving that vertical plates placed along the barge perimeter cannot be used as vibration control devices for these kinds of structures.

It is also interesting to highlight that in this case, the low-frequency peaks in the roll and pitch RAOs are significantly greater than in the previous cases, proving the existence of an important coupling between sway and the rotational degrees of freedom.

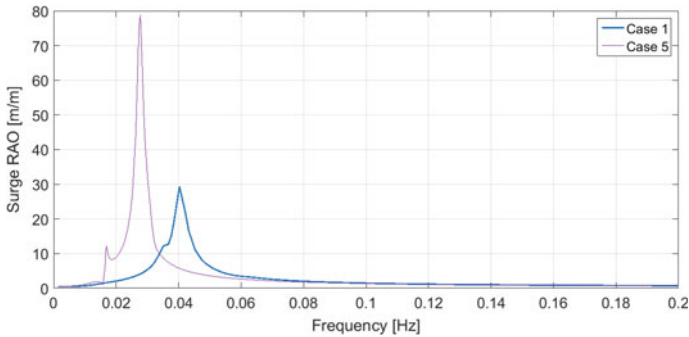


Fig. 13 Surge RAOs of the barge model obtained in Ansys AQWA for Case 5 and Case 1

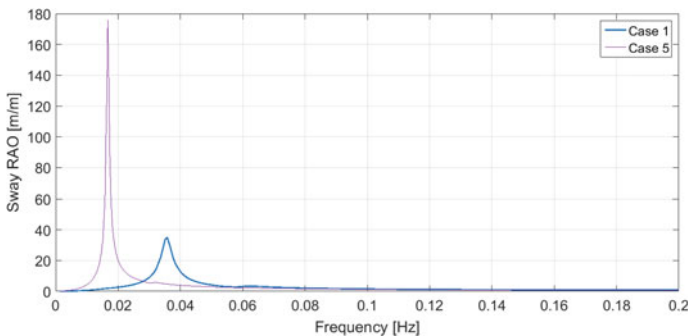


Fig. 14 Sway RAOs of the barge model obtained in Ansys AQWA for Case 5 and Case 1

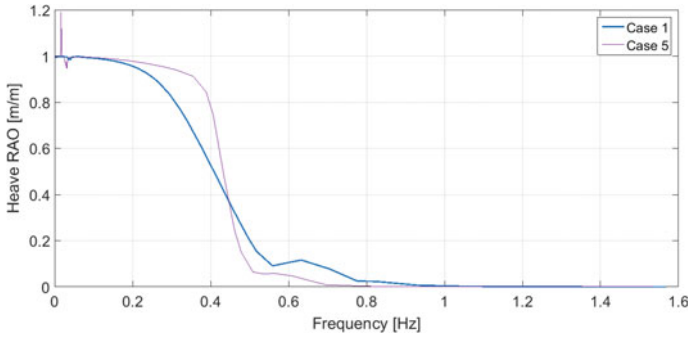


Fig. 15 Heave RAOs of the barge model obtained in Ansys AQWA for Case 5 and Case 1

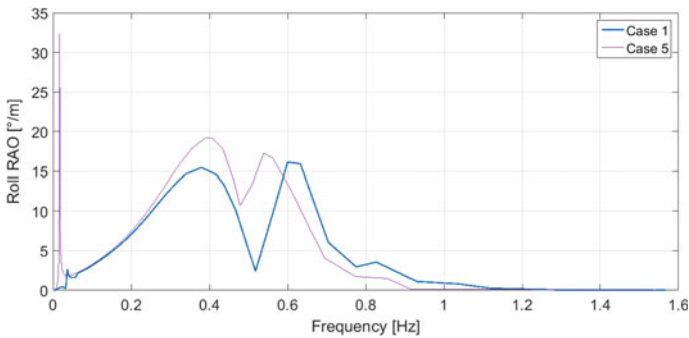


Fig. 16 Roll RAOs of the barge model obtained in Ansys AQWA for Case 5 and Case 1

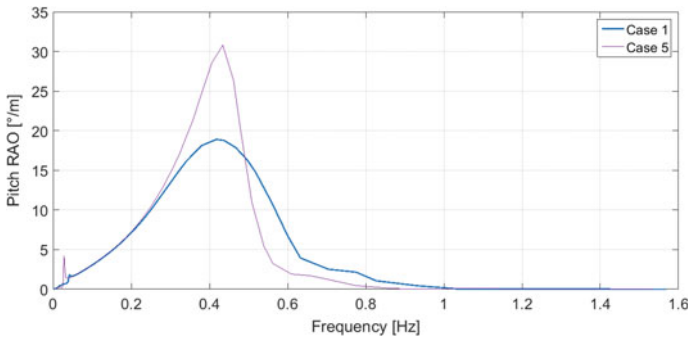
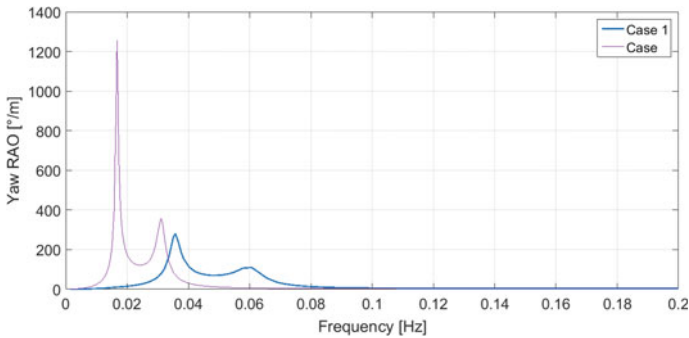


Fig. 17 Pitch RAOs of the barge model obtained in Ansys AQWA for Case 5 and Case 1

## 4 Conclusions and Future Work

This paper presents the arrangement of an intermediate-scale open-sea experimental activity on a barge model. The tests conducted at NOEL laboratory in Reggio Cal-



**Fig. 18** Yaw RAOs of the barge model obtained in Ansys AQWA for Case 5 and Case 1

abria, Italy, to evaluate the effects of vertical plates on the dynamics of large floating bodies are reported in this paper. In particular, the barge model considered can be regarded as a scaled model of a LFS or of a VLFS module, given an opportune scale factor. In the first part of the paper, the experimental set-up is discussed in detail, including installation site peculiarities and mooring system design. To investigate the effects of the submerged vertical plates on the structure dynamics, the barge model has been equipped with movable steel laminas, which can be used either as external walls or submerged vertical plates. Four relevant structural configurations have been chosen, and the barge mass properties have been calculated for each of them.

In the second part of the paper, a numerical analysis has been carried out to evaluate the effect of the submerged vertical plates on the structure dynamics, using the software Ansys AQWA. The analysis revealed that an increase in the radiation damping induced by the vertical plates is insufficient to compensate the increase of wave force in the frequency domain, resulting in the increase of structure motions when the plates are submerged. Similar results have been obtained by considering a fifth case with deeper submerged vertical plates, showing that such devices are not viable for motion reduction of VLFS. Secondary effects of the vertical plate introduction are the decrease of the natural frequencies of surge, sway, roll and pitch motions of the barge, due to the increased added mass, and the insurgence of some couplings, mainly between sway and the other degrees of freedom.

The experimental activity that will be carried out in a near future is expected to confirm such numerical predictions and to give additional information about the real behaviour of such structures in open-sea. Moreover, since vertical plates have proved not to be feasible for motion reduction of the structure considered, further numerical and experimental works will be carried out in a near future to find alternative solutions. Among the others, vertical plates could be moved to the internal part of the barge, where the wave action is smaller, or horizontal plates could be adopted instead of the vertical ones.

**Acknowledgements** This paper was developed during the Marie Curie IRSES project “Large Multi-Purpose Platforms for Exploiting Renewable Energy in Open Seas (PLENOSE)” funded by the European Union (Grant Agreement Number: PIRSES-GA-2013-612581).

## References

1. Chakrabarti SK (2005) Handbook of offshore engineering. Elsevier, London. <https://doi.org/10.1016/b978-0-08-044381-2.50014-x>
2. El-Reedy MA (2012) Offshore structures. Gulf Professional Publishing, Boston. ISBN 9780123854749
3. Wang CM, Tay ZY (2011) Very large floating structures: applications, research and development. Proc Eng 14:62–72. <https://doi.org/10.1016/j.proeng.2011.07.007>
4. Lamas-Pardo M, Iglesias G, Carral L (2015) A review of very large floating structures (VLFS) for coastal and offshore uses. Ocean Eng 109:677–690. <https://doi.org/10.1016/j.oceaneng.2015.09.012>
5. Quevedo E, Carton M, Delory E, Castro A, Hernandez J, Llinas O, De Lara J, Papandroulakis N, Anastasiadis P, Bard J, Jeffrey H, Ingram D, Wesnigk J (2013) Multi-use offshore platform configurations in the scope of the FP7 TROPOS Project. In: OCEANS—Bergen, 2013 MTS/IEEE conference. <https://doi.org/10.1109/oceans-bergen.2013.6608061>
6. H2Ocean Project. Information: <http://www.h2ocean-project.eu/>
7. Mermaid Project. Information: <http://www.vliz.be/projects/mermaidproject/>
8. Utsunomiya T, Watanabe E, Nakamura N (2001) Analysis of drift force on VLFS by the near-field approach. In: 11th international offshore and polar engineering conference (ISOPE 2001)
9. Watanabe E, Utsunomiya T, Kuramoto M, Ohta H, Torii T, Hayashi N (2002) Wave response analysis of VLFS with an attached submerged plate. In: 12th international offshore and polar engineering conference (ISOPE 2002)
10. Ohta H, Torii T, Hayashi N, Watanabe E, Utsunomiya T, Sekita K, Sunahara S (1999) Effect of attachment of a horizontal/vertical plate on the wave response of a VLFS. In: Ertekin RC, Kim JW (eds), Proceedings of the 3rd international workshop on very large floating structures (VLFS '99)
11. Hong DC, Hong SY, Hong SW (2006) Reduction of hydroelastic responses of a very long floating structure by a floating oscillating water column breakwater system. Ocean Eng 33(5–6):610–634. <https://doi.org/10.1016/j.oceaneng.2005.06.005>
12. Arena F, Barbaro G (2013) The Natural Ocean Engineering Laboratory, NOEL, in Reggio Calabria, Italy: a commentary and announcement. J Coastal Res 29(5):vii–x
13. Natural Ocean Engineering Laboratory. Information: <http://noel.unirc.it/>
14. Ruzzo C, Fiamma V, Nava V, Collu M, Failla G, Arena F (2016) Progress on the experimental set-up for the testing of a floating offshore wind turbine scaled model in a field site. Wind Eng 40(5):455–467. <https://doi.org/10.1177/0309524X16660023>
15. Ruzzo C, Failla G, Collu M, Nava V, Fiamma V, Arena F (2016) Operational modal analysis of a spar-type floating platform using the frequency domain decomposition method. Energies 9(11):870. <https://doi.org/10.3390/en9110870>
16. ANSYS®, Academic Research, Release 16.1
17. ANSYS® AQWA, v. 16.1, Help system, theory manual, ANSYS, Inc.
18. Arena F, Ruzzo C, Romolo A, Fiamma V, Malara G, Barbaro G (2016) Test Water: approcci avanzati per la realizzazione in mare di isole offshore galleggianti. In: Lauria M, Trombetta C (eds) Building Future Lab: Ricerca sperimentale per la Sostenibilità nel Settore delle Costruzioni. ISBN: 8891612830
19. Boccotti P (2014) Wave mechanics and wave loads on marine structures. Butterworth-Heinemann, Waltham. ISBN 9780128003435



20. Ruzzo C, Fiamma V, Collu M, Failla G, Nava V, Arena F (2018) On intermediate-scale open-sea experiments on floating offshore structures: feasibility and application on a spar support for offshore wind turbines. *Mar Struct* 61:220–237
21. Quallen S, Xing T, Carrica P, Li Y, Xu J (2014) CFD simulation of a floating offshore wind turbine system using a quasi-static crowfoot mooring-line model. *J Ocean Wind Energy* 1(3):143–152

# Experimental Investigation on Effect of Submerged Solid Baffle in a Barge Carrying Liquid Sloshing Tank



T. Nasar and S. A. Sannasiraj

**Abstract** An experimental programme is conducted to investigate, barge responses, sloshing dynamics and sloshing pressure in a partially liquid-filled baffled tank which is equipped in a floating barge. The barge was subjected to regular wave excitations with wave height of 0.1 m and frequencies ranging from 0.45 to 1.54 Hz under beam sea condition. An aspect ratio ( $h_s/l$ , liquid depth,  $h_s$  to length of tank  $l$ ) of 0.488 corresponds to 75% fill level is considered. In addition, a solid baffle wall at  $l/2$  (height of solid baffle wall as  $h/2$ ,  $h$ =tank height) is considered which is a typical arrangement in LNG sloshing tank. The effectiveness of solid baffle is investigated in comparison with unbaffled conditions. The barge responses at liquid-filled condition and equivalent dry weight conditions are compared.

**Keywords** Barge response · Harmonics · Solid baffle · Sloshing pressure

## 1 Introduction

The intricate phenomenon of liquid sloshing in a partially filled container has been subject of study over the past few decades due to its association with several engineering problems. In maritime applications, the violent sloshing in LNG-FPSO/FSRU units and storage tanks/ballast tanks in all floating systems causes instability in its static behaviour as well as leads to localised structural damage. Numerous studies have been focussed to understand nonlinear sloshing behaviour and sloshing pressure on the walls of containment. Sloshing suppression devices have also been proposed by various authors.

---

T. Nasar (✉)

National Institute of Technology Karnataka, Surathkal, Karnataka, India

e-mail: [t.nasar@gmail.com](mailto:t.nasar@gmail.com)

S. A. Sannasiraj

Indian Institute of Technology Madras, Chennai, Tamilnadu, India

e-mail: [sasraj@iitm.ac.in](mailto:sasraj@iitm.ac.in)

© Springer Nature Singapore Pte Ltd. 2019

K. Murali et al. (eds.), *Proceedings of the Fourth International Conference in Ocean Engineering (ICOE2018)*, Lecture Notes in Civil Engineering 22,

[https://doi.org/10.1007/978-981-13-3119-0\\_21](https://doi.org/10.1007/978-981-13-3119-0_21)

Since 1980s considerable works have been carried out on sloshing dynamics, Nakayama and Washizu [1] developed finite element formulation to study the non-linear behaviour of liquid sloshing in a pitch excited 2D rectangular tank. Ockendon et al. [2–4] explored the nonlinear characteristics of sloshing by using shallow water theory. The importance of dynamic coupling between roll excitation and liquid oscillation has been examined by Liu and Lin [5] using analytical approach. The presence of harmonics on modal behaviour of sloshing oscillations for the aspect ratio ranging between  $h_s/l$  of 0.1 and 1.0 [6], [7, 8] was explored. In the following numerical works, Frandsen [9] reported the multiple resonance conditions in a combined sway and heave excitations. Kim et al. [10] predicted the unexceptional behaviour in the free surface oscillation by using volume of fluid-based numerical algorithm for combined degrees of excitations of tank. Two-Dimensional and Three-Dimensional (six degrees freedom of excitation) sloshing behaviour in a rectangular tank impetus the necessity of combined translational and rotational accelerations, which would lead to unexpected reaction force against the oil tanker.

Importance of coupled effect of surge, heave and roll motions and the reciprocal action of the sloshing fluid with freely floating tank motion were reported by Chen and Chiang [11]. The interaction effect in a roll excited tank shifts the roll resonance peak towards lower frequencies as reported by Francescutto and Contento [12]. Also, a secondary peak was observed in the roll response amplitude operator (RAO) at the natural sloshing frequency. A numerical study by Lee et al. [13] on the interaction of barge-type FPSO subjected to random excitation showed similar results. Nasar et al. [14] also observed bimodal peaks in the roll response due to interaction between floating barge and sloshing in a rectangular tank. Nasar et al. [15] emphasised the necessity of the interaction study and also stated that as the excitation degrees of freedom increases, the modal behaviour of free surface oscillations is chaotic. As a result, higher sloshing pressure on the side walls and top panel of rectangular containment can be expected.

In view of suppressing the sloshing energy/improving the damping characteristics, authors have proposed anti-slosh devices such as bottom fixed wedge-shaped obstacles or sloping bottom (Modi and Akinturk [16], submerged nets/poles [17], floating baffles/slat screens [18] and slotted screens [19], [20]. A numerical study by Armenio and La Rocca [21] reported the effect of the bottom mounted solid baffle in reducing the sloshing load. Kim [22] reported the combined effectiveness of vertical baffle and side wall stringers. Panigrahy et al. [23] experimented the combination of horizontal and vertical baffle to attenuate the sloshing pressure in a sway excited tank. Xue et al. [24] simulated the sloshing behaviour and traced the pressure in a surge excited cubic tank. The effectiveness of different baffle wall configurations such as horizontal baffle, perforated vertical baffle, and their combinations is discussed, and the results are compared with experimental data. Akyildiz [25] used volume of fluid (VOF) technique to simulate the effect of vertical baffle height in the pitch excited two-dimensional rectangular tank. The side wall pressure distribution and roof impact for the different filling conditions are discussed, and the results are compared with experimental work. Xue et al. [24] investigated the effectiveness of the vertical baffles in suppressing the sloshing pressure in a horizontally excited tank.

Four configurations such as submerged solid baffle, surface piercing baffle, surface flush baffle, and porous baffle are considered. It is concluded that the porous baffle gives better results in reducing side wall impact pressure. Iranmanesh [26] proposed a numerical model based on VOF technique and discussed the potentiality of the constrained surface floating and submerged cylinder in suppressing sloshing pressure. Cho et al. [27] examined the effect of horizontal baffle wall in reducing sloshing energy and sloshing pressure on the tank walls in a sway excited tank. Boundary element equations were developed for different porous wall conditions to compare with the experimental results. In maritime applications, it is conventional practice to use solid baffle walls (bottom stringers and side stringers at different elevations of tank) as flow damping systems in cargo oil tanks. Kim [28] carried out computational study to assess the effect of internal members on the sloshing flows for various filling levels. The liquid tank system was subjected to sway/surge, pitch/roll, combined sway/surge (with and without phase difference) and combined pitch/roll (with and without phase difference) mode of excitation.

Although there are considerable numerical/analytical models are reported in the literature, experimental procedures are more preferred to study the barge responses, sloshing dynamics and calculation of pressure on tank walls as well as pressure on tank ceiling. Further, the theoretical models are less efficient in predicting the unusual behaviour in the free surface, hydraulic jump, roof impact, etc. In addition, experimental work is rather suited to study the damping characteristics of baffle in which vorticity involves. By considering the importance of combined excitations and interaction study, a freely floating barge with a rectangular tank fixed in it is allowed to oscillate in three degrees of freedom, namely sway, heave and roll. The present paper aims to explore the efficacy of submerged solid baffle.

## 2 Experimental Investigations

### 2.1 Model Details

An acrylic sloshing tank of dimensions 1.0 m ( $l$ )  $\times$  0.4 m ( $b$ )  $\times$  0.65 m ( $h$ ) and thickness of 12 mm is equipped inside fibre-reinforced plastic barge with dimensions' breadth ( $B$ ) 1.32 m  $\times$  0.65 m ( $D$ ) deep. To receive the beam sea waves, barge of length 1.95 m was kept along the flume width. The longitudinal axis of sloshing tank is aligned with traverse width of the barge. The beam sea condition excites the liquid along the longitudinal axis of sloshing tank. Figure 1 represents the experimental setup of sloshing tank equipped inside the floating barge. A solid baffle was made using acrylic sheet of 5 mm thickness, and Fig. 2 exhibits the baffle arrangement in the sloshing tank.

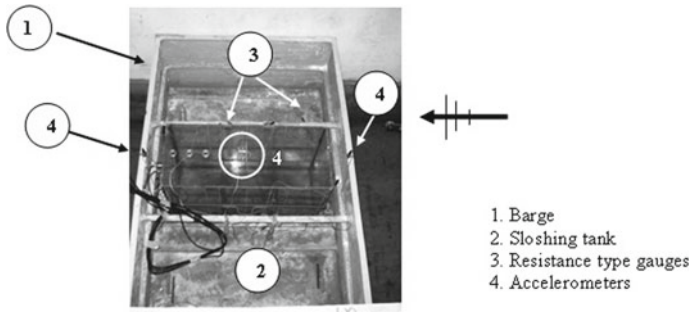
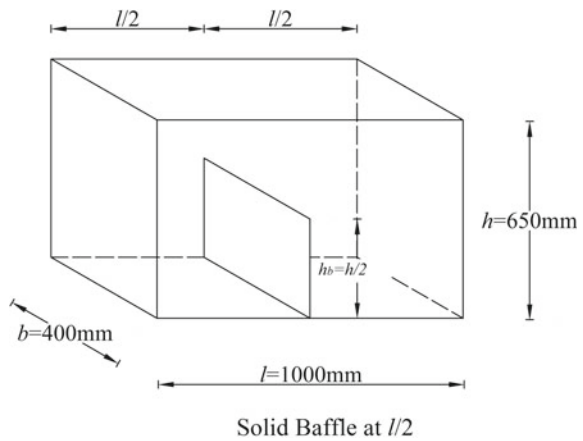


Fig. 1 Photographic view of sloshing tank inside the barge

Fig. 2 Baffle arrangement in the sloshing tank



### 2.2 Flume Facilities and Experimental Procedures

The experimental investigations were carried out in a wave flume at Department of Ocean Engineering, IIT Madras, India. The flume is about 50 m length, 2 m width and 2.7 m depth. The wavemaker is controlled by a hydraulic servo actuator and can be operated both in piston and hinged modes. During the course of experiment, the wavemaker is operated in the piston mode and the water depth ( $d$ ) was maintained as 1.0 m. The model was placed at a distance of 34 m from the mean position of the wave paddle. Two-wave probe method was adopted to trace the incident wave field. Figure 3 shows the position of barge model and the wave probe locations in the flume. Single-axis HBM accelerometers with a measuring range of up to 100 Hz were used to trace the sway, heave and roll responses of barge model. The liquid oscillations inside sloshing tank were recorded with help of four resistive gauges (RP1–RP4) on the walls. The tank walls were instrumented with strain gauge-type pressure transducers (P1–P8), and the schematic representation of sloshing tank is shown in Fig. 4.

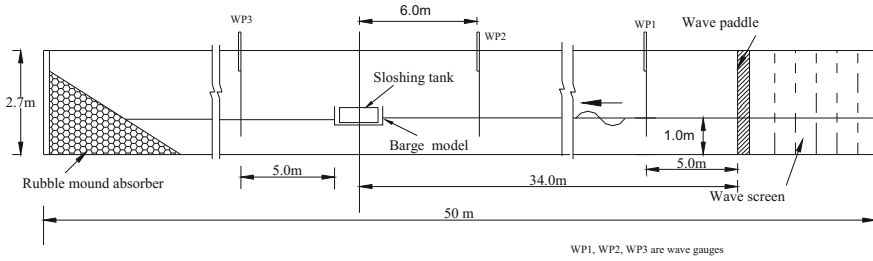


Fig. 3 Experimental setup in the wave flume

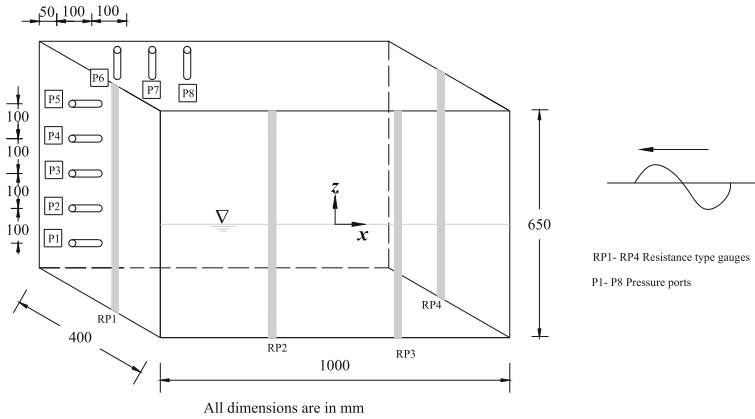


Fig. 4 Position of resistive type run-up probes (RP1–RP4) and pressure port locations (P1–P8) on the sloshing tank

The liquid oscillation behaviour in the partially filled tank depends on the excitation frequency and amplitude, size and geometry of the tank of the tank, fill depth and internal baffle arrangements if any. The complexity in the free surface behaviour escalates due to coupled transitional and rotational movements. Ibrahim [29] gave the linear approximation of resonant liquid sloshing frequencies (in Hz) for the  $n$ th mode in a rectangular tank as follows:

$$f_n = \frac{1}{2\pi} \sqrt{\frac{n\pi g}{l} \tanh\left(\frac{n\pi h_s}{l}\right)} \quad n = 1, 2, 3 \dots \tag{1}$$

where  $l$  is the length of the tank,  $h_s$  is the static liquid depth, and  $n$  is the surface mode number. Faltinsen and Timokha [30] proposed the modified equations of sloshing frequency (rad/s) for centrally placed bottom mounted submerged vertical baffle in a 2D sloshing tank is given in Eq. 2.

$$\frac{\omega_1'^2}{\omega_1^2} = 1 - \frac{2\pi^2 \sin^2(\pi/2)}{\sinh(2\pi h_s/l)} \left(\frac{h_b}{l}\right)^2 \tag{2}$$

**Table 1** Tank sloshing frequencies for 75% fill depth

	$f_1$ (Hz)	$f_2$ (Hz)	$f_3$ (Hz)	$f_4$ (Hz)	$f_5$ (Hz)
Without baffle (Eq. 1)					
Tank length, $l$	0.84	1.25	1.53	1.77	1.98
Tank length, $l/2$	1.25	1.77	2.16	2.50	2.79
Tank length, $l/3$	1.53	2.16	2.65	3.06	3.42
Solid baffle @ $l/2$ (Eq. 2) ( $h_b = h/2$ )	0.75	1.12	1.38	1.59	1.77

**Table 2** Barge model parameters and barge frequencies

Fill depth in sloshing tank $h_s = (h^* \%)$	Draft of barge (m)	Total mass (kg)	KG (m)	(MI) <sub>CG</sub> (kg m <sup>2</sup> )
0.75	0.123	293	0.260	54.83
Draft of barge (m)	Experimental analysis ( $f_z$ )	Eigenvalue analysis (FEM) ( $f_z$ )	Experimental analysis ( $f_\varphi$ )	Eigenvalue analysis (FEM) ( $f_\varphi$ )
0.123	0.67	0.66	0.81	0.81

where  $h_b$  is height of baffle.

The sloshing modal frequencies (Eq. 1) and modified frequencies (Eq. 2) for the liquid depth ( $h_s$ ) of 75% tank depth ( $h$ ) are provided in Table 1. The model parameters for the liquid-filled condition and the heave and roll natural frequencies for the equivalent dry weight condition of the barge derived from the measured free response time histories in calm water condition are stated in Table 2. The experimental frequencies are compared with numerical values predicted by using FEM model [31].

Table 3 explains the wave parameters considered in the present experimental work. The wave frequencies are varied from 0.46 to 1.54 Hz which encompasses third-mode sloshing frequency. For each of the tests, the wave surface elevations at two locations in front and rear of the barge model, sloshing surface elevation, sloshing pressure and barge accelerations were acquired simultaneously for duration of 60–90 s with a sampling frequency of 40 Hz.

**Table 3** Wave parameters

Test case	Fill depth $h_s = (h^* \%)$	Incident wave height, $H_i$ (m)	Wave frequency range, $f_w$ (Hz)
Without baffle	0.75	0.1	0.46–1.54
With baffle [submerged solid baffle]	0.75	0.1	0.46–1.54

### 3 Results and Discussion

#### 3.1 Barge Responses

The steady-state barge responses, sway ( $X$ ), heave ( $Z$ ) and roll ( $\phi$ ), due to combined action of wave and induced sloshing are presented in Fig. 5. The partially liquid-filled condition, liquid filled with submerged solid baffled and equivalent dry weight conditions are compared. The RAOs are compared with the solutions using the finite element method (FEM) of Sannasiraj et al. [31]. The characteristics of barge response amplitude operators (RAO) for 75% liquid-filled condition and the corresponding equivalent dry weigh conditions are detailed in Nasar et al. [14]. The influence of the submerged solid baffle placed at  $l/2$  on RAOs' is herein discussed. An inconsequence of baffle is noted on the characteristics of heave and roll RAOs; however, the peak amplitude of roll RAO is further reduced. It is observed that the sway RAO is greatly influenced by the baffle.

#### 3.2 Analysis of Sloshing Oscillations

##### 3.2.1 General

In the present study, the effect of submerged solid baffle on sloshing run-up, sloshing energy, frequency spectra of sloshing oscillation and induced sloshing pressure for an aspect ratio ( $h_s/l$ ) of 0.488 in comparison with without baffled condition have been discussed. The harmonics/spectral peaks are identified based on the resonance conditions as reported in Nasar et al. [32] and are referred to discuss the spectral peaks. The influence of internal baffle arrangements on resonant sloshing frequency is reported by Falinsen and Timokha [30], and hence, an attempt is made to identify the spectral peaks based on the modified sloshing frequency (Eq. 2) as well. The effectiveness of baffle is assessed as follows:

$$\% \text{ of attenuation in sloshing} = \frac{\zeta_{\max(\text{or})}m_0(\text{without baffle}) - \zeta_{\max(\text{or})}m_0(\text{with baffle})}{\zeta_{\max(\text{without baffle})}} \quad (3)$$



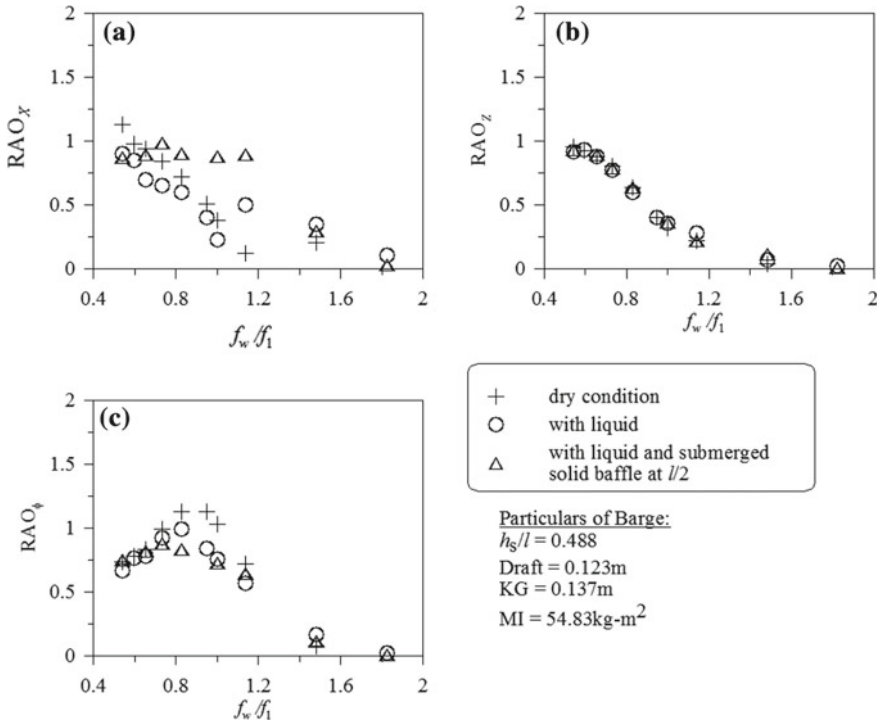


**Fig. 5** Response amplitude operator of the barge for the liquid fill level ( $h_s/l$ ) of 0.488: **a** sway, **b** heave and **c** roll

**3.2.2 Sloshing Run-up and Sloshing Energy**

The variation of normalised maximum sloshing oscillation ( $\zeta_{max}/H_i$ ) as a function of different frequencies' ratio ( $f_w/f_1$ ) subjected to normalised incident wave height  $H_i/d = 0.1$  for without baffle and baffled condition is given in Fig. 6a. By gauging the variation due to baffled condition, it is noticed that maximum sloshing run-up ( $\zeta_{max}/H_i$ ) is obtained at  $f_w/f_1 = 1.14$  which corresponds to wave excitation frequency,  $f_w = 0.96$  Hz. For the frequencies' ratio of  $f_w/f_1 = 0.98$  and  $f_w/f_1 = 1.14$ , normalised sloshing run-up is found to be lesser than the unbaffled condition. On contrary, there is a marginal increase in sloshing run-up at the excitation frequency ratio,  $f_w/f_1 = 1.48$  ( $f_w = f_2$ ), when compared with unbaffled condition. At  $f_w/f_1 = 1.82$  ( $f_w = f_3$ ) and at  $f_w/f_1 = 0.74$ , higher sloshing run-up is obtained. The percentage attenuation of sloshing run-up is illustrated in Fig. 6b. The solid baffle performs up to the expectation for the frequencies' ratio of  $f_w/f_1 = 0.98$  and  $f_w/f_1 = 1.14$  with attenuation of 28 and 48%, respectively. At the frequency ratio of  $f_w/f_1 = 1.48$  corresponds to second-mode frequency, there is an attenuation of -3% which is unappreciable due to being on undesired side. The excitation ratio  $f_w/f_1 = 1.82$  which corresponds to third-mode sloshing frequency in unbaffled condition closer to third-mode frequency ( $f_w/f_1$

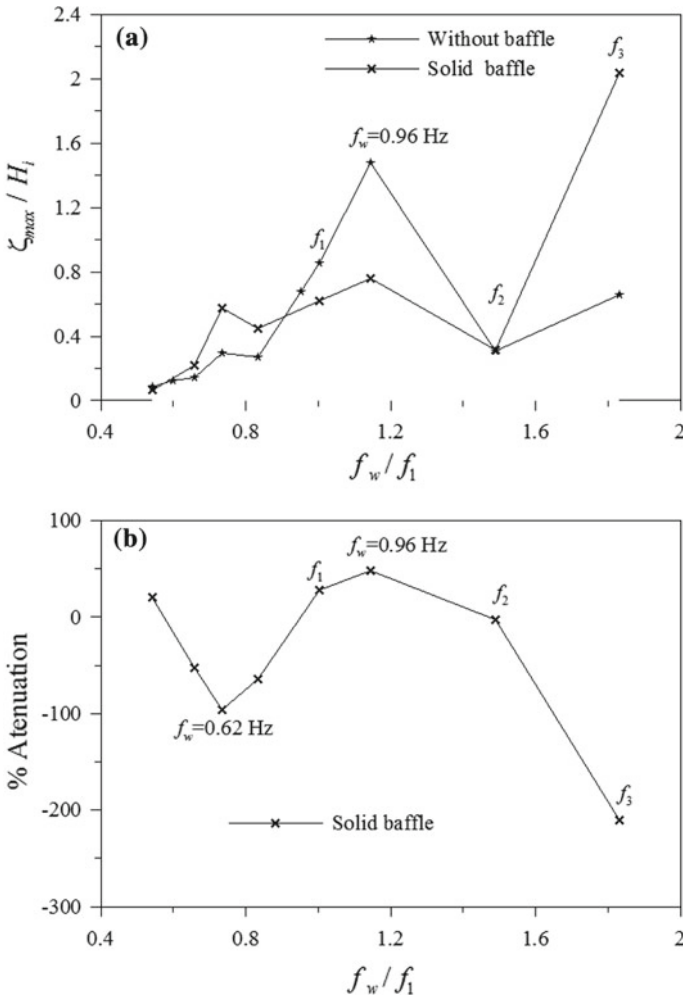


**Fig. 6** a Variation of  $\zeta_{max}/H_i$  with different frequencies' ratio ( $f_w/f_1$ ) for  $H_i/d=0.1$ ,  $h_s/l=0.488$  and solid baffle at  $l/2$ , b percentage attenuation for different frequencies' ratio ( $f_w/f_1$ ) for  $H_i/d=0.1$ ,  $h_s/l=0.488$  and solid baffle at  $l/2$

= 1.84) of submerged baffle at  $l/2$  condition results in an attenuation of  $-210\%$ . Similarly the excitation ratio of 0.73 corresponds to secondary parametric resonance of second mode ( $f_w=f_2/2$ ) in unbaffled condition closer to parametric resonances of second mode ( $2f_2/4, 2f_2/3$ ) of submerged baffle at  $l/2$  condition results in an attenuation of  $-100\%$ .

The variation of zeroth spectral moment ( $m_0$ ) with different frequencies' ratio ( $f_w/f_1$ ) is given in Fig. 7a. It is observed that sloshing energy and sloshing run-up go hand in hand and follow similar pattern. On usage of solid baffle, zeroth

spectral moment is found to be 0.0011 and 0.0012 for  $f_w/f_1 = 0.98$  and  $f_w/f_1 = 1.14$ , respectively. It is interesting to see that even though there is an increase in sloshing run-up (Fig. 6b), a decrease in sloshing energy is observed at  $f_w/f_1 = 1.48$ . The sloshing energy at excitation frequency ratio of  $f_w/f_1 = 1.86$  has a magnitude of 0.0006 which is quite high when compared with un baffled condition. Figure 7b demonstrates the total energy reduction in the system. The attenuation is in the order of 24, 78 and 25% for the frequencies' ratio of  $f_w/f_1 = 0.98$ ,  $f_w/f_1 = 1.14$  and  $f_w/f_1 = 1.48$ , respectively. For the excitation at third-mode sloshing frequency, the sloshing energy was observed to be about ten times of the corresponding without baffled condition and resulted in undesired  $-900\%$  reduction in sloshing energy.

### 3.2.3 Modal Behaviour and Identification of Harmonics

The sloshing modes occurring in the system for solid baffle at  $l/2$  are presented in Table 1. The sloshing oscillations, phase plot and spectra are projected in Figs. 8a–f and 8g–l, for frequencies' ratio of  $f_w/f_1 = 0.98$  and  $f_w/f_1 = 1.48$ , respectively, for without baffle condition as well as solid baffle at  $l/2$ . The projected spectral response for solid baffle (Fig. 8f) subjected to wave excitation frequency ratio ( $f_w/f_1$ ) of 0.98 shows bimodal spectra similar to without baffle condition. The secondary peak at  $2f_w$  is due to third-mode contribution, and the dominant peak at  $f_w$  is a result of first mode in the system. The presence of solid baffle leads to redistribution of energy with reduction in secondary energy peak and increase in dominant peak. The high crests with wideness and deep trough with narrowness in the sloshing oscillation are reflected in the phase plot (Fig. 8e). The frequency ratio of 1.48 corresponds to excitation at second-mode sloshing frequency. Solid baffle has led to reduced bimodal spectra (Fig. 8l) with peaks at  $f_w$  (second-mode contribution) and  $f_3$ . The strong modal interaction is visible through phase plots and the presence of solid baffle increased the dominance of second mode in the system. Figure 9a–f presents the sloshing run-up, phase plot and sloshing spectra for with and without baffle condition at excitation frequency equals to third natural sloshing frequency. Figure 9f exhibits a single dominant peak at  $f_w$  with tremendous increase in energy in comparison with un baffled condition. The phase plot (Fig. 9e) shows the presence of single mode in system and reflects the unstable behaviour available in the sloshing run-up. Also, it reflects the increased peakedness by solid baffle. Figure 9g–l represents the behaviour of the system for the excitation frequency ratio of 1.14. The dominant peak at  $f_w$  (Fig. 9i) in without baffle condition is significantly subdued with the help of solid baffle (Fig. 9l). Also, nominal increase in energy concentration is observed at  $2f_w$ .

The sloshing run-up corresponding phase plot and spectra for with and without baffle condition at excitation frequency ratio of 0.73 is illustrated in Fig. 10a–f. It is observed that the solid baffle has increased the sloshing run-up. Further, the baffle has increased the participation of second mode (occurred due to parametric resonance condition) and third mode. As a result, increase in energy peak is observed at  $f_w$  (first-mode contribution),  $2f_w$  (second-mode contribution) and  $3f_w$  (third-mode contribution). At wave excitation frequency ratio of 0.54, the presence of solid baffle

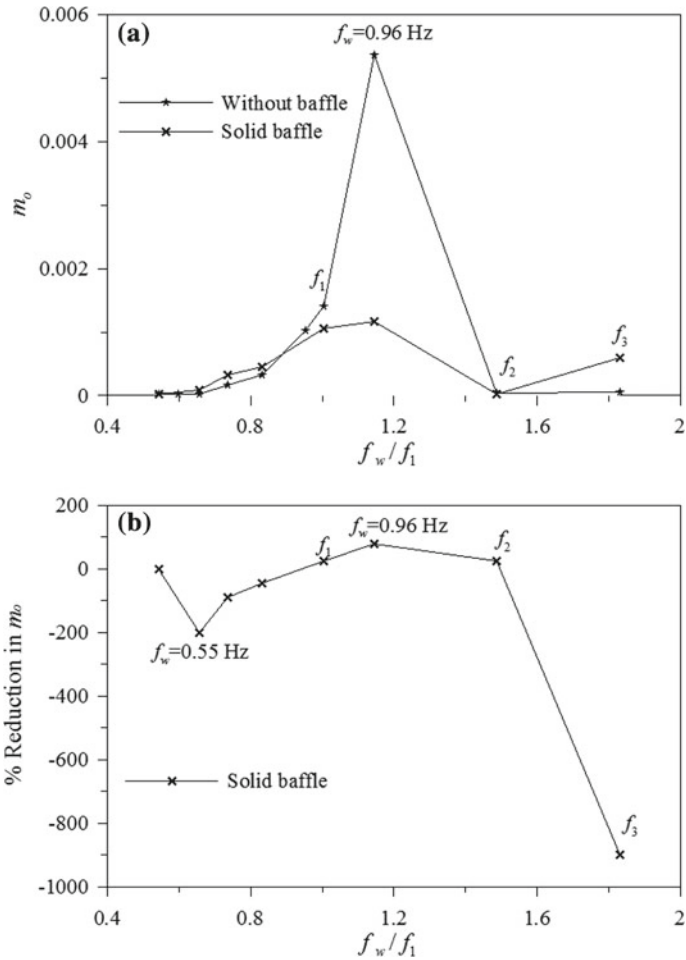


**Fig. 7** **a** Variation of  $m_0$  for different frequencies' ratio ( $f_w/f_1$ ) for  $H_i/d=0.1$ ,  $h_s/l=0.488$  and solid baffle at  $l/2$ , **b** percentage reduction in  $m_0$  for different frequencies' ratio ( $f_w/f_1$ ) for  $H_i/d=0.1$ ,  $h_s/l=0.488$  and solid baffle at  $l/2$

interchanged the dominant energy peak between  $f_w$  and  $2f_w$  (Fig. 10i and l) which are occurred due to first-mode contribution. The energy peak at  $3f_w$  due to third-mode contribution is undisturbed.

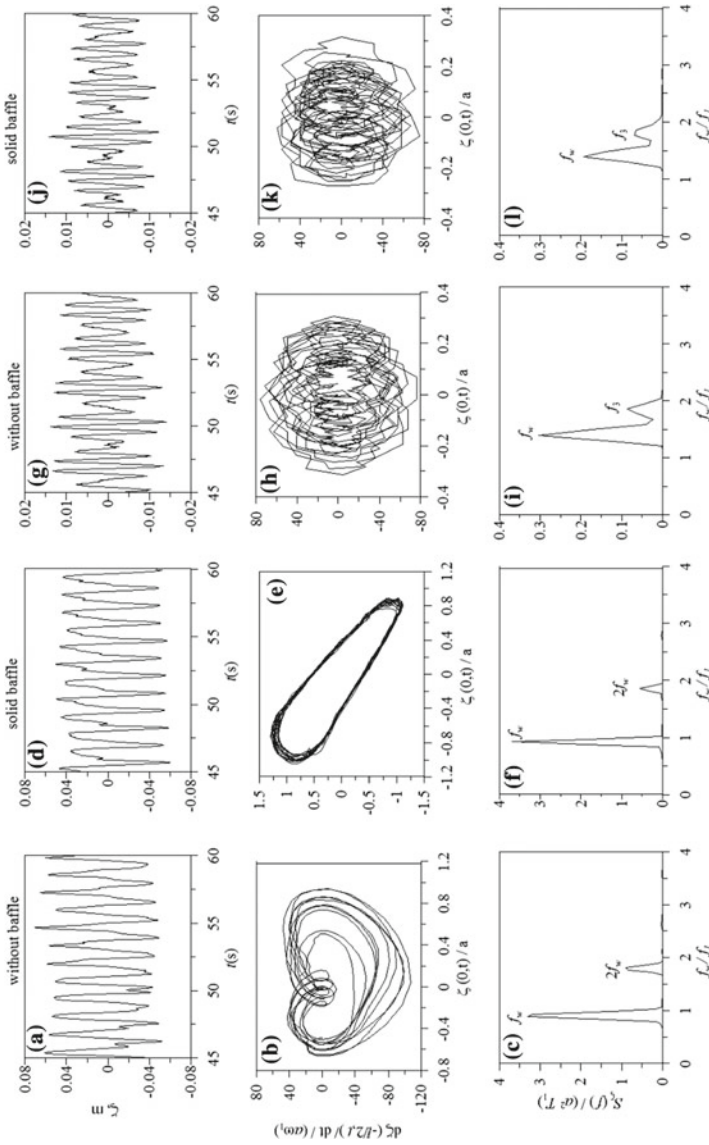


**Fig. 8** Sloshing oscillations for  $H_1/d = 0.1$  and  $h_s/l = 0.488$ . Without baffle wall,  $f_w/f_1 = 0.98$ : **a** surface elevation at end wall, **b** phase plot and **c** surface elevation spectrum corresponding to **(a)**; solid baffle at  $l/2$ ,  $f_w/f_1 = 0.98$ , **d** surface elevation at end wall, **e** phase plot and **f** surface elevation spectrum corresponding to **(d)**. Without baffle wall,  $f_w/f_1 = 1.48$ , **g** Surface elevation at end wall, **h** phase plot and **i** surface elevation spectrum corresponding to **(g)**; solid baffle at  $l/2$ ,  $f_w/f_1 = 1.48$ , **j** surface elevation at end wall, **k** phase plot and **l** surface elevation spectrum corresponding to **(j)**

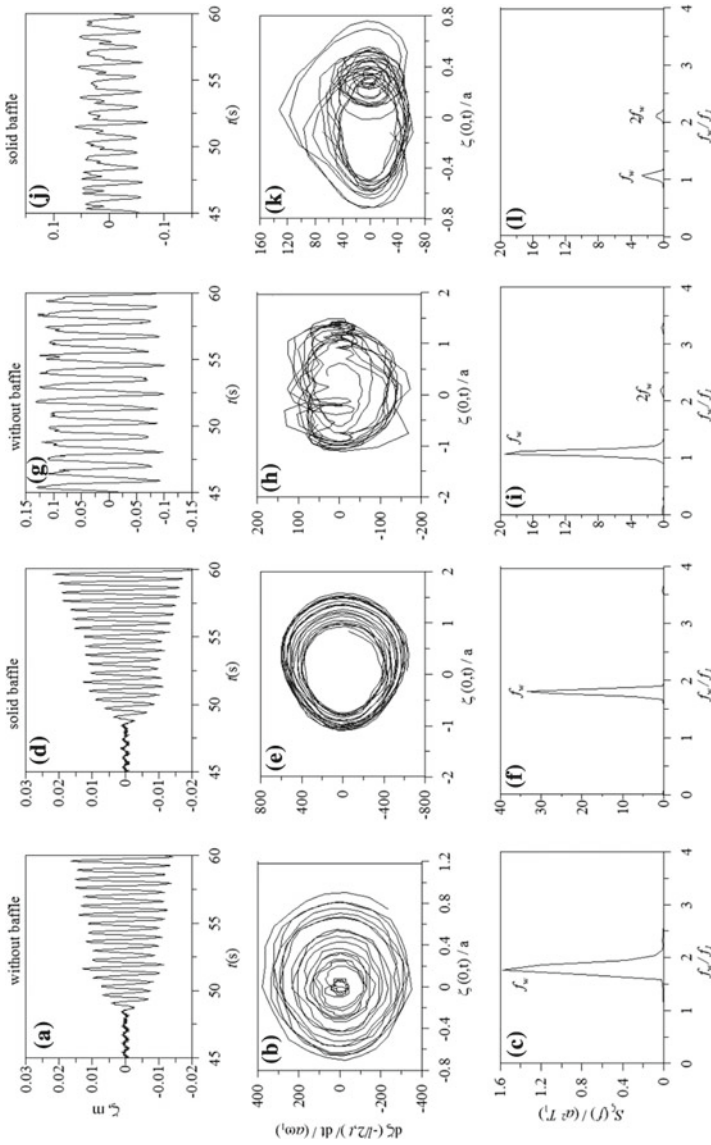


**Fig. 9** Sloshing oscillations for  $H_i/d = 0.1$ , and  $h_s/l = 1.83$ ; **a** surface elevation at end wall, **b** phase plot and **c** surface elevation spectrum corresponding to **(a)**; **d** surface elevation at end wall, **e** phase plot and **f** surface elevation spectrum corresponding to **(d)**. Without baffle wall,  $f_w/f_1 = 1.14$ , **g** surface elevation at end wall, **h** phase plot and **i** surface elevation spectrum corresponding to **(g)**; solid baffle at  $l/2$ ,  $f_w/f_1 = 1.14$ , **j** surface elevation at end wall, **k** phase plot and **l** surface elevation spectrum corresponding to **(j)**

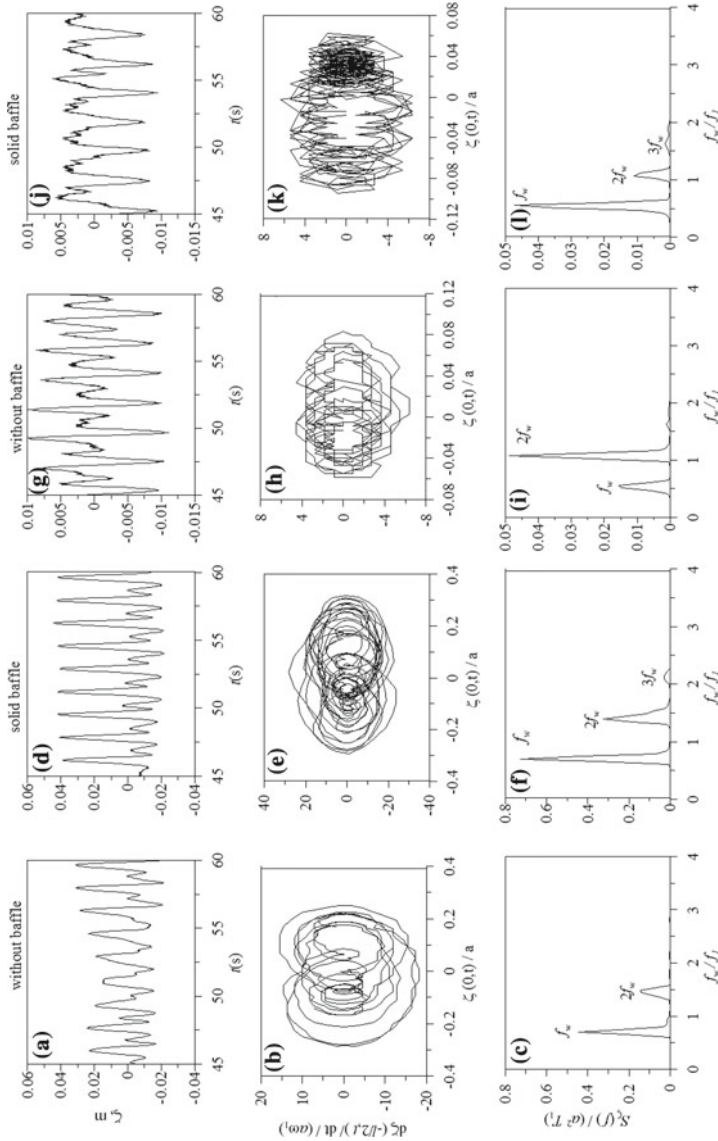


**Fig. 10** Sloshing oscillations for  $H_w/d = 0.1$  and  $h_w/l = 0.488$ . Without baffle wall condition,  $f_w/f_1 = 0.73$ : **a** surface elevation at end wall, **b** phase plot and **c** surface elevation spectrum corresponding to **(a)**; solid baffle at  $l/2$ ,  $f_w/f_1 = 0.73$ , **d** surface elevation at end wall, **e** phase plot and **f** surface elevation spectrum corresponding to **(d)**. Without baffle wall condition,  $f_w/f_1 = 0.54$ , **g** surface elevation at end wall, **h** phase plot and **i** surface elevation spectrum corresponding to **(g)**; solid baffle at  $l/2$ ,  $f_w/f_1 = 0.54$ , **j** surface elevation at end wall, **k** phase plot and **l** surface elevation spectrum corresponding to **(j)**

### 3.3 Sloshing Pressure

Baffle walls considerably suppress the sloshing motion and it is expected that there would be significant reduction in sloshing pressure on the liquid containment. The pressure fluctuations at pressure port locations near to the free surface are pragmatic to be high compared to deeper surface in the liquid sloshing tank [23]. Hence, the discussion is presented for pressure port location (P4) by considering the fact that the free surface exists just above the P4. The induced sloshing pressure-time traces in the steady-state phase are considered for the analysis. Within the time history, the crest values are picked up and the root mean square of sloshing pressure ( $p_{rms}^c/H_i$ ) and maximum sloshing pressure ( $p_{max}^c/H_i$ ) are obtained. The percentage of attenuation in sloshing pressure is calculated as follows:

$$\% \text{ of attenuation} = \frac{\text{P4 (without baffle)} - \text{P4 (with baffle)}}{\text{P4 (without baffle)}} \quad (4)$$

The variation of  $p_{rms}^c/H_i$  and  $p_{max}^c/H_i$  with  $f_w/f_1$  at pressure port location P4 for all the porosities and also the percentage reduction in pressure are shown in Figs. 11 and 12, respectively. For without baffle wall and the baffle wall at  $l/2$ , the maximum responses of  $p_{rms}^c$  (Fig. 11a) and  $p_{max}^c/H_i$  (Fig. 12a) are observed at excitation frequency of 0.96 Hz ( $f_w/f_1 = 1.14$ ). The percentage reduction in  $p_{rms}^c$  and  $p_{max}^c$  is about an average of 50% for  $f_w/f_1 = 1.14$ . However, the reduction in sloshing pressure ( $p_{rms}^c$ ) at  $f_w/f_1 = 1$  is about 32% whilst  $p_{max}^c$  is reduced by 23%. Baffle at  $l/2$  condition gives an undesirable response in reducing the sloshing pressure at wave excitation  $f_w = f_3$  Hz, and the reduction in  $p_{rms}^c$  and  $p_{max}^c$  is about -1130 and -510%, respectively.

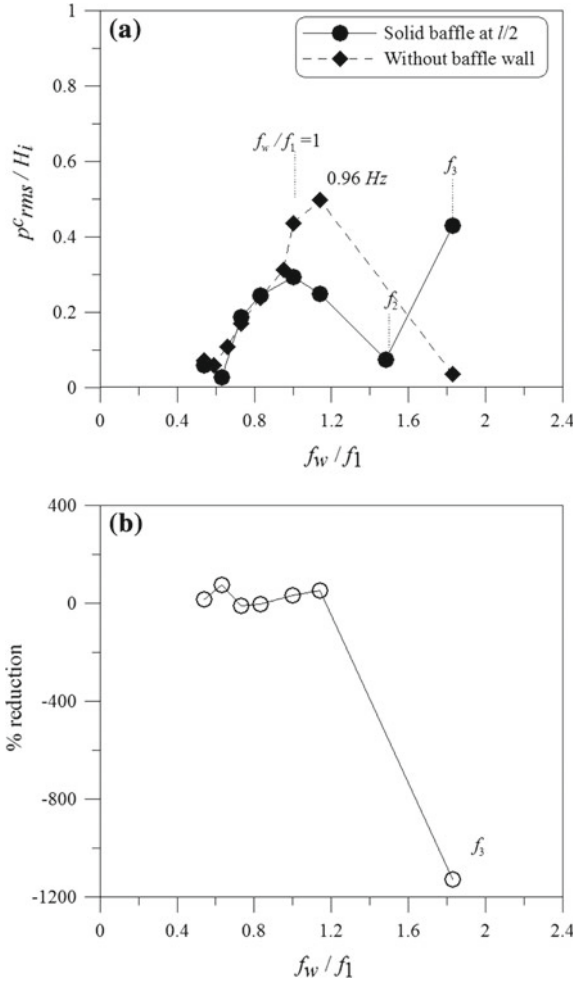
## 4 Concluding Remarks

The effectiveness of solid baffle is presented in terms of reduction in sloshing run-up, spectral energy and percentage reduction in  $p_{rms}^c$ . The harmonics are identified in line with the studies of Nasar et al. [32] and Faltinsen and Timokha [30]. The effect of baffle on barge RAOs' is discussed in comparison with Nasar et al. [14]. The following conclusions are drawn in each of the above aspects:

- The submerged solid baffle's effect on heave RAO is absent. Peak amplitude of roll RAO is further reduced which is a positive aspect. The sway RAO around the excitation of first-mode sloshing frequency is greatly disturbed by the presence of the submerged baffle.
- The solid baffle performs up to the expectation for the frequencies at  $f_w/f_1 = 1$  and  $f_w/f_1 = 1.14$  with sloshing run-up attenuation of 28 and 48%, respectively. Solid baffle at  $l/2$  leads to an undesirable behaviour at wave excitation of third-

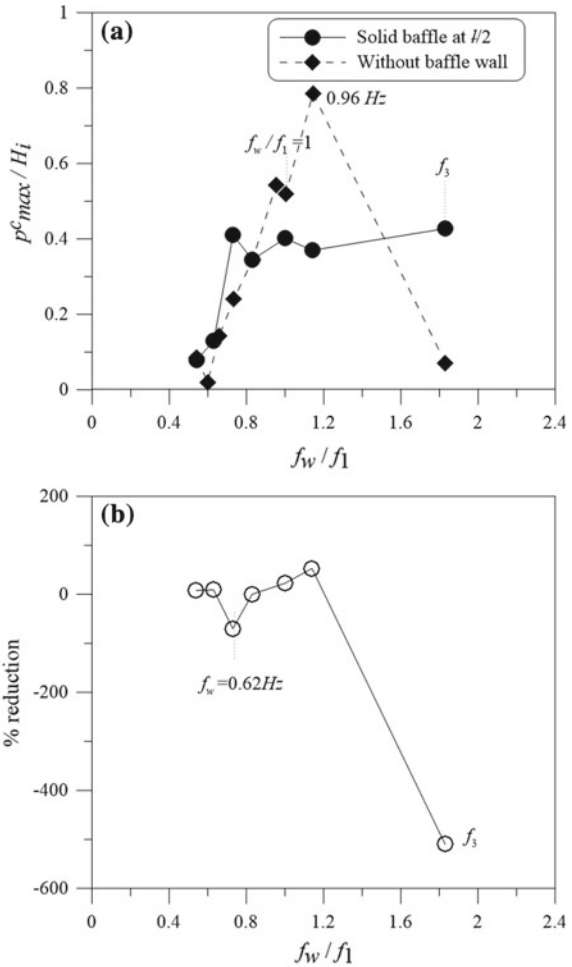


**Fig. 11** Variation of **a**  $p_c^{rms}/H_i$  and **b** percentage reduction at P4 with  $f_w/f_1$  for  $H_i/d=0.10$  and  $h_s/l=0.488$



- mode sloshing frequency,  $f_w=f_3$ . The attenuation of maximum sloshing run-up and zeroth spectral moment are about  $-210$  and  $-900\%$ , respectively.
- The presence of submerged solid baffle interchanged the dominant energy peak between  $f_w$  and  $2f_w$  at wave excitation frequency ratio of  $0.54$ .
  - The undesirable condition at  $f_w=f_3$  is reflected in the induced sloshing pressure as well. The attenuation in  $p_{rms}^c$  and attenuation in  $p_{max}^c$  are about  $-1130$  and  $-510\%$ , respectively.

**Fig. 12** Variation of **a**  $p_{max}^c/H_i$  and **b** percentage reduction at P4 with  $f_w/f_1$  for  $H_i/d=0.10$  and  $h_s/l=0.488$



**References**

1. Nakayama T, Washizu K (1980) Nonlinear analysis of liquid motion in a container subjected to forced pitching oscillation. *Int J Numer Meth Eng* 15(8):1207–1220. <https://doi.org/10.1002/nme.1620150808>
2. Ockendon H, Ockendon JR, Johnson AD (1986) Resonant sloshing in shallow water. *J Fluid Mech* 167(1):465. <https://doi.org/10.1017/S0022112086002926>
3. Ockendon H, Ockendon JR, Peake MR, Chester W (1993) Geometrical effects in resonant gas oscillations. *J Fluid Mech* 257:201. <https://doi.org/10.1017/S0022112093003040>
4. Ockendon H, Ockendon JR, Waterhouse DD (1996) Multi-mode resonances in fluids. *J Fluid Mech* 315:317. <https://doi.org/10.1017/S0022112096002443>
5. Liu D, Lin P (2009) Three-dimensional liquid sloshing in a tank with baffles. *Ocean Eng* 36:202–212. <https://doi.org/10.1016/j.oceaneng.2008.10.004>

6. Faltinsen OM, Rognebakke OF, Lukovsky IA, Timokha AN (2000) Multidimensional modal analysis of nonlinear sloshing in a rectangular tank with finite water depth. *J Fluid Mech* 407:201–234. <https://doi.org/10.1017/S0022112099007569>
7. Faltinsen OM, Timokha AN (2001) An adaptive multimodal approach to nonlinear sloshing in a rectangular tank. *J Fluid Mech* 432:167–200
8. Faltinsen OM, Timokha AN (2002) Asymptotic modal approximation of nonlinear resonant sloshing in a rectangular tank with small fluid depth. *J Fluid Mech* 470:319–357. <https://doi.org/10.1017/S0022112002002112>
9. Frandsen JB (2004) Sloshing motions in excited tanks. *J Comput Phys* 196:53–87. <https://doi.org/10.1016/j.jcp.2003.10.031>
10. Kim MS, Park JS, Lee W II (2003) A new VOF-based numerical scheme for the simulation of fluid flow with free surface. Part II: Application to the cavity filling and sloshing problems. *Int J Numer Meth Fluids* 812:791–812
11. Chen BF, Chiang HW (2000) Complete two-dimensional analysis of sea-wave-induced fully non-linear sloshing fluid in a rigid floating tank. *Ocean Eng* 27:953–977. [https://doi.org/10.1016/S0029-8018\(99\)00036-0](https://doi.org/10.1016/S0029-8018(99)00036-0)
12. Francescutto A, Contento G (1994) An experimental study of the coupling between roll motion and sloshing in a compartment. In: Proceedings of the fourth international offshore and polar engineering conference, Osaka, Japan, 10–15 April 1994
13. Lee SJ, Kim MH, Lee DH, Kim JW, Kim YH (2007) The effects of LNG-tank sloshing on the global motions of LNG carriers. *Ocean Eng* 34:10–20. <https://doi.org/10.1016/j.oceaneng.2006.02.007>
14. Nasar T, Sannasiraj SA, Sundar V (2010) Motion responses of barge carrying liquid tank. *Ocean Eng* 37:935–946. <https://doi.org/10.1016/j.oceaneng.2010.03.006>
15. Nasar T, Sannasiraj SA, Sundar V (2009) Wave-induced sloshing pressure in a liquid tank under irregular waves. *Proc Inst Mech Eng, Part M: J Eng Marit Environ* 223(2):145–161. <https://doi.org/10.1243/14750902JEME135>
16. Modi VJ, Akinturk A (2002) An efficient liquid sloshing damper for control of wind-induced instabilities. *J Wind Eng Ind Aerodyn* 90:1907–1918
17. Warnitchai P, Pinkaew T (1998) Modelling of liquid sloshing in rectangular tanks with flow-dampening devices. *Eng Struct* 20(97):593–600. [https://doi.org/10.1016/S0141-0296\(97\)00068-0](https://doi.org/10.1016/S0141-0296(97)00068-0)
18. Tait MJ, El Damatty AA, Isyumov N, Siddique MR (2005) Numerical flow models to simulate tuned liquid dampers (TLD) with slat screens. *J Fluids Struct* 20:1007–1023. <https://doi.org/10.1016/j.jfluidstructs.2005.04.004>
19. Crowley S, Porter R (2012) The effect of slatted screens on waves. *J Eng Math* 76:33–57. <https://doi.org/10.1007/s10665-011-9529-6>
20. Molin B, Remy F (2015) Inertia effects in TLD sloshing with perforated screens. *J Fluids Struct* 59:165–177. <https://doi.org/10.1016/j.jfluidstructs.2015.09.00>
21. Armenio V, La Rocca M (1996) On the analysis of sloshing of water in rectangular containers: numerical study and experimental validation. *Ocean Eng* 23(8):705–739. [https://doi.org/10.1016/0029-8018\(96\)84409-X](https://doi.org/10.1016/0029-8018(96)84409-X)
22. Kim Y (2001) Numerical simulation of sloshing flows with impact load. *Appl Ocean Res* 23(1):53–62. [https://doi.org/10.1016/S0141-1187\(00\)00021-3](https://doi.org/10.1016/S0141-1187(00)00021-3)
23. Panigrahy PK, Saha UK, Maity D (2009) Experimental studies on sloshing behavior due to horizontal movement of liquids in baffled tanks. *Ocean Eng* 36(3–4):213–222. <https://doi.org/10.1016/j.oceaneng.2008.11.002>
24. Xue M, Zheng J, Lin P, Yuan X (2017) Experimental study on vertical baffles of different configurations in suppressing sloshing pressure. *Ocean Eng* 136:178–189. <https://doi.org/10.1016/j.oceaneng.2017.03.031>
25. Akyildiz H (2012) A numerical study of the effects of the vertical baffle on liquid sloshing in two-dimensional rectangular tank. *J Sound Vib* 331(1):41–52. <https://doi.org/10.1016/j.jsv.2011.08.002>

26. Iranmanesh A (2017) A 2D numerical study on suppressing liquid sloshing using a submerged cylinder. *Ocean Eng* 138:55–72. <https://doi.org/10.1016/j.oceaneng.2017.04.022>
27. Cho IH, Choi J, Kim MH (2017) Sloshing reduction in a swaying rectangular tank by an horizontal porous baffle. *Ocean Eng* 138:23–34. <https://doi.org/10.1016/j.oceaneng.2017.04.005>
28. Kim Y (2001) Numerical simulation of sloshing flows with impact load. *Appl Ocean Res* 23:53–62. [https://doi.org/10.1016/S0141-1187\(00\)00021-3](https://doi.org/10.1016/S0141-1187(00)00021-3)
29. Ibrahim RA (2005) *Liquid sloshing dynamics—theory and applications*. Cambridge University Press, Newyork
30. Faltinsen OM, Timokha AN (2009) *Sloshing*. Cambridge University Press, Newyork
31. Sannasiraj SA (1996) *Dynamics of long floating structures in directional waves*. Ph.D. Thesis, Indian Institute of Technology Madras, India
32. Nasar T, Sannasiraj SA, Sundar V (2008) Liquid sloshing dynamics in a barge carrying container. *Fluid Dyn Res* 40:427–458

# Design Approach for Reducing the Wave Added Resistance by Hull Form Optimisation



M. Kumar Sanchana, R. Vijayakumar and V. V. S. Prasad

**Abstract** The primary objective of this project is to investigate if the designed hull form when realistic wave conditions are taken into account should be more slender than the current blunt bows. The added resistance is also highly dependent upon environmental forces like wave conditions the vessel experiences. Also, ship operators are mostly interested in fuel savings with minimum modifications in hull form; thus, a study has been made on one operation regime considering the wave data for all the design variations. MOERI KVLCC2 has been considered for this study <http://www.simman2008.dk/KVLCC/KVLCC2/tanker2.html>, as it is available in public domain and widely used for CFD calculations in industry. Hull forms have been transformed using FFD transformation in NAPA looped with optimisation and CFD tools in NAPA. Systematic algorithm was used to do optimisation. Six designs have been investigated changing the water lines and entrance angles resulted from blunt to sharp. In this thesis, KVLCC2\_0 is the original design of MOERI tanker with no flare. KVLCC2\_-1.5, KVLCC2\_-1 and KVLCC2\_-0.5 are blunt designs than the other design variations used. KVLCC2\_0.5, KVLCC2\_1 and KVLCC2\_2 are more slender ships by moving the volume from the shoulder to the bulb area. KVLCC2\_-1.5 is more blunt ship and has some restrictions in calculating the full-scale resistance after CFD study, so this design variation is neglected in the reports. However, to show the design variations, it has been shown at some places. KVLCC2\_0 has been elongated by 8 m and can be seen in KVLCC2\_2 design. One route has been chosen to represent the actual operational areas of a similar vessel. The route selected is from Arabian Gulf (AG) to Japan. Resistance of calm water has been calculated and verified with experimental data. The wave resistance was calculated numerically using

---

M. K. Sanchana (✉)  
NAPA Ltd., Mumbai, India  
e-mail: [manoj.kumar@napa.fi](mailto:manoj.kumar@napa.fi)

R. Vijayakumar  
Indian Institute of Technology Madras, Madras, India  
e-mail: [vijay2028@iitm.ac.in](mailto:vijay2028@iitm.ac.in)

V. V. S. Prasad  
Andhra University, Visakhapatnam, India  
e-mail: [prasadau@gmail.com](mailto:prasadau@gmail.com)

NAPA. KVLCC2\_-1 has the greatest calm water resistance compared to rest of the designs. Designs KVLCC2\_0, KVLCC2\_0.5 and KVLCC2\_1 have very similar calm water resistance but slightly lower than KVLCC2\_-0.5 and KVLCC2\_2. The added resistance was calculated by NAPA seakeeping subsystem. Sharper bow designs have lower resistance in the regime considered as expected. Fuel consumption calculations were done by including operational profile of the voyage, viscous resistance, added resistance, and propulsion characteristics in NAPA. The results show that KVLCC2\_0.5 and KVLCC2\_1 have good fuel efficiency of 11.8 and 12.6%, respectively. From the results, it is obvious that a sharper bow will have better advantage over a blunter bow when actual operational conditions are considered.

**Keywords** Design optimisation · Hull optimisation · Wave added resistance

## Nomenclature

MOERI	Maritime and Ocean Engineering Research Institute
KVLCC	K Tanker; Very Large Crude Carrier
KVLCC1	First variant of MOERI tanker with relatively V-shaped stern frame lines
KVLCC2	Second variant of MOERI tanker with more U-shaped stern frame lines
KVLCC2_x	Hull Design variations of the bow and shoulder part to optimise wave resistance using NAPA software
NAPA	NAPA Group, a software house or NAPA software, depending on the context
FFD	Free Form Deformation tool in NAPA software for transformations
SYSTEMATIC	Systematic is an optimisation algorithm which studies all possible combinations of design parameters
NAPA RANS	RANS code solves the Reynolds-averaged Navier Stokes equations for the flow field around the hull. This is based on FLOWPACK code by Professor Yusuke Tahara
TAHARA	Potential flow solver in NAPA used to calculate bow resistance based on FLOWPACK code by Professor Yusuke Tahara

## 1 Introduction

The primary objective of this project is to investigate if the designed hull form when realistic wave conditions are taken into account should be more slender than the current blunt bows. The added resistance is also highly dependent upon environmental forces like wave conditions the vessel experiences.

**Table 1** Main dimensions of the original KVLCC2 design

<i>Main particulars</i>	
Lpp (m)	320.0
Lwl (m)	325.5
Bwl (m)	58.0
<i>D</i> (m)	30.0
<i>T</i> (m)	20.8
Displacement (m <sup>3</sup> )	312,622
S w/o rudder (m <sup>2</sup> )	27,194
CB	0.8098
CM	0.9980
LCB (%), fwd+	3.48
<i>Rudder</i>	
Type	Horn
S of rudder (m <sup>2</sup> )	273.3
Lat. area (m <sup>2</sup> )	136.7
Turn rate (deg/s)	2.34
<i>Propeller</i>	
Type	FP
No. of blades	4
<i>D</i> (m)	9.86
<i>P/D</i> (0.7R)	0.721
<i>Ae/A0</i>	0.431
Rotation	Right hand
Hub ratio	0.155
<i>Appendages</i>	
Bilge keels	None

Also, ship operators are mostly interested in fuel savings with minimum modifications in hull form; thus, a study has been made on one operation area considering the wave data for all the design variations.

MOERI KVLCC2 has been considered for this study <http://www.simman2008.dk/KVLCC/KVLCC2/tanker2.html> as it is available in public domain and widely used in industry. Dimensions are as shown in Table 1.

One route has been chosen to represent the actual operational areas of a similar vessel. The route selected is from Arabian Gulf (AG) to Japan.

Resistance of calm water has been calculated and verified with experimental data. The wave resistance was calculated numerically using NAPA.

Six hull form variants have been evaluated including the original hull form by changing entrance angles and varying bulbous bow parameters like length breadth and height with realistic operational conditions. Both blunt and slender shapes were

obtained using FFD transformations. NAPA RANS is used for viscous calculations and hydrostatic and hydrodynamic pressure coefficient calculations. TAHARA is used to calculate bow resistance by varying bow dimensions. Added wave resistance is calculated by Gerritsma and Beukelman's methods in seakeeping calculations. All these calculations are looped with SYSTEMATIC algorithm for optimisation.

A considerable improvement is noticed by evaluating all the designs compared to original hull form by introducing the concept of using operational data for design work.

The core elements of this project were:

- Estimation of calm water resistance, added wave resistance and total fuel oil consumption by combining all weather conditions
- Optimisation of the bow shape and shoulders for minimum resistance on a route selected
- Concept of using operational data for design work
- Improving ship design by ship operation
- Optimisation of framework
- Design variations and calculations.

## 2 Hypothesis

Ship resistance is increased when incident waves are reflected and broken at the ship bow. For blunt bow shapes, waves are reflected forward and resistance increases in waves as shown in Fig. 1. The resistance in waves acting on blunt hull form is larger than slender ships.

The power loss in blunt ships is estimated more compared to conventional high-power engine. To improve the performance in waves for ships with low-power engine, the resistance increase in waves needs to be reduced and this can be done by designing less blunt ships. Ship with sharper bow, incident wave is reflected to sideward, thus reducing the wave resistance acting backward as shown in Fig. 2.

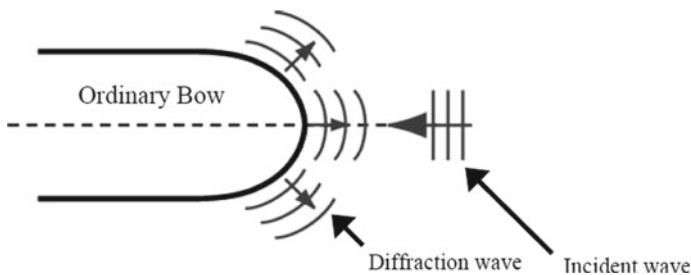


**Fig. 1** Wave reflection of a blunt bow



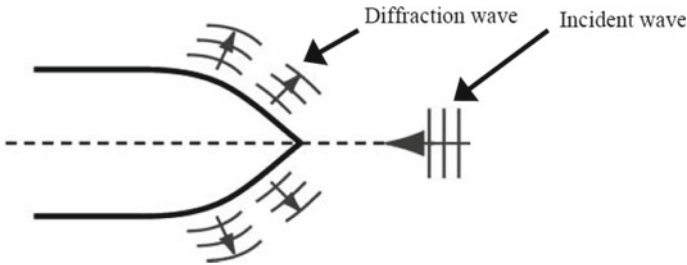


**Fig. 2** Wave reflection of a sharp bow

Larger ships have fixed voyage routes, and the operational sea states are limited. Waves with shorter wavelengths for longer term will have more effect on the added resistance. There are different methods to reduce the reflection of waves; one way is to reduce the half angle of entrance to have sharper bow. A comparatively simple theoretical approach by Gerritsma and Beukelman [2] considered the added resistance to be primarily the result of the damping waves radiated from the oscillating ship's hull.

It is assumed in this study that the added resistance in sea waves would compensate the calm water resistance increase due to sharper bow. Hence, the total resistance would be reduced which leads to better overall performance, reducing less fuel oil consumption and less emissions.

A ship can experience about 15–30% of resistance increase in seaway. Prediction of added resistance due to waves is vital and used in following problems:

- Weather margin
- Weather routing
- Performance analysis.

The final result of this study however depends on the vessel's operational conditions, sea states and time spent in calm water and waves.

### 3 Optimisation Framework

A framework for optimisation of bow shape and shoulders to optimise effective power and fuel oil consumption is created as shown in Fig. 3.

#### 3.1 Free-Form Deformation

NAPA has a relatively new tool free-form deformation (FFD) for transformations of surfaces locally.

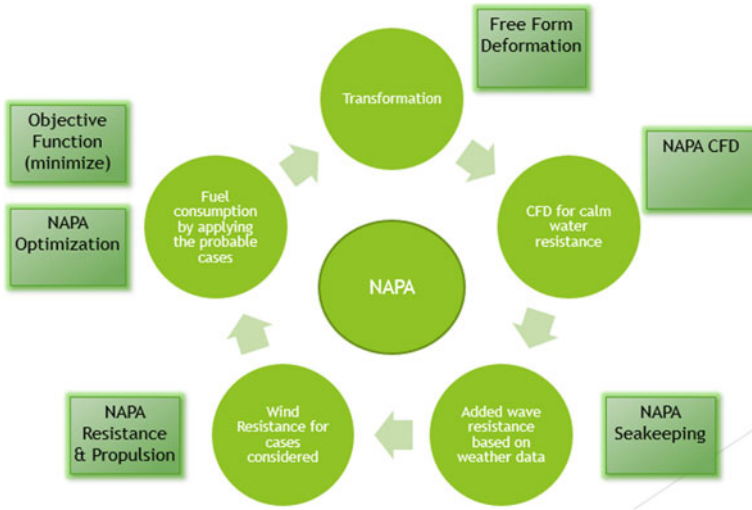


**Fig. 3** Optimisation of framework

Transformation is done so that the user first defines a three-dimensional box. It is also possible to define the number and locations of the control points between the corners separately in all the directions. Only the part of the surface that is located inside the box will be affected by the transformation.

Then, the user defines which points are moved to which direction the box is transformed and the surface inside accordingly (Fig. 4).

Blending factor defines the magnitude of the transformation (between  $-10$  and  $10$ ).  $0$  will result in no transformation,  $1$  will make a complete transformation, and values between these will provide results linearly interpolated between the extremes. If  $5$  is selected as the blending factor, then transformation will be five times the differential values ( $dx$ ,  $dy$  and  $dz$ ).

Six different hull form designs are obtained by varying bow shapes and shoulders. Blending factor is used to control the change in hull forms.

Changes can be seen from original hull form in Fig. 5.

### 3.2 Calm Water Resistance

Calm water resistance is calculated using CFD tool in NAPA. It solves **Reynolds-Averaged Navier–Stokes** equation developed by **Professor Yusuke Tahara, Japan** (Figs. 6 and 7) .

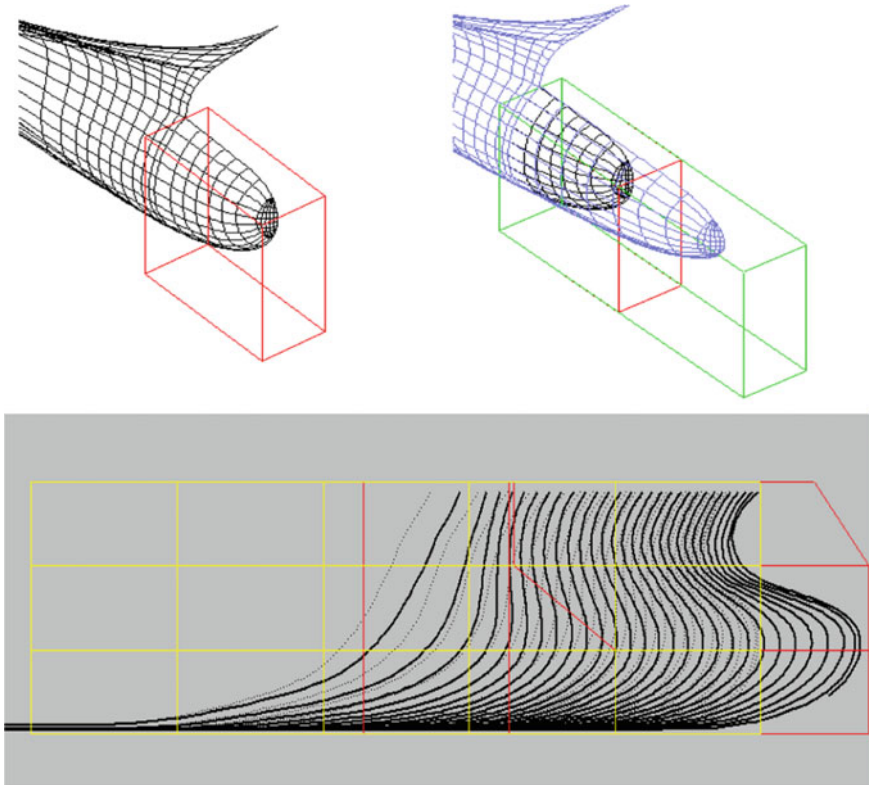


Fig. 4 FFD tool in NAPA for local surface transformation

Model CFD calculations results from NAPA

Vs knots	Fn	Iter	Ct E-3	CF E-3	Cpres E-3	Rn E6
15.700	0.143	16000	5.113	3.298	2.661	5.075
RANS?						

Full Scale CFD calculations results from NAPA

RANS?>lis						
Vs knots	Fn	Ct E-3	Cf E-3	CRapp E-3	Cr E-3	Rn E9
15.700	0.143	2.970	1.390	0.042	1.223	2.213

NAPA CFD calculates total resistance. Flat plate resistance is calculated using ITTC 57 formula. Form factor is obtained as a result.

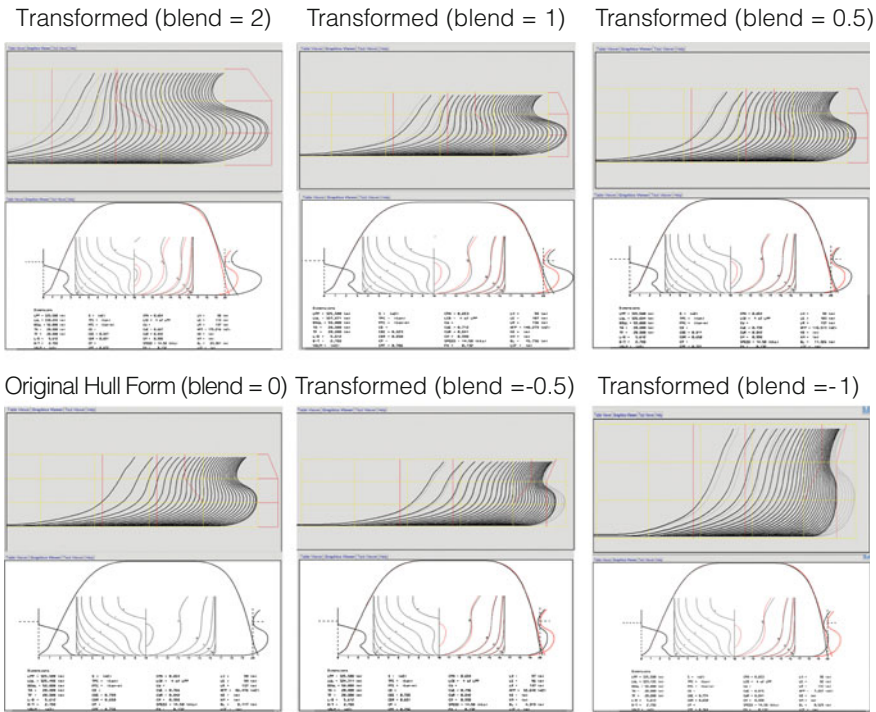


Fig. 5 Various designs with different blending factors

### 3.3 Added Resistance in Waves

The added resistance is calculated using seakeeping module in NAPA. It is developed in Finland in NAPA Ltd. Seakeeping module is used for calculating responses and motions based on the low-speed strip theory formulation by Tuck et al.

Figure 8 shows variation of added wave resistance and effective power with change in designs.

The software gives a choice between strip theory and pressure integration for calculating responses. Choosing to calculate added resistance based on pressure integration gives a choice of methods in the long-wave (radiation) region, either Gerritsma and Benkelman or a pressure integration approach based on the methods in Faltinsen et al. [6].

TABLE 5.2 - RESULTS FROM MARINTEK EXPERIMENTS, FORM FACTOR K = 0.2021

Model						
$F_N$	$R_{Nm}$	$C_{Tm}$	$C_{Fm}$	$C_{Appm}$	$C_{BDm}$	$C_R$
0.101	3.80E+06	5.81E-03	3.58E-03	0.00E+00	5.00E-06	1.50E-03
0.121	4.56E+06	5.23E-03	3.46E-03	0.00E+00	5.00E-06	1.07E-03
0.143	5.39E+06	5.34E-03	3.36E-03	0.00E+00	5.00E-06	1.31E-03
0.157	5.91E+06	5.29E-03	3.29E-03	0.00E+00	5.00E-06	1.33E-03
0.161	6.07E+06	5.14E-03	3.28E-03	0.00E+00	5.00E-06	1.19E-03
0.181	6.83E+06	5.54E-03	3.21E-03	0.00E+00	5.00E-06	1.67E-03

Ship							
$F_N$	$R_{Ns}$	$C_R$	$C_{Fs}$	$C_{Vs}$	$C_{BDs}$	$C_{Apps}$	$C_{Ts}$
0.101	1.56E+09	1.50E-03	1.45E-03	1.87E-03	8.00E-06	0.00E+00	3.25E-03
0.121	1.87E+09	1.07E-03	1.42E-03	1.87E-03	8.00E-06	0.00E+00	2.83E-03
0.143	2.21E+09	1.31E-03	1.39E-03	1.87E-03	8.00E-06	0.00E+00	3.06E-03
0.157	2.43E+09	1.33E-03	1.38E-03	1.87E-03	8.00E-06	0.00E+00	3.08E-03
0.161	2.49E+09	1.19E-03	1.37E-03	1.87E-03	8.00E-06	0.00E+00	2.94E-03
0.181	2.80E+09	1.67E-03	1.35E-03	1.87E-03	8.00E-06	0.00E+00	3.42E-03

Fig. 6 Comparison of results with Marintek experimental data to NAPA results

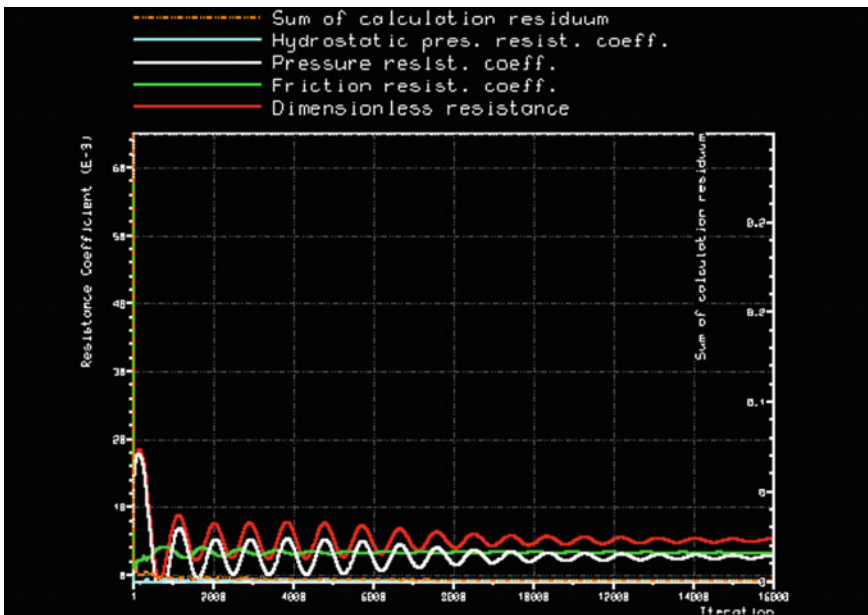


Fig. 7 Convergence plot from NAPA showing resistance coefficients vs iterations

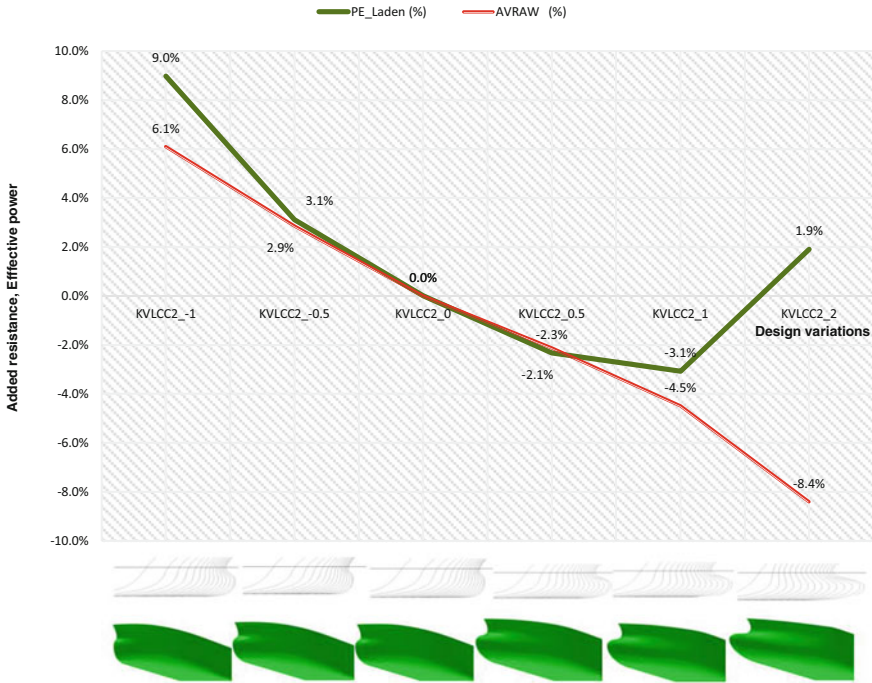


Fig. 8 Added resistance and effective power for each design



Fig. 9 Traditional method of ship design

### 3.4 Optimisation

Traditionally, hull forms are designed for a design draft, speed in calm sea conditions. Later, CFD calculations are used to optimise the hull form and it is a cyclic process in design (Fig. 9).

But in reality ideal hull form demands actual conditions. Actual ship in sea will have wind, wave and draft, speed depending on operational conditions. This data will be very useful in ship design. If this data is made available to designer which

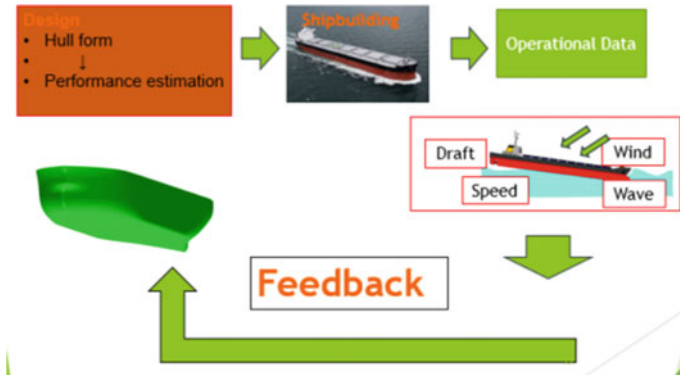


Fig. 10 Feedback to ship design department

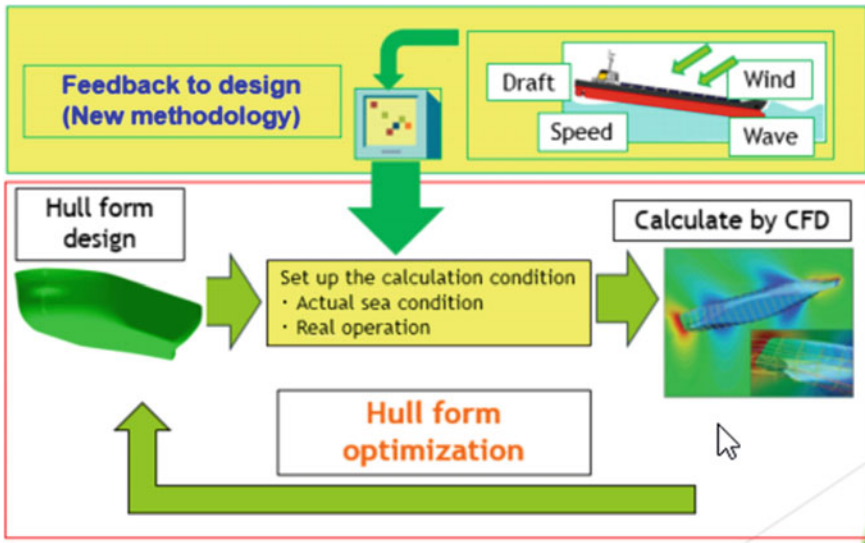


Fig. 11 Feedback data collected in a voyage is stored and fed to design department in the initial design stage to improve the design

acts a kind of feedback to design, then hull form optimisation can be done for actual operational conditions (Fig. 10).

By introducing feedback loop, the next-generation designs can be improved considering all the actual sea conditions (Fig. 11).

Hull form optimisation is done based on feedback from operation data. This will solve the operational problems and help the designer to create better hull forms.

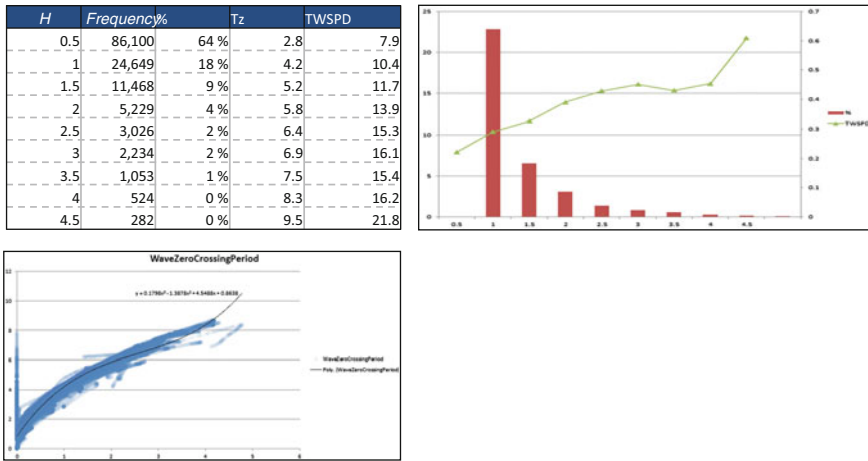


Fig. 12 Weather data collected for one year for a similar vessel

### 3.5 Weather Conditions

Weather conditions are considered based on the probability of encounter. Zero-crossing period (Tz) is approximated by third-degree polynomial fit as a function of wave height (Fig. 12).

- H** is significant wave height
- Tz** is zero-crossing period
- TWSPD** is true wind speed for wind resistance calculations

## 4 Design Variations and Results

Six hull variants are run through optimisation algorithm by changing the blending factor ranging from  $-1.5$  to  $2$  at a step  $0.5$ . Optimising objectives are effective power in laden condition, fuel oil consumption and added wave resistance.

From the below results, it is noticed that for blunt ships, average added wave resistance and effective power are more. Results show very good improvement for slender ships in calm sea and waves.

KVLCC2\_-1 has the greatest calm water resistance compared to rest of the designs. Designs KVLCC2\_0, KVLCC2\_0.5 and KVLCC2\_1 have very similar calm water resistance but slightly lower than KVLCC2\_-0.5 and KVLCC2\_2. The added resistance was calculated by NAPA seakeeping subsystem. Sharper bow designs have lower resistance in the regime considered as expected (Figs. 13, 14, 15, 16, and 17).



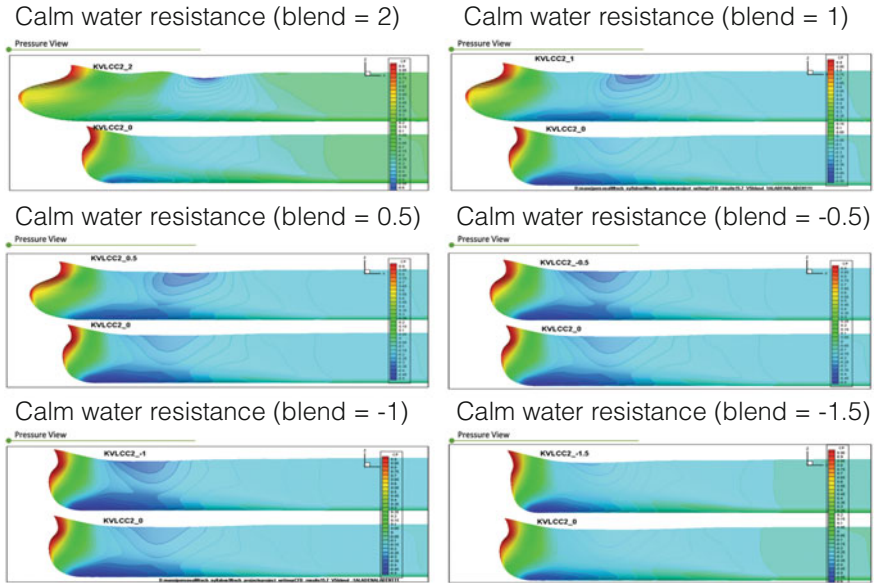


**Fig. 13** Pressure resistance comparison of design variants with original KVLCC2

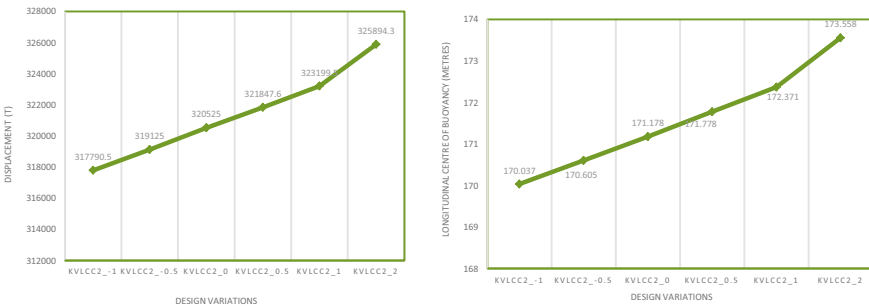


**Fig. 14** Displacement and LCB versus design variations

- Blend** Amount factor of hull form change
- PE** Effective power in calm sea in laden condition
- Tot FOC** Total fuel oil consumption in a year
- Avr RAW** Average wave added resistance in a year

Fuel consumption calculations were done by including operational profile of the voyage, viscous resistance, added resistance and propulsion characteristics in NAPA. The results show that KVLCC2\_0.5 and KVLCC2\_1 have good fuel efficiency of 11.8 and 12.6%, respectively. From the results, it is obvious that a sharper bow will have better advantage over a blunter bow when actual wave conditions are considered.

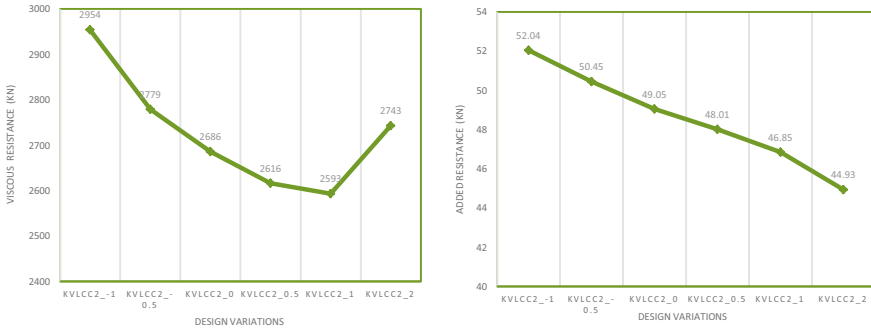


Fig. 15 Viscous and added wave resistance versus design variations

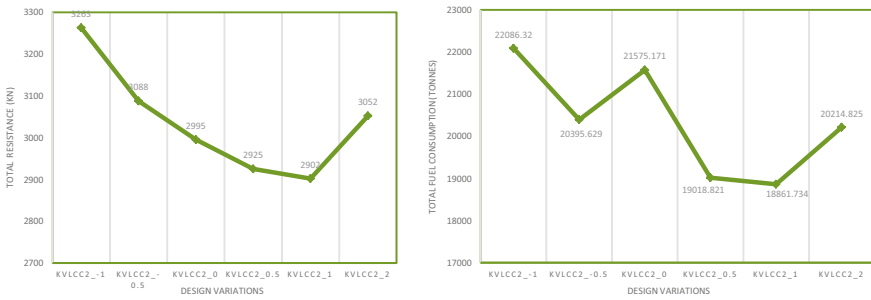


Fig. 16 Total resistance and total FOC versus design variations

Models (Blend)	LPP (m)	PE Laden (KW)	Avr RAW (kN)	Tot FOC (t)	Pbt (KW)	Pd (KW)	PE Laden (KW)	AVRAW (kN)	Tot FOC (t)
KVLCC2_-1	321.7	26358	52.04	22086.32	41385	40557	9.0%	6.1%	2.4%
KVLCC2_-0.5	324.3	24940	50.45	20395.629	38099	37334	3.1%	2.9%	-5.5%
KVLCC2_0	328.1	24186	49.05	21575.17	40422	39613	0.0%	0.0%	0.0%
KVLCC2_0.5	331.9	23625	48.01	19018.821	35532	34821	-2.3%	-2.1%	-11.8%
KVLCC2_1	335.7	23441	46.85	18861.734	35115	34413	-3.1%	-4.5%	-12.6%
KVLCC2_2	343.3	24647	44.93	20214.825	37932	37174	1.9%	-8.4%	-6.3%

Fig. 17 Results of PE, Avr RAW and total FOC of all designs

KVLCC2\_1 seems to have good performance considering added resistance due to waves and calm water resistance. The increase in design length of 8 m would still keep calm water resistance low due to sharper bows which leads to better performance compared to blunter bows.

## 5 Conclusions

This study is just an attempt to show that there are still possibilities for design improvements using actual operational data as a feedback to designers/shipyards. Operators and shipowners could show some interest by giving relevant data to naval architects to develop eco-friendly designs. By considering the above study, it is noticed that there is huge potential for fuel savings.

Other future studies which can be considered:

- Optimisation of stern for better performance
- Optimisation of seakeeping characteristics
- Calculating pressure forces acting on the hull form to optimise plate thickness and further to make ship more lighter
- Optimisation of structures as an ultimate goal
- Calculations to be performed for several ship speeds also considering dynamic trim and sinkage.

**Acknowledgements** We thank those numerous colleagues in NAPA, who have helped and given their valuable contribution to make this presentation possible.

## References

1. Faltinsen OM, Svensen T (1990) Incorporation of seakeeping theories in CAD. In: Oortmerssen GV (ed) Proceedings of the international symposium on CFD and CAD in ship design, Wageningen, the Netherlands. Elsevier Science Publishers B.V.
2. Gerritsma J, Beukelman W (1972 Sept) Analysis of the resistance increase in waves of a fast cargo ship. *Int Shipbuild Progress* 19(217)
3. Fujii H, Takahashi T (1975 Sept) Experimental study on the resistance increase of a ship in regular oblique waves. In: Proceedings of 14th ITTC, Ottawa, vol 4, p 351
4. Faltinsen OM (1990) Sea loads on ships and offshore structures. Cambridge University Press, Cambridge
5. Faltinsen OM (2010) Hydrodynamics of high-speed marine vehicles. Cambridge University Press, Cambridge
6. Faltinsen OM, Minsaas KJ, Liapis N, Skjördal SO (1980) Prediction of resistance and propulsion of a ship in a seaway. In: Proceeding of the 13th symposium on naval hydrodynamics, pp 505–529
7. von Kerczek C, Tuck EO (1969) The representation of ship hulls by conformal mapping function. *J Ship Res*

**Manoj Kumar Sanchana** holds a master's in naval architecture from Andhra University, PG Diploma in Business Administration from Symbiosis and holds the current position of Sales Director at NAPA Group. His previous experience includes 6 years of working at shipyards and design consultancies in India and 10 years in NAPA Group.

**Dr. R. Vijayakumar** is a graduate of naval architecture from the Cochin University of Science and Technology. He has completed his PG Diploma in Naval Construction from Indian Institute

of Technology Delhi, M. Tech. in ocean engineering from Indian Institute of Technology Madras and Ph.D. from Indian Institute of Technology Delhi. Prior to joining IIT Madras, he had served in the Indian Navy for a period of 21 years and retired as Commander. During his tenure in the Navy, he had worked in dockyards (Mumbai and Visakhapatnam) and design directorate. He had also served as Adjunct Faculty at the Naval Construction Wing, Department of Applied Mechanics at Indian Institute of Technology Delhi. Presently, he is working as Assistant professor in the Department of Ocean Engineering, IIT Madras, since February 2016. His fields of interest include advance marine vehicle, ship hydrodynamics, ship dynamics, and computational fluid dynamics (CFD).

**Dr. V. V. S. Prasad** is presently working as Professor and Head of the Department, Department of Marine Engineering, Andhra University College of Engineering, Visakhapatnam-530003.

# Hydrodynamic Aspects of Turret-Moored FPSOs



Balakrishnan G. Nair, R. Vijayakumar and P. Ananthkrishnan

**Abstract** As oil and gas exploration moves toward deeper, harsher waters, and marginal fields, the issues concerning the associated floating production storage and offloading ships (FPSOs) get more complex. Traditionally, at the early stage of the design of FPSOs, subsystem design is individually taken up and subsystem interactions are accounted for through an uncoupled approach, as against a more rigorous fully coupled approach. In fully coupled approach, the system components and mutual interactions are coupled concurrently. Issues related to mooring system of FPSOs are some of the key aspects needing close attention. Approaches for determining the peak behavior belonging to turret-moored FPSOs to random wind, seawater flow, and wave forces for a specified life are still evolving. In the case of weathervaning FPSOs, special consideration is essential for the representation of realistic non-collinear environments. Also, choice of location of turret inside hull is an important design decision, as turret position influences motions. Similarly, another aspect requiring attention is the development of resonant sloshing due to excitation owing to external waves. Also combined piston modes happen within the turret and in the volume between turret and moon pool walls, which is an important hydrodynamic phenomenon. The flow parting via chain table openings heavily damps the piston mode. The paper reviews the literature on some of these hydrodynamic aspects concerning motion response of turret-moored FPSOs.

**Keywords** FPSO · Turret · Mooring · Risers · Degrees of freedom · Instability

---

B. G. Nair (✉)

Structural & Naval Engineering, Saipem India Projects Pvt. Ltd., Chennai, India  
e-mail: [balakrishnangnair@ymail.com](mailto:balakrishnangnair@ymail.com)

R. Vijayakumar · P. Ananthkrishnan

Department of Ocean Engineering, Indian Institute of Technology Madras, Chennai, India  
e-mail: [vijay2028@iitm.ac.in](mailto:vijay2028@iitm.ac.in)

P. Ananthkrishnan

e-mail: [ananthkrishnan@iitm.ac.in](mailto:ananthkrishnan@iitm.ac.in)

© Springer Nature Singapore Pte Ltd. 2019

K. Murali et al. (eds.), *Proceedings of the Fourth International Conference in Ocean Engineering (ICOE2018)*, Lecture Notes in Civil Engineering 22,  
[https://doi.org/10.1007/978-981-13-3119-0\\_23](https://doi.org/10.1007/978-981-13-3119-0_23)

## 1 Introduction

The global quest for energy is constantly on the rise. While renewables are yet to become viable options, fossil fuels continue to be the mainstay. It is well known that coastal and shallow water reservoirs of oil and gas are fast depleting, pushing the industry to explore progressively deeper and harsher waters. Fixed platforms do not offer technically viable and cost-effective solutions beyond a few hundred meters of seawater depths. Today, the demand is to undertake exploration and exploitation at depths of 2000 m and more. An FPSO is an integral part of this pursuit. It is a floating refinery and forms an interface between the upstream and downstream offshore oil and gas industry. Also, it makes economic sense not to go for a fixed platform on marginal fields and instead use an FPSO, even if the water depth is less, since an FPSO can be redeployed over a different field, once the field gets exhausted. Therefore, FPSOs find application even in relatively shallower waters. Despite the current slump in the petroleum prices, conservative estimates show that as much \$60 billion worth of FPSOs may be commissioned by early 2020, with around 130 deployments expected worldwide. This tendency is likely to endure for a conceivable future. The paper takes a brief look at the various hydrodynamic aspects concerning turret-moored FPSOs currently under scrutiny. FPSOs are home to cutting-edge technology, particularly in terms of mooring and anchoring beside receiving and processing of hydrocarbons.

Station keeping by FPSO by active or passive means invokes tremendous interest among practicing Naval Architects and Ocean Engineers as it has a direct bearing on the functional efficacy of the FPSO, not just in receiving, processing, and storage but even in transferring the hydrocarbon to a shuttle tanker. Understanding of FPSO motion under the influence of the Metocean factors is constantly evolving while individual and collective contribution of mooring chains and even risers in restraining the vessel motion raises justifiable curiosity.

## 2 FPSO Mooring

Traditionally, FPSOs are moored either by spread mooring or turret mooring systems. England and Duggal [1] bring out the principal features of these systems. There are two variants to the turret mooring. They are internal and external turret mooring. Also, there are other means of mooring such as yoke mooring. While turret and yoke mooring allow the FPSO to weathervane, spread mooring does not allow the same degree of freedom. The latter imposes relatively much more restraints on the vessel, with the consequence that the mooring lines experience larger loads, whereas weathervaning ability provided by a turret enables the ship to choose its alignment in comparison with the currently existing environment in order to lessen the relative ship–environment orientation and consequent forces on mooring, thus allowing for the best possible offloading direction, in comparison with spread-moored system.

Depending on specific characteristics of the mooring systems, there are a number of variants to the Mooring types. Wichers [2] provides the broad categories of floaters mooring systems.

Spread mooring on an FPSO may induce vessel motions based on the original vessel orientation and the instantaneous environmental parameters. It leads to huge accelerations and reaction forces. Further, it puts some restrictions on the approach of the shuttle tanker that approaches the FPSO for receiving the hydrocarbon products, especially on account of the large number of anchor legs. Restrictions are imposed on the onboard activity during extreme weather conditions leading to operational downtime. Mooring lines undergo strain and fatigue over period of time in case of spread mooring.

A turret mooring on the contrary reduces vessel motions by weathervaning. Therefore, turret mooring is more desirable and conducive for onboard operations and good for lowering annual downtime. There is relatively less restriction on the approach of the shuttle tanker towards the FPSO in the case of turret mooring. However, spread mooring has certain advantages over turret mooring. Table 1 provides a comparison between the features of spread-moored and turret-moored systems as brought out in [1]. It may be noted that the present paper is focusing on some hydrodynamic aspects of turret-moored FPSOs.

**Table 1** Comparison between spread and turret mooring [1]

Parameter	Spread-Moored	Turret-Moored
Ship orientation	Fixed orientation, can impact flare	360° weathervaning
Environment	Moderate, unidirectional to fairly directional	Mild to extreme, directional to spread
Field layout	Prefers flowline arrangement to approach beam-on	Fairly adaptable, partial to distributed flowline arrangements
Riser number and arrangement	Can design for flexibility	Requires commitment, moderate expansion capability
Riser system	For different kinds of risers	Positioning of turret (bow) requires healthy riser arrangement
Station keeping	Larger number of anchors, offsets	Lesser number of anchors, offsets reduced
Ship movements	Depends on comparative ship and environment orientation	Weathervaning ability reduces motion
Ship’s arrangement	Parts arranged on deck require extensive interfaces	Turret gives compact force and hydrocarbon transfer arrangement
Offloading efficiency	Subject to ship–environment direction	Broadly, FPSO matching in direction with mean environment

### 3 Turret Mooring

In accordance with [2], the turret mooring system is passive in nature that holds the FPSO in place without assistance from external sources such as tugs. In this system, when the vessel is disturbed by environmental forces from an equilibrium position, the restoring forces are provided by the asymmetrical tension generated in mooring lines and to a certain extent, the risers. These forces push the vessel through the turret structure back to the original position. Therefore, the turret transfers large dynamic load originating from mooring lines. It also transfers forces from large mass of steel/risers besides mooring lines via bearings onto the ship hull. Further, the chain table secures mooring legs to turret while I-tubes receive the risers. Figure 1 shows typical schematic deepwater mooring lines and riser configuration [2].

The mooring system applies partial restraint on the three linear degrees of freedom, viz. surge, sway, heave of the vessel. It also provides restraint on two of the angular degrees of freedom, viz. roll and pitch. However, it does not restrain the vessel from the angular motion of yaw. The bearing system between the vessel hull and the turret allows the vessel to revolve with respect to the axis of the turret, providing to the vessel what is known as weathervaning capability. In this paper, we focus on hydrodynamics of internal turret-moored FPSO.

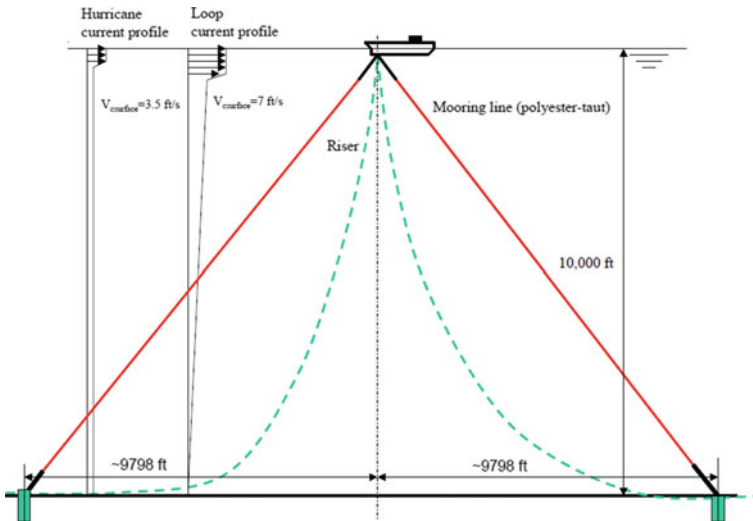


Fig. 1 Typical deepwater mooring lines and riser configuration, schematic [2]



### 4 Internal Turret

The subsystems of mooring of an internal turret are constituted by anchor legs and turret shaft besides the bearing system. While the turret offers load transfer between mooring and the ship and provides weathervaning capability to the vessel, the fluid transfer subsystem gives support for risers, manifold, and the swivel stack. The turret typically includes installation subsystems such as winches, sheaves, subsea controls. Together the bearing and swivel stack give all-round weathervaning ability to the ship. Main features of internal turret system consist of those indicated in Fig. 2. Typical roller bearings in the horizontal plane that enables weathervaning are shown in Fig. 3 [2].

A moon pool is created within the hull to accommodate the turret. It is a watertight circular boundary with a vertical axis placed within the hull symmetrically about the centerline of the ship. The moon pool cuts across all the decks right up to the bottom of the ship providing clear access for the turret mechanism and allowing all the umbilicals to pass through to the swivel stack above the turret located above the main deck. Through the system of bearings, the turret transfers loads to the moon pool structure of the hull. The position of the moon pool and hence that of the turret along the length of the vessel depends on a number of factors which will be discussed subsequently in the paper.

Irrespective of the position, the moon pool introduces a weakness to the cross section of the hull which needs to be strengthened by additional stiffening, so that

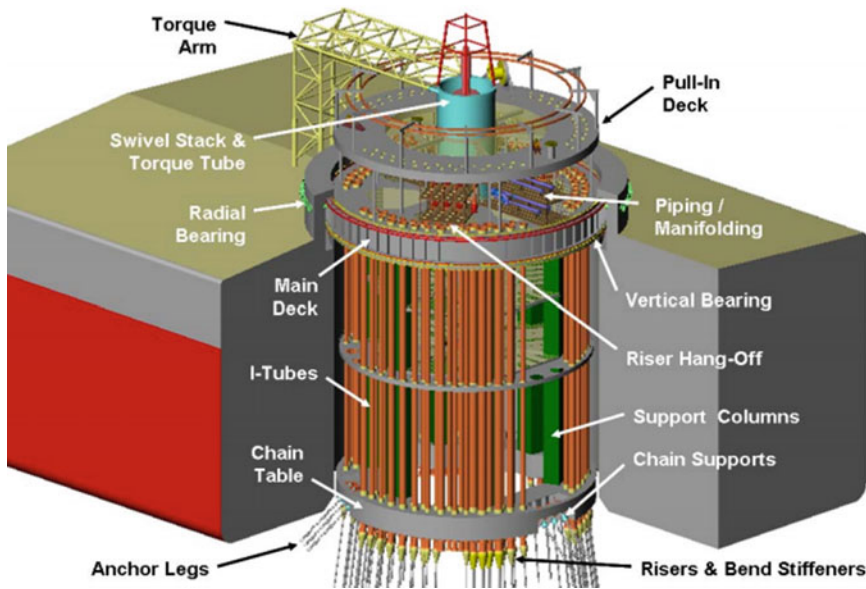


Fig. 2 Main features of internal turret system [2]

**Fig. 3** Turret roller bearing with a typical diameter of 12.5 m (Courtesy of SBM) [2]



it provides both local strengths and compensates for the loss of hull girder strength. A typical very large turret (VLT) for water depths of 2000 m or more may have a diameter of 25–30 m as indicated by Ihonde et al. [3]. Subject to position of turret along the length of the FPSO, this may lead to about 40–45% reduction in effective cross-sectional area. This in turn reduces the effective material and section modulus. The hull girder has to be strengthened to account for the bending loads, local whipping effects, besides to strengthen the structure surrounding moon pool so as to withstand the rigors of sloshing within the moon pool, etc.

## 5 Turret Position Within the Hull

The internal turret occupies huge volume within the hull of an FPSO and therefore has a direct bearing on the layout, process flow, flare location, etc. Consequently, a decision on its location within the hull is taken earlier on in the design of an FPSO, irrespective of whether it is new-build or conversion. The overriding factor that dictates the position of turret within the hull has to be its efficacy in terms of hydrodynamics, its ability to provide motion stability from functional point of view. Several studies have been carried out in the recent past to have an insight into this aspect. Fernandes et al. [4] examined a central turret while extreme surge as well as mooring loads on FPS structures was studied by Dogliani and Pittaluga [5]. Turret-moored FPSO response with changing turret location as well as wind orientation was studied by Liu and Brown [6]. Donoghue and Linfoot [7] presented a study of the turret-moored FP systems. The turret-moored FPS response in conjunction with changing turret position as well as wind orientation was the subject of a similar study by Liu and Brown [6].

Kannah and Natarajan [8] carried out experimental investigation on the effect of position of turret within the hull and brought out interesting conclusions. Motion loads and mooring loads of a typical FPSO under seawaves for varying loading

conditions of dead weight (DWT) with changing turret locations (e.g., midships and semi-aft) locations were studied. It was found that the forward turret position was very well-suited position, in order to have favorable as well as safe working environment. For this position of turret, heave and pitch were found to be approximately 20–30% less as compared to midship and semi-aft locations for all loading.

The paper [8] concludes that the forward turret position is very good for internal turret FPSOs, so that there will be favorable working opportunity in all loading which, incidentally, is one of the most important functional requirements of turret FPSOs. The maximum motion response of FPSO also happens at full load, and therefore, internal turret FPSO along with catenary anchor leg should be designed catering for full load for safe and efficient exploitation. However, it may be noted that the experimental setup in this case was an oversimplified one with mooring lines arranged only in the fore and aft direction. The experiments were conducted under regular waves and head sea condition. A future study may attempt a closer replication of actual mooring arrangement. This study provides qualitative insight into relative merits of various turret locations within the hull. The results, however, cannot be lifted to predict the actual response of full-scale vessel for which a well-established model theory would be needed.

## 6 Design Considerations

The design of mooring systems for FP units has been studied by several authors. Winterstein et al. [9] investigated environmental parameters for extreme vessel response. Coupled analysis for FPS/FPSO motion and mooring characteristics of a vessel which is turret moored was looked into by Ormberg and Larsen [10]. Low and Langley [11] attempted time and frequency domain analysis in coupled mode for deepwater FPSs in a bid to identify the crucial environmental factors for the floaters. Mazaheri and Downie [12] adopted a response-based approach for determining extreme behavior of FPSs. Naess et al. [13] went for simulation based on Monte Carlo method for prediction of extreme behavior of floating offshore structures. Morton and Bowers published a paper [14] on large value study in given multivariate environment.

The design study of mooring systems of FP units normally examines extreme environments considering them as main design parameters. But the worst response may be related to sea state conditions other than extreme environmental conditions on account of the fact that the extreme response may be related to resonant periods and not necessarily extreme wave heights, in accordance with Vázquez-Hernández et al. [15]. The authors bring out that a good method to handle this situation is by conducting long-term study for obtaining extreme response.

## 7 Low-Frequency Mooring Forces

Having looked at the contemporary work on design considerations of mooring system, we take a quick look at one of the individual factors of forces on the mooring lines, viz. low-frequency mooring forces and how they are computed. The paper by van den Boom [16] deals with the dynamic behavior of mooring lines. Huse and Matsumoto [17] devised practical estimation method for mooring line damping. Wichers [18] examined wave and current interaction on the tankers which are moored in the high seas. Pinkster and Wichers [19] dealt with the statistics of low-frequency motions, particularly concerning nonlinearly moored tankers. Kim and Yue [20] studied slowly changing wave drift forces in irregular seas. Wichers and Huijsmans carried out oscillation tests. They did calculations on chain legs in static sea and while under the influence of current [21].

## 8 Assessment of Reliability of Mooring Systems

There have been considerable amount of efforts to assess the reliability of structures from early 1980s. Thoft-Christensen et al. [22] authored 'Structural Reliability Theory and Its Applications' in 1982. Also, Winterstein [9] contributed towards this effort. Subsequently, the efforts got extended to fixed offshore platforms. Winterstein et al. [23] worked on design sea states in connection with extreme response pertaining to Jackup Structures drawing upon such principles. Mid-1990s saw the efforts for assessing reliability of floaters gaining momentum. Winterstein et al. [24] produced the first prominent paper on environmental parameters and extreme response in relation to deepwater floating structures. This work was undertaken around 1995. Winterstein and Kumar [25] brought out extreme response as well as reliability of load factor design of floaters, the same year. Morton and Bowers [26] undertook extreme value investigation in multivariate environment at offshore (1996). Later (1998) Winterstein and Engebretsen [27] worked on 'Reliability-Based forecast of Forces and Response for design for the Floating offshore Structures'. The same year, Manuel et al. [28] authored a paper on a design format which was reliability-based for jacket platforms subjected to wave loads. Bhattacharya et al. [29] published combination of environmental parameters which were reliability-based for design of innovative floating structures. Fontaine et al. [30] attempted re-assessment of reliability of the mooring of existing FPSOs, using field data on wind, waves as well as current. They concurrently undertook measurements of the vessel offset and line tensions.

## 9 Yaw Instability

Simos et al. [31] worked on dynamics of an FPSO with turret system and the associated hydrodynamic models in 1998. Paton et al. [32] investigated on sway and yaw motions of a deepwater FPSO. Pistani and Thiagarajan [33] undertook campaign based on experiments on an FPSO positioned in bidirectional seas. Munipalli et al. [34] made contribution towards instability of weathervaning of FPSO as also consequences on RAOs. Problems relating to yaw instability in various FPSO systems operating around the globe disrupting the production/deck operations were well known. The same was studied by Yadav et al. [35].

Some initial findings are presented by Yadav et al. [35] on the basis of two important parameters—position of turret and hull length. In the paper, the authors go on to assess the effect of the said parameters. They compare the same with model test results. The author states, further parametric studies would be necessary for examining the influence of position of CoG, hull geometry, and slenderness of the hull among other parameters.

## 10 Piston Mode Resonance and Sloshing and Inertia of Turret-Entrapped Water

Miles [36] investigated slow oscillations in coupled wells. Molin [37] worked on the piston mode and sloshing mode occurrence widely observed in moon pools. Newman [38] studied low-frequency resonance of moon pools. Sphaier et al. [39] worked on monocolumn in waves. The issue was investigated by Molin et al. [40]. Figures 4 and 5 show typical decay test results for annular space and moon pool.

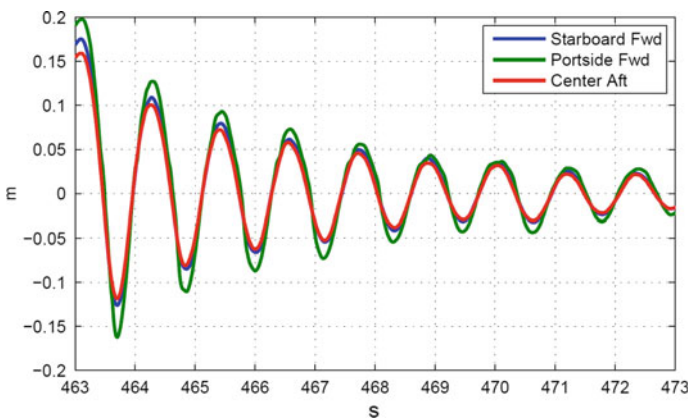
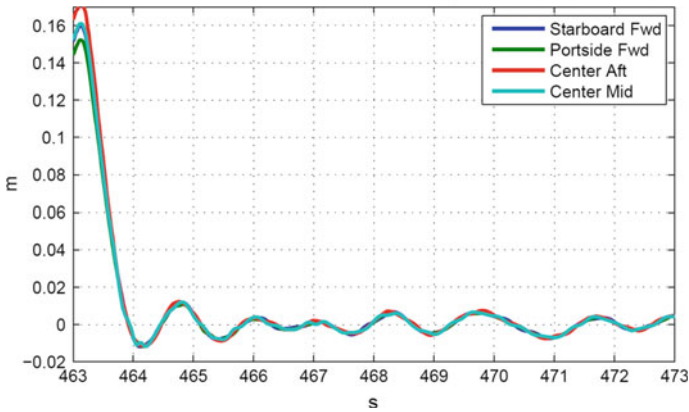


Fig. 4 Decay test time series—annular space [40]



**Fig. 5** Decay test time series—turret moon pool [40]

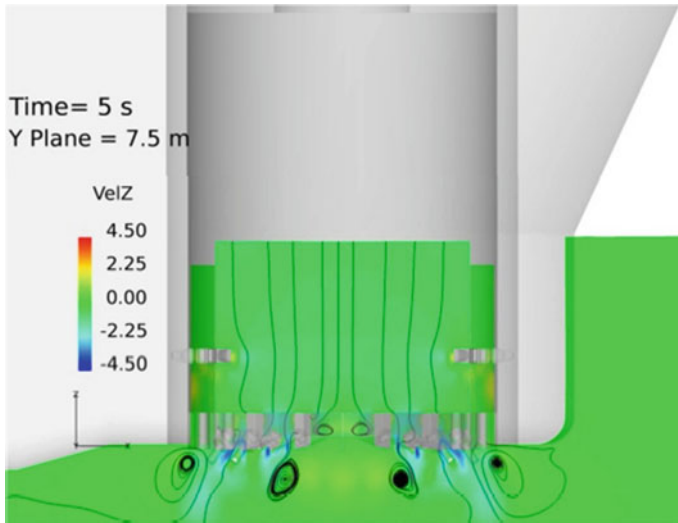
In the late 1990s, Molin [41] worked on the piston mode in moon pools. Molin [37] published a paper on piston mode and sloshing mode that happen in moon pools. Low-frequency resonance associated with moon pools was the theme worked on by Newman [42]. Maisondieu and Le Boulluec [43] worked on flow dynamics in moon pool by both experimental and numerical determination. Torres et al. [44] worked on moon pool numerical model as a minimization tool of monocolumn hull, while Sphaier [39] explored monocolumn behavior in waves by experiments.

Figure 6 shows the liquid formation during decay tests conducted in piston mode decay. de Vries et al. [45] investigated this phenomenon. The paper proposes practical analysis and design recommendations.

## 11 FPSOs in Shallow Water

Li [46] summarizes new development of offshore engineering technology, which was followed by Yang et al. [47] who investigated motions of a model of a tanker in shallow water. Ward et al. [48] brought out the response of a tanker FPSO in hurricane. Yang et al. [49] conducted out experimental investigation on motions of large FPSO operating in relatively shallow water.

Based on the above studies among others, the motion performance of an SPM 320K DWT FPSO in shallow water was investigated with varying depths by Li et al. [50]. This was undertaken for studying the behavior of FPSOs in the offshore of Bohai Bay, where water depth varies between 20 and 30 m. The model tests in 100-year condition, including the collinear wind and wave and the crossed current, were undertaken at the State Key Laboratory. The study is based on ideal and irrotational fluid assumptions and that the velocity potential satisfies the Laplace equation, the



**Fig. 6** Liquid formation (during decay tests) shown in figure is piston mode decay [41]

**Table 2** Main particulars of vessel and the scaled model [50]

Symbol	Unit	Full load	
		Full size	Model
LOA	m	352.83	4.833
<i>B</i>	m	62.05	0.850
<i>D</i>	m	29.64	0.406
<i>T</i>	m	19.49	0.267
$\Delta$	MT	390,000	0.977
LCG	m	-4.05	-0.055
GM	m	10.23	0.140
LGM	m	489.92	6.711
<i>K<sub>yy</sub></i>	m	85.78	1.175
<i>T<math>\varphi</math></i>	s	15.00	1.760

linearized free surface condition, radiation condition at infinity and solid boundary. Table 2 provides main particulars of the vessel and model.

Comparisons between the results of numerical calculation and experiment on water depth of 26, 23.5, 22.0, and 21.0 m are carried out for the power spectrum of pitch, roll, and heave. Also, a comparison of the time series for heave, roll, and pitch was undertaken. Good agreement between calculation and experiment was observed. It was observed that the pitch, roll, and heave of the fully loaded vessel considerably decrease when water depth reduces from 26 to 21 m (corresponding water depth in Ocean Engineering Basin varying from 0.356 to 0.288 m). The decreasing trend and

amplitude variation are consistent with that in the calculation. The result of numerical simulation agrees well with the value of the model test.

It means that the linear 3D potential theory and time domain simulations can be adopted to predict the motions of relatively bigger vessels in shallow water. The research result is expected to provide insight into optimizing design of the FPSO in the oil fields with shallow water.

## 12 Full-Scale Investigation of FPSO Hydrodynamics Under Typhoon

Some papers published prior to 2012 provided the precursor to the theoretical background for the full-size hydrodynamic study of the turret FPSOs. de Souza and Morishita [51] studied dynamic performance of a turret FPSO in single configuration as well as tandem configuration in actual kind of sea environs. Luo and Baudic [52] attempted forecasting FPSO response with the help of model test/numerical analysis. Kim et al. [53] reported coupled mode dynamic analysis of a turret FPSO matched with OTRC (Offshore Technology Research Center, University of Texas) experiment. Esperanca et al. [54] brought out results of an experimental study of roll motions of FPSO. Hu [55] reported full-size motion study on the performance of a floating production and storage vessel in South China Sea. Zhao et al. [56] analyzed the FPSO's motion performance during the typhoon 'Koppu'. Figure 7 shows catenary element configuration in the local  $x$ - $z$  plane.

A decoupled analysis between floater motions and the mooring system was employed, and the calculation process consists of the following: Determination of

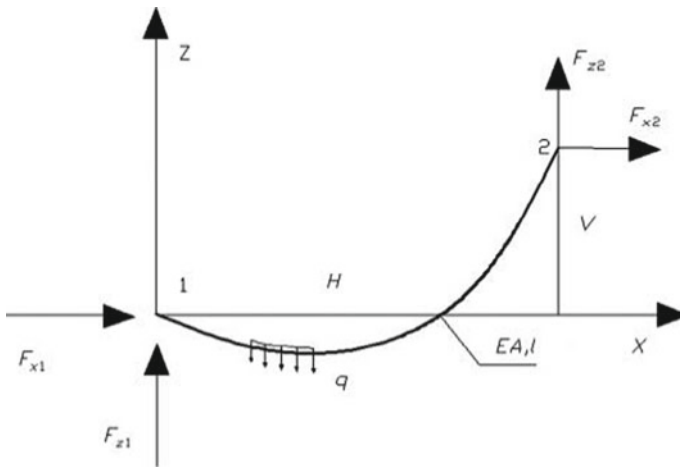


Fig. 7 Catenary element configuration in the local  $x$ - $z$  plane [56]



floaters motions and dynamic response analysis of mooring system with the help of top-end motions projected in the first step. Typical inadequacies in the separated approach were the lack of or generalization of current loads and low-frequency damping from the moorings. It was brought out that if the floater motions can be measured and then serve as the input into the dynamic response analysis, the decoupled analysis would give a more exact simulation of the mooring loads than the coupled analysis.

The most exact way to estimate mooring loads is arguably through the full-scale measurement in the operation field of the FPSO system. However, there are practical difficulties to realize this since the available technology places some restrictions both on account of the limitation on the size of the load cell with a large enough measuring range, and due to the fact that installing the instruments between the vessel and mooring would weaken mooring lines. One set of time series data from the passage of a typhoon from 15:00 to 18:00 on September 14, 2009, was selected.

The detailed procedure for the decoupled analysis can be abridged as (1) calculate the translational displacement of turret point on the FPSO hull in surge, heave, and sway motions, (2) configure the finite element (FE) model for the FPSO system with the help of 'DeepC', and input the FE model directly into the line model code, 'Riflex'. Run the numerical code with the time series obtained in the first step as the input data and calculate the loads acting on mooring system.

Also, the loads acting on mooring legs are very sensitive to the conditions of environment. During the passage of the typhoon, the tension forces acting on the mooring system were less than the allowable maximum tension, indicating the capability and strength of the FPSO mooring system. Because of difficulties in executing full-scale measurements and high cost, there has been hardly any research published on full-scale measurements to characterize the FPSO. Such works would help to verify the design of the FPSO involved in the study and may serve as guidance for the future FPSO system design. Though interesting relationships were uncovered between the roll and pitch motions that were possibly related to the ratio of the length between the perpendiculars and the breadth of the vessel, during the above study, further studies are needed for corroboration.

### 13 Model Testing for FPSO Hydrodynamics

Experimental approach has yielded good results in the field of FPSOs. Stansberg et al. [57–59] worked on reliable approaches for laboratory confirmation of station keeping and the associated mooring in deepwater, challenges in deepwater experiments and model testing for ultra-deepwater. Waals and Van Dijk [60] worked on truncation approach for deep-sea moorings for moored vessel and a partially tensioned moored semisub. API [61] brought out their RP 2SK for station keeping systems meant for floaters. In 2008, ITTC [62] published procedures recommended and guidelines, testing, and extrapolation.



**Fig. 8** Model, scale 1/64, used to represent the FPSO in deepwater Gulf of Mexico [63]

Model testing of floaters along with mooring lines and risers at deep sea may be the most dependable methodology to investigate intricate hydrodynamic response of the comprehensive system, according to Lopez et al. [63] (Fig. 8).

## 14 Coupled Dynamic Response in Case of FPSO with Risers

Studies towards coupled dynamic response of floaters commenced in the early 1980s. Pioneers were Paulling and Webster [64], Huse and Matsumoto [65]. Aranha [66], Bompais et al. [67] took the process forward. Chakrabarti [68] brought out the approach for scrutinizing the effect of incorporating riser/mooring design. Karunakaran [69] dealt with efficient metal riser arrangement for production systems based on ship and semis. Ma et al. [70] brought out a deepwater nonlinear coupled analysis tool. Chaudhury [71] and Gupta [72] led the development in the year 2000. Wichers and Ji [73] outlined coupling terms in viscous reaction which are of the low-frequency kind in deepwater tankers.

Dynamic response to sea loads by floaters with moorings and risers has invoked considerable interest in the industry. Usually, each component is investigated individually, and subsystem exchanges are then taken into account in a simplified way. Fundamentally, this kind of modeling based on uncoupled approach remains restricted to cases of feeble interactions. Heurtier et al. [74] have examined a wholly coupled approach wherein motions of say, FPSO mooring lines/risers are calculated concurrently in time domain. Comparisons of coupled/uncoupled results are offered for a moored FPSO in severe environment. For the test case considered, viz. an FPSO

anchored in deepwater, by 2000 m depth, the previous computations lead to conclude that:

- The horizontal motion of the vessel (surge) arises mainly in the low-frequency range and must be computed including the line dynamics.
- The quasi-static uncoupled investigation tends to over-forecast surge amplitude on account of an imprecise evaluation of drag load acting on mooring system.
- The coupled approach allows to take into account properly the low-frequency damping associated with the mooring system.
- Contrary to the surge motion, the vertical motion (heave) at the wave frequency does not vary significantly whether or not the dynamics of the lines are considered.
- The top tension in the mooring lines must also be computed using a dynamic analysis, for both the low-frequency and peak spectrum wave frequency parts.
- As far as the top tension is concerned, either the uncoupled or coupled methods can be said to be always conservative, thus the need for dynamic simulations.

The uncoupled approach offers an interesting compromise between complexity, accuracy, and CPU time, thus is efficient to use in early design stage of a mooring system. Despite the relatively good agreement between uncoupled and fully coupled signals, the maximum values are found different. From the case studied here, it seems that coupling effects are relatively small for FPSO. This has to be confirmed by more case studies. However, fully coupled simulations are probably needed to model smaller floating units in extreme waves yielding to survival conditions.

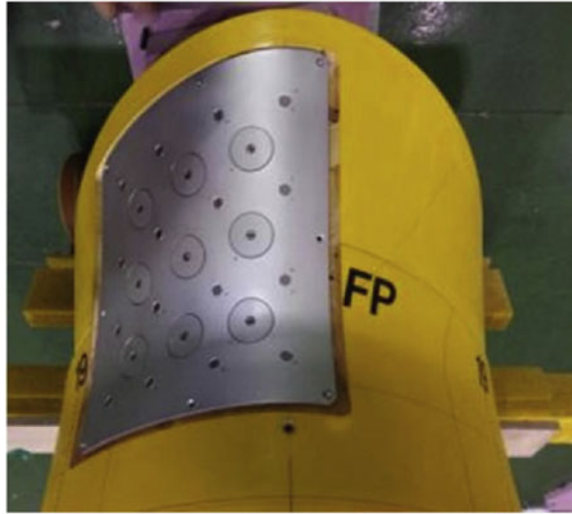
## 15 Wave Run-up Along the Broadside

Green water shipping has been a matter of concern for FPSOs for decades now. Typical were the experimental studies toward mitigation in the 1990s. Watanabe [75], Hamoudi and Varyani [76] and Vestbøstad [77] took the lead in this direction. During the years from 2000 to 2010, a large number of studies has been carried out. Buchner and Voogt [78], Faltinsen et al. [79], Drobyshevski [80], Xu et al. [81], Touzé et al. [82], Stansberg et al. [83] were prominent among them. FPSOs suffer from wave run-up and green sea occurrence in severe oceanic environs. An investigation was undertaken by Xiao et al. [84] to study the shipment of green sea on an FPSO (300k DWT) in shallow water. Hong et al. [85] studied the effect of impact load otherwise known as slapping force by steep waves on FPSO bow by way of model test (Fig. 9).

## 16 Innovations

Change is the only constant on any technology front, and the same is true with FPSOs. There are innovative developments in applied technology as well as the theoretical

**Fig. 9** Bow panel with pressure sensors [85]



approaches. A key necessity for FPSO is to withstand severe meteorological conditions in some of the fields such as the GoM. Usage of large disconnectable buoy mooring (Buoyant Turret Mooring or BTM) is one such development which has taken place in the recent past. This will allow the ship to safely sail away from oncoming hurricanes. This disconnectable capability allows the FPSO to rapidly reconnect and restart production when the hurricane passes the location. Feature of steel lazy wave risers (SLWRs) also brought in an element of innovation.

Shell's Stones FPSO in the GoM has incorporated both disconnectability as well as SLWR. It operates at a seawater depth of 2900 m, the deepest till date. Yet another innovative aspect developed is the opportunity to re-adjust each of the mooring lines' tension without having any device installed on board the FPSO. It pioneers use of what is known as ILMC which is in-line mooring connector that gives direct access to mooring line for the purposes of re-tension. This allows more options when need arises to fine-tune tension of mooring lines during the early phase of system installation. Lamport and Josefsson [86] carried out a research to study the advantage of round-shaped FPSO over the traditional ship-shaped FPSO. The comparisons were made in terms of motion response, mooring system design, constructability and fabrication, operability, safety and costing between both the structures. One of the findings of the study was, unlike their traditional counterparts, round FPSOs' motions which were similar for any direction of incident wave. Siow et al. [87, 88] investigated wave response and dynamic stability of new design round-shaped FPSO in ocean environments.

The primary aim of the investigation was to forecast wave-induced motion of round-shaped FPSO. (Refer Fig. 10 for a classic round-shaped or cylindrical FPSO). In this investigation, the motion response of FPSO is replicated by diffraction poten-



**Fig. 10** Cylindrical FPSO, ‘Sevan Voyageur’ while under construction [86]

**Fig. 11** Model test setup for tandem arrangement of a round-shaped FPSO [87]



tial with Morrison heave damping amendment method. Wave tank experiment on a scaled model was conducted (see Fig. 11) to validate the simulated results.

The study of the wave frequency motion was conducted by numerical method and experimental method. The experimental and numerical results were observed to be in very good agreement between each other for heave, surge, and pitch motions. The simulation results showed that the round-shaped FPSO has good wave frequency response, and the motion response is kept in low amplitude in most of ocean environment. From the research, it is obtained that the designed round-shaped FPSO has good dynamic stability. This is an important factor to reduce the functional downtime of FPSO in normal operation. Besides, this FPSO is also suitable to operate with more stringent requirement, such as design for a LPG or LNG FPSO installed with the fractionating columns. It is believed that maximum roll amplitude of the round-shaped FPSO can remain below  $2^\circ$  for most of the wave conditions due to

low roll or pitch RAO in wind sea and swells sea condition and the roll/pitch natural period is designed far away from the most frequently occurring ocean condition.

In future, the round-shaped FPSO design should be focused in heave motion response due to the fact that the heave natural period is still likely to fall in the ocean swells condition at some of the FPSO operating environment. It is concluded that the round-shaped FPSO can be considered as an alternative to replace ship hull due to the good wave motion response characteristic. Further, study may reinforce confidence in concept of round-shaped FPSO.

## 17 Conclusion

Review of the literature on hydrodynamic aspects of FPSOs reveals the following:

- (a) Design of moorings meant for floaters normally takes into consideration severe environment as the main parameter for design. The worst response for mooring system in case of FPSOs can be related to those other than extreme environment since response extreme in nature can be related to resonant period and not largest wave amplitude.
- (b) FPSOs show a large degree of yaw instability. Equilibrium angle for yaw is considerably larger for internal turreted floaters particularly as length of wave is near to length of ship.
- (c) The uncoupled approach to environmental loads in determining vessel response offers a good compromise between complexity, accuracy and CPU time; hence, it is efficient in early design phase of a mooring system.
- (d) The motion modes of surge, sway, and yaw are primarily affected by typical low-frequency forces, whereas the motion modes of heave, roll, pitch are mainly influenced by wave frequency loads.
- (e) Round-shaped FPSO can be considered as alternate to traditional ship-shaped hull on account of superior wave response of the former.

## References

1. England LT, Duggal AS, Allen Queen L (2001) A comparison between turret and spread moored F(P)SOs for deepwater field developments. Deep offshore technology
2. Wichers IJ (2013) Guide to single point moorings. [www.info@wmooring.com](http://www.info@wmooring.com)
3. Ihonde O, Mattinson J, England LT (2002) FPSO mooring & offloading system alternatives for deepwater West Africa. In: 6th annual offshore West Africa conference
4. Fernandes AC et al (1998) The feasibility of a central turret in FPSO system. In: Proceedings of 17th international conference on offshore mechanics and arctic engineering (OMAE)
5. Dogliani M, Pittaluga A (1993) Extreme surge and mooring loads of FPS structures. In: Proceedings of offshore technology conference, 7198, pp 117–131
6. Liu F, Brown DT (1998) Turret moored floating production system response with varying turret location and wind direction. In: Proceedings of 17th international conference on offshore mechanics and arctic engineering (OMAE)

7. Donoghue TO, Linfoot BT (1992) An experimental study of turret moored floating production systems. *J Appl Ocean Res* 14:127–139
8. Rajesh Kannah T, Natarajan R (2006) Effect of turret location on the dynamic behaviour of an internal turret moored FPSO system. *J Nav Archit Mar Eng*
9. Winterstein SR, Ude TC, Cornell CA, Bjerager P, Haver S (1993) Environmental parameters for extreme response: inverse form with omission factors. In: *Proceedings of the international conference on structural safety and reliability (ICOSSAR)*
10. Ormberg H, Larsen K (1998) Coupled analysis of floater motion and mooring dynamics for a turret-moored ship. *Appl Ocean Res* 20:55–67
11. Low YM, Langley RS (2006) Time and frequency domain coupled analysis of deepwater floating production systems. *Appl Ocean Res* 28:371–385
12. Mazaheri S, Downie MJ (2005) Response-based method for determining the extreme behaviour of floating offshore platforms. *Ocean Eng* 32:363–393
13. Naess A, Gaidai O, Teigen PS (2007) Extreme response prediction for nonlinear floating offshore structures by Monte Carlo simulation. *Appl Ocean Res* 29:221–230
14. Morton D, Bowers J (1996) Extreme value analysis in a multivariate offshore environment. *Appl Ocean Res* 18:303–317
15. Vázquez-Hernández AO, Ellwanger GB, Sagrilo LVS (2011) Long-term response analysis of FPSO mooring systems. *Appl Ocean Res*
16. van den Boom HJJ (1985) Dynamic behaviour of mooring lines. In: *Proceeding BOSS conference, Delft*
17. Huse E, Matsumoto K (1988) Practical estimation of mooring line damping. In: *Proceedings of the twentieth annual offshore technology conference, paper no. 5676*
18. Wichers JEW (1988) Wave-current interaction effects on moored tankers in high seas. In: *Proceedings of the twentieth annual offshore technology conference, paper no. 5631*
19. Pinkster JA, Wichers JEW (1987) The statistical properties of low frequency motions of nonlinearly moored tankers. In: *Proceedings of the nineteenth annual offshore technology conference, paper no. 5457*
20. Kim MH, Yue DK (1989) Slowly varying wave drift forces in short crested irregular seas. *J Appl Ocean Res*
21. Wichers JEW, Huijsmans RHM (1990) The contribution of hydrodynamic damping induced by mooring chains on low-frequency vessel motions, OTC
22. Thoft-Christensen P, Baker MJ (1982) *Structural reliability theory and its applications*. Springer
23. Winterstein SR, Torhaug R, Kumar S (1994) Design seastates for extreme response of jackup structures. *Proc OMAE Conf* 2:77–84
24. Winterstein SR, Kumar S, Kleiven G. (1995) Environmental contours and extreme response of deep-water floating structures. In: *Proceedings of ASCE engineering mechanics conference, pp 1187–1190*
25. Winterstein SR, Kumar S (1995) Reliability of floating structures: extreme response and load factor design. In: *Proceedings of OTC (OTC 7758), pp 1–10*
26. Morton ID, Bowers J (1996) Extreme value analysis in a multivariate offshore environment. *Appl Ocean Res* 18(6):303–317
27. Winterstein SR, Engebretsen K (1998) Reliability-based prediction of design loads and responses for floating ocean structures. In: *Proceedings of OMAE conference, pp 1–11*
28. Manuel L, Schmucker DG, Cornell CA, Carballo JE (1998) A reliability-based design format for jacket platforms under wave loads. *Mar Struct* 11(10):413–428
29. Bhattacharya B, Wang S, Basu R et al (1999) Reliability-based combination of environmental parameters for the design of novel floating structures. In: *Proceedings of OMAE (99-6019), pp 1–6*
30. Fontaine E, Orsero P, Ledoux A, Nerzic R, Prevosto M, Quiniou V (2013) Reliability analysis and response based design of a moored FPSO in West Africa. Elsevier
31. Simos AN, Tannuri EA, Pesce CP (1998) Dynamics of a turret-FPSO system and hydrodynamic models, OMAE98-0410

32. Paton CG, Carra CJ, Sincock P (2006) Investigation of sway yaw motions of a deep water FPSO, OTC 18039, Houston
33. Pistani F, Thiagarajan KP (2007) Experimental campaign on a moored FPSO in complex, bi-directional seastates. In: Proceedings of international conference on water waves floating bodies (IWWWFB), Plitvice, Croatia
34. Muniipalli J, Pistani F, Thiagarajan KP, Winsor F, Colbourne B (2007) Weathervaning instabilities of a FPSO in regular waves and consequences on response amplitude operators, OMAE2007-29359
35. Yadav A, Varghese S, Thiagarajan KP (2007) Parametric study of yaw instability of a weathervaning platform. In: 16th Australasian fluid mechanics conference
36. Miles J (2002) On slow oscillations in coupled wells. *J Fluid Mech* 455:283–287
37. Molin B (2001) On the piston and sloshing modes in moon pools. *J Fluid Mech* 430:27–50
38. Newman JN (2003) Low-frequency resonance of moon pools. In: Proceedings of 18th international workshop on water waves and floating bodies, Le Croisic
39. Sphaier SH, Torres FGS, Masetti IQ, Costa AP, Levi C (2007) Monocolumn in waves: experimental analysis. *Ocean Eng* 34:1724–1733
40. Molin B, de Vries I, Cinello A Hydrodynamic analysis of the piston mode resonance inside a large FLNG turret
41. Molin B (1999) On the piston mode in moon pools. In: Proceedings of the 14th IWWWFB Port Huron Michigan U.S.A
42. Newman JN (2003) Low-frequency resonance of moon pools. In: Proceedings of the 18th IWWWFB, Le Croisic, France
43. Maisondieu C, Le Boulluec M (2001) Flow dynamics in a moon pool. Experimental and numerical assessment In: Proceedings of the 20th international conference on offshore mechanics and arctic engineering, Rio de Janeiro, Brazil
44. Torres FGS, Cueva M, Malta EB, Nishimoto K, Ferreira MD (2004) Study of numerical modeling of moon pool as minimization device of monocolumn hull. In: Proceedings of the 23rd international conference on offshore mechanics and arctic engineering. Paper 51540 Vancouver, British Columbia, Canada
45. de Vries I, Roux Y, Naciri M, Bonnaffoux G (2013) Dynamics of entrapped water in large diameter turret moon pools. OMAE
46. Li Y (1998) The new development of offshore engineering technology. *China Offshore Platform* 13(1):9–12
47. Yang J, Longfei X, Tao P et al (2000) Investigation of motions of a oil tanker model in shallow water with irregular waves. *Ocean Eng* 18(3):25–29
48. Ward EG, Mehernosh BI, Robert PJ (2001) The behavior of a tanker-based FPSO in hurricane waves, winds, and currents. In: Proceedings of the 11th ISOPE conference, Stavanger, Norway, vol IV, pp 650–653
49. Yang J, Xiao L et al (2001) Experimental research on motion performance of large FPSO in shallow water
50. Li X, Yang J, Xiao L (2003) Motion analysis on a large FPSO in shallow water. In: International offshore and polar engineering conference
51. de Souza JR Jr, Morishita HM (2002) Dynamic behavior of a turret FPSO in single and tandem configuration in realistic sea environments. In: Proceedings of the 21st international conference on offshore mechanics and arctic engineering (OMAE). ASME, Oslo, Norway
52. Luo Y, Baudic S (2003) Predicting FPSO response using model test and numerical analysis. In: Proceedings of the thirteenth international offshore and polar engineering conference. ISOPE, Honolulu, Hawaii, USA, 25–30 May 2003
53. Kim MH, Koo BJ, Mercier RM, Ward EG (2005) Vessel/mooring/riser coupled dynamic analysis of a turret-moored FPSO compared with OTRC experiment. *Ocean Eng* 32:1780–1802. *Ships Offshore Struct* 295
54. Esperanca PTT, Sales JS Jr, Liapis S, Matsuura JPJ (2008) An experimental investigation of roll motions of an FPSO. In: Proceedings of the 27th international conference on offshore mechanics and arctic engineering (OMAE). ASME, Estoril, Portugal, pp 15–20



55. Hu Z (2010) Report for the full-scale measurement on the motion response of FENJIN FPSO in South China Sea and investigations on the deduction of the mooring line loads. State Key Lab of Ocean Engineering, Shanghai Jiao Tong University, Shanghai
56. Zhao W-h, Yang J-m, Hu Z-q, Wei Y-f (2011, May) Full-scale measurement investigation of the hydrodynamics of a turret-moored FPSO in a typhoon and deduction of its mooring loads. *Ships Offshore Struct* 7
57. Stansberg CT, Oritsland O, Kleiven G (2000) Verideep: reliable methods for laboratory verification of mooring and stationkeeping in deepwater. Paper #12087, OTC2000 conference, Houston, Tx, USA
58. Stansberg CT, Ormberg H, Oritsland O (2002) Challenges in deepwater experiments-hybrid approach. *JOMAE (ASME)* 124(2):90–96
59. Stansberg CT, Karlsen SI, Ward EG, Winchers JEW, Irani MB (2004) Model testing for ultra-deep waters, OTC 16587
60. Waals O, Van Dijk RRT (2004) Truncation methods for seep water mooring systems for a catenary moored FPSO and a semi taut moored semisubmersible. In: *Proceedings, deep offshore technology conference (Dot)*, New Orleans, USA
61. API RP 2Sk (2005) Design and analysis of station keeping systems for floating structures, 3rd edn, Oct 2005
62. ITTC 07-3.5-Recommended procedures and guidelines (2008) Testing and extrapolation methods, loads and responses, ocean engineering, truncation of test models and integration with numerical simulations
63. Lopez JT, Tao L, Xiao L, Hu Z (2015) Experimental study on hydrodynamics of a FPSO in deepwater Gulf of Mexico. In: *International conference on ocean, offshore and arctic engineering, OMAE2015*
64. Paulling JR, Webster WC (1986) A consistent, large amplitude analysis of the coupled response of a TLP and tendon system. In: *Proceedings of 5th OMAE conference*, vol 3, pp 126–133
65. Huse E, Matsumoto K (1989) Mooring line damping due to first and second order vessel motions. OTC
66. Aranha JAP (1993) A formula for wave damping in the drift of a floating body. *JFM* 275:147–155
67. Bompais X, Le Boulluec M, Dekint F, Marin S, Molin B (1994) Slow drift motion: practical estimation of mooring line damping. *OMAE* 1:383–391
68. Chakrabarti P, Chandwani R, Larsen I (1996) Analyzing the effect of integrating riser/mooring line design. *OMAE*, vol 1, part B, offshore technology. ASME
69. Karunakaran D, Nordsve NT, Olufsen A (1996) An efficient metal riser configuration for ship and semi based production systems. In: *Proceedings of the six international offshore and polar engineering conference (ISOPE)*, Los Angeles, USA, vol 2, pp 156–162
70. Ma W, Lee M, Zou J, Huang W (2000) Deepwater nonlinear coupled analysis tool. In: *Proceedings of offshore technology conference*, paper no. 12085
71. Chaudhury G, Ho CY (2000) Coupled dynamic analysis of platforms, risers, and mooring. In: *Proceedings of offshore technology conference*, paper no. 12084
72. Gupta H, Finn L, Weaver T (2000) Effects of spar coupled analysis. In: *Proceedings of offshore technology conference*, Houston
73. Wichers J, Ji C (2000) On the coupling terms in the low frequency viscous reaction forces of moored tankers in deep water. In: *Proceedings of offshore technology conference*
74. Heurtier JM, Le Buhan P, Fontaine E, Le Cunff C, Biolley F, Berhault C (2001) Coupled dynamic response of moored FPSO with risers. In: *International offshore and polar engineering conference*, Stavanger, Norway
75. Watanabe I (1990) Remarks on influence of bow flare form on deck wetness. In: *Proceedings of 19th international towing tank conference*, Madrid, Spain, vol 2, pp 167–172
76. Hamoudi B, Varyani KS (1998) Significant load and green water on deck of offshore units/vessels. *Ocean Eng* 25(8):715–731
77. Vestbøstad TM (1999) Relative wave motions along the side of an FPSO hull. In: *Proceedings of 18th international conference on offshore mechanical and arctic engineering*, St. John's, Newfoundland, Canada, paper OMAE4239

78. Buchner B, Voogt A (2000) The effect of bow flare angle on FPSO green water loading. In: Proceedings of 19th international conference on offshore mechanical and arctic engineering, paper OMAE4092
79. Faltinsen OM, Greco M, Landrini M (2002) Green water loading on FPSO. *J Offshore Mech Arctic Eng* 124:94–103
80. Drobyshevski Y (2004) Hydrodynamic coefficients of a two-dimensional, truncated rectangular floating structure in shallow water. *Ocean Eng* 31(3–4):305–341
81. Xu L, Barltrop N, Okan B (2008) Bow impact loading on FPSOs 1—experimental investigation. *Ocean Eng* 35(11–12):1148–1157
82. Le Touzé D, Marsh A et al (2010) SPH simulation of green water and ship flooding scenarios. *J Hydrodyn* 22(5):231–236
83. Stansberg CT, Baarhom R, Berget K et al (2010) Prediction of wave impact in extreme weather. In: Proceedings of the annual offshore technology conference, Houston, USA, vol 2, pp 1070–1080
84. Xiao L, Tao L, Yang J, Li X (2014) An experimental investigation on wave runup along the broadside of a single point moored FPSO exposed to oblique waves. *Ocean Eng*
85. Hong S-K, Lew J-M, Jung D-W, Kim H-T, Lee D-Y, Seo J-S (2016) A study on the impact load acting on an FPSO bow by steep waves. *Int J Nav Archit Ocean Eng*
86. Lampert WB, Josefsson PM (2008) The next generation of round fit-for-purpose hull form FPSOs offers advantages over traditional ship-shaped hull forms, 2008 deep Gulf conference, 9–11 Dec, New Orleans, Louisiana, USA
87. Siow CL, Koto, Yasukawa, Matsuda, Terada, Soares, Samad (2014) Experiment study on hydrodynamics characteristic of rounded-shape FPSO. In: Conference on ocean, mechanical and aerospace
88. Siow CL, Koto J, Yasukawa H, Matsuda A, Terada D, Guedes Soares C, Samad MZbM, Priyanto A (2015) Wave induce motion of round shaped FPSO. *J Subsea Offshore*

# Duct Optimization and Performance Evaluation Using CFD for the Reefer Container Hold



Elangovan Muniyandy, Ananth Kumar and Sunil Arora

**Abstract** In the conversion of a container vessel from the standard 20-ft container into high cube reefer container, maximum number of container is accommodated with an improved ventilation system. For the proper ventilation system, each duct has been modelled in 3D and analysed using CFD to make sure that defined airflow is achieved. Each hold is modelled with structure, containers, fan, duct and natural outlet to remove the heated air. Using CFD simulations, duct design was improved and hot spots were removed by modifying the grid opening in duct and few changes in structures to circulate the air easily towards an outlet.

**Keywords** Duct design · Container hold · Reefer container · CFD analysis  
Duct optimization · Thermal analysis and performance evaluation

## 1 Introduction

Shipping is the economic transport when compared to other modes of transport. For the type of vessel need, current market decides and many cases, existing vessel can go for major changes to carry other than a designated cargo. A similar requirement was raised to convert 20-ft container carrier into a high cube container to carry a banana. Transporting cargo needs to be given special thought on equipment, ducting system piping system, external temperature and internal temperature [1]. Other shipboard factors are functions of refrigeration, method of stowage, interpretation of carriage instructions and duration of the voyage [2]. Common issue in banana transportation is heat, which can spoil the cargo. The studies were carried out in temperature conditions inside the containers [3, 4] because homogeneous distribution of gaps is crucial to maintain airflow rate and temperature. It was observed that the difference in internal

---

E. Muniyandy (✉) · A. Kumar  
Bond Marine Consultancy, Kandigai, Chennai 600127, India  
e-mail: [muniyandy.e@gmail.com](mailto:muniyandy.e@gmail.com)

S. Arora  
Bond Marine Consultancy, London, UK

© Springer Nature Singapore Pte Ltd. 2019  
K. Murali et al. (eds.), *Proceedings of the Fourth International Conference in Ocean Engineering (ICOE2018)*, Lecture Notes in Civil Engineering 22,  
[https://doi.org/10.1007/978-981-13-3119-0\\_24](https://doi.org/10.1007/978-981-13-3119-0_24)

and external temperatures [4] can affect the banana. Altogether, adequate ventilation system is required in the enclosed cargo space to maintain the average temperature [5]. Airflow and heat transfer model was developed and analysed using CFD [6].

Based on earlier published paper review, the researchers were studied single container but for entire hold, not many papers to refer. Therefore, special care was taken from the beginning of placement of a container to the ventilation system. As this project is the conversion of the vessel to carry a banana in a high cube reefer container, maintaining a ventilation system is most important. Because of height variation for the high cube container from the existing grid opening position, walkway and access were modified from the maintenance point of view. Maximums of 457 containers were placed within the space and accepting the class rule.

In this project, two major researches were carried out because of complexity in the ventilation system. The first part is duct design and optimization and the second part is to analyse the complete hold which includes container, duct, fan and air outlet. These two parts can be well analysed further in this paper.

## 2 Definition of Problem

As a part of consultancy cum research project, the initial study was made to increase the number of reefer container by doing changes in the structure and in the ventilation system. As per the design, it is possible to place 457 reefer containers but doing small changes in structure for the maintenance and air circulation; total container below deck was increased from 372 to 457. General arrangement which shows the number container and highlighting the hold number 2 is shown in Fig. 1. As per the rule [7, 8], the refrigerated container needs 4500 m<sup>3</sup>/h of air supply, and if it is water cooled, 700 m<sup>3</sup>/h is required. The outlet velocity of air should not be more than 13 m/s, and recommended velocity is 10 m/s.

To make this ventilation system works better, and whole project has been grouped into two. First part is designing the duct, and make sure that required flow rate is achieved at the grid which faces the container equipment located face. Due to the height difference of a reefer container, all grid locations are changed and accordingly, opening at the inner wall is changed to reach air from grid to container. In the second part, whole domain is covered from an inlet of air, container hold and outlet air.

### 2.1 Duct Design for Air Distribution

Duct is designed to distribute the required at port and starboard side of the hold. Fan capacity is estimated based on the number of containers to be supplied by the fan. For the better airflow and improving the performance of the ducting system, branching was restricted to supply the single vertical duct. Though it was designed as per standard HVAC designer, it was recommended to verify the flow rate using

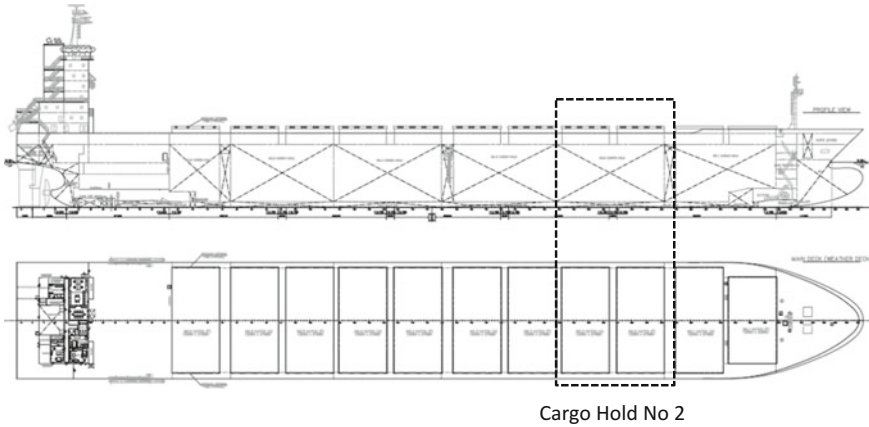


Fig. 1 Container vessel with highlighting of single cargo hold

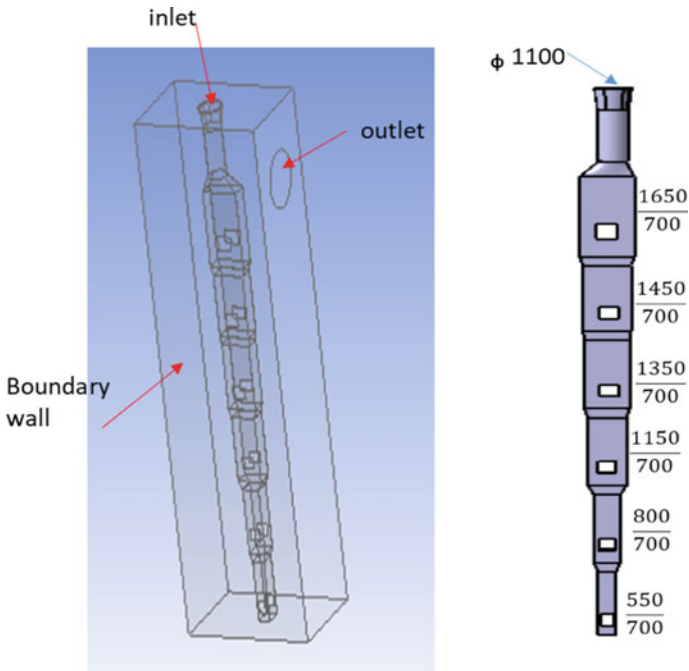


Fig. 2 Single duct with domain used in CFD

CFD simulation, refer to Fig. 2. It depends upon the size of the hold; maximums of 11 ducts were placed for each hold. Due to the strength member in the steel structure, containers at port and starboard are not the same number of container for each side. This leads to many duct designs for each hold.

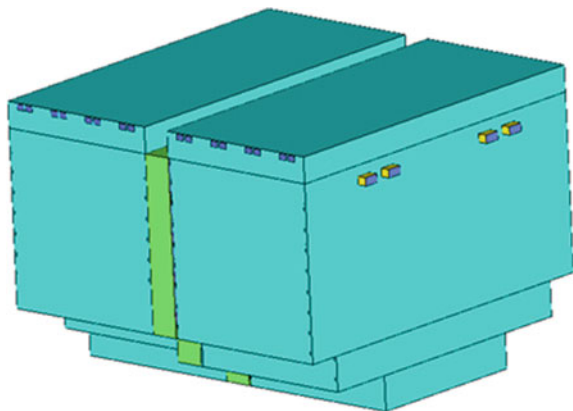
In the container hold, space between a container (i.e. walkway), there is a restriction to increase the duct depth along the ship length because of insufficient space for maintenance and repair access. Therefore, duct depth is kept constant for the complete length and only width get changes.

## 2.2 Hold Performance Evaluation

Due to the development in computer technology and computing machine, it has happened to analyse the complete hold using CFD. Ventilation duct is placed at the centre of the hold, and aft and forward are placed with containers. The size of the hold is around  $27\text{ m} \times 20\text{ m} \times 27\text{ m}$ . Each hold contains the maximum of 122 containers, and the maximum ducts are 11. Each duct is connected with fan to supply sufficient air to the assigned containers which are six at each side. It can vary depending on the hull width and structure restrictions (Fig. 3).

As per the design, required, flow is calculated based on the manual calculation of fan capacity, duct size and grid opening. In the hold, wall is placed between container and duct, which might change the airflow circulation. It was assumed that complete system works without any issue. Based on our experience, we decided to verify using CFD simulation because of space between containers and space between a duct and a container. As we predicted, standard design was not performed well and we modified the design to suit the required airflow.

**Fig. 3** Single hold domain used in CFD



### 3 Duct Modelling and Boundary Conditions

From our experience, usually ducts are designed using standard, and execution is carried for the installations. To avoid the critical situation, designed duct was modelled and did meshing for the simulation, please refer to Fig. 4. Duct design can affect the flow rate at the grid, and there are no points to add temperature in the simulation because there is no heat source. Therefore, calculated fan capacity was given as an input for the inlet in terms of mass flow rate and outlet boundary is atmospheric pressure.

Initially, mesh dependency study was carried to avoid mesh influence. At the final stage, four million elements were selected to get a proper result without promising on accuracy. Keeping the optimum mesh size, this has been introduced for entire hold analysis to attain mesh size. As this vessel is for conversion, existing duct and newly designed ducts were simulated with respect to grid opening.

#### 3.1 Analysis of Duct Simulations

For the existing duct and new ducts design simulation, result shows that flow rates were not reached as per calculations. In fact, initial duct grid and last grid which are at bottom of the domain were failed to stratify the requirements. From the CFD, we have done our calculation for duct and grid opening. Simulation was repeated for each duct. By doing minor changes in grid opening, required flow rate was achieved (Fig. 5).

It was observed that flow from the grid reaches to the side wall much lower height than expected. If it does not reach, then containers heat source and heat removal process might come down. To avoid that, different sizes like 30, 50, 75, 100 mm plates were with different angle likes 0, 15, 30, 45, with respect to grid direction.

**Fig. 4** Single duct meshing  
(four million elements)

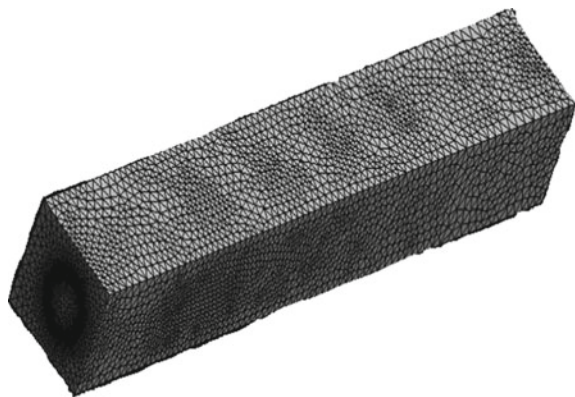
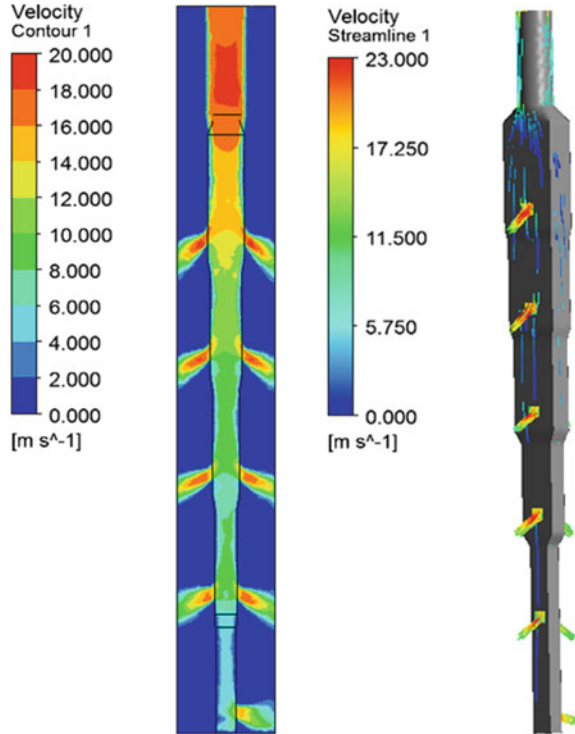


**Fig. 5** Single duct with domain used in CFD



After the details, it was decided based on the performance that 50 mm plate with an angle of zero degrees can work well.

After completing the individual duct study, as an additional check to make sure the flow rate, all ducts have been modelled but the domain size was limited between containers. In this study, walkway and accesses were not added as this aimed to study the flow rate at each grid. Mass flow rate for each duct is varying because of the number of containers supplied by the individual duct (Fig. 6).

This study has been repeated for each hold before going for complete hold analysis. It was observed that duct does not influence the flow and guide plate is adding value to flow direction to reach the container heat source area. At the end, same size of grid was executed though there is an acceptable flow difference of 1–5% which from experience. Keeping same size grid helps for the fabrication easier.

### 3.2 Observations and Suggestions

As per the standard, ducts were designed considering the frictional loss and reduction of duct size. After the CFD simulation, complete duct has been redesigned, and grids



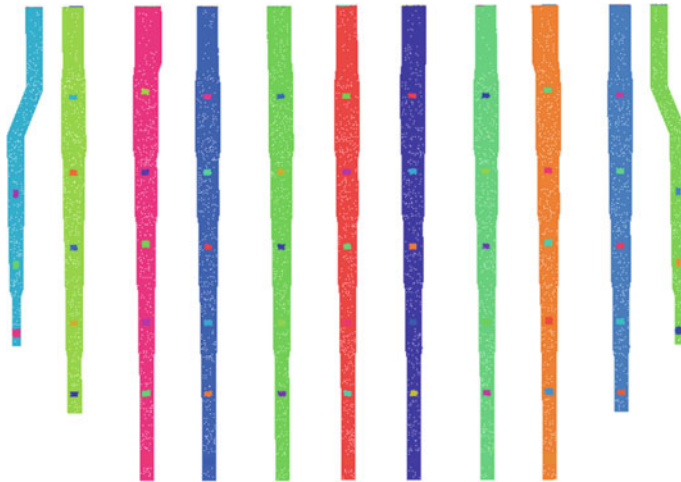


**Fig. 6** Single hold with all ducts

were modified to get the required. Please refer to Fig. 5 which shows the velocity contour and 3D duct view with flow rate and flow. Providing additional guiding plates, improve the direction of flow, which is the exit from the grid. All flow rates are achieved with an accuracy of 5–10% difference. Refer to Fig. 7 which shows the flow rate for single duct, and similar study was carried out all single ducts. All the duct designs must be constructed, and grid needs to be done at the proper location. Grid size is kept same for each hold, which makes easier for fabrication.

#### 4 Hold Modelling and Boundary Conditions

Each hold is different size and inside hold also not symmetry to reduce the domain. Complete hold is modelled from the air inlet which is fan supply flow rate. Flow rate has been entered in terms of mass flow rate, which is an inlet boundary condition. For the inlet air, ambient air condition was set as 35° and RH 70%. As first step, complete hold is modelled and meshing was done. Because of the domain size, total element has been increased to 15 million without compromising on result, and the minimum cell size is 0.299. Whole domain is grouped into three parts. First is duct area, which is in between aft and forward container face. Other two domains are aft, refer to Fig. 8. In the middle of the container, thin wall is placed and proper opening is provided to access container equipment from the walkway. For natural exhaust, ventilation is provided with rectangular opening at port and starboard side of the hold. At forward and aft, few circular ducts were provided to remove heated air from hold. Heat source is introduced in container equipment area, and the heat source is 10.5 kW.

Fig. 7 Airflow rate in %

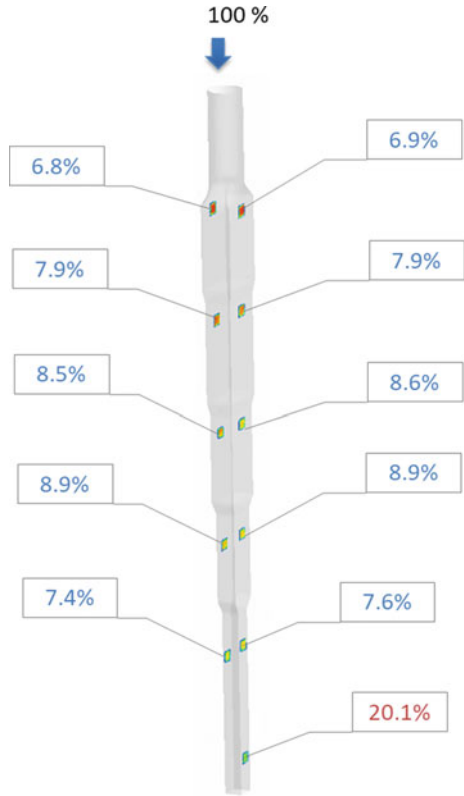
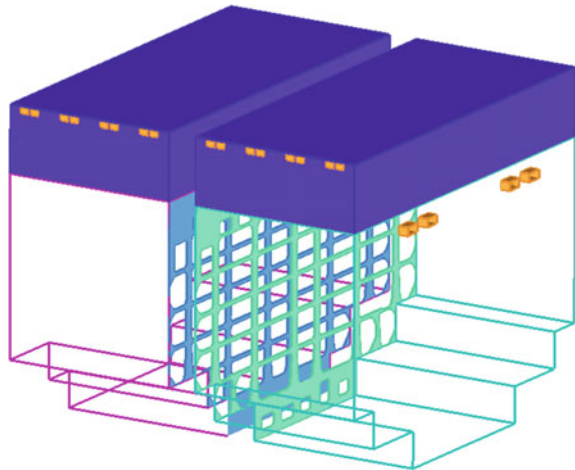
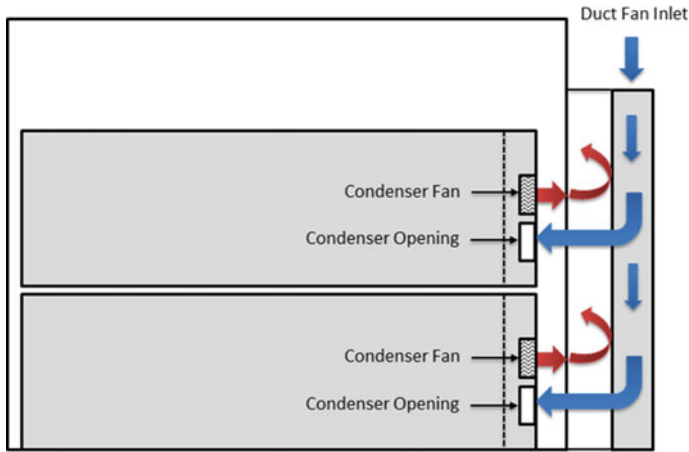


Fig. 8 Container hold view





**Fig. 9** Flow schematic inside the hold

Refer to Fig. 9 for the schematic flow of air circulation in the container. Heat source was introduced at the condenser fan. Therefore, there is an inlet is introduced by defining as an opening.

### 4.1 Analysis of Hold Simulations

Due to the complexity of the domain and having 15 million of elements, simulation has completed within a day. Even for small mismatch in the grid and condenser director, heat can go up in that area. Based on the simulation, temperature at each condenser was noted, refer to Fig. 10, and it shows the hot spot in the container hold of one side. Most of the cases, top layer containers were identified. In many cases, we did some changes in the structure and at the grid to overcome the hot spot. In some cases, there was no possibility to change a structure because of strength members.

### 4.2 Observations and Suggestions

For the simulation purpose, heat source was taken as 10.5 kW, which is worst condition. This heat source at the initial stage and after few hours of cooling, heat energy comes down. Though one container is shown as hot spot, this can be used to carry cargo because the heat energy can be considered as 8.5 kW for running vessel. Grid position facing the heat source is important because the removal ratio comes down which in turn increases the temperature at the container. Please refer to Fig. 11 where, in top layer, two containers more than the allowable limit but this can be used because

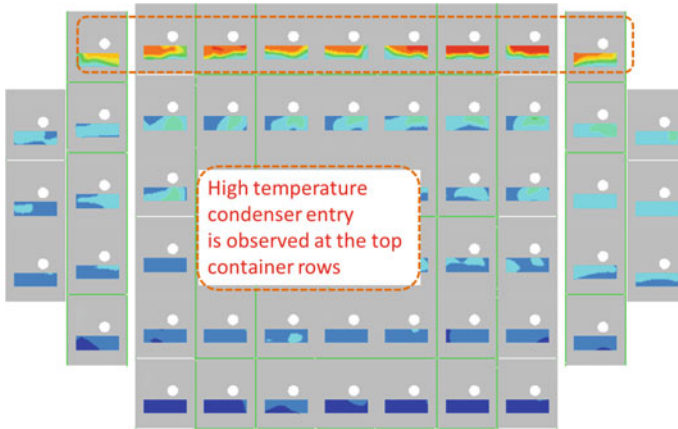


**Fig. 10** Hot spot at one side of hold

T-avg	C-01	C-02	C-03	C-04	C-05	C-06	C-07	C-08	C-09	C-10	C-11
R-01		41.8	38.5	44.8	40.8	48.4	41.9	47.2	39	44.3	
R-02	39.9	41	39.4	39.3	38.1	39.6	38	40.7	39.1	40.1	39.3
R-03	39.3	40.4	39.8	40.2	39.3	39.1	40	40.3	39.9	40.1	39.7
R-04	37.5	39.8	40	41.3	40.5	38.9	41.1	41.7	39.5	39.4	37.5
R-05		49	38.4	40.9	39.6	38.8	40.4	40.2	38.2	50.4	
R-06				39.1	39.6	38.7	39.6	38.7			

**Fig. 11** Identified hot spot

during the running condition, heat source comes down. Whereas, at the right corner down, one container is shown in red colour because of higher temperature. This container is not recommended because even the heat source is reduced during the voyage, there can be a possibility that temperature can be more than the allowable.

## 5 Conclusions

Initial duct was designed based on existing practice, and it has been identified during CFD simulation that manual way of calculation is not sufficient to get proper airflow in practical condition. From the existing 372 containers space, it has been improved to accommodate 457 high cube reefer containers by improving ventilation and duct optimization. From the CFD simulation to improve the flow rate, grid guiding plates were introduced to improve the performance of the duct. It has been extended to analyse the complete hold, and hot spots were identified (temperature more than 45 °C) and corrected to improve the ventilation of the hold. This has been repeated for all holds. Doing CFD analysis for duct and complete hold, increased containers get sufficient ventilation. This has been evaluated by doing CFD analysis, and authors advised all HVAC design companies to use the CFD analysis to improve the chilled cargo carrying system.

## References

1. Kohli P (2000) E\_book-refrigerated ships
2. Snowdon AL (2008) Carriage of bananas in refrigerated ships and containers: pre-shipment and shipboard factors influencing cargo out-turn condition. In: IV international symposium on banana: international conference on banana and plantain in Africa: harnessing international partnerships to increase research impact
3. Jedermann R, Geyer M, Praeger U, Lang W (2013) Sea transport of bananas in containers—parameter identification for a temperature model. *J Food Eng* 115(3):330–338
4. Rodriguez-Bermeji J, Barreriro P, Robla JI, Ruiz-Garcia L (2007) Thermal study of a transport container. *J Food Eng* 80(2):517–527
5. Lee U, Kim D, Lee D, Choi K (2007) Analysis of thermal behaviour in a cargo hold of LILW transport ship. In: Transaction of the Korean nuclear society spring meeting, Jeju, Korea
6. Zou Q (2002) A CFD modelling system for airflow and heat transfer in ventilated packing systems during forced-air cooling of fresh produce. Thesis, Massey University
7. GL Rule. 19 guidelines for the carriage of refrigerated containers on board ships. Edition 2003
8. DNV GL AS Rule. 6 additional class notations—4 cargo operations. Edition 2005

# Technological Trends for Ocean Research Vessels



Nitin Agarwala

**Abstract** Research vessels undertake detailed analysis and studies of the oceanic arena for myriad roles and in diverse oceanic regions. Some of these roles can be combined into a single vessel, while others may require a dedicated vessel. These vessels are majorly customized during design and construction to suit their operational needs and to face the toughest environmental conditions at sea. The early research vessels were fairly basic and simplistic compared to the state-of-the-art research vessels we see today. The present paper focuses on the design characteristics and the technological trends that would bear pioneering hallmarks in the future research vessels.

**Keywords** Technological trends · Research vessels · Deep sea

## 1 Introduction

Research vessels which fall in the category of *Special Purpose Ship* fulfill an important task of researching the various facets of the oceanic arena. The structural composition of such ships is majorly customized to face the toughest environmental conditions at sea and to suit their operational needs. The role of a research vessel is to measure and collect data about the ocean and its environment in varied scientific aspects (physical, chemical, biological, geological, geophysical, meteorological, ecological, etc.) for scientific studies toward exploration and exploitation, conservation and control of the ocean resources and environment. A research vessel thus has a very wide scientific role to play and accordingly needs to be equipped with a whole range of equipment.

The earliest known utilization of a research vessel predates back to the mid-1700s when James Cook was commissioned to study the planetary movements from the Pacific Ocean. The vessel employed was not officially recognized as a research ship,

---

N. Agarwala (✉)

Directorate of Naval Design (Surface Ship Group), New Delhi 110048, India  
e-mail: [nitindu@yahoo.com](mailto:nitindu@yahoo.com)

© Springer Nature Singapore Pte Ltd. 2019

K. Murali et al. (eds.), *Proceedings of the Fourth International Conference in Ocean Engineering (ICOE2018)*, Lecture Notes in Civil Engineering 22,  
[https://doi.org/10.1007/978-981-13-3119-0\\_25](https://doi.org/10.1007/978-981-13-3119-0_25)

435

but the nature and the characteristics of the work demarcated it to be as one of the pioneering vessels to be applied in the field of researching the surface below the water.

The design of a research vessel is one of the most complex subsets of ship design. This is primarily because, a research vessel needs to undertake a large variety of oceanographic missions, viz. physical, biological, and chemical oceanography; marine geology and geophysics; ocean engineering; and atmospheric science, with each discipline having its own unique set of mission requirement which in turn are cross-linked to disciplines of geochemistry, biochemistry, geophysics, and biophysics. Accordingly, the design of these research vessels varies significantly with the changing research activity the vessel may undertake. Since a research vessel may be called upon to perform work for a number of different disciplines during the same research cruise, these vessels need to be able to perform in all areas of the ocean, including the polar seas. With scientific objectives and the available equipment required to be changed many times during the lifetime of a ship, flexibility to meet these changes becomes a key requirement for these vessels. The present paper aims to discuss the characteristics that influence the design of a research vessel while bringing out the technological trends that are likely to bear pioneering hallmarks in such vessels of the future.

## 2 Design Characteristics

A research vessel is a working platform for the scientists to carry out research work at sea and for the equipment used in that research. The amount of time that can be spent in this scientific work is a basic measure of the efficiency of the vessel. An otherwise good research vessel will be inefficient if the work is interrupted frequently due to excessive roll motion which causes the scientists to be seasick or if computer failure occurs due to electric disturbances. Hence, vessel characteristics and essential design considerations that place a definite limitation on the choice of the hull form, machinery and equipment, play an important part in determining the size of a research vessel, and are critical for the design of such ships are discussed in the subsequent paragraphs.

### 2.1 Characteristics

Some typical characteristics for these research vessels are [1, 2]:

- (a) Have to be as general as possible to allow multidisciplinary studies and research.
- (b) Though size is determined by various requirements, the LOA should not exceed 100 m.
- (c) Cruising speed of 15 knots should be sustainable at sea state 4 (1.25–2.5 m).

- (d) Seakeeping should be able to permit research work in the following speeds and sea states:
  - (i) 15 knots cruising through sea state 4 (1.25–2.5 m),
  - (ii) 13 knots cruising through sea state 5 (2.5–4 m),
  - (iii) 8 knots cruising through sea state 6 (4–6 m),
  - (iv) 6 knots cruising through sea state 7 (6–9 m).
- (e) Laboratory spaces and arrangements should be highly flexible to accommodate large, heavy, and portable equipment.
- (f) Suite of modern cranes should reach all working deck areas, be able to offload heavy items (vehicles, equipment, etc.), and be able to work close to the water surface.
- (g) Oceanographic winches should provide a wire monitoring system with inputs to laboratory panels allowing local and remote data and operational controls.

## 2.2 *Minimum Requirement*

The research ship must embody the following as a minimum requirement [1]:

- (a) A satisfactory working platform at minimum sea state 5 and preferably at sea state 6.
- (b) High degrees of maneuverability (easy movement) and directional stability (maintain the desired heading).
- (c) Ability to maintain position during heavy weather in the neighborhood of the observation area.
- (d) Provide stability for sensitive instrumentation in various sea states.
- (e) Cost of fuel to be of secondary consideration, when compared with the ability to continue the work at hand.
- (f) A deep draft and a well-balanced above water profile for safe handling of instruments and nets in and out of the water.
- (g) Higher reliability than for normal ships as they sail alone and to the least travelled reaches of the ocean for long periods.
- (h) Adequate range (usually well over 6000 miles) at reasonable speeds to reach the remotest areas of the oceans and be able to stay there a sufficient time to perform her assigned task.
- (j) Quietness and effective noise control to ensure accurate and reliable readings.
- (k) Ample space and facilities for science.
- (l) A high degree of habitability and versatility.
- (m) Trawling capabilities.
- (n) Over-the-side sampling.
- (p) State-of-the-art computer systems.
- (q) Ability to accommodate future technological advancements in assessment techniques.



### **2.3 *Specific Requirements***

To perform these observation activities accurately and efficiently, these ships are required to satisfy the following elements different from the general ships.

- (a) Availability of auxiliary facilities such as a winch and crane for lifting and putting into the sea of various observation devices.
- (b) A sufficiently wide work deck.
- (c) Work deck height to take into consideration the requirement of lifting and putting into the sea of various observation devices.
- (d) The winch and associated system to have a heave compensation capability against motion generated by lifting to ensure minimum swing of the vessel.
- (e) Laboratory spaces and arrangements should be highly flexible to accommodate large, heavy, and portable equipment.
- (f) A system for efficiently processing the obtained large amounts of data so obtained.
- (g) To maintain the performance of acoustic equipment, noise generated by the propeller, and the vessel during sailing to be a minimum. Bubbles generated by the ship are not to enter into the position of the transmitter/receiver mounted on the bottom of the ship.
- (h) Improved fuel efficiency in traveling to the test sea area.
- (j) Continuous efficient low-speed sailing for observation work.

### **2.4 *Other Design Attributes***

A number of other scientific and operational trends that drive oceanographic research vessel design includes:

- (a) Larger, multidisciplinary science parties to collect interdisciplinary and/or complementary data.
- (b) Longer cruise durations over larger areas of the ocean.
- (c) Round the clock operations while in the test area.
- (d) Specialized hull-mounted swath bathymetry and sonar systems.
- (e) Larger and heavier portable science equipment.
- (f) Deployment, recovery, and maintenance of specialized science equipment.
- (g) More specialists (in addition to marine technicians) to service complex equipment.
- (h) Need for operational safety.

## 2.5 Equipment

Research vessels undertake a plethora of scientific measurements and sampling for which a host of equipment needs to be provided. This equipment that makes the heart of the research vessel is:

- (a) **Scientific equipment** that is dictated by the science they are researching. These scientific equipment include Doppler Current Meter and Profiler, Complete Meteorology station (includes sensors for air temperature, humidity, temperature, and water temperature), Multi-frequency Biological Sounder, bathymetry devices (side-scan sonars and echosounders), Net Sonar, and hull hydrophones.
- (b) **Sampling equipment** is used to collect samples at different depths to determine the various parameters of the water (salinity, oxygen content, temperature, turbidity, etc.) through analysis and quantity of suspended matter (nutrient, phytoplankton, and zooplankton). The sampling equipment onboard depends on the type of sampling that needs to be undertaken and is different for physical/chemical sampling (Carousel, Acoustic Doppler Current Profiler (ADCP), Chirp Sub-bottom Profiler, CTD, spectrophotometers), biological sampling (bathyphotometer, Chlorophyll-a Fluorometer, Meter Nets, Neuston, Phytoplankton Net, Tucker Trawl Net Remotely Operated Vehicles), and geological sampling (Shipek Grab, Gravity Core, Rock Dredges, Fisher Sediment Scoop). Some general use sampling equipment includes Zeiss stereo dissecting microscope, compound microscope with epifluorescence, oceanographic rosette, Niskin bottle, Van Veen dredger, Secchi disk, oceanographic buoys, and data management system to control the oceanographic winches and the fishing winch control information [3].
- (c) **Handling equipment** is required for safe handling of increasingly large and complex platforms and instruments over-the-side in high sea states (up to sea state 6). General-purpose research vessels require a permanently installed suite of winches (direct pull and traction) with active heave compensation. This handling equipment is preferably run on an electric system rather than hydraulic to ensure minimum acoustic signature and ease of maintenance. This equipment consists of a variety of winch equipment such as trawl winches, net drums, oceanographic winches, and sonar net cable winches. Other handling equipment used is collapsible davits, cranes, A-frames, launching and retrieval system (LARS).

## 3 Design Essentials

The function of a research vessel is so varied that there are a host of parameters that need to be accounted for as design essentials before one can think of sizing a vessel. These design essentials are discussed herein. As ship design is a calculated

compromise, one would realize that meeting all these design essentials may not be possible, thus forcing the designer to undertake conflict resolution of requirements.

### ***3.1 Hull Shape and Appendages***

The research vessel should have a fine and slender form with a waterplane entrance half-angle not more than  $18^\circ$ , a prismatic coefficient of 0.62–0.65 to achieve speed, fuel economy during the exploitation, and low hydrodynamic noise level. The bow is to have a flare to improve seakeeping and habitability and a transom stern to ensure greater deck area aft. A retractable keel which hangs a gondola may be used for transducers for acoustic detection and control of other equipment.

### ***3.2 Main Dimensions***

A large ship will perform better than a small one and be quieter; its transit voyages will be faster, have better fuel economy, and a relatively smaller crew as compared to the scientific payload. However, the main dimensions of a research vessel are determined by the space required by laboratories, operational deck areas, accommodation, storage spaces, etc., with the upper limits being usually dictated by the available funds.

### ***3.3 Internal Spaces***

Accommodation trends onboard research vessels include more single berthing for the crew, specialized technicians, and scientists; berthing with natural light to promote natural sleep patterns; and galley and relaxation spaces that promote a healthy lifestyle at sea. The quality and design of crew living spaces are paramount for employee retention and morale. The laboratory facilities, computers and the offices and accommodation for the scientists should be placed in the quietest areas, in terms of engine and propeller noise and in terms of ship motions.

### ***3.4 Working Deck Space***

The working deck must be open, clear, with tie-downs for equipment and containers, capable of handling increasingly heavy gear, including moorings, fleets of autonomous vehicles, and ROV equipment and winches. The working decks need

to be designed with flexibility in mind. However, research vessels often end up with insufficient open working deck space.

### ***3.5 Freeboard***

It should be as low as possible to allow for optimal handling of over-the-side equipment while keeping decks dry. Ideally, research ships would be designed with low freeboard to facilitate deployment and recovery of over-the-side equipment, but in a rough sea this leads to these decks becoming submerged regularly, limiting working conditions.

### ***3.6 Ice Class***

To be able to work in ice-covered areas, research vessels need to be designed as per “ice class” which includes a strengthened hull, additional watertight bulkheads, two rudder pintles with strengthened propeller tips and heating arrangements for fuel tanks, ballast tanks, and other tanks vital to the ship’s operation.

### ***3.7 Acoustic Quieting***

To ensure that the results of the investigations at sea are reliable, the ship-emitted sound should be a minimum. The research vessel thus must be designed to minimize air, structural, and radiated noise to the water. It must comply with the requirements of ship-radiated noise recommendations set forth in the International Council for the Exploration of the Sea (ICES) 209 specifications [4].

### ***3.8 Dynamic Positioning System (DPS)***

To ensure safe handling of over-the-side equipment, accurate navigation of ROVs, deployment, and retrieval of buoys, deep-sea crawler, etc., a dynamic positioning system is required. With a DPS, even at sea state 5 (wave height 4–5 m), the ship’s position can be fixed to within a variation of less than 50 m.

### 3.9 *Laboratories*

To ensure research in multiple sciences, plentiful laboratory spaces often subdivided into ultraclean, clean, normal, and temperature-controlled areas are required. These laboratories should have ease of and logical access into and between laboratory spaces for personnel and sample movements. Specialist laboratory needs are often provided through the use of containerized laboratories. A requirement for a substantial scientific stores area, including areas for frozen and refrigerated sample storage, also exists. The cold room in these ships is designed to maintain up to  $-20\text{ }^{\circ}\text{C}$  temperature to store the samples.

### 3.10 *Scientific Personnel*

The size of the scientific personnel influences the size of a research vessel and should, therefore, be kept to a minimum. A large scientific team may create a human and organizational problem of its own. The upper limit of scientific accommodation in a 70 m vessel may be said to be limited to 16 personnel.

### 3.11 *Efficiency*

It is a vital consideration in the design of a research vessel. There are a variety of efficiencies that are seen.

- (a) **Propulsion efficiency.** High propulsion efficiency leads to a lower operating cost and hence a “greener” ship. Achieving this efficiency requires an addition of equipment to reduce emissions, which requires space and adds weight thus increasing ship construction costs. Further, increasing fuel cost requires improving propulsion plant efficiency and reducing ship hull resistance.
- (b) **Performance efficiency.** A research vessel performance is evaluated based on the quantity and quality of the data she produces. Thus, the performance efficiency is affected by the time taken to deploy equipment (to full depth and recover it), change over (from one piece of equipment to another), and breakdown (of winching and OTS handling equipment).

### 3.12 *Propulsion*

The propulsion system of a research vessel needs to provide adequate cruising speed, feasibility to tow large loads and to keep station using dynamic positioning. These requirements are fulfilled by a diesel-electric installation, main propellers of con-

trollable pitch type, and 2–4 bow and stern thrusters, preferably of the azimuth type. From the *acoustic point* of view, a diesel-electric propulsion system allows for silent navigation.

### **3.13 *Electric Power***

Critical equipment such as computers and data acquisition systems requires very clean electric power (free of voltage and frequency disturbances). This requires data transmission lines to be kept isolated from the ship's power lines and from machinery and well-designed electric ground connections.

### **3.14 *Speed***

The research vessels may use high speed only when proceeding from the base to the research station, maybe once in 3 weeks. For the remaining period when undertaking scientific cruise, the vessel may make 6–8 knots. Thus high speed is hardly called for in such vessels. The upper limit of the speed of an ocean research vessel can thus be taken as 12 knots.

### **3.15 *Seaworthiness***

This requires consideration of the following aspects

- (a) *Deck wetness*: Need for a bigger and longer ship, with a higher and flared forecastle and higher reserve buoyancy forward to have reduced deck wetness.
- (b) *Ship motion*: Need for a larger ship to sustain lesser sea motion.
- (c) *Seakeeping*: Good seakeeping needs to be achieved to allow the scientists onboard to work efficiently. This may be achieved by a high freeboard, especially forward, deep draught, large beam, low block coefficient, large bilge keels, roll damping tanks, roll and pitch damping fins, use of sails to name a few.
- (d) *Stability*: IMO does not lay stability criterion for ships greater than 90 m, while for smaller ships, such as fishing vessels, the criterion is a higher standard of stability.

### ***3.16 Navigation Systems***

In ocean exploration work, precise navigation is considered to be more important than in ordinary shipping. Surveys must not be contaminated with position errors. The navigation systems that may be used are terrestrial, astronomical, radio (Radar, Decca, Loran, and Omega), inertial and satellite navigation. Of these, satellite navigation will probably be the dominant navigation system in the future.

### ***3.17 Communication Equipment***

Radio communications of short, medium wave and intermediate broadcast band as well as modern satellite equipment used onboard ships are part of the global marine distress and safety system (GMDSS). These include VHF radiotelephone (156–162 MHz), radar, EPIRB, single-sideband radiotelephone (2–27.5 MHz), satellite radio, radiotelegraph, survival craft radio, onboard radio. Ships communicate with other ship stations or coast stations primarily for safety and secondarily for navigation and operational efficiency.

## **4 Technological Trends**

The computational power and capabilities we use today are doubling every year. In the 1950s, our cutting-edge data storage capability was 5 MB which stands at a terabyte today. The computing technology available presently is greater than the technology used to launch man into space in the 1960s. Similarly, remarkable progress in deep ocean science has been made in the past 40 years due to development in observational platforms and instruments whose capabilities have continued to improve over the years. Some of these platforms support human observers while others do not. Today, a variety of platforms are used for research such as research ships, stationary observation systems (moorings and bottom-supported platforms), mobile observation systems (submersibles, ROVs, AUVs, fixed observatories, drifters, gliders), and satellites with remote sensing capabilities. If ocean exploration program were to include archeology then the diversity of platforms is even larger. Marine technology has evolved exponentially with artificial intelligence, virtual reality, and 3D printing being adapted for use in the marine environment. Fiber optics and Internet2, combined with telepresence, high-definition cameras, remotely operated underwater vehicles (ROVs), and state-of-the-art networking, allow experts to plumb the ocean depths and instantly share their findings with others who are on dry land. In the 1970s, deep-sea explorers got around in slow-moving mini-submarines armed with flashlights called “underwater jeeps.” These submarines provided a mere three hours

a day for actual exploration. Today, ROVs and AUVs allow continuous exploration for over 6 months at a length.

Development in the field of instrumentation, electronics, computation, sensors, digital processing, and communication has helped in remote monitoring of various aspects of the ocean environment. The data so collected through these remote processes outweighs the data that can possibly be collected by research ships. Though many other technologies have been developed, these have not been able to withstand the harsh marine environment. However, these budding technologies are certain to affect future research vessels as they are developed further.

Even with all these advancements, it is unlikely that mobile observation systems, autonomous mobile platforms, or fixed observatories will have sufficient sensing capabilities to replace traditional research vessels in the next 10–20 years. However, their inputs would act as drivers for future research of these new discoveries along with the requirement of training students of oceanography. Technological advancement for shipborne equipment is thus natural to continue with future research vessels required to support increasingly complex, multidisciplinary, multi-investigator research projects using autonomous technologies, ocean observing systems, remote sensing, and modeling. These vessels will be needed to investigate and explore all areas of the ocean, from tidal zones to deep trenches.

Analysis of the technological trends in the last 20 years reveals:

- (a) Increased trend in use of floats, gliders, remotely operated vehicles, autonomous underwater vehicles, and scientific seafloor cables.
- (b) Stable trend in the use of ships, drifters, moorings, and towed platforms. Of these, ships form an essential component of ocean research infrastructure with an increased range of their capabilities by the use of autonomous and unmanned assets.
- (c) Decline in trend in the use of human-occupied vehicles.
- (d) Increase in longevity, stability, data communications, adaptability, and access to harsh environments of sensors primarily due to innovations occurring outside the ocean science field.
- (e) Enabling technologies of 2009 such as the global positioning system (GPS), satellite communications and the Internet, remotely operated vehicles (ROVs), autonomous platforms, and sensors such as multibeam mapping systems and improved vessel-deployed chemical sensors have developed to a state of maturity.

The earliest technique for ocean research was bathymetry which was conducted by lowering a weighted-down rope or cable over-the-side of a ship. This technique was replaced in the 1920s by echo sounding. Improvements in transducer technology and timing accuracy allowed the introduction of precision depth sounders (PDRs) in the 1950s, with 30°–60° beam width allowing large-scale maps of the seabed. A multibeam echosounder system called Swath Array Sonar Systems of the 1960s was further modified by the use of frequency-modulated (FM) pulses in place of continuous wave (CW) pulses to allow improved range resolution and better data quality due to less signal fading.



Over the years, many areas of the ocean have been researched and hundreds of products have been developed. Today, the focus is primarily on widely different areas, such as more precise bottom detection algorithms, seabed classification, image processing, acoustical modeling of the backscattering process, and high-resolution methods for direction finding of plane waves. With hundreds of products available to serve oceanographic applications, major equipment arising from technological developments can best be organized in the following categories.

#### ***4.1 Sensors for Oceanographic Data Collection***

These include Acoustic Doppler Current Profiler (ADCP) which may be portable or hull mounted; Sondes used for profiling and monitoring water conditions to measure temperature, conductivity, salinity, dissolved oxygen, pH, turbidity, and depth; Conductivity, Temperature, and Depth (CTD) to measure conductivity, temperature, and depth; underway CTD measurements used while a vessel is underway; seafloor/object imaging for investigating shipwrecks, monitoring pollution, tracking whales and dolphins, and studying fish stock; multibeam and single beam echosounders for seafloor mapping; imaging sonars for monitoring infrastructure below the water line; forward-looking sonars for obstacle avoidance and inspection in AUVs and ROVs; sub-bottom profiling systems to identify and characterize layers of sediment or rock under the seafloor, satellites that can detect and observe different characteristics and features of the Earth's atmosphere, lands, and ocean to provide information such as temperature and color of the ocean thus allowing scientists to detect the presence of algal blooms, river plumes, map features in the water such as coral reefs [3].

#### ***4.2 Systems for Deploying Sensors***

These systems include bottom-mounted frames to deploy oceanographic instrumentation such as ADCPs, transponders, cameras, CTDs, and virtually any other type of compact oceanographic instrumentation package on the seafloor; moorings to deploy oceanographic sensors; profiling floats to collect data such as temperature, salinity profiles, currents and for biogeochemistry studies; electric drives winches with permanent magnet electric motor to provide a smooth drive/high torque property but with much reduced sound; cabled hydrophones to detect submarine volcanic eruptions; acoustic observatory in deep ocean to monitor ambient ocean noises and their effects on the marine environment; light detection and ranging (LIDAR) technology to measure elevation or depth in complex areas and rugged shorelines where surface vessels cannot operate efficiently or safely, autonomous vehicles such as remotely operated vehicles (ROVs), gliders, autonomous surface vehicles (ASVs), autonomous underwater vehicles (AUVs), human-occupied submersibles (HOV), towed camera and sonar sled, and towed sonar sled [3].

### **4.3 Navigation for Oceanographic Platform Tracking**

Underwater vehicles which house many oceanographic sensors need to understand where they have been, where they are going, and how to pinpoint an exact location of interest. The best-known methods to address this need are the Doppler-aided navigation, Doppler Velocity Logs (DVLs), and Inertial Navigation Systems (INSS).

### **4.4 Communication for Oceanographic Sensors**

To ensure that the sensors, platforms, and navigation systems can function efficiently and can speak to each other; interconnect, power and communication solutions are required. These include the use of highly robust and reliable standard and custom electrical, fiber optic, and/or hybrid electro-optic connectors. Interconnect solutions include wet-mate, splash-mate, and dry-mate connectors, differential pressure penetrators, cable assemblies, cable terminations, and custom-engineered encapsulation and molding. Further, for data transfer; cabled networks, integrating wireless nodes and modems working over a variety of frequency ranges may be used. To process, display, and archive data from the navigational and scientific sensors on research ships, Shipboard Computer System (SCS) is used.

### **4.5 Communication to Collaborate**

Technologies to collaborate and transmit data more quickly between scientists are changing the way that we explore. These technologies are increasing the pace, efficiency, and scope of ocean exploration, and the ones in use include Telepresence technology wherein an individual or group of individuals can participate in an event live even when they are not physically present for the event. Similarly, SeaNet communications system allows availability of the Internet to ships at sea.

## **5 Drivers for the Future**

In the last four decades of technological advancements, many developments have been achieved, while there are many more those need to be achieved. The focus is on undersea vehicles such as the advanced underwater vehicles (AUVs) and the remotely operated vehicles (ROVs) and their systems with numerous achievements to their credit such as the discovery of the *Titanic*, the *Bismark*, the *Yorktown* to name a few. The AUVs undertake survey with a variety of sensors and can provide higher resolution mapping than what is possible with conventional deep-tow technology.

They offer an estimated fivefold improvement in survey productivity over the ROV technology. With time, the AUVs have evolved to being self-contained robotic diesel-electric submarines capable of setting out on its own for up to 6 months at a time [5]. They set out from port like a submarine, carry out its mission, and then return by itself when the mission is complete. Some drivers for the future of ocean research technology are:

- (a) Research vessels require both surface support (support from ship for lowering and retrieval of equipment) and the shore-side support (support in harbor) to function efficiently which need to be developed for better coordination.
- (b) **Robots** have taken over underwater exploration, and their involvement will increase with time. These robots are controlled via a haptic system that permits the pilot to feel resistance as he presses against or grips objects, via a motorized pushback in the control system. Efforts to pair them with a modern off-the-shelf VR headset are in progress to provide stereoscopic 3D, head-tracked immersion that will create the sensation of being in the body of the robot deep underwater [6].
- (c) **Around View Monitor (AVM)** technology is being developed to help remotely operated vehicles search for natural resources, avoid obstacles, and navigate the ocean seafloor more easily. This deep-sea crawler robot can be used with greater precision and accuracy, avoiding obstacles and performing its tasks more efficiently. This technology will help to save time and collect more data about the floor of the oceans.
- (d) **High-resolution geophysical mapping**, used on ROVs, is being successfully exploited to define conductive copper-sulfide-bearing SMS mineralization to a depth of less than six meters below the seafloor, even within areas covered by a superficial veneer of sediment.
- (e) **High-resolution multibeam echosounder** surveys undertaken from 40 m above the seafloor by an ROV enables mapping of the seafloor at decimeter-scale resolution thus allowing mapping of SMS chimney structures. High-resolution side-scan sonar has also been used to successfully map chimney fields. This higher resolution mapping capability is critical for discovering inactive SMS systems.
- (f) Developments with *gravity measuring system* deployment on an AUV platform are an emergent technology with the potential capability to enable detection of SMS targets.
- (g) There is an increasing need to define the SMS orebody in 3D using geophysical techniques for which the use of desktop modeling is being pursued to reduce cost and time consumed by the existing procedures.
- (h) Use of 3D seismic technology will provide confidence in defining the 3D nature and extent of SMS mineralization zones to aid drilling programs thus reducing drilling costs and provide critical geological and geotechnical detail for future mine planning and mine extraction operations.
- (j) Undersea drone is an area of future development in deep-sea exploration.

- (k) New CTD development focuses on ultra-low-power-specialized electronic to eliminate fouling of electrodes during long-term deployments in shallow water and on dynamic calibration.
- (l) Smaller gravimeters are being developed that could be used on both ROVs and AUVs. These accurate compact systems are still expensive and complex.
- (m) Good short-range communications for AUVs is available. Use of optic fibers in ROV tethers has helped increase the available bandwidth providing enhanced control capability of the systems.
- (n) **Undersea vehicle system.** Various subsystem technologies for a highly effective undersea vehicle system are required. These include developmental effort of fuel cells in the range of 200–400 kWh/kg, acoustic systems navigation over small to medium distances (less than 3.5 km, or 2 nm) and accuracies in the range of centimeters, high-precision positioning over longer times and distances, improvement in guidance and control systems of ROVs and AUVs, development of new lightweight material for deep-ocean, pressure-resistant housings and buoyancy structures, advances in wideband acoustic communications with parallel advances in computing power, AUV onboard data logging and manipulation, in situ analyses and systems management using low power, high-volume data storage, and innovative manipulation techniques; launch and recovery needs constant evolving, with emphasis on reducing size so that smaller, lower cost surface support vessels can be used, adapting industrial robot manipulators for greater dexterity during working in AUVs, improvement in acoustic, optical, chemical, magnetic, and other sensors to improve abilities of undersea vehicles and to present human operators with visual information [6, 5].
- (p) There is a need for inertial navigation systems that can function when wet with seawater while being small in size and having integrated sensors and control system.
- (q) There is a need for developing a nodal station (for recording and collecting data from surrounding sensors), docking station (for battery charging, data transfer and communication).
- (r) Areas of swath sonars, obstacle avoidance, path planning, laser line scanner—all of low power—need development. Similarly, areas of increased data storage and power to extend mission endurance also need development.
- (s) Basic technologies for use in the deep sea such as pressure-free, cost-efficient, and modular AUVs are being progressed. Additional information such as from intelligent multisensors and ultrasound imaging sensors will improve the inspection and exploration capabilities of the AUVs.
- (t) **Hybrid vehicles.** Scientists and engineers are testing innovative hybrid vehicles to revisit the astounding depths of the ocean. These vehicles can function as an AUV and an ROV both allowing the advantages of both these types of vehicles to be fruitfully utilized in the same expedition [6].

## 6 Drivers Affecting Ship Design

The drivers of the future discussed in the preceding section are those that are aimed at the technology associated with the ocean research. The drivers that are likely to have an impact on the design of the research vessel itself include:

- (a) **Unique platforms.** Learning from experimental platforms such as the Floating Instrument Platform (FLIP) [7] and the fully autonomous manned ship Mayflower Autonomous Research Ship (MARS) when implemented in research vessels would have an impact on the design of a research vessel.
- (b) **Emission regulations.** With stricter emission regulations being implemented toward emission reduction measures and implementing control measures such as the carbon tax, the traditional propulsion plants are likely to see a drastic change thus forcing a space and weight definition for these plants onboard [8].
- (c) **Recovery mechanism.** Gliders, AUVs, UAVs, and ROVs require specific deployment and recovery procedures and equipment. Research vessels have high freeboard (due to damage stability and personal safety) that makes recovery more difficult. Hence, over-the-side (OTS) lifting equipment will be necessary to protect equipment and personnel while undertaking deployment and recovery as and when required. Such designs of handling equipment optimized for OTS would have a serious impact on the design and layout of a research vessel.
- (d) **Hydrodynamic design considerations.** Bubble sweep down which is an important consideration for placement of sensors and affects the hull form design has been a persistent problem on research vessels which is aggravated by the ship motion. To date, no definite solution is available to address this problem; however, studies to follow would definitely have an impact on the design of future research vessels.
- (e) **Use of a small waterplane area twin hull (SWATH) vessel.** To be able to achieve good seakeeping, good stability, wide laboratory, work deck area, ability to set the research equipment and crew comfort mix of catamarans (large deck area) and semi-submersibles (controlled motion and reduced wave making), SWATH have been tried out. Future research vessels could be SWATH; however, presently cost considerations inhibit such a shift.
- (f) **Green ships.** Environmental considerations are forcing ship design to focus on green ships. The designer hence needs to focus on issues such as reduction of air emissions, ship waste disposal, bilge water treatment, black wastewater treatment, gray wastewater treatment, ballast water treatment, innovative anti-fouling systems, optimized hull and rudder design, use of LNG as fuel, reducing the underwater radiated noise, and waste heat recovery systems. Incorporating these features is definitely going to affect the research ship design drastically [8].
- (g) **Acoustic quieting.** Modern sensors on research ship operate best at minimized acoustic interference levels. Hence, the design of these ships is to minimize air, structural, and radiated noise to the water for which it must comply with the requirements of Silent Platform ICES 209 [7]. Achieving such a compli-

ance shall affect design procedures presently being followed. Some necessary changes would involve; selection of low noise air and structural machinery, selection of appropriate mounting, selection of appropriate flexible connections, selection of auxiliary machinery, appropriate design of hydrodynamic form, wake-adapted propeller design, masking radiated noise from the hull by using bubbles generated by compressed air, controlling ambient internal noise around cabins by providing dampening/panes of different grades and adopting design features to reduce hull-induced flow noise to avoid interference with scientific equipment.

- (h) **Automation.** Use of automation onboard such as remote diagnosis of onboard equipment, integral management of vibration and noise, integration of bridge equipment and communications with scientific systems to allow working on the ship from land laboratories in real time would bring about changes in the layout.
- (j) **Innovation in handling equipment.** Winches and gantry cranes are critical to research ships. They need to be made reliable and easier to handle with flexibility to handle changing roles of the research vessel. Though the present trend is to arrange the winches so as to allow all wires to be permanently rigged up and quickly connected, while a system of sheaves allows any wire to be led over any of the main OTS handling equipment; however, with innovations in handling equipment this may change bringing about requirement in design changes.
- (k) **Scientific equipment.** Increased use of heavier and more sophisticated tools, landers, observatories, moorings, buoys, and drilling equipment which require vessels with large, open working decks and heavy-duty cranes, A-frames and winches would require design philosophies to be reworked.
- (l) **Innovations in sampling devices.** New coring devices such as a hydraulic piston corer used within the drill string have increased sample recovery and reduced core disturbance. Drilling can be sited very accurately using DP of the ship drilling platform, and very deep samples can be obtained by means of re-entering the boreholes after replacing worn bits. Boreholes can also be re-entered for insertion of seismic and other sensors. All these innovations are forcing the designer to reshape the designing methodology of research vessels.
- (m) **Pollution.** MARPOL, 2007 amendment to Annex 1 requires ships with fuel capacity of more than 600 m<sup>3</sup> to enclose the fuel tanks within a double hull. This regulation is likely to have a significant effect on the design, cost, and operation of future research vessels since several research vessels have fuel tanks with a greater capacity than 600 m<sup>3</sup> [8].

## 7 Conclusion

One can conclude based on the discussions in the paper that the future research vessels will be required to support complex, multidisciplinary, and multi-investigator

research. The design of these future vessels is naturally expected to be more challenging. These multidisciplinary requirements would have a direct bearing on design aspects such as power plant, propulsion, working deck area and layout, handling equipment. The design of such research vessels needs to cater for the presently available technology while being future ready for the technology to follow. Because a research ship is based on conflicting design requirements which must strike a balance of the best understanding and projection of the directions science may take, decisions on the design may be out of date or found to be impractical before the vessel is launched. In a class design, whose construction is to be repeated over a period of years, this obsolescence is unfortunate.

**Acknowledgements** This paper is simply a brief overview of a substantial field. The author appreciates the support of Adm A. K. Chatterjee, Research Fellowship through National Maritime Foundation, New Delhi, India, for undertaking this study [9].

## References

1. Rosenblatt L (1960) The design of modern oceanographic research ships. 26–28 May 1960, SNAME
2. Marcelli M, Pannocchi A, Piermattei V, Mainardi U (2012) New technological developments for oceanographic observations. In: oceanography; IntechOpen: Rijeka, Croatia [www.intechopen.com](http://www.intechopen.com)
3. Moore C, Barnard A, Fietzek P, Lewis MR, Sosik HM, White S, Zielinski O (2009) Optical tools for ocean monitoring and research. *Ocean Sci* 5:661–684. [www.ocean-sci.net/5/661/2009/](http://www.ocean-sci.net/5/661/2009/)
4. Basáñez N, Fernando J (2012) Project and construction of oceanographic and fisheries research vessels in Spain. *Ship Sci Technol* 6(11)
5. Meyer D (2016) Glider technology for ocean observations: a review. *Ocean Sci Discuss*. <https://doi.org/10.5194/os-2016-40>
6. Brandt A, Gutt J, Hildebrandt M, Pawlowski J, Schwendner J, Soltwedel T, Thomsen L (2016) Cutting the umbilical: new technological perspectives in benthic deep-sea research. *J Mar Sci Eng* 4:36. <https://doi.org/10.3390/jmse4020036>
7. Lisnyk JA (2014) Research vessel floating instrument platform II (R/V FLIP II). Student Ship Competition Design Report, 14 June, 2014, University of Michigan Naval Architecture and Marine Engineering Department
8. Catrijsse A, Rogers R, van Vliet H, Huyskens P (2013) Eco-design of research vessels. *J Ocean Technol* 8(2)
9. Agarwala, N (2019) Deep seabed mining in the Indian Ocean: economic and strategic dimensions. Book under publication by National Maritime Foundation, New Delhi, India. Due March 2019

# Feature Extraction of Underwater Images by Combining Fuzzy C-Means Color Clustering and LBP Texture Analysis Algorithm with Empirical Mode Decomposition



M. Somasekar and S. Sakthivel Murugan

**Abstract** Submerged objects discovery has been broadly completed by utilizing an acoustic device like side-scan sonar (SSS) which captured the pictures of seabed silt and structures. Such pictures are known as SSS image and it is of low contrast due to pixels intensity exists wider in a restricted range of the histogram. Therefore, the items in this sort of pictures are not clear and distinct. This paper presents fuzzy c-means (FCM) with local binary pattern. (LBP) and empirical mode decomposition (EMD) combined for enhancement of the SSS images. In this, EMD is used for image enhancement and FCM utilized to segment the image in order to extract the feature of the SSS image and Local Binary Pattern (LBP) algorithm is used to find texture of the enhanced image. The EMD is a versatile algorithm helpful for breaking down nonlinear and non-stationary signals. Thereby, intrinsic mode functions (IMF) of the three shading channels (Red, Green, and Blue) is calculated independently. Then, all the three channels IMFs are combined with ideal weights. It induces that the pixels of enhanced SSS images are uniformly distributed in the histogram range and also improved the color contrast problem. Therefore, the proposed approach has better density upgrade and the ocean bed structure will be fortified concentrate and dregs easily.

**Keywords** Empirical mode decomposition · Contrast stretching  
Side-scan sonar image · Average gradient · FCM · LBP

---

M. Somasekar  
Department of Electronics and Communication Engineering, PERI Institute of Technology,  
Chennai, India  
e-mail: [somasekar109@gmail.com](mailto:somasekar109@gmail.com)

S. Sakthivel Murugan (✉)  
Department of Electronics and Communication Engineering, SSN College of Engineering,  
Chennai, India  
e-mail: [sakthivels@ssn.edu.in](mailto:sakthivels@ssn.edu.in)

© Springer Nature Singapore Pte Ltd. 2019  
K. Murali et al. (eds.), *Proceedings of the Fourth International Conference in Ocean Engineering (ICOE2018)*, Lecture Notes in Civil Engineering 22,  
[https://doi.org/10.1007/978-981-13-3119-0\\_26](https://doi.org/10.1007/978-981-13-3119-0_26)



## 1 Introduction

The submerged prehistoric objects identification and investigation are the fundamental task of maritime archaeologist. It is highly essential to acquire the trace of ancient humankind. Nowadays, the autonomous underwater vehicles (AUVs) and remotely operated vehicles (ROVs) carry special devices which are involved and analysis the submerged objects in the seabed levels. There are many such devices are available, but sonar is widely used because of its varying depths across the ocean. Again, sonar has different types such as color sector sonar (CSS), searchlight sonar (SLS), and side-scan sonar (SSS). Among them, SSS [1] provides better image resembles of submerged objects even in zero visibility range. This can be achieved by using echo principle in which objects are detected by sending sound waves and listening for echoes. It has been shown in the study track and each side of the track, a solitary line portion responds to the echoes and counted one for every transmission—reception cycle from the ocean bottom. The inclination range (time) or horizontal range can be clearly identified by proper reception of the refracted waves. Likewise, a time-varying gain adjusts for transmission losses caused by circular spreading and immersion of sound waves in water. Nevertheless, in the absence of remedies made, the images taken subsequently lead to adverse effect like falsification and artifacts of various kinds. The reasons are: (1) different types of external impedances brought by other acoustic gadgets that work in the meantime are added to the procedure (2) The review track is rarely straight and the attitude of the tow fish changes with time (3) the beam arrangements of the sonar are not uniform in the angular sector in the area of eagerness.

Moreover, back projections may be added crosstalk between the two sides or may get echoes reflected from the ocean surface. Despite free from these impediments, at present, the images may be hard to interpret because they lack contrast. Such images are normally referring as SSS images. Thus, image enhancement approaches will improve the visual quality but SSS image enhancement is quite different because captured image object itself damage and blurring. Therefore, algorithms need to be developed and applied to enhance the SSS images quality. Garcia et al. presented a significant literature addressing the lightning problems in underwater images. Conventional histogram equalization [2] and contrast stretching [3] are another most widely used enhancement methods. According to this, the images are decomposed into band-pass images and histogram equalization technique is used for brightness and contrast improvement [4–7]. In Hariharan et al. [8], EMD has been used for image fusion and enhancement, and images from different imaging modalities are decomposed into their IMFs and fusion is done at the decomposition level. IMFs are fused with various weights in order to obtain the reconstructed image. Not only it has been adopted, this approach for underwater image is described in Tas et al. [9]. Iqbal et al. [3] discusses an integrated color model for submerged image enhancement. Based on this model, different types of filters such as homomorphic filtering, anisotropic filtering, and wavelet deionizing are used for underwater image preprocessing [10] and [11]. All the above methods can be applicable for image which has

low contrast and almost have same frequencies. The empirical mode decomposition (EMD) is an adaptive algorithm used for image enhancement [12] in underwater images. In [13, 14], EMD is applied to hyper-spectral image data which is used to rise accuracy in organization of hyper-spectral images. Compared to other decomposition techniques like Fourier and wavelets transform, EMD has vital advantage. Alternatively, EMD does not have basic functions and decomposes a signal based on its intrinsic properties. Depending on signal characteristics at different signal locations, IMFs obtained by EMD can contain both high- and low-frequency detail. In [15] describes an effective algorithm to remove noise in sonar images utilizing EMD. Taşyapı Çelebi and Ertürk [16] describes EMD for better target detection in sonar images. Sowmyashree et al. [17] presents a comparative study of the various image enhancement techniques used for enhancing underwater image such as integrated color model, histogram equalization and an image-based technique. The proposed system uses empirical mode decomposition (EMD)-based image enhancement technique for improving the quality of sonar images. The organization of chapters as follows: Sect. 2 describes process involved in EMD, Sect. 3 presents enhancement made in the sonar images using EMD, Sect. 4 discusses the comparison of results obtained using different techniques and Sect. 5 concludes this paper.

## 2 Empirical Mode Decomposition

It is a nonlinear and non-stationary time–frequency data analysis which makes it a highly efficient method for real-time applications. The procedure involved in EMD is easy to comprehend. It does not have any basic function and decomposes the image into various frequency components. The process is very simple and performs shift operations on the original data series until the final series are stationary, and thereby decompose the original signal into several intrinsic mode functions (IMFs) and a residue. The main step is to apply sifting process to the original image for obtaining the IMFs. This decomposition process starts from the original image  $Input(i, j)$ . The input signal is the image itself and assigns as  $Im(i, j) = Input(i, j)$ . Where  $i$  and  $j$  are the dimensions of the input image.

1. Identify all the points of local maxima and local minima of the given Input image  $Im(i, j)$ .
2. Construct the upper, lower envelope ( $env_{Max}(i, j)$ ,  $env_{Min}(i, j)$ ) with Cubic spline interpolating local maxima and local minima, respectively.
3. Compute the  $Env\_mean(i, j)$  based on the upper and the lower envelopes as in Eq. (1)

$$Env\_mean(i, j) = (env_{Max}(i, j) + env_{Min}(i, j))/2 \quad (1)$$

4. The mean of the two envelopes is subtracted from the input to get their difference as given

$$H(i, j) = \text{Im}(i, j) - \text{Env\_mean}(i, j) \quad (2)$$

5. The stopping criterion defined in Eq. (4) should be used for stopping the iterative procedure for finding IMF.

$$\text{Eps} = \frac{\sum_{i=1}^H \sum_{j=1}^W |\text{Env\_mean}(i, j)|}{H*W} \quad (3)$$

6. If  $\text{Eps} < \tau$ , ( $0 < \tau < 1$ ) the shifting process is stopped and  $\text{IMF} = H(i, j)$ . If the current IMF is obtained successfully, the residue signal  $R(i, j)$  is computed as in Eq. (4)

$$R(i, j) = \text{Input}(i, j) - \text{IMF} \quad (4)$$

It is completed when the residue does not contain any extrema points. In this manner, the original image is decomposed into n number of IMFs depending on the stopping criterion. The enhanced image is obtained by combining the IMFs of Red, Green, and Blue channels with various weights and the final residue.

### 3 Enhancement of Sonar Images Using EMD

Figure 1 shows the block diagram for EMD with optimal weight enhancement of acoustic images. The input SSS image is divided into three color channels: Red (R), Green (G), and Blue (B). The EMD algorithm is applied to three colors channels separately. Each channel image is then decomposed to several frequency components called intrinsic mode functions (IMFs). The enhanced image is constructed by using the lower order IMFs since it contains the higher frequency components. Higher order IMFs that basically contain low-frequency components are discarded in this process. The IMFs are multiplied with weight and summed up to get enhanced R, G, and B channels. The weight sets  $[w1 \ w2 \ w3]$  are chosen in such a way that it is normalized to 1. Finally, the enhanced R, G and B channels are combined together to get the enhanced SONAR image.

$$\text{Avg.Grad} = \frac{1}{S * T} \sum_{i=1}^S \sum_{j=1}^T \sqrt{(\partial \text{Im}(i, j) / \partial i)^2 + (\partial \text{Im}(i, j) / \partial j)^2} \quad (5)$$

### 4 Result and Simulation

In this section, the experimental results of five test SSS images are demonstrated as follows. The proposed technique is being evaluated under both quantitative as

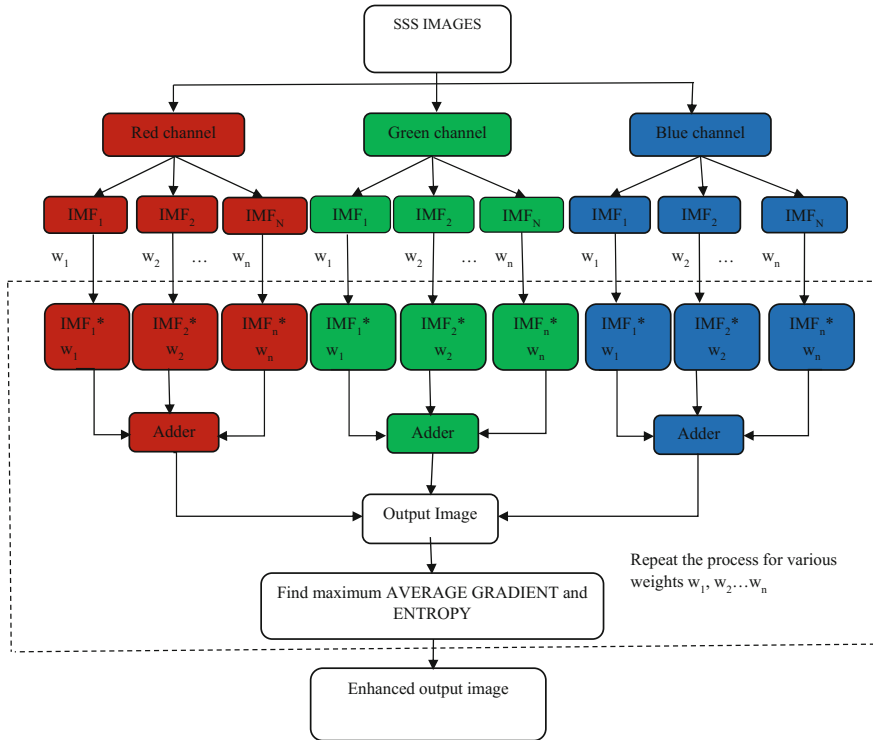
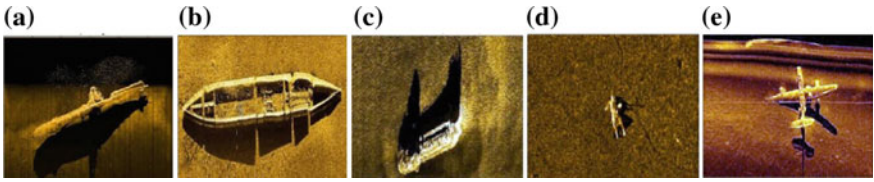


Fig. 1 Block diagram for EMD with optimal weight enhancement

well as qualitative, respectively. Figure 2 shows the five test SSS images used for experimentation (a) U-Boat submarine [18] (b) midget submarine [19] (c) deep sea submergence vehicle [20] (d) human torpedoes [21] (e) submerged aeroplane [22]. These images are captured by side-scan sonar device under different levels of seabed conditions. Figure 3 describes the different image enhancement schemes are applied in the five test SSS images such as histogram equalization, contrast stretching, EMD minimum average gradient and EMD optimal weight maximum average gradient. Table 1 represents reconstructed enhanced images using different weights for u-boat submarine. According to proposed algorithm, the SSS images are divided into Red, Green, and Blue channels, and intrinsic mode functions (IMF) are segregated from each color channels in which optimal weight is multiplied. This process can be continued until maximum average gradient selected. Table 2 shows the maximum average gradient values of the proposed algorithm. It is observed that whenever the weight of the first IMF is larger, then, the visual quality of the enhanced image must be superior. So, the first three IMFs are more than enough to attain sufficient image enhancement with reasonable adequate weights.

Based on that, the visual quality of the SSS images is improved by enhancing the intensity values in the narrow range of the SSS image. In Fig. 4 represents the



**Fig. 2** Experimental results for side-scan sonar images: **a** U-boat submarine **b** midget submarine **c** deep sea submergence vehicle **d** human torpedoes **e** submerged aeroplane

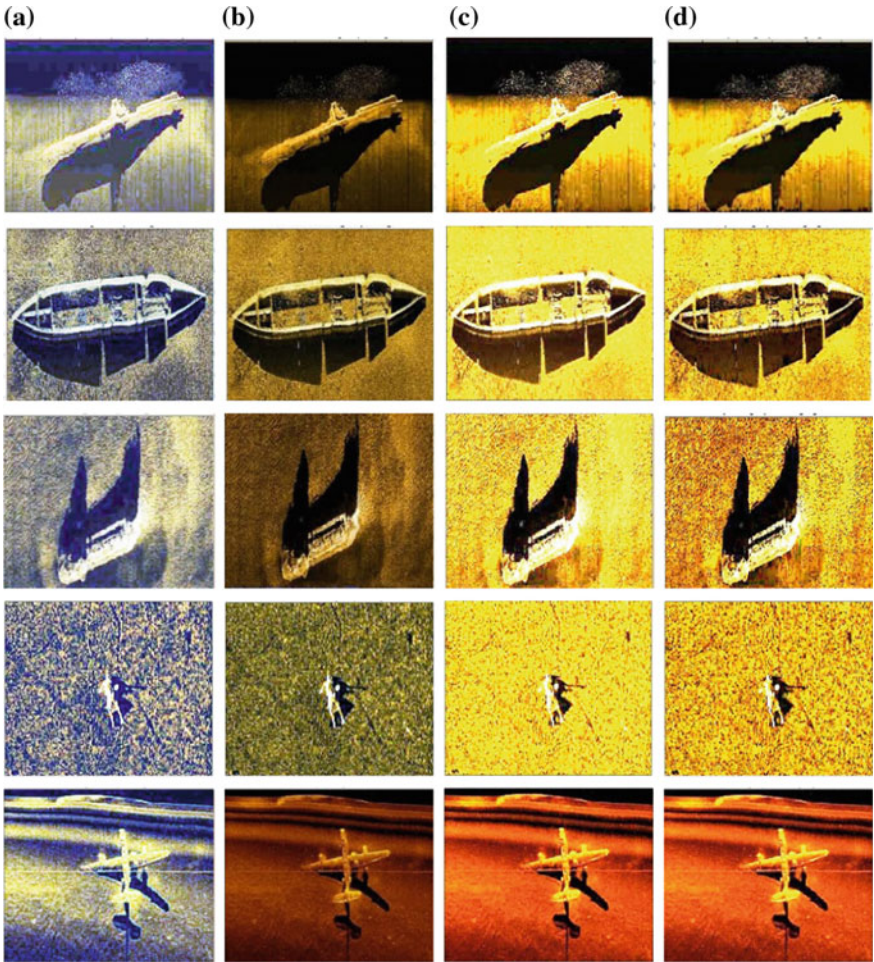


**Fig. 3** Experimental result for side-scan sonar images: **a** histogram equalization images, **b** contrast stretching images, **c** EMD minimum average gradient images and **d** EMD optimal weight maximum average gradient images

histogram comparison of the (a) five test SSS images, (b) EMD enhanced images, (c) Histogram equalized images. Finally, the enhanced vision of the visually affected images provides visual details with good image quality compared to the original image.

In further, the enhanced images are segmented with the help of K-means and fuzzy c-means (FCM) color clustering and LBP methods for feature extraction. Comparison of K-means and FCM color clustering method outputs are shown in Fig. 5. Figure 5a depicts the K-Means with optimal weight EMD output images and Fig. 5b shows the output images of FCM with optimal weight EMD. Among these two color clustering methods, FCM color clustering gives more details about the enhanced image. So the FCM with optimal weight empirical mode decomposition can be used for feature extraction of the underwater SSS images.

It's already known that the images using sonar are captured by the intensity of the reflected acoustic signal. Based on the intensity of reflected acoustic signal, Sonar will assign a pixel value; hence, by considering only the color information we cannot segment the sonar image commendably. For this purpose, we combine both the color and texture information to segment the sonar image. Figure 6 represents the flow diagram of FCM with LBP. The segmentation results of SSS images are shown in Fig. 5c. As per our analysis, the combined results of FCM color clustering with LBP texture analysis are far better than considering only the color. Hence, combining the features will be helpful to classify the sediments in the sonar image suitably

**Table 1** Reconstructed enhanced images using different weights for U-boat submarine

w1	w2	w3	Average gradient	Entropy
0.50	0.40	0.10	17.88	5.44
0.50	0.50	0.00	17.82	5.01
0.50	0.50	0.50	17.57	5.52
0.60	0.00	0.40	17.81	5.44
0.60	0.10	0.30	17.86	5.43
0.60	0.20	0.20	17.88	5.25
0.60	0.30	0.10	17.88	5.35
0.60	0.40	0.00	17.84	4.97
0.60	0.60	0.60	17.41	5.53
0.70	0.00	0.30	17.84	5.36
0.70	0.10	0.20	17.88	5.26
0.70	0.30	0.00	17.87	4.92
0.70	0.70	0.70	17.26	5.53
0.80	0.00	0.20	17.88	5.27
0.80	0.20	0.00	17.90	4.86
0.80	0.80	0.80	17.06	5.54
0.90	0.00	0.10	17.89	5.07
0.90	0.10	0.00	17.91	4.74

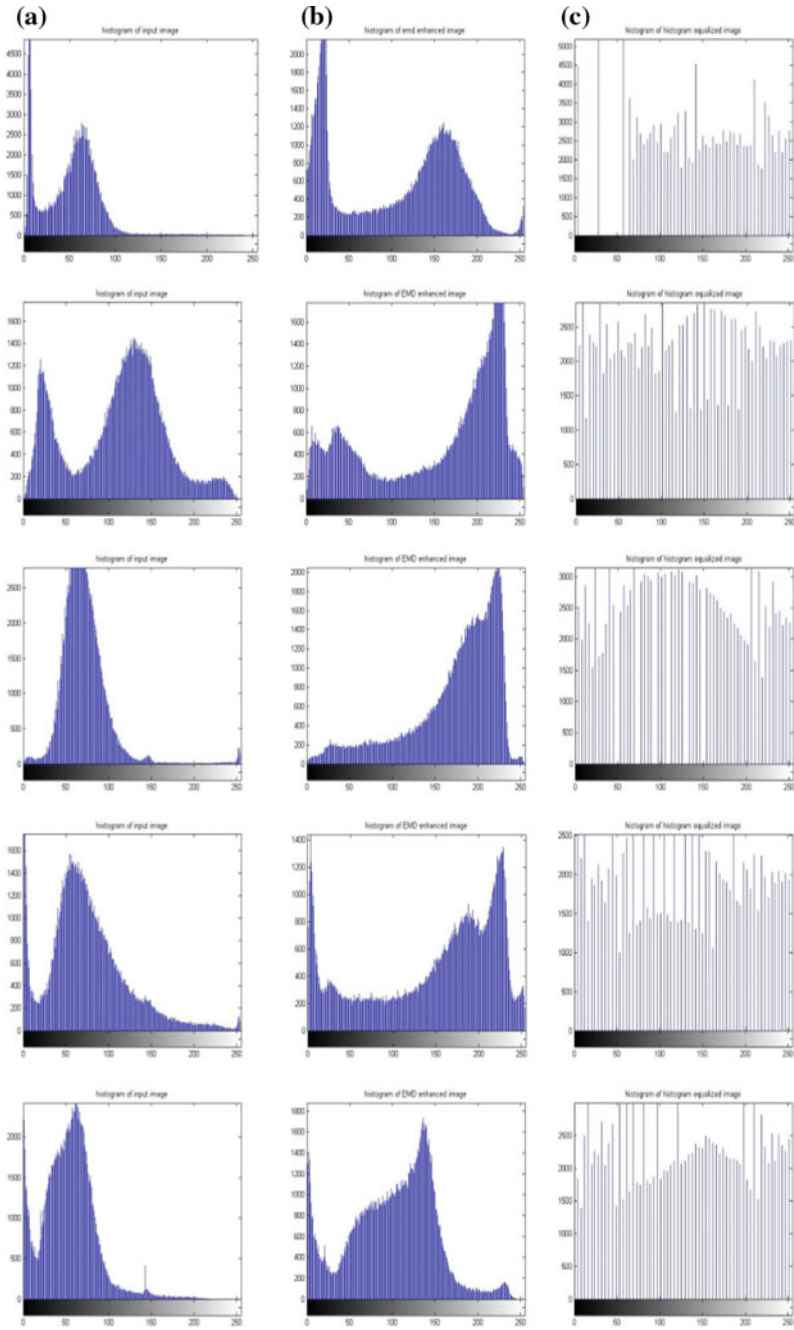
**Table 2** Sample weight combination and corresponding average gradient and entropy

Image	Optimal weight for the corresponding images			Average Gradient for input image	Average Gradient for optimal weighted image
	w1	w2	w3		
U-boat submarine	0.90	0.10	0.00	9.41	17.90
Midget submarine	0.70	0.20	0.10	20.88	26.80
Deep sea submergence vehicle	0.80	0.20	0.00	16.85	34.30
Human torpedoes	0.90	0.10	0.00	15.39	31.90
Submerged aeroplane	0.9	0	0.1	7.88	18.36

than considering only either of the color or texture. The number of segments can be improved for accuracy.

## 5 Conclusion

In this paper, a novel image enhancement algorithm is proposed based on empirical mode decomposition with optimal weights (EMD-OW) for submerged SSS images. According to this, SSS images are divided into Red, Green, and Blue channels and each color channels intrinsic mode functions (IMF) are segregated in which optimal weight has been multiplied. After, each IMFs of Red, Blue and Green channels are added and recombined each channel in which average gradient of the SSS image has been calculated. Hence, the highest graded average is identified which induce the enhanced version of the SSS image. The quality of the images is statistically illustrated by plotting the histogram of Red, Green and Blue channels of the SSS image before and after enhancement. The reconstructed enhanced image provides visual details with good image quality compared to the original image. Further, segmentation of image was performed using texture and color features. Future work will include comparison of advanced texture analysis methods and classifying the segmented image using classification algorithm like support vector machine (SVM).



**Fig. 4** Histogram images **a** input images, **b** EMD with optimal weight enhanced images, and **c** histogram equalized images



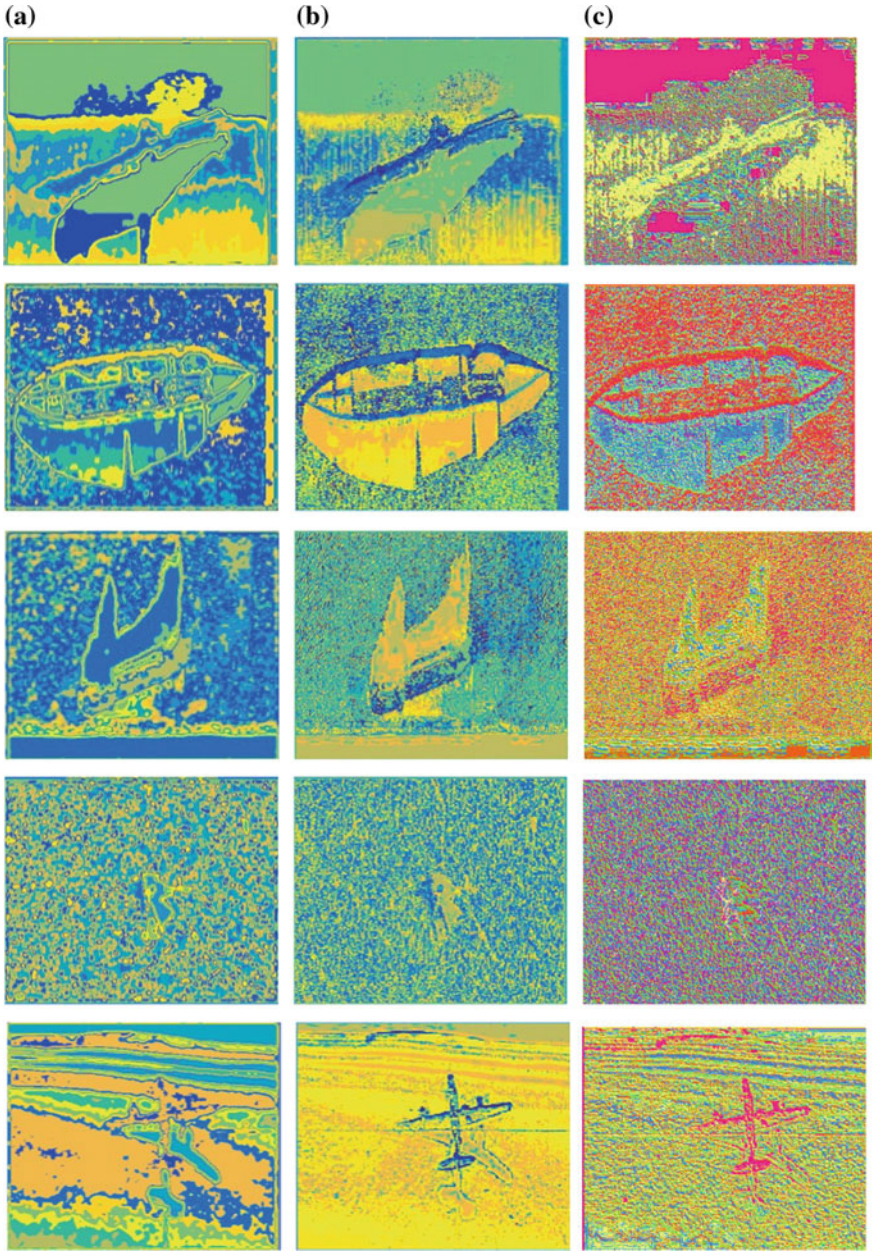


**Fig. 5** Comparison of K-Means clustering (a), FCM color clustering (b), and FCM with LBP (c)

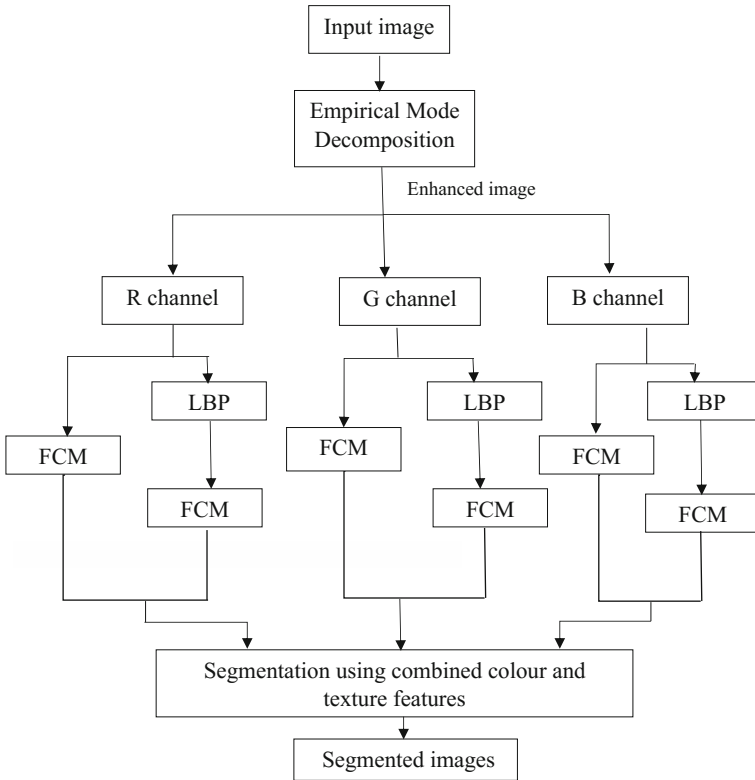


Fig. 6 Flow diagram of FCM with LBP

## References

1. Cervenka P, de Moustier C (1993) Side scan image processing techniques. *IEEE J Oceanic Eng* 18(2):108–122
2. Thakur V, Tripathi N (2010) On the way towards efficient enhancement of multi-channel underwater images. *Int J Appl Eng Res* 5(5):895–903
3. Iqbal K, Abdul Salam R, Osman A, Talib A (2007) Underwater image enhancement using an integrated colour model. *IAENG Int J Comput Sci* 34:2–8
4. Hasikin K, Isa NAM (2014) Adaptive fuzzy contrast factor enhancement technique for low contrast and nonuniform illumination images. *SIViP* 8(8):1591–1603
5. Santhi K, Banu RW (2015) Contrast enhancement by modified octagon histogram equalization. *SIViP* 9(1):73–87
6. Thangaswamy SS, Kadarkarai R, Thangasamy SRR (2013) Developing an efficient techniques for satellite image denoising and resolution enhancement for improving classification accuracy. *J Electron Imaging* 22(1):1–7
7. Garcia R, Nicosevici T, Cufi X (2002) On the way to solve lightning problems in underwater imaging. In: *IEEE OCEANS conference*, pp 1018–1024
8. Hariharan H, Gribok A, Abidi M, Koschan A (2006) Image fusion and enhancement via empirical mode decomposition. *J Pattern Recogn Res* 1(1):16–32
9. Tas yapı Çelebi A, Ertürk S (2010) Empirical mode decomposition based visual enhancement of underwater images. In: *2nd international conference on image processing theory tools and applications (IPTA)*, Paris, pp 221–224
10. Bazeille S, Quidu I, Jaulin L, Malkasse JP (2006) Automatic underwater image pre-processing. In: *Proceedings of the characterisation du Milieu Marin (CMM'06) Brest, France, Oct 2006*, pp 16–19
11. Padmavathi G, Subashini P, Kumar MM, Thakur SK (2010) Comparison of filters used for underwater image pre-processing. *IJCSNS Int J Comput Sci Net Secur* 10(1):58–65
12. Huang NE, Shen Z, Long SR, Wu MC, Shih HH, Zheng Q, Yen NC, Tung CC, Liu HH (1998) The empirical mode decomposition and the hilbert Spectrum for nonlinear and non-stationary time series analysis. *Proc R Soc London A* 454:903–995
13. Liu Z, Liao Z, Sang E (2005) Noise removal of sonar image using empirical mode decomposition. *Proc SPIE* 6044:60440N-1–60440N-9
14. Linderhed A (2004) Image compression based on empirical mode decomposition. In: *Proceeding of SSAB Symposium Image Analysis, Uppsala*, pp 110–113
15. Janusauskas A, Jurkonis R, Lukosevicius A, Kurapkiene S, Paunksnis A (2005) The empirical mode decomposition and the discrete wavelet transform for detection of human cataract in ultrasound signals. *Inf Lith Acad Sci* 16(4):541–556
16. Taşyapı Çelebi A, Ertürk S (2010) Target detection in sonar images using empirical mode decomposition and morphology. *Undersea Defence Technology (UDT) Europe*, pp 22–24
17. Sowmyashree MS, Bekel SK, Sneha R, Priyanka N (2014) A survey on the various underwater image enhancement techniques. *Int J Eng Sci Invention* 40–45. , ISSN: 2319-6734
18. <http://www.geotech1.com/forums/attachment.php?s=6315799d1a3e2c73a4d99e0b47d8b0da&attachmentid=13384&d=1285895680>
19. <http://geoviewinc.com/methods/marine/side-scan-sonar>
20. [http://www.blacklaserlearning.com/images/pauline\\_marie\\_web.jpg](http://www.blacklaserlearning.com/images/pauline_marie_web.jpg)
21. <http://kleinmarinesystems.com/products/side-scan-sonar/system-3900/#prettyPhoto/gallery2/0/>
22. <http://static.seattletimes.com/wp-content/uploads/2007/08/2003847265-300x0.jpg>
23. Demir B, Ertürk S (2008) Empirical mode decomposition pre-process for higher accuracy hyperspectral image classification. In: *International conference on geoscience and remote sensing symposium, Boston, Massachusetts, U.S.A.*, pp. II-939–II-941

# Embedded System Design for Autonomous Unmanned Surface Vehicles in Laboratory Environment



Awanish C. Dubey, V. Anantha Subramanian and V. Jagadeesh Kumar

**Abstract** Sea-keeping, maneuvering, and motion tests of surface vehicle/ship model need self-propelled scale model which can perform different maneuvers. The present work describes the design implementation and testing of embedded system of an autonomous system for unmanned surface vehicles (USVs)/ship model in the laboratory environment. This is a first-time national development test in the wave basin has demonstrated full-free running self-controlled model in a disturbance environment. The central unit of the system is an embedded controller, compact reconfigurable input–output (cRIO) which features a field-programmable gate array (FPGA) and a processor running Linux-based real-time operating system. It performs the main propulsion control, rudder control data logging and telemetry. The peripherals are interfaced with main controller through multifunction input–output module. The RS-232 communication is used to interface the MRU sensor with main controller. LabVIEW is used as programming tool to develop a program to control the peripherals connected to the main controller and data acquisition over a wireless link using Wi-Fi. A graphical user interface is developed to send control commands and visualize the 4-degree of motion at base station in real time.

**Keywords** Embedded system · Real-time operating system · Dataflow programming language · USVs · PD controller

## 1 Introduction

Study of motion responses of USVs/ship in waves and calm water is very important to evaluate maneuverability and also helps in designing autopilots for the ship using Nomoto model obtained from these tests. The dynamics of the ship are determined traditionally by performing the model tests in towing tank or wave basin with umbili-

---

A. C. Dubey (✉) · V. A. Subramanian  
Department of Ocean Engineering, Indian Institute of Technology-Madras, Chennai, India  
e-mail: [awanish.dubey@gmail.com](mailto:awanish.dubey@gmail.com)

V. J. Kumar  
Department of Electrical Engineering, Indian Institute of Technology-Madras, Chennai, India

© Springer Nature Singapore Pte Ltd. 2019  
K. Murali et al. (eds.), *Proceedings of the Fourth International Conference in Ocean Engineering (ICOE2018)*, Lecture Notes in Civil Engineering 22,  
[https://doi.org/10.1007/978-981-13-3119-0\\_27](https://doi.org/10.1007/978-981-13-3119-0_27)

cal cables or mechanical link from a captive follower towing carriage which controls the self-propelled model or by a follower bridge in a wave basin. A recent development of a self-propelled, self-controlled scaled ship model for towing tank-based tests described in [1]. Another recent development of an autonomous system with azimuth steering system ship model testing is presented in [2]. Present work focuses on the embedded system design of an autonomous system which facilitates the surface vehicle/ship models to perform different maneuvers in calm water and wave conditions. The model is controlled via base station computer over Wi-Fi, which allows the model to perform tests such as turning circle, zigzag spiral without any mechanical link. The architecture and design of the system are described below. The system uses a main controller which controls the peripherals and different motors which is described in Sects. 5 and 6. A graphical language-based programming environment Laboratory Virtual Instrument Engineering Workbench (LabVIEW) is used to code the main controller. LabVIEW has become more popular in the measurement and test field, which has the flexibility of a programming language combined with built-in tools designed specifically for test, measurement, and control [3]. Also, a GUI is developed to enter control commands for the system, discussed in Sect. 7. Wireless communication between model and base station is established using Wi-Fi which is discussed in detail in Sect. 8. The data acquisition system measures all four degrees of freedom, i.e., roll, heave, pitch, and yaw and stores data on onboard USB flash drive and also transmits to the base station over Wi-Fi to maintain the data redundancy.

## 2 USVs/Ship Model Dynamics

The ship dynamic equations are well established and are obtained from Newton–Euler or Lagrange equations. In maneuvering theory, the model is subjected to a constant speed in calm water with the assumption that the hydrodynamic coefficients are frequency independent. So the maneuvering model can be formulated as coupled surge–sway–yaw model and thus neglect heave, roll, and pitch motions [4]

$$m[\dot{u} - vr - x_g r^2 - y_g \dot{r}] = X \quad (1)$$

$$m[\dot{v} + ur - y_g r^2 - x_g \dot{r}] = Y \quad (2)$$

$$I_z \dot{r} + m[x_g(\dot{v} + ur) - y_g(u - vr)] = N \quad (3)$$

where  $m$  is the mass of the model,  $u$  is the velocity of model in  $x$ -direction,  $v$  is the projection of the models velocity on  $Y$ -axis,  $r$  is the angular velocity in yaw,  $I_z$  is the moment of inertia about the  $z$ -axis  $X$ ,  $Y$ , and  $N$  denote the external forces and moment and,  $x_g$  and  $y_g$  represent center of gravity relative to a fixed point on the hull.

### 3 Transfer Function

The ship model dynamics can be represented by the input–output relation with rudder angle as an input and heading angle as output. The transfer function of the ship model can be described as

$$T(s) = \frac{\psi}{\delta} = \frac{b_1s + b_2}{s(s^2 + a_1s + a_2)} \tag{4}$$

This transfer function model has been proposed by Nomoto [5] where  $\psi$  is a model motion excited by  $\delta$ . The simultaneous measurements of an arbitrary  $\delta$  and  $\psi$  excited by particular  $\delta$  give us the transfer function. There are several methods that are proposed to determine the values of  $a_1$ ,  $a_2$ ,  $b_1$ , and  $b_2$  [6].

### 4 Heading Control Design

To perform different maneuvering and station keeping tests in wave conditions, it is crucial to maintain the heading of the model when subjected to external disturbances. The model is subjected to a constant speed by setting to corresponding rpm of the motor. The control objective is to make the error to zero, i.e.,  $\lim_{t \rightarrow \infty} (\psi_d - \psi) = 0$ , where  $\psi$  and  $\psi_d$  are the current heading from MRU sensor and desired heading from the pilot, respectively.

A proportional derivative (PD) control law given in Eq. (5) is designed for the heading control to maintain the desired course.

$$\delta_r = K_p(\psi_d - \psi) - K_d\dot{\psi} \tag{5}$$

where  $K_p$  and  $K_d$  are proportional and derivative gains, respectively.

The saturation of the rudder and the rudder rate is typically in the range of  $\delta_{max} = 35^\circ$  and  $\frac{7}{3} (\circ/s) < \dot{\delta}_{max} < 7 (\circ/s)$  [4], which is shown by the saturation block in the Simulink block diagram in Fig. 1. The step response of the model is shown in Fig. 2.

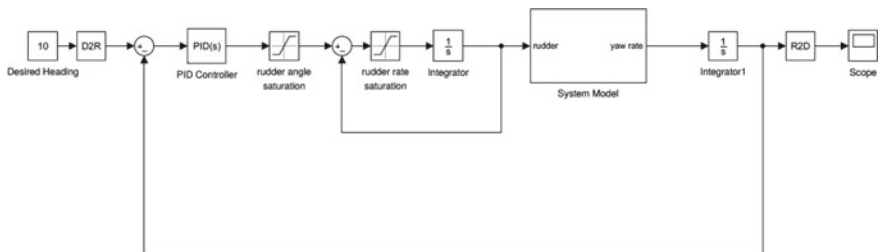
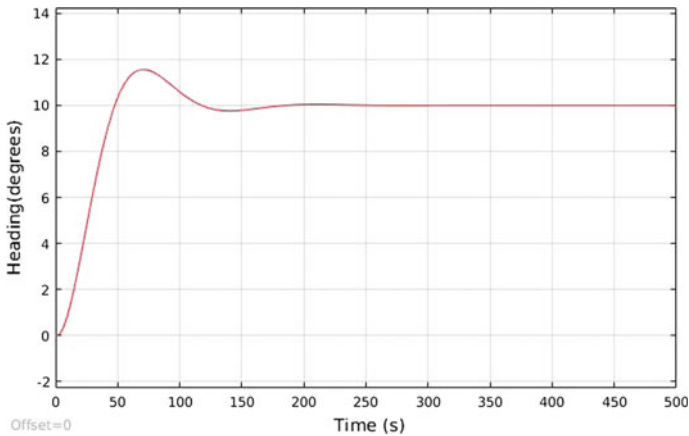


Fig. 1 Block diagram of model simulation in Simulink



**Fig. 2** Simulation response of heading control

## 5 System Architecture

The autonomous system architecture for self-propelled ship model has shown in Fig. 3 and has three main components as described below.

### 5.1 Propulsion System

The direct propulsion system is used to propel the ship model, where a twin propeller is connected with a 400 W brush-less DC (BLDC) motor through a transmission shaft and twin-motor gearbox with 1:1 ratio. The BLDC motor is interfaced to the main controller through a motor drive and a relay. The rpm and the direction of the motor are controlled by the multifunction I/O module connected with the main controller. For a set of known forward speeds of the model, the corresponding propeller rpm is determined from the towing tank tests.

### 5.2 Steering System

The steering system consists of twin Becker rudder and timing belt system. The system is actuated by a stepper motor with step angle of  $1.8^\circ$  and holding torque capacity of 1 Nm which is interfaced with main controller through a stepper motor drive and a stepper module. There are two modes of operations for steering system:

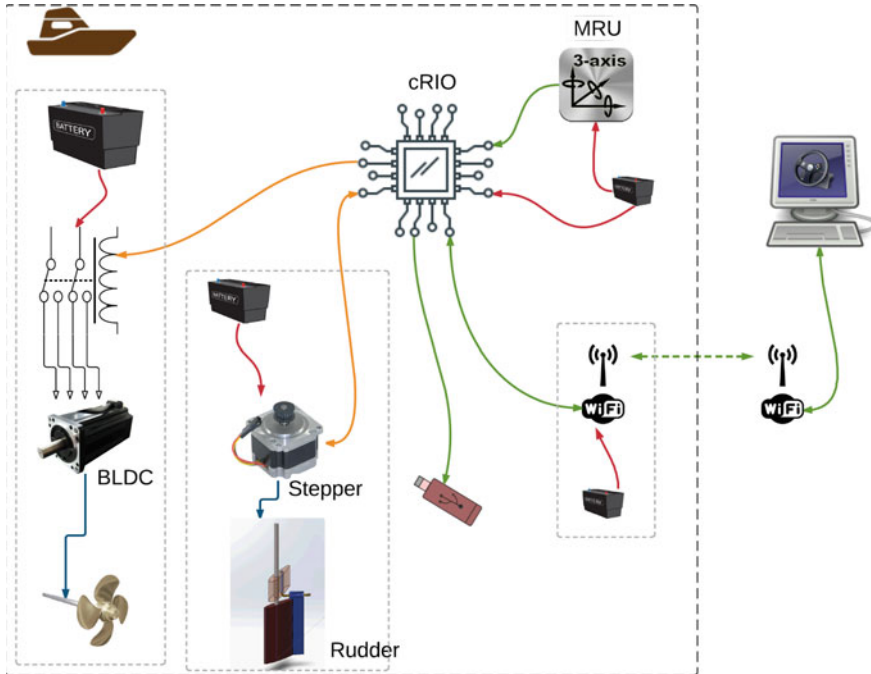


Fig. 3 Overview of system architecture

- Open loop: In open loop, the heading correction is done with the help of human intervention, where the user sends command to correct the heading by changing the rudder angle over wireless link.
- Closed loop: In closed loop, the model is set to follow a desired heading in external disturbances, where the steering system takes the heading data from the MRU sensor and perform heading correction using feedback control law and keep the desired heading.

### 5.3 Data Acquisition System

The MRU sensor connected to the serial port of the main controller, senses the roll, pitch, heave and yaw motion of the ship model and gives output in string format using serial communication protocol. The sensor is placed at the center of gravity of loaded ship model. The MRU data is stored in a USB flash drive which is mounted on the USB port available at main controller on board and at the same time data is transferred from the ship model to the base station through a wireless communication. The two-way data storage, i.e., via USB and Wi-Fi gives data redundancy for safety.



## **6 Hardware Architecture**

### **6.1 Processor**

The cRIO9064 is used as a main controller which suits for advanced control, data acquisition, and monitoring applications. It features an FPGA and a Linux-based real-time processor. It controls the main propulsion motor and steering motor by generating logic as per the program through different modules connected to the main controller.

### **6.2 I/O Module**

The BLDC motor is interfaced with the main controller through an multifunction I/O module NI9381. It is a single system which combines common I/O circuitry into a single module. The digital I/O pins generate the logic signals to switch the controls of the BLCD drive circuit. The analog output of the I/O module controls the rpm of the motor.

### **6.3 Stepper Module**

The stepper motor is interfaced with main controller through NI9512 which provides stepper drive interface signals, position compare and as direct connectivity to P7000 series stepper drives. The NI9512 processor runs the spline interpolation step generation algorithm to produce smoother motion, resulting in precise stepper motion control.

### **6.4 Motion Reference Unit (MRU)**

The motion reference unit (MRU) is used to determine the roll, pitch, heave, and yaw motion of the vessel model to which it is fixed. The output of the sensor is in string format over serial communication port. Further, the sensor can be configured for different format of output string with the update rate of 24 Hz.

## **6.5 Communication Ports**

The main controller provides a different type of connectivity ports, which include two Ethernet, one USB host, one USB port, and one serial port. The Wi-Fi router is connected to the Ethernet port which provides wireless connectivity with the base station. The MRU sensor is connected to the main controller through serial (RS-232) port to acquire motion data. The acquired data from MRU is stored to the USB flash drive which is connected to the USB port of the main controller.

## **6.6 Power Supply**

All the components on board are powered by three sets of hermetically sealed batteries.

- 1 24 V 26 Ah batteries. A set of 4 batteries is connected in series to power the BLDC motor.
- 2 12 V 7 Ah batteries. A set of 4 batteries is connected in series which powers the stepper motor, controller unit, and MRU.
- 3 12 V 7 Ah batteries. A single battery is used to power the Wi-Fi router.

# **7 Software Architecture**

## **7.1 Data Flow Programming Language**

The programming language that used in LabVIEW is a dataflow programming language. Structure determines the execution of a graphical block diagram on which the different function nodes are connected by drawing wires. The variable propagates through these wires and any node can execute as soon as all its input data become available. Multi-processing and multi-threading function are exploited by the built-in scheduler, which multiplexes multiple OS threads over the nodes ready for execution.

The main controller is programmed to generate logic signal to enable, stop, and control the direction of rotation of the propeller. The BLDC motor drive receives logic signal through the multifunction I/O module which is connected to the main controller. The rpm of the BLDC motor is controlled by using on-chip digital-to-analog converter (DAC) that generates analog signal at the analog output pin of the I/O module.

The stepper motor of the steering system is controlled by sending command in form of rudder deflection and desired heading to operate the system in open loop and closed loop, respectively. These control commands are set through GUI, and the main controller generates the signal to the stepper module. The position for the

stepper motor is calculated by converting the angle for rudder deflection into step angle by multiplying with a factor which includes the size of the timing pulley and stepper module settings. In the closed-loop scenario, the reference heading compared with the current heading and uses the PD control law to generate the actuator signal in terms of position to keep the desired heading of the scaled ship model [4]. In zigzag mode of maneuver, the model is deflected from its initial course by deflecting the rudder to a fixed angle (5, 10, and 15) and allows model to reach to the desired heading defined by user (such as 10, 20, and 30). Program compares the current heading sensed by MRU sensor and compares it to the overshoot heading angle. Once it matches the condition of overshoot, the main controller generates the signal to set the rudder to the negative of the initial deflected angle, which makes the ship model to move in opposite direction.

## **7.2 Block Diagram**

The block diagram is the back end of the virtual instrument (VI) which includes the building blocks of a program such as terminals, sub-VIs, functions, constants, structures, and wires, which transfer data among other block diagram objects. The program's logics are implemented using these structures and VIs using data flow programming language.

## **7.3 Graphical User Interface (GUI)**

A user interface provides a link to the pilot to interact with the source code. It allows the user to change the parameters passed to the program code and see the output data that the back-end code computes. In LabVIEW, the user interface is the front panel. The GUI facilitates pilot to control the model during run by assigning certain commands. GUI also provides user to process and visualize the data in real time as shown in Fig. 4. The GUI is made accessible through a web browser by assigning a dedicated Internet Protocol (IP) address. It provides numeric indicator and control buttons to transmit control command to the main propulsion unit and steering unit. The speed control is implemented by generating the lookup table from set of experiments done at towing tank for speed calibration, where the model is set to different rpm to match the speed of the towing carriage.

## **8 Communication**

The onboard system and the base station computer communicate over wireless link. This end-to-end communication uses client-server model, where the onboard system



Fig. 4 GUI is used to exchange data and control command between base station and model

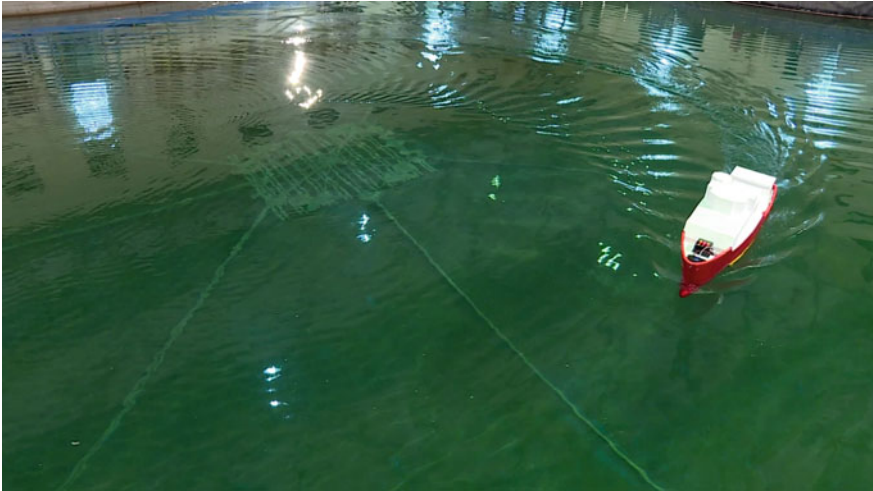
works as server, which shares its resources to the base station, which acts as a client. This architecture provides the operating system in-dependency and scalability of the whole setup. A wireless dual-band router is used for wireless communication. The router uses the latest high-speed wireless technology which provides fast Wi-Fi speeds of up to 300 Mbps on the 2.4 GHz frequency band.

## 9 Results

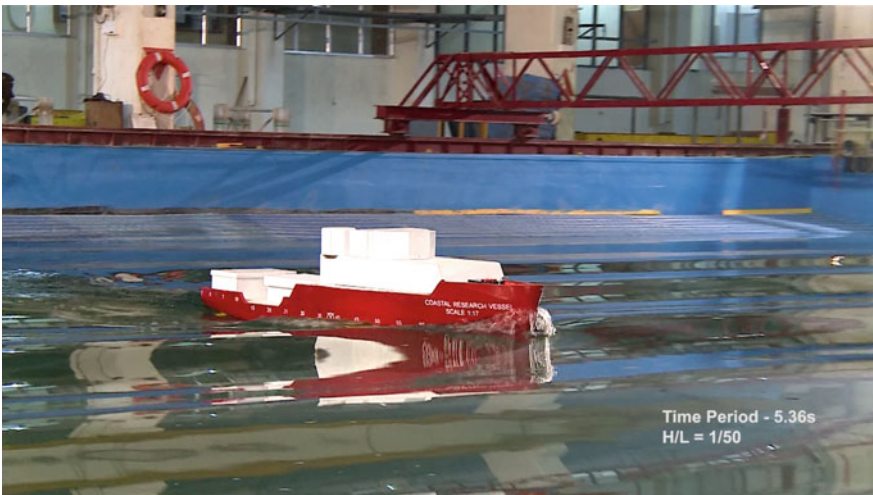
The system is developed and tested successfully on a scaled ship model for different maneuvering tests. The model is deployed in a wave basin (30 m × 30 m) and controlled from base station over Wi-Fi.

Figure 5 shows the model during run-in wave basin, where the model is subjected to a constant speed and rudder angle in calm water condition. The motions data are acquired and processed at the base station.

To study the different motions response of the model in waves, the model is subjected to the different wave conditions such as head sea, beam sea, and oblique sea, with different wave heights and time periods as shown in Fig. 6. The sensor data transferred over wireless communication to base station is processed and analyzed for different maneuver tests in different wave conditions. Figure 7 shows the time series plot of heading of the ship model in head sea condition, where model maintains the desired heading. The ship is subjected to a constant rpm which corresponds to 1.5



**Fig. 5** Model performing turning circle test in wave basin



**Fig. 6** Model subjected to head sea to perform straight line

m/s (speed in calm water condition) and the wave of period and height is generated as an external disturbance for duration of 20–30 s as shown in time series plot (Figs. 7, 8 and 9). The model is programmed to maintain a desired heading in closed loop with feedback from MRU sensor. The roll, pitch, and yaw motions are analyzed to study the dynamic stability of the model when subjected to waves.

**Fig. 7** Heading control in head sea condition with forward speed of 0.75 m/s

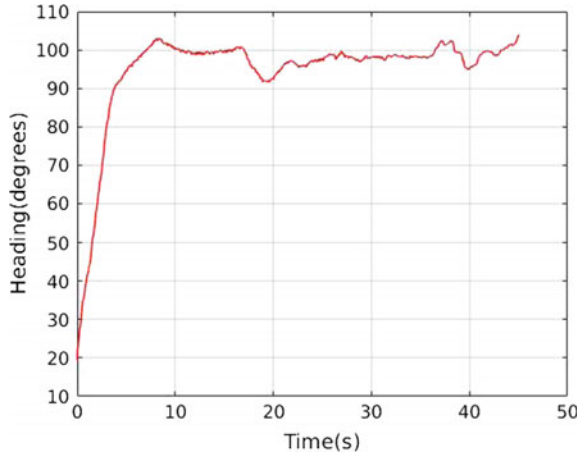


**Fig. 8** Roll response in beam sea condition with model running at 0.75 m/s

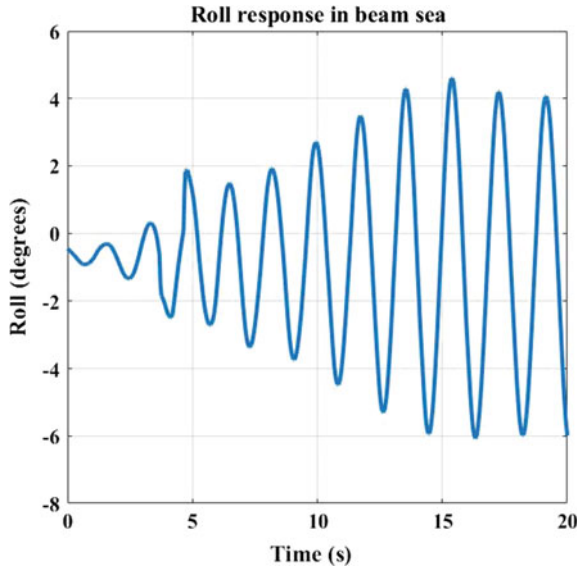
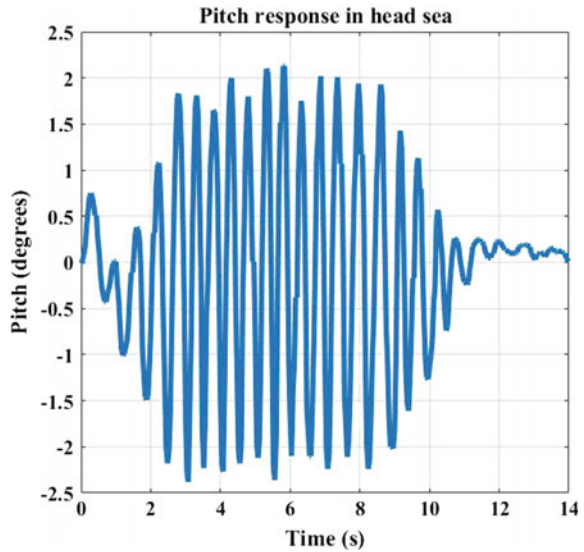


**Fig. 9** Roll response in head sea condition with model running at 0.75 m/s



## 10 Conclusion

A robust autonomous self-propulsion system with full data storage and transmission without any physical link has been developed and demonstrated. The system allows user to study the dynamic stability of the ship model in different wave conditions. This offers the basis for further analysis and simulating complex maneuvers which are listed below.

- Nomoto second-order model identification for steering control.
- Path following and way point guidance.
- Multiple vehicle control and obstacle avoidance.

## References

1. Lopez Pea F, Miguez Gonzalez M, Deibe A, Pena D, Orjales F (2013) An autonomous scale ship model for towing tank testing. In: 7th IEEE international conference on intelligent data acquisition and advance computing systems, Sept 2013
2. Dubey AC, Subramanian VA, Kumar VJ, Bhikkaji B (2016) Development of autonomous system for scaled ship model for seakeeping tests. In: OCEANS 2016 MTS/IEEE Monterey. IEEE, pp 1–5
3. Chen Y, Jin JX (2011) Real-time measurement and control system for PMLSM based on virtual instrument. In: 2011 IEEE international conference on applied superconductivity and electromagnetic devices, Sydney, Australia, 14–16 Dec 2011, pp 243–247
4. Fossen TI (1994) Guidance and control of ocean vehicle. Wiley, New York

5. Nomoto K, Taguchi T, Honda K, Hirano S (1957) On the steering qualities of ships. *Int Shipbuild Prog* 4(35)
6. Tzeng C-Y, Chen J-F (1999) Fundamental properties of linear ship steering dynamic models. *J Marine Sci Technol* 7(2):79–88



# Design and Development of Unmanned Underwater and Aerial Vehicle



A. Palaniappan, P. Ganesh, S. B. Pranesh, D. Sathianarayanan  
and G. A. Ramadass

**Abstract** The quadcopter-based unmanned underwater and aerial vehicle has been designed. The vehicle electronics pressure casing has been designed and fabricated using acrylic material which can withstand an atmospheric pressure in aerial condition and external pressure of 10 bar in underwater condition to fly in both aerial and underwater conditions up to 100 m. This type of vehicle will be used in both civil and military applications for surveillance in the air and underwater conditions. Total payload of the quadcopter is 3 kg. The propeller assembly is tested to measure the maximum thrust force developed under bollard pull condition. The brushless DC motor and aerial fixed pitch propellers combination has been selected for the quadcopter type vehicle, and each motor is capable of producing a required thrust force for aerial as well as underwater condition. The flow analysis is carried out using water as the fluid medium for 3-knot speed, and drag force is found along the vertical direction is maximum. The developed quadcopter has been tested in underwater. The vehicle is found to be stable, and wireless control is working for about 1 m from the surface of the water.

**Keywords** Quadcopter · Aerial vehicle · Underwater vehicle  
Fixed pitch propellers

## 1 Introduction

Unmanned underwater vehicles are necessary tools for underwater inspection and it is a self-propelled unmanned submersible vehicle. The unmanned underwater vehicles are classified into two types—one is autonomous underwater vehicles (AUVs) and

---

A. Palaniappan (✉) · P. Ganesh  
Anna University, MIT Campus, Chennai, India  
e-mail: [palaniappan.12.12@gmail.com](mailto:palaniappan.12.12@gmail.com)

S. B. Pranesh · D. Sathianarayanan · G. A. Ramadass  
National Institute of Ocean Technology (NIOT), Velachery–Tambaram Main Road,  
Narayanapuram, Pallikaranai, Chennai 600100, Tamil Nadu, India

© Springer Nature Singapore Pte Ltd. 2019  
K. Murali et al. (eds.), *Proceedings of the Fourth International Conference in Ocean Engineering (ICOE2018)*, Lecture Notes in Civil Engineering 22,  
[https://doi.org/10.1007/978-981-13-3119-0\\_28](https://doi.org/10.1007/978-981-13-3119-0_28)

another one is remotely operated vehicles (ROVs), these are the most important vehicles used to explore the underwater environment. The ROVs consist of the number of thrusters, sensors, cameras, and other electronic components [1]. The ROVs are the most significant tools to explore an underwater environment because they are necessary to use the marine technique for underwater observation [2]. The ROVs are controlled and powered from the ship or surface operated by using umbilical or joystick control. The ROVs are performing a wide variety of tasks in the underwater environment [3].

Unmanned aerial vehicle (UAV) is an aircraft that manipulates aerodynamic forces to provide lift without a human on board operator. There are several types of aerial vehicles such as a fixed wing, flapping wing, and roto crafts. The quadcopter is a kind of roto crafts aerial vehicle. Quadcopter, also known as a quadrotor. It is a multicopter aerial vehicle and to take off using four rotors actuated two in clockwise and another two in counter-clockwise [4]. These vehicles are vertical take-off and landing (VTOL). UAV is an aircraft that is capable of vertical take-off and landing from the static or dynamic position [5, 6]. There are several advantages to quadcopters over comparably scaled helicopters. In case, the quadcopter hits anything the damage is significantly lesser than the similar-sized helicopter. The quadcopter direction changes by control individual rotor speed.

Our work focuses on developing the combined aerial and underwater vehicle. The designed vehicle should be capable of flying in the air and swimming in underwater, and it has been of great interest for decades. The developed vehicle based on quadcopter type vehicle that can fly in the air and submerged into the underwater with the help of own propeller and without using buoyancy chamber. The vehicle electronics pressure casing has been designed and fabricated using suitable material which can withstand the underwater pressure up to 100 m and quadrotor-type vehicle configuration based on aerodynamics as well as hydrodynamics. The fixed pitch aerial propeller has been used for both aerial and underwater conditions. There is a continuous increase in these unmanned vehicle applications in areas like surveillance, photography, environmental, geological, and biological monitoring and testing, as well as some military and civilians applications.

## 2 Quadcopter Type Aerial and Underwater Vehicle

The vehicle dynamics are introduced by using two frames, i.e., two coordinate systems [7, 8]. One attached to the moving vehicle, and the other, the inertial coordinate system. The inertial frame is defined by the ground, with gravity pointing in the negative  $zz$  direction. The body frame is denoted by the orientation of the vehicle, with the rotor axis denoting the positive  $zz$  direction and the arms denoting the  $xx$  and  $yy$  directions. The vehicle dynamics of body-fixed frame and inertial frame coordinates are shown in Fig. 1.

The  $b_1$ ,  $b_2$ , and  $b_3$  constitute the set of unit vectors that describe the body-fixed coordinate system, and likewise  $a_1$ ,  $a_2$ , and  $a_3$  describe a coordinate system that is

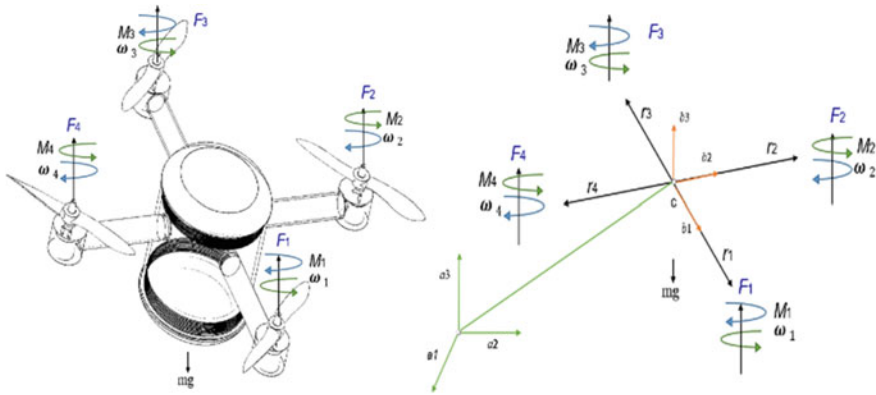


**Fig. 1** Body and inertial coordinate frames

fixed to the inertial frame. The four rotors are each independently actuated. The  $r$  is the position vector of the center of mass.

The axis of the body-fixed frame is indicated as  $x$ ,  $y$ , and  $z$ , and the axis of the rotated frame is indicated as  $X$ ,  $Y$ , and  $Z$ . The geometrical definition produces to explain the line of nodes as the intersection of the planes  $xy$  and  $XY$ . It can also denote as the common perpendicular to the axis  $z$  and  $Z$ , and then drafted the vector product  $Z \times Z$ . Euler angles are used for representing rotations in the  $zxy$ -connection, the first rotation is about the  $z$ -axis to  $\varphi$  [9]. The second one about the  $x$ -axis and the third one about the  $y$ -axis. So, the first axis is yaw, and the second one is rolling, and the third one is the pitch [10]. The first rotation about the  $Z$ -axis through  $\varphi$ , the second rotation about the  $X$ -axis through  $\theta$ , this is the roll angle, and finally, the pitch about the  $Y$ -axis through  $\theta$ .

### 3 Propeller Selection and Performance Study

The propeller assembly is tested to measure the maximum thrust force developed under bollard pull condition. The mechanical setup for thrust measurement is shown in Fig. 2. The motor and propeller are connected to the steel frame at one end, and another end of the frame was attached to the string, and another end of string is connected to the mass  $M$ . The two different sets of motors were selected based on motor  $Kv$  value, and propeller has been chosen based on different lengths and same pitch angle. The thrust measurement is conducted for the aerial and underwater conditions. The hydrophobic coating has been applied to BLDC motor to avoid corrosion. The length of the frame is  $L1 = L2$ .

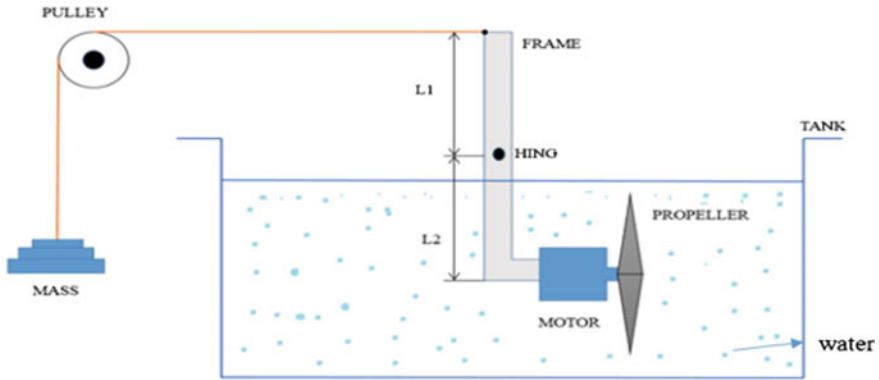


Fig. 2 Mechanical setup for thrust measurement

### 3.1 Propellers and Thrust

The propeller dynamic thrust equation has been used to determine the thrust force in aerial as well as in underwater condition. Assume, air density of  $1.255 \text{ kg/m}^3$ , the “standard” air pressure at sea level and water density  $\rho = 1000 \text{ kg/m}^3$  Static thrust if  $V_0 = 0$ .

$$F = 4.392399 * 10^{-8} * \text{RPM} * \frac{d^{3.5}}{\sqrt{\text{Pitch}}} * (4.23333 * 10^{-4} * \text{RPM} * \text{Pitch} - V_0) \tag{1}$$

where “ $F$ ” is the thrust, “ $d$ ” is the propeller diameter in an inch, RPM is propeller rotations/min,  $V_0$  is the propeller-forward airspeed and pitch is the propeller pitch in an inch.

Designing a vehicle which will carry 3 kg of payload and each motor will carry in one-fourth of weight, and the total thrust needed for four rotors is taken to be twice the weight of your vehicle.

## 4 Design and Fabrication of Vehicle

The vehicle frame is developed based on quadcopter type such as X-frame. This kind of frame has been selected with four arms which are equal in length. The length can vary depending upon maximum payload. Usually, the frame is categorized as a motor to motor distance or diameter of the circular of frame area. This type structure is suitable for the aerial condition, but underwater condition cylindrical shape is suitable to withstand the underwater pressure in 100-m length.

### 4.1 Thickness Calculation of Cylindrical Body

The underwater pressure depends on depth range and the pressure  $P = 10$  bar and seawater condition  $P = 11$  bar in 100 m range. The factor of safety is 1:2 will be considered to take the value of the casing design pressure  $P = 22$  bar. The thickness of the cylindrical body and endcaps are found by using crush depth of simple cylinders and endcaps equation. The length of the X-frame is made up of the cylindrical tube in the acrylic material to withstand the underwater pressure. The length of X-frame is taken from the center of a propeller spinner to the vehicle body.

$$\frac{t}{OD} = \left[ p \left( \frac{1 - \nu^2}{2E} \right) \right]^{\frac{1}{3}} \tag{2}$$

where  $p$  is the pressure, OD is the outer diameter,  $E$  is the elastic modulus,  $\nu$  is the Poisson’s ratio, and  $t$  is the thickness.

The thin cylindrical shape frame or tube is designed by using solid modeling. The frame material is selected based on the lightweight and high strength; it can withstand the working pressure. Acrylic material is chosen as the body material. The isometric view of the 3D model and assembled vehicle are shown in Fig. 3.

The vehicle pressure casing has been designed and fabricated using the acrylic material. The material which can withstand an atmospheric pressure in aerial condition and external pressure in underwater condition maximum 10 bar and to fly in both aerial and underwater conditions up to 100 m. The acrylic components are joined by using an adhesive. In the present case, chloroform is used, and it acts as an adhesive. The O-ring is placed on both endcaps which act as a sealant.

The brushless DC motor and aerial fixed pitch propellers combination have been selected for the quadcopter type vehicle based on the thrust measurement, and each motor is capable of producing a required thrust force for aerial as well as the underwater condition of about the power source of the entire system is using lithium polymer

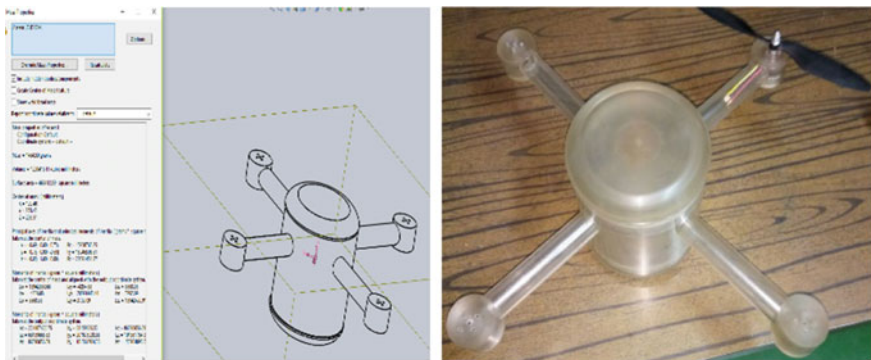


Fig. 3 3D model and assembled vehicle

**Fig. 4** Prototype

battery 5200 mAh and 12 V. The four actuators are controlled by using four electronic speed controllers (ESCs) and flight controllers. The flight controller consists of ardupilot Mega is an open-source UAV platform, and incorporates with sensors and it will be controlled multicopters [11, 12]. The inertial measurement unit (IMU) consists of accelerometer, gyroscope, and magnetometer. The prototype of the entire setup is shown in Fig. 4.

## 5 CFD Analysis of Vehicle

Computational fluid dynamics (CFD) analysis has been performed for both aerial and underwater conditions. Drag is a resistive force acting on a body moving through a fluid. Drag force is determined based on the fluid properties, object size, shape, and speed of the object or velocity of the object. One way to express this is utilizing the drag equation. The drag coefficient  $C_D$  is determined based on the shape of the object and Reynolds number.

$$F_d = \frac{1}{2} \rho V^2 C_D A \quad (3)$$

where  $F_d$  is the drag force,  $\rho$  is the density of the fluid,  $V$  is the speed of the object relative to the fluid,  $A$  is the cross-sectional area, and  $C_D$  is the drag coefficient.

CFD analysis is used to determine the drag force and coefficient of drag. The vehicle will move in that particular axis  $X$ ,  $Y$ , and  $Z$  to simulate in the air and underwater condition to determine the drag value. The vehicle can move in 6 DOF, and the CFD analysis is conducted based on the water condition; the flow velocity of water is 1.54 or 3 knots, and density  $\rho$  of water is  $1000 \text{ kg/m}^3$ . The aerial condition of the flow velocity of air is 2 m/s, the density  $\rho$  of air is  $1.225 \text{ kg/m}^3$ , and area of

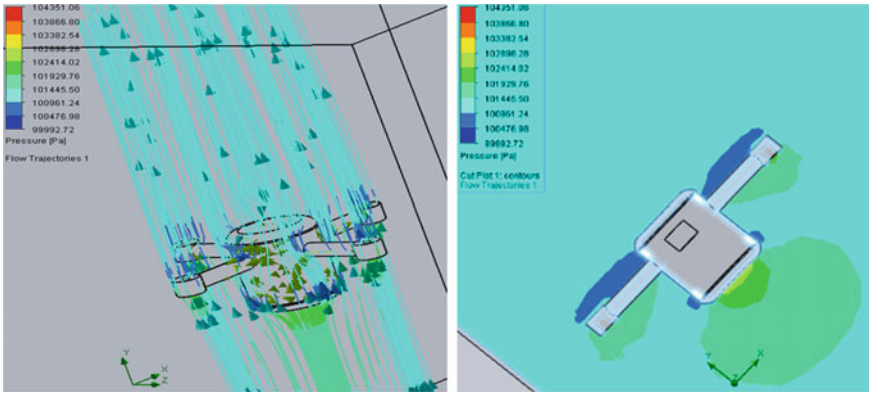


Fig. 5 CFD analysis in water

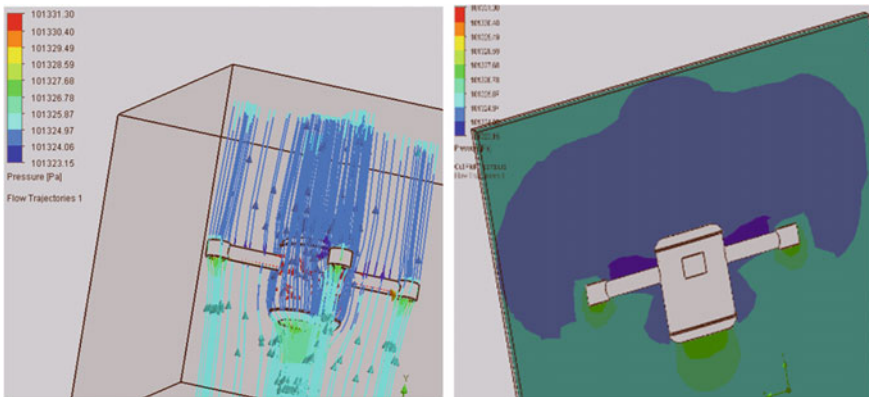


Fig. 6 CFD analysis in aerial

the cross section of a vehicle is 0.233 m. Based on this condition, flow analysis is used to measure the drag force  $F_d$  and drag coefficient  $C_D$  based on the drag equation parameters. The CFD analysis of water and air flow trajectory was in vertical axis are shown in Figs. 5 and 6.

## 6 Performance Test Results

### 6.1 Thrust Measurement

Mechanical setup has been developed to study the thrust force for both aerial and underwater conditions. When the load increases and the current value will also

**Table 1** Aerial condition for thrust measurement

Current (A)	Weight (g)	Propeller (inch)	Motor condition
0.1	40	5 × 4.5	Run
3.4	140	5 × 4.5	Run
5.2	240	5 × 4.5	Run
1.25	40	8 × 4.5	Run
2.15	80	8 × 4.5	Run
5.2	140	8 × 4.5	Run

**Table 2** Underwater condition for thrust measurement

Current (A)	Weight (g)	Propeller (inch)	Motor condition
1.4	40	5 × 4.5	Run
3	240	5 × 4.5	Run
5	340	5 × 4.5	Stop
1.5	40	8 × 4.5	Run
3	140	8 × 4.5	Stop

increase. The thrust force is indirectly estimated based on the added weight (g). The aerial and underwater conditions for thrust values and motor condition are provided in Tables 1 and 2.

The BLDC motor and propeller have been selected based on the experiments. The motor is selected based on low  $K_v$  value for the underwater condition. The aerial fixed pitch propellers have been selected as the propeller length increases and the corresponding thrust force all so increases in the aerial condition. When the aerial propeller length increases, there is a decrease in corresponding thrust force when it is operated in underwater condition using same BLDC motor.

## 6.2 Stress Analysis for Vehicle Body

The design and simulation are carried out using solid works platform as shown in Fig. 7. The pressure force of 1.1 MPa was applied normally on all external surfaces, as seen in was added to the pressure at the design depth of 100 m depth, to account for variations in the hydrostatic pressure. The stress distribution of the cylindrical body and extruder frame is made up of acrylic material. Maximum stresses were below the yield stress of 45 MPa, and there were no pronounced stress concentrations. The underwater condition vehicle can withstand the pressure of 11 bar and apply the pressure to estimate the stress and displacement for the aerial and underwater conditions.



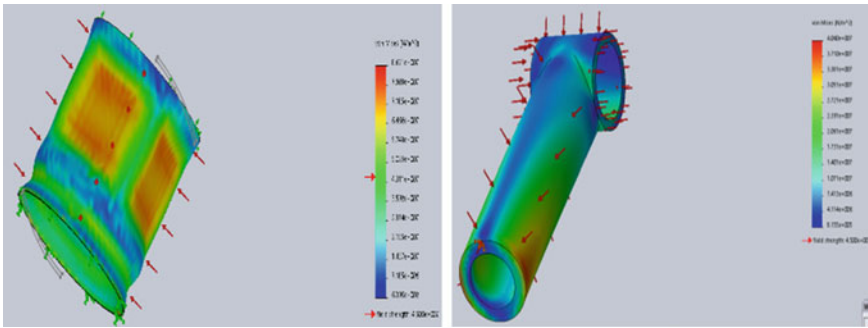


**Fig. 7** Stress analysis for cylindrical body and extruder frame

**Table 3** Drag force in aerial and underwater conditions

Name	Unit	Underwater condition	Aerial condition
Drag force (X)	N	30.297	0.068
Drag force (Y)	N	52.911	0.118
Drag force (Z)	N	34.121	0.064
Coefficient of drag (X)	–	1.155	0.119
Coefficient of drag (Y)	–	0.201	0.208
Coefficient of drag (Z)	–	0.130	0.111

### 6.3 Determining the Drag Force Using CFD Analysis

The drag force and drag coefficient are provided in Table 3. When the drag force is compared to the thrust force and if the thrust force is greater than the drag force for both aerial as well as underwater condition the vehicle can move.

### 6.4 Vehicle Testing Under Underwater and Aerial

The vehicle testing for both static and dynamic conditions in the aerial and underwater environment. The underwater conditions such as buoyancy vehicle, stability, cavitation, and added mass due to the inertia of the surrounding fluid. The experimental results show that the aerial propellers can operate effectively under water at low rotational speed without cavitation, providing enough thrust for the movement and maneuvering with high thrust-to-power ratio in the air. The added mass will affect the vehicle performance in underwater condition. The vehicle body moves in underwater condition at this moment surrounding fluid is quickly moved along with the body. Figure 8 shows the vehicle testing setup in water. The thruster speed will be increased, and the vehicle will be a float, and then it will be fly in aerial condition.

**Fig. 8** Vehicle testing

## 7 Conclusions

The developed underwater and aerial vehicle is capable of operating in air and underwater convertible. The unmanned air and underwater vehicles can be converted to operate under the aerial condition and the same can be controlled in underwater condition up to 100 m of water depth. The motor is selected based on low  $K_v$  value for the underwater condition. When the propeller length increases, the thrust force increases for the aerial condition. The quadcopter type vehicle has been designed and fabricated to withstand a working pressure of 10 bar. The total payload of the vehicle is 3 kg. Each motor is capable of producing a thrust force in aerial as well as underwater condition.

The drag force for the underwater condition has been determined using CFD analysis for 3-knot speed. The maximum value is found to be 52.91 N drag force along the vertical direction. The drag force for the aerial condition has been determined using CFD analysis for 2 m/s speed. The maximum value of the drag force is 0.118 N along the vertical direction. A vehicle performance and change instability have been tested under the static and dynamic conditions in underwater as well as aerial condition. The vehicle is found to be stable and wireless control is working for about 1 m from the surface of the water.

**Acknowledgements** I would like to express my gratitude toward Ministry of Earth Science, Government of India for funding this research. I would like to express my special thanks to the Director of National Institute of Ocean Technology for helped me to do research. The authors are very grateful to Madras Institute of Technology, Anna University for providing the necessary facilities for this study.

## References

1. Bian J, Xiang J, Liang H (2015) A quad rotor-like unmanned underwater vehicle. In: Chinese control and decision conference (CCDC), pp 12–11
2. Anwar BMM, Ajim MA, Alam S (2015) Remotely operated underwater vehicle with surveillance system. In: International conference on advances in electrical engineering (ICAEE), pp 255–258
3. Xiang X, Liu H, Yu C, Niu Z (2016) A newly developed hybrid underwater robotic vehicle (HURV): communication design and tests. In: OCEANS, Shanghai, pp 1–6
4. Tashreef S, Iftekhar L, Azmeen-ur-Rahman S (2016) Design of a crash-resistant PD-controlled quad copter using coaxial propeller system. In: International conference on unmanned aircraft systems (ICUAS), pp 986–992
5. Alzu'bi H, Akinsanya O, Kaja N, Mansour I, Rawashdeh O (2015) Evaluation of an aerial quad-copter power-plant for underwater operation. In: 10th international symposium on mechatronics and its applications (ISMA), pp 1–4
6. Maia MM, Soni P, Diez-Garias FJ (2015) Demonstration of an aerial and submersible vehicle capable of flight and underwater navigation with seamless air-water transition. In: ArXiv: robotics, pp 4–7
7. Emran BJ, Dias J, Seneviratne L, Cai G (2015) Robust adaptive control design for quad copter payload add and drop applications. In: 34th Chinese control conference (CCC), pp 3252–3257
8. Magnussen Ø, Ottestad M, Hovland G (2013) Experimental validation of a quaternion-based attitude estimation with direct input to a quad copter control system. In: International conference on unmanned aircraft systems (ICUAS), pp 480–485
9. Lukmana MA, Nurhadi H (2015) Preliminary study on unmanned aerial vehicle (UAV) quad copter using PID controller. In: International conference on advanced mechatronics, intelligent manufacture, and industrial automation (ICAMIMIA), pp 34–37
10. Tao C, Da X, Jiajia Z, Anzuo J (2016) Observer based 3-D path following control of underactuated underwater vehicle in the presence of ocean currents. In: Chinese control and decision conference (CCDC), pp 5268–5273
11. Zuo M, Xu G, Xiang X, Yu C, Chen Y (2015) Design of a newly developed hybrid underwater robotic vehicle. In: The twenty-fifth international offshore and polar engineering conference, pp 584–589
12. Chirtel E, Knoll R, Le C, Mason B, Peck N, Robarge J, Lewin GC (2015) Designing a spatially aware, autonomous quad copter using the android control sensor system. In: Systems and information engineering design symposium (SIEDS), pp 35–40

# Effect of Rudder and Roll Control Mechanism on Path Prediction of Autonomous Underwater Gliders



R. V. Shashank Shankar and R. Vijayakumar

**Abstract** Autonomous underwater gliders are a class of AUVs that execute motions using change in buoyancy in conjunction with wings. Lack of conventional propeller restricts the speed of the vehicle. Speed of vehicle depends on operation of the buoyancy engine. Gliders follow a saw-tooth profile path and spiral path for undertaking motions in 2D and 3D planes. Traditionally, “legacy gliders” have been using roll and pitch correction mechanisms for conducting the 3D motion. This paper attempts to characterize the mass definitions of one laboratory-based AUG being developed at IIT Madras and predicts the path the glider will execute with participation of roll and pitch correction mechanisms that are being developed. The laboratory-scale gliding fish (small-scale glider) consists of a rudder and a roll control mechanism. The roll control mechanisms consist of movable mass, rotating and traversing about the principal axis of the glider. The effect of rudder and roll control mechanism on the path traversed by glider in 3D steady state is studied individually and in combination by solving the equations of motion using FSOLVE algorithm of MATLAB.

**Keywords** AUG · Underwater glider · Spiral path · Manoeuvrability · FSOLVE  
Robotic fish

## 1 Introduction

Underwater gliders are a class of underwater vehicles that work on principle of change of buoyancy for propulsion. These vehicles do not have an external active propulsion mechanism. The change of buoyancy is actuated by a buoyancy engine (an internal pumping system) which makes the vehicle positively and negatively buoyant. This change in buoyancy converts to vertical translation of the vehicle. In conjunction of wings, this linear translation is converted to forward motion. Commercially available gliders are capable to undertake long-range missions for extended duration of time.

---

R. V. Shashank Shankar (✉) · R. Vijayakumar  
Indian Institute of Technology Madras, Chennai 600036, Tamil Nadu, India  
e-mail: [shashankrayaprou@gmail.com](mailto:shashankrayaprou@gmail.com)

© Springer Nature Singapore Pte Ltd. 2019  
K. Murali et al. (eds.), *Proceedings of the Fourth International Conference in Ocean Engineering (ICOE2018)*, Lecture Notes in Civil Engineering 22,  
[https://doi.org/10.1007/978-981-13-3119-0\\_29](https://doi.org/10.1007/978-981-13-3119-0_29)

They have found broad application in oceanography. Hence a glider does not require extra energy consumption to move horizontally, other than adjusting the buoyancy. As a result, the glider usually follows a saw-tooth motion pattern in the vertical plane and progresses along a straight line in the horizontal plane. The three-dimensional motion of glider is studied by the spiral path traversed by the vehicle in steady state.

The dynamics of an underwater glider driven by a movable internal mass was established by Leonard and Graver [1] and Bhatta and Leonard [2]. The estimation of hydrodynamic coefficients for underwater gliders has been undertaken by many authors. These include Singh et al. [3], S. Zhang et al. [4], and F. Zhang et al. [5]. The authors of these papers formulate a dynamic model of an underwater glider and have undertaken CFD-based estimation of hydrodynamic coefficients for different gliders. Study of spiral path manoeuvres is the topic of interest for this study. The spiralling motion is the outcome of hydrodynamic forces. It is also considered to be energy efficient as it can be used to change the direction of the glider movement under water without motion of the external surface like rudder. The motion can be adjusted by rotating an internal weight like a battery. The study of spiralling motion is complex in nature as it involves a dynamic model and coupled hydrodynamics. This affects the computation of the relationship between inputs that control the motion and the motion itself. The studies made by different authors on this motion are as follows:

- Leonard and Graver [1] established the equations of manoeuvring for buoyancy driven, underwater gliders.
- Bhatta and Leonard [2] brought out the numerical solutions for above equations of spiralling motion.
- Mahmoudian et al. [6] worked on the study of analytical solution of equations developed by Graver using perturbation theory.
- MATLAB-based solution of the equations of motion was undertaken with a Simulink model by Kan et al. [7].
- Modelling and analysis of spiral path were attempted by S. Zhang et al. [4] by translation and rotation of a semi-elliptical mass and calculating the steady-state glide parameters using recursive equation solution. The recursive equations are principally derived from [1].
- A gliding robotic fish and the spiral path manoeuvre of the same were described by F. Zhang et al. [8]. The authors describe a spiralling manoeuvre enabled by a rudder position at the aft of the fish.

In this study, we focus on the equations formulated by F. Zhang et al. [8] and solution of the same is attempted using computation tools of MATLAB. The control inputs are selected as per the study and comparison of the results of the dependent properties of the spiral path, published in [8] and calculated by MATLAB is undertaken. Then, effects of rudder (Tail fin), roll control mass and both on glide parameters such as radius of glide and roll angle of the body are investigated.

The paper is organized in the following way. Section 2 describes the dynamic model used for describing the glider motion and the equations of motion are derived. The hydrodynamic coefficients used are from the earlier work of F. Zhang et al. [8]. Section 3 discusses the solution of equations derived and the validation of the method

used in comparison with the published literature. Section 4 discusses the effect of change in input variables, namely rotatable mass and pitch moment mass. Section 5 provides the conclusion and future work.

## 2 Dynamic Model

The kinematics and dynamics of the motion of underwater glider have been discussed by Leonard and Graver [1]. The dynamics of gliding robotic fish developed by F. Zhang et al. [8] is based on similar lines. We discuss the gliding fish model in the following section. The nomenclature used is presented in Table 1.

### 2.1 Full Dynamic Model

A robotic gliding fish is a miniature underwater glider with an idea of exploring the platform by fitting fins/tails/control planes in future. The tail fin (hereby designated as rudder) is a control surface and one of the sources for forces and moments. The model of the gliding fish is considered as a rigid body which also includes two internal movable masses (one for roll and another for pitch control) and a bladder-type buoyancy engine (which will be studied in future work). The deflected rudder provides forward thrust, side force and yaw moment. Figure 1 shows the reference frames and hydrodynamic forces on the glider, and Fig. 2 shows the mass distribution.

A total of three reference frames are designated, and the body position, velocity and other parameters are defined as per one of these three axes. These are the inertial frame  $I_0$ , the body-fixed frame  $B_0$  and the flow frame  $\pi_0$ . The body-fixed frame ( $B_0$ ) of reference has its origin at the geometry centre of the vehicle.  $Bx_b$  axis is along the

**Fig. 1** Reference frames and hydrodynamic forces on the robotic gliding fish

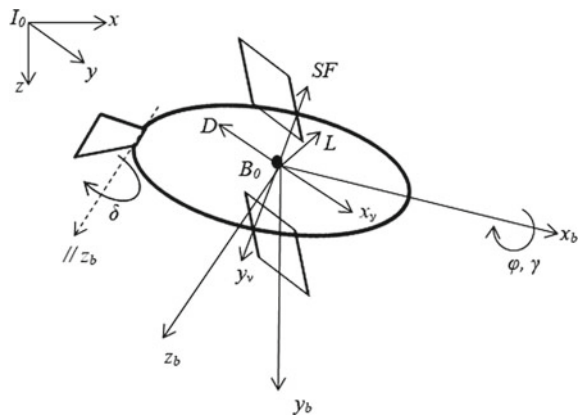


**Table 1** Nomenclature used

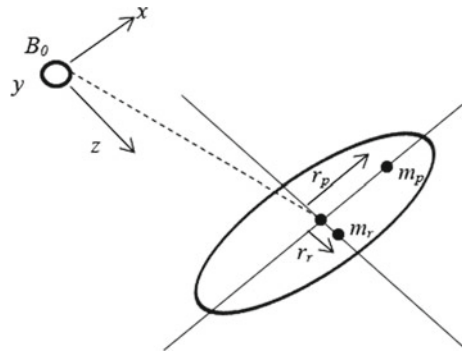
Notation	Description	Notation	Description
$B_0$	Body frame	$r_p$	Position of pitch control mass
$I_0$	Inertial frame	$r_r$	Position of roll control mass
$\pi_0$	Flow frame	$F_{ext}$	Total external force generated by the wings in the flow frame
$V = [V_1, V_2, V_3]^T$	Translational velocity in body frame	$T_{ext}$	Hydrodynamic moments in the flow frame
$\Omega = [p, q, r]^T$	Angular velocity in body frame	$\alpha$	Angle of attack
$b = [x, y, z]^T$	Fish position in inertial frame	$\beta$	Angle of sideslip
$\theta = [p, q, r]^T$	Fish attitude in inertial frame	$\gamma$	Angle executed by roll control mass
$m_s$	Static mass of fish	$\delta$	Angle executed by rudder
$m_h$	Hull mass of fish	$\varphi$	Vehicle roll angle
$m_r$	Roll control mass	$\theta$	Vehicle pitch angle
$m_p$	Pitch control mass	$\psi$	Vehicle yaw angle
$m_b$	Ballast mass of fish	$R_{bf}$	Rotation matrix between body and flow frames
$m$	Mass of the displaced fluid by the fish	$R_{eb}$	Rotation matrix between body and inertial frames
$m_0$	Excess mass	$K_{D0}, K_D^\alpha$	Drag coefficients with respect to $V^2$ and $\alpha V^2$
$M$	Generalized inertial matrix	$K_{SF}^\beta$	Sideforce coefficient with respect to $\beta V^2$
$m_1, m_2, m_3$	Diagonal elements of mass matrix	$K_{SF}^\delta$	Sideforce coefficient with respect to $\delta V^2$
$I_1, I_2, I_3$	Diagonal elements of inertial matrix	$K_{L0}, K_L^\alpha$	Lift coefficient with respect to $V^2$ and $\alpha V^2$
$K_{q1}$	Roll moment coefficient with respect to $V^2$	$K_{M0}$	Pitch moment with respect to $V^2$
$K_{q2}$	Pitch moment coefficient with respect to $V^2$	$M_{MR}^\beta$	Roll moment with respect to $\beta V^2$

(continued)

**Table 1** (continued)

Notation	Description	Notation	Description
$K_{q3}$	Yaw moment coefficient with respect to $V^2$	$M_{MP}^\alpha$	Pitch moment with respect to $\alpha V^2$
$S$	Surface area	$M_{My}^\beta$	Yaw moment with respect to $\beta V^2$
$M_{My}^\delta$	Yaw moment with respect to $\delta V^2$		

**Fig. 2** Mass distribution of the robotic gliding fish



body’s longitudinal axis pointing forward (towards the head of the fish); the  $B_{y_b}$  and  $B_{z_b}$  axes are formed as per the right-hand orthonormal principle and are as shown in Fig. 1. In the inertial frame,  $I_0(xyz)$ ,  $I_0z$  axis is along the gravity direction and  $I_0x/I_0y$  are defined in the horizontal plane and origin is a fixed point in space.

The stationary mass of the robotic gliding fish  $m_s$  comprises of three parts: hull mass  $m_h$ , point mass  $m_r$  used for roll control with displacement  $r_p$  and ballast mass  $m_b$ . Here we assume that the buoyancy engine is positioned and effects of change in buoyancy occur at the origin of body axis (being the CG of the fish). The pitch control mass  $m_p$  is located at  $r_p$  distance from body-fixed axis origin. The pitch control mass provides a moment to the fish. The motion of  $m_p$  is restricted to longitudinal axis and  $m_r$  is restricted to move in  $y_b-z_b$  plane. The robot hull displaces a volume of fluid mass  $m$ . We assume that  $m_0 = m_s + m_p - m$  represents the additional mass (negative net buoyancy). The fish will sink if  $m_0 > 0$  and ascend if  $m_0 < 0$ .

$R$  is the notation used to denote the rotation matrix from the body-fixed axis to the inertial axes. Here, we follow the 3–2–1 intrinsic rotation sequence [insert paper reference].  $R$  is based on three Euler angles: roll  $\phi$ , pitch  $\theta$ , yaw  $\psi$ .

$$R = \begin{pmatrix} \cos \theta \cos \varphi \sin \varphi \sin \theta \cos \psi - \cos \varphi \sin \psi & \cos \varphi \sin \theta \cos \psi + \sin \varphi \sin \psi \\ \cos \theta \sin \psi \cos \varphi \cos \psi + \sin \varphi \sin \theta \sin \psi & -\sin \varphi \cos \psi + \cos \varphi \sin \theta \sin \psi \\ -\sin \theta & \sin \varphi \cos \theta & \cos \varphi \cos \theta \end{pmatrix} \tag{1}$$



The translational velocity of the robotic gliding fish is denoted by  $v_b = (v_1 \ v_2 \ v_3)^T$  and angular velocity by  $\omega_b = (\omega_1 \ \omega_2 \ \omega_3)^T$  in the body-fixed frame. The rudder is assumed to be a rigid body fixed with a pivot at junction at aft of fish. The rudder creates an external thrust force  $F_{\text{ext}}$  on the robot when it moves. The other hydrodynamic forces and moments are created by relative moment between rudder and surrounding water. These are the yaw moments and side forces.

Based on the modelling work undertaken by F. Zhang et al. [9], the dynamic model for robotic gliding fish with deflected tail and roll control mass is as follows:

$$\dot{v}_b = M^{-1}(Mv_b \times \omega_b + m_0g\mathbf{R}^T\mathbf{k} + \mathbf{F}_{\text{ext}}) \quad (2)$$

$$\begin{aligned} \dot{\omega}_b = I^{-1}(-\dot{I}\omega_b + I\omega_b \times \omega_b + Mv_b \times v_b + \mathbf{T}_{\text{ext}} + m_r g \mathbf{r}_r \\ \times (\mathbf{R}^T\mathbf{k}) + m_p g \mathbf{r}_p \times (\mathbf{R}^T\mathbf{k})) \end{aligned} \quad (3)$$

where  $M = (m_s + m_p)I_3 + M_f$ , where  $I_3$  is the  $3 \times 3$  identity matrix, and  $M_f$  is the added mass matrix, calculated using strip theory [10].  $I$  is the sum of the inertial matrix due to the stationary mass and the added inertial matrix.  $\mathbf{k}$  is the unit vector along the  $I_z$  direction in inertial frame.  $\mathbf{r}_r$  is the vector that describes the position of the roll control mass and  $\mathbf{r}_p$  is the pitch control mass vector which moves in  $B_0x_b$  direction.

$\mathbf{F}_{\text{ext}}$  is the sum of all external forces: the external thrust force  $\mathbf{F}_t$  induced by rudder deflection and other hydrodynamic forces like lift, drag and side force acting on the robotic fish.  $\mathbf{T}_{\text{ext}}$  is the hydrodynamic moment caused by  $\mathbf{F}_{\text{ext}}$ .

## 2.2 Hydrodynamic Model (Forces and Moments)

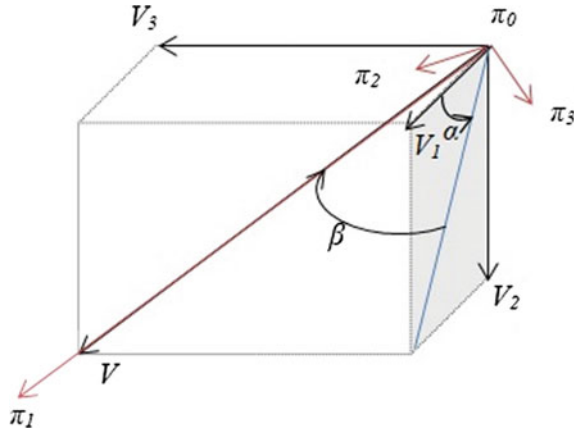
We utilize a rotation matrix  $\mathbf{R}_{bf}$  that represents the rotation operation from the flow reference frame to the body-fixed frame (Fig. 3). The derivation of this rotation matrix is from Euler angle transformation of the order yaw and pitch from fluid frame to body frame. The first transformation gives the matrix

$$\mathbf{R}_{bf}(\text{yaw}) = \begin{pmatrix} \cos(-\beta) & -\sin(-\beta) & 0 \\ \sin(-\beta) & \cos(\beta) & 0 \\ 0 & 0 & 1 \end{pmatrix}$$

$$\mathbf{R}_{bf}(\text{pitch}) = \begin{pmatrix} \cos(\alpha) & 0 & \sin(\alpha) \\ 0 & 1 & 0 \\ -\sin(\alpha) & 0 & \cos(\alpha) \end{pmatrix}$$

The final rotation matrix takes the form

**Fig. 3** Body and flow reference frames of the gliding robotic fish



$$\mathbf{R}_{bf} = \begin{pmatrix} \cos\alpha \cos\beta & -\cos\alpha \sin\beta & -\sin\alpha \\ \sin\beta & \cos\beta & 0 \\ \sin\alpha \cos\beta & -\sin\alpha \sin\beta & \cos\alpha \end{pmatrix} \quad (4)$$

where angle of attack  $\alpha = \tan^{-1}\left(\frac{v_3}{v_1}\right)$  and sideslip angle  $\beta = \sin^{-1}(v_2/\sqrt{v_1^2 + v_2^2 + v_3^2})$ .

The hydrodynamic forces and moments acting on the body are:

$$\text{Lift Force } L = \frac{1}{2}\rho V^2 S(K_{D0} + K_D^\alpha \alpha^2 + K_D^\delta \delta^2) \quad (5)$$

$$\text{Side Force } SF = \frac{1}{2}\rho V^2 S(K_{Fs}^\beta \beta + K_{Fs}^\delta \delta) \quad (6)$$

$$\text{Drag Force } D = \frac{1}{2}\rho V^2 S(K_{L0} + K_L^\alpha \alpha) \quad (7)$$

$$\text{Roll Moment } M_1 = \frac{1}{2}\rho V^2 S(K_{MR}^\beta \beta + K_{q1} \omega_1) \quad (8)$$

$$\text{Pitch Moment } M_2 = \frac{1}{2}\rho V^2 S(K_{M0} + K_{MP}^\alpha \alpha + K_{q2} \omega_2) \quad (9)$$

$$\text{Yaw Moment } M_3 = \frac{1}{2}\rho V^2 S(K_{MY}^\beta \beta + K_{q3} \omega_3 + K_{MY}^\delta \delta) \quad (10)$$

The external forces and moments can now be formulated as per the equations below:

$$\mathbf{F}_{\text{ext}} = \mathbf{R}_{bf} \begin{pmatrix} -D & SF & -L \end{pmatrix}^T \quad (11)$$

$$\mathbf{T}_{\text{ext}} = \mathbf{R}_{bf} \begin{pmatrix} M_1 & M_2 & M_3 \end{pmatrix}^T \quad (12)$$

**Table 2** Values of parameters used in steady-state spiralling equations

Parameter	Value	Parameter	Value
$m_1$	3.88 kg	$K_{q1}$	-0.1 m s/rad
$m_2$	9.9 kg	$K_{q2}$	-0.5 m s/rad
$m_3$	5.32 kg	$K_{q3}$	-0.1 m s/rad
$m_p$	0.8 kg	$I_1$	0.8 kg m <sup>2</sup>
$K_{D0}$	0.45	$I_2$	0.05 kg m <sup>2</sup>
$K_D^\alpha$	17.59 rad <sup>-2</sup>	$I_3$	0.08 kg m <sup>2</sup>
$K_{FS}^\beta$	-2 rad <sup>-1</sup>	$K_{MY}^\beta$	5 m/rad
$K_{FS}^\delta$	1.5 rad <sup>-1</sup>	$K_{MY}^\delta$	-0.2 m/rad
$K_{L0}$	0.075	$K_{MR}^\beta$	-0.3 m/rad
$K_L^\alpha$	19.58 rad <sup>-1</sup>	$K_{MP}^\alpha$	0.57 m/rad
$K_{M0}$	0.0076 m		

As shown in the equations above, the hydrodynamic forces and moments are dependent on the angle of attack  $\alpha$ , the sideslip angle  $\beta$ , the velocity magnitude  $V$  and the rudder angle  $\delta$ .

The other symbols that are used (mentioned in Table 1) are:

- $\rho$  Density of water (taken 1000 kg/m<sup>3</sup>);
- $S$  Frontal cross-sectional area of the robotic gliding fish (characteristic area of the fish taken as 0.012 m<sup>2</sup>);
- $\delta$  Rudder angle defined as angle between longitudinal axis  $B_0x_b$  and centre line of the tail projected into the  $B_0x_b y_b$  plane with  $B_0z_b$  axis as the positive direction.

$K_{q1}, K_{q2}, K_{q3}$  are rotation-damping coefficients. The other constants mentioned in the equations (with ‘K’ in notation) are hydrodynamic coefficients. The values used have been from F. Zhang et al. [8]. The evaluation procedure used by the author is based on computational fluid dynamics (CFD)-based water tunnel simulation. The list of values used in the equations is placed in Table 2.

### 3 Spiralling Motion of the Robotic Gliding Fish

In this section, derivation of the steady-state spiralling equations with control inputs fixed is discussed. The solution of the equations using Newton’s method is described in F. Zhang et al. [8]. In this paper, we use MATLAB’s FSOLVE algorithm for solving the equations.

The parameters for determining the spiralling motion in steady state for an under-water glider like body are described in S. Zhang et al. [4]. The updated parameters for our fish are as follows:

- $V, \alpha, \beta$  describe the velocity of the fish;
- $\omega_{3i}, \varphi, \theta$  describe the angular velocity;
- $r_r, r_p, \gamma$  describe the position of roll and pitch control mass;
- $m_0, R$  are excess mass and turning radius of the spiral;
- $\delta$  Rudder angle.

We designate four control variables (used as inputs) to influence the motion profile of the fish; excess mass  $m_0$ , position of pitch control mass  $r_p$ , angle of roll control mass  $\gamma$  and rudder angle  $\delta$ .

### 3.1 Spiralling Equations

The steady-state linear motion has been discussed in Leonard and Graver [1]. Here, we analyse the steady-state motion where yaw angle changes at a constant rate while pitch and roll angles are constant. This implies that the rotation matrix  $\mathbf{R}^T \mathbf{k}$  is constant as

$$\mathbf{R}^T \mathbf{k} = \mathbf{R}^T \begin{pmatrix} 0 \\ 0 \\ 1 \end{pmatrix} = \begin{pmatrix} -\sin\theta \\ \sin\varphi \cos\theta \\ \cos\varphi \cos\theta \end{pmatrix} \tag{13}$$

Taking derivative with respect to time of  $\mathbf{R}^T \mathbf{k}$ , we get

$$\omega_b \times (\mathbf{R}^T \mathbf{k}) = 0 \tag{14}$$

From this, we get that the angular velocity has a single degree of freedom with angular amplitude  $\omega_{3i}$  in the  $B_{0z}$  direction in the inertial frame. Hence

$$\omega_b = \omega_{3i} (\mathbf{R}^T \mathbf{k}) \tag{15}$$

The other important variables of the robot’s motion can be now expressed in the body-fixed frame of reference as

$$\mathbf{v}_b = \mathbf{R}_{bf} (V \ 0 \ 0)^T \tag{16}$$

Two central parameters in the spiralling motion: the turning radius  $R$  and the vertical speed  $V_{\text{vert}}$ . By projecting the trajectory of fish into horizontal plane and velocity into vertical direction, we get the values for turning radius and vertical speed

$$R = V \cos(\theta - \alpha) / \omega_{3i} \tag{17}$$

$$V_{\text{vert}} = V \sin(\theta - \alpha) \tag{18}$$

By equating time derivatives to zero in Eqs. (2) and (3), we get the steady-state spiralling equations

$$0 = (M v_b \times \omega_b + m_0 g \mathbf{R}^T \mathbf{k} + \mathbf{F}_{\text{ext}}) \quad (19)$$

$$0 = -\dot{I} \omega_b + I \omega_b \times \omega_b + M v_b \times v_b + \mathbf{T}_{\text{ext}} + m_r g \mathbf{r}_r \times (\mathbf{R}^T \mathbf{k}) \\ + m_p g \mathbf{r}_p \times (\mathbf{R}^T \mathbf{k}) \quad (20)$$

The independent states for describing the steady spiral motion:  $(\theta \ \varphi \ \omega_{3i} \ V \ \alpha \ \beta)$  are obtained from expansion of Eqs. (1), (4), (15) and (16). Further, we expand Eqs. (2) and (3) to get steady-state non-linear equations as shown below:

$$0 = m_2 \sin \beta \ V \ \cos \varphi \ \cos \theta \ \omega_{3i} - m_3 \sin \alpha \ \cos \beta \ V \ \sin \varphi \ \cos \theta \ \omega_{3i} - m_0 \ g \ \sin \theta \\ + L \ \sin \alpha - SF \ \cos \alpha \ \sin \beta - D \ \cos \alpha \ \cos \beta \quad (21)$$

$$0 = -m_3 \sin \alpha \ \cos \beta \ V \ \sin \theta \ \omega_{3i} - m_1 \ \cos \alpha \ \cos \beta \ V \ \cos \varphi \ \cos \theta \ \omega_{3i} - D \ \sin \beta \\ + SF \ \cos \beta + m_0 \ g \ \sin \varphi \ \cos \theta \quad (22)$$

$$0 = m_1 \ \cos \alpha \ \cos \beta \ V \ \sin \varphi \ \cos \theta \ \omega_{3i} + m_2 \ \sin \beta \ V \ \sin \theta \ \omega_{3i} - D \ \sin \alpha \ \cos \beta \\ - SF \ \sin \alpha \ \cos \beta - L \ \cos \alpha + m_0 \ g \ \cos \varphi \ \cos \theta \quad (23)$$

The above three Eqs. (21)–(23) constitute the force balance equations. The moment balance equations are as follows:

$$0 = (I_2 - I_3) \sin \varphi \ \cos \theta \ \cos \varphi \ \cos \theta \ \omega_{3i}^2 + (m_2 - m_3) \sin \beta \ \sin \alpha \ \cos \beta \ V^2 \\ - \frac{1}{2} \rho V^2 S (K_{M0} + K_{MP}^\alpha \alpha + K_{q2} \sin \varphi \ \cos \theta \ \omega_{3i}) \cos \alpha \ \sin \beta + \frac{1}{2} \rho V^2 S (K_{MR}^\beta \beta \\ - K_{q1} \omega_{3i} \sin \theta) \cos \alpha \ \cos \beta - \frac{1}{2} \rho V^2 S (K_{MY}^\beta \beta + K_{q3} \omega_{3i} \cos \varphi \ \cos \theta + K_{MY}^\delta \delta) \sin \alpha \\ - m_r g r_r \cos \gamma \ \cos \theta \ \sin \varphi + m_r g r_r \cos \varphi \ \cos \theta \ \sin \gamma \quad (24)$$

$$0 = (I_1 - I_3) \sin \theta \ \cos \varphi \ \cos \theta \ \omega_{3i}^2 + (m_3 - m_1) \cos \alpha \ \cos \beta \ \sin \alpha \ \cos \beta \ V^2 \\ - m_r g r_r \cos \gamma \ \sin \theta - m_p g r_p \cos \varphi \ \cos \theta + \frac{1}{2} \rho V^2 S (K_{MR}^\beta \beta - K_{q1} \omega_{3i} \sin \theta) \sin \beta \\ + \frac{1}{2} \rho V^2 S (K_{M0} + K_{MP}^\alpha \alpha + K_{q2} \sin \varphi \ \cos \theta \ \omega_{3i}) \cos \beta \quad (25)$$

$$0 = (I_2 - I_1) \sin \theta \ \sin \varphi \ \cos \theta \ \omega_{3i}^2 + (m_1 - m_2) \cos \alpha \ \cos \beta \ \sin \beta \ V^2 + m_p g r_p \sin \varphi \ \cos \theta \\ - \frac{1}{2} \rho V^2 S (K_{M0} + K_{MP}^\alpha \alpha + K_{q2} \sin \varphi \ \cos \theta \ \omega_{3i}) \sin \alpha \ \sin \beta + \frac{1}{2} \rho V^2 S (K_{MR}^\beta \beta \\ - K_{q1} \omega_{3i} \sin \theta) \sin \alpha \ \cos \beta + \frac{1}{2} \rho V^2 S (K_{MY}^\beta \beta + K_{q3} \omega_{3i} \cos \varphi \ \cos \theta + K_{MY}^\delta \delta) \cos \alpha \\ + m_r g r_r \sin \gamma \ \sin \theta \quad (26)$$

The above equations, mass matrix and inertial matrix are having the following form:

$$M = \begin{pmatrix} m_1 & 0 & 0 \\ 0 & m_2 & 0 \\ 0 & 0 & m_3 \end{pmatrix} \tag{27}$$

$$I = \begin{pmatrix} I_1 & 0 & 0 \\ 0 & I_2 & 0 \\ 0 & 0 & I_3 \end{pmatrix} \tag{28}$$

### 3.2 Program Algorithm

Equations (21)–(26) are solved by using FSOLVE method in MATLAB. A code was formulated and written for this purpose. The algorithm uses Levenberg–Marquardt and trust-region methods for the solution of non-linear equations. It is an iterative method which gives the roots of equations. More information on the algorithm can be obtained from [11]. In our program, we solve the six equations for six unknowns ( $\theta \ \varphi \ \omega_{3i} \ V \ \alpha \ \beta$ ).

## 4 Results and Discussion

### 4.1 Validation

Series of iterations were run using the code for solving Eqs. (21)–(26). The control inputs were varied initially to validate with the results published by F. Zhang et al. [8]. The results are placed at Figs. 4 and 5.

In Fig. 4, the blue plot indicates the values of radius as published by F. Zhang et al. [8] and the red plot indicates values calculated by FSOLVE algorithm. Both the plots have matching values at lower angles and at higher angles ( $50^\circ$  and more) of rudder, the variation is about 0.124 m at  $\delta = 60^\circ$ .

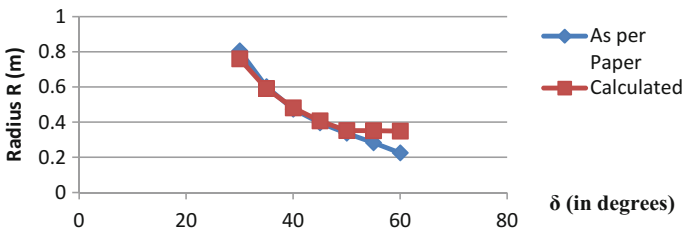
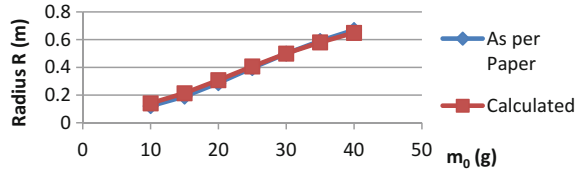


Fig. 4 Variation of radius of spiral path with varying rudder angle ( $\delta$ )

**Fig. 5** Variation of radius of spiral path with varying excess mass ( $m_0$ )



Then the excess mass ( $m_0$ ) has been varied while keeping the rudder angle constant at  $45^\circ$ , and radius of spiral path has been plotted in Fig. 5. The blue plot indicates the values of radius as published by [8] and the red plot indicates values calculated by FSOLVE algorithm. There is a close match between both the plots. This gives us a sureness regarding the applicability of the algorithm for understanding the effects of both rudder and roll control mass. (For validation purpose, the roll control mass was kept at  $\gamma = 0^\circ$ ).

#### 4.2 Results for Varying Rudder Angle ( $\delta$ ) with a Constant Roll Control Mass Angle $\gamma = 0$

Code for solving Eqs. (21)–(26) was run for finding the radius of spiral executed by the fish for different rudder angles. The same is plotted in Fig. 6. The figure brings out the direction and radius of the spiral path executed by the fish for two different rudder angles ( $\delta = 10$  and  $-10^\circ$ ) with rotatable mass (or roll control mass) kept at zero-degree position ( $\gamma = 0^\circ$ ). The  $z$ -axis represents depth, with the gliding fish starting from the surface and executing a downward spiral. For these two rudder angles, the glider executes two opposite spirals.

Figure 7 brings out variation in the radius of the spiral path ( $R$  plotted on  $y$ -axis) executed by the fish for varying rudder angle (from  $\delta = -40$  to  $+40^\circ$ , plotted on  $x$ -axis) and rotatable mass kept at zero-degree position ( $\gamma = 0^\circ$ ). It is observed that as rudder angle increases, there is a sharp decrease in radius of the spiral at higher angles and as the angle magnitude increases, the decrease in radius diminishes. The same is observed for both sides of rudder action (positive and negative).

Similarly, Fig. 8 brings out variation in the roll angle of the fish ( $\varphi$  as plotted on  $y$ -axis) for varying rudder angle (from  $\delta = -30$  to  $+30^\circ$  as plotted on  $x$ -axis) with rotatable mass kept at zero-degree position ( $\gamma = 0^\circ$ ). It is observed that roll angle increases in the negative direction as rudder angle executed increases in the positive direction (as per sign convention discussed) i.e., roll angle is executed in the opposite direction to the direction of rudder.

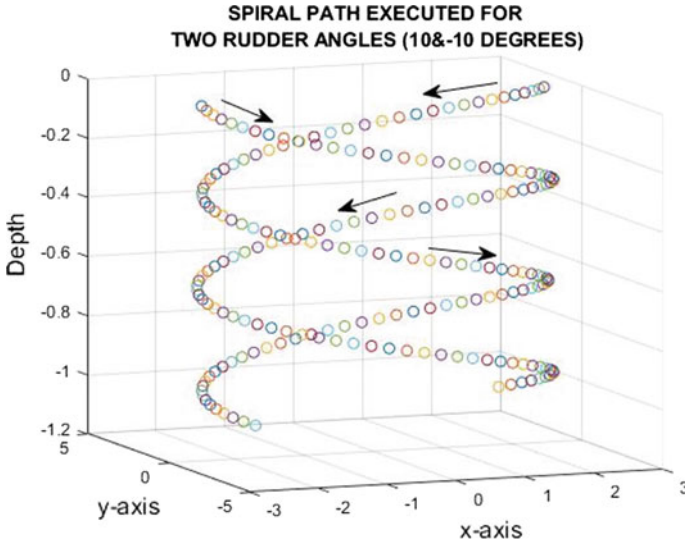
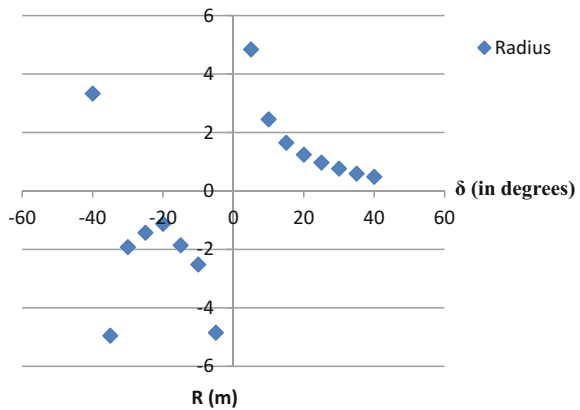


**Fig. 6** Spiral path executed by the fish for two different rudder angles ( $\delta = 10$  and  $-10^\circ$ )

**Fig. 7** Variation in the radius of the spiral path executed by the fish for varying rudder angle (from  $\delta = -40$  to  $+40^\circ$ )



### 4.3 Results for Varying Roll Control Mass Angle ( $\gamma$ )

The MATLAB code is run with the control input of rudder  $\delta$  set at a  $30^\circ$  angle and  $\gamma$  varied from  $0$  to  $360^\circ$ . The roll angle of the fish ( $\varphi$ ) and radius of the spiral path executed by the fish ( $R$ ) are plotted. Figure 9 brings out the  $\varphi$  and  $R$  variation from  $-45$  to  $+45^\circ$ . Here  $R$  (in metres) is plotted on vertical on left and roll angle  $\varphi$  (in degrees) is plotted on vertical axis on right.  $\gamma$  (in degrees) is plotted on horizontal axis. Also shown in the figures is the position of variation of roll control mass from  $-45$  to  $+45$  as seen from aft of the fish. Figure 10 plots the  $\varphi$  and  $10R$  variation from  $185$  to  $225^\circ$  and the respective position of roll control mass seen from aft of fish.  $10R$



**Fig. 8** Variation in the roll of the fish for varying rudder angle (from  $\delta = -30$  to  $+30^\circ$ )

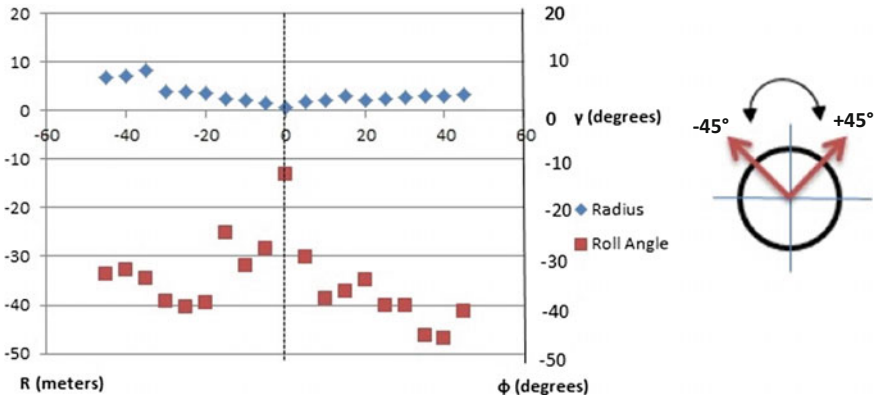
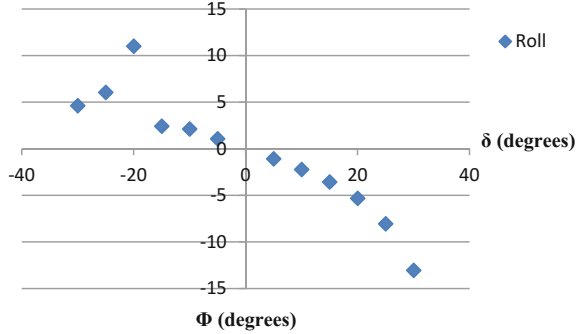


**Fig. 9** The graph (on the left) brings out the variation of roll angle  $\phi$  and radius of spiral path  $R$  for varying roll control mass angle  $\gamma$  (from  $-45^\circ$  to  $+45^\circ$ ) at a constant rudder angle ( $\delta = 30^\circ$ ). The picture on right shows the position of roll control mass as seen from aft of the fish

(in metres) is plotted on vertical axis on left and roll angle  $\phi$  (in degrees) is plotted on vertical axis on right.  $\gamma$  (in degrees) is plotted on horizontal axis.

It can be observed in both cases that a near reflection occurs in behaviour of the both parameters at  $0^\circ$  and  $180^\circ$  (in Figs. 9 and 10, respectively). The radius of the glide path is found to be minimum when roll control mass is at zero degree. Any deviation from this position (with rudder acting) will lead to an increase in the roll of the body and also the radius of the spiral executed by the fish during the glide. Further, from the study undertaken for roll control mass varied from 0 to 360, it is observed that the behaviour of fish at multiples of  $90^\circ$  ( $90, 180$  and  $270$ ) cannot be effectively calculated as the ‘‘Gimbal Lock’’ comes into play. This can be avoided by taking the quaternions approach rather than the Euler angles approach. Additional study on this issue is planned to be undertaken in future work.

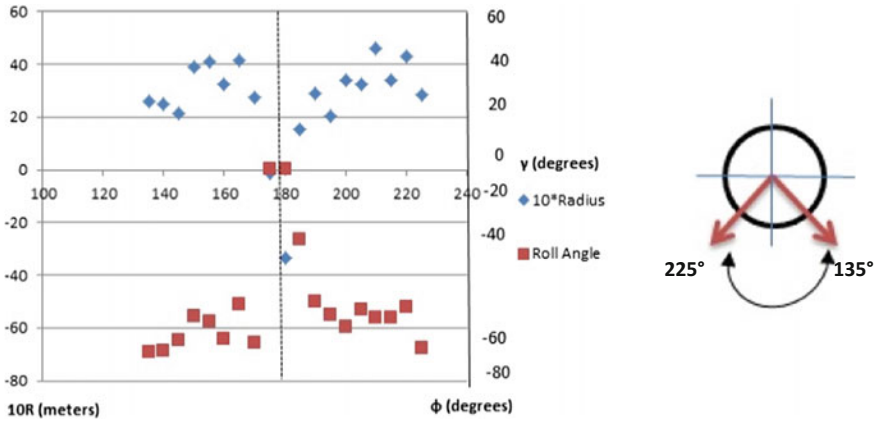


**Fig. 10** The graph brings out the variation of roll angle  $\phi$  and radius of spiral path  $R$  for varying roll control mass angle  $\gamma$  (from  $185^\circ$  to  $225^\circ$ ) at a constant rudder angle ( $\delta = 30^\circ$ ). The picture in the right shows the position of roll control mass as seen from aft of the fish. Here  $10R$  (in metres) is plotted on vertical axis on left and roll angle  $\phi$  (in degrees) is plotted on vertical axis on right.  $\gamma$  (in degrees) is plotted on horizontal axis

### 5 Conclusion and Future Work

In this paper, a dynamic model of a robotic gliding fish is discussed and formulated. The numerical model consists of a tail rudder and a roll control mass acting in combination and effect of same on roll of the body of robot and radius of the spiral path executed is studied. Derivation of motion equations has been discussed and programs have been written for same. All calculations are based on steady-state conditions. The results of MATLAB program (using FSOLVE algorithm) has been validated with the published result for effect of rudder angle. Then effect of rudder and combination of rudder and roll control mass has been observed on the spiral path of the fish. Study of effect of rudder and roll control mass in separation has been studied before but combination of same together has not been undertaken before.

The results achieved are

- Radius of spiral path executed by gliding fish reduces with increase in rudder angle (from zero position).
- The vehicle executes a roll angle which is opposite to the angle of turn executed by rudder.
- When participation of roll control mass is included with rudder, the radius of glide is minimum when roll control mass is at zero-degree position.
- Radius of spiral path and roll of body show near mirror image for the position of roll control mass kept at  $0^\circ$  and  $180^\circ$ .
- Gimbal lock effect is seen when calculating the fish parameters using Euler angles at multiples of  $90^\circ$ .

In future, it is aimed to design and model a laboratory-scale underwater gliding robotic fish with controllable rudder and internal roll and pitch mechanisms. The robot is planned to be run on a Raspberry Pi system computer with LabVIEW software of National Instruments at the heart. Study of manoeuvrability characteristics of the robotic gliding fish will be attempted to achieve minimal turning radius with the combined effect of wings, rotatable mass and rudder.

**Acknowledgements** The authors acknowledge the information shared by Dr. Feitian Zhang, Assistant Professor, George Mason University, Fairfax.

## References

1. Leonard NE, Graver JG (2001) Model-based feedback control of autonomous underwater gliders. *IEEE J Ocean Eng* 26(4):633–645. <https://doi.org/10.1109/48.972106>
2. Bhatta P, Leonard NE (2008) Nonlinear gliding stability and control for vehicles with hydrodynamic forcing. *Automatica* 44(5):1240–1250
3. Singh Y, Bhattacharyya S, Idichandy V (2017) CFD approach to modelling, hydrodynamic analysis and motion characteristics of a laboratory underwater glider with experimental results. *J Ocean Eng Sci*. <https://doi.org/10.1016/j.joes.2017.03.003>
4. Zhang S, Yu J, Zhang A, Zhang F (2013) Spiraling motion of underwater gliders: modeling, analysis, and experimental results. *Ocean Eng* 60:1–13. <https://doi.org/10.1016/j.oceaneng.2012.12.023>
5. Zhang F, Zhang F, Tan X (2012) Steady spiraling motion of gliding robotic fish. In: *IEEE international conference on intelligent robots and systems*, pp 1754–1759. <https://doi.org/10.1109/iros.2012.6385860>
6. Mahmoudian N, Geisbert J, Woolsey C (2010) Approximate analytical turning conditions for underwater gliders: implications for motion control and path planning. *IEEE J Ocean Eng* 35(1):131–143. <https://doi.org/10.1109/JOE.2009.2039655>
7. Kan L, Zhang Y, Fan H, Yang W, Chen Z (2007) MATLAB-based simulation of buoyancy-driven underwater glider motion. *J Ocean Univ China* 7(1):113–118. <https://doi.org/10.1007/s11802-008-0113-2>
8. Zhang F, Zhang F, Tan X (2014) Tail-enabled spiraling maneuver for gliding robotic fish. *J Dyn Syst Meas Control* 136(4):41028. <https://doi.org/10.1115/1.4026965>
9. Zhang F, Thon J, Thon C, Tan X (2014) Miniature underwater glider: design and experimental results. *IEEE/ASME Trans Mechatron* 19(1):394–399. <https://doi.org/10.1109/TMECH.2013.2279033>
10. Milgram JH (2007) Strip theory for underwater vehicles in water of finite depth. *J Eng Math* 58(1–4):31–50. <https://doi.org/10.1007/s10665-006-9101-y>
11. FSOLVE algorithm information in MATLAB website. <http://www.mathworks.com/help/optimg/ug/fsolve.html>

# Development of Controller for Robotic Fish



M. P. R. Prasad and A. M. R. B. Aminur

**Abstract** Fish Robot can be used in numerous applications nowadays, and hence, they are gaining popularity in research in today's world. Here, in this paper mathematical modeling of a fish robot with four degrees of freedom is presented. Controlling of the kinematics and the dynamics of it using a robust control strategy is proposed. The swimming motion of a fish Robot, which is inspired by motion of a tuna fish, has been considered. It needs to generate an undulatory motion with the help of its tail peduncle and caudal fin, which means that the dynamics of it is unstable and have nonlinear properties. A few of the existing control strategies for the same are also presented for its motion control and stabilization. The control schemes are developed as per its specific design. The comparative study of result shows a significant improvement with this control strategy over previous others. It is observed that its performance is better with this robust control method.

**Keywords** Fish robot · Robust control · Sensitivity · Stability

## 1 Introduction

The sea is a source of vast resources, even though in this age of advanced science and technology there are still numerous untapped resources that are available beneath the sea, this fact raised a lot of interest in underwater research. As it is known fact that, it is highly impossible for mankind to reach every part of this vast underwater area, so developing an underwater vehicle, underwater robot or a fish robot is the alternate option. As the operation under the sea, viz. supervision, observation of aquatic life, pollution observation and controlling measures, military detection, are some of examples that puts a demand for the development of underwater robots,

---

M. P. R. Prasad (✉) · A. M. R. B. Aminur  
NIT Kurukshetra, Kurukshetra, India  
e-mail: [mprp823@gmail.com](mailto:mprp823@gmail.com)

A. M. R. B. Aminur  
e-mail: [aamin.hcl@gmail.com](mailto:aamin.hcl@gmail.com)

© Springer Nature Singapore Pte Ltd. 2019  
K. Murali et al. (eds.), *Proceedings of the Fourth International Conference in Ocean Engineering (ICOE2018)*, Lecture Notes in Civil Engineering 22,  
[https://doi.org/10.1007/978-981-13-3119-0\\_30](https://doi.org/10.1007/978-981-13-3119-0_30)

507

which is capable enough to replace humans or at least perform the necessary. But, an underwater vehicle might look like a threat to underwater creatures, and hence a fish robot, the bio-inspired robots are better option. Since, the Fish Robot looks like a normal fish but works as per our requirement to provide us with requisite important information. This is the reason due to which advanced types of fish robots and advanced control strategies are being developed. As it is known that, these fish robots generally possess nonlinear and unstable in nature, the dynamics and the kinematics of them are critical. Thus, proper and appropriate control strategies are to developed. An attempt for the same is made in this paper. The control of a Fish Robot in such a constrained aquatic environment is always a significant challenge, and designers are to take care of all odds due to this fact [1]. The hydrodynamic forces acting on the motion of a Fish Robot are critical, the contain nonlinearity and mostly drawing the system to unstable state. Also, it is generally difficult to measure all the parameters without facing that exact aquatic environment in practical, hence four degrees of freedom are considered while developing the Fish Robot.

Here the motion equations are represented as per axes so as to manage all four degrees of freedom, and they vastly depend on the fish geometry, i.e., its hydrodynamics and kinematics, and they mostly remain constant when fish orientation is as per global coordinate changes.

Figure 1 shows a typical Robotic Fish.

With these three degrees of freedom, rotational motions in all axes usually called surge, sway and heave are obtained. These three are just as similar as roll, pitch, and yaw. The orientation of the body coordinate with respect to the global axes is set as per described by its Euler Angles, i.e., yaw, pitch, and roll. An intelligent Fish Robot generally exhibits three major functions, viz. guidance, control, and navigation.

Till now many types of Fish Robots or sometimes underwater vehicles are being developed in many research laboratories and universities. Fish robots which can

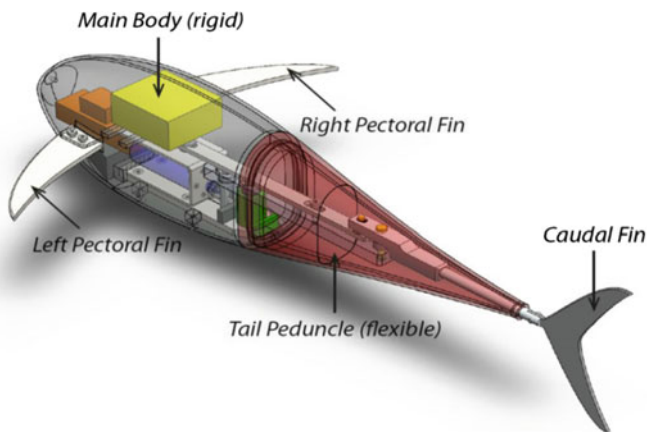


**Fig. 1** Computer-aided design of a typical Fish Robot with various functioning parts [11]

also help a lot in underwater research without being a threat to aquaculture. The spherical underwater vehicles are generally propelled by water-jet Motors. A smooth spheroidal body can show considerably good enough hydrodynamic behaviors, but for quick and smooth maneuvering during low speeds, sometimes they may not perform well enough. Thus, a well-controlled automated Fish Robot is always a better option.

The munk moment helps to make an orientation perpendicular to flow stream for a smooth, elongated fish robot. In a marine environment, bio-inspired Fish Robots could be highly efficient, maneuverable and noiseless. For example, propulsion systems for few types of bio-inspired Fish Robots achieve high efficiency. On the other hand, existing fish robots also shows deficiency in their swimming behavior as well. Fish Robots are designed to perform a specific way swimming. For example, some are designed to swim with the help of their tail undulation, while others to swim with the help of their pectoral fins. Both of these type exhibit different performances, one is efficient for cruising long distances; on the other hand other is for hovering around and slow swimming. It is basically a problem because for the navigation of a large distance Fish Robot needs to be acquainted with both of the abilities, i.e., swimming and hovering [2].

To overcome above problem, a novel fish robot has to be designed which is capable of exploiting different swimming ways. So, designing a new fish robot is required, but swimming behavior of a Fish Robot requires critical analytical modeling, which is necessary for the analysis of their swimming behavior and to improve their respective performance. The modeling of a Fish Robot is a challenging task due to its complication in interacting with fluid environment, and it requires healthy knowledge regarding computational fluid dynamics (CFD). Implementation of CFD in modeling of swimming motion can be studied [3–5]. But on the contrary, this method of CFD cannot be employed for control and optimization purposes. Thus besides CFD, mechanical approaches based modeling are also tried. Lighthill [6, 7] and Wu [8] are prime example of those. Lighthill [6, 7] also presented the Elongated Body Theory (EBT) which has got crucial applications in designing of many modern Fish Robots. The structure of the paper as follows. Section 1 is about introduction. Modeling aspects are explained in Sect. 2. Existing controlling methods details are given in Sect. 3. Proposed control technique is presented in Sect. 4. Conclusions are highlighted in Sect. 5.

## 2 Fish Robot Modeling

A basic Fish Robot can be modeled mathematically by the following two approaches.

**Dynamic Modeling Approach** The dynamic modeling takes consideration of all actual forces, resulting motion and dynamic constraints. The equations for both translational motion and rotational motion are established with the help of Newton–Euler’s equation for rigid body in a flow. Three Dimensional equations of motion

for a hydrodynamically balanced Fish Robot using a body-fixed coordinate frame and a global reference frame. The equations of motion of Fish Robot are represented in two coordinate systems and can be written as [1].

**Kinematic Modeling Approach** For the Fish Robot, reference frame and Euler angles along with their requisite state space representations are explained from its Kinematics. Here for the Fish Robot, two basic reference frames are considered, viz. body-fixed reference frame and Earth-fixed reference frame. The Earth-fixed reference frame means its coupling is with respect global axes at any place, where north is pointed by the  $x$ -axis, east by  $y$ -axis, the  $z$ -axis refers Earths center. Similarly, the body of the Fish Robot is coupled with its own reference axes, forward direction is pointed in  $x$ -axis, the right of it is in  $y$ -axis and vertical down with  $z$ -axis. With those reference frames one can easily determine the orientations of Fish Robot with respect to the Earth axis, and hence it helps to determine the movement characteristics, velocity, acceleration, etc. in reference with the Earth-Coordinates and vehicle-coordinates, which are generally used for the Fish Robot navigations. When we need any orientation from a coordinate system to other one, it is sometimes required all three rotational sequences, and  $z$ - $y$ - $x$  convention for coordinates of earth is described from Euler Coordinate conventions whenever it is necessary. The modeling and analysis of Fish Robot are carried out in state space representation since it gives a convenient, easy and compact way of modeling. Translational velocity and Rotational velocity between Body-fixed frame and Earth-fixed frame are related with the help of coordinate transformation [9].

**Autonomous Fish Robot Controlling** The Fish Robot is capable of performing numerous underwater ventures viz. surveying of seafloor, cable inspections and sensing in oceanic environment, underwater pollution inspection, and aquatic life survey, etc. Further with addition of sensing modules and robotic hands like parts in the fish itself that comes out only when it is required just like wheels in flights we can do few more extra tasks with it, viz. petroleum drilling stations underwater parts maintenance, underwater rescue, seabed fuel inspection, etc., can also be performed. All such applications require precise, accurate and strict positioning of the robot, and it requires to exert adequate forces for the same. Dynamics of Fish Robot are time variant as well as nonlinear which means there may be changes in mass and buoyancy in accordance with different working conditions. There can also be numerous uncertain disturbances from outside environment and there can be difficulty in controlling the hydrodynamic forces. This in turn makes controlling of the Fish Robot as a very difficult as well as a challenging task.

Here, undulatory motion of a basic tuna fish is considered, since its geometry and mechanism plays a vital role in its efficient cruising. Its tail mechanism is mainly responsible for generating this undulatory motion. We can observe its functioning in UC-Ika, a tuna-mimetic robot. This UC-Ika has significant benefit of its unique tail mechanism, so we considered it to implement a better control strategy to this. Although it is much more complicated compared to others robots of such kind, but its mechanism is very similar to a typical fish [10]. The link mechanism of the tail

peduncle of UC-Ika is considered, which consists of three links. All those links are typically internally linked and their actuation is provided by only single DC motor which is connected to the Link-1. This means, only Link-1 is provided with oscillatory motion and it in turns actuates other two links as they are typically internally linked.

A schematic fish robot is shown in Fig. 2.

The kinematics of it is modeled by analyzing the behavior about point  $F$  with regard to fixed frame (reference), and the performance of the robot swimming is analyzed with respect to main reference frame. Now, Consider Fig. 2, all the mathematical calculations were done. The mathematical relations obtained are discussed as follows, actuation angle,  $\theta_1$  is provided by a DC motor and it is calculated as

$$\theta_1 = A \sin(2\pi ft) \tag{1}$$

where  $A$  is the amplitude,  $f$  is the frequency and  $t$  is the time, and the design will result  $\theta_3$  become

$$\theta_3 = \lambda\theta_1 \tag{2}$$

The value of  $\lambda$  is dependent on the lengths of links of the various parts of fish-tail mechanism, that includes  $\overline{DE}$ ,  $\overline{OB}$ ,  $\overline{BC}$ ,  $\overline{EC}$ , and  $\overline{CF}$ . The four degrees of freedom for this model will be  $X$ ,  $Y$ ,  $\Phi$ , and  $\theta_4$ ,  $X$  is translation in  $X$  direction,  $Y$  is translation in  $Y$  direction, the  $\Phi$  will be rotation around the center of mass of the robot and  $\theta_4$  will be the rotation of the caudal fin. From all the calculations, the resultant velocity about point  $G$ , which is defined as  $U$  will be expressed as

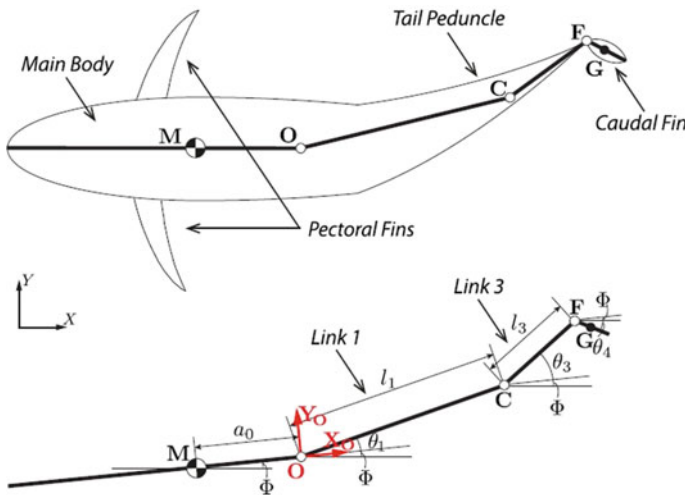


Fig. 2 A schematic diagram of UC-Ika 1 [11]



$$U = (\dot{X}_G^2 + \dot{Y}_G^2)^{0.5} \quad (3)$$

Here, movement of point  $F$ , with respect to the corresponding reference frame is considered. Performance of Fish robot is analyzed with respect to the absolute body reference frame. The various hydrodynamic forces are considered on the basis of following assumptions [11].

- Rotation of the main body considered as negligible.
- The caudal fin is exerting all the propulsion.
- The fluid viscosity is zero or it has negligible effect on Fish Robot.

From all mathematical relations, the final four motion equations for Fish Robot are obtained as

$$M\ddot{X} = F_{Cx} - F_{Dx} \quad (4)$$

$$M\ddot{Y} = F_{Cy} - F_{Dy} \quad (5)$$

$$I_M\ddot{\Phi} = (X_G - X)F_{Cy} - (Y_G - Y)F_{Cx} - M_{Dp} \quad (6)$$

$$I_c\ddot{\theta}_4 = (X_G - X)F_{Cy} - (Y_G - Y)F_{Cx} - k(\theta_4 - \theta_3) \quad (7)$$

### 3 Existing Control Methods

Controlling of a Fish Robot is indeed a tedious task and one has to go through several obstacles and challenges. Thus to increase the capabilities of Fish Robot for various underwater functions and automated decision-making ability, it is required to develop a control scheme which is high performing and robust with high stability. Various control schemes can be used for designing a controller. Few of the most common Fish Robot or underwater robot control methods obtained from various source are summarized here.

#### 3.1 PID Controller

The most common type of controller used is PID control, but PID controller with fixed gain does not meet all the requirements of Fish Robot. Since, a PID controller does not need any information from the Fish Robot for its implementation. Considering the fact that the modeling uncertainties are generally more critical and sophisticated, this control scheme is not efficient, although a well-tuned PID can serve the purpose but with a lot of limitation. Also, when dynamic characteristics of Fish Robot are time and environment dependent, it is compulsory to return the gains so as to obtain desired performance [1, 10].

### ***3.2 Sliding Mode Control***

The Fish Robot is basically a time variant and a nonlinear system. Sliding mode control (SMC) proves a great potential for achieving optimum stability and performance even in parametric uncertainty and outer disturbances which makes it as a best suitable control scheme for Fish Robots or Underwater Robots. SMC was used by Vuilmet [2] for speed controlling, steering controlling, and diving controlling individually. Global asymptotic convergence for a system can also be obtained with the help of SMC with pole placement approach or by LQR Method as well.

### ***3.3 Adaptive Control***

The Fish Robot possesses hydrodynamics generally consists of numerous parametric variations, disturbances, and uncertainties. An adaptive control based on model can make the system nearly linear in a certain specific range of operation or operating condition, it can estimate system parameters with the help of recursive least square algorithm. Then controller is developed using pole placement method which results in a better performance for this adaptive control [9].

### ***3.4 Fuzzy Logic Control***

We take the help of fuzzy logic when the mathematical model for the system is not known with certainty or totally unknown or if the system exhibits a considerable amount of dynamic changes. Generally, a fuzzy model expresses a complex nonlinear dynamic terms of a system in linguistic variables form or we say ‘if-then’ rules. As the fuzzy controllers contain robustness and have numerous applicable variations in while designing, they are really handy for a nonlinear and time-varying system [1].

### ***3.5 Model Predictive Control (MPC)***

MPC is a very efficient control strategy but mostly it is non-suitable for an unstable open-loop system but when it comes to astable closed-loop system MPC can be efficiently applied. To apply the MPC to an unstable system, we have to apply a state feedback control so as to stabilize the main system and then we can apply MPC and get a desired result in any system. Application of such can be seen for an underwater vehicle can be seen in [5].

### 3.6 Robust Control

In this paper, the approach of robust control using the  $H_\infty$  ( $H$ -infinity) approach.  $H_\infty$  is applied when the system has to undergo through a number of uncertainties, most importantly when the system consists of complex dynamics. The robust controller is observed so that if it can achieve desired performance level of robustness for its stability. A complex  $H$ -infinity approach for solving a system with four DOF structure, then developing a controller for that with it gives better performance and also ensures a better stability.

## 4 Development of Controller

Robust control is an important research area to control the trajectory of robotic fish in the presence of external disturbances. It is also used to find the stability and sensitivity of the robotic fish. Stability and sensitivity play an important role in the trajectory and terrain following of robotic fish. It can easily handle bounded modeling errors to maintain robust performance.  $H_\infty$ -infinity is mathematical tool to analyze the sensitivity and stability of the robotic fish. Control law is used to optimize the trajectory of robotic fish. The robust control is internally stable when all the closed-loop poles are within the specified region (Fig. 3).

Conventional control system design considers the robotic fish model, controller and fixed parameters. The system model will always be not accurate representation of the actual l system because of the following [5],

- parameter variations,
- un-modeled time delays,
- un-modeled dynamics,
- changes in operating point,
- sensor noise,
- unpredicted disturbances.

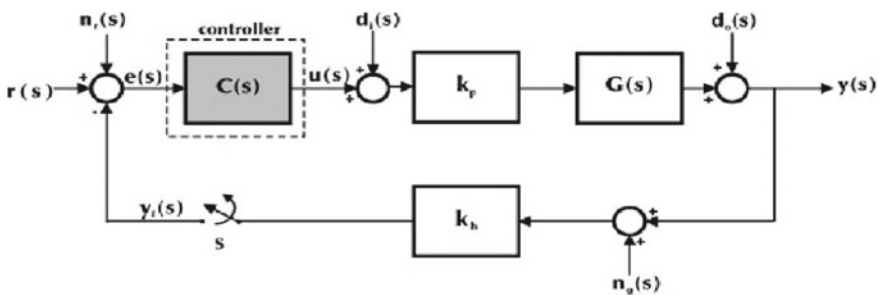


Fig. 3 Block diagram of robust controller [1]

The goal of robust systems design is to retain assurance of the systems performance in spite of model inaccuracies and changes.

A system is said to be robust when the system has acceptable changes in performances due to model changes or inaccuracies.

### Sensitivity and Robustness

A system is robust if it has following properties

- It has minimum sensitivities.
- It must be stable over a span of variations in parameters.
- Performance should be maintained in the presence of un-modeled dynamics and external disturbances.

Sensitivity is defined as  $S_{\alpha}^T = \frac{\partial T/T}{\partial \alpha/\alpha}$

where  $T$  is the transfer function and  $\alpha$  is the parameter of the system.

### Design of Robust Control Systems

Main objective is that output should exactly and instantaneously reproduce its input. In other words, Bode plot of the system should have 0 dB gain of infinite bandwidth and zero phase shifts. But it is ideal. One possible design objective is to maintain the response curve as flat and as close unity for large bandwidth as possible. Design steps are as follows

- Modeling of the nominal plant and perturbed plant,
- Experimental determination of parameters of the system,
- Selection of uncertainty and performance weights,
- Setting up the interconnection structure,
- Robustness analysis.

### Selection of Uncertainty and Performance Weights

1. Model selected is additive:

$$G_p(s) = G(s)(1 + W_{\text{add}}(s)\Delta_{\text{add}}(s)), \quad |\Delta_{\text{add}}(s)| < 1 \quad \forall \omega$$

2. The uncertainty weighting covers all the model perturbations

$$W_{\text{add}} = \frac{1 \times 10^{-5} \left(1 + \frac{s}{8}\right) \left(1 + \frac{s}{170}\right) \left(1 + \frac{s}{420}\right)}{\left(1 + \frac{s}{30}\right) \left(1 + \frac{s}{35}\right) \left(1 + \frac{s}{38}\right)}$$

3. To reject the disturbance at low frequency band, we select the performance
4. weighting

$$W_p = \frac{200}{\left(1 + \frac{s}{0.1}\right)}$$

### Results and Discussion

The model of fish robot and system parameters are taken from [11] for implementing the proposed robust control. The simulation results are obtained and presented here. All these simulations are developed in MATLAB environment.

Figure 4 represents linear motion of fish robot in translation direction and it has good settling time.

Figure 5 represents the response of uncertainty weighting matrices. Amplitude response is settling at 100 Hz. Here,  $\sigma(S(j\omega))$  is represented with solid black line,  $\sigma(T(j\omega))$  is represented with dashed red line and  $\sigma(GK(j\omega))$  is represented with dash-dot blue line.

Figure 6 represents Singular value of weighted closed-loop system. It has flat frequency response.

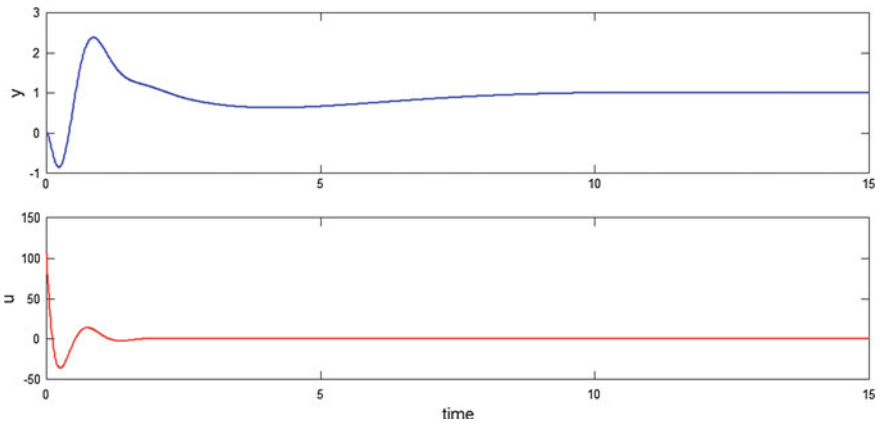


Fig. 4 Step response of fish robot in linear motion

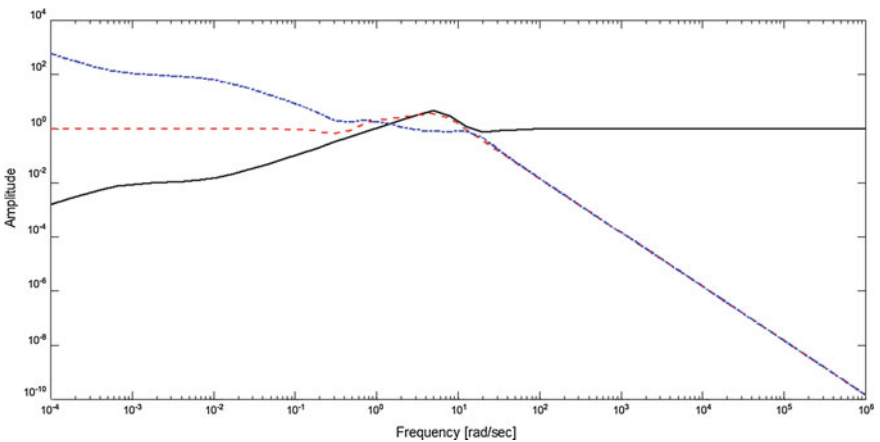
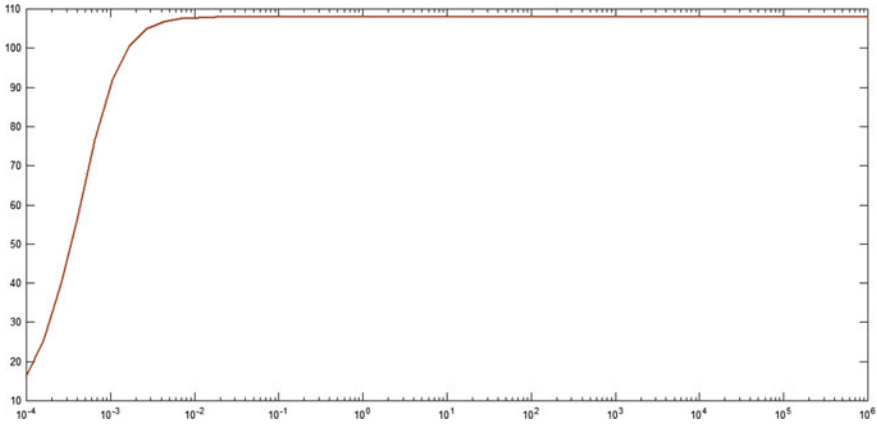


Fig. 5 Plot of uncertainty weighting



**Fig. 6** Singular value of weighted closed-loop system

## 5 Conclusions

In this paper, a robust control-based approach of controlling a Fish Robot is presented.  $H$ -infinity control method is proposed. The problems of uncertainty, nonlinearity, and stability are improved to a good extent. Robust control is not limited to any engineering discipline but equally applicable to environmental, civil and electrical engineering. There is a concern for the extremes of operation in a control system that has safety implications. The presented robust control is based on a dynamic model of the robotic fish and it is flexible to be used for multi-input and multi-output systems. Finally, MATLAB simulation result demonstrates the improvements of the proposed control method. Further the high level or advanced robust control is used to improve the performance of the fish robot.

## References

1. Fossen T (2009) Guidance and control of ocean vehicles. Wiley, New York
2. Vuilmet C (2005) Higher order sliding mode control applied to a heavyweight torpedo. In: IEEE conference on control applications, Toronto
3. Hao L, Wassersug R, Kawachi K (1996) A computational fluid dynamics study of tadpole swimming. *J Exp Biol* 199(6):1245–1260
4. Yong-Hua Z, Jian-Hui H, Jie Y, Shi-Wu Z, Kin-Huat L (2006) A computational fluid dynamics (CFD) analysis of an undulatory mechanical fin driven by shape memory alloy. *Int J Autom Comput* 3(4):374–381
5. Anton M, Zheng C, Kruusmaa M, Xiaobo T (2009) Analytical and computational modeling of robotic fish propelled by soft actuation material based active joints. In: Intelligent robots and systems IEEE/RSJ international conference, pp 2126–2131
6. Lighthill MJ (1960) Note on the swimming of slender fish. *J Fluid Mech* 9(2):305–317

7. Lighthill MJ (1970) Aquatic animal propulsion of high hydromechanical efficiency. *J Fluid Mech* 44(02):265–301
8. Wu T (1961) Swimming of a waving plate. *J Fluid Mech* 10(03):321–344
9. Basant KS, Bidyadhar S (2014) Adaptive tracking control of autonomous underwater vehicle. *Int J Autom Comput* 11(3):299–307
10. Khalid I, Arshad MR (2013) Modelling and motion control of a hybrid driven underwater glider. *Int J Geo-Mar Sci* 42(8):971–979
11. Masoomi SF, Gutschmidt S, Chen XQ, Sellier M (2015) The kinematics and dynamics of undulatory motion of a tuna-mimetic robot. *Int J Adv Robot Syst*

**Part III**  
**Computational Modelling**



# Multi-directional Irregular Wave Modelling with CFD



Weizhi Wang, Hans Bihs, Arun Kamath and Øivind Asgeir Arntsen

**Abstract** The design of coastal structures requires accurate simulations of the wave conditions. Computational fluid dynamics (CFD) captures most complexities of the wave physics with few assumptions and therefore is considered to be an ideal alternative for the offshore wave simulation. However, the conventional uni-directional regular wave CFD simulation does not represent the reality and tends to overestimate the wave conditions. The irregular bottom topography and varying water depth in the coastal area make the simulation more complicated. To give a more realistic simulation in a coastal area, a directional irregular wave model is to be implemented in a CFD code. This paper presents a multi-directional irregular wave implementation in the open-source CFD model REEF3D. The non-directional frequency spectra Joint North Sea Wave Observation Project (JONSWAP) together with a cos-squared-type directional spreading function is used for the simulation. REEF3D solves the incompressible Navier–Stokes equations with the finite difference method on a staggered Cartesian grid and uses the level-set method to capture the free surface under the two-phase flow approximation. The relaxation method is used for the wave generation and numerical beaches. The irregular waves are generated by the superimposition of a finite number of regular waves. The resulting significant wave heights are compared with another numerical model SWASH. The comparisons show good performance of CFD simulations in predicting irregular wave behaviours. The differences are also discussed for future references.

**Keywords** Multi-directional irregular wave · CFD · REEF3D · SWASH

---

W. Wang (✉) · H. Bihs · A. Kamath · Ø. A. Arntsen  
Norwegian University of Science and Technology, 7491 Trondheim, Norway  
e-mail: [weizhi.wang@ntnu.no](mailto:weizhi.wang@ntnu.no)

© Springer Nature Singapore Pte Ltd. 2019  
K. Murali et al. (eds.), *Proceedings of the Fourth International Conference in Ocean Engineering (ICOE2018)*, Lecture Notes in Civil Engineering 22,  
[https://doi.org/10.1007/978-981-13-3119-0\\_31](https://doi.org/10.1007/978-981-13-3119-0_31)

## 1 Introduction

Ocean waves are random by nature. An accurate prediction of the random seas requires a good knowledge of the energy distribution over both frequencies and directions. A conventional uni-directional irregular wave study tends to overestimate the wave condition. The study of the directionality in a random wave field is the key for an accurate prediction of the wave properties and the design of coastal structures.

Many spectra describing the energy density distribution have been developed in the past decades. Pierson and Moskowitz [18], Hasselmann et al. [9] and Bouws et al. [3] developed different frequency spectra based on their observations to describe the fully developed sea, the non-fully developed sea and to include shallow water effects. To describe the directionality, Pierson et al. [17] proposed the Pierson-Neumann-James (PNJ) directional spreading function as a function of only the directional angles. Longuet-Higgins et al. [14], Mitsuyasu [15] and Ochi [16] further developed directional spreading functions of both angles and frequencies.

Many studies have been conducted using the empirical spectra. Even though most studies have been focusing on the uni-directional irregular wave, some experimental and numerical studies of the multi-directional irregular waves are also progressing. Li et al. [12, 13] and Ji et al. [10] experimentally studied the interaction between multi-directional irregular waves and a vertical cylinder. Numerical models HOS-NWT [6] and HOS-Ocean [5] were also developed in Ecole Centrale de Nantes for the multi-directional irregular wave simulation in wave basin and larger scale.

However, the coastal region presents more complicated scenarios compared to the idealised studies in experiments. The dramatic change of the bottom topography and water depth cause complicated wave transformation phenomena. Few studies have been made to numerically investigate the multi-directional random sea over irregular bottoms. The complexity, however, can be accounted for to a great extent by the Computational Fluid Dynamics (CFD) method, as CFD solves most of the kinematics and dynamics in the fluid domain with few assumptions. Wang et al. [20, 21] has explored the application of the CFD method on the regular wave and uni-directional irregular wave modelling over irregular bottom topography using the wave model REEF3D. REEF3D is an open-source CFD wave model developed in NTNU specialising in wave hydrodynamics and free-surface flow. It has been widely used to simulate various wave phenomena, such as six degree-of-freedom floating body [2], the breaking wave kinematics [1] and breaking wave-structure interactions [11].

Therefore, it is an important task to implement the multi-directional irregular wave module in the REEF3D framework. In order to fulfil the task, the first step is to verify the model using a simple numerical tank. In this paper, a flat bottom numerical wave tank without any structures is used for the verification of the newly developed module. The results are also compared to another numerical model SWASH [23].

## 2 Numerical Model

### 2.1 The Governing Equations

The CFD model REEF3D solves the incompressible Navier–Stokes equation together with the continuity equation as shown in Eqs. (1) and (2).

$$\frac{\partial u_i}{\partial x_i} = 0 \quad (1)$$

$$\frac{\partial u_i}{\partial t} + u_j \frac{\partial u_i}{\partial x_j} = -\frac{1}{\rho} \frac{\partial p}{\partial x_i} + \frac{\partial}{\partial x_j} \left[ \nu \left( \frac{\partial u_i}{\partial x_j} + \frac{\partial u_j}{\partial x_i} \right) \right] + g_i \quad (2)$$

where  $u$  is the velocity,  $\rho$  stands for the fluid density,  $p$  represents the pressure,  $\nu$  is the kinematic viscosity and  $g$  is the acceleration due to gravity.

REEF3D uses a finite difference method to solve the governing equations on a structured Cartesian grid. High-order numerical schemes such as a conservative fifth-order weighted essentially non-oscillatory (WENO) scheme [8] and a third-order total-variation-diminishing (TVD) Runge–Kutta scheme [19] are used in REEF3D. The Poisson pressure equation is solved using the PFMG preconditioned BiCGStab algorithm provided by HYPRE library [7].

SWASH solves the non-linear shallow water equations using a finite element framework on a staggered grid. Different from a Boussinesq-type model, SWASH compensates the dispersion relation by increasing the number of vertical layers rather than increasing the order of derivatives [23].

### 2.2 Multi-directional Irregular Wave Generation in a Numerical Tank

The 3D irregular wave can be regarded to be a superposition of a finite number of regular wave components travelling in different directions at different frequencies and phases. The properties of each wave components are ramped up to the theoretical values in the wave generation zone using a relaxation method. The theoretical values for the wave components are calculated from the directional energy spectrum, which is formed by multiplying a frequency spectrum with a directional spreading function. For the frequency spectrum, the JONSWAP spectrum recommended by DNV [4] is used in this paper, as shown in Eq. (3).

$$S = \frac{5}{16} \frac{H_s^2 \omega_p^4}{\omega^5} \exp\left(-\frac{5}{4} \left(\frac{\omega}{\omega_p}\right)^{-4}\right) (1 - 0.287 \ln(\gamma)) \gamma^{\exp(-0.5(\frac{\omega - \omega_p}{\sigma \omega_p})^2)} \quad (3)$$

where  $\omega_p$  is the peak frequency in the unit of rad,  $\gamma$  is a constant,  $\gamma = 3.3$  in this paper.

The PNJ [17] directional spreading function is used in this paper due to its simplicity and wide application, as shown in Eq. (4). In the formula,  $\bar{\beta}$  is the principal direction representing the main energy propagation direction and  $\beta_i$  is the incident wave direction of each wave components, as illustrated in Fig. 1.

$$G(\beta) = \begin{cases} \frac{2}{\pi} \cos^2(\beta - \bar{\beta}), & \text{if } |\beta| < \frac{\pi}{2} \\ 0, & \text{else} \end{cases} \quad (4)$$

By multiplying Eqs. (3) and (4), one gets the directional spectrum JONSWAP-PNJ. The velocities and surface elevations can be derived based on the directional spectrum using a single-array method. As an example, the formulation of the surface elevation is shown in Eq. (5).  $k_n$  can be calculated based on wave theory and the amplitude is calculated in Eq. (6) using the spectrum. N denotes the total number of the wave components, which is a multiplication of the number of frequency components and directional components.  $\varepsilon_n$  is the phase generated randomly between 0 and  $2\pi$ .

$$\eta(\vec{r}, t) = \sum_{i=1}^N a_n \cos(\vec{k}_n \cdot \vec{r} - \omega_n t + \varepsilon_n) \quad (5)$$

$$a_n = \sqrt{2S(\omega_n, \beta_n)\Delta\omega\Delta\beta} \quad (6)$$

**Fig. 1** Definition of the principal angle and the incident wave angle

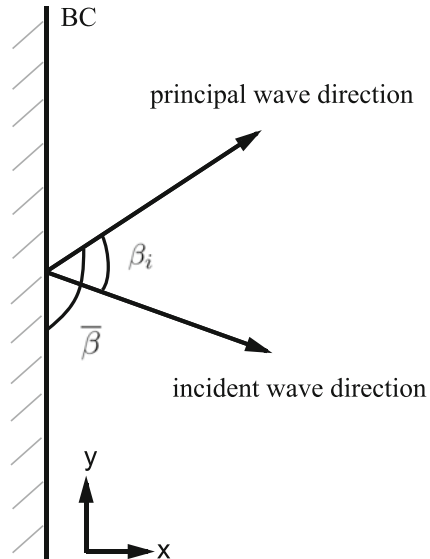
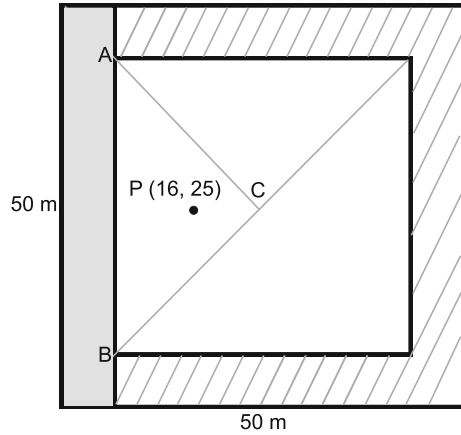


**Fig. 2** Configuration of the numerical wave tank. The shaded zone to the left-hand side is the wave generation zone. Numerical beaches are shown in the zones with stripes



### 2.3 Numerical Tank Configurations

A numerical wave tank 50 m long and 50 m wide is used with a water depth of 0.5 m. As shown in Fig. 2, a wave generation zone of one wavelength is provided on the left-hand side of the tank and numerical beaches are located both at the end of the tank and also along the side walls. The wave probes are located near the geometric centre of the triangle  $\triangle ABC$  formed by the diagonals of the numerical tank in Fig. 2. This arrangement helps to minimise the influence of reflected waves from the boundaries.

## 3 Numerical Simulation Results

The input wave has a  $H_s$  of 0.1 m and a  $T_p$  of 2 s. The principal direction is  $45^\circ$  counter-clockwise from the  $x$ -axis. The corresponding wave directional spectrum based on the wave input is plotted in Fig. 3. The mesh convergence study is conducted with three mesh sizes:  $dx = 0.08$  m,  $dx = 0.10$  m and  $dx = 0.20$  m. The frequency spectra obtained at the probes at different mesh sizes are compared with the theoretical spectrum in Fig. 4. Concluding from the comparison, a mesh size of  $dx = 0.08$  m is considered to be sufficient to obtain accurate information about the irregular wave field. The following CFD results are all based on this mesh size. With the mesh size of 0.20, 0.25 and 0.50 m, SWASH gives very similar predictions of the significant wave height. A mesh size of 0.20 m is considered to be sufficient for the SWASH model. Two vertical layers are used in the SWASH simulation. The simulation time is 200 s for both REEF3D and SWASH simulations. As the first verification study, a small number of wave components are used in the CFD simulation. Twenty frequencies are used with the range of  $[2.26, 4.82]$  rad/s. Six directional angles are used within the range of  $[-\frac{\pi}{2}, \frac{\pi}{2}]$  rad.

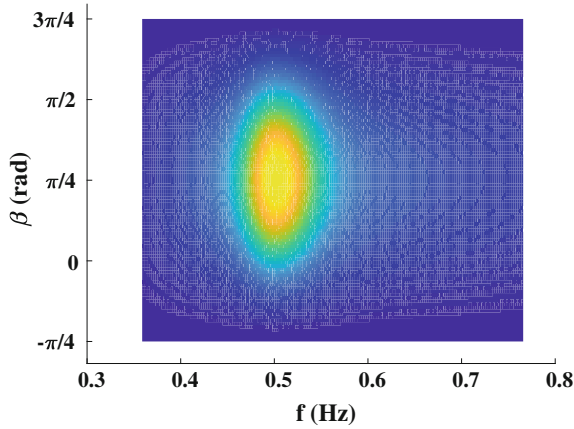


**Fig. 3** Plot of the spectrum density of the directional spectrum combining the JONSWAP frequency spectrum and the PNJ directional spreading function

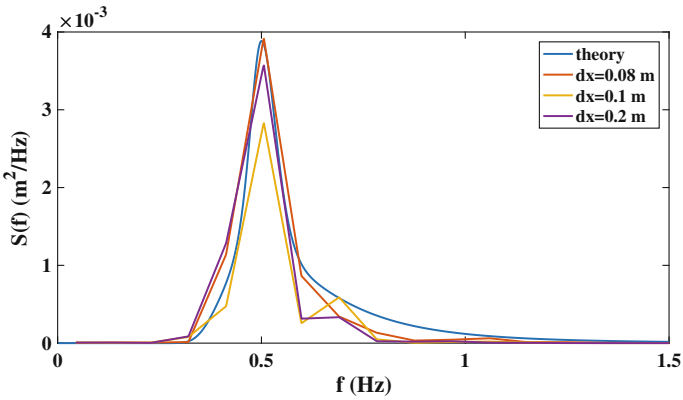


**Fig. 4** Comparison of the frequency spectrum in the tank with different mesh sizes

Figures 5 and 6 show the surface elevation results from the REEF3D and SWASH simulations, respectively. The principal direction of the irregular wave field is clearly visible in both simulations. The  $H_s$  at the probe from both simulations are compared to the input wave data as shown in Table 1. The  $H_s$  in the numerical tank from the REEF3D simulation gives a very satisfactory agreement with the input data. SWASH gives a lower value in this simulation.

**Fig. 5** Surface elevation in the numerical tank of the REEF3D simulation at  $t=200$  s

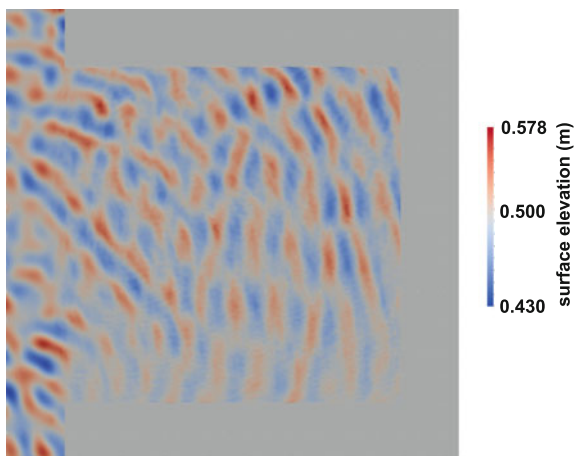


**Fig. 6** Surface elevation in the numerical tank of the SWASH simulation at  $t=200$  s

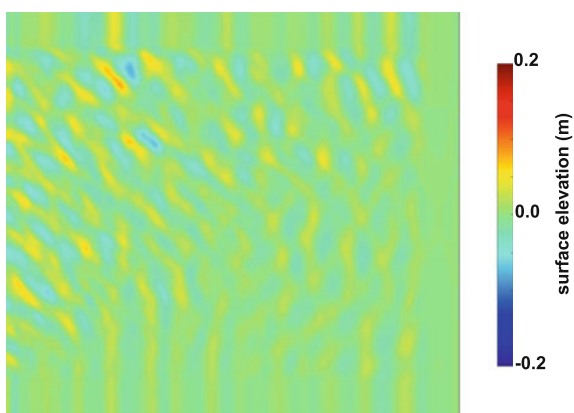


**Table 1** Comparison of the  $H_s$  in the REEF3D and SWASH simulations

	$H_s$ (m)
Input	0.1000
REEF3D	0.1001
SWASH	0.07103

## 4 Conclusion Remarks and Future Work

In order to develop a CFD model for directional random sea over irregular bottom near the coastal area, a study of the newly developed multi-directional irregular wave module in REEF3D is described in this paper. A flat bottom tank is used for verification. The CFD simulation successfully produced a directional random sea in the numerical wave tank and gives a good prediction of the frequency spectrum and

$H_s$ . SWASH performs well in producing a random sea, but the prediction of  $H_s$  is not very accurate based on the current set-up. Due to the complexity in the random wave field, more thorough studies are needed for further conclusions. The following works are to be completed in the future: (1) A sensitivity study of the number of the frequency and direction components; (2) A sensitivity study of the simulation time; (3) The reconstruction of the directional spectrum using an array of probes in the numerical wave tank; (4) A validation study to compare the numerical results with the data from physical experiments.

**Acknowledgements** This study has been carried out under the E39 fjord crossing project (No. 304624) and the authors are grateful to the grants provided by the Norwegian Public Roads Administration. This study was supported in part with computational resources at the Norwegian University of Science and Technology (NTNU) provided by NOTUR project (No. NN2620K), <http://www.notur.no>.

## References

1. Alagan-Chella M, Bihs H, Myrhaug D, Muskulus M (2017) Breaking solitary waves and breaking wave forces on a vertically mounted slender cylinder over an impermeable sloping seabed. *J Ocean Eng Marine Energy* 3(1):1–19. <https://doi.org/10.1007/s40722-016-0055-5>
2. Bihs H, Kamath A, Alagan-Chella M, Aggarwal A, Arntsen ØA (2016) A new level set numerical wave tank with improved density interpolation for complex wave hydrodynamics. *Comput Fluids* 140(Supplement C):191–208. <https://doi.org/10.1016/S0045793016302729>
3. Bouws E, Günther H, Rosenthal W, Vincent CL (1985) Similarity of the wind wave spectrum in finite depth water: 1. spectral form. *J Geophys Res Oceans* 90(C1):975–986. <https://doi.org/10.1029/JC090iC01p00975>
4. DNV. Modelling and analysis of marine operations. Standard DNV-RP-H103, Det Norske Veritas, Veritasveien 1, Hvik, Norway, April 2011
5. Ducrozet G, Bonnefoy F, Le Touzé D, Ferrant P HOS-ocean: open-source solver for nonlinear waves in open ocean based on high-order spectral method. *Comput Phys Commun* 203:245–254, June 2016. <https://doi.org/10.1016/j.euromechu.2012.01.017>
6. Ducrozet G, Bonnefoy F, Le Touzé D, Ferrant P A modified high-order spectral method for wavemaker modelling in a numerical wave tank. *Eur J Mech B/Fluids*, July 2012. <https://doi.org/10.1016/j.euromechu.2012.01.017>
7. Falgout RD, Jones JE, Yang UM Conceptual interfaces in hypre. *Future Gener Comput Syst* 22(1-2):239–251, Jan 2006. <https://doi.org/10.1016/j.future.2003.09.006>
8. Jiang GS, Shu CW (1996) Efficient implementation of weighted ENO schemes. *J Comput Phys* 126(1):202–228
9. Hasselmann K et al (1973) Measurements of wind-wave growth and swell decay during the joint north sea wave project (jonswap). *Ergänzung zur Deut. Hydrogr. Z., Reihe A* (8), 12:1–95
10. Ji X, Liu S, Li J, Jia W (2017) Numerical investigation of multidirectional random wave interaction with a large cylinder. *Proc Inst Mech Eng Part M J Eng Maritime Environ* 231(1):271–283. <https://doi.org/10.1177/1475090216642464>
11. Kamath A, Alagan-Chella M, Bihs H, Arntsen ØA (2016) Breaking wave interaction with a vertical cylinder and the effect of breaker location. *Ocean Eng* 128:105–115. <https://doi.org/10.1016/S0029801816304590>
12. Li J, Wang Z, Liu S (2012) Experimental study of interactions between multi-directional focused wave and vertical circular cylinder, part i: wave run-up. *Coast Eng* 64(Supplement C):151–160. <https://doi.org/10.1016/S0378383912000270>



13. Li J, Wang Z, Liu S (2014) Experimental study of interactions between multi-directional focused wave and vertical circular cylinder, part ii: wave force. *Coast Eng* 83(Supplement C):233–242. <https://doi.org/10.1016/S0378383913001129>
14. Longuet-Higgins MS, Cartwright DE, Smith ND (1963) Observations of the directional spectrum of sea waves using the motions of a floating buoy. *Proceedings of the conference of ocean wave spectra*, pp 111–132
15. Mitsuyasu HEA (1975) Observations of the directional spectrum of ocean waves using a clover-leaf buoy. *J Phys Oceanogr*, pp 750–760
16. Ochi MK (1998) *Ocean waves: the stochastic approach*. Cambridge University Press
17. Pierson WJ, Neumann G, James RW (1955) Practical methods for observing and forecasting ocean waves by means of wave spectra and statistics
18. Pierson WJ, Moskowitz L (1964) A proposed spectral form for fully developed wind seas based on the similarity theory of S. A. Kitaigorodskii. *J Geophys Res* 69(24):5181–5190. <https://doi.org/10.1029/JZ069i024p05181>
19. Shu CW, Osher S Efficient implementation of essentially non-oscillatory shock-capturing schemes. *J Comput Phys* 77(2):439–471, Aug 1988
20. Wang W, Bihs H, Kamath A, Arntsen ØA (2017) Large-scale CFD modelling of wave propagation in Sulafjord for the e39 project. In: *Proceedings of MekIT17—9th national conference on computational mechanics*
21. Wang W, Bihs H, Kamath A, Arntsen ØA (2017) Large-scale CFD modelling of wave propagation into Mehamn harbour. In: *Proceedings of MARINE 2017 computational methods in marine engineering VII*
22. You ZJ (2008) A close approximation of wave dispersion relation for direct calculation of wavelength in any coastal water depth. *Appl Ocean Res* 30(2):113–119. <https://doi.org/10.1016/S0141118708000382>
23. Zijlema M, Stelling G, Smit P (2011) Swash: an operational public domain code for simulating wave fields and rapidly varied flows in coastal waters. *Coast Eng* 58(10):992–1012. <https://doi.org/10.1016/S0378383911000974>

# Numerical Study of Superposition Principle for Surface Gravity Waves



Vinay Kumar Gupta, Alok Khaware, Ashok Sivanandham  
and K. V. S. S. Srikanth

**Abstract** The study of surface gravity wave is very important for the safety of marine vessels and the design of coastal and offshore structures. Gravity-induced sea waves mostly show a nonlinear behaviour, but at a low wave steepness, these waves can be approximated as linear waves and superposition principles can be applied. Various wave phenomena such as standing waves, constructive and destructive interference, wave groups and generation of random waves are based on superposition principle. Random waves are generally modelled using wave spectrum, which is a representation of wave energy in the specified frequency range. Wave spectrum is broken into different wave components which are superposed to produce a random wave. In the present work, volume of fluid method is used for numerical simulation of surface gravity waves. Implicit formulation for volume fraction equation along with the bounded second order in time is used, which allows better temporal accuracy and numerical stability at larger time step size. The surface gravity wave is modelled by providing the wave profiles and velocities at upstream boundary. In the downstream, pressure outlet boundary is used for the specification of the hydrostatic pressure profile. Numerical beach zone is defined adjacent to the pressure outlet boundary to suppress the wave reflections propagating upstream. Random waves are modelled using JONSWAP spectrum. Formation of constructive and destructive interference, standing wave, wave pockets and modelling of random wave is achieved with numerical approach, and wave kinematics are validated against the analytical results.

**Keywords** Computational fluid dynamics (CFD) · Volume of fluid method (VOF) · Surface gravity waves · JONSWAP spectrum · Numerical wave tank

---

V. K. Gupta (✉) · A. Khaware (✉) · A. Sivanandham · K. V. S. S. Srikanth  
Ansys Inc, Pune, India  
e-mail: [vinaykumar.gupta@ansys.com](mailto:vinaykumar.gupta@ansys.com)

A. Khaware  
e-mail: [alok.khaware@ansys.com](mailto:alok.khaware@ansys.com)

A. Sivanandham  
e-mail: [ashok.sivanandham@ansys.com](mailto:ashok.sivanandham@ansys.com)

K. V. S. S. Srikanth  
e-mail: [kvss.srikanth@ansys.com](mailto:kvss.srikanth@ansys.com)

© Springer Nature Singapore Pte Ltd. 2019

K. Murali et al. (eds.), *Proceedings of the Fourth International Conference in Ocean Engineering (ICOE2018)*, Lecture Notes in Civil Engineering 22,  
[https://doi.org/10.1007/978-981-13-3119-0\\_32](https://doi.org/10.1007/978-981-13-3119-0_32)

## 1 Introduction

Wave interactions in nature lead to several interesting wave phenomena such as standing waves, wave groups or beats, constructive and destructive interference and random waves. Gravity waves on a liquid surface play an important role for coral movement, motion of hydraulic vessels, design of ships and offshore structures, and in understanding sedimentation at the entrance of a port. Consequently, the ability to simulate these phenomena accurately is important for many branches of engineering.

Standing surface gravity waves are observed at a variety of scales. Small-scale standing waves are seen in a swimming pool or bathtub where water sloshing happens back and forth. Large-scale standing waves are observed near storm centres or from the reflection of swell at the shore. Standing waves are typically formed when strong winds push waves forward and later waves rebound back when the wind stops. Water then oscillates back and forth for hours.

Wave groups are observed at the open sea coast when a series of high waves follow a series of low waves with a large spread in wave heights, wave direction and wave frequencies. Oscillations caused by wave groups are also called surf beats, where wave frequencies can vary significantly compared to the mean wave frequency.

Random waves on the sea surface are generated by the action of wind and depend on wind speed, wind direction, wind duration and fetch area. The disturbed sea surface is not regular and contains many different oscillatory motions at different frequencies. Wave spectra are often used to describe the distribution of wave energy within a frequency range.

In general, waves are nonlinear in nature and can be considered as a superposition of several waves with different wave characteristics. A superposition principle is ideally applicable to linear waves; therefore, numerical analysis of complex nonlinear wave interactions is approximated often by linear wave interactions [1]. The importance of linear systems is that they are easier to analyse mathematically. Some of the wave components during superposition may not satisfy the linear wave assumption; hence, it might lead to error while modelling wave phenomena.

Wave theories can be classified as small amplitude and finite amplitude wave theories. Applicability of wave theory is decided by wave steepness and relative height which are defined as the ratio of wave height to wavelength and ratio of wave height to the liquid depth, respectively. Small amplitude wave theories are first order and linear in nature which are applicable for waves with low steepness and low relative height. Finite amplitude wave theories are higher order and nonlinear in nature which are applicable for waves with high steepness or high relative height.

Progress in CFD techniques and the availability of large computing resources allow a close prediction of waves using numerical computational methods. In this paper, the numerical simulations of various wave phenomena using ANSYS Fluent are validated successfully by comparing with analytical results. The volume of fluid method (VOF) and numerical wave tank are used for modelling free surface gravity waves. A numerical beach is used in vicinity of the downstream boundary to damp wave reflections propagating upstream. A bounded second-order time formulation

and implicit volume fraction discretization are chosen as that is critical for simulations to be run with higher time step size without compromising on accuracy. Different case studies are used to analyse the formation of nodes and anti-nodes, constructive and destructive interference, wave groups and random waves using the JONSWAP spectrum. Consistency with linear wave theory is observed for waves of sufficiently small amplitude with deviations being observed at larger wave amplitudes.

## 2 Superposition Principle

According to superposition principle, when two or more waves travelling in same nondispersive medium pass through each other at the same time without being disturbed then the net displacement of medium at any point is the sum of individual displacements. Superposition principle is ideally valid for linear waves, which is used in modelling various physical phenomena such as interference, beats, standing waves and random waves.

Wave profile as per linear wave theory is given as [2],

$$\eta(x, t) = A \cos(k_x x + k_y y - \omega_e t + \phi) \quad (1)$$

Wave number  $k$  and its components in flow directions  $\hat{x}$  and  $\hat{y}$  are specified as,

$$k = 2\pi/L, \quad k_x = k \cos \theta \text{ and } k_y = k \sin \theta$$

The wave frequency  $\omega$  is defined as,

$$\omega = \sqrt{gk \tanh(kh)} \quad (2)$$

The effective wave frequency is given by,

$$\omega_e = \omega + \vec{K} \cdot \vec{U} \quad (3)$$

Effective wave speed and time-period are given by,

$$c_e = \omega_e/k, \text{ and } T_e = 2\pi/\omega_e \quad (4)$$

where  $h$  is the liquid height,  $g$  is the acceleration due to gravity opposite to the direction of  $\hat{z}$ ,  $t$  is time,  $\vec{U}$  is averaged flow velocity,  $\vec{K}$  is wave number in vector form,  $L$  is wavelength,  $\theta$  is the wave heading angle.

Velocity components for shallow or intermediate waves are given as,

$$\begin{bmatrix} u \\ v \end{bmatrix} = \frac{gkA}{\omega} \frac{\cosh[k(z+h)]}{\cosh(kh)} \begin{bmatrix} \cos \theta \\ \sin \theta \end{bmatrix} \cos(k_x x + k_y y - \omega_e t + \phi) \quad (5)$$

$$w = \frac{gkA \sinh[k(z+h)]}{\omega \cosh(kh)} \sin(k_x x + k_y y - \omega_e t + \phi) \tag{6}$$

Effective wave and velocity profiles are calculated by superposing  $n$  number of wave components given as

$$\eta(x, t) = \sum_{i=1}^n A_i \cos(k_{x,i} x + k_{y,i} y - \omega_{e,i} t + \phi_i) \tag{7}$$

$$\vec{V} = \vec{U} + \sum_{i=1}^n u_i \hat{x} + \sum_{i=1}^n v_i \hat{y} + \sum_{i=1}^n w_i \hat{z} \tag{8}$$

### 3 Numerical Methodologies

#### 3.1 Governing Equations

The governing equations for CFD are based on conservation of mass, momentum and energy which are solved using Finite Volume Method (FVM). VOF method is used to track the interface between the fluids which are not interpenetrating. If the volume fraction of one fluid in the cell is denoted as  $\alpha$ , then the following three conditions are possible:

- $\alpha = 0$  means that the cell is completely filled with primary fluid;
- $\alpha = 1$  means that the cell is completely filled with secondary fluid;
- $0 < \alpha < 1$  means that the cell is partially filled and contains the interface.

Summation of volume fraction for all the fluids should be equal to one

$$\sum_a \alpha = 1 \tag{9}$$

Volume fraction equation is given as,

$$\frac{\partial \alpha}{\partial t} + \nabla \cdot (\vec{u} \alpha) = 0 \tag{10}$$

Total continuity equation for incompressible fluid is given as,

$$\nabla \cdot \vec{u} = 0 \tag{11}$$

A single momentum equation is solved throughout the domain, and the resulting velocity field is shared among the phases.

$$\frac{\partial \rho \vec{u}}{\partial t} + \nabla \cdot (\rho \vec{u} \otimes \vec{u}) = -\nabla p + \nabla \cdot \vec{\bar{T}} + \vec{F}_b \tag{12}$$

The properties in the total continuity and momentum equations are volume-weighted averaged properties.

### 3.2 Solver Methods

**Pressure–Velocity Coupling:** PISO is used for pressure–velocity coupling which solves pressure corrections in two steps named as predictor and corrector. It allows large under-relaxation factors for pressure and momentum to achieve faster convergence.

**Gradient Method:** Green–Gauss node-based method is used for gradient calculation. Node values are constructed using least square system, and finally, gradients are calculated using Gauss divergence theorem.

**Time Formulation:** Bounded second-order time implicit formulation is used which ensures that variables are bounded when extrapolated in time. This formulation allows better accuracy and stability at much larger time step size compared to unbounded methods.

**Volume Fraction Formulation:** Volume fraction equation can be solved in explicit or implicit manner. For explicit formulation, very accurate interface-tracking schemes are available based on geometric construction; however, they require rather low time step sizes to ensure Courant number-based stability criterion. For implicit formulation, various interface-capturing schemes are available which allow rather larger time step sizes. The interface-capturing schemes are numerically more diffusive compared to interface-tracking schemes. For simulations running for longer time, explicit formulation becomes impractical due to time step size constraint. Therefore, implicit formulation is used with bounded second-order time formulation to achieve better accuracy at larger time step size.

**Volume Fraction Discretization:** In volume fraction equation, face values of volume fraction used in the convection term are discretized using the second-order reconstruction scheme based on slope limiters [3].

$$\alpha_f = \alpha_d + \beta \nabla \alpha_d \cdot dr \quad (13)$$

where  $\alpha_f$  is face volume fraction,  $\alpha_d$  is donor cell volume fraction,  $\nabla \alpha_d$  is donor cell volume fraction gradient,  $\beta$  is slope limiter, and  $dr$  is position vector between cell and face centroid.

### 3.3 Boundary Conditions

**Upstream:** Open channel wave boundary condition is applied at velocity inlet, which requires wave inputs depending on the type of wave. Typically, wave height, wave frequency, phase angle and wave heading angle are provided as wave inputs. Averaged

flow velocity is specified to model the effect of flow current. Specification of the free surface level is required to find liquid depth for shallow and intermediate waves.

**Downstream:** Hydrostatic pressure profile is applied at the outlet. Numerical beach region is considered adjacent to pressure outlet to suppress the numerical reflections propagating upstream which might significantly affect the actual wave interaction.

**Numerical Beach Treatment:** A damping sink term is added in the momentum equation for the cell zone near the pressure outlet boundary to avoid wave reflection [4]. Damping effect is two-dimensional which is maximum at the end of beach and at the mean free surface level.

$$S = - \left[ C_1 \rho V + \frac{1}{2} C_2 \rho |V|V \right] f(z) f(x) \quad (14)$$

$$f(x) = r_x^2, \quad f(z) = 1 - r_z \quad (15)$$

$$r_x = (x - x_s)/(x_e - x_s), \quad r_z = (z - z_{fs})/(z_b - z_{fs}) \quad (16)$$

where  $x$  is distance along the flow direction  $\hat{x}$ ,  $z$  is distance from the free surface level,  $S$  and  $V$  are source term and velocity in the  $\hat{z}$ -direction,  $C_1$  and  $C_2$  are linear and quadratic damping resistances,  $f(x)$  and  $f(z)$  are damping terms.  $x_s$  and  $x_e$  are the start and end points of the damping zone in the  $\hat{x}$ -direction.  $z_{fs}$  and  $z_b$  are the free surface and bottom level along the  $\hat{z}$ -direction.

## 4 Case Studies

The case studies for various wave phenomena are validated with analytical results and presented in the following sections. In all the cases, upstream boundary is prescribed with open channel wave inlet. Except for standing wave case, downstream boundary is taken as pressure outlet with the specification of hydrostatic pressure profile. Numerical beach is used in the region adjacent to pressure outlet to damp numerical reflections; thus, solution in this region is ignored in the analysis. Top, bottom and side boundaries are taken as symmetry boundaries. Quadrilateral or hexahedral mesh is used, and the free surface region is well refined. The free surface level is extracted by taking  $y$ -coordinate on an iso-surface of volume fraction = 0.5. In all the cases, the time step size is selected in the range of  $T_e/100$  to  $T_e/200$ , which is based on best practice guidelines while using bounded second-order time formulation for wave simulations.

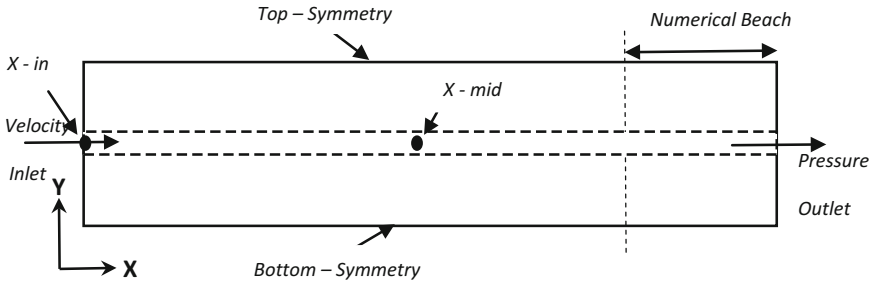


Fig. 1 Schematic representation of the computational flow domain

### 4.1 Constructive and Destructive Interference

If two or more waves having same amplitude, wavelength and frequency travel in the same direction but with different phase angles, constructive interference occurs for waves in same phase and destructive interference occurs for opposite phases. Wave displacement for two waves using superposition principle can be represented as,  $\eta(x, t) = A \cos(kx - \omega t + \phi_1) + A \cos(kx - \omega t + \phi_2)$

$$\eta(x, t) = 2A \cos\left(kx - \omega t + \frac{\phi_1 + \phi_2}{2}\right) \cos\left(\frac{\phi_1 - \phi_2}{2}\right) \tag{17}$$

$$\begin{aligned} \phi_1 = \phi_2 = \phi & \qquad \phi_1 = \phi, \quad \phi_2 = \phi + \pi \\ \eta(x, t) = 2A \cos(kx - \omega t + \phi) & \quad \eta(x, t) = 0 \end{aligned} \tag{18}$$

**Problem Description:** Two-dimensional rectangular domain of 60 m × 2 m is considered with the mesh size of 0.96 million cells. Schematic view of the flow domain is shown in Fig. 1. Two waves having wave height and wavelength of 0.01 m and 1.5 m propagate either in the same or opposite phase to produce constructive and destructive interferences. Length of numerical beach zone is 5 m. Average flow velocity is 1 m/s, and effective time-period is about 0.593 s. Time step size is 0.005 s, and simulation time is 8 s which is approximately 14 time-periods. Wave steepness ratio for individual wave is 0.0067 which satisfies linear wave assumption for superposition.

**Results and Discussions:** Time history of free surface level at inlet ( $x = 0$  m) and at mid-section ( $x = 30$  m) of the channel are shown in Fig. 2. Effective amplitude is 0.01 m in Fig. 2a as waves are adding in amplitudes causing constructive interference, and effective amplitude is zero in Fig. 2b as waves are cancelling each other causing destructive interference.

Case studies are performed using bounded second-order time formulation with a time step size of 0.01 s ( $T_e/60$ ) and 0.005 s ( $T_e/120$ ). Waves have distorted when run with  $T_e/60$  which can be seen in Fig. 3a. Solving several simulations, it is found that optimal time step size for obtaining wave profiles without any distortions lies in



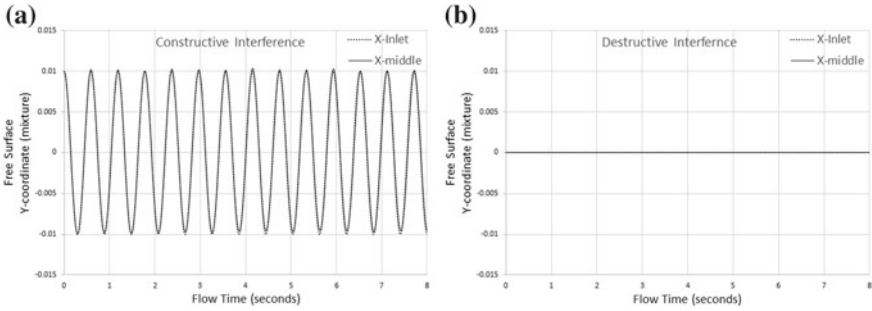


**Fig. 2** Free surface height monitored along the flow domain with respect to time: **a** constructive interference and **b** destructive interference

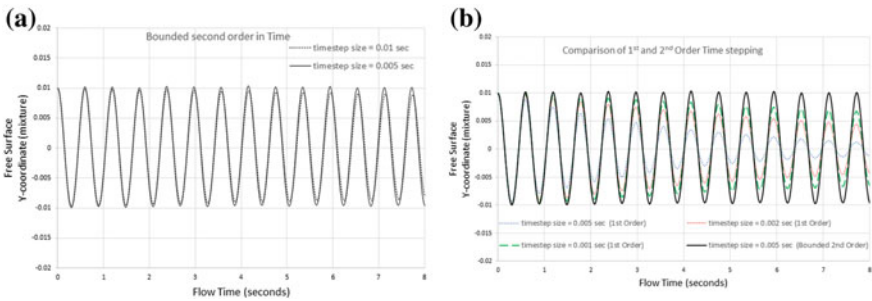


**Fig. 3** Free surface profiles monitored along the flow domain with respect to time: **a** bounded second-order time formulation with time step sizes 0.01 and 0.005 s; **b** comparison of first-order time formulation with multiple time step sizes against bounded second-order time formulation

the range of  $T_e/100$  to  $T_e/200$ . This case study also includes multiple simulations using time step sizes of  $T_e/120$ ,  $T_e/300$ ,  $T_e/600$  with first-order time formulation. Waves are significantly damped in amplitude for first order even with very small time step size compared to bounded second-order time formulation and distort more with simulation time.

### 4.2 Standing Wave

If two waves having same amplitude, wavelength, frequency and phase angle travel in the opposite directions, then using superposition principle resulting wave displacement can be represented as,

$$\eta(x, t) = A \cos(kx - \omega t + \phi) + A \cos(-kx - \omega t + \phi) \tag{19}$$

$$\eta(x, t) = 2A \cos(kx) \cos(-\omega t + \phi) \text{ and } A_{\text{eff}} = 2A \cos(kx) \tag{20}$$

As the position and time dependence have been separated, this wave is no longer a travelling wave. This wave stands still and oscillates up and down with respect to time, therefore called as standing wave.

### 4.3 Spatial and Temporal Analysis

Assuming the phase difference to be zero and representing locations in terms of quarter wavelengths  $L/4$  and time in terms of quarter time-periods  $T/4$ , effective amplitude and wave profile at various locations and time instances are given as

$$A_{\text{eff}} = \begin{cases} 0 & \text{at } x = nL/4 \\ 2A & \text{at } x = 2nL/4 \end{cases} \text{ and } \eta(x, t) = \begin{cases} 0 & \text{at } t = nT/4 \\ -A_{\text{eff}} & \text{at } t = 2nT/4 \\ A_{\text{eff}} & \text{at } t = 2(n - 1)T/4 \end{cases} \quad (21)$$

where  $n$  is an odd integer. The wave locations with zero displacement at odd multiples of quarter wavelengths are called as nodes, whereas wave locations with maximum displacement at even multiple of quarter wavelengths are called anti-nodes. Constructive interference occurs at even multiples of quarter time-periods, whereas destructive interference occurs at odd multiples of quarter time-periods.

**Problem Description:** Three-dimensional cuboid domain of  $20 \text{ m} \times 10 \text{ m} \times 18 \text{ m}$  is considered with the mesh size of 0.52 million cells. Two waves having wave height and wavelength of 0.02 m and 4 m, respectively, propagate in opposite directions to produce standing wave. Time-period in this case is 1.6 s. Simulation time is 5 s which is about 3 time-periods.

**Results and Discussions:** Wave steepness ratio for individual wave is 0.005 which satisfies linear wave assumption for superposition. According to the best practices of using bounded second-order time formulation for wave propagation problems, time step size is chosen as 0.01 s which is about  $T_e/160$ . Figure 4a shows the free surface contours at  $t = T$ . Figure 4b represents time history of free surface level at different positions. Nodes are located at  $x_5 = 5L/4$ ,  $x_7 = 7L/4$ ,  $x_9 = 9L/4$ , whereas anti-nodes are located at  $x_4 = 4L/4$ ,  $x_6 = 6L/4$ ,  $x_8 = 8L/4$ ,  $x_{10} = 10L/4$  (Eq. 21).

Free surface level at different time instances is presented in Fig. 5. Destructive interference occurs at time instances  $t = T/4$ ,  $3T/4$ . Constructive interference occurs at  $t = 2T/4$  and  $t = 4T/4$  with inverted wave pattern. All the results match closely with the analytical results. Minor deviation from analytical results is due to numerical errors.

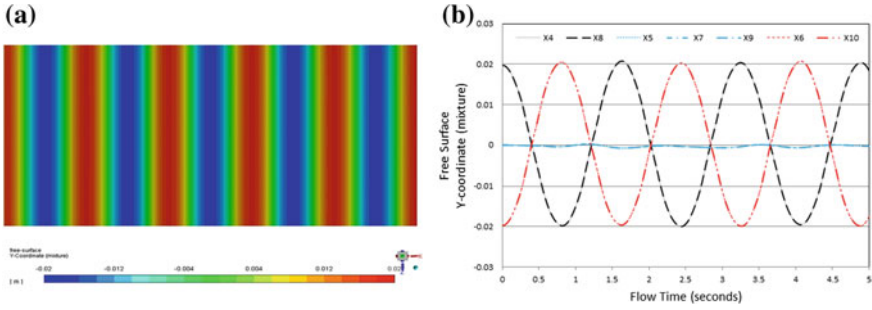


**Fig. 4** **a** Contours of free surface level at  $t = T$ . **b** Time history of free surface level at different positions, where nodes and anti-nodes are observed

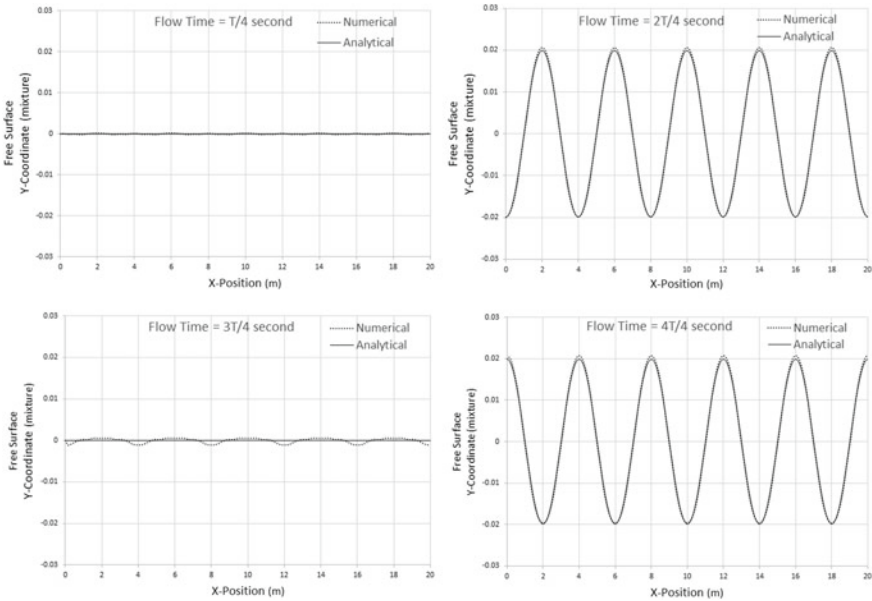


**Fig. 5** Free surface profiles at different time instances in terms of time-period

### 4.4 Beats or Wave Groups

Wave groups are generated when two waves having same amplitude and phase angle are travelling in the same direction with small differences in frequencies and wavelengths. The effective amplitude depends on the increase or decrease in the resultant frequency of the waves over time.

$$\eta(x, t) = A \cos(k_1x - \omega_1t + \phi) + A \cos(k_2x - \omega_2t + \phi) \tag{22}$$

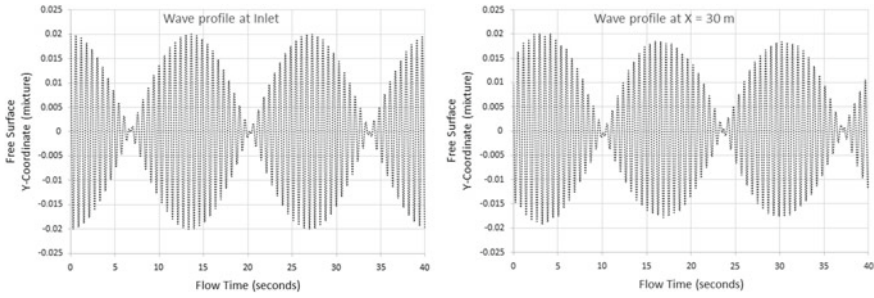


**Fig. 6** Comparing the time history of numerical and analytical wave profile at inlet ( $x = 0$  m) and mid-section ( $x = 30$  m) of the channel

$$\eta(x, t) = 2A \cos\left(\frac{k_1 - k_2}{2}x - \frac{\omega_1 - \omega_2}{2}t\right) \cos\left(\frac{k_1 + k_2}{2}x - \frac{\omega_1 + \omega_2}{2}t + \phi\right) \quad (23)$$

$$A_{\text{eff}} = 2A \cos\left(\frac{\Delta k}{2}x - \frac{\Delta \omega}{2}t\right) \quad (24)$$

Each amplitude envelope contains group of internal waves; therefore, the speed of this envelope is usually called group speed which is defined in terms of phase speed as following,

$$c_g = \frac{d\omega}{dk} = \frac{1}{2} \sqrt{\frac{g}{k}} = \frac{c}{2} \quad (25)$$

**Problem Description:** Two-dimensional rectangular domain of  $60 \text{ m} \times 2 \text{ m}$  is considered with the mesh size of 0.96 million cells. Two waves with wave height of 0.02 m and wavelengths of 1.5 and 1.6 m, respectively, interact with each other to produce wave group. Length of numerical beach zone is 5 m. Average flow velocity is 1 m/s; thus, effective time-periods for waves are 0.5928 and 0.62 s. Simulation time is 50 s which is about 84 time-periods.

**Results and Discussions:** Wave steepness ratio for both the waves is 0.13 which satisfies linear wave assumption for superposition. Time step size is 0.005 s which is about  $T_e/120$ . Figure 6 shows the time history of wave profile at inlet ( $x = 0$  m) and mid-section ( $x = 30$  m) of the channel.

Figure 7 shows the wave profiles at time instances  $t = 10$  and 50 s along the domain where damping effect due to numerical beach zone is visible between  $x = 55$  m and  $x = 60$  m. Numerical beach treatment suppresses the numerical reflections moving upstream; thus, all the results match closely with analytical results in the zone of interest.

Numerical group speed for this case study is obtained by analysing wave profiles as a function of position at a given time instance and wave profiles as a function of time at a given location. From the analysis of wave profiles at  $t = 10$  s in Fig. 7, length ( $L_g$ ) of the envelope is found to be 24 m. From time history of wave profile at

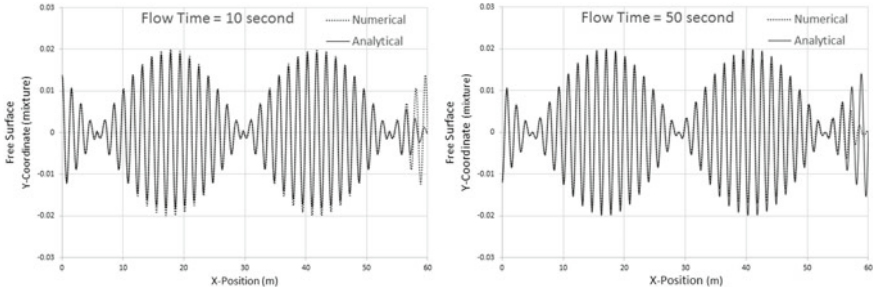


**Fig. 7** Comparison of numerical and analytical wave profiles at various time instances ( $t = 10$  and  $50$  s) along the flow domain

$x = 30$  m in Fig. 6, time ( $T_g$ ) taken by the envelope to travel the length  $L_g$  is found to be 13.65 s. Numerical group speed in case of nonzero averaged flow velocity is calculated as  $c_g = L_g/T_g - U = 0.758$  m/s, which deviates from the analytical group speed value of 0.777 m/s (Eq. 25), as wave frequency is a nonlinear function of wave number for surface gravity waves and can be approximated as linear only in small frequency range.

### 4.5 Irregular Waves

Irregular waves are formed if wave group envelope with large difference in frequencies interacts where linear assumption for wave frequency in small range is violated.

**Problem Description:** Two-dimensional rectangular domain of  $20\text{ m} \times 20\text{ m}$  is considered with the mesh size of 0.013 million cells. Two waves with wave height of 0.02 m and wavelengths of 3 and 6 m, respectively, interact with each other to produce an irregular wave. Length of numerical beach zone is 4 m. Average flow velocity is 1 m/s; thus, effective time-periods for waves are 0.9481 and 1.4776 s. Simulation time is 5 s which is about 4 time-periods.

**Results and Discussions:** Wave steepness ratios for individual waves are 0.0066 and 0.0033 which satisfy linear wave assumption for superposition. Time step size is 0.01 s which is about  $T_e/120$ . Distortion in wave envelope is visible in this case as wave components are travelling with different phase speeds. Wave profiles are validated at two different time instances and results show a good match with analytical (Fig. 8).

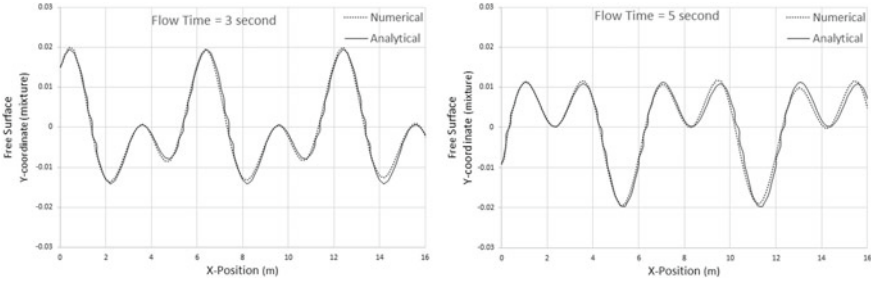


**Fig. 8** Comparison of numerical and analytical wave profiles at flow time of 3 and 5 s along the flow domain

### 4.6 Random Wave

Random waves are most commonly modelled using JONSWAP spectrum which is a fetch-limited version of Pierson–Moskowitz spectrum with more pronounced peak energy. This wave spectrum is never fully developed and continues to develop due to nonlinear wave–wave interactions for a very long period of time and distance. The spectral density is defined as,

$$S_{JS} = S_{PM}(1 - 0.287 \ln(\gamma))\gamma^e^{-0.5\left(\frac{\omega - \omega_p}{\sigma\omega_p}\right)^2} \quad \text{and} \quad S_{PM} = \frac{5}{16} \frac{H_S^2 \omega_p^4}{\omega^5} e^{-\left(\frac{5\omega_p^4}{4\omega^4}\right)} \quad (26)$$

$S_{PM}$  is Pierson–Moskowitz spectral density,  $S_{JS}$  is JONSWAP spectral density,  $H_S$  is significant wave height,  $\omega$  is wave frequency,  $\omega_p$  is peak wave frequency,  $\gamma$  is peak shape parameter,  $\sigma$  is spectral width parameter. In general,  $\sigma$  is taken between 0.07 and 0.09 depending on the wave frequency and  $\gamma$  is taken as 3.3.

Wave spectrum is divided into number of segments, where each segment determines the inputs for individual wave component. Phase angles for different segments are random and distributed between 0 and  $2\pi$ . Amplitude of individual wave component  $A_i$  is calculated using the spectral density at a given frequency  $\omega_i$  and interval  $d\omega$ .

$$A_i = \sqrt{2S(\omega_i)d\omega} \quad (27)$$

Sea steepness is important criterion from the stability perspective which is defined as,

$$s = \frac{2\pi H_s}{g T_p^2} \quad (28)$$

Sea steepness should be less than 0.0667 for waves to be stable based on numerical observations [3].

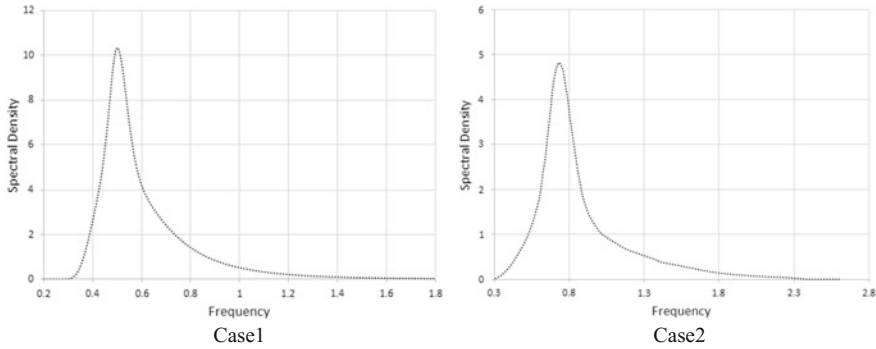


**Fig. 9** Wave frequency versus spectral density for JONSWAP frequency spectrum with sea steepness of 0.0243 (Case 1) and with sea steepness of 0.09 (Case 2)

**Table 1** JONSWAP wave spectrum input parameters for Case 1 and Case 2

JONSWAP wave spectrum input parameter	Case 1	Case 2
Significant wave height, $H_s$ (m)	6	5
Peak wave frequency, $\omega_p$ (rad/s)	0.5	1
Frequency range (rad/s)	0.4–0.7	0.667–1.667
Averaged flow velocity, $U$ ( $m\ s^{-1}$ )	4	20.578
Peak time-period, $T_p$ (s)	12.566	6.28
Mean time-period, $T_m$ (s)	9.996	5.16

**Problem Description:** Propagation of random waves in numerical wave tank without any obstacle is modelled using JONSWAP Frequency Spectrum. We have considered two cases with different sea steepness to verify superposition principle (Fig. 9). JONSWAP wave spectrum input parameters for Case 1 and Case 2 are given in Table 1.

**Case 1:** In first case (Fig. 9 Case 1), sea steepness is 0.0243 based on peak time-period which is lower than the permissible stability limit of 0.0493 (Eq. 28). A 2D computational domain of 1197 m  $\times$  130 m is created with 244K quadrilateral cells. Frequency range is selected falling in the region of maximum wave energy. Wave spectrum is divided into 20 components. Simulation is carried out for 100 s which is about 10 mean time-periods. Numerical beach zone of two wavelengths is applied from outlet; therefore, the effective domain for numerical analysis is about 750 m from upstream boundary along the flow direction.

**Results and Discussions:** Time step size of 0.05 s is used in this simulation which is about  $T_m/200$ . The time history of wave profiles at locations  $x = 200$  m and  $x =$

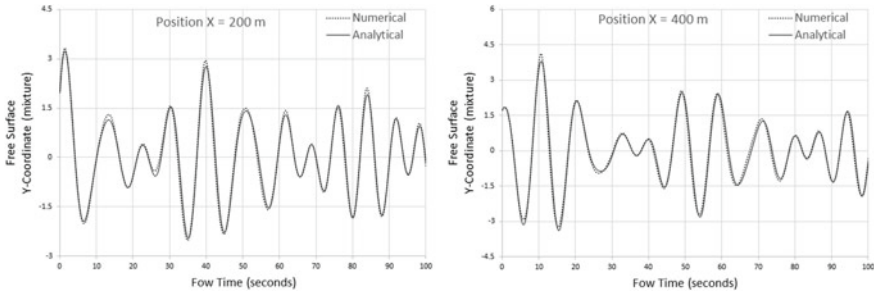


**Fig. 10** Comparison of numerical and analytical wave profiles at 200 and 400 m from the inlet

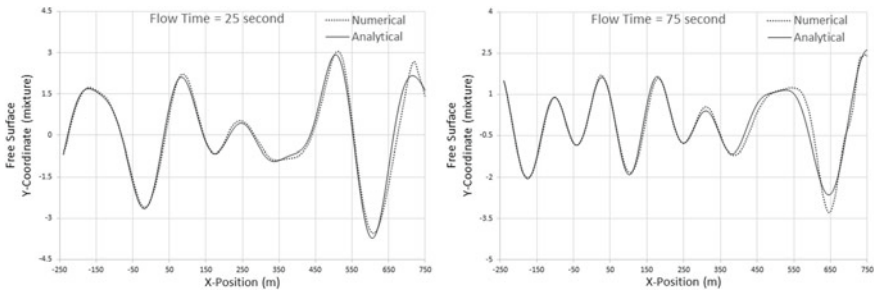


**Fig. 11** Comparison of numerical and analytical wave profiles at time = 25, 75 s along the flow domain

400 m is shown in Fig. 10. Wave profiles at time instances of 25 and 75 s along the domain are shown in Fig. 11. Effective zone of interest for numerical analysis lies between  $-250$  and  $500$  m after excluding numerical beach zone. Results match closely with analytical wave profiles in the zone of interest when sea steepness is below the stability limit.

**Case 2:** In second case (Fig. 9 Case 2), sea steepness based on peak time-period is  $0.09$  which is higher than the stability limit of  $0.066$ . A 2D computational domain of  $500\text{ m} \times 50\text{ m}$  is created with mesh size of 1 million cells. Damping zone length used for numerical beach is  $100\text{ m}$ . Wave spectrum is resolved with 50 wave components. Simulation is being carried out for  $75\text{ s}$  which is about 15 mean time-periods.

**Results and Discussion:** One of the important aspects in this case study is to analyse superposition principle for sea steepness higher than the stability limit [5, 6]. When the wave components are superposed, it is expected that some of the wave components fall within wave-breaking regime and their effect might reflect in the final free surface profile. Time step size used in this study is  $0.01\text{ s}$  which is about  $T_m/500$ . Wave profiles at time instances  $t = 30$  and  $75\text{ s}$  are shown in Fig. 12. As expected, deviations from analytical solutions at higher sea steepness observed through the case have been solved well below the optimal time step size range with bounded second-order time formulation.



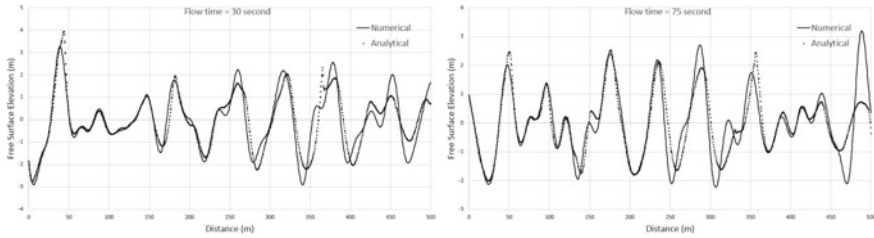


**Fig. 12** Comparison of numerical and analytical wave profiles at time = 30 and 75 s along the flow domain

## 5 Conclusion

In this study, we have successfully demonstrated that CFD can be used to model kinematics of surface gravity waves accurately. Superposition principle is validated through numerical approach for modelling constructive and destructive interferences, standing wave, wave groups and random waves. Random wave studies clearly demonstrate the applicability of superposition using linear wave assumption when sea steepness is within the permissible limits. Bounded variant of second-order transient formulation is very critical to obtain accurate and stable results with much larger time step size compared to first-order time formulation. Optimal time step size has been increased to one-hundredth of effective time-period by using bounded second-order time formulation without losing any accuracy. Effect of numerical beach treatment at the pressure outlet boundary to suppress wave reflection towards upstream is presented. All the results obtained using ANSYS Fluent are in a good agreement with the analytical results. Minor differences are observed between numerical and analytical results for specific scenarios due to discretization errors in numerical schemes. The present study thus covers fundamental aspects of wave phenomena from mathematical and numerical perspective.

## References

1. Tanaka M (2001) A method of studying nonlinear random field of surface gravity waves by direct numerical simulation. *Fluid Dyn Res* 28(1):41
2. Dean RG (1984) *Water wave mechanics for engineers and scientists*. Advanced series on ocean engineering, vol. 2
3. ANSYS Fluent 18.0 theory guide
4. Park JC, Kim MH, Miyata H (1999) Fully non-linear free-surface simulations by a 3D viscous numerical wave tank. *Int J Numer Meth Fluids* 29:685–703
5. DNV-RP-C205 (2010) *Environmental conditions and environmental loads*
6. Lubeena R, Gupta VK, Agrawal M (2014) Wet deck slamming analysis of twin-hulled offshore ship in irregular sea waves

# Numerical Modelling of Hydrodynamic Impact of Tsunami on Coastal Structures in the Presence of Curved Sea Wall



Aditya Gupta , Manasa R. Behera  and Amin Heidarpour 

**Abstract** Tsunami, after arrival at the shore, flows and inundates hundreds of metre inland. The only way of shelter is to take cover on a high elevated structure as it is not possible to evacuate horizontally due to unpredicted nature and high approach velocity of tsunami bore. This high-velocity bore can impact the nearshore structures with extreme loads resulting in catastrophic losses. Therefore, it is necessary to adopt coastal protection measures such as sea walls which can reduce the effect of high impact and hydrodynamic loads on structures. In this study, three-dimensional Reynolds-averaged Navier–Stokes (RANS) equations were solved using finite volume method (FVM) for incompressible two-phase flow (air–water) utilizing numerical solver “interFoam”. Dam-break condition was used to generate the extreme bore to study its interaction with the square structure that represents the coastal elevated structure. The variation of the tsunami force on the structure was investigated by considering two types of curved sea walls as protection measures. The curved face sea wall having nine different radii increasing from bottom to top and another with parabolic profile at the bottom and circular at the top are placed at a distance  $1D$  ( $D$  being the width of structure) from structure face. The results showed that the force on the structure reduced substantially and also differs with the change in geometric shape of the front face of the sea wall and thus helped in achieving an overall understanding of physical mechanisms that occurs due to extreme bore impact on the onshore structures. These results will help in guiding the practicing engineering for proper design of the tsunami shelter buildings as well as the design of sea walls in the tsunami risk zones.

---

A. Gupta (✉)

IIT Bombay-Monash Research Academy, Mumbai 400076, Maharashtra, India

e-mail: [adityagupta1906@gmail.com](mailto:adityagupta1906@gmail.com)

M. R. Behera

Department of Civil Engineering, Indian Institute of Technology Bombay, Mumbai 400076, Maharashtra, India

e-mail: [manasa.rb@iitb.ac.in](mailto:manasa.rb@iitb.ac.in)

A. Heidarpour

Department of Civil Engineering, Monash University, Melbourne, VIC 3800, Australia

e-mail: [amin.heidarpour@monash.edu](mailto:amin.heidarpour@monash.edu)

© Springer Nature Singapore Pte Ltd. 2019

K. Murali et al. (eds.), *Proceedings of the Fourth International Conference in Ocean Engineering (ICOE2018)*, Lecture Notes in Civil Engineering 22,

[https://doi.org/10.1007/978-981-13-3119-0\\_33](https://doi.org/10.1007/978-981-13-3119-0_33)

**Keywords** Tsunami bore · Curved sea walls · Hydrodynamic loads  
Finite volume method · Reynolds-average Navier–Stokes equation

## 1 Introduction

National Oceanic and Atmospheric Administration (NOAA) [1] has reported an overall trend of the increasing frequency of significant earthquake over the last century. The 1990s and latter part of the century have also seen tsunami events causing great damage to life and property in Indonesia (1992, 1994, 1996), Peru (1996), Turkey (1999) and recent devastating event in Indian Ocean (2004) and Japan (2011). The serious effect of tsunami on coastal zone and their countermeasures have been widely studied [2–4]. Inoue et al. [5, 6] investigation showed that the existing coastal structures have lost their original hydrodynamic performance in extreme events and appropriate modifications are required to maintain their efficiencies under tsunami bore impacts. On a dry-bed condition, the run-up of tsunami bore is similar to dam-break condition [7]. Nistor et al. [8–10] have carried out extensive experimental and numerical studies measuring pressure and horizontal forces on square and circular cross-sectional structures by impounding water in reservoir and then generating the dam-break condition by rapidly opening the hinged gate. The studies showed three phases of forces acting on the elemental structure due to incoming bore; they are impulsive, run-up and quasi-steady hydrodynamic forces. Similar forces are also obtained in the present numerical study using OpenFOAM 16.04 [11]. Sea walls have been widely used to protect nearshore structures. Several types of sea walls have been proposed for the reduction of wave overtopping [12–14]. However, these walls could not save the downstream region from the danger of overtopping of wave. There are limited studies on the interaction of incoming extreme bore with faces of curved sea walls. Sarjamee et al. [15] evaluated the performance of low-height, single-radius curve and inclined mitigation wall to assess the loading on the free-standing structure and found noticeable reduction in the net force. In this numerical study, two different types of curved sea walls, suggested by Sundar and Anand [16], were adopted to reduce the impact of extreme tsunami force on the nearshore structure. The numerical model was generated by adopting a model scale of 1:5. The first seawall shape is a combination of parabolic curve at the bottom and circular arc at the top [17], and the second has a circular arc of nine different radii increasing from bottom to top [18, 19]. A computational model was set up in line with the laboratory experiment conducted by Al-Faesly et al. [20] by placing the sea walls in front of the square structure at a distance of 1D ('D' being the width of the square structure). The numerical results were analysed and validated with experimental data.

## 2 Numerical Model Set-Up

The set-up of the computational domain and the numerical study of bore interaction with sea wall are analysed using Open Field Operation and Manipulation (OpenFOAM 16.04). “InterFoam” solver is used for reproducing water–air interaction in extreme condition (dam break). The 3D-averaged Navier–Stokes equations are solved using finite volume method (FMV) discretization for two-phase flow (incompressible) and volume of fluid (VOF) method. Graphic visualizations of the model results were generated using the internally linked version of the open-source software ParaView. Parallel computation of individual cases is achieved through the study “simple geometric decomposition” method, whereby the mesh is divided into a number of subdomains equal to the number of processors.

### 2.1 Governing Equation

In this study, Reynolds-averaged Navier–Stokes (RANS) equation is used to solve the movement of incompressible and immiscible fluids, while volume of fluid (VOF) method is used to capture interface. The RANS equations for continuity and momentum in differential form respectively are given as [21]

$$\frac{\partial \bar{u}}{\partial x} + \frac{\partial \bar{v}}{\partial y} + \frac{\partial \bar{w}}{\partial z} = 0 \tag{1}$$

$$\frac{\partial \bar{u}_i}{\partial t} + \bar{u}_j \frac{\partial \bar{u}_i}{\partial x_j} = -\frac{\partial \bar{P}}{\partial x_i} + \nu \frac{\partial^2 \bar{u}'_i}{\partial x_i \partial x_j} - \left( \frac{\partial \bar{u}_i \bar{u}_j}{\partial x_j} \right) + f_i \tag{2}$$

where  $\bar{u}$ ,  $\bar{v}$ ,  $\bar{w}$ ,  $\bar{P}$  are the mean velocity and pressure components in  $x$ ,  $y$  and  $z$  directions

$$u(t) = \bar{u} + u' \quad v(t) = \bar{v} + v' \quad w(t) = \bar{w} + w' \quad p(t) = \bar{p} + p'$$

### 2.2 Turbulence Model

OpenFOAM includes various turbulence closure models for incompressible flow such as SSG model,  $k - \epsilon$  model,  $k - \omega$ , realizable  $k - \epsilon$  model. For this study, standard  $k - \epsilon$  model [22] is used that parameterizes turbulence into turbulent kinetic energy,  $k$  [Eq. 3], and turbulent dissipation rate,  $\epsilon$ , [Eq. 4] which are simultaneously solved with continuity and momentum equation.

$$\frac{\partial \rho k}{\partial t} + \nabla \cdot \left( \rho U k - \left[ \mu + \frac{\mu_t}{\sigma_k} \right] \nabla k \right) = \tau \nabla U - \rho \epsilon \tag{3}$$

$$\frac{\partial \rho \epsilon}{\partial t} + \nabla \cdot \left( \rho U \epsilon - \left[ \mu + \frac{\mu_t}{\sigma_\epsilon} \right] \nabla \epsilon \right) = C_{\epsilon 1} \frac{\epsilon}{k} \tau \nabla U - C_{\epsilon 2} \frac{\epsilon^2}{k} \quad (4)$$

The turbulent dynamic viscosity is calculated as

$$\mu_t = \frac{C_\mu \rho k^2}{\epsilon} \quad (5)$$

The value of coefficients used in the study are taken as  $C_\mu = 0.09$ ,  $C_{\epsilon 1} = 1.44$ ,  $C_{\epsilon 2} = 1.92$ ,  $\sigma_k = 1.0$ ,  $\sigma_\epsilon = 1.3$ .

### 2.3 Volume of Fluid Model (VOF)

This technique developed by Hirt and Nicholas [23] can capture complicated interface by employing indicator function ‘ $\alpha$ ’ which is a function bound between 0 and 1 and determines the fractional volume of each mesh cell. A grid cell carrying phase fraction value 1 means it is entirely water and 0 means entirely air.

$$\alpha = \begin{cases} 0 & (\text{air}) \\ 0 < \alpha < 1 & (\text{intransition}) \\ 1 & (\text{water}) \end{cases} \quad (6)$$

The fluid physical properties can be simply weighted using the VOF method where the dynamic viscosity

$$\mu = \alpha \mu_{\text{water}} + (1 - \alpha) \mu_{\text{air}} \quad (7)$$

It obeys transport equation described by an advection equation such that

$$\frac{\partial \alpha}{\partial t} + \nabla \cdot U \alpha + \nabla \cdot U_c \alpha (1 - \alpha) = 0 \quad (8)$$

Here,  $U_c = U_i - U_g$  (note that  $U_c$  is the relative velocity between liquid phase and gaseous phase representing water and air).

### 2.4 Time-Step Control

The automatic time-step adjustment is implemented for proper stability of calculations. In a given domain, Courant number  $C_o = 1$  is assumed and then the smallest mesh size ‘ $\Delta x$ ’ and maximum velocity ‘ $U$ ’ of the domain are selected and  $\Delta t$  is calculated using these data. The Courant number is defined as

$$C_o = \frac{|U_f S_f|}{d} \Delta t \tag{9}$$

where  $d$  is a vector between the adjacent faces of two control volumes. The quantities  $U_f$  and  $\Delta t$  are obtained from the previous time step. Based on these values, the new time step can be measured.

### 3 Description of Physical Experiment

The experiments were carried out by Al-Faesly et al. [20] in high-discharge flume (HDF) as shown in Fig. 1 at Ocean Engineering Laboratory at National Research Council Canada (NRC) in Ottawa. Dimensions of HDF were  $14.56 \times 2.7 \times 1.4$  m. Tsunami-like bores were generated by using dam-break mechanism by adapting Lauber and Hager [24] criteria by maintaining gate removal non-dimensional time of  $\sqrt{2}$ . At downstream end of flume, vertical drain was provided to avoid bore reflection. The square structure of  $0.305 \times 0.305 \times 1$  m (acrylic sheet) was placed at 4.92 m from gate. Thirteen wave gauges numbering from WG1 to WG13 were placed at regular interval to measure bore depth. A six-DOF dynamometer was attached at structure base to measure the force. Inundation depth of 0.55 m was considered to generate tsunami-like bores.

#### 3.1 Computational Domain

The configuration of the experimental flume is modelled as shown in Fig. 2. The grid shown in the figure is in metres. To acquire more accurate result of bore behaviour and its interaction with structure, refined mesh of  $1.5 \times 1.5 \times 2$  cm in  $x$ ,  $y$  and  $z$  directions, respectively, was considered.

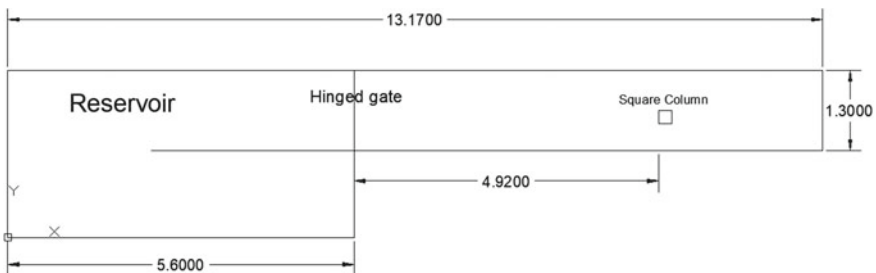


Fig. 1 Plan view of high-discharge flume

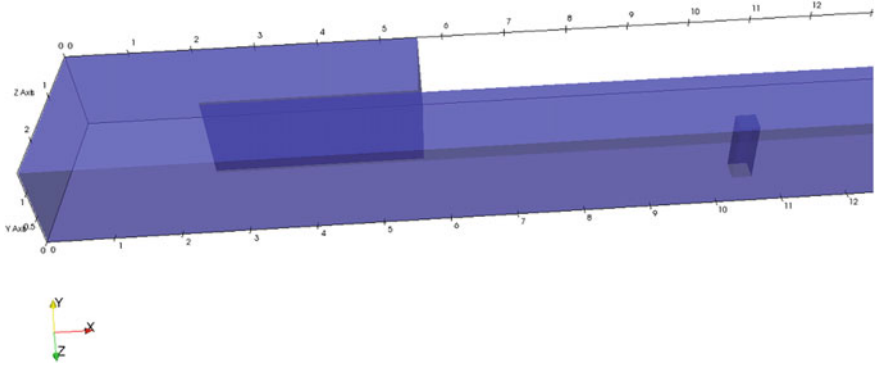


Fig. 2 Computational domain modelled in OpenFOAM

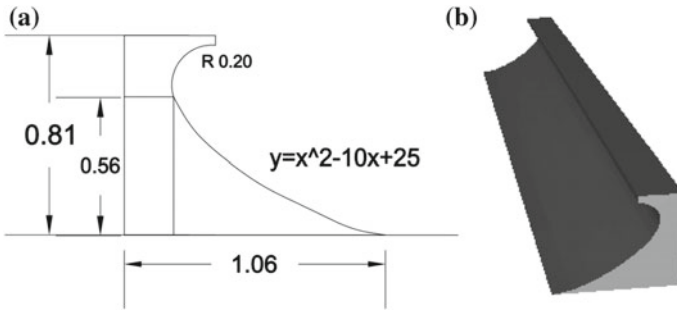
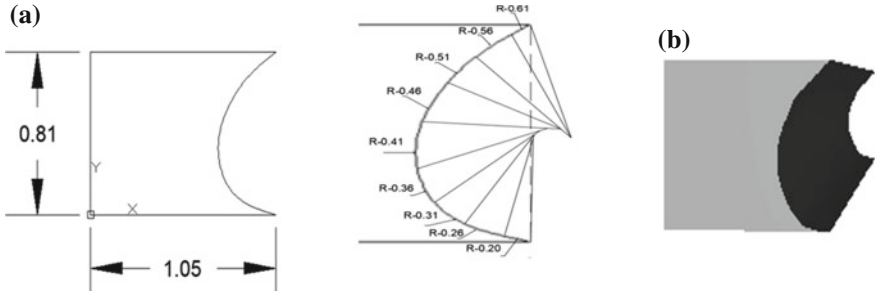


Fig. 3 a Geometry of sea wall proposed by Weber [17] having parabolic profile at the bottom and circular profile at top (dimensions in 'm'), b sea wall modelled for the numerical study

The design of the sea walls was adopted from Sundar and Anand [16] and was modelled to scale 1:5 for this numerical study. The meshing of the curved surface was done by “SnappyHexMesh” utility which generates the 3D meshes containing hex(box) mesh from triangulated geometries creating very fine quality of mesh across edges and curves (Figs. 3 and 4).

### 3.2 Mesh Resolution

To reduce the amount of truncation error, the 3D computational grid cells have to be refined. The cubic grid cells were used to calibrate the mesh resolution. It can be seen from the graph below that the stream bore force changes, the oscillations become damped, and finer details can be observed when the mesh cell size is refined. The  $2.5 \times 2.5 \times 2.5$  cm cell size evaluated lower value of initial impact. The model was unable to capture the sudden drawdown of force after the initial impact at around 2.5 s. The



**Fig. 4** **a** Geometry of sea wall proposed by Kamikubo [19] with nine different radii increasing from bottom to top (dimensions in 'm'), **b** sea wall modelled for the numerical study

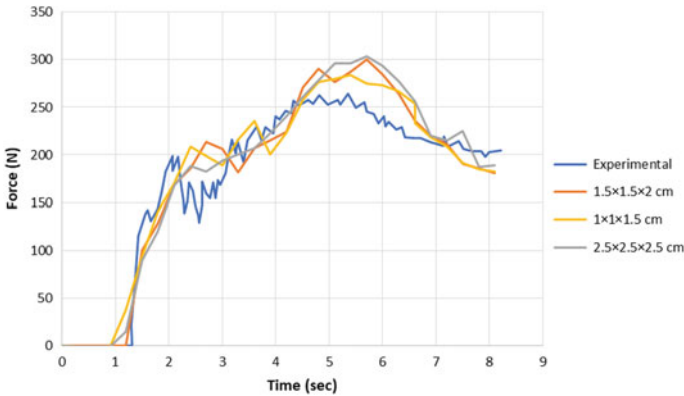


**Fig. 5** Sensitivity analysis for the mesh resolution

peak hydrodynamic force was also in high range as compared to experimental value. As the mesh size is refined to  $1.5 \times 1.5 \times 2$  cm, the rise of initial impact load and its sudden fall were captured as observed in the case of the experiment. Also, the run-up and quasi-steady hydrodynamic load were similar to experimental results. Mesh size  $1 \times 1 \times 2$  gives approximately the same result as  $1.5 \times 1.5 \times 2$  cm refinement, but the computational time increases by 48 h, and thus, for further study,  $1.5 \times 1.5 \times 2$  cm is considered for the simulation (Fig. 5).

## 4 Results and Discussion

### 4.1 Bore Force

The force–time history plot of bore–structure interaction for inundation depth of 0.55 m when there is no sea wall placed is shown in Fig. 6. By integrating the



product of pressure and normals generated over the surface of square structure, force value was obtained. The three phases of force, i.e. impulsive, run-up and quasi-steady hydrodynamic forces, were clearly obtained in numerical modelling. The peak impact force in experiment occurred at 2.0 s, but in numerical modelling, the impact force is delayed which may be due to the non-inclusion of flume roughness. Also, the peak hydrodynamic force is overestimated by approximately 40 N which was also observed in LES model by Sarjamee et al. [15]. After 7.0 s, it was observed that the drawdown rate was much more compared to the experiment as the facility of continuous pumping was provided in physical modelling. So, for the further study, the analysis was considered till 6.5 s only.

#### 4.2 Variation in Force–Time History on Square Structure Due to the Presence of Curved Sea Wall with Front Face Having Nine Different Radii Placed at 1D

The force–time history plot shown in Fig. 7 reveals that the time of impact force on the structure has been delayed by almost 1 s as the curve face of sea wall diverts the water back to the oncoming flow that can be observed from Fig. 8a, thus decreasing the incident energy which could be observed in the reduction of impact force by 60 N or by 30%. The oncoming bore then overtops the sea wall and hits the structure as shown in Fig. 8b and d at time interval of 1.8 and 2.4 s. Although the change in peak hydrodynamic load is not significant, it can be observed that the development of hydrodynamic surge from 2 to 5 s is still low compared to the experimental data.

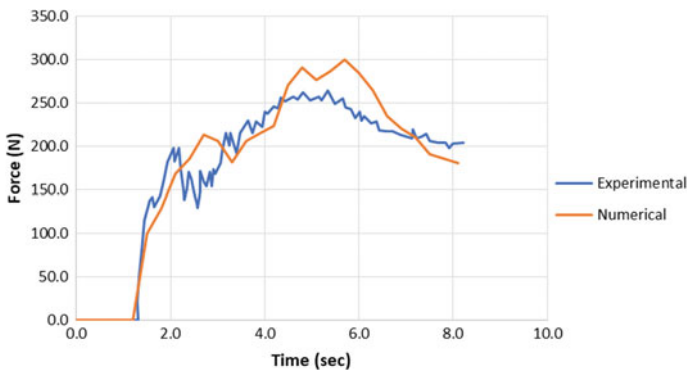


**Fig. 6** Force–time history series on a square structure due to bore generated with 0.55 m impoundment depth

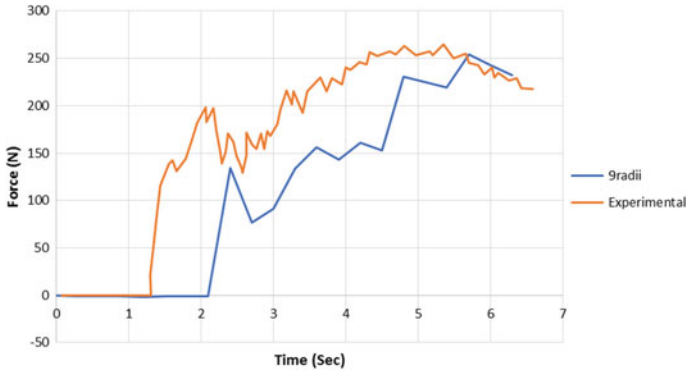


**Fig. 7** Force–time history series on a square structure due to the presence of curved sea wall having nine different radii placed at 1D

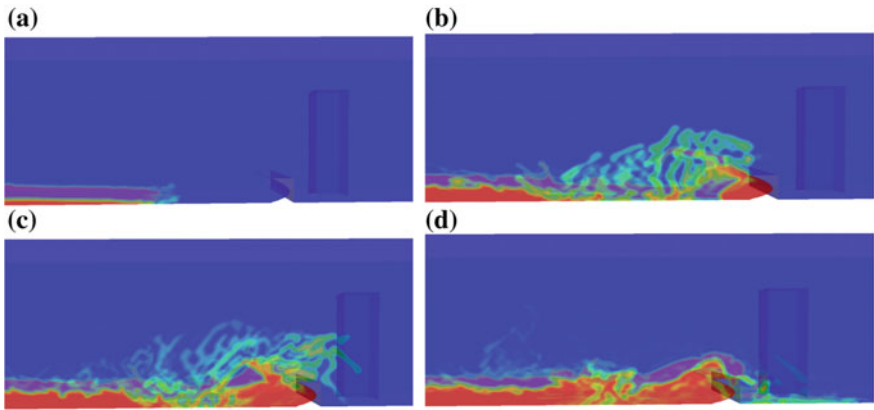


**Fig. 8** Interaction of generated bore with sea wall and structure at interval of 0.9, 1.8, 2.1 and 2.4 s, respectively

**4.3 Variation in Force–Time History on Square Structure Due to the Presence of Curved Sea Wall Having Parabolic and Circular Profile at Bottom and Top of the Front Face, Respectively, Placed at 1D**

The force–time plot shown in Fig. 9 shows that although the first impact force of the bore was reduced by 30%, there was a generation of transient phase at around 3 s due to the reflection of bore from initial impact that collapses on incoming bore also observed by Kihara and Lincoln [25, 26]. The peak hydrodynamic load also exceeds by 30 N. The interaction of bore with sea wall and structure is shown in Fig. 10. In this case, the bore instead of diverting back towards oncoming shore is launched

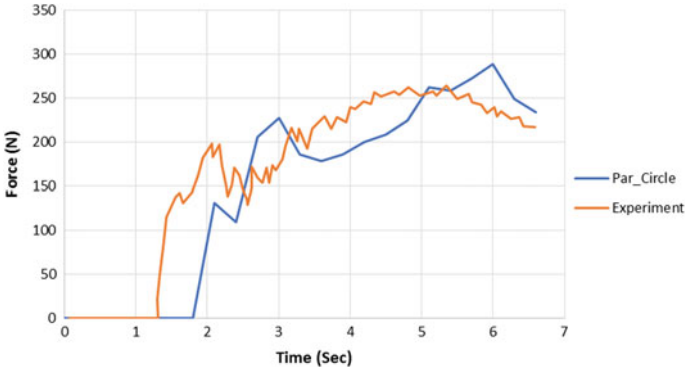


**Fig. 9** Force–time history series on a square structure due to the presence of curved sea wall having parabolic–circular profile placed at 1D

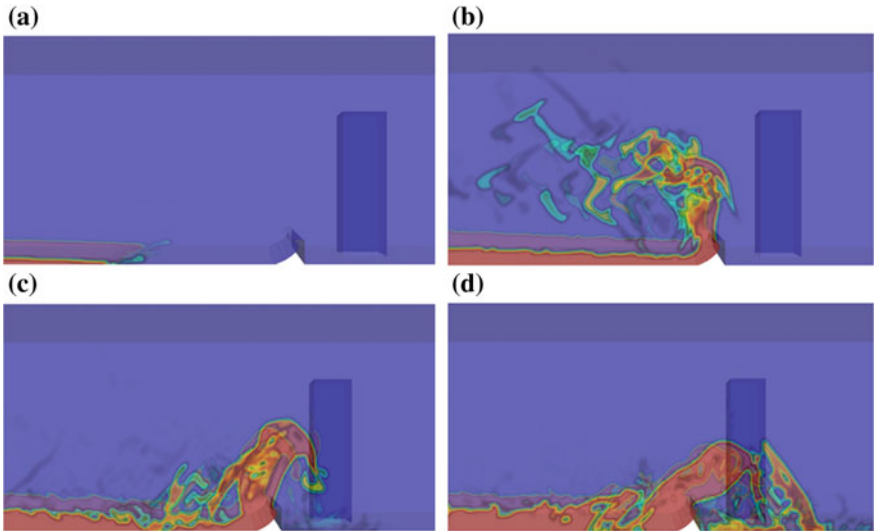


**Fig. 10** Interaction of generated bore with sea wall and structure at interval of 0.9, 1.8, 2.1 and 3.0 s

upwards as shown in Fig. 10b at time 1.8 s. Figure 10c shows the first impact of bore with structure at 2.1 s. The height of the impact was more when compared to nine radii curved wall. Figure 10d shows the generation of transient phase at interval of 3.0 s.

## 5 Conclusion

In this study, the interaction of force induced by extreme bore on a square structure in the presence of two different curved shaped sea walls is modelled. The two walls, i.e. one wall with front face varying with nine different radii increasing from bottom to top and the other wall having parabolic profile at the bottom and circular profile at the top, are kept at a distance of 1D from the square structure. Although the curvature of the wall is inadequate to direct the waves towards ocean, it was observed that the effect of force changes on the structure in the presence of sea wall. The circular arc wall was able to reduce the impact load on the structure by 30%. The peak hydrodynamic load was not reduced significantly, but the development of hydrodynamic load was still low compared to experimental conditions when there was no sea wall present. The analysis of force due to the presence of wall designed by Weber [17] showed that the combination of parabolic and circular profile is not that effective in reducing the load as its profile was unable to divert much water towards ocean instead the bore launched towards the structure at hitting it at much greater height resulting in the increase of hydrodynamic load.

In conclusion, the presence of sea wall can affect the load on a structure, but the shape of the wall plays an important role in reducing the peak load. The curve wall with nine radii was more effective than parabolic–circular profile wall as it was able to divert more water towards ocean resulting in dissipation of incident energy.

## References

1. National Geophysical Data Center/World Data Service (NGDC/WDS) (2017) Significant earthquake database. National Geophysical Data Center, NOAA. <https://doi.org/10.7289/v5td9v7k>
2. Daigle R (2006) Impacts of sea level rise and climate change on the coastal zone of southeastern New Brunswick. Environment Canada
3. Matsui T, Tateishi H, Isobe M, Watanabe A, Mimura N, Shibasaki A (1992) The vulnerability assessment of sea coastal zone in Japan under the sea-level rise. *Proc Coast Eng JSCE* 39:1031–1035
4. Hosomi Y, Kadoyu K, Uchida S, Gomi H, Itahashi H, Mimura N (2005) Public awareness toward sea level rise caused by global warming and future directions of coastal management. *J Coast Eng JSCE* 52:1291–1295
5. Inoue M, Shimada H, Sakamoto Y (1993) Effect of sea level rise on wave overtopping over a seawall. *Proc Coast Eng JSCE* 40:696–700
6. Inoue M, Shimada H, Sakamoto Y (1994) Malfunfunction of wave overtopping over seawall due to sea level rise. *Proc Coast Eng JSCE* 41:676–680
7. Chanson H (2006) Tsunami surges on dry coastal plains: application of dam break wave equations. *Coast Eng J* 48(04):355–370
8. Nistor I, Palermo D, Nouri Y, Murty T, Saatcioglu M (2009) Tsunami-induced forces on structures. In: *Handbook of coastal and ocean engineering*, pp 261–286
9. Nouri Y, Nistor I, Palermo D, Cornett A (2010) Experimental investigation of tsunami impact on free standing structures. *Coast Eng J* 52(01):43–70
10. Palermo D, Nistor I, Al-Faesly T, Cornett A (2013) Impact of tsunami forces on structures. *Int J Tsunami Soc* 32(2):58–76

11. OpenCFD O (2009) The open source CFD toolbox. User guide. OpenCFD Ltd
12. Inoue M (1974) Hydraulic characteristics of seawall with inverted slope. In: Proceedings of 21st conference on coastal engineering in Japan, pp 417–421
13. Itakata A, Yoshida Y, Fujikawa H (1979) Relationships of sectional forms of seawall and wave overtopping. In: Proceedings of 26th conference on coastal engineering in Japan, pp 285–289
14. Kono T, Takano S, Tsuda H (1993) Comparison of wave overtopping rate between seawalls with various kind of cross section. In: Proceedings of 40th conference on coastal engineering in Japan, pp 681–685
15. Sarjamee S, Nistor I, Mohammadian A (2017) Large eddy simulation of extreme hydrodynamic forces on structures with mitigation walls using OpenFOAM. *Nat Hazards* 85(3):1689–1707
16. Sundar V, Anand KV (2010) Dynamic pressure and run-up on curved seawalls compared with vertical wall under cnoidal waves
17. Weber C (1934) U.S. patent no. 1,971,324. U.S. Patent and Trademark Office, Washington, DC
18. Murakami K, Irie I, Kamikubo Y (1997) Experiments on a non-wave overtopping type seawall. In: *Coastal engineering 1996*, pp 1840–1851
19. Kamikubo Y, Murakami K, Irie I, Hamasaki Y (2001) Study on practical application of a non-wave overtopping type seawall. In: *Coastal engineering 2000*, pp 2215–2228
20. Al-Faesly T, Palermo D, Nistor I, Cornett A (2012) Experimental modeling of extreme hydrodynamic forces on structural models. *Int J Prot Struct* 3(4):477–505
21. Rodi W (1993) *Turbulence models and their application in hydraulics*. CRC Press
22. Launder BE, Spalding DB (1974) The numerical computation of turbulent flows. *Comput Methods Appl Mech Eng* 3(2):269–289
23. Hirt CW, Nichols BD (1981) Volume of fluid (VOF) method for the dynamics of free boundaries. *J Comput Phys* 39(1):201–225
24. Lauber G, Hager WH (1998) Experiments to dam-break wave: horizontal channel. *J Hydraul Res* 36(3):291–307
25. Kihara N, Niida Y, Takabatake D, Kaida H, Shibayama A, Miyagawa Y (2015) Large-scale experiments on tsunami-induced pressure on a vertical tide wall. *Coast Eng* 99:46–63
26. Linton D, Gupta R, Cox D, Lindt J, Oshnack M, Clauson M (2013) Evaluation of tsunami loads on wood-frame walls at full scale. *J Struct Eng* 139(8):1318–1325

# Numerical Study on Secondary Flow Characteristics After Dual Stepped Cylinder at Low Reynolds Number



Junxian Wang, Qingwei Ma and Shiqiang Yan

**Abstract** A dual stepped cylinder consists of two small slender cylinders of the same diameter being co-axially connected by a large one. Flow travelling over the step surface can generate strong ‘end flow’, which goes and develops downstream, approaching the large cylinder. This ‘end flow’, defined as ‘downwash’, gives rise to the impact of three-dimensional vortex shedding in the wake area, which is numerically investigated in the present paper at the Reynolds number of 150 (Reynolds number is estimated based on the diameter of the large cylinder.). Apart from that, the vertical velocity in the wake goes downstream, at the same time transferring up and down periodically. This periodic vertical flow, together with the ‘end flow’, can be attributed to ‘secondary flow’. In the present paper, flow passing two stepped cylinders with diverse diameter ratios ( $D/d$ ) are modelled numerically. Results about the corresponding vertical velocity and ‘end flow’ are comprehensively studied. The relationship between velocity field and vortex structures in the wake is also investigated in this present paper.

**Keywords** Stepped cylinder · Vortex shedding · Laminar flow · Secondary flow

## 1 Introduction

In offshore oil and gas industry field, catenary risers are widely used to connect wells at seabed and platforms near the ocean surface. Considering its long arch length, which can reach several kilometres, there could be extremely huge tension near the

---

J. Wang · Q. Ma (✉) · S. Yan

School of Mathematics, Computer Science and Engineering, City, University of London, London, UK

e-mail: [Q.Ma@city.ac.uk](mailto:Q.Ma@city.ac.uk)

J. Wang

e-mail: [Junxian.Wang@city.ac.uk](mailto:Junxian.Wang@city.ac.uk)

S. Yan

e-mail: [Shiqiang.Yan@city.ac.uk](mailto:Shiqiang.Yan@city.ac.uk)

© Springer Nature Singapore Pte Ltd. 2019

K. Murali et al. (eds.), *Proceedings of the Fourth International Conference in Ocean Engineering (ICOE2018)*, Lecture Notes in Civil Engineering 22,

[https://doi.org/10.1007/978-981-13-3119-0\\_34](https://doi.org/10.1007/978-981-13-3119-0_34)

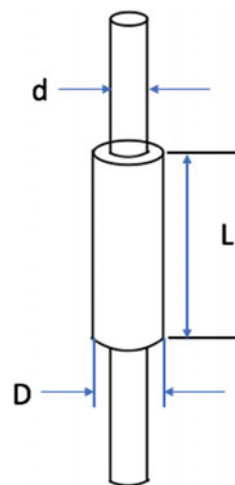
top end owing to its self-weight. Hence, the buoyancy modules are utilized and assembled round the middle of the risers, which can greatly reduce the top tension. Whilst with the existence of the buoyancy modules, geometrical profile along the risers' spanwise direction is no longer uniform. When flow goes around this kind of structure, the pressure distribution on the surface of such structure is different from the cases of cylinders with uniform profile. Besides, flow characteristic in the wake will vary distinctly along its spanwise direction.

In the present paper, the structure of risers with multiple buoyancy modules could be truncated and simplified as a dual stepped cylinder, which can be shown in Fig. 1, where ' $d$ ' denotes the diameter of the small cylinder and ' $D$ ' denotes the diameter of the large cylinder. The normalized term of diameter ratio is defined as  $D/d$ . Considering the diameter variation, the properties of the vortices after the large cylinder and the small cylinder are very different in terms of the vortex intensity, formation length and the shedding frequency. In consequence, the step junction with this sudden change of the diameter can give rise to strong vortex interaction in the wake near these discontinuous sections. Besides, there are part of flow travelling over the step surface, which can be named as 'end flow'. With the impact of 'end flow', the vortex interaction gradually develops and travels downstream.

Previously, researchers have studied the issues of flow passing a cylinder with geometrical variation along the axial direction for several decades, such as a tapered cylinder (usually a cone) [1–3], and the cylinder with a free end, namely a cantilever cylinder [4, 5]. It reveals that flow patterns in the wake show strong three-dimensional features in space. Besides, the surficial pressure coefficient and sectional force coefficients are no longer uniform, especially near the free end.

For the single stepped cylinder, three-dimensional characteristics of flow after the structure are governed by the diameter ratio and the Reynolds number. At low Reynolds number, Lewis and Gharib [6] carried out a series of experiments and put

**Fig. 1** Diagram of the dual stepped cylinder [14]



forward two diverse regimes based on the diameter ratio, i.e. direct mode ( $D/d < 1.25$ ) and indirect mode ( $D/d > 1.55$ ). At the direct mode, the in-phase vortex connection and the out-of-phase connection occur alternately, owing to vortex shedding frequency difference after the small cylinder and the big cylinder. S-cells (vortex shedding cells after the small cylinder) directly connects with L-cells (vortex shedding cells after the large cylinder) located at the other side of the step surface plane. If there is no L-cells matching S-cells, the out-of-phase situation occurs, when two neighbouring S-cells with the same direction connect with each other near the step surface plane, forming the so-called half-loop. As for the indirect mode, a new type of vortex cell emerges after the big cylinder near the step junction, which can be named as the N-cell. It possesses a lower frequency than S-cell and L-cell. With its development downstream, it grows and disappears periodically. Terms of 'S-cell', 'L-cell' and 'N-cell' were defined and introduced by Dunn and Tavoularis [7]. In addition, Norberg [8] implemented a series of relevant researches, focusing on the impact of the Reynolds number, and found the N-cell zone reduces with the increasing of the Reynolds number.

The dual stepped cylinder introduces a new core factor which also affects the flow structure in the wake, namely the aspect ratio of the large cylinder ( $L/D$ ). Williamson [9] investigated dual stepped cylinders with a low aspect ratio ( $L/D = 0.5$ ) and low diameter ratios of 1.1–2 experimentally. He found that vortex dislocation happens near the step junction and the frequency of vortex dislocation is equal to the frequency difference between the small cylinder and the big cylinder. After that, Morton and Yarusevych [10, 11] studied the impact of the aspect ratio at the Reynolds number ( $Re_D$ ) of 150 and the diameter ratio at 2. Referring to vortex interaction visualization after the dual stepped cylinder, they put forward to four regimes by the magnitude of  $L/D$ . Recently, McClure et al. [12] studied the combined effect of diameter ratio ( $4 \geq D/d \geq 1.1$ ) and aspect ratio ( $5 \geq L/D \geq 0.2$ ) at the Reynolds number ( $Re_D$ ) of 150. In their study, four regimes were detected and given the name, as shedding of hairpin vortices, transient asymmetric shedding, primarily spanwise shedding and no vortex shedding.

In terms of the N-cell, Morton and Yarusevych [13] numerically recorded spanwise component of velocity near the step junction of a single stepped cylinder, which could represent the downwash. They found the variation of downwash with time can be decomposed into high-frequency fluctuations and low-frequency fluctuations, the former of which is governed by vortex shedding. They found the low-frequency fluctuations show great consistency with N-cell development.

The aforementioned studies on stepped cylinders provide the background of vortex interaction after the step junction. The downwash, which can be attributed to a kind of 'secondary flow', has been proved to affect vortex interaction after the single stepped cylinder. Wang et al. [14] numerically investigated the characteristic of dual stepped cylinders with different diameter ratios. The sectional force and surficial pressure distribution on big cylinder were discussed in that paper. The present study will investigate secondary flow characteristics near step surface and in the wake numerically by using OpenFOAM v2.3.0, and furthermore establish the link between secondary flow and the vortex interaction in the wake of dual stepped cylinder.



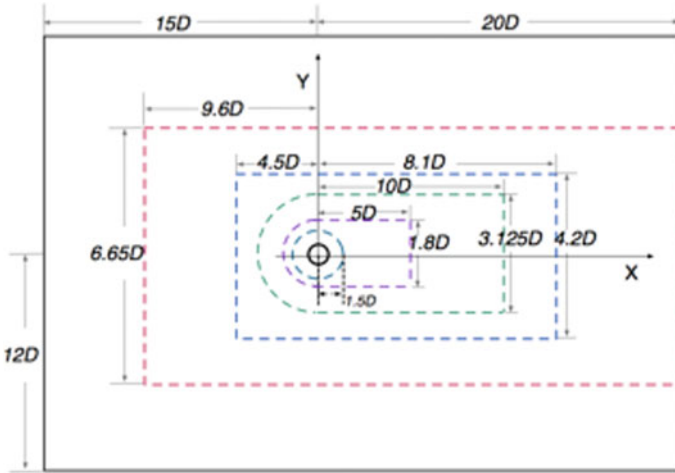
## 2 Numerical Configuration and Validation

In this study, dual stepped cylinders with the diameter ratio ( $D/d$ ) of 2, 4 are numerically studied. All the cylinder segments have the same length of  $L = 5D$ . The dual stepped cylinders' dimensions, as well as the computational domain size, keep the same with that in McClure et al. [12]. Numerical configurations utilized in the present study have already been made comprehensive in our previous study [14]. Figure 2 gives a sketch of the entire computational domain, including the arrangement in  $X$ - $Y$  plane and  $X$ - $Z$  plane. A total of five blocks marked in Fig. 2 help to divide the whole domain. Size of each block is decided by implementing a series of convergence tests, which has been narrated in [14]. The inlet velocity is assigned as  $u = (U, 0, 0)$ , and the pressure at the outlet boundary is set as zero. The Reynolds number ( $Re_D = UD/\nu$ ) of both cases are fixed to 150, where  $\nu$  represents the kinematic viscosity. No-slip condition is employed on the cylinder surface, and free-slip condition is assigned at the remaining boundaries. The numerical simulations are implemented at the platform of OpenFOAM v2.3.0, and the unstructured meshing strategy, namely the cut-cell mesh, is utilized by means of software Star-CCM+ v11.02.009.

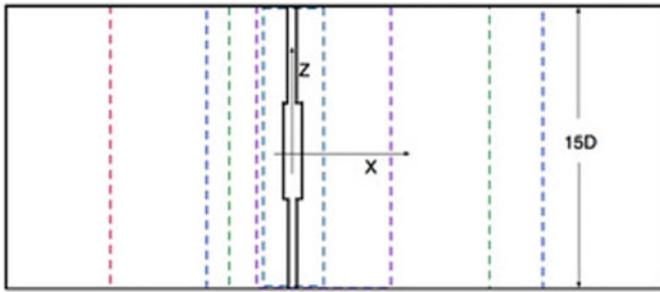
To verify numerical models used in this study, the drag force coefficients ( $C_d$ ) and lift force coefficients ( $C_l$ ), together with base pressure coefficient ( $C_{bp}$ ) of the big cylinder, are compared with results presented in [12]. The comprehensive validation processing was presented in [14], where great consistency with the reference paper is shown.

## 3 Streamline and Vertical Velocity Analysis

In this section, three-dimensional instantaneous streamline distribution ( $t = 357.6$  s) after stepped cylinders with diameter ratio of 2 and 4 is displayed and analysed, contrastively. The reference line is selected from point A ( $5D, 0.75D, 7.5D$ ) to point B ( $5D, 0.75D, -7.5D$ ), which allows all the streamlines that go through the reference line are displayed in Figs. 3 and 4.  $X$ -axis and  $Z$ -axis represent the streamwise direction and spanwise direction, respectively. The colours in Figs. 3 and 4 stand for vertical velocity component value, the blue of which denotes drop flow and the red of which denotes rising flow. The incident flow, coming from the negative  $X$  direction, hits the upwind surface and goes around the cylinder. There is a flow component, called 'end flow', travelling over the step surface. It goes downstream, gradually approaching the middle plane ( $Z = 0$ ), owing to the strong negative pressure after the big cylinder. The 'end flow' interacts with vortices detached from the small cylinder and the big cylinder and further affects the 'vortex interaction'. It could be found in Figs. 3 and 4 that the vertical velocity (defined as  $U_v$ ) can be detected near the step surface, and it changes periodically in the wake of the stepped cylinder.



(a) Plan view of the computational domain (X-Y plane)



(b) Side view of the computational domain (X-Z plane)

**Fig. 2** Sketch of the computational domain. Dash lines from outer to inner indicate blocks 1~5, respectively [14]

By comparing Figs. 3 and 4, it could be found  $U_v$  near the upwind step surface of  $D/d = 2$  has higher magnitude than that of  $D/d = 4$ , which reveals that the bigger step surface can contribute to the increasing of vertical velocity component near the step junction. After travelling over the step surface, ‘end flow’ in Fig. 3 suddenly and quickly goes towards the middle plane ( $Z = 0$ ), whilst in Fig. 4, it goes with slight slope and slowly touches the middle plane ( $z = 0$ ) at  $X/D = 4$ . It can be inferred the ‘end flow’ in Fig. 4 experiences a further horizontal distance to arrive near the middle plane. At  $X/D = 5$ , the spanwise vertical velocity distribution at  $D/d = 2$  is wider than that of  $D/d = 4$ . It means that  $U_v$  exists after the small cylinder and this vertical velocity component continuously connects the neighbour wake of big cylinder, whilst flow after the small cylinder at  $D/d = 4$  does not produce vertical flow component.

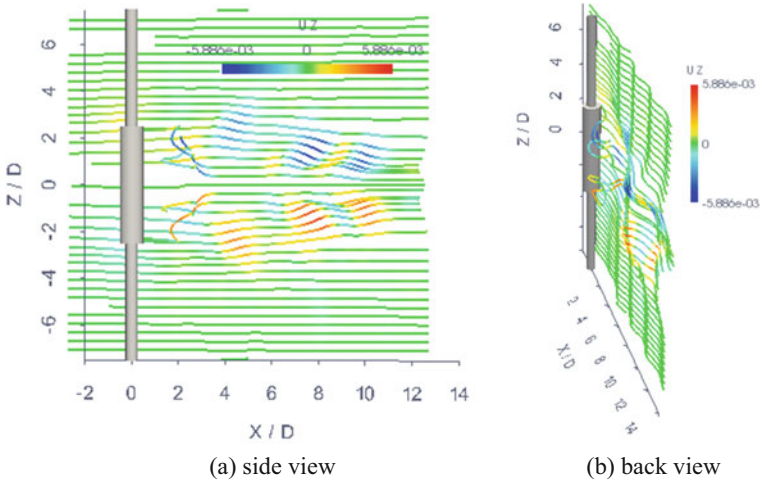


Fig. 3 Instantaneous streamline distribution ( $D/d = 2, t = 357.6$  s)

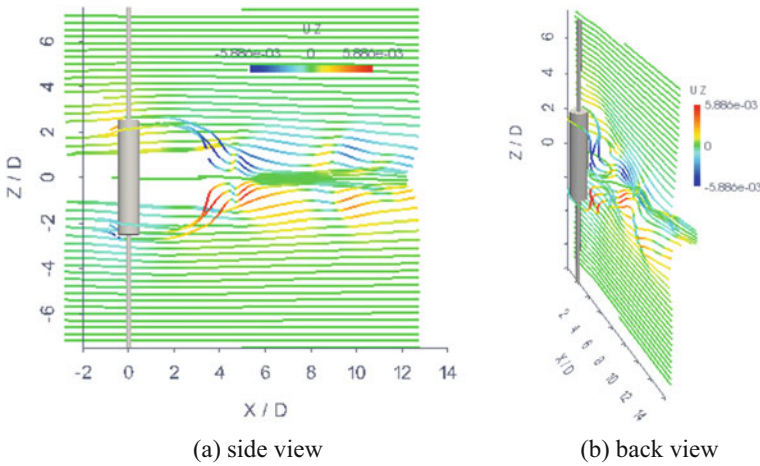
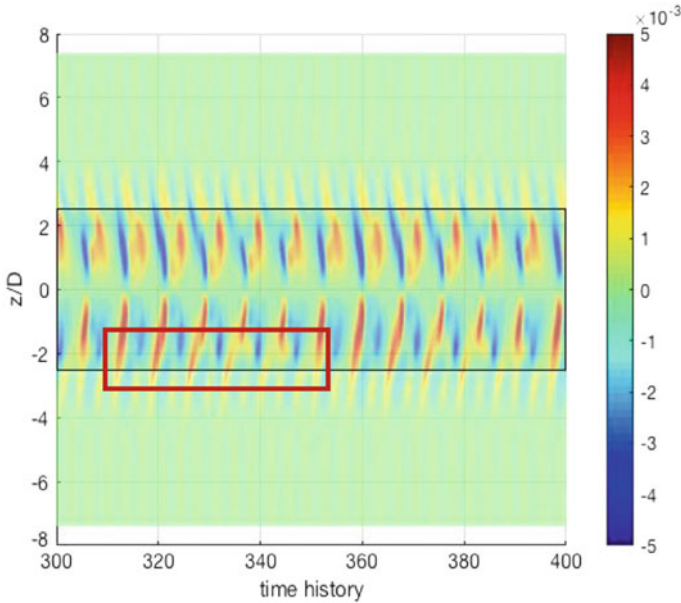


Fig. 4 Instantaneous streamline distribution ( $D/d = 4, t = 357.6$  s)

In order to gain insight into the variation of vertical flow in time in the wake, the vertical velocity component is captured along a spanwise line at  $X/D = 5$  and  $Y/D = 0.75$ . The corresponding results of  $D/d = 2$  and  $D/d = 4$  are presented in Figs. 5 and 6, respectively. The  $X$  coordinate stands for time history, and the  $Z$  coordinate stands for the spanwise location. The colour represents the vertical velocity value. It should be noted that the dark shadow area in Figs. 5 and 6 represents results in the wake after the big cylinder. Thus, the top boundary and the bottom boundary of the dark shadow area can be thought of as interfaces of the step surface planes in the wake.  $U_v$  shown in Figs. 5 and 6 changes periodically in time. Most part of  $U_v$  emerges in



**Fig. 5** Vertical velocity component variation depending on time history ( $D/d = 2$ , time = [300 s, 400 s])

the wake of big cylinder. When we focus on one specific cycle, vertical velocity on both sides of the middle plane ( $Z = 0$ ) transfers symmetrically. The first half cycle, vertical flow on both sides travels towards the middle plane ( $Z = 0$ ), and they move away the middle plane ( $Z = 0$ ) at the other half cycle. Velocity value at the first half cycle and the rest half cycle are different owing to the sample line locating at  $Y/D = 0.75$ .

Several differences of the vertical flow behaviour can be detected in Figs. 5 and 6. Apart from most vertical flow existing after the big cylinder, vertical velocity can be found in the wake of small cylinder in Fig. 5. Vertical flow after the big cylinder seems to be more concentrated in Fig. 6, whilst vertical velocity after the big cylinder is widely distributed in Fig. 5, almost from upper step surface to the lower step surface. Besides, vertical flow near the step surface plane shows a long-period behaviour (seeing the red frame region in Fig. 5).  $U_v$  after the big cylinder exists a strong connection with that after the small cylinder at  $t = 311.7$  s. As time goes on,  $U_v$  after the big cylinder gradually loses the matching (seeing  $t = 343.9$  s) and establishes a new connection with the next branch of  $U_v$  after the small cylinder at  $t = 350.8$  s. Vertical flow along both sides of the step surface connects with each other, and then gradually dis-match, after that they reconnect again and start the next loop.

Figure 7 gives a comprehensive illustration about  $U_v$  fluctuation after dual stepped cylinders with  $D/d = 2$  and  $D/d = 4$ . The dark shadow area denotes results after the

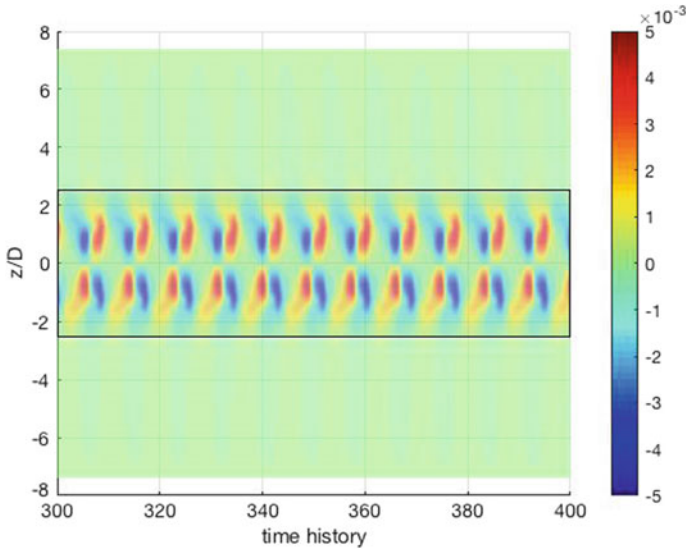
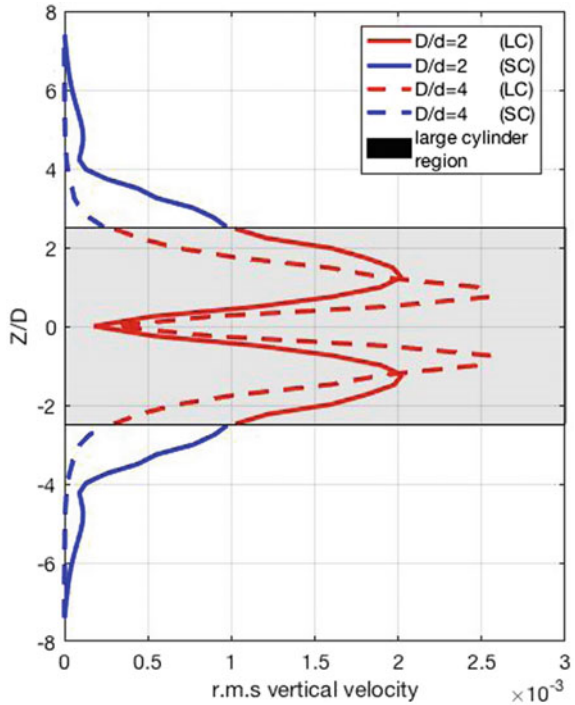


**Fig. 6** Vertical velocity component variation depending on time history ( $D/d = 4$ , time = [300 s, 400 s])

large cylinder region, and red lines and blue lines represent results after the large cylinder and small cylinder, respectively. The  $X$ -axis stands for the r.m.s vertical velocity, and the  $Z$ -axis stands for the spanwise location. It could be found that the curves are symmetrical along the middle plane and vertical velocity near the step surface plane shows clear continuity. The fluctuation gradually becomes strong with it moving towards the middle plane and reaches the highest level at a specific plane in the large cylinder region. After that, it starts to weaken till the middle plane. Compared with the curve of  $D/d = 4$ , the maximum velocity fluctuation of  $D/d = 2$  is weaker and the spanwise location where it is captured is further away from the middle plane ( $Z = 0$ ). As for the curve of  $D/d = 2$ , the maximum velocity fluctuation with the value of 0.002017 happens at  $Z = 1.241D$  and  $-1.241D$ , whilst the maximum velocity fluctuation is detected at  $Z = 0.744D$  and  $-0.744D$ , with the value of 0.002551. Besides, vertical flow can be markedly observed after the small cylinder under the condition of ' $D/d = 2$ '. At the spanwise region of  $4.228 \leq Z/D \leq 2.52$  and  $-4.228 \leq Z/D \leq -2.52$ , the r.m.s value increases dramatically, from  $8.89E-05$  to  $0.9E-3$ . With respect to the case of ' $D/d = 4$ ', no distinct vertical velocity can be found after the small cylinder.

**Fig. 7** Vertical velocity fluctuation distribution along the spanwise direction



#### 4 Relationship Between Vertical Velocity and Vortex Interaction

Based on the analysis of previous sections, the ‘end flow’ travels over two step surfaces and then goes downstream, gradually approaching the middle plane ( $Z = 0$ ). With the development of the vertical flow in the wake after the big cylinder, the vertical flow transfers up and down, periodically. The occurrence of this periodic vertical flow component owns to some other factors, instead of the ‘end flow’. Another issue is that a periodic vertical flow component can be detected after the small cylinder at ‘ $D/d = 2$ ’. This periodic vertical flow component connects, dis-matches and reconnects with the periodic vertical flow after the big cylinder, which forms a loop with long period. Figure 8 gives a description of instantaneous vorticity iso-surface, together with the streamline distribution. This section tries to establish the link between the vortex development and the vertical velocity component, and further solve these two issues.

Referring to the vortices analysis in the wake of dual stepped cylinder from McClure et al. [12], vortices detached from the small cylinder make a complex interaction with vortices in the wake of big cylinder, and vortices in the wake of small cylinder and big cylinder can be defined as S-cell and L-cell, respectively. For the most part, a specific S-cell connects with a neighbouring L-cell. The ends of the

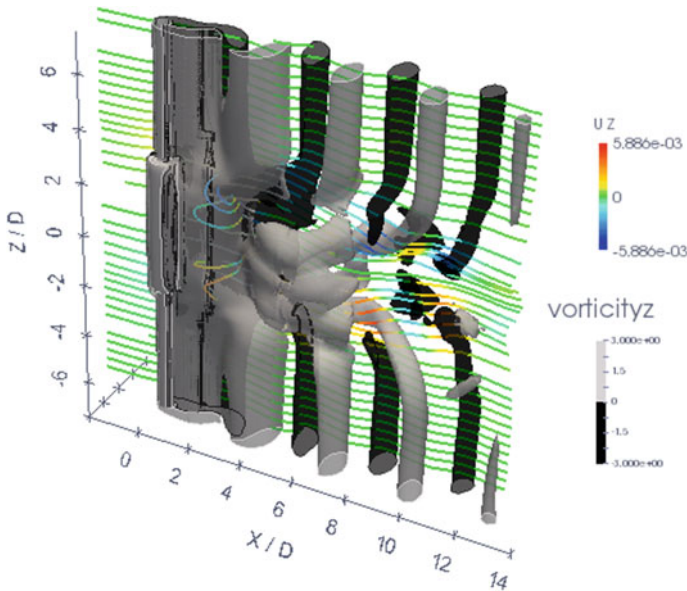


**Fig. 8** Instantaneous vorticity iso-surface ( $D/d = 2$ ,  $t = 357.6$  s)

corresponding vortex tube become bending owing to the higher vortex shedding frequency of S-cells. As the ‘end flow’ travels over the step surface and goes towards the middle plane, vortex connections will be dragged towards the middle plane, which induces S-cells extend across the step surface plane into the wake of the big cylinder. Besides, with the combined effect of ‘end flow’ near the upper step surface and the lower step surface, vortex tubes detached from the big cylinder gradually change the shape into a ‘hairpin shape’ [12]. Considering the imbalanced vorticity strength between S-cells and L-cells, it can be detected that one single L-cell can connect with more than one single S-cell with the same vorticity direction. As a result, vortices detached from the small cylinder make a complex interaction with vortices in the wake of big cylinder.

Figure 9 gives a close-up view of instantaneous vorticity iso-surface, including several vortex connection nodes. A total of six black frames (A, B, C, D, E, F) are marked, to recognize six vertical flow regions. It could be obviously found the shape of vortex tubes near the connection nodes bends clearly. Odd-shaped vortex tubes near connection nodes make the velocity field near connection nodes complex. There are vertical flow existing in Frames A, C, D and F, the vertical flow of which goes through the corresponding vortex connection nodes. With the vortex connection nodes periodically developing downstream, vertical velocity components in Frames A, C, D and F transfer downstream periodically as well. It should be noted that there is the relatively slight vertical velocity existing in Frames B and F, which could be explained that streamlines, going across the neighbouring connection nodes, become bending and generate the vertical velocity components. As a result, the bending of

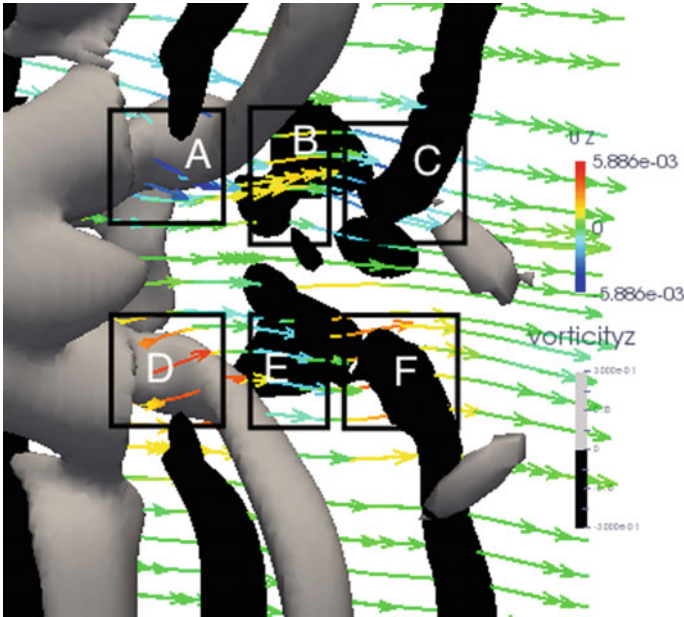


**Fig. 9** Close-up view of instantaneous vorticity iso-surface ( $D/d = 2, t = 357.6$  s)

vortex tubes can generate the vertical velocity component. The Reynolds number of the small cylinder at ' $D/d = 4$ ' is 37.5 which does not meet the minimum value which allow the vortex shedding occurrence. Consequently, the vertical velocity can be detected after the small cylinder at ' $D/d = 2$ ' and cannot emerge in the wake of the small cylinder at ' $D/d = 4$ ' (see Figs. 5 and 6). Besides, the primary  $U_v$  regions in Fig. 3 are accompanied by the vortex connection nodes, and the slight  $U_v$  regions which exist in the middle of the neighbouring primary  $U_v$  regions are caused by the bending of streamlines between the neighbouring vortex connection nodes.

## 5 Vortex Interaction Transition

It has been detected and analysed in Fig. 5,  $U_v$  near the lower step surface plane experiences a long-period loop, when it breaks and establishes the connection periodically (seeing the red frame marked in Fig. 5). According to the analysis of relationship between  $U_v$  and vortex interaction, the periodic occurrence of  $U_v$  after the stepped cylinder is accompanied with the development of the vortex connection nodes. It could be inferred that the break and establishment of vortex interaction take place periodically when the long-period  $U_v$  phenomenon happens. In consequence, Fig. 10 presents a series of consequent vorticity contour slice ( $Y/D = 0.75$ ) which captures near the lower step junction, at the moments of 374, 377.6, 381.2, 384.8, 388.2 and



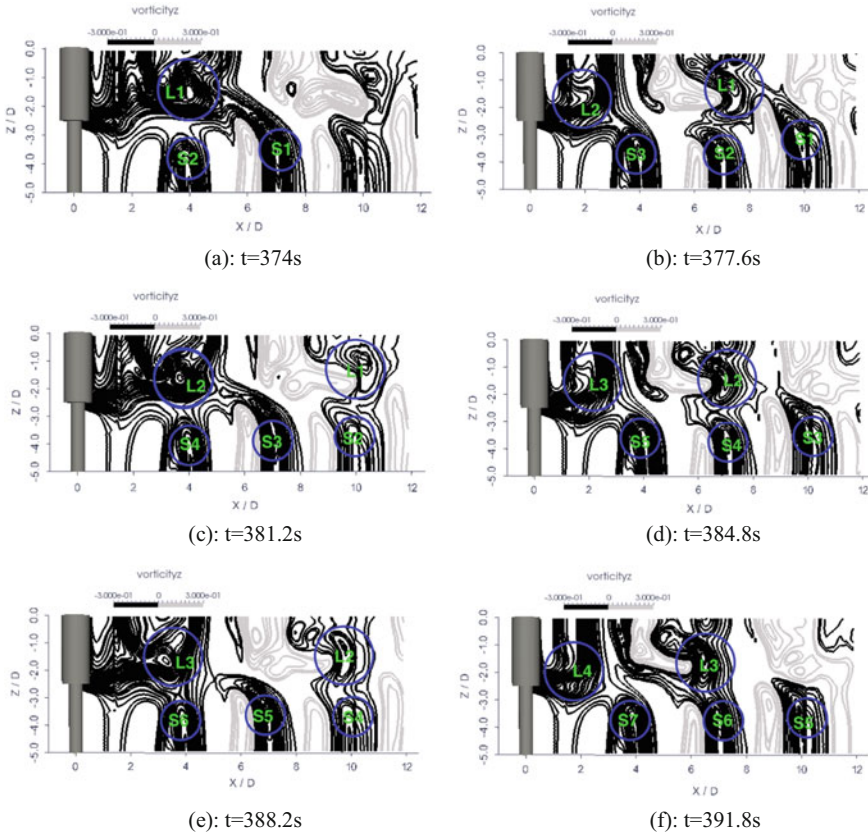


**Fig. 10** Close-up view of instantaneous vorticity contour ( $D/d = 2$ ,  $t = 374, 377.6, 381.2, 384.8, 388.2, 391.8$  s)

391.8 s, respectively. A series of L-cells are defined as L1, L2, L3 and L4, and S-cells are defined as S1, S2, S3, S4, S5, S6 and S7, respectively. To make S-cells in every capture located at the same phase, the newest S-cells in every capture, i.e. S2 (a), S3 (b), S4 (c), S5 (d), S6 (e), S7 (f), are assigned at  $X = 4D$ .

Firstly, by observing Fig. 5 again, it could be found the  $U_v$  gradually breaks the connection between the component after the big cylinder and the component comes from the small cylinder at  $t = 374, 381$  and  $388.2$  s. As  $U_v$  in Fig. 5 are selected at the line of  $X/D = 5, Y/D = 0.75$ , the corresponding vorticity results in Fig. 10 can be linked at  $X/D = 5$ . With the analysis of (a), (c) and (e) in Fig. 10, it could be found that vortex connections of L1-S1, L2-S3, L3-S5 are gradually become weaker, and finally L3 and S5 break the connection with each other at  $t = 388.2$  s. Meanwhile, vortex connections of L1-S2, L2-S4, L3-S6 at (a), (c), (e) become stronger. This phenomenon can be described as ‘vortex interaction transition’. At (b), (d) and (f) of figure, it could be found that the phase difference of L1-S1, L2-S3 and L3-S5

gradually becomes bigger. In consequence, a short conclusion can be made here that the vortex connection near the step surface plane is a long-period loop by connection, dis-matching and reconnection repeatedly. This long-period vortex connection loop has a strong link with the long-period loop of  $U_v$  near the stepped surface plane.

## 6 Conclusion

The present paper numerically investigates secondary flow characteristics after dual stepped cylinders with the diameter ratio of  $D/d = 2$  and 4 under the Reynolds number ( $Re_D$ ) of 150. By making comparisons between results of  $D/d = 2$  and  $D/d = 4$ , a series of secondary flow traits are obtained. In addition, some unique phenomenon after dual stepped cylinder with  $D/d = 2$  is observed, of which this study aims to explain by linking the secondary flow and vortex interaction. Some new findings and interesting conclusions are summarized below.

- (1) The ‘end flow’ travels over the step junction and goes downstream, gradually approaching the middle plane ( $z = 0$ ). At the same time, it pulls S-cells (if exist) extending across the step surface plane into the wake of big cylinder.  $U_v$  near the front step surface at  $D/d = 2$  has a higher magnitude than that at  $D/d = 4$ . Besides, the ‘end flow’ at  $D/d = 2$  reaching the middle plane displays a larger slope.
- (2)  $U_v$  in the wake of big cylinder changes its location and magnitude periodically. The fluctuation of  $U_v$  is symmetrical along the middle plane, and the fluctuation magnitude is continuous near step surface plane. Two maximum fluctuation magnitudes are detected after the big cylinder, and the maximum fluctuation magnitude at  $D/d = 4$  is bigger than that at  $D/d = 2$ .  $U_v$  is found after the small cylinder at  $D/d = 2$ , whilst it disappears after the small cylinder at  $D/d = 4$ . At  $D/d = 2$ ,  $U_v$  breaks into two pieces and reconnected with each other repeatedly near the lower step surface plane.
- (3) Some links between the secondary flow and vortex interaction are established. For example, when  $D/d = 2$ , the influence of the ‘end flow’ is to pull the vortex interaction nodes approaching the middle plane ( $Z = 0$ ). The periodical features of  $U_v$  in the wake of big cylinder are caused by vortex bending and vortex deformation near the connection nodes. Hence, the long-period  $U_v$  variation loop near the lower step surface plane is induced by the loop of ‘vortex connection, dis-matching and reconnection’ between S-cell and L-cell, whereas the occurrence of the loop of vortex interaction is due to the vortex shedding phase difference between S-cell and L-cell.

**Acknowledgements** The authors gratefully acknowledge the financial support of EPSRC projects (EP/N006569/1, EP/N008863/1 and EP/M022382/1) and DST-UKIERI project (DST-UKIERI-2016-17-0029). The first author also appreciates the support provided by the China Scholarship Council (PhD program No. 201406330078).

## References

1. Gaster M (1969) Vortex shedding from slender cones at low Reynolds numbers. *J Fluid Mech* 38(03):565–576
2. Hsiao FB, Chiang CH (1998) Experimental study of cellular shedding vortices behind a tapered circular cylinder. *Exp Thermal Fluid Sci* 17(3):179–188
3. Papangelou A (1992) Vortex shedding from slender cones at low Reynolds numbers. *J Fluid Mech* 242:299–321
4. Ayoub A, Karamcheti K (1982) An experiment on the flow past a finite circular cylinder at high subcritical and supercritical Reynolds numbers. *J Fluid Mech* 118:1–26
5. Park CW, Lee SJ (2000) Free end effects on the near wake flow structure behind a finite circular cylinder. *J Wind Eng Ind Aerodyn* 88(2):231–246
6. Lewis CG, Gharib M (1992) An exploration of the wake three dimensionalities caused by a local discontinuity in cylinder diameter. *Phys Fluids A* 4(1):104–117
7. Dunn W, Tavoularis S (2006) Experimental studies of vortices shed from cylinders with a step-change in diameter. *J Fluid Mech* 555:409–437
8. Norberg C (1992) An experimental study of the flow around cylinders joined with a step in diameter. In: Proceedings of the 11th Australasian fluid mechanics conference, Hobart, Australia, pp 507–510
9. Williamson CHK (1992) The natural and forced formation of spot-like ‘vortex dislocations’ in the transition of a wake. *J Fluid Mech* 243:393–441
10. Morton C, Yarusevych S (2012) An experimental investigation of flow past a dual step cylinder. *Exp Fluids* 52(1):69–83
11. Morton C, Yarusevych S (2014) On vortex shedding from low aspect ratio dual step cylinders. *J Fluids Struct* 44:251–269
12. McClure J, Morton C, Yarusevych S (2015) Flow development and structural loading on dual step cylinders in laminar shedding regime. *Phys Fluids* 27(6):063602
13. Morton C, Yarusevych S (2009) Modeling flow over a circular cylinder with a stepwise discontinuity. In: Proceedings of the 39th AIAA fluid dynamics conference, San Antonio, TX, USA, pp 22–25
14. Wang JX, Ma QW, Wang JH (2017) Numerical study on hydrodynamics of dual stepped cylinder at low Reynolds number. In: International conference on computational & experimental engineering and science (ICCES 2017)

# Modelling Wave Interaction with Porous Structures Using Boussinesq Equations



Shagun Agarwal, V. Sriram and K. Murali

**Abstract** The paper presents a numerical model of the two-dimensional enhanced Boussinesq equations to simulate wave transformations in the near-shore region. The finite element-based discretisation over unstructured mesh with triangular elements uses mixed linear and quadratic shape functions. The domain integrals are calculated analytically. The model is extended to study flow through porous structures using Darcy velocity, with the energy dissipation within the porous medium modelled through additional laminar and turbulent resistance terms. A single set of empirical constants gives accurate prediction for various stone sizes and porosity. This paper reports the model development and its validation using existing experimental studies. Application of the model is demonstrated by studying the interaction between ship-generated waves in a narrow channel and the porous walls of the channel.

**Keywords** Boussinesq equation · Porous structure wave interaction

## 1 Introduction

Boussinesq-type equations are widely used for modelling wave transformations in near-shore region. The increasing use of this equations stems from the fact that it reduces the three-dimensional potential flow problems to a two-dimensional problem based on depth-averaged velocity, thus reducing the computational cost drastically in modelling the large domain while capturing the important phenomenon. Early formulations based on depth-averaged velocities were linear and limited to shallow

---

S. Agarwal (✉) · V. Sriram (✉) · K. Murali (✉)  
Indian Institute of Technology Madras, Chennai, India  
e-mail: [shagun.1994@gmail.com](mailto:shagun.1994@gmail.com)

V. Sriram  
e-mail: [vsriram@iitm.ac.in](mailto:vsriram@iitm.ac.in)

K. Murali  
e-mail: [murali@iitm.ac.in](mailto:murali@iitm.ac.in)

© Springer Nature Singapore Pte Ltd. 2019  
K. Murali et al. (eds.), *Proceedings of the Fourth International Conference in Ocean Engineering (ICOE2018)*, Lecture Notes in Civil Engineering 22,  
[https://doi.org/10.1007/978-981-13-3119-0\\_35](https://doi.org/10.1007/978-981-13-3119-0_35)

573

water regions. Modifications in [1] extended it to intermediate water depths. Further non-linear improvements in [2, 3] saw practical use in coastal engineering problems.

Wave interaction with porous structures, like rubble mound breakwater and sea wall, is an important phenomenon for coastal engineering. Their partially reflecting nature is favourable in dissipating wave energy. A comprehensive wave model should incorporate porous structure interaction for practical application. A comparison of different porous flow equations was done in [4, 5]. Early diffraction around porous breakwater model by [6] was limited to thin breakwater. A rigorous comparison with experiment results on transmission and reflection of solitary wave was done in [7]. Some notable Boussinesq models based on Darcy porous flow equation are [8, 9].

This work presents a finite element-based numerical model of Boussinesq equation with mixed spatial interpolation, covering shallow to intermediate water depth regions. Interaction with porous structure is modelled using Darcy velocity along with linear and turbulent resistance terms. The basic model is validated using experimental results from standard Berkhoff shoal test. The porous flow model is validated through results on reflection and transmission coefficients for porous breakwater. A potential application of the model is presented by studying interaction of ship-generated waves in a narrow channel with its partially reflecting walls.

## 2 Governing Equations

This work uses enhanced Boussinesq equations as derived in [1], which is valid for slowly varying bathymetry and incorporates linear dispersion characteristics. They are evaluated in depth-integrated form, with  $P$  and  $Q$  as depth-integrated velocity flux along  $x$  and  $y$  Cartesian coordinates axes respectively,  $\eta$  as water surface elevation,  $h$  as still water depth,  $d = h + \eta$  as total water depth,  $g$  as acceleration due to gravity and  $\rho$  as density of water.

The enhanced Boussinesq terms  $\Psi_x$  and  $\Psi_y$ , as defined in [1] involve third-order spatial derivatives of surface elevation. A linear shape function for  $\eta$  estimation in finite element would not be able to calculate this higher order derivative. Therefore, an auxiliary variable  $w$  was introduced in [10] as defined by Eq. 1. This work uses these modified Boussinesq equations as a basis for deriving the flow equation through porous medium.

$$w = \frac{\partial}{\partial x} \left( h \frac{\partial \eta}{\partial x} \right) + \frac{\partial}{\partial y} \left( h \frac{\partial \eta}{\partial y} \right) \quad (1)$$

Flow in a porous medium of porosity  $\lambda$  is modelled using the Darcy velocity or seepage velocity. If  $P_d$  is the depth-integrated Darcy flux, then

$$P_d = \lambda P \implies P = \frac{P_d}{\lambda} \quad (2)$$

The energy dissipation inside the porous medium is modelled using the laminar and turbulent drag resistance terms,  $f_l u$  and  $f_t |u|u$ , where  $f_l$  and  $f_t$  are the respective coefficients and are obtained using the empirical relations from [11].

$$f_l = \alpha_0 \frac{(1 - \lambda)^3 \nu}{\lambda^2 s^2} \quad f_t = \beta_0 \frac{(1 - \lambda) 1}{\lambda^3 s} \tag{3a}$$

where  $\nu$  is the kinematic viscosity of water,  $s$  is the characteristic size of the stone and  $\alpha_0$  and  $\beta_0$  are empirical constants with recommended range of 780–1500 and 1.8–3.6, respectively. The final form of the Boussinesq equations for flow through porous medium is given in Eq. 4. This is used for the final finite element formulation. Putting  $\lambda = 1$  makes  $f_l = 0$  and  $f_t = 0$  thus returning them to the original form as in [10].

$$\frac{\partial \eta}{\partial t} + \frac{\partial}{\partial x} \left( \frac{P}{\lambda} \right) + \frac{\partial}{\partial y} \left( \frac{Q}{\lambda} \right) = 0 \tag{4a}$$

$$\frac{\partial P}{\partial t} + \frac{\partial}{\partial x} \left( \frac{P^2}{\lambda d} \right) + \frac{\partial}{\partial y} \left( \frac{PQ}{\lambda d} \right) + \lambda g d \frac{\partial \eta}{\partial x} + \lambda f_l P + \lambda f_t \frac{P}{d} \sqrt{P^2 + Q^2} + \Psi'_x = 0 \tag{4b}$$

$$\frac{\partial Q}{\partial t} + \frac{\partial}{\partial x} \left( \frac{PQ}{\lambda d} \right) + \frac{\partial}{\partial y} \left( \frac{Q^2}{\lambda d} \right) + \lambda g d \frac{\partial \eta}{\partial y} + \lambda f_l Q + \lambda f_t \frac{Q}{d} \sqrt{P^2 + Q^2} + \Psi'_y = 0 \tag{4c}$$

with the Boussinesq terms  $\Psi'_x$  and  $\Psi'_y$  given by

$$\begin{aligned} \Psi'_x = & - \left( B + \frac{1}{3} \right) h^2 \left( \frac{\partial^3 P}{\partial x^2 t} + \frac{\partial^3 Q}{\partial x y t} \right) - h \frac{\partial h}{\partial x} \left( \frac{1}{3} \frac{\partial^2 P}{\partial x t} + \frac{1}{6} \frac{\partial^2 Q}{\partial y t} \right) \\ & - h \frac{\partial h}{\partial y} \left( \frac{1}{6} \frac{\partial^2 Q}{\partial x t} \right) - \lambda B g h^2 \frac{\partial w}{\partial x} \end{aligned} \tag{5a}$$

$$\begin{aligned} \Psi'_y = & - \left( B + \frac{1}{3} \right) h^2 \left( \frac{\partial^3 P}{\partial x y t} + \frac{\partial^3 Q}{\partial y^2 t} \right) - h \frac{\partial h}{\partial y} \left( \frac{1}{6} \frac{\partial^2 P}{\partial x t} + \frac{1}{3} \frac{\partial^2 Q}{\partial y t} \right) \\ & - h \frac{\partial h}{\partial x} \left( \frac{1}{6} \frac{\partial^2 P}{\partial y t} \right) - \lambda B g h^2 \frac{\partial w}{\partial y} \end{aligned} \tag{5b}$$

### 3 Numerical Formulation

The finite element formulation is done using standard Galerkin method. The two-dimensional computational domain is meshed with irregular triangles. Each triangular element consists of six nodes; three vertices and middle points of each side. The variable  $P$  and  $Q$  are evaluated on the six nodes and interpolated using quadratic shape function  $\phi$  to handle high order derivatives in Eq. 4. The variables  $\eta$  and  $w$  are evaluated on the three vertices of each triangle and interpolated using linear shape function  $\delta$ . The derivatives of the unknowns are evaluated using the Jacobian matrix and standard triangle element. The governing equations are converted to integral

form using  $\delta_i$  as trial function for Eqs. 1 and 4a; and  $\phi_i$  as trial function for Eqs. 4b and 4c. Certain higher order derivatives are converted to weak form using Gauss divergence theorem. The integration was carried out analytically over a standard triangular element and then scaled using the Jacobian. This avoids the approximations of Gauss quadrature method and involves lesser computation. The discretised weak form of governing equations is given in Eq. 6 using matrix notation. The definition of each matrix in Eq. 6 is excluded from this manuscript.

$$M_2 w = f_w - D\eta \quad (6a)$$

$$M_2 \dot{\eta} = C_x P + C_y Q \quad (6b)$$

$$\begin{bmatrix} M_1 + B_1 & B_2 \\ B_3 & M_1 + B_4 \end{bmatrix} \begin{bmatrix} \dot{P} \\ \dot{Q} \end{bmatrix} = \begin{bmatrix} f_{p1} & f_{p2} & f_{p3} \\ f_{q1} & f_{q2} & f_{q3} \end{bmatrix} \begin{bmatrix} \dot{P} \\ \dot{Q} \\ w \end{bmatrix} - \begin{bmatrix} B_5 \\ B_6 \end{bmatrix} w \quad (6c)$$

$$- \begin{bmatrix} N + R_l & 0 & G_x \\ 0 & N + R_l & G_y \end{bmatrix} \begin{bmatrix} P \\ Q \\ \eta \end{bmatrix} - \begin{bmatrix} R_{tx} \\ R_{ty} \end{bmatrix} \sqrt{P^2 + Q^2}$$

$\dot{P}$ ,  $\dot{Q}$  and  $\dot{\eta}$  denotes the time derivatives. The time integration is done using explicit three-point Adams-Bashforth method. The algebraic Eq. 6 is of form  $AX = B$ . The solution for the unknown  $X$  is obtained using iterative-type GMRES solver using PARALUTION library [12] with OpenMP-based parallel implementation. There are four types of boundary conditions that are modelled—fully reflection slip wall, fully reflecting no-slip wall, inlet boundary condition and absorbing layer boundary condition. The Dirichlet-type boundary conditions are implemented using penalty method [13, Chap. 4], and Neumann-type boundary conditions are applied using iterative method. Finally, the absorbing layer boundary condition is applied using a sponge layer.

## 4 Numerical Experiments

### 4.1 Regular Waves over Berkhoff Shoal

Berkhoff shoal bathymetry is widely used to validate numerical models on surface waves. The bathymetry is a constant 1:50 slope with water depth range of 0.1–0.45 m. It consists of an elliptical shoal with the centre at a distance of 5.84 m from the shoal toe, with 4 m major axis and three minor axes. The depth contours are aligned at an angle of 20° to the incident regular waves. The computational domain is of size 36 m × 20 m with the origin located at the centre of the ellipse. The analytical expression for this bathymetry can be found in [14].

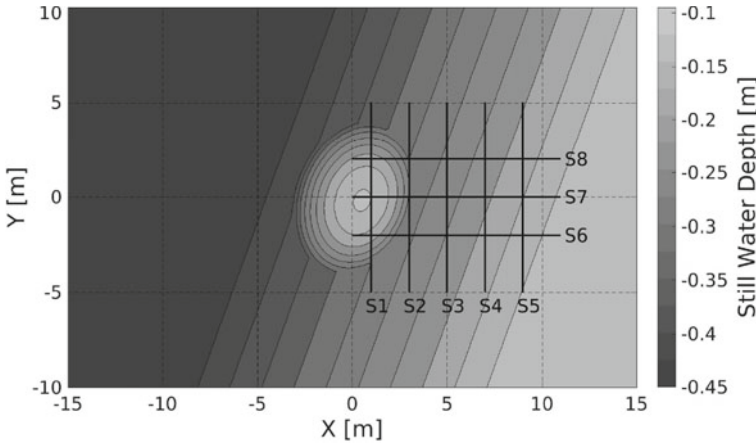


**Fig. 1** Contour plot of Berkhoff shoal bathymetry; measurements along lines ( - - )

The wave inlet boundary is located at side  $x = -15$  m, generating regular waves of period 1 s and height 0.0464 m. The sides  $y = \pm 10$  m are fully reflecting slip walls. A 6 m sponge layer is located at side  $x = 15$  m to absorb the waves.

The irregular mesh implementation allows the use of variable mesh size. The region between  $x = -8$  m and  $x = 15$  m is meshed with mean element area of  $0.005 \text{ m}^2$ , and the remaining space has element area of  $0.02 \text{ m}^2$ . The mesh has 97,062 elements with 48,915 linear nodes and 194,891 total nodes. Simulation time step is 0.005 s, obtained after time convergence study. The simulated time is 40 s.

The results from this simulation are compared with experimental wave height measurements from [15] in Fig. 2. The figure also shows comparison with numerical results obtained using FUNWAVE 1.0 [16] with similar mesh characteristics. The measurements are made along the line sections S1–S8, as shown in Fig. 1. The model correctly captures the location and magnitude of peaks in the wave height along the line sections, thus validating the implementation of the numerical model.

### 4.2 Flow of Solitary Wave Through Porous Breakwater

The numerical modelling of flows through porous structures is verified through the study of the interaction of solitary wave with porous breakwater. Solitary waves are non-dispersive in nature and can keep a constant elevation profile over a long distance of propagation. The solitary wave profile with wave height ( $H$ ) at water depth ( $h$ ) used in the present study is given in [17].

$$\eta(x, t) = H \operatorname{sech}^2[\kappa(Ct - X_0)] \quad \kappa = \sqrt{\frac{3H}{4h^3}} \quad C = \sqrt{g(h + H)} \quad (7)$$



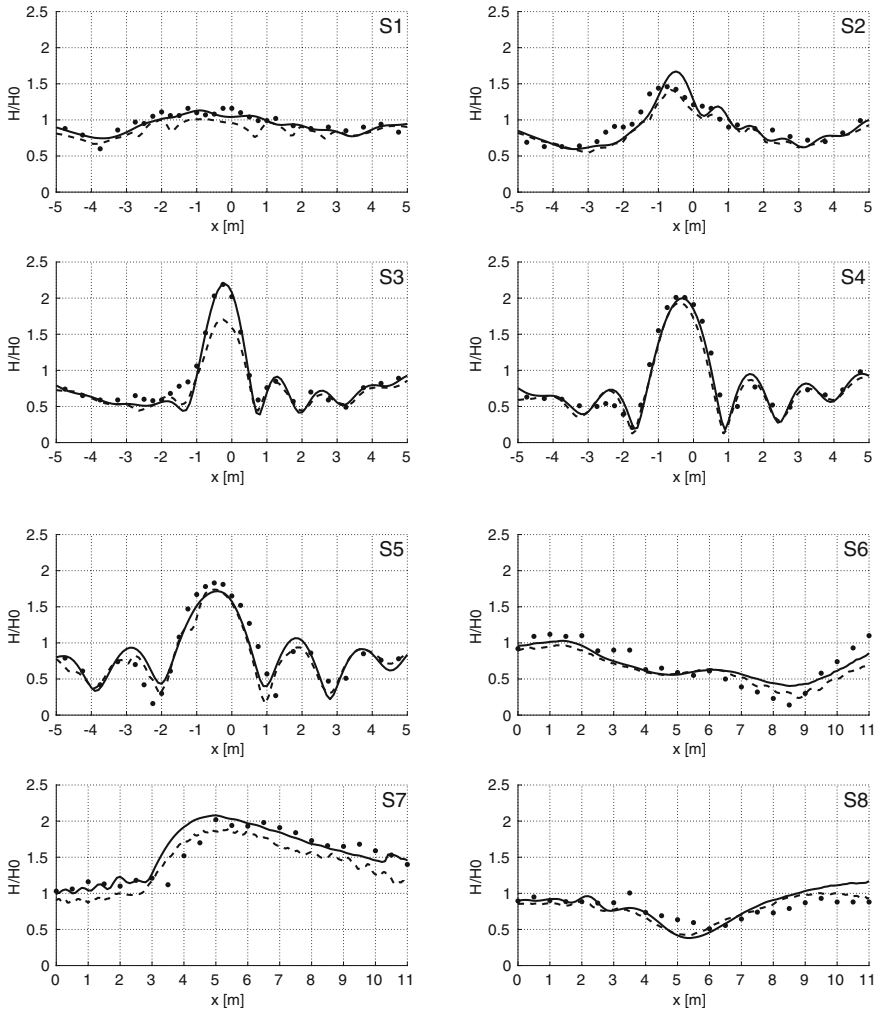


**Fig. 2** Graphs showing comparison with results on wave height along various sections; present work numerical (—), experimental [15] (•), FUNWAVE 1.0 numerical [16] (- -)

with the depth-integrated velocity profile given by

$$P(x, t) = CH \operatorname{sech}^2[\kappa(Ct - X_0)] \tag{8}$$

The governing equations for this model are weakly non-linear and hence will not be able to match the conventional non-linear initial condition for solitary wave. To obtain a constant profile, the solitary wave is first allowed to propagate for long distance at a constant water depth. At the beginning of these computations, the wave height and shape keep changing. But over some distance of propagation, the solitary

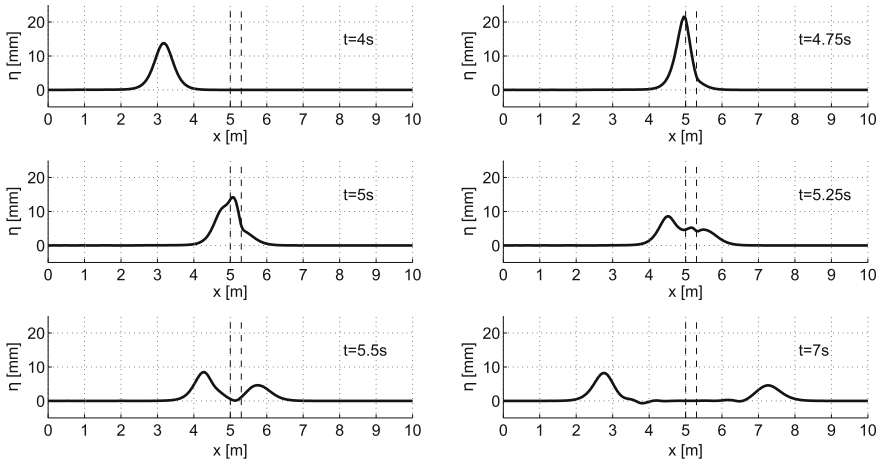


**Fig. 3** Snapshots of surface elevation at different time instants depicting splitting of solitary wave through the porous breakwater

wave achieves a stable shape and is then used for the study of interaction with porous breakwater. This is similar to the approach taken in [2].

The computational domain is  $10 \text{ m} \times 2 \text{ m}$ . A uniform element size of 0.05 m and time step of 0.005 s is used for all cases. The breakwater is located in the middle of the domain. Porosity of the gravel is taken as 50% with drag resistance coefficients  $\alpha = 1100$  and  $\beta = 1.50$ . Two sizes of irregular gravel are studied with median diameters 1.6 and 2.0 cm. Widths of breakwater are taken as 15 and 30 cm. The water depth is kept constant at 0.1 m, and wave heights are in the range of 0.01–0.035 m.

As shown in Fig. 3, the solitary wave on hitting the breakwater splits into two parts and is partly reflected and transmitted. The heights of these two waves are non-dimensionalised using the initial wave height to obtain the reflection and transmission coefficients ( $\zeta_R, \zeta_T$ ), which are used to compare the results with reference studies. Figure 4 shows comparison of results from the present work with numerical and experimental results from [7] (using  $\alpha = 1100$  and  $\beta = 0.81$ ) for different gravel sizes and breakwater widths. The present model can accurately estimate the transmission coefficient for all cases in  $H/h$  range of 0.1–0.35. Reflection coefficient is predicted well for low  $H/h$  but is over-predicted for higher  $H/h$ . This is possible because the model is linearly dispersive, and with increase in wave height, the non-linearity of the solitary wave increases, leading to modelling errors. The turbulence modelling done in the present work is based on depth-integrated properties and hence cannot include the effects of eddies formed along the depth. This is supported by the observation stated in [17], according to which surface wave models tend to over-estimate reflection from porous structure due to improper turbulence modelling.

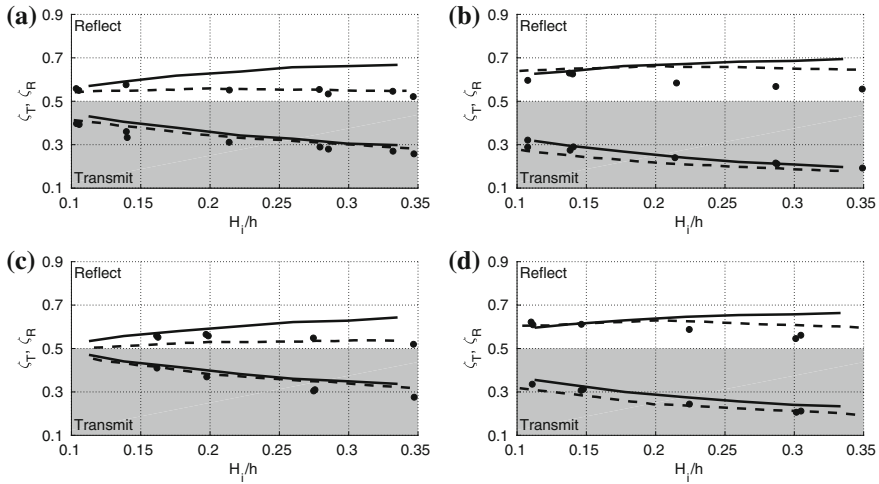


**Fig. 4** Graphs showing estimated transmission and reflection coefficient for 1D solitary waves through porous breakwater; shaded region shows transmission; **a**  $s = 1.6 \text{ cm } b = 15 \text{ cm}$ ; **b**  $s = 1.6 \text{ cm } b = 30 \text{ cm}$ ; **c**  $s = 2.0 \text{ cm } b = 15 \text{ cm}$ ; **d**  $s = 2.0 \text{ cm } b = 30 \text{ cm}$ ; present work (—); referred numerical [7] (- -); experimental [7] (•)

### 4.3 Study of Ship Motion in Narrow Channel

This numerical experiment presents a possible extension of this model. Inland waterways, in form of river, canals, backwaters and creeks are utilised for freight transport at low cost. The long waves generated by the motion of cargo vessels in these narrow channels can cause damage to the riverbanks and surrounding region through erosion. There is a need to study this interaction between ship-generated waves and riverbank along the navigation length.

A riverbank can be simplified as a partially reflecting wall, similar to a porous breakwater. The characteristics of riverbank are tuned using stone size and porosity parameters. The ship waves are generated using moving pressure field based on the formulation of [18]. This approach can be used to study the interaction over long navigation channels.

The schematic describing numerical setup for a parametric example study is shown in Fig. 5. A narrow channel of width 23 m has a porous bank, denoted by lines P1 and P2. The width of each porous region is 5 m. Water depth is 2.5 m in the entire region. A slender vessel of length  $L = 5 \text{ m}$ , width  $B = 1 \text{ m}$  and draft  $T = 0.2 \text{ m}$  is moved along midline of this channel at a constant speed corresponding to  $Fr_d = 0.7$ . The moving pressure field with respect to centre of ship is given by

$$p(x, y) = p_0 [1 - c_L(x/L)^4] [1 - c_B(y/B)^2] \exp[-a(y/B)^2] \tag{9}$$

with peak pressure  $p_0 = \rho g T$  and shape constants  $a = 16, c_b = 2, c_l = 16$ .

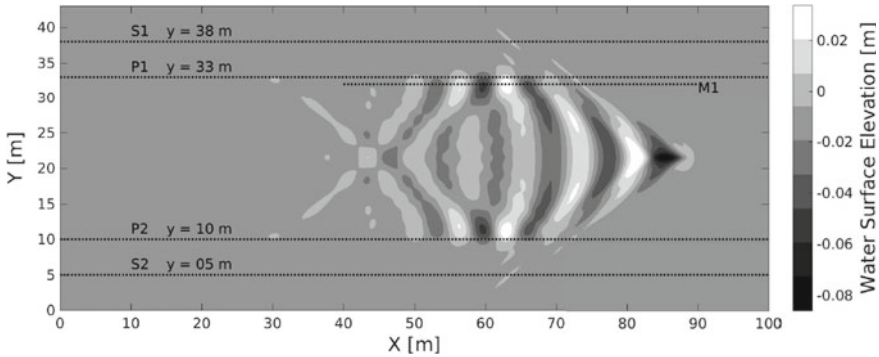


**Fig. 5** Schematic for numerical experiment setup and contour plot of water elevation at 22 s for  $\lambda = 0.15$

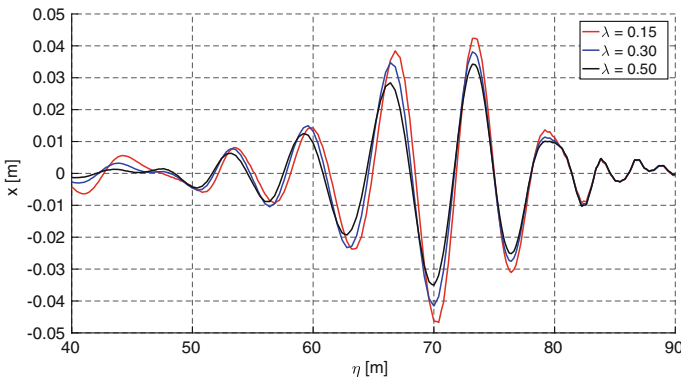


**Fig. 6** Graph showing surface elevation at 25 s along M1 for three different porosities

The computational domain is  $100\text{ m} \times 43\text{ m}$ . The ship moves along the centre line. Therefore, to successfully capture the sharp gradient of the moving pressure field, the region between  $y = 20\text{ m}$  and  $y = 23\text{ m}$  is meshed with mean element area  $0.02\text{ m}^2$  and the remaining region with mean element area  $0.08\text{ m}^2$ . A 5 m wide sponge layer is placed at each boundary. This gives a mesh with 70,398 elements, 35,570 linear nodes and 141,537 total nodes. Time step is 0.01 s.

Wave elevation is measured along a line parallel to the bank at a distance of 1 m as denoted by M1. Porosity and stone size are two parameters that can be adjusted for the bank. For this study, the stone size is kept constant at 20 cm. Three values of porosity, 15, 30 and 50%, are tested. Figure 6 shows the wave elevation measurement on M1 at 25 s for these three porosities. The measured maximum wave height for the three porosities values is 0.0934 m, 0.0819 m and 0.0705 m, respectively. The wave height measurement and the wave train in Fig. 6 show a reduction in reflection from the bank with increasing porosity value. The magnitude of wave height can be used to estimate erosion at riverbank. Due to the unstructured mesh formulation, the

channel shape is not limited to rectangles. This approach can be used to study curved channels too.

## 5 Conclusion

This manuscript presented a numerical model of Boussinesq equations incorporating flow through porous structures. The version of equations used was capable of simulating waves transformation process in shallow to intermediate water depths. The model uses porous flow equations derived based on Darcy velocity with laminar and turbulent drag resistance terms.

The finite element formulation was done using standard Galerkin method. The spatial interpolation of water elevation and auxiliary variable was done using linear polynomial, and a quadratic shape function was used for depth-integrated velocities. The domain integrals were calculated analytically for standard triangle and scaled using the Jacobian, which improve accuracy and efficiency.

The basic wave model was tested using standard Berkhoff shoal experiment. The wave height was measured along pre-defined lines and compared with the experiment results with acceptable accuracy.

Numerical formulation of porous flow was validated using the interaction of solitary wave with porous breakwater. The tuning coefficients for laminar and turbulent resistance terms were obtained by minimising error in transmission and reflection coefficients. The tuned model was tested for various stone sizes and breakwater widths with constant porosity. The results of transmission coefficient show good agreement with experiment in every test case with the same set of empirical constants. Reflection coefficient was found to be over-estimated with increasing non-linearity of incident wave.

The application of model was demonstrated through the study of interaction of ship-generated waves with porous walls in a narrow channel. Porosity of the walls of constant depth channel was varied and wave train formed by the interaction of incident wave and partially reflected wave was measured near the wall. The trend of decreasing wave height with increasing wall porosity was obtained, and their values for the specific ship characteristics were presented.

This manuscript reported the development and validation of the new numerical model. The potential real-world application of the model was exhibited for both off-shore and inland waterways problems.

## References

1. Madsen PA, Sørensen OR (1991) A new form of the Boussinesq equations with improved linear dispersion characteristics. Part 2: a slowly-varying bathymetry. *Coast Eng* 18(3–4):183–204

2. Wei G, Kirby JT, Grilli ST, Subramanya R (1995) A fully nonlinear Boussinesq model for surface waves. Part 1: highly nonlinear unsteady waves. *J Fluid Mech* 294:71
3. Madsen PA, Bingham HB, Liu H (2002) A new Boussinesq method for fully nonlinear waves from shallow to deep water. *J Fluid Mech* 462:1–30
4. Karunarathna SASA, Lin P (2006) Numerical simulation of wave damping over porous seabeds. *Coast Eng* 53(10):845–855
5. Burcharth HF, Andersen OK (1995) On the one-dimensional steady and unsteady porous flow equations. *Coast Eng* 24(3–4):233–257
6. Yu X, Togashi H (1996) Combined diffraction and transmission of water waves around a porous breakwater gap. In: Coastal engineering 1996, New York, NY, Aug 1997. American society of civil engineers, pp 2063–2076
7. Lynett PJ, Liu PL, Losada IJ, Vidal C (2000) Solitary wave interaction with porous breakwaters. *J Waterw Port Coast Ocean Eng* 126(6):314–322
8. Woo S-B, Liu PLF (2004) Finite-element model for modified Boussinesq equations. I: model development. *J Waterw Port Coast Ocean Eng* 130(1):1–16
9. Pinheiro L, Fortes CJ, Santos JA, Walkley M (2009) Implementation of partial reflection boundary conditions in wave propagation model BOUSSIIW. *J Coast Res SI* 56:1040–1044
10. Sørensen OR, Schäffer HA, Sørensen LS (2004) Boussinesq-type modelling using an unstructured finite element technique. *Coast Eng* 50(4):181–198
11. Engelund F (1953) On the laminar and turbulent flows of ground water through homogeneous sand. *Akademiet for de tekniske videnskaber*
12. PARALUTION Labs. Paralution v1.1.0 (2016)
13. Liu GR, Gu YT (2005) An introduction to meshfree methods and their programming. Springer, Netherlands
14. Kirby JT, Dalrymple RA (1984) Verification of a parabolic equation for propagation of weakly-nonlinear waves. *Coast Eng* 8(3):219–232
15. Berkhoff JCW, Booy N, Radder AC (1982) Verification of numerical wave propagation models for simple harmonic linear water waves. *Coast Eng* 6(3):255–279
16. Kirby JT, Wei G, Chen Q, Kennedy AB, Dalrymple RA (1998) FUNWAVE 1.0. Fully nonlinear Boussinesq wave model. Documentation and user's manual. Technical report, University of Delaware, Newark
17. Hughes SA (1993) Physical models and laboratory techniques. *Coast Eng* 7
18. Bayraktar Ersan D, Beji S (2013) Numerical simulation of waves generated by a moving pressure field. *Ocean Eng* 59

# Breaking Focused Waves Generated Using the Transient Wave Packet Method and the Breaking Impact Forces on a Vertical Cylinder



Arun Kamath, Mayilvahanan Alagan Chella and Hans Bihs

**Abstract** The presence of vital offshore infrastructure in deeper waters makes it essential to be able to evaluate the properties of steepness-induced breaking waves. An extreme wave event in deep water can be modelled with a transient wave packet approach where shorter waves follow longer waves resulting in a steep, large extreme wave (focused wave) at a point of concentration. Wave breaking occurs when the steepness of the large wave crest front satisfies the breaking criteria. Generation of such extreme waves with phase-focussing waves through a spectrum such as the JONSWAP spectrum can be challenging. This paper shows the interaction of a focussed extreme wave generated using the transient wave packets method with a vertical cylinder under different impact scenarios.

**Keywords** CFD · Focussed waves · Breaking waves · Wave forces · REEF3D

## 1 Introduction

The two major types of breaking waves in the marine environment are depth-induced breaking waves and steepness-induced breaking waves. Depth-induced breaking waves are a feature of the coastal environment while the steepness-induced breaking is a phenomenon observed in deeper waters away from the coast. The presence of offshore infrastructure in deeper waters makes it essential to be able to evaluate the properties of steepness-induced breaking waves which vary from depth-induced breaking waves. The steepness-induced wave breaking is a transient wave phenomenon where shorter waves followed by longer waves result in a focussed wave at a point of concentration. This steepness of this focussed wave induces wave breaking. Such a wave train is called a transient wave train are generated using a wave packet-based approach.

---

A. Kamath (✉) · M. A. Chella · H. Bihs  
Department of Civil and Environmental Engineering, Norwegian University of Science and Technology, NTNU Trondheim, Trondheim, Norway  
e-mail: [arun.kamath@ntnu.no](mailto:arun.kamath@ntnu.no)

© Springer Nature Singapore Pte Ltd. 2019  
K. Murali et al. (eds.), *Proceedings of the Fourth International Conference in Ocean Engineering (ICOE2018)*, Lecture Notes in Civil Engineering 22,  
[https://doi.org/10.1007/978-981-13-3119-0\\_36](https://doi.org/10.1007/978-981-13-3119-0_36)

Some of the notable numerical studies on focussed wave generation are [2, 6, 15] among others. Here, irregular waves are generated based on an idealised wave spectrum such as the JONSWAP wave spectrum, and the components are phase focussed such that the generated wave components focus at a predetermined point in the wave tank, to produce a focussed extreme wave event. Due to the inherent nature of the wave spectra, the individual wave components generated using this method to obtain a target focussed wave amplitude have large amplitudes themselves. This can result in wave breaking at a premature location and time than intended due to the superpositioning of certain large components. Thus, the desired focussed wave amplitude cannot be reached [4].

The principle of transient waves was investigated by [9], where a wave train is generated with wave components of increasing wavelength. The longer, faster moving wave components then lead to the wave train converging at a certain location in the wave flume, producing a large focussed wave amplitude. The transient wave method was further improved by [14] for the generation of freak waves. A special Gauss-modulated amplitude spectrum to produce focussed extreme waves was presented by [8] with wave groups of limited length being generated that converge at a predetermined location in the wave tank at a prescribed point in time. This technique has the advantage that a transient wave train can be generated, that needs a finite short duration of time for propagation and focussing at a predetermined location in the wave tank.

In this study, the open-source CFD model REEF3D [3] is used to generate a transient wave train using the wave packets approach and a breaking focussed plunging wave is simulated. The transient wave packets method [8] implemented in the numerical model is validated in [4]. In the current paper, the interaction of a breaking wave produced using this method with a slender vertical cylinder is studied under three different impact scenarios. The wave propagation in the numerical wave tank, the breaking wave characteristics and the total breaking wave forces on the vertical cylinder are calculated.

## 2 Numerical Model

The open-source CFD model REEF3D [3] used in this study solves the incompressible Navier–Stokes equations:

$$\frac{\partial u_i}{\partial x_i} = 0 \quad (1)$$

$$\frac{\partial u_i}{\partial t} + u_j \frac{\partial u_i}{\partial x_j} = -\frac{1}{\rho} \frac{\partial p}{\partial x_i} + \frac{\partial}{\partial x_j} \left[ \nu \left( \frac{\partial u_i}{\partial x_j} + \frac{\partial u_j}{\partial x_i} \right) \right] + g_i \quad (2)$$

where  $u$  is the time-averaged velocity,  $\rho$  is the density of water,  $p$  is the pressure,  $\nu$  is the kinematic viscosity,  $t$  is time and  $g$  is the acceleration due to gravity. Chorin's projection method [7] is used for the pressure treatment. The high performance



solver library HYPRE [5] is employed to solve the Poisson pressure equation using the PFMG-preconditioned BiCGStab algorithm [1].

The fifth-order conservative finite difference Weighted Essentially Non-Oscillatory (WENO) scheme proposed by Jiang et al. [12] is used for the discretization of convective terms for the velocity  $u_i$ , the level set function  $\phi$ , turbulent kinetic energy  $k$  and the specific turbulent dissipation rate  $\omega$ . A TVD third-order Runge-Kutta explicit time scheme developed by Harten [10] is employed for time discretization in the model. It is a three-step scheme and involves the calculation of the spatial derivatives three times per time step. This scheme is used for the time advancement of the level set function and the reinitialisation equation.

A Cartesian grid is used in the numerical model for spatial discretisation. The Immersed Boundary Method (IBM) [16] is used to incorporate the boundary conditions for complex geometries. The free surface is obtained using the level set method where the zero level set of a signed distance function,  $\phi(\mathbf{x}, t)$  is used to represent the interface between air and water. Moving away from the interface, the level set function gives the closest distance of the point from the interface. The sign of the function represents the two fluids across the interface. The level set function is reinitialised after every iteration using a partial differential equation (PDE) based reinitialisation procedure presented by Sussman et al. [18] to retain its signed distance property after convection.

Wave generation and absorption is carried out using the active wave absorption (AWA) method [17]. At the wave absorption boundary, the velocities opposite to the reflected wave are imposed so that the reflected wave is cancelled out. In this study, since a focussed wave train is used, the effect of reflection on the solution is negligible as the reflection occurs only after some duration after the focussed wave interaction with the structure in the tank. The focussed waves are generated using a Fourier amplitude spectrum as follows [11]:

$$|F| = \frac{27 (\omega - \omega_{beg}) (\omega - \omega_{end})^2}{4 (\omega_{end} - \omega_{beg})^3} \tag{3}$$

where  $\omega$  is the angular frequency, the  $\omega_{beg}$  and  $\omega_{end}$  define the extent of the Fourier spectrum on the frequency axis. The free surface,  $\eta^{(1)}$  at the wave generation is then calculated as:

$$\eta^{(1)} = \sum_{i=1}^N A_i \cos \theta_i \tag{4}$$

where  $A_i$  is the amplitude of the each wave component and  $\theta_i$  is the phase of the each wave component generated. defined as:

$$\theta_i = k_i x - \omega_i t - \epsilon_i \tag{5}$$

where  $k_i$  is the wave number of each component. The parameter  $\epsilon_i$  is the phase angle, which is chosen in such a way that each wave component focuses at a specified time  $t_f$  and location  $x_f$ .

### 3 Results and Discussion

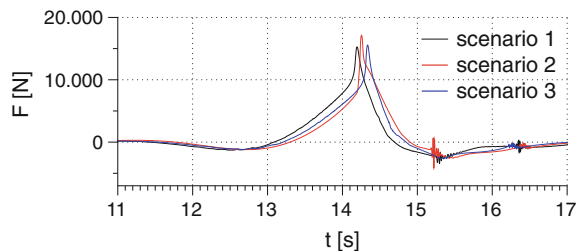
The numerical simulations are carried out in a 25 m long, 5 m wide and 8 m high wave tank with a water depth of 4 m and a cylinder of diameter 0.7 m is placed using a grid size of  $dx = 0.05$  m. The wave generation, focussing and breaking point are first confirmed using a 2D study in a numerical wave tank of the same dimensions. A grid resolution study is also carried out to verify the representation of the breaking wave. The focussed wave amplitude is set to 2.13 m with a focus distance of 15 m from the inlet boundary at 15 s with 500 wave components used in the wave generation. The wave breaking point is determined to be  $x_b = 14.30$  m.

The 3D studies are carried out for three different impact scenarios:

- scenario 1: focussed wave breaking point at cylinder front surface
- scenario 2: focussed wave breaking point  $1D$  in front of cylinder
- scenario 3: focussed wave breaking point  $2D$  in front of cylinder.

The resulting total breaking wave forces on the cylinder in the three different impact scenarios are presented in Fig. 1. It is seen that the maximum peak breaking wave force is seen in the scenario where the overturning focussed wave crest impacts the cylinder around crest level. This is slightly different from the numerical investigation with regular breaking waves on a slope [13] due to the varying nature of the breaking wave kinematics. The free surface features associated with the focussed breaking wave impact in scenario 1 are presented in Fig. 2. The vertical wave crest front impacting the cylinder, the separation of the wavefront around the cylinder and the subsequent overturning of the wave crest are clearly seen.

**Fig. 1** Breaking wave forces on a vertical cylinder due to focussed breaking wave impact at different cylinder locations



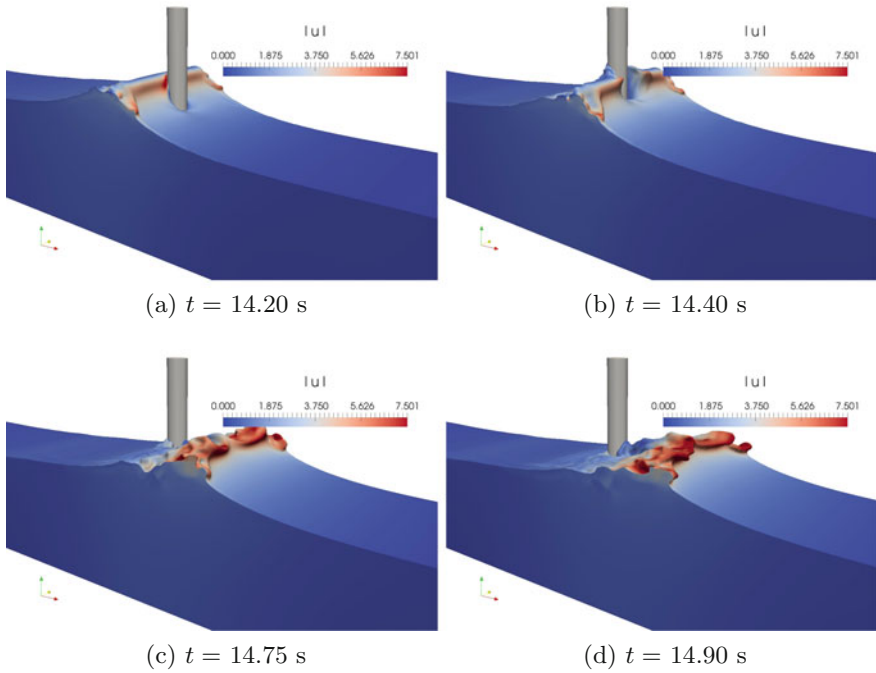


**Fig. 2** Free surface features around the cylinder under the impact of a focussed breaking wave

## 4 Conclusion

The open-source CFD model REEF3D is used to generate focussed breaking waves using the method of transient wave packets. The method produces extreme breaking waves without premature breaking of the individual wave components and different impact scenarios with a vertical cylinder are simulated. The results show that the maximum peak breaking wave forces are calculated for the scenario where the overturning focussed breaking wave impacts the cylinder just below the wave crest level. Free surface features involved in the different impact scenarios are presented and discussed. Further studies regarding the distances of the cylinder from the breaking location of focussed waves produced using wave packets are to be carried out.

**Acknowledgements** This work was supported in part by computational resources provided at NTNU by the Norwegian Metacentre for Computational Science (NOTUR) under project no. NN2620K.

## References

1. Ashby SF, Falgout RD (1996) A parallel multigrid preconditioned conjugate gradient algorithm for groundwater flow simulations. *Nucl Sci Eng* 124(1):145–159
2. Bihs H, Alagan Chella M, Kamath A, Arntsen ØA (2017) Numerical investigation of focused waves and their interaction with a vertical cylinder using REEF3D. *J Offshore Mech Arctic Eng* 139(4):041101–1–8
3. Bihs H, Kamath A, Alagan Chella M, Aggarwal A, Arntsen ØA (2016) A new level set numerical wave tank with improved density interpolation for complex wave hydrodynamics. *Comput Fluids* 140:191–208
4. Bihs H, Kamath A, Alagan Chella M, Arntsen ØA (2017) Extreme wave generation, breaking and impact simulations with reef3d. In: SME 2017 36th international conference on ocean, offshore and arctic engineering. American Society of Mechanical Engineers, pp V002T08A004–V002T08A004
5. Center for Applied Scientific Computing (2006) HYPRE high performance preconditioners—user’s manual. Lawrence Livermore National Laboratory
6. Chen LF, Zang J, Hillis AJ, Morgan GCJ, Plummer AR (2014) Numerical investigation of wave-structure interaction using OpenFOAM. *Ocean Eng* 88:91–109
7. Chorin A (1968) Numerical solution of the Navier-Stokes equations. *Math Comput* 22:745–762
8. Clauss GF, Kuehnlein WL (1997) A new tool for seakeeping test—nonlinear transient wave packets. In: 8th international conference on the Behaviour of offshore structures, Delft, The Netherlands
9. Davis MC, Zarnick EE (1966) Testing ship models in transient waves. Technical report, David Taylor Model Basin Washington DC Hydromechanics Lab
10. Harten A (1983) High resolution schemes for hyperbolic conservation laws. *J Comput Phys* 49:357–393
11. Henning J (2005) Generation and analysis of harsh wave environments. PhD thesis, Technical University Berlin
12. Jiang GS, Shu CW (1996) Efficient implementation of weighted ENO schemes. *J Comput Phys* 126:202–228
13. Kamath A, Alagan Chella M, Bihs H, Arntsen ØA (2016) Breaking wave interaction with a vertical cylinder and the effect of breaker location. *Ocean Eng* 128:105–115
14. Kjeldsen SP (1982) 2- and 3-dimensional deterministic freak waves. *Coast Eng* 1982:677–694
15. Paulsen BT, Bredmose H, Bingham HB (2014) An efficient domain decomposition strategy for wave loads on surface piercing circular cylinders. *Coast Eng* 86:57–76
16. Peskin CS (1972) Flow patterns around the heart valves. *J Comput Phys* 10:252–271
17. Schäffer HA, Klopman G (2000) Review of multidirectional active wave absorption methods. *J Waterw Port Coast Ocean Eng* 126(2):88–97
18. Sussman M, Smereka P, Osher S (1994) A level set approach for computing solutions to incompressible two-phase flow. *J Comput Phys* 114:146–159

# Effect of Emerged Coastal Vegetation on Wave Attenuation Using Open Source CFD Tool: REEF3D



H. S. Arunakumar, Praveen Suvarna, P. A. Abhijith, Ashwin S. Prabhu, U. Pruthviraj and Arun Kamath

**Abstract** Coastal vegetation is a soft solution for protecting the coast from the action of waves by attenuating the wave height and reducing the energy of the waves. Effect of wave height attenuation as a result of the presence of emerged coastal vegetation is studied numerically by resolving the Reynolds-averaged Navier–Stokes (RANS) equations. A three-dimensional numerical wave tank model is simulated using an open source computational fluid dynamics (CFD) software REEF3D, and wave attenuation due to emerged coastal vegetation is determined. An artificial, rigid, emerged vegetation for a length of 2 m is developed in a numerical wave tank of REEF3D. The model is tested for regular waves of height 0.08, 0.12, and 0.16 m and wave periods of 1.8 and 2 s in a water depth of 0.40 and 0.45 m. The wave heights are measured at different locations along the vegetation meadow at 0.5 m intervals. The devolved numerical model is corroborated by comparing the obtained numerical results with the experimental results as reported by John et al. (Experimental investigation of wave attenuation through artificial vegetation meadow, ISH—HYDRO, [1]). The numerically obtained results are concurrent with the experimental results.

---

H. S. Arunakumar (✉) · P. Suvarna · U. Pruthviraj  
Department of Applied Mechanics and Hydraulics, NITK Surathkal, Surathkal 575025, Karnataka, India  
e-mail: [arunsaligram17@yahoo.com](mailto:arunsaligram17@yahoo.com)

P. Suvarna  
e-mail: [civilsuvarna@gmail.com](mailto:civilsuvarna@gmail.com)

U. Pruthviraj  
e-mail: [pruthviu@gmail.com](mailto:pruthviu@gmail.com)

P. A. Abhijith · A. S. Prabhu  
Department of Civil Engineering, NITK Surathkal, Surathkal 575025, Karnataka, India  
e-mail: [abhpa247@gmail.com](mailto:abhpa247@gmail.com)

A. S. Prabhu  
e-mail: [ashwinsp1997@gmail.com](mailto:ashwinsp1997@gmail.com)

A. Kamath  
Department of Civil and Transportation Engineering, NTNU, Trondheim 7491, Norway  
e-mail: [arun.kamath@ntnu.no](mailto:arun.kamath@ntnu.no)

**Keywords** Coastal vegetation · Numerical model  
Computational fluid dynamics (CFD) · Wave attenuation

## 1 Introduction

A close relationship has been maintained by the mankind with the sea for the centuries, because of his activity along the coast. Urbanization and industrialization of coastal areas compelled the mankind to develop the coastal facilities to cater the demand. The intent of coastal engineering is to deliver a sustainable enlargement of the susceptible coastal zone facing catastrophic scenarios and also meeting the requirements for the safeguarding of coastline. Coastlines are dynamic systems which are vulnerable to storm surges, tsunamis, cyclones, and erosion. The usage of hard solution like conventional breakwaters, seawalls, and groynes will dissipate and reflect wave energy and thereby protect that part of the region. When hard solutions are adopted, it will indulge erosion or accretion in the adjacent shorelines due to the alteration of natural hydrodynamics and sediment movement.

Coastal plant life can diminish the wave height and the energy of the waves. Reports on the assessment of damage due to the 1999 Odisha cyclone along the coast of the Indian state of Odisha and the 2004 Indian Ocean tsunami on some of the coastal districts of Tamil Nadu (in India) reveal that intact and healthy mangroves saved many lives by dramatically reducing the intensity of the storm surge due to the cyclone and decelerated the gush of tsunami wave shoreward [2, 3].

The energy of the wave depends on the wave steepness, crest angle, depth, the impact on the structure, etc. The shape of the structure plays a major role while interacting with highly nonlinear waves, including reflection, overtopping, transmission, breaking, and evolution of vortices. These flow problems are resolved numerically by using different computational fluid dynamics (CFD) software. REEF3D is an open source software and free. REEF3D software has been used to solve the continuum mechanics problems in coastal engineering. For the calculation of wave propagation and wave hydrodynamics, a three-dimensional new level set with better density interpolation is established by resolving the incompressible Navier–Stokes equations. The level set method is used for modeling the free surface [4] under the approximation of two-phase flow, allowing for the simulation of complicated phenomena such as breaking wave forces [5], wave transformation [6], and floating bodies in waves [7].

Many experimental and numerical studies on coastal vegetation have been conducted to observe the efficacy of coastal vegetation in wave attenuation. Previous studies include studies on coastal kelp forests [8–11] and mangroves [12–15] and numerical studies [9, 16]. In India, the soft measures of coastal protection have gained importance after tsunamis. Some of the early works include experimental investigations on the effect of vegetation on reducing the wave run-up [17] and experimental investigation of wave attenuation through an artificial vegetation meadow [1].

This work aims at simulation and validation of emerged artificial rigid coastal vegetation using CFD software REEF3D. The numerical wave tank is used for the

simulation, and the numerical solutions are well suited to assess the effect of emerged artificial rigid vegetation on the attenuation of the waves. Thus, an initial study is presented on the attenuation of waves with rigid emerged vegetation, and the numerically obtained results are validated with the experimental results which are carried out in a wave flume at the Department of Applied Mechanics and Hydraulics, NITK Surathkal.

## 2 Numerical Model of Emerged Vegetation

REEF3D is an open source computational fluid software package and can be used to solve complex problems in coastal engineering, hydrodynamics, offshore and environmental engineering, as well as marine CFD.

In the present numerical model, the incompressible Navier–Stokes equations are solved with RANS turbulence closure. Cartesian mesh is used to achieve wave propagation with higher stability and accuracy. Fifth-order WENO scheme is used for the convection terms of the momentum equations. Third-order TVD Runge–Kutta scheme is used for performing time stepping. Staggered grid with projection method is used to solve the pressure which ensures tight pressure–velocity coupling. Ghost cell-immersed boundary method is used to consider boundaries with irregularity. The numerical model is completely parallelized on the basis of domain decomposition strategy and MPI (message passing interface).

### 2.1 Governing Equations

Incompressible RANS equations are solved using REEF3D along with the continuity equation to resolve the flow problems.

$$\frac{\partial U_i}{\partial x_i} = 0 \quad (1)$$

$$\frac{\partial U_i}{\partial t} + U_j \frac{\partial U_i}{\partial X_j} = -\frac{1}{\rho} \frac{\partial P}{\partial X_i} + \frac{\partial}{\partial X_j} \left[ (v + \nu_t) \left( \frac{\partial U_i}{\partial X_j} + \frac{\partial U_j}{\partial X_i} \right) \right] + g_i \quad (2)$$

where  $\rho$  is the density,  $u$  is the time-averaged velocity,  $p$  is the pressure,  $\nu_t$  is the eddy viscosity,  $\nu$  is the kinematic viscosity, and  $g$  is the acceleration due to gravity. Projection method is used to determine the pressure, and BiCGStab is adopted to resolve the subsequent Poisson's equation.  $K-\omega$  model is adopted for the modeling of turbulence.

## 2.2 Free Surface

The free surface of the waves is modeled by adopting the level set method. The signed distance function is the shortest distance from the interface determined by level set function. The interface of the two fluids can be differentiated by using the sign of the function, and it is described in the equation below:

$$\Phi(\vec{x}, t) \begin{cases} > 0 \text{ if } \vec{x} \text{ is in phase 1} \\ = 0 \text{ if } \vec{x} \text{ is in interphase} \\ < 0 \text{ if } \vec{x} \text{ is in phase 2} \end{cases} \quad (3)$$

Under the effect of external velocity  $u_j$ , the level set function is moved with the convection equation as mentioned below:

$$\frac{\partial \Phi}{\partial t} + U_j \frac{\partial \Phi}{\partial X_j} = 0 \quad (4)$$

The convection term in Eq. (4) is resolved by adopting the Hamilton–Jacobi version of the WENO scheme [18], and third-order TVD Runge–Kutta scheme is adopted for the time stepping [19]. When the interface between two fluid changes, the level set function modifies its signed distance property. To maintain mass conservation and ensure signed distance property, the level set function is reinitialized after every time step. In the current study, a PDE-based reinitialization equation is solved [20].

## 2.3 Assumptions

In experimental investigation, the emerged plant model is made up of nylon rods and it is observed that the nylon rods show negligible sway movement in the wave-propagating direction for the action of waves generated. Therefore, in the present numerical study, in REEF3D, the flexibility of the vegetation is neglected and vegetation is assumed and modeled as rigid solid cylindrical structure. The placement of cylinders is in line with experimental setup.

## 2.4 Numerical Model Validation

The numerical validation is based on the physical experiments carried out in the wave flume by John [1]. Figure 1 shows a schematic diagram of the experimental setup. The physical model of emerged artificial rigid vegetation meadow shown in Fig. 2 is of 2 m width, placed on the horizontal part of the flume bed and tested for wave



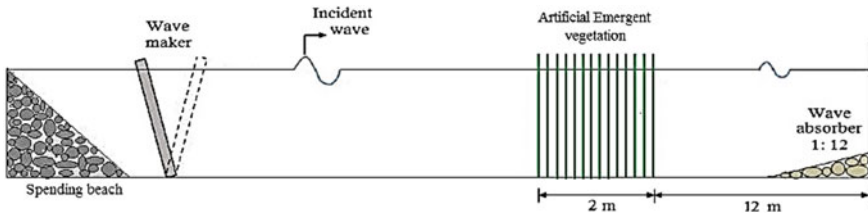


**Fig. 1** Experimental setup of emerged vegetation in wave flume [1]



**Fig. 2** Experimental model arrangement to investigate wave attenuation over emergent vegetation [1]

**Table 1** Vegetation physical characteristics and experimental conditions [1]

Plant	Characteristics of modeled vegetation		Wave height $h$ (m)	Wave period $T$ (s)	Water depth $d$ (m)	Relative vegetation height ( $hs/d$ )
Emergед rigid vegetation	Length of rod	0.50 m	0.08 0.12 0.16	1.8 2.0	0.40 0.45	1.25 1.11
	Diameter of rod	0.16 m				
	Density (plants/m <sup>2</sup> )	108				

heights 0.08, 0.12, and 0.16 m and different wave periods of 1.8 and 2 s in distinct water depths of 0.40 and 0.45 m. The vegetation characteristics and experimental conditions are described in Table 1.

The wave heights at different places along the vegetation are recorded using numerical wave probes along the meadow. The vegetation rods are of 0.016 m diameter and 0.50 m long, and the density of the vegetation is 108 plants/m<sup>2</sup>.

The dimensions of emerged vegetation and wave parameters are similar to the physical experiment. The simulated time is 20 s. Waves are generated in the intermediate water depth using linear wave theory. The 3D numerical wave tank used in this study is illustrated in Figs. 3 and 4, respectively. The numerical tank is 20.0 m long, 0.71 m wide, and 0.7 m high. Waves of height 0.08, 0.12, and 0.16 m are generated at different water depths of 0.40 and 0.45 m with time periods of 1.8 and 2 s,

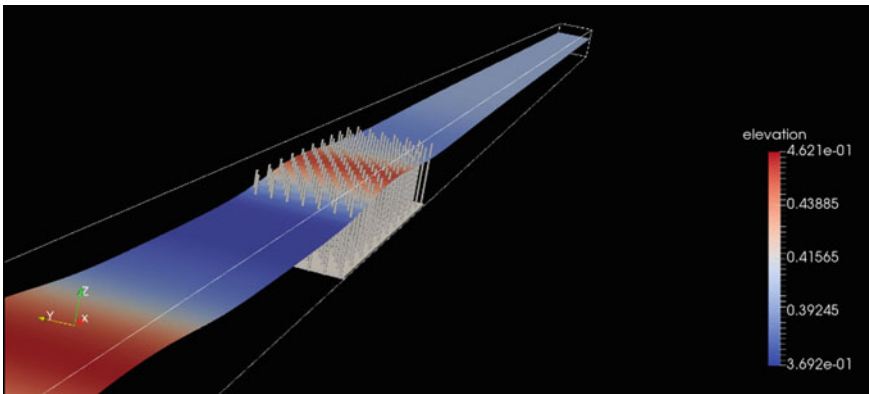


Fig. 3 Three-dimensional numerical wave tank with emerged vegetation

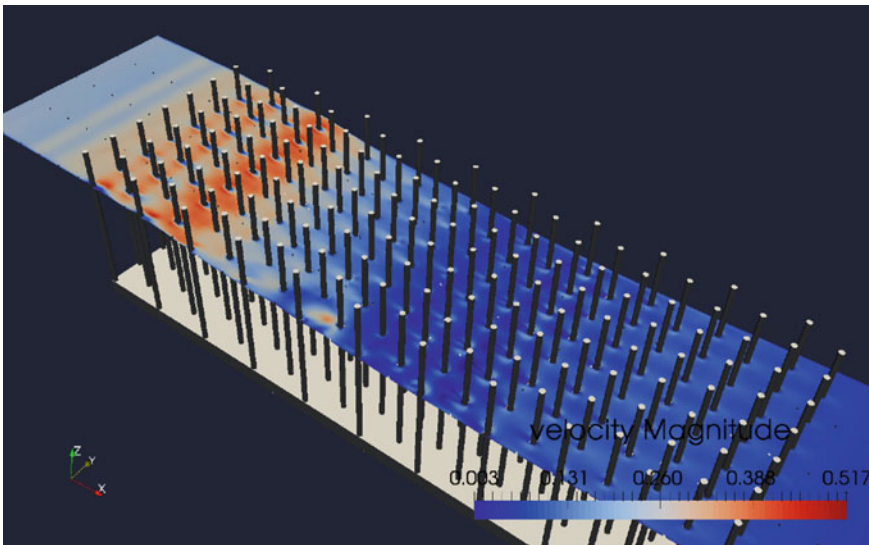


Fig. 4 Interaction of waves with emerged vegetation in numerical wave tank

respectively. A grid size of 0.0125 m is used for the modeling of the numerical wave tank. Water surface elevation along the vegetation meadow is measured by using the numerical probes.

### 3 Results and Analysis

#### 3.1 Grid Convergence Study

The performance of the numerical wave tank is carried out in a two-dimensional rectangular wave tank of length 12 m. Regular waves of wave height 0.08 m are generated based on the linear wave theory in a water depth of 0.4 m. The elevation of the water depth is measured using the numerical wave probe in the working zone. Mesh sizes of 0.05, 0.025, 0.0125, and 0.00625 m are used for studying grid convergence, and the results obtained for different mesh sizes are compared as illustrated in Fig. 5.

It is evident from Fig. 5 that for the mesh size of 0.05 m, the crests and troughs of the waves are damped out and the results are improved for mesh size of 0.025 m. There is no much variation in the wave profile for 0.0125 and 0.00625 m as both converge to a single solution and give the same results.

From the grid convergence study, it can be concluded that 0.0125 m is the optimum grid size, and hence, the same grid size is used to study the effect of emerged coastal vegetation on attenuation of the waves.

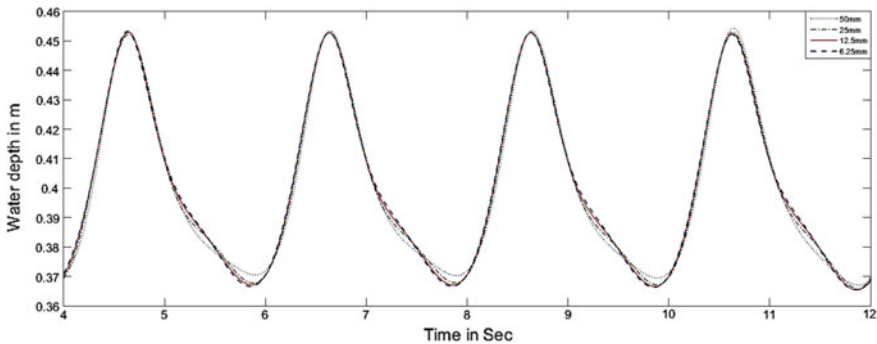
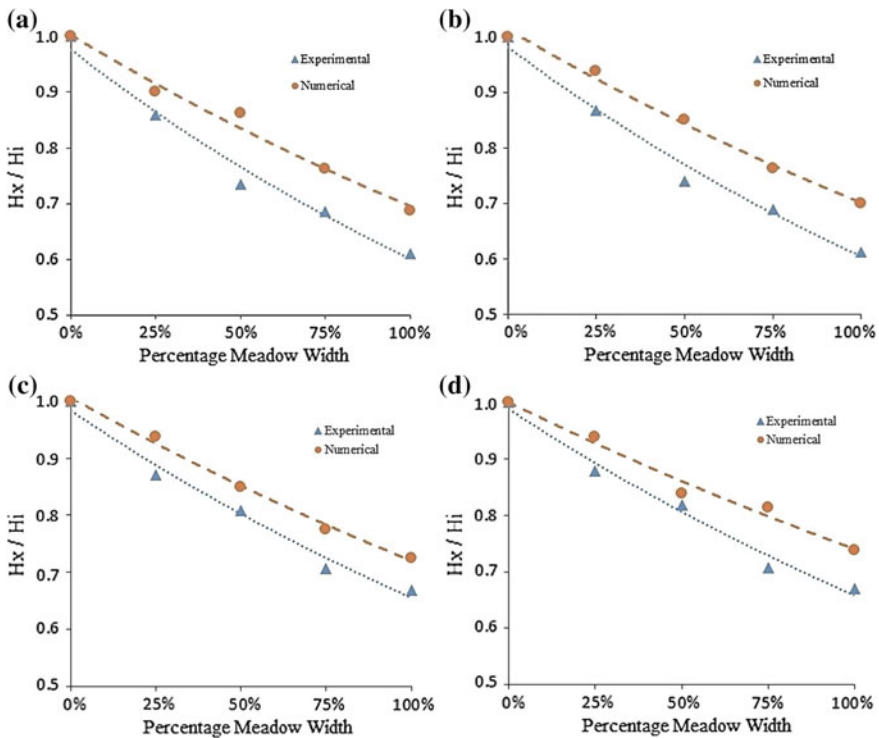


Fig. 5 Results of grid convergence study for mesh sizes of 0.05, 0.025, 0.0125, and 0.00625 m

### 3.2 Attenuation of Waves Due to Emerged Vegetation

The wave heights measured at different locations in the numerically simulated model along the 2-m meadow of emerged vegetation model are compared with the experimental results. It is observed that attenuation of wave height along the meadow is following exponential decay. For the wave height of 0.08 m, different relative vegetation heights ( $hs/d = 1.25, 1.11$ ), and different time periods ( $T = 1.8, 2$  s), the wave heights measured along the vegetation meadow of length 2 m at 0.5-m intervals are illustrated in Fig. 6.

The attenuation of wave height observed at the exit of the emerged vegetation meadow for  $hs/d = 1.25$  and  $T = 1.8$  and 2 s is 39.00 and 31.80% in the case of experimental study and 32.80 and 30.00% in the present numerical study, respectively. Further, the attenuation of wave height observed at the exit of the emerged vegetation meadow for  $hs/d = 1.11$  and  $T = 1.8$  and 2 s is 33.10 and 32.90% in the case of experimental study and 27.50 and 26.20% in the present numerical study, respectively.



**Fig. 6** Relative wave height ( $H_s/H_i$ ) measured along the emerged vegetation meadow for **a**  $h = 0.08$  m,  $T = 1.8$  s,  $hs/d = 1.25$ ; **b**  $h = 0.08$  m,  $T = 2$  s,  $hs/d = 1.25$ ; **c**  $h = 0.08$  m,  $T = 1.8$  s,  $hs/d = 1.11$ ; and **d**  $h = 0.08$  m,  $T = 2$  s,  $hs/d = 1.11$

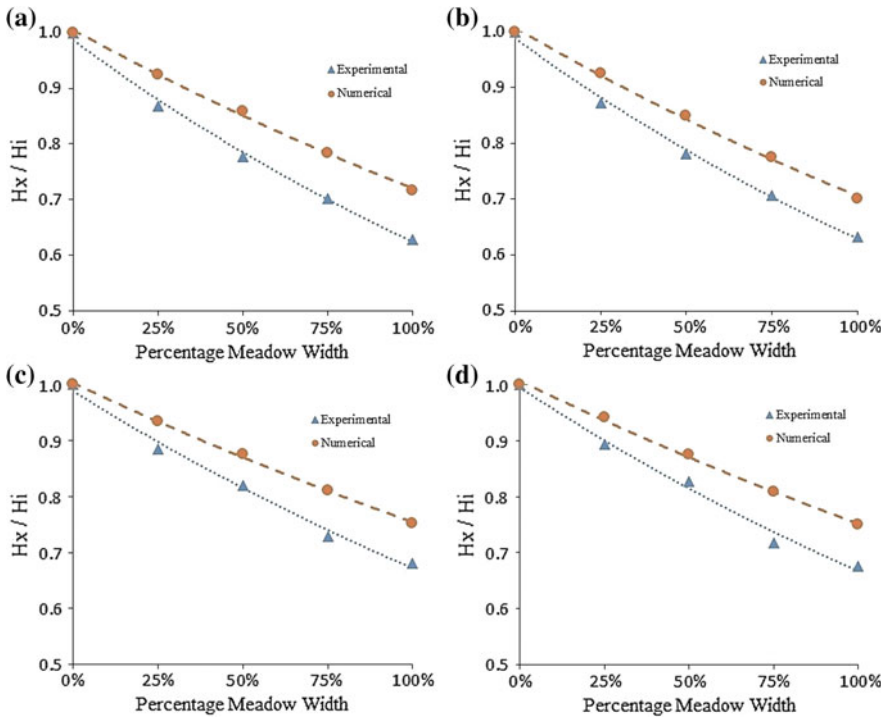


**Fig. 7** Relative wave height ( $H_x/H_i$ ) measured along the emerged vegetation meadow for **a**  $h = 0.08$  m,  $T = 1.8$  s,  $h_s/d = 1.25$ ; **b**  $h = 0.08$  m,  $T = 2$  s,  $h_s/d = 1.25$ ; **c**  $h = 0.08$  m,  $T = 1.8$  s,  $h_s/d = 1.11$ ; and **d**  $h = 0.08$  m,  $T = 2$  s,  $h_s/d = 1.11$

For the wave height of 0.12 m, different relative vegetation heights ( $h_s/d = 1.25, 1.11$ ), and different time periods ( $T = 1.8, 2$  s), the wave heights measured along the vegetation meadow of length 2 m at 0.5-m intervals are illustrated in Fig. 7.

The attenuation of wave height observed at the exit of the emerged vegetation meadow for  $h_s/d = 1.25$  and  $T = 1.8$  and 2 s is 37.20 and 36.80% in the case of experimental study and 28.30 and 30.00% in the present numerical study, respectively. Further, the attenuation of wave height observed at the exit of the emerged vegetation meadow for  $h_s/d = 1.11$  and  $T = 1.8$  and 2 s is 32.00 and 32.30% in the case of experimental study and 24.80 and 25.00% in the present numerical study, respectively.

For the wave height of 0.16 m, different relative vegetation heights ( $h_s/d = 1.25, 1.11$ ), and different time periods ( $T = 1.8, 2$  s), the wave heights measured along the vegetation meadow of length 2 m at 0.5-m intervals are illustrated in Fig. 8.

The attenuation of wave height observed at the exit of the emerged vegetation meadow for  $h_s/d = 1.25$  and  $T = 1.8$  and 2 s is 34.40 and 33.90% in the case of experimental study and 26.90 and 28.10% in the present numerical study, respectively. Further, the attenuation of wave height observed at the exit of the emerged vegetation

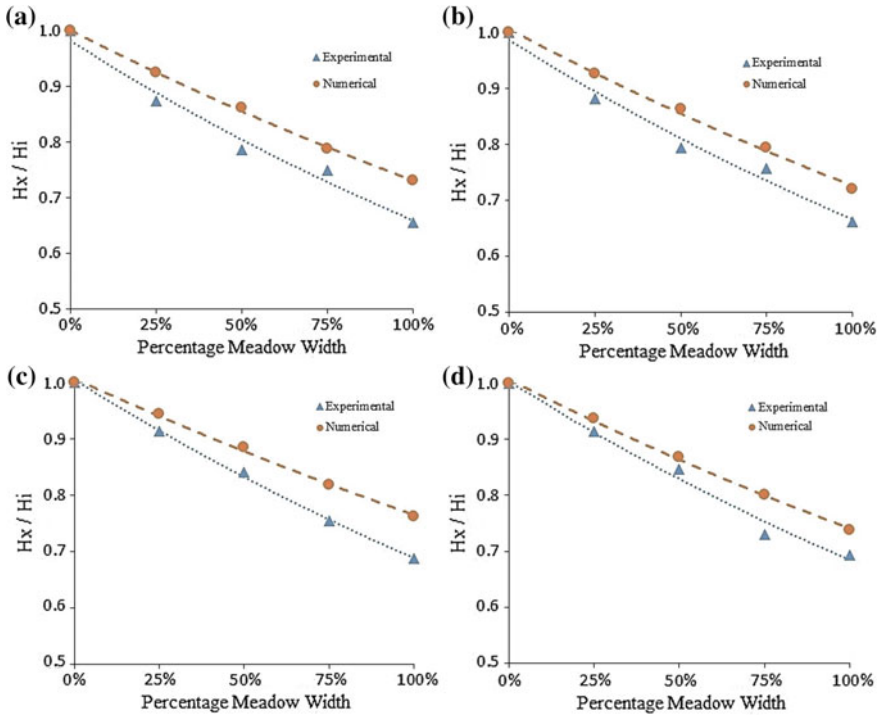


**Fig. 8** Relative wave height ( $H_s/H_i$ ) measured along the emerged vegetation meadow for **a**  $h = 0.08$  m,  $T = 1.8$  s,  $h_s/d = 1.25$ ; **b**  $h = 0.08$  m,  $T = 2$  s,  $h_s/d = 1.25$ ; **c**  $h = 0.08$  m,  $T = 1.8$  s,  $h_s/d = 1.11$ ; and **d**  $h = 0.08$  m,  $T = 2$  s,  $h_s/d = 1.11$

meadow for  $h_s/d = 1.11$  and  $T = 1.8$  and 2 s is 31.30 and 31.70% in the case of experimental study and 23.70 and 26.20% in the present numerical study, respectively.

### 3.3 Influence of Relative Vegetation Height on Attenuation of Wave

The relative vegetation height indicates the depth of submergence of the vegetation with respect to the depth of water. An increase in relative plant height ( $h_s/d$ ) results in higher attenuation of incident wave height as evident from experimental and numerical results illustrated in Fig. 9a, b for  $h_s/d = 1.25$  and  $h_s/d = 1.11$ , respectively.

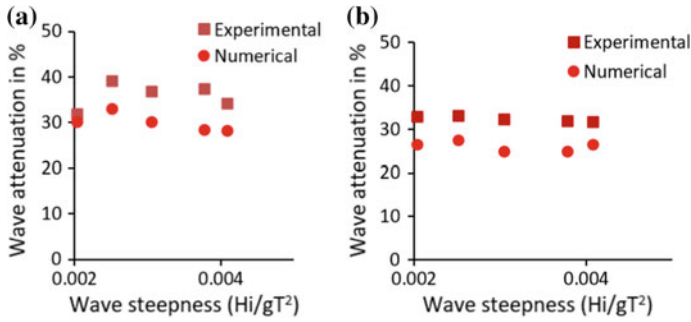


**Fig. 9** Influence of relative vegetation height ( $h_s/d$ ) on wave attenuation for emerged vegetation for **a**  $h_s/d = 1.25$  and **b**  $h_s/d = 1.11$

## 4 Conclusions

The open source CFD tool REF3D is used for the simulation of emerged vegetation placed in a three-dimensional numerical wave tank. The influence of water depth, incident wave height, and wave period on wave attenuation is investigated numerically. Numerical results are in good agreement with the experimental results, and the wave attenuation due to emerged vegetation is following the same trend as experimental for the variation of wave height, wave period, and water depth.

The orbital velocity of the propagating waves is captivated by emerged vegetation resulting in developing turbulence which in turn results in loss of wave energy and wave height. The waves are attenuated in exponential trend as it propagates along the vegetation meadow. The increase in relative vegetation height ( $h_s/d$ ) results in higher attenuation of the waves. The numerical results obtained for emerged vegetation, attained an average of 85% agreement with that of experimental results. The variances between experimental results and numerical results are probably due to the assumptions based on which models are simulated; that is, vegetation is assumed to be rigid and does not move in any direction for the action of waves.

**Acknowledgements** The authors are grateful to Dr. Kiran G. Shirlal, professor, Department of Applied Mechanics and Hydraulics, Dr. Subba Rao, professor, Department of Applied Mechanics and Hydraulics, Beena Mary John, research scholar, and authorities of Department of Applied Mechanics and Hydraulics and Centre for System Design (CSD), NITK Surathkal, for providing the experimental data and computational resource for the study.

## References

1. John BM, Shirlal KG, Rao S (2016) Experimental investigation of wave attenuation through artificial vegetation meadow, ISH—HYDRO
2. Das S, Vincent JR (2009) Mangroves protected villages and reduced death toll during Indian super cyclone. *Proc Natl Acad Sci USA* 106(18):7357–7360. <https://doi.org/10.1073/pnas.0810440106>
3. NIO (2005) Observations of post tsunami reconnaissance investigations along eastern coastal tract of India following the devastating tsunami of 26th December 2004. National Institute of Oceanography Technical Report no. NIO/TR-08/2005
4. Bihs H, Kamath A, Chella MA, Aggarwal A, Arntsen ØA (2016) A new level set numerical wave tank with improved density interpolation for complex wave hydrodynamics. *Comput Fluids* 140:191–208. <https://doi.org/10.1016/j.compfluid.2016.09.012>
5. Alagan Chella M, Bihs H, Myrhaug D, Muskulus M (2017) Breaking solitary waves and breaking wave forces on a vertically mounted slender cylinder over an impermeable sloping seabed. *J Ocean Eng Mar Energy* 3(1):1–19
6. Kamath A, Alagan Chella M, Bihs H, Arntsen ØA (2017) Energy transfer due to shoaling and decomposition of breaking and non-breaking waves over a submerged bar. *Eng Appl Comput Fluid Mech* 11(1):450–466
7. Bihs H, Kamath A (2017) A combined level set/ghost cell immersed boundary representation for floating body simulations. *Int J Numer Meth Fluids* 83(12):905–916
8. Rosman JH, Denny MW, Zeller RB, Monismith SG, Koseff JR (2013) Interaction of waves and currents with kelp forests (*Macrocystis pyrifera*): insights from a dynamically scaled laboratory model. *Limnol Oceanogr* 58(3):790–802. <https://doi.org/10.4319/lo.2013.58.3.0790>
9. Zeller RB, Weitzman JS, Abbott ME, Zarama FJ, Fringer OB, Koseff JR (2014) Improved parameterization of seagrass blade dynamics and wave attenuation based on numerical and laboratory experiments. *Limnol Oceanogr* 59(1):251–266. <https://doi.org/10.4319/lo.2014.59.1.0251>
10. Bouma TJ, De Vries MB, Low E, Peralta G, Táncoz IC, van de Koppel J, Herman PJ (2005) Trade-offs related to ecosystem engineering: a case study on stiffness of emerging macrophytes. *Ecology* 86(8):2187–2199
11. Coops H, Geilen N, Verheij HJ, Boeters R, van der Velde (1996) Interaction between waves, bank erosion and emergent vegetation: an experimental study in a wave tank. *Aquat Bot* 53:187198. [https://doi.org/10.1016/0304-3770\(96\)01027-3](https://doi.org/10.1016/0304-3770(96)01027-3)
12. Struve J, Falconer RA, Wu Y (2003) Influence of model mangrove trees on the hydrodynamics in a flume. *Estuar Coast Shelf Sci* 58:163–171. [https://doi.org/10.1016/S0272-7714\(03\)00072-6](https://doi.org/10.1016/S0272-7714(03)00072-6)
13. Vo-Luong P, Massel S (2008) Energy dissipation in non-uniform mangrove forests of arbitrary depth. *J Mar Syst* 74(1):603–622. <https://doi.org/10.1016/j.jmarsys.2008.05.004>
14. Husrin S, Strusińska A, Oumeraci H (2012) Experimental study on tsunami attenuation by mangrove forest. *Earth Planet Space* 64(10):973–989. <https://doi.org/10.5047/eps.2011.11.008>
15. Strusińska-Correia A, Husrin S, Oumeraci H (2013) Tsunami damping by mangrove forest: a laboratory study using parameterized trees. *Nat Hazards Earth Syst Sci* 13(2):483. <https://doi.org/10.5194/nhess-13-483-2013>
16. Eldina F, Wahab AK, Hadibah I (2008) Numerical modeling approach of an artificial mangrove root system (ArMS) submerged breakwater as wetland habitat protector COPEDEC VII, Dubai, UAE
17. Sundar V, Murali K, Noarayanan L (2011) Effect of vegetation on run-up and wall pressures due to conoidal waves. *J Hydraul Res* 49(4):562–567. <https://doi.org/10.1080/00221686.2010.542615>



18. Jiang GS, Peng D (2000) Weighted ENO schemes for Hamilton Jacobi equations. *SIAM J Sci Comput* 21(6):2126–2143. <https://doi.org/10.1137/S106482759732455X>
19. Shu CW, Osher S (1988) Efficient implementation of essentially non-oscillatory shock capturing schemes. *J Comput Phys* 77(2):439–471. [https://doi.org/10.1016/0021-9991\(88\)90177-5](https://doi.org/10.1016/0021-9991(88)90177-5)
20. Sussman M, Smereka P, Osher S (1994) A level set approach for computing solutions to incompressible two-phase flow. *J Comput Phys* 114(1):146–159. <https://doi.org/10.1006/jcph.1994.1155>

# CFD Study of Regular Waves on a Jacket Structure



Ankit Aggarwal and Hans Bihs

**Abstract** The jacket-type platforms are one of the most common kinds of offshore structures used worldwide. These structures are installed in the open oceans. When the waves in open ocean interact with the jacket structure, it leads to a highly intricate free surface around the structure. These waves exert wave forces on the jacket members. This makes the study of the wave–jacket interaction very important. The numerical investigation of regular waves on the jacket structure is quite challenging due to their highly complex free surface during the interaction. Computational fluid dynamics (CFD) can be used as an effective tool to study regular waves interacting with the jacket structure. The present investigation is performed using the open-source computational fluid dynamics (CFD) model REEF3D. A highly turbulent free surface during the wave–jacket interaction is observed due to the increased contribution of the nonlinear wave components. The complex turbulent flow features around the jacket structure due to wave–structure interaction are well captured by the CFD model. The model uses the Reynolds-averaged Navier–Stokes (RANS) equations to provide detailed information about the wave hydrodynamics. The level set method (LSM) is used for modelling the free surface. For time discretization, third-order total variation diminishing (TVD) Runge–Kutta scheme is used. The complex geometries are implemented in the model using a ghost-cell immersed boundary method. The numerical code is fully parallelized using the message passing interface (MPI).

**Keywords** Jacket structure · CFD · Complex geometry · Turbulent free surface

## 1 Introduction

There has been an increasing focus towards offshore energy in the last few decades. The offshore platforms which are installed in the open oceans often experience

---

A. Aggarwal (✉) · H. Bihs  
Department of Civil and Environmental Engineering, Norwegian University of Science and Technology, 7491 Trondheim, Norway  
e-mail: [ankit.aggarwal@ntnu.no](mailto:ankit.aggarwal@ntnu.no)

© Springer Nature Singapore Pte Ltd. 2019  
K. Murali et al. (eds.), *Proceedings of the Fourth International Conference in Ocean Engineering (ICOE2018)*, Lecture Notes in Civil Engineering 22, [https://doi.org/10.1007/978-981-13-3119-0\\_38](https://doi.org/10.1007/978-981-13-3119-0_38)

605

complex wave–structure interactions. This leads to a complicated wave hydrodynamics around the substructures and the associated deck. The jacket structure is the commonly used substructure worldwide for offshore platforms. The waves impact the jacket members and can induce fatigue during the complex wave–structure interaction. A detailed study of the wave hydrodynamics around jacket structures is required in order to ensure the safety and structural integrity of the structure.

Many researchers in the past have performed experiments to study the wave hydrodynamics around offshore platforms. Murray et al. conducted experimental and analytical studies in order to investigate the wave hydrodynamics and wave impact forces on the Ekofisk platform structures [20]. They concluded that the wave diffraction plays an important role in deciding the significant vertical wave impact. Stansberg et al. investigated the extreme wave amplification on offshore structures [23]. They identified the higher-order effects from schematic variations in the wave steepness. Buchner et al. [12] and Finnigan et al. [13] suggested methods to evaluate the wave crest heights for decks. Experimental tests are a good way to investigate the wave hydrodynamics and crest heights for offshore platforms, but usually they are expensive and involve scale effects [25].

Computational fluid dynamics (CFD) have been used previously by many researchers to model different types of waves [5–7, 16, 18]. CFD results can be used in supplement with the experimental studies for investigating such complex wave hydrodynamics around the jacket structure. However, few researchers in the past have made an attempt to validate their CFD results. Grønbech et al. used the concept of change of fluid momentum taking into account the additional effects from buoyancy and drag in their CFD model in order to validate their hydrodynamic model for offshore platforms [15]. Pázkodi et al. conducted a CFD case study with wave-in-deck loads on a gravity-based structure (GBS) platform and validated their results against the model test data. Their results showed a good comparison with the experimental wave surface elevations, but the estimated numerical peaks were lower than the experiments for the cases with the large wave steepnesses. Only a few studies are available in the literature about the complex free surface and turbulence investigation during wave–jacket interaction.

The aim of the present paper is to study and investigate the complex wave–structure interaction and resulting hydrodynamic phenomena like wave diffraction and the free surface turbulence during the regular wave propagation around the jacket structure. The present study is conducted using the open-source CFD software REEF3D [10]. The numerical model is able to simulate these complex hydrodynamic processes, free surface turbulence and resulting nonlinearity in the free surface elevation.

## 2 Numerical Model

The present numerical model is based on the governing equations of fluid dynamics: continuity equation and the Reynolds-averaged Navier–Stokes equations (RANS) with the assumption of an incompressible fluid given as:

$$\frac{\partial u_i}{\partial x_i} = 0 \quad (1)$$

$$\frac{\partial u_i}{\partial t} + u_j \frac{\partial u_i}{\partial x_j} = -\frac{1}{\rho} \frac{\partial p}{\partial x_i} + \frac{\partial}{\partial x_j} \left[ (v + \nu_t) \left( \frac{\partial u_i}{\partial x_j} + \frac{\partial u_j}{\partial x_i} \right) \right] + g_i \quad (2)$$

where  $u$  is the velocity averaged over time  $t$ ,  $\rho$  is the fluid density,  $p$  is the pressure,  $\nu$  is the kinematic viscosity,  $\nu_t$  is the eddy viscosity,  $i$  and  $j$  denote the indices in  $x$  and  $y$  direction, respectively, and  $g_i$  is the acceleration due to gravity.

The numerical model uses a fifth-order finite difference weighted essentially non-oscillatory (WENO) scheme in multi-space dimensions for the spatial discretization [17]. The third-order TVD Rung–Kutta scheme is used for the time discretization [22]. An adaptive time stepping scheme is used in the numerical model [14]. The present study uses the  $k$ - $\omega$  model [24] along with the Reynolds-averaged Navier–Stokes (RANS) equation. The level set method is used to capture the free surface [21]. The level set function can be written as:

$$\phi(\mathbf{x}, t) \begin{cases} > 0 & \text{if } \mathbf{x} \text{ is in phase 1} \\ = 0 & \text{if } \mathbf{x} \text{ is at the interface} \\ < 0 & \text{if } \mathbf{x} \text{ is in phase 2} \end{cases} \quad (3)$$

The relaxation method [19] is used in the present study for the wave generation. A three-dimensional ghost-cell immersed boundary method (GCIBM) [8] is implemented to model the complex geometries. Parallel computation is employed in the numerical model which is based on the domain decomposition method and message passing interface (MPI). The detailed information about the numerical model can be obtained in Bihs et al. [10]. REEF3D has been used in the past for a wide range of marine applications, such as wave–structure interaction [18], breaking wave forces [11], floating body dynamics [9], irregular wave analysis [2–4] and sediment transport [1].

## 3 Results

### 3.1 Numerical Set-up

In this section, the numerical simulations are performed in a three-dimensional numerical wave tank (NWT) to study the wave propagation and wave hydrodynamics of regular waves around the jacket structure. The numerical wave tank is 15 m long, 5 m wide and 4.5 m high with a water depth  $d = 2.5$  m (Fig. 1a). A jacket structure with the multiple horizontal and vertical members is placed at a distance of 1.5 m from the wave generation. The diameter of each member of the jacket structure is

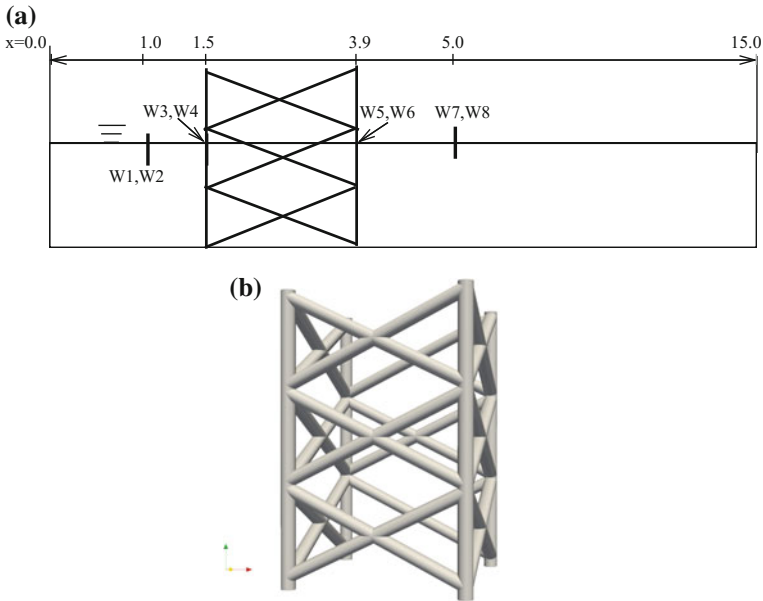


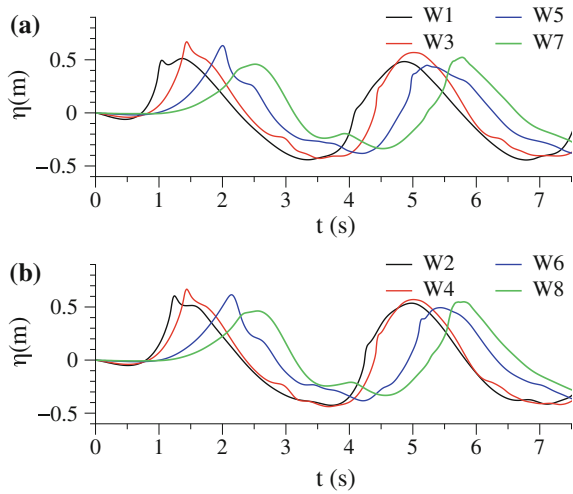
**Fig. 1** Schematic sketch of the **a** numerical wave tank with the wave gauge , **b** jacket structure

$D = 0.2$  m. The jacket structure is shown in Fig. 1b. In the numerical set-up, eight different wave gauges are placed along the numerical wave tank (NWT) at  $[x, y]$  (m) = W1(1.0, 0.8), W2(1.0, 3.2), W3(1.5, 0.8), W4(1.5, 3.2), W5(3.9, 0.8), W6(3.9, 3.2), W7(5.0, 0.8) and W8(5.0, 3.2).

### 3.2 Changes in the Free Surface Elevation

The numerical test is performed with the input wave height  $H = 0.60$  m and period  $T = 3.5$  s. The profile of the wave surface elevation  $\eta$  becomes more asymmetric and nonlinear, when the wave propagates along the NWT and interacts with the jacket members. Figure 2 presents the comparison of the numerical regular wave free surface elevation at eight different wave gauge locations. The wave free surface elevations measured at the wave gauges located at  $x = 1$  m (W1 and W2) are mostly regular. However, there is some nonlinearity and skewness in the wave crest and wave trough due to the superposition of the incident waves with the diffracted and reflected waves from the jacket members. When the waves propagate further (W3 and W4), the wave crest is about to hit the jacket members. The wave crest becomes more skewed, sharp and vertically and horizontally asymmetric due to the wave–wave and wave–structure interactions. When the wave crest reaches the rear side of the jacket (W5 and W6), the wave crest is very nonlinear, skewed and asymmetric. Also, some

**Fig. 2** Numerical regular wave free surface elevation at the different wave gauges located at the **a** front XZ-plane, **b** back XZ-plane



percentage of wave energy is dissipated during this process in the form of turbulence and transfer of wave energy towards higher harmonics. For the wave gauges located after the jacket (W7 and W8), the computed numerical free surface elevations are similar to irregular wave free surface elevation. It is clearly observed that the wave train now contains the waves with different amplitudes and frequencies. This is due to the superposition of the shorter waves generated because of the wave diffractions and wave reflections during the wave-jacket interaction.

Figure 3 presents the computed wave profile with the velocity variation during the jacket-wave interaction. Both the top and side views are shown at the different time steps. The wave crest at  $t/T = 1.31$  which is about to hit the jacket structure can be seen in Fig. 3a. A highly irregular and nonlinear free surface is observed due to the complex wave-structure interaction. The wave diffraction takes place due to the wave obstruction by the jacket members. The diffracted waves travel radially outwards in the form of the semicircles, when the waves interact with the vertical members of the jacket. The diffracted waves from the four vertical members interact with each other, and a semi-elliptical wave diffraction pattern is observed around the midway of the jacket. At  $t/T = 1.43$ , the wave crest is propagated further after impacting the front face of the jacket. A very turbulent and irregular wave field is noticed due to the diffracted and reflected waves from the vertical and horizontal jacket members. The diffraction pattern around the midway of the jacket is no longer uniform and semicircular; rather, it becomes more irregular and random. However, the waves which are diffracted by the members located on the rear face of the jacket still show the semicircular diffracted waves propagating radially outwards. Due to the complex wave-wave interaction, the free surface does not look regular anymore and some energy is dissipated as turbulence during this process. The members located on the lateral faces distribute the energy of wave crest, and the primary wave crest propagates in three parts in three different regions located in the same vertical plane.

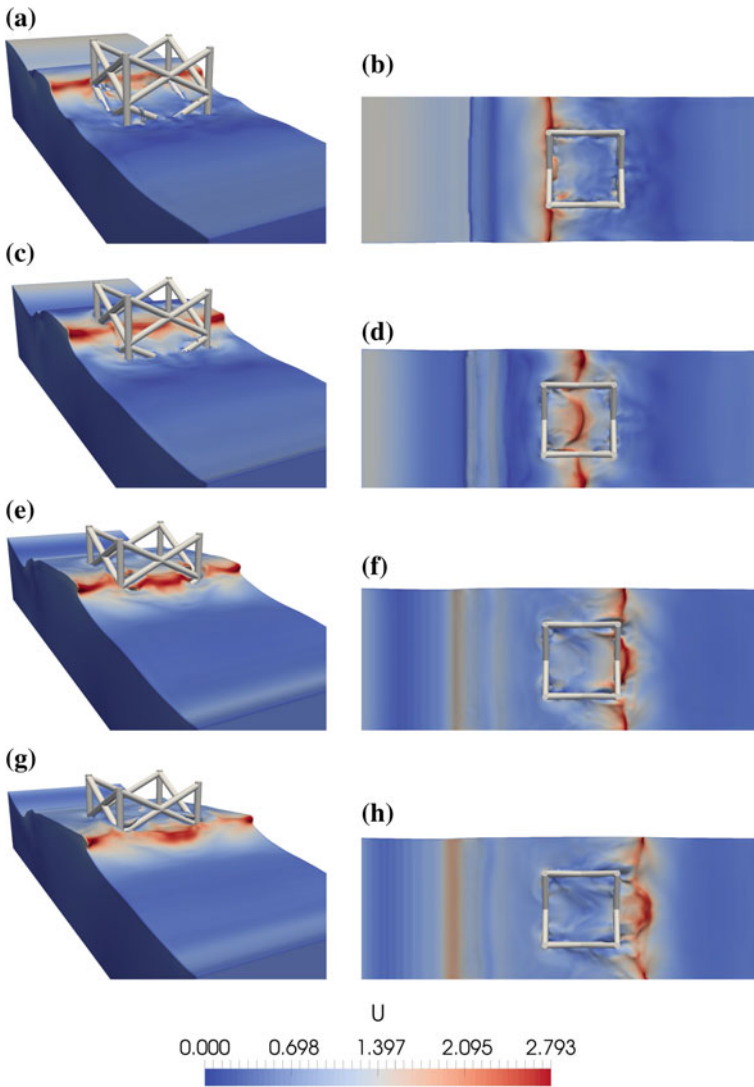


**Fig. 3** Computed wave profile with the velocity variation (m/s) during the wave-jacket interaction at  $t/T$  **a** 1.31 **b** 1.31 **c** 1.43 **d** 1.43 **e** 1.54 **f** 1.54 **g** 1.60 **h** 1.60

The part of the wave crest which propagates inside the jacket after interacting with the jacket members on the front face takes the form of a propagating semicircular primary wave crest. At  $t/T = 1.54$ , the wave crest hits the members located on the rear face of the jacket. The diffraction pattern around the members located on the front face becomes more regular and semicircular again, since the wave crest is already propagated. A semicircular-shaped wave crest is observed around the midway of the jacket, but the crest velocities are significantly reduced as compared

to the previous time step. The waves are diffracted in a more irregular and random fashion around the rear members of the jacket due to the primary propagating waves and secondary diffracted and reflected waves (by the members located on the front and rear face). When the wave crest is propagated over the jacket members located in the rear face, the wave diffraction pattern around the front jacket members is more semicircular (at  $t/T = 1.60$ ). The wave pattern around the midway of the jacket becomes sharp V-shaped due to the complex hydrodynamic wave–wave and wave–structure interactions. The waves around the rear members also start to diffract in more uniform and a semicircular manner. The wave crest velocities are also reduced due to the dissipation of the wave energy during the wave–jacket interaction.

## 4 Conclusions

The numerical model REEF3D is used to simulate the interaction of the regular waves with the jacket structure. The study of such interaction is very complicated due to many hydrodynamic processes like wave diffraction, wave reflection, redistribution of wave energy occurring at the same time. The changes in the wave free surface elevation are studied during the wave propagation along the numerical wave tank. As the wave propagates along the wave tank, the wave crests become more sharp, skewed and asymmetric. The diffraction and reflection generate the shorter waves which interact with the incident waves leading to the redistribution of wave energy. Some percentage of the wave energy is dissipated in the form of turbulence, which is observed by highly nonlinear and turbulent wave profile. Due to this, the incident wave crest loses some of its initial energy and wave crest height is reduced after it propagates through the jacket structure. The wave surface elevation looks more alike to irregular wave surface elevation due to the presence of the waves with different frequencies and amplitudes. The numerical model REEF3D is able to simulate these complex hydrodynamic processes during the wave–jacket interaction. However, the present work is a preliminary study, and the model should be further validated with the experimental data for further applications.

**Acknowledgements** The research work has been funded by the Research Council of Norway through the project Hydrodynamic Loads on Offshore Wind Turbine Substructures (project number: 246810). The authors gratefully acknowledge the computing time granted by NOTUR (project number: NN2620k).

## References

1. Afzal MS, Bihs H, Kamath A, Arntsen ØA (2015) Three dimensional numerical modeling of pier scour under current and waves using level set method. *J Offshore Mech Arctic Eng-Trans Asme*



2. Aggarwal A, Alagan Chella M, Bihs H, ákozdi CP, Petter A, Arntsen Ø (2017) Numerical investigation of irregular breaking waves for extreme wave spectra using CFD. In: Proceedings of international ocean and polar engineering conference
3. Aggarwal A, Alagan Chella M, Kamath A, Bihs H, Arntsen ØA (2016) Irregular wave forces on a large vertical circular cylinder. *Energy Proc* 94:504–516
4. Aggarwal A, Alagan Chella M, Kamath A, Bihs H, Arntsen ØA (2016) Numerical simulation of irregular wave forces on a horizontal cylinder. In: ASME 2016 35th international conference on ocean, offshore and arctic engineering, volume 2: CFD and VIV
5. Alagan Chella M, Bihs H, Myrhaug D (2015) Characteristics and profile asymmetry properties of waves breaking over an impermeable submerged reef. *Coast Eng* 100:26–36
6. Alagan Chella M, Bihs H, Myrhaug D, Michael M (2016) Hydrodynamic characteristics and geometric properties of plunging and spilling breakers over impermeable slopes. *Ocean Model* 103:53–72
7. Alagan Chella M, Bihs H, Myrhaug D, Michael M (2017) Breaking solitary waves and breaking wave forces on a vertically mounted slender cylinder over an impermeable sloping seabed. *J Ocean Eng Mar Energy* 3(1):1–19
8. Berthelsen PA, Faltinsen OM (2008) A local directional ghost cell approach for incompressible viscous flow problems with irregular boundaries. *J Comput Phys* 227:4354–4397
9. Bihs H, Kamath A (2017) A combined level set/ghost cell immersed boundary representation for simulations of floating bodies. *Int J Numer Methods Fluids*
10. Bihs H, Kamath A, Alagan Chella M, Aggarwal A, Arntsen ØA (2016) A new level set numerical wave tank with improved density interpolation for complex wave hydrodynamics. *Comput Fluids* 140:191–208
11. Bihs H, Kamath A, Alagan Chella M, Arntsen ØA (2016) Breaking-wave interaction with tandem cylinders under different impact scenarios. *J Waterw Port Coast Ocean Eng*
12. Buchner B (2010) Public summary crest JIP. *Pub Summ CresT JIP*
13. Finnigan T (2013) Review and summary of recent industry w-i-d work, group recommendations. *Review and Summary of Recent Industry WI-D Work, Group Recommendations*
14. Griebel M, Dornseifer T, Neunhoffer T (1998) *Numer Simul Fluid Dyn*. SIAM
15. Grønbech J, Sterndorff MJ, Grigorian H (2001) Hydrodynamic modelling of wave-in-deck forces on offshore platform decks. In: *Offshore Technology Conference, USA*
16. Jacobsen NG, Fuhrman DR, Fredsøe J (2012) A wave generation toolbox for the open-source CFD library: openfoam. *Int J Numer Methods Fluids* 70:1073–1088
17. Jiang GS, Peng D (2000) Weighted ENO schemes for Hamilton-Jacobi equations. *SIAM J Sci Comput* 21:2126–2143
18. Kamath A, Alagan Chella M, Bihs H, Arntsen ØA (2015) CFD investigations of wave interaction with a pair of large tandem cylinders. *Ocean Eng* 108:734–748
19. Larsen J, Dancy H (1983) Open boundaries in short wave simulations—a new approach. *Coast Eng* 7:285–297
20. Murray J, Kaplan JP, Yu CW (1995) Experimental and analytical studies of wave impact forces on Ekofisk platform structures. In: *27th Offshore Technology Conference, USA*, pp 783–795
21. Osher S, Sethian JA (1988) Fronts propagating with curvature-dependent speed: algorithms based on Hamilton-Jacobi formulations. *J Comput Phys* 79:12–49
22. Shu CW, Gottlieb S (1998) Total variation diminishing range kutta schemes. *Math Comput* 67:73–85
23. Stansberg CT, Baarholm R, Kristiansen T, Hansen EWM, Rortveit G (2005) Extreme wave amplification and impact loads on offshore structures. In: *Offshore technology conference, USA*, pp 783–795
24. Wilcox DC (1994) *Turbulence modeling for CFD*. DCW Industries Inc. La Canada, California
25. Wu G, Danmeier D (2014) Practical application of cfd modeling of air gap and wave loads in offshore structure design. In: *Offshore technology conference, USA*

# Computational Study on the Hydrodynamic Effects of Interceptors Fitted to Transom of Planing Vessel



Suneela Jangam, V. Anantha Subramanian and P. Krishnankutty

**Abstract** The use of stern flaps, either fixed or controllable and interceptors in high-speed boats, has become an acceptable option to control the running trim of the vessel to enhance its speed and powering performance. The interceptor changes the pressure distribution underneath the hull over a certain distance forward of the transom. The stern interceptor effect on planing craft performance depends on its parameters and also on those of the craft. The aim to improve the performance on already built high-speed crafts has become an important issue for ecological and economic aspects. So, an in-depth study of the hydrodynamic behaviour of interceptor is essential, before it is adapted to a vessel, to get the best performance during the craft operation. Computational fluid dynamics (CFD) is being used for modelling ship flows due to the advances in computational methods. The aim of this paper is to predict the pressures and resistance characteristics of a high-speed planing craft equipped with an interceptor. The data regarding trim and resistance is generated for a planing hull with interceptor using CFD. In view of the above, an interceptor with 1 mm height is used to study the performance of a planing hull and compared with the experimental studies of Savitsky, Steen, and Srikanth. The numerical model predicts favourable trim and reduced drag for the planing hull with an interceptor.

**Keywords** Hydrodynamics · Stern interceptor · Planing hull · Resistance · Trim

## Nomenclature

LCG	Longitudinal centre of gravity
$C_f$	Schoenherr turbulent friction coefficient
$\nabla$	Volume of displacement
$\rho$	Mass density of water
$\Delta$	Displacement

---

S. Jangam (✉) · V. Anantha Subramanian · P. Krishnankutty  
Department of Ocean Engineering, Indian Institute of Technology Madras, Chennai, India  
e-mail: [suneelajangam4@gmail.com](mailto:suneelajangam4@gmail.com)

© Springer Nature Singapore Pte Ltd. 2019  
K. Murali et al. (eds.), *Proceedings of the Fourth International Conference in Ocean Engineering (ICOE2018)*, Lecture Notes in Civil Engineering 22,  
[https://doi.org/10.1007/978-981-13-3119-0\\_39](https://doi.org/10.1007/978-981-13-3119-0_39)

$\beta$	Deadrise angle
$V_1$	Average bottom velocity
$V$	Forward speed
$h_i$	Height of interceptor
$C_{D_{int\_S}}$	Coefficient of drag by Steen
$C_{L\beta}$	Lift coefficient for a deadrise surface
$A_D$	Additional drag force due to interceptor
$b$	Maximum beam at chine
$D_f$	Viscous component of drag
$c$	Distance between $N$ and CG
$N$	Resultant of pressure forces acting normal to bottom
$\tau$	Trim angle of keel, deg
$\lambda$	Wetted length to beam ratio
$\varepsilon$	Turbulent energy dissipation rate
$i$	Interceptor height
$L_w$	Mean wetted length
$D_{int\_S}$	Added drag due to interceptor

## 1 Introduction

The application of interceptor to high-speed planing crafts is a relatively recent innovation. The idea for interceptor design discussed herein originated from transom flaps research conducted in the 1900s. Interceptor is a stern appendage which consists of a thin plate fitted on or near the transom of a boat whose sharp tip follows the shape of the transom edge. Interceptors do not extend aft of the transom but go vertically downwards at the transom. Stern wedges, flaps are all been used commonly on many high-speed small crafts such as work boats, patrol crafts, and pleasure crafts. However, the principal reasons for the effectiveness of these devices on high-speed crafts are significantly different from that on large ships such as destroyers and frigates. The stern interceptors create a vertical lift force at the transom and modify the pressure distribution on the aft portion of the hull. The knowledge of the hydrodynamic action of the interceptor, which changes the surrounding flow, is important for selecting its size, form, and orientation. The practice shows that the blade always experiences a decelerated mean flow at the aft by Brizzolara [1]. On planing crafts which operate at high speed and derive a significant portion of the total hull lift from dynamic forces, the vertical forces from interceptor affect the hull trim angle by as much as  $2^\circ$ – $4^\circ$ . The effect of interceptor on the drag and trim of prismatic hulls for different deadrise angles is presented by Luca and Pensa [5]. On these hulls, the key to minimizing resistance is to reduce the hull trim angle. The most effective planing surface that maximizes hull dynamic lift and minimizes wetted surface, friction drag, and wave resistance is derived at this reduced trim angle. John et al. [3] studied experimentally the effect of flaps, wedges, and interceptor on displacement vessel, catamaran, and a planing hull. They found that interceptor with

wedge gave good performance in planing hull compared to other vessels. Salas and Tampier [6] made a CFD study on a displacement hull with flaps and interceptor and used spray rail for semiplaning hull. They found the resistance reduction in all three devices is around 5–10% and evaluated them as energy-saving devices. Karimi and Abbaspoor [4] made an experimental study on a scaled-down model of a high-speed planing catamaran and tested with and without controllable stern interceptors in calm water and regular head waves, to investigate the effect of automatically controlled interceptors on vertical motion reduction of the model.

The interceptor powering benefit is attributable to the induced change in the field flow around the hull. This flow field changes cause a reduction in drag on the ships aft body and modify the wave resistance of the craft. The pressure changes are verified computationally by RANS solver using STAR CCM+ on high-speed craft for interceptor of 1 mm height. In this work, numerical modelling has been undertaken to simulate the flow past the bare hull and later with interceptor in the aft region.

## 2 Interceptor Development

The study on interceptor by Brizzolara [1] is carried out by one of the first and most thorough published studies on interceptor hydrodynamics. He utilized a CFD approach to study the local flow around a 2D interceptor fitted to a flat boundary representing the bottom of the ship, at a Reynolds number of  $1.4 \times 10^9$ . He used a standard boundary layer approach to specify the inflow and computed the free surface in the region behind the interceptor and the pressure distribution in the region upstream of the interceptor for several interceptor sizes. Interceptors are also installed on displacement and semi-displacement hulls as given by Deng et al. [2]. Figure 1 shows the shape of the interceptor at the transom.

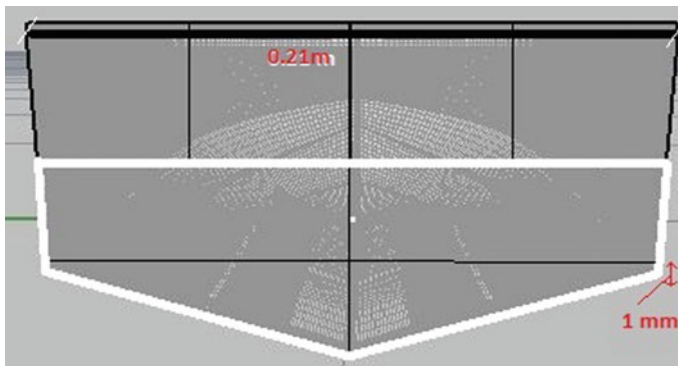


**Fig. 1** Interceptor of 1 mm height at the transom

The results indicated good performance improvements with reduction of trim and resistance. Thus, plans are made to test interceptor with 1 mm height on the high-speed planing craft. This appendage follows exactly the shape of the transom with interceptor of 1 mm height. The height of the interceptor is considered according to Tsai et al. [10]. They considered a planing boat of 20 m length with 1 mm as the efficient height of interceptor from the tested results [10].

### 2.1 Methodology

In a planing hull, there is an alteration of trim and draft in the running condition due to dynamic lift condition. Savitsky [7] proposed the use of average bottom velocity instead of free stream velocity in the calculations for frictional resistance component. The scheme predicted the performance of planing hull based on empirical equations for lift, drag, wetted area, the centre of pressure, trim angle, and deadrise angle. It is an iterative method based on choosing trim angles, which are then used in the empirical equation to obtain values of lift, drag, and trim. Forces acting on planing hull are shown in Fig. 2.

The planing hull is said to be in equilibrium when it satisfies the equation

$$\Delta \left\{ \frac{[1 - \sin \tau \sin (\tau + \epsilon)]c}{\cos \tau} - f \sin \tau \right\} + Df(a - f) = 0 \tag{1}$$

$$c = LCG - C_p \lambda b, \quad a = VGC - (b/4) \tan \beta$$

$$C_p = 0.75 \frac{1}{5.21CV^2/\lambda^2 + 2.39}, \quad V_1 = V(1 - 2Pd/\rho V^2)^{0.5}$$

The empirical equations for the planing craft of a deadrise surface are given by

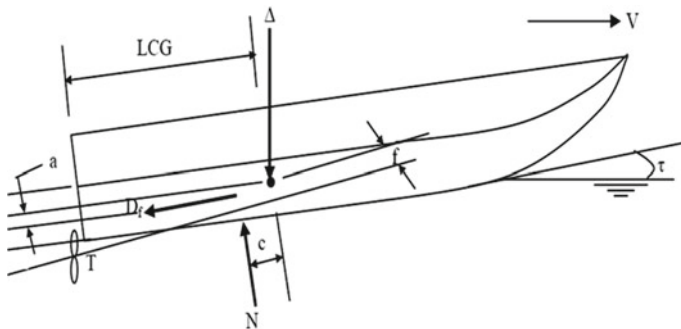


Fig. 2 Forces acting on planing hull

$$C_{L\beta} = \Delta / (1/2)\rho V^2 b^2 \quad (2)$$

$$D_f = C_f \rho V_1^2 (\lambda b^2) / 2 \cos \beta \quad (3)$$

These basic planing equations are used for predicting the performance of planing hull. The computational procedure involves the determination of running trim and resistance which provide for equilibrium conditions of the hull at a given running speed, load, and centre of gravity location. The above scheme is used iteratively, ensuring that first equation is satisfied by the iterative choice of values of trim angle. The hydrodynamic drag is obtained once the correct trim angle is obtained. The total hydrodynamic drag of planing surface is composed of pressure drag developed by pressure acting normal to the inclined bottom and viscous drag acting tangentially to the bottom in both the pressure area and spray area. It is assumed that the pressure acting normal to the bottom of the hull would be same as that acting on the interceptor. Along with the pressure at the transom, the interceptor also causes additional drag but is found to be very insignificant according to Srikanth and Datla [8]. Considering the formula to calculate additional drag produced due to the interceptor and the bare hull drag gives us the total drag acting on the high-speed craft.

Srikanth and Datla [8] mentioned interceptor as a surface imperfection which adds drag to the vessel where the boundary layer is forced to turn turbulent. The flow at the transom will not be laminar except for very low speeds. Depending on the size and shape, the drag is affected. In their experimental investigation on the performance of planing hull with interceptor found that there is exponential rise in drag with speed and substantial reduction of trim. They assumed that the added pressure at the bottom of hull at the transom will be same as that of the interceptor. The additional normal force they found is five times the additional drag force. The additional drag force is given by

$$A_D = 0.5\rho v^2 ib \quad (4)$$

Steen's formulas for added drag due to interceptor for a planing hull is given below in Eq. 5. Since the drag is dependent on wetted length and height of interceptor the coefficient of drag, the added drag is given by

$$C_{D_{int_S}} = 292.18 \left( \frac{h_i}{L_w} \right)^2 + 7.183 \left( \frac{h_i}{L_w} \right) \quad (5)$$

$$D_{int_S} = C_{D_{int_S}} (0.5\rho V^2 b L_w \tau) \quad (6)$$

The wetted length is assumed to be the mean wetted length used by Savitsky.

### 3 Numerical Modelling

Numerical solution of any problem related to fluid dynamics is associated with a solution of conservation of equations, namely the mass and momentum conservation equations. The governing equations of fluid flow represent the mathematical statements for the conservation of mass and momentum. Numerical modelling is performed to simulate the high-speed free running condition of the vessel with consequent dynamic changes in trim, sinkage, and bottom pressure. The differential form of the Navier–Stokes equations combined with the Reynolds averaged form of the N–S equation (RANSE) gives the solution of governing equations for practical engineering applications. The determination of resistance and trim angle of a planing craft at speed involves simulation in calm water on the free surface, and for this purpose, the volume of fluid (VOF) method is used. This study is carried out using the commercial CFD software STAR CCM+.

#### 3.1 Computational Domain and Boundary Conditions

A large domain was created in order to avoid effects from the domain boundaries to affect the flow near the hull. The vessel is enclosed by 3D rectangular parallelepiped computational domain over which the flow is solved. In Fig. 3, the computational domain is illustrated and its dimensions are expressed in terms of the overall hull length, LOA. These dimensions agree well with the minimum recommendations of ITTC.

The top, side, and bottom of the domain were prescribed with symmetry boundary conditions, and the hull was set to a wall with no slip. At the inlet, located in front of the hull, the velocity of the incident air and water was set to the hull speed that was simulated. The outlet located behind the hull was set to a pressure outlet. The inlet boundary conditions were used to initialize the flow field (Table 1).

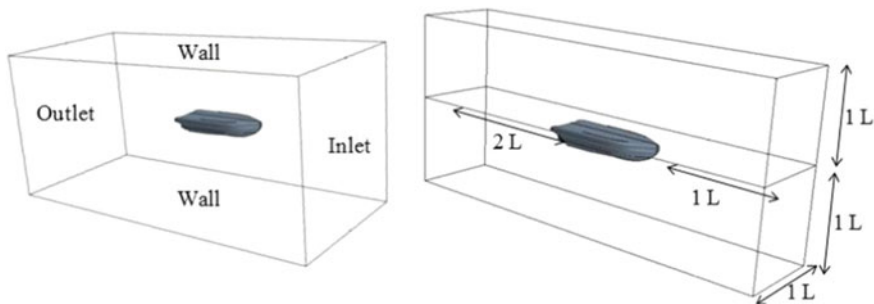


Fig. 3 Computational domain

**Table 1** Boundary conditions for 20 m medium craft in calm water simulation

Inlet	Velocity inlet
Outlet	Pressure outlet
Walls	Slip
Body	No slip

### 3.2 Solver Parameters

The flow equations are solved sequentially in segregated solver where the pressure and velocity change with time. This means an appropriate pressure–velocity coupling procedure is to be adopted. The procedure adopted in this study for coupling the pressure and velocity is semi-implicit method for pressure-linked equations (SIMPLE). The turbulence model used is realizable  $k-\epsilon$  which gives better results compared to standard  $k-\epsilon$  because of the new equation used for dissipation rate. VOF is a free-surface modelling technique for tracking and locating free surface. This means an appropriate pressure–velocity coupling procedure is to be adopted. The procedure adopted in this study for coupling the pressure and velocity is SIMPLE (Semi-Implicit Method for Pressure-Linked Equations). A summary of the solver settings is given in Table 2 and the principal particulars of the vessel is shown in Table 3.

## 4 Results

High-speed planing craft of 20 m length with a design speed of 25 knots is considered for the study. To validate the current solution, the resistance of the craft in calm water is obtained and compared against experiments for the bare hull. The obtained CFD results of resistance and trim are shown in Fig. 4.

The present numerical model is used to analyze:

1. The effect of trim and drag on the hull in calm water for bare hull and interceptor.
2. The longitudinal distribution of pressure on the hull for bare hull and interceptor.

**Table 2** Solver parameters used for 20 m craft in calm water simulation

Parameter	Setting
Solver	3S segregated, unsteady, implicit
Viscous model	Realizable $k-\epsilon$
Pressure–velocity coupling	SIMPLE
Free-surface scheme	VOF
Discretization of convective acceleration for transport equations	Second-order upwind scheme



3. The effect of the stern wave for the craft with and without interceptor.

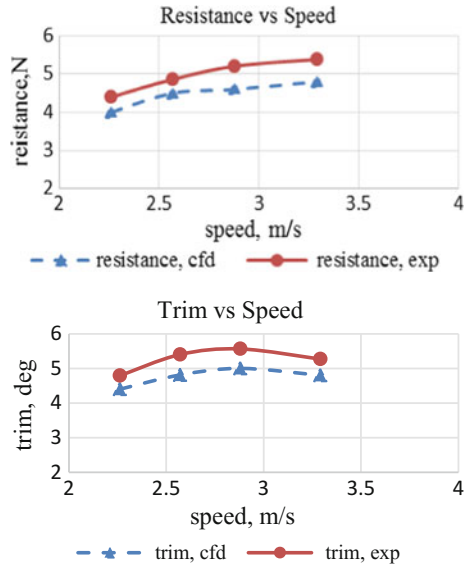
### 4.1 Effect of Trim and Drag

Figure 5 shows the resistance and trim for the bare hull and interceptor of the model. To study the effect of trim angle, the planing hull with deadrise angle 20° is evaluated and compared with bare hull. The increase in speed will result in an overall decrease in drag and trim compared with bare hull and hull with an interceptor. For the 1-mm-height interceptor, the resistance is increasing as speed is increasing and

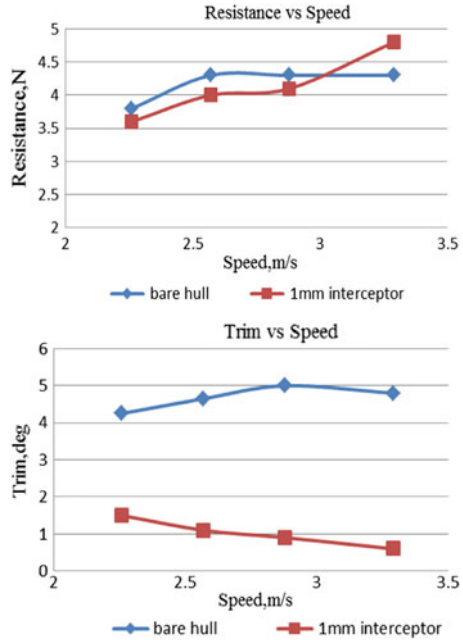
**Table 3** Principal particulars of the high-speed planing hull taken for study

Particulars	Prototype	Model
Length, $L$ (m)	20.5	0.873
Breadth, $B$ (m)	5.3	0.212
Draft, $T$ (m)	1.062	0.046
Depth, $D$ (m)	1.03	0.412
Displacement, $\Delta$ (kg)	46,000	2.94
Block coefficient, $C_b$	0.41	
Design speed, $V$	25 knots	2.57 m/s
Scale	1:25.011	

**Fig. 4** Comparison of total resistance and trim for the bare hull model



**Fig. 5** Total resistance and trim of craft without and with interceptor of 1 mm height



trim is decreasing with increase in speed. When compared with bare hull, there is a reduction of 5–7% in resistance. There is better performance with interceptor at a design speed of 2.57 m/s.

#### 4.2 Pressure Distribution on the Hull with and Without Interceptor

The longitudinal pressure distribution at the design speed is given in Figs. 6 and 7 for CFD simulations. To study the longitudinal pressure distribution, hull without interceptor and with interceptor is taken. The result for interceptors of 1 mm height is compared with the bare hull. As shown in Fig. 6, the pressure distribution on the bottom of bare hull is less at the stern when compared to the hull with an interceptor. Due to this high pressure at the stern, the hull experiences a lift force at the transom and rises up which gives trim on the vessel with less drag. Figure 7 describes well that there is no pressure at the transom of bare hull, whereas the pressure is acting at the transom where the interceptor is fitted.

**Fig. 6** Pressure distribution at the bottom of hull without and with an interceptor at design speed (model)

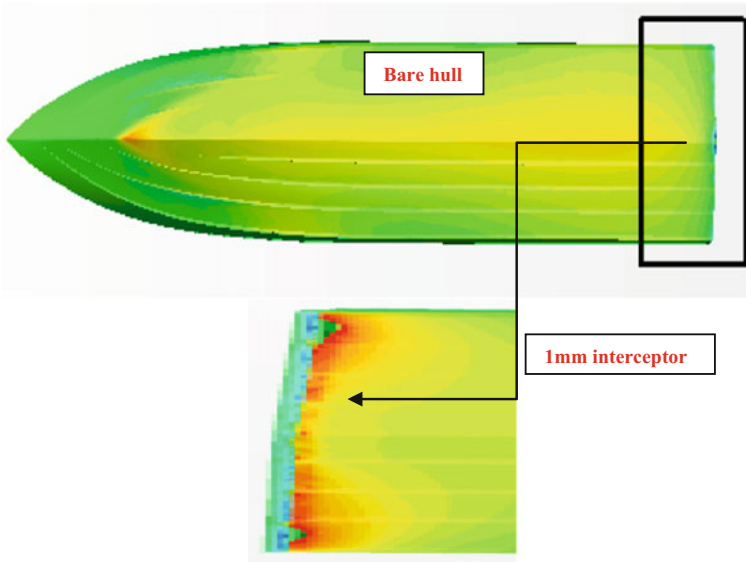
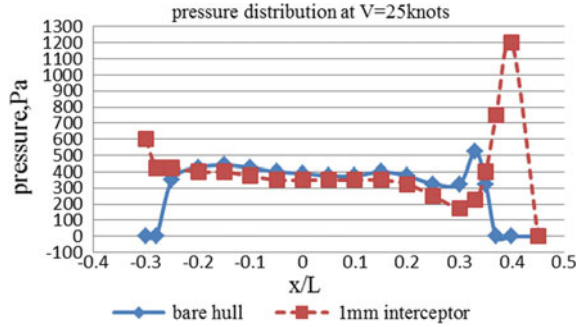


**Fig. 7** Pressure distribution along the wetted surface of the model boat and at the stern interceptor of 1 mm height

### 4.3 Effect of Stern Wave

The free-surface wave pattern is shown in Fig. 8 which shows the wake at the stern is actually modified when compared with the bare hull. The energy transfer from hull to the water is more in the bare hull which increases the resistance of the craft. The effect of rooster tail is experienced in the stern region of planing hull and is not seen in the forward region. As a result, the effect of rooster tail is studied for 1-mm-height interceptor.

The results of stern wave height are presented in Fig. 9 in terms of height of stern wave over speed. The localized flow around the transom is greatly modified by the stern interceptor. Thus, the interceptor reduces the height of this peak traditionally

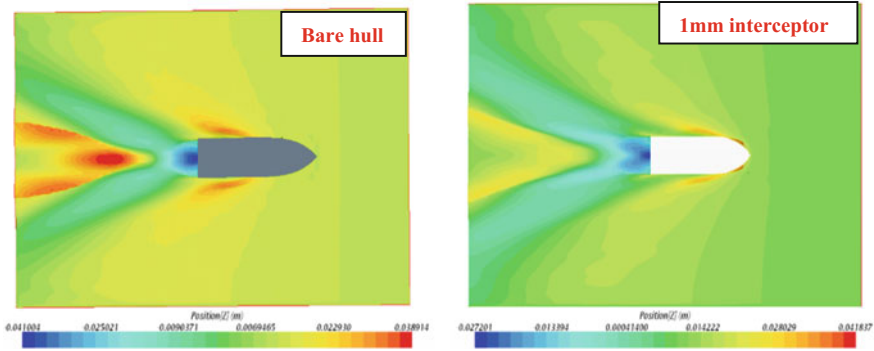
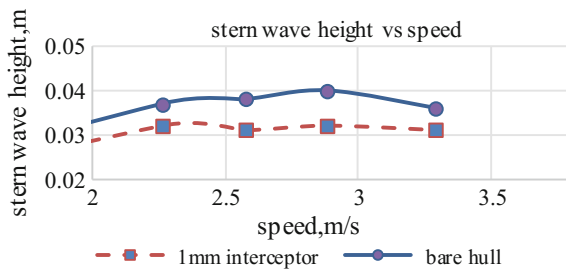


**Fig. 8** Free-surface wave pattern for the bare hull and with interceptor at design speed

**Fig. 9** Stern wave effect for bare hull and 1-mm-height interceptor



known as rooster tail. It has been observed that the best performance is reached by the interceptor of 1 mm height in comparison with bare hull.

### 5 Comparison of Resistance Between CFD and Standard Formulation

The numerical results of resistance described in the previous Sect. 4.1 are used as a reference to compare the standard Eqs. (2) and (3) proposed by Savitsky for bare hull. Srikanth and Datla [8] gave formulas to calculate drag produced by interceptor which says that the drag produced by interceptor is not very significant. Rest of the equations are used same as Savitsky [7]. So, Fig. 10 shows the comparison of CFD calculated resistance for the craft with interceptor of 1 mm height with Steen [9] and Srikanth and Datla [8] which follows the trend. Both Steen and Srikanth gave the formulations for added drag due to interceptor from the experimental results.

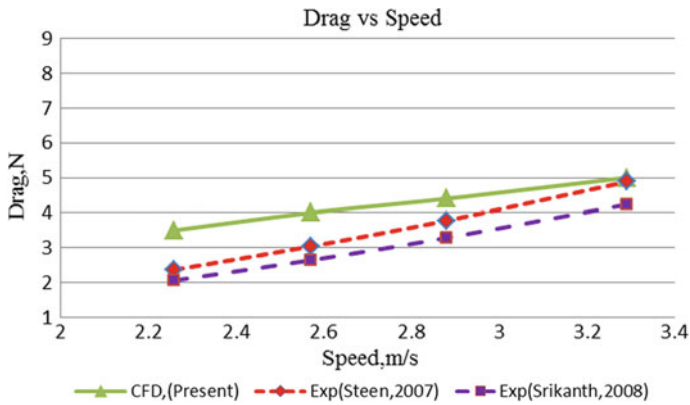


**Fig. 10** Comparison between RANS prediction and those obtained by Srikanth and Datla [8] and Steen [9] with an interceptor

## 6 Conclusion

From this study, the following conclusions are envisaged:

- Stern interceptors represent viable mechanisms for reducing the powering of high-speed crafts.
- The stern interceptor causes the flow to slow down at the forward of the interceptor. This decreases flow velocity, increases pressure under the hull, and in turn causes reduction in resistance acting on ships aft body.
- The reduction in resistance is of 7% compared to bare hull.
- The trim of the craft is very less in case of the bare hull and so the resistance is increasing with speed as the wetted surface area is more.
- The stern wave height decreases with speed for the craft installed with interceptor when compared to the bare hull.
- Planing crafts experience large changes in trim due to interceptors, which can greatly affect the dynamic lift because of the pressure created at the transom due to the interceptor.

## References

1. Brizzolara S (2003) Hydrodynamic analysis of interceptors with CFD methods. In: 7th international conference on fast sea transportation
2. Deng R et al (2011) Preliminary numerical investigation of effect of interceptor on Ship resistance
3. John S, Kareem Khan MD, Praveen PC, Manu K, Panigrahi PK (2011) Hydrodynamic performance enhancement using stern wedges, stern flaps and interceptors. In: ICSOT

4. Karimi MH, Abbaspoor M (2015) A study on vertical motions of planing boats with automatically controlled stern interceptors in calm water and waves. *Ships and offshore struct* 10(3):335–348
5. Luca FD, Pensa C (2011) Experimental data on interceptor effectiveness. In: IX HSMV, Naples
6. Salas M, Tampier G (2013) Assessment of appendage effect on forward resistance reduction. *Ship Sci Technol* 7(13):37–45, July 2013, Cartagena (Colombia)
7. Savitsky D (1964) The hydrodynamic design of planing hulls. *Mar Technol* 1(1):71–95
8. Srikanth S, Datla R (2008) Performance prediction of high-speed planing craft with interceptors using a variation of the Savitsky method. In: The first Chesapeake power boat symposium
9. Steen (2007) Experimental investigation of interceptor performance. Norwegian University of Science and Technology, Trondheim
10. Tsai JF, Hwang JL, Chou SK (2004) Study on the compound effects of the interceptor with stern flap for two fast monohulls with transom stern. In: *Oceans'04, MTTS/IEEE Tecno-ocean'04*, vol 2, pp 1023–1028

# Numerical Modelling of Scour Around an Offshore Jacket Structure Using REEF3D



Nadeem Ahmad, Hans Bihs, Arun Kamath and Øivind A. Arntsen

**Abstract** In the present paper, a numerical investigation of the scouring around offshore jacket structure is carried out. The open-source CFD model REEF3D is used for the numerical modelling. The model solves the Reynolds-averaged Navier–Stokes equations with  $k-\omega$  turbulence closure to calculate the flow hydrodynamics. The simulated flow field is coupled with sediment transport module in the model to calculate the scouring process. The scouring calculations are based on the Exner formula. The free surface and sediment bed topography are captured with the level set method. Results discuss the numerical modelling of an in situ local scour around the jacket foundations at the C-power wind farm Thornton bank. The key finding from the paper is the local scour around the individual jacket foundations and the global scour which takes place in form of a saucer-shaped. Additionally, the hydrodynamics and the temporal evolution of the scouring process under the wave and current action are discussed. The implication of the study is to set up a CFD model for the hydrodynamics and the scour calculations around offshore jacket foundations.

**Keywords** Jacket foundations · Local scour · Global scour · Wave and current Free surface · CFD · REEF3D

## 1 Introduction

Increased renewable energy generation and the development of the larger offshore turbine generators are one of the prime tasks, the offshore industry has to deal with. In this context, the stability of jacket structure is an important concern and needs to be analysed thoroughly against the possible scour around the jacket structure foundations.

---

N. Ahmad (✉) · H. Bihs · A. Kamath · Ø. A. Arntsen  
Department of Civil and Environmental Engineering, Norwegian University of Science and Technology, 7491 Trondheim, Norway  
e-mail: [nadeem.ahmad@ntnu.no](mailto:nadeem.ahmad@ntnu.no)

© Springer Nature Singapore Pte Ltd. 2019  
K. Murali et al. (eds.), *Proceedings of the Fourth International Conference in Ocean Engineering (ICOE2018)*, Lecture Notes in Civil Engineering 22,  
[https://doi.org/10.1007/978-981-13-3119-0\\_40](https://doi.org/10.1007/978-981-13-3119-0_40)

There is a limited knowledge about the scouring process around the offshore platforms such as the jacket foundations, tripods and the other type of wind turbine foundations [15][?, ?]. This is due to the fact that the field measurement of the flow hydrodynamics and the temporal variation of the erosion process are challenging and time-consuming process. Thus, the estimation of the maximum scour around the jacket foundations is carried out by using the scour formula for the group of the vertical foundations [14], developed for vertical foundations and does not account for the effect of the scouring process around the horizontal and the tangential bracings assembled with the vertical foundations, i.e. the jacket structure. The calculation of the maximum scour depth around the jacket foundations using the formula might be ambiguous and consequently unexpected expenditure on the scour protection measures [9]. CFD modelling of the scouring process around the jacket foundations could be a suitable approach to analysing scour problems more accurately. A growing body of literature has investigated sediment transport under the local flow field. These studies discuss the 2D and 3D numerical modelling of local scouring process around the single horizontal foundation and vertical foundations [1, 2, 4, 13]. However, there is still a need for a discussion on the scour process around the jacket foundations, which comprises an assembly of the horizontal and the tangential bracings attached with the vertical foundations.

Hence, the primary objective of the present study is to investigate 3D scour around jacket foundations. The numerical model is implemented for the modelling of an in situ local scour case around the jacket foundations at the C-power wind farm Thornton bank, which is a sandbank. According to the available field data [7], the storm of the significant wave height  $H_s = 3.5\text{--}4.5$  m occurred during the period of December 2011–January 2012 and resulted in the scour around the jacket foundations. To study the same case, two case scenarios are run. The first case discusses the scour calculations for the waves of  $H = 4.5$  m; the Keulegan–Carpenter number  $KC = \pi H/D = 14$ . The second case shows the scouring process under the typical steady current flow, i.e. the  $KC = \infty$ . The simulated results discuss hydrodynamics, the maximum scour depth and the temporal variation of the scour process around jacket foundations.

## 2 Numerical Model

### 2.1 Hydrodynamic Model

The open-source CFD model REEF3D [5, 6, 12] is used for the numerical modelling of the wave hydrodynamics and the sediment transport. The model solves the incompressible Reynolds-averaged Navier–Stokes (RANS) equations, along with the continuity equation to calculate the velocity field in the numerical wave tank. The  $k\text{-}\omega$  model is used to calculate the eddy viscosity by solving for the turbulent



kinetic energy  $k$  and the specific turbulent dissipation  $\omega$ . Details of the equations and the method can be found in [6].

### 2.2 Morphological Model

Sediment transport is calculated based on the flow field simulated by the hydrodynamic module in REEF3D. The bed shear stress is determined considering a logarithmic velocity profile near the sediment bed. The bed shear stress  $\tau$  is defined as follows:

$$\tau = \rho u_*^2 \tag{1}$$

where  $u_*$  is the shear velocity and is defined as:

$$\frac{u}{u_*} = \frac{1}{\kappa} \ln\left(\frac{30z}{k_s}\right) \tag{2}$$

here  $u$  is the velocity at a height  $z$  above the bed,  $\kappa = 0.4$  is the von Karman constant,  $k_s = 3d_{50}$  is the equivalent sand roughness and  $d_{50}$  is the median grain size. The bed-load calculations are made with the formulation proposed by [16]. It is based on the sediment particle mobility which suggests that when the bed shear stress just exceeds the critical bed shear stress, the motion of the particles is initiated. The formulation for the bed-load transport rate  $q_b$  [16] is defined as follows:

$$\frac{q_b}{d_{50}^{1.5} \sqrt{(s-1)g}} = 0.053 \frac{T^{2.1}}{D_*^{0.3}} \tag{3}$$

Here,  $T$  is the transport stage parameter and  $D_*$  is the particle parameter. The critical bed shear stress calculated with the Shields diagram leads to underestimation of the sediment transport because it does not account for the effects of a sloping bed. This problem is handled with the modified critical shear stress formulation on sloping beds proposed by [8]. The effect of the sloping bed is accounted for by considering the longitudinal bed slope  $\theta$ , the transverse bed slope  $\alpha$ , the angle of repose of the sediment  $\varphi$  and the drag and lift forces, yielding to the expression for the critical bed shear stress reduction factor  $r$ . Thus, the modified critical bed shear stress  $\tau_{cr}$  is calculated by multiplying the Shields critical bed shear stresses  $\tau_0$  with the reduction factor  $r$  [8]. The change in bed elevation is calculated with Exner’s formula. The method is based on the conservation of sediment mass where the horizontal spatial variation in the bed load is conserved with the spatial change in the vertical bed elevation. The morphological evolution occurs as a nonlinear propagation of the bed-level deformation in the direction of the sediment transport. The transient change in bed level is defined as follows:

$$\frac{\partial z_b}{\partial t} + \frac{1}{(1-n)} \left[ \frac{\partial q_{b,x}}{\partial x} \right] + E - D = 0 \quad (4)$$

where  $z$  is the bed level,  $q_{b,x}$  is the bed load,  $n$  is the sediment porosity,  $D$  is the deposition rate and  $E$  is the entrainment rate from the suspended load. The sediment surface is modelled with the level set method approach which is an implicit representation of the sediment bed as the zero level set. The driving velocity  $F = \partial z_b / \partial t$  moves the interface in the vertical direction to represent the change in the sediment bed due to the scouring action.

### 3 Model Validation

The model has already been validated for the scouring under the steady and unsteady flow conditions. Results from these validation cases discussed the scour around the vertical piles, horizontal piles and the piles in a group. Details of the papers can be found in [1, 3].

### 4 Scour Around the Jacket Foundations

The model is implemented to simulate the scour around the jacket foundations at the C-power wind farm Thornton bank, which is a sandbank. The height of the jacket foundations on the site is between 40 and 50 m. The jacket foundations comprise of the four vertical foundations connected with horizontal and the diagonal bracings. The diameter of the vertical foundations is  $D = 2$  m, and the gap between the individual foundation is  $G/D = 10$ . The jacket foundations are located in water depths ranging from 12 to 30 m. According to the hydrodynamic measurements available from the Flemish banks monitoring network [7], only two storms of the significant wave height  $H_s = 3.5\text{--}4.5$  m occurred during the period of December 2011–January 2012 and resulted in the major scour.

The numerical modelling is carried out by the scaling the in situ incident waves and sediment characteristics. The selected scaling factor satisfies two scaling criteria. First is the Froude criterion for hydrodynamics that arises when the ratio of the inertia force to gravity force is held constant between prototype and model. The second criterion maintains the speed parameter of the sediment particles between prototype and model. Thus, the calculated scaling factor for the sediment bed material is 2.7 and the incident wave characteristics are scaled down by a factor of 7.5. The details of the scaling method and calculations can be found in the article by [10]. After the scaling, the height of the jacket foundations is considered to be 6 m. The diameter of the vertical foundations is  $D = 0.26$  m, and the diameter of the diagonal bracings is 0.13 m. The gap between the vertical foundations is  $G/D = 10$  which replicate the actual gap ratio between the foundations on site. The still water level is  $d = 4$  m. The

fifth-order Stokes waves of wave height  $H = 0.6$  m; assuming the wave period of  $T = 4.5$  s are generated in the NWT. The bed material consists of non-cohesive sand with median particle diameter  $d_{50} = 0.13$  mm. The sediment density is  $\rho_s = 2700$  kg/m<sup>3</sup>, and the angle of repose of the sediment is  $\varphi = 35^\circ$ . The Shields parameter for the bed material is  $\theta_c = 0.047$ . The wave generation in the numerical wave tank is managed with the active wave absorption method (AWA). The method is considered to be a good choice to manage both the wave generation and the absorption in a relatively shorter numerical domain [11].

#### 4.1 Scour Under Waves

In this section, results of the scouring process around the jacket foundations for the observed waves are discussed. The foundations are exposed to the regular waves of wave height to water ratio  $H/d = 0.15$  and the  $KC = 14$ . The simulation is run for  $t = 60$  min. Figure 1a shows a 3D view of the simulated maximum scour depth with the free surface profile, and Fig. 1b shows a zoom-in view of the simulated scour around the jacket foundations. It can be seen that the maximum scour is taking place around the vertical foundations and the area under the longitudinal bottom bracings is equally affected. However, the foundations at the downstream side and the area under the lateral bracings show relatively less scour. Figure. 1c demonstrates the velocity profile at  $XY$ -plane to elaborate on the change in the velocity around the jacket foundations. The higher velocity around the vertical foundations and under the lateral bottom bracings indicates a flow contraction and the formation of the flow jet, respectively. In addition, despite being the shadow region, there is significant flow velocity under the longitudinal bottom bracings which indicate a converging flow into the shadow region for the  $KC = 14$ . Thus, the presence of relatively higher velocity due to the flow contraction around the vertical foundations, the formation of the flow jet under the lateral bracings and a converging flow regime under the longitudinal bracings results in the higher local scour, the wake erosion and the tunnel erosion, respectively, consequently a global scour around the jacket structure [15].

Figure 1d shows the temporal variation of the erosion and the deposition process. The spikes in the graphs represent the change in the maximum scour depth or deposition changing with the back-forth action of the waves. It is seen that temporal variation of the maximum scour and the deposition is almost the same, and it grows rapidly in the beginning and slows down as it approaching an equilibrium state after  $t = 60$  min. The magnitude of the maximum scour depth is  $S/D = 0.65$  that is almost double of the maximum deposition. The result agrees with the field observation [7] of the average scour depth measured after the storm, compared to the expected value of  $S/D = 1.3$  for high foundations calculated using the empirical formula [9, 14].

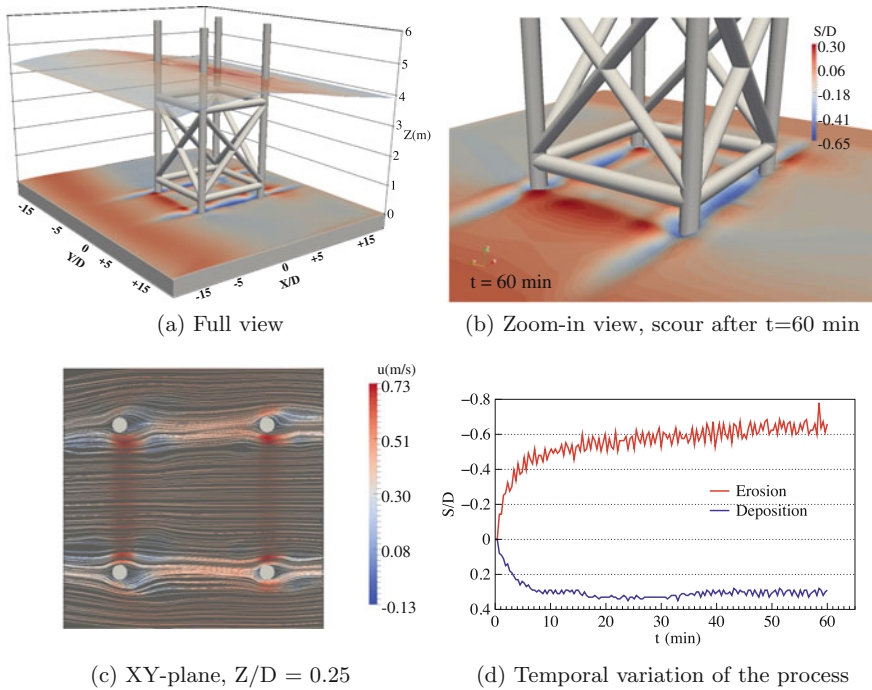


**Fig. 1** Scouring under the wave action around the jacket foundations

### 4.2 Scour Under the Steady Current

In this section, scour under the steady current is discussed. The incident flow velocity is  $u = 0.6$  m/s which represents a typical flow condition on the field [7].

The simulation is run for  $t = 60$  min, and the results of the hydrodynamics and the resulting scour around the jacket foundations are discussed. Figure 2a shows a 3D view of the simulated maximum scour depth with the free surface profile, and Fig. 2b shows a zoomed view of the simulated scour around the jacket foundation. It can be seen that the maximum scour is taking place around the vertical foundations connected with the lateral bottom bracings at the upstream side of the structure. The foundations at the downstream side of the structure show relatively less scour. However, the area under the longitudinal bottom bracings seems safe against the erosion. Figure 2c shows the velocity profiles at XY-plane. Results show a higher velocity around the vertical foundations, relatively low velocity under the bottom lateral bracing and the lowest velocity under the longitudinal bottom bracings. Consequently, the higher local scour around the vertical foundations, relatively strong tunnel erosion and almost no wake erosion. In addition, It can be seen that the sediments eroded from the upstream side foundations and are depositing in low-velocity regime inside the jacket. Figure 2d reveals that both the scour depth and the deposition grow rapidly

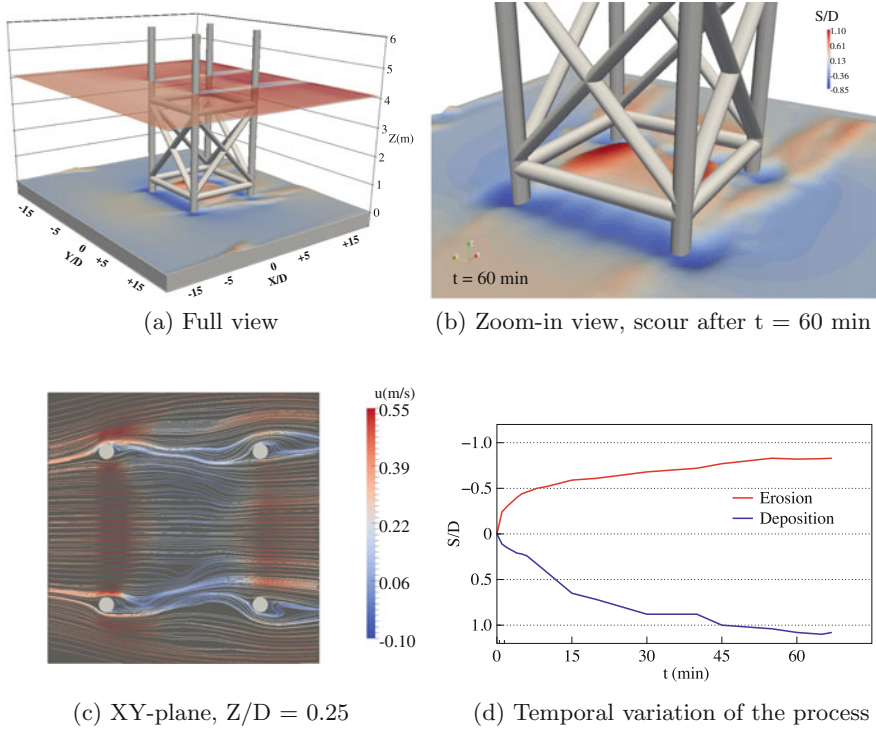


Fig. 2 Scouring under the current flow around the jacket foundations

and attain equilibrium state with an almost equal magnitude of the maximum erosion and the deposition. The magnitude of the maximum deposition is  $S/D = 0.85$ . The result supports the field observation that under the typical conditions of the steady current, the averaged scour depth ranges between  $S/D = 0.7-0.95$ .

### 5 Conclusion

The main objective of the study was to implement a CFD model to predict the scour around the offshore jacket structures in the deep water. The open-source CFD model REEF3D is successfully implemented and the results of the maximum scour under the waves and current action predicted satisfactorily with a good agreement with the field measurements. The following conclusions can be drawn from the study:

- Model provides sharp capturing of 3D scour featured with the free surface profile for the large domain, the problem encountered around the deepwater offshore jacket structure.

- The study revealed the scour pattern under the waves ( $KC = 14$ ) and the steady current ( $KC = \infty$ ).
- In case of the wave flow, the maximum scour takes place under the longitudinal bottom bracings attached with the vertical foundations, which indicates significant wake scour compared to tunnel scour.
- In case of the steady current flow, the maximum scour takes place under the lateral bottom bracings attached with vertical foundations, which indicates significant tunnel erosion compared to wake erosion.
- The current approach will help to solve the hydrodynamics and the associated scour problems, combining the reliable design of protection measures.

**Acknowledgements** This study has been carried out under the POL- NOR/200336/95/2014, and the authors are grateful to the grants provided by the Research Council of Norway. This study was supported in part with computational resources at the Norwegian University of Science and Technology (NTNU) provided by NOTUR, <http://www.notur.no>.

## References

1. Ahmad N, Bihs H, Chella MA, Arntsen ØA, Aggarwal A (2017) Numerical modelling of arctic coastal erosion due to breaking waves impact using REEF3D. In: The 27th international ocean and polar engineering conference. International Society of Offshore and Polar Engineers
2. Afzal MS, Bihs H, Kamath A, Arntsen ØA (2015) Three-dimensional numerical modeling of pier scour under current and waves using level-set method. *J Offshore Mech Arctic Eng* 137(3):032,001
3. Ahmad N, Bihs H, Alagan Chella M, Arntsen ØA (2017) A numerical investigation of erosion around offshore pipelines. In: MekIT' 17—9th national conference on computational mechanics, Norway
4. Ahmad N, Bihs H, Kamath A, Arntsen ØA (2016) 3D numerical modelling of pile scour with free surface profile under wave and current using level set method in model REEF3D. In: 8th international conference on local scour and erosion, ICSE 2016, Oxford, UK
5. Bihs H, Kamath A (2017) A combined level set/ghost cell immersed boundary representation for floating body simulations. *Int J Numer Methods Fluids* 83(12):905–916
6. Bihs H, Kamath A, Alagan Chella M, Aggarwal A, Arntsen ØA (2016) A new level set numerical wave tank with improved density interpolation for complex wave hydrodynamics. *Comput Fluids* 140:191–208
7. Bolle A, Winter JD, Goossens W, Haerens P, Dewaele G (2012) Scour monitoring around offshore jackets and gravity based foundations. In: 6th international conference on scour and erosion
8. Dey S (2003) Threshold of sediment motion on combined transverse and longitudinal sloping beds. *J Hydraul Res* 41(4):405–415
9. DNV (2014) Design of offshore wind turbine structures. Offshore standard DNV-OS-J101. Det Norske Veritas AS
10. Hughes SA, Fowler JE (1990) Technical report CERC-90-8: midscale physical model validation for scour at coastal structures. Technical report, Coastal Engineering Research Center Vicksburg, MS
11. Jacobsen NG, Fuhrman DR, Fredsøe J (2012) A wave generation toolbox for the open-source CFD library: openfoam. *Int J Numer Methods Fluids* 70(9):1073–1088
12. Kamath A, Alagan Chella M, Bihs H, Arntsen ØA (2016) Breaking wave interaction with a vertical cylinder and the effect of breaker location. *Ocean Eng* 128:105–115

13. Olsen NRB (2010) A three-dimensional numerical model for simulation of sediment movements in water intakes with multiblock option, users manual
14. Sumer BM, Fredsøe J (1998) Wave scour around group of vertical piles. *J Waterw Port Coast Ocean Eng* 124(5):248–256
15. Sumer BM, Roulund A, Fredsøe J, Michelsen J (2002) Three-dimensional numerical modeling of flow and scour around a pile. In: *Proceedings of 1st international conference on scour of foundations*, pp 795–809 (2002)
16. van Rijn LC (1984) Sediment transport, part I: bed load transport. *J Hydraul Eng* 110(10):1431–1456

# Numerical Modelling of Bed Shear Stress in OpenFOAM



Nandakumar Visuvamithiran, V. Sriram and Jaya Kumar Seelam

**Abstract** In coastal zones, erosion is the major threat to the livelihood as it leads to the water inundation into the human premises. Sediment transport results in erosions causes morphological changes and also affects the coastal ecosystem. The sediment transport processes are primarily driven by bed shear stress induced by waves and currents. As bed shear stress plays a major role in the determining sediment transport rates, the accuracy of sediment transport models mainly rely on the basis of bed shear stress measurements. So, there is a need to measure the reliable bed shear stress to improve the effectiveness of sediment transport models. In coastal zones when the waves enter into the low water depth, it starts to feel the bottom and the effect of shear stress at the bottom will be high. In this paper, bed shear stress is estimated from the numerical simulations using OpenFOAM. In OpenFOAM, bed shear stress is calculated from viscous force on the bed by integrating the pressure and the skin frictional forces. Surface elevation and flow velocity were measured using the numerical gauges. This bed shear stress can be directly incorporated into the shields parameter. In this study, numerical simulations in OpenFOAM were carried out for the regular sinusoidal waves with a time step of 0.001 s for a total duration of 16 s. OpenFOAM uses the waves2Foam toolbox for wave generation in the numerical wave tank.

**Keywords** Bed shear stress · OpenFOAM · Waves2Foam · Friction factor  
Sediment transport

---

N. Visuvamithiran · V. Sriram (✉)  
Department of Ocean Engineering, Indian Institute of Technology Madras, Chennai, India  
e-mail: [vsriram@iitm.ac.in](mailto:vsriram@iitm.ac.in)

N. Visuvamithiran  
e-mail: [nandacivil92@gmail.com](mailto:nandacivil92@gmail.com)

J. K. Seelam  
CSIR-National Institute of Oceanography, Goa, India  
e-mail: [jay@nio.org](mailto:jay@nio.org)

© Springer Nature Singapore Pte Ltd. 2019  
K. Murali et al. (eds.), *Proceedings of the Fourth International Conference in Ocean Engineering (ICOE2018)*, Lecture Notes in Civil Engineering 22,  
[https://doi.org/10.1007/978-981-13-3119-0\\_41](https://doi.org/10.1007/978-981-13-3119-0_41)



## 1 Introduction

Fluvial processes due to water waves are important reason for the morphological changes in the coastal environments. Sediment instability in the sea floor occurs when the sea bed's shear resistance is exceeded by bed shear stresses, and dynamic pressure results in the propagation of waves. Prediction of erosion and sediment transport rate is important in the conservation and development of coastal ecosystem. When a wave enters the shallow water regions, it starts to feel the bottom and the effect of bed shear stress on the sea bed will be greater. Bottom shear stress induced by the water waves is important in the coastal sediment transport modelling. So, the accuracy of sediment transport modelling can be improved by the calculating reliable bed shear stress value. Bed shear stress also has the impacts on coastal structures, as well as during cyclonic events, storm surge and in wave-structure modelling. In boundary layer, bed shear stress is usually measured from the following four methods viz., log law fit, momentum integral method, Reynolds stress and shear plate method. The measurements of the bottom shear stress under regular waves may be classified as direct and indirect methods [1]. The indirect method includes the pressure difference method, hot film sensors [2] and velocity measurements method [3]. But there are some difficulties in indirect method like the direction of shear stress is not measured by hot film, and it is difficult to measure the boundary layer velocity accurately in the turbulent conditions in experiments. These uncertainties in the bed shear stress measurements affect the accuracy of the sediment transport modelling. Ippen and Mitchell [4] measured the bed shear stress by using shear plate method and relate it with the damping of wave height. Jonsson [5] found the empirical friction factor from the relationship between the bed shear stress and the near bottom velocity for an oscillatory flow. Kamphuis [6] measured the bed shear stress directly by using the shear plate method. Rankin and Hires [7] related the bed shear stress with friction factor by measuring the energy dissipation in the ripple geometry. Sleath [8] analysed the boundary layer by the velocity measurements with a laser Doppler anemometer. Recently, Barnes et al. [9], Pujara and Liu [10], Lin et al. [11] directly measured the bed shear stress from force–displacement relationship of the shear plate. Barnes and Baldock [12] developed the new Lagrangian boundary layer model for analysing the friction coefficient in the boundary layer for the swash zone. Although many experimental and theoretical studies are carried out for direct measurement of bed shear stress, there is a need of feasible numerical modelling for direct bed shear stress measurement. In this study, numerical modelling of bed shear stress is simulated using open-source CFD solver OpenFOAM.

Computational fluid dynamics is the tool for solving the real world fluid flow problems by a set of algebraic equations using the digital computers. Open Field Operation and Manipulation, known as OpenFOAM, is an open-source CFD solver with the package of C++ libraries and codes that are created to simulate the numerical modelling of continuum mechanics problems. OpenFOAM consists of large number of solvers, libraries and utilities to solve a wide range of problems. It is also possible for users to create their own codes and solvers for their specific problems or to

modify the existing solvers [13]. Waves2Foam is a toolbox recently developed by OpenFOAM users to simulate free surface wave generation and absorption [14]. It uses the relaxation method to generate and adsorb the waves. OpenFOAM uses Navier–Stokes equation which were given below

$$\rho \left( \frac{\partial u}{\partial t} + u \frac{\partial u}{\partial x} + v \frac{\partial u}{\partial y} + w \frac{\partial u}{\partial z} \right) = -\frac{\partial p}{\partial x} + \rho g_x + \mu \left( \frac{\partial^2 u}{\partial x^2} + \frac{\partial^2 u}{\partial y^2} + \frac{\partial^2 u}{\partial z^2} \right) \quad (1)$$

$$\rho \left( \frac{\partial v}{\partial t} + u \frac{\partial v}{\partial x} + v \frac{\partial v}{\partial y} + w \frac{\partial v}{\partial z} \right) = -\frac{\partial p}{\partial y} + \rho g_y + \mu \left( \frac{\partial^2 v}{\partial x^2} + \frac{\partial^2 v}{\partial y^2} + \frac{\partial^2 v}{\partial z^2} \right) \quad (2)$$

$$\rho \left( \frac{\partial w}{\partial t} + u \frac{\partial w}{\partial x} + v \frac{\partial w}{\partial y} + w \frac{\partial w}{\partial z} \right) = -\frac{\partial p}{\partial z} + \rho g_z + \mu \left( \frac{\partial^2 w}{\partial x^2} + \frac{\partial^2 w}{\partial y^2} + \frac{\partial^2 w}{\partial z^2} \right) \quad (3)$$

The objective of this paper is to simulate the periodic waves in an OpenFOAM numerical wave tank and to investigate the characteristics of bed shear stress under laminar conditions and to analyse the relationship between wave friction factors with the Reynolds number.

## 2 Numerical Modelling of Bed Shear Stress

Numerical modelling of bed shear stress is done in OpenFOAM using waves2Foam solver. In this numerical model, numerical wave tank shown in Fig. 1 and meshing created by using blockMesh utility in OpenFOAM. Geometry was divided into five hexagonal blocks with each block has eight vertices. Cell size in the  $y$  direction is 0.003 m, and in the wave propagation direction, it was 0.02 m. Bed shear stress measured in the plate created in the tank numerical tank using patches to measure the bed shear stress. Patches were created for 0.1 m length and 0.02 m width at 7.5 m from the paddle. Bed shear stress at the plate (patches) were measured by integrating the pressure and skin frictional force at the bed. Mesh near the patches where the bed shear stress measured, were made finer cells than the remaining cells to increase the accuracy of the results. OpenFOAM uses volume of fraction method (VOF) for tracking and locating free surface in the interface of air and water. VOF will calculate the fraction of each fluid (air and water) in each cell [15]. Physical properties used in this numerical study are presented in Table 1.

Using waves2Foam toolbox, periodic waves of time period 1.5, 1 s and wave height of 1.8–6.6 cm were simulated and the wave elevation, flow velocity and viscous force were measured at every time step of 0.001 s in the duration of 16 s. Schematic view of wave propagation was shown in Fig. 2. In this study, Stokes second-order wave theory used for regular wave generation. WaveGaugesNprobes utility is used to define the type and orientation of the numerical probes. SetWaveParameter and setWaveField utilities were used to compute the required wave parameters and to set the initial condition according to the defined theory. The meshing of numerical wave tank created from blockMesh utility was shown in Fig. 3. Horizontal ( $u$ ) and vertical ( $v$ )

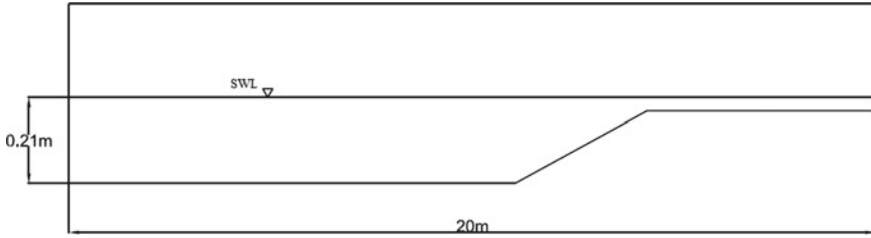


**Fig. 1** Schematic view of numerical wave tank

**Table 1** Physical properties

Property	Value
Acceleration gravity (g) (m/s <sup>2</sup> )	9.81
Density (kg/m <sup>3</sup> )	1000 (water) 1.2 (air)
Kinematic viscosity (m/s <sup>2</sup> )	10 <sup>-6</sup> (water) 1.48 × 10 <sup>-5</sup> (air)
Surface tension (N/m)	0.07

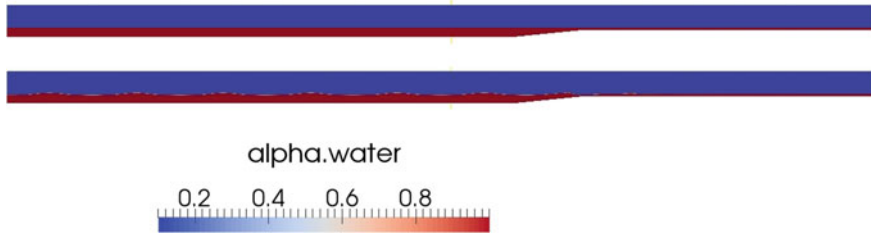


**Fig. 2** Wave propagation in OpenFOAM

components of particle velocity which are partial derivatives of the velocity potential  $\Phi$  in the model use the Stokes second-order wave theory given below

$$u = \frac{H}{2} \frac{gh}{\omega} \frac{\cosh k(h+y)}{\cosh kh} \cos(kx - \omega t) + \frac{3}{16} \frac{H^2 \omega k}{\sinh^4 kh} \frac{\cosh 2k(h+y)}{\sinh^4 kh} \cos 2(kx - \omega t) \tag{4}$$

$$v = \frac{H}{2} \frac{gh}{\omega} \frac{\sinh k(h+y)}{\cosh kh} \cos(kx - \omega t) + \frac{3}{16} \frac{H^2 \omega k}{\sinh^4 kh} \frac{\sinh 2k(h+y)}{\sinh^4 kh} \sin 2(kx - \omega t) \tag{5}$$

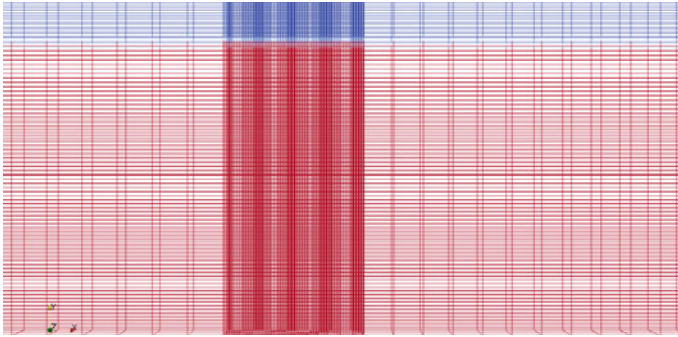


Fig. 3 Meshing of the numerical wave tank

### 3 Experimental Setup

Experiments were carried out in the wave flume in Gordon McKay hydraulics laboratory at the University of Queensland by Seelam and Baldock [16]. In the experiments of Seelam et al. [17], the shear cell developed by Barnes et al. [9] was used for direct bed shear stress measurement. The shear cell consists of the 1.21 mm thick plate with the length and breadth of 0.1 and 0.25 m. The shear cell was supported by four flexible legs. Displacement of the leg due to shear stress was measured by eddy current sensor. From the displacement, shear force can be calculated by force–stiffness relationship. Shear cell was placed at 7.8 m from the paddle. Pressure in the gap between shear cell edges was measured by the pressure sensors, flow velocity at the centre of shear cell was measured by ADV, and surface elevation at the cell edges was measured by the ultrasonic gauges. Schematic view of experimental setup was shown in Fig. 4.

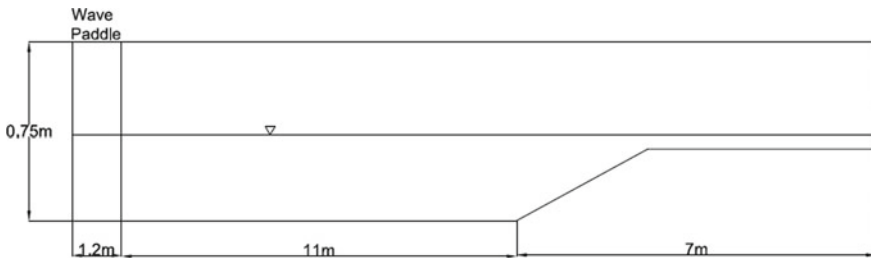


Fig. 4 Schematic view of experimental setup

### 4 Results and Discussion

The typical time series of experimental and numerical wave height was shown in Fig. 5, and the typical time series of bed shear stress for the water depth ( $d$ ) of 0.21 m, the wave height of 0.05 m and the wave period = 1.5 s was shown in Fig. 6. Surface elevation was measured at both upstream and downstream edges of the plate. Surface elevation measured using volume of fraction method which tracks and locates the air water fraction at free surface. Bed shear stress calculated from the dividing bed's viscous force with the area of the plate (patches). Bed shear stress value varies from 0.034 to 0.134 Pa. Velocity obtained from the numerical study was compared with experimental results. Velocities were measured at the 6 mm above the centre of the plate. Experimental and numerical velocity comparison time series were shown in Fig. 7, from that plot it knows that numerical results were very well match with the experimental results.

From the velocity and shear stress measurements, wave friction factor can be back calculated using the quadratic drag law given in Eq. 6. Numerical friction factor and Reynolds number results were compared with theoretical and experimental results [16]. Theoretical friction factor was calculated from Eq. 7. The relationship between the wave friction factor and Reynolds number shows in Fig. 8. It can be seen that numerical results were in good agreement with the theoretical and experimental results. Numerical results were slightly lower than the theoretical results because of smooth bed conditions. Friction factor decreased with increase in Reynolds number as the flow transition happens from laminar to transition flow. The friction factor decreases with increase in Reynolds number because skin frictional drag gets minimum in the boundary layer. In this study, friction factor varies from 0.03 to 0.14.

$$\tau_b = \frac{1}{2} \rho f_w u^2 \tag{6}$$

$$f_w = \frac{2}{\sqrt{Re}} \tag{7}$$

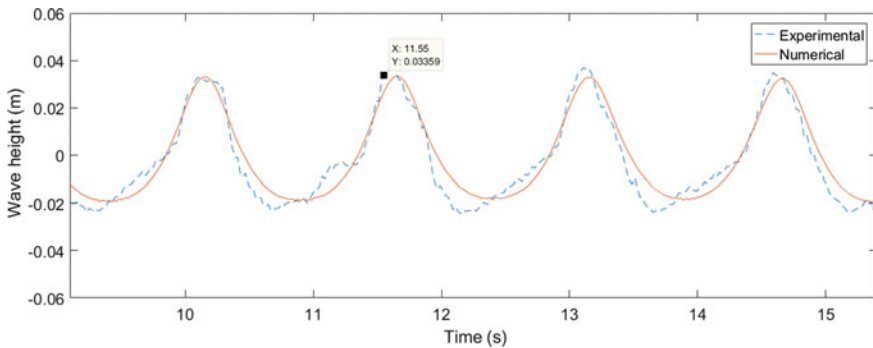
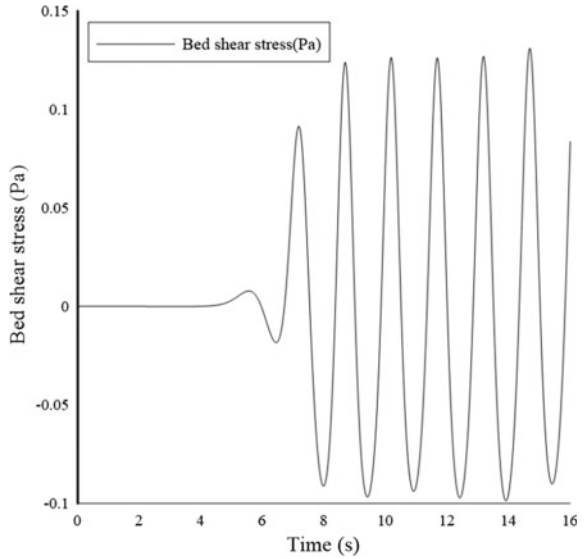
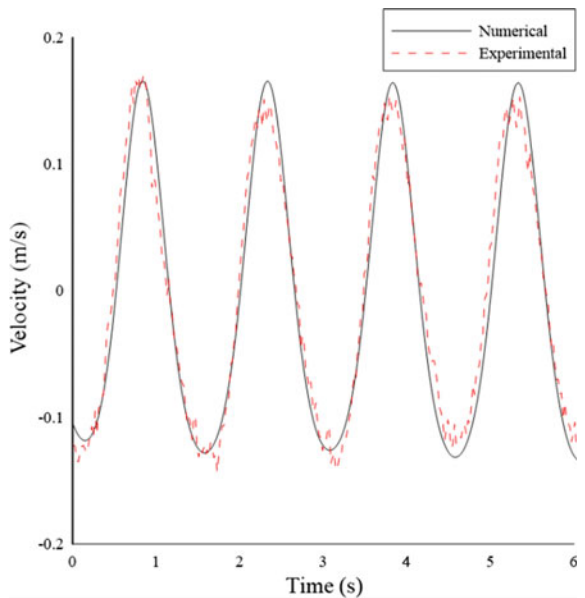


Fig. 5 Typical time series of wave elevation ( $T = 1.5$  s,  $H = 5$  cm,  $d = 0.21$  m)

**Fig. 6** Typical time series of bed shear stress ( $T = 1.5$  s,  $H = 5$  cm,  $d = 0.21$  m)



**Fig. 7** Typical time series of experimental and numerical velocity results at 6 mm above the bed ( $T = 1.5$  s,  $H = 5$  cm,  $d = 0.21$  m)



where  $\tau_b$  is bed shear stress,  $\rho$  is density,  $f_w$  is the wave friction factor,  $u$  is flow velocity, and  $R_e$  is Reynolds number. The relationship between the bed shear stress and the relative wave height was shown in Fig. 8. In this study, the relative wave height was in the range of 0.05–0.35. Figure 9 shows the bed shear stress increases linearly with increase in wave height.

**Fig. 8** Friction factor and reynolds number comparison

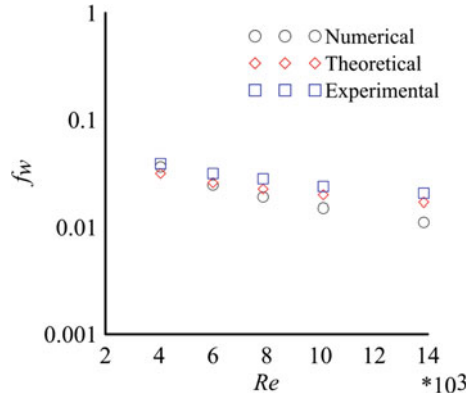
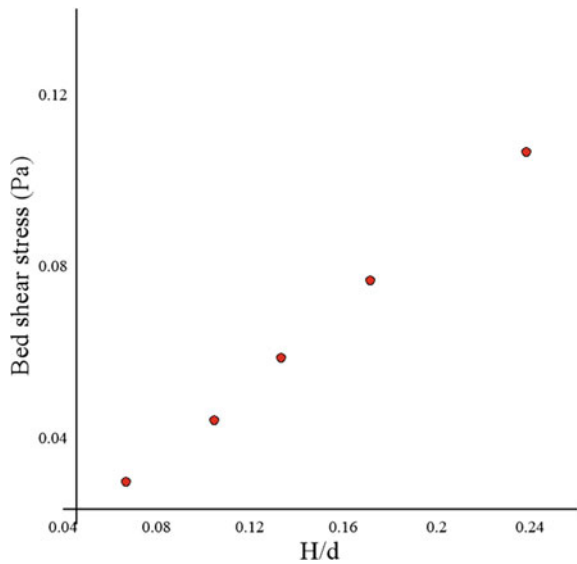


**Fig. 9** Bed shear stress versus relative wave height



### 5 Conclusions

In this paper, bed shear stress due to periodic waves was modelled in OpenFOAM using waves2Foam toolbox. Wave friction factors were found from the velocity and shear stress measurements using quadratic drag law. Numerical results from this study were compared with the theoretical and experimental results. Wave friction factors were decreasing with increase in Reynolds number because of flow transition from laminar flow to transitional flow. From the results obtained from this study, it is seen that OpenFOAM model results match very well with the theoretical and experimental results. Wave friction factor back calculated using the bed shear stress

and velocity measurements can also be related to the wave energy dissipation factor [7]. These numerical studies can also be extended to solitary waves.

## References

1. Haritonidis JH (1989) Advances in fluid mechanics measurements. In: The measurement of wall shear stress. Springer, pp 229–261
2. Sumer BM, Sen MB, Karagali I, Ceren J, Fredsoe J, Sottile M, Zilioli L, Fuhrman DL (2011) Flow and sediment transport induced by a plunging solitary wave. *J Geophys Res* 116(C01008):1–15
3. Cowen EA, Sou IM, Liu PL-F, Raubenheimer B (2003) Particle image velocimetry measurements within a laboratory-generated swash zone. *J Eng Mech* 129:1119–1129
4. Ippen AT, Mitchell MM (1957) The damping of the solitary wave from boundary shear measurements. Tech. Rep., Hydrodynamics Laboratory, Massachusetts Institute of Technology
5. Jonsson IG (1966) Wave boundary layers and friction factors. In: Tenth international conference on coastal engineering, Tokyo, Japan
6. Kamphuis JW (1975) Friction factor under oscillatory flows. *J Waterw Harbors Coast Eng Div, ASCE* WW2, 135–145
7. Rankin KL, Hires RI (2000) Laboratory measurement of bottom shear stress on a movable bed. *J Geophys Res* 105(C7):17011–17019
8. Sleath JFA (1987) Turbulent oscillatory flow over rough beds. *J Fluid Mech* 182:369–409
9. Barnes MP, O'Donoghue T, Alsina JM, Baldock TE (2009) Direct bed shear stress measurements in bore-driven swash. *Coast Eng* 56:853–867
10. Pujara N, Liu PLF (2014) Direct measurements of local bed shear stress in the presence of pressure gradients. *Exp Fluids* 55:1767
11. Lin JH, Chen GY, Chen YY (2012) Laboratory measurement of seabed shear stress and the slip factor over a porous seabed. *J Eng Mech* 139(10):1372–1386
12. Barnes MP, Baldock TE (2010) A Lagrangian model for boundary layer growth and bed shear stress in the swash zone. *Coast Eng* 57:385–396
13. Chen G, Xiong Q, Morris PJ, Paterson EG, Sergeev A, Wang Y (2014) *Notices AMS* 61:354–363
14. Jacobsen NG (2012) Waves2Foam toolbox bejibattjes validation case tutorial [Online]. Available: <http://openfoamwiki.net/index.php/Contrib/waves2Foam>
15. Chenari B, Saadatian SS, Ferreira Almerindo D (2015) Numerical modelling of regular waves propagation and breaking using Waves2Foam. *J Clean Energy Technol* 3(4):276–281
16. Seelam JK, Baldock TE (2010) Measurements and modeling of direct bed shear stress under solitary waves. In: Proceedings of ninth international conference on hydro-science and engineering, Chennai, India, ICHE 2010
17. Seelam JK, Guard PA, Baldock TE (2011) Measurements and modelling of bed shear stresses under solitary waves. *Coast Eng* 58(9):937–947



# Fully Coupled Aero-Hydrodynamic Simulation of Floating Offshore Wind Turbines with Overset Grid Technology



Ping Cheng and Decheng Wan

**Abstract** The fully coupled aero-hydrodynamic simulation of the OC4 Phase II semi-submersible floating offshore wind turbine (FOWT) is conducted. The three-dimensional (3D) Reynolds-Averaged Navier–Stokes (RANS) equations, enclosed with the  $k-\omega$  SST turbulence model are solved. The in-house code naoe-FOAM-SJTU solver, based on OpenFOAM and coupled with overset grid technology, is employed. The aerodynamic forces which decrease with the coupling effect of platform motions oscillate in wave period. With the aerodynamic forces applying on the platform through tower, the platform motions show significant variation on the equilibrium position of surge and pitch DOFs. Detailed flow information also clarifies the flow fields and indicates the coupling effects.

**Keywords** Fully coupled Aero-hydrodynamic simulation  
Floating offshore wind turbine (FOWT) · Overset grid technique  
Naoe-FOAM-SJTU solver

## 1 Introduction

Floating offshore wind turbines (FOWTs) are considered more economically viable compared to bottom-fixed ones when water depth is larger than approximately 50 m [1]. FOWTs have attracted more attention in recent years, especially in coastal countries with enormous ocean wind energy resource. Since the first multi-megawatt FOWT in the world installed at the west coast of Norway in June 2009 [2], more FOWTs have been designed and served for coastal cities [3]. However, designing FOWT system is still a quite challenging task due to the complicated structure, the complex environmental loading, and the coupling effects.

---

P. Cheng · D. Wan (✉)

State Key Laboratory of Ocean Engineering, School of Naval Architecture, Ocean and Civil Engineering, Collaborative Innovation Center for Advanced Ship and Deep-Sea Exploration, Shanghai Jiao Tong University, 200240 Shanghai, China  
e-mail: [dcwan@sjtu.edu.cn](mailto:dcwan@sjtu.edu.cn)

© Springer Nature Singapore Pte Ltd. 2019

K. Murali et al. (eds.), *Proceedings of the Fourth International Conference in Ocean Engineering (ICOE2018)*, Lecture Notes in Civil Engineering 22,  
[https://doi.org/10.1007/978-981-13-3119-0\\_42](https://doi.org/10.1007/978-981-13-3119-0_42)

647

Basic research methods consist of model test and numerical simulations. As an indispensable tool for research, model test plays an important role in study on FOWT. Model tests including intermediate-scale models monitored in offshore water areas [4] and scaled-down models tested in wave basin and wind tunnel [5] can provide more intuitionistic and practical data for further study. However, there underlies a problem that the Froude scaling law and the Reynolds similarity law cannot be guaranteed at the same time, which makes the model test data less valuable in FOWT designing. On the other hand, model test is quite expensive, especially the intermediate-scale models.

The numerical methods successfully cut down the research cost and avoid the scale effect by conducting simulations with full-scale models. Recently, fully coupled aero-hydrodynamic simulation solvers for FOWTs have been developed, which are mainly based on the traditional aerodynamic tools for fixed wind turbine and conventional hydrodynamic codes well developed in offshore ocean engineering. In early studies, most numerical tools for coupling simulation of FOWT are developed based on BEM method, such as HAWC2, 3Dfloat, etc. [6]. As is known, BEM is an empirical method with various correction models (such as Glauert correction, skewed wake correction, etc.), some researchers [7] suggested that the BEM is still questionable in unsteady aerodynamic prediction for FOWTs. Based on blade element momentum (BEM) method and potential-flow theory, the National Renewable Energy Laboratory (NREL) developed a fully coupled aero-hydro-servo-elastic tool named FAST [8]. However, depending on data-inputting from external potential-flow-based hydrodynamic solvers, such as WAMIT, restricts its usage for more accurate predictions with the viscous effect.

With rapidly developed compute technology and computing methods, more and more fully coupled studies have been conducted with CFD method. Based on OpenFOAM package, Liu [9] established a fully coupled CFD analysis tool for FOWTs and studied the coupling effect of the OC4-DeepCWind semi-submersible FOWT. Tran has also conducted the fully coupled aero-hydrodynamic analysis of this semi-submersible FOWT, while in his study a dynamic fluid body interaction approach is used [10] with Star CCM+ software combined with overset grid technique. Based on OpenFOAM, the open source CFD platform, our research team developed the CFD solver naoe-FOAM-SJTU to investigate hydrodynamic problems in the field of ship and ocean engineering. By introducing the unsteady actuator line model (UALM) [11] into OpenFOAM for aerodynamic simulation and combining with naoe-FOAM-SJTU solver, the fully coupled aero-hydrodynamic simulation model for FOWTs is established, which is named the FOWT-UALM-SJTU solver. The FOWT-UALM-SJTU solver achieves higher computational efficiency. On the other hand, the absence of accurate expression of the blades surface with refined mesh leads to lack of detailed flow information near blades, which plays critical role in deeply mechanism research. To improve the numerical accuracy, the full structured blades are directly simulated by employing overset grid technique to deal with the independent blades rotating motion and platform's 6DOFs motions problem, which is utilized in this present work.

## 2 Numerical Method

### 2.1 Governing Equations

In the numerical simulations in this paper, the incompressible Reynolds-Averaged Navier–Stokes (RANS) equations are solved, which contain the continuity equations and the momentum equations:

$$\frac{\partial U_i}{\partial x_i} = 0 \quad (1)$$

$$\frac{\partial U_i}{\partial t} + \frac{\partial}{\partial x_j}(U_i U_j) = -\frac{1}{\rho} \frac{\partial P}{\partial x_i} + \frac{\partial}{\partial x_j} \left( \nu \frac{\partial U_i}{\partial x_j} - \overline{u_i' u_j'} \right) \quad (2)$$

In these equations,  $U_i$  is the averaged flow velocity component, while  $u_i'$  is the fluctuation part;  $\rho$  is the density of the fluid;  $P$  is the pressure;  $\nu$  is the kinematic viscosity.

But the equations are not closed as they contain more variables than there are equations. In order to meet the closure requirement and solve the above equations, the two-equation turbulence model  $k$ – $\omega$  SST [12] is employed, and the turbulent kinetic energy  $k$  and the turbulent dissipation rate  $\omega$  can be described as:

$$\frac{\partial}{\partial t}(\rho k) + \frac{\partial}{\partial x_i}(\rho k u_i) = \frac{\partial}{\partial x_j} \left( \Gamma_k \frac{\partial k}{\partial x_j} \right) + G_k - Y_k + S_k \quad (3)$$

$$\frac{\partial}{\partial t}(\rho \omega) + \frac{\partial}{\partial x_i}(\rho \omega u_i) = \frac{\partial}{\partial x_j} \left( \Gamma_\omega \frac{\partial \omega}{\partial x_j} \right) + G_\omega - Y_\omega + D_\omega + S_\omega \quad (4)$$

where  $\Gamma_k$  and  $\Gamma_\omega$  are the effective diffusion coefficients for the turbulent kinetic energy  $k$  and the turbulent dissipation rate  $\omega$ , respectively,  $G_k$  and  $G_\omega$  are turbulence generation terms for  $k$  and  $\omega$ ,  $Y_k$  and  $Y_\omega$  are turbulent dissipation terms for  $k$  and  $\omega$ ,  $S_k$  and  $S_\omega$  are the source term for  $k$  and  $\omega$ ,  $D_\omega$  is the cross-diffusion term for  $\omega$ .

### 2.2 Naoe-FOAM-SJTU Solver

Based on the open source CFD platform, the in-house code naoe-FOAM-SJTU solver [13, 14] is designed for computing viscous flows of ships and ocean structures. It inherits the data structure and CFD libraries in OpenFOAM, such as FVM, RANS, VOF, and PISO algorithm. The two-phase incompressible RANS equations are solved in this solver. The governing equations are discretized with finite volume method (FVM) which is capable to handle arbitrary polyhedral cells. The interface between two phases is captured using a VOF method with bounded compression technique. The turbulence models of  $k$ – $\omega$  SST and  $k$ – $\varepsilon$  can be used for turbulence

closure. The pressure–velocity coupling equations are solved by pressure-implicit with splitting of operations (PISO) algorithm. Based on the above, a numerical tank system including wave generation and absorption module is built up, six degrees of freedom (6DOF) motion module is developed, and finally the mooring system module is added (Fig. 1).

The wave generation system is able to use boundary inlet to generate first-order regular waves and high order nonlinear waves, transient extreme waves, and freak wave. The sponge layer for wave absorption is adopted to avoid wave reflection. The mooring system module is built for hydrodynamic analysis of floating offshore structures which are moored in waters, such as semi-submersible, TLP, Spar, and FPSO. Several quasi-static models including spring, catenary, piecewise extrapolation method as well as a dynamic model lumped mass method, are utilized for simulation of mooring lines. To solve 6DOF equations, two coordinate systems are used, which are the earth-fixed coordinate system and the body-fixed coordinate system. And both dynamic deformation mesh method and overset grid technique are employed to deal with the 6DOF issues. With these modules, naoe-FOAM-SJTU solver can be applied to the simulation of ship advancing, seakeeping, superposition of complex motions, and hydrodynamics of floating platforms.

### 2.3 Overset Grid Technique

Using overset grid technique, the separated overlapping grids for each part with independent movement are allowed, which makes it powerful in simulating large amplitude motion problems. And the information transformation between each grid domain is built by interpolation at appropriate cells or points using DCI (domain connectivity information) which is produced by SUGGAR++ [15]. There are four main steps when using DCI in the overset grid technique: The first step is to pick out the hole cells which are located outside the simulation domain or of no interest

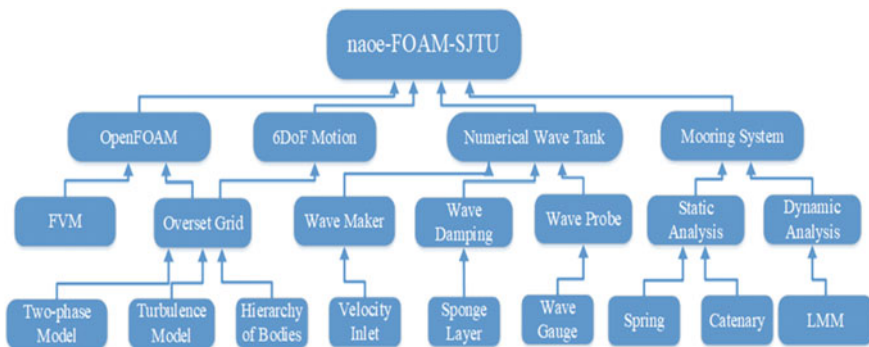


Fig. 1 Frame diagram of naoe-FOAM-SJTU solver

and exclude them from computation. As shown in Fig. 2, in overset grid, there exist series of fringe cells around hole cells, and for each fringe cell there are several donor cells which receive information from the donor cells, so the second step is to seek for the donor grids of each fringe cell and provide information from the donor grids. The third step is to obtain the value of a variable  $\phi$  of the fringe cell by interpolation from the donor cells with:

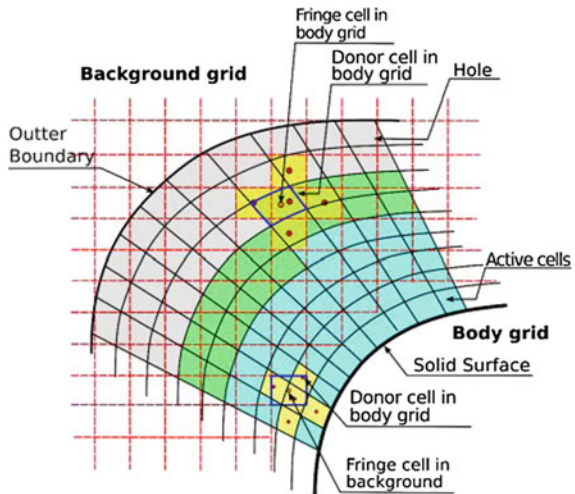
$$\phi_I = \sum_{i=1}^n \omega_i \cdot \phi_i \tag{5}$$

where  $\phi_I$  is the value of a variable  $\phi$  of the fringe cell,  $\phi_i$  is the value for the  $i$ th donor cell,  $\omega_i$  is the dimensionless weight coefficient and follows:

$$\sum_{i=1}^n \omega_i = 1 \tag{6}$$

And the last step is to optimize the overlapping area and improve the accuracy of interpolation.

**Fig. 2** Diagram of overset grid



### 3 The Semi-Submersible Floating Offshore Wind Turbine

#### 3.1 Physical Model

In the present simulation work, a semi-submersible FOWT system, Phase II of OC4 project, is adopted. The FOWT contains several main parts: the NREL 5-MW baseline wind turbine [16], a tower connecting wind turbine and platform, the semi-submersible platform [17], and the mooring system. Figure 3 shows the sketch of this FOWT system, and Table 1 lists the basic properties.

The wind turbine in Phase II of OC4 FOWT system is NREL 5-MW baseline line wind turbine, which is a conventional three-bladed, upwind, variable speed wind turbine. The floating support platform is a semi-submersible floating system which consists of a main column attached to the tower, three offset columns covering significant portion of buoyancy, a couple of smaller diameter pontoons and cross braces to link the main column and offset columns and to strengthen the structure. The semi-submersible floating system for Phase II of OC4 is moored with three catenary lines spread symmetrically about the platform Z-axis (Table 2).

**Fig. 3** Phase II of OC4 floating offshore wind turbine system

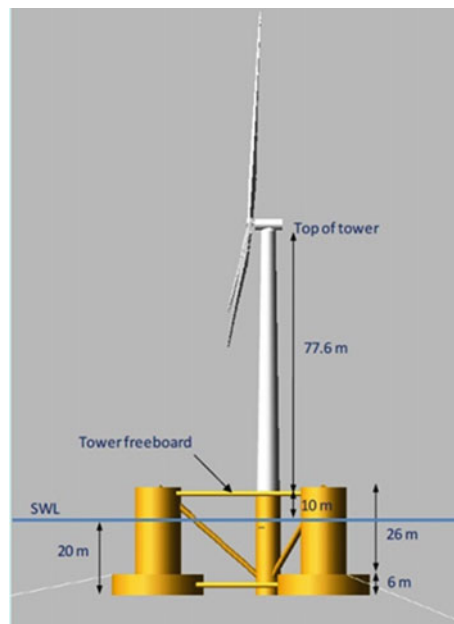


**Table 1** Specification of the phase II of OC4 FOWT system

Rotor orientation, configuration	Upwind, 3 blades
Rotor, hub diameter	126, 3 m
Hub height	90 m
Rotor mass	110,000 kg
Nacelle mass	240,000 kg
Tower mass	347,460 kg
Coordinate location of CM (rotor, nacelle, and tower)	(-0.2, 0.0, 64.0 m)
Total draft of platform	20 m
Platform mass	1.347E7 kg
Coordinate location of CM (platform)	(0.0, 0.0, -13.46 m)
Number of mooring lines	3
Angle between adjacent lines	120°
Depth to anchors/fairleads below SWL	200 m, 14 m
Radius to anchors/fairleads from platform centerline	837.6, 40.868 m
Unstretched mooring line length	835.5 m
Mooring line diameter	0.0766 m
Equivalent extensional stiffness	7.536 E+8 N
Equivalent mass density/in water	113.35, 108.63 kg/m

**Table 2** Structural properties of the FOWT system

Structural mass	1.407E7 kg
CM location below SWL	9.9376 m
Total structure roll inertia about CM	1.1E10 kg m <sup>2</sup>
Total structure pitch inertia about CM	1.1E10 kg m <sup>2</sup>
Total structure yaw inertia about CM	1.226E10 kg m <sup>2</sup>

### 3.2 Setup of Simulation Domain and Grid Structure

The optimum domain should be large enough to avoid boundary effects. Since the numerical simulations are conducted under the regular wave with wavelength of 156.13 m, the domain is set as cuboid with  $X$  (-200 to 400 m),  $Y$  (-150 to 150 m),  $Z$  (-100 to 240 m), as shown in Fig. 4. As the overset grid technique is utilized, three grid systems are generated, respectively. The green color in Fig. 4 represents for the background mesh covering the whole simulation domain, which is refined along the wave surface to reach grid density requirement for surface capture and also refined near the other two mesh system for better interpolation. The yellow cylinder sub-domain contains the wind turbine including turbine blades, nacelle, and hub. In

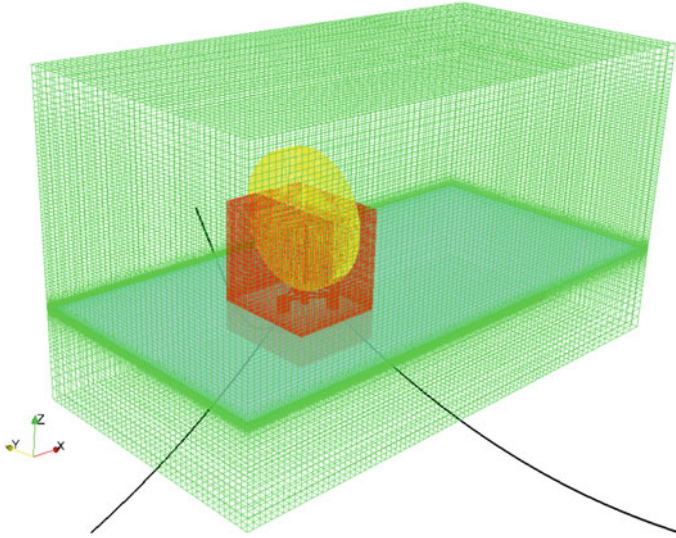


**Fig. 4** Simulation domain

this paper, all the solid structures are treated as rigid body, so the red part of grid is generated with the platform and tower.

## 4 Results and Discussions

In the present work, the fully coupled aero-hydrodynamics of a FOWT in coupling wave-wind conditions are investigated. Two simulations are conducted with same wave condition in which the wave height is 4 m and the wavelength is 156.13 m, while the inlet wind velocities are set as 8 and 11 m/s, respectively. At the beginning of simulation, the platform is fixed until  $t = 20$  s, while the wind turbine accelerates from rotating speed 0 rpm to the required speed gradually in 5 s. Comparisons are done on both hydrodynamics and aerodynamics to study the coupling effects between the aerodynamic forces and the hydrodynamic motions.

### 4.1 Hydrodynamic Responses

In regular heading waves, a moored platform with symmetrically distributed mooring lines oscillates with wave period in three main degrees of freedom (DOFs): surge, heave, and pitch, while the motions in other DOFs are negligible. Despite the hydrodynamic forces on platform, a floating offshore wind turbine is also subject to



aerodynamic loads mainly on turbine blades. As the turbine rotor is mounted on the top of tower and the tower is fixed on the floating platform, the aerodynamic loads also play essential roles in hydrodynamic responses.

Besides the periodic oscillations corresponding to the wave effect, additional surge motions are also observed in Fig. 5a. With the constraints of mooring system, the effect of aerodynamic loads acts as an additional increase of the equilibrium position. The equilibrium position is determined depending on the aerodynamic loads and the natural properties of the mooring system, where the total forces from the three mooring lines balances out the external loads from the aerodynamics of wind turbine. In Fig. 5a, the red curve shows the surge motion of the FOWT with incoming wind speed set as 8 m/s, and the green one represents for surge motion with wind velocity of  $U = 11$  m/s. With rotating speed of rotor increasing with wind speed, the aerodynamic thrust improves significantly just as Fig. 6 shows, thus larger mooring forces are required for the balance. However, the aerodynamic forces are too small compared to the instantaneous wave loads to have obvious influence on the periodic oscillation. Despite the variation on equilibrium position, the oscillating amplitude with wave period does not show much difference with increased inlet wind speed.

The rotating turbine rotor acts as an appendage part of the whole floating offshore wind turbine with both gravity center and rotating center located on the semi-submersible floating platform. So the additional pitching moment from aerodynamics of turbine blades is computed by integral of the moments on each blade surface cell to the rotating center. As the time history of pitch motion shown in Fig. 5c, this additional pitching moment plays a similar role in the pitching motion just as the additional thrust force does in surging motion DOF. Similar conclusions are drawn for the pitching motion.

But it's totally different for heaving component. The main loading effect on this DOF is the additional gravity from the tower and wind turbine, which never changes with working conditions. So the heave curves almost overlap each other despite tiny phase difference.

## 4.2 Aerodynamic Loads

With different incoming wind velocity from 8 to 11 m/s, the rotational speed of turbine rotor varies from 9.7 to 12.1 rpm, and the averaged aerodynamic thrust increases rapidly from 420 to 710 kN. The time history of aerodynamic thrust is plotted in Fig. 6. Both aerodynamic thrust curves show oscillating regularity with different wave period. Magnification during 260–300 s in right figure tells that the oscillating amplitude with wave period increases with incoming wind speed. This oscillation is resulted from the periodic motions of platform as mentioned above. When turbine blades move toward  $+x$  direction with positive velocity component  $U_x$ , the relative flow velocity near blades decrease below the incoming wind speed. On the other hand, when the blades move backward with negative velocity component  $U_x$ , the relative

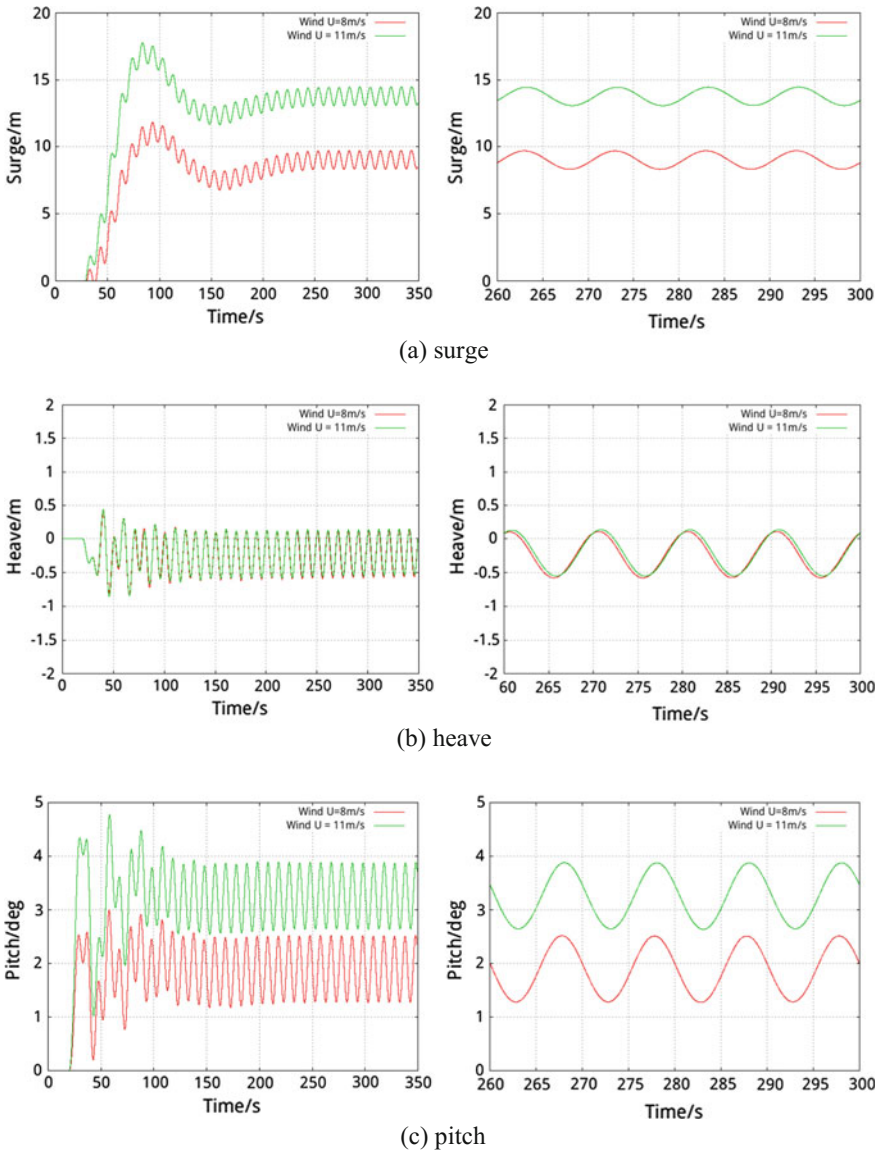
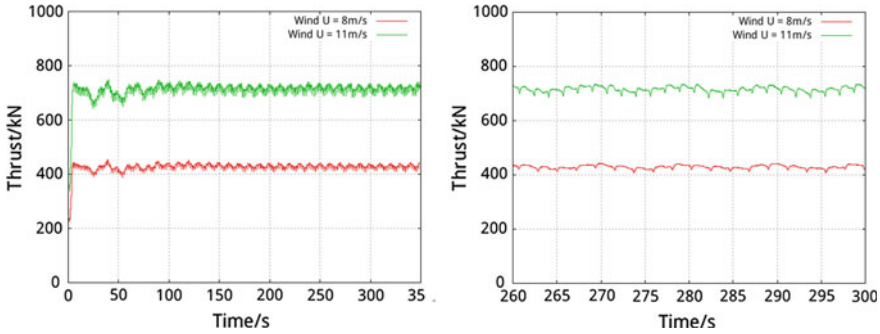


Fig. 5 Hydrodynamic responses of FOWT

flow velocity near blades increases over the inlet wind speed. From curves in the right figure, periodic variation with higher frequency is presented, which results from the tower effect and has a three times frequency of the rotating turbine.

As discussed above, the oscillating amplitudes with wave period differ little with increased inlet wind speed in both surge and pitch DOFs, but significant difference



**Fig. 6** Aerodynamic thrust on turbine blades

between the oscillating amplitude in two cases are observed in Fig. 6. With careful comparison and analysis, we believe that the key factor should be the pitching angle. To confirm this point of view, more analysis work needs to be done.

### 4.3 Wake Flow

The spiral wake vortex of turbine blades is generated with two key factors: firstly, incoming flow generates vortex while passing the blade surface. Secondly, the rotating blades disturb the initial uniform wind flow and induce rotating velocity component of the flow around turbine blades. Figures 7 and 8 show the visualization of wake vortex of turbine blades and pressure distribution on platform surface in two cases. The visualized wake vortex is colored by magnitude of velocity. The rotating velocity induced with the rotating blades is quite high near the blades surface, where thin but strong vortex tubes are generated. Interaction with neighbor flow field smooth the flow velocity distribution and leads to the expansion of vortex tube, while the  $U_x$  components make the wake vortex shedding downstream, and the finally the spiral vortex is generated. Because of the additional motion of turbine blades in sync with platform, the induced flow velocity also varies periodically. So the distance between two neighbor vortex cubes is not exactly the same.

The platform surface is colored with pressure distribution. Four figures in Fig. 7 or Fig. 8 represents for four moments during one wave period: the platform reached the minimum pitch position at  $t = 263$  s, then moves to the equilibrium position at  $t = 265.5$  s, then keeps moving until  $t = 268$  s to the maximum pitching position, then turns back again and moves to the equilibrium position at  $t = 270.5$  s, in the next quarter of cycle, the FOWT arrives at the minimum pitch position again, then round and round. The pressure distribution shows the immersed height of cylinders and the periodic pitching and heaving motions, also indicates the variations of hydrodynamic loads. Because of the pitching effect, the immersed area of downstream cylinder is

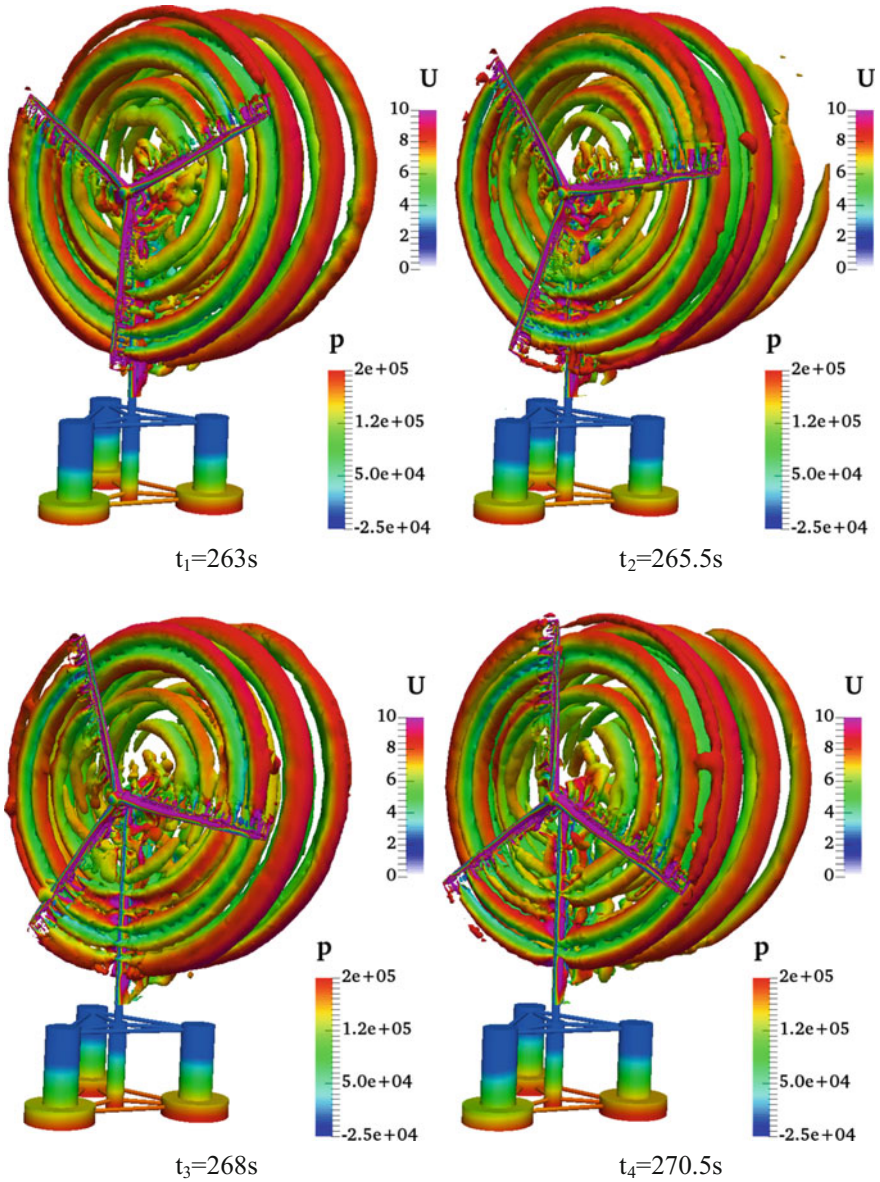


**Fig. 7** Visualization of wake vortex of turbine blades and pressure distribution on surface of platform with inlet wind speed  $U = 8$  m/s

much larger than that of the upstream one, and more significant difference is observed with higher inlet wind speed.

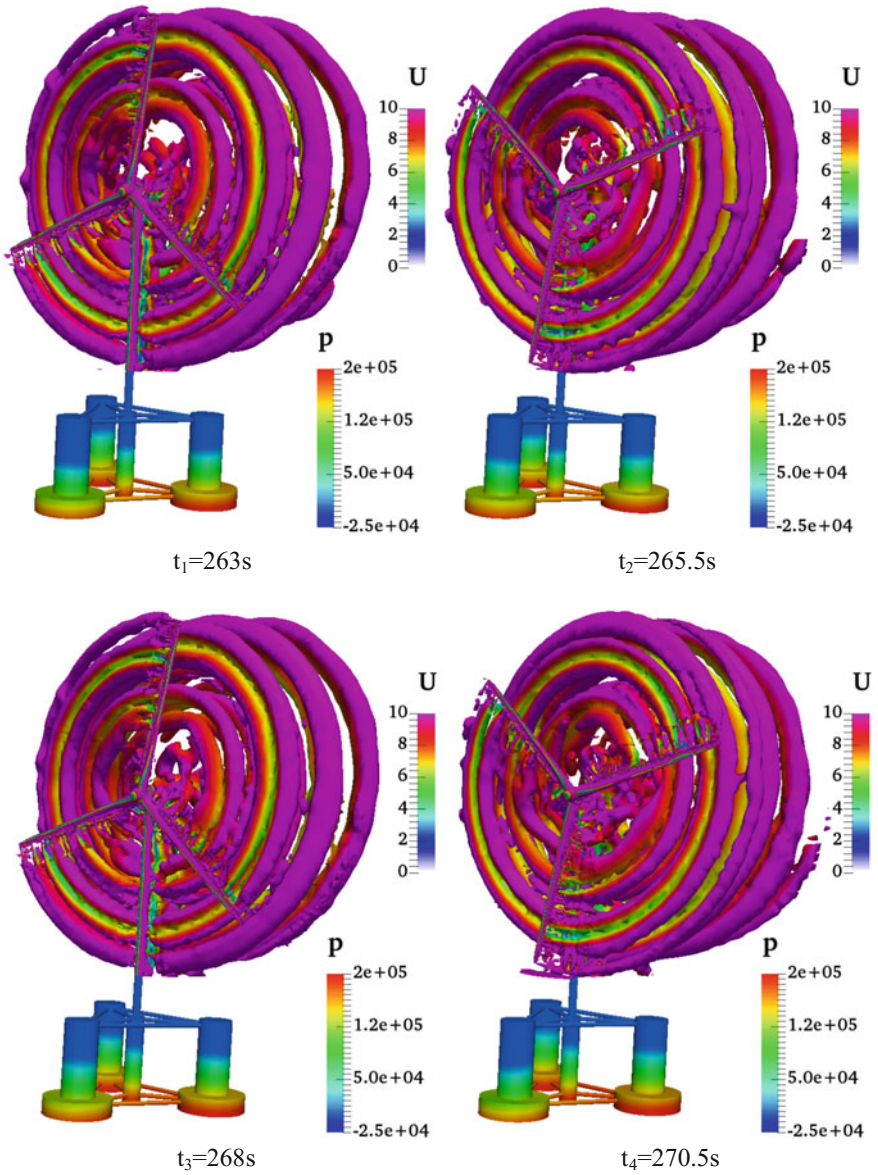


**Fig. 8** Visualization of wake vortex of turbine blades and pressure distribution on surface of platform with inlet wind speed  $U = 11$  m/s

## 5 Conclusions

The fully coupled aero-hydrodynamic simulation of the Phase II of OC4 FOWT system is conducted. The in-house code naoe-FOAM-SJTU solver, based on OpenFOAM and coupled with overset grid technology, is employed. The additional aerodynamic forces on turbine blades mainly effect the equilibrium position of the FOWT system in surge and pitch DOFs. When the aerodynamic forces on turbine blades increase with rotating speed as well as the inflow wind velocity, the new equilibrium position gets further from the initial one, in which case larger mooring forces are required for force balancing. But the oscillating amplitude with wave period does not show much difference with increased inlet wind speed, because the aerodynamic forces are too small compared to the instantaneous wave loads to have obvious influence on the periodic oscillation.

The periodic motion of blades in sync with platform causes the variations of the relative flow velocity near blades surface. So the aerodynamic thrust on turbine blades shows periodic oscillating regularity with wave period same as the platform motion period. Besides, the oscillating amplitudes increase with inlet wind speed is observed, and we believe that the key factor should be the equilibrium pitching angle. To confirm this point of view, more analysis work needs to be done.

Detailed flow information also clarifies the flow fields and indicates the coupling effects. Due to the axial exponent of flow velocity inherited from the inlet flow and the rotational component induced with rotating blades, series of spiral wake vortex are generated and shedding downstream. For the semi-submersible floating platform, because of the equilibrium pitching angle resulted from the additional aerodynamic forces, the immersed area of downstream cylinder is much larger than that of the upstream one.

**Acknowledgements** This work is supported by the National Natural Science Foundation of China (51879159, 51490675, 11432009, 51579145), Chang Jiang Scholars Program (T2014099), Shanghai Excellent Academic Leaders Program (17XD1402300), Program for Professor of Special Appointment (Eastern Scholar) at Shanghai Institutions of Higher Learning (2013022), Innovative Special Project of Numerical Tank of Ministry of Industry and Information Technology of China (2016-23/09) and Lloyd's Register Foundation for doctoral student, to which the authors are most grateful.

## References

1. Wang CM, Utsunomiya T, Wee SC, Choo YS (2010) Research on floating wind turbines: a literature survey. *IES J Part A: Civil Struct Eng* 3(4):267–277
2. Skaare B, Nielsen FG, Hanson TD (2015) Analysis of measurements and simulations from the Hywind Demo floating wind turbine. *Wind Energy* 18(6):1105–1122
3. BBC (2015) Floating wind farm to be installed off Peterhead. Available from: <http://www.bbc.co.uk/news/uk-scotland-scotland-business-34694463>
4. Viselli AM, Goupee AJ, Dagher HJ (2015) Model test of a 1:8-scale floating wind turbine offshore in the gulf of maine. *J Offshore Mech Arct Eng* 137(4):041901
5. Koo BJ, Goupee AJ, Kimball RW (2014) Model tests for a floating wind turbine on three different floaters. *J Offshore Mech Arct Eng* 136(2):020907
6. Cordle A (2010) State-of-the-art in design tools for floating offshore wind turbines. Deliverable report Under (SES6), UpWind project, Bristol, UK, Contract
7. Sebastian T, Lackner MA (2013) Characterization of the unsteady aerodynamics of offshore floating wind turbines. *Wind Energy* 16(3):339–352
8. Jonkman JM (2009) Dynamics of offshore floating wind turbines—model development and verification. *Wind Energy* 12(5):459–492
9. Liu Y, Xiao Q, Incecik A, Incecik A, Peyrard C, Wan DC (2017) Establishing a fully coupled CFD analysis tool for floating offshore wind turbines. *Renew Energy* 112:280–301
10. Tran TT, Dong HK (2015) The aerodynamic interference effects of a floating offshore wind turbine experiencing platform pitching and yawing motions. *Indian J Thorac Cardiovasc Surg* 29(2):549–561
11. Li PF, Cheng P, Wan DC (2015) Numerical simulations of wake flows of floating offshore wind turbines by unsteady actuator line model. In: *Proceedings of the 9th international workshop on ship and marine hydrodynamics*, Glasgow, UK, 26–28 August
12. Menter FR (1994) Two-equation eddy-viscosity turbulence models for engineering applications. *AIAA J* 32(8):1598–1605
13. Shen Z, Wan D (2016) An irregular wave generating approach based on naoe-FOAM-SJTU solver. *China Ocean Eng* 30(2):177–192
14. Cao H, Wan D (2014) Development of multidirectional nonlinear numerical wave tank by naoe-FOAM-SJTU solver. *Int J Ocean Syst Eng* 4(1):52–59
15. Carrica PM, Huang J, Noack R (2010) Large-scale DES computations of the forward speed diffraction and pitch and heave problems for a surface combatant. *Comput Fluids* 39(7):1095–1111
16. Jonkman J, Butterfield S, Musial W, Scott G (2009) Definition of a 5-MW reference wind turbine for offshore system development. National Renewable Energy Laboratory, Golden, CO
17. Robertson A, Jonkman J, Masciola M (2012) Definition of the semisubmersible floating system for phase II of OC4. *Offshore Code Comparison Collaboration Continuation (OC4) for IEA Task*, 30

# A Parallelized Inflow-Boundary-Based Numerical Tank: Performance on Individual SMA Nodes



Shaswat Saincher, Sagar Dave, Chetan Anghan and Jyotirmay Banerjee

**Abstract** State of the art in numerical wave tank (NWT) development demands that emerging algorithms be capable of utilizing most of the computing power available from today's multi-core CPU architectures. Based on this motivation, we attempt MPI-based parallelization of our (in-house) Navier–Stokes equation (NSE)-based NWT algorithm. Parallelization strategy adopted in this paper involves domain decomposition along the direction of wave propagation. The parallelized NWT code is tested on single, multi-core, shared-memory nodes for both regular wave generation and wave-rigid structure interaction (WSI) scenarios. It is demonstrated that the resultant wave topology is independent of number of threads considered in the parallel computation ( $N_p$ ). It is further observed that proposed parallelization strategy results in appreciable reduction in computation time ( $CT$ ). However, maximum speedup ( $\psi_{max}$ ) is observed to be limited by the number of physical cores ( $\mathfrak{N}$ ) available on the computing node. Nonetheless, the results demonstrate that, for the same grid size, proposed NWT code is significantly faster than ANSYS® FLUENT for WSI simulations.

**Keywords** Navier–Stokes · NWT · Parallelization · MPI · Speedup

## 1 Introduction

Numerical wave tanks (NWTs) act as computational counterparts of wave flumes. Whilst an obvious classification of NWTs emerges from the system of governing equations used for describing wave hydrodynamics, the proposed algorithms can

---

S. Saincher (✉) · S. Dave · J. Banerjee  
Sardar Vallabhbhai National Institute of Technology, Surat 395007, Gujarat, India  
e-mail: [shaswat.saincher@gmail.com](mailto:shaswat.saincher@gmail.com)  
URL: <http://www.svnit.ac.in>

C. Anghan  
Shroff S. R. Rotary Institute of Chemical Technology, Ankleshwar-Valia Road,  
Valia, District Bharuch 393135, Gujarat, India

© Springer Nature Singapore Pte Ltd. 2019  
K. Murali et al. (eds.), *Proceedings of the Fourth International Conference in Ocean Engineering (ICOE2018)*, Lecture Notes in Civil Engineering 22, [https://doi.org/10.1007/978-981-13-3119-0\\_43](https://doi.org/10.1007/978-981-13-3119-0_43)



also be classified based on the “environment” used for NWT design. To be specific, NWTs have been developed using commercial codes such as PHOENICS, ANSYS® FLUENT, ANSYS® CFX [1] and STAR-CCM+ [2]; open-source codes such as OpenFOAM and REEF-3D [3] as well as “pure” FNPT-based [4–6], “pure” NSE-based [7, 8] and “hybrid” FNPT-NSE-based [9] in-house codes. Taking these NWT designs and the authors’ own experience (of developing commercial software-based as well as in-house code-based NWT models) into consideration, an interesting distinction emerges between commercial and in-house codes. Commercial CFD codes such as ANSYS® FLUENT are highly general purpose and applicable to a wide category of problems, domain geometries and mesh configurations. Unfortunately, given a high level of versatility, it is generally the case with commercial CFD codes that:

- debugging and “problem interrogation” (especially quantitative querying of solution variables during intermediate stages of a simulation) are difficult,
- specification of “user-defined” functions/field variables is possible; however, modification or alteration of existing solution methods/models is (generally) not possible, and
- monotonically  $\downarrow \mathcal{CT}$  for a fixed problem size is challenging, especially on multi-core (not to be confused with “multi-node”) computing architectures.

In contrast, development of in-house CFD codes is not impeded by the above-mentioned limitations. Thanks to availability of the source code, solution interrogation is possible up to any level within individual subroutines. Considering the example of PLIC-VOF based NWTs [2, 8], in-house codes offer greater flexibility in terms of algorithm modification and querying typical quantitative data from the solution. For instance, higher-order interface reconstruction methods such as LVIRA [10] could be introduced to reduce artificial surface tension effects in the PLIC-VOF routine. In addition, advection of volume fraction ( $f$ ) could be made operator-split [7] or even semi-Lagrangian [10] to eliminate “double-fluxing” errors (in  $f$ ) at large Courant numbers ( $C > 0.25$ ). Further, exact coordinates of the reconstructed PLIC-VOF interface can be queried [10] in an in-house NWT code which would ensure that local free-surface elevation signals ( $\eta(t)$ ) are continuous [7, 8]. Hence, once developed, in-house NWT algorithms are poised to outperform commercial CFD codes. This can certainly be accomplished if  $\downarrow \mathcal{CT}$  were somehow achieved on multi-core CPUs for a fixed problem size.

In case of CFD algorithms,  $\downarrow \mathcal{CT}$  can be achieved through OpenMP (suitable for shared-memory architectures; SMAs) or MPI (suitable for both SMAs and distributed-memory architectures; DMAs)-based parallelization. Generally speaking, the goal of parallel code development is to achieve linear speedup (where speedup ( $\psi$ ) is defined as ratio of time consumed in a serial computation to that consumed in a parallel computation). Achieving linear speedup ( $\psi = N_p$ ) for parallel CFD codes is not straightforward given the following challenges:

- selecting uni-axial/bi-axial/tri-axial decomposition of the domain such that load balance is ensured amongst individual threads [11, 12]

- data communication (in MPI-based codes) between threads and at the same time minimizing communication overheads [11]
- ensuring partitioning independence of the solution
- identifying (and resolving) latencies inducing saturation in  $\psi$  [11, 12]
- minimizing inherently serial fraction ( $e$ ) of the code [13]
- ensuring that  $\psi = N_p \ni N_p \leq \mathfrak{N}$  holds across a variety of problems [3, 11, 12]
- identifying whether hyper-thread control within a single node is beneficial or detrimental to parallel performance.

Motivated by a desire to improve (computing) resource harnessing capabilities of our in-house NSE-based NWT algorithm [8] and also towards addressing (some of) the above-mentioned challenges, we attempt MPI-based parallelization of our serial code. Mathematical model of our (existing) numerical tank is briefly described in Sect. 2. Parallelization strategy is based on domain decomposition along the direction of wave propagation [11, 14]; said methodology is described in detail in Sect. 3. The parallelized code is benchmarked in Sect. 4 against regular wave propagation ( $Ur = 1.65, 19.5$ ) [8, 15] and WSI experiments of Beji and Battjes [15]. Performance of the proposed NWT parallelization methodology is assessed in Sect. 5 through evaluation of  $\psi$  and  $CT$  (for  $N_p = 1 \div 24$ ) and also by comparing the proposed code against ANSYS<sup>®</sup> FLUENT for WSI simulations in serial and parallel modes. The paper is summarized, and future outlook is proposed in Sect. 6.

## 2 Numerical Wave Tank

Serial version of our inflow-boundary-based NWT algorithm has already been explained in detail elsewhere [8]; only a brief description is provided here.

The present NWT model is based on the two-phase Navier–Stokes equations (NSE). Wave propagation is assumed to be a viscous, incompressible two-phase flow with gravity ( $g$ ) being the dominant restoring force. Influence of the air phase on generated waves is modelled using an operator-split PLIC-VOF technique adopting a “single-fluid formulation” where fluid density ( $\rho$ ) and viscosity ( $\mu$ ) are replaced by mixture properties  $\rho^*$ ,  $\mu^*$  which are in turn evaluated from the volume fraction ( $f$ ) field [8]. The system of equations (governing momentum  $\vec{V}$  and  $f$  transport) have been discretized on a finite volume staggered grid in a semi-explicit framework, and continuity ( $\vec{\nabla} \bullet \vec{V} = 0$ ) is satisfied using the velocity projection method based on a predictor–corrector approach.

Referring to previous works by the authors [7, 8], a generalized approach has been adopted for selecting domain and mesh configuration for the NWT. Considering regular incident waves having characteristics  $H$ ,  $\lambda$  and  $h$ ; length of wave simulation region (excluding sponge layers/beaches) is selected within:  $5\lambda \leq \mathbb{L} \leq 10\lambda$  and height of the NWT is selected such that  $\mathbb{H} \geq h + 2H$ . The mesh size ( $n_x \times n_y$ ) is correlated to incident wave characteristics [7] through the variables  $n_{x_\lambda}$  (cells per wavelength) and  $n_{y_H}$  (cells per wave height). Guidelines for selecting  $n_{x_\lambda}$ ,  $n_{y_H}$  are reported elsewhere [7].

Incident waves are generated using a “wave-inflow” condition applied at the left-most boundary. This involves a Dirichlet prescription of  $\eta(t)$  and  $\vec{V}(y, t)$  (determined from Stokes  $\nabla$  theory). Given that  $\int_T \int_{h+\eta(t)} U(y, t) dy dt \neq 0$  for *any* wave theory, a central issue with inflow-boundary-based NWTs is a net addition of volume at the end of a wave period ( $T$ ) which induces a nonzero set-up  $\vartheta_+$  in the numerically generated waves over several periods ( $t > 10T$ ). The authors have recently demonstrated that said volume addition issue can be resolved using the kinematic stretching-based “modified inflow technique” [8]. In this paper, we propose an equally effective strategy for achieving volume preservation. Here, we progressively eliminate net volume added over one wave period by truncating an equivalent amount from the interfacial region;

$$f_m \rightarrow f_m - \left( \int_T \int_{h+\eta(t)} U(y, t) dy dt \cdot \Delta t \right) \cdot (T \mathfrak{M} \Delta x \Delta y)^{-1} \quad (1)$$

where ( $0 < f_m < 1$ ) is fraction of water in a “mixed” cell [10],  $\Delta x \cdot \Delta y$  is volume of the mixed cell,  $\mathfrak{M}$  is the total number of mixed cells in the interfacial region and  $\Delta t$  is time step size. It is demonstrated in Sect. 4 that the proposed “VOF truncation algorithm” is effective in ensuring that  $\vartheta_+ \cong 0$  during generation of strongly nonlinear waves without inducing height reduction. Lastly, wave absorption is achieved in the present NWT model using sponge layers (regular wave generation) or beaches (WSI simulations [15]). These algorithms have directly been adopted from our previous works [7, 8] without any modifications; implementation details are hence excluded for the sake of brevity. Methodology adopted for parallelizing the NWT code is presented in the next section.

### 3 Parallelization Methodology

The present NWT code (written in C) has been parallelized using MPI which makes execution possible on both DMAs and SMAs [13]. Parallelization is initiated using the functions `MPI_Init()`, `MPI_Comm_size()` and `MPI_Comm_rank()` which identify the total number of threads ( $N_p$ ) as well as individual threads ( $np = 0, 1, 2, \dots, N_p - 1$ ) involved in the parallel computation. Based on  $N_p$ , the domain is uni-axially partitioned along the direction of wave propagation [11]. Referring to Fig. 1, partitioning generates  $N_p$  sub-domains each having  $i_{cl} \times ny$  cells where  $ny$  is the total number of cells normal to the partitioning direction and  $i_{cl} = nx/N_p$  where  $nx$  is the total number of cells along the partitioning direction. Cell “columns” normal to partitioning direction are assigned `MPI_Datatype layer` [11]. Datatypes and memory addresses of variables within each `layer` are in turn defined using the functions `MPI_Type_vector()` and `MPI_Type_commit()`. Given that mesh generation within a NWT is not CPU intensive, the same was carried out in “serial mode” (the same calculation assigned to all threads) and later, running indices ( $i \rightarrow 3 \div nx + 2$ ) of the global mesh were shifted to local indices ( $i \rightarrow 3 \div i_{cl} + 2$ )

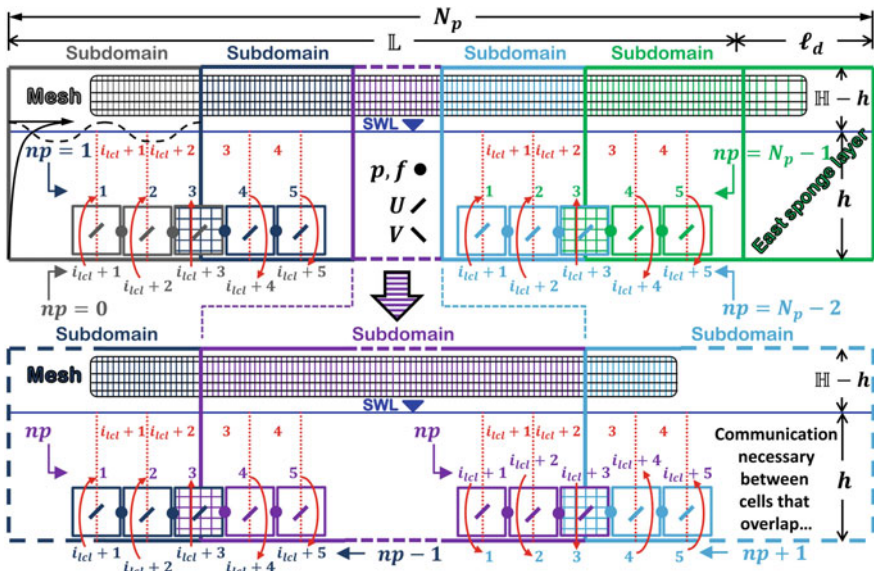


**Fig. 1** Representative sketch of a parallelized inflow-boundary NWT illustrating difference in communication overheads between “boundary” and “interior” sub-domains

in individual sub-domains. Beyond this point, all subroutines in the NWT code (solution initialization, variable time-stepping, calculation of  $\rho^*$ ,  $\mu^*$ , VOF truncation routine, PLIC-VOF solver, NSE-solver projection step and pressure correction step) have been strictly executed in parallel mode ( $i \rightarrow 3 \div i_{tcl} + 2$ ). It is worth noting that data communication of layers between threads, realized using the function `MPI_Sendrecv()` [13, 14], precedes any sub-routine which queries neighbor values for computing a “cell-centered” variable. Referring to Fig. 1, it is also evident that communication overheads are twice as large for interior sub-domains ( $0 < np < N_p - 1$ ) that need two “supplemental” boundary conditions compared to boundary sub-domains ( $np = 0, N_p - 1$ ) that require just one supplemental condition.

The primary concern surrounding parallelization is that of achieving “partitioning independence”: Do serial and parallel versions of the code generate same output irrespective of  $N_p$ ? This question is addressed in the next section.

## 4 Benchmarking of the Parallelized NWT

Wave generation performance as well as partitioning independence of the parallelized NWT is evaluated through three test cases; two cases involve regular wave generation [8, 15] whilst the third scenario pertains to WSI [15].

### 4.1 Monochromatic Wave Generation

Regular waves have been generated by coupling the wave-inflow boundary condition with the VOF truncation approach described in Sect. 2. Two distinct wave designs have been considered: (a) sinusoidal high-frequency (**SH**) waves ( $h = 0.4$  m;  $T = 1.25$  s;  $H = 2.5$  cm  $\vdash$   $Ur = 1.65$ ) [15] and (b) case **C** waves ( $h = 0.3$  m;  $T = 1.5$  s;  $H = 9$  cm  $\vdash$   $Ur = 19.5$ ) [8]. Considering [7], following NWT set-up is selected for **SH** waves:  $L = 20$  m,  $H = 0.44$  m,  $\ell_d = 10$  m;  $n_x = 864 \vdash n_{x_\lambda} \approx 84, n_y = 100 \vdash n_{y_H} \approx 19; T/\Delta t = 10,000$ . For case **C** waves, the NWT set-up is identical to one reported in [8] but with  $n_x = 1392$  instead of  $n_x = 1380$ . Results of regular wave simulations in the NWT are shown in Fig. 2. Partitioning independence is demonstrated for **SH** waves through a comparison of  $\eta(x)$  profiles (at  $t = 20T$ ) between serial ( $N_p = 1$ ) and parallel ( $N_p = 8$ ) simulations (see top in Fig. 2). For case **C**, volume preservation characteristics of the VOF truncation algorithm (given by Eq. (1)) are illustrated for a parallel simulation considering four sub-domains (see bottom in Fig. 2). It is observed that the proposed strategy is effective in ensuring that  $\vartheta_+ \cong 0$  is retained even after twenty wave periods. In both cases, a near-exact match is obtained between simulations and analytical  $\eta(x)$  profiles predicted by Stokes  $\nabla$  theory.

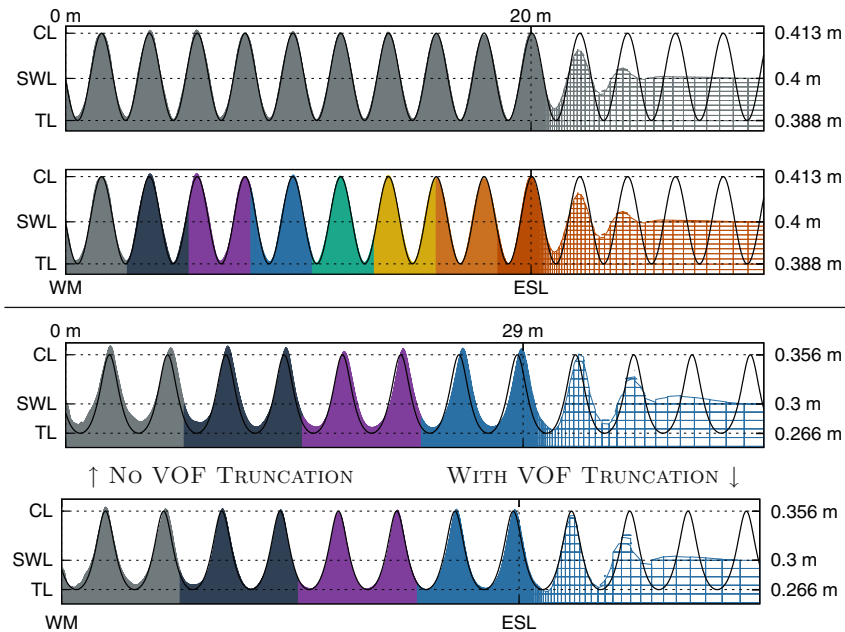


**Fig. 2** Spatial profiles ( $\eta(x)$ ) of regular (*top*) **SH** waves [15] and (*bottom*) case **C** waves [7, 8] in the NWT at  $t = 20T$  superimposed with analytic profiles (predicted using Stokes  $\nabla$  theory) for (*top*)  $N_p = 1, 8$  and (*bottom*)  $N_p = 4$

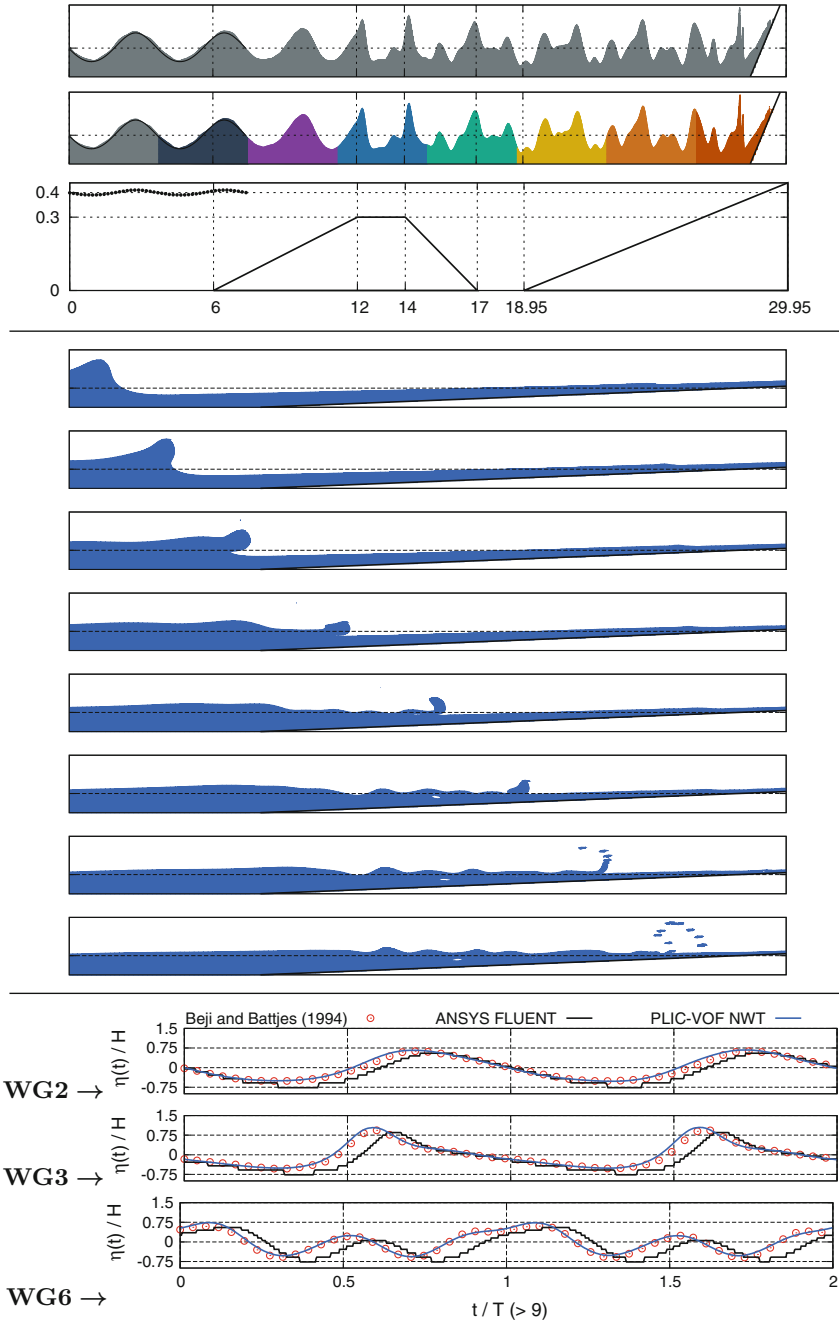


**Fig. 3** SL wave transformation over a submerged trapezoidal bar: (top)  $\eta(x)$  profiles at  $t = 15T$  showing partitioning independence, (center) breaking-induced absorption of incident waves over the beach and (bottom) validation of normalized  $\eta(t)$  profiles [15]

## 4.2 Wave-Rigid Structure Interaction

Third test case considered is that of WSI occurring during sinusoidal low-frequency (**SL**;  $h = 0.4$  m;  $T = 2.0$  s;  $H = 2$  cm  $\vdash$   $Ur = 4.27$  [15]) wave propagation over a submerged trapezoidal bar (see Fig. 3). NWT set-up and numerical treatment of non-Cartesian submerged/emergent boundaries adopted for this problem are identical to the serial design reported in [8] but with  $n_x = 1536$  instead of  $n_x = 1500$ . Remainder of the simulation specifications are excluded for sake of brevity. Nonetheless, it is worth mentioning that we capitalize on capabilities of the two-phase NSE solver by modeling a physical beach for wave absorption (see Fig. 3), thereby achieving closer resemblance with experimental conditions of Beji and Battjes [15]; breaking-induced absorption of incident waves is not possible in FNPT-based NWTs [4, 6]. Partitioning independence of WSI simulations in the NWT is demonstrated through  $\eta(x)$  profiles in Fig. 3. Comparison of normalized  $\eta(t)$  signals (recorded at  $x = 10.5$  m (**WG2**),  $x = 12.5$  m (**WG3**) and  $x = 15.7$  m (**WG6**)) with experiments [15] and with ANSYS® FLUENT simulations is also shown in Fig. 3. Owing to PLIC-VOF coordinate information [7], proposed NWT records more continuous  $\eta(t)$  signals compared to FLUENT and hence accurately predicts occurrence of zero downcrossings. This, in turn, is critical in sustaining simultaneous phase agreement between topologies (attained in Fig. 3) at multiple wave gauge locations [3].

## 5 Assessment of Parallel Performance

Performance assessment of our parallelization methodology is done by evaluating  $\psi$  and  $\mathcal{CT}$  (in hours) against an increasing number of threads ( $N_p$ ) for a fixed problem size (strong scaling [11–13]). The strong scaling study has been undertaken for case **C** and WSI scenarios on two SMA nodes having following configurations: a desktop having an Intel® i7-4770 CPU with  $\mathfrak{N} = 4$  and a server having two Intel® Xeon E5 2620 v2 CPUs with  $\mathfrak{N} = 12$ . Results of the strong scaling study are reported in Fig. 4. It is seen that the proposed algorithm scales better on the dual processor Xeon compared to i7. However,  $\psi$  is observed to *not* increase monotonically with  $N_p$ . Performance gain/degradation is observed to be both problem and architecture-dependent. This is mainly attributable to Intel® Hyper-Threading (HT) technology which allows addressing  $2\mathfrak{N}$  logical cores for a system having  $\mathfrak{N}$  physical cores. However, as explained in [16], all logical cores “must share the same resources” available in the physical processor (such as L1, L2 and L3 cache memories); said resource sharing “creates potential for performance degradation” [16]. As learned from dedicated processor-benchmarking studies, HT-based performance gains are “modest for real applications” [17] and HT may “help or hinder<sup>1</sup> performance” [16]. Speedup oscillations observed in Fig. 4 are also attributable to (comparatively)

---

<sup>1</sup>quite interestingly, performance degradation was observed for benchmarking tests involving FFT-based solution of PDEs [16].

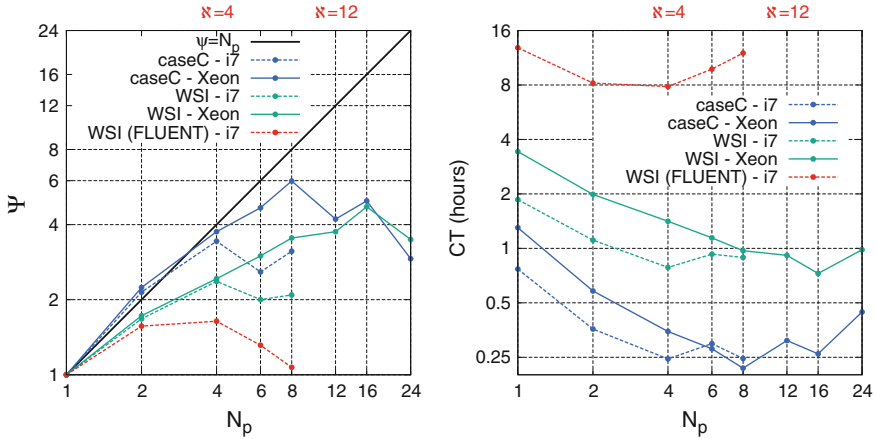


Fig. 4 Variation of  $\psi$  and  $CT$  against increasing  $N_p$

small problem sizes ( $n_x \times n_y \sim 7 \times 10^4$ ) considered in the strong-scaling study. It is hence anticipated that the experimental  $\psi$  versus  $N_p$  curves would shift closer to the ideal  $\psi = N_p$  law with increasing problem size. Nonetheless, it is demonstrated through Fig. 4 that proposed NWT code is considerably faster and has superior scaling characteristics compared to ANSYS® FLUENT for WSI simulations performed on a  $\sim 7 \times 10^4$  structured mesh.

## 6 Summary and Outlook

In the present paper, we successfully parallelize our in-house PLIC-VOF-based NWT code using MPI. The parallel code has been benchmarked for topological quality of generated waves, volume preservation and partitioning independence during monochromatic wave generation and WSI simulations. Under strong scaling, the proposed code achieves:

- $\psi_{max} \cong 6 \leftarrow N_p = 8$  for trochoidal wave generation [7]
- $\psi_{max} \cong 5 \leftarrow N_p = 16$  for WSI simulations [15]

executed on a dual-Xeon server ( $\mathfrak{N} = 12$ ). It is worth noting that whilst (the trend of)  $\psi$  may continue increasing for  $N_p > \mathfrak{N}$ ,  $\psi_{max} \leq \mathfrak{N}$  would always hold regardless of the nature of problem/type of architecture considered for benchmarking due to inherent limitations of Intel® Hyper-Threading (HT) technology [16]. It is also demonstrated that proposed NWT algorithm is considerably faster than ANSYS® FLUENT (in both serial and parallel modes) during WSI simulations. Future studies would be focused towards identifying and resolving bottlenecks in  $\psi$  so that  $\psi \approx \mathfrak{N}$  could be achieved for the range of problems considered in this paper.



## References

1. Finnegan W, Goggins J (2015) Linear irregular wave generation in a numerical wave tank. *Appl Ocean Res* 52:188–200
2. Perić R, Abdel-Maksoud M (2015) Generation of free-surface waves by localized source terms in the continuity equation. *Ocean Eng* 109:567–579
3. Bihs H, Kamath A, Chella MA, Aggarwal A, Arntsen ØA (2016) A new level set numerical wave tank with improved density interpolation for complex wave hydrodynamics. *Comput Fluids* 140:191–208
4. Sriram V, Sannasiraj SA, Sundar V (2006) Simulation of 2-D non-linear waves using finite element method with cubic spline approximation. *J Fluids Struct* 22:663–681
5. Sriram V, Sannasiraj SA, Sundar V, Schlenkhoff A, Schlurmann T (2010) Quantification of phase shift in the simulation of shallow water waves. *Int J Numer Methods Fluids* 62:1381–1410
6. Zhang T, Ren Y-F, Yang Z-Q, Fan C-M, Li P-W (2016) Application of generalized finite difference method to propagation of nonlinear waves in numerical wave flume. *Ocean Eng* 123:278–290
7. Saincher S, Banerjee J (2017) On wave damping occurring during source-based generation of steep waves in deep and near-shallow water. *Ocean Eng* 135:98–116
8. Saincher S, Banerjee J (2017) A volume-preserving inflow boundary based numerical tank applied to wave-structure interaction in near-shallow water. In: *Proceedings of the 7th international conference on computational methods in marine engineering (MARINE 2017)*, Nantes, France
9. Sriram V, Ma QW, Schlurmann T (2014) A hybrid method for modelling two dimensional non-breaking and breaking waves. *J Comput Phys* 272:429–454
10. Zinjala HK, Banerjee J (2015) A Lagrangian-Eulerian volume-tracking with linearity-preserving interface reconstruction. *Numer Heat Trans Part B Fundam* 68:459–478
11. Aggarwal V, Gada VH, Sharma A (2013) Parallelization methodology and performance study for level-set-method-based simulation of a 3-D transient two-phase flow. *Numer Heat Trans Part B Fundam* 63:327–356
12. Oger G, Le Touzé D, Guibert D, de Lefle M, Biddiscombe J, Soumagne J, Piccinali J-G (2016) On distributed memory MPI-based parallelization of SPH codes in massive HPC context. *Comput Phys Commun* 200:1–14
13. Quinn MJ (2004) *Parallel programming in C with MPI and OpenMP*. McGraw-Hill Higher Education
14. Anghan C (2016) Direct numerical simulation (DNS) of spatially and temporally developing free round jet using message passing interface (MPI). Thesis of Master of Technology, Mechanical Engineering Department, S V National Institute of Technology, Surat, India
15. Beji S, Battjes JA (1994) Numerical simulation of nonlinear wave propagation over a bar. *Coastal Eng* 23:1–16
16. Leng T, Ali R, Hsieh J, Mashayekhi V, Rooholamini R (2002) An empirical study of hyper-threading in high-performance computing clusters. In: *Proceedings of the 3rd LCI international conference on Linux clusters: the HPC revolution*, St. Petersburg, Florida
17. Margo W, Petersen P, Shah S (2002) Hyper-threading technology: impact on compute-intensive workloads. *Intel Technol J* 6:1–9

# Simulation of Floating Bodies in Waves and Mooring in a 3D Numerical Wave Tank Using REEF3D



Tobias Martin, Hans Bihs, Arun Kamath and Øivind Asgeir Arntsen

**Abstract** Mooring systems ensure the safety of structures near the shore like floating breakwaters and aquaculture cages by keeping them in position. Their design has to either provide enough flexibility to allow large displacements or enough strength to withstand the hydrodynamic loads while restraining the structural motion. The accurate determination of the motion of the moored-floating structure and the resulting tension forces in the cables is, therefore, of high significance to produce a safe and economical design. At the same time, the dynamics of the cables can be neglected in the early design process due to their minor contribution to the forces acting on the structure. Hence, an analytical solution for the cables can be found, which provides a fast solution to the problem. The mooring model is implemented in the open-source CFD model REEF3D. The solver has been widely used to study various problems in the field of wave hydrodynamics. It solves the incompressible Reynolds-averaged Navier–Stokes equations for two-phase flows using a finite-difference method and a level set method to model the free surface between water and air. Floating structures are represented by an additional level set function. Its motion is calculated from the Newton and Euler equations in 6DOF and in a non-inertial coordinate system. The fluid–structure interaction is solved explicitly using an immersed boundary method based on the ghost cell method. The application shows the accuracy of the solver and effects of mooring on the motion of a floating structure.

**Keywords** CFD · REEF3D · Mooring · Fluid–structure interaction

---

T. Martin (✉) · H. Bihs · A. Kamath · Ø. A. Arntsen  
Norwegian University of Science and Technology, 7491 Trondheim, Norway  
e-mail: [tobias.martin@ntnu.no](mailto:tobias.martin@ntnu.no)

A. Kamath  
e-mail: [arun.kamath@ntnu.no](mailto:arun.kamath@ntnu.no)

© Springer Nature Singapore Pte Ltd. 2019  
K. Murali et al. (eds.), *Proceedings of the Fourth International Conference in Ocean Engineering (ICOE2018)*, Lecture Notes in Civil Engineering 22,  
[https://doi.org/10.1007/978-981-13-3119-0\\_44](https://doi.org/10.1007/978-981-13-3119-0_44)

## 1 Introduction

Coupled fluid–structure interaction plays a major role in the fields of coastal and ocean engineering. Most applications require the solution of a two-phase problem as well as an accurate determination of rigid body dynamics. Some examples are floating breakwater, aquaculture cages or ship motion prediction. As a first attempt, fluid–structure interaction problems based on the Navier–Stokes equations have been calculated with Arbitrary Lagrangian–Eulerian methods [18]. In this approach, the interface between solid and fluid is tied to the numerical mesh for which reason the mesh needs to be adjusted dynamically. The re-meshing procedure can have a detrimental effect on the numerical accuracy and stability, especially for more arbitrary solid body movements. A way to avoid constant re-meshing is the usage of dynamic overset grids. The method consists of a Eulerian mesh for the fluid and a overset mesh which follows the movement of the solid and overlaps with the base mesh. A stable scheme for establishing the connections between the overset mesh points and the underlying grid points in the overlapping region has to be introduced (see, e.g. [7]). As an alternative, a direct forcing immersed boundary method was developed for describing the fluid–structure interaction [26]. This immersed boundary method requires just one Eulerian grid, and the interaction is incorporated by an additional forcing term in the Navier–Stokes equations. Special attention was also given to the field extension method [24], which accounts for solid cells becoming fluid cells and vice versa. With the field extension, unphysical values for the pressure and the velocities are avoided. More recently, [6] presented a level set-based two-phase flow solver for the simulation of floating structures. In this work, an extension of the local directional immersed boundary method [2] using the field extension method is presented. The geometry of the solid is described by a level set function. Hence, forces and moments can be calculated without explicitly defining the intersections between the surface mesh and the grid of the flow domain. Like other immersed boundary methods, the solid body is immersed into the fluid and re-meshing or overset grids are avoided. The presented results are all obtained with a weakly coupled scheme. In combination with the robust two-phase flow solver REEF3D [4], this results in a stable fluid–structure interaction model. If the motion of the floating structure is large, mooring dynamics can have a significant impact on the response of the structure. The general solution for the dynamics of mooring systems has to be found numerically due to the underlying nonlinear system of equations. Several discretisation methods have been developed, like the finite differences [13] and finite element-based methods [1] or the lumped mass method [12]. A general overview of the methods can be found in [9]. For structures with small responses in mild environmental conditions, a quasi-static mooring model is suitable. By neglecting the dynamic effects of the mooring system, dependencies of mass, damping and fluid acceleration on the system are omitted. The mooring line shape and tension can then be found analytically as shown by [10]. It has the advantage of computational efficiency and simplicity of implementation. Therefore, the analytical approach is taken into account in this paper as a starting point for more advanced models in further research. In Sect. 2,

the CFD model REEF3D is shortly described. Afterwards, details about the implemented 6DOF algorithm and mooring model are given in Sects. 2.1 and 2.2. The application of the solver is presented in Sect. 3. Final remarks and prospects for further developments can be found in Sect. 4.

## 2 Numerical Model

The basic equations of the numerical model arise from the conservation law of mass and momentum for incompressible fluids. Using tensor notation, the resulting equations read for a whole-domain formulation

$$\frac{\partial u_i}{\partial x_i} = 0, \quad (1)$$

$$\frac{\partial u_i}{\partial t} + u_j \frac{\partial u_i}{\partial x_j} = -\frac{1}{\rho} \frac{\partial p}{\partial x_i} + \frac{\partial}{\partial x_j} \left( \nu \cdot \left( \frac{\partial u_i}{\partial x_j} + \frac{\partial u_j}{\partial x_i} \right) \right) + g_i, \quad (2)$$

with  $u_i$  the velocity components,  $\rho$  the fluid density,  $p$  the pressure,  $\nu$  the kinematic viscosity and  $\mathbf{g}$  the gravity acceleration vector. Here, the Reynolds-averaged Navier–Stokes (RANS) equations are solved by replacing the fluid properties with time-averaged values and add turbulent viscosity to  $\nu$ . The additional viscosity is calculated with a modified  $k$ - $\omega$  model as given in [4].

The spatial domain is discretised by a finite-difference method (FDM) on a Cartesian grid. System (1), (2) is solved on a staggered grid to avoid decoupling of pressure and velocity. Convection terms are evaluated in a non-conservative form because the violation of the mass conservation during an explicit solution procedure might cause numerical instabilities in a conservative formulation [21]. For this purpose, the fifth-order accurate weighted essentially non-oscillatory (WENO) scheme of [15] adapted to non-conservative terms by [27] is applied. The discretised system is solved using Chorin’s projection method for incompressible flows [8]. The pressure is calculated from a Poisson equation and by applying the fully parallelised BiCGStab algorithm [23]. For progressing in time, the third-order accurate Total Variation Diminishing (TVD) Runge–Kutta scheme [20] is employed. Adaptive time stepping controls the time stepping according to the required CFL condition.

The location of the free water surface is represented implicitly by the zero level set of a smooth signed distance function  $\Phi(\mathbf{x}, t)$  which is defined as the closest distance to the interface [16]. Its motion can be described by the advection equation

$$\frac{\partial \Phi}{\partial t} + u_j \frac{\partial \Phi}{\partial x_j} = 0. \quad (3)$$

The convection term in (3) is discretised by the fifth-order accurate Hamilton–Jacobi WENO method of [14]. In order to conserve the signed distance property,

the level set function is reinitialised after each time step. Here, the PDE-based reinitialisation equation of [21] is taken into account. The material properties of the two phases are finally determined for the whole domain in accordance with the continuum surface force model of [5] (see [4] for details).

## 2.1 6DOF Algorithm

The geometry of the rigid body is described by a primitive triangular surface mesh neglecting connectivity. For this purpose, the intersections of the surface mesh with the underlying Cartesian grid are determined with the ray-tracing algorithm of [25]. It efficiently provides inside–outside information and, for each grid point, the shortest distance along the coordinate axis to the body describing triangles. Afterwards, the mentioned reinitialisation algorithm of [17] is applied to obtain signed distance properties for a level set function in the vicinity of the solid body. This has the advantage that the intersections of the surface mesh with the underlying grid do not have to be calculated explicitly. The obtained level set function can be used for calculating the six force and moment components of the fluid on the body as given by [3].

Any point relating to a rigid body can be described by the location of the centre of gravity and orientation of the body in the inertial coordinate system. Here, the orientation is described by Euler angles which results in the position vector

$$\mathbf{x} = (x_1, x_2, x_3, x_4, x_5, x_6)^T, \quad (4)$$

where the first three components are the coordinates of the centre of gravity and the last three components are the Euler angles  $\phi$ ,  $\theta$  and  $\psi$ . The calculation of the motion of a body in the inertial system would include several time derivatives of moments which can be avoided by applying a coordinate transformation to the Euler equations. The rotation components in the principal coordinate system of the body reads then

$$\boldsymbol{\xi} = (\xi_1, \xi_2, \xi_3)^T. \quad (5)$$

In this paper, it is assumed that the principal axes of the body are known. Thus, the inertia tensor reduces to the three principal moments of inertia which yields

$$\mathbf{I} = \begin{bmatrix} I_x & 0 & 0 \\ 0 & I_y & 0 \\ 0 & 0 & I_z \end{bmatrix} = \begin{bmatrix} mr_x^2 & 0 & 0 \\ 0 & mr_y^2 & 0 \\ 0 & 0 & mr_z^2 \end{bmatrix}, \quad (6)$$

with  $m$  the mass of the body and  $r_x$ ,  $r_y$  and  $r_z$  the distances of a point from the centre of gravity along the  $x$ -,  $y$ - and  $z$ -direction. Since the fluid flow is calculated in the inertial system, the acting moments in this system  $\mathbf{M}_x$  have to be transformed to the non-inertial system by applying the transformation [11]

$$\mathbf{M}_{\xi} = (M_{1,\xi}, M_{2,\xi}, M_{3,\xi})^T = \mathbf{J}_1^{-1} \cdot \mathbf{M}_x, \quad (7)$$

with  $\mathbf{M}_{\xi}$  the moments in the system of the body and  $\mathbf{J}_1^{-1}$  the rotation matrix ( $s$  stands for sin and  $c$  for cos)

$$\mathbf{J}_1 = \begin{bmatrix} cx_6cx_5 & -sx_6cx_4 + cx_6sx_5sx_4 & sx_6sx_4 + cx_6cx_4sx_5 \\ sx_6cx_5 & cx_6cx_4 + sx_4sx_5sx_6 & -cx_6sx_4 + sx_5sx_6cx_4 \\ -sx_5 & cx_5sx_4 & cx_5cx_4 \end{bmatrix}. \quad (8)$$

Hence, the dynamics of the rigid body can be described by the three equations of translational motion

$$\begin{pmatrix} \ddot{x}_1 \\ \ddot{x}_2 \\ \ddot{x}_3 \end{pmatrix} = \frac{1}{m} \cdot \begin{pmatrix} F_{x_1,x} \\ F_{x_2,x} \\ F_{x_3,x} \end{pmatrix}, \quad (9)$$

where  $F_x$  are the acting forces in the inertial system and the three Euler equations in the non-inertial system are [11]

$$\begin{aligned} I_x \ddot{\xi}_1 + \dot{\xi}_2 \dot{\xi}_3 \cdot (I_z - I_y) &= M_{1,\xi}, \\ I_y \ddot{\xi}_2 + \dot{\xi}_1 \dot{\xi}_3 \cdot (I_x - I_z) &= M_{2,\xi}, \\ I_z \ddot{\xi}_3 + \dot{\xi}_1 \dot{\xi}_2 \cdot (I_y - I_x) &= M_{3,\xi}. \end{aligned} \quad (10)$$

The position of the body can be calculated analytically by integrating (9) twice. System (10) is solved explicitly with the second-order accurate Adams–Bashforth scheme which reads for a generic variable in the new time step  $q^{(n+1)}$

$$\dot{q}^{(n+1)} = \dot{q}^{(n)} + \frac{\Delta t}{2} \cdot (3\ddot{q}^{(n+1)} - \ddot{q}^{(n)}), \quad (11)$$

$$q^{(n+1)} = q^{(n)} + \frac{\Delta t}{2} \cdot (3\dot{q}^{(n+1)} - \dot{q}^{(n)}). \quad (12)$$

The Euler angles in the body system cannot be calculated from the body angular velocities due to missing physical interpretation [11]. Instead, the angular velocities are transformed back using the rotation matrix [11] ( $s$  stands for sin,  $c$  for cos and  $t$  for tan)

$$\mathbf{J}_2 = \begin{bmatrix} 1 & sx_4tx_5 & cx_4 + cx_6tx_5 \\ 0 & cx_4 & -sx_4 \\ 0 & sx_4/cx_5 & cx_4/cx_5 \end{bmatrix}. \quad (13)$$

Afterwards, the necessary Euler angles are calculated from (12) in the inertial frame. It might be noticed that (13) has a singularity at  $x_5 = \pm \frac{\pi}{2}$ . In practice, this angle does not occur for typical floating structures in ocean engineering.

In this paper, the fluid–structure coupling is arranged in a weak form without sub-iterations. First, acting forces are calculated from the fluid, and the body position is determined as described above. Afterwards, the fluid properties are updated to the new time level using the ghost cell immersed boundary method [2] for incorporating the boundary conditions of the solid. For both the velocities and the pressure, these conditions are calculated from the motion of the body with respect to its centre of gravity [3]. Even though the weak coupling has been reported to lead to numerical stability problems for complex cases (e.g. [6] or [7]), the current implementation shows good numerical stability throughout the range of application. However, pressure oscillations can occur in the vicinity of the solid body because of solid cells turning into fluid cells. The fresh fluid cells lack physical information about velocities from previous time steps. It is solved by implementing the field extension method of [22, 24] adapted to the ghost cell immersed boundary method.

### 2.2 Mooring Model

The mooring systems considered in this paper consist of a number of cables which are attached to the floating structure at arbitrary points. Their lower ends are anchored at the seabed. In order to avoid high vertical forces on the anchor, a part of the cable lies on the bottom and damps the vertical motion of the structure. An illustration of this configuration can be seen in Fig. 1. The general equations describing the unsteady motion of a cable are nonlinear and have to be solved numerically. For practical purposes, an analytical solution can be found if static conditions and no current forces are assumed. Following the derivation of [10], a catenary equation, describing the shape of a line, arises as

$$z(x, y) = \frac{F_h}{w} \cdot \left( \cosh \left( \frac{w}{F_h} \cdot \sqrt{x^2 + y^2} \right) \right), \tag{14}$$

with  $F_h$  the horizontal force, which is constant along the cable, and  $w$  the weight per unit length of the cable in water. The tension forces  $F_t$  are calculated as

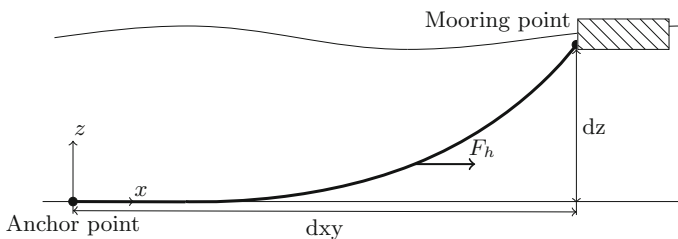


Fig. 1 Definition of a mooring line in two dimensions

$$F_t(z) = F_h + wdz + (z - dz) \cdot (w + \rho gA), \tag{15}$$

where  $g$  is the acceleration due to gravity and  $A$  is the cross-section area of the cable. The area is assumed to be constant; i.e. elasticity of the material is neglected. In the current algorithm, the effect of the mooring lines on the dynamics of the structure is taken into account explicitly in a weakly coupled manner. For this purpose, the forces of each cable acting on the structure have to be calculated from the known distance  $dxy$  from the time-invariant anchor point to the current position of the mooring point. The corresponding equation is written as [10]

$$dxy = \sqrt{dx^2 + dy^2} = l - dz \cdot \sqrt{1 + 2 \cdot \frac{F_h}{wdz}} + \frac{F_h}{w} \cosh^{-1} \left( 1 + \frac{wdz}{F_h} \right), \tag{16}$$

which provides a function transcendental in  $F_h$ . A solution can be determined using the Newton–Raphson algorithm

$$F_h^{(k+1)} = F_h^{(k)} - \frac{f(F_h^{(k)})}{f'(F_h^{(k)})}, \quad k = 1, 2, \dots \tag{17}$$

Once, a converged solution for  $F_h$  has been found, the forces at each mooring point  $X, Y, Z$  result from

$$X = F_h \cos \left( \tan^{-1} \left( \frac{dy}{dx} \right) \right), \tag{18}$$

$$Y = F_h \sin \left( \tan^{-1} \left( \frac{dy}{dx} \right) \right), \tag{19}$$

$$Z = F_h dz \cdot \sqrt{1 + \frac{2F_h}{wdz}}, \tag{20}$$

and moments by multiplication with the appropriate distances to the centre of gravity of the body.

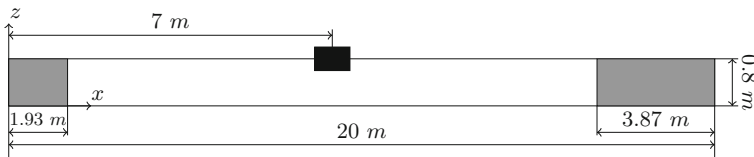


**Fig. 2** Setup for the test case of a 2D barge in waves



### 3 Results for a 2D Barge in Waves

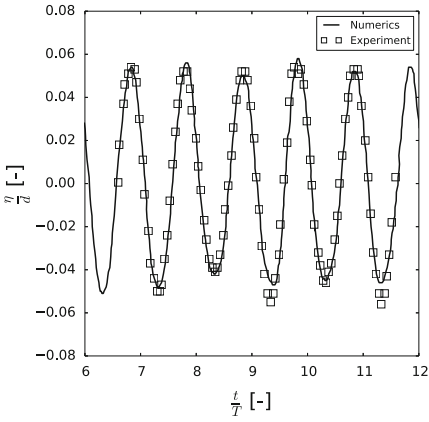
The capability of the presented 6DOF algorithm is presented for a rigid floating barge in two dimensions under the effect of waves with and without mooring. The results are compared to the experimental data of Ren et al. [19]. The laboratory experiment was performed in a wave flume of 20 m length, 0.8 m height and 0.44 m width, which is modelled with the numerical wave tank of REEF3D [4]. The barge is 0.30 m long and 0.2 m high. Since the gap between body and flume walls is small, the case can be considered as 2D, with surge, heave and pitch motion. The initial position of the barge is defined by its centroid at  $(x, z) = (7.0 \text{ m}, 0.4 \text{ m})$  (see Fig. 2). Its density is  $500 \text{ kg/m}^3$ . The water depth in the tank is  $d = 0.4 \text{ m}$ . The incoming waves are regular and have a height of 0.04 m, a period of  $T = 1.2 \text{ s}$  and wavelength of 1.936 m. In the calculations, these are modelled using a second-order Stokes wave theory. A numerical beach is applied in order to avoid wave reflections at the outlet. For the discretisation, a cell size of 0.005 m is chosen which equals 640,000 cells.

#### 3.1 Free-Floating Condition

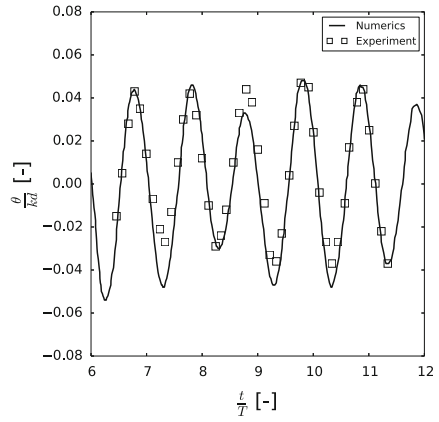
The results from the free-floating simulation are compared with the experiment for the period between  $t/T = 6.36 \text{ s}$  and  $t/T = 12 \text{ s}$ . The wave elevation shown in Fig. 3a shows a good agreement with the experimental data, which confirms the chosen wave theory for modelling the waves. In accordance with the quality of the incoming waves, the distribution of the pitch motion predicts accurate results for the most part of the simulation. Small undershoots are given which correspond to underpredicted wave troughs at  $t/T = 9.3$  and  $t/T = 11.3$  (see Fig. 3b). Also, underresolved damping effects from vortex detaching at the immersed edges might influence the accuracy of the pitch motion. The frequency of the heave motion follows the frequency of the experimental data accurately. However, the amplitudes of this motion are 10% smaller in the simulations. This might be caused by the coupled physics of heave and pitch motion. In contrast, the surge motion is predicted much better, showing a good accordance of the drift with the experiments. This drift is mainly caused by inertia effects driven by the wave motion which is accurately predicted here (Fig. 3b).

#### 3.2 Moored Condition

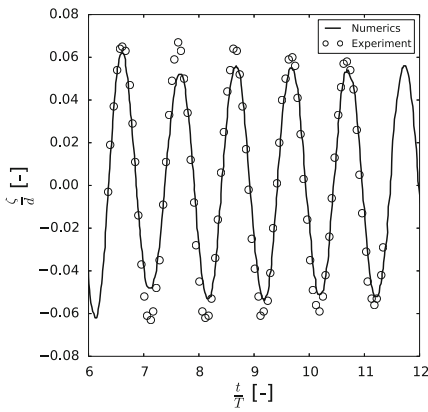
The effect of mooring and capability of the presented mooring model are shown for the 2D barge in waves. For this purpose, two mooring lines are fixed to the body at  $z = 0.4 \text{ m}$  (Fig. 4). The cables are 1.6 m long, 0.01 m thick and have a weight per unit length of  $w = 4 \text{ kg/m}$  in water. A comparison to the motion from above is ensured by increasing the weight of the free-floating body resulting in the same draft as the



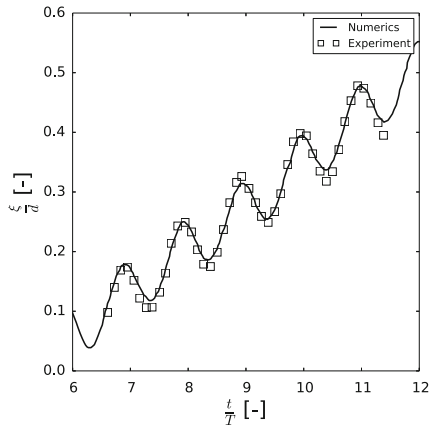
(a) Wave elevation at  $x = 5.5$  m.



(b) Pitch motion.



(c) Heave motion.



(d) Surge motion.

**Fig. 3** Numerical results of the two-dimensional barge in comparison to the experiment data

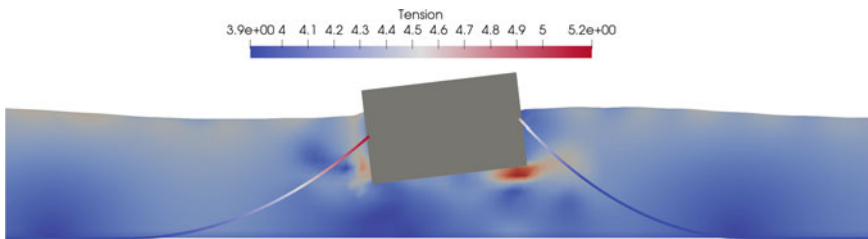


**Fig. 4** Tension force distribution in the mooring cables during a wave trough situation

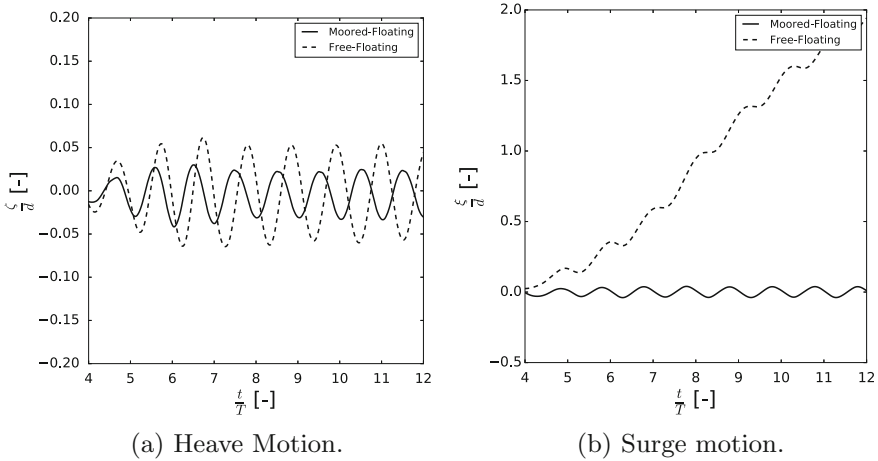


**Fig. 5** Numerical results of the free-floating and moored-floating two-dimensional barge

initial condition. As result, the heave and surge motions over time are shown in Fig. 5. The vertical motion of the structure is significantly damped by installing the mooring system. Further, surging is prevented almost completely.

## 4 Conclusion

This paper gives an overview of the implementation of a weakly coupled 6DOF algorithm in the open-source CFD code REEF3D. The floating body is represented by the combination of a surface mesh, a level set function and the ghost cell immersed boundary method. This results in a method that does not require re-meshing or overset grids. In addition, a simple mooring model is presented which provides analytical solutions for the shape and forces of mooring systems. The application confirms the accuracy of REEF3D in modelling fluid–structure interactions. The mooring model is able to provide the damping effects on the motion of floating bodies. However, for more advanced mooring applications, like tension-leg platforms and extreme weather situations, a dynamic model is preferable.

**Acknowledgements** The calculations were supported in part with computational resources at the Norwegian University of Science and Technology (NTNU) provided by NOTUR project (No. NN2620K), <http://www.notur.no>.

## References

1. Aamo OM, Fossen TI (2001) Finite element modelling of Moored vessels. *Math Comput Model Dyn Syst* 7(1):47–75
2. Berthelsen PA, Faltinsen OM (2008) A local directional ghost cell approach for incompressible viscous flow problems with irregular boundaries. *J Comput Phys* 227:4354–4397
3. Bihs H, Kamath A (2017) A combined level set/ghost cell immersed boundary representation for floating body simulations. *Int J Numer Meth Fluids* 83:905–916
4. Bihs H, Kamath A, Alagan-Chella M, Aggarwal A, Arntsen ØA (2016) A new level set numerical wave tank with improved density interpolation for complex wave hydrodynamics. *Comput Fluids* 140:191–208
5. Brackbill JU, Kothe DB, Zemach C (1992) A continuum method for modeling surface tension. *J Comput Phys* 100(2):335–354
6. Calderer A, Kang S, Sotiropoulos F (2014) Level set immersed boundary method for coupled simulation of air/water interaction with complex floating structures. *J Comput Phys* 277:201–227
7. Carrica PM, Noack RW, Stern F (2007) Ship motions using single-phase level set with dynamic overset grid. *Comput Fluids* 36:1415–1433
8. Chorin A (1968) Numerical solution of the Navier-Stokes equations. *Math Comput* 22:745–762
9. Davidson J, Ringwood J (2017) Mathematical modelling of mooring systems for wave energy converters—a review. *Energies* 10:666
10. Faltinsen OM (1990) *Sea loads on ships and offshore structures*. Cambridge University Press, Cambridge
11. Fossen TI (1994) *Guidance and control of ocean vehicles*. Wiley, Chichester, England
12. Hall M, Goupee A (2015) Validation of a lumped-mass mooring line model with DeepCwind semisubmersible model test data. *Ocean Eng* 104:590–603
13. Huang S (1994) Dynamic analysis of three-dimensional marine cables. *Ocean Eng* 21:587–605
14. Jiang GS, Peng D (2000) Weighted ENO schemes for Hamilton Jacobi equations. *SIAM J Sci Comput* 21:2126–2143
15. Jiang GS, Shu CW (1996) Efficient implementation of weighted ENO schemes. *J Comput Phys* 126(1):202–228
16. Osher S, Sethian JA (1988) Fronts propagating with curvature-dependent speed: algorithms based on Hamilton-Jacobi formulations. *J Comput Phys* 79:12–49
17. Peng D, Merriman B, Osher S, Zhao H, Kang M (1999) A PDE-based fast local level set method. *J Comput Phys* 155:410–438
18. Ramaswamy B, Kawahara M, Nakayama T (1986) Lagrangian finite element method for the analysis of two-dimensional sloshing problems. *Int J Numer Methods Fluids* 6:659–670
19. Ren B, He M, Dong P, Wen H (2015) Nonlinear simulations of wave-induced motions of a freely floating body using WCSPPH method. *Appl Ocean Res* 50:1–12
20. Shu CW, Osher S (1988) Efficient implementation of essentially non-oscillatory shock-capturing schemes. *J Comput Phys* 77(2):439–471
21. Sussman M, Smereka P, Osher S (1994) A level set approach for computing solutions to incompressible two-phase flow. *J Comput Phys* 114:146–159
22. Udaykumar HS, Mittal R, Rampungoon P, Khanna A (2001) A sharp interface cartesian grid method for simulating flows with complex moving boundaries. *J Comput Phys* 174:345–380
23. van der Vorst H (1992) BiCGStab: a fast and smoothly converging variant of Bi-CG for the solution of nonsymmetric linear systems. *SIAM J Sci Comput* 13:631–644
24. Yang J, Balaras E (2006) An embedded-boundary formulation for large-Eddy simulation of turbulent flows interacting with moving boundaries. *J Comput Phys* 215:12–40
25. Yang J, Stern F (2014) Robust and efficient setup procedure for complex triangulations in immersed boundary simulations. *J Fluids Eng* 135(10):101107.1101107.11
26. Yang J, Stern F (2012) A simple and efficient direct forcing immersed boundary framework for fluidstructure interactions. *J Comput Phys* 231:5029–5061
27. Zhang J, Jackson TL (2009) A high-order incompressible flow solver with WENO. *J Comput Phys* 228:146–159

# Application of an Efficient Numerical Model for CO<sub>2</sub> Sequestration in Deep Saline Aquifers



P. Dinesh, M. R. Behera, P. G. Ranjith and N. Muthu

**Abstract** In this paper, the element-free Galerkin (EFG) method is applied to study the vertically averaged multiphase flow of CO<sub>2</sub> and brine in the deep saline aquifer. The methodology involves solving two governing partial differential equations (PDEs), namely pressure and saturation equations sequentially using implicit pressure and explicit saturation (IMPES) solution strategy. The governing PDEs are obtained by combining mass conservation (continuity equation) and momentum conservation (Darcy's law of multiphase extension) equations. In order to capture the asymptotic pressure behaviour near injection well, a local nodal refinement zone was introduced around the well. The computed pressure and average saturation were compared with an existing approximate grid-based FEM and extended FEM (XFEM) numerical solutions to demonstrate the robustness of the developed model.

**Keywords** Multiphase flow · Carbon sequestration  
Element-free Galerkin method · Caprock

## 1 Introduction

The rise in atmospheric CO<sub>2</sub> level causes global warming, melting of ice in the polar regions and, consequently, climate change. In order to store a large quantity of CO<sub>2</sub> in a subsurface, the best possible solution is injecting it into deep saline aquifers (sandstone) having brine (dissolved salts more than 5%) as the formation

---

P. Dinesh  
IITB-Monash Research Academy, IIT Bombay, Powai, 400076 Mumbai, Maharashtra, India

P. Dinesh · M. R. Behera (✉)  
Department of Civil Engineering, IIT Bombay, Powai, 400076 Mumbai, Maharashtra, India  
e-mail: [manasa.rb@iitb.ac.in](mailto:manasa.rb@iitb.ac.in)

P. Dinesh · P. G. Ranjith  
Department of Civil Engineering, Monash University, Melbourne, VIC 3800, Australia

N. Muthu  
Department of Mechanical Engineering, IIT Guwahati, Guwahati 781039, Assam, India

© Springer Nature Singapore Pte Ltd. 2019

K. Murali et al. (eds.), *Proceedings of the Fourth International Conference in Ocean Engineering (ICOE2018)*, Lecture Notes in Civil Engineering 22,  
[https://doi.org/10.1007/978-981-13-3119-0\\_45](https://doi.org/10.1007/978-981-13-3119-0_45)

water [1]. Thus, the injected CO<sub>2</sub> will get trapped over time in the aquifer by means of four different stages of trapping mechanisms namely, “structural and stratigraphic trapping, residual trapping, solubility trapping and mineral trapping and its dominating processes such as advection dominated multiphase behaviour (viscous, buoyant, capillary), dissolution and diffusion-based phase transfer processes and geochemical reactions will vary in a different period of time” [2].

The objectives of the present study are (a) to demonstrate the application of meshless methods, especially EFG for solving the coupled system of PDE equations in the vertically averaged multiphase flow model and (b) to accurately account for the pressure field near the injection well (discontinuity) in the domain.

The present study aims to obtain the pressure and saturation of the respective fluid phases by solving the carbon sequestration model in a deep saline aquifer using the nonlinear multiphase flow equations. The focus is based on solving the coupled PDEs of the vertically averaged multiphase flow model using one of the well-known EFG meshless methods. To the best of authors’ knowledge, this is the pioneering attempt to apply the meshless method (especially EFG) for solving the vertically averaged multiphase flow model in a horizontal aquifer with and without the consideration of local nodal refinement zone around the injection well present in the domain. As the shape functions used in EFG method are based on moving least square (MLS) approximants and higher order in nature [3, 4], EFG method can capture the pressure field reasonably well closer to the discontinuity with less number of nodal density than that of FEM.

## 2 The Essentials of the EFG Method

In this study, the meshless EFG method based on the MLS scheme which was developed by Belytschko et al. [5] is applied to study the vertically averaged multiphase flow equations in porous media. The following description of the essentials of the EFG method is same as reported in Muthu et al. [6] but is given here for the sake of completeness. Muthu is one of the co-authors of the current study. Unlike FEM, the element topology is lost in the EFG, and it helps to (a) generate the nodal shape functions used to approximate the solution and not to interpolate the solution as in the case of FEM and to (b) integrate the weak form of the governing boundary value problem. In this EFG method, a background mesh is used for domain integration and the MLS technique [3] is used to generate nodal shape functions [4]. Each support domain has a background mesh with its own sampling points or Gauss points of the required degree of polynomial to perform numerical integration. The support set for a sampling point is connected through nodes, and each node is initially assigned a compact domain of influence (DMI), through a bell-shaped weight function, which can be of a variety of shapes and sizes (circular, rectangular in 2D, fixed size or determined from the third closest node, and so on). The support set is used to generate the MLS shape functions to compute the field approximation [6]. Figure 1 shows the circular domains of influence of a fixed size ( $1.75 \times \delta$ ) where  $\delta$  is the distance between

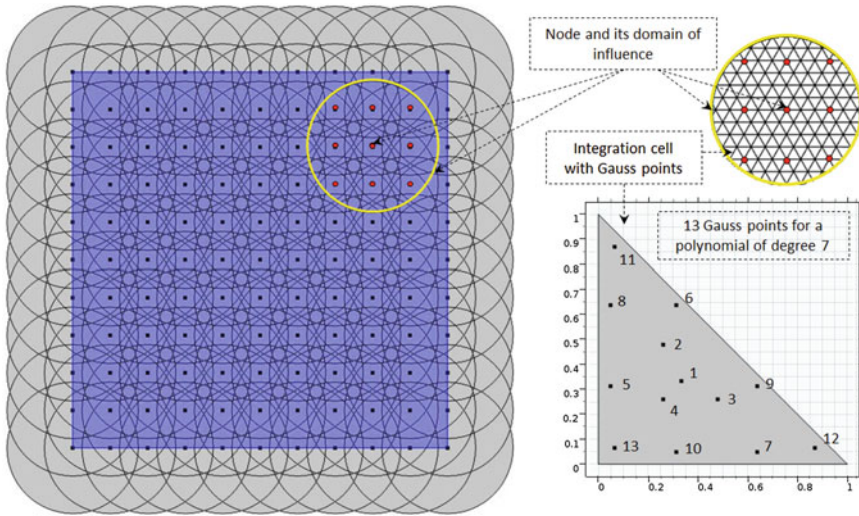


**Fig. 1** DMI for the field nodes with background integration cells and Gauss points

two adjacent nodes for a square-shaped aquifer domain having  $11 \times 11$  nodes with the closer view of a triangular background mesh or integration cells using 13 Gauss point quadrature of seventh-order polynomial.

The representation of the field variable in the EFG method follows the conventional FEM form. The bottom pressure ( $p_{bot}$ ) and height of brine ( $h_1$ ) in the coupled system of PDE equations in the vertically averaged multiphase flow model (will be discussed below) can be approximated with the MLS scheme method [6]. The MLS approximations are depending on the set of coefficients, a weight function and a polynomial basis. The MLS approximation for the bottom pressure and height of brine can be written as  $\hat{p}_{bot}(x)$  for  $p_{bot}(x)$  and  $\hat{h}_1(x)$  for  $h_1(x)$ , respectively. Let us write the approximation for a general variable, e.g.  $\hat{u}(x)$  for  $u(x)$ , which can be evaluated at a point  $x \in \Omega$  as

$$u(x) \approx \hat{u}(x) = \sum_{j=1}^m p_j(x)a_j(x) = p^T(x)a(x) \quad (j = 1, 2, \dots, m), \quad (1)$$

where  $P(x)$  is a standard complete polynomial of order  $m$ . In this study, a linear basis is used in two dimensions of the form,  $p^T(x) = [1 \ x \ y]$ . The term “Moving” in MLS refers to the varying coefficient vector with spatial coordinates. The term  $a(x)$  is the unknown coefficient vector, and it can be determined using the weighted residual least square technique.

$$a(x) = A^{-1}(x)B(x)u \quad (2)$$

where the matrices  $A(x)$  and  $B(x)$  can be expanded as,

$$A(x) = \sum_{k=1}^N W(x - x_k)p(x_k)p^T(x_k) = \sum_{k=1}^N W(x - x_k) \begin{bmatrix} 1 & x_k & y_k \\ x_k & x_k^2 & x_k y_k \\ y_k & x_k y_k & y_k \end{bmatrix},$$

$$B(x) = W(x - x_k)p(x_k) = W(x - x_k) \begin{pmatrix} 1 \\ x_k \\ y_k \end{pmatrix}, \quad (k = 1, 2, \dots, N);$$

where  $N$  is the total number of nodes in the domain. At each Gauss point  $x$ , the residual is minimized with respect to the unknown coefficient vector  $a(x)$ .  $x_k$  is coordinate of the node in the domain. The term  $W$  is the weight/window or the kernel function, and it is necessary to obtain shape functions. The weight function must have a *compact support* which is also known as dilatation parameter or smoothing length or domain of influence (DMI). The compact support gives the local behaviour of the meshless methods. It is analogous to the element size in the FEM [7]. In this study, the weight function at any given point in two dimensions is obtained using the cubic B-spline with a circular domain of influence [8] as shown below:

The cubic B-spline weight function is given by

$$W(r) = \begin{cases} \frac{2}{3} - 4r^2 + 4r^3 & \text{for } r \leq \frac{1}{2} \\ \frac{4}{3} - 4r + 4r^2 - \frac{4}{3}r^3 & \text{for } \frac{1}{2} < r \leq 1 \\ 0 & \text{for } r > 1 \end{cases} \quad (3)$$

$$W(x - x_I) = W(r) = W\left(\frac{\|x - x_I\|}{R_{dmi}}\right) \quad (4)$$

where  $R_{dmi}$  is the radius of the domain of influence of node  $I$ , ( $R_{dmi} = 1.75 \times \delta$ ). Finally, substituting the above-obtained unknown coefficient vector Eq. (2)  $a(x)$  into the approximation Eq. (1) leads to the MLS-based EFG shape function that can be written as

$$\hat{u}(x) = \sum_{j=1}^m p^T(x)A^{-1}(x)B(x)u = \sum_{k=1}^N N_k(x)u_k \quad (k = 1, 2, \dots, N), \quad (5)$$

where  $N_k$  is the shape function or basis function of the MLS approximation of node  $k$  which is given by

$$N_k(x) = p^T(x)A^{-1}(x)B_k(x), \quad (6)$$



### 3 The Governing Equations and Its EFG Solution Methodology

The governing PDE of the vertically averaged multiphase flow model for pressure and saturation equations is developed by combining the mass conservation (continuity equation) for brine and CO<sub>2</sub> that are combined with the momentum conservation (multiphase extension of Darcy’s law) equation. Figure 2 shows the description of the terms involved in the governing equation and its pictorial representation of a conceptual CO<sub>2</sub> sequestration model in the saline aquifer and its defining parameters. The governing equations were obtained using the below simplifying assumptions and its detailed explanation with derivation that can be found in the literature [9–12].

- (a) Both pore fluids (brine and CO<sub>2</sub>) and solid matrix are incompressible.
- (b) Fluid properties such as viscosity and density are constant.
- (c) The sharp interface exists between the fluids which separate them by gravity and leads to simple linear functions of average saturation (or effective relative permeability), and capillary pressure is zero.
- (d) Vertical pressure variation exists across the depth of the aquifer.
- (e) Thermal, mechanical and chemical effects are negligible.

The mass balance equations for the brine and CO<sub>2</sub> phases in the aquifer are similar to Ladubec et al. [12]:

$$\begin{aligned} \phi(1 - S_{res,1}) \frac{\partial h_1}{\partial t} + \nabla \cdot \vec{u}_1 &= 0 \\ \phi(1 - S_{res,1}) \frac{\partial h_2}{\partial t} + \nabla \cdot \vec{u}_2 &= q_2 \end{aligned} \tag{7}$$

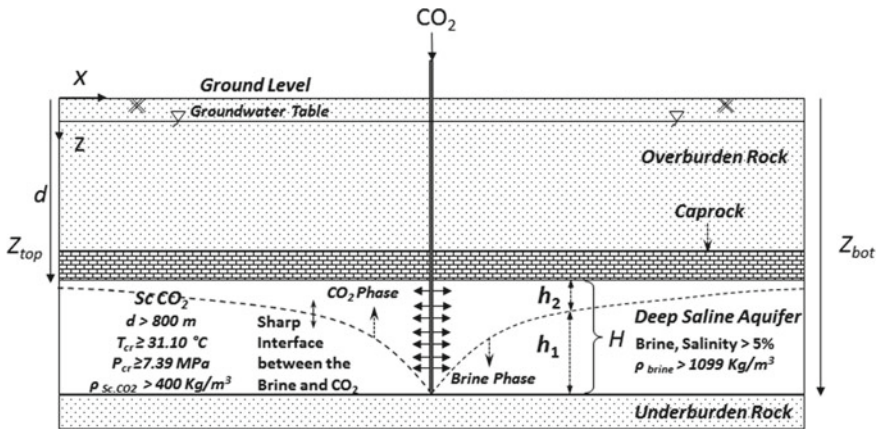


Fig. 2 A conceptual diagram of CO<sub>2</sub> sequestration model with defining parameters

where the subscripts 1 and 2 are for wetting phase (brine) and non-wetting phase (CO<sub>2</sub>),  $\phi$  is the porosity of the aquifer,  $S_{res,1}$  is residual saturation of the brine,  $h_1(x, y, t)$  is the depth of CO<sub>2</sub> from  $Z_{top}(x, y)$ ,  $h_2(x, y, t)$  is the depth of brine from  $Z_{bot}(x, y)$ , the total aquifer depth is  $H = h_1 + h_2$ , and  $q_2(x, y, t)$  is the source term or recharge rate to account for the injection of CO<sub>2</sub> into the aquifer as a point source,

$$q_2 = \sum_{i=1}^n Q_2 \delta(x - x_i) \tag{8}$$

where  $Q_2$  is the rate of injection (e.g. m<sup>3</sup>/day),  $\delta(x - x_i)$  is the Dirac delta function and  $i = (1, 2, \dots, n)$  is the number of wells in the domain.  $\vec{u}_1(x, y, t)$  and  $\vec{u}_2(x, y, t)$  are the vector representations of vertically averaged brine flux and CO<sub>2</sub> flux, respectively, and it can be written using the multiphase extension of Darcy’s Law

$$\begin{aligned} \vec{u}_1 &= -h_1 \frac{k}{\mu_1} (\nabla p_{bot} + \rho_1 g \nabla z_{bot}) \\ \vec{u}_2 &= -h_2 \frac{kk_{r2}}{\mu_2} (\nabla p_{bot} - \rho_1 g \nabla H + \Delta \rho g \nabla h_2 + \rho_2 g \nabla z_{top}) \end{aligned} \tag{9}$$

where  $p_{bot}(x, y, t)$  is the bottom pressure acting on the  $Z_{bot}(x, y)$  plane, and it is evolved due to the injection of CO<sub>2</sub> into the brine-filled aquifer;  $k$  is the intrinsic permeability tensor of the aquifer;  $\mu_1$  and  $\mu_2$  are the dynamic viscosities of the respective phases;  $\Delta \rho = \rho_1 - \rho_2$  is the density difference between fluids; and  $g$  is the acceleration due to gravity. Therefore, by substituting  $\vec{u}_1$  and  $\vec{u}_2$  into the corresponding mass balance equations, we can get the governing mass balance equations for the respective phases as written as,

$$\begin{aligned} \phi(1 - S_{res,1}) \frac{\partial h_1}{\partial t} + \nabla \cdot \left( -h_1 \frac{k}{\mu_1} (\nabla p_{bot} + \rho_1 g \nabla z_{bot}) \right) &= 0 \\ \phi(1 - S_{res,1}) \frac{\partial h_2}{\partial t} + \nabla \cdot \left( -h_2 \frac{kk_{r2}}{\mu_2} (\nabla p_{bot} - \rho_1 g \nabla H + \Delta \rho g \nabla h_2 + \rho_2 g \nabla z_{top}) \right) &= q_2 \end{aligned} \tag{10}$$

### 3.1 Pressure Equation

The pressure equation is obtained by summing the individual phases of mass balance equations, and its simplicity results in a single equation without a time derivative [12]. Because it is convenient to sum the phase equations, “this summed equation is sometimes called the total pressure equation, or simply the pressure equation” [13].

$$\phi(1 - S_{\text{res},1}) \frac{\partial(h_1 + h_2)}{\partial t} + \nabla \cdot \vec{u}_1 + \nabla \cdot \vec{u}_2 = q_2$$

$$\nabla \cdot \vec{u}_T = q_2, \quad \text{where } \vec{u}_T = \vec{u}_1 + \vec{u}_2 \quad (11)$$

$$\nabla \cdot \left( -h_1 \frac{k}{\mu_1} (\nabla p_{\text{bot}} + \rho_1 g \nabla z_{\text{bot}}) \right)$$

$$+ \nabla \cdot \left( -h_2 \frac{k k_{r2}}{\mu_2} (\nabla p_{\text{bot}} - \rho_1 g \nabla H + \Delta \rho g \nabla h_2 + \rho_2 g \nabla z_{\text{top}}) \right) = q_2 \quad (12)$$

The first term in Eq. (11) is equal to zero because aquifer depth is constant over time (neglecting the mechanical effect). Therefore, the sum of saturation is equal to 1 or the depth of aquifer. The summation of depth-averaged total flux is equal to  $\vec{u}_T$ . The boundary conditions for the pressure equation can be specified as the Dirichlet boundary condition (specified pressure,  $p_{\text{bot}}$ ) or Neumann boundary condition (specified flux,  $\vec{u}_1$  and  $\vec{u}_2$ ) throughout the boundary, or combination of both can be distributed throughout the boundary depending upon the type of problem interest. In this study, the specified pressure boundary condition is used throughout the study.

### 3.2 Saturation Equation

The saturation equation is taken as one of the phases of mass balance equations. In this study, the brine phase is taken as the saturation equation,

$$\phi(1 - S_{\text{res},1}) \frac{\partial h_1}{\partial t} + \nabla \cdot \vec{u}_1 = 0$$

$$\phi(1 - S_{\text{res},1}) \frac{\partial h_1}{\partial t} + \nabla \cdot \left( -h_1 \frac{k}{\mu_1} (\nabla p_{\text{bot}} + \rho_1 g \nabla z_{\text{bot}}) \right) = 0 \quad (13)$$

The boundary conditions for the saturation equation can be specified as the Dirichlet boundary condition. Initially, the aquifer depth is fully saturated with brine, i.e. ( $H = h_1$  at the time,  $t = 0$ ). The average saturation for the brine phase— $S_1 = h_1/H$  and for CO<sub>2</sub> phase— $S_2 = h_2/H$  (i.e.  $S_1 + S_2 = 1$  or  $h_1 + h_2 = H$ ).

### 3.3 Initial and Boundary Conditions

The aquifer is initially filled with brine before the CO<sub>2</sub> injection starts; therefore, the initial condition will be the height of brine (i.e.  $h_1(x, 0) = H$ ) and its respective hydrostatic equilibrium pressure will be considered throughout the aquifer domain. Dirichlet boundary conditions of the hydrostatic pressure (i.e.  $\rho g H$ ) and the height of the aquifer are equal to the height of brine (i.e.  $h_1(x, t) = H$ ) and are applied to the pressure and saturation equations, respectively, in this study along the whole

boundary of the domain. One of the difficulties associated with the EFG method is an imposition of Dirichlet or EBCs due to the lack of Kronecker delta property for shape functions. Several methods based on the modification of the weak form and modified shape functions have been proposed by researchers to overcome this problem. Some of the popular techniques are the Lagrange multiplier method, the penalty function method and Nitsche’s method [5]. In this study, the Lagrange multiplier method is used to enforce EBC for pressure and saturation equation.

**Imposition of Source Node or Injection Well**

The source node or injection well is positioned exactly matching over the field node. The injection rate (source term  $q_2$  in the pressure Eq. 8) is distributed among the influence nodes using EFG shape function that falls under the domain of influence due to the source node. If the problem domain involves multiple injection wells, their injection rate will be distributed correspondingly to its adjacent influence nodes that fall under its support domain. Figure 3 shows the square aquifer domain having a source node at its centre with the circular domain of influence with its nodal size shown in the first row (\*) of Table 1. The size of DMI is getting reduced in the refined nodal density having  $15 \times 15$  central nodal patch around the source node than that of the unrefined node as shown in Table 1.

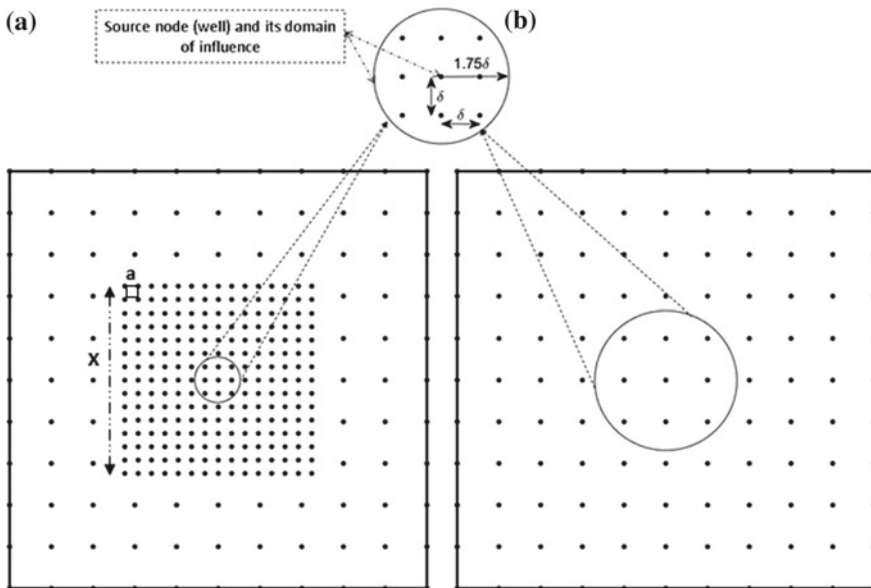


**Fig. 3** An imposition of the source or well node and its domain of influence for the central source node **a** with and **b** without nodal refinement

**Table 1** Geometrical property of local nodal refinement around the injection well

<i>n</i>	Divisions ( <b>10 × <i>n</i></b> ) div 1 div = 3.2 m	Distance between two nodes ( <b><i>a</i> = 32/<i>n</i></b> ) m		Side length of the square refinement zone ( <b><i>X</i> = 14 × <i>a</i></b> ) m	
1*	10 div (11 × 11 nodes)	32	m	448	m
2	20 div (21 × 21 nodes)	16	m	224	m
4	40 div (41 × 41 nodes)	8	m	112	m
5	50 div (51 × 51 nodes)	6.4	m	89.6	m
7	70 div (71 × 71 nodes)	4.571	m	64	m
10	100 div (101 × 101 nodes)	3.2	m	44.8	m
14	140 div (141 × 141 nodes)	2.286	m	32	m

\* This grid is shown in Fig. 3

### 3.4 Discrete System of Equations

The weak form of the governing coupled system of PDE equations in the vertically averaged multiphase flow model follows the similar work of Ladubec et al. [12]. The discrete system of the equation obtained using EFG shape functions will be required to solve for pressure and saturation by substituting it into the corresponding weak form governing PDE. Then, the derived PDE with appropriate initial and boundary conditions will be discretized both spatially (EFG) and temporally (FDM) using the Bubnov–Galerkin weak form method and Crank–Nicolson scheme ( $\theta = 0.5$ ), respectively. The discrete system of pressure and saturation equations which are formulated using the Galerkin’s formulation of a weighted residual principle with MLS approximation leads to,

$$\iint_{\Omega} [N]^T (\nabla \cdot \vec{u}_1 + \nabla \cdot \vec{u}_2 - q_2) d\Omega = 0 \tag{14}$$

$$\iint_{\Omega} [N]^T \left( \phi (1 - S_{res,1}) \frac{\partial h_1}{\partial t} + \nabla \cdot \vec{u}_1 \right) d\Omega = 0 \tag{15}$$

where  $[N]$  is the MLS shape function. After substituting the flux terms  $\vec{u}_1$  and  $\vec{u}_2$  in the above equations, the unknowns of bottom pressure  $p_{bot}$  and height of brine  $h_1$  can be obtained in an equivalent manner as Ladubec et al. [12],

$$K_p p_{bot} = F_p = F_{p1} + F_{p2} + F_{p3} + F_{p4} \tag{16}$$

$$[C_S] \left\{ \frac{\partial h_1}{\partial t} \right\} + [K_S] \{h_1\} = F_s \tag{17}$$

Combining the above two equations in matrix form, it can be written as,

$$\begin{bmatrix} 0 & 0 \\ 0 & C_S \end{bmatrix} \begin{Bmatrix} \dot{p}_{bot} \\ \dot{h}_1 \end{Bmatrix} + \begin{bmatrix} K_p & 0 \\ 0 & K_S \end{bmatrix} \begin{Bmatrix} p_{bot} \\ h_1 \end{Bmatrix} = \begin{Bmatrix} F_p \\ F_s \end{Bmatrix} \tag{18}$$

where

$$K_{p,IJ} = \iint_{\Omega} B_I^T \left( \frac{h_1}{\mu_1} + \frac{h_2 k_{r2}}{\mu_2} \right) k B_J d\Omega \tag{19}$$

$$F_p = \begin{cases} F_{p1,I} = \iint_{\Omega} N_I^T q_{c,inj} d\Omega \\ F_{p2,I} = - \oint_{\Gamma} N_I^T (\vec{u}_1 + \vec{u}_2) n d\Gamma \\ F_{p3,I} = - \iint_{\Omega} B_I^T \frac{k k_{r2}}{\mu_2} \Delta \rho g h_2 \nabla h_2 d\Omega \\ F_{p4,I} = \iint_{\Omega} B_I^T \left( h_2 \frac{k k_{r2}}{\mu_2} (\rho_1 g \nabla H - \rho_2 g \nabla z_{top}) - h_1 \frac{k}{\mu_1} \rho_1 g \nabla z_{bot} \right) d\Omega \end{cases} \tag{20}$$

$$C_S = \iint_{\Omega} N^T \phi (1 - S_{res,1}) N d\Omega \tag{21}$$

$$F_s = \oint_{\Gamma} N^T \vec{u}_1 n d\Gamma \tag{22}$$

$$K_S = K_{adv} + K_{SU}; K_{adv} = \iint_{\Omega} B^T \frac{k}{\mu_1} (\nabla p_{bot} + \rho_1 g \nabla z_{bot}) N d\Omega \tag{23}$$

$$K_{SU} = \iint_{\Omega^e} B^T \tau \frac{H}{\phi(1 - S_{res,1})} \frac{k}{\mu_1} |\nabla p_{bot} + \rho_1 g \nabla z_{bot}| B d\Omega \tag{24}$$

$K_p$  is the stiffness matrix or pressure diffusion of the aquifer, and it can be written in expanded form as follows;  $F_p$  is the total flux vector which is composed of:  $F_{p1}$ —the injection vector,  $F_{p2}$ —the boundary flux vector,  $F_{p3}$ —the buoyancy vector,  $F_{p4}$ —the aquifer slope vector. The term  $K_{adv}$  is the advection matrix,  $K_{SU}$  is the additional artificial diffusion term to stabilize the saturation equation, following the work of Ladubec et al. [12], and  $\tau$  is the very crucial parameter that controls the numerical oscillation. Therefore, depending upon the selection of  $\tau$  value, the solution will keep changing. In the next section, we have identified ways to correctly predict the value of  $\tau$  especially for EFG-based meshless methods.  $N$  and  $B$  are shape

functions and the shape function derivatives for a node in its domain of influence using the EFG method.

Finally, the strongly coupled system of equations obtained from the discretization of pressure (16) and saturation Eqs. (17) is solved using the implicit pressure and explicit saturation (IMPES) or single-step (SS) solution strategy [12, 14] as shown in Fig. 4. In this method, the pressure equation is first solved by assuming that the initial height of brine is same as the height of the aquifer. Then, for each time step, the saturation equation is solved and it is getting updated from the solution of previous time step pressure equation. The pressure solution is sequentially computed using the solution of current time step saturation equation. Thus, the pressure and saturation solutions are obtained for every time step till it reaches the end of the simulation time period. The integrals appear in the weak form of governing PDE can be evaluated by using numerical Gaussian integration. The location of the sampling points and their corresponding weights are taken from Dunavant [15] for performing numerical integration of pressure and saturation equations. In this study, fifth order is used and it itself gives accurate results and increasing its polynomial order to a seventh degree slightly improves the accuracy of numerical integration.

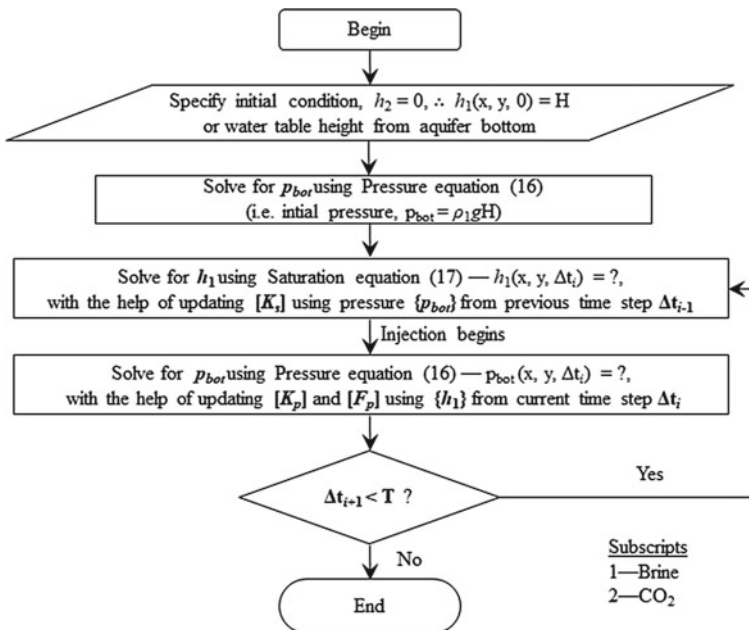


Fig. 4 IMPES or single-step solution strategy [12, 14]

## 4 Application of Element-Free Galerkin Method

This section aims to fix the stabilization parameter ( $\tau$ ) and maximum Courant number ( $Cr_{\max}$ ) to perform the mesh (nodal)-independent study. The fixation of Courant number helps us to select the maximum time step for a corresponding nodal distribution in EFG (similar to an element size in FEM). Finally, these fixed values are used to demonstrate the application of the present EFG model for solving a simple square-shaped horizontal aquifer problem.

### 4.1 Stabilization Parameter Study

The stabilization parameter term  $\tau$  appearing in the  $[K_{SU}]$  Eq. (24) needs to be fixed to control numerical oscillations occur while solving the advective nature of saturation equation. This term needs to be fixed for a constant Courant number to perform nodal independence analysis. The Courant number can be obtained from the following expression,

$$Cr_{\max} = \frac{\|a\| \Delta t}{h^e} \quad (25)$$

where  $a$  is the advective velocity and  $h^e$  is the element size which is equal to the total length of the domain divided by the number of divisions in the respective coordinate direction for uniformly distributed nodes. In this study, the field nodes are uniformly distributed in both x and y directions.

$$a = -\frac{k}{\phi(1 - S_{res,1})\mu_1} (\nabla p_{bot} + \rho_1 g \nabla z_{bot}) \quad (26)$$

The existing benchmark XFEM model was adopted from Ladubec et al. [12] to validate the developed EFG model. The top and cross-sectional views of the conceptual horizontal model are shown in Fig. 5. The pressure plot for different nodal divisions at the beginning of the injection is shown in Fig. 6. In this model, the water table is placed on the top of the aquifer. In general, any confined aquifer, the water table height will be above the piezometric height and its effect will get simply added by the pressure solution using the corresponding hydrostatic pressure boundary conditions. The aquifer and fluid properties are shown in Table 2.

The advective velocity  $a$  is obtained from the pressure solution of several nodal divisions as shown in Fig. 6. The pressure gradient  $(\nabla p_{bot})_{\max}$  is maximum after the first time step pressure solution, or in other words at the start of the injection. In this study, the maximum velocity is taken from the pressure gradient occurring near the well, which is almost same at a particular location (say at 680 m in  $x$ -axis) irrespective of the nodal divisions. After calculating the advective velocity from  $(\nabla p_{bot})_{\max}$ , the



**Fig. 5** Set-up of the horizontal aquifer problem adapted from Ladubec et al. [12]

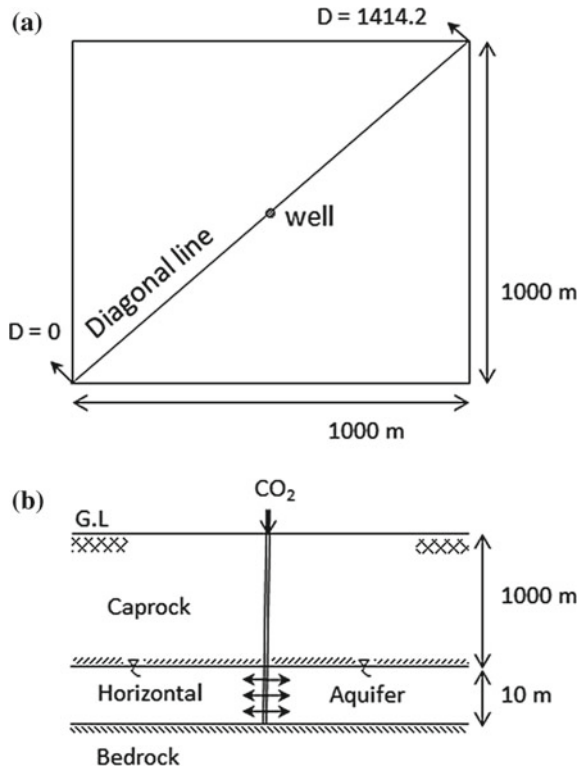


**Table 2** System properties used in the model example problem adapted from Ladubec et al. [12]

Property	Value	Units
$\mu_1$	$5.11e-4$	N s/m <sup>2</sup>
$\mu_2$	$6.11e-5$	N s/m <sup>2</sup>
$\rho_1$	1099	kg/m <sup>3</sup>
$\rho_2$	400	kg/m <sup>3</sup>
$S_{res,1}$	0	–
$\phi$	0.15	–
$k$	$1e-15$	m <sup>2</sup>
$k_{r,2}$	1	–
$q_2$	1600	m <sup>3</sup> /d

time step for different element sizes (the minimum distance between the two field nodes in the respective direction) can be determined using known Courant number.

Table 3 shows the relative error for pressure and head for three days of CO<sub>2</sub> injection into the horizontal aquifer of EFG  $41 \times 41$  nodal density (40 divisions) model results compared against the FEM  $150 \times 150$  elements (150 divisions) results

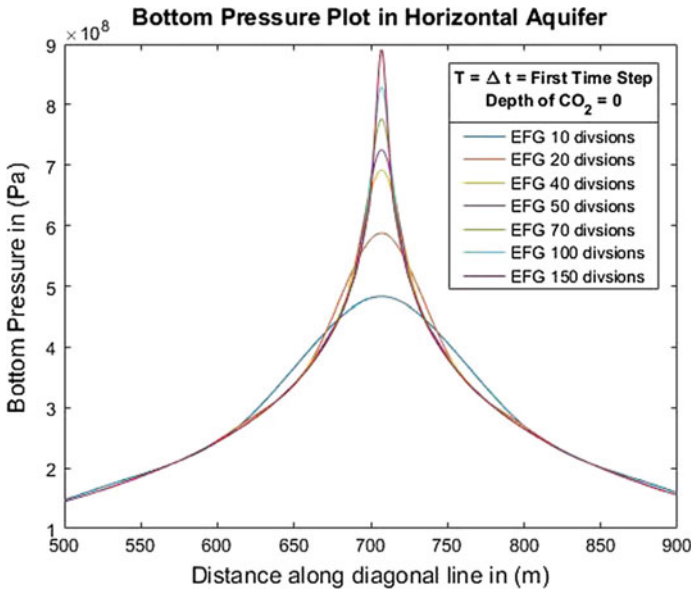


**Fig. 6** Bottom pressure plot at the beginning of the injection for different nodal densities

of Ladubec et al. [12]. The relative error for pressure is calculated at far-field location (at 500 m), and that of head or height of CO<sub>2</sub> from the top of the aquifer is calculated at well location (at 707 m) along the diagonal line. The individual cell values in the table show first the relative error for pressure and then the relative error for the height of CO<sub>2</sub> with respect to FEM 150 × 150 results of Ladubec et al. [12] in three days of CO<sub>2</sub> injection into the horizontal aquifer. Three days’ result of the height of CO<sub>2</sub> shows that EFG 40 divisions can capture FEM 150 divisions of benchmark results with a very less relative error. The idea of finding minimum  $\tau$  and maximum  $\Delta t$  is to fix the parameters for nodal-independent analysis. When the value of  $\tau$  is increased, pressure increases and correspondingly head decreases due to overdiffusion or damping of the head. With less  $\tau$  value and increased Courant number (maximum  $\Delta t$ ), obtained solution will be smooth represented as “S” and there are no oscillations; if there are oscillations in the solution, then it is represented as “O” in the table values. It is evident from the tables that as the value  $\tau$  increases the simulation results are smooth. But in case of the decreased value of  $\tau$ , the simulation results are getting oscillated. Figures 7 and 8 show the relative error plot for Table 2 results of pressure and saturation. It is understood from Fig. 7 that the relative error is approaching a minimum value for the time step 0.5 and the corresponding stabilization parameter in the range of 0.15–0.20. In this numerical study, even using the less conservative  $\tau$  value of 0.2 itself shows the better result which is highlighted in the below Figs. 7 and 8 using the square box.

Figures 9 and 10 show the results of the horizontal aquifer simulated for 3 days with the time step of 0.5 day for the various stabilization parameter ( $\tau$ ) from Table 3.

**Table 3** Simulation results after 3 days of CO<sub>2</sub> injection for  $\tau = 0.5$  and the SS method  
 $\tau$  (three-day horizontal aquifer EFG results are compared with Ladubeac et al. [12] of FEM 150  $\times$  150)

$\Delta t$ (days)	$C_{r\text{-max}}$	Relative Error = $\frac{ E_{EFG} - E_{FEM} }{E_{FEM}} \times 100$									
		Values in the table show the relative error (pressure at far field in %, height of CO <sub>2</sub> at injection well in %)									
		0.05	0.10	0.15	0.2	0.25	0.3	0.35	0.4		
0.25	0.1890	O	S (0.19%, 3.68%)	S (0.46%, 11.08)	S (0.69%, 17.29%)	S (0.89%, 22.54%)	S (1.06%, 27.01%)	S (1.22%, 30.85%)	S (1.37%, 34.19%)		
0.5	0.3780	O	S (0.48%, 0.65%)	S (0.13%, 8.95%)	S (0.12%, 15.79%)	S (0.31%, 21.50%)	S (0.47%, 26.30%)	S (0.61%, 30.39%)	S (0.73%, 33.91%)		
1	0.7560	O	O	S (0.08%, 1.35%)	S (0.13%, 10.66%)	S (0.25%, 18.40%)	S (0.32%, 24.88)	S (0.38%, 30.36%)	S (0.43%, 35.02%)		
1.5	1.134	O	O	O	O	O	O	O	S (0.63%, 2.06%)		

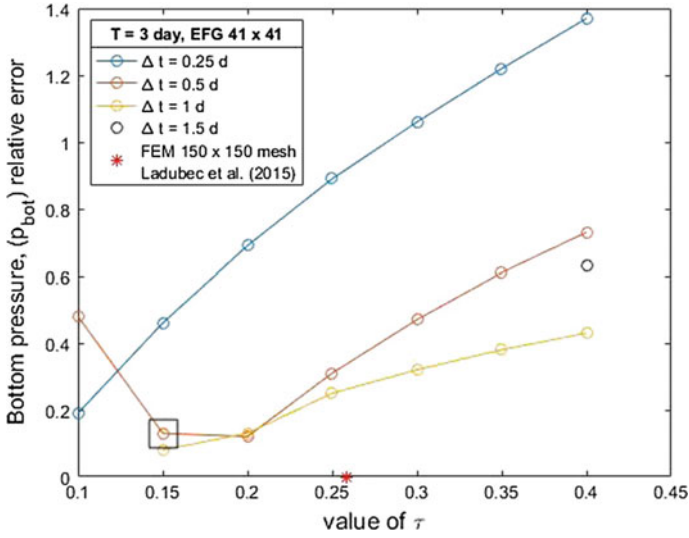


Fig. 7 Relative error plot for far-field bottom pressure and its effect on  $\tau$

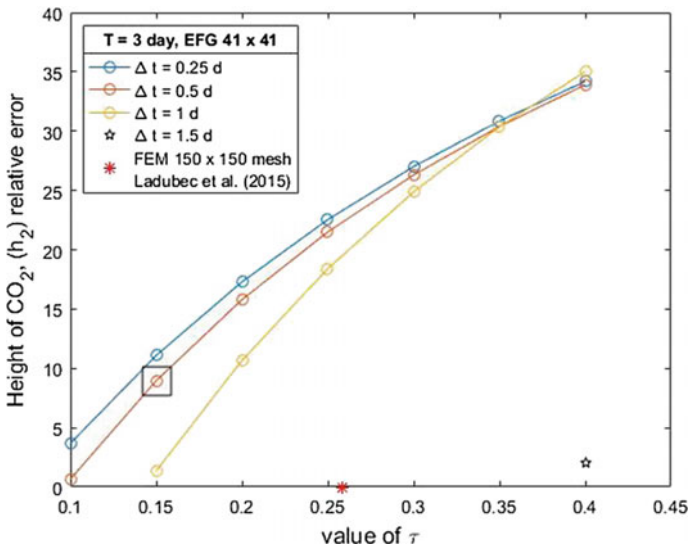
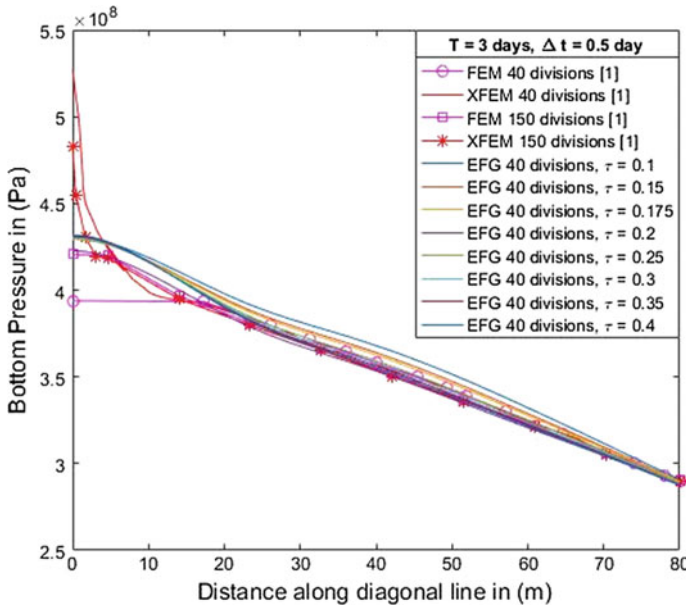


Fig. 8 Relative error plot for the height of CO<sub>2</sub> at the injection well and its effect on  $\tau$

This depicts that the height of CO<sub>2</sub> matches very well with the Ladubec et al. [12] results at the well location with a less relative error. At the same time, the pressure results are not matching at the well location due to its asymptotic variation pressure behaviour near the well. From these simulation results, the value of  $\tau$  can be specified as the range in between 0.15 and 0.2 for EFG. The value 0.15 is a conservative result.



**Fig. 9** Bottom pressure plot along the diagonal line from the centre of the well and its effect on  $\tau$

But in this research, even the less conservative value 0.2 shows the best comparison results. From these numerical experiments, the values of  $\tau$  and  $Cr_{max}$  are fixed as the 0.2 and 0.3780 for EFG meshless analysis.

### 4.2 The Nodal Independence Study

The accuracy of the pressure results near the well can be improved by introducing a local nodal refinement zone near the well. The comparative results with the relative error for pressure are shown below without and with local nodal refinement.

#### Without Refinement

Figure 11 shows the pressure plots for different nodal divisions of 20, 40, 50, 70, 100 and 140 without refinement. The results of 20 divisions are unphysical because the height of CO<sub>2</sub> exceeds the aquifer height. Therefore, the minimum nodal divisions will be 40 which can capture the higher nodal discretization with a less relative error. Figure 12 shows the improvement in the increasing trend of the pressure results as we increase the nodal divisions 40–140 and its corresponding decreasing trend of relative error was estimated with respect to 140 nodal divisions’ result.

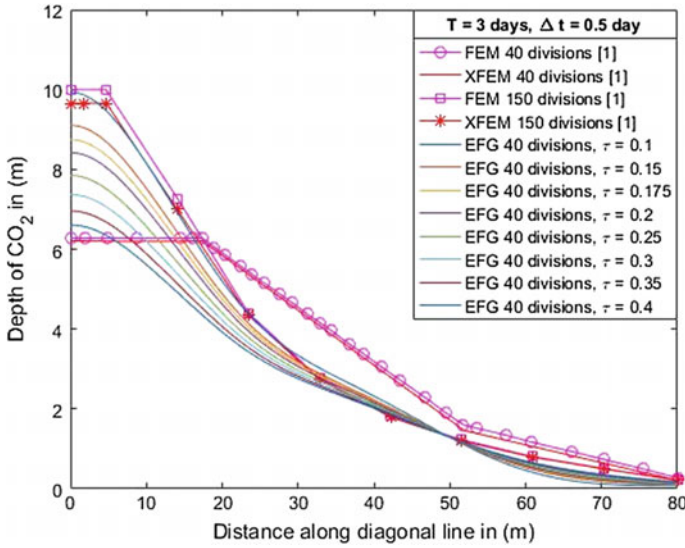


Fig. 10 Height of CO<sub>2</sub> along the diagonal line from the centre of the well and its effect on  $\tau$

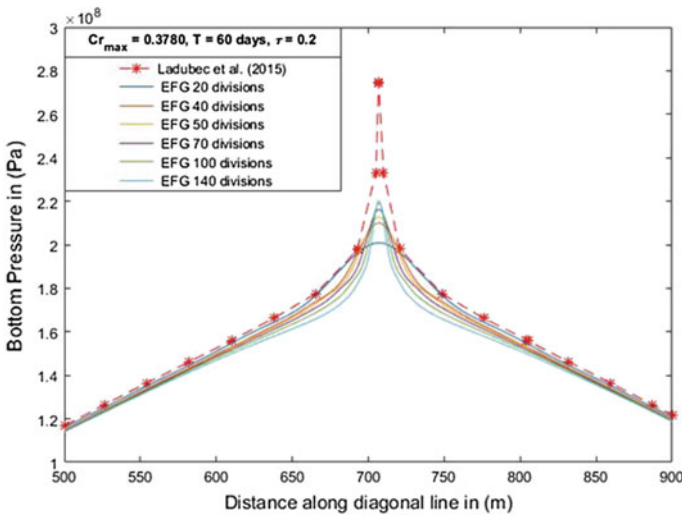


Fig. 11 Bottom pressure plot for different nodal divisions

### With Refinement

Figure 13 shows the local EFG nodal refinement of  $15 \times 15$  nodal density with its position around the central well node. Figure 14 shows the pressure distribution for different nodal divisions of 20, 40, 50, 70, 100 and 140 with its nodal refinement around the central well node. The results of 20 divisions with refinement were suffi-

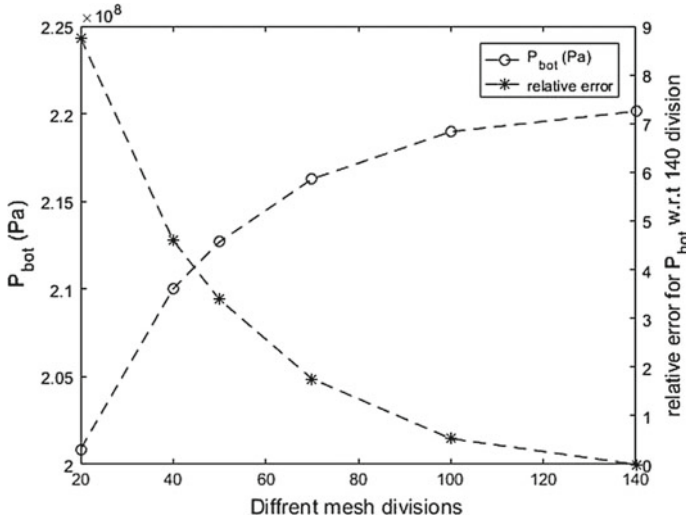


Fig. 12 Bottom pressure and its relative error plot for different nodal divisions

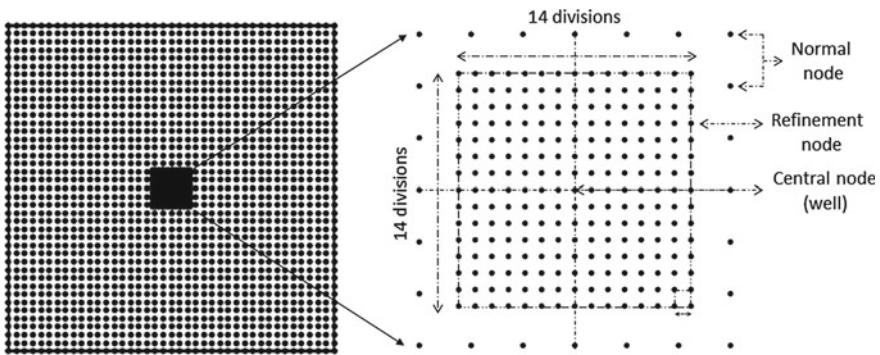


Fig. 13 Local EFG nodal refinement properties with its position around the injection well as a centre node

cient to capture the height of CO<sub>2</sub> within the aquifer height. But in our simulations, the minimum nodal divisions of 40 are adapted to better capture the pressure variation near the well. Figure 15 shows the improvement in the increasing trend of the pressure results as we increase the nodal divisions 40–140 and its corresponding decreasing trend of relative error was estimated with respect to 140 nodal divisions’ result.

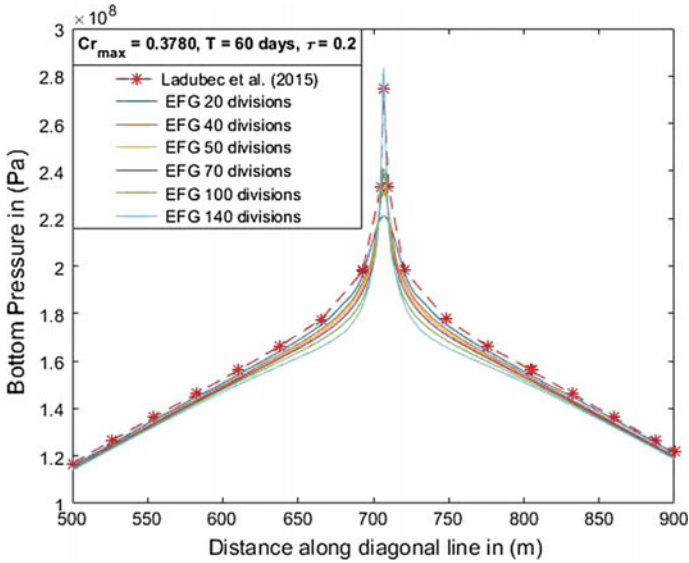


Fig. 14 Bottom pressure plot for different nodal divisions with refinement

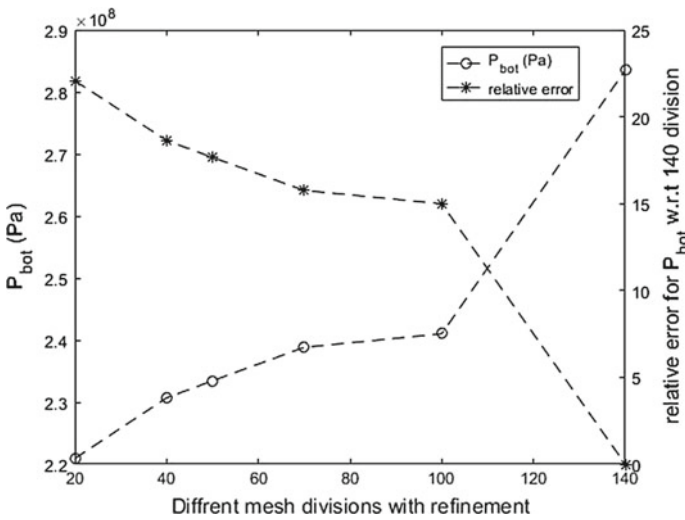
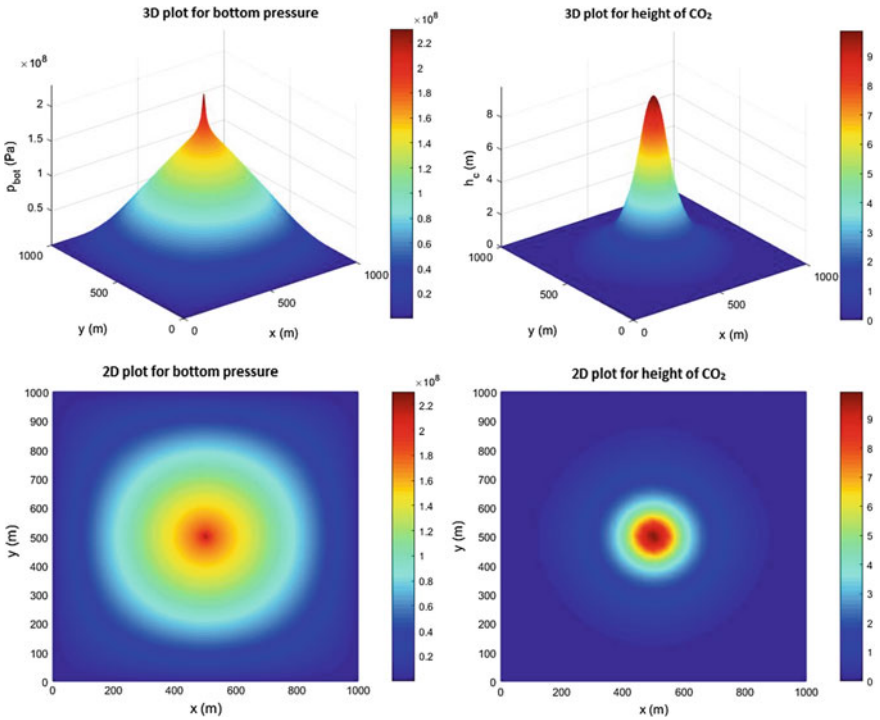


Fig. 15 Bottom pressure and its relative error plot for different nodal divisions with refinement

### 5 Numerical Result

In this section, the simulations were performed for 60 days of CO<sub>2</sub> injection with the same aquifer and fluid properties shown in Table 2, and the value of  $\tau$  is taken as 0.2 throughout the simulations. The simulation results were carried out for the





**Fig. 16** 3D and 2D plot for pressure and saturation after 60 days of injection in the horizontal aquifer

square-shaped horizontal aquifer domain having 40 nodal divisions ( $41 \times 41$  nodal density) with local nodal refinement around the injection well. Initially, the aquifer pressure ( $1099 \times 9.81 \times 10 = 107811.9$  Pa) was in an equilibrium state. Once the injection started (i.e. at the beginning of the injection), the pressure in the aquifer reached its maximum value at the injection well; consequently, the aquifer system was not in an equilibrium state. At the same time, the pressure in the far field and in the system boundary was much lower than that at the injection well. This difference in the pressure over a length of the domain (i.e. pressure gradient) caused the CO<sub>2</sub> plume to spread radially outward and enter the aquifer and consecutively displaced the in situ or formation brine from its own position. Thus, the pressure in the aquifer tried to attain an equilibrium state in a pressure diffusion process during the injection as well as after the injection. The CO<sub>2</sub> saturation started spreading radially outward after the injection began. Figure 16 shows the 3D and 2D plot of pressure and saturation of the square-shaped horizontal aquifer after 60 days of CO<sub>2</sub> injection. Figures 17 and 18 show the comparison of pressure and saturation results of present EFG model with Ladubec et al. [12]. It is evident from the results that the pressure field near the well with local refinement is captured accurately. However, these field variables (pressure and saturation) are matching very well with those in the study of Ladubec et al. [12].

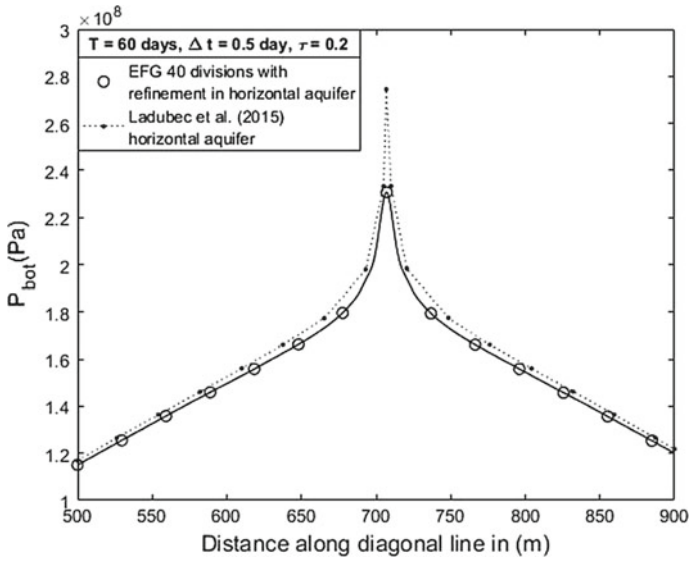


Fig. 17 EFG pressure distribution after 60 days of injection in a square-shaped horizontal aquifer

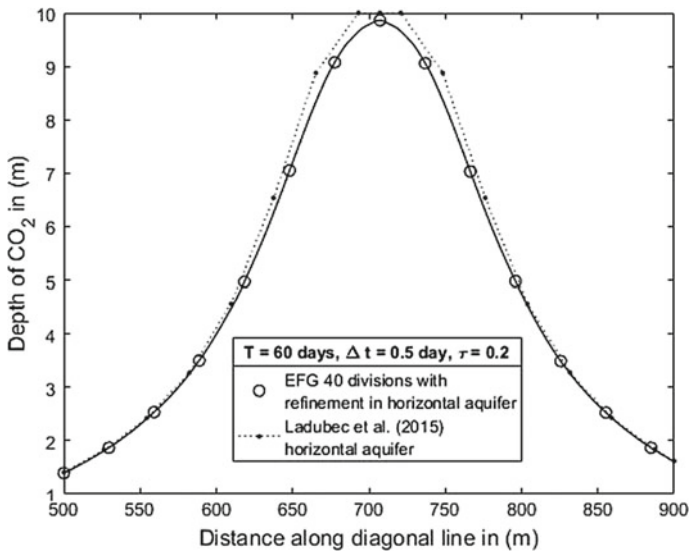


Fig. 18 EFG saturation distribution after 60 days of injection in a square-shaped horizontal aquifer

## 6 Conclusions

The present study demonstrated the application of the EFG method to solve the coupled system of PDEs in the vertically averaged multiphase flow model. In order to accurately account for the strong discontinuity in the pressure field, EFG formulations were developed with and without considering a local refinement zone around the injection well. The developed model is also capable of capturing the pressure field accurately. Finally, the developed EFG model successfully simulated the pressure and saturation results of the square-shaped horizontal aquifer with a minimum number of nodal densities. These obtained results could be used to study the integrity of caprocks (such as to study the deformation behaviour and to further investigate the fracture initiation and propagation of the caprock system due to developed pressure in the aquifer system) and storage capacity of the aquifers. The developed model could easily be extended for varying aquifer depths and heterogeneous aquifer properties with multiple sources and sinks.

## References

1. Bachu S, Adams JJ (2003) Sequestration of CO<sub>2</sub> in geological media in response to climate change: capacity of deep saline aquifers to sequester CO<sub>2</sub> in solution. *Energy Convers Manag* 44(20):3151–3175
2. IPCC (2005) IPCC special report on carbon dioxide capture and storage, prepared by the working Group III of the intergovernmental panel on climate change. Cambridge University Press, Cambridge, p 442
3. Lancaster P, Salkauskas K (1981) Surfaces generated by moving least squares methods. *Math Comput* 37(155):141–158
4. Levin D (1998) The approximation power of moving least-squares. *Math Comput Am Math Soc* 67(224):1517–1531
5. Belytschko T, Lu YY, Gu L (1994) Element-free Galerkin methods. *Int J Numer Meth Eng* 37(2):229–256
6. Muthu N, Maiti SK, Falzon BG, Guimatsia I (2013) A comparison of stress intensity factors obtained through crack closure integral and other approaches using eXtended element-free Galerkin method. *Comput Mech* 52(3):587–605
7. Nguyen VP, Rabczuk T, Bordas S, Dufflot M (2008) Meshless methods: a review and computer implementation aspects. *Math Comput Simul* 79(3):763–813
8. Dolbow J, Belytschko T (1999) Numerical integration of the Galerkin weak form in meshfree methods. *Comput Mech* 23(3):219–230
9. Celia MA, Nordbotten JM (2009) Practical modeling approaches for geological storage of carbon dioxide. *Groundwater* 47(5):627–638
10. Gasda SE, Nordbotten JM, Celia MA (2009) Vertical equilibrium with sub-scale analytical methods for geological CO<sub>2</sub> sequestration. *Comput Geosci* 13(4):469–481
11. Bandilla KW, Celia MA, Birkholzer JT, Cihan A, Leister EC (2015) Multiphase modeling of geologic carbon sequestration in saline aquifers. *Groundwater* 53(3):362–377
12. Ladubec C, Gracie R, Craig J (2015) An extended finite element method model for carbon sequestration. *Int J Numer Meth Eng* 102(3–4):316–331
13. Nordbotten JM, Celia MA (2011) Geological storage of CO<sub>2</sub>: modeling approaches for large-scale simulation. Wiley, Hoboken

14. Ladubec C, Gracie R (2017) Stabilized finite element methods for vertically averaged multi-phase flow for carbon sequestration. *Int J Numer Methods Eng*
15. Dunavant DA (1985) High degree efficient symmetrical Gaussian quadrature rules for the triangle. *Int J Numer Meth Eng* 21(6):1129–1148

# Prediction of Motions and Wave-Induced Loads on a Container Ship Using Nonlinear 3D Time-Domain Panel Method



Ranadev Datta and C. Guedes Soares

**Abstract** In this paper, a relatively simplified nonlinear method based on three-dimensional time-domain panel method is used to predict the motions and vertical bending moment of a container ship with and without forward speed. The numerical formulation is developed using transient free-surface Green's function. Froude–Krylov and hydrostatic restoring forces are computed considering the nonlinearities arising from the large-amplitude incident waves. To deal with this phenomenon, an appropriate algorithm is developed which is capable of finding the exact wetted surface under the incident wave profile. In case of estimation of radiated–diffracted forces, a modified approach of body kinematic condition is proposed. The methodology is validated for a simplified structure such as Wigley hull, rectangular barge. In the present paper, a realistic container ship (S175) is taken for the analysis. Heave, pitch motions, and vertical bending moments are calculated and have been compared with available experimental results for head sea condition. The comparison shows the present methodology which is efficient and robust enough to estimate the wave-induced responses. Once the method is validated, to check the effect of nonlinearity, the motions and force results are computed for different steepness. Results show beyond a steepness factor of 0.08, and nonlinear effects are significant.

**Keywords** Time domain · Panel method · Container ship · Forward speed  
Nonlinearity

---

R. Datta (✉)  
Indian Institute of Technology Kharagpur, Kharagpur, India  
e-mail: [ranadev@naval.iitkgp.ernet.in](mailto:ranadev@naval.iitkgp.ernet.in)

C. Guedes Soares  
Centre for Marine Technology and Ocean Engineering (CENTEC), Instituto Superior Técnico,  
University of Lisbon, Lisbon, Portugal  
e-mail: [c.guedes.soares@centec.tecnico.ulisboa.pt](mailto:c.guedes.soares@centec.tecnico.ulisboa.pt)

© Springer Nature Singapore Pte Ltd. 2019  
K. Murali et al. (eds.), *Proceedings of the Fourth International Conference in Ocean Engineering (ICOE2018)*, Lecture Notes in Civil Engineering 22,  
[https://doi.org/10.1007/978-981-13-3119-0\\_46](https://doi.org/10.1007/978-981-13-3119-0_46)

## 1 Introduction

Prediction of motions or wave-induced load in extreme sea conditions for a vessel is extremely challenging task. For large-amplitude motion problems, the classical linear theory may not produce results within engineering accuracy and perhaps nonlinear theories are more adequate. Especially the ship with larger flare, even hydrostatic forces are no longer act like linear restoring forces and proper nonlinear model is required to develop in such cases. Within the framework of potential theory, several nonlinear theories are developed for the last couple of decades. In a review on this topic [1], potential flow theory has been used to identify all five levels of prediction methods and level 6 is based on traditional CFD-based approach. The methods are fully linear at the lowest level 1, whereas they tend to be fully nonlinear at the highest level 6. In between, levels 2–5 can be explained as Froude–Krylov (F–K) nonlinear, body-nonlinear, body-exact—weak scatterer, and full nonlinear—smooth waves, respectively. As expected, the advanced levels of computational methods showcase gradually lesser approximations in the problem setup at the cost of increasing difficulty level and numerically enriched procedures. The level 2 or F–K nonlinear method is most simplified method to approximate the nonlinearities. Here, the disturbed potentials are solved based on full linear assumptions; however, the incident wave forces (i.e., F–K forces) and hydrostatics are considered as nonlinear taking the displaced hull under the incident wave profile.

Though the level 2 methods are relatively simple to include the nonlinearities, it is widely used and accepted as practical tool for predicting nonlinear loads and responses arising due to large-amplitude waves. Various methods have been proposed to combine the linear potential theory to define the radiation and diffraction wave field with nonlinear F–K and hydrostatic forces. Because of the inclusion of nonlinearities, the solution procedures are mostly based on the time-domain approach. One popular scheme in this regard is to employ the formulation based on Cumming's impulse response function (IRF) for the equations of motions, whereas the radiation and diffraction effects are determined from frequency domain calculations. In order to predetermine these radiation and diffraction effects, either 3D methods or 2D strip theory based methods are being employed. This approach can be seen in many sources [2, 3]. The other alternative approach is to solve the linear perturbation potential itself in the time domain, for example, using a 3D method as can be seen in [4, 5].

In this paper, nonlinear loads and responses based on a level 2 method have been studied, wherein a direct 3D time-domain solution using transient free-surface Green's function has been incorporated to get the perturbation potentials. The formulation for the perturbation potential follows the approach originally proposed by Lin and Yue [5] and subsequently followed in several other works [6, 7]. Besides nonlinear F–K and hydrostatics, a modified form of the body kinematic condition has been introduced for the numerical solution of the perturbation potential. This scheme is supposed to incorporate partial nonlinearities in the diffraction potential in an approximate way. In this regard, the approach may be considered as an attempt somewhere between level 2 and level 4 methods, however, maintaining the simplicity

of level 2 method in its applicability and computational effort. The idea proposed in the present paper is similar to the methodology used in [8] in the context of 3D zero-speed diffraction solution scheme based on a numerical tank approach; however, the detailed application of the modified body boundary condition is somewhat different in the present analysis. Also, the exact pressure integration above mean free surface is discussed extensively in [9, 10].

The present method is validated with simple ship-like structure such as Wigley Hull [11]. However, the effect of nonlinearities for a real ship structure is not being studied extensively using the proposed scheme. Therefore, in this paper a realistic container ship (S175) is taken for the present study. Heave motions and vertical bending moments are computed, and the nonlinear effects are studied for both the cases. It is found that beyond a steepness factor of 0.08, nonlinear effects are significant especially for the calculation of the bending moment.

## 2 Brief Mathematical Formulation

The details description of the methodology is given in many [6, 11, 12]. However, for the completeness, a very brief description of the problem formulation as well as the numerical implementation is given.

The following equation gives the six degrees of equations of motion:

$$[m]\dot{\bar{v}} + [m]\{\bar{\Lambda} \times \bar{v}\} = \bar{F}; \quad [I]\dot{\bar{\Lambda}} + \bar{\Lambda} \times [I]\bar{\Lambda} = \bar{M} \tag{1}$$

In the above equations,  $[m]$  and  $[I]$  represent the mass and moment of inertia matrices, respectively.  $\bar{v}$  and  $\bar{\Lambda}$  are the linear and angular velocities in the  $G x' y' z''$  system.  $\bar{F} = \{F_x, F_y, F_z\}$  and  $\bar{M} = \{M_x, M_y, M_z\}$  represent the three external forces and moments on the body, also defined in the  $G x' y' z''$  system. Motions of a ship can be determined from direct integration of Eq. (1), provided all the information about the forces and moments are known at each time instant. These are obtained by solving the hydrodynamic problem.

For the solution of the hydrodynamic problem, potential theory is used. Under the assumptions of potential flow theory, the fluid motion can be described by the velocity potential  $\phi_T(\vec{x}; t)$ . This can be split into:

$$\phi_T(\vec{x}; t) = \phi_I(\vec{x}; t) + \phi(\vec{x}; t) \tag{2}$$

where  $\phi_T(\vec{x}; t)$  denotes the total fluid potential in the earth-fixed system,  $\phi_I(\vec{x}; t)$  denotes the incident wave potential, and  $\phi(\vec{x}; t) = \phi_T(\vec{x}; t) - \phi_I(\vec{x}; t)$  is defined as the total disturbed potential. It can be shown that based on a time-dependent (transient) Green's function for this problem,  $\phi(p, t)$  can be expressed in the form of an integral equation as follows:

$$\phi(p, t) = -\frac{1}{4\pi} \left\{ \iint_{S_B(t)} \sigma(q, t) G^o(p, q) dS + \int_0^t d\tau \left[ \iint_{S_B(\tau)} \sigma(q, t) G^f(p, q; t - \tau) dS \right. \right. \\ \left. \left. - \frac{1}{g} \int_{\Gamma(\tau)} \sigma(q, t) G^f(p, q; t - \tau) V_N V_n dL \right] \right\} \tag{3}$$

$G^o(p, q)$  and  $G^f(p, q; t - \tau)$  above are the Rankine and memory part of the time-domain Green’s function.

Let  $P(\vec{x}, t)$  be the total pressure on the body including hydrodynamic and hydrostatic components. According to Bernoulli’s theorem, we have:

$$P(\vec{x}, t) = -\rho \left( \frac{\partial \phi_T}{\partial t} + \frac{1}{2} (\nabla \phi_T)^2 + gz \right) \tag{4}$$

From Eqs. (2) and (4), pressure can be written as:

$$P(\vec{x}, t) = -\rho \left( \frac{\partial(\phi + \phi_I)}{\partial t} + \frac{1}{2} (\nabla \phi + \nabla \phi_I)^2 + gz \right) \tag{5}$$

This splits into two parts as:

$$P^L(\vec{x}, t) = -\rho \left( \frac{\partial \phi}{\partial t} + (\nabla \phi) \cdot (\nabla \phi_I) + \frac{1}{2} (\nabla \phi) \cdot (\nabla \phi) \right) \tag{6}$$

$$P^{NL}(\vec{x}, t) = -\rho \left( \frac{\partial \phi_I}{\partial t} + \frac{1}{2} (\nabla \phi_I) \cdot (\nabla \phi_I) + gz \right) \tag{7}$$

In the present calculation, the  $P^L(\vec{x}, t)$  part of the pressure is integrated over the mean surface  $S_B(0)$  while  $P^{NL}(\vec{x}, t)$  part of pressure is integrated over the instantaneous surface  $S'_B(t)$ , which is the wetted hull under the incident wave profile considering the body’s displaced location. The unknown perturbation potential  $\phi(\vec{x}; t)$  being computed using fully linear boundary value problem and pressure component arises from  $\phi(\vec{x}; t)$  is integrated over the mean surface to get the force. Note that  $S'_B(t)$  is the wetted surface under the incident wave profile based on the total potential.

While carrying out the force integrations and summing up of the forces, special attention should be paid as there are two coordinate systems being considered on which these two components are being integrated.  $P^{NL}$  is defined and integrated in the body system while  $P^L$  is defined and integrated in the system which is parallel to the inertial system but having its origin fixed on the body. Hence, appropriate coordinate transformations between these two systems are required while transforming the panel coordinates and the body normal as well as while adding the forces and moments coming from the two pressures  $P^L$  and  $P^{NL}$ . The detailed calculations in this respect can be seen in [6].



### 3 Modifying Body Boundary Condition

Since the boundary condition is imposed on mean wetted surface, and the F–K forces are calculated on the exact wetted surface Eq. (6), two different techniques were employed to include nonlinear effects in the scattered potential [8]. In the present analysis, based on momentum conservation principle, the following formulation is proposed in the present work.

We assume that  $d$  is the draft of the vessel and  $\eta$  is the wave elevation. The distance between wave elevations to draft is divided into  $n$  segments. In each segment,  $\partial\phi_1/\partial n$  is calculated with respect to  $z'$ , i.e., actual elevation of the incident wave. Since it is assumed that total momentum is preserved along depth, the following area is stored:

$$\text{Area} = \int_{-d}^{\eta} (\nabla\phi_1) dz' \tag{8}$$

Next, as the gradient exponentially decays, it is assumed that the profile of the  $\nabla\phi_1$  is of the form  $Ce^{kz}$  where

$$\int_{-d}^0 Ce^{kz} dz = \text{Area} \tag{9}$$

From Eqs. (8) and (9), the constant  $C$  can be obtained, and hence, the distribution of  $\nabla\phi_1$  from mean free surface can be approximated. The above approach is capable of counting the extra contribution coming from wave crest and eliminates the extra contribution coming from linear theory at wave trough.

### 4 Results and Discussions

In this paper, a realistic S175 hull is considered for the analysis. This is a well-known hull which was used by ITTC to perform a comparative numerical examine on wave-induced motions and structural loads. The database that has been generated from this study includes numerical results from various institutions validated against experimental data. In this paper, results are computed for both zero-speed cases of the vessel and different forward speeds. The main particulars of this hull are given in Table 1.

Figure 1 represents the linear and nonlinear heave time history for zero forward speed at  $\lambda/L = 1$ . In Fig. 1, LTD denotes the formulation based on linear theory, and NLTD30 and NLTD50 denote nonlinear results for the steepness  $2A_w/\lambda = 1/30, 1/50$ , respectively.

**Table 1** S175 hull—main particulars

Description	Unit	Value
Length between perpendiculars	m	175.0
Beam	m	25.4
Draft	m	9.5
Total mass	ton	24,742
Block coefficient	–	0.5716
Longitudinal center of gravity aft midship	m	2.34
Long radius of gyration	m	42.0

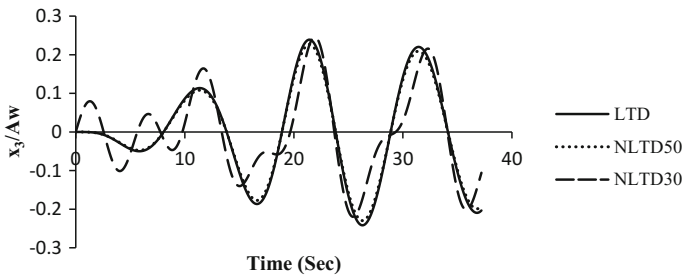


**Fig. 1** Heave motion time history

The nonlinear results are computed for two different steepness factors  $2A_W/\lambda = 1/50, 1/30$ , i.e.,  $kA_W = 0.06, 0.1$ . One can observe that both linear and nonlinear formulations give almost identical results for lower steepness range; however, significant change can be observed for higher steepness; also nonlinear effects are prominent at  $2A_W/\lambda = 1/30$  or  $kA_W = 0.1$ . It can also be observed from Fig. 1 that at the higher wave steepness region, not only there are differences in the amplitude, the nonlinear calculations start to show double peaks in the force history indicating the presence of higher harmonics.

In order to check the influence of nonlinearities in prediction of the heave response, non-dimensional heave amplitudes over a range of wave steepness are shown in Fig. 2. As it is observed in practical scenario that relative motions are usually largest at the region of  $\lambda/L = 1$ , results are given only for  $\lambda/L = 1$ . It can be seen that beyond  $kA_W = 0.08$ , the linear and nonlinear results differ by 10%. Figure 3 shows the comparison between LTD and NLTD30 results for heave response RAO. In the plots, NLTD+ represents the positive peak, and NLTD– represents the negative peak. It can be observed from the plots that at lower frequency range, surprisingly the difference is more. This could be because of the influence of nonlinear hydrostatic force. Since the present ship is having some flare, the nonlinear contribution from the hydrostatic force becomes important at lower frequency region as at that frequency, the dominant forces are hydrostatic and Froude–Krylov forces.

**Fig. 2** Heave transfer function over a range of non-dimensional wave steepness

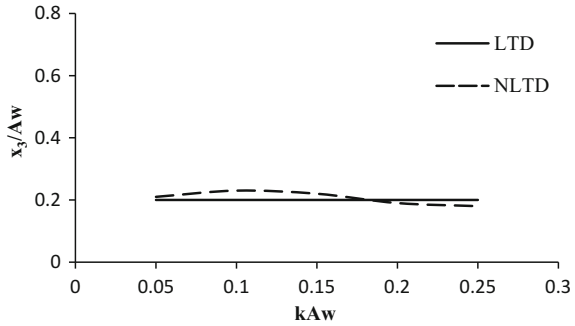


**Fig. 3** Heave RAO

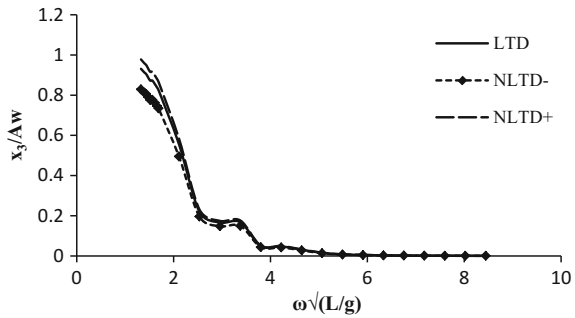


Figure 4 shows the VBM time signals at midship obtained from both linear and nonlinear computations for head waves when  $\lambda/L = 1$ . These calculations are performed with wave height to length ratio of  $2A_w/\lambda = 1/50, 1/30$  and denoted in the plots by NLTD50 and NLTD30, respectively. It can be observed from the figure that for  $2A_w/\lambda = 1/50$ , the computations are almost identical; however, for the latter case, the influence of nonlinearities is visible in the plots. The most relevant point can be made out in this case is that nonlinear calculations produce different positive and negative peak values. According to the convention used in these plots, positive and negative peaks are as sagging and hogging moments, respectively. Hence, the results show that nonlinear computations can estimate different sagging and hogging moments. It can also be noted that there occurs a phase gap between the time signals obtained from the linear and nonlinear predictions, which may be justified from the fact that the force peak between linear and nonlinear computations does not occur at the same time instant as wave steepness increases. The non-dimensional bending moment at midship against non-dimensional frequencies is plotted in Fig. 5. The result shows maximum bending moment occurs at  $\omega\sqrt{L/g} = 2.5$ , which is equivalent to  $\lambda/L = 1$  where the nonlinear results are significantly different (for the sagging moment, almost 15%) from linear computations.

Next set of computations are carried out for the forward speed. Figure 6 shows the non-dimensional heave and pitch amplitudes against wave steepness for a range of non-dimensional frequency region. As it is well-established fact that motions are

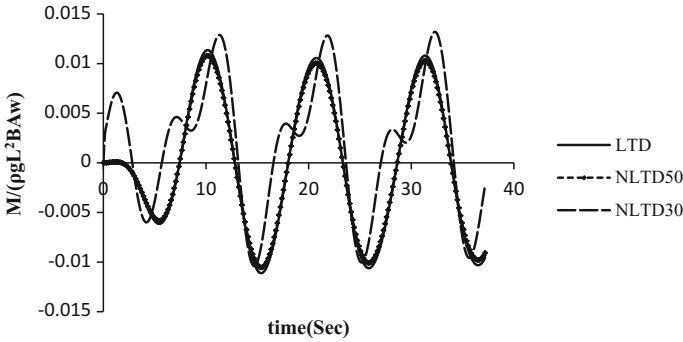


Fig. 4 VBM time history at midship

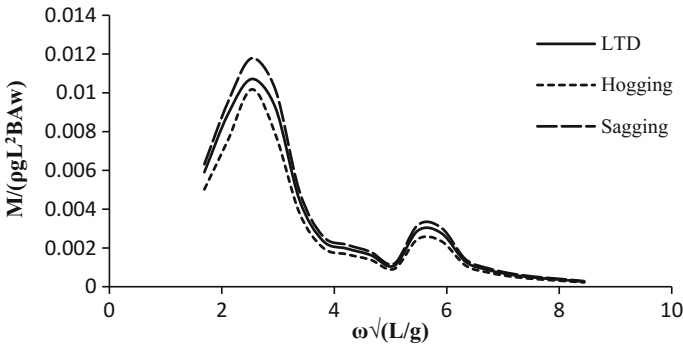
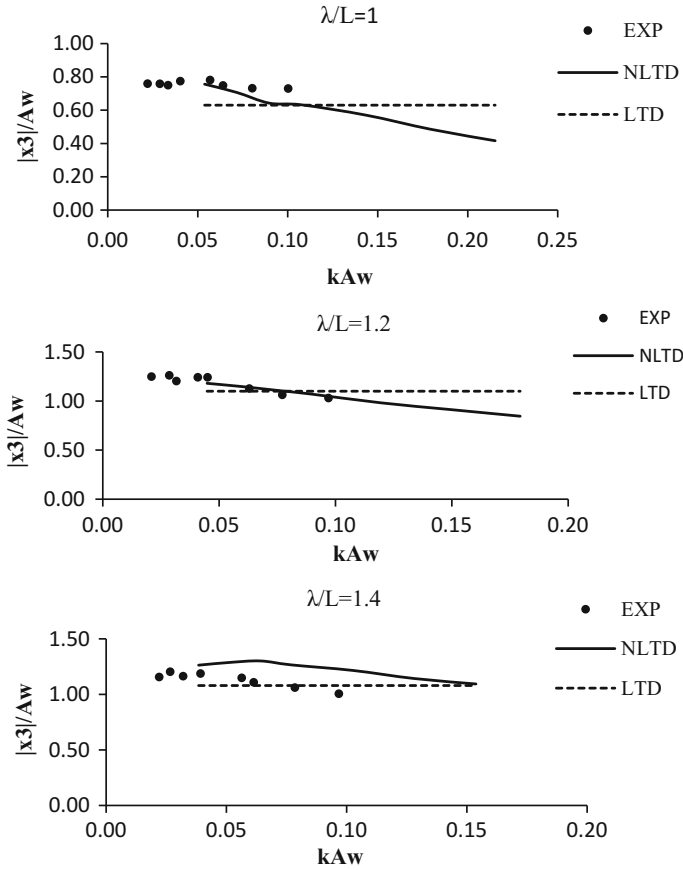


Fig. 5 VBM transfer function (midship)

usually largest at around  $\lambda/L = 1$ , the results for  $\lambda/L = 1, 1.2, 1.4$  with the forward speed of  $F_n = 0.25$  have only been discussed. Since experimental results for these cases are available in [13], attempts have been taken to produce results for these ratios only.

The motion amplitudes for the nonlinear calculations are obtained from averaging peak-to-peak values. It is seen that the influence of nonlinearity is clearly visible in the NLTD calculations. It may be noted that experimental data cover a relatively lower range of wave steepness, and there appears a strong nonlinear influence at low wave steepness for this particular hull. The reason may be justified due to the influence of so-called geometric nonlinearity of the S175 hull because of its large flare at bow and stern region.



**Fig. 6** Variation of heave transfer function over a range of wave steepness and for different frequencies ( $F_n = 0.25$ )

Figure 7 shows the VBM time histories obtained from both linear and nonlinear computations for  $F_n = 0.25$  in head waves at  $\lambda/L = 1.2$ . These calculations are performed with wave height to length ratio of  $2A_w/\lambda = 1/30$ . Thus, the computations are for moderately steep waves, but still the influences of nonlinearities are visible in the plots.

The influence of nonlinearities in the predicted VBM is showcased in Fig. 8 where a comparison study between the non-dimensional hogging and sagging moment amplitudes from NLTD along with results from the LTD calculations has been highlighted over a range of wavelengths. These results have been computed here while keeping the forward speed, wave heading angle, and wave steepness as same as reported in Fig. 6.

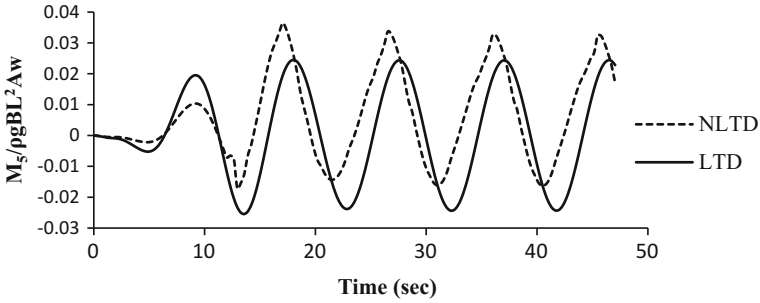
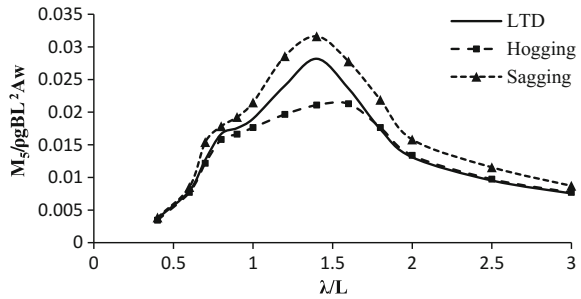


**Fig. 7** Time signal of VBM from linear and nonlinear calculations with forward speed case ( $F_n = 0.25$ ,  $\lambda/L = 1$ ,  $2A_w/\lambda = 1/30$ )

**Fig. 8** VBM over a range of wavelengths from linear and nonlinear computation with forward speed ( $F_n = 0.25$ ,  $2A_w/\lambda = 1/30$ )



This figure clearly indicates that there is a high influence of nonlinearities in the computed VBM. When compared to the estimations from linear calculations, it is found out that sagging moments are at the higher side while hogging moments are lower than the previous one. When bending moments are considered at the peak value, which is obtained at around  $\lambda/L = 1.5$ , linear computations seem to under-predict sagging moment by about 30% while over-predict hogging moment by about 15%. This also indicates that nonlinearities may cause a noticeable difference of about 45% between sagging and hogging moments. It can be noted that these values are all computed for a reasonably moderate wave steepness of  $2A_w/\lambda = 1/30$ .

In the final plot of Fig. 9, the amplitudes of VBM from linear and nonlinear computations over the range of wave steepness have been plotted for the case of  $\lambda/L = 1.2$  at forward speed,  $F_n = 0.25$ . In terms of full-scale values, wave amplitudes here range from 1 to 5 m for this 175 m long hull with draft 9.5 m. It can be seen from the plot that the influence of nonlinearities on hogging and sagging moments is clearly differentiable. In particular, linear computations over-predicts the hogging moment at the 5-m wave amplitude region by nearly 40% when compared to the nonlinear calculations.

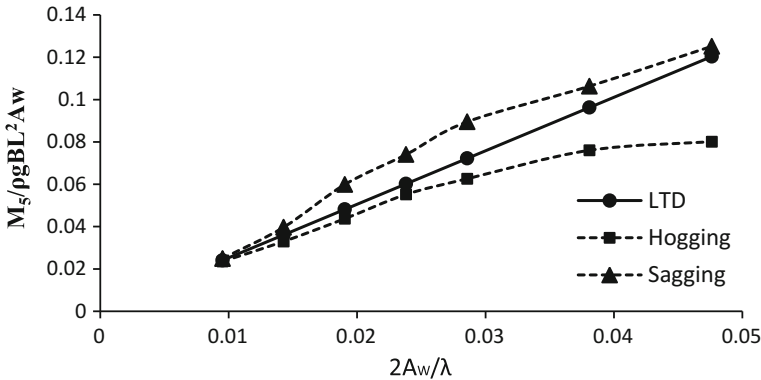


Fig. 9 VBM as a function of wave amplitude from linear and nonlinear formulations

### 5 Conclusion

In the present study, a nonlinear time-domain 3D lower-order panel method is developed to analyze the hydrodynamic forces and motions of ships for a realistic S175 hull. Nonlinearities reported here are incorporated in the formulation of F–K and hydrostatic forces. An attempt is made to include partial nonlinearities of the wave diffraction through a modified body boundary condition in the numerical solution of the perturbation potential. The effect of nonlinearities is analyzed in order to compute the vessel motions, vertical bending moments, etc. Results show that the influence of nonlinearities can be important especially for the calculation of bending moment. Therefore, it can be concluded that the proposed numerical methodology could be a useful technique to predict the wave induces responses of a realistic ship hull in terms of displacement, VBM, etc., at initial design stage. This methodology also enables us to guess some of the parameters like sagging bending moment where non-inclusion of nonlinearities may result in a fairly significant under-prediction of wave-induced loads.

### References

- Hirdaris SE, Bai W, Dessi D, Ergin A, Gu X, Hermundstad OA, Huijsmans R, Iijima K, Nielsen UD, Parunov J, Fonseca N, Papanikolaou A, Argyriadis K, Incecik A (2014) Loads for use in the design the ship and offshore structures. *Ocean Eng* 78:131–174
- Chitrapu AS, Ertekin RC (1995) Time-domain simulation of large-amplitude response of floating platforms. *Ocean Eng* 22(4):367–385
- Fonseca N, Soares CG (1998) Time domain analysis of large amplitude vertical motions and wave loads. *J Ship Res* 42(2):100–113
- Bingham HB, Korsemeyer FT, Newman JN, Osborne GE (1993) The simulation of ship motions. In: *Proceedings of 6th international conference in numerical ship hydrodynamics*. National Academy Press, Washington DC, pp 561–579

5. Lin WM, Yue DKP (1991) Numerical solutions for large amplitude ship motions in the time domain. In: Proceedings of 18th symposium on naval hydrodynamics. National Academy Press, Washington DC, pp 41–66
6. Sen D (2002) Time domain computations of large amplitude 3D ship motions with forward speed. *Ocean Eng* 29:973–1002
7. Datta R, Sen D (2007) The simulation of ship motion using a B-spline based panel method in time domain. *J Ship Res* 51(3):267–284
8. Sen D, Srinivasan N (2007) Long duration simulation of wave-structure interactions in a numerical wave tank. In: Proceeding of PRADS
9. Rodrigues J, Guedes Soares CC Ship vertical loads from using an adaptive mesh pressure integration technique for Froude-Krylov forces calculation. In: ASME, international conference on offshore mechanics and arctic engineering, vol 7A: ocean engineering
10. Rodrigues J, Guedes Soares C (2017) Froude-Krylov forces from exact pressure integrations on adaptive panel meshes in a time domain partially nonlinear model for ship motions. *Ocean Eng* 139:169–183
11. Sengupta D, Datta R, Sen D (2016) A simplified approach for computation of nonlinear ship loads and motions using a 3D time-domain panel method. *Ocean Eng* 117:99–113
12. Datta R, Rodrigues JM, Soares CG (2011) Study of the motions of fishing vessels by a time domain panel method. *Ocean Eng* 38:782–792
13. Fonseca N, Soares CG (2004) Experimental investigation of the nonlinear effects on the vertical motions and loads of a containership in regular waves. *J Ship Res* 48(2):118–147



**Part IV**  
**Ocean Modelling**

# Estimation and Analysis of Extreme Maximum Wave Heights



S. Satish, S. A. Sannasiraj and V. Sundar

**Abstract** Extreme wave height is the most decisive parameter in the design and survival of variety of coastal engineering activities like port and harbour infrastructures, beach management schemes and flood risk analysis. Although the initial focus of this study was in the estimation of return values for significant wave heights, it is important to arrive at the design wave height with utmost caution after a rigorous analysis, as both safety, as well as the cost of investment, are involved. Hence, in the present study, the extreme wave heights for different return periods were estimated not only for significant wave heights ( $H_s$ ) but also for the maximum individual wave heights ( $H_{max}$ ), assuming the individual wave height measurements are Rayleigh distributed. In order to carry out the analysis envisaged herein, long-time series of ERA-Interim significant wave height hindcast data covering a period of 36 years i.e., from 1979 to 2014 were employed along with the polynomial approximation method of extreme wave analysis.

**Keywords** Survival · Design wave height · Wave hindcast · Extreme wave maps  
Uncertainty · Optimal design

## 1 Introduction

Extreme wave conditions influence all the coastal and offshore engineering applications. Therefore, the prediction of extreme wave climate is prerequisite for a variety of coastal activities like the structural design of port and harbour infrastructures,

---

S. Satish (✉) · S. A. Sannasiraj · V. Sundar  
Department of Ocean Engineering, Indian Institute of Technology Madras, Chennai, Tamil Nadu, India  
e-mail: [satish946@gmail.com](mailto:satish946@gmail.com)

S. A. Sannasiraj  
e-mail: [sasraj@iitm.ac.in](mailto:sasraj@iitm.ac.in)

V. Sundar  
e-mail: [vsundar@iitm.ac.in](mailto:vsundar@iitm.ac.in)

© Springer Nature Singapore Pte Ltd. 2019  
K. Murali et al. (eds.), *Proceedings of the Fourth International Conference in Ocean Engineering (ICOE2018)*, Lecture Notes in Civil Engineering 22,  
[https://doi.org/10.1007/978-981-13-3119-0\\_47](https://doi.org/10.1007/978-981-13-3119-0_47)

optimisation of marine energy converters, planning of beach management schemes and for flood risk analysis. In recent years, marine energy from tidal currents and waves [1, 2] has been identified as an important source of low carbon sustainable energy. This incentive is evident in the countries with large potential for exploiting these wave energy resources like Australia, the UK and also developing countries like India. This is imperative as the prevailing marine environment is expected to change in the coming years due to global warming.

Regarding the efficiency and survivability of the marine energy-converting devices, coastal and offshore structures, one critical factor is the information on the prevailing extreme sea-state parameters in the vicinity of these structures, like 100 and 1000-year extreme wave heights. The lesser return period would be associated with a lesser wave height return values but more risk and vice versa, depending on the structural importance. The design wave provides ample opportunity to decide on the risk involved as it is associated with a return period that is proportional to the life of the structure. For example, in the design of sea defences safety control system of The Netherlands, return values of up to 10,000-year are used as the country lies below the mean sea level. Also for flood risk area mapping in the UK, a 1000-year return value is used.

Any underestimation of these extreme conditions could adversely affect the survivability of the structures leading to catastrophic failure, while an overestimate would inevitably lead to over design, making the return on investment financially unattractive. The understanding of extreme conditions of waves is of interest not only to the research community but also to the industries because of the economic aspect. Any traditional method of estimating extreme wave heights consists of gathering all the available  $H_s$  data for a number of years in a single sample and fitting a suitable parametric model to the data. As the extreme values are unique occurrence events and fall outside the range of the available observations, which implies that an extrapolation to the desired low probability of occurrence is required [3–5].

Many researchers in the past have proposed different approaches for extreme wave analysis. As there are no theoretical means to determine the most appropriate method for extreme wave analysis, a number of methods were typically used in different studies and the one achieving the best fit to the data and the method which results in reliable return values generally is being accepted.

In many studies, the interest is being centred on identifying the most reliable approach for estimating the extreme order statistics. Samayam et al. [6] investigated different approaches for the return value estimation like the generalised extreme value distribution (GEV) method based on annual maxima sample, the generalised Pareto distribution (GPD) method based on peaks over threshold sample, equivalent triangular storm (ETS) model based on the concept of replacing the sequence of actual storms with a sequence of equivalent triangular storms and the polynomial approximation method [7] based on extrapolating the tail of the provision function. In their study, they have also introduced a statistical approach to validate the reliability of the return values from a particular extreme wave estimation method and thereby identified GEV and GPD methods showing high variation in underestimating or overestimating of return values whereas the polynomial approximation method showed

consistency in estimating return values for both buoy and simulated data. Hence, in this study, the extreme wave heights for different return periods were estimated by considering the polynomial approximation method of extreme wave analysis.

Majority of the Indian seas experience comparatively mild waves under normal weather conditions. When strong monsoon winds prevail due to cyclones, higher waves can be experienced at the exposed locations. When these cyclones pass over or in the close vicinity of the shore, which results in higher wave heights. Extreme wave conditions in India occur mainly due to tropical cyclones. Isolated maritime structures such as wind turbine towers and oil-drilling rigs have to be designed to resist the largest possible wave at the site. In view of this variable and often unpredictable character of the wave forces to which marine structures are subjected to, it is of utmost importance to arrive at the design wave height with greater caution after a rigorous analysis. Hence, in the present study, the extreme wave heights for different return periods were estimated not only for  $H_s$  but also for  $H_{max}$ , assuming the individual wave height measurements are Rayleigh distributed.

## 2 Description of the Significant Wave Height Data and Study Area

For the modelling of extreme wave conditions in space and time, space-time significant wave height ( $H_s$ ) data is needed. It is evident that a quality data set with sufficient resolution in both time and space is a necessary requirement for a better prediction of the extremes. Several sources of data acquisition have been explored such as observations from in situ measurements, altimeter measurements, modelling of waves from winds and also data assimilation techniques. In this particular study, we chose ERA-Interim significant wave height data from European Centre for Medium-Range Weather Forecasts (ECMWF) because they have a regular coverage for the whole World Oceans, in particular, the Indian coast. The wave climate parameters with 6-hourly fields covering the whole globe can be obtained, with the best spatial resolution of  $0.125^\circ \times 0.125^\circ$ . Furthermore, these numerically simulated ERA-Interim wave data sets have regular and long continuous series, which is important for the statistical aims of extreme wave analysis.

The Indian coastline has a wide territory which extends from  $5^\circ\text{N}$  to  $25^\circ\text{N}$  latitudes and at longitudes,  $65^\circ\text{E}$ – $90^\circ\text{E}$ . In order to carry out the extreme wave analysis, 11 important major port locations in India were considered. The selected sites are shown in Fig. 1 and presented in Table 1 along with their coordinates. The main criterion for the choice of these locations is the rapid development of major infrastructure in and around these port locations. The estimates of extreme wave height return values are based on ERA-Interim significant wave height data, covering a period of 36 years i.e., from 1979 to 2014 obtained by extracting this data of resolution  $0.125^\circ \times 0.125^\circ$  nearest to the selected port locations.

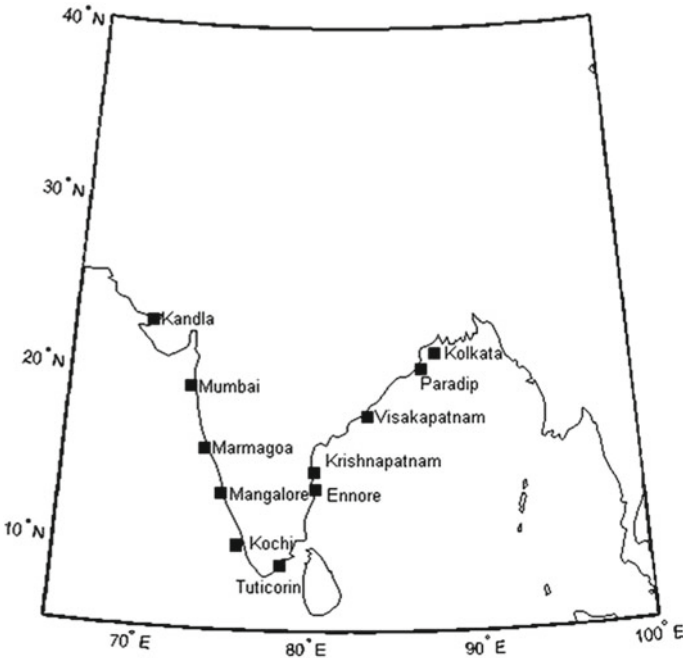


**Fig. 1** Major port locations along the Indian coast

**Table 1** Coordinates of the major ports along the Indian coast and extreme wave heights (m) for different return periods

S. No.	Location	Latitude	Longitude
1	Kolkata	21.125°N	87.75°E
2	Paradip	20.25°N	86.875°E
3	Visakhapatnam	17.50°N	83.50°E
4	Krishnapatnam	14.25°N	80.25°E
5	Ennore	13.25°N	80.375°E
6	Tuticorin	8.75°N	78.375°E
7	Kochi	10.0°N	76.125°E
8	Mangalore	12.875°N	74.75°E
9	Marmagoa	15.50°N	73.625°E
10	Mumbai	19.0°N	72.50°E
11	Kandla	22.75°N	69.875°E

### 3 Methodology of Polynomial Approximation Method

The polynomial approximation method involves the construction of an analytical approximation  $F_{ap}(H)$ , aimed for its extrapolation beyond an observed maximum

value  $H_M$ . The approximation should be restricted to a shorter domain lying above the uppermost mode of the histogram considered of the function  $F(H)$ . The domain suitable for constructing approximation  $F_{ap}(H)$  can be determined by the following condition,

$$H_l \leq H \leq H_h \leq H_M \tag{1}$$

where  $H_l$  and  $H_h$  are the lower and the upper edges of the domain of  $F(H)$ .

The number of points ( $N_M$ ) considered in the histogram is  $H_M/\Delta H$  and  $N_S$  is defined as,

$$N_S = (H_M - H_h)/\Delta H \tag{2}$$

The number of points ( $N_T$ ) used for constructing the approximation function,  $F_{ap}(H)$  is defined as,

$$N_T = (H_h - H_l)/\Delta H + 1 \tag{3}$$

The approximation function,  $F_{ap}(H)$  should be constructed in the logarithmic coordinates due to few values in the tail of  $F(H)$ , providing importance to the values in the tail. This allows accounting for a strong variability of the tail of function  $F(H)$  in the domain near the maximum value of the series ( $H_M$ ) depending on the length of the series.

To exclude the application of fixed statistics, the approximation function  $F_{ap}(H)$  should be considered in the form of a polynomial of degree  $n$ , the value of which may vary.

The statistical distribution fitted to the provision function is given as,

$$F_{ap}(H) = \exp \left[ \sum_{i=0}^{i=n} a_k H^k \right] \tag{4}$$

After obtaining the approximation function,  $F_{ap}(H)$  from Eq. (4), the return value,  $H_R$ , appearing once for  $N_R$  years, can be deduced from the following formula,

$$F(H_R) = \Delta t/8760 \cdot N_R \tag{5}$$

where  $\Delta t$  is the interval of significant wave height data observations.

### 4 Analysis of Extreme Waves Using Significant Wave Height Data

The polynomial approximation method has been used to evaluate extreme wave heights for different return periods at major port locations. Figure 2 shows the application of polynomial approximation method for a series of  $H_s$  at four of the port locations from which we can observe the adaptation of polynomial approximations to the real behaviour of the tail of the provision function. The provision function has been built in logarithmic coordinates due to a fewer number of values in the tail of  $F(H)$ , ensuring importance to the tail values.

### 5 Extreme Wave Analysis Using Maximum Wave Height Data

The marine structures and devices operating in marine environments are continuously exposed to the forces from the waves. During extreme events, or over a period of time, for example, by fatigue, wear, corrosion, failure to withstand such forces may lead to severe consequences. Hence, these extreme wave conditions need to be analysed with a high degree of confidence to minimise the chances of such failures to acceptable levels. Even though the future marine environment will tend to be rougher than the historic and current marine environment, the uncertainty of the future wave climate is considerably large. In view of this variable and often unpredictable character of the wave forces to which marine structures are subjected to, it is important to arrive at the design wave height with utmost caution after a rigorous analysis.

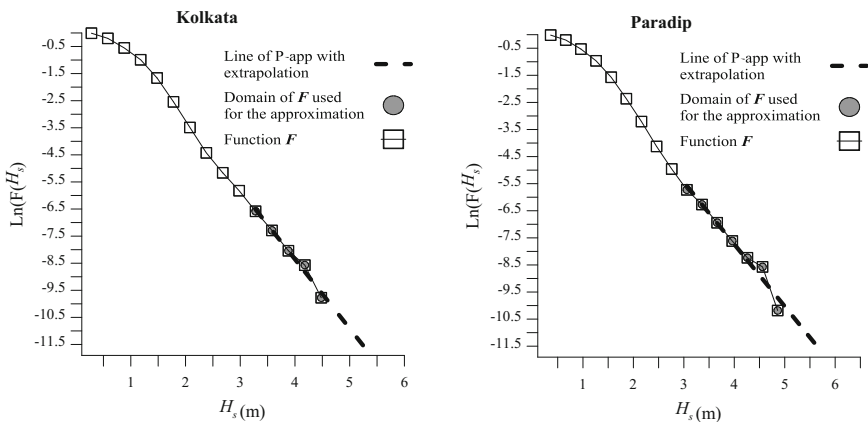


Fig. 2 Application of polynomial approximation method for the series of  $H_s$  data at Kolkata and Paradip

According to Liu and Burcharth [8], the conservative method for the estimation of the design individual maximum wave height involves first to obtain the design significant wave height corresponding to a certain exceedance probability within a lifetime of the structure, based on the statistical extreme wave analysis. The design individual maximum wave height is then calculated with the assumption that the individual wave heights follow the Rayleigh distribution, as the expected maximum individual wave height associated with the design significant wave height. According to them, the expected maximum individual  $H_{\max}$  associated with the design  $H_s$  is given as,

$$(H_{\max})_{\text{mean}} \approx \left( \sqrt{\frac{\ln N}{2}} + \frac{0.577}{\sqrt{8 \ln N}} \right) H_s^{100} \tag{6}$$

where  $N$  is the number of individual waves related to  $H_s^{100}$ . However, the exceedance probability of such a design individual maximum wave height within the lifetime of the structure is unknown, which calls for an additional site-specific analysis.

In the present study by an assumption that the individual wave heights of ERA-Interim data follow the Rayleigh distribution, in which case Longuet Higgins [9] suggested that the range of  $H_{\max}$  could be  $1.6H_s-2H_s$ . Using this assumption, short-term statistics of individual waves and long-term statistics of sea states may be combined to obtain long-term distributions of individual waves. Hence, in this section, the extreme wave heights for different return periods were estimated not only from  $H_s$  but also from the maximum wave heights like  $1.6H_s$ ,  $1.8H_s$  and  $2.0H_s$  at the major ports. At each of these locations, the assessment was carried out by the polynomial approximation method of extreme wave analysis.

The resulted return values for different return periods are mentioned as  $H_{1.6\max}^R$ ,  $H_{1.8\max}^R$  and  $H_{2.0\max}^R$ , respectively. On the other hand, it is illuminating to perceive whether the variability and trend statistics of the  $H_{1.6\max}^R$ ,  $H_{1.8\max}^R$  and  $H_{2.0\max}^R$  values are analogous to the values  $1.6H_s^R$ ,  $1.8H_s^R$  and  $2.0H_s^R$ , which are nothing but the extreme wave heights for different return periods ( $R$ ) estimated from  $H_s$  and multiplied with 1.6, 1.8 and 2.0, respectively. The aforementioned analysis at all of the 11 major port locations along the Indian coast is presented in Fig. 3. From the figures, it can be observed that the trends and slopes of both of the approaches are almost similar at most of the locations except at Kochi. This is because at Kochi the outlier  $H_s$  values in the time series are much higher and when these outliers are again multiplied by 1.8 or 2.0, the attained values became more assertive which resulted in anomalous return values. This kind of anomaly can be perceived rarely, but it is a major shortcoming of this approach.

Further comparison of these two different return value series was performed by obtaining the Covariance and Root mean square error (RMSE), which is depicted in Table 2. Covariance is a measure of the joint variability of two different random variables. Therefore, the sign of the covariance shows the tendency in the linear relationship between the variables. The RMSE was estimated in order to check the level of deviation between these two different return value series. From the aforemen-



tioned table, we can notice that the covariance values are always positive indicating the similar linear behaviour between them and at Paradip and Kochi, higher RMSE values can be seen, indicating the outlier  $H_s$  values, which results in anomalous return values.

Considering the above observations and results, both the approaches of estimating design individual maximum wave height have several uncertainties, however, the estimated return values  $1.6H_s^R$ ,  $1.8H_s^R$  and  $2.0H_s^R$  are very close to the values of  $H_{1.6max}^R$ ,  $H_{1.8max}^R$  and  $H_{2.0max}^R$ , and the anomalous outlier phenomenon (Kochi in Fig. 3) does not appear in the former approach. Further, this approach is straightforward and results in the same values as that of  $H_{1.6max}^R$ ,  $H_{1.8max}^R$  and  $H_{2.0max}^R$ . The aforementioned analysis will offer guidance on the design of marine works and

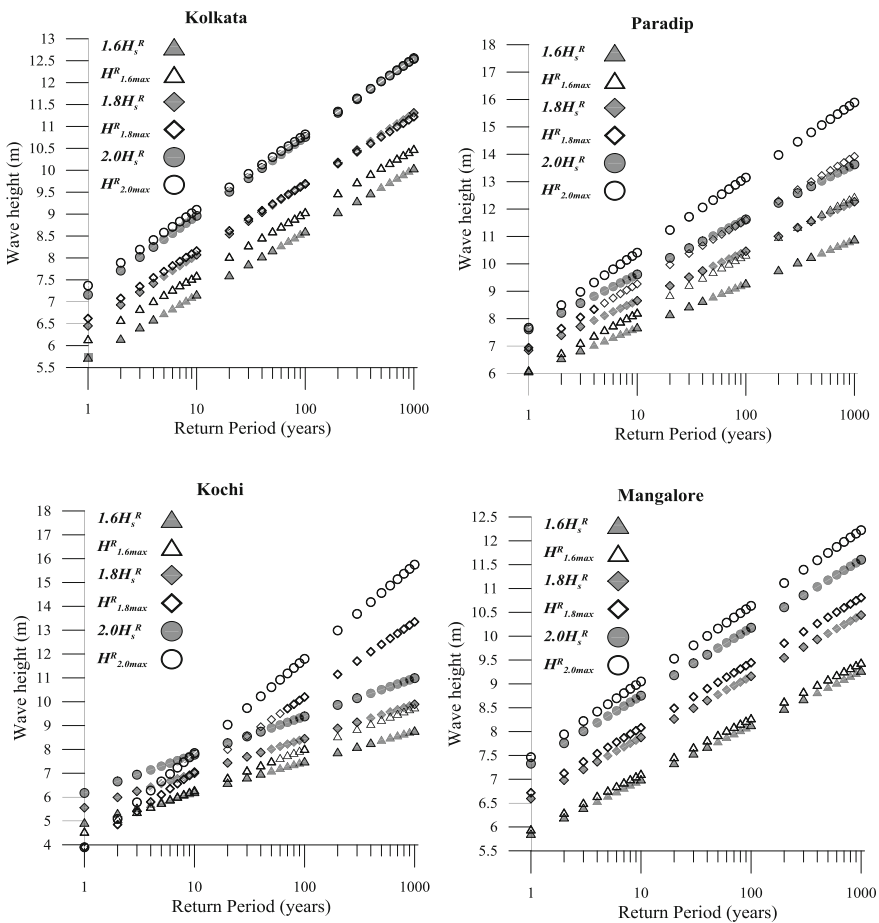


**Fig. 3** Variation of wave height return values for  $H_s$  and  $H_{max}$  at different port locations along the Indian coast

**Table 2** Statistical relation between different return value series

Location	$1.6H_s^R - H_{1.6\max}^R$		$1.8H_s^R - H_{1.8\max}^R$		$2.0H_s^R - H_{2.0\max}^R$	
	COV	RMSE	COV	RMSE	COV	RMSE
Kolkata	1.65	0.430	1.97	0.084	2.46	0.106
Paradip	2.69	0.986	3.33	1.067	4.36	1.441
Visakhapatnam	1.51	0.113	1.66	0.449	2.17	0.322
Krishnapatnam	1.19	0.211	1.55	0.322	1.88	0.301
Ennore	2.09	0.541	2.48	0.667	2.85	0.887
Tuticorin	0.11	0.031	0.15	0.058	0.19	0.099
Kochi	1.76	0.548	3.61	1.925	5.02	2.652
Mangalore	1.05	0.134	1.38	0.266	1.79	0.430
Marmagoa	2.70	0.159	3.69	0.419	4.27	0.226
Mumbai	1.06	0.177	1.42	0.326	1.74	0.321
Kandla	0.45	0.049	0.56	0.074	0.63	0.169

structures normally related to the port infrastructure and also for the design of beach management schemes.

## 6 Conclusions

The polynomial approximation method has been used to evaluate extreme wave heights for different return periods at major port locations along the Indian coast. This awareness aids in the efficient design of the structures related to ports, so as to withstand the wave forces that impact on them resulting from extreme wave conditions during their lifetime. To arrive at the design wave height, a rigorous analysis was carried out with utmost caution by estimating extreme wave heights for different return periods not only from  $H_s$  but also from the maximum wave heights like  $1.6H_s$ ,  $1.8H_s$  and  $2.0H_s$  and a detailed analogous investigation was carried out between the return values series of  $H_{1.6\max}^R$ ,  $H_{1.8\max}^R$  and  $H_{2.0\max}^R$  and  $1.6H_s^R$ ,  $1.8H_s^R$  and  $2.0H_s^R$ . This analysis will provide an ample opportunity to decide on the risk involved as it is associated with different return periods that is proportional to the life of the port-related structures.

**Acknowledgements** This paper has been developed during the joint Russian–Indian (RFBR–DST) project “Developing a new method of regime characteristics assessment for wind and waves along the Indian coast” funded by Department of Science and Technology (DST), Government of India (Sanction No. INT/RU/RFBR/P-177).

## References

1. Pelc R, Fujita RM (2002) Renewable energy from the ocean. *Mar Policy* 26(6):471–479
2. Boyle G (ed) (2012) *Renewable energy: power for a sustainable future*, 3rd edn. Oxford University Press and Open University, Oxford
3. Ochi MK, Whalen JE (1980) Prediction of the severest significant wave height. In: *Coastal engineering 1980*, pp 587–599
4. Isaacson MDSQ, MacKenzie NG (1981) Long-term distributions of ocean waves: a review. *J Waterw Port Coast Ocean Div* 107(2):93–109
5. Goda Y (1988) On the methodology of selecting design wave height. In: *Proceedings 21st coastal engineering conference*. ASCE, pp 899–913
6. Samayam S, Laface V, Annamalaisamy SS, Arena F, Vallam S, Gavrilovich PV (2017) Assessment of reliability of extreme wave height prediction models. *Nat Hazards Earth Syst Sci* 17(3):409–421
7. Polnikov V, Sannasiraj SA, Satish S, Pogarskii FA, Sundar V (2017) Estimation of extreme wind speeds and wave heights along the regional waters of India. *Ocean Eng* 146:170–177
8. Liu Z, Burcharth HF (1999) Encounter probability of individual wave height. In: *Coastal engineering 1998*, pp 1027–1038
9. Longuet Higgins MS (1952) On the statistical distribution of height of sea waves. *J Mar Res* IX(3):245–268

# Seasonal Variability of Circulation Along the North-East Coast of India Using Princeton Ocean Model



P. S. Swathy Krishna and Hari V. Warrior

**Abstract** The coastal circulation of northern Bay of Bengal, highlighting the West Bengal-Orissa coast is subjected to seasonal reversing of monsoon circulation. Additional forcing occurs due to freshwater flux from rivers. The surface circulation patterns and SST were analysed in former studies for the whole Bay of Bengal coast, and the effect of freshwater influx on circulation patterns was also studied in detail. We have corroborated those results by studying the surface circulation patterns in the north-east coast of India, on a month-to-month basis using Princeton Ocean Model (POM) forced by wind, salinity, heat flux and temperature for the year 2001. The reversal of surface current along the coast is observed between summer and winter monsoons. The study location shows signature of upwelling during the month of July, along with low-pressure cold-core cyclonic eddy. The presence of upwelling was also confirmed in our study by comparing the result with SeaWiFS chlorophyll data. The upwelling phenomenon was investigated for the July month of the years 1998 and 1996 and it is inferred that there is no correlation of upwelling with former and subsequent El-Niño and La-Nina years.

**Keywords** Bay of Bengal · Upwelling · POM · Monsoon

## 1 Introduction

It has always been a challenge to understand and depict the ocean circulation features, especially in the case of India and the monsoons. For a semi-enclosed basin such as Bay of Bengal which comes under the tropical monsoon belt and possessing a seasonally reversing circulation, it is found very essential to have knowledge of the coastal circulation patterns. There is a decreasing gradient in the bathymetry which

---

P. S. Swathy Krishna (✉)  
Cochin University of Science and Technology, Kochi, India  
e-mail: [swathy43734@gmail.com](mailto:swathy43734@gmail.com)

H. V. Warrior  
Indian Institute of Technology, Kharagpur, India

© Springer Nature Singapore Pte Ltd. 2019  
K. Murali et al. (eds.), *Proceedings of the Fourth International Conference in Ocean Engineering (ICOE2018)*, Lecture Notes in Civil Engineering 22,  
[https://doi.org/10.1007/978-981-13-3119-0\\_48](https://doi.org/10.1007/978-981-13-3119-0_48)

ranges from 4 km at 5°N to about 2 km at about 20°N. The continental shelf extends from 150 to 200 km in width at the Head Bay region. Majority studies have been carried out in the coastal and surface circulation of Bay of Bengal region using models such as ROMS, OGCM and satellite data analysis and by hydrographic studies. The more recent studies of the circulation pattern along the east coast of India were done by measuring the sea level anomalies estimated from satellite altimetry.

The coastal currents along the east coast of India are subjected to seasonal reversal so that it shows different nature in the northern and southern part along the East coast of India. The southward flow of coastal waters is found to appear first in the northern Bay of Bengal by the end of September and then it goes down gaining more strength as it reaches the Sri Lanka. The south-west monsoon and North-East monsoon winds push the surface water southwards from June to September and northwards from November to January, respectively. This is the usual trend observed along the East coast of India throughout the year. In this study, we have considered a small region, the north-east coast of India, which is subjected to both the summer and winter monsoons, so that the seasonal variability of surface circulation patterns can be identified on a local basis and the physical features followed by the monsoon winds can also be identified. Mostly, earlier studies on coastal circulation over BoB were done focussing on the region below 17°N and the localized feature such as upwelling mainly over the Vishakhapatnam coast were studied in detail. A cyclonic gyre off Visakhapatnam in the deep ocean was detected using numerical model MITgcm [1].

The model studies on the circulation over Bay of Bengal reveals a large anti-cyclonic gyre centred at 15°N, 86°E, fully established in February and this gyre is driven by the north-easterly wind of the winter monsoon [2]. It has been found from past observations that the southward shifting of a cyclonic gyre from the head BoB region and seemed much prominent at a depth less than 200 m for the month of July. In BoB, upwelling has been detected off Walthair in February and June [3]; it probably extends up the coast to Sagar Island off Calcutta in June–July. The observations from the coastal circulation in the northern region of BoB suggests that the dominant factor which affects the salinity and thus the stratification is the estuarine process with a predominant low salinity plume cascading as far south as 17°N [4]. The freshwater influx from the major river Subarnarekha which flows into the southern part of West Bengal coast have not been considered in our study as we need to analyse the sole effect of heat flux on the surface water circulation over the specified region.

## 2 Data and Methodology

### 2.1 Site Specification and Bathymetry

The region under study is the West Bengal-Orissa coast which extends from 20.5–22°N to 86.8–88°E. The region is exposed to tropical climate. It annually receives a moderate amount of freshwater through river input from Subarnarekha

River ( $392 \text{ m}^3/\text{s}$ ) and by heavy precipitations, especially during summer monsoon period. During the arrival of monsoons, low pressure in the BoB often leads to the occurrence of storms in the coastal areas. The region under study is shown in Fig. 1.

The bathymetry data was derived from the ETOPO1 global relief model from National Geophysical Data Center (NGDC). It is a 1 arc-minute global relief model for the earth surface which integrates land topography and bathymetry. The bathymetry data was digitalized and given as an input for our model for a depth of 200 m. The model bathymetry is shown in Fig. 2.

For understanding the circulation patterns in north-east coast of India a higher resolution model is needed. The analysis area of the model extends from  $20.5\text{--}22^\circ\text{N}$  to  $86.8\text{--}88^\circ\text{E}$ , with an approximate width of 105 km from the Orissa coast, for a depth of 200 m which includes the continental shelf region. There are  $73 \times 91$  grid points in the horizontal plane and 20 levels in vertical direction, comprising  $73 \times 91 \times 20$  computational grid points. We have used a uniform grid having resolution of 0.016 km in  $x$ -direction and 0.015 km in  $y$ -direction.

## 2.2 Input Parameters

The model is forced with wind stress, derived from QSCAT monthly climatology data for the year 2001, 1998 and 1996. Other input parameters are Sea Surface Temperature (SST), Sea Surface Salinity (SSS), Heat flux and Short Wave Radiation (SWR) are taken from Wood Hole Oceanographic Institution (WHOI) OAFflux. The

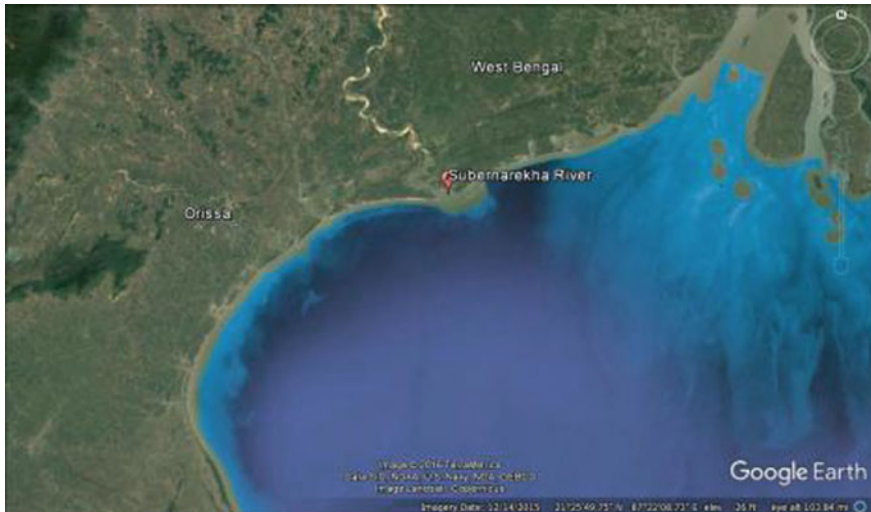
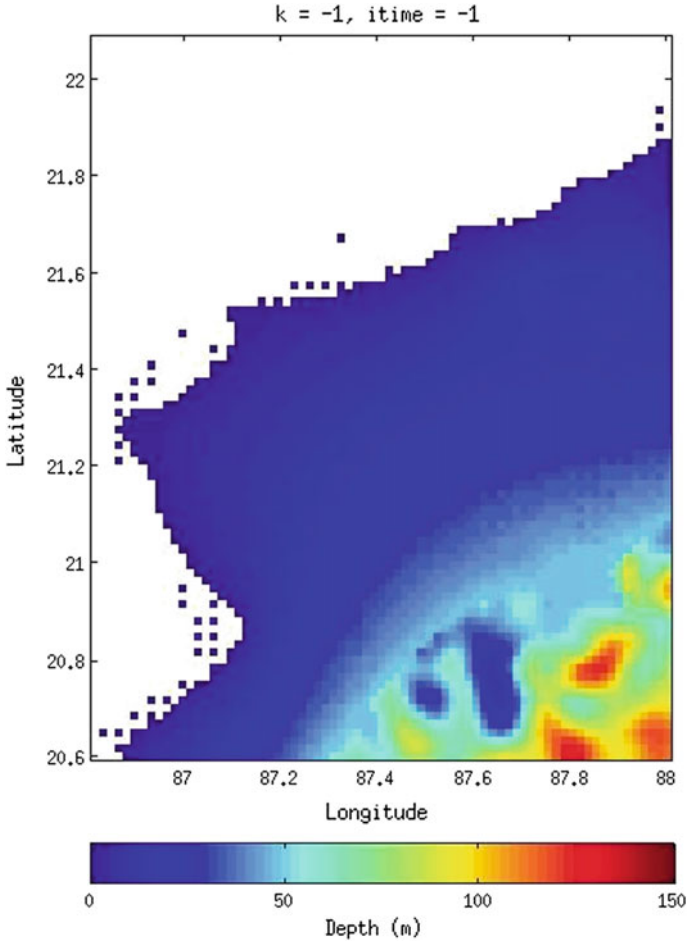


Fig. 1 Google Earth image of site



**Fig. 2** Model bathymetry

latent and sensible heat flux for the study area was found out using the Eqs. (1) and (2). The required data for these fluxes, humidity, wind, atmospheric temperature were downloaded for each month from (WHOI) OAFflux.

The turbulent exchange of heat between ocean and water is due to sensible heat and latent heat fluxes. The latent and sensible heat flux estimates are computed from the objectively analysed surface meteorological variables by using the COARE bulk flux algorithm 3.0.

They are commonly computed from the parameterization of the fluxes as a function of surface meteorological observables, such as wind speed, sea-air humidity and temperature gradients. These flux-related variables are obtained from three major sources.

- (1) Marine surface weather reports from voluntary observing ships (VOS)
- (2) Satellite remote sensing
- (3) Numerical weather prediction (NWP) reanalysis and operational data.

The expression for the respective latent and sensible heat fluxes are:

$$Q_{LH} = \rho L_e C_e U (q_s - q_a) \quad (1)$$

$$Q_{sh} = \rho C_p C_h U (T_s - \theta) \quad (2)$$

$\rho$  is the density of air,  $L_e$  is the latent heat of evaporation  $C_p$  is the specific heat capacity of air at constant pressure  $U$  is the wind speed relative to sea surface at a height  $z$ .  $C_e$ ,  $C_h$  are the turbulent exchange coefficients for latent and sensible heat fluxes and they are function of wind speed, height and atmospheric stability  $q_s$  and  $q_a$  are the surface and near surface atmospheric specific humidity,  $T_s$  is the sea surface skin temperature and  $\theta$  is the near surface air potential temperature. Table 1 shows the input parameters for the model run.

### 3 Model Description

#### 3.1 Princeton Ocean Model

Numerical models are used to simulate oceanic flows with realistic and useful results. The most recent models include heat fluxes through the surface, wind forcing, mesoscale eddies, realistic coasts and sea-floor features, and more than 20 levels in vertical. The model to be used in this circulation study is the Princeton Ocean Model. POM is a community general circulation numerical ocean model the can be used to simulate and predict oceanic currents, temperatures, salinities and other water properties. The code was originally developed at Princeton University [5] in collaboration with Dialysis of Princeton (H. James Herring, Richard C. Patchen). POM is widely used to describe coastal currents. It is a direct descendant of the Bryan–Cox model. It includes thermodynamic processes, turbulent mixing, Boussinesq and hydrostatic approximations. The model incorporates the Mellor–Yamada turbulence scheme developed in the early 1970s by George Mellor and Ted Yamada; this turbulence sub-model is widely used by oceanic and atmospheric models. Considering the need for a high-resolution numerical model for coastal ocean, and POM was developed with many features to handle tides and coastal circulation it was best suited for the circulation study particularly in our area of study. In POM, the vertical equations are restructured by sigma coordinate system (where  $\sigma$  is used to represent a scaled pressure level) and horizontal equations are recast in a curvilinear coordinate system which provides variable grid sizing. This feature made the model to better handle the coastline features, complex topographies and shallow region. It uses an ‘Arakava C’ grid differencing scheme and has a free surface and split time step. Using



**Table 1** Input parameters

Month	January	February	March	April	May	June	July	August	September	October	November	December
u_wind	-2.101	0.847	-0.197	3.112	1.309	4.488	4.617	4.229	0.929	-1.501	-3.743	-0.77
v_wind	-1.342	2.684	3.909	6.15	6.546	5.805	5.273	3.759	4.286	-0.596	-2.152	-3.417
SST	24.45	25.8	28.8	29.7	30.75	30.45	29.4	30.6	29.25	31.5	29.4	26.85
Salinity	31.49	31.59	31.76	32	32.23	32.26	32.26	32.27	32.32	32.31	32.33	32.08
SHF	-1.244	-2.66	-2.68	-2.92	-3.16	-3.85	-3.23	-3.865	-2.45	-2.57	-3.515	-1.275
LHF	131.7	256.9	299.6	374.8	456.3	538.1	439.9	534.5	369.2	367.2	385.4	115.2
SWR	194.9	224.6	253.8	259.2	240.8	130.6	152.5	180.5	190.1	197.1	151	172.9

Mellor–Yamada turbulence scheme, it solves time dependent, 3-D equations for the conservation of mass, momentum, salt, temperature and turbulence quantities in an incompressible hydrostatic fluid.

In a semi-enclosed region like the Bay of Bengal, the typical forcing at the open boundary includes temperature and salinity, while typical free surface forcing includes the wind stress and flux of heat and freshwater. Along the lateral boundaries, rivers can be prescribed with temperature, salinity and flow rates and in our particular simulation; we have excluded the river salinity at the lateral boundary and used 20 sigma levels in vertical.

## 4 Model Results

### 4.1 Circulation Study for the Year 2001

The model clearly depicts the annual surface water circulation that alters twice a year. These surface water currents change their direction from season to season in response to the seasonal rhythm of monsoons. The surface circulation in the West Bengal–Orissa coast is characterized by the coastal current that flows northward from November to February with maximum intensity along the coast during December, and from March to September it flows southward with maximum intensity near the coast during June and July. Then in between months are the transition period from winter to the summer monsoon period (January–March) and from the summer to the winter monsoon period (September–November). The strength of EICC varies from month to month and eventually it will reverse its direction twice in a year during November and February.

During North-East monsoon (winter monsoon) the winds blowing from the north-east direction will move the surface water southwards along the coast of West Bengal. By October which is the onset of north-east monsoon, southward flow starts along the coast of west Bengal which seems to be very weak downwards.

The coastal current moving along the Orissa coast weakens and flow with no such particular direction of flow (Fig. 3a). The SST varies from 28 near the coast to 32 at a depth of 100 m. The current starts gaining more strength by the beginning of November along the coast of Orissa and the southward moving monsoon current flows further south near to the West Bengal coast and found decaying by the end of November. This drives the surface water to circulate in an anticlockwise direction as shown in (Fig. 3b). The temperature along the coast varies from 26 to 29 as it is moving away from the coast. The SST is observed to be less in December and a strong northward flow is found with intense surface currents, whole along the north-east coast of India (Fig. 3c) extending to Head Bay. It can be analysed that during north-east monsoon the coastal currents is less affected by local winds and is more forced with wind stress. A westward flow is also observed at 20.6°N with very less

intensity which is the way it should be. The northward flow starts weakening during January and is observed with minimum SST for the whole year as shown in (Fig. 3d).

Weak currents are flowing southwards near the coast for the month of February. SST shows a uniform variation of around 26 °C except for the coastal region as shown in Fig. 4a. Most of the winds are weaker which does not show a particular direction of flow but depicts wind reversal. By March, the wind is getting more intensified and a small clockwise (eddy like formation) is found near the coast of Orissa at about

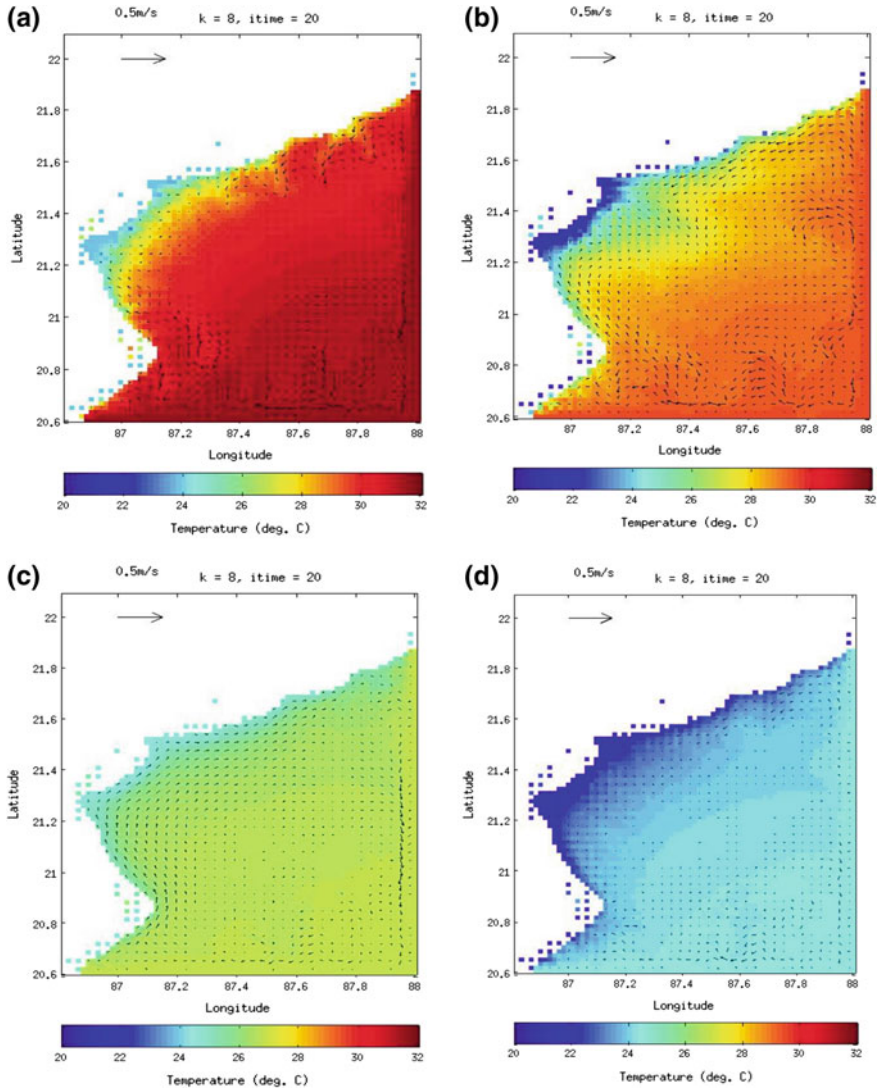


Fig. 3 a–d Surface circulation patterns for the month October–January, respectively

20.8°N as shown in Fig. 4b. The SST is getting higher and rose to 28 °C. The wind pattern is not clear for the centre portion of our domain where the intensity is much less. For the month of April, the southward flow is found to be more intensified below 21.4°N and a weak eastward flow is also noticed as in Fig. 4c. The SST is increased to 30 °C. Since it is a pre-monsoon period the SST should increase and as it can be observed in the Fig. 4d. It is increasing uniformly and reaching to 32 °C in May. The winds gain more strength by May and circulation pattern is clearer with an anticlockwise pattern of flow. The weak easterly flow still prevails at around 20.9°N.

For the month of June, (Fig 5a), it is observed that at 21.6°N, a freshwater intrusion from the Subarnarekha river changes the circulation pattern north of 21.6°N. Below this latitude coastal current flowing southward is of greater strength and further flows down along the coast of Orissa. A countercurrent flowing northward is also observed. South-west monsoon is building up along the West Bengal coast, above 21.7°N which is pushing the surface water northwards. Due to the seasonal wind change, there is clockwise circulation in the north of 21.6°N and anticlockwise in the south of it. The SST decreases to 30 °C and it found less than 28 °C near the coast. The SST reduces to 26 °C where the river inflow is found. By this time, the currents flowing away from the coast starts losing strength.

The month of July clearly depicts the phenomenon of upwelling which stretches from 21 to 22°N and found up to a depth of 30–35 m. The southward moving coastal current prevails over the Orissa coast with lesser intensity compared with the month of June. The along shore current gains more strength as it moves to the north and is directed north-eastward. This north-eastward wind stress shifts offshore and leads to Ekman transport, thereby causes upwelling. A low-pressure cold-core cyclonic eddy is observed around 21.2°N and 87.5°E. Since it is a cold-core eddy, more nutrients rich water is seen to appear there, which is confirmed by comparing the result with chlorophyll data obtained from SEAWiFS which can be seen in Fig. 5b, c. From the figure, it can be inferred that there is a high chlorophyll concentration at the centre of the eddy, which is due to upwelling. The centre of the eddy is characterized with a temperature of 26 °C. The SST went down to 22 °C at the up-welled region where the sub-surface cold water comes to the surface. To the east of eddy a strong southward flow which further moves to the right of it at around 21°N and a portion of it merges with the counter current which is flowing northward off the coast and this again merges with the eddy. Since the south-west monsoon is getting stronger, this intensifies the northward flow along the west Bengal coast. There is further decrease in SST from 31 to 29 °C at a depth of around 150 m.

For the month of august, it is observed that the upwelling region is reduced to the near coast region and cold (<22 °C) is replaced by warmer water (Fig. 6a). The south-west monsoon starts retreating so that the northward flow along BoB is less intensified but still the flow prevails. By this time, the coastal current is also reduced but continues to flow in the same direction as it was in July (southward). The SST varied between 22 and 31 °C with a uniform temperature of 30 °C over a larger area. By September, the whole coast is influenced by EICC which flows southward with lesser intensity as shown in Fig. 6b. The flow is getting more intensified as it flows southward. The SST is lesser as compared to the month of august with a temperature

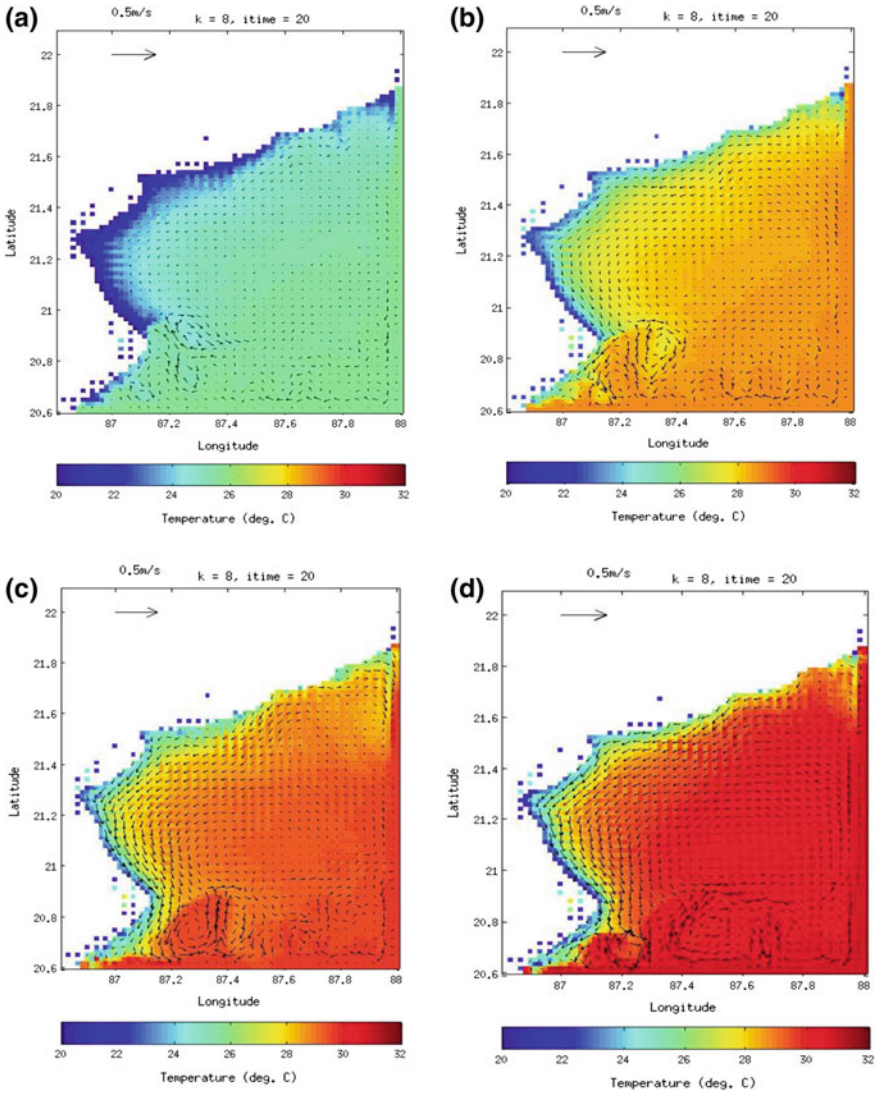


**Fig. 4** a–d Surface circulation patterns for the month February–May, respectively

of 29 °C over a large area offshore. South-east monsoon is completely vanished and the flow in the northern region is reversed.

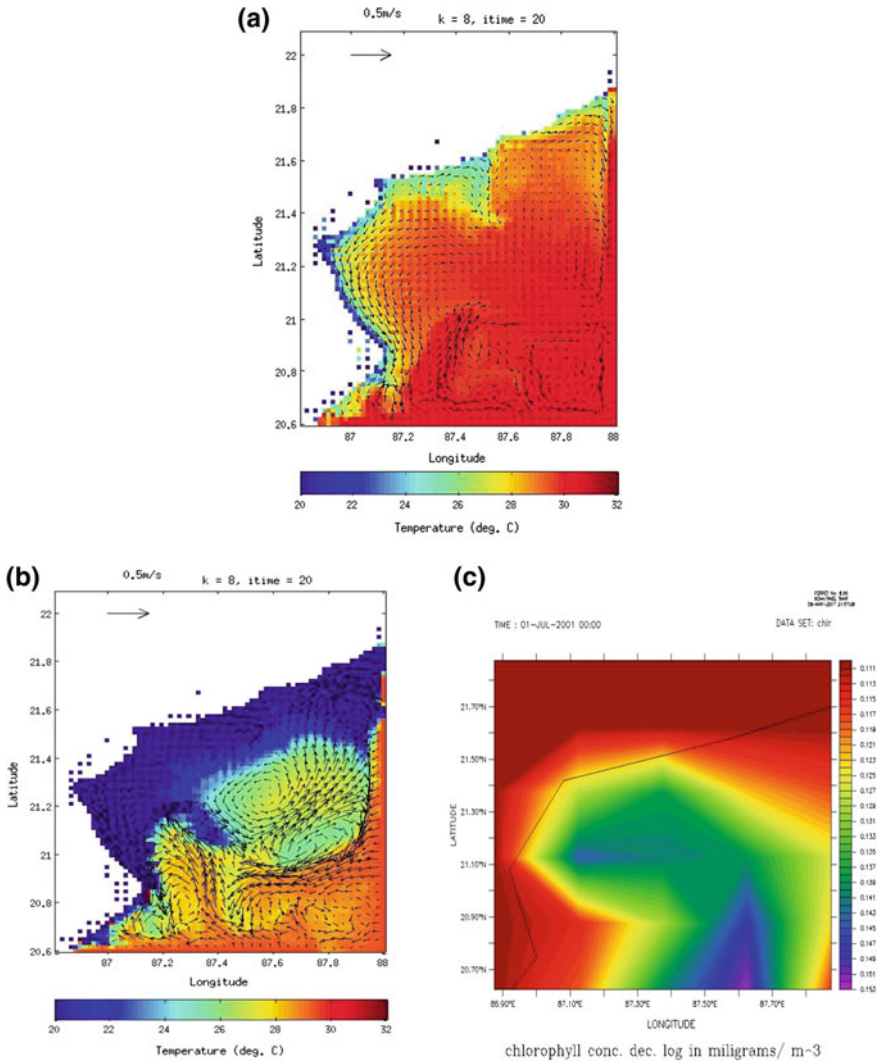


**Fig. 5** a Surface circulation pattern for the month of June. b The surface circulation of coastal currents for the month of July. It clearly depicts the upwelling phenomenon. c Chlorophyll concentration along the same region (SeaWiFS chlorophyll data)

### 4.2 Circulation Study for the Month of July 1998 (Strong El Nino Year)

1997–1998 is a strong El Nino year and the Indian summer monsoon rainfall was above normal during this period. In our present study, the effect of El Nino on the upwelling along the north-east coast of India is done and is inferred that there is no

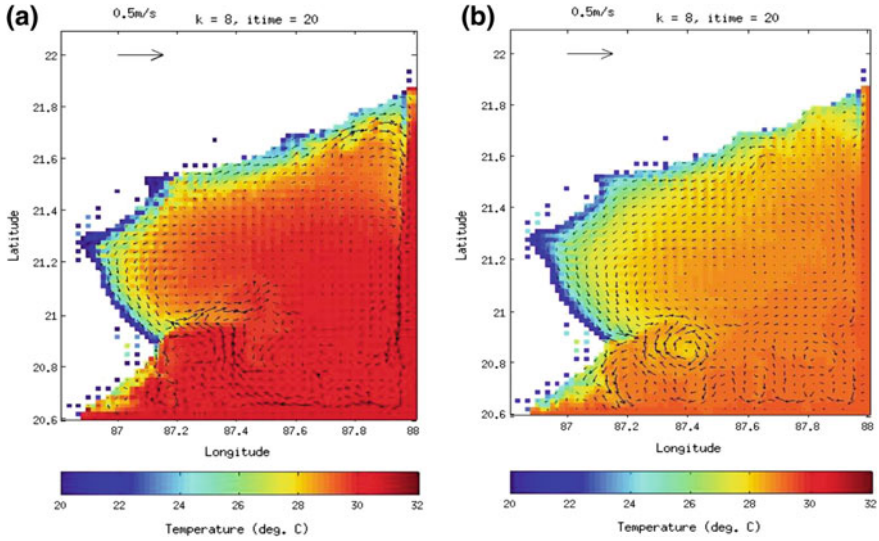


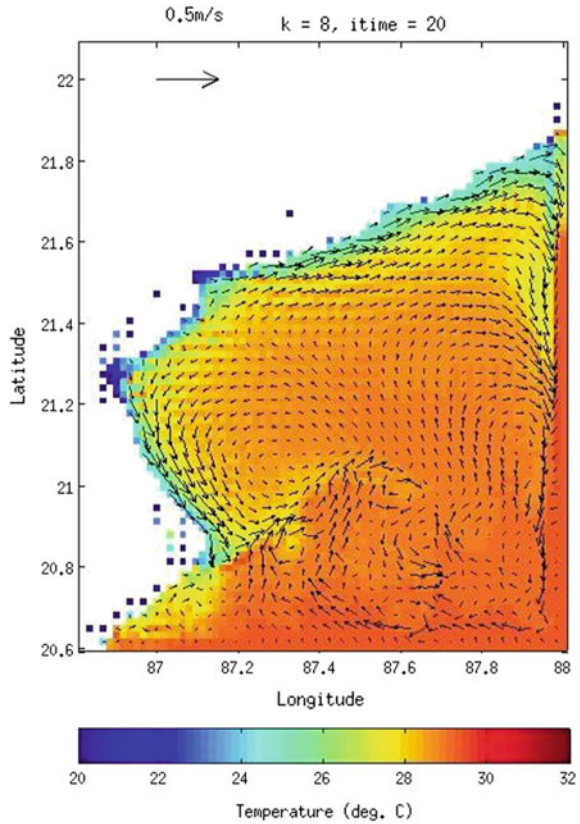
**Fig. 6** a, b Surface circulation patterns for the month August and September, respectively

trace of upwelling observed during the month of July nor an eddy formation is found even though the circulation pattern remains the same (Fig. 7). The counter current which was flowing upward off the coast with much intensity in 2001 was found to decay and forms a clockwise circulation pattern near 21°N in 1998. The SST was also found to be high than the year 2001. There is no such traces of a severe cyclonic activity either. The coastal current flowing southward due to the seasonal monsoon winds (south-west monsoon) is not at all affected by the impact of El-Niño. A counter rotating flow prevails to the south of 21.3°N and the currents are found to weaken as it reaches the Orissa coast.

### 4.3 Circulation Study for the Month of July 1996 (Weak La-Niña Year)

During July 1996, the northward flow found to the north of 21.6°N was observed to flow eastward moving away from the coast. The SST is found to be decreased to 26 near to the shore areas when compared with 1998 case, and the upwelling phenomenon is also absent in this case with no such evidence of a cyclonic eddy (Fig. 8). It has been thus inferred that La-Nina brings down the SST but the replacement of sub-surface cold water with the warm surface water along the coast is not found. Instead of the westward moving current for the year 2001, in this case, to the south of 21°N an eastward flow is found prominent. The absence of the counter current

**Fig. 7** Surface circulation pattern for July 1998



flowing northwards away from the coast is another important factor which is noticed in this weak La-Nina year.

#### 4.4 Sea Surface Temperature (SST) Validation for the Year 2001

The SST variation for the year 2001s is being validated with Hadley Center SST data (HadISST) downloaded from APDRC site. Monthly averaged values for the specific region are taken to validate with the model result and the scatter plot is shown in Fig. 9. The correlation coefficient was calculated and found to be 0.988. The model output is showing a similar trend with the Hadley SST data, and so the difference seen can be attributed to some model errors Fig. 10. It shows two peaks for the months of May and October, and SST is found to be maximum during May with average value



**Fig. 8** Surface circulation pattern for July 1996

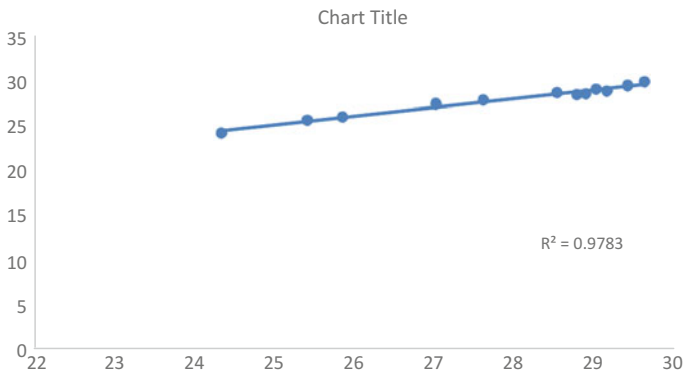
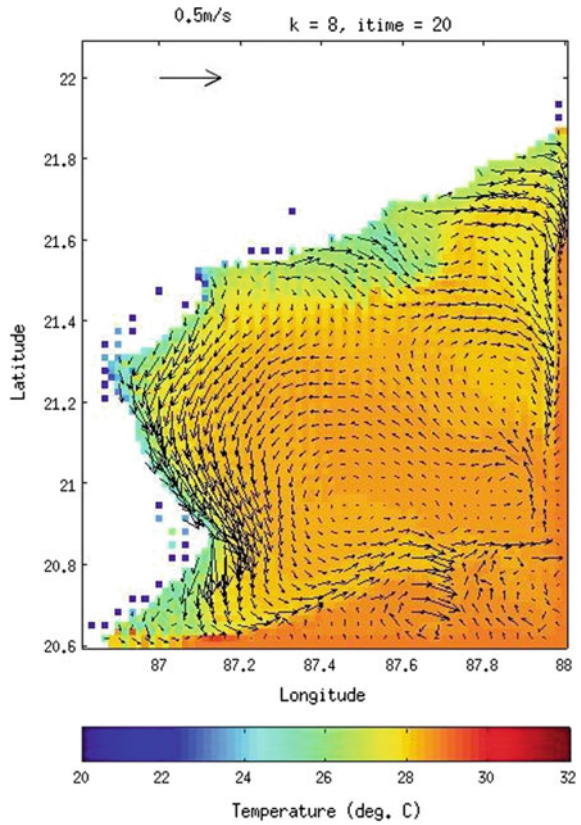


**Fig. 9** Scatter plot comprising the model SST result with Hadley SST result

around 30 °C. During south-west monsoon, the SST decreases up to 28.5 °C for the month of august.

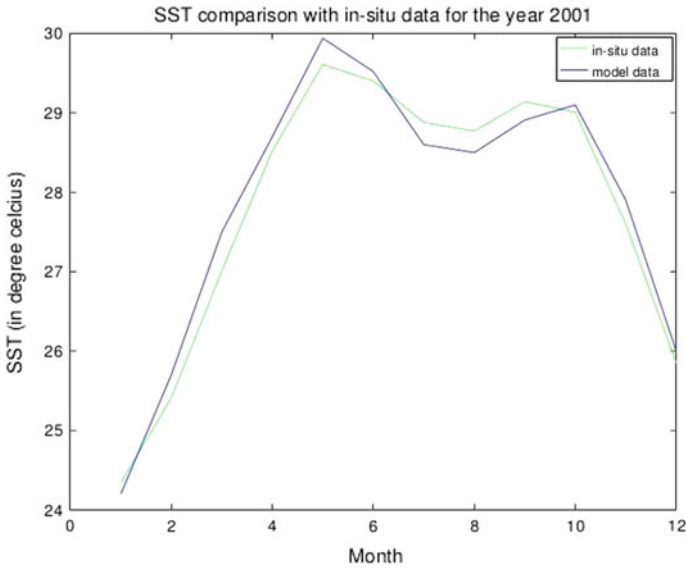


Fig. 10 Comparison of model SST data and Hadley SST data

## 5 Conclusions

The paper is a numerical simulation of the circulation in the coastal Bay of Bengal near the West Bengal coast. We have used the Princeton Ocean Model to study the current patterns of the Head Bay. The flow in this area is highly determined by a coastal current EICC. The strength of EICC varies from month to month and seasonally it reverses its direction twice in a year; during November and February. The influence of El Nino in the coastal pattern is found to be negligible.

A low-pressure cold-core cyclonic eddy is observed around 21.2°N and 87.5°E at certain period of the year. Since it is a cold-core eddy, more nutrients rich water is seen to appear there, which is confirmed by comparing the result with chlorophyll data obtained from SEAWiFS. It can be inferred that there is a high chlorophyll concentration at the centre of eddy which is due to the strong upwelling features there.

The coastal circulation of the Bay of Bengal near the Head Bay needs to be studied in more detail to discern the effects of the Hooghly and Ganga rivers on the flow. These rivers make the circulation pattern there much more complicated and interesting. Since studying circulation pattern is the first step to the determination of nutrients and phytoplankton concentrations and eventually fisheries, it is important that we study these patterns at length.

## References

1. Pradhan HK, Rao AD, Mohanty S (2015) Surface circulation and temperature inversions in the western Bay of Bengal using MITgcm. *Indian J Appl Res* 5
2. Potemra JT, Luther ME, O'Brien JJ (1991) The seasonal circulation of the upper ocean in the Bay of Bengal. *J Geophys Res: Oceans* 96(C7)
3. Lafond EC (1954) On upwelling and sinking off the east coast of India. *Mem Oceangr Andhra Univ* 1(49):117–121
4. Chamarthi S, Shree Ram P (2008) Role of fresh water discharge from rivers on oceanic features in the Northwestern Bay of Bengal. *J Mar Geodsy* 64–76
5. Blumberg AF, Mellor GL (1987) A description of a three-dimensional coastal ocean circulation model. In: Heaps N (ed) *Three-dimensional coastal ocean models, coastal estuarine Science*, vol 4. AGU, Washington, D.C, pp. 1–16
6. Mariano AJ, Ryan EH, Perkins BD, Smithers S (1995) *The Mariano Global surface velocity analysis 1.0*; USCG Report CG-D-34-95. Office of Engineering, Logistics, and Development, U.S. Coast Guard

# Water-Level Forecasting Using Neuro-wavelet Technique



Pradnya Dixit and Shreenivas Londhe

**Abstract** In the support of all ocean-related activities, it is necessary to predict the actual seawater levels as accurate as possible. The present work aims at forecasting the water levels from 3 to 6 weeks in advance at three locations: Dauphin Island, AL (Gulf of Mexico); Portland, ME (Gulf of Maine); and Cordova, AK (Gulf of Alaska) of divergent oceanic environment along the US coastline using neuro-wavelet technique (NWT) which is a combined approach of wavelet transform (WT) and artificial neural network. For this, time series of water-level anomaly (difference between the observed water level and harmonically predicted tidal level) was used to develop the NWT models at respective stations to predict the water levels for three different lead times from 3 to 6 weeks ahead. For this, hourly observed water levels along with harmonic tides were obtained from the National Oceanic and Atmospheric Administration of USA. The time series of water-level anomaly was decomposed using discrete wavelet transform (DWT) into low (approximate) and high (detail) frequency components. Further, these approximate coefficients were decomposed up to the desired level of decomposition (third and fifth levels) by multiresolution analysis of WT in order to provide more detailed and approximate components which ultimately provides relatively smooth varying amplitude series to develop the NWT models. Thus, the effect of autocorrelation in time series analysis was removed by decorrelating it using WT. Neural networks were trained with these decorrelated approximate and detailed wavelet coefficients. The outputs of networks during testing were reconstructed back using inverse DWT. Network-predicted anomaly was then added to harmonic tidal level to predict the water levels. Performance of NWT models was judged by drawing the water-level plots and other error measures. The NWT models performed reasonably well for all forecasting intervals at all the locations.

**Keywords** Water levels · Harmonic tides · Water-level anomaly  
Artificial neural networks · Neuro-wavelet technique

---

P. Dixit (✉) · S. Londhe  
Civil Engineering, Vishwakarma Institute of Information Technology, Pune, India  
e-mail: [pradnya.dixit@viit.ac.in](mailto:pradnya.dixit@viit.ac.in)

S. Londhe  
e-mail: [shreenivas.londhe@viit.ac.in](mailto:shreenivas.londhe@viit.ac.in)

© Springer Nature Singapore Pte Ltd. 2019  
K. Murali et al. (eds.), *Proceedings of the Fourth International Conference in Ocean Engineering (ICOE2018)*, Lecture Notes in Civil Engineering 22,  
[https://doi.org/10.1007/978-981-13-3119-0\\_49](https://doi.org/10.1007/978-981-13-3119-0_49)

## 1 Introduction

Accurate information of seawater levels and their variations is required for planning, construction, operation, and maintenance works of various coastal as well as off-shore structures. Generally, variations in seawater level are large enough to disturb the day-to-day operations of different coastal structures in nearby areas, particularly in shallow water depth as well as safety of maritime activities and human lives. It generates the necessity of accurate prediction of seawater levels. Traditionally, harmonic analysis is used for tide predictions, but often the values of predicted tide and the measured (observed) water levels are not identical [1]. In recent years as an alternative modeling approach to overcome the drawbacks of traditional methods, researchers have applied the domain of data-driven techniques in which applications of artificial neural networks and genetic programming are predominant. Though these techniques proved their efficiency in prediction accuracy when modeling using univariate time series is concerned the competency of these techniques becomes a question as ‘phase lag’ or ‘time lag’ occurs in most of all the forecasts. This can be attributed to the ‘effect of autocorrelation’ which inherently occurs in any univariate time series modeling. Many researchers earlier have used the same ‘seawater anomaly’ to predict the correct seawater-level anomaly, and from the predicted anomaly, further they had predicted the tides. But the use of seawater-level anomaly as input tends toward the univariate time series modeling and effect of autocorrelation plays its role which ultimately results through a ‘time lag or phase lag’ in prediction and then tide prediction exercise becomes ineffective one.

Captivating this as motivation, the present study aims in predicting the accurate seawater levels by removing the prediction lag not only at short lead time intervals but long as 3–6 weeks in advance at three locations: Dauphin Island, AL (Gulf of Mexico); Portland, ME (Gulf of Maine); and Cordova, AK (Gulf of Alaska) of divergent oceanic environment along the US coastline using neuro-wavelet technique (NWT) which is a combined approach of wavelet transform (WT) and artificial neural network. For this, time series of water-level anomaly (difference between the observed water level and harmonically predicted tidal level) was used to develop the NWT models at respective stations to predict the water levels for different lead times: 3 weeks (3w), 4 weeks (4w), 5 weeks (5w), and 6 weeks (6w) ahead. For this, hourly observed water levels along with harmonic tides were obtained from the National Oceanic and Atmospheric Administration of USA. The time series of water-level anomaly was decomposed using discrete wavelet transform (DWT) into low (approximate) and high (detail) frequency components. Further, these approximate coefficients were decomposed up to the desired level of decomposition (third and fifth levels) by multiresolution analysis of WT in order to provide more detailed and approximate components which ultimately provides relatively smooth varying amplitude series to develop the NWT models. Thus, the effect of autocorrelation in time series analysis was removed by decorrelating it using WT. Neural networks were trained with these decorrelated approximate and detailed wavelet coefficients. The outputs of networks during testing were reconstructed back using inverse DWT.

Network-predicted anomaly was then added to harmonic tidal level to predict the water levels. Performance of NWT models was judged by drawing the water-level plots and other error measures. The NWT models performed reasonably well for all forecasting intervals at all the locations.

## 2 Study Area and Data

For the present work, three tidal stations, namely Dauphin Island, AL (Gulf of Mexico); Portland, ME (Gulf of Maine); and Cordova, AK (Gulf of Alaska), were selected which are from different oceanic and meteorological environments and maintained by the National Water Level Program (NWLP) of National Oceanic and Atmospheric Administration (NOAA) of the USA. Hourly observed water-level data from the year 2000 to 2005 along with harmonic tidal data was used to train and test the model. The locations of these stations are depicted in Table 1 and Fig. 1. It can be observed from Fig. 1 that, station Dauphin Island is inside the Gulf of Mexico region which experiences very severe hurricane events every year from June to November and where the effect of hurricane winds will be of greater extent on water levels. On the other hand station Portland, ME in Gulf of Maine facing an open sea which experiences extreme cold weather conditions along with wind forcing due to tropical storms. The difference between maximum and minimum tidal levels at these locations also indicates that there is a large variation in water levels. The third station Cordova, AK, which is in Gulf of Alaska experiences a diverse wind condition than the previous two stations as it is located in the different meteorological environments than those previous stations. Thus, in the present work, the applicability of the neuro-wavelet technique in various oceanic conditions will be judged characteristically for removing the lag in prediction as well as for accurate prediction at higher lead time intervals. Readers are directed to '<http://tidesandcurrents.noaa.gov>' for further details.

**Table 1** Location of tidal stations

Sr. No.	Station	Location	Maximum WL (m)	Minimum WL (m)	Difference
1	Dauphin AL 8735180	30° 15'N, 88° 4.5'W	2.136	-0.405	2.541
2	Portland ME 8418150	43° 39.4'N, 70° 14.8'W	3.85	-0.948	4.798
3	Cordova AK 9454050	60° 33.5 N, 145° 45.1 W	5.172	-1.245	6.417

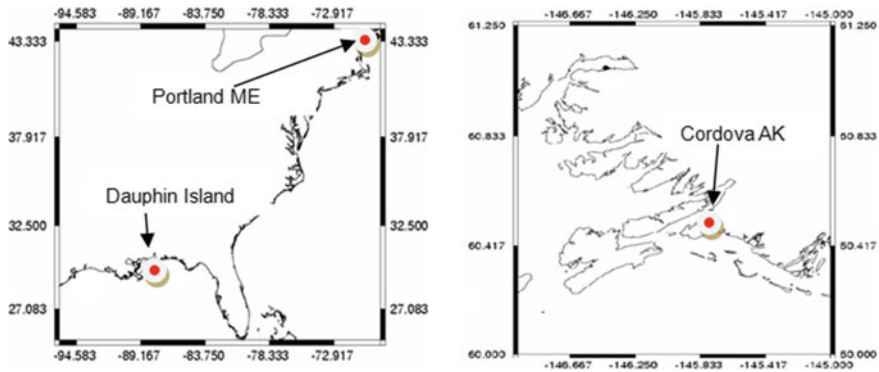


Fig. 1 Study area (Gulf of Mexico, Gulf of Maine, and Gulf of Alaska)

### 3 Neuro-Wavelet Technique

As mentioned in the introduction, a neuro-wavelet technique (NWT) is the combination of artificial neural network and the discrete wavelet transform. The discrete wavelet transform analyzes the frequency of the signal with respect to time at different scales. It decomposes time series into low (approximate) and high (detail) frequency components. The decomposition of approximate can be carried out further up to desired multiple levels in order to provide more detailed and approximate components which provides relatively smooth varying amplitude series. The neural network is thus trained with decorrelated approximate and detailed wavelet coefficients. The outputs of networks during testing are generally reconstructed back using inverse DWT. Figure 2 shows the generalized algorithm for the neuro-wavelet model. The total data set of observed water-level anomaly values is filtered into approximate (CA1) and detailed (CD1) components at the first decomposition level. Further, first approximate coefficient (CA1) is filtered into approximate (CA2) and detailed (CD2) components in the second-level decomposition. At the third-level decomposition, the second approximate coefficient (CA2) is again decomposed in approximation (CA3) and detailed (CD3) components. Finally, for third-level decomposition system, three detailed components and one approximate component are used to train the neural network (Fig. 3). This is called the multiple-level decomposition using wavelet transform. As authors have successfully applied the NWT for forecasting the ocean waves, readers are directed to Dixit et al. [2–4] for further details of neuro-wavelet technique along with the details of artificial neural network (ANN) and wavelet transforms (WTs). The choice of wavelet transformation is in fact an important part of wavelet analysis and depends very much upon both the properties of the signal under investigation and what the investigator is looking for.

Fig. 2 Algorithm of NWT

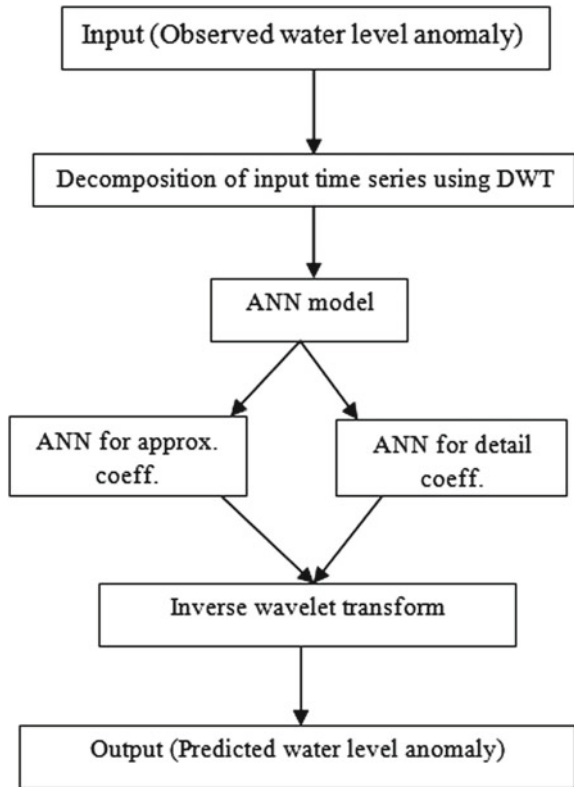
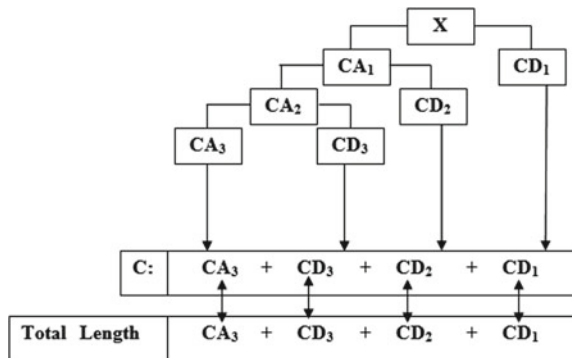
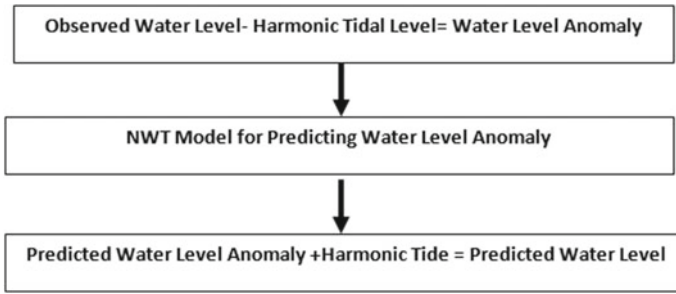


Fig. 3 Multilevel decomposition by wavelet transform



As mentioned earlier, instead of observed water-level time series, the time series of water-level anomaly (difference between the observed water level and harmonically predicted tidal level) is used in the present work to develop the NWT models at the respective stations to predict the water levels for different lead time intervals. For this, time series of water-level anomaly was decomposed using discrete wavelet





**Fig. 4** Flowchart for water-level modeling

transform (DWT) into low (approximate) and high (detail) frequency components as mentioned earlier up to third-level (3d) and fifth-level (5d) decomposition system wherever necessary. This decomposition helps to remove the effect of autocorrelation in the time series analysis to get the outputs. Thus, the network-predicted anomaly was then added to harmonic tidal level to predict the water levels. This methodology is elaborated further in Fig. 4 also.

It was noticed by the authors in earlier attempt of waves using NWT, that higher order Daubechies wavelets gives better results for higher lead time intervals [2, 3], to forecast the water level anomaly from 3 to 6 week ahead Daubechies wavelet 'db35' is used in the present work to develop all the models. Though the available water-level anomaly series is of hourly basis, for the present study one time step of 1 week is used for model development. The model for 3 weeks ahead forecast consists of four values as inputs. The first input is the anomaly for the current time step ' $t$ ', the second input is the anomaly obtained at 1 week behind the current time step, i.e., ' $t - 1w$ ', and similarly, the third input is the anomaly obtained at 2 weeks behind the current time step, i.e., ' $t - 2w$ ', while fourth input consists the anomaly obtained at 3 weeks behind the current time step, i.e., ' $t - 3w$ '. Therefore, the four inputs were:  $t$ ,  $t - 1w$ ,  $t - 2w$ , and  $t - 3w$  where the output is the 3 weeks ahead water-level anomaly, i.e., ' $t + 3w$ '. Though the forecasting interval varies from 3 to 6 weeks specifically to judge the performance of NWT, a number of inputs were kept the same while developing all the models. Thus, model for 4 weeks ahead forecast consists the same inputs:  $t$ ,  $t - 1w$ ,  $t - 2w$ ,  $t - 3w$ , and output will be 4 weeks ahead water-level anomaly value; likewise, 5 weeks ahead and 6 week ahead also include the same inputs, but output will be the 5 and 6 weeks ahead water-level anomaly values. These inputs and outputs of the various models can be expressed as

Input	Output
For 3 weeks ahead model: $t, t - 1w, t - 2w, t - 3w$	$t + 3w$
For 4 weeks ahead model: $t, t - 1w, t - 2w, t - 3w$	$t + 4w$
For 5 weeks ahead model: $t, t - 1w, t - 2w, t - 3w$	$t + 5w$
For 6 weeks ahead model: $t, t - 1w, t - 2w, t - 3w$	$t + 6w$

Instead of taking serially values of water-level anomaly on hourly basis with continuous time steps like ' $t, t - 1, t - 2$  h...' as inputs, here the specific time steps as ' $t, t - 1w, t - 2w, t - 3w$ ' were selected purposely as inputs which indirectly helps to break the autocorrelation effect in removal of phase lag [5, 6]. The models were calibrated with 70% of the total data, and the remaining data is used for the testing. Separate models were developed for 3w, 4w, 5w, and 6w ahead forecasts. Separate three-layered feedforward networks are developed for both approximate and detailed components of the wave data along with Levenberg–Marquardt (LM) as an algorithm, 'log-sigmoid' and 'linear' as transfer functions. Ultimately, the performance of NWT models was judged by drawing the water-level plots and other error measures like correlation coefficient (CE), root-mean-squared error (RMSE), mean absolute error (MAE), and scatter index (SI) between the observed and corrected water levels (after adding/subtracting the predicted water-level anomalies from the tidal levels).

## 4 Results and Discussions

As mentioned earlier, all the developed models are tested with the unseen data sets and their performance is judged by the traditional error measures like root-mean-squared error (RMSE), mean absolute error (MAE), coefficient of efficiency (CE), scatter index (SI), and correlation coefficient ' $r$ ' along with the water-level plots and scatter plots. Tables 2 and 3 showcase the results and error measures of Portland and Cordova, respectively, where the third-level decomposition (3d) system was used to predict the water-level anomaly from 3 to 6 weeks ahead in time. From Table 2, it is clear that for Portland for all the four time intervals, i.e., from 3 to 6 weeks, ' $r$ ' values are above 0.99 which showcases the superiority of NWT over the traditional techniques. Also, range of RMSE varies from 0.0987 to 0.1104 for 3–6w ahead forecasts, whereas the range of MAE varies from 0.0093 to 0.1452 for 3–6 W forecasts, respectively. Higher values of CE and lower values of SI again indicate the good performance of developed NW models. Like Portland, NWT models developed for Cordova also proclaimed better quality results for all the time intervals from 3 to 6 weeks (Table 3). Figures 5 and 6 present the observed and predicted water levels at Portland and Cordova stations, respectively. From these figures, it is evident that

**Table 2** Results of Portland

Forecasting interval	Decomposition level	$r$	RMSE	MAE	CE	SI
3w	3d	0.999	0.0987	0.0093	0.99	0.001
4w	3d	0.998	0.1001	0.0998	0.98	0.099
5w	3d	0.995	0.1098	0.0121	0.978	0.095
6w	3d	0.992	0.1104	0.1452	0.971	0.0910

**Table 3** Results of Cordova

Forecasting interval	Decomposition level	$r$	RMSE	MAE	CE	SI
3w	3d	0.999	0.0977	0.0089	0.99	0.001
4w	3d	0.999	0.0976	0.0092	0.99	0.001
5w	3d	0.998	0.0999	0.0105	0.97	0.009
6w	3d	0.994	0.1120	0.0113	0.96	0.010

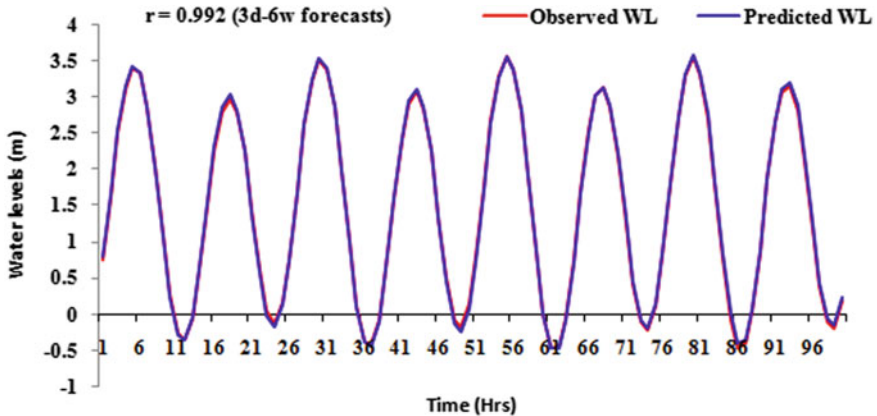


**Fig. 5** Six weeks ahead forecast at Portland by third-level decomposition

the phase lag is completely removed in the prediction and due to which prediction accuracy is improvised up to 0.99:  $r$  at higher lead time interval also.

But at Dauphin, the results obtained were not in agreement with these two stations. It can be seen from Table 4 that when third-level decomposition (3d) system was used, as the lead time interval increased from 3 to 6 weeks, ' $r$ ' values decreased from 0.904 to 0.834, respectively. Therefore, to improvise the results for higher precision, it was decided to decompose the input time series up to fifth-level decomposition (5d) as higher-order decomposition facilitates more number of filters than the lower one and thus helps to remove the autocorrelation effect in the input time series which exactly helps to improve the prediction accuracy [3]. Table 4 also presents the '5d' results for all the four lead time intervals from 3 to 6 weeks, and it can be said from these results that '5d' system had dominated the '3d' system as values of ' $r$ '

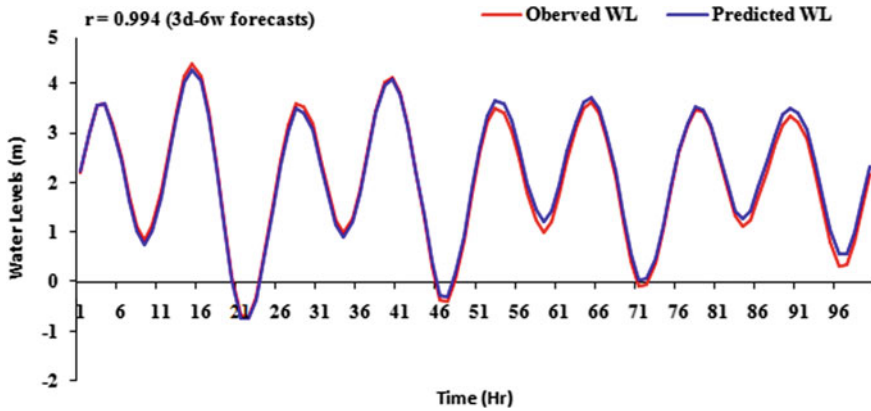


Fig. 6 Six weeks ahead forecast at Cordova by third-level decomposition

Table 4 Results of Dauphin Island

Forecasting interval	Decomposition level	<i>r</i>	RMSE	MAE	CE	SI
3w	3d	0.904	0.104	0.011	0.900	0.87
	5d	0.989	0.080	0.002	0.970	0.36
4w 24 h	3d	0.890	0.115	0.018	0.893	0.92
	5d	0.960	0.086	0.008	0.918	0.45
5w	3d	0.871	0.108	0.021	0.826	1.12
	5d	0.952	0.089	0.011	0.896	0.76
6w	3d	0.834	0.210	0.028	0.743	1.20
	5d	0.911	0.098	0.019	0.820	0.87

improved from 0.904 to 0.989 for 3w, 0.890 to 0.960 for 4w, 0.871 to 0.952 for 5w, and 0.834 to 0.911 (6w) ahead forecasts. As not only ‘*r*’ values were improvised but all other error measures values also improved with better range. This indicates the competency of NWT in forecasting the water levels at comparatively longer lead times from 3 weeks (504–1176 h or 3/4th of a month) to 6 weeks (1176 h or 1 1/2th of a month). It is evident from all 5d results in Table 4 that the range of SI is decreased from 3 to 5d level. Also, it can be said that as decomposition level increased the model accuracy is increased at higher lead time intervals with reduced values of SI. This authenticated the superiority of higher-level decomposition than the lower ones in precise prediction a time series. Figures 7 and 8 represent the performance of 3 and 5d decomposition models and endorse the superiority of higher-level decomposition on lower-level decomposition system clearly. Also, it is clear from all these figures that phase lag is removed completely from prediction.

These all results depict the excellent performance of the developed NWT models at each station. Though all the three stations Dauphin, Portland, and Cordova were from

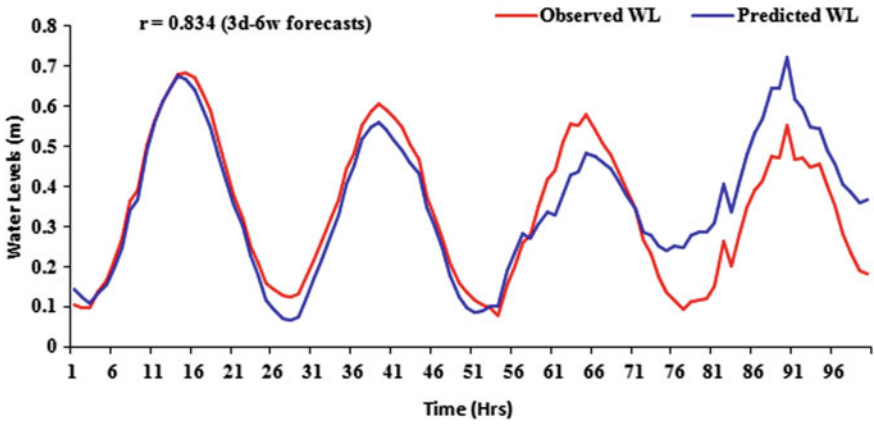


Fig. 7 Six weeks ahead forecast at Dauphin by third-level decomposition

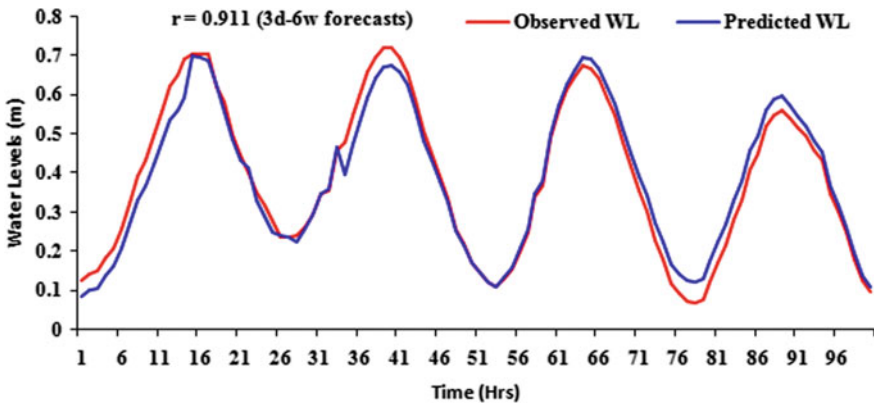


Fig. 8 Six weeks ahead forecast at Dauphin by fifth-level decomposition

different oceanic environments, NWT proved its proficiency at all the stations for all the lead time intervals with ‘no phase lag’. Thus, NWT is successful in predicting the accurate water levels at longer lead time as well as with highest precision with all error measures.

Hence, it can be said that the application of NWT is proved to be worthy in the diversified oceanic environments as well.

## 5 Conclusions

This paper presents the application of neuro-wavelet technique (NWT) for forecasting seawater levels at a different lead time interval from 3 to 6 weeks ahead at three

US coastline stations, namely Dauphin, Cordova, and Portland. The objective of the work is to judge the performance of neuro-wavelet technique in removing the prediction lag water-level forecasting and to improve the prediction accuracy at high lead time intervals in three complete different environments.

Therefore, a combination of wavelet transform and artificial neural networks (neuro-wavelet technique, NWT) when applied for seawater level at three US stations, it is observed that the phase lag in prediction is removed completely. NWT is successful in maintaining the prediction accuracy at higher lead time intervals also. It is confirmed that higher-level decomposition is quite useful for improvising the prediction accuracy at higher lead time intervals. From all the above-mentioned results, it can be said that the performance of neuro-wavelet technique is highly satisfactory in different oceanic environments. As per authors' best knowledge, NWT is applied very first time to predict the seawater level in a view to remove the phase lag and to improve the prediction accuracy as high lead time intervals up to 6 weeks ahead. Taking into account all these facts, it can be said that the application of NWT for accurate prediction of oceanic water levels is pretty useful and can be used in time series predictions successfully as both the major impediments about the 'timing lag' problem and 'prediction' at higher lead can be overcome by neuro-wavelet technique.

## References

1. Nitsure SP, Londhe SN, Khare KC (2014) Prediction of sea water levels using wind information and soft computing techniques. *Appl Ocean Res* 47:344–351
2. Dixit PR, Londhe SN, Dandawate YH (2015) Wave forecasting using neuro-wavelet technique. *Int J Ocean Clim Syst* 5(4):237–248
3. Dixit PR, Londhe SN, Dandawate YH (2015) Removing prediction lag in wave height forecasting using Neuro-wavelet modeling technique. *Ocean Eng* 93:74–83
4. Dixit PR, Londhe SN (2016) Prediction of extreme wave heights using neuro wavelet technique. *Appl Ocean Eng* 58:241–252
5. Abrahart RJ, Heppenstall AJ, See LM (2007) Timing error correction procedure applied to neural network rainfall-runoff modeling. *Hydrol Sci J* 52(3):414–431
6. De Vos NJ, Rientjest THM (2005) Constraints of artificial neural networks for rainfall-runoff modeling: trade-offs in hydrological state representation and model evaluation. *Hydrol Earth Syst Sci* (9):111–126
7. Indian National Centre for Ocean Information Services, Hyderabad, India. <http://www.incois.gov.in>
8. Babovic V, Keijzer M (2000) Genetic programming as a model induction engine. *J Hydroinform* 1(02):35–60

# Seasonal and Inter-Annual Variations in Wave Characteristics of Vizhinjam, South-West Coast of India



Sisir Kumar Patra, Basanta Kumar Jena, V. Suseentharan  
and M. V. Ramanamurthy

**Abstract** Understanding of nearshore wave characteristics is vital for beach processes, sediment transport, the design of coastal structures and shoreline management. Identification and separation of wind sea and swell wave characteristics provide more realistic depiction of sea state and are of great importance in sea safety, offshore structure design and ship operations. Seasonal and inter-annual wave characteristics based on observed wave data collected for the period March 2015–February 2017 from 2 km off Vizhinjam coast at 25 m water depth are studied. The separation of wind sea and swell components from the wave spectrum was done by wave steepness method that separates by a separating frequency ( $f_s$ ) into sea and swell parts and their components, viz. significant wave heights ( $H_s$ ,  $H_{sw}$  and  $H_{ss}$ ), zero crossing periods ( $T_z$ ,  $T_{sw}$  and  $T_{ss}$ ) and mean wave periods ( $\theta_{sw}$ ,  $\theta_{ss}$ ). The predominant wave direction is SSW (202.5°) followed by South (180°) and SW (225°), recorded annually. The maximum and significant wave height of 4.7 and 2.85 m, respectively, was recorded during June 2015; however, there was no major cyclone impact in the study duration. The result of long-term (two years) wave characteristics of Vizhinjam shows the monthly and seasonal variations of wave parameters are within a range and repetitive.

**Keywords** Sea and swell · Wave rider buoy · Wave spectrum

## 1 Introduction

The study on short- and long-term wave characteristics primarily helps coastal engineers and oceanographers for proper planning and design of coastal structures, navigation, forecasting and shore protection measures [1]. Long-term measured wave data collection along Indian coast is not adequate till date to derive wave climate of

---

S. K. Patra (✉) · B. K. Jena · V. Suseentharan · M. V. Ramanamurthy  
National Institute of Ocean Technology, NIOT Campus, Velachery-Tambram Main Road,  
Pallikaranai, Chennai 600100, India  
e-mail: [sisir.skp@gmail.com](mailto:sisir.skp@gmail.com)

© Springer Nature Singapore Pte Ltd. 2019  
K. Murali et al. (eds.), *Proceedings of the Fourth International Conference in Ocean Engineering (ICOE2018)*, Lecture Notes in Civil Engineering 22,  
[https://doi.org/10.1007/978-981-13-3119-0\\_50](https://doi.org/10.1007/978-981-13-3119-0_50)

761

Indian coast as a whole; however, there are few site-specific observation since last decade [2–5].

Sea waves are generated by wind and as they propagate away from the generating area, are called swell waves. Swell waves are known to travel long distances across the world. Wind waves are generated locally and are strongly coupled to the local wind field, surpassing the contribution of tides, tsunamis, coastal surges. Separation of wave from wave spectrum into wind sea and swell provides a more realistic depiction of the sea state and is of great importance to oceanography and engineering applications [6]. The wave characteristics along west coast (Karwar to Ratnagiri) dominated by long swells during SW monsoon period and found the seasonal average wave height and period did not vary significantly [7]. However, there is an increase in wave height from June to August from south to north direction along eastern Arabian Sea [8]. The seasonal average wave height and period did not vary significantly. The Indian coast is governed by southwest monsoon (June–September) to the northeast monsoon (October and January) and fair weather (February–May) period [9].

Vizhinjam is situated along the south-west coast of India with a shore line orientation of approximately  $310^\circ$  with respect to north (Fig. 1). The Government of Kerala is developing the existing Vizhinjam harbour into International Deepwater Multipurpose Seaport. It has named a separate company, viz. Vizhinjam International Seaport Limited (VISL), as a special purpose Government company (fully owned by Government of Kerala) that would act as implementing agency for development of the Greenfield port at Vizhinjam under Public Private Partnership component on a design, build, finance, operate and transfer (DBFOT) basis with Adani port as private partner. Therefore, the present study on wave characteristics is useful to understand seasonal and inter-annual variation of the sea, swell and other wave characteristics for port development, design of coastal structures (groyne, breaker water, pier, etc.), shoreline management planning and monitoring of future geo-morphological changes along Vizhinjam coast.

## 2 Data and Methodology

As a part of long-term coastal observational studies, National Institute of Ocean Technology (NIOT), Chennai under Ministry of Earth Sciences, Government of India, has been collecting various coastal oceanography and hydrodynamics data along Indian coasts (Fig. 1). Under this programme, NIOT in collaboration with Vizhinjam International Seaport Limited (VISL) has deployed a Datawell which makes Global Positioning System (GPS)-based directional wave rider buoy in 25 m water depth [10], 1.5 km offshore off Vizhinjam (Lat/Long— $8^\circ 21.089'N/76^\circ 59.571'E$ ) since March 2015, to cater the need of future upgradation of NIOT Technical Criteria Atlas (TCA) for wave and coastal sedimentation budget planning under Sustainable Shoreline Management (SSM) project.

Data were recorded for 30 min duration at every one hour interval and sampled at a frequency of 1.28 Hz using fast Fourier transform of 6 series, each consisting





**Fig. 1** Study map showing wave rider buoy location at 25 m water depth off Vizhinjam

of 256 data points. The high-frequency cut-off was set at 0.6 Hz, and the frequency resolution was 0.005 Hz. The measurement principle of the GPS wave buoy is based on the Doppler shift phenomenon. The system calculates the velocity of the buoy from changes in the frequency received in the observed GPS signals 14. The velocities are integrated with time to determine buoy displacement. In practice, the system uses signals from multiple satellites to determine three-dimensional buoy motions. In GPS buoy, data were sampled at a frequency of 2 Hz and measured velocities are digitally filtered using integrated high-pass filter with a cut-off frequency of 0.01 Hz. These velocities are converted into north–south, east–west and vertical motions at 1.28 Hz sample interval. The wave parameters, viz. significant wave height ( $H_s$ ), average wave period ( $T_{02}$ ), wave period corresponding to maximum spectral energy ( $T_p$ ), were obtained from spectral analysis. The sharpness or flatness in the shape of the wave spectrum is judged through the spectral peakedness parameter ( $Q_p$ ). Spectra with sharper peaks will have larger value of peakedness parameter. The width of the spectra is determined using spectral width parameter ( $\epsilon$ ) and spectral narrowness parameter ( $\nu$ ).

The separation of sea and swell components from the wave spectra was done by wave steepness method adopted by US National Data Buoy Centre, based on the frequency of the wave [11]. Estimations are made by selecting a separation frequency  $f_s$  that partitions the wave spectrum into its sea and swell parts and their components, viz. significant wave height ( $H_{sw}$  and  $H_{ss}$ ), zero crossing period ( $T_{sw}$  and  $T_{ss}$ ), mean wave direction ( $\theta_{sw}$  and  $\theta_{ss}$ ). The steepness function  $\xi(f)$  and separation frequency  $f_s$  are given by Eqs. (1) and (2).

$$\xi(f) = \frac{8\pi m_2(f)}{g\sqrt{m_0(f)}} \quad (1)$$

$$f_s = Cf_m \quad (2)$$

where  $f_m$  is the frequency of maximum of  $\xi(f)$ ,  $g$  is acceleration due to gravity,  $m_0$  and  $m_2$  are the zeroth and second-order spectral moments, and  $C = 0.75$  is an empirically determined constant.

### 3 Results and Discussion

#### 3.1 Observed Wave Characteristics of Vizhinjam

The percentage occurrence of significant wave height ( $H_s$ ), periods ( $T_z$  and  $T_p$ ) and direction ( $\theta$ ) is analysed for March 2015–February 2016 and depicted in Fig. 2. However, the data for the period March 2016–February 2017 are analysed for comparison purpose only with previous year to understand seasonal and inter-annual change, due to gaps in data set. During the study periods, the maximum ( $H_{\max}$ ) and significant ( $H_s$ ) wave height of 4.7 and 2.85 m were recorded on 22 June 2015, respectively. Moreover,  $H_{\max}$  also exceeded 4 m during May and September 2015 and 2016 by south west monsoon impact although there was not major cyclone recorded during these days.

The significant wave height ( $H_s$ ) for one-year period (2015–2016) ranged from 0.38 to 2.85 m with an average of 1.11 m and the distribution is shown in Fig. 2a. The percentage distribution of significant wave height shows that 47.1% of waves are within the range of 0.5–1 m, 30.3% of waves are in the range of 1–1.5 m, and only 2.8% of waves are less than 0.5 m. During SW monsoon, 49.4% of waves are between 1 and 1.5 m, 50% of waves are more than 1.5 m, and only 0.6% are less than 1 m. During the SW monsoon season, the sea was rougher with due to high wave intensity by 99% of wave recorded more than 1 m in height. The period during December–February was recorded calm with 96.4% of wave less than 1 m and only 3.6% are more than 1 m in height.

The distribution of zero crossing periods ( $T_z$ ) is shown in Fig. 2b. One year of  $T_z$  analysis shows within the range of 3.67–10 s, with average of 6.35 s. The wave periods are ranged between 4 and 6 s with 37.7% and 6–8 s with 58.4%, respectively. During SW monsoon period, nearly 80.8% occurs in the range of 6–8 s and 19% are in the range 4–6 s. However, during December to February,  $T_z$  in the range of 4–6 s contributes nearly 55.5% of the distribution; 32.7% are in the range of 6–8 s; and 9.2% are ranged 8–10 s. This above distribution indicates that long swells dominate during SW monsoon over sea waves and the presence of very long swells during fair weather period (December–February).

The peak period ranged from 4 to 20 s with an average of 12.8 s and the distribution of peak period is presented in Fig. 2c. During one-year observation, the  $T_p$  ranged

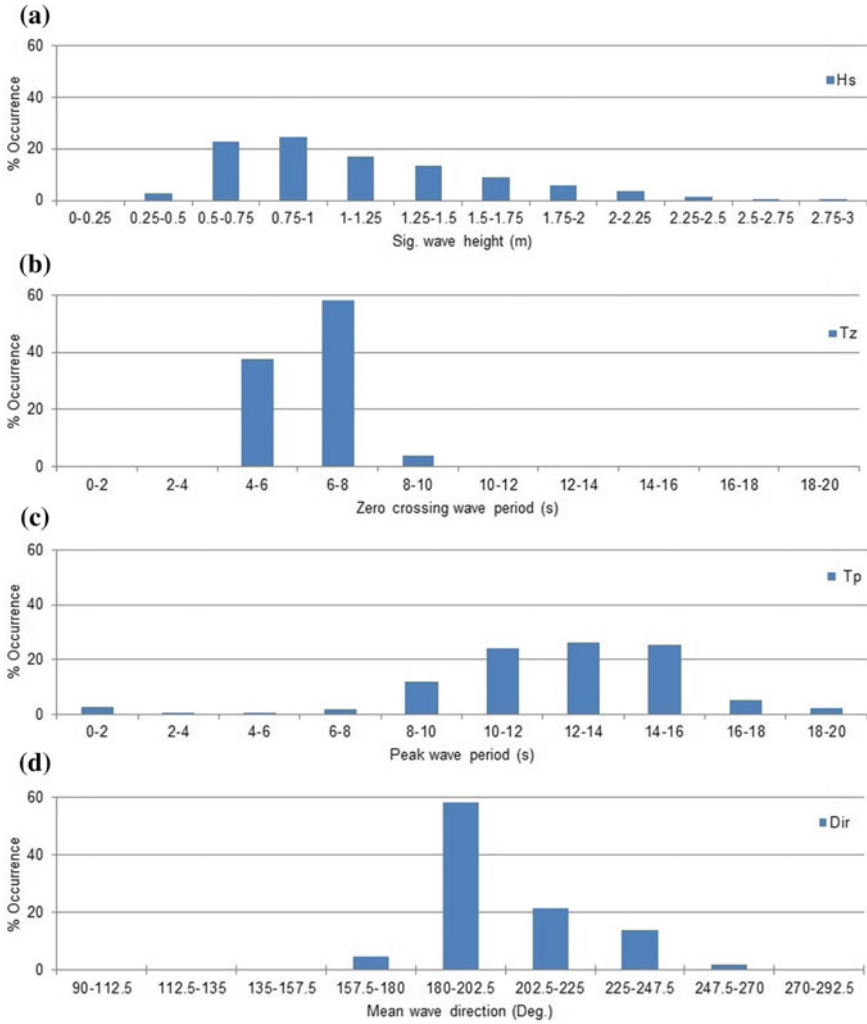


**Fig. 2** Percentage occurrence of significant wave height ( $H_s$ ), zero crossing wave period ( $T_z$ ), peak wave period ( $T_p$ ) and mean wave direction ( $\theta$ )

between 8 and 12 s by 36%, 12–16 s by 51.5%, and more than 16 s by 7.5% of waves. During SW monsoon,  $T_p$  range is maximum between 8 and 12 s by 53.2%, followed by 12–16 s with 34.6 and 8.8% with greater than 16 s waves. During fair weather period, the  $T_p$  distribution for 8–12, 12–16 and >16 s are 31.8, 51.5 and 5.6%, respectively. The distribution of  $T_p$  did not specify the dominance of any types of wave (sea or swell), due to its dependence on spectral peak where power density is maximum, and small stochastic effects easily modify the peak of the spectra and yield a different peak period [12].

The wave direction distribution clearly indicates that 58% of waves are South–SSW, 21.5% are SSW–SW, and 13.8% are SW–WSW directions (Fig. 2d). The dominant wave direction for SW monsoon is SW and SSW, and the rest of year is South and SSW. The seasonal reversal of wave direction is not fairly understood from the mean wave direction distribution. Hence, the necessary splitting of the total wave spectrum into sea and swell components is estimated separately and explained in sea and swell section.

### 3.2 Spectral Wave Characteristics

The directional wave energy spectra provide a complete description of the wave energy distribution over spectral frequencies ( $f$ ) and direction ( $\theta$ ). As sea state consists of local wind-generated waves and swells of distant storms, the wave energy spectra often show two or more spectral peaks corresponding to different generation sources (Fig. 3). The measure of spectral energy density ( $S_{\max}$ ) depicts the sea state condition, which largely depends upon spectral peakedness parameter ( $Q_p$ ) known as Goda's peakedness parameter suggested by [13] is a measure of the irregularity of the sea state. Theoretically,  $Q_p$  becomes very large for narrowband spectra and low value for broad band spectra, and under natural conditions, it remains within the interval 1.5–5.

The observed maximum spectral energy density ( $S_{\max}$ ) varies between 0.23 and 13.23  $\text{m}^2/\text{Hz}$  with average value of 2.21  $\text{m}^2/\text{Hz}$ . The % occurrences of  $S_{\max}$  between 0–2, 2–4 and 4–6  $\text{m}^2/\text{Hz}$  are 57.2, 28.1 and 10.9%, respectively. The high value of  $S_{\max}$  observed during SW monsoon, due to prevalent rough condition over the sea monsoonal wave and prevailing wind. During the study period,  $Q_p$  varied between 1 and 7.81 with an average of 1.83. Majority of the wave spectra are broader in

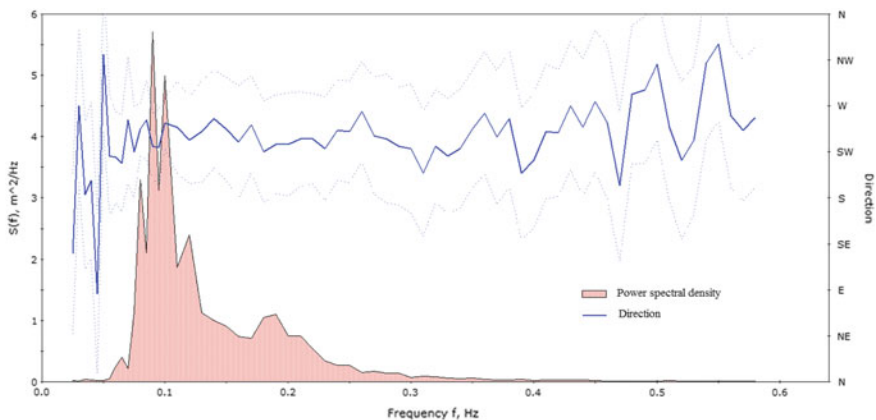
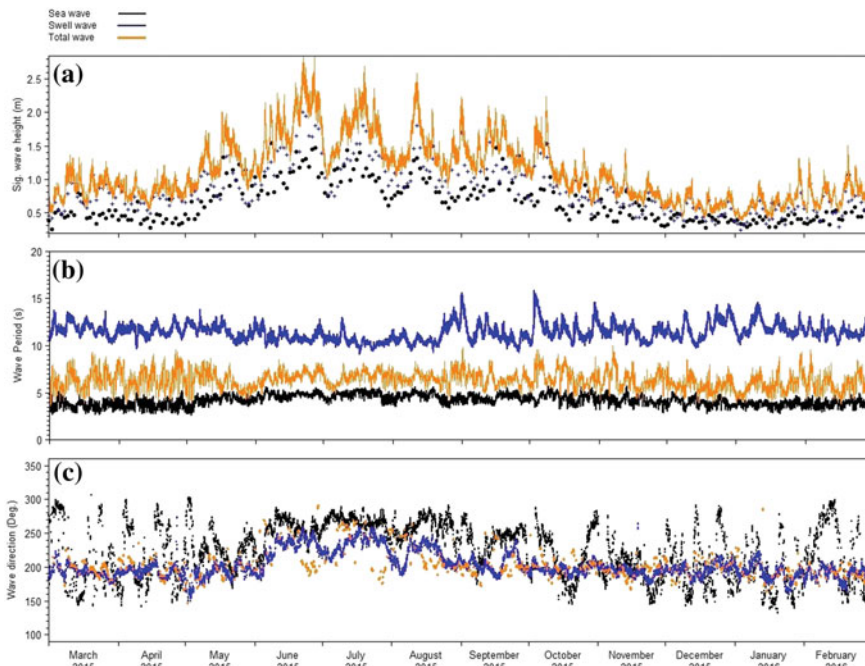


Fig. 3 Measured wave spectra observed during 25 June 2015 at 3:30 pm

shape and  $Q_p$  value fall within the range of 1–2 (72.3%). The spectral width ( $\epsilon$ ) and narrowness ( $\nu$ ) parameters vary from 0 to 1 and have smaller values for narrower spectra and larger for broader spectra. The spectral width parameter for one-year period ranged from 0.66 to 0.94 with a mean value of 0.83, out of which major portion in the range of 0.8–1 (75.6%). The high spectral width parameter indicates the dominance of the swell waves over sea waves. The spectral narrowness parameter ranged from 0.37–0.96 with a mean average value of 0.62. About 95.3% of waves fall within the range of 0.4–0.8.

### 3.3 Sea and Swell Characteristics

The significant wave height of  $H_s$ ,  $H_{sw}$  and  $H_{ss}$  is plotted in Fig. 4a. The range of  $H_{sw}$  and  $H_{ss}$  varies from 0.19–2 m to 0.22–2.46 m, respectively. The annual average of  $H_{sw}$  and  $H_{ss}$  is recorded as 0.67 and 0.86 m, respectively. The swell wave height ( $H_{ss}$ ) exceeded more than 1 m during May–September. The dominance (above 50% in wave heights) of sea and swell waves over total  $H_s$  is analysed and depicted in Table 1.



**Fig. 4** Time series plot for sea, swell and total wave height, period and direction for March 2015–February 2016

**Table 1** Percentage occurrence of sea and swell waves during January–December

Month	% Sea waves	% Swell waves
January	24.0	76.0
February	23.7	76.3
March	12.6	87.4
April	10.0	90.0
May	37.7	62.3
June	13.4	86.6
July	22.0	78.0
August	10.3	89.7
September	22.4	77.6
October	23.3	76.7
November	20.8	79.2
December	28.0	72.0
Total	20.7	79.3

Annually, 79.3% of waves are dominated by swell and 20.7% by sea. The swell waves are dominant throughout the year. However, the highest percentage of sea waves found during onset of summer monsoon in May. Similar study conducted along the Gulf of Mannar shows 55.5% of the waves dominated by seas and 45.5% by swell waves annually [14] and 30% of the waves by seas and 70% by swell waves annually along west coast [15]. This result confirms that the magnitude of the significant wave height of the study area is dominated by long swell waves by south Indian Ocean.

The range of  $T_z$  for sea and swell waves is from 2.6 to 5.8 s and 9.1 to 15.8 s, with mean value of 4.2 and 11.4 s, respectively. The measured  $T_{sw}$  is closely distributed over the periods 3–6 s (95%) and  $T_{ss}$  between 10 and 14 s (90%). The distribution of  $H_s$  with  $T_{sw}$  and  $T_{ss}$  is fairly uniform and is range bound due to its dominance by long swells throughout the year and the absence of any extreme events (cyclones).

The time series plot of sea, swell and total wave direction is depicted in Fig. 4c. The sea wave direction varies diurnally with daily reversal of sea and land breeze. There is no distinct shift in sea wave direction SW monsoon to NE monsoon, with respect to prevailing wind condition of the subcontinent [3]. The dominant swell wave direction during SW monsoon is SW, followed by SSE and WSW and South; it is SSW and South during rest of the year (Fig. 5). The mean (total) wave direction follows the pattern of swell direction due to its complete dominance (79.3%) over sea wave throughout the year.

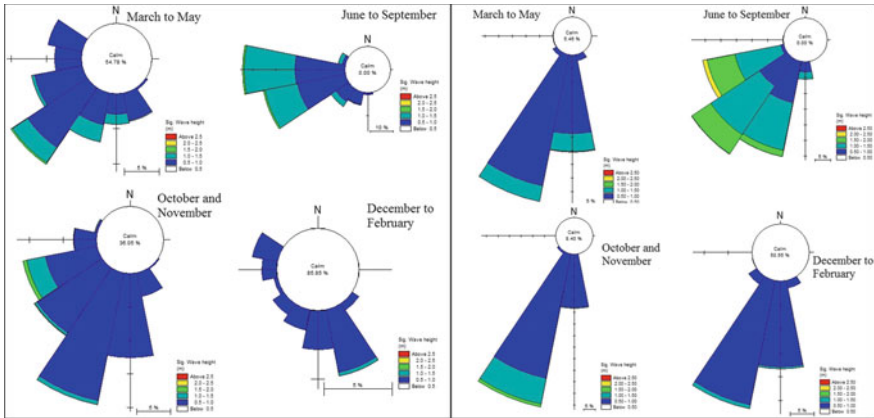


Fig. 5 Rose plot for sea (left side) and swell waves (right side) for four different seasons

### 3.4 Seasonal and Inter-Annual Wave Characteristics

In the present study, wave data of two complete years (2015–2016 and 2016–2017) are compiled and are presented (Fig. 6). The standard deviations for all the wave parameters for two years are less than 10% and quite comparable. Monthly mean  $H_s$  are higher ( $>1.5$  m) during SW monsoon and lower ( $<0.8$  m) during fair weather (DJF) period. The wave period  $T_z$  is higher ( $>6.5$  s) during SW monsoon and lower ( $<5.5$  s) during rest of the periods. There is no explicit seasonal trend of the wave period  $T_p$  (10–14 s) due to its dependence on spectral peak [16]. The mean wave direction (mode of monthly mean) is SW and SSW direction during June to September, and it is South and SSW for the rest of the year.

## 4 Conclusion

The study on wave characteristics of Vizhinjam in south west coast of India is dominated by long swell waves originated from south Indian Ocean. The swell wave is dominant by 79.3% annually, compared to sea waves. The long-term wave data (2015–2017) reveal that the monthly and seasonal wave parameters vary within a range, repetitive and cyclic. The analysis of the spectral width ( $\epsilon$ ) and narrowness ( $\nu$ ) parameters shows that majority of the wave spectra are broader in shape (72.3%) and are of high spectral energy (42%). During the SW monsoon season, the sea condition was rough with due to high wave intensity (99% of wave recorded more than 1 m in  $H_s$ ) and during December–February was recorded calm with 96.4% of wave less than 1 m. The predominant mean wave direction is SSW, followed by South and SW.

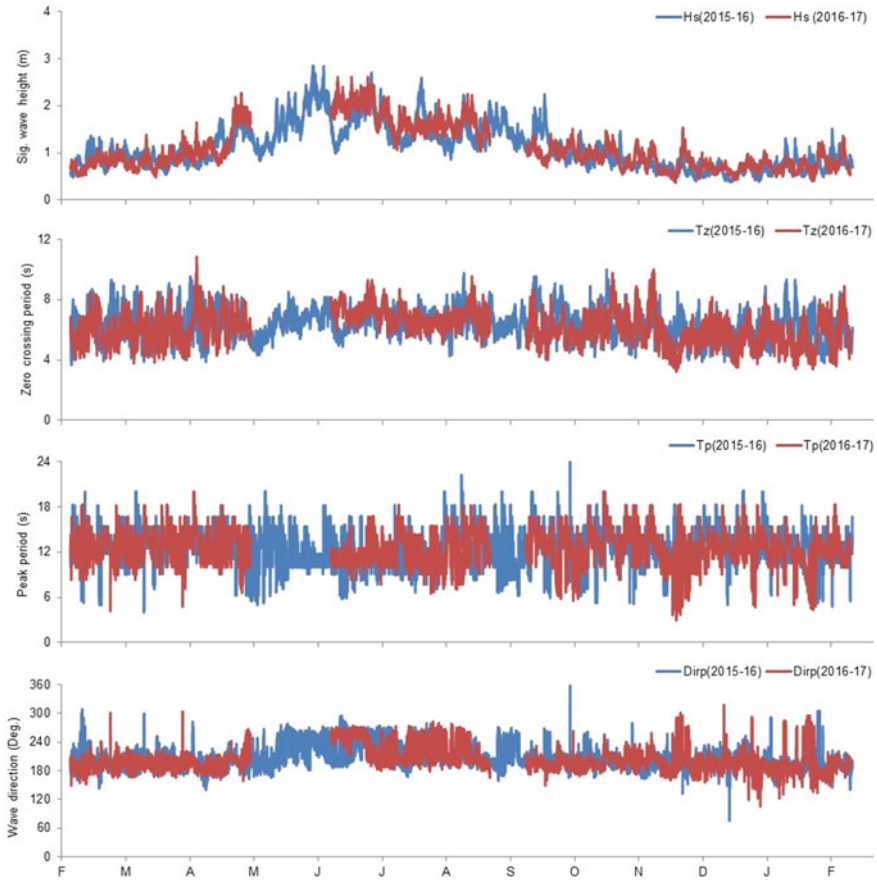


**Fig. 6** Inter-annual variability (2015–2016 and 2016–2017) for wave height, period and direction

The result of the study is helpful for the ongoing port construction near Vizhinjam and shoreline management prospective in future.

**Acknowledgements** The present study is a part of the ongoing research project ‘Technical Criteria Atlas (TCA)’ sponsored by the Ministry of Earth Sciences (MoES), Government of India. We are grateful to Secretary, MoES, Government of India, New Delhi, for necessary funding support, and The Director, National Institute of Ocean Technology, Chennai, for his encouragement and support. The help rendered by the Vizhinjam Port authorities is acknowledged.

## References

1. Earle MD (1984) Development of algorithms for separation of sea and swell. National data Buoy Center Tech. Rep. MEC-87-153



2. Sanil Kumar V, Dubhashi KK, Balakrishnan Nair TM (2014) Wave spectral characteristics off Gangavaram, East coast of India. *J Oceanogr* 70:307–321. <https://doi.org/10.1007/s10872-014-0223-y>
3. Patra SK, Mishra P, Mohanty PK, Pradhan UK, Panda US, Ramanamurthy MV, Sanil Kumar V, Balakrishnan Nair TM (2016) Cyclone and monsoonal wave characteristics of northwestern Bay of Bengal: long-term observations and modeling. *Nat Hazards* 82:1051–1083. <https://doi.org/10.1007/s11069-016-2233-0>
4. Glejin J, Sanil Kumar V, Balakrishnan Nair TM (2013) Monsoon and cyclone induced wave climate over the near shore waters off Puduchery, south western Bay of Bengal. *Ocean Eng* 72:277–286. <https://doi.org/10.1016/j.oceaneng.2013.07.013>
5. Glejin J, Sanil Kumar V, Amrutha MM, Singh J (2016) Characteristics of long-period swells measured in the in the near shore regions of eastern Arabian Sea. *Int J Nav Arch Ocean Eng* 8:312–319. <https://doi.org/10.1016/j.ijnaoe.2016.03.008>
6. Semedo A, Suselj K, Ruthersson A, Sterl A (2011) A global view on the wind sea and swell climate and variability from ERA-40. *J Clim* 24:1461–1479. <https://doi.org/10.1175/2010JCLI3718.1>
7. Anoop TR, Sanil Kumar V, Shanas PR (2014) Spatial and temporal variation of surface waves in shallow waters along the eastern Arabian Sea. *Ocean Eng* 81:150–157. <https://doi.org/10.2016/j.oceaneng.2014.02.010>
8. Glejin J, Sanil Kumar V, Balakrishnan Nair TM, Singh J (2013) Influence of winds on temporally varying short and long period gravity waves in near shore regions of the eastern Arabian Sea. *Ocean Sci* 9:343–353. <https://doi.org/10.5194/os-9-343-2013>
9. Sanil Kumar V, Pathak KC, Pednekar P, Raju NSN, Gowthaman R (2006) Coastal processes along the Indian coastline. *Curr Sci* 91:530–536
10. Datawell BV (2006) Datawell wave rider reference manual; Datawell BV, Zumerlustra 4 (2012) LM Haarlem, The Netherlands
11. Wang WD, Hwang PA (2001) An operational method for separating wind sea and swell from ocean wave spectra. *J Atm Oceanic Tech* 18:2052–2062. [https://doi.org/10.1175/1520-0426\(2001\)018%3c2052:AOMFSW%3e2.0.CO;2](https://doi.org/10.1175/1520-0426(2001)018%3c2052:AOMFSW%3e2.0.CO;2)
12. Patra SK, Jena BK (2014) Inter-comparison of wave measurement by accelerometer and GPS wave buoy in shallow water off Cuddalore, east coast of India”. *Indian J Geo-Mar Sci* 43(1):45–49
13. Goda I (1970) A synthesis of breaker indices. *Jpn Soc Civ Eng* 2(2):227–230
14. Gowthaman R, Sanil Kumar V, Dwarakish GS, Mohan SS, Singh Jai, Ashok Kumar K (2013) Waves in Gulf of Mannar and Palk Bay around Dhanushkodi, Tamil Nadu. *India Curr Sci* 104(10):1431–1435
15. Aboobacker VM, Rashmi R, Vethamony P, Menon HB (2011) On the dominance of pre-existing swells over wind seas along west coast of India. *Cont Shelf Res* 31:1701–1712. <https://doi.org/10.1016/j.csr.2011.07.010>
16. Jeans G, Bellamy I, De Vries JJ, Van Weert P (2003) Sea trial of the new Datawell GPS direction wave rider. In: Proceedings of the IEEE/OES seventh working conference on current measurement technology, IEEE, San Diego, CA, USA, pp 145–147

# Multidecadal Fluctuations of Storminess of Black Sea Due to Teleconnection Patterns on the Base of Modelling and Field Wave Data



Yana Saprykina , Sergey Kuznetsov  and Nikolay Valchev 

**Abstract** The connections of Black Sea storminess activity with teleconnection patterns (climatic indexes) were performed on the base of visual wave observations (Voluntary Observing Ship) and WAM modelling. The annual maximal waves are more affected by AMO and PDO, but annual mean waves by NAO. It is shown that for qualitative analysis of climatic variability of waves on short- and middle-time periods, in general, one can use numerical simulation data even at one point of sea combining classical correlation analysis with wavelet analysis methods and parametric spectral analysis. In WAM modelling data, a long-term periodicity cannot be defined.

**Keywords** Teleconnection patterns · Storminess variability · Black Sea North Atlantic oscillation · Pacific decadal oscillation  
Atlantic multidecadal oscillation

## 1 Introduction

Storminess variability is one of the key importance for many marine applications, naval and coastal engineering. Recent investigation had shown that extreme wave climate and coastal hazards are strongly affected by teleconnection patterns of atmospheric and oceanic variability on interannual and multidecadal timescales [1–3]. The teleconnection pattern defines a recurring and permanent, large-scale pattern of

---

Y. Saprykina (✉) · S. Kuznetsov  
Shirshov Institute of Oceanology of the Russian Academy of Sciences, Moscow, Russia  
e-mail: [saprykina@ocean.ru](mailto:saprykina@ocean.ru)

S. Kuznetsov  
e-mail: [kuznetsov@ocean.ru](mailto:kuznetsov@ocean.ru)

N. Valchev  
Institute of Oceanology of the Bulgarian Academy of Sciences, Varna, Bulgaria  
e-mail: [valchev@io-bas.bg](mailto:valchev@io-bas.bg)

pressure and circulation anomalies that span some geographical areas [4, 5]. Teleconnection patterns are also defined as preferred modes of low-frequency (or long timescale) variability of the atmospheric circulation. Detailed description of teleconnection patterns, its calculating and importance can be found, for example, on <http://www.cpc.ncep.noaa.gov>. Studying the evolution of storminess along with large-scale atmospheric connection patterns and being able to predict them is crucial in the context of problem of global climate change. This is the main aim of the work on example of Black Sea's wave climate.

## 2 Teleconnections Patterns

For analysis of multidecadal fluctuations of storminess of Black Sea such teleconnection patterns as North Atlantic oscillation (NAO), Pacific decadal oscillation (PDO), Arctic oscillation (AO), East Atlantic–West Russian and Atlantic multidecadal oscillation (AMO) were chosen. The North Atlantic oscillation (NAO) index is calculated on the surface sea-level pressure difference between the Subtropical (Azores) High and the Subpolar Low. The Pacific decadal oscillation (PDO) indicates a long-lived El Niño-like pattern of Pacific climate variability. The Atlantic multidecadal oscillation (AMO) is a coherent mode of natural variability occurring in the North Atlantic Ocean with long-time period of 60–80 years. It is based on the average anomalies of sea surface temperatures in the basin of North Atlantic and associated with such important climate impacts as the variability of hurricane activity in Atlantic basin, changes of European summer climate and northern hemispheric mean surface temperature. The Arctic oscillation (AO) is a climate pattern characterized by winds circulating counterclockwise around the Arctic at around 55°N latitude. AO reflects the climate variability connected with a penetration of colder arctic air and increasing storminess into the mid-latitudes. The East Atlantic/West Russia (EA/WR) pattern affects Eurasia throughout year. The main surface temperature anomalies associated with the positive phase of the EATL/WRUS pattern reflect above-average temperatures over Eastern Asia and below-average temperatures over large portions of western Russia and north-eastern Africa.

## 3 Wave Data

The Black Sea is the inner sea of Atlantic Ocean located between Eastern Europe and Western Asia. The Black Sea connects with the Mediterranean Sea and then with the Atlantic Ocean, through the Aegean Sea and various straits. According to classification suggested in [6], the Black Sea can be divided into five regions differed by wind-wave activity (Fig. 1). The main problem of analysing the variability of wave climate is long-term wave data. Usually, there are no such data of measurements and modelling data are analysed. But there are some questions about modelling data: (a)



**Fig. 1** Black Sea region, characteristic parts of Black Sea, points of modelling data (O1) and hydrometeorological service observation (O)

how many modelling data we need or how many points of investigated region we need and (b) how does an accuracy of modelling influence on analysis and predictions of wave climate variability? To answer these questions, we will compare three types of data for one of the regions of Black Sea and data for all sea.

The analysis of Black Sea storminess activity was performed on the base of:

- (a) Visual wave observations (Voluntary Observing Ship or VOS data) for the period 1955–2007 years [7, 8]. In total for this period for all parts of Black Sea, there are 125,142 observations available for analysis. Wave data of swell and wind-driven sea are registered separately;
- (b) Open-source data of anomalies ( $A_i$ ) of heights of maximal waves:

$$A_i = (H_i - \text{mean}(H))/\text{std}(H), \tag{1}$$

where  $H = H(\text{year})$ —height of maximum wave in year,  $i$ —year,  $\text{std}$ —standard deviation, based on visual and semi-instrumental observations on hydrometeorological station on Black Sea near Khersoness lighthouse (Fig. 1) for the period 1955–2007 years [9];

- (c) Hindcasting wave data was modelled using the spectral wave model WAM Cycle 4 [10]. Historical wind data for the Black Sea region for 59-year period (1948–2006) were extracted from NCEP global reanalysis [11]. The modelling was performed on a regular spherical grid, covering the Black Sea basin at  $0.5^\circ$  spatial resolution. During modelling, following source terms in wave action equation were taken into account: wind input, quadruplet nonlinear interactions and white capping. Previously validated WAMC4 model for the Black Sea had

shown a good agreement between the modelling results and observations [12]. Continuous hourly time series of root-mean-square wave height are simulated. From all massive of modelling data for analysis, the wave data in one point were chosen (Fig. 1). VOS data annual means and annual maximal heights of wind-driven seas and swell were investigated separately. For all data, the wavelet analysis with wavelet function Morlet and the parametric spectral analysis using Yule-Walker method were applied.

## 4 Discussion of Results

In Fig. 2, the wavelet transforms of all teleconnection indices are shown. It is well visible that changes all of indices are non-stationary process. There are trends of changes in frequency, which are not resolved by spectral analysis. But long-term variability of indices is well visible on wavelet transforms.

In Fig. 3, the changes of maximal annual wave heights of swell and wind-driven sea for all Black Sea and wavelet transforms are shown. The same data for mean annual waves are in Fig. 4. It is well visible that for all analysed wave data of maximal and mean annual waves have on average the same trends of change: since the mid-1980s, there has been a sharp decrease in the heights of waves. For annual mean wave heights of wind-driven sea, this decreasing is not so clear pronounced, especially for wind waves. For annual mean wave heights, the general increasing of wave height in period of 1955–2007 and heights of swell waves increase more than wind waves. In general, increasing of heights of mean annual height of swell waves was 25%. The average mean annual wave height for period of 1955–2007 years is 1.1 m for wind waves and 1.486 m for swell. The average annual maximal height of wind waves is 8.88 m, and swell waves are 9.18 m.

The decreasing of heights of annual maximal waves beginning in the mid-1980s is described in [13]. In this work, it is associated with the 50-year period of the Atlantic multidecadal oscillation (AMO). Also it is pointed out that the Pacific decadal oscillation (PDO) also affects the change in storm conditions and wave heights in the Black Sea, especially when both PDO and AMO are in the negative phase. Our analysis showed that (1) a sharp change in the heights of waves occurs when the PDO is in the maximum phase and the AMO is still in the negative phase, and (2) if the sharp change in the maximum wave heights is due to the minimum phase of the low-frequency AMO fluctuation, a time delay is about 4–5 years.

Wavelet analysis of variability of heights of waves shown that the characteristic periods of fluctuations in the heights of annual mean and maximal waves, on the whole, are non-stationary (Figs. 3 and 4).

The low-frequency changes in annual maximal waves, both wind-driven and swell, are affected mainly by the AMO index, and influence of the PDO index is also traced. The changes in wind waves are followed also (a) by AMO in decreasing frequency 0.09; (b) by AO, especially after 1970, at the scale of 17 years—frequency 0.06; and (c) NAO with decreasing frequency of fluctuations from 0.08 to 1.2. It can be

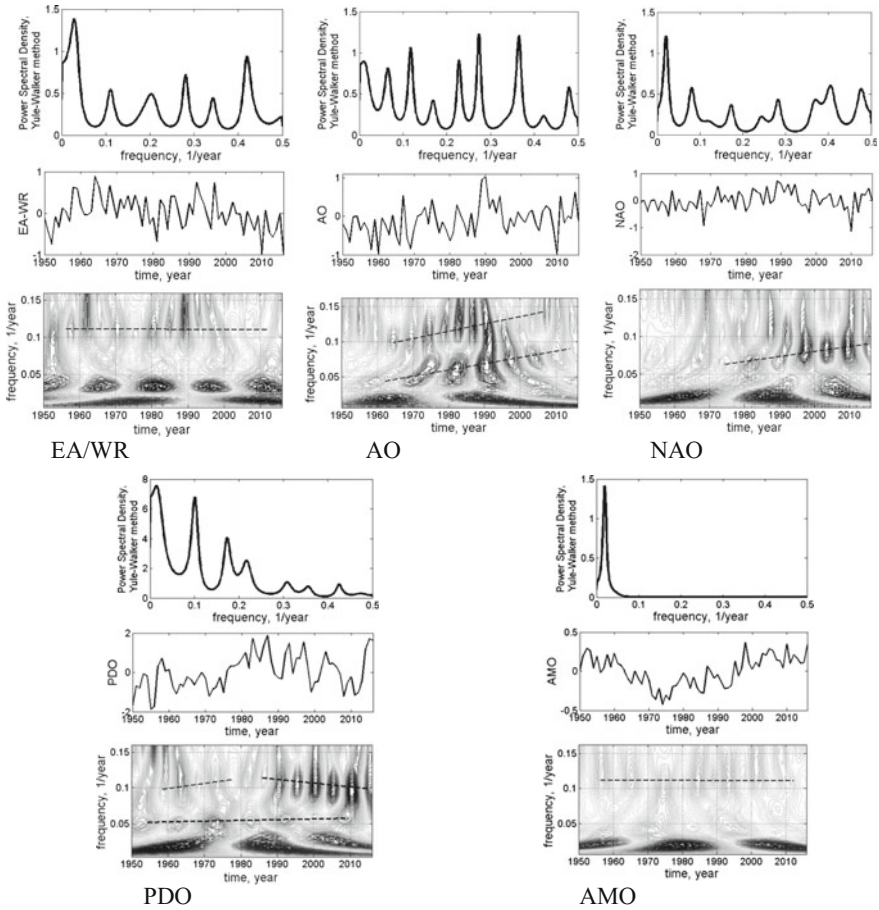


**Fig. 2** Teleconnection patterns, its spectra and wavelet transforms. Some trends in frequency variability are shown by dotted lines

said that until the mid-1980s, AMO had a greater influence and now index NAO. In swell waves, the changes are in the antiphase with PDO (the frequency scale of 0.05). But fluctuations with this frequency scale are not observed in wind-driven sea waves. Until 1980, the frequency scale about 1.2–1.5 associated with AMO is clearly traced.

The changes in annual mean wind-driven waves are connected with the PDO on frequency 0.05 which increases, starting from the 80 s, to frequency about 0.1, that can be connected with fluctuations of AMO. The low-frequency fluctuations associated with the AMO are not traced. The influence of NAO (especially in 2000s) is traced. The changes in annual mean swell waves are on frequencies 0.03 (connected with fluctuations of EA/WR index), 0.06 (with AO) and 0.1 (with AMO). Wavelet analysis had shown that the relationship between the variation of the wave heights and

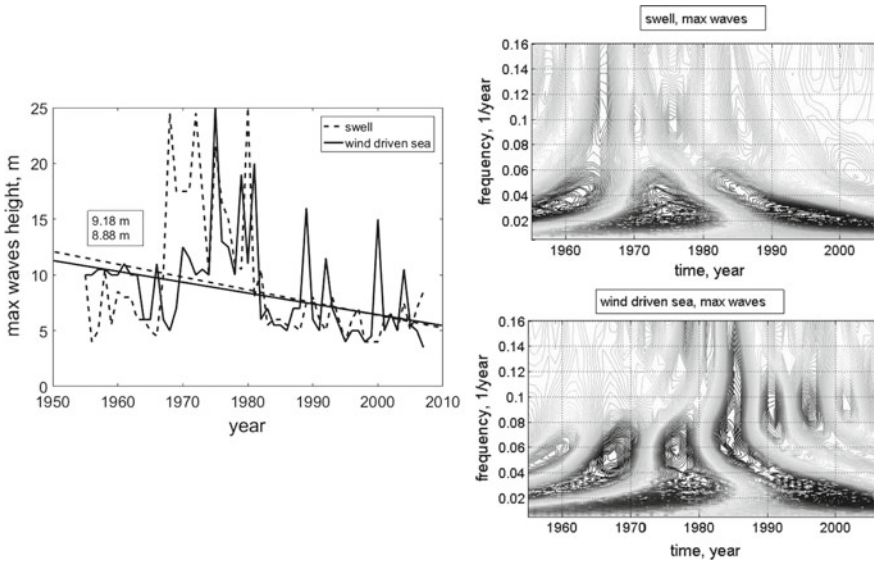


**Fig. 3** Variability of heights of annual maximal swell and wind-driven sea waves (left) and its wavelet transforms (right), swell—upper, wind-driven sea—lower

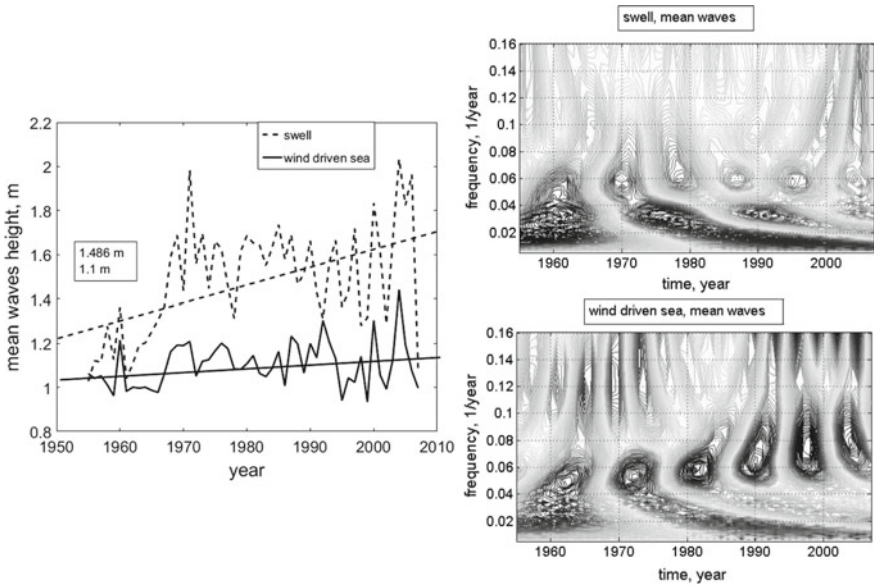


**Fig. 4** Variability of mean heights of swell and wind-driven sea waves in year (left) and wavelet transforms of variability of mean heights of waves in year (right), swell—upper, wind-driven sea—lower

**Table 1** Correlation coefficients with indices and height of annual maximal and mean waves

Teleconnection patterns	Annual maximal height of waves		Annual mean heights of waves	
	Wind-driven sea	Swell	Wind-driven sea	Swell
NAO	0.45	0.45	0.4	0.4
AO	0.3	0.38	0.35	0.35
AMO	0.40	0.56	0.32	0.4
PDO	0.40	0.46	0.3	0.4
EA/WR	0.30	0.37	0.3	0.35

climatic indices is rather complicated. It can be said that all fluctuations in climatic indices are reflected in changes in the heights of wind waves. However, for changes of mean annual waves, a connection with NAO index fluctuations is typical, with a period of 12–14 years and 3–4 years. For annual maximal wave heights, a low-frequency variability is more characteristic with large periods (about 45–50 years), which is mainly influenced by the Atlantic (AMO) and Pacific (PDO) oscillations. The connection with the NAO is weaker. It should also be noted that the use of spectral and classical correlation analysis to establish these relationships is complicated by the non-stationarity of the analysed data; classical correlation analysis will give lower values of correlation coefficients (Table 1).

Let us compare data of annual maximal and mean wave heights for wind waves of modelling and observed data for region 1 of Black Sea. It should be mentioned that in general, modelling data have wave heights of annual maximal waves that are twice lower than observed. For observed and modelled annual mean wave height, the difference is not so significant. But comparisons of anomalies (1) of wave heights of modelling data, HMS observations and VOS data have a good agreement (Fig. 5). Wavelet analysis demonstrates that in general, the fluctuations of wave heights are similar for modelled and observed waves. The fluctuations of modelled annual maximal waves better correspond to visual observation, than of modelled mean waves. For region 1 of Black Sea, there are correlations between NAO, EA/WR and PDO indices (correlation coefficients about 0.4). However for modelled data, correlation coefficients with all indices are less than 0.33. Using wavelet transform and parametric spectral analysis is possible to define similar periods of fluctuations in indices and heights of waves, but predominantly in middle and short periodicity. No clear low-frequency periodicity and no connections with AMO and PDO low-frequency variability are observed in modelling data. Wavelet structure of annual maximal and mean modelling waves is similar on EA-WR index wavelet transform. Wavelet structure of field observed and modelled waves has time lags practically in all frequency scales.



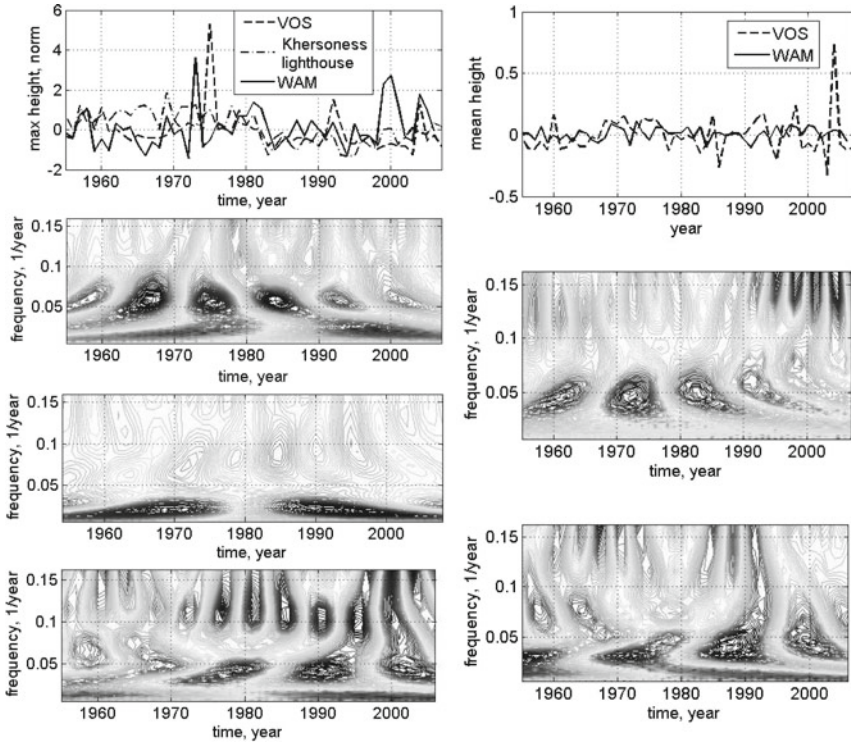


**Fig. 5** Variability of heights of mean waves in year relatively its average height (left) and anomalies of maximum wind-driven sea waves (right) in year of modelling (WAM) and field observation data (VOS, HMS) and its wavelet transforms

### 5 Conclusions

The connections of Black Sea storminess activity with teleconnection patterns (climatic indexes) were performed on the base of visual wave observations (Voluntary Observing Ship) and WAM modelling results for the periods 1955–2007. The indexes NAO, PDO, and AMO are that well correlated the maximal and mean annual wave heights as the swell of wind-driven sea. The annual maximal waves are more affected by AMO and PDO, but annual mean waves by NAO. Wavelet analysis had shown that fluctuations of teleconnection patterns and heights of waves are non-stationary processes, so application of classical correlation analysis is not correct in this case. Wavelet analysis demonstrates also good correlation between variability of wave heights and fluctuations of AO and EA/WR teleconnection patterns. There are regional differences in connection of variability of wave heights with teleconnection patterns. The wind-driven sea waves at region 1 of the Black Sea are better connected with the index EA-WR, NAO and PDO. The variability of heights of swell waves is better connected with the fluctuation of index AMO and NAO. It is shown

that for qualitative analysis of climatic variability of waves on short- and middle-time periods, in general, one can use numerical simulation data even at one point of region combining classical correlation analysis with wavelet analysis methods and parametric spectral analysis. But in modelling data, a long-term periodicity cannot be defined.

**Acknowledgements** The study was supported by RFBR grant 16-55-76002 ERA\_a in the frame of BS STEMA project. The analysis of data of waves of maximal heights was performed in the frame of project 14-50-00095 of the Russian Science Foundation.

## References

1. Bromirski PD, Cayan DR (2015) Wave power variability and trends across the North Atlantic influenced by decadal climate patterns. *J Geophys Res Oceans* 120:3419–3443. <https://doi.org/10.1002/2014JC010440>
2. Masselink G et al (2014) Role of wave forcing, storms and NAO in outer bar dynamics on a high-energy, macro-tidal beach. *Geomorphology* 226:76–93
3. Hurrell JW, Deser C (2009) North Atlantic climate variability: the role of the North Atlantic oscillation. *J Mar Syst* 78(1):28–41
4. Barnston AG, Livezey RE (1987) Classification, seasonality and persistence of low-frequency atmospheric circulation patterns. *Mon Weather Rev* 115:1083–1126
5. Wallace JM, Gutzler DS (1981) Teleconnections in the geopotential height field during the northern hemisphere winter. *Mon Weather Rev* 109:784–812
6. Lopatuhin LI (2006) Reference data on the regime of wind and waves in the Baltic, Northern, Black, Azov and Mediterranean seas. Saint-Petersburg, Russian maritime register of shipping, 450 p (in Russian)
7. Gulev S, Grigorieva V (2016) World oceans waves (WOW). [www.sail.msk/wow](http://www.sail.msk/wow)
8. Grigorieva VG, Gulev SK, Gavrikov AV (2017) Global historical archive of wind waves based on voluntary observing ship data. *Oceanology* 57(2):229–231
9. Naumova VA et al (2010) Wind-wave conditions of the Azov-Black Sea coast of Ukraine. *Nauk UkrNDGMI*, vol 259, pp 263–283 (in Russian)
10. Günther H, Hasselmann S, Janssen PAEM (1992) Wave model cycle 4: technical report no. 4. In: Modellberatungsgruppe Hamburg (ed) *Deutsches Klima Rechen Zentrum*, Germany, p 102
11. Kalnay E et al (1996) The NCEP/NCAR reanalysis project. *Bull Am Meteorol Soc* 77:437–471
12. Cherneva Z et al (2008) Validation of the WAMC4 model for the Black Sea. *Coast Eng* 55:881–893
13. Polonsky A et al (2014). Low-frequency variability of storms in the northern Black Sea and associated processes in the ocean-atmosphere system. In: *The regional environmental change*, vol 14, issue 5, pp 1861–1871

# Climate Change Impact on Design Waves Using Climate Models



Pooja Jain and M. C. Deo

**Abstract** The significant wave height,  $H_s$ , with a return period of 100 years or the design wave height is traditionally evaluated on the basis of historical observations or simulated wave data. This work examines what can happen if the same is done on the basis of projected or futuristic wave data at a series of coastal locations along the country's coastline. The design waves were derived at each location  $n$  on the basis of numerically simulated wave heights over two time slices of past and future. The wave model was forced by the CanESM2 regional climate model (RCM) run for a moderate warming scenario. The simulated daily values of  $H_s$  were fitted to the Generalized Pareto Distribution using the peak-over-threshold (POT) scheme, and 100-year  $H_s$  was derived separately for past and projected data at each site. The comparison of design  $H_s$  values derived as per projected data with those obtained from the historical data generally showed rise in the design  $H_s$  at most of the locations with some exceptions. The western coastal sites showed higher change than the eastern ones.

**Keywords** Regional climate models · General circulation models · Wave statistics  
Design waves

## 1 Introduction

As established by the Inter-Governmental Panel on Climate Change, the earth is warming and the effect of such warming on coastal and ocean environment is significant [1]. The rising temperature would alter atmospheric pressure and wind in terms of magnitudes and patterns, and hence, the wind-generated waves will accordingly change. There are many studies in the past in which changes in extreme significant wave height ( $H_s$ ) values have been worked out considering likely changes in the

---

P. Jain · M. C. Deo (✉)  
Indian Institute of Technology Bombay, Mumbai, India  
e-mail: [mcdeo@civil.iitb.ac.in](mailto:mcdeo@civil.iitb.ac.in)

climate in future as reviewed in [2]. More information of some of the noteworthy works is as below.

In a project called WASA, waves were simulated numerically with the help of wind fields belonging to the periods of 30 years each of past and future and comparatively analysed [3]. Wang et al. [4] derived wave heights for three different climate forcing scenarios in the North Atlantic on the basis of a coupled climate model. Ensemble of two regional climate models (RCMs) and two global warming scenarios was studied to evaluate extreme wave conditions in North Sea by Grabermann and Weisse [5]. Mori et al. [6] used an ensemble of several general circulation models (GCMs) available under an older modelling experiment called Climate Model Inter-comparison Project—version 3 (CMIP-3), and projected mean wave heights globally till the year 2100 by empirically relating waves to wind. They found that as per the region, 15% rise or fall in mean wave heights can be expected. Perez et al. [7] followed a similar statistical and empirical approach but predicted that future pressure changes might reduce the wave activity in Atlantic Europe. Erikson et al. [8] numerically simulated waves using four GCMs under the modelling experiment called Climate Model Inter-comparison Project—version 5 (CMIP-5) and two warming scenarios for time slices of past 30 years and future 20 years and found that an increase or decrease in mean and extreme waves can happen as per the region under consideration. Dobrynin et al. [9, 10] reported that the climate change impact in the Southern Ocean was in the form of an increase in wave activity there as per latest CMIP-5 wind models and WAM wave model. Shimura et al. [11] derived future wave climate using a general circulation model (GCM) and a numerical wave model and found 0.3 m rise or fall in annual mean  $H_s$  over the world as per the location. Bennet et al. [12], however, did not find significant changes in storm wave heights around UK in future based on an atmospheric GCM and a numerical wave model. Roshin and Deo [13] derived design  $H_s$  at 39 locations around India using past and projected waves and found a considerable rise in general in their values.

The aim of this work is to expand on the earlier study of Roshin and Deo [13] and Bhat et al. [14]. In this work, we have considered a large number of coastal sites, namely 110, and a different and reliable regional climate model (RCM). The overall aim is to evaluate design  $H_s$  at all these stations on the basis of past and projected periods of around 30 years each and compare their values so derived on the basis of historical as well as projected wave conditions. For this purpose, following procedure was followed. The wave data are generated by a numerical model driven by the RCM of Canadian Centre for Climate Modelling and Analysis (CCCMA). This choice is as per the recommendation of this RCM by Kulkarni et al. [15], in which it was found to perform better than some other RCMs. These wind forced a numerical wave model: Mike21 Offshore Spectral Wave (OSW) model, which includes a new generation spectral wind-wave model based on unstructured meshes. Before using the RCM wind, it was corrected for likely bias and this was done using the target wind of National Centre for Environmental Prediction/National Centre for Environmental Research (NCEP/NCAR). The long-term statistical analysis of historical and projected waves so generated was done by fitting Generalized Pareto Distribution

(GPD) using the peak-over-threshold (PoT) method. Finally, a comparison is made between the design  $H_s$  so obtained from both past and future data at each location.

## 2 Methods

This section presents details of the study locations and wave simulation along with the wind forcing.

### 2.1 *The Locations of Study*

This work is carried out at 110 sites spread evenly along the 7000-km-long coastline of peninsular India shown in Fig. 1. These sites include the coastal stations in water depths varying from 10 to 20 m. The distance between two sites is kept as small as 25 km in case of highly irregular coastlines and as large as 50 km or more in case of straight and smooth coastal stretches. It is well known that the total coastline is approximately equally divided into two halves exposed to Arabian Sea at the west and Bay of Bengal at the east side and that the ocean environment along the west coast is considerably different than the one along the east coast. The west coast has shallow continental shelf and flatter slopes of sea bed, while the east coast has deep shelf and steeper bed slopes. In Arabian Sea, strong winds blow along the south-west (SW) direction during the SW monsoon season, and they reverse during the north-east (NE) season.

Waves in the coastal Bay of Bengal have higher seasonality effects and lower  $H_s$  values in general than Arabian Sea [16, 17]. Several investigators in the past have studied the wave climate for Arabian Sea, Bay of Bengal, and northern Indian Ocean using variety of data such as climate models, satellite sensing, reanalysis wind and waves [9, 17–23]. Many past works have indicated the dominance of swells in Arabian Sea [24, 25]. These swells have their origin in the Southern Ocean [19, 26–28].

### 2.2 *The Wave Simulation*

The numerical wave model employed in this study is a third-generation spectral wave model—Mike21—developed by Danish Hydraulics Institute (DHI [29]). In this work, it was used to simulate hourly wave conditions over a period of past 27 years and future 35 years and ranging from 1979 to 2005 and from 2006 to 2040, respectively. The usefulness of Mike21 SW in modelling the significant wave height,  $H_s$ , off Indian coastlines is shown by many past investigators including Teena

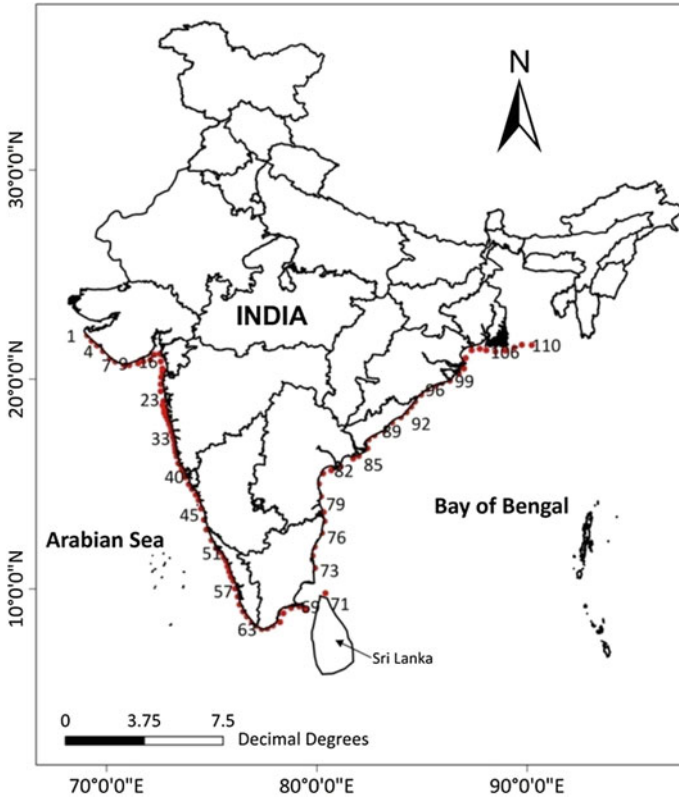


**Fig. 1** Location points along the Indian coast

et al. [30] and Satyavathi et al. [31]. The basic governing equation in this modelling protocol is the wave action balancing equation written below:

$$\frac{\partial N}{\partial t} + \nabla \cdot (vN) = \frac{S}{\sigma} \tag{1}$$

where  $N$  or  $N(\sigma, \theta)$ =the wave action density spectrum related to wave energy density spectrum  $E$  or  $E(\sigma, \theta)$  by:

$$N = \frac{E}{\sigma} \tag{2}$$

where  $\sigma$  is the relative angular frequency  $=2\pi f$ ;  $f$  = wave frequency in Hz and  $\theta$  is the direction of wave propagation. Further,  $\nabla$  = spatial operator;  $v$  = propagation velocity;  $S$  = energy source function;  $t$  = time. The above equation is solved for the unknown  $N$ , which in turn yields the required average spectral parameters, using an implicit finite difference scheme with appropriate boundary conditions. The impor-

tant wave transformation processes of shoaling, refraction, diffraction, nonlinear wave–wave interaction, dissipation of wave energy are taken into consideration in this model [29].

The physical domain covered the Indian Ocean region extending from 19°S to 30°N and 20°E to 110°E. The domain was divided into a large number of meshes of different sizes such that the resolution of the flexible triangular mesh was 1.5° for the region varying from 40° south to 0°, 0.75° above equator and 0.25° along the Indian coastline. To construct the bathymetry meshes over the domain, the toolboxes of Mike C-map and National Hydrographical Office (NHO) charts were utilized. Availability of high-resolution bathymetry scatter data near-shore in Mike C-map contributed to the best possible interpolation of the triangular mesh nodes. The wave spectrum was derived by considering 25 frequency bins with minimum frequency of 0.055 Hz and 16 direction bins. The model was calibrated using buoy data deployed at Mangalore Port location (code named: SW3) and at Ennore Port (code named: SW6) lying along the west and east coasts of India, respectively. The various model parameters such as breaking parameter, bottom friction and white capping were tuned to provide better wave predictions. Finally, the wave breaking parameter  $\gamma = 0.5$ , bottom friction or Nikuradse roughness  $KN = 0.04$  m and white capping coefficient  $C_{dis} = 3.5$  were found to be optimum and used in further work. The option of instantaneous time formulation was chosen with no separation of wind sea and swell. To account for nonlinear transformation in shallow water and nonlinear energy transfer, triad-wave and quadruplet-wave interactions are chosen.

### 2.3 *The Wind Data*

The RCMs are derived from GCMs which operate on global scales and which describe movement of the weather system as per laws of conservation of mass, momentum, energy, water mass and include heat and moisture balance principles. In climate change studies, scenarios or representative concentration pathways (RCPs) describe probable path of different aspects of the future that are combined using various driving forces such as physical, ecological, socio-economic and potential societal responses to investigate the likely consequences of anthropogenic climate change. These scenarios may work well from one parameter as compared to another in a given region. For example, one scenario may work well for simulating rainfall for a particular region but may not function satisfactorily for another parameter like say oceanic wind. Better climate models are being continuously developed to take into account scientific advances in understanding of the climate system as well as to incorporate updated data on recent historical emissions, climate change mitigation and impacts.

As mentioned earlier, in this work the main input to simulate waves with the help of the numerical model was historical and projected wind from a regional climate model, RCM, called CanESM2 of Canadian Centre for Climate Modelling and Analysis (CCCMA) tuned for the South Asian region. The variation in mean and extreme

wind over the entire Indian coastline was earlier evaluated by Kulkarni et al. [15] based on ten general circulation models (GCMs) and their multi-model ensemble, and the same were further compared with reference reanalysis data, which showed the excellent performance of CanESM2 data. The run of this climate model belonging to a moderate global warming scenario, called representative concentration pathway, RCP 4.5, was used, avoiding thereby mild as well as harsh changes into the future. The RCP 4.5 is associated with a radiative forcing on earth of the order of  $4.5 \text{ W/m}^2$ , temperature rise of  $2.4 \text{ }^\circ\text{C}$ , emission of  $\text{CO}_2$  of 650 ppm and a stabilized pathway—all until the end of the present century.

The CanESM2 wind used in this work comes under the umbrella of a modelling experiment called “Coordinated Regional Climate Downscaling Experiment” (CORDEX) targeted for South Asia (<http://cccr.tropmet.res.in/cordex>). The daily wind data of the CanESM2 RCM resulted from process-based downscaling of corresponding parent GCM.

Considering that for designing structures around 30-year data are necessary [6], the time slice of 27 years in the past and 35 years in the future was considered. The choice of these durations was governed by availability of reanalysis data for benchmarking as described subsequently. The historical data thus belonged to years 1979–2005, while the projected time slice pertained to 2006–2032. The spatial resolution of the wind was  $0.5^\circ \times 0.5^\circ$ . Although the resolution of wind data was low, the evaluation of  $H_s$  has been done at higher resolutions dictated by the size of the computational mesh.

The climate model data vary from real observations due to modelling and computational limitations, and this is counteracted by benchmarking them with some standard data. For this purpose, we have used the method of quantile mapping [32] which is based on equating the cumulative distribution function of a given approximate data set with that of a more reliable one. The latter data set used as standard reference was Climate Forecast System Research (CFSR) from National Centre for Environmental Prediction/National Centre for Atmospheric Research (NCEP/NCAR). This was selected in view of its enhanced performance checks [33, 34]. The CFSR wind specified over  $0.5^\circ \times 0.5^\circ$  resolutions at every 6-h interval was required to be regridded for this purpose owing to its different spatial resolution than that of the RCMs, and this was achieved through bilinear interpolation.

### 3 The Long-Term Wave Statistics

The long-term statistical analysis of the  $H_s$  data simulated as above was carried out on the basis of Generalized Pareto Distribution (GPD) fitted to past as well as projected wave data separately. This involved the use of daily  $H_s$  values selected on the basis of the peak-over-threshold (PoT) method in which the threshold was selected as per conditional mean exceedence plots. Refer to [35–37] for theoretical details. The usefulness of GPD in evaluating extreme wave heights has been indicated by many investigators in the past [8, 38, 39]. Some earlier studies on Indian seas [13, 31] had



indicated that the theoretical extreme value distribution of GPD type was statistically most appropriate compared with other extreme value distributions. This distribution is as follows:

$$P\left(\frac{H \leq H_s}{H \geq u}\right) = 1 - \left[1 + \frac{\xi(H_s - u)}{\Psi}\right]^{-\frac{1}{\xi}} \tag{3}$$

where P() = cumulative probability distribution of the bracketed quantity,  $H$  = dummy variable, representing the significant wave height;  $u$  = selected threshold or location parameter;  $\Psi$  = scale parameter and  $\xi$  = shape parameter. To determine the distribution parameters, the method of maximum likelihood, which involves maximization of a likelihood function, is used.

The choice of the threshold wave height,  $u$ , is based on the linearity of the plot of sample mean exceedence (SME),  $e_n(u)$ , against changing threshold values. The SME is given as:

$$e_n(u) = \frac{\sum_{i=1}^n (X_i - u)^+}{\sum_{i=1}^n N_{i\{X_i > u\}}} \tag{4}$$

where  $x_i$  =  $i$ th value of given or observed  $H_s$  out of total values  $n$ ;  $N_i()$  = number of  $H_s$  which exceeds  $u$ . The lowest value of  $u$  from where the SME graph becomes linear is selected.

## 4 Results and Discussion

The following paragraphs discuss the results obtained from model validation and application.

### 4.1 Validation of the Numerical Model

As stated earlier, the generated  $H_s$  data were validated by comparing with Wave Rider Buoys data collected earlier by National Institute of Ocean Technology. Table 1 gives details of the locations where the buoys were deployed. The west coast site (SW3) was off the port of Mangalore where the water depth was 17 m, while the east coast location (SW6) was off the port of Ennore Port at water depth of 1050 m. The duration of data collection was around 2 years each. A comparison with respect to the 3-hourly  $H_s$  values showed (Table 1) satisfactory model performance as reflected in the error statistics of correlation coefficient,  $R$ , root mean square error, RMSE, and mean absolute error, MAE, in that  $R$  was high and RMSE and MAE were low for the two buoy locations.

**Table 1** Validation of numerical wave data with buoy data

Buoy	Latitude	Longitude	Test period	Water depth (m)	Corr. coeff. <i>R</i>	Root mean square error (RMSE) (m)	Mean absolute error MAE (m)
SW3	12°58'06"	74°45'36"	01/01/2001–01/01/2003	17	0.83	0.42	0.31
SW6	13°10'03"	80°41'31"	01/01/2003–12/12/2004	1050	0.75	0.34	0.19

### 4.2 Projected versus Historical Conditions

After validation as above and using the wind input discussed in the preceding section, historical hourly  $H_s$  data belonging to years 1979–2005 as well as projected  $H_s$  data pertaining to years 2006–2032 were simulated.

For every site and for past as well as projected data, the threshold  $H_s$  values used in the GPD fitting (done as per the peak-over-threshold (PoT) method) were selected by changing the sample mean exceedence evaluated from Eq. (4) with varying thresholds,  $u$ , and selecting that threshold from where the graph became linearly varying.

The design  $H_s$  with a return period of 100 years was extracted from the GPD fits so provided to past as well as projected wave data. Figure 2 shows the same for the west coast stations, while Fig. 3 indicates the same for the east coast sites. From these figures, it can be observed that at most of the locations, design  $H_s$  calculated on the basis of projected data was higher than the one evaluated as per the historical data.

Along the west coast, majority of sites showed 20–40% rise in the design  $H_s$ . The increase is slightly above 40% at sites 12–14 at the entrance of the Gulf of Khambhat and off central Maharashtra coast (29–37). There are 14 out of 64 sites where a decreasing trend is seen; however, such changes are smaller in magnitude compared to the rising  $H_s$ . It appears that local level met-ocean and geo-morphological features and interactions, likely changes in wind fetch and durations in future, configuration

**Fig. 2** The design  $H_s$  along the west coast sites based on past (RCM) and projected (RCP-4.5) data

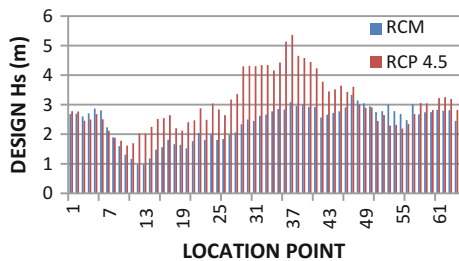


**Fig. 3** The design  $H_s$  along the east coast sites based on past (RCM) and projected (RCP-4.5) data

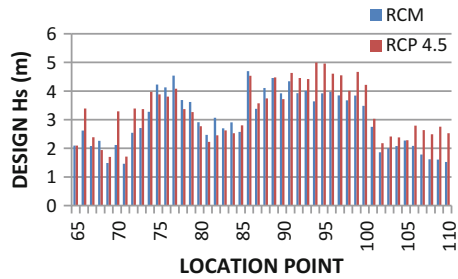


**Table 2** Statistics of past and future  $H_s$  at selected west and east coast locations (values in m)

Location point	Past min. value	Past max. value	Past std. deviation value	Past mean value	Future min. value	Future max. value	Future std. deviation value	Future mean value
25	0.11	1.70	0.15	0.65	0.12	2.46	0.25	0.60
40	0.14	2.50	0.20	0.72	0.16	3.71	0.35	0.75
59	0.25	2.61	0.24	0.72	0.33	3.22	0.38	0.95
76	0.13	3.72	0.26	0.57	0.23	3.82	0.39	0.95
88	0.16	3.61	0.23	0.62	0.18	4.05	0.45	1.03
99	0.18	3.47	0.30	0.71	0.21	4.42	0.51	1.11

of the adjacent land boundaries, change in circulation and shifting of storms govern the amount and nature of the change.

The percentage difference of the  $H_s$  along the eastern locations is much smaller and generally less than 20%. This shows higher impact of the changing climate along the west coast compared to the east. Like the west in the east coast as well 14 out of 45 sites showed a decreasing design  $H_s$ . The reductions were seen at the central east coast where curved land boundaries were present.

In order to see whether the above changes were associated with the same in the basic statistics of  $H_s$  data of entire past and future durations (considered separately), namely mean, standard deviation and maximum values, the same were worked out for all sites. An example for six typical stations along the west and east coasts is given in Table 2 showing the minimum, maximum, standard deviation and mean values for both past and projected conditions. It may be noticed that these statistical parameters indicate an intensification of waves into the future at these stations.

It, thus, appears that the difference in the design  $H_s$  will be very site-specific and non-uniform along the coast and needs to be worked out on case-to-case basis, although some amount of generalization is possible.

It is felt that the cause of the intensified wave activity in future could be the rise of local wind as well as global wind as well as swells coming from the southern directions and further due to intensification of “shamal” wind and waves coming from

the Persian Gulf and hitting the central west coast as documented in past studies in Arabian Sea, Bay of Bengal and Indian Ocean [9, 15, 17, 24, 31, 40].

While the reason for the increase in the design  $H_s$  could be due to intensification of wind and swell conditions in future as above, the same for the decrease could be reasons such as local changes in circulation and shifting of storm tracks in future.

## 5 Conclusions

The preceding sections described an attempt to understand likely changes in the design wave environment around India's coastline if such waves are derived from the future climate in place of the historical conditions.

It is found that at most of the 110 coastal sites considered, along the 7000-km-long coastline the magnitude of the design wave height might rise, although at some stations a reverse trend is also likely. Such rise will be highly site-specific and would depend on a number of factors including the location along the west or east coast, or at the tip of the coastline, proximity to complex shoreline geometry, likely changes in wind characteristics such as wind fetch and duration, complex met-ocean-morphological interactions, local changes in wind circulation and in wave propagation.

Potential shifts in the direction of wave approach can also be an important factor behind the local changes. Similarly, an intensification of wind in Arabian Sea, Bay of Bengal and Indian Ocean in future as well as rise in swells coming from the southern side as well as from the north-eastern side, documented by past investigators, can also cause the rise in the design waves seen in this work.

The study points to the necessity of considering the changing climate in future structural design after carrying out station-specific data analysis.

## References

1. IPCC (2013) Climate Change (2013) The physical science basis, contribution of working group I to the fifth assessment report of the intergovernmental panel on climate change. Cambridge University Press
2. Komar PD, Allan JC, Ruggiero P (2010) Ocean wave climates: trends and variations due to earth's changing climate. In: Kim YC (ed) Handbook of coastal and ocean engineering, chap 35. World Scientific, pp 971–995
3. WASA Group (1998) Changing waves and storms in the northeast Atlantic? Bull Am Meteorol Soc 69:741–760
4. Wang XL, Zwiers FW, Swail VR (2004) North Atlantic ocean wave climate change scenarios for the twenty-first century. J Clim 17(12):2368–2383
5. Grabemann I, Weisse R (2008) Climate change impact on extreme wave conditions in the North Sea: an ensemble study. Ocean Dyn 58:199–212

6. Mori N, Shimura T, Yasuda T, Mase H (2013) Multi-model climate projections of ocean surface variables under different climate scenarios—future change of waves, sea level and wind. *Ocean Eng* 71(1):122–129
7. Perez J, Menendez M, Camus P, Mendez FJ, Losada IJ (2015) Statistical multi-model climate projections of surface ocean waves in Europe. *Ocean Model* 96:161–170
8. Erikson LH, Hegermiller CA, Barnard PL, Ruggiero P, Van Ormondt M (2015) Projected wave conditions in the eastern north Pacific under the influence of two CMIP5 climate scenarios. *Ocean Model* 96:171–185
9. Dobrynin M, Murawski J, Yang S (2012) Evolution of the global wind wave climate in CMIP5 experiments. *Geophys Res Lett* 39:L18606. <https://doi.org/10.1029/2012GL052843>
10. Dobrynin M, Murawski J, Baher J, Ilyina T (2015) Detection and attribution of climate change signal in ocean wind waves. *J Clim* 28:1578–1591
11. Shimura T, Mori N, Mase H (2015) Future projection of ocean wave climate: analysis of SST impacts on wave climate changes in the western north Pacific. *J Clim* 28:3171–3190. <https://doi.org/10.1175/JCLI-D-14-00187.1>
12. Bennet WG, Karunarathna H, Mori N, Reeve DE (2016) Climate change impacts on future wave climate around the UK. *J Mar Sci Eng* 4:78. <https://doi.org/10.3390/jmse4040078>
13. Roshin E, Deo MC (2017) Derivation of design waves along the Indian coastline incorporating climate change. *J Mar Sci Technol* 22(1):61–70. <https://doi.org/10.1007/s00773-016-0393-y> Springer
14. Bhat S, Jain P, Deo MC (2017) Application of regional climate models (RCMs) for coastal design parameters along India, under review
15. Kulkarni S, Deo MC, Ghosh S (2016) Evaluation of wind extremes and wind potential under changing climate for Indian offshore using ensemble of 10 GCMs. *Ocean Coast Manag* 121:141–152. <https://doi.org/10.1016/j.ocecoaman.2015.12.008>
16. Chandramohan P, Sanil Kumar V, Nayak BU (1991) Wave statistics around Indian Ocean. *Indian J Mar Sci* 20:87–92
17. Bhaskaran PK, Gupta N, Dash MK (2014) Wind-wave climate projections for the Indian Ocean from satellite observations. *Mar Sci Res Dev*. <http://dx.doi.org/10.4172/2155-9910.S11-005>
18. Hemer MA, Wang XL, Church JA, Swail VR (2010) Coordinating global ocean wave climate projections. *Bull Am Meteorol Soc* 91(4):451–454
19. Hithin NK, Sanil Kumar V, Shanas PR (2015) Trends of wave height and period in the Central Arabian Sea from 1996 to 2012: a study based on satellite altimeter data. *Ocean Eng* 108(2015):416–425
20. Patra A, Bhaskaran PK (2016) Trends in wind-wave climate over the head Bay of Bengal region. *Int J Climatol* 36:4222–4240
21. Shanas PR, Sanil Kumar V (2014) Temporal variations in the wind and wave climate at a location in the eastern Arabian Sea based on ERA-Interim reanalysis data. *Nat Hazards Earth Syst Sci* 14:1371–1381
22. Anoop TR, Sanil Kumar V, Shanas PR, Johnson G (2015) Surface wave climatology and its variability in the North Indian Ocean based on ERA-Interim reanalysis. *Atmos Ocean Technol* 32:1372–1385
23. Wu L, Qin J, Wu T, Li X (2017) Trends in global ocean surface wave characteristics as represented in the ERA-Interim wave reanalysis for 1979–2010. *J Mar Sci Technol* 1–8. <https://doi.org/10.1007/s00773-017-0450-1>
24. Aboobacker VM, Vethamony P, Rashmi R (2011) Shamal swells in the Arabian Sea and their influence along the west coast of India. *Geophys Res Lett* 38:L03608. <https://doi.org/10.1029/2010/10GL045736>
25. Glejin J, Kumar VS, Nair TMB, Singh J (2013) Influence of winds on temporally varying short and long period gravity waves in the near shore regions of the eastern Arabian Sea. *Ocean Sci* 9:343–353
26. Kumar VS, Anand NM (2004) Variations in wave direction estimated using first and second order Fourier coefficients. *Ocean Eng* 31:2105–2119

27. Young IR, Ziege S, Babanin A (2011) Global trends in wind speeds and wave height. *Science* 332(6028):451–455
28. Semedo A, Sušelj K, Rutgersson A, Sterl A (2011) A global view on the wind sea and swell climate and variability from ERA-40. *J Clim* 24:1461–1479
29. DHI (2014) MIKE21: spectral waves FM module scientific documentation. Danish Hydraulic Institute, DHI, Water and Environment, Copenhagen, Denmark
30. Teena NV, Sanil Kumar V, Sudheesh K, Sajeev R (2012) Statistical analysis on extreme wave height. *Nat Hazards* 64(1):223–236
31. Satyavathi P, Deo M C, Kerkar J, Vethamony P (2016) Re-evaluation of design waves off the western Indian coast considering climate change. *Mar Technol Soc J Wash* 50(1):88–98
32. Li H, Sheffield J, Wood EF (2010) Bias correction of monthly precipitation and temperature fields from intergovernmental panel on climate change AR4 models using equidistant quantile matching. *J Geophys Res Atmos* 115:D10
33. Lileo S, Petrik O (2011) Investigation on the use of NCEP/NCAR, MERRA and NCEP/CFRSR reanalysis data in wind resource analysis. In: EWEA, Brussels, Belgium. <http://proceedings.ewea.org/annual2011/papers/81.pdf>
34. Sharp E, Dodds P, Barrett M, Spataru C (2015) Evaluating the accuracy of CFRSR reanalysis hourly wind speed forecasts for the UK, using in situ measurements and geographical information. *Renew Energy* 77:527–538
35. Sarpkaya T, Issacson M (2000) Mechanics of wave induced forces on offshore structures. Van Nostrand Reinhold, Amsterdam, The Netherlands
36. Goda (2000) Random seas and design of maritime structures. World Scientific, Singapore
37. Kamphuis JW (2006) Introduction to coastal engineering and management. World Scientific, Singapore
38. Caires S, Swail VR, Wang XL (2006) Projection and analysis of extreme wave climate. *J Clim* 19:5581–5605
39. Ruggiero P, Komar PD, Allan JC (2010) Increasing wave heights and extreme value projections: the wave climate of the U.S. Pacific northwest. *Coast Eng* 57:539–552
40. Sajiv PC, Kumar V S, Glejin J, Udhaba DG, Vinayaraj P (2012) Interannual and seasonal variations in nearshore wave characteristics off Honnavar, west coast of India. *Curr Sci* 103:286–292

# Assessment of Nonlinear Quadruplet Interactions for Measured Spectra in Deep Waters on the East Coast of India Through Gauss–Legendre Quadrature Method



M. Kamalakannan, M. Kalyani, V. Prabhakar, Basanta Kumar Jena and R. Venkatesan

**Abstract** Existing methods, such as Discrete Integration Algorithm (DIA) or Multiple DIA (MDIA) for evaluating Boltzmann integral to assess the nonlinear energy transfer within a given energy spectrum at a given location, do not account for all the contributing wave resonating quadruplets (QPs) for want of computational ease in the wave models such as WAM and WWIII. By virtue of employing the state-of-the-art Gauss–Legendre Quadrature Method (GLQM), the transfer integral becomes free of singularities, and fast estimation of all the contributing QPs is possible; and hence, this method provides both accuracy and efficiency. It also works for different frequency and angular resolutions of the input spectral grid. In this paper, GLQM is validated with EXACT-NL and WRT methods for a theoretical spectrum. It is then applied to a measured spectrum of a moored buoy of National Institute of Ocean Technology, off Machilipattinam (DS5) in deep waters for evaluating the nonlinear QP interactions based on one-month data during July 2005. A characteristic monthly averaged 1D frequency spectrum has been chosen which represented a double-peaked sea-dominated spectrum. It is then fitted with a theoretical JONSWAP spectrum with 99.5% confidence. The nonlinear energy transfer rate ( $S_{nl}$ ) between the higher and lower frequencies of this fitted spectrum has been evaluated using GLQM and are quantified. The nonlinear coupling between the sea and swell parts is found to be absent as the ratio of the swell and sea frequencies is less than 0.6 (Masson in *J Phys Oceanogr* 23:1249–1258, 1993 [1]). Few hypothetical cases have been studied to understand  $S_{nl}$  behaviour further.

---

M. Kamalakannan  
Tamil Nadu Dr. J. Jayalalithaa Fisheries University, Nagapattinam, India

M. Kalyani (✉) · B. K. Jena · R. Venkatesan  
National Institute of Ocean Technology, NIOT Campus, Velachery–Tambaram Main Road,  
Pallikaranai, Chennai 600100, India  
e-mail: [kalyani.niot00@gmail.com](mailto:kalyani.niot00@gmail.com)

M. Kamalakannan · V. Prabhakar  
School of Advanced Sciences, VIT University, Chennai, India

**Keywords** Nonlinear energy transfer rate · Quadruplets · EXACT-NL · WRT  
GLQM · Deep water · Wave model

## 1 Introduction

Characterization of wave field at a specific location of interest has been a dearth study for decades, which is evolving with the advent of state-of-the-art numerical techniques, advanced computational facilities and measurement techniques. Wave models that have evolved from first, second to the present third generation are governed by the action balance equation and account for different wave phenomena consisting of various source terms, such as wind input, white capping, nonlinear wave-wave interactions in deep waters, and in addition depth breaking and dissipation due to bottom friction in shallow waters. In deep waters, nonlinear interactions occur between wave vector quadruplets that satisfy resonance conditions and also ensure conservation of wave energy, action and momentum. A full solution of the Boltzmann integral (six-dimensional integral over three wave number vectors) requires an accurate determination of all the possible wave resonating quadruplets. There are several computation techniques proposed by various researchers for the evaluation of full Boltzmann integral for deep waters.

EXACT-NL method [2] was based on a symmetric integration technique using the property of detailed balance (single-point applications). Another significant contribution was due to the method of Webb [3] who presented a set of integrable equations by using analytical transformations to eliminate the delta functions in the Boltzmann integral for deep waters (computationally not feasible for implementation in wave models). Hasselmann and Hasselmann [4] introduced an efficient and first approximate method, called Discrete Interaction Approximation, for deep waters. Implementation of DIA led to the development of the first 3G wave model WAM [5] and followed by other 3G wave models. The Webb-Resio-Tracy (WRT) formulation is an improvement of the method of Webb by [6, 7]. A detailed description of this WRT method can be found in [8]. Resio and Perrie [9] introduced the Two-Scale Approximation (TSA) which attempts to retain the effect of the overall spectral shape on nonlinear transfer while allowing the effect of decomposing a directional spectrum into a parametric (broad-scale) spectrum and a residual (local-scale) nonparametric component. They used empirical test cases such as the JONSWAP-type wave spectra and showed that TSA results are more accurate than those of DIA, relative to results from their highly accurate evaluations of the full Boltzmann integral based on WRT formulations. Prabhakar and Pandurangan [10] developed a new formulation based on Quadrature Method for the computation of the nonlinear source term for deep waters in which different input polar grids were employed. Prabhakar and Pandurangan [11] employed an explicit polar method for the determination of wave resonating quadruplets in which the number of quadruplets varies with each input pair of wave number vectors ( $\mathbf{K}_1, \mathbf{K}_3$ ), but computationally expensive.



As an extension and improvement of Quadrature Method, the present paper covers a new computational method called Gauss–Legendre Quadrature Method (GLQM) that aims to achieve both accuracy and efficiency. So far GLQM is applied to theoretical spectra. In this paper, GLQM has been applied to a measured spectrum of a moored buoy of National Institute of Ocean Technology, off Machilipattinam (DS5) at a depth of 3267 m for evaluating the nonlinear quadruplet interactions based on one-month data during July 2005. The  $S_{nl}$  behaviour of this measured case (mixed spectrum with sea dominance) is compared with few hypothetical cases (mixed with swell dominance; single swell and sea cases fitting the mixed spectrum components to understand the  $S_{nl}$  behaviour of all the four types of spectra that occur in North Indian Ocean (NIO) during different seasons. Curve fitting errors and their effect on  $S_{nl}$  are also discussed.

## 2 Nonlinear Energy Transfer Rate—GLQM

Following [12], the nonlinear energy transfer rate is described by the following Boltzmann integral.

$$\frac{\partial N_1}{\partial t} = \iiint G_{1,2,3,4} N_{1,2,3,4} \delta(\mathbf{K}_S) \delta(\omega) d\mathbf{K}_2 d\mathbf{K}_3 d\mathbf{K}_4 \tag{1}$$

Here,  $\mathbf{K}_i = (k_i, \theta_i)$  and  $N_i = N(\mathbf{K}_i)$  are the  $i$ th interacting wave number vector and action density at  $\mathbf{K}_i$  respectively,  $\omega = \omega_1 + \omega_2 - \omega_3 - \omega_4$  and  $\mathbf{K}_S \equiv \mathbf{K}_1 + \mathbf{K}_2 - \mathbf{K}_3 - \mathbf{K}_4$  represent wave angular frequency and wave vector resonance conditions, respectively. The terms  $G_{1,2,3,4} = G(\mathbf{K}_1, \mathbf{K}_2, \mathbf{K}_3, \mathbf{K}_4)$  and  $N_{1,2,3,4} = N_1 N_3 (N_4 - N_2) + N_2 N_4 (N_3 - N_1)$  represent the coupling coefficient and product of action density functions, respectively. In the deep water case,  $\omega_i^2 = gk_i$ . Because of the Dirac  $\delta(\dots)$  terms, the interactions occur between quadruplets of spectral wave components  $\{\mathbf{K}_1, \mathbf{K}_2, \mathbf{K}_3, \mathbf{K}_4\}$  that satisfy the following resonance conditions:

$$\mathbf{K}_S = 0 \quad \text{and} \quad \omega = 0 \tag{2}$$

The first step in GLQM consists of expressing Eq. (1) in the form

$$\frac{\partial N_1}{\partial t} = \int T(\mathbf{K}_1, \mathbf{K}_3) d\mathbf{K}_3, \tag{3}$$

with the transfer integral  $T(\mathbf{K}_1, \mathbf{K}_3)$  given by

$$T(\mathbf{K}_1, \mathbf{K}_3) = \iint G_{1,2,3,4} N_{1,2,3,4} \delta(\mathbf{K}_S) \delta(\omega) d\mathbf{K}_2 d\mathbf{K}_4. \tag{4}$$

The second step in GLQM consists of reducing the transfer integral to a line integral over a simple closed curve (or locus) separately for each of the cases  $k_1 < k_3$

and  $k_1 > k_3$  using the properties of the delta function in polar form [10] which can then be expressed in the form

$$T(\mathbf{K}_1, \mathbf{K}_3) = \frac{2}{L} \oint G_{1,2,3,4} J_{1,2,3,4} N_{1,2,3,4} ds \tag{5}$$

in which the integration parameter along the closed curve  $\Gamma$  is the arc length(s). In Eq. (5),  $J_{1,2,3,4} = |\nabla\omega|^{-1}$  is the gradient term,  $L$  is the total length of the closed locus  $\Gamma$ ,  $\Gamma$  represents the locus of  $\mathbf{K}_2$  for the case when  $k_1 < k_3$  and represents the locus of  $\mathbf{K}_4$  for the case  $k_1 > k_3$ . In order to evaluate Eq. (5), an accurate estimation of all possible resonating quadruplets needs to be determined. The third step in GLQM uses a simple procedure for accurate determination of all possible resonating quadruplets. Prabhakar and Pandurangan [11] derived a polar equation from the resonance conditions in Eq. (2) for given input pair  $(\mathbf{K}_1, \mathbf{K}_3)$  which is quadratic in the radial variable.

A simple closed curve  $\Gamma$  can be obtained from this polar equation which represents a conic. There are two different approaches to determine the distribution of points on the locus  $\Gamma$ . In the first approach, the polar equation can be used to determine each point on the locus and the resulting locus will be an approximate form of an ellipse. In the second approach, one needs to obtain end points on the lines of symmetry from the polar equation which helps in obtaining the centre point and radii along the symmetry lines of the closed locus. Since there are two radii along the symmetries and the polar equation is quadratic in the radial variable,  $\Gamma$  represents an ellipse. The present formulation uses the second approach and hence considered the parametric form of the ellipse for  $\Gamma$ . The last step in GLQM consists of applying Gauss–Legendre quadrature rules for the estimations of the transfer integral in Eq. (5) and the double integral in Eq. (3). Let  $N_{loc}$  be the number of points on  $\Gamma$ . Applying  $N_{loc}$ -Gauss–Legendre quadrature rule, discretized form of the transfer integral is given by

$$T(\mathbf{K}_1, \mathbf{K}_3) \approx \sum_{i=1}^{N_{loc}} W_i G(s_i) \times J(s_i) \times N(s_i), \tag{6}$$

where  $s_i$  denote the abscissas of the Legendre polynomial of order  $N_{loc}$  and  $W_i$  the associated weights. In order to evaluate the double integral in Eq. (3), a polar grid for the input wave number vector  $\mathbf{K}_i$  ( $i = 1, 3$ ) is required. Let the size of the input spectral  $\mathbf{K}_1$  polar grid be  $(N_r, N_\theta)$ , where  $N_r$  and  $N_\theta$  denote the total number of radial and angular points, respectively.

Divide the radial interval of the  $\mathbf{K}_3$  polar grid into  $Q$  sub-intervals with a constant geometric spacing and  $R$  the number of interior points in each sub-interval. Let  $\ell$  be the number of angular points in the angular interval  $[0, 2\pi]$  of the  $\mathbf{K}_3$  polar grid. Applying  $\ell$ -point Gauss–Legendre quadrature formula for the angular direction ( $\theta_3$ ) and using composite Gauss–Legendre quadrature formula for the radial wave number direction  $k_3$ , discretized form of the double integral in Eq. (3) can be expressed as

$$\Delta N(k_{1,p}, \theta_{1,t}) \approx C \sum_{q=1}^Q \lambda^{q-1} \left[ \sum_{r=1}^R W_r \sum_{n=1}^{\ell} W_n T(k_{1,p}, \theta_{1,t}, k_{3,q,r}, \theta_{3,n}) k_{3,q,r} \right]; \quad (7)$$

$$p = 1, 2, \dots, N_r, \quad t = 1, 2, \dots, N_{\theta}.$$

Here,  $k_0$  is the minimum wave number,  $k_{1,p} = \lambda^{p-1}k_0$ ,  $C = \pi(\lambda - 1)k_0/2$  and  $Q = N_r - 1$ . Also,  $\theta_{3,n}$  represent the abscissas of Legendre polynomial of order  $\ell$  with the associated weight  $W_n$ ,  $k_{3,q,r}$  denotes the abscissas of Legendre polynomial of order  $R$  in the  $q$ th sub-interval and  $W_r$  the associated weights. An advantage in the present method is that  $k_{3,q,r} = \lambda^{q-1}k_{3,1,r}$ . Since composite Gauss–Legendre quadrature rule is employed, the input case of  $\mathbf{K}_1 = \mathbf{K}_3$  does not arise at all. As a result, the transfer integral for an input pair is free from singularities. Thus, the present method gets rid of the singularities of the Boltzmann integral. In terms of frequency-direction polar grid, the nonlinear transfer rate is given by

$$S_{nl}(f_{1,p}, \theta_{1,t}) = \left[ \frac{2\pi k_{1,p} \omega_{1,p}}{C_{g,p}} \right] \Delta N(k_{1,p}, \theta_{1,t}), \quad (8)$$

where  $f_{1,p}$  and  $C_{g,p}$  are the radial frequency and group velocity corresponding to the wave number  $k_{1,p}$ . The parameters of the present formulation to estimate  $S_{nl}$  are represented by the set  $(Q, R, \ell, \mathbf{N}_{loc})$ . By identifying and fixing these parameters, the 2D nonlinear energy transfer  $\mathbf{S}_{nl}(f)$  in Eq. (8) can be evaluated for an input wave energy spectrum at a finite depth. The 1-D nonlinear energy transfer rates  $\mathbf{S}_{nl}(f)$  and  $\mathbf{S}_{nl}(\theta)$  are then determined by integrating  $\mathbf{S}_{nl}(f, \theta)$  with respect to  $\theta$  and  $f$ , respectively.

### 3 Results and Discussion

We present the results of  $\mathbf{S}_{nl}(f)$  obtained, using GLQM. All the computations were carried out with the integration parameters  $Q = N_r - 1$ ,  $R = 1$ ,  $\ell = 30$  of Eq. (7) and  $\mathbf{N}_{loc} = 15$  of Eq. (6), unless otherwise specified.

#### 3.1 Validation of GLQM for a Theoretical Wave Spectrum

Figure 1 shows a comparison of  $\mathbf{S}_{nl}(f)$  obtained from the present GLQM with EXACT-NL and WRT methods for the case 15 of [2] and for the input standard JONSWAP spectrum which is defined by the following expression.

$$E(f) = \alpha g^2 (2\pi)^{-4} f^{-5} \exp^{-\frac{5}{4} \left(\frac{f}{f_p}\right)^{-4}} \gamma^{\exp\left(-\frac{(f-f_p)^2}{2\sigma^2 f_p^2}\right)}, \quad (9)$$

The directional spreading function (DSF) is chosen to be cosine square spreading function given by

$$D(\theta) = \cos^2(\theta - \theta_m), \tag{10}$$

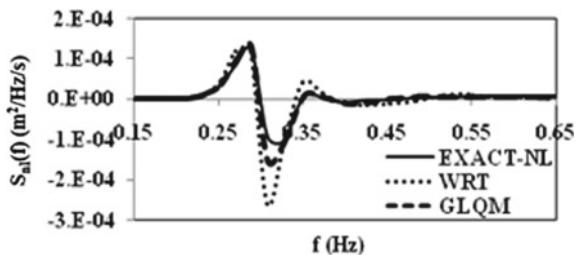
The mean direction  $\theta_m$  is taken as  $0^\circ$ . The input spectral parameters (JONSWAP) are given by,  $\alpha = 0.01$ ,  $\gamma = 7$ , peak frequency  $f_p = 0.3$  Hz and  $\sigma = \sigma_a = 0.07$  for  $f < f_p$  and  $\sigma = \sigma_b = 0.09$  otherwise. The size of the input polar grid considered is  $(N_r, N_\theta) = (50, 30)$ .

Figure 1 exhibits good agreement of  $S_{nl}(f)$  between the three methods, viz. EXACT-NL, WRT and GLQM. Present GLQM closely matches EXACT-NL method and showed good improvement over WRT method. EXACT-NL seems to provide minimum positive and negative peak amplitudes of energy transfer rates, whereas WRT showed the maximum among the three methods. GLQM showed a via-media between the exact and approximate methods. This difference is more pronounced at the peak of the negative lobe, though the occurrence is observed at the same frequency from the three methods. The trend of GLQM is similar to that of WRT, while its accuracy is improved over WRT.

### 3.2 Application of GLQM for a Measured Wave Spectrum

The monthly average spectrum of July 2005 at the moored buoy of National Institute of Ocean Technology at DS5 ( $83^\circ 16' 16''$ E,  $13^\circ 59' 28''$ N; 3267 m depth) location in Bay of Bengal (BoB) has been obtained by averaging every three hourly spectra spanning the entire month. It exhibited a *double-peaked spectrum* with *sea-dominated condition* ( $E_p\text{-sea} > E_p\text{-swell}$ ). Swells from distant storms in the Southern Indian Ocean (SIO) reach the Bay of Bengal and hence constituted approximately 11% (up to 0.5 Hz) of the total energy. Coexistence of locally generated wind seas and pre-existing swells results in a diurnal pattern of wave parameters. The role of SIO swells on the North Indian Ocean (NIO) wave field has been detailed by [13]. In the present case, the measured spectrum is fitted with a *double-peaked (DP) JONSWAP spectrum* (6 parameter) by curve fitting (MATLAB tool) using the appropriate

**Fig. 1** Comparison of  $S_{nl}$  from GQLM with WRT and EXACT-NL for case 15 [2]



separation frequency ( $f\text{-sep} = 0.082$  Hz) and by adjusting other five spectral parameters (Tables 1 and 2) with 99.5% confidence and with Root Mean Square Error of 0.02788 and correlation coefficient as 0.9955. This fitted DP spectrum is denoted as 1A. Torsethaugen [14] has developed a two-peaked 1A-type spectrum using curve fitting of experimental data from the North Sea in Norwegian waters by using a separation frequency. The comparison of measured spectrum with fitted (1A) is shown in Fig. 2. The fitted 1A spectrum slightly over-predicted (by 5%) the measured one. Further, swell and sea components of 1A (DP) are fitted [15] with separate single-peaked (SP) JONSWAP spectra (pure swell; 1B and pure sea, 1C) by defining their respective peak frequencies ( $f_p$ ) using curve fitting (MATLAB tool) (Tables 1 and 2).

**Table 1** Description of hypothetical cases

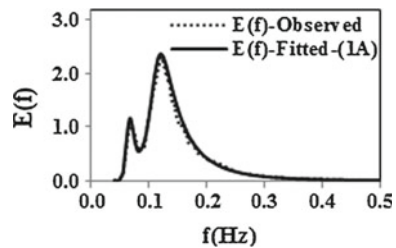
Case	Description
1A	Double-peaked sea-dominant spectrum (DP-sea.dom)
1B	Single-peaked swell spectrum (fitted to 1A); (SP-swell)
1C	Single-peaked sea spectrum (fitted to 1A); (SP-sea)
2A	Double-peaked swell-dominant spectrum; (DP-swell.dom)
2B	Single-peaked swell spectrum (fitted to 2A); (SP-swell)
2C	Single-peaked sea spectrum (fitted to 2A); (SP-sea)

**Table 2** Fitted JONSWAP parameters for hypothetical cases

Case	$\alpha$	$\gamma$	$f_p$ or $f\text{-sep}$	$\sigma_a$	$\sigma_b$	$P$
1A	0.007500	0.1	0.082*	0.130	0.21	4.25
1B	0.000215	3.0	0.067	0.130	0.21	4.25
1C	0.008500	3.3	0.120	0.200	0.20	4.00
2A	0.006000	0.1	0.075*	0.030	0.29	4.00
2B	0.000530	5.0	0.067	0.035	0.10	4.00
2C	0.001600	7.0	0.120	2.000	5.00	4.00

\*Refers to separation frequency,  $f\text{-sep}$

**Fig. 2** Monthly averaged measured wave spectrum fitted with six-parameter double-peaked JONSWAP spectrum using  $f\text{-separation}$



### 3.3 Hypothetical Cases

In this paper, two types of double-peaked spectra 1A (*sea-dominated; fitted to measured DS5 location in BoB, July 2005*) and 2A (*swell-dominated; hypothetical spectrum with same nonlinear coupling status to that of 1A*) are chosen, and their  $S_{nl}$  behaviour is compared. 1A and 2A are treated as wave conditions pertaining to different locations and seasons with varying intensities. The total energies, separation frequencies and compositions are different for the two. 2A spectrum is obtained (from 1A) by magnifying swell energy (by 1.62 times) and curtailing sea energy (by 52%) with a net total energy reduction (by 34%), while the sum total of sea and swell peak energies is increased by 5% than that of 1A.  $f_p$ -sea,  $f_p$ -swell and  $f$ -ratio are kept constant to have identical nonlinear coupling status between the sea and swell systems for both 1A and 2A, which is governed by  $f$ -ratio [1]. It is also associated with a reduction in separation frequency (1A: 2A = 0.082: 0.075 Hz). These statistics apply only when the sea and swell systems are decoupled for DP spectra ( $f_p$ -ratio (sw/sea) < 0.6). Here, 2A is not an observed spectrum at the same location of 1A. The spectral energy balance between 1A and 2A is not resorted to. If so, it would have changed the  $f$ -ratio and altered the nonlinear coupling status.

2A-type swell-dominant spectrum can occur due to pre-existing swells from SIO/cyclones/distant storms superposed with relatively lesser local wind seas to that of 1A which might belong to a different season/different place [16]. The 2A spectrum is also decomposed into single-peaked spectra; pure swell (2B) and pure sea (2C), respectively, are analysed for  $S_{nl}$ . The description of the six cases is given in Table 1 with the fitted JONSWAP parameters in Table 2. The peak energies for all the six cases are shown in Table 3, while the total energies are detailed in Table 4 (upper bound  $f = 0.5$  Hz). The nonlinear energy transfer rate,  $S_{nl}(f)$ , for all the six cases is evaluated using the GLQM as detailed in Sect. 2, for a constant monthly mean wave direction of  $198^\circ$  and with  $90^\circ$  constant spread. Here, the size of the input polar grid considered is  $(N_r, N_\theta) = (60, 24)$ . The magnitude of peak positive and negative  $S_{nl}$  ( $S_{nl+}$ ,  $S_{nl-}$ ) and associated shift from  $f_p$  (sh+, sh-) for all the six cases is given in Table 5.

**Table 3** Peak frequency and energy statistics for different cases  $f$ -sep for (1A)=0.082 Hz and (2A)=0.075 Hz

Case	$f_p$		$E_p$				
	Swell	Sea	sw	Sea	Total	%sw	%Sea
1A	0.067	0.12	1.162	2.362	3.524	33.0	67.0
1B and 1C	0.067	0.12	1.113	2.420	3.533	31.5	68.5
2A	0.067	0.12	2.572	1.126	3.698	69.5	30.5
2B and 2C	0.067	0.12	2.327	1.162	3.489	66.7	33.3

**Table 4** Energy of sea and swell and % wrt measured and fitted (1A) spectra

Case	sw	s	$T(\text{sw} + s)$	$\text{sw}/T$	$s/T$	$\text{sw}/\text{sw}(o)$	$s/s(o)$	$T/T(o)$	$\text{sw}/\text{sw}(f)$	$s/s(f)$	$T/T(f)$
Obs(O)	0.020	0.166	0.186	0.11	0.89	1	1	1	0.97	0.95	0.96
1A(fit)	0.021	0.174	0.195	0.11	0.89	1.03	1.05	1.05	1	1	1
1B + 1C*	0.036	0.144	0.181	0.20	0.80	1.83	0.87	0.97	1.77	0.83	0.93
2A	0.034	0.095	0.128	0.26	0.74	1.69	0.57	0.69	1.63	0.54	0.66
2B + 2C*	0.045	0.114	0.159	0.28	0.72	2.25	0.68	0.85	2.17	0.65	0.81

\*Addition of energies of the respective fitted single-peaked swell and single-peaked sea spectra

**Table 5** Peak  $S_{nl}$  and its shift from  $f_p$  for swell and sea for different cases

Case	sh+	sh-	Tot sh ( $bw-snl$ )	$S_{nl+}$	$S_{nl-}$	Total	$S_{nl}$ slope
<i>Swell</i>							
1A	0.003	0.004	0.007	1.3E-07	1.1E-07	2.4E-07	3.44E-05
1B	0.003	0.015	0.018	2.0E-08	3.2E-08	5.2E-08	2.91E-06
2A	0.003	0.004	0.007	2.2E-07	4.4E-07	6.6E-07	9.39E-05
2B	0.007	0.007	0.014	1.0E-07	1.1E-07	2.1E-07	1.51E-05
<i>Sea</i>							
1A	0.005	0.04	0.045	4.5E-05	6.7E-05	1.1E-04	2.49E-03
1C	0.005	0.024	0.029	3.9E-05	5.9E-05	9.8E-05	3.37E-03
2A	0.005	0.053	0.058	5.2E-06	7.9E-06	1.3E-05	2.27E-04
2C	0.005	0.071	0.076	1.1E-05	2.1E-05	3.2E-05	4.25E-04

The single-peaked spectra are obtained by curve fitting SP-sea or SP-swell to the mixed spectra separately. Their intensities are taken in accordance with the *mixed-sea* and *mixed-swell* of DP spectra, respectively. This curve fitting can induce two types of differences in spectral energies, (a) (**Mode 1**): due to the cut-off of the swell and sea components by separation frequency in the mixed spectrum which is absent for SP spectrum. This induces an apparent added energy in the high-frequency (HF) band for SP-swell and in the low frequency (LF) band for SP-sea of single-peaked spectra when compared to their counterparts in the mixed spectrum, respectively, (b) (**Mode 2**): discrepancies in any frequency band as the case may be. In the present paper, these differences in energies of the fitted spectra are pictorially depicted for clearly understanding the source of error. The  $S_{nl}$ -curves obtained using GLQM are plotted in Figs. 3 and 4 for 1A (DP-sea.dom) and 2A (DP-swell.dom) cases, respectively.

**1A versus fitted SP-swell (1B):** From Fig. 3 and Tables 3, 4 and 5 (left panel), it can be seen that the net swell energy increase (from 1A to 1B, 0.021–0.036 m<sup>2</sup>/Hz) *did not increase the  $S_{nl}$* , as significant part of this energy is added in the HF portion (mode 1) beyond  $f$ -sep (0.082 Hz) which is away from  $f_p$ -swell (where the  $S_{nl}$  transfer is concentrated). Moreover, the *loss in swell energy at the  $f_p$  by 1B due to mode 2* reduced  $S_{nl}$  of 1B and is associated with an *increase of bandwidth* (shift towards HF). Gain in swell energy (mode 2) by 1B, adjacent to  $f_p$  shifted  $f$ -further towards HF till separation frequency ( $f$ -sep = 0.082 Hz) for SP case. The net significant increase of *bandwidth between  $S_{nl+}$  and  $S_{nl-}$  ( $bw-snl$ )* by 4 times to that of 1A, with reduced energy at the peak, has reduced the  $S_{nl}$  at the peak for 1B spectrum drastically. The shift of  $f-$  of swell spectrum is restricted by  $f$ -sep for both DP spectrum (DPS) and its fitted SP spectrum (SPS). It is also verified in case of 2B.



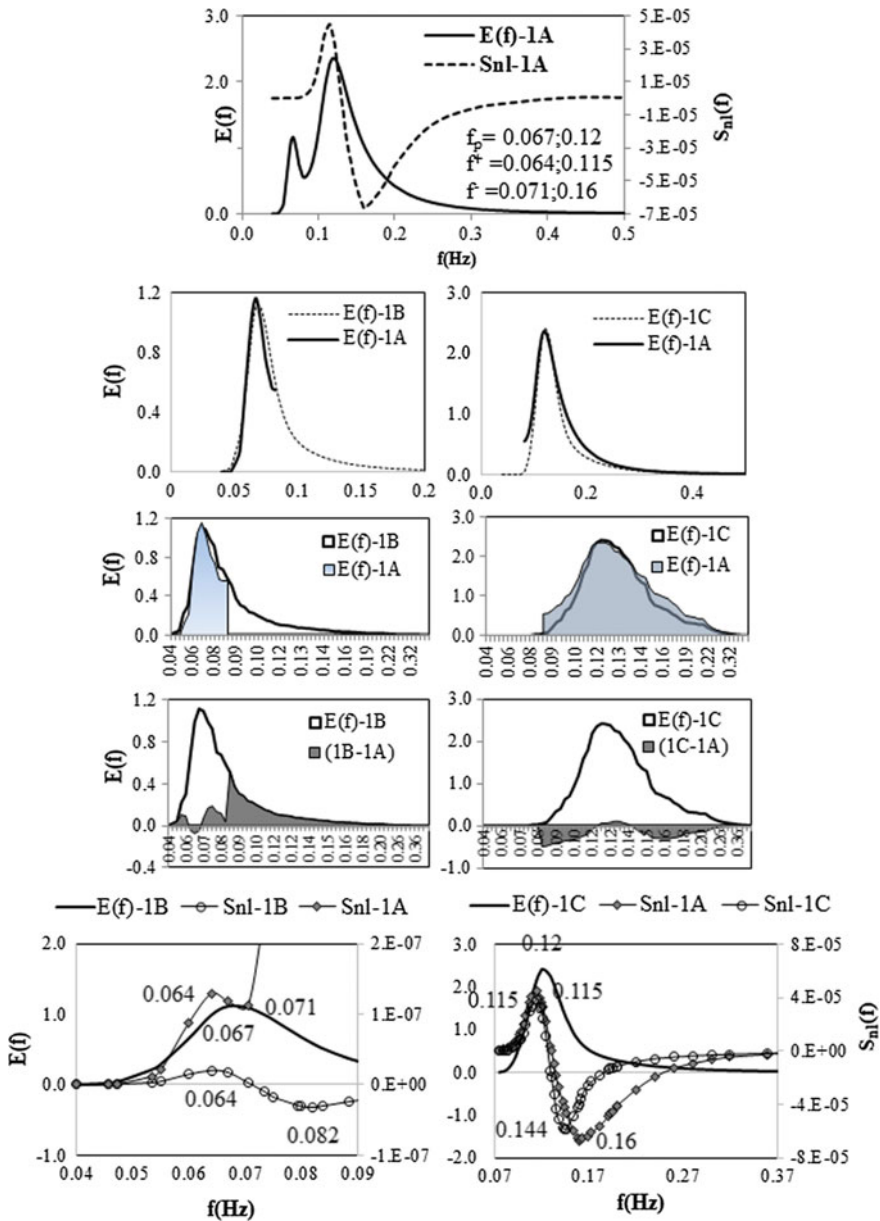


**Fig. 3** (r1) Energy and  $S_{nl}$  of 1A (DPS); (r2) DPS-component fitted to SPS; (r3) area overlap between target and fitted spectra; (r4) loss/gain in energy by SPS wrt to DPS; (r5)  $S_{nl}$  of DPS-counterpart with its SPS (E of SPS superimposed) (left panel: swell (1B) and right panel: sea (1C))

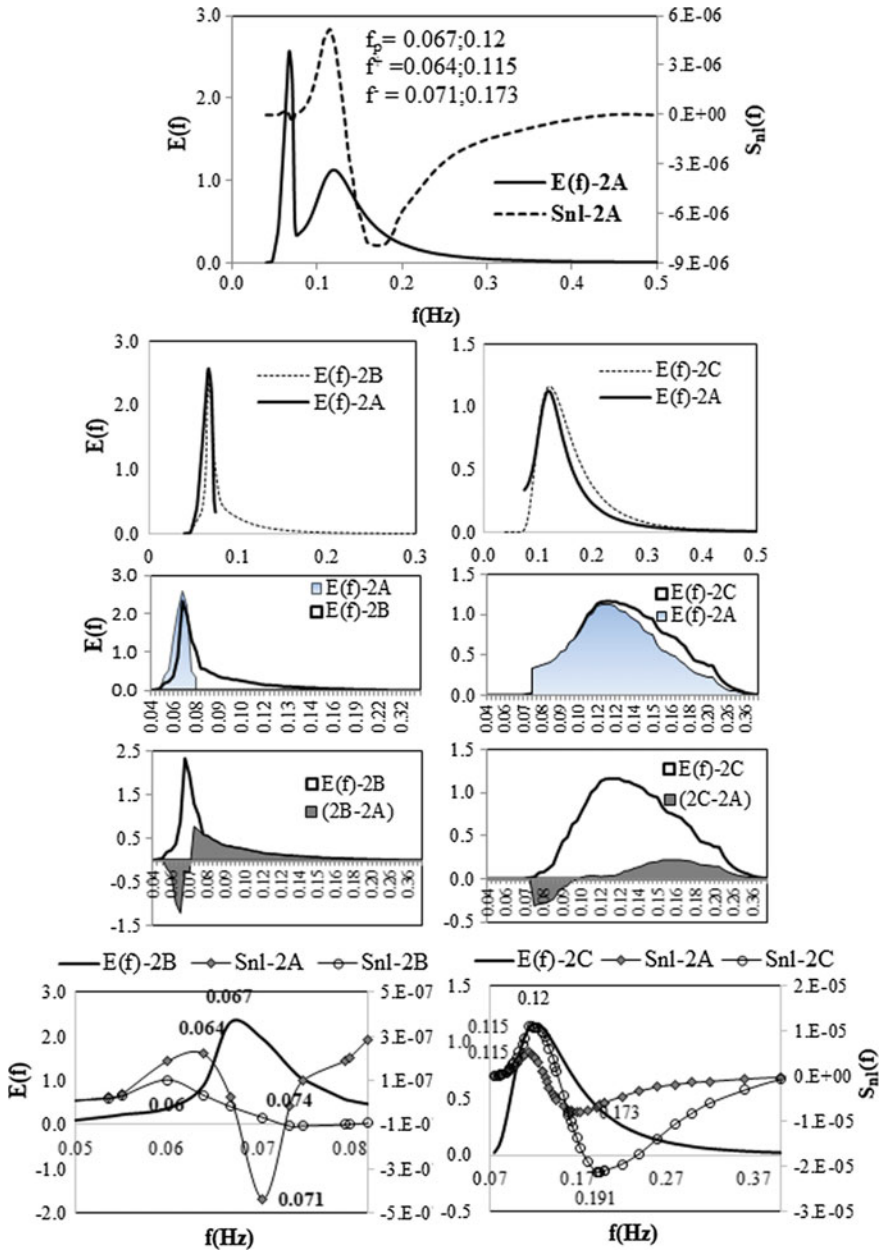


**Fig. 4** (r1) Energy and  $S_{nl}$  of 2A (DPS); (r2) DPS-component fitted to SPS; (r3) area overlap between target and fitted spectra; (r4) loss/gain in energy by SPS wrt to DPS; (r5)  $S_{nl}$  of DPS-counterpart with its SPS (E of SPS superimposed) (left panel: swell (2B) and right panel: sea (2C))

**1A versus fitted SP-sea (1C)** From Fig. 3 and Tables 3, 4 and 5 (right panel), it can be seen that though there is a net reduction in sea energy (from 1A to 1C; from 0.174 to 0.144  $\text{m}^2/\text{Hz}$ ), it *did not cause reduction in  $S_{nl}$  transfer rate of 1C and also did not increase the total shift, as it did not occur at the peak frequency*. At the  $f_p$ -sea and adjacent to it, there is a *gain in sea energy by 1C, due to mode 2*. This has increased the total peak  $S_{nl}$  and reduced the bw-snl. Further, net loss in sea energy in other frequencies (away from  $f_p$ ) due to curve fitting (mode 2) has shifted  $f-$  towards LF (0.144 Hz) than that of 1A-sea (0.160 Hz). The minute amount of energy added in the LF below  $f$ -sep due to mode 1 is not much contributive to any significant changes for 1C (SPS-sea), when compared to its counterpart in the mixed spectrum, 1A-sea. These are associated with individual discrepancies of mode 1 and mode 2, but the net effect resulted in the above specific  $S_{nl}$  behaviour. Hence, a tiny change at and near the peak frequency due to curve fitting causes significant changes in the total behaviour of the nonlinear transfer rates, bw-snl and at what pace the transfer occurs.

**2A versus fitted SP-swell (2B)** From Fig. 4 and Tables 3, 4 and 5 (left panel), it can be seen that the apparent increase in swell energy of 2B to that of 2A (0.034, 0.045  $\text{m}^2/\text{Hz}$ ) should increase  $S_{nl}$  of 2B (*but decreased*), should decrease the bw-snl of 2B (*but increased*) and should increase the  $S_{nl}$  slope (*but decreased*). The loss of swell energy at  $f_p$  and in its neighbourhood on either side, due to mode 2, has decreased the total peak  $S_{nl}$  of 2B and increased the bw-snl. Further loss in energy of 2B (SPS) when compared to that of mixed-swell (2A), in the entire LF region below  $f_p$ -swell, has shifted the  $f+$  towards LF by extra 0.004 Hz while the  $f-$  has shifted to HF further by extra 0.003 Hz due to mode 1, which has resulted in a total shift of 2 times that of 1A. The reduction in total  $S_{nl}$  associated with doubled (2 times) bw-snl has drastically reduced the  $S_{nl}$  slope of 2B to that of 2A.

**2A versus fitted SP-sea (2C)** From Fig. 4 and Tables 3, 4 and 5 (right panel), an increase in net sea energy from (2A to 2C: 0.095 to 0.114  $\text{m}^2/\text{Hz}$ ) as well as addition of energy in the peak frequency and in its neighbourhood has increased the total peak  $S_{nl}$  of 2C when compared to that of 2A-mixed-sea. The net energy gain in the other frequency regions away from the peak frequency is contributed by (i) increase of sea energy in the entire HF range of SPS-sea (2C), (ii) increase in energy below separation frequency in the LF region due to mode 1 as well as (iii) decrease of energy in other parts of the LF. The resultant gain in other frequencies (HF) away from  $f_p$  caused a shift of  $f-$  towards HF and resulted in a total bw-snl greater than that of 2A (from 0.058 Hz for 2A to 0.076 Hz for 2C). The net effect is to increase the slope of  $S_{nl}$  curve between the two peaks. Less than 10% of total shift is observed on LF side (6.6%) while the predominant shift is found on HF side (93.4%) to that of respective total shifts for 2A and 2C.

The fitted SPS-swell (1B and 2B) underpredicted the net energy transfer rates ( $S_{nl}$ ) and exhibited a relatively slower transfer rates of energy in a relatively broad band of frequencies compared to that of their corresponding DPS-swell (1A and 2A).

SPS-sea (1C) showed a relatively good fit to 1A and showed a rapid rate of transfer of energy in a relatively lesser band of frequencies in the neighbourhood of  $f_p$ -sea.

2C exhibited net increase in total  $S_{nl}$  which is associated with increase in the  $S_{nl}$  slope, but its bandwidth also increased from 0.058 to 0.076 Hz. The net difference in their energies was so high that even with increased bandwidth, 2C showed a rapid dissipation rate than that of mixed-sea of 2A (2A is 66% of 1A and is mostly reflected in sea energy apart from curve fitting errors). These predictions are shadowed by differences in the net energies due to mode 1 and mode 2 type of discrepancies. The comparison of  $S_{nl}$  between the two DP spectra, 1A and 2A, is shown in Fig. 5, while the comparison of  $S_{nl}$  between the two SP-swell (1B, 2B) and the two SP-sea (1C, 2C) cases is shown in Fig. 6.

**$S_{nl}$  of Swell Component (1A versus 2A)** A magnification of peak swell energy from (1A to 2A) 1.162 to 2.572  $\text{m}^2/\text{Hz}$  (2.21 times; 121% increase) and *total swell energy* from 0.021 to 0.034  $\text{m}^2/\text{Hz}$  (62% increase) resulted in increase of  $S_{nl+}$  by 1.69 times and of  $S_{nl-}$  by 4.0 times (refer Tables 3, 4 and 5). It is associated with equal  $f+$  (43%) and  $f-$  (57%) to that of 1A-swell, respectively, and *equal bw-snl* (0.007 Hz). The differences in total energies (2A = 66% of 1A) and the separation frequencies (0.082, 0.075 Hz) but with same peak frequency (0.067 Hz) and same  $f$ -ratio (0.558) for 1A and 2A spectra, respectively, have resulted in this combination. The slope of peak  $S_{nl}$  of 2A is increased by 2.73 times (from 3.44 to  $9.39 \times 10^{-5} \text{m}^2/\text{Hz/s/Hz}$ ) indicating a *rapid rate of transfer of peak swell energy* in an equal bandwidth when compared to that of the original (1A). This suggests that the high intensity swell with sharp peak (2A-swell) transfers the peak energy faster (for equal bandwidth) than that of the one with relatively lesser intensity (1A-swell).

**$S_{nl}$  of Sea Component (1A versus 2A)** Increase of energy increases the amplitude of peak  $S_{nl}$ . A reduction of peak sea energy from (1A to 2A) 2.362 to 1.126  $\text{m}^2/\text{Hz}$  (52% reduction) and total sea energy from 0.174 to 0.095  $\text{m}^2/\text{Hz}$  (45% reduction) resulted in reduction of  $S_{nl+}$  from 4.5 to  $0.52 \times 10^{-5} \text{m}^2/\text{Hz/s}$  (88%) and reduction of  $S_{nl-}$  from 6.7 to  $0.79 \times 10^{-5} \text{m}^2/\text{Hz/s}$  (88%) (refer Tables 3, 4 and 5). *It is associated with an equal  $f+$  and an increased  $f-$  by 0.013 Hz (29%) to that of original (1A). [bw-snl(2A-sea) > bw-snl(1A-sea)].*

Consequently, the slope of total peak  $S_{nl}$  is reduced by 88% (from 11.2 to  $1.32 \times 10^{-5} \text{m}^2/\text{Hz/s/Hz}$ ), indicating a slow transfer rate of sea energy (1/11th) in relatively wide frequencies (29% more) when compared to that of the original (1A). A 1.63 times magnification in swell energy resulted in the magnification of  $S_{nl}$  slope of 2.73 times in equal bw-snl. 45% reduction in sea energy resulted in reduction of  $S_{nl}$  slope to 1/11th, and resulted in an increase of bw-snl by 29%. The magnification factor for swell ( $2.73/1.63 = 1.68$ ) and sea ( $(1/11)/0.54 = 0.168$ ) are 1.68 and 0.168, respectively. Swell dissipation is ten times faster than that of sea. The  $S_{nl}$  amplitude of swell is two orders less (1/100th) than that of the wind seas.

**$S_{nl}$  of SPS-Swell (1B versus 2B)** 1B and 2B are SP-swell spectra with energy of  $2B > 1B$  ( $1B = 80\%$  of 2B). The  $S_{nl}$  of  $2B > 1B$ . The bw-snl of 2B and 1B are 0.014 and 0.018 Hz, respectively. Low-intensity swell of 1B has transferred energy to a relatively wider band on either side of the peak (17% to LF and 83% to HF). A 20%

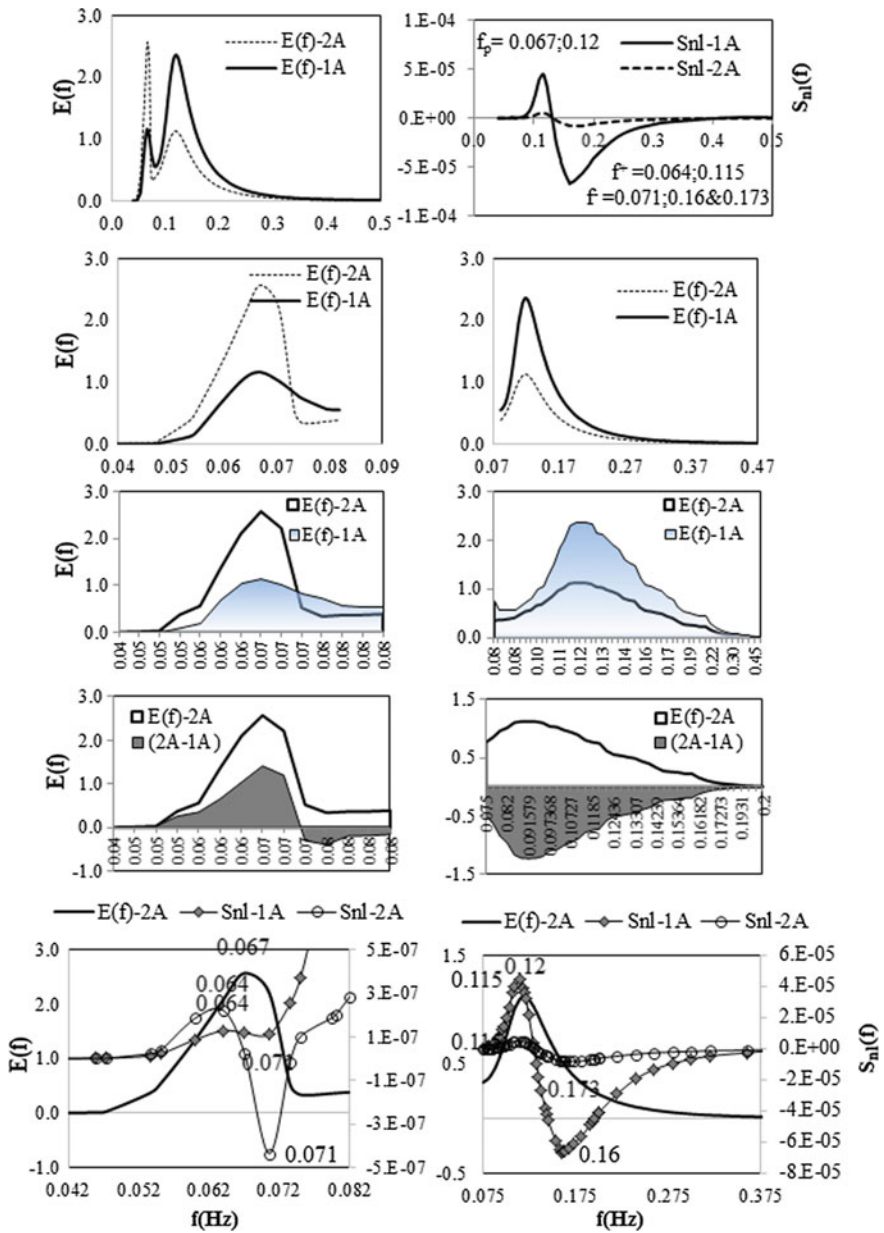


**Fig. 5** (r1) Comparison of 1A and 2A double-peaked spectra (r1) spectral energy ( $lt$ ) and  $S_{nl}$  ( $rt$ ); (r2) swell energy ( $lt$ ) and sea energy ( $rt$ ); (r3) area overlap of two spectra; (r4) loss/gain in energy by 2A wrt to 1A; (r5)  $S_{nl}$  of swell ( $lt$ ) and sea ( $rt$ ) ( $E$  of 2A superimposed)

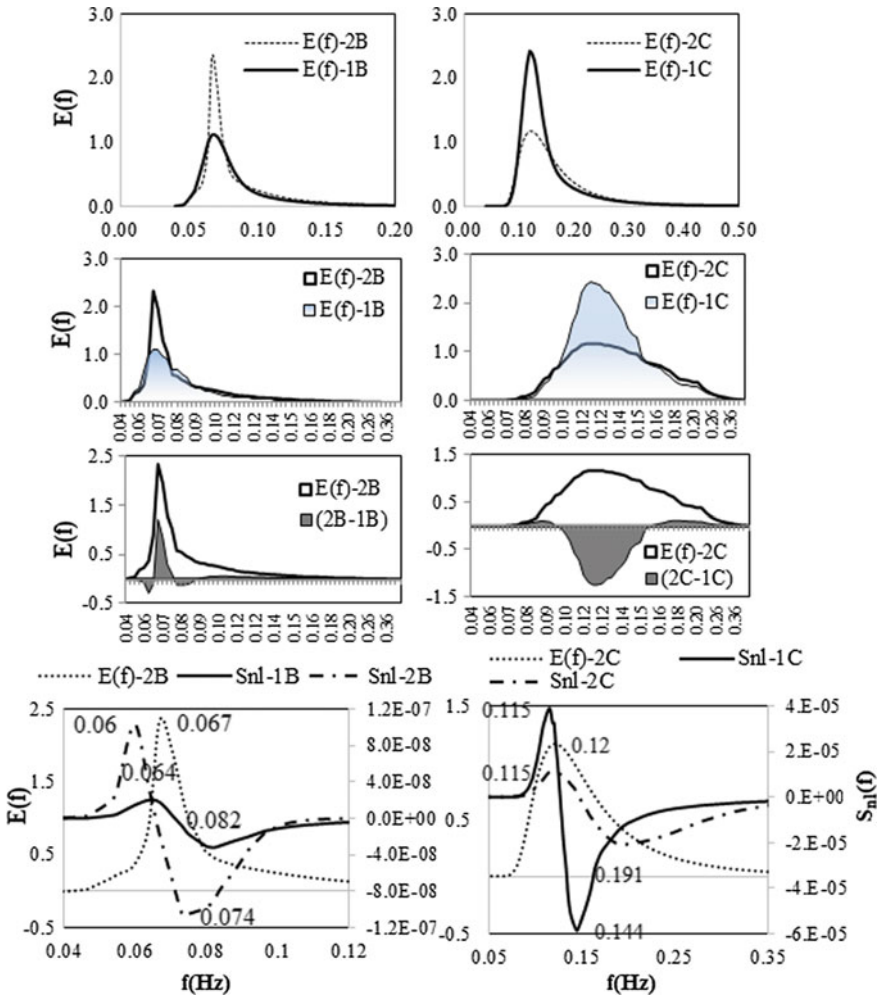


**Fig. 6** Comparison of 1 and 2 single-peaked spectra fitted to 1A and 2A double-peaked spectra, respectively; (1B, 2B: Swell in left panel and 1C, 2C: Sea in right panel); (r1) spectral energy; (r2) area overlap; (r3) loss/gain in energy by 2 wrt 1; (r4) comparison of  $S_{nl}$  ((E of 2 superimposed))

reduction in swell energy of SP spectrum (from 2B to 1B) has increased bw-snl by 29% and resulted in reduced  $S_{nl}$ -swell slope (1/5th) of that of 2B.

**$S_{nl}$  of SPS-Sea (1C versus 2C)** 1C and 2C are SP-sea spectra with energy of  $1C > 2C$  ( $=79\%$  of 1C). The peak  $S_{nl}$  of 1C is more than that of 2C. The bw-snl of 1C is decreased by 62% to that of 2C. The  $S_{nl}$  slope of 1C is 7.9 times to that of 2C. A reduction of 21% of wind sea energy (from 1C to 2C) has increased the bw-snl by 2.6 times, and correspondingly, the  $S_{nl}$  sea slope is decreased to 1/8th to that of 1C.

## 4 Conclusions

In this paper, two types of double-peaked spectra 1A (*sea-dominated; fitted to measured spectrum at DS5 location in BoB, July 2005*) and 2A (*swell-dominated; hypothetical spectrum with same nonlinear coupling status to that of 1A*) are chosen and their  $S_{nl}$  behaviour, computed using the state-of-the-art Gauss–Legendre Quadrature Method is compared. 1A and 2A (DP spectra) are treated as wave conditions pertaining to different locations and seasons. The sea and swell compositions, total energies and separation frequencies are different for the two.

- These statistics apply *only when the sea and swell systems are decoupled for DP spectra ( $f_p$ -ratio (sw/sea) $<0.6$ ) and exhibit two distinct  $S_{nl}$  curves separately in the swell and sea frequency regions:  $S_{nl}$ -swell following the structure of a narrow peak spectrum and  $S_{nl}$  sea following a typical 3-lobe structure. The results from this study establish the same fact.*
- Increase of peak energy increased the amplitude of peak  $S_{nl}$ , decreased the bandwidth between  $S_{nl+}$  and  $S_{nl-}$  (bw-snl) and increased the pace of nonlinear transfer of energy for both DP and SP spectra. When the intensity of swell and sea is varied in a DP spectrum, the rate of nonlinear transfer of peak energy is ten times faster in swell system and is distributed to a relatively lesser band of frequencies than that for wind sea system. The same behaviour is observed for SP spectra also. The magnitude of  $S_{nl}$  of swell is two orders less than (1/100th) that of  $S_{nl}$  of wind sea.
- Fitting of DPS to measured spectrum and SPS to DP-component spectrum are done using curve fitting (6 parameter JONSWAP) with the help of MATLAB tool. For DP spectrum, a separation frequency is used in place of peak frequency as per the literature.
- This study also revealed the importance of curve fitting errors on the  $S_{nl}$  behaviour.
- The resultant  $S_{nl}$  amplitude is governed by the magnitude of error, whereas the shift of peak  $S_{nl}$  from  $f_p$  is dependent on the frequency band in which the errors are induced and both depend on the mode of error (gain/loss).
- An error due to curve fitting at and near peak frequency is profound and can even reverse  $S_{nl}$  behaviour. Hence, care should be administered while fitting the measured spectrum with any standard theoretical spectrum. In this paper, the difference in energies of the target and fitted spectra are pictorially depicted for clear understanding of the source of error.

**Acknowledgements** This work is a part of the research project (Sanction No. 25 (0275)/17/EMR-II) funded by CSIR, New Delhi, India, to the third author. The authors thank INCOIS and MOES for providing the moored buoy data. We thank the Director, Dr. S.S.C. ShenoI and the Group Head of CEE group Dr. M. V. Ramanamurthy, for giving an opportunity to conduct the work. We thank the technical and scientific staff who assisted in the field data collection.




## References

1. Masson D (1993) On the nonlinear coupling between swell and wind waves. *J. Phys. Oceanogr.* 23:1249–1258
2. Hasselmann K, Hasselmann S (1981) A symmetrical method of computing the non-linear transfer in a gravity wave spectrum. *Hamburger Geophys Einzelschriften* 52
3. Webb, D. J.: Non-linear transfers between sea waves. *Deep Sea Res* 25:279–298
4. Hasselmann S, Hasselmann K (1985) Computations and parameterizations of the nonlinear energy transfer in a gravity-wave spectrum. Part I: A new method for efficient computations of the exact nonlinear transfer integral. *J Phys Oceanogr* 15:1369–1377
5. Hasselmann S, Hasselmann K, Komen GK, Janssen P, Ewing JA, Cardone V (1988) The WAM model—a third generation ocean wave prediction model. *J Phys Oceanogr* 18:1775–1810
6. Tracy BA, Resio DT (1982) Theory and calculation of the nonlinear energy transfer between sea waves in deep water. WIS Technical Report, 11. US Army Engineer Waterways Experiment Station, Vicksburg, Mississippi, USA, pp 47
7. Resio DT, Perrie W (1991) A numerical study of nonlinear energy fluxes due to wave-wave interactions. Part 1: Methodology and basic results. *J Fluid Mech* 223:609–629
8. Van Vledder GPh (2006) The WRT method for the computation of nonlinear four-wave interactions in discrete spectral wave models. *Coastal Eng* 53:223–242
9. Resio DT, Perrie WA (2008) A two-scale approximation for efficient representation of nonlinear energy transfers in a wind wave spectrum. Part I: Theoretical development. *J Phys Oceanogr* 38:2801–2816
10. Prabhakar V, Pandurangan J (2006) A quadrature method for computing nonlinear source term due to wave-wave interactions. *Curr Sci* 90(6):812–817
11. Prabhakar V, Pandurangan J (2006) A polar method for obtaining wave resonating quadruplets in finite depths. *Ocean Eng* 33(6):1044–1055
12. Hasselmann K (1962) On the non-linear energy transfer in a gravity-wave spectrum: Part 1. General theory. *J Fluid Mech* 12:481–500
13. Samiksha SV, Vethamony P, Aboobacker VM, Rashmi R (2012) Role of south Indian Ocean swells in modulating the north Indian Ocean wave climate through modelling and remote sensing. *Geophys Res Abstr* 14:EGU2012-714
14. Torsethaugen K (1993) A two peak wave spectral model. In: *The 12th International Conference on Offshore Mechanics and Arctic Engineering*, 2, pp 175–180, ASME
15. Gabin WG (2015) Wave bimodal spectrum based on swell and wind sea components. *IFAC-PapersOnline* 48–16:223–228
16. Glejin J, Sanil Kumar V, Amrutha MM, Singh J (2016) Characteristics of long-period swells measured in the near shore regions of eastern Arabian Sea. *Int J Naval Archit Ocean Eng* 8:312–319



# Sensitivity Study of Wind Drag Coefficient on Surge Modelling for Tropical Cyclone



C. Gowri Shankar , Manasa Ranjan Behera  and P. Vethamony 

**Abstract** The Bay of Bengal (BoB) is the breeding ground for the tropical cyclones, accompanied by very strong winds, torrential rains and storm surges with severe intensity during the pre- and post-monsoon seasons. Modelling this storm surge is involved with many uncertainties; among those, the wind stress (associated with wind drag coefficient,  $C_d$ ) over ocean surface is a crucial surface forcing and a thriving factor. The present study examines the sensitivity of  $C_d$  that was used to simulate storm surge in the BoB region using the coupled ADCIRC and SWAN model. In general, ADCIRC uses the formulation of Garratt [1] and SWAN uses that of Wu [2] to evaluate  $C_d$ . Both these relations are empirical, and  $C_d$  increases linearly with wind speed. Hence, cut-off values ( $C_d$  cap) are proposed for  $C_d$ , ranging from  $2.0 \times 10^{-3}$  to  $3.5 \times 10^{-3}$  and a no-cap condition in SWAN. The simulations were performed for cyclone ‘Vardah’, and significant wave heights, surge heights and landfall time were computed. Results show that the parameters estimated through the cut-off  $C_d$  values reasonably match with the observed values than the no-cap case. The results and analysis interpreted from the current study will be used on a significant scale to understand and determine the sensitive behaviour of  $C_d$  for very high wind speeds of a tropical cyclonic condition.

**Keywords** Storm surge · Wind stress · ADCIRC-SWAN · Drag coefficient  
Significant wave height

---

C. Gowri Shankar (✉) · M. R. Behera · P. Vethamony  
Department of Civil Engineering, Indian Institute of Technology Bombay, Powai, 400076  
Mumbai, Maharashtra, India  
e-mail: [gowrishankar1805@gmail.com](mailto:gowrishankar1805@gmail.com)

M. R. Behera  
e-mail: [manasa.rb@iitb.ac.in](mailto:manasa.rb@iitb.ac.in)

P. Vethamony  
e-mail: [vethamony@iitb.ac.in](mailto:vethamony@iitb.ac.in)

© Springer Nature Singapore Pte Ltd. 2019  
K. Murali et al. (eds.), *Proceedings of the Fourth International Conference in Ocean Engineering (ICOE2018)*, Lecture Notes in Civil Engineering 22,  
[https://doi.org/10.1007/978-981-13-3119-0\\_54](https://doi.org/10.1007/978-981-13-3119-0_54)

## 1 Introduction

Among all the natural hazards, storm surges remain as the world's leading ones, especially due to their frequent occurrences in many coastal regions and heavy loss of life, property and damage to coastal structures. The extensive coastline of India ( $\approx 7500$  km), especially the east coast of India, is suffering from the effect of storms in varying degrees. Some of the devastating cyclones and the associated storm surges over the east coast of India and Bangladesh coast show the propensity and destructive violence of cyclones emanating from the Bay of Bengal. Although only about seven per cent of the global tropical cyclones occurs in the northern Indian Ocean, they are the deadliest in the world. Factors like the shallow waters of the Bay of Bengal, the low and flat coastal terrain of India and Bangladesh and the funnel-shaped coastline combinations tend to produce intensive surges. The most severe cyclone-related event in the recorded history, with respect to inundation and loss of life, occurred in Bangladesh in November 1970 which produced a maximum surge height of  $\sim 10$  m, and the loss of life was estimated to be 300,000–500,000 [3]. The October 1999 cyclone that hit the Orissa coast of India produced a 7.5 m surge [4]. Around the globe nearly one billion people and in India almost 14% of the population have their habitats along the coastline and are vulnerable to such extreme sea-level events. Thus, forecasting, modelling and prediction of such events would be of great interest in safeguarding the lives and interest of the nation.

Numerical storm surge modelling has always been a challenging task and had taken a few decades to come to this stage of development. It involves several input parameters such as wind velocity, central pressure of the cyclone, local bathymetry, tidal input and wave stress gradients. These input parameters are collected and generated through field observations and models, and then given as input to surge model for simulating vertical surge height and inundation levels. A comprehensive review of such studies is reported in [5–7]. It is a well-known fact that ocean currents and waves are driven by momentum fluxes across the air–sea interface. The bulk formula that calculates boundary layer parameterisations uses either roughness length  $Z_0$  or drag coefficient,  $C_d$  for the cyclonic storm surge models [e.g. Sea, Lake and Overland Surges from Hurricanes (SLOSH) by NOAA [8] for surge and Advanced Circulation Multidimensional Hydrodynamic Model (ADCIRC) [9, 10] and the Finite Volume Coastal Ocean Model (FVCOM) [11, 12] for surge and waves]. The present study investigates the sensitivity of the drag coefficient parameter by modifying its cut-off values used in the current storm surge and wave models. To execute the same, the very severe cyclonic storm (VSCS) that hit the east coast of India (Tamil Nadu) cyclone 'Vardah' was considered, and simulations were performed. Cyclone Vardah formed as a depression in the morning hours of 6 December 2016 over the south-east Bay of Bengal, and lay centred approximately  $8.5^\circ\text{N}$ ;  $91.0^\circ\text{E}$  (about 1320 km south-south-east of Visakhapatnam, 1360 km south-south-east of Gopalpur and 210 km west-south-west of Car Nicobar). The system intensified into a 'deep depression' after 33 h with wind speed exceeding  $14\text{ ms}^{-1}$  and transformed into a 'cyclonic storm' (wind speed crossed  $17\text{ ms}^{-1}$ ) at 0030 UTC on 8 December 2016. Further it

intensified into a severe and very severe cyclonic storm at 1200 UTC on 10 December 2016. Vardah attained its maximum intensity of  $36 \text{ ms}^{-1}$  and made its landfall around 0900 to 1130 UTC on 12 December 2016 near Chennai. Vardah reduced to a severe cyclonic storm (SCS) just before making its landfall and moved westwards by dissipating its intensity into a depression and finally as a low-pressure system. The havoc caused by Vardah to the coastal structures and properties was enormous. It was observed that a maximum of 1 m height of storm surges above the astronomical tide inundated the coastal stretches of Ennore, Chennai and Thiruvallur districts of Tamil Nadu and Nellore district of Andhra Pradesh.

## 2 Model Description

The present study uses the coupled hydrodynamic (circulation) and wave model (ADCIRC and SWAN) for the simulation of storm surge and its corresponding waves. ADCIRC model was developed through the combined efforts of the Engineering Research and Development Centre (U.S. Army Corps of Engineers (USACE)), University of Notre Dame and University of North Carolina. Through the axis of rotating coordinate system, the model is solving for the moving fluid with the equation of motion. Finite element method and finite difference method are adopted to discretize the governing equations in space and time, respectively, which was formulated using Boussinesq approximation.

The current version of ADCIRC used in the present study is highly capable to run with two-dimensional depth-integrated (2DDI) mode on a flexible unstructured grid. The model solves the vertically integrated continuity equation and vertically integrated momentum equations for water surface elevation ( $\zeta$ ) and currents, respectively [13], with a sophisticated algorithm for wetting and drying that activates and deactivates the entire grid elements during inundation and recession of coastal topography [10]. The model requires wind and pressure fields and tidal forcing along open ocean boundary as essential inputs. Simulating Waves Nearshore (SWAN) is a third-generation wave model that was developed at the Delft University of Technology, The Netherlands. It is governed by the action balance equation with phase averaging analogue Gauss-Siedel sweeping algorithm technique to propagate wave action density spectrum on an unstructured mesh [14]. SWAN describes the waves with the two-dimensional wave action density spectrum, even when nonlinear phenomena dominate (e.g. in the surf zone). The latest version of SWAN 41.10 has been used in this study, coupled with ADCIRC to simulate surges and waves for cyclone Vardah. When the coupling is initiated, ADCIRC runs first using radiation stresses of SWAN from the previous interval to extrapolate the wave forcing forwards in time. When the time steps of the coupling interval is complete, ADCIRC passes on the wind velocity, water levels, currents and roughness length to SWAN. The gradient of each element will be projected to the vertices considering the area-weighted average of gradients from elements adjacent to each vertex [10].

### 3 Model Composition and Implementation

The simulations were carried out for the east coast of India, where it is encircled by the Bay of Bengal basin. The domain starts in the north from southern Andhra Pradesh coast (Kavali) and extends in the south till Vedaranyam (Tamil Nadu coast) as shown in Fig. 1. The total length of the inland boundary is approximately 570 km, while the offshore extent to the open ocean boundary is about 600 km. Storm surges are well known for its complexity in simulation, and hence, a finite element grid was generated with a fine spatial resolution along the coast ( $\sim 100$  m) and increases to a coarse grid ( $\sim 20$  km) in the offshore extent [15, 16].

A coarse grid has been chosen for the offshore region because of its large bathymetric depths for longer extents that makes the geometry simpler to solve. The total number of triangular elements and nodes in the mesh are 340,221 and 172,854,

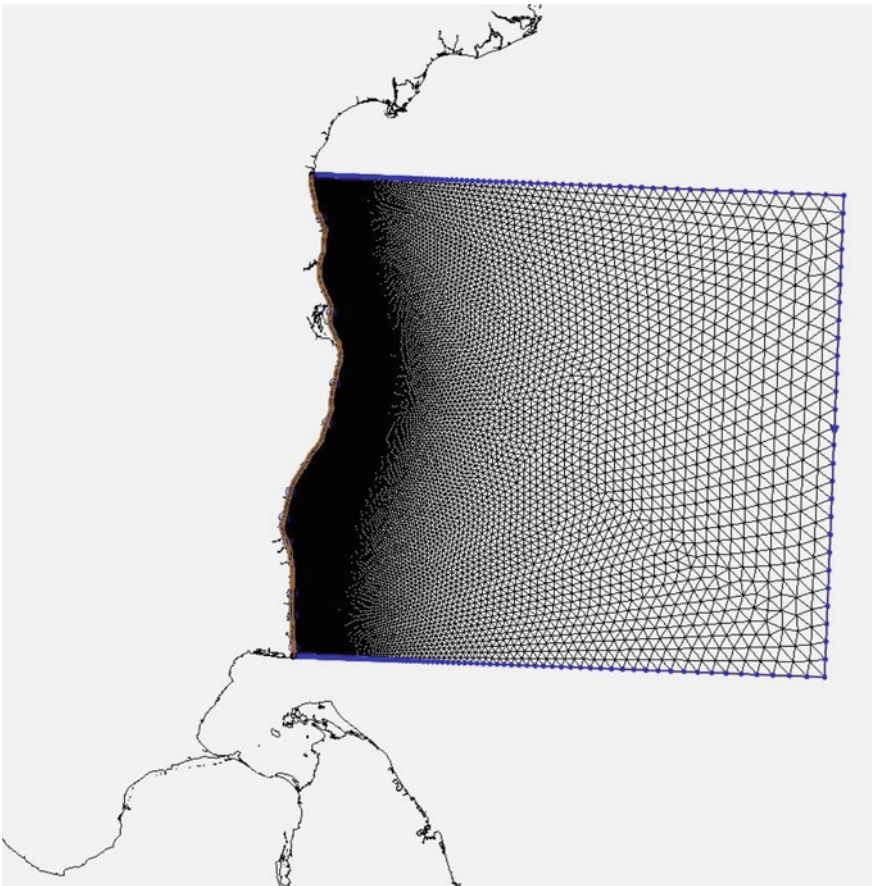


**Fig. 1** Study area with a finite element mesh and rectangular open ocean boundary

respectively, with a rectangular offshore boundary connecting to the mainland. A rectangular-shaped boundary was preferred over a semi-circular-shaped boundary (although the number of nodes and computational time would be less) because of its computational stability along the corner node points. The gridded bathymetry used for the current study was obtained from the open source database General Bathymetric Chart of the Oceans (GEBCO) which comes under the division of British Oceanographic Data Centre. GEBCO's bathymetry is the finest spatial resolution available currently with a global grid of 30 arc second data as represented in Fig. 2 for the current study domain.

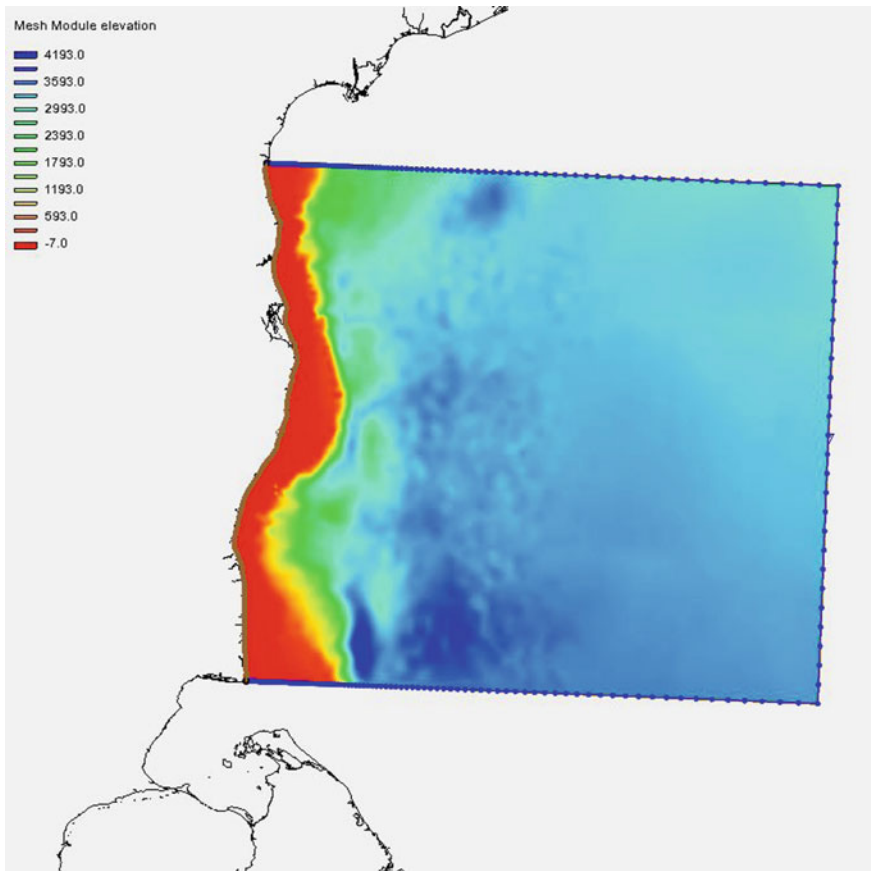


Fig. 2 Spatial extent of the bathymetry for the model domain (in m)

### 3.1 Methodology

Wind stress component is completely dependent on the factor, wind drag coefficient ( $C_d$ ). Most of the storm surge models use either a linearly increasing  $C_d$  or a fast increasing  $C_d$  as the wind speed increases. However, the trend was found to be different from the recent field, laboratory, theoretical and numerical studies that show a levelling-off or even a decreasing  $C_d$  at high wind speeds. Both ADCIRC and SWAN use a linear relationship to calculate the drag coefficient that was developed by Garratt [1] and Wu [2], respectively. A cut-off value has been introduced to the drag coefficient, as these models tend to give unrealistic values at very high wind speeds besides using a linear relation. In earlier studies, the cut-off value for the hydrodynamic model was fixed at 0.002, and now, it has been reformed to 0.0035 for better predictions. However, to understand the sensitivity of this drag coefficient in the storm surge model, the cut-off values were set to 0.002, 0.0025, 0.0030 and 0.0035 for the coupled model.

The model inputs required for the simulations are bathymetry data, cyclone best track (that includes the location of the cyclone w.r.t its wind intensity and central pressure) and tidal potential constituents. As earlier stated, the bathymetry data was imported to the model from GEBCO with 30 arc second resolution with reference to the study domain, and six tidal constituents (K1, M2, N2, O1, P1 and S2) were prescribed at the open ocean boundary. These six tidal constituents were only used as they portray the true tidal field that exists in the Bay of Bengal basin [16]. The phase and amplitude of the six tidal constituents synchronize with model start time (i.e. 6 Z of 6 December 2016) at the open ocean boundary and progress ahead with time into the nearshore areas. Cyclone Vardah's best track details were obtained from Joint Typhoon Warning Center (JTWC) and imposed to the study area as shown in Fig. 2. The best track data avails information like coordinates of the cyclone position (latitude and longitude), maximum wind intensity and central pressure along the cyclone's path at every 6 h interval to the model. The coordinate system was set to spherical with a cold start, and a constant quadratic bottom friction coefficient ( $C_b = 0.0028$ ) was used. The wetting and drying scheme was also enabled by assigning the minimum water depth and minimum velocity for wetting to 0.05 [17]. The weighting factor that relates to the relative contribution of primitive and wave portions in Generalized Wave Continuity Equation (GWCE) was set to 0.005. The simulation was for a total of 7 days (6–13 December 2016) with a ramp function set to 1 day that is the spin-up time taken by the model. The time step for the current simulations was assigned to 2.0 s which was correlated with the Courant number. The recommended value for Courant number is 1.0 [18] and thus should not exceed the same.

A high performance computing (HPC) cluster IBM 7915-x3650 M4 system with a processor clock speed of 1200 MHz was used to perform the model simulations. All the three nodes with 24 processors were used since the model has a very fine resolution (approximately 100 m) along the nearshore regions. Totally, eight virtual probe stations were set, out of which six are along the coastline (Nellore, Krishnapatnam, Ennore, Chennai, Pondicherry (Puducherry) and Nagapattinam) to capture the surge

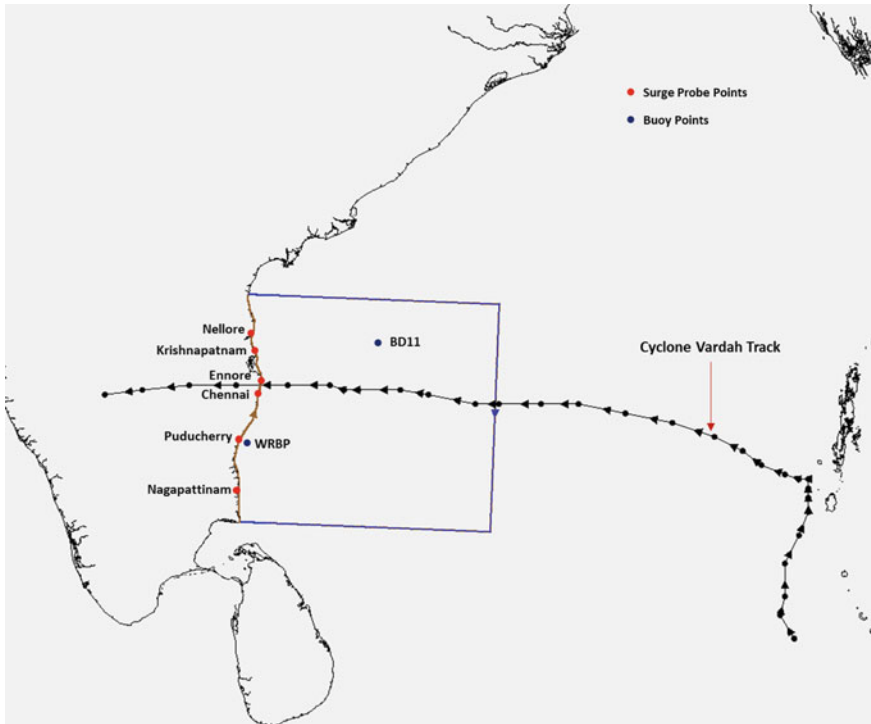


**Fig. 3** Virtual probe locations along the study domain to measure the surge and significant wave height

and two buoy stations within the study domain (deep water moored buoy—BD11 and shallow water buoy—wave rider buoy Pondicherry (WRBP)) as represented in Fig. 3. The two buoy locations, namely BD11 and WRBP, are situated approximately 300 km north-east and 150 km south, respectively, from the cyclone’s landfall point. The output, recorded with a time step of 30 min interval from the model simulations, was used for the final analysis.

## 4 Results and Discussion

The model was simulated and recorded under different case scenarios that are mentioned in the previous sections. The outputs simulated by the coupled model are the total water-level elevations, wind velocity and atmospheric pressure (ADCIRC), radiation stress gradients, significant wave heights, mean wave directions, mean wave periods and peak wave periods (SWAN) at all the nodal points. As stated, there were six virtual probe stations fixed along the nearshore (coastline) areas to

record the water-level elevations. These six probe stations were fixed with reference to the cyclone track, two stations to the northern side of the cyclone, two stations in the near vicinity of the landfall point and two stations on the southern side of the cyclone as shown in Fig. 3. Vardah was categorized as a very severe cyclonic storm (VSCS—wind intensity exceeding  $33 \text{ ms}^{-1}$ ) and reported that it generated a storm surge of 1 m height above the astronomical tide for Chennai, Kanchipuram, Thiruvallur districts along the Tamil Nadu coast and Nellore district of Andhra Pradesh. The simulated results with the mentioned case scenarios were compared with the reported values of IMD. Figures 4 and 5 represent the results of maximum water levels and the corresponding residuals obtained during the cyclone's progress at all the six probe locations for different cut-off values of the drag coefficient.

According to the solutions obtained from the hydrodynamic coupled model, it is noticeable that the cut-off value of 0.0035 shows the highest surge values which are the closest to the observed value of 1 m on the Chennai and Ennore coasts. The residuals that are shown in Fig. 6 explain the disturbances caused in the water levels by the cyclone over and above the predicted astronomical tide (pure surge component). These residuals are computed by removing the tide and considering only the pure forcing of the surface winds that emerged during the cyclone to produce the surge. Figure 6 illustrates the spatial variation of the maximum water levels obtained from the model computations for a drag coefficient cut-off value of 0.0035. It also clearly points out that the locations towards the right of the cyclone track experience higher surge than that of the left side locations (as seen in the locations of Pondicherry and Nagapattinam). This is because of the anticlockwise rotation of the wind field in a moving cyclonic storm, which causes a higher surge elevation on the northern side.

To evaluate the performance of the wave model (SWAN), the computed significant wave heights were compared with a deep water moored buoy (BD11) and shallow water buoy (WRBP) observed data obtained from the Indian National Centre for Ocean Information Services (INCOIS). The significant wave heights, both in the deep water and shallow water locations, were overestimated (Fig. 7) by the model for the no-cap condition as well as for the cut-off value of 0.0035 when the cyclone passed these locations. However, for the cut-off values of 0.0025 and 0.0030, the model wave heights are found to be in good agreement with the observed values. Though there is a shift in the peak wave height's phase in the deep water location, it is understandable that SWAN is particularly built for nearshore regions, and it is quite evident that its efficiency for deep water wave modelling is low unless it is nested with global models like WW3 [19, 20]. It is also recognized that there is a huge difference (underestimation of  $H_s$ ) in the wave heights for the initial days of simulation. This is because of not including the pre-existing wind conditions of the region, rather, the forcing was made only with the cyclone wind intensities and also non-inclusion of swell effects from the rest of the north Indian Ocean as well as the Southern part of the Indian Ocean into the model domain. The  $H_s$  of both the probe locations for the entire cyclone duration is shown in Fig. 7. The maximum significant



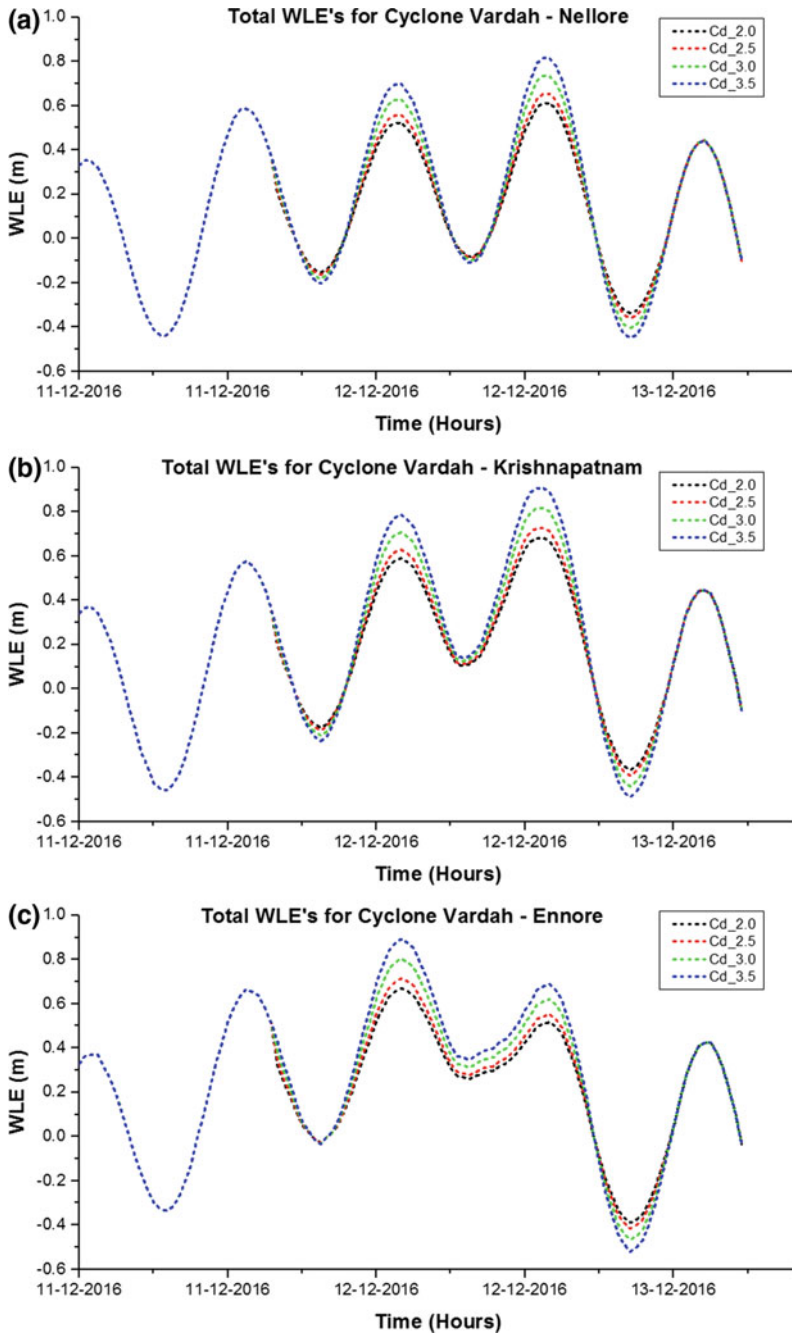


Fig. 4 Total water-level elevation at all the surge probe locations during Vardah's landfall (in m)

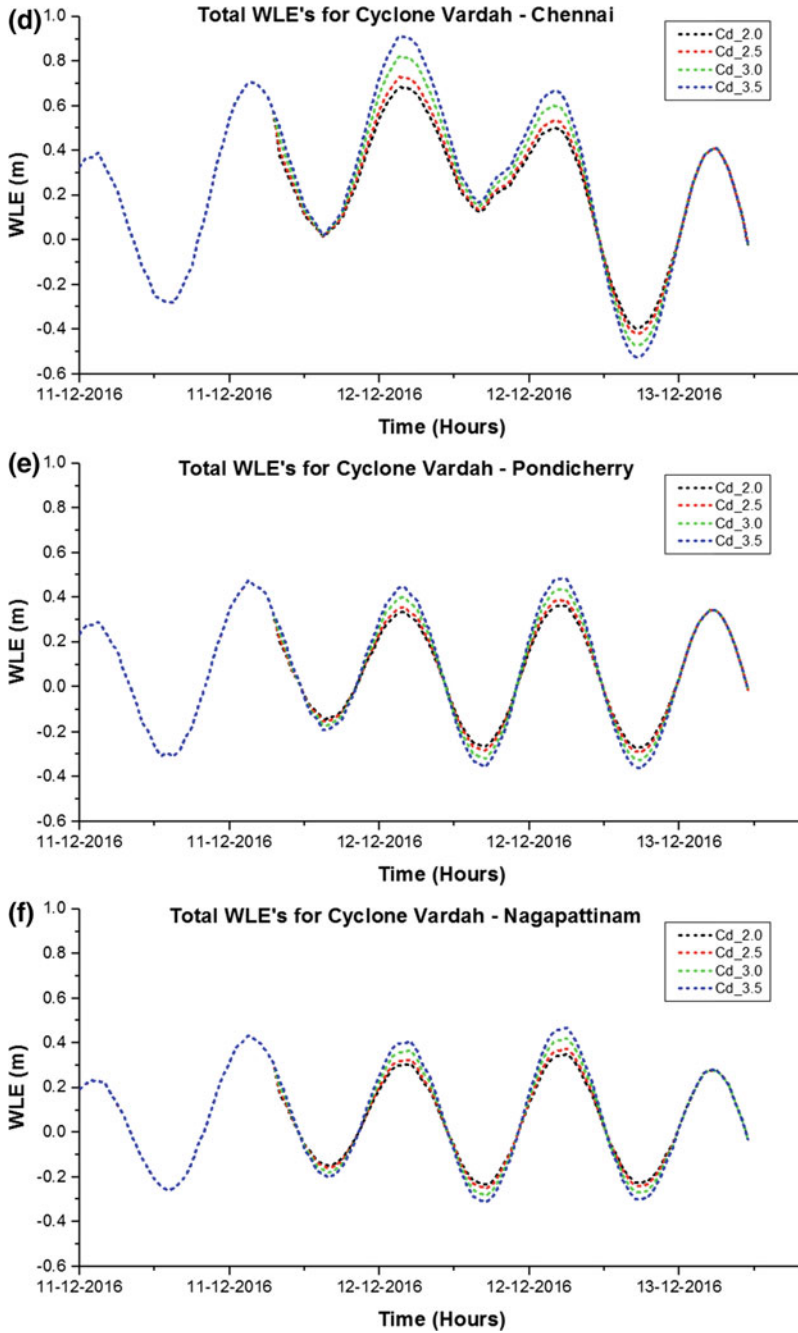
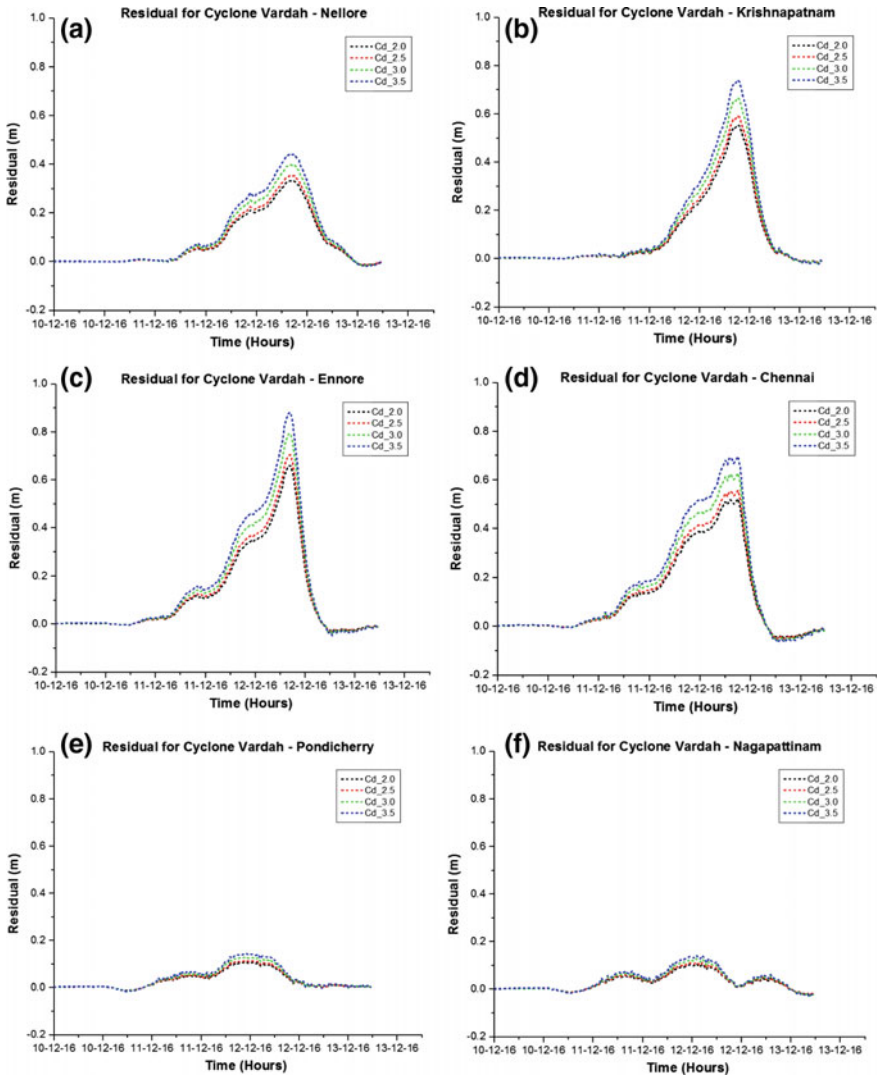
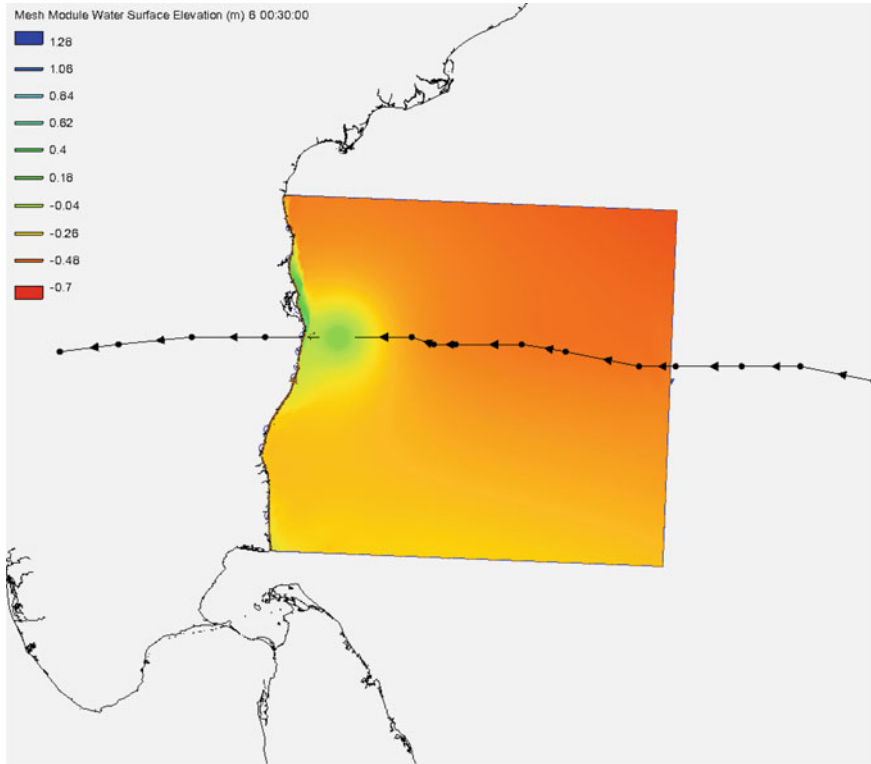


Fig. 4 (continued)



**Fig. 5** Residual at all the surge probe locations during Vardah’s landfall (in m)

wave heights exceeded 14 m (Fig. 8) along the cyclone track in the deep waters, and when the waves started experiencing the drag from the sea bottom as they moved towards the shore, the waves started breaking due to shoaling effect and wave heights started reducing as they approached the coast.



**Fig. 6** Spatial variation of maximum water level (in m) in the entire domain for  $C_d = 0.0035$

## 5 Summary and Conclusions

A coupled (ADCIRC+SWAN) model was used to simulate the storm surges generated by the cyclone ‘Vardah’, and subsequently, significant wave heights, surge heights and landfall time were computed. The simulated results from the coupled model for the cut-off  $C_d$  cases were compared with observed data, and it was found that for a cut-off value of  $C_d = 0.0035$ , the model tends to produce much better surge values, whereas, other simulations were greatly underestimated. The significant wave heights computed from the wave model is also prone to water depth, as it estimates better wave heights in the shallow water location than the deep water for a cut-off value of 0.003. Therefore, it is obvious that SWAN model results based on the default wind input settings for tropical cyclones are reliable for areas shallower than the continental shelf (20–30 m) region regardless of the tendency to overestimate the significant wave heights in deep waters [21]. Hence, these cut-off values cannot be uniform for both the models in a coupled environment, rather they are model dependent. Though the simulated wave heights match reasonably well in comparison with the observed values for the case of 0.003 (cut-off of  $C_d$ ), there can still be an

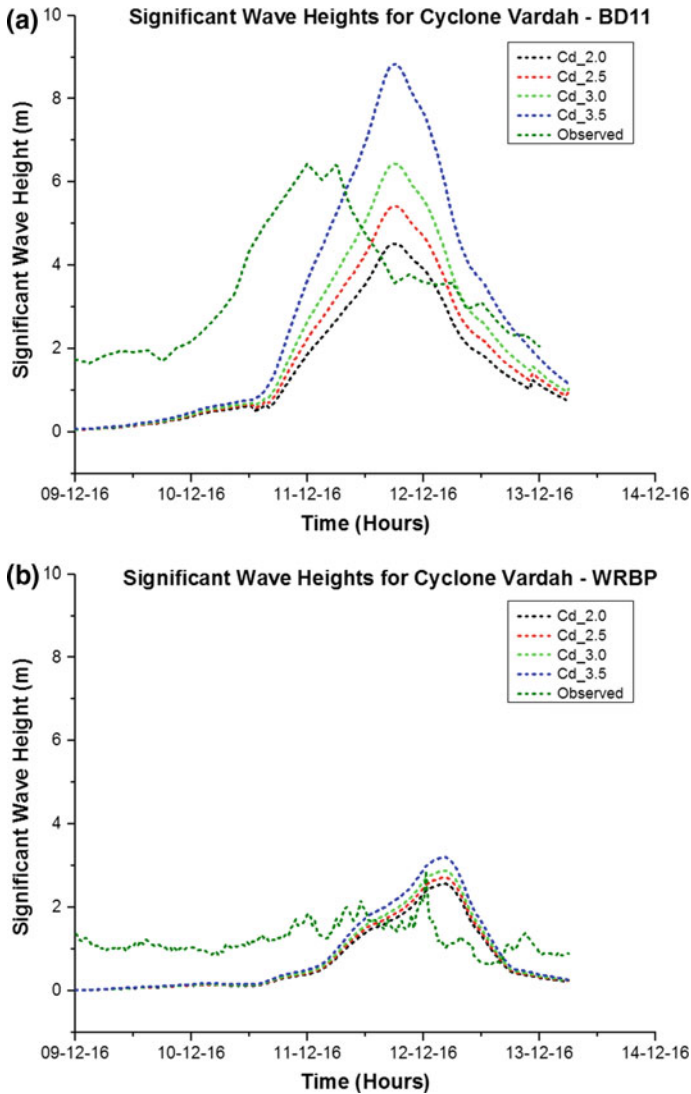


**Fig. 7** Significant wave height at the two buoy probe locations (in m)

improvement in the representation of the drag coefficient formulation that is affected by very high wind speeds during an extreme weather event. The results and analysis interpreted from the present study will be extended further on a significant scale to understand and determine the sensitive behaviour of  $C_d$  in storm surge modelling, as it can improve the accuracy of the latter to a great extent. Thus, the results could be used for effective planning and design of mitigation and protection mechanisms for better coastal resilience.

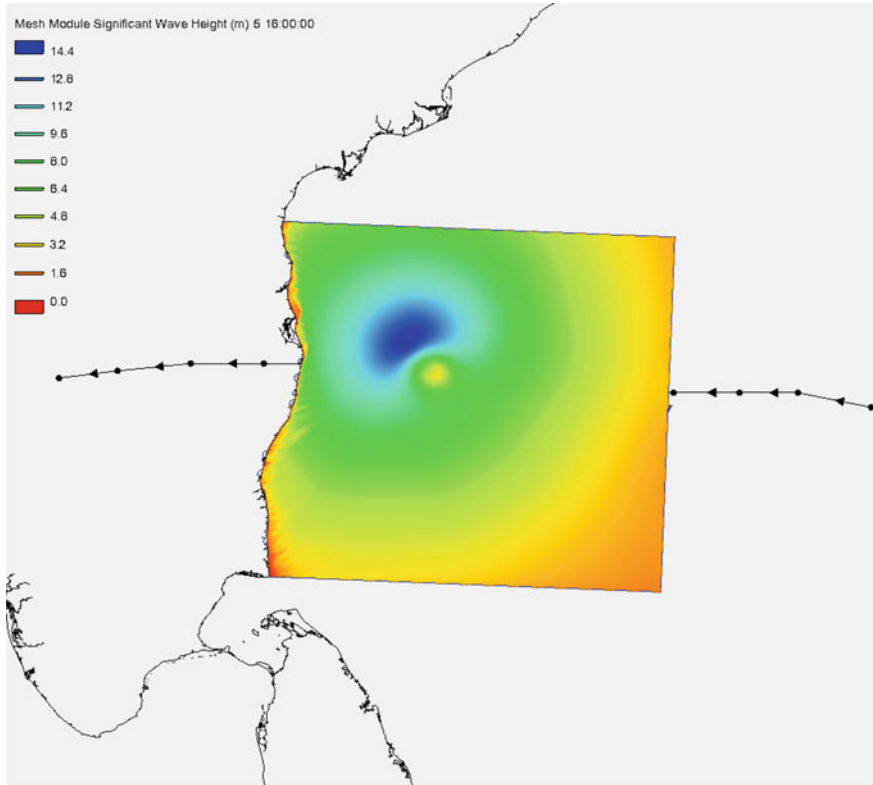


**Fig. 8** Spatial variation of maximum significant wave height (in m) in the entire domain for  $C_d = 0.0035$

## References

1. Garratt JR (1977) Review of drag coefficients over oceans and continents. *Mon Weather Rev* 105(7):915–929
2. Wu J (1980) Wind-stress coefficients over sea surface near neutral conditions—a revisit. *J Phys Oceanogr* 10(5):727–740
3. Madsen H, Jakobsen F (2004) Cyclone induced storm surge and flood forecasting in the northern Bay of Bengal. *Coast Eng* 51(4):277–296
4. Dube SK, Chittibabu P, Rao AD, Sinha PC, Murty TS (2000) Extreme sea levels associated with severe tropical cyclones hitting Orissa coast of India. *Mar Geodesy* 23(2):75–90
5. Murty TS, Flather RA, Henry RF (1986) The storm surge problem in the Bay of Bengal. *Prog Oceanogr* 16(4):195–233
6. Dube SK, Rao AD, Sinha PC, Murty TS, Bahulayan N (1997) Storm surge in the Bay of Bengal and Arabian Sea: the problem and its prediction
7. Dube SK, Jain I, Rao AD, Murty TS (2009) Storm surge modelling for the Bay of Bengal and Arabian Sea. *Nat Hazards* 51(1):3–27
8. Jelesnianski CP, Chen J, Shaffer WA (1992) SLOSH: sea, lake, and overland surges from hurricanes. NOAA Technical Report NWS 48, 77 pp, National Weather Service, National Oceanic and Atmospheric Administration, Silver Spring, Md

9. Westerink JJ, Luettich RA (1991) Tide and storm surge prediction in the Gulf of Mexico using model ADCIRC-2D. Report to U. S. Army Engineers Waterways Experiment Station, 112 pp, Vicksburg, Miss., July
10. Dietrich JC, Zijlema M, Westerink JJ, Holthuijsen LH, Dawson C, Luettich RA, Stone GW (2011) Modeling hurricane waves and storm surge using integrally-coupled, scalable computations. *Coast Eng* 58(1):45–65
11. Huang Y, Weisberg RH, Zheng L (2010) Coupling of surge and waves for an Ivan-like hurricane impacting the Tampa Bay, Florida region. *J Geophys Res Oceans* 115(C12)
12. Zheng L, Weisberg RH, Huang Y, Luettich RA, Westerink JJ, Kerr PC, Akli L (2013) Implications from the comparisons between two-and three-dimensional model simulations of the Hurricane Ike storm surge. *J Geophys Res Oceans* 118(7):3350–3369
13. Luettich RA, Westerink JJ (2004) Formulation and numerical implementation of the 2D/3D ADCIRC finite element model version 44.XX, p 74
14. Booij NRRC, Ris RC, Holthuijsen LH (1999) A third-generation wave model for coastal regions: 1. Model description and validation. *J Geophys Res Oceans* 104(C4):7649–7666
15. Rao AD, Jain I, Murthy MR, Murty TS, Dube SK (2009) Impact of cyclonic wind field on interaction of surge–wave computations using finite-element and finite-difference models. *Nat Hazards* 49(2):225–239
16. Bhaskaran PK, Gayathri R, Murty PLN, Bonthu S, Sen D (2014) A numerical study of coastal inundation and its validation for Thane cyclone in the Bay of Bengal. *Coast Eng* 83:108–118
17. Dietrich JC (2005) Implementation and assessment of ADCIRC’s wetting and drying algorithm. Doctoral dissertation, University of Oklahoma
18. Westerink JJ, Luettich Jr RA, Blain CA, Scheffner NW (1994) ADCIRC: an advanced three-dimensional circulation model for shelves, coasts, and estuaries. Report 2. User’s manual for ADCIRC-2DDI (No. WES/TR/DRP-92-6-2). Army Engineer Waterways Experiment Station, Vicksburg, Ms
19. Sandhya KG, Nair TB, Bhaskaran PK, Sabique L, Arun N, Jeykumar K (2014) Wave forecasting system for operational use and its validation at coastal Puducherry, east coast of India. *Ocean Eng* 80:64–72
20. Vethamony P, Rashmi R, Samiksha SV, Aboobacker VM (2013) Recent studies on wind seas and swells in the Indian Ocean: a review. *Int J Ocean Clim Syst* 4(1):63–73
21. Huang Y, Weisberg RH, Zheng L, Zijlema M (2013) Gulf of Mexico hurricane wave simulations using SWAN: bulk formula-based drag coefficient sensitivity for Hurricane Ike. *J Geophys Res Oceans* 118(8):3916–3938

# Tidal Circulation Studies Using Regional Model in the Bay of Bengal



Saikat Pramanik, Samiran Mandal, Abhijit Shee, Subrota Halder and Sourav Sil

**Abstract** Ocean circulation is very much important for ocean engineering in terms of building offshore structures, navigation, renewable energy and designing marine instruments. This study discusses the impact of tides on ocean circulation using high-resolution (spatial resolution  $1/9^\circ$  with 45 vertical levels) Regional Ocean Modelling System (ROMS) for the coastal region of the Bay of Bengal (BoB). A climatological simulation is performed with Comprehensive Ocean-Atmosphere Data Set (COADS05) air–sea fluxes and ten major tidal components from TOPEX/POSEIDON global tidal model (TPXO7). The simulation reproduced the tidal elevations well as validated with observation (at R1, near Paradeep, Odisha). In the head bay (R2) and the Gulf of Martaban (R3), the broad continental shelf and shape of the coastline largely contribute the amplification of tidal currents, which are around 0.9 and 1.7 m/s, respectively. In the BoB, semi-diurnal tide M2 achieves the highest amplitude 320 cm, followed by the amplitude of S2 tide (120 cm) at R3. The tidal-driven current changes its direction in every 6 h, which indicates that the shallow water constituents have significant impact in the R2 and R3 regions. The vertical structures of the currents denote tidal-driven current in those regions are more baroclinic.

**Keywords** ROMS · Bay of Bengal · Tide · Current · M2

## 1 Introduction

Circulations in the coastal regions of the global oceans are very much important in our daily lives. However, coastal ocean is more complex compared to the open ocean

---

S. Pramanik (✉) · S. Mandal · A. Shee · S. Halder · S. Sil  
School of Earth, Ocean and Climate Sciences, Indian Institute of Technology Bhubaneswar,  
Bhubaneswar, India  
e-mail: [sp22@iitbbs.ac.in](mailto:sp22@iitbbs.ac.in)

S. Halder  
Indian Institute of Tropical Meteorology, Pune, India

© Springer Nature Singapore Pte Ltd. 2019  
K. Murali et al. (eds.), *Proceedings of the Fourth International Conference in Ocean Engineering (ICOE2018)*, Lecture Notes in Civil Engineering 22,  
[https://doi.org/10.1007/978-981-13-3119-0\\_55](https://doi.org/10.1007/978-981-13-3119-0_55)



as it is additionally driven by the tides, and interaction with the bottom topography is more. The topography of the Bay of Bengal (BoB) is very unique in nature, and it has less shelf region on the western boundary and very large shelf in the north and eastern boundary. Therefore, the tidal characteristics along the coastline of the BoB are different with locations. There are numerous observational and modelling studies on tidal characteristics over the BoB. It was reported that the major semi-diurnal and diurnal tidal constituents in the BoB are (M2, S2, N2) and (K1 and O1), respectively [1, 2]. Rose and Bhaskaran [3] determine the major tidal constituents at the Ganges location, estuary over the BoB from tide gauge data set using ADvanced CIRCulation (ADCIRC) hydrodynamic model with special focus on mouth point of two major rivers Meghna and Hooghly. The higher order constituents have been studied in the north-west European shelf region for the first time from the satellite TOPEX/POSEIDON (TP) altimetry data sets [4, 5].

But short duration and spatially sparse tidal and hydrographic data along the BoB coast limit the understanding of the tidal characteristics and their impact on the ocean parameters in this basin. Therefore, the circulation models are one of the options to investigate the above. For tidal studies, topography is very crucial. The topography in the earlier two-dimensional barotropic model studies were of 5 min horizontal resolution or coarser. Therefore, we have used a finer resolution (2 min) topography in our model. The aim of this work is to investigate the tidal-driven current and identify the significant regions in northern part of the BoB using a three-dimensional ocean circulation model (details are given in Sect. 2). The paper is organized in the following manner: a brief description of model configuration and validation are presented in Sect. 2. In Sect. 3, the impact of tides on sea level and the circulation are discussed.

## 2 Model Configuration

The Regional Ocean Modelling System (ROMS), a terrain following three-dimensional ocean model [6, 7], is configured for the BoB region (Fig. 1). The model topography fields are extracted from Earth Topography (etopo2) with 2-min resolution data sets. A finer horizontal resolution  $1/9^\circ$  with 45 vertical levels is considered to simulate the vertical structures of the oceanic parameters accurately. The model is forced with the climatologically varying monthly air–sea fluxes from Comprehensive Ocean-Atmosphere Data Set (COADS05). Ten major components of tides (K2, N2, S2, M2, P1, O1, K1, Q1, Mm and Mf) are forced from TOPEX/POSEIDON global tidal model (TPXO7) to simulate the tidal-driven currents as well as sea level. The initial and boundary conditions are taken from latest  $0.25^\circ$  World Ocean Atlas 2013 (WOA13) [8, 9]. The open oceanic boundary conditions and lateral vertical mixing are same as described by Dey [7]. The model is simulated for one year to spin-up, and results are discussed for the last month, i.e. December.

For validation of the model, we compared the simulated sea surface height anomaly (SSHA) with the sea-level anomaly from the tide gauge observation (source:

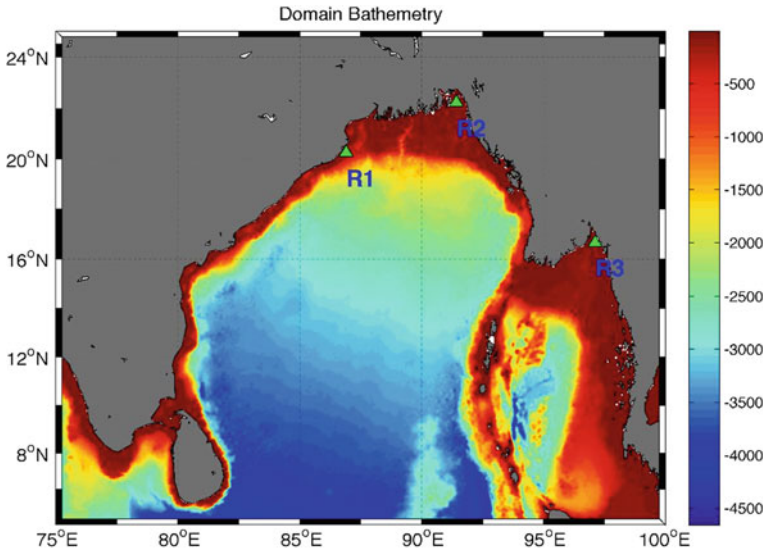


**Fig. 1** Domain bathymetry (m) extracted from etopo2 (shaded colour) with the locations R1 (at Paradeep), R2 (on the head Bay of Bengal) and R3 (on Gulf of Martaban)

Indian National Centre for Oceanic Information Services (INCOIS), Hyderabad, India) at Paradeep location (R1) for the period of 31 days in December 2014 (Fig. 2). Time evaluations of observed and simulated tides show that ROMS captured the spring and neap tidal cycle very well, although ROMS simulated tidal height is slightly more than the observation.

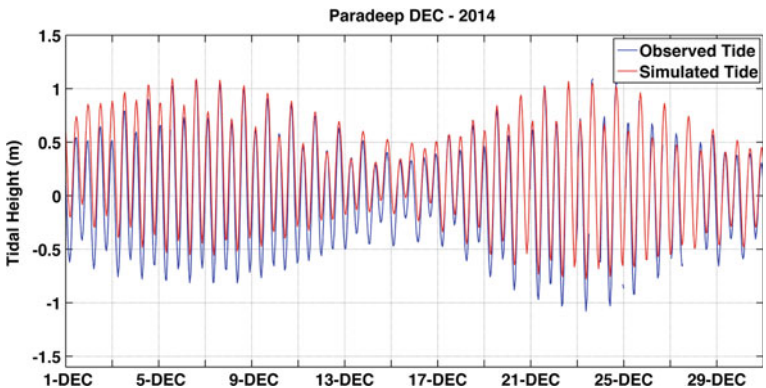


**Fig. 2** Comparison of observed sea surface height anomaly (m) from tide gauge observation (blue line) and ROMS simulation (red line) at R1 (Paradeep) location in the month of December 2014

### 3 Results and Discussions

#### 3.1 Sea Level

Figure 3 comprises the amplitude of 28 tidal constituents from harmonics analysis using T\_Tide toolbox [10] of the sea level at the locations of Paradeep (R1), head Bay of Bengal (R2) and Gulf of Martaban (R3). Semi-diurnal tide M2 has highest amplitude in R3 location (320 cm), whereas 290 cm and 55 cm in R2 and R1, respectively. But the amplitude of S2 tide is maximum (140 cm) at R2 location and 120 and 20 cm at R3 and R1 location, respectively. The values match reasonably well with the observational study [1, 2].

Co-range charts for M2, N2, S2 and K1 tides over the northern BoB are shown in Fig. 4. The amplitude of M2 tide is more in north-eastern and northern BoB when approaching towards the Gulf of Martaban and head BoB. Over the BoB, M2

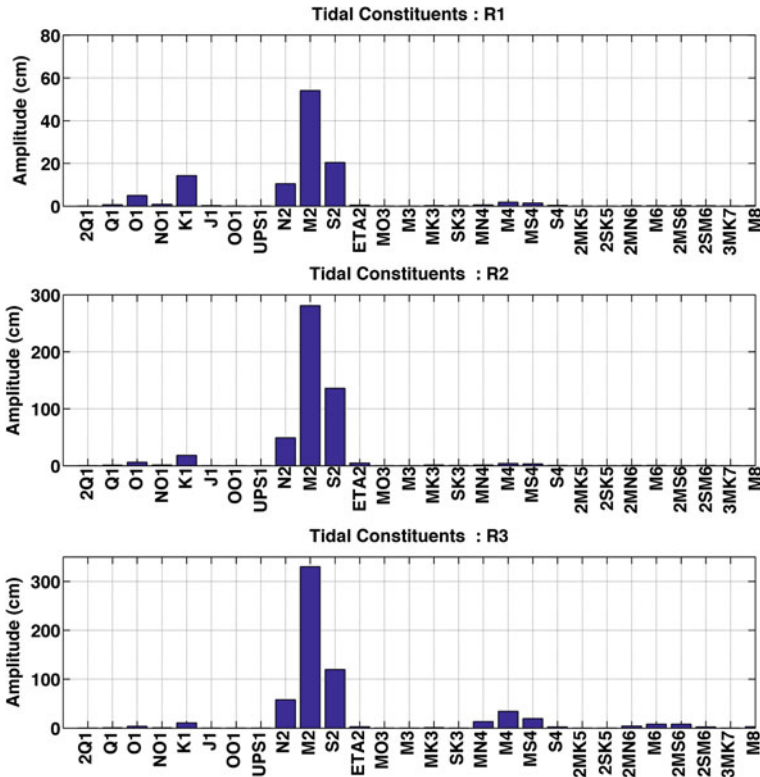
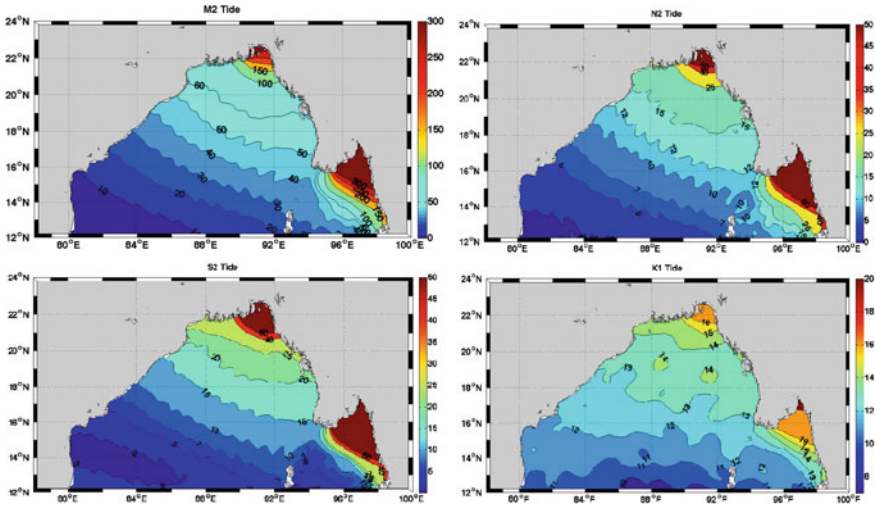


Fig. 3 Amplitude of diurnal and semi-diurnal tidal constituents obtained from harmonic analysis of model-simulated sea surface height at R1 (Paradeep) in upper panel, R2 (Head BoB) in middle panel and R3 (Gulf of Martaban) in lower panel. Locations are depicted in Fig. 1



**Fig. 4** Distribution of amplitude of dominated semi-diurnal tides M2, S2, N2 and diurnal tides K1 over the BoB

tide propagates north-westwards in the central bay and the northwards in the head bay from the amphidromic point in the central BoB. In the Andaman Sea, M2 tide travels north-eastwards and enters in the Gulf of Martaban. M2 tide attains its maximum value at the Gulf of Martaban nearly about 250 and 140 cm in the head BoB. Its amplitude increases in the northern BoB and attains maximum in the western BoB and Gulf of Martaban. The propagation of S2 tide is similar to the variation of M2 tide, but its amplitude is half of the amplitude of M2 tide over BoB. It has peak in the Gulf of Martaban (120 cm) and 70 cm in the head BoB. The amplitude of N2 tide is less compare to M2 and S2 tides, although maximum amplitude occurs in the Gulf of Martaban (40 cm) and the head BoB. Propagation of diurnal tide K1 is not similar to the propagation of M2, S2 and N2.

### 3.2 Ocean Current

Model-simulated tidal currents at the locations R1, R2 and R3 are depicted in Fig. 5. The range of current magnitude is more (0.1–1.7 m/s) at R3 location. Also, the variations of spring and neap tidal currents are very clear at this location. Spring tide during new or full moon has highest magnitude 1.7 m/s, and neap tide varies 0.1–1 m/s during the month of December. At R2 location, the range of current is less in compare to R3 location and it varies within the range 0.01–0.9 m/s. The range of tidal current variation in less in R1 location, and it varies from 0.3 to 0.7 m/s.

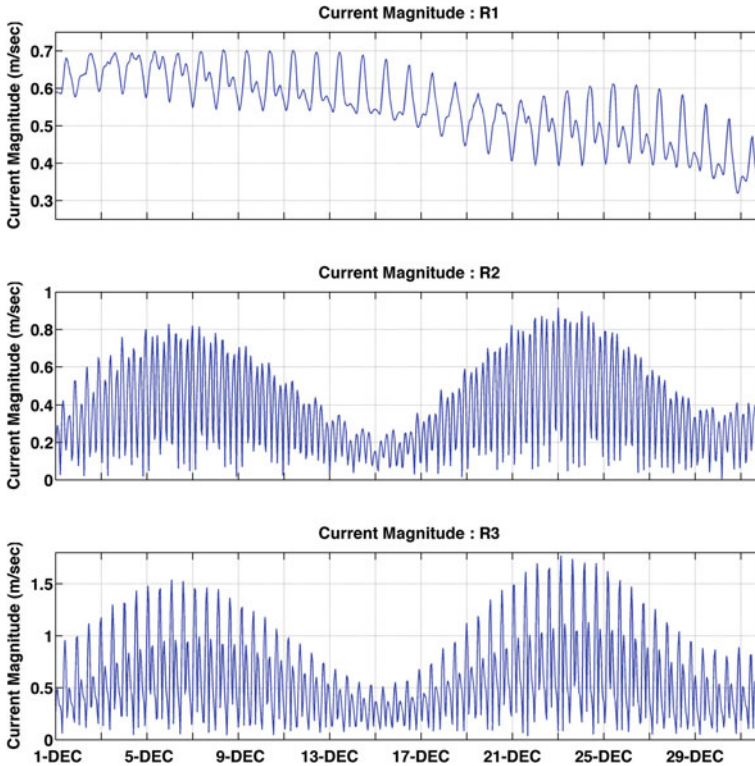


**Fig. 5** ROMS-simulated tidal current magnitude at R1 (Paradeep) in upper panel, R2 (Head BoB) in middle panel and R3 (Gulf of Martaban) in lower panel. The x-ticks are for zero hours of the corresponding dates. Location depicted in Fig. 1

It is important to note that in every six hours, current direction changes at R2 and R3 locations (figure not shown). First 6 h of a day tidal current propagates towards the head bay, and next six hours, it propagates southwards. This is due to the geometrical configuration of the coastline and shallow bathymetry in the region of head BoB and the Gulf of Martaban.

## 4 Conclusions

A 3D ocean circulation model is developed for the simulation of tidal currents over the Bay of Bengal. The model is forced with climatologically varying air–sea fluxes from COADS along with ten major tidal constituents (K2, N2, S2, M2, P1, O1, K1, Q1, Mm and Mf) from TOPEX/POSEIDON global tidal model (TPXO7). The model well captured the sea-level variation as validated against the existing tide gauge

observation data near Paradeep location. The co-range chart for the tidal components M2, N2, S2 and K1 form the model-simulated SSH over BoB are analysed, which are reasonably well matched with earlier studies. Semi-diurnal tidal constituents S2, N2 and M2 are amplified near the head BoB and Gulf of Martaban. The tidal current at R3 (on Gulf of Martaban) showed variation of its direction in every 6 h. The simulated tidal currents in this region showed the magnitude of around 1.5 m/s. However, wide validation and analysis are needed for this simulation which will be carried out in future. Study on the temperature and salinity variations in those regions will also be carried out. This study resulted the currents in the head bay and the Gulf of Martaban are tidal driven, which is important for storm surge cases [11, 12].

**Acknowledgements** We would like to acknowledge the financial assistance from Science and Engineering Research Board (SERB), Department of Science and Technology (DST), Government of India and the infrastructural support from the IIT Bhubaneswar. We are grateful to INCOIS for providing the tide gauge data.

## References

1. Murty TS, Henry RF (1983) Tides in the Bay of Bengal. *J Geophys Res* 88(C10):6069. <https://doi.org/10.1029/JC088iC10p06069>
2. Sindhu B, Unnikrishnan AS (2013) Characteristics of tides in the Bay of Bengal. *Mar Geod* 36(4):377–407. <https://doi.org/10.1080/01490419.2013.781088>
3. Rose L, Bhaskaran PK (2017) Tidal asymmetry and characteristics of tides at the head of the Bay of Bengal. *Q J Royal Meteorol Soc*. <https://doi.org/10.1002/qj.3122>
4. Ray RD, Mitchum GT (1997) Surface manifestation of internal tides in the deep ocean: observations from altimetry and island gauges. *Prog Oceanogr* 40(1–4):135–162. [https://doi.org/10.1016/S0079-6611\(97\)00025-6](https://doi.org/10.1016/S0079-6611(97)00025-6)
5. Anderson OB (1999) Shallow water tides in the northwest European shelf region from TOPEX/POSEIDON altimetry. *J Geophys Res* 104(C4):7729–7741. <https://doi.org/10.1029/1998JC900112>
6. Shchepetkin AF, McWilliams JC (2005) The regional oceanic modelling system (ROMS): a split-explicit, free-surface, topography-following-coordinate oceanic model. *Ocean Model* 9(4):347–404. <https://doi.org/10.1016/j.ocemod.2004.08.002>
7. Dey D, Sil S, Jana S, Pramanik S, Pandey PC (2017) An assessment of TropFlux and NCEP air-sea fluxes on ROMS simulations over the Bay of Bengal region. *Dynam Atmos Ocean* 80:47–61. <https://doi.org/10.1016/j.dynatmoce.2017.09.002>
8. Locarnini RA, Mishonov AV, Antonov JI, Boyer TP, Garcia HE, Baranova OK, Seidov D (2013) World ocean atlas 2013, vol 1: Temperature. In: Levitus S (ed), Mishonov A (Technical Ed.) NOAA Atlas NESDIS 73:40. <https://doi.org/10.1182/blood-2011-06-357442>
9. Zweng MM, Reagan JR, Antonov JI, Mishonov AV, Boyer TP, Garcia HE, Bidlle MM (2013) World ocean atlas 2013, vol 2: Salinity. NOAA Atlas NESDIS 2(1):39. <https://doi.org/10.1182/blood-2011-06-357442>
10. Pawlowicz R, Beardsley B, Lentz S (2002) Classical tidal harmonic analysis including error estimates in MATLAB using T\_TIDE. *Comput Geosci* 28(8):929–937
11. Sinha PC, Rao YR, Dube SK, Murty TS (1997) Effect of sea level rise on tidal circulation in the hooghly estuary, Bay of Bengal. *Mar Geod* 20(4):341–366. <https://doi.org/10.1080/01490419709388114>

12. Sinha PC, Jain I, Bhardwaj N, Rao AD, Dube SK (2008) Numerical modeling of tide-surge interaction along Orissa coast of India. *Nat Hazards* 45(3):413–427

**Part V**  
**Marine Foundations**



# Vertical Pull-Out Capacity of Torpedo Anchors



S. Keerthi Raaj , R. Sundaravadivelu and Nilanjan Saha

**Abstract** In recent years, the novel concept of dynamically installed anchors like torpedo-shaped anchors has a significant development in offshore gas exploration and platform construction. Torpedo anchors are those which breach to the designated embedment depth by the kinetic energy acquired in the process of free fall and develop vertical as well as horizontal pull-out resistances. The large scale of uncertainties in pull-out capacity theoretical prediction often requires a finite element analysis. Hence, this paper investigates the vertical pull-out resistance offered by torpedo pile anchors through numerical simulation using PLAXIS. The kaolin clay soil properties are assumed, and modified cam clay (MCC) soil model is assigned throughout the entire numerical simulation. The cylindrical-shaped torpedo pile anchor was modelled with “wished in place” configuration as zero fin, blunt tip with four different aspect ratios ( $l/d = 5, 10, 15, 30$ ), and each anchor is analysed under four different embedment depths to anchor height ratios ( $D/l = 2, 2.5, 3, 3.5$ ). The effects of embedment ratio and aspect ratio and their influence on the anchoring capacity were studied, and the numerical results are validated through the established empirical results. The pull-out capacities of the anchors are further studied for varying disturbed zone diameter of (1D, 2D, 3D and 4D). And hence, it is concluded that the character of the remoulded soil significantly influences the vertical pull-out resistance and the extent of remoulded soil zone due to anchor penetration is between 3D to 4D.

**Keywords** Torpedo pile anchors · Pull-out capacity · Embedment depth  
PLAXIS

## 1 Introduction

The demands for underwater fossil fuel exploration are exponentially increasing from olden times, which created the need for developing a new kind of anchoring system for deep offshore drilling platform construction. Schmid [1] stated that ocean floor is

---

S. Keerthi Raaj (✉) · R. Sundaravadivelu · N. Saha  
Indian Institute of Technology, Chennai, India  
e-mail: [mskraaj44@gmail.com](mailto:mskraaj44@gmail.com)

© Springer Nature Singapore Pte Ltd. 2019  
K. Murali et al. (eds.), *Proceedings of the Fourth International Conference in Ocean Engineering (ICOE2018)*, Lecture Notes in Civil Engineering 22,  
[https://doi.org/10.1007/978-981-13-3119-0\\_56](https://doi.org/10.1007/978-981-13-3119-0_56)

one of the last unexplored frontiers on earth and the activity of man on the ocean floor will increase quickly and enormously. And this statement is made truthful during the last five decades of man's interest in deep-sea studies. In the early twenty-first century, Medeiros [2] successfully performed the novel concept of torpedo pile anchors with the field test conducted by a Brazilian Petroleum Corporation *Petróleo—Brasileiro* (Petrobras). Torpedo anchors are called so not only as their shape is alike to a torpedo or a dart but also because of the kinetic energy obtained through a free fall released from a designated height to penetrate the target depth below the ocean floor. The height of free fall is predetermined to achieve the target penetration depth. Thus, the obtained kinetic energy from self-weight and free fall is spent in the process of penetration deep into the soft ocean floor.

In marine geotechnical design perspective, the prediction of anchor pull-out capacity and embedment depth is key challenges [3]. Since the vast scale of uncertainties exists in pull-out capacity, theoretical prediction often requires a finite element analysis. In this paper, holding capacity of torpedo pile anchors subjected to tensile loading test is performed using finite element analysis and validated to the established theoretical results. In the real field scenario, the torpedo pile anchor suffers from inclined loading, which could be resolved into vertical and horizontal components. O'Loughlin et al. [4] and Lieng et al. [5] illustrate that torpedo pile anchor has enough horizontal capacity and most of the anchor failures are due to low load when the anchor is subjected to pure vertical loading. And so, in this study, torpedo pile anchors are subjected to pure vertical tensile loading. The benefit of this study are, (i) the effect of embedment depth and aspect ratio of torpedo pile anchor on pull-out capacity, (ii) the effect of remoulded zoned due to anchor penetration on vertical pull-out capacity, is studied.

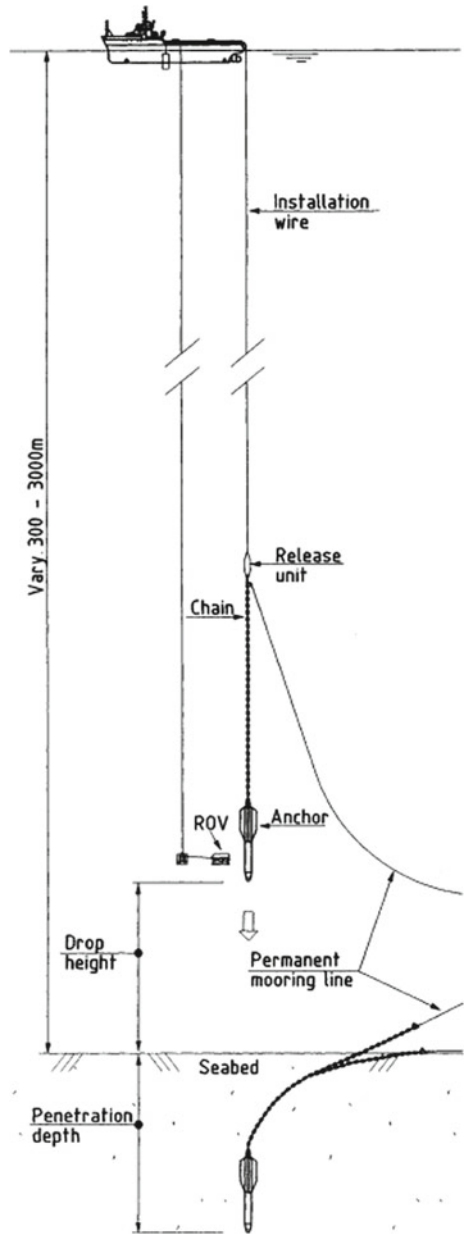
A series of vertical pull-out simulation and the theoretical prediction was conducted for various embedment ratios and aspect ratios. The diameter of the torpedo pile was kept constant ( $d = 0.7$  m), and the length of the anchor was varied according to the aspect ratios ( $l/d = 5, 10, 15, 30$ ). Similarly, the embedment depth for every individual aspect ratio (pile length) was varied ( $D/l = 2, 2.5, 3, 3.5$ ), and the pull-out capacity was calculated. Though the aspect ratio of  $l/d = 30$  and embedment ratio of  $D/l = 3.5$  are unrealistic in the field, a comprehensive study has been conducted.

## 2 Origin and Installation of Torpedo Anchors

Torpedo pile anchors are evolved from penetrometers. Initially, in late 1960s, penetrometers are used in the estimation of offshore sub-surface stratigraphy and ocean floor sediment strength determination [6–8] and later used in the ballistic studies and nuclear waste disposal, military application and extra-terrestrial exploration [8–10]. In the early twenty-first century, Lieng and Medeiros [2, 5] made use of these penetrometers in sub-seabed as a new concept for anchoring floaters. Since deep-sea pile driving is relatively expensive and requires large barges for operational field works, the traditional method of pile driving for anchoring is wearily time-consuming and uneconomical.

Lieng et al. [5] noted that in traditional anchoring system, cost increases with water depth, whereas in case of torpedo anchor due to simple installation procedure with no external driving source made them too economical anchoring system mainly for mobile offshore drilling units, floating production storage and offloading system

**Fig. 1** Installation procedure of torpedo anchor. After Lieng et al. [5]



(FPSOs) and flexible risers. Figure 1 shows the schematic arrangement for torpedo anchor installation. Temporary installation wires are used for holding the releasing unit and torpedo anchor pile, where the initial anchor is attached to both permanent and temporary installation cables. After reaching pre-calculated releasing height, ROV is used for releasing the anchor from temporary installation cable, but the permanent cable is connected to anchor loosely. Then, the anchor falls freely and penetrates the ocean floor. Finally, the loosely connected permanent installation wire is tightened and moored to the structure to be anchored.

### 3 Anchor Geometry and Soil Properties

A typical torpedo pile anchor consists of a central cylindrical shaft and may have stabilizing fins around the shaft. The lateral 3–4 stiffeners fins provide directional stability during free fall and penetration of the anchor in the seabed, whereas the central cylindrical shaft consists of hollow steel tube usually filled with scrap material or concrete fill to increase self-weight. The typical shapes and properties of a torpedo pile anchor are shown in Fig. 2 and Table 1.

Soh et al. [11] studied the hydrodynamic behaviour of torpedo anchors and concluded that drag effect is most sensitive towards change in aspect ratio ( $l/d$ ) which is nearly 50% in comparison with other parameters. O’Loughlin et al. [4] studied the fluke geometries of dynamic anchors and summarized that geometry aspect of torpedo anchors is noteworthy. Importance of pull-out resistance is considered in this investigation. Hence, the nose shape does not influence the vertical pull-out estimation, so the nose shape is configured as blunt. One of the important observations from the literature review on torpedo anchor is that increase in a number of flukes

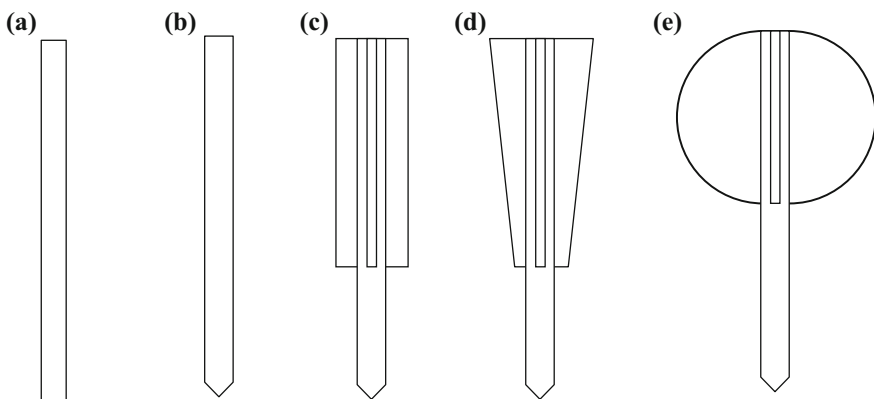


**Fig. 2** a Finless blunt nose, b finless conical nose, c uniform fin width conical nose, d varying fin width—conical nose, e ellipsoidal fin width—conical nose (nose shape may be blunt, conical and ellipsoidal)

decreases the actual embedment depth due to more frictional drag effect, and so for, a simple case finless anchor is accounted. The cylindrical-shaped torpedo pile anchor was modelled with “wished in place” configuration as zero fin, blunt tip with four different aspect ratios ( $l/d = 5, 10, 15, 30$ ), and each anchor is analysed under four different embedment depths to anchor height ratios ( $D/l = 2, 2.5, 3, 3.5$ ). Table 2 shows the pre-calculated “design basis” embedment depth for different aspect ratios and different embedment ratio combinations.

Wang et al. [12] attempted to study the penetration behaviour of torpedo anchor in cohesive soil by free fall and concluded that soil characters like grain size, effective stress history greatly influence the undrained shear strength and bearing capacity factors of cohesive soil. The behaviour of underwater sea sediments is mostly similar to kaolin clay soils, so, the geotechnical properties of kaolin clay are accounted as given by O’Loughlin et al. [4] used in laboratory test of a reduced scale model of torpedo piles (1:200) performance in centrifuge test. The geotechnical properties of kaolin clay soil are tabulated in Table 3. In general, the strength of soil is appropriated by the undrained shear strength which is represented as  $S_u = (n_1 + n_2x)$ , where  $x$  is the depth of which  $S_u$  to be estimated,  $n_1 = 0$  implies shear strength at free surface is zero, and  $n_2 = 1.15$  represents the shear strength gradient of kaolin clay. Moreover, the shear strength of the soil increases linearly with depth from the mud line level.

**Table 1** Typical properties of a torpedo pile anchor

Length	10–17 m
Diameter	0.4–1.2 m
Dry weight	24–1500 kN
Penetration depth	2–3 times of anchor length ( $l$ )
Dropping height	30–150 m
Impact velocity	20 m/s to 30 m/s
Number of fins	3–4
Fluke height and lateral length	Varies
Pad eye location	Top of anchor (generally)
Anticipated anchor capacity	3–5 times the dry anchor weight

**Table 2** Embedment depth for different aspect ratios and embedment ratio combinations

Diameter $d$ (m)	Anchor height $l$ (m)	Aspect ratio $l/d$	Embedment depth $D$ (m)			
			$D/l=2$	$D/l=2.5$	$D/l=3$	$D/l=3.5$
0.7	3.5	5	7	8.75	10.5	12.25
0.7	7	10	14	17.5	21	24.5
0.7	10.5	15	21	26.25	31.5	36.8
0.7	21	30	42	52.5	63	73.5

**Table 3** Geotechnical properties of kaolin clay (data after O'Loughlin et al. [16])

Liquid limit, LL (%)	61
Plastic limit, PL (%)	27
Plastic index, $I_p$ (%)	34
Specific gravity, $G$	2.6
Angle of internal friction, $\varphi$ (degrees)	23
Void ratio at $p' = 1$ kPa on critical state line, $e_{cs}$	2.14
Slope of normal consolidation line, $\lambda$	0.205
Slope of swell line, $\kappa$	0.044
Strength ratio, $S_u/\sigma'_v$	0.19
Coefficient of vertical consolidation, $C_v$ (m <sup>2</sup> /year)	4.5
Sensitivity, $S_t$	2.5–3

## 4 Pull-Out Capacity

The pull-out resistances are mainly due to the anchor submerged weight in the soil, reverse end bearing and side adhesion developed along soil-structure interaction as represented in Fig. 3. In the case of marine sediments, the consistency of the deposit is between very soft to medium stiff. Due to this, the reverse end bearing is too small and negligible in comparison with anchor submerged weight and side adhesion. In this study, the effect of reverse end bearing is neglected. The effect of the inclination of the anchor during installation on holding capacity influences predominately; in this analysis, the effect of initial anchor inclination is ignored and considered as perfectly straight [13, 14]. Added, neglecting the installation effects, the pile is modelled as “wished in place” in numerical simulation, which means with the initial state of stress in the soil equal to the in situ state of stress as before anchor installation [2, 5].

### 4.1 Theoretical Prediction

The theoretical pull-out capacity of a torpedo anchor is estimated similarly as for uplift capacity of tension piles. The vertical capacity of torpedo anchor pile was predicted using API's guidelines [15]. According to API's guidelines, pull-out capacity  $F_v$  is the sum of the submerged weight of anchor  $W'_s$ , side frictional resistance  $F_f$  and reverse bearing resistance  $F_b$ .

$$F_v = W'_s + F_f + F_b \quad (1)$$

$F_v$  Ultimate pull-out Capacity

$W'_s$  Submerged weight of anchor in soil

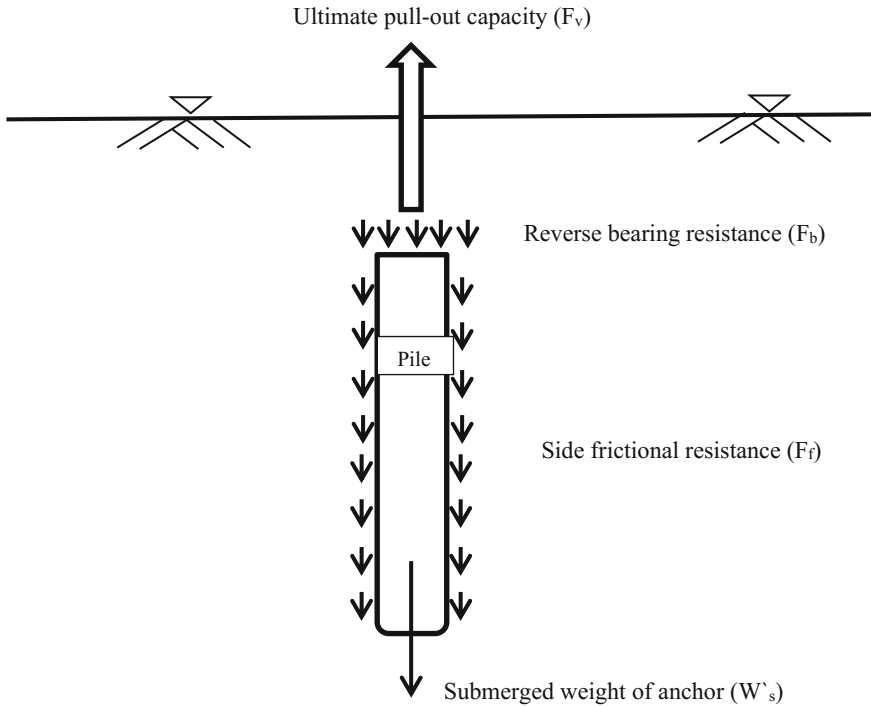


**Fig. 3** Force acting on finless torpedo pile during pull-out

$F_f$  Frictional resistance along anchor shank and fluke wall

$F_b$  Reverse bearing resistance @ top and bottom of shank

$$F_f = \alpha S_u A_s \tag{2}$$

$$\alpha = 0.5 \left( \frac{S_u}{\sigma'_v} \right)^{-0.5} \quad \text{when} \quad \left( \frac{S_u}{\sigma'_v} \right) \leq 1 \tag{3}$$

$$\alpha = 0.5 \left( \frac{S_u}{\sigma'_v} \right)^{-0.25} \quad \text{when} \quad \left( \frac{S_u}{\sigma'_v} \right) > 1 \tag{4}$$

where  $\alpha$  is the friction ratio which accounts varying shear strength along the pile length and introduces average resistance force,  $S_u$  is the undrained shear strength,  $A_s$  is the surface area of anchor, and  $\sigma'_v$  is the effective vertical stress.

$$F_b = N_c S_u A_p \tag{5}$$

where  $N_c$  is the bearing capacity factor and  $A_p$  is the bearing area of the anchor.

Figure 4 shows the theoretical prediction of vertical pull-out capacity concerning the aspect ratio and embedment ratio. It could be observed that there is a monotonous increase of vertical pull-out capacity with an increase in both aspect ratio and embedment ratio. As the embedment ratio for a particular aspect ratio increases, then the vertical pull-out capacity increases and vice versa. Hence, it is so obvious that aspect ratio and embedment ratio have the significant effect on the vertical pull-out capacity of a torpedo anchor.

### 4.2 Numerical Prediction

For analysing the pull-out capacity of torpedo pile anchors, tremendous uncertainty exists, and hence, often analysing using finite element method is essential. PLAXIS-2D was utilized for the numerical simulation, and the input parameters for modelling the kaolin clay and torpedo pile anchor are shown in Tables 3 and 4. The horizontal boundary of the simulation is set to 10 times the anchor diameter, and the vertical limit is set to sum of embedment depth, anchor length and 0.5 times the anchor length below the pile tip (to minimize the boundary effect). The vertical pull-out effect in kaolin clay has been modelled as an axis-symmetric problem. The kaolin clay soil properties are used after O’loughlin et al. [16] and Modified Cam Clay (MCC) soil model is assigned for kaolin clay throughout the entire numerical simulation. The linear elastic model was used to characterize the torpedo pile behaviour. The bottom boundary is made rigid, where the lateral boundaries are made fixed in the x-direction and free in the y-direction. The water boundary conditions are given as consolidated water boundary in the lateral directions, where in the top and bottom direction, water

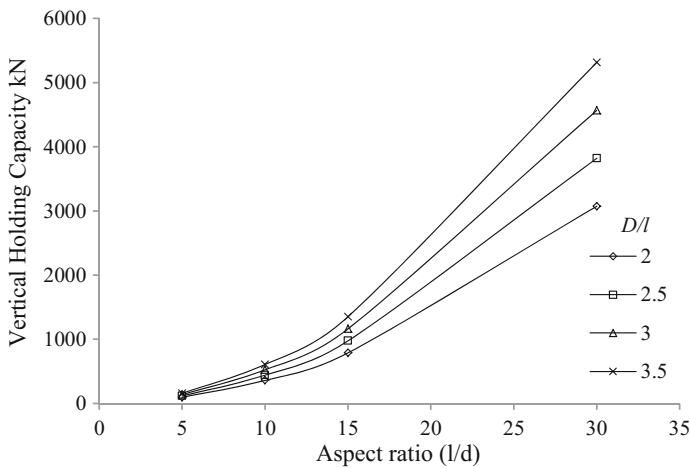


Fig. 4 Theoretical prediction of vertical pull-out capacity



**Table 4** Torpedo pile anchor model properties

Model type	Linear elastic
Drainage type	Non-porous
Unit weight of anchor	25 kPa
Modulus of elasticity	260000 kPa
Poisson's ratio	0.33

is allowed to flow. The coarseness of the mesh is set to fine, and the typical PLAXIS generated mesh is shown in Fig. 5a, b.

One of the greatest advantages of using finite element programs is a simulation of the real field working condition scenario. Thus, in PLAXIS, installation process of torpedo anchor could be made as close as demonstrated by Lieng et al. [5], as represented in Fig. 1. In the analysis, the installation of torpedo anchor consists of

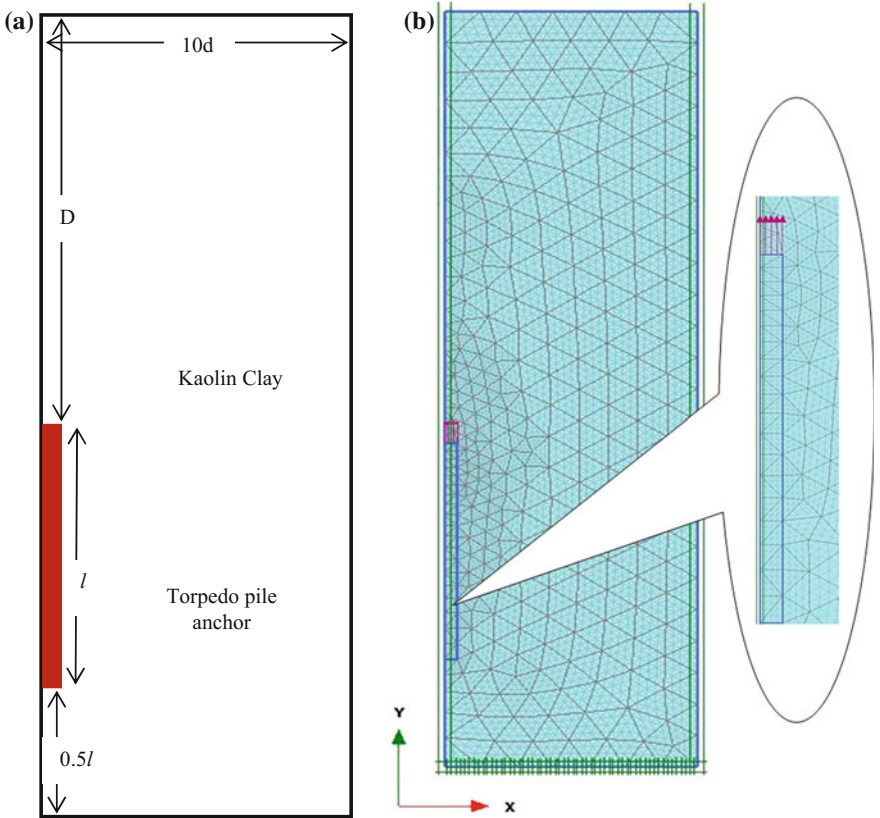


**Fig. 5** a Numerical simulation typical boundary condition, b meshing for torpedo anchor with 0.35 m radius, 7 m anchor height and 14 m embedment depth

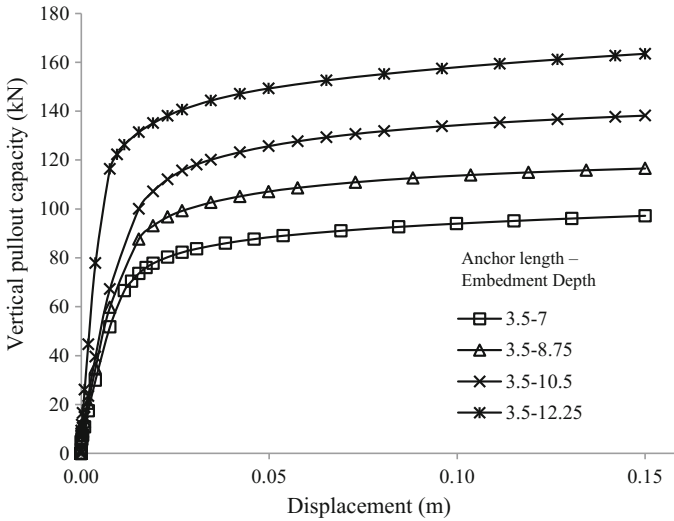
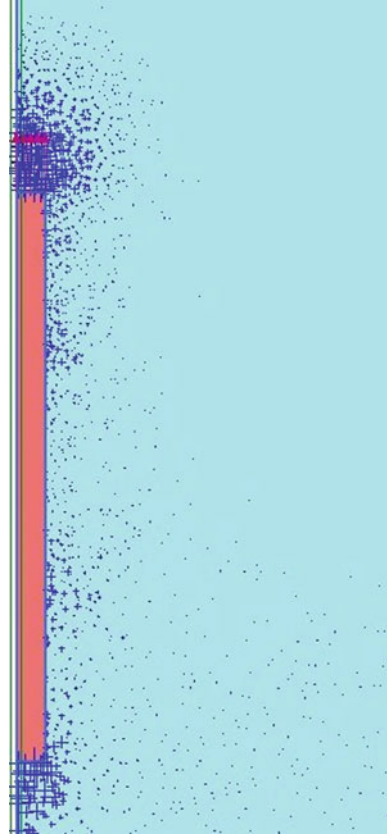


**Fig. 6** Variation of pull-out capacity with embedment depth for torpedo anchor height 3.5 m

three phases: initial phase, installation phase and pull-out phase. The initial phase consists of the in situ soil condition without any structural members and loading conditions. Followed by the second phase, neglecting the installation effect, the pile is modelled as “wished in place”, which means with the initial state of stress in the soil equal to the in situ state of stress as before anchor installation. So, the developed excess pore pressure is made less than 1 kPa. Finally, the anchor loading is applied using prescribed displacement in an upward direction. The upward displacement is applied to the top of anchor for a total displacement of 0.15 m over a time span of 60 s [3, 17]. A displacement larger than serviceability limits would cause failure conditions, so a vertical displacement of 0.15 m represents the serviceability limit of the anchor which is considered.

A series of vertical pull-out simulation was conducted for various embedment ratios and aspect ratios. Figure 6 shows one of the typical numerical simulation results, variation of pull-out capacity for 3.5 m anchor height case with different embedment depths (7, 8.75, 10.5 and 12.25). Similarly, for every individual aspect ratio ( $D/l = 2, 2.5, 3, 3.5$ ) and embedment ratio ( $D/l = 2, 2.5, 3, 3.5$ ), the pull-out capacity was calculated numerical and discussed later in validation section. The development of excess pore pressure during anchor pull-out is observed at top and bottom as well, as shown in Fig. 7.

**Fig. 7** Excess pore pressure development due to anchor pull-out



## 5 Validation and Discussion

The PLAXIS numerical simulation results are validated by established theoretical results. Figure 8 displays the variation of pull-capacity in logarithmic scale to the embedment ratio. It can be accepted that the numerical and theoretical results are well enough in agreement, and only for the aspect ratio of  $l/d = 15$ , the trend shows the slight discrepancy. Sturm et al. [18] noticed that the monotonous increase in shear strength directly causes the achievable penetration depth to decrease monotonically. Moreover, penetration depth decreases for higher shear strength. Similarly in this investigation, monotonous increase in aspect ratio directly causes the achievable embedment ratio to increase monotonically. Added, monotonous increase in both aspect ratio and embedment ratio causes a tremendous increase in vertical pull-out resistance.

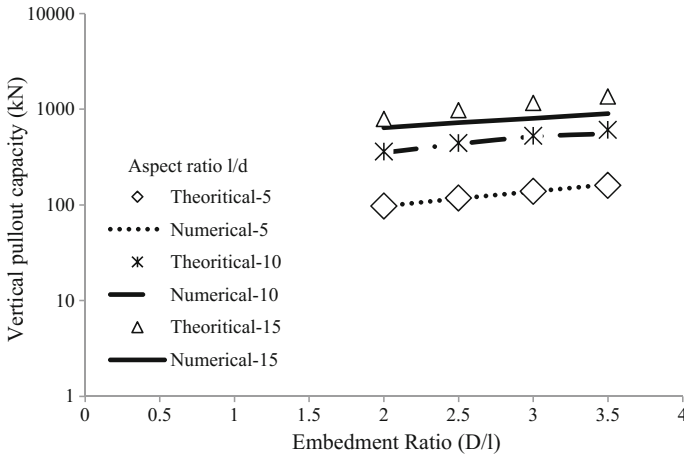


Fig. 8 Comparison of numerical and theoretical vertical pull-out capacity

### 5.1 Effect of Remoulded Soil Zone

Another important aspect of this study is the effect of the remoulded zone on the vertical pull-out capacity. Due to the torpedo anchor free fall, a tremendous amount of energy has been created, which is spent in the process of anchor penetration. Therefore, in the process of penetration, the surrounding soil vicinity is disturbed to a certain extent. This disturbed zone has decreased strength and permeability, which causes slow dissipation rate of excess pore pressure during anchor pull-out. So, the horizontal width of the remoulded zone is one of the prime aspects to be considered in the anchor installation. Hence, the pull-out capacities of the anchors are further studied for varying disturbed zone diameter of 1D, 2D, 3D and 4D, where D is the diameter of torpedo pile anchor. The typical remoulded zone extending 2D with torpedo anchor in PLAXIS finite element simulation is shown in Fig. 9. The sensitivity of the remoulded soil zone was mobilized to 1.5 times the undisturbed soil zone.

The anchor aspect ratio and embedment ratio of  $l/d = 10$  and  $D/l = 2$  are chosen for this analysis. The remoulded soil zone width is varied for this case from 1D to 4D, and the vertical pull-out capacity was estimated numerically. The estimated vertical pull-out capacity is plotted against the remoulded soil zone diameter, and it is shown in Fig. 10. It is so clear that initially with an increase in remoulded soil zone diameter, the vertical pull-out capacity falls steeply. After three times the anchor diameter, the trend follows nearly a linear path. Thus, the effect of the remoulded soil zone is significant between 1D and 3D. Beyond the 3D spacing, the effect is stabilized and the influence of the remoulded zone is constant. Pecorini and De [3] reported that due to ball penetrometer free fall simulation, higher the free fall velocity, the extent of remoulded soil zone is greater and vice versa. Added, a normalized distance of 7R

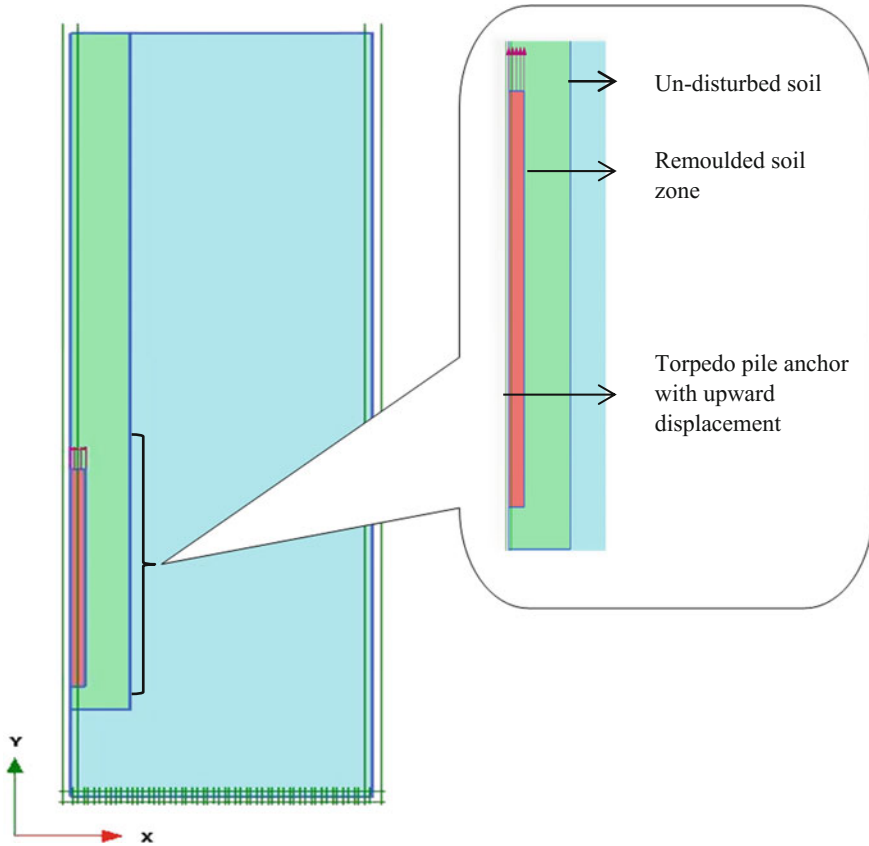
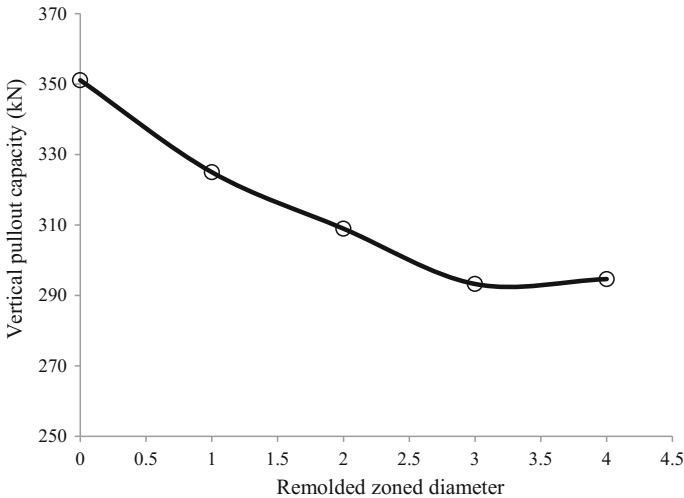


Fig. 9 Typical remoulded zone extending 2D with torpedo anchor

from the centre line was considered as remoulded soil zone in that analysis. Thus, it could be strongly agreed form this analysis that the effect of remoulded soil zone was extended from 3D to 4D.

## 6 Conclusion

A parametric study analysing the effect of the embedment depth ratio and aspect ratio of the anchor has been performed in this paper. The numerical results are validated through the established empirical results, and the extent of remoulded soil zone of torpedo pile anchor model is proposed based on the ultimate capacity. And, it is concluded that the character of the remoulded soil greatly influences the vertical pull-out resistance and the extent of remoulded soil zone due to anchor penetration is between 3D and 4D.



**Fig. 10** Vertical pull-out capacities with different remoulded zone diameters

**Acknowledgements** The authors are thankful to acknowledge the support from the Department of Ocean Engineering and Department of Civil Engineering, Indian Institute of Technology, Madras, for authorizing the work described here to occur.

## References

- Schmid WE (1969) Penetration of objects into the ocean bottom (the state of the art). Technical Report AD0695434. Naval Civil Engineering Laboratory, Port Hueneme, California
- Medeiros CJ (2002) Low cost anchor system for flexible risers in deep waters. Offshore Technology. Offshore Technology Conference, Texas U.S.A. <https://doi.org/10.4043/14151-ms>
- Pecorini, D., and De, A.: Pull-Out Capacity Analysis of Offshore Torpedo Anchors Using Finite-Element Analysis, International Society of Offshore and Polar Engineers, Hawaii, USA. ISSN 1098-6189 (2015)
- O'Loughlin CD, Randolph MF, Richardson M (2004) Experimental and theoretical studies of deep penetrating anchors. In: Offshore technology conference, Texas, USA. <https://doi.org/10.4043/16841-ms>
- Lieng JT, Hove F, Tjelta TI (1999) Deep penetrating anchor: subseabed deepwater anchor concept for floaters and other installations. In: The ninth international offshore and polar engineering conference. International Society of Offshore and Polar Engineers, Brest, France
- Beard RM (1984) Expendable Doppler penetrometer for deep ocean sediment strength measurements. Technical Report R-905. Naval Civil Engineering Laboratory, Port Hueneme, California
- Robertson RM (1965) Expendable instrumentation. In: Knopf WC, Cook HA (eds) Marine sciences instrumentation, vol 3. Plenum Press, New York, pp 99–121
- Scott RF (1970) In-place ocean soil strength by accelerometer. Proc Am Soc Civil Eng J Soil Mech Found Div 96:199–211
- Dawson PR, Chavez PF (1978) Seabed waste disposal program: one-dimensional hole-closure simulation: SAND 78-1275. Sandia National Laboratories, Albuquerque

10. Lott D, Poeckert RH (1996) Extending co-operative research: Canada, New Zealand, United States in joint effort in British Columbia to evaluate penetrometers for ground truthing acoustic classifiers for mine countermeasures. *Sea Technol* 56–61
11. Soh BP, Pao W, Al-Kayiem HH (2015) Numerical analyses for improved hydrodynamics of deep water torpedo anchor. In: *OP conference series: material science engineering*, vol 100. <https://doi.org/10.1088/1757-899x/100/1/012059>
12. Wang W, Wang X, Yu G (2016) Penetration depth of torpedo anchor in cohesive soil by free fall. *Ocean Eng* 116, 286–294. ISSN 0029-8018. <http://dx.doi.org/10.1016/j.oceaneng.2016.03.003>
13. Ehlers CJ, Young AG, Chen J (2004) Technology assessment of deepwater anchors. In: *Proceedings of 36th annual offshore technology conference*, Houston, Texas, Paper No. OTC 16840
14. Raie MS, Tassoulas JL (2009) Installation of torpedo anchors: numerical modeling. *J Geotech Geoenviron Eng* 135:1805–1813. [https://doi.org/10.1061/\(ASCE\)GT.1943-5606.0000159](https://doi.org/10.1061/(ASCE)GT.1943-5606.0000159)
15. American Petroleum Institute (2002) Recommended practice for planning, designing and constructing fixed offshore platforms—working stress design. API RP 2A-WSD, Washington D.C., USA
16. O’Loughlin, CD, Richardson MD, Randolph MF (2009) Centrifuge tests on dynamically installed anchors. ASME. In: *International conference on offshore mechanics and arctic engineering*, vol 7: Offshore geotechnics; petroleum technology, pp 391–399. <https://doi.org/10.1115/omae2009-80238>
17. Raie MS (2009a) A computational procedure for simulation of torpedo anchor installation, set-up and pull-out. Ph.D. thesis, The University of Texas at Austin
18. Sturm H, Lieng JT, Saygili G (2011) Effect of soil variability on the penetration depth of dynamically installed drop anchors. In: *Offshore technology conference*, Rio de Janeiro, Brazil. <https://doi.org/10.4043/22396-ms>

# Design of Piles for a Berthing Structure on Artificial Slope



S. V. Sivapriya, R. Sundaravadivelu and S. R. Gandhi

**Abstract** In present study, a new berthing structure is proposed for slope stable dredging activity. A slope with a weak soil structure comprising gravel, sand–silt clay, stiff silty clay, and terra firma at various depths is stabilized with ground improvement techniques. The pile makes dredging difficult for a single-slope angle. To overcome this difficulty, different slopes are recommended for different depths. This study analyses the slope stability for such a design by finite element modeling. Modeling shows that the factor of safety is  $> 1.5$  for the varied slope structure, thus proving that the design is effective in preserving the slope stable.

**Keywords** Slope stability · Static · Dredging

## 1 Introduction

Dredging activities may result in slope instability caused by factors such as saturation, swell, coupled with seepage, and pore pressure. For example, dredging of slopes comprising cohesive soil leads to negative pore pressure, which increases the short-term safety of the slope. The most important factor that influences slope stability is the slope angle; it is particularly sensitive when the slope angle is  $15^\circ$ . Soil type and vegetation are other factors that affect slope stability [1], and it is important to understand the stability of slopes during dredging activities and erection of piles.

---

S. V. Sivapriya (✉)

Department of Civil Engineering, SSN College of Engineering, Chennai 603110, India  
e-mail: [sivapriyavijay@gmail.com](mailto:sivapriyavijay@gmail.com)

R. Sundaravadivelu

Department of Ocean Engineering, Indian Institute of Technology Madras, Chennai 600042, Tamil Nadu, India

S. R. Gandhi

Department of Civil Engineering, SVNIT, Surat 395007, India

© Springer Nature Singapore Pte Ltd. 2019

K. Murali et al. (eds.), *Proceedings of the Fourth International Conference in Ocean Engineering (ICOE2018)*, Lecture Notes in Civil Engineering 22,  
[https://doi.org/10.1007/978-981-13-3119-0\\_57](https://doi.org/10.1007/978-981-13-3119-0_57)

855

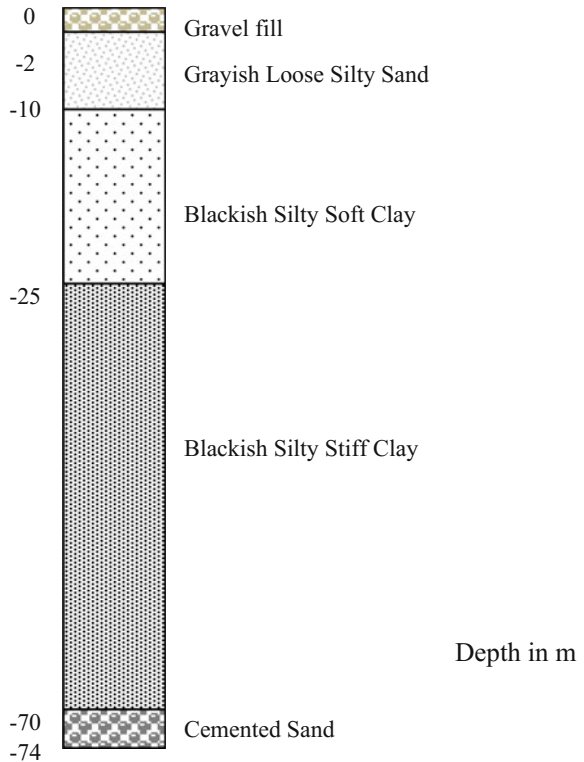


A number of stability analysis studies have been reported [2–7] which is mostly based on 2D planar strain. Hence, a 2D model is generated; the material type of the soil is not varied parallel to the slope, as is seen in reality. The present study reports several results of numerical analysis performed to understand slope stability, considering the comprehensive soil profile. The nature of slope required for stability is also assessed, and a new berthing structure is proposed.

## 2 Soil Profile and Foundation Design

An earlier borehole investigation of the test site showed that gravel comprises top 2 m of the soil surface. Below this, 25 m of the soil is silty sand–silty clay. The soil below this depth is blackish stiff silty clay, which is followed by firm strata below 70 m. Dense cemented sand follows below 70 m and until 74 m dense (Fig. 1).

Fig. 1 Borehole description



### 2.1 Design of Foundation

Figures 2 and 3 shows the typical cross section of the proposed berthing structure and dredging area. For this, 1.2 m diameter and 50 m long pile were chosen. The calculation involved axial load capacity and the uplift capacity of the pile.

#### 2.1.1 Capacity of the Pile

The worst soil condition was considered for numerical analysis. The calculation was performed according to IS 2911 [8] given in Eq. (1).

$$Q_u = Q_b + Q_f \tag{1}$$

where  $Q_u$  is the ultimate load carrying capacity of the pile,  $Q_b$  is the ultimate base resistance, and  $Q_f$  is the ultimate shaft resistance.

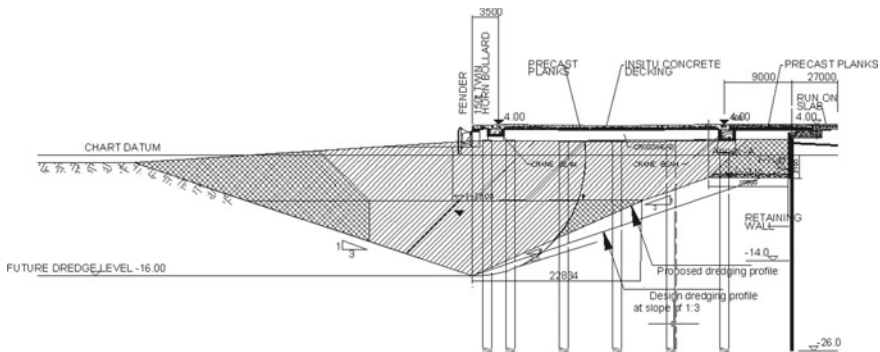


Fig. 2 Cross section of the berth with the platform

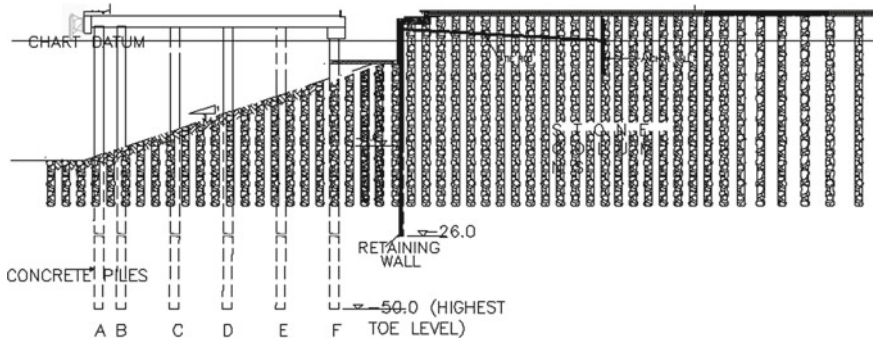


Fig. 3 Dredging between sheet pile wall and pile row

**Table 1** Different type of load values

Type	Value (kN)
Axial	17,000
Lateral	330
Uplift	6000
Drag	2770

**Table 2** Soil properties

Layer	Soil type	$c$ (kPa)	$\Phi^\circ$	$\gamma_{\text{sat}}$ (kN/m <sup>3</sup> )	$E_s$ (kPa)	$\mu$
I	Soft clay	20	2	14	15,000	0.41
II	Silty sand	2	30	18	20,000	0.32
III	Soft clay	30	3	15	15,000	0.41
IV	Cemented sand	6	38	20	50,000	0.31

The effective overburden pressure at pile toe was limited to 20 times the diameter of the pile. Due to the presence of soft clay from 10.0 to 25.0 m, the drag force was also calculated. Table 1 shows the axial, lateral, and uplift capacity along with the drag force using Eqs. (2) and (3). The ultimate axial bearing capacity of the pile is 1700 kN (with factor of safety is 2.5), and lateral capacity was taken as 5% the axial capacity.

$$Q_{\text{up}} = Q_s + W_p \quad (2)$$

$$Q_n = \frac{1}{2} L^2 k_o \gamma \delta \quad \text{Perimeter of the pile} \quad (3)$$

where  $W_p$  is the weight of the pile,  $L$ —length of the pile,  $k_o$ —earth pressure coefficient,  $\gamma$ —unit weight of the soil,  $\phi$ —angle of internal friction,  $\delta$ —coefficient of friction ( $3/4 \phi$ ),  $E_s$ —modulus of the soil, and  $\mu$ —Poisson's ratio with the soil properties as listed in Table 2.

### 3 Dredging Method

The location of the berth was initially subjected to a ground improvement technique with a stone column due to low shear strength of the soil. A slope of 1V:3H was recommended for dredging.

**Table 3** Details of dredging

Stage	Slope	Depth (m)
I	1V:0.15H	8
II	1V:0.54H	12.5
III	1V:2.5H	16

The barge was mounted between the retaining wall and the pile for the dredging process. The dredging was performed between the piles to form a slope of 1V:3H. There was difficulty during dredging and the desired slope could not be achieved. To overcome this problem, three different slopes were adopted at various depths. It was a challenge to dredge the soil for installation of the pile and to maintain stability of the slope.

The three different slopes were as follows: a slope of 1V:0.15H was proposed until a depth of 8 m (Stage I). This was followed by a slope of 1V:0.54H till 12.5 m (Stage II) and 1V:2.5H until a depth of 16 m (Stage III). The different slope dimensions with the corresponding depths are given in Table 3.

The slope was analyzed to acquire a factor of safety greater than 1.5 (US Army Corps of Engineers) to have a stable slope.

## 4 Numerical Modeling

A plane strain analysis [9] was performed, in which the piles were replaced as equivalent sheet pile wall with flexibility equal to the average thickness of the piles. This type of approach was extended [10] by connecting the sheet pile wall to the soil with the support of link elements, therefore allowing displacement of the soil and the wall, which shows more close approximation of 3D behavior around the piles. For the analysis of stabilizing piles installed at a slope, an elastic–plastic soil model was used and limiting soil pressure is exerted on the piles to allow plastic flow around the soil and piles [11].

The analysis of slope stability was performed using PLAXIS. The slope stability analysis involved three phases of calculation. The initial phase included development of geometry model, material generation, location of water table, and mesh generation. The boundary conditions were assigned as standard fixities in the bottom and rollers in the sides of the model generated. To achieve optimal safety, the model embankment was divided into a number of finite elements using fine mesh refinement option. A 15-node element was constructed. The material was modeled for *plane strain* analysis, which is a straightforward approach of finite element modeling which is ideal for representing pile configuration and geometry, without much complication. The pile and the deck were modeled with beam–column elements. Mohr–Coulomb elastic–plastic constitutive model was considered to represent the shear strength response of the various geomaterial.

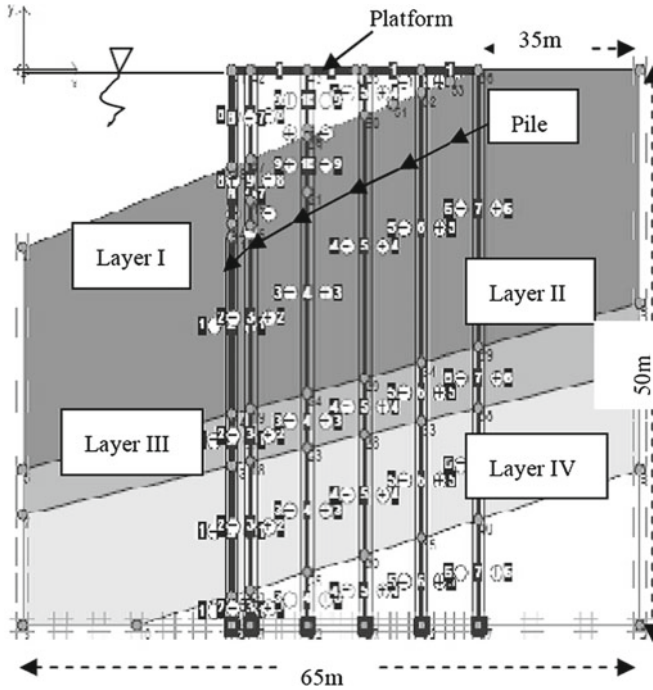


**Fig. 4** Model generated for slope of 1V:3H

The calculation involved two phases: 1. *plastic analysis* and 2.  $\Phi$ -*c reduction*. In *plastic analysis*, the in situ stresses were developed and in  $\Phi$ -*c reduction* the cohesion and tangent of the friction angle were reduced in the same proportion to calculate the global safety factor.

Initially, the proposed model was generated and analyzed for slope stability. Due to the difficulty in forming a slope of 1V:3H, three different slopes were modeled along the soil profile in the berthing area and analyzed. The value of Young's modulus was taken, considering the improvements in properties caused by the ground improvement techniques employed. Figures 4 and 5 show the model and deformed mesh for a slope of 1V:3H. The material properties of the soil platform are given in Tables 4. Slope stability analysis was carried out stepwise for the different stages.

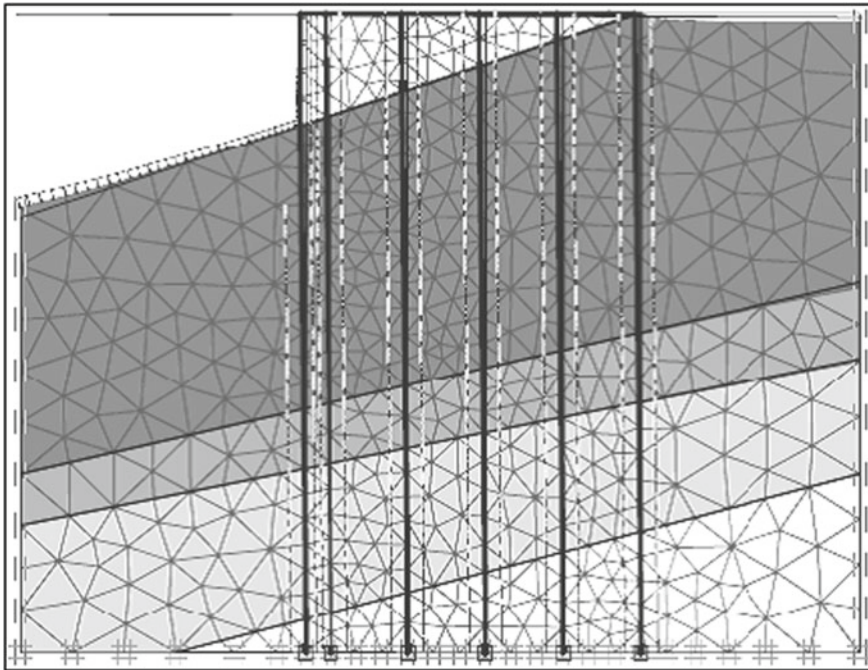


**Fig. 5** Deformed mesh after slope stability analysis for slope 1V:3H

**Table 4** Material properties of pile and platform

Material	Type	EA (kN/m)	EI (kN m <sup>2</sup> /m)	w (kPa)	$\mu$	$\alpha$ and $\beta$
Pile	Elastic	8.553e4	1.603e7	23.5	0.2	0.5
Platform	Elastic	3.346e7	3.017e6	23.5	0.2	0.5

Figures 6, 7, 8, 9, 10 and 11 show the models generated at each stage with the corresponding deformed mesh. In the calculation, the initial phase was gravity loading, where the initial stresses are applied by the overburden stress. This was followed by the plastic analysis and  $\Phi$ - $c$  reduction analysis, where the shear strength parameters such as  $\Phi$  and  $c$  of the soil were reduced for failure conditions. The factor of safety is defined as the ratio between the available strength and the strength at failure. This approach resembles the slip circle method which is conventionally used to calculate the safety factor.

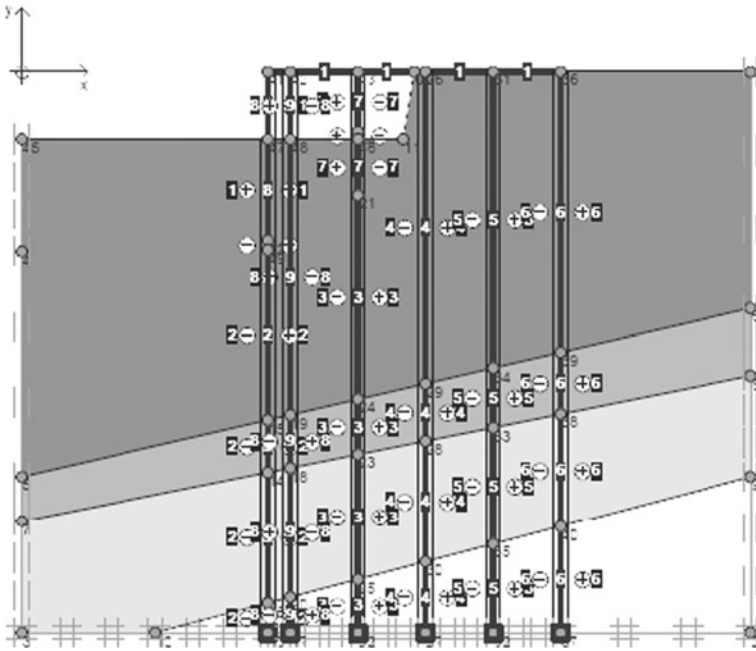


Fig. 6 Model generated for slope of 1V:0.15H—Stage I

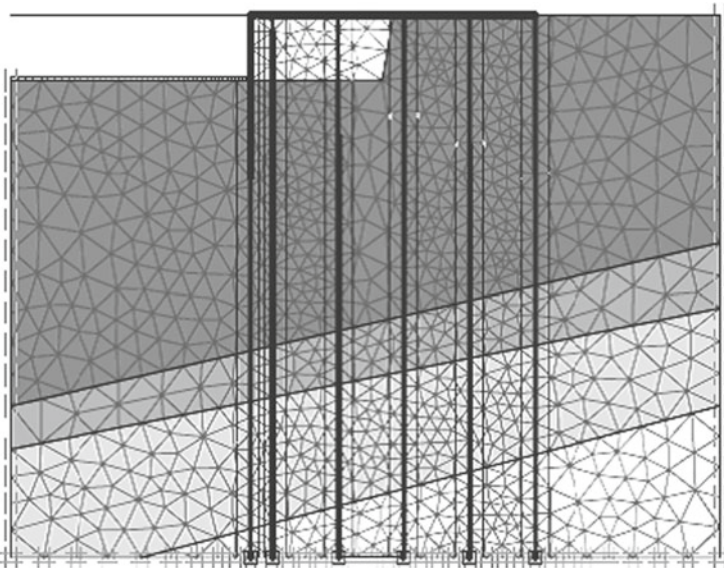


Fig. 7 Deformed mesh after slope stability analysis for slope—Stage I

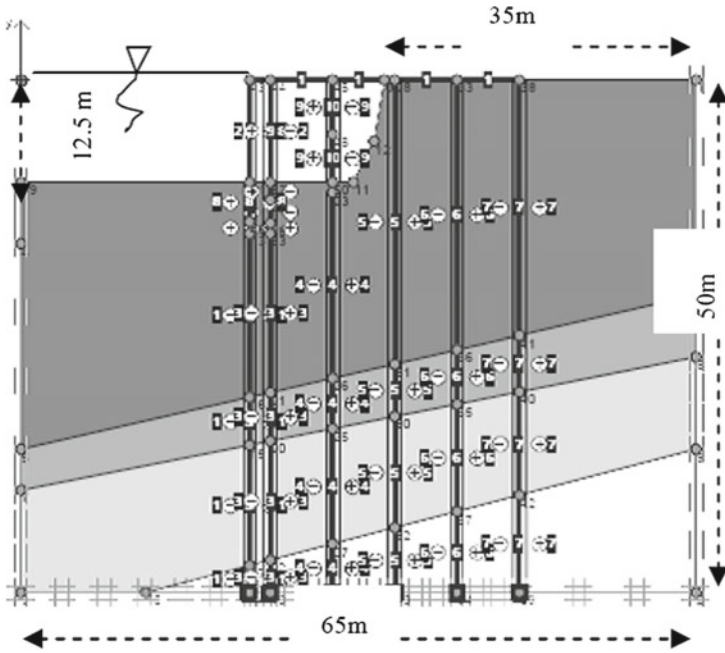


Fig. 8 Model generated for slope of 1V:0.54H—Stage II

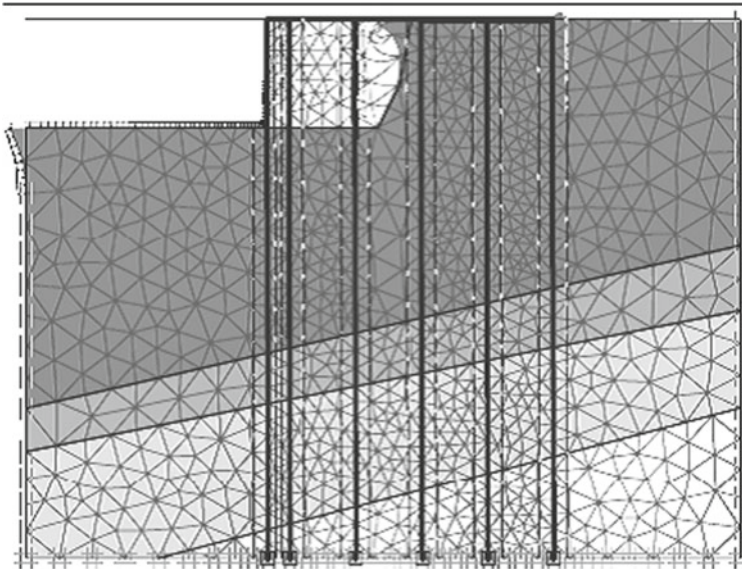


Fig. 9 Deformed mesh after slope stability analysis for slope—Stage II



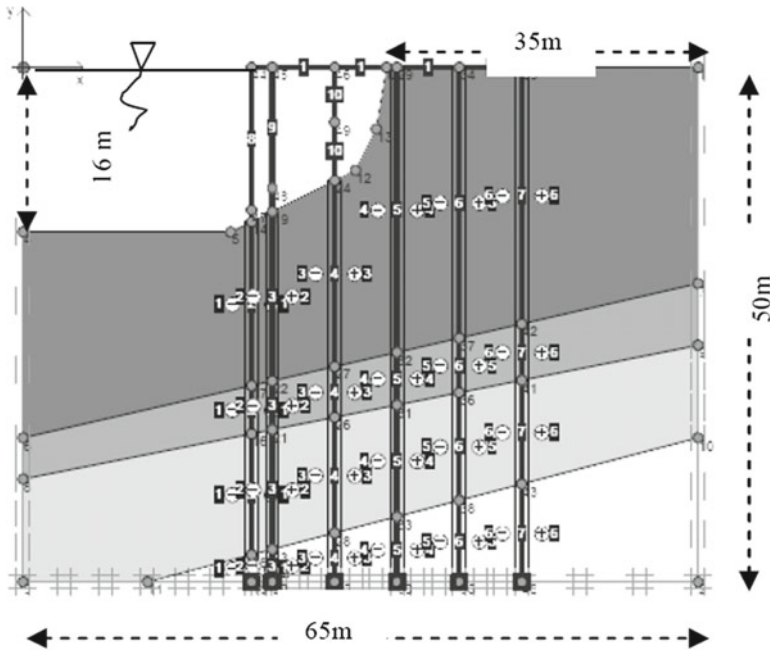


Fig. 10 Model generated for slope of 1V:2.5H—Stage III

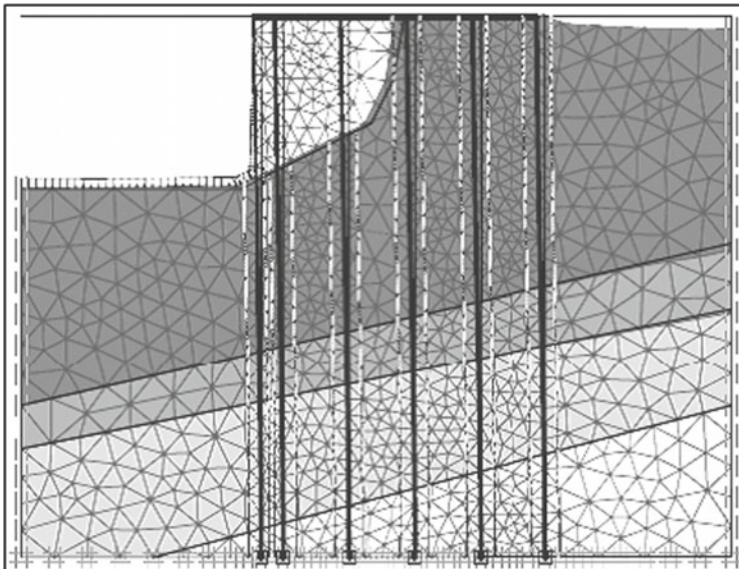


Fig. 11 Deformed mesh after slope stability analysis for slope

**Table 5** Model generated for slope of 1V:3H

Phase	Phase no	Start phase	Calculation type	Load input
Initial	0	0	Gravity loading	–
Phase-I	1	0	Plastic	Staged construction
Phase-II	2	1	<i>Ph/c Reduction</i> (safety analysis)	Incremental multipliers

**Table 6** Factor of safety after each stage

Stage	Factor of safety
I	2.865
II	2.637
III	2.514

The sequential steps followed and factor of safety obtained at each stage are given in Tables 5 and 6, respectively.

As the factor of safety was found to be greater than 1.5 after complete dredging in all three stages, the dredged slope can be considered stable against sliding.

## 5 Conclusion

Soil movement during dredging causes an increase in soil volume, and hence, pore pressure becomes negative; which makes the slope stable for short term. The geometry and the nature of the slope determine the short-term or long-term factor slope stability. If the factor of safety is greater than 1.5, it is ensured that the slope is stable for a long term.

Finite element modeling was used to study the stability of a slope on which piles are installed, using the soil profile from the site. The area of installation was initially treated with a stone column, as the virgin soil posses poor shear strength. Piles were installed to the desired depth (–50.0 m), but it was difficult to attain the desired slope. Hence, finite element analysis was performed to find the desired slope for dredging without compromising slope stability. A non-uniform slope structure was recommended to ensure stability of the slope.

Three different slopes 1V:0.15H, 1V:0.54H, and 1V:2.5H slope were recomended from the ground level until a depth of –8.0, –12.5, and –16.0 m, respectively. The analysis resulted in a factor of safety greater than 1.5, ensuring the stability of the slope against failure.

## References

1. Roth RA (1983) Factors affecting landslide-susceptibility in San Mateo Country, California. *Bull Assoc Eng Geol* 20(4):353–372
2. Bishop AW (1955) The use of the slip circle in the stability analysis of slopes. *Geotechnique* 5:7–17
3. Fredlund DG, Krahn J, Pufahl DE (1980) The relationship between limit equilibrium slope stability methods. In: *Proceedings of the 10th international conference on soil mechanics and foundation engineering*, vol 3, pp 409–416
4. Janbu N (1973) *Slope stability computations-Embankment dam engineering*, Casagrande memorial Volume. Wiley, New York, pp 47–86
5. Lowe J, Karafiath L (1960) Stability of earth dams upon drawdown. In: *Proceedings of the first pan-American conference on soil mechanics and foundations*, vol 2, pp 537–552
6. Morgenstern NR, Price VE (1965) The stability of general slip surfaces. *Geotechnique* 15:79–93
7. Spencer E (1967) A method of analysis of embankment assuming parallel inter-slice forces. *Geotechnique* 17:11–26
8. IS 2911 Part 1-sec 2 1979-Reaffirmed (2002) *Code of practice for design and construction of pile foundations*. Bureau of Indian Standards, New Delhi
9. Randolph MF (1981) *Pilot study of lateral loading of piles due to movement caused by embankment loading*. Report for the Department of Transport, Cambridge University
10. Naylor DJ (1982) *Finite element study of embankment loading on piles*. Report for the Department of Transport, Department of Civil Engineering, University College of Swansea
11. Rowe RK, Poulos HG (1979) A method for predicting the effect of piles on slope behaviour. In: *Proceedings of 3rd international conference on numerical method in geomechanics*, Balkema, Aachen

# Numerical Study of the Behaviour of Pipe Sheet Pile Wall and Diaphragm Wall in Vertical Face Berthing Structure



P. Kavitha and R. Sundaravadivelu

**Abstract** Port and harbour structures are constructed along with the coast to provide berthing facilities to ships for loading and unloading of cargo or for embarking and disembarking passengers. Soil found in coastal areas is generally soft marine clay or loose sand. Such kind of soil has very low shear strength. Pile foundations are adopted in these areas in order to bypass the weak shear layers. Vertical face-type berthing structures are preferred if the soil has enough strength and the earth pressure on the vertical wall can be efficiently shared by piles. This type of structure is constructed using pile sheet pile wall instead of diaphragm wall. If mooring force is applied on the structure, active soil pressure which is acting on the wall is increased and it becomes critical. The purpose of this study is to compare the behaviour of pipe sheet pile wall and diaphragm wall on seaside using PLAXIS 3D.

**Keywords** Berthing structure · Pile foundation · Dredging depth  
Soil–structure interaction

## 1 Introduction

Piles and wall of a vertical face berthing structure on coastal soils are subjected to axial and lateral loads. Pile foundations are used to transfer loads from surface to lower level of soil and sometimes used to control the movement of earth. Lateral forces are significantly applied on pile supporting structures such as quays, jetties, wharfs, offshore structures and tall structures. Predominant lateral forces are wind and earth pressure in the case of land structures. Wind, currents, waves, berthing load, mooring load, lateral earth pressure are primary forces in coastal and offshore structures. As a result of siltation or dredging, unstable slope is formed, and it will

---

P. Kavitha (✉) · R. Sundaravadivelu  
Indian Institute of Technology Madras, Chennai 600042, Tamil Nadu, India  
e-mail: [gcekavitha@yahoo.co.in](mailto:gcekavitha@yahoo.co.in)

R. Sundaravadivelu  
e-mail: [rsun@iitm.ac.in](mailto:rsun@iitm.ac.in)

© Springer Nature Singapore Pte Ltd. 2019  
K. Murali et al. (eds.), *Proceedings of the Fourth International Conference in Ocean Engineering (ICOE2018)*, Lecture Notes in Civil Engineering 22,  
[https://doi.org/10.1007/978-981-13-3119-0\\_58](https://doi.org/10.1007/978-981-13-3119-0_58)

cause lateral earth pressure. It leads to lateral movements of structural elements. To study the behaviour, either the theory of subgrade reaction [1] or the theory of elasticity [2] is used. The subgrade reaction approach is modified by introducing p-y curves [3]. Budhu et al. [4] analysed the laterally loaded pile, to account for soil non linearity, elastic solutions are modified using the yield factors. Pile behaviour under lateral load will have nonlinearity in nature. Thus, nonlinear analysis is needed. The following factors are considered for the behaviour of pile, i.e. characteristic of soil, pile stiffness and conditions of loading. This paper compares the behaviour of pipe sheet pile wall-supported berthing structure and diaphragm wall-supported berthing structure under dredging.

## 2 Nomenclature

$\gamma_s$ —Unit weight of sand	(kN/m <sup>3</sup> )
$C$ —Cohesive strength of sand	(kN/m <sup>2</sup> )
$\nu$ —Poisson's ratio	(no unit)
$\phi$ —Angle of friction	(°)
$U_x$ —Displacement in horizontal direction	(mm)
$E_s$ —Young's modulus of sand	(kN/m <sup>2</sup> )
$D$ —Pile diameter/diaphragm wall width	(m)
$E_p$ —Elastic modulus of pile	(kN/m <sup>2</sup> )
$I_p$ —Moment of inertia of pile	(m <sup>4</sup> )
$y$ —Displacement of vertical wall	(m)
$D_d$ —Depth of dredging at each phase	(m)
$D_t$ —Total dredging depth	(m)

## 3 Details of Berthing Structure

Berthing structure width is 24 m. This structure is assembled with vertical face wall and four rows of 1.25 m diameter piles, spacing 6 m centre to centre. The height of vertical face wall and piles are 30 m. Mean sea level is +5 m. The level of ground is required to be dredged up to -15 m for accommodating the vessel. Two types of berthing structure in sandy soil are considered for the analysis. The dimensions of diaphragm wall and pipe sheet pile (PSP) wall are chosen by equating the moment of inertia of diaphragm wall and PSP wall. Types of case are listed below.

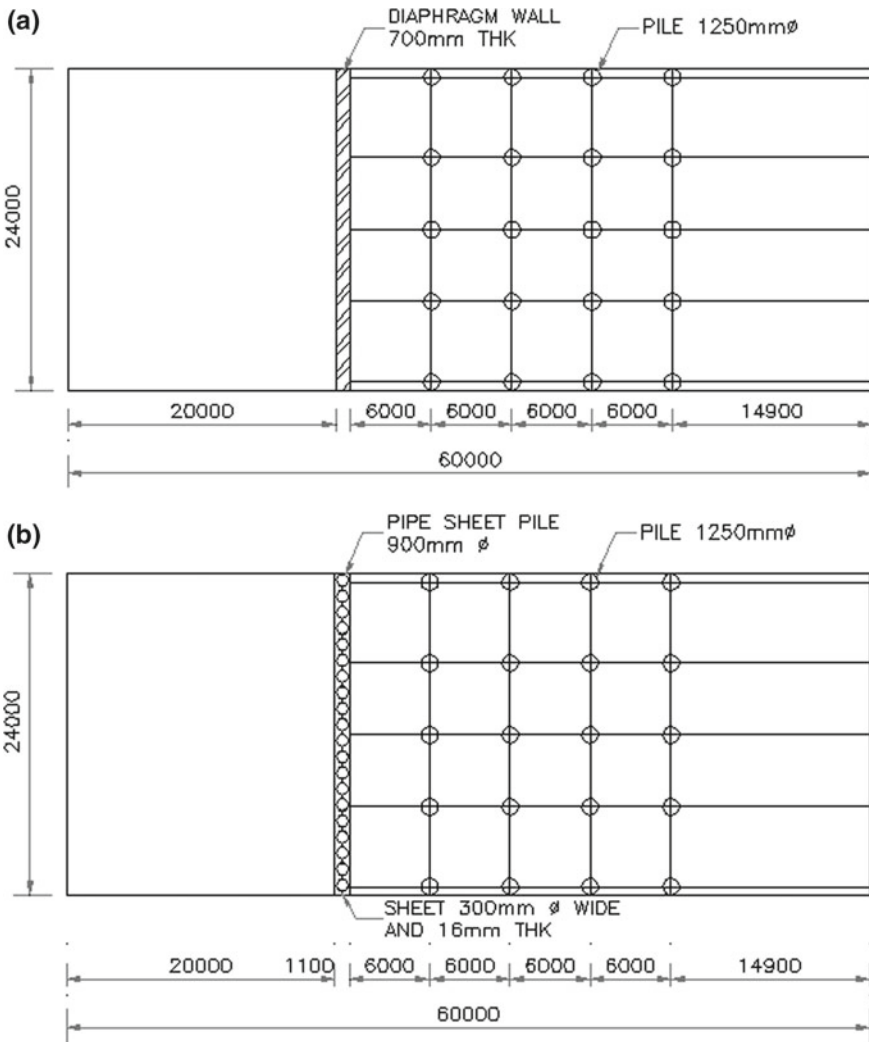


Fig. 1 a Plan of diaphragm wall berthing structure. b Plan of pipe sheet pile wall berthing structure

Case I Diaphragm wall is modelled as vertical face (Fig. 1a).

Case II Pipe sheet pile wall is modelled as vertical face (Fig. 1b).

Diaphragm wall having 0.7 m thickness is modelled in case I, and in case II, 0.9 m diameter of piles are connected by steel sheet which has 300 mm width and 16 mm thick.

## 4 Numerical Modelling—Plaxis 3D Model

Finite element software Plaxis 3D is used for numerical modelling. This tool is used to simulate geotechnical problems. It has inbuilt soil models, beam, plate elements, embedded beam, anchors and geo-grid elements.

### 4.1 Soil Models

Soil stratigraphy is formed in soil mode by giving borehole details (Fig. 2). Mohr—Coulomb model is used for the present analysis. It is considered as a first-order approximation of soil behaviour. This model requires five basic input parameters, namely density, Young's modulus, Poisson's ratio, friction angle and cohesion of soil.

### 4.2 Structural Elements and Boundary Conditions

Structural elements such as plate, beam, anchor, embedded pile, geo-grid and boundary conditions can be defined in structures mode in Plaxis. An embedded pile is

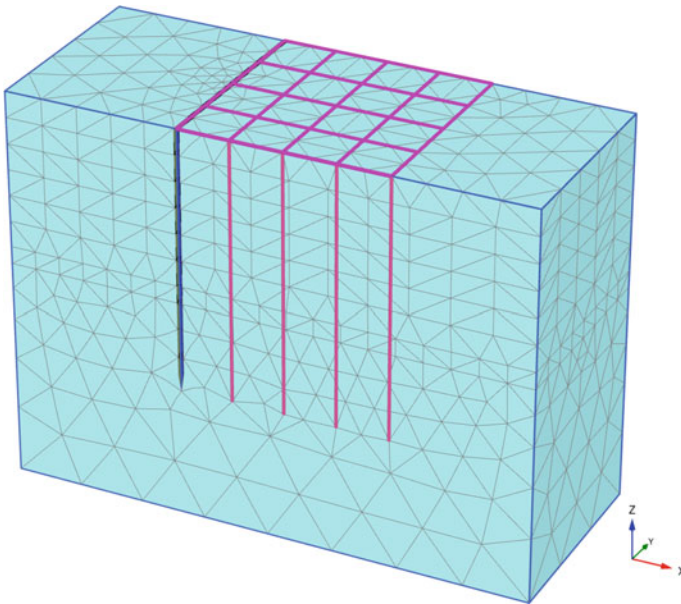


Fig. 2 Three-dimensional finite element mesh of the model

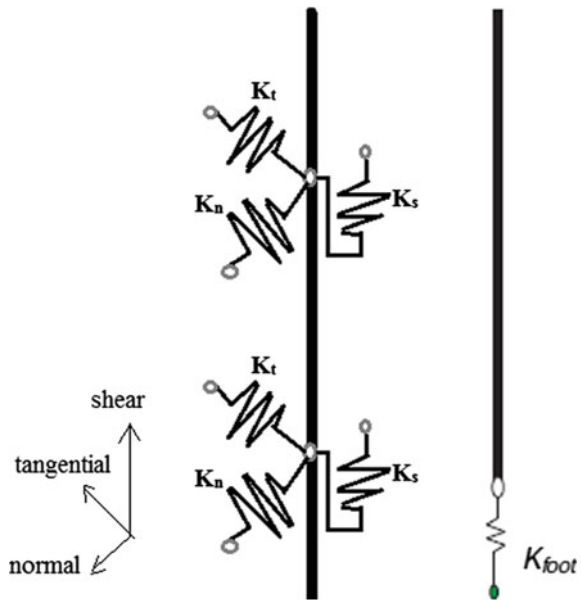
created in the subsoil, and it interacts with the surrounding soil by means of skin resistance and foot resistance. The support condition of pile like free, hinges and fixed can be defined. The beam elements are defined to model one-dimensional structures with bending and axial stiffness (Fig. 3).

Plate element is used to model two-dimensional structures with bending stiffness. Structures such as diaphragm wall and retaining wall are defined as plate element. Plaxis automatically imposes a set of boundary conditions to the geometry model.

### 4.3 Description of Model

The soil domain of dense sand is generated in Plaxis 3D. The length, width and depth of soil domain are 60, 24 and 45 m, respectively. It accommodates vertical wall, group of piles and top beam which is used to connect the top of piles and wall. Total excavation depth is 20 m and is carried out in seven phases. The pile displacement profile at each phase is obtained from the output of Plaxis. Pile-soil interaction is studied through these values.

Fig. 3 Stiffness at skin and foot of the interface element in pile





#### 4.4 Generation of Mesh

The soil–structure model is divided into elements for performing finite element calculations. An arrangement of finite element is called a mesh. Mesh generation process considers the soil stratigraphy, all structural elements, loads and boundary conditions. Mesh is adequately fine to get precise numerical results. Or else, very fine meshes should be avoided since it will take to excessive calculation time. Global coarseness is refined into five levels: very coarse, coarse, medium, fine and very fine. Six node triangular elements are used to mesh the diaphragm wall. It has six-degree of freedom per node. Three node special elements are used for embedded pile.

#### 4.5 Stages of Calculation

In this numerical modelling, the calculation is carried out in two stages: initial condition and plastic condition. In initial condition, initial stresses are influenced by weight of soil and previous history of soil. It is generated by using  $K_0$  procedure. At the end of this analysis, the entire soil mass is activated. In plastic condition, the elastic–plastic deformation analysis is carried out according to the small deformation theory. This calculation does not account the time effects. This type of calculation is more suitable for practical geotechnical applications.

### 5 Material Parameters

The parameter used in Mohr–Coulomb model for the analysis is shown in Table 1, and the material properties are shown in Table 2.

**Table 1** Properties of soil

Parameter	Unit	Dense sand
Young's modulus	kN/m <sup>2</sup>	48,000
Density	kN/m <sup>3</sup>	20
Poisson's ratio	No unit	0.2
Angle of friction	°	30
Cohesive strength	kN/m <sup>2</sup>	0

**Table 2** Properties of materials used in Plaxis 3D

Parameter	Unit	Variable	
Element		Pile, diaphragm wall, top beam	Plate
Unit weight	kN/m <sup>3</sup>	25	80.5
Young's modulus	MPa	29,580	210,000
Poisson's ratio	no unit	0.33	0.3

## 6 Validation of FE Model

Through the experimental results of single pile test, the finite element model is validated. Numerical analysis of single pile subjected to lateral load in horizontal ground was done and compared with experimental result. It is also compared with the classical solutions, and thus, the validation FE model is done. It gave confidence in extending the study in Plaxis. The results have been reported previously by Kavitha et al. [5].

## 7 Results and Discussion

Soil displacement of berthing structure after 20 m dredging is shown in Fig. 4. Total displacement after 20 m dredging in two cases is given in Table 3. It shows that soil displacement is nearly equal in case I and II-type berthing structures in which vertical walls are constructed as diaphragm wall and pipe sheet pile wall, respectively. From Fig. 5, it is observed that pipe sheet pile wall (PSP wall) has lesser displacement than diaphragm wall (Dwall). Figure 6a–d shows that pile displacement in four rows in each phase of excavation. From these figures, it is known that pile displacement behind PSP wall is lesser than piles behind diaphragm wall. Pile in row 3 and row 4 has nearly equal amount of displacement. Displacement of vertical wall after each phase of excavation is shown in Fig. 7.

**Table 3** Soil displacement after 20 m dredging

Types of case	Displacement after 20 m dredging in m
Case I Diaphragm wall in sand	0.2392
Case II Pipe sheet pile wall in sand	0.2379

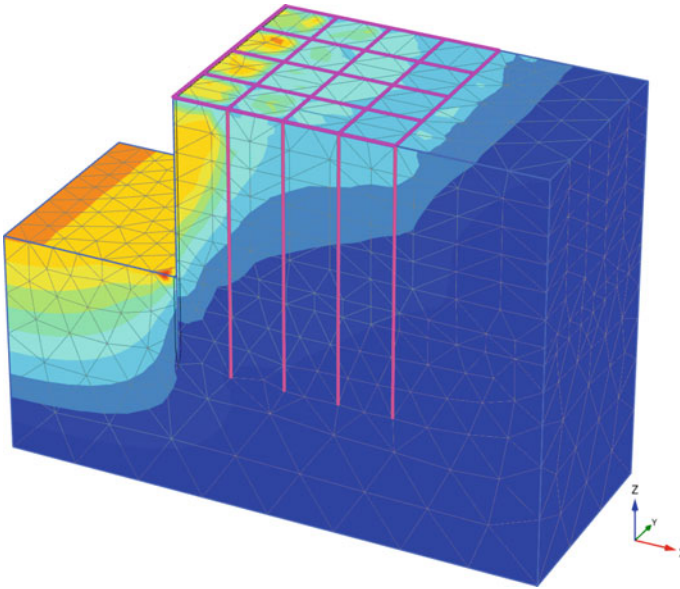


Fig. 4 Soil displacement contour

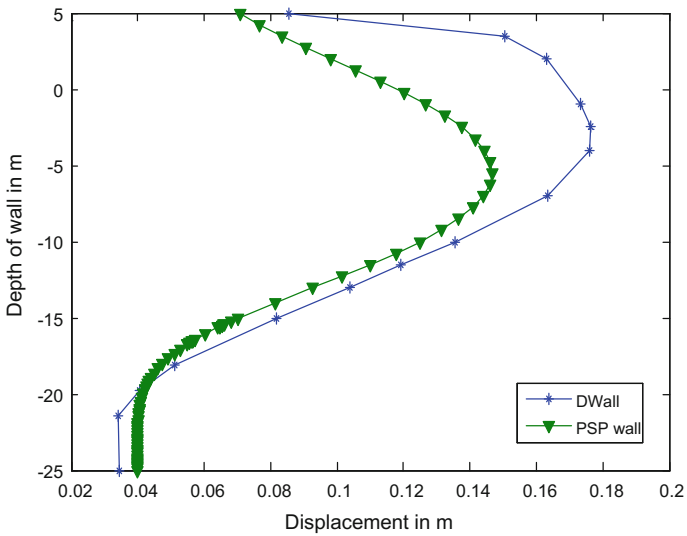
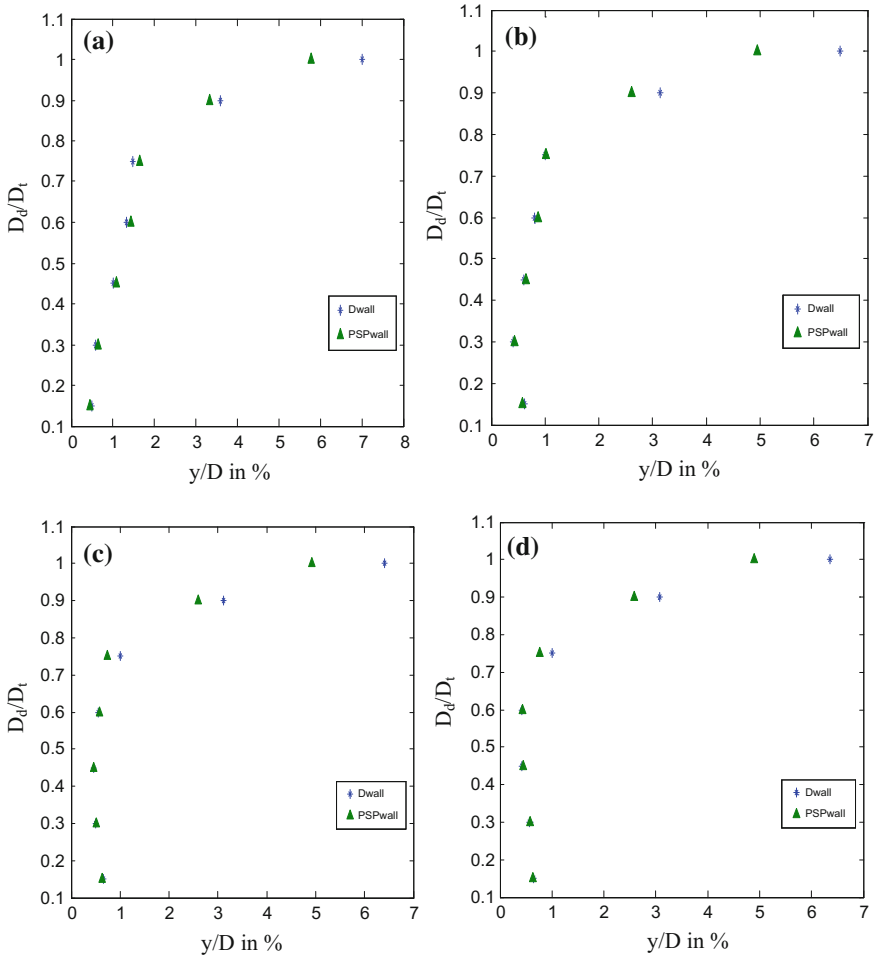


Fig. 5 Displacement of vertical wall in sand along its depth



**Fig. 6** **a** Displacement of pile in row 1 versus depth of dredging. **b** Displacement of pile in row 2 versus depth of dredging. **c** Displacement of pile in row 3 versus depth of dredging. **d** Displacement of pile in row 4 versus depth of dredging

### 8 Conclusion

This paper has been described the numerical analysis examining the response of the pipe sheet pile wall, diaphragm wall and pile-supported berthing structure under excavation. Three-dimensional finite element analysis is performed and a Mohr—

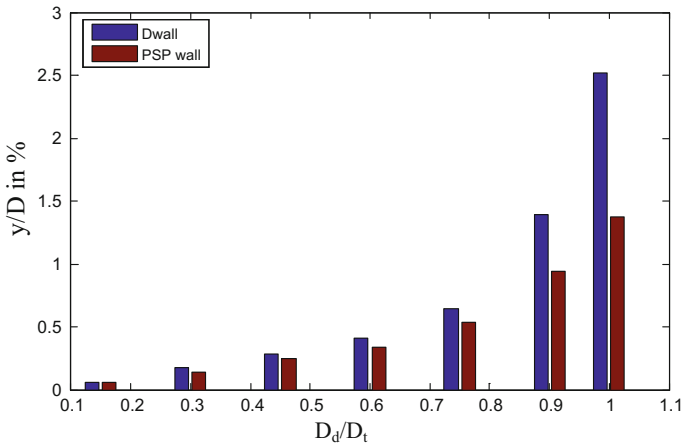


**Fig. 7** Displacement of vertical wall in sand after each phase of excavation

Coulomb model used for the soil profile. If pipe sheet pile wall is constructed as vertical wall, then the vertical wall displacement is considerably less. And also piles behind vertical wall have less displacement as compared with piles behind diaphragm wall. From these analyses, it is concluded that the lateral response of the berthing structures is reduced if pipe sheet pile wall is used as vertical wall.

## References

1. Matlock H, Ripperger EA (1956) Procedure and instrumentation for tests on a laterally loaded pile. In: Proceedings of the 8th Texas conference on soil mechanics and foundation engineering, vol 29. Bureau of Engineering Research, University of Texas, Special Publication, pp 1–39
2. Pise PJ (1984) Lateral response of free-head pile. *J Geotech Eng ASCE* 110:1805–1809
3. Matlock H (1970) Correlations for design of laterally loaded piles. In: Proceedings of 2nd Annual offshore technology, Conference, Houston, Texas, pp 577–593
4. Budhu M, Davies TG (1987) Nonlinear analysis of lateral loaded piles in cohesionless soils. *Can Geotech J* 24:289–296
5. Kavitha P, Sundaravadivelu R (2017) Soil structure interaction analysis of a berthing structure under lateral loading—by numerical approach. In: 36th international conference on ocean, Offshore & Arctic Engineering OMAE

# Field and Numerical Study of Vibration on Existing Berthing Structure Due to Pile Driving



Jeena Mary John, R. Sundaravadivelu and Nilanjan Saha

**Abstract** The tremendous inflow of goods from different parts of the world to ports in India has created an increased demand for renovation of existing berthing structure and also extension of the port. The ports have to be extended so as to harbour large number of incoming vessels. The extension will have to be near the existing berth in order to get proper connectivity to other port facilities and also to obtain the pros of site like the water depth requirement and water area protection. The new berthing structure construction involves several vibratory processes like chiselling and pile driving. These construction activities cause vibration on adjacent berthing structure which may lead to non-serviceability of those. Hence, it is essential to find that these lie much below the permissible limits. The field test was done at Tuticorin where the chiselling process was going on adjacent to an existing berthing structure. The site predominantly had weathered basalt rock, and this has to be bored using chisel before concreting. The vibration measurement was taken at the deck of adjacent existing berthing structure. This was repeated by placing instrument at various distances from pile on deck. The geophone, a vibration-measuring instrument, records vibration and peak particle velocity along all the three perpendicular directions, i.e. transverse, longitudinal and vertical directions. The vibration measurements were found to be much lesser than permissible limits, and hence, the structure is safe. The site details, pile details and pile hammer details were collected and are modelled in Plaxis to confirm that the field measurements taken were proper.

**Keywords** Pile driving · Vibration · Permissible limits  
Three-dimensional finite element analysis

---

J. M. John (✉) · R. Sundaravadivelu · N. Saha  
Department of Ocean Engineering, Indian Institute of Technology Madras,  
Chennai 600042, Tamil Nadu, India  
e-mail: [jeena9993@yahoo.com](mailto:jeena9993@yahoo.com)

© Springer Nature Singapore Pte Ltd. 2019  
K. Murali et al. (eds.), *Proceedings of the Fourth International Conference in Ocean Engineering (ICOE2018)*, Lecture Notes in Civil Engineering 22,  
[https://doi.org/10.1007/978-981-13-3119-0\\_59](https://doi.org/10.1007/978-981-13-3119-0_59)

## 1 Introduction

The extension and deepening of port and other berthing structures have increased phenomenally with the flourishing trade and commerce across the world. Due to various factors like high lateral load on berthing structure, space limitation and ease of installation, pile foundation is found suitable for deepening and extending berthing structure. Driving of pile adjacent to an existing berthing structure poses high risk to the serviceability of the structure. The machineries like conveyer belts, cranes and other cargo-handling equipment placed on berthing structure may also get damaged due to this vibration. A vibration is generated when hammer hits the pile, which will further lead to the formation of stress waves. These stress waves (of short duration) are radiated from the shaft and/or the toe of the pile and will propagate into the surrounding soil. The vibration generated from pile travels through the soil and attenuates with increase in distance. These waves transmit vibration on to the soil layers and structures that come across their path. This leads to vibration of nearby ground surface and adjacent structures both above ground and under the ground. To ensure that the adjacent structures and ground surfaces are least affected by pile driving, various techniques and measures have to be adopted to transmit the minimum amount of vibration onto them. For this purpose, a study on vibration transmitted onto existing berthing structures becomes necessary.

Finite element analysis of the soil and the existing berthing structure will serve as an effective means to study the propagation of vibration. Hence, we make use of a finite element software, Plaxis 3D AE, to study this problem. For this, pile and the surrounding soil structure are to be modelled in Plaxis 3D AE software. Further, a dynamic load that will replicate the pile-driving load is applied on the pile. The vibration induced on nearby structure due to the impact load generated from pile driving is studied for varying distances from the vibration source.

Abdel-Rahman [1] stated that characteristics of vibration generated from pile-driving vibrator is nonlinear. Massarsch and Fellenius [2] stated that ground vibrations are not directly affected by the driving energy and reducing the drop height of the hammer will decrease ground vibration. They further added that the length of the pile hammer influences the length of the stress wave. Also, ground vibrations increase with decreasing pile impedance and increasing specific soil impedance. The vibration on the structure will disturb occupants and may damage the machineries and sensitive equipment housed in the structure. Deckner et al. [3] observed that the factors having the highest impact on ground vibrations due to pile driving are the geotechnical conditions, the vibration generated at the source, the distance from the source and the installation method.

## 2 Problem Definition

The extension of the port at Tuticorin requires driving of pile just beside the existing berthing structure due to space constraints which will induce vibration on the structure. Hence, a study on vibration at critical points on the deck of existing berthing structure will be helpful in predicting the impending damage on the structure. In this case, the study is done by evaluating the propagation of vibration in terms of variation of peak particle velocity across the length of the existing berthing structure on the deck slab.

## 3 Field Study

The instrument (micromate instancel) was set up by attaching connection wire between the geophone and the recorder. The recorder is programmed based on the requirement. The geophone, a vibration-measuring instrument, records vibration (in Hz) and peak particle velocity (in mm/s) along all with the three perpendicular directions, i.e. transverse, longitudinal and vertical directions. Geophone is placed on the structure at a measured distance from the point of pile driving. The geophone is operated simultaneously to pile driving. The readings are recorded for about 3 min and are saved in the recorder. The same procedure is repeated at different points on the deck slab of the structure. The points at which geophone was placed were measured out using tape simultaneous to recording.

The site plan, pile details, hammer details and soil details were collected from the site engineer. The hammer was dropped once in 30 s. The soil properties have been given medium quality rock from Sultana [4] (Tables 1 and 2).

Figure 1 shows that all the vibrations measured at field were less than 1 mm/s. Hence, vibrations measured along all the three directions are much below the per-

**Table 1** Soil properties

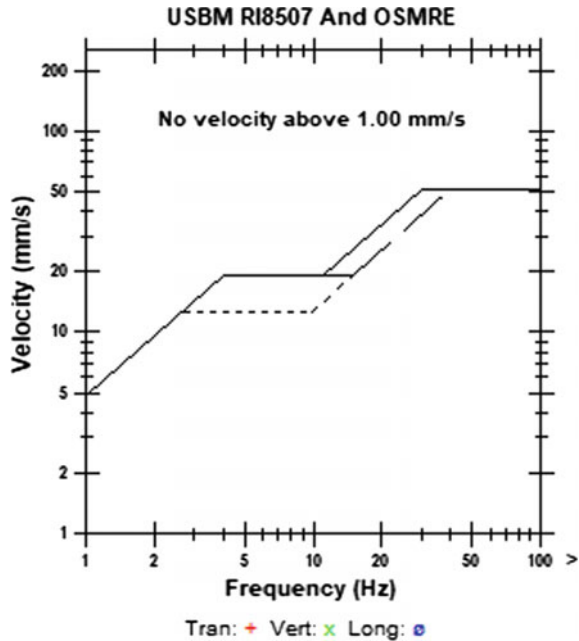
Soil type	Weathered basalt rock
Material model	Mohr–Coulomb
Drainage type	Non-porous
Unit weight $\gamma$ (kN/m <sup>3</sup> )	24
Poisson ratio	0.25
Elastic modulus $E$ (kN/m <sup>2</sup> )	$45 \times 10^6$
Cohesion $C$ (kN/m <sup>2</sup> )	3500
Internal friction $\phi$	32
Interface $R_{inter}$	0.57
Coefficient of lateral earth pressure at rest $K_0$	1



**Table 2** Field properties

Pile hammer weight	2 t
Pile hammer drop height	2 m
Rock parameter	Weathered basalt rock
Depth of water	+1.5 m
Pile diameter	750 mm

**Fig. 1** Peak particle velocity (mm/s) versus frequency of vibration (Hz)



missible limit (50 mm/s for frequency above 4 Hz) according to codal provision in BS 7385-2:1993.

Figures 2, 3 and 4 show that the peak particle velocity reduces with distance and all the readings conform to the codal provision.

### 4 Numerical Modelling of Problem

A finite element study was done to study the effect of pile driving on existing berthing structure. A three-dimensional finite element software, namely Plaxis 3D AE, was used to study the vibration at various positions on the floor slab of adjacent berthing structure. The soil layer is idealized with ten-noded tetrahedral element with three degrees of freedom per node. The soil was modelled using Mohr–Coulomb model. The steel liner is modelled by means of the linear elastic model with non-porous

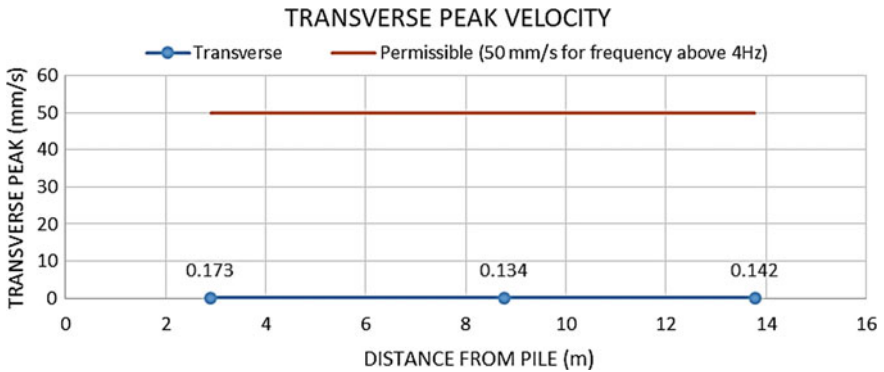


Fig. 2 PPV in transverse direction (mm/s) versus distance from pile (m)

behaviour. The interface elements that lie between the steel liner and soil were placed at a metre into the soil layer. A steel liner is driven into the soil using hammer weighing 2 tonne falling over a height of 2 m. The forcing function is selected from Mabsout and Tassoulus [5] and is applied at the head of steel liner. The forcing function was chosen so as to replicate the hammer drop. Since the frequency of both hammer drop and forcing function were same, this could suit the model well. The forcing function was reduced to 0.15 times function based on impact energy calculation. The dynamic time step of 0.001 s was used to study the structural response due to driving of steel liner. Standard viscous boundary conditions were used at bottom and all sides to avoid spurious reflection of waves from the boundary. The bottom is given an additional boundary condition by giving surface groundwater flow boundary condition as seepage throughout bottom boundary (Fig. 5).

The model is then meshed with medium coarseness. The structure along with soil medium and pile is analysed in two phases, namely initial phase and dynamic phase.

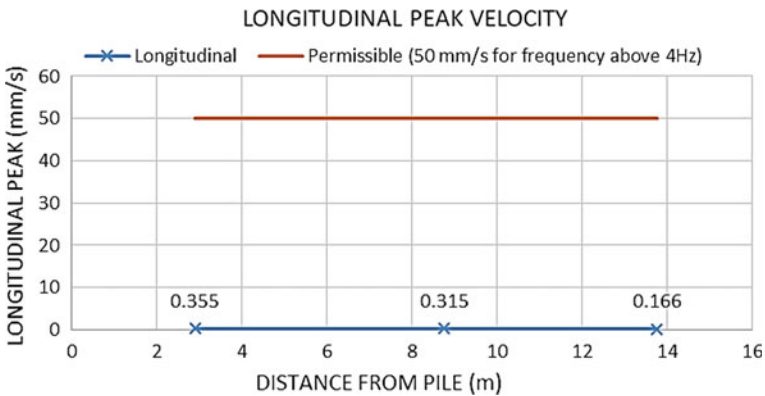


Fig. 3 PPV in longitudinal direction (mm/s) versus distance from pile (m)

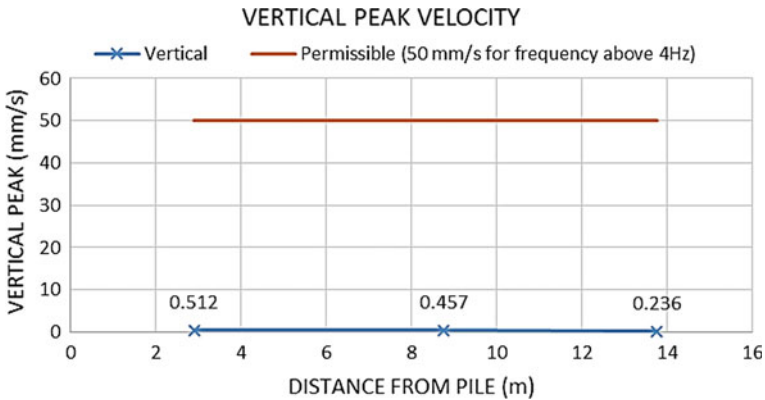


Fig. 4 PPV in vertical direction (mm/s) versus distance from pile (m)

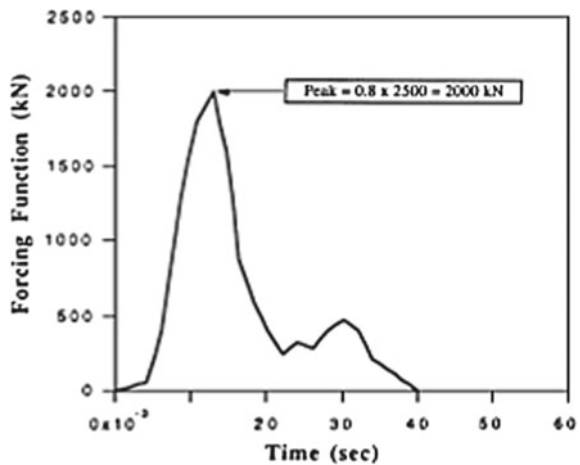
In initial phase, the soil and the berthing structure are analysed. Further, the steel liner with dynamic load is analysed in dynamic phase. After analysis, the result is viewed in the output window (Figs. 6, 7 and 8).

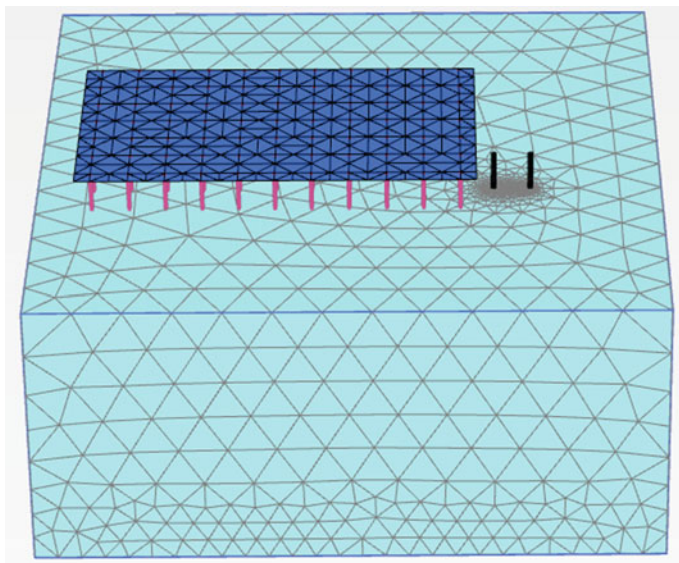
The graph is plotted for variation of velocity across the length of the berthing structure; i.e. the transverse point  $x$  is kept constant and velocity at various points along the longitudinal axis is recorded and studied.

The graphs are plotted for varying  $y$  coordinate, keeping  $x$  and  $z$  coordinate constant ( $x = 11.62, z = 1.4$ ).

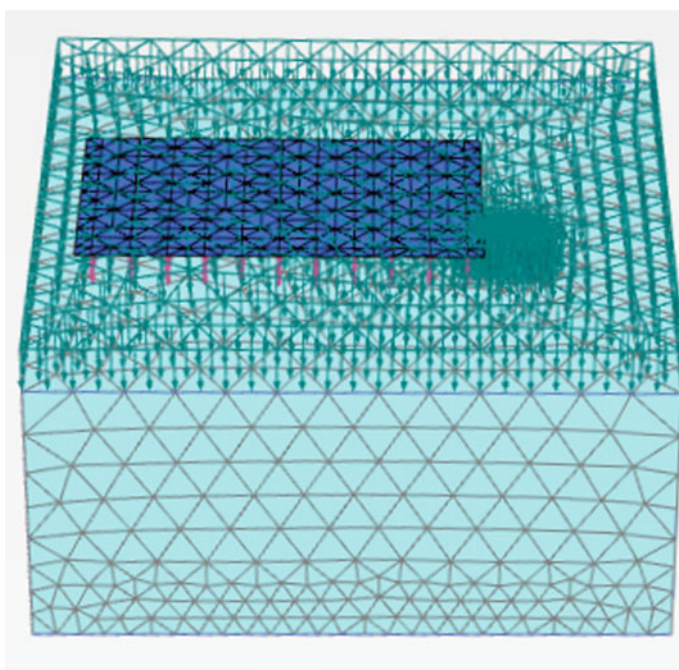
Figures 9 and 10 show that the transverse and longitudinal peak particle velocity reduces as we move away from source of vibration. The pile was driven at 23 m away from the origin, and the velocity decreases on moving away from pile. Figure 11 shows that the vertical peak particle velocity is almost a constant with slightly a

Fig. 5 Forcing function simulating a hammer blow on pile head (from Mabsout [5])





**Fig. 6** Model is meshed for medium coarseness



**Fig. 7** Model at the end of initial phase analysis

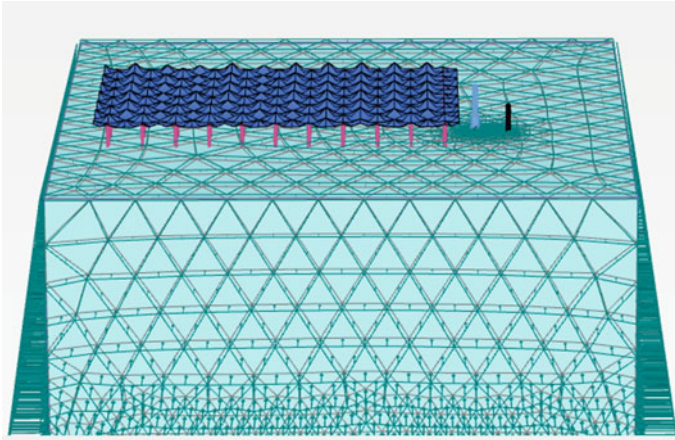


**Fig. 8** Deformed model at the end of dynamic phase analysis

higher peak at points near pile driving. All the three velocities satisfy the codal provision, i.e. no velocity exceeded 50 mm/s.

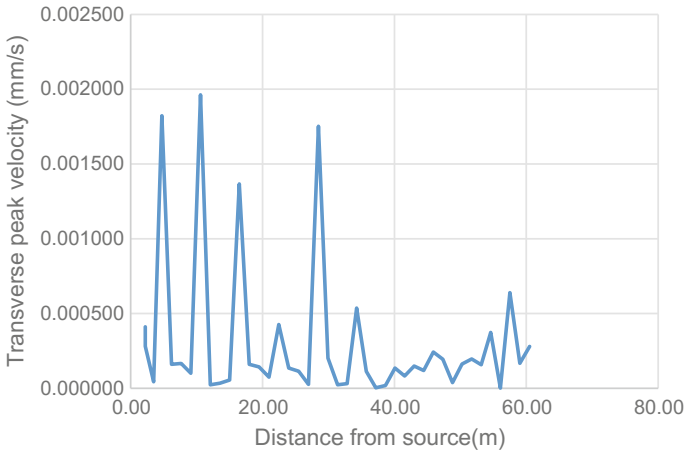


**Fig. 9** Distance across length (m) versus transverse velocity (mm/s)

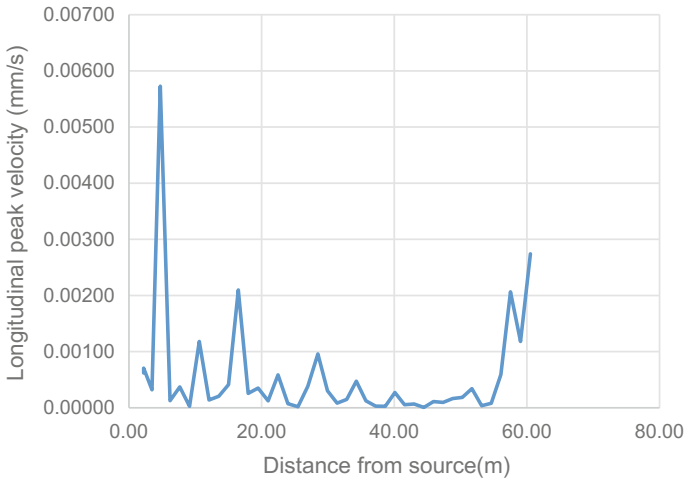


Fig. 10 Distance across length (m) versus longitudinal velocity (mm/s)

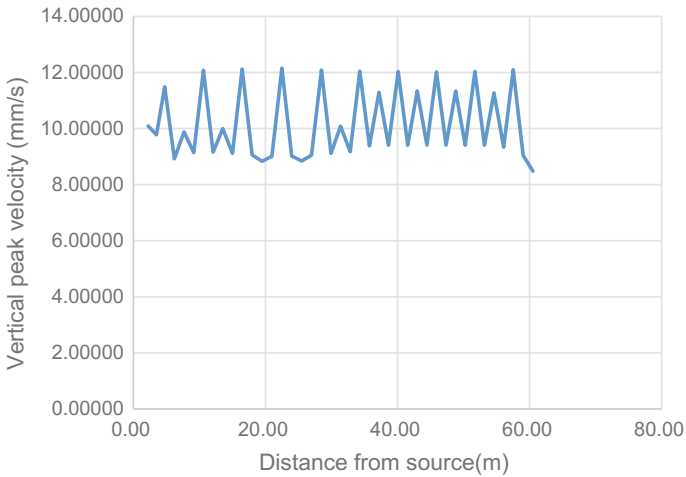


Fig. 11 Distance across length (m) versus vertical velocity (mm/s)

### 5 Codal Provision from BS 7385-2:1993 [6]

Table 3 and Fig. 12 explain the vibration limits for reinforced and unreinforced structures based on BS 7385-2:1993. In our case, since the structure is reinforced the vibration limit is 50 mm/s for all vibrations above 4 Hz.

**Table 3** Transient vibration guide values for cosmetic damage (from BS 7385-2: [6])

Line (see Fig)	Type of building	Peak component particle velocity in frequency range of predominant pulse	
		4–15 Hz	15 Hz and above
1	Reinforced or framed structures Industrial and heavy commercial buildings	50 mm/s at 4 Hz and above	
2	Unreinforced or light-framed structures residential or light commercial-type buildings	15 mm/s at 4 Hz increasing to 20 mm/s at 15 Hz	20 mm/s at 15 Hz increasing to 50 mm/s at 40 Hz and above

Note 1 Values referred to are at the base of the building

Note 2 For line 2, at frequencies below 4 Hz, a maximum displacement of 0.6 mm (zero to peak) should not be exceeded

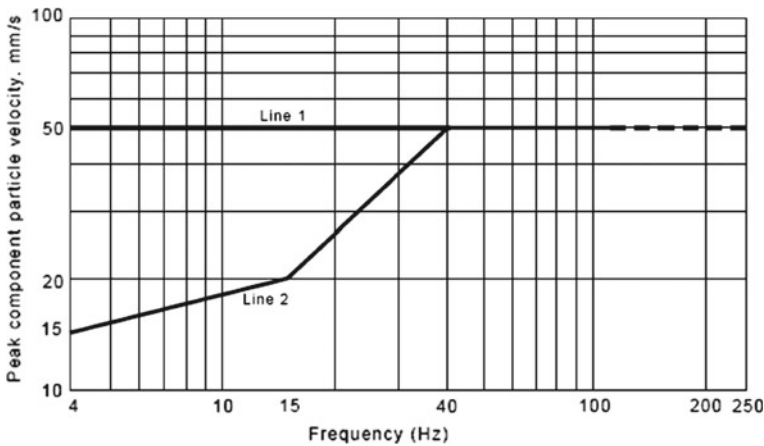


**Fig. 12** Transient vibration guide values for cosmetic damage (from BS 7385-2: [6])

## 6 Conclusion

From the field observations, it is found that all three perpendicular directions, i.e. transverse, longitudinal and vertical, have ppv much below the permissible limit (less than 1% of permissible limit), and so the existing structure is safe. The maximum transverse peak particle velocity obtained numerically is 0.001962 mm/s and from field test is 0.173 mm/s. The maximum longitudinal peak particle velocity obtained numerically is 0.00573 mm/s and from field test is 0.355 mm/s. The maximum vertical peak particle velocity obtained numerically is 12.12 mm/s and from field test is 0.512 mm/s. It is observed that the vibration is maximum and the dissipation

of energy of the stress waves is minimum along vertical direction. In both the other directions, it is observed that as the distance between pile-driving point and point on the existing structure increases, the vibration (expressed as ppv) is found to decrease drastically. The numerical study using Plaxis 3D AE further conforms to the field observation that the vibration reduces on moving away from the point of disturbance. It is further observed that all the results obtained from numerical modelling satisfy the codal provision set by BS 7385-2:1993.

## References

1. Abdel-Rahman SM (2002) Vibration associated with pile driving and its effects on nearby historical structures. In: IMAC-XX conference & exposition on structural dynamics, 1251–1258
2. Massarsch, KR, Fellenius, BH (2008) Ground vibrations induced by impact pile driving. In: Prakash S (ed) Proceedings of the sixth international conference on case histories in geotechnical engineering, Arlington, USA, pp 1–38
3. Deckner F, Viking K, Hintze S (2011) Aspects of ground vibrations due to pile and sheet pile driving. *EJGE* 20(19):11161–11176 Bund
4. Sultana P, Manikandan R (2015) Behaviour on joint spacing and settlement of pile raft foundation resting on Jointedhoek-Brown Rocks. In: 50th Indian geotechnical conference
5. Mabsout ME, Tassoulas JL (1994) A finite element model for the simulation of pile driving. *Int J Numer Eng* 37(2):257–278
6. BS 7385-2 (1993) Evaluation and measurement for vibration in buildings, part 2: guide to damage levels from groundborne vibration. British Standard Institution



# Alternative Foundation Methods for Upgradation of Oil Jetty



R. Sundaravadivelu, S. Sakthivel, S. Srinivasalu, A. Chitra  
and J. Bharath Priyan

**Abstract** Marine civil structures in the harbour are used to handle various types of cargoes. Liquid cargo terminal berth vessels are used for loading and unloading of petroleum, oil, lubricants and other liquid chemical products. These liquid cargoes move through pipelines. India is keen to explore the possibilities of increasing the capacity utilization of oil berths and to improve the existing liquid terminals to handle the ever-growing demand for POL and other liquid cargoes. The objective of the present study is to assess and suggest the most suitable among the proposed three alternative methods for upgrading the oil berth at Visakhapatnam Port Trust (VPT). The existing oil berths at VPT have a dredge level of  $-10$  m, which were built using caissons more than 40 years back and will be dismantled after constructing new berths which will have dredge level of  $-16$  m. The space available between the existing berths and current pipeline layout is limited and restricted posing a challenge for capacity augmentation. The alternative methods for substructure configuration are as follows (i) T-diaphragm wall + pile + anchor wall, (ii) T-diaphragm wall + pile + anchor wall + anchor rod and (iii) pile + rectangular diaphragm wall, respectively. The proposed structural configurations have been analysed to withstand the maximum forces acting on the berth. In addition, these three alternative foundation options once implemented will handle vessels up to 85,000 DWT (Panamax size). This techno-commercial exercise was carried out through STAAD Pro V8i software to analyse the structural integrity and foundation stability in collapse and service conditions for all three alternative methods. The comparison of results indicates that the first alternative has better structural stability and is also cost-effective.

---

R. Sundaravadivelu · A. Chitra · J. Bharath Priyan (✉)  
Department of Ocean Engineering, Indian Institute of Technology Madras,  
Chennai 600042, Tamil Nadu, India  
e-mail: [bharathbp92@gmail.com](mailto:bharathbp92@gmail.com)

S. Sakthivel  
Ocean Engineering & Consultancy Private Limited, Chennai, India

S. Srinivasalu  
Institute of Ocean Management, Anna University, Chennai, India

**Keywords** Oil berth · Structural stability · Capacity utilization of berths  
Alternative methods · STAAD Pro analysis · Stability

## 1 Introduction

Oil berths are marine civil structures used to berth oil tankers and vessels for loading and unloading of petroleum, oil and lubricant products and other harmful chemicals through pipelines. India's oil demand has risen up and is imported. POL is a global commodity sold on international market, and the vessels used to transport them are getting bigger every decade. India is keen to explore possibilities to increase the capacity utilization of oil berths and to improve the existing structures to cater for the increasing demand for oil. India is the world's fourth-largest oil consumer. The oil industry is among the six core industries, which plays a major role in the Indian economy. To address this increase in oil imports, the ports are required to increase in the capacity utilization of their oil berths. The Visakhapatnam Port has three harbours, and they are outer harbour, inner harbour and fishing harbour.

The outer harbour is mainly designed to handle ore and gas and has offshore tanker terminal and container terminal. The north-western arm is part of the inner harbour handling liquid cargo and fertilizer cargo. With natural deepwater basins, the outer harbour is capable of accommodating vessels up to 200,000 DWT with draft up to 18.10 m. The inner harbour is capable of accommodating fully laden handymax vessels accommodating up to 65,000 DWT with draft up to 10.06 m. The fishing harbour handles high-tech fishing boats. The vessel characteristics govern the design of berthing structures. This paper highlights the assessment of the most optimal among the three alternative foundation systems which have been studied to handle vessels with draft of 14.5 m.

## 2 Objective of the Study

- Carry out analysis and design of the proposed new structure with three alternative foundation systems.
- Assess the most suitable among the three alternatives based on technical, design and commercial consideration.

## 3 Proposed Structure

The site is located in the western arm of the inner harbour at Visakhapatnam Port Trust. The existing berth is monolithic in nature and at present handles only handymax-type vessels (40,000–60,000 DWT). To address the increase in liquid



**Fig. 1** Aerial view of inner harbour of Visakhapatnam Port (Google earth source)

cargo volumes, it is necessary to increase the dredge level of the berths in alignment with the capital dredging of navigational channel to handle larger size vessels up to 85,000 DWT in the future. The dredge depth shall be maintained as (-) 16.1 m to cater the Panamax vessels with the draft of 14.5 m. Hence, the proposed development plan is to demolish the existing oil berths and to construct new oil berths to handle the 9.81 MTPA (Fig. 1).

### 3.1 Vessel Specifications

The proposed berth shall be designed for a maximum vessel size of 85,000 DWT. The vessel specifications are given as per IS 4651 part 3 (Table 1).

**Table 1** Vessel specifications

Vessel size	Approximately up to 85,000 DWT
Vessel type	Panamax size
Draft	14.5 m
Length	230 m
Width	32.5 m

### 3.2 General Arrangements of the Proposed New Structure

The proposed length of the new berth is 426 m with width of 12.8 m. Expansion joints are provided every 60 m.

#### 3.2.1 General Arrangements of Alternative-I

This alternative substructure is proposed with a T-diaphragm wall, pile and anchor wall. The T-diaphragm wall is proposed on the seaside, and the piles are placed at the distance of 5.0 m in transverse direction from the diaphragm wall. The anchor wall is placed on the land side at the distance of 5.0 m from the pile. The proposed dredge level is (-) 16.1 m to accommodate the vessel with draft of 14.5 m. The deck structure shall consist of main beam; it is placed at a distance of 4 m in the longitudinal direction. The long beams are placed at intervals of 5.0 m in transverse direction. The deck slab thickness shall be 300 mm, and wearing coat is 100 mm thick. The precast fender beam with suitable fender and bollards is recommended. Refer Fig. 2 for details of structural components.

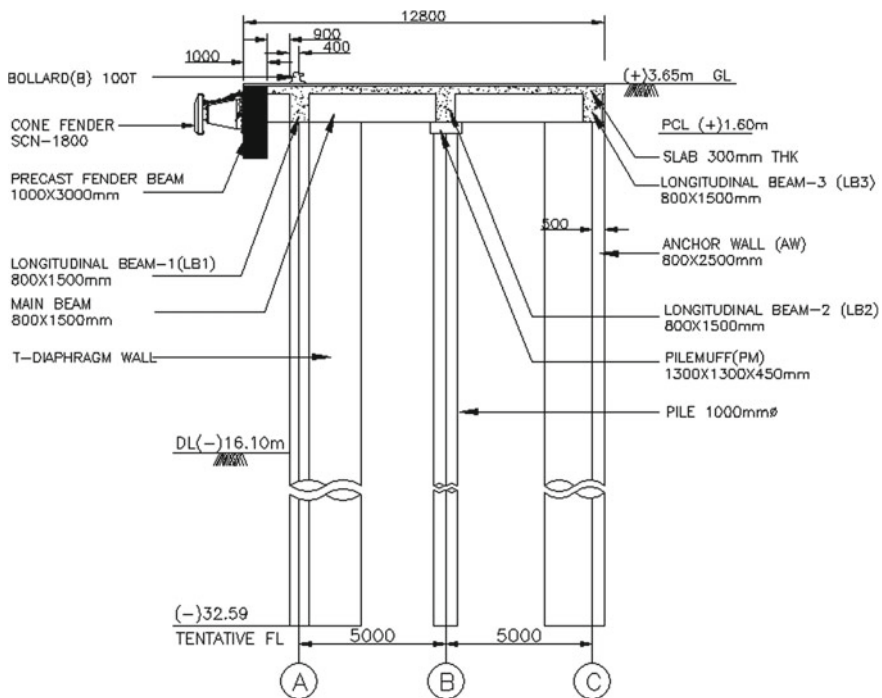


Fig. 2 Sectional view of Alternative-I

### 3.2.2 General Arrangements of Alternative-II

The proposed general arrangement of alternative-II consists of T-diaphragm wall proposed on seaside with dimensions of 4000 × 800 mm flange, 800 × 2200 mm web and anchor wall with the size of 800 mm × 2500 mm which shall be provided on rear side of the structure. One row of vertical RCC pile with diameter of 1000 mm is placed between diaphragm wall and anchor wall. The structural components are placed at 4 m c/c in longitudinal direction and 5.0 m in transverse direction. The proposed dredge level is (-) 16.1 m to accommodate the vessel with draft of 14.5 m. The T-diaphragm wall and pile shall be connected by main beam with dimensions of 800 mm × 1500 mm, and it is placed at a distance of 4 m in the longitudinal direction. The anchor wall piles are connected by 120-mmϕ tie rod. The long beams of size 800 mm × 1500 mm are placed at intervals of 5.0 m in transverse direction. The deck slab thickness shall be 300 mm, and wearing coat is 100 mm thick. The precast fender beam of size 1000 mm × 3000 mm with suitable fender and bollards is recommended (Fig. 3).

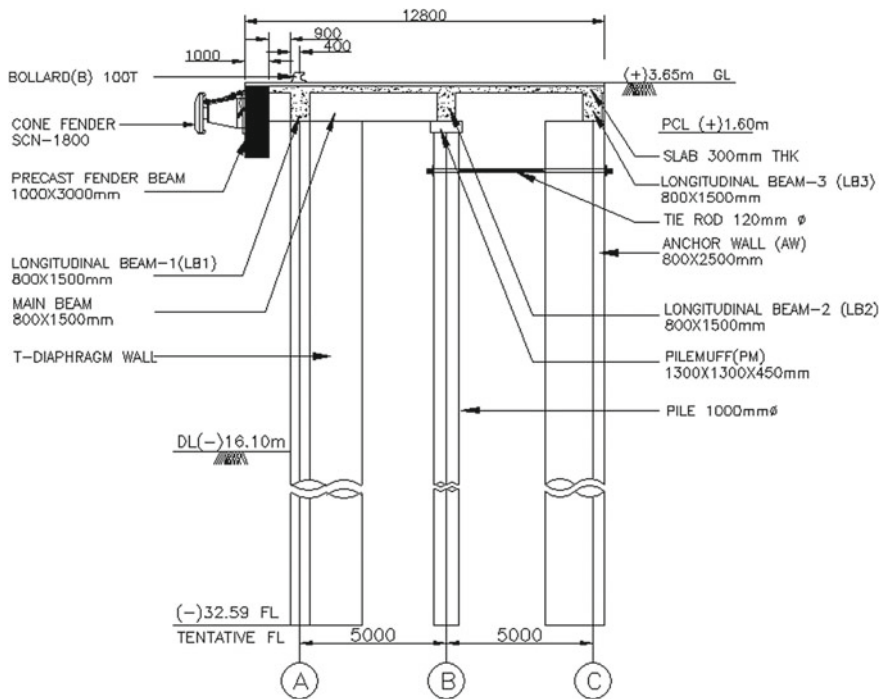


Fig. 3 Sectional view of Alternative-II

### 3.2.3 General Arrangement of Alternative-III

This proposed alternative consists of two rows of RCC piles with 1000 mm dia on berthing side and one row of rectangular diaphragm wall with thickness of 800 mm on land side. The structural components are placed at 4 m c/c in longitudinal direction and 5.0 m in transverse direction. The pile muff with the dimensions of 1300 mm × 1300 mm × 450 mm is placed above the pile. The deck structure shall consist of main beam with dimensions of 800 mm × 1500 mm, and it is placed at a distance of 4 m in the longitudinal direction. The long beams of size 800 mm × 1500 mm are placed at intervals of 5.0 m in transverse direction. The deck slab thickness shall be 300 mm, and wearing coat is 100 mm thick. The precast fender beam of size 1000 mm × 3000 mm with suitable fender and bollards is recommended (Fig. 4).

## 4 General Design Criteria

The main considerations followed in the design of the proposed alternatives are

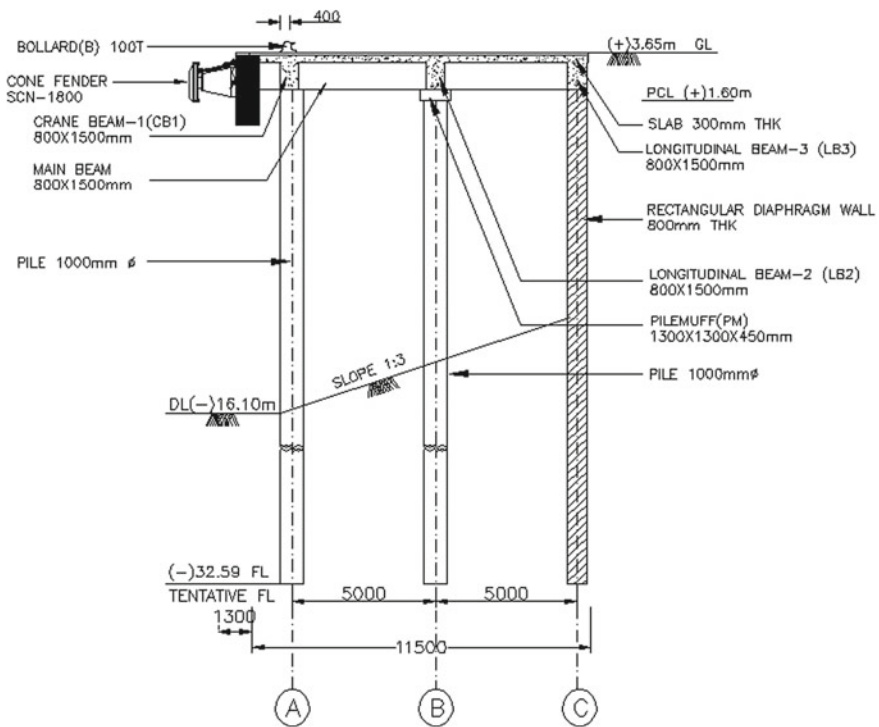


Fig. 4 Sectional view of Alternative-III

- a. Structural stability.
- b. Durability of the structure.
- c. Design vessel size of 85,000 DWT.
- d. M40 grade of concrete shall be used.
- e. High yield strength deformed bars of grade Fe 500 D conforming to IS 1789 shall be used.
- f. Live load of 50 kN/m<sup>2</sup> is considered for the design of deck structure.
- g. Earth pressure will be calculated based on the code IS 2911-2011.
- h. Differential water pressure shall be considered as per IS 4651 part 3.
- i. Seismic force shall be calculated according to IS 1893-2002, and Visakhapatnam is in zone II.
- j. Calculation of soil spring values using Vesic's equation.
- k. Berthing and mooring forces as per IS 4651 part 3.

## 5 Analysis

Three-dimensional analysis shall be carried out using conventional STAAD Pro V8i package for various critical load combinations. The P- $\delta$  analysis will be carried out. Soil-structure interaction analysis is performed by using springs as a representation of soil. The analysis of the structure shall be carried out using STAAD Pro, by idealizing the soil support using springs for diaphragm wall, piles and anchor wall.

The springs will be placed at 0.8 m interval for diaphragm wall and anchor wall and 1.0 m interval for piles. The spring spacing shall be less than equal to the thickness of diaphragm wall or the pile diameter or thickness of anchor wall for effective modelling of soil support in finite element method of analysis. These spring values are calculated by spring constant for every layer of soil to idealize the soil interaction of the foundation alternative structure.

## 6 Results and Discussion

Percentage of reinforcements is provided to satisfy the crack width limit as per IS 4651 part 4. By comparing the percentage reinforcement for all three alternatives, Alternative-I gives the most optimal reinforcement percentage and least among the three. Alternative-I structure is having less deflection compared with Alternative-II and Alternative-III. Therefore, by comparison of Alternative-I, Alternative-II and Alternative-III details, Alternative-I structure is having less deflection through all combination of loads (Tables 2 and 3) (Fig. 5).

**Table 2** Details of reinforcement percentage provided

	Components	Maximum bending moment (kNm)	Maximum shear force (kN)	Percentage of reinforcement provided (%)
Alternative-I	T-diaphragm wall	1.83E+04	2.8E+03	Pt = 0.42
	Pile	(-)1.8E+03	193.01	Pt = 3.07
	Anchor wall	6.36E+03	818.35	Pt = 0.33
Alternative-II	T-diaphragm wall	2.19E+04	(-)3.01E+03	Pt = 0.52
	Pile	(-)2.4E+03	(-)689.95	Pt = 3.28
	Anchor wall (anchor rod connected)	7.58E+03	960.26	Pt = 1.26
Alternative-III	Pile-1 (seaside)	(-)3.12E+03	953.9	Pt = 6.15
	Pile-2 (centre)	(-)3.84E+03	1.13E+03	Pt = 6.35
	Rectangular diaphragm wall	9.0E+03	(-)2.16E+03	Pt = 2.88

**Table 3** Percentage reinforcement of pile, T-diaphragm wall and anchor wall for Alternative-I

S. No	Components	Percentage of reinforcement required (%)	Percentage of reinforcement provided (%)	Crack width limit (mm)
1	Pile	2.40	3.07	0.3
2	T-diaphragm wall	0.17	0.42	0.3
3	Anchor wall	0.28	0.33	0.3

## 7 Conclusion

This redevelopment project is complex involving demolition of existing oil berths, dredging the channel from (-) 14.5 m to (-) 16.1 m and construction of new oil berths at the same location to cater for 85,000 DWT oil tankers. In such brown field port development project, there are a lot of constraints and the port planners need to overcome the same by choosing the most optimal option among the proposed three alternatives. The alternative needs to have a robust and cost-effective design. This oil berth reconstruction is a very complicated operation as it involves multiple pile lines, and there are various dismantling, construction sequences along with multiple interphase issues between marine civil works, electrical and mechanical works. In



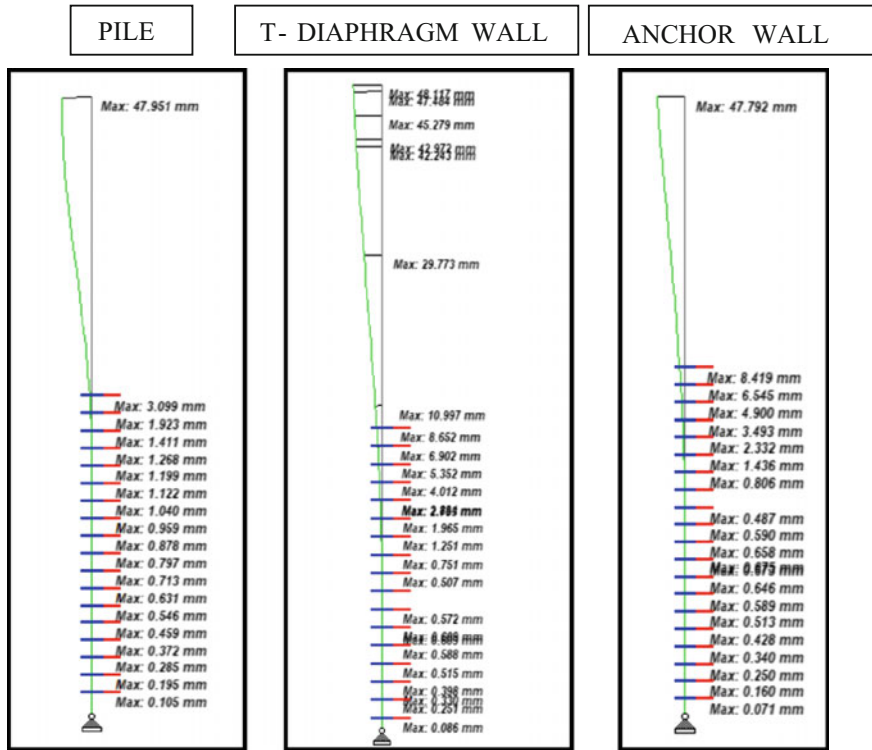


Fig. 5 Pile, T-diaphragm wall and anchor wall deflection for Alternative-I

this project, such attempts were made to reach at an optimal alternative by suggesting the most suitable substructure system for the development of the oil berth in a very short timeline of 42 months. The exhaustive detailed studies reveal that Alternative-I requires relatively lesser percentage of reinforcement and is more cost-effective by 20 crores. It also has the best performance in serviceability and collapse conditions among the three alternatives.

### References

1. Houston TW et al (2002) Foundation design considerations for a pile supported critical facility. 22:1169–1174
2. Comodromos EM et al (2005) Evaluation of negative skin friction effects in pile foundations using 3D nonlinear analysis. 34:383–421
3. Maheshwari BK et al (2003) Three-dimensional nonlinear analysis for seismic soil–pile-structure interaction. 24:343–356
4. Eicher JA et al (2003) Stress and deformation of offshore piles under structural and wave loading. 30:369–384

5. Tokimatsu K et al (2005) Effects of inertial and kinematic interaction on seismic behavior of pile with embedded foundation. 25:753–762
6. Fuji H et al (2015) Design of mooring system of oil storage barges in shallow water
7. Yajneswaran B et al (2015a) Analysis of the effect of anchor rod on the behavior of diaphragm wall using PLAXIS 3D. 4:240–247
8. Yajneswaran B et al (2015b) Effect of stiffness on performance of diaphragm wall. 116:343–349
9. Witker T et al (1976) Horizontal forces on piles and pile groups, Chapter 17, pp 176–190
10. Murthy VNS (2011) Textbook of Soil mechanics and foundation engineering
11. Gue SS et al (1984) Ground heave around driven piles in clay. 32:345–367
12. Evans KM et al (1987) A model study of the end bearing capacity of piles in layered calcareous soils. 34:427–445
13. Chaudhry AR et al (1994) Static Pile-soil-pile interaction in offshore pile groups. 14:213–234
14. Bell RW (1991) The analysis of offshore foundations subjected to combined loading
15. Martin CM (1994) Physical and numerical modelling of offshore foundations under combined loads

# Influence of Grouser Geometrical Parameters of Deep-Sea Crawler Vehicle on Soft Clays



C. Janarthanan , K. Gopkumar , V. Sundaramoorthi , N. R. Ramesh   
and G. A. Ramadass 

**Abstract** India has been involved in developing the technology for deep-sea mining in the Central Indian Ocean Basin (CIOB) from approximately 6000 m water depth. The Central Indian Ocean Basin is abundant in nodules which are rich sources of minerals like manganese, copper, cobalt, and nickel. The mining machine has to collect the nodules from the seabed, crush them, and pump to the mother ship at the sea surface. The mining machine has to be supported on very soft sediments of shear strength less than 2 kPa. The maneuverability of mining machine becomes very critical while operating in such soft soils. One of the major challenges involved in deep-sea mining is the mobility of the mining machine on the soft seabed. Predicting the traction of the mining machine is very important for determining the mobility of the mining machine in such soft soils. To analyze the influence of geometrical parameters of the grouser on soft soil for traction performance, the conventional teramechanics approach of Mohr–Coulomb failure criteria method was used to obtain the traction parameters. The shear strength–shear displacement model of deep-sea soft sediments were obtained experimentally using a customized bevameter in bentonite soil to simulate soft soil deep-sea conditions. The traction force model for the various geometrical configurations of the grouser was numerically studied in ABAQUS software using coupled Eulerian–Lagrangian (CEL) technique. The influence of the grouser parameters, viz. shape and size, on the traction performance and the soil displacement was examined. To validate the analysis, experimental studies were undertaken with a scaled-down locomotion vehicle in simulated soft soil tank. The proposed paper brings out the studies undertaken and further analysis planned in the field.

**Keywords** Grouser · Traction · Soft soil · CEL · ABAQUS

---

C. Janarthanan (✉) · K. Gopkumar · V. Sundaramoorthi · N. R. Ramesh · G. A. Ramadass  
National Institute of Ocean Technology (NIOT), Velachery–Tambaram Main Road,  
Narayanapuram, Pallikaranai, Chennai 600100, Tamil Nadu, India  
e-mail: [janarthanan.c@niot.res.in](mailto:janarthanan.c@niot.res.in)

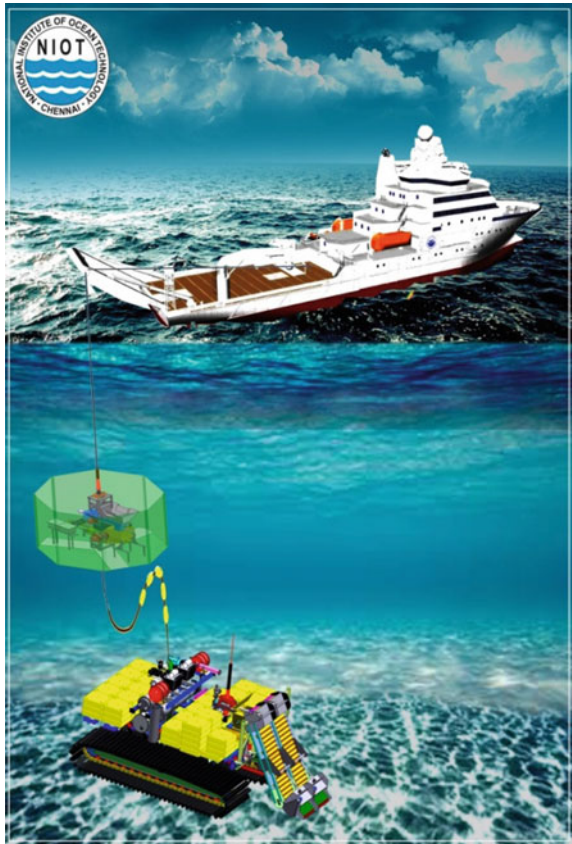
© Springer Nature Singapore Pte Ltd. 2019  
K. Murali et al. (eds.), *Proceedings of the Fourth International Conference in Ocean Engineering (ICOE2018)*, Lecture Notes in Civil Engineering 22,  
[https://doi.org/10.1007/978-981-13-3119-0\\_61](https://doi.org/10.1007/978-981-13-3119-0_61)

# 1 Introduction

The deep seas have rich mineral resources, one of them being polymetallic nodules. Development of a deep-sea mining vehicle, which moves on the seabed and collects the polymetallic nodules, is in progress. India is working on a mining system using the flexible riser concept (Fig. 1). The concept was demonstrated for pumping fine seafloor material in the Indian seas at 451 m depth for short-term operations in 2000 [1]. The system was augmented with pressure compensation systems and buoyancy packs, and the system was used for mining fine seafloor materials like sand and silt in 2006.

Subsequently, the qualification of undercarriage system with the three module collector and pickup device of the machine was done. The system was tested near Angria Bank off Malvan coast in Arabian Sea at 512 m depth during October 2010 using artificial nodules laid on the seabed [2].

**Fig. 1** Integrated mining system using flexible riser concept



The grouser geometrical parameters of the tracked vehicle play a critical role in predicting the traction of the mining machine, and the following literatures discussed the various effects of the trafficability of the mining machine.

Schulte [3] studied the evaluation of trafficability of a tracked mining vehicle for manganese nodule mining which is one important aspect of the complete mining system. The trafficability was studied by using traction force potential, static sinkage, dynamic sinkage, and ground failure analysis.

Bekker's [4] derived terramechanics model (BDTM) is an analytical tool for evaluating vehicle off-road mobility. BDTM has been developed using Bekker's equations for vehicle soil interactions and has modified the Mohr–Coulomb equation considering the grouser width and height.

Nuttal [5] examined the applicability of the existing estimation methods for maximum net traction of tracked vehicles ashore to the tracked vehicles crawling on the seafloor.

Muro [6, 7] studied the trafficability of tracked vehicle on very soft bottom and investigated grouser effect on tractive performance of a bulldozer running on soft marine sediment.

Bode [8] studied the parameter which influences the tractive performance of tracked vehicle in deep snow through experiments.

Rehorn [9] developed a tracked vehicle model distinguished by an articulated chassis structure, and flexible rubber tracks equipped with grousers of involute shape were used for the sand mining system.

Hong [10] performed experiments to investigate grouser shape effects on trafficability of extremely soft seabed. The effects of shape and height of grouser on tractive force and slip sinkage were investigated.

Hong [11] conducted an experimental investigation into the performance of tracked vehicle on soft and cohesive soil which has been carried out in a soil bin facility based on design of experiments.

Shaojun [12] performed kinematic and dynamic characteristics of deep-sea mining system which have been investigated and evaluated by using computational dynamic method of multi-body system.

Li [13] experimentally investigated the trafficability of the tracked vehicle and Archimedean screw vehicles on soft soil and lots of tractive tests of the special tracks with various grousers on soft soil with 1–4 kPa shear strength.

Manuwa [14] studied the traction characteristics of the grouser in the sandy clay with different water contents and confirmed the traction model by the polynomial regression equation.

Wenbo [15] performed an experimental research on grouser traction of deep-sea mining machine by combining the traction model parameters, and the traction–displacement curve of the grouser with a certain group values of tooth width, tooth height, and ground pressure can be predicted. Therefore, the slip of the mining machine can be prevented to improve the mining efficiency.

The various literature studies of tracked vehicle suggested that the grousers enhance the traction force of tracked vehicle on soft clays.

This paper analyzes the influence of geometrical parameters of the grouser on soft soil for the traction performance of cohesive soft soil. Various shapes and speeds of grouser models are analyzed in cohesive soil model simulated by the conventional terramechanics approach of Mohr–Coulomb failure criteria based on the measured geotechnical data on the bentonite soil using a customized bevameter test setup.

## 2 Grouser Studies

### 2.1 Bevameter

The deep-seabed sediments at CIOB are mostly medium to highly plastic clay or silty clay with very low shear strength, less than 5 kPa [16, 17], which can easily make the deep-sea mining machine to slip. The in situ soil tester was developed and tested at 5462 m water depth in the Central Indian Ocean Basin (CIOB) for measuring same soil properties at locations [18].

Based on the CIOB soil property data, the bentonite mixture was prepared for varying shear strength and a customized bevameter shear test setup as shown in Fig. 2 was developed to determine the shear parameters for numerical simulation studies.

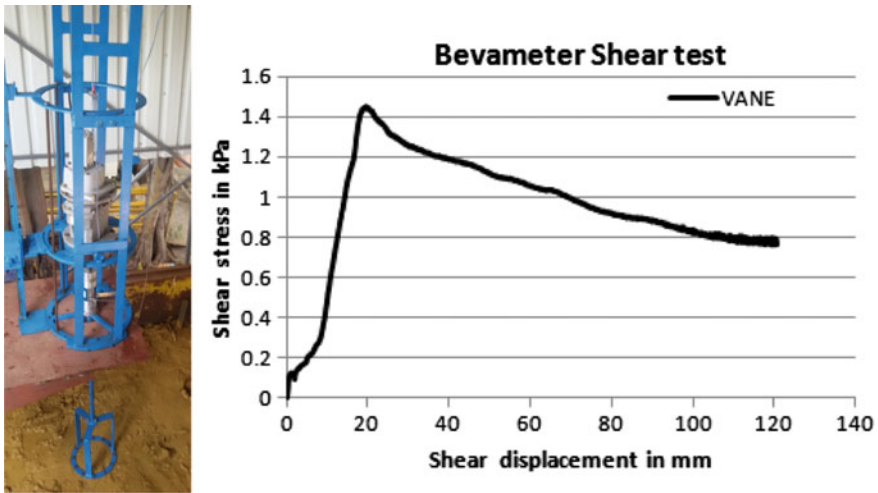
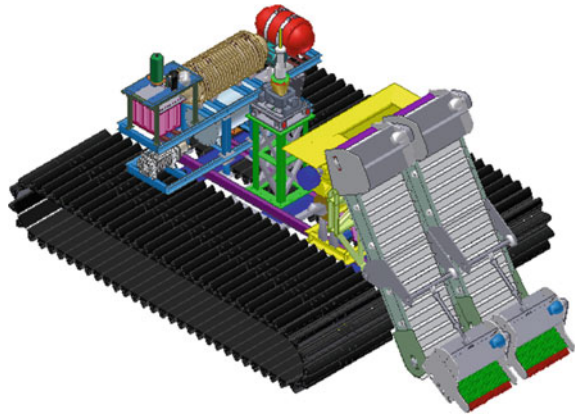


Fig. 2 Bevameter shear test setup

**Fig. 3** Mining machine

## 2.2 Mining Machine

The deep-sea mining machine consists of undercarriage unit with track belts, mechanical tined pickup device, conveyor, crusher, HPU system, enclosures, and pump for slurry transportation. The intended mining machine is shown in Fig. 3. The major design criteria are low contact bearing pressure and high traction which make a tracked vehicle suitable for locomotion on soft seabed at CIOB.

Maneuverability studies of tracked vehicles recommend the grouser which is used in the track belt which improves the trafficability on soft clays [19].

## 2.3 Grouser Model

The studies on the geometrical parameters of the grouser are very important for the soft cohesive soil since it is directly affecting the traction forces of a tracked vehicle and the soil deformation pattern. Traction was developed on the soft soil due to the shearing between the grouser and soil during locomotion. Bekker's equation shows that the traction force will be higher in the case of the vehicle having the grouser [20].

The existing empirical methods did not consider the geometrical parameters of the grouser for determining the traction force, but Bekker's theory [19] proposed an empirical relationship considering the grouser height for determining the traction force; however, the influence of the grouser parameters, viz. shape, size, and speed, on the traction performance and the soil displacement was not considered in any of the empirical relationships.

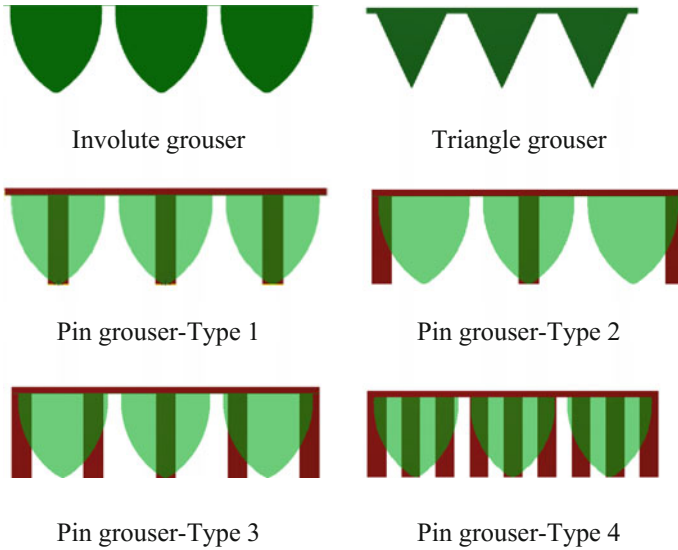


Fig. 4 Various grouser models

The present numerical study aims to examine the traction effect of the various grouser profiles and displacement speeds of the grouser on the soft soil, and the grouser profiles shown in Fig. 4 were used in the numerical simulation. The experiments are being performed to validate the numerical studies.

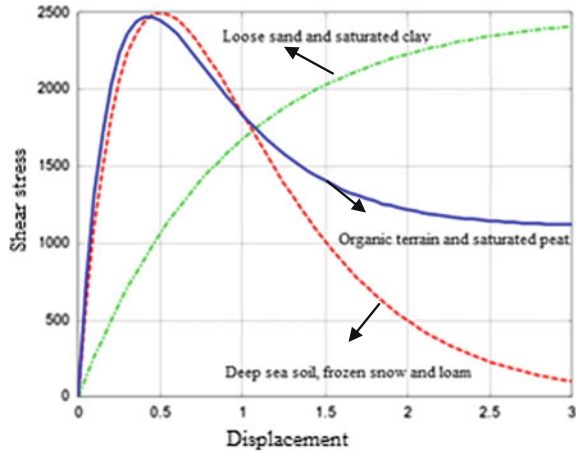
### 2.4 Soil–Machine Interaction

Bekker’s theory is widely used to estimate the traction force of the tracked vehicle. The traction force of the tracked vehicle on soil depends on the following relationship as shown in Fig. 5 [21].

In order to study the locomotion of the tracked vehicle on soft soil, the sinkage and shear stress parameters of the particular soil are vital to determine the traction and mobility. The maximum traction force will be developed based on the shear strength of the terrain and the bearing contact area of the tracks. The Mohr–Coulomb criteria [22] were used to determine the maximum shear strength of the soil according to the criteria the soil fails when the shear stresses developed in the soil become equal to the shear strength of the soil.



**Fig. 5** Shear stress–shear displacement curves for various soil types



The maximum shear strength was calculated by using the following equation.

$$\tau_{\max} = (c + \sigma \tan\phi) \tag{1}$$

where

- c* Cohesion of soil
- $\sigma$  Normal stress
- $\phi$  Angle of internal friction of soil.

### 2.5 Finite Element Method Model of Numerical System

The finite element model was prepared in ABAQUS software for a soft soil bed of 1 m × 0.5 m × 0.5 m dimension as shown in Fig. 6.

The soft soil was modeled using Mohr–Coulomb failure criteria material model with elastic–plastic material behavior, which is widely used for geotechnical applications. The property of the soil used in the simulation was based on the bevameter results.

The seabed soil undergoes large deformations during the locomotion of the tracked vehicle. Traditional Lagrangian-based finite element analysis often fails in these situations due to the excessive element distortion; however, Eulerian-based analysis offers significant advantages because the soil material can move relative to mesh [23].

The ABAQUS/explicit coupled Eulerian–Lagrangian (CEL) technique combines the advantages of both the Eulerian and Lagrangian approaches by allowing grouser model that does not deform significantly to be modeled as Lagrangian, and soil model that undergoes large deformations to be modeled as Eulerian. The interaction

between the Lagrangian and Eulerian regions is maintained by the general contact algorithm.

The cross section, initial position, and FEM model of the grouser–soil model are shown in Fig. 7.

The bottom of the soil domain was restricted in all the directions, and the vertical walls of the soil domain were only allowed to move in vertical directions. Grouser was constrained in all the directions except the linear direction ( $x$ -direction), and rate of change of distance constraint is provided in the linear direction. The general contact provided in between grouser and soil domain and the initial material content of the Eulerian domain must be specified as an initial condition.

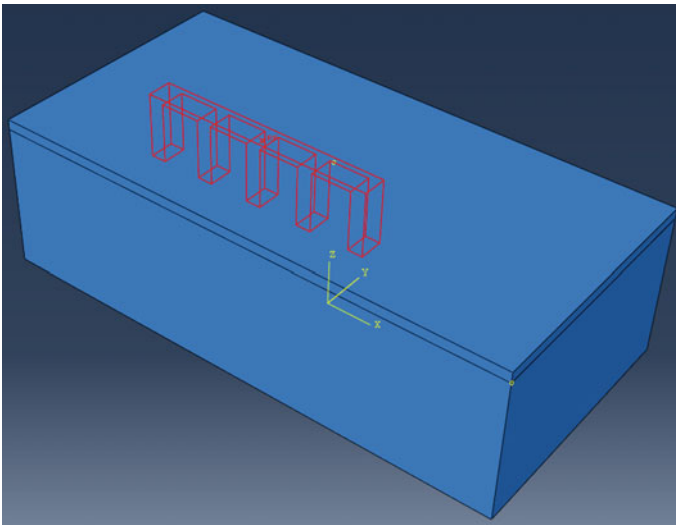


**Fig. 6** Soil bed model in ABAQUS

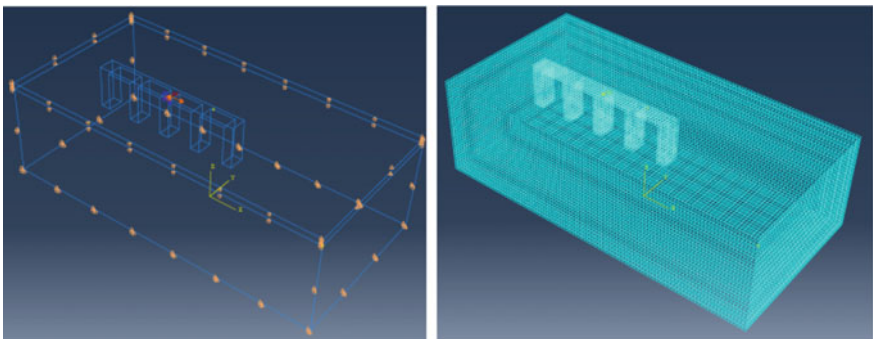


**Fig. 7** Model constraints and FEM model

The indented mining machine grouser has a dimension of 1300 mm × 155 mm × 130 mm, wherein in the numerical simulation studies, it was considered 50 mm × 155 mm × 130 mm by considering the solving time of the large deformation simulation domain.

For investigating the behavior of the grouser–soil interaction, the grouser was subjected to a translational load with a horizontal velocity of 0.015 m/s until a translation of 0.15 m was achieved. The same procedure was applied to the various grouser profile simulations.

## 2.6 Experimental Test Setup

The experiments are being performed to validate the numerical simulation results and to examine the influence of the grouser parameters on the traction performance and the soil displacement. The grouser parametric test setup consists of chain sprocket arrangements for various grouser sizes with variable pitch and height. The grouser parametric experimental test setup is shown in Fig. 8. It has an electric motor coupled with gearbox to rotate the grouser configuration at a speed ranging from 1 to 10 RPM. The test setup has a torque sensor capable of measuring a maximum torque of 500 Nm to measure the resistance offered by the soil. The data were logged using data acquisition and control system.

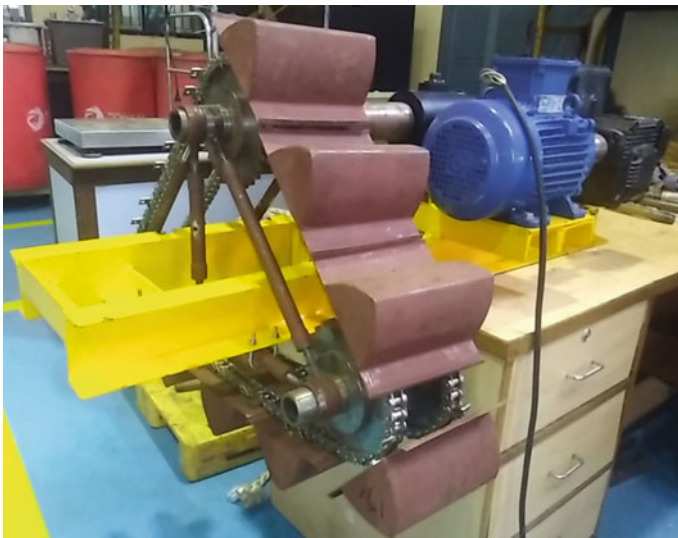


**Fig. 8** Grouser parametric experimental setup

### 3 Result and Discussion

Numerical simulations were performed with various grouser profiles by considering the same loading and boundary constraints. Figure 9 shows the results of reaction force on the grouser due to soil displacement.

Numerical simulation results show that the measured value of the reaction force of the grouser model curve trend was dependent on the soft soil characteristics. The results show significant difference in the reaction force values with a variation in the grouser profiles. The reaction force was highest for the pin grouser type-4 configuration which can be attributed to the higher contact area within the boundary.

Figures 10 and 11 show the value of the maximum principal plastic strain in the soil after the grouser movement, and it shows that the involute grouser configuration has influence over large area than the pin-type grouser configuration.

Figures 12 and 13 show the experimental results of the scaled-down locomotion vehicles track pattern in simulated soft soil tank, and it shows the higher disturbance induced by the involute grouser configuration than the pin-type grouser configuration by retaining the same bearing pressure and soil strength during the experiments.

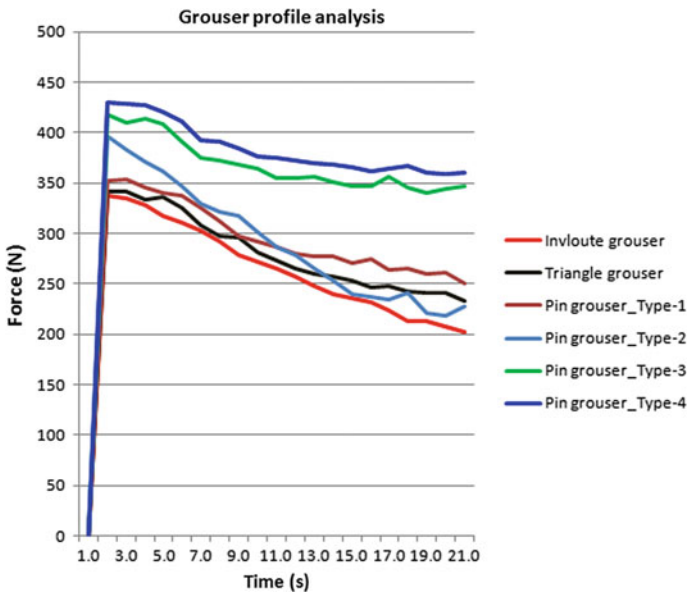
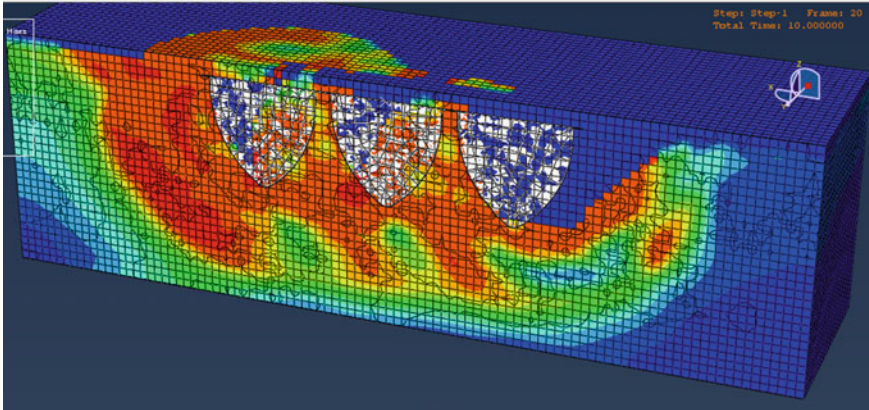
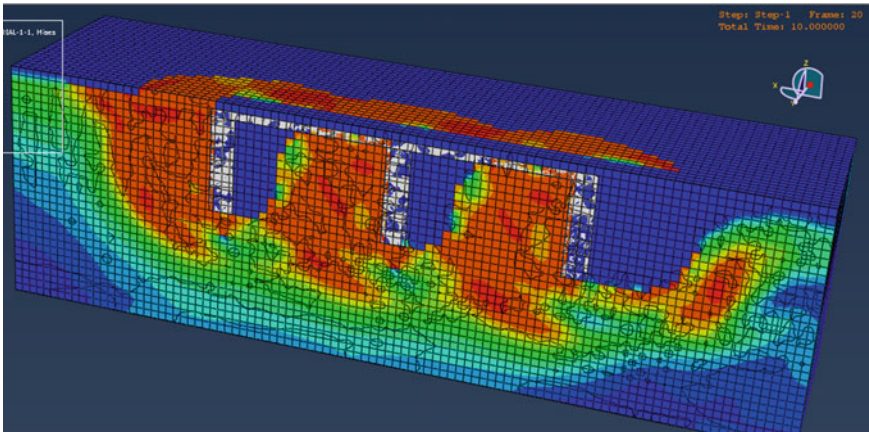


Fig. 9 Grouser profile analysis results



**Fig. 10** Numerical results of involute grouser configuration



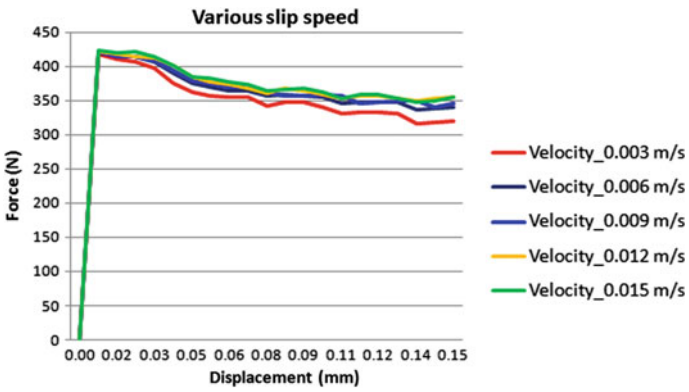
**Fig. 11** Numerical results of involute grouser configuration

Figure 14 shows the numerical results of reaction forces of various shear rates of the pin-type grouser configuration to study the viscous effect on the soil. However, no significant difference in behavior was observed for varying the grouser speed which can be attributed to the lesser speed (0.15 m/s) of the indented tracked vehicle.

**Fig. 12** Experimental results of involute grouser configuration



**Fig. 13** Experimental results of pin grouser configuration



**Fig. 14** Numerical results of pin grouser in various speeds

## 4 Conclusion

The traction force model for the various geometrical configurations of the grouser was numerically estimated in the conventional terramechanics approach used in coupled Eulerian–Lagrangian (CEL) technique. The influence of the grouser shapes on the traction performance was simulated and examined. The pin-type grouser configuration develops higher traction force than the other grouser-type configuration. The soil displacement of the grousers was simulated and compared with experimental studies. Simulation of the grouser shear tests on varying speeds showed no significant difference in traction force.

The grouser parametric experimental test setup was developed, and experiments are being performed to validate the numerical results. It is also intended to study the shear test on varying normal load on the grouser to examine the static and dynamic sinkage behavior of the soft soil. The test setup can also be used to examine the height and width effect of the grouser on very soft clays which is valuable input for developing the deep-sea mining machine.

**Acknowledgements** The authors sincerely thank Ministry of Earth and Sciences, Government of India, for funding the technology development programs of deep-sea technologies group of NIOT and for encouraging us to carry out the research work.

## References

1. Deepak CR, Shajahan MA, Atmanand MA, Annamalai K, Jeyamani R, Ravindran M, Schulte E, Panthel J, Grebe H, Schwarz W (2001) Developmental tests on the underwater mining system using flexible riser concept. In: Proceedings of 4th ocean mining symposium of international society of offshore and polar engineers, Szczecin, Poland, 23–27 Sept 2001
2. Rajesh S, Gnanaraj AA, Velmurugan A, Ramesh R, Muthuvel P, Babu MK, Ramesh NR, Deepak CR, Atmanand MA (2011) Qualification tests on underwater mining system with manganese nodule collection and crushing devices. In: Proceedings of the ninth ISOPE ocean mining symposium, Maui, Hawaii, USA, 19–24 June 2011
3. Schulte E, Schwarz W (2009) Simulation of tracked vehicle performance on deep sea soil based on soil mechanical laboratory measurements in bentonite soil OMS-ISOPE
4. Bekker MG (1969) Introduction to terrain-vehicle systems. University of Michigan Press, Ann Arbor, MI
5. Nuttal CL (1971) Traction limit for tracked vehicles crawling the sea bottom. *J Eng Ind Trans ASME* 717–730
6. Muro T (1983) Trafficability of tracked vehicle on super weak ground (in Japanese). *Ill/emoirs Fac Eng* 10(2)
7. Muro T (1988) Grouser effect on tractive performance of a bull-dozer running on a superweak marine sediment. In: Proceedings of 2nd Asia-Pacific conference, ISTVS, Bangkok, Thailand, 6–10 Dec
8. Bodin A (2001) Study of the influence parameter on tractive performance in deep snow. *J Terramech* 47–59
9. Rehorn L (1994) Entwicklung eines Tiefseeraupenfahrzeugs und Untersuchung seiner inneren Fah7' l' ffliderstaende, doctoral thesis (in German), University of Giegen

10. Hong S, Choi JS (2001) Experimental study on grouser shape effects on trafficability of extremely soft seabed. In: Proceedings of the 4th ocean mining symposium, Szczecin, Poland, pp 115–121
11. Hong JSS, Kim H, Lee TH (2003) An experimental study on tractive performance of tracked vehicle on cohesive soft soil. *Isopce* 139–143
12. Liu S, Wang G, Li L, Wang Z, Xu Y (2003) Virtual reality research of ocean poly-metallic nodule mining based on COMRA's mining system, OMS-ISOPE
13. Li L, Jue Z (2005) Research of China's pilot-miner in the mining system of poly-metallic nodule, OMS ISOPE
14. Manuwa S, Ademosun O (2007) Draught and soil disturbance of model tillage tines under varying soil parameters. *Agric Eng Int* 4:1–17
15. Wenbo MA, Qihua RAO<sup>†</sup>, Feng K, Xu F (2015) Experimental research on grouser traction of deep-sea mining machine. *Appl Math Mech*
16. Khadge NH (2000) Geotechnical properties of surface sediments in the INDEX Area. *Mar Geosour Geotechnol* 18:251–258
17. Khadge NH (1992) Geotechnical Properties of deep sea sediments from the Central Indian Ocean Basin. *Indian J Mar Sci* 21:80–82
18. Muthukrishna Babu S, Ramesh NR, Muthuvel P, Ramesh R, Deepak CR, Atmanand MA (2013) In-Situ soil testing in the Central Indian Ocean Basin at 5462 m water depth. In: Tenth ISOPE ocean mining and gas hydrates symposium, 22–26 Sept, Szczecin, Poland
19. Bekker MG (1969) Introduction to terrain-vehicle systems. University of Michigan Press
20. Laughery S, Gerhart G (1999) Bekker's terramechanics model for off-road vehicle research. In: Ground mobility conference 1999, Houghton MI
21. Grebe H, Schulte ES (2005) Determination of soil parameters based on the operational data of a ground operated tracked vehicle. In: Proceedings of 6th ocean mining symposium of international society of offshore and polar engineers, Changsha, Hunan, China, 9–13 Oct 2005
22. Wong JY (2001) Theory of ground vehicles, 3rd edn. Wiley Inc., USA, pp 144–153. ISBN 0-471-35461-9
23. Simulia DS (2010) Installation and extraction of spudcans using Abaqus/Explicit. Abaqus technology brief, June 2010



# Testing of Soft Clays Using Bevameter for Deep-Sea Mining Machine



K. V. Reshma , C. Janarthanan , V. Sundaramoorthi , K. Jayanthi ,  
B. O. Vishwanath , P. Muthuvel , K. Gopkumar  and G. A. Ramadass 

**Abstract** India has been developing technology for deep-sea mining in the Central Indian Ocean Basin from 6000 m water depth. The Central Indian Ocean Basin (CIOB) is abundant in nodules which are rich sources of minerals like manganese, copper, cobalt, and nickel. The intended mining machine has to collect the nodules from the seabed, crush them, and pump it to an interim station before transfer to the mother ship at the sea surface. The mining machine has to be supported on very soft seabed of shear strength less than 5 kPa. The maneuverability of mining machine becomes very critical while operating in such soft soils. One of the major challenges involved in deep-sea mining is the mobility of the mining machine on the soft seabed with predictable and controlled sinkage. Prediction of traction force for a tracked vehicle on very soft clays has been difficult. The existing studies in this area are mainly for soft clay of shear strength about 5 kPa. Conventional terramechanics approach for the prediction of traction forces for tracked vehicle is based on Bekker's Theory. Bekker's Theory uses bevameter shear tests to understand the shear behavior of soil. The shear tests help to establish the shear stress–shear displacement relationship of soil which helps to predict the traction forces. The present study aims to identify the shear parameters for very soft clays of less than 3 kPa shear strength, which can in turn be used to predict the traction developed in vehicles. Experimental studies were performed using a bevameter setup to determine the shear parameters of very soft clays. The influence of the variables like ring size, height of blades, number of blades, and normal stress on the shear behavior of the soil was examined experimentally.

**Keywords** Deep-sea mining · Mining crawler · Bevameter · Shear ring  
Bentonite–water mixture · Seabed soil

---

K. V. Reshma · C. Janarthanan (✉) · V. Sundaramoorthi · K. Jayanthi · B. O. Vishwanath  
P. Muthuvel · K. Gopkumar · G. A. Ramadass  
National Institute of Ocean Technology (NIOT), Velachery–Tambaram Main Road,  
Narayanapuram, Pallikaranai, Chennai 600100, Tamil Nadu, India  
e-mail: [janarthanan.c@niot.res.in](mailto:janarthanan.c@niot.res.in)

© Springer Nature Singapore Pte Ltd. 2019  
K. Murali et al. (eds.), *Proceedings of the Fourth International Conference in Ocean Engineering (ICOE2018)*, Lecture Notes in Civil Engineering 22,  
[https://doi.org/10.1007/978-981-13-3119-0\\_62](https://doi.org/10.1007/978-981-13-3119-0_62)

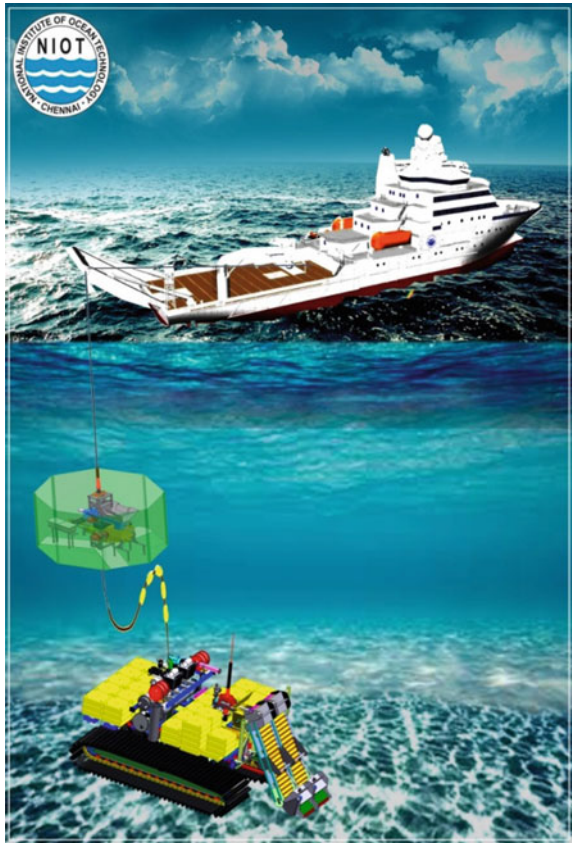
# 1 Introduction

The deep seas have rich mineral resources, one of them being polymetallic nodules. The development of a deep-sea mining vehicle, which moves on the seabed and collects the polymetallic nodules, has been in progress worldwide. India is working on a mining system using the flexible riser concept (Fig. 1). The concept was demonstrated for pumping fine seafloor material in the Indian seas at 451 m depth in 2000 [1]. The system was augmented with pressure compensation systems and buoyancy packs and used for mining fine seafloor materials like sand and silt.

Subsequently, the qualification of undercarriage system with the three modules of collector and pickup device of the mining machine was completed. The system was tested near Angria Bank off Malvan coast in Arabian Sea at 512 m depth using artificial nodules laid on the seabed [2].

The geotechnical properties of the seabed play a critical role in predicting the maneuverability of the mining machine. The seabed sediments at CIOB are mostly

**Fig. 1** Integrated mining system using flexible riser concept



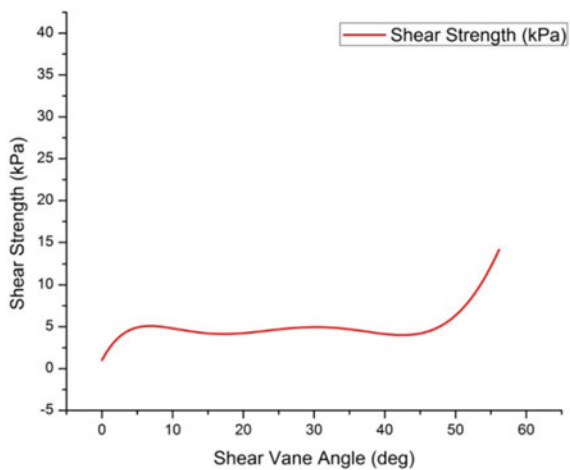
medium to highly plastic clay or silty clay with very low shear strength, less than 5 kPa [3, 4]. An electrically operable sub-sea in situ soil tester was developed and tested at 5462 m water depth in the Central Indian Ocean Basin (CIOB) to measure the soil properties more accurately on location. The result of the in situ vane shear test performed at location 13°33' S 74°48' E in CIOB is shown in Fig. 2 [5]. Soil property measurements in the nodule bearing areas of the Clarion–Clipperton fracture zones in the Pacific Ocean indicate soft sediments of shear strength less than 10 kPa [6].

The intended mining machine has a bottom undercarriage track with involute teeth to facilitate movement on the soft seabed at CIOB (Fig. 3). Low contact pressure and high traction make a tracked vehicle suitable for locomotion on soft clays. Maneuverability studies of tracked vehicles recommend consistency index to be used as a guiding factor for predicting trafficability on soft clays [7].

Shear behavior of soil is to be established for predicting the traction for tracked vehicles. Bekker had proposed employing bevameter for vehicle mobility studies [8]. It comprises two types of tests—plate penetration tests and shear tests. Bevameter shear tests aim at evaluating traction force for undercarriage at various slip percentages under different normal loads. Shear stress–shear displacement curves are obtained from the bevameter shear tests from which the shear deformation parameters can be estimated. A comparative study on the shear behavior of bentonite soil measured using a bevameter shear ring and a track segment has been reported by Schulte and Schwarz [9]. There are few studies related to the effect of grouser shape and height on traction of tracked vehicles [10]. The studies however to determine traction parameters for locomotion of tracked vehicle on very soft clays are very limited.

A bevameter shear test setup was developed to determine the shear parameters for estimating the traction force developed by the vehicle. The present study focuses on the effect of soil–machine interaction using bevameter shear test setup variables like ring size, number of blades, height of blades, and normal pressure on the shear

**Fig. 2** Measurement of shear strength at 5462 m depth at 492 mm penetration into seabed



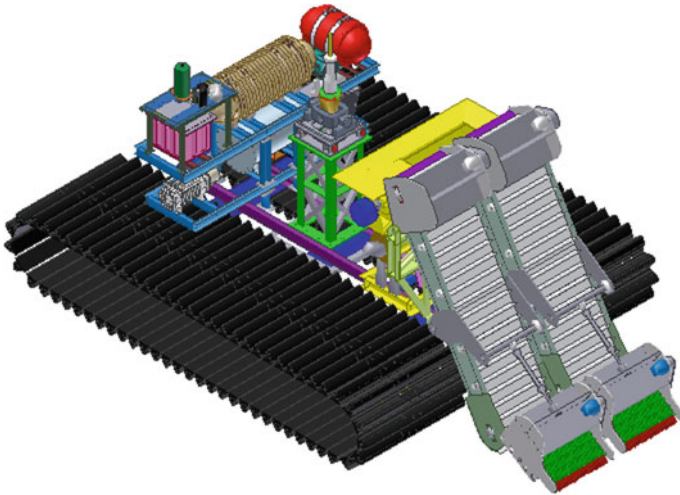


**Fig. 3** Intended mining machine

stress–shear displacement curves. Similar study using bevameter had been performed on frictional soil for the planetary rover by Apfelbeck et al. [11].

## 2 Shear Behavior of Soil

Empirical equations based on Bekker’s Theory are widely used in the field of teramechanics for predicting the traction of tracked vehicles. However, it requires the estimation of soil constants which represent the soil characteristics [11, 12]. The shear behavior of deep-sea soil needs to be established in order to predict the traction forces for the undercarriage track. The shear stress–shear displacement characteristics exhibited by a soil depend on the soil type. The shear stress–shear displacement curves for various soils are shown in Fig. 4 [13].

Soil type **A** exhibits a smooth shear stress–shear displacement curve. The shear stress initially increases with shear displacement and then remains constant after reaching the peak. This type of behavior is shown by loose sand, saturated clay, and dry fresh snow. The behavior of such soil can be represented by the Janosi and Hanamoto’s equation as below:

$$\tau = \tau_{\max}(1 - e^{-\frac{i}{k}}) \tag{1}$$

where

$$\tau_{\max} = (c + \sigma \tan \phi)$$

- $\tau_{\max}$  is the maximum shear strength of the soil
- $c$  is the cohesion of soil
- $\phi$  is the angle of internal friction of soil
- $\sigma$  is the normal stress
- $j$  is the shear displacement
- $K$  is the shear deformation parameter.

Soil type **B** shows an increase in shear stress with the increase in shear displacement up to the peak; thereafter, it decreases and reaches almost zero. This type of behavior is shown by peat and organic terrain. This type of behavior is represented by the following equation:

$$\tau = \tau_{\max}(j/K_w)e^{(1-\frac{j}{K_w})} \tag{2}$$

where

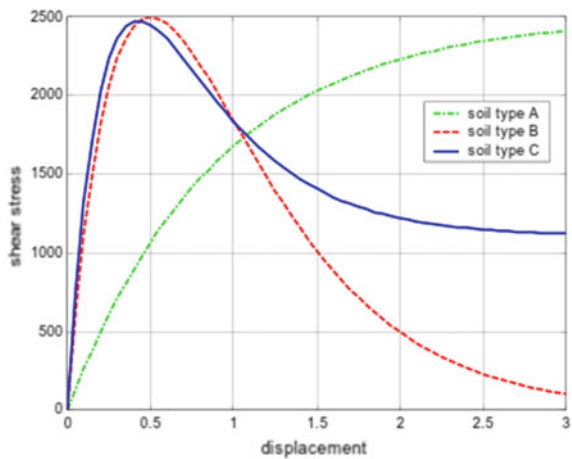
$K_w$  is the shear displacement at maximum shear stress.

The behavior of compact sand, silt and loam and frozen snow is represented by soil type **C**, wherein the shear stress increases with the increase in displacement up to the peak and then reduces to a residual value at higher displacements. Deep-sea soil also exhibits this type of behavior as deep soil is predominantly clays or silty clays with residual shear strength value more than zero [13]. The behavior of this type of soil is characterized by the following function:

$$\tau = \tau_{\max}K_r\left(1 + (1/(K_r(1 - 1/e)) - 1)e^{(1-\frac{j}{K_w})}\right)\left(1 - e^{-\frac{j}{K_w}}\right) \tag{3}$$

where  $K_r$  is the ratio of residual shear strength to maximum shear strength.

**Fig. 4** Shear stress–shear displacement curves for various soil types



The shear parameters  $K_r$  and  $K_w$  are obtained from the bevameter tests. The influence of test setup variables on the shear behavior was also studied using the bevameter test setup.

### 3 Experimentation

#### 3.1 Description of the Test Setup

The bevameter shear test setup consists of annular shear rings of various sizes with variable pitch and height as shown in Table 1. The test setup is shown in Fig. 5. It has an electric geared motor to rotate the annular ring at an rpm ranging from 0.016–0.9 to 5–15. The electric motor has an inbuilt gearbox with a gear reduction ratio of 1:1800 which is in turn coupled to a second-stage gearbox of gear ratio 1:25. The test setup has a torque sensor capable of measuring a maximum torque of 50 Nm to measure the resistance offered by soil. The data is logged using data acquisition and control system. The test progress is monitored using a GUI screen.

A provision to vary the motor rpm is incorporated in the setup to study the rate-dependent shear behavior of soil and to establish the viscous parameters of very soft soil. The setup also has an arrangement for loading the deadweights for applying a constant normal pressure ranging from 5 to 15 kPa and an arrangement for lifting and lowering the test plates. A linear variable differential transformer (LVDT) of measurement range 500 mm is also provided in the test setup for recording the static and dynamic sinkage under various normal stresses. For the study of variation of ring size, number, and height of pin on the shear stress–shear displacement curves, no normal load is applied on the shear ring.

#### 3.2 Preparation of Soil

Experiments were performed on bentonite mud mixed with potable water to simulate properties similar to that of the deep-sea soil. Deep-sea soil at the CIOB has been

**Table 1** Shear ring configuration

Sl. No.	Parameters		Type 1	Type 2	Type 3
1	Plate sizes	Outer dia (mm)	200	250	300
		Inner dia (mm)	80	190	240
2	Height of pin (mm)		20	40	60



**Fig. 5** Bevameter shear test setup: **a** bevameter shear tester, **b** shear ring, **c** data acquisition system

noted to be predominantly soft clays with high water content [4]. Similar soft soil bed has been made by mixing bentonite and water in a tank of dimensions 8 m × 3 m and depth about 0.8 m and mixed using an electrically operated mixer (Fig. 6).

The water content of the bentonite mixture was varied to obtain various shear strengths. For the bevameter tests, bentonite was mixed with water to obtain shear strength ranging from 1 to 3 kPa. The bentonite bed was divided into grids in order to perform the parametric study. Average shear strengths were determined using a manually operated field vane of diameter 0.15 m and height 0.20 m as shown in Fig. 7.

**Fig. 6** Bentonite mixing in bentonite tank



### 3.3 Test Procedure

The shear ring was lowered into bentonite bed by means of a rack and pinion arrangement. After contact with soil surface, dead load was transferred to the soil by releasing the pin for normal stress variation studies. The soil was then sheared by rotating the shear ring at a specified rate, and the resulting torque was measured with a torque

**Fig. 7** Vane shear testing of bentonite





sensor. The test was repeated to study the effect of variables like ring size, number of blades, height of blade, and normal stress. In order to study the effect of variables like ring size, number of blades, and height of blade, experiments were performed as defined in Indian standards for in situ vane shear test [14]. The shear angle was calculated from the shear rate and time of operation. The tests were performed till the residual shear strength values were sensed and recorded.

The shear stress was estimated from the measured torque as follows:

$$\tau = \frac{2T}{\pi \left( \frac{1}{6}(d_o^3 - d_i^3) + h(d_o^2 + d_i^2) \right)} \quad (4)$$

where

- $\tau$  is the shear stress
- $T$  is the measured torque
- $d_o$  is the external diameter of the annular ring
- $d_i$  is the inner diameter of the annular ring
- $h$  is the height of the blade of shear ring.

The shear displacement is obtained as follows:

$$j = \frac{r_o + r_i}{2} \times \alpha \quad (5)$$

where

- $r_o$  is the external radius of the annular ring
- $r_i$  is the inner radius of the annular ring
- $\alpha$  is the measured shear angle.

The shear stress–shear displacement curve was thus plotted using the above-mentioned estimates.

## 4 Result and Discussion

Experiments to analyze the effect of number of blades of shear ring on the shear behavior were performed for number of blades 4, 6, and 12 for various ring configurations. The height of the blades of shear ring was maintained as 40 mm for experiments varying the number of blades. The results are shown in Figs. 8, 9, and 10. Experiments with two blades were performed on Types 1 and 2 shear rings to observe the difference in shear behavior.

Experimental results show a decrease in peak shearing resistance with a decrease in the number of blades. However, no significant difference in behavior was observed for higher number of blades 6 and 12. There was significant difference in the residual shear strength values with a variation in the number of blades. The residual shear strength was lowest for the 12-blade configuration which can be attributed to the

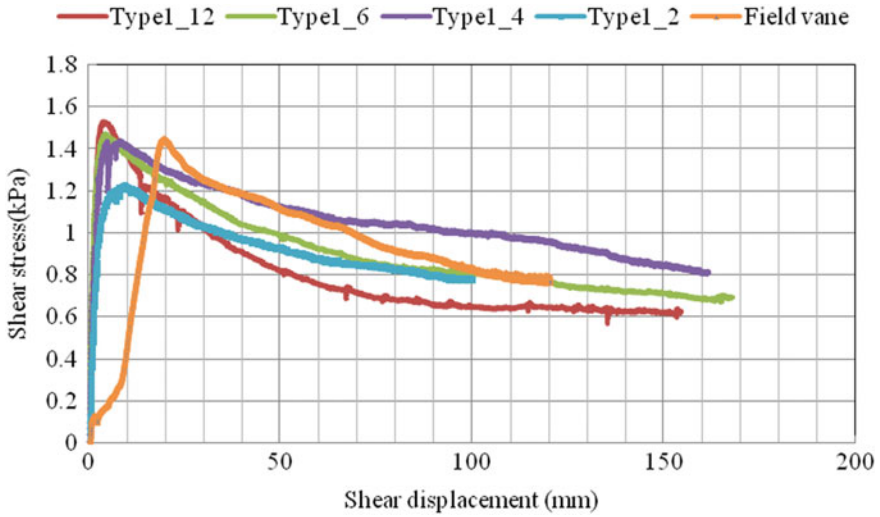


**Fig. 8** Effect of number of blades on shear behavior—Type 1 (where, Type1\_12 is the Type 1 with 12 numbers of blades, Type1\_6 is the Type 1 with 6 numbers of blades, Type1\_4 is the Type 1 with 4 numbers of blades, Type1\_2 is the Type 1 with 2 numbers of blades, Field vane is the In Situ Vane Shear Test Apparatus)

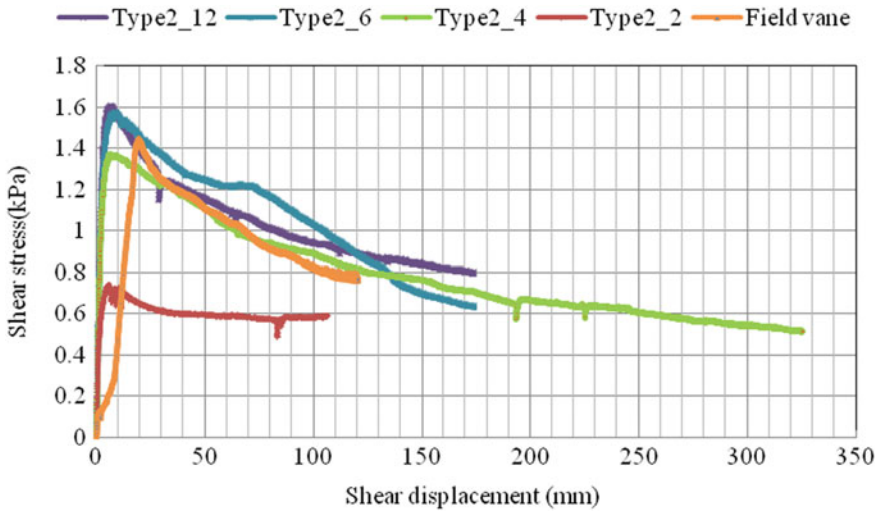


**Fig. 9** Effect of number of blades on shear behavior—Type 2

higher disturbance caused by more number of blades. The expression for computation of shear stress from the measured torque is independent of the number of blades.

A comparison of shear behavior observed using annular shear ring and field vane shear shows that displacement required to mobilize the shear resistance is higher in

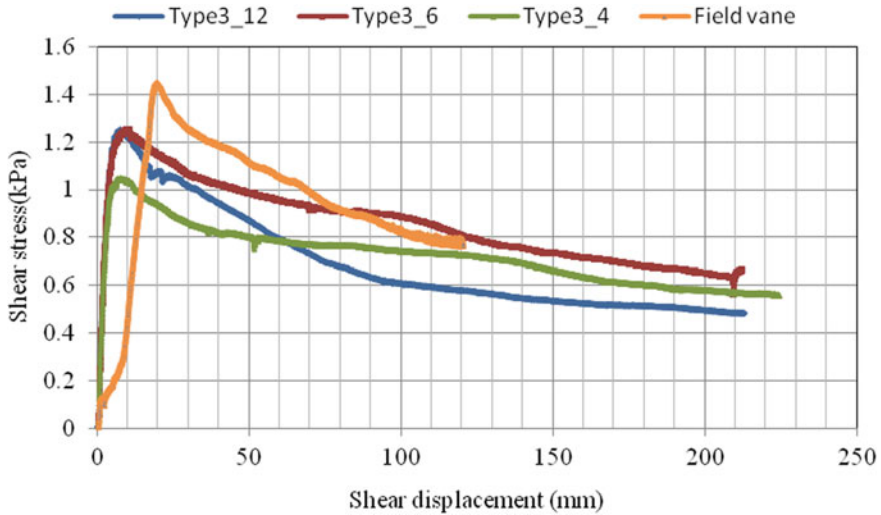


Fig. 10 Effect of number of blades on shear behavior

case of field vane. The parameters  $K_w$  and  $K_r$  required for estimating traction were computed from the shear stress vs shear displacement curves. The value of  $K_w$  ranges from 3.7 to 9.7 mm, and  $K_r$  ranges from 0.4 to 0.8.

The trend observed was confirmed by repeating the shear test on soil of slightly higher shear strength. The results are shown in Fig. 11. The residual shear strength was found to decrease with increase in the number of blades as observed for tests on lower shear strength soil. However, the peak values did not follow the same trend.

Experiments were also performed for various heights of blades 20, 40, and 60 mm for various shear ring configurations. The number of blades was maintained as 12 for these tests. The results are shown in Fig. 12. Experiments on various heights of blades show that lower the blade height, higher the peak shear strength. The residual shear strength also decreases with the increase in blade height for all the ring configurations. The value of  $K_w$  ranges from 3.8 to 8.9 mm, and  $K_r$  ranges from 0.2 to 0.5.

It can be inferred from these tests that an undercarriage track with less pitch having more grousers for the same contact length decreases the residual shear strength of soil resulting in more sinkage. Very high pitch may also cause a reduction in peak shear strength as full shear strength may not be mobilized in such cases. Similarly, an increase in grouser height may also decrease the peak and residual strength as observed from the bevameter studies on height of blades. There is an optimum value of pitch and height which should be arrived based on experiments on large-scale models or numerical methods.

The effect of normal stress on shear behavior was also examined experimentally on annular shear ring with outer diameter 250 mm and inner diameter 130 mm. The height of the blades was fixed as 20 mm and number of blades 12 for the normal

stress variation studies. Tests were performed under zero normal stress and normal stress ranging from 5.2 to 9.2 kPa in 1 kPa increments.

The shear ring was lowered to establish contact with soil, and then, load pin was released to transfer the load onto soil. Static and dynamic sinkage values was measured using LVDT mounted on the bevameter shear setup. Tests were performed for higher normal stress by adding more deadweights.

The test results are shown in Fig. 13. It was observed that residual strength was increasing at higher displacements at higher normal stresses. This might be because the soil fails in shear at higher loads and the failed soil which accumulated on the top of the ring was creating additional torque. Peak shear stress values failed to show any trend for the normal stresses considered. Static and dynamic sinkage values recorded using LVDT for a normal stress of 8.2 kPa are shown in Fig. 14. As shown in Fig. 14, dynamic sinkage values were not stabilized at higher stresses as the tests were stopped once the residual shear strength was reached.

Static and dynamic sinkage values recorded for various normal stresses are shown in Table 2. As expected, static sinkage values are negligible for normal stress below 7.2 kPa. However, dynamic sinkage values are high and found to increase with the increase in normal load. It can be noted from these tests that dynamic sinkage of mining machine is critical and needs to be determined for the safe maneuverability of mining machine.

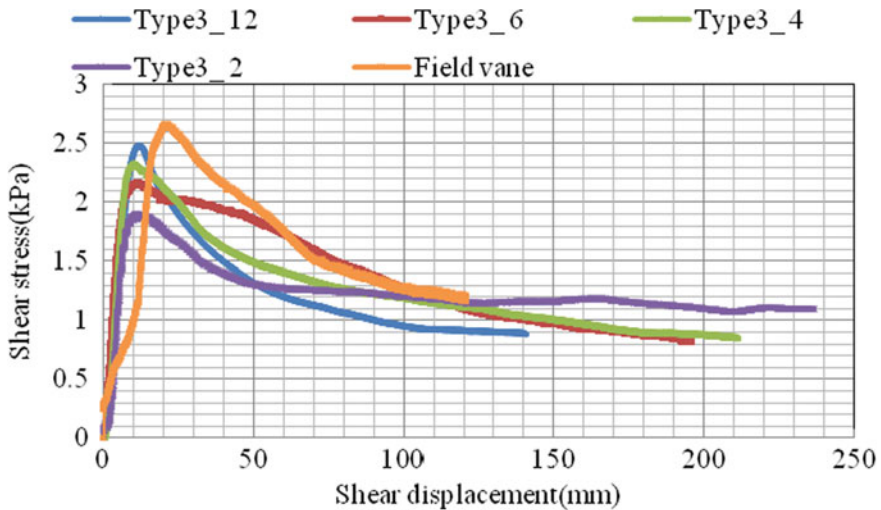


Fig. 11 Effect of number of blades on shear behavior for higher shear strength

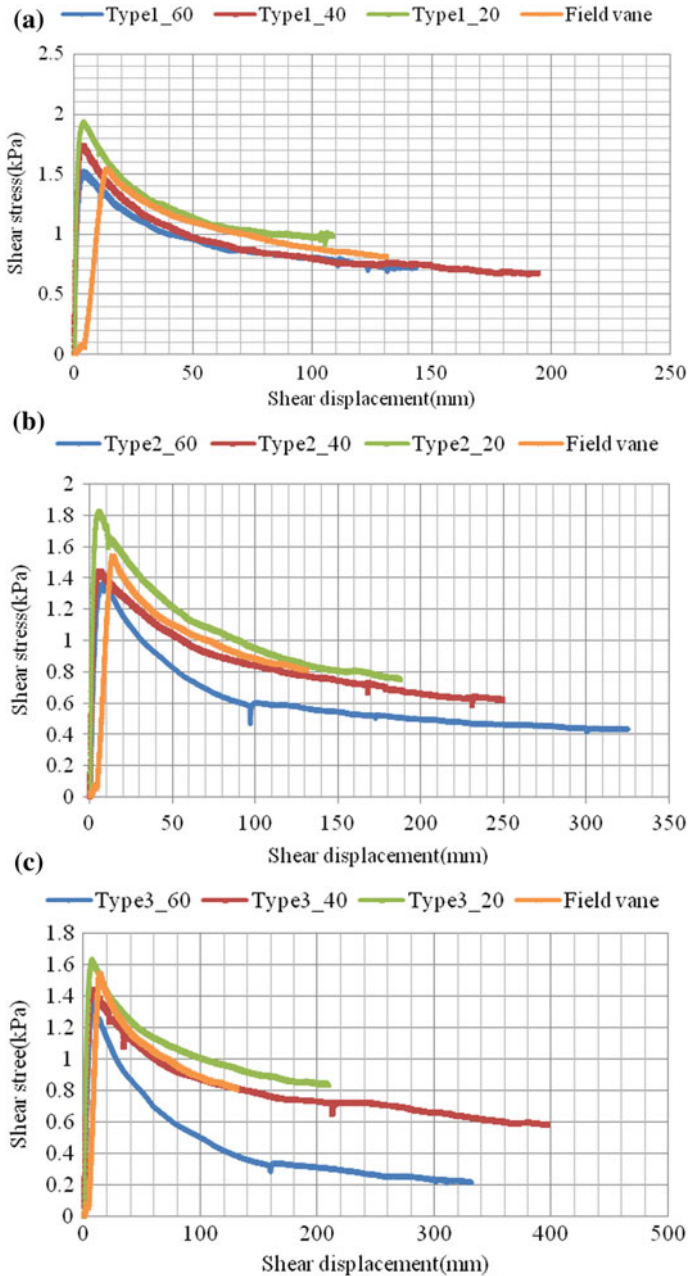
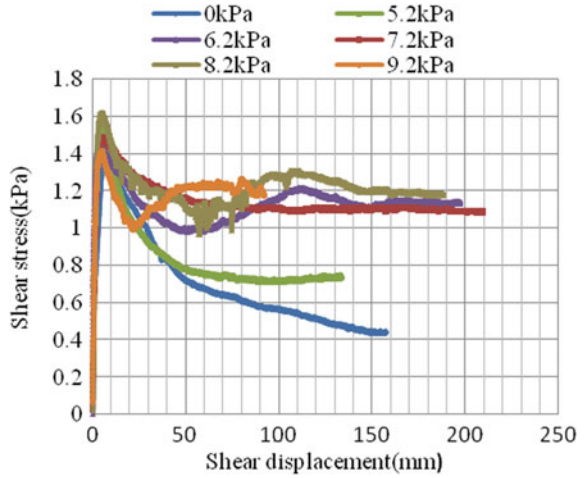
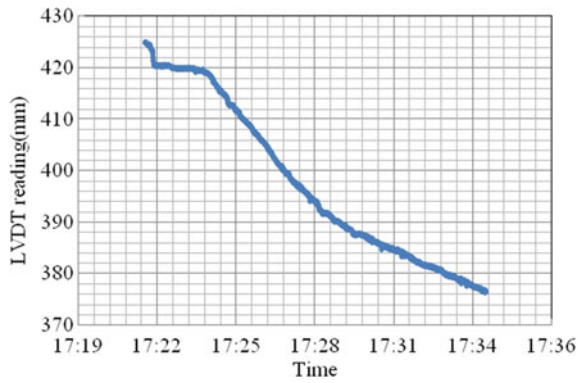


Fig. 12 Effect of height of blades on shear behavior: a Type 1, b Type 2, c Type 3 configuration

**Fig. 13** Effect of normal stress on shear behavior for Type 3 configuration



**Fig. 14** Static and dynamic sinkage for Type 3 configuration



**Table 2** Static and dynamic sinkage

Sl. No.	Bearing strength (kPa)	5.2	6.2	7.2	8.2	9.2
1	Static sinkage (mm)	1	3	3	4.5	9
2	Dynamic sinkage (mm)	6	26.69	39.77	42.77	58.69

## 5 Conclusion

The parameters  $K_w$  and  $K_f$  required for estimating traction were deduced from the tests. Bevameter shear tests on varying blades with blade height and rate of shear maintained as constant showed a decrease in residual strength for higher number of blades irrespective of the ring size. Experiments on various heights of blades with number of blades and rate of shear maintained as constant showed that lesser the height of blades, higher the peak and residual shear strength. For normal stress variation studies, residual strength was found to be increasing at higher displacements for higher normal stresses. Static sinkage values are negligible for normal stresses below 7.2 kPa, and dynamic sinkage values are high and found to increase with the increase in normal load.

It is indented to establish an optimum value of grouser height and pitch of under-carriage track using numerical models after validating with the experimental data presented in this study. Dynamic sinkage needs to be established for the mining machine as it may become critical for the locomotion of mining machine. It is also indented to study the effect of rate of loading on the shear behavior of soil using this test setup. The test setup can also be used to determine the viscous parameters of very soft clays by performing tests at various shear rates which is a valuable input for numerical modeling.

**Acknowledgements** The authors sincerely thank Ministry of Earth and Sciences, Government of India, for funding the technology development programs of deep-sea technologies group of NIOT and for encouraging us to carry out the research work.

## References

1. Deepak CR, Shajahan MA, Atmanand MA, Annamalai K, Jeyamani R, Ravindran M, Schulte E, Panthel J, Grebe H, Schwarz W (2001) Developmental tests on the underwater mining system using flexible riser concept. In: Proceedings of 4th ocean mining symposium of international society of offshore and polar engineers, Szczecin, Poland, 23–27 Sept 2001
2. Rajesh S, Gnanaraj AA, Velmurugan A, Ramesh R, Muthuvel P, Babu MK, Ramesh NR, Deepak CR, Atmanand MA (2011) Qualification tests on underwater mining system with manganese nodule collection and crushing devices. In: Proceedings of the ninth ISOPE ocean mining symposium, Maui, Hawaii, USA, 19–24 June 2011
3. Khadge NH (2000) Geotechnical properties of surface sediments in the INDEX area. *Mar Georesour Geotechnol* 18:251–258
4. Khadge NH (1992) Geotechnical Properties of deep sea sediments from the Central Indian Ocean Basin. *Indian J Mar Sci* 21:80–82
5. Muthukrishna Babu S, Ramesh NR, Muthuvel P, Ramesh R, Deepak CR, Atmanand MA (2013) In-Situ soil testing in the Central Indian Ocean Basin at 5462 m water depth. In: Tenth ISOPE ocean mining and gas hydrates symposium, 22–26 Sept, Szczecin, Poland
6. Yamazaki T, Komine T, Kawakami T (2005) Geotechnical properties of deep-sea sediments and the in-situ measurement techniques. In: Proceedings of the sixth ISOPE ocean mining symposium, 9–13 Oct, Hunan, China, pp 48–55

7. Morgan N, Cathie D, Pyrah J, Steward J (2007) Tracked subsea trencher mobility and operation in soft clays. In: Proceedings of the seventeenth (2007) international offshore and polar engineering conference, 1-6 July, Lisbon, Portugal, pp 1366–1373
8. Bekker MG (1969) Introduction to terrain-vehicle systems. University of Michigan Press
9. Schulte E, Schwarz W (2009) Simulation of tracked vehicle performance on deep sea soil based on soil mechanical laboratory measurements in bentonite soil. In: Proceedings 8th ocean mining symposium of international society of offshore and polar engineers, Chennai, India, 20–24 Sept 2009
10. Hong S, Choi J-S (2001) Experimental study on grouser shape effects on trafficability of extremely soft seabed. In: Proceedings of the fourth ISOPE ocean mining symposium, 23–27 Sept, Szczecin, Poland, pp 115–121
11. Apfelbeck M, Kuß S, Rebele B, Schafer B (2011) A systematic approach to reliably characterize soils based on Bevameter testing. *J Terramech*
12. Wong JY (2001) Theory of ground vehicles, 3rd edn. Wiley Inc., USA, pp 144–153. ISBN 0-471-35461-9
13. Grebe H, Schulte ES (2005) Determination of soil parameters based on the operational data of a ground operated tracked vehicle. In: Proceedings of 6th ocean mining symposium of international society of offshore and polar engineers, Changsha, Hunan, China, 9–13 Oct 2005
14. IS 4434-1978 Indian standard code of practice for In-situ vane shear test for soils



**Part VI**  
**Petroleum Engineering & Technology**

# Estimating Belowground Free Phase Gas (FPG) in Tropical Peatlands of South-West Coast of India Using Ground Penetrating Radar (GPR)



Koravangatt Devi and Rajesh R. Nair

**Abstract** The south-west depression of Kerala-Konkan onshore peatland is one of the most promising areas for shallow biogenic methane existence in India. The shallow biogenic methane gas in the area is intimately linked to the sedimentary environments and palaeo-drainage system emerged due to the evolution of the West coastal system as the result of sea level fluctuations. Depressions caused by such fluvial incisions were drowned and filled up by sediments during a subsequent transgression in the study sites. The main purpose of this study is to identify the spatial distribution of hotspots by surface-based non-invasive GPR surveys as the tool for estimating free phase gas fractional volume from multi-offset profiles by using Complex Refractive Index Model (CRIM). The peat layers of Holocene–Pleistocene age in the sub-coastal areas of Southern Kerala Sedimentary Basin (SKSB) were mapped with ground-penetrating radar (GPR) with frequencies of 100 MHz. The formation of biogenic gas from the peat is either by acetate fermentation pathway or CO<sub>2</sub> reduction pathway and is accumulated as the by-product of anaerobic decomposition of organic materials. The escape biogenic methane encountered at the depth of 3–4 m and 16–18 m on the coastal inland area few kilometre far from the present coastline. Cross-sectional plots display the spatial variation of gas dynamics identified based on the shadow zone due to the variations in electromagnetic wave velocity and amplitude of radar signals have significant correlation with direct measurement of free phase gas (FPG) volume. A conceptual model developed from the present study based on the escape or loss of methane from peatlands via two mechanisms—one, by shallow diffusion and episodic ebullition (from 3 to 5 m depth) of methane from the peat pores matrix and second is, the deep ebullition (from >16 m depth) processes due to the breakage of confining woody peat layer, which causes a large rates of abrupt escape of methane from peatlands to the atmosphere evidenced by the GPR measurements.

---

K. Devi (✉) · R. R. Nair

Department of Ocean Engineering, IIT Madras, Chennai, India  
e-mail: [k.devi190@gmail.com](mailto:k.devi190@gmail.com)

R. R. Nair

e-mail: [rajeshnair@iitm.ac.in](mailto:rajeshnair@iitm.ac.in)

© Springer Nature Singapore Pte Ltd. 2019

K. Murali et al. (eds.), *Proceedings of the Fourth International Conference in Ocean Engineering (ICOE2018)*, Lecture Notes in Civil Engineering 22,  
[https://doi.org/10.1007/978-981-13-3119-0\\_63](https://doi.org/10.1007/978-981-13-3119-0_63)

**Keywords** Biogenic methane · Ebullition · Ground-penetrating radar · Peatlands Kerala

## 1 Introduction

Peatlands are a type of wetlands formed by the slow accumulation of partly decayed vegetal matter deposited in a basin flooded with water, prevents oxygen flow from atmosphere and forms an anoxic condition leads to a slow decay of organic matter. These are locations are well known for the generation, accumulation and release of methane. Though south-west India has extensive wetland system in which the total estimated wetland area of Kerala extends up to 1279.30 km<sup>2</sup> comprising 342 km<sup>2</sup> of “inland wetlands” and 937.30 km<sup>2</sup> of “coastal wetlands” [1], stands first in having large area of wetlands in India [2], received less attention except peat swamp of (a) Late Pleistocene from Nilgiri Hills of 2,000 m above mean sea level in south India [3] and in (b) basin of Himalayan mountains [4]. Both these studies were limited to exploring the palaeoclimate potential of this unique sedimentary record. The biogenic gas has formed in two pathways: (1) acetic fermentation pathway and, (2) CO<sub>2</sub> reduction pathway [5–9]. The acetic fermentation pathway is primarily linked with continental freshwater environments, while CO<sub>2</sub> reduction pathways occur largely in marine environments [6, 7].

The study of quaternary peat deposits in west coast of India has been done by many researchers [8–10] for palaeoclimate reconstruction [11], landform evolution [12] and palynological studies [13]. Our study is the first attempt into explore the shallow deposits methane associated with the peat using ground-penetrating radar method. The main goal of our study is to estimate the spatial and vertical variations in of biogenic gas saturation and dynamics in SW coast of India, especially Alappuzha region, which is selected as the most potential site established from ground-penetrating radar (GPR) studies and supported by direct gas flux measurement.

## 2 Study Area

The study site, Alappuzha, SW coast of India (9°13.624' N–76°32.533' E) located in ~2 km far from present-day coastline falls under Viyyam formation. The litho-units of Viyyam surface comprises fluvio-marine deposits and the formation consists of the deposits of tidal flats, mud flat, estuarine landforms, kol land and delta. The distinct lithology in this formation consists of a top layer of black/grey black, sticky, plastic clay with pockets of fine sand (~50 cm thick), followed by a middle layer of black clay with shells and buried wood (~1 m thick) and lastly a black organic clay layer of >1 m thick. The low land area of Alappuzha, occurred with thick pile of buried wood at shallow depth is reminiscent of subsidence of the terrain and burial of luxuriant mangrove forest that existed along coastal area. The rapid and complete

carbonization of this buried wood undergoes with lower sandy stratum and upper clay layer with overburden pressure. The resultant carbonized wood has been found in highly decomposed state and preserved in sheath of sediments in west coast of India [14]. During this process of carbonization methane evolved and getting trapped by overlain clay (Fig. 1).

### 3 Methodology

#### 3.1 Ground-Penetrating Radar

The non-destructive electromagnetic (EM) technique, GPR has been used for this shallow subsurface investigation to reveal the internal stratigraphy and FPG accumulation in peatlands by using common offset method and common midpoint method (CMP) with GSSI's 100 MHz antennas. In the first method, both transmitter and

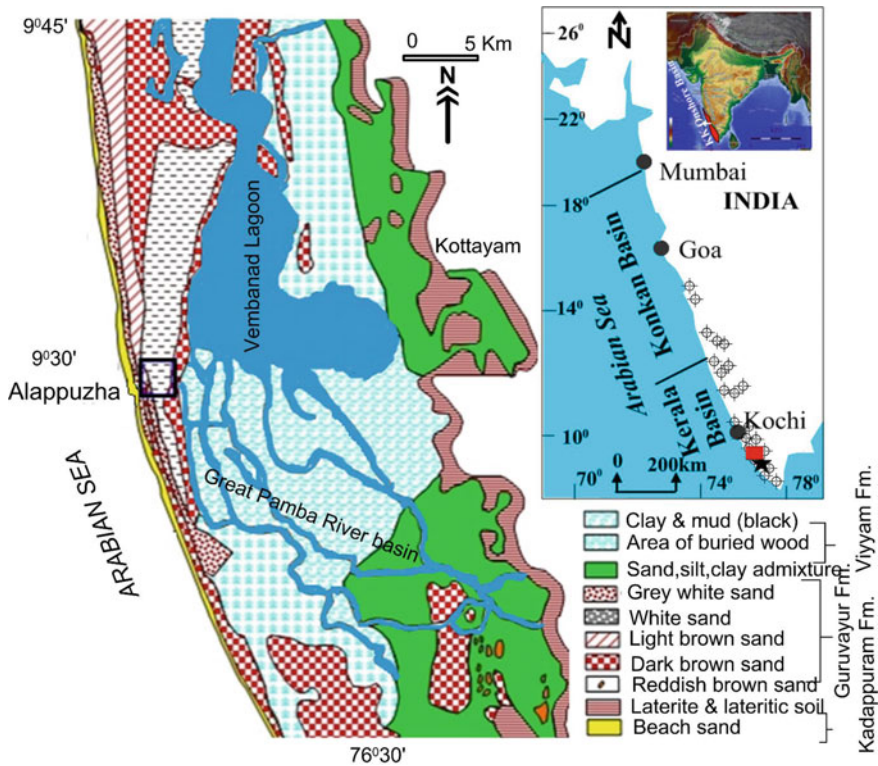


**Fig. 1** Study area in Alappuzha, where extensive study carried out and inset map showing the GPR data acquired locations along SW coast of India, modified from [1]

receiver kept in a fixed distance and move along the ground to image the stratigraphy, peat depth and confining layers from EM wave two-way travel time. The presence of FPG results EM wave scattering with attenuated signals in radargrams [15, 16]. The second type of data collection by moving transmitter and receiver from a centre point stepwise and records velocity profiles from offset-depth graph. The radargrams from both the methods processed by applying band-pass filtering and gain function in each wavelet to enhance signal-to-noise ratio.

The EM velocity ( $v$ ) used to determine spatial and vertical variability of FPG in peatlands [17], and it is related to relative dielectric permittivity ( $\epsilon_r$ ) (Eq. 1) which is dependent on moisture content ( $\theta$ ) in the soil and hence gas content.

$$v \approx \frac{c}{\sqrt{\epsilon_r}} \quad (1)$$

The travel time changes in the CMP estimated for each reflector related to the gas content accumulation within the peat and adjacent layers. For that, we have adopted petrophysical model, otherwise known as Complex Refractive Index Model (CRIM) (Eq. 2), which is a three-phase soil mixing model [gas ( $a$ ), water ( $w$ ) and soil ( $s$ )] to estimate gas contents from EM wave velocities [18].

$$\epsilon_b^\alpha = \theta \epsilon_w^\alpha + (1 - n) \epsilon_s^\alpha + (n - \theta) \epsilon_a^\alpha \quad (2)$$

The equation has rewrite to calculate  $\theta$ , since porosity ( $n$ )—volumetric water content ( $\theta$ ) is the gas content.

$$\theta = \frac{\epsilon_b^\alpha - (1 - n) \epsilon_s^\alpha - n \epsilon_a^\alpha}{\epsilon_w^\alpha - \epsilon_a^\alpha} \quad (3)$$

In Eqs. (2) and (3),  $\alpha$  indicates orientation of EM field to the soil, here for peat it assumed as 0.35 [19–22]. As GPR is an indirect measurement method, the direct gas emission measurement from the ground is necessary to calibrate the results.

## 4 Results and Discussions

The stratigraphy of Alappuzha peatlands revealed by common offset radargrams displayed as EM wave travel time through layers with varying contrasting dielectric contrast (Fig. 2). Lithological units are differentiated based on the amplitude of EM waves correlated with borehole data (Fig. 2c). The six units identified with their reflectors geometry with continuous nature on upper layers with feeble signal scattering. The top sand layer is coarse nature probably accumulated by high energy

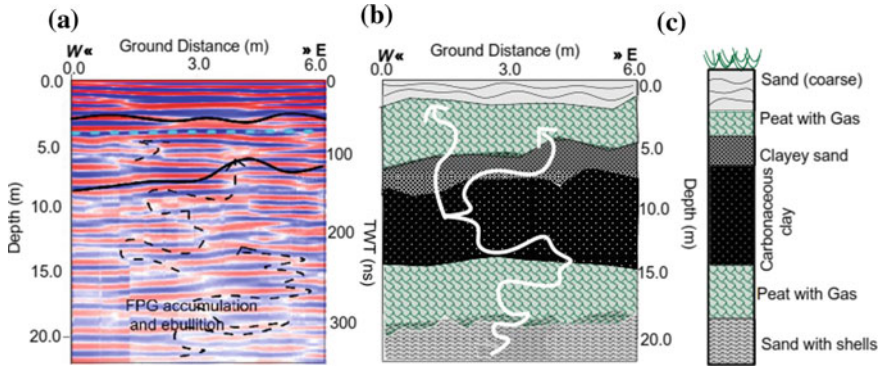


**Fig. 2** Surface constant offset GPR profiles collected from Alappuzha using 100 MHz monostatic antenna shows **a** Processed radargram showing absence of EM shadow zone at depths of 5 and 18 m overlie by high amplitude reflections of carbonaceous clay and peat **b** interpreted stratigraphic units and pathway of biogenic gas escaping to the surface shown by white arrow **c** borehole data collected from the site by drilling [23]

process. The thick peat layers at two different depths might be formed during Early to Middle Holocene sea level rise by the submergence of coastal lowland mangrove forests. These buried vegetal matter decomposed under anaerobic condition (created by transgression flooding) by methanogens generates the biogenic methane trapped within the peat under favourable conditions or migrated through the weaker zone and release to the atmosphere. The scattering of EM wave energy coincides with the biogenic pathway or accumulation and the strong reflectors with high amplitude reflections are the confining layers act as the trapping mechanism of generated biogenic gas [24, 25].

Figure 3 shows six reflectors have interpreted from CMP analysis in which peat layers lies in average depths of ~5 and ~17 m coincides with velocity of 0.0385 m/ns. Course sand layer on the top layer with velocity of 0.055 m/ns boosts the methane diffusion from peat layers to atmosphere. The clayey sand at the depth of ~7 m with velocity of 0.07 m/ns overlies the thick carbonaceous clay of ~6 m thickness with velocity of 0.08 m/ns creates confined strata to trap the biogenic methane generated from peat layers positioned in ~17 m depth peat layers. The installation of borehole sample collection results methane escape to the surface may be due to the disturbance in the confining layers. Peat itself acts as source and reservoir. Figure 2 shows an “EM blanking” with migration pathways through the weaker zones in the strata to the surface. The volume of methane emission from varies vertically throughout the profile in arrange of 0–39%.

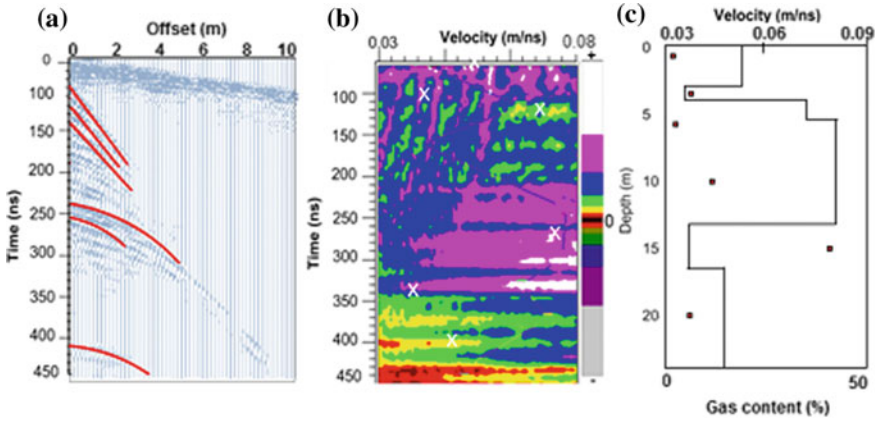


**Fig. 3** a CMP profile b semblance plot c gas content scale is calculated from the CRIM model. 1-D vertical velocity model showing CRIM-estimated gas content ranges from 0 to 40%

Conceptual model in FPG release and storage in peatlands has developed from this study (Fig. 4a) by comparing two existing models from Northern Peatlands. From the GPR investigation, we have developed a “ultra deep model” in which gas trapped by confined layer at depths of 4–5 m and >16m from where FPG is released either by steady or episodic ebullition pathways in SW Indian Peatlands. The existing two models are “shallow” and “deep” peat model by considering different patterns of gas accumulation and release [28]. In “deep gas” model, the methane bubbles formed from around 1 m depth and accumulated below the confined woody peat layer [26]. The ebullition events are related to this mode, in which huge amount of methane escaped to the atmosphere in short interval of time, also related to the drop in atmospheric pressure. In “shallow gas” peat model, FPG accumulates close to the upper peat layer below the depth of 1 m and it loses to the atmosphere by diffusion [27] due to the absence of confined wood to trap the escaping gas [28].

## 5 Conclusions

Current study demonstrates the spatial variations of EM wave shadow zone coincide with area of biogenic gas accumulation at the depth of ~4–5 m and >16 m in Alapuzha peatlands of SW India. Higher concentrations of free phase gas relate to the peat layers have EM wave velocity of 0.038 m/ns recorded in CMPs and common offset profiling correlate with shadow zones. The presence of strong reflectors above shadow zones represents confining layers with carbonaceous clay act as gas traps. The subsurface saturation of biogenic gas is 0–39% with dominating methane of ~92% from isotopic studies (unpublished data). These findings also have implications for

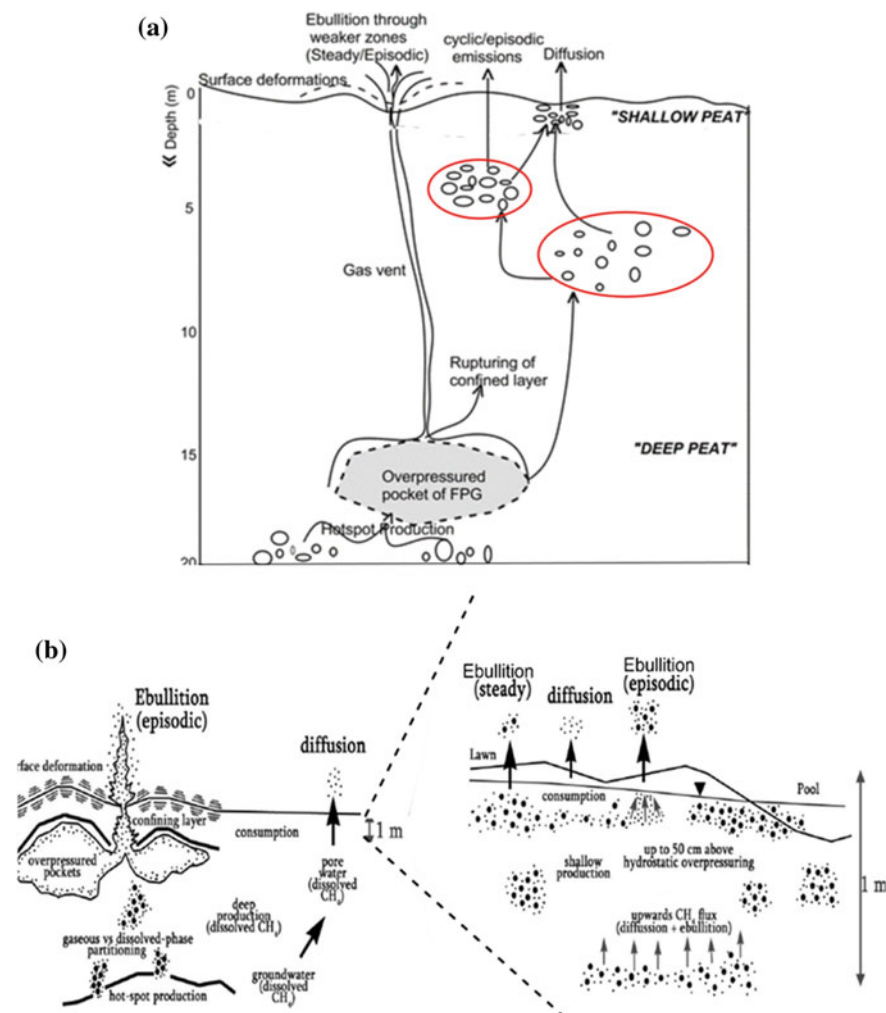


**Fig. 4** a Illustrate conceptual model of methane formation and escape mechanisms in the study area. The figure modified from b “deep peat” ebullition model (>1 m) [27] and “shallow peat” (<1 m) ebullition model modified from [28], in northern peatlands. The upward flux of biogenic gas from the study area occurs at two different depths (~4–5 m and >16 m) categorized as “ultra-deep peat models”

the monitoring of spatial and temporal behaviours and variability of biogenic gas emissions from south-west Indian Peatlands.

**Acknowledgements** Authors are thankful to the laboratory fellows who helped to collect GPR data from the field and grateful for the financial support provided by Gas Authority of India Limited and IIT Madras to carry out this research.



## References

1. Nair KK (2007) Quaternary geology and geomorphology of the coastal plains of Kerala. Geological Survey of India, Special publications 73
2. Nayar S, Nayar NM (1997) Wetlands. In: Thampi KB, Nayar NM, Nayar CS (eds) The natural resources of Kerala. WWF State Office, Trivandrum, pp 369–374
3. Rajagopalan G, Sukumar R, Ramesh R, Pant RK, Rajagopalan G (1997) Late quaternary vegetational and climate changes from tropical peats in southern India extended record up to 40,000 years BP. *Curr Sci* 73:60–63
4. Phadtare NR, Pant RK (2006) A century-scale pollen record of vegetation and climate history during the past 3500 years in the Pinder Valley, Kumaon Higher Himalaya, India. *J Geol Soc India* 68:495–506
5. Rice DD, Claypool GE (1981) Generation, accumulation, resource potential of biogenic gas. *AAPG Bull* 65:5–25
6. Whiticar MJ, Faber E, Scheoll M (1986) Biogenic methane formation in marine and fresh-water environments: CO<sub>2</sub> reduction versus acetate fermentation-isotope evidence. *Geochim Cosmochim Acta* 50:693–709
7. Whiticar M (1989) A geochemical perspective of natural gas and atmospheric methane. *Org Geochem* 16:531–547
8. Mascarenhas J (1993) Molecular mechanisms of pollen tube growth and differentiation. *Plant Cell* 5:1303–1314
9. Rajendran CP, Rajagopalan G, Narayanaswamy (1989) Quaternary geology of Kerala: evidence from radiocarbon dates. *J Geol Soc India* 33:218–222
10. Nair KM, Padmalal D, Kumaran KPN, Sreeja R, Limaye RB, Reji S (2010) Late quaternary evolution of Ashtamudi-Sasthamkotta lake systems of Kerala, south west India. *J Asian Earth Sci* 37:361–372
11. Kumaran KPN, Nair KM, Shindikar M, Limaye RB, Padmalal D (2005) Stratigraphical and palynological appraisal of the late quaternary mangrove deposits of the west coast of India. *Q Res* 64:418–431
12. Padmalal D, Kumaran KPN, Nair KM, Baijula B, Limaye RB, Vishnu Mohan S (2011) Evolution of the coastal wetland systems of SW India during the Holocene: evidence from marine and terrestrial archives of Kollam coast, Kerala. *Q Inter* 237:123–139
13. Limaye RB, Kumaran KPN, Padmalal D (2014) Mangrove habitat dynamics in response to Holocene sea level and climate changes along southwest coast of India. *Q Int* 325:116–125
14. Jayalakshmi K, Nair KM, Kumai H, Santosh M (2004) Late pleistocene—holocene palaeoclimatic history of the southern Kerala Basin, Southwest India. *Gondwana Res* 7:585–594
15. Daniels JJ, Roberts R, Vendl M (1995) Ground penetrating radar for the detection of liquid contaminants. *J Appl Geophys* 33:195–207
16. Lopes de Castro D, Branco RMGC (2003) 4-D ground penetrating radar monitoring of a hydrocarbon leakage site in Fortaleza (Brazil) during its remediation process: a case history. *J Appl Geophys* 54:127–144
17. Neal A (2004) Ground penetrating radar and its use in sedimentology: principles, problems and progress. *Earth Sci Rev* 66:261–330. <https://doi.org/10.1016/j.earscirev.2004.01.004>
18. Davis JL, Annan AP (1989) Ground penetrating radar for high resolution mapping of soil and rock stratigraphy. *Geophys Prospect* 37:531–551
19. Huisman JA, Hubbard SS, Redman JD, Annan AP (2003) Measuring soil water content with ground penetrating radar: a review. *Vadose Zone* 2:476–491
20. Parsekian AD, Slater L, Comas X, Glaser PH (2010) Variations in free phase gases in peat landforms determined by ground-penetrating radar. *J Geophys Res* 115:G02002. <https://doi.org/10.1029/2009JG001086>
21. Kellner E, Lundin LC (2001) Calibration of time domain reflectometry for water content in peat soil. *Nord Hydrol* 32:315–332
22. Keller JK, White JR, Bridgman S, Pastor P (2004) Climate change effects on carbon and nitrogen mineralization in peatlands through changes in soil. *Glob Change Biol* 10:1053–1064

23. Kumaran KPN, Nair KM, Shindikar M, Limaye RB, Padmalal D (2005) Stratigraphical and palynological appraisal of the late quaternary mangrove deposits of the west coast of India. *Q Res* 64:418–431
24. Comas X, Slater L, Reeve A (2008) Seasonal geophysical monitoring of biogenic gases in a northern peatland: implications for temporal and spatial variability in free phase gas production rates. *J Geophys Res Biogeosci* 113:G01012. <https://doi.org/10.1029/2007JG000575>
25. Comas X, Terry N, Slater L, Warren M, Kolka R, Kristijono A, Sudiana N, Nurjaman D, Darusman T (2015) Imaging tropical peatlands in Indonesia using ground penetrating radar (GPR) and electrical resistivity imaging (ERI): implications for carbon stock estimates and peat soil characterization. *Biogeosciences* 12:2995–3007. <https://doi.org/10.5194/bg-12-2995-2015>
26. Romanowicz EA, Siegel DI, Chanton JP, Glaser PH (1995) Temporal variations in dissolved methane deep in the Lake Agassiz Peatlands, Minnesota. *Global Biogeochem Cycles* 9:197–212
27. Glaser P, Chanton H, Morin P, Rosenberry DO, Siegel DI, Ruud O, Chasar LI, Reeve AS (2004) Surface deformations as indicators of deep ebullition fluxes in a large northern peatland. *Global Biogeochem Cycles* 18:GB1003. <https://doi.org/10.1029/2003gb002069>
28. Coulthard T, Baird AJ, Ramirez J, Waddington JM (2009) Modelling methane dynamics in peat: future prospects, in *Northern Peatlands and Carbon Cycling*. In: Baird AJ et al (ed) AGU, Washington, D. C. vol 184, p 299

# Integrating, Predicting and Preventing Flow Assurance Issues—A Review



Anchit Khanna  and Samarth Patwardhan 

**Abstract** This paper reviews the multiple aspects of flow assurance problems, from a production standpoint, with an aim to provide a deeper understanding of the work that needs to be done to mitigate them. It is seen in multiple case studies that proposed solutions to specific problems do not work well and need to be reinvestigated. Hydrate plugging, wax deposition and asphaltene and scale build-up are typical flow assurance problems. Generally, it has been seen that, under conducive circumstances, these three issues take place in conjunction with each other, which further intensifies the problem; e.g. low temperatures lead to an acceleration of both hydrate formation and rate of wax deposition. An integrated study of the crude with the surrounding conditions would provide a clearer picture, which would help in diagnosing the best possible measure to prevent it. Work done in this paper builds on the initial overview and discusses methods of assessing and analytically predicting flow assurance problems that might arise during the course of the production. Integrating the three issues together and then predicting the problems that might arise would significantly lower the chances of escalation of the situation. From a safety perspective, the paper further discusses the measures that need to be taken during the planning phase of the project, to omit any future situations of such problems once a risk has been identified during the prediction phase. Preventive measures for each of the three flow assurance problems give an integrated outlook of how to tackle these issues together. This paper further sheds light on how to plan an integrated approach for the management of the flow assurance problems in a multiphase flow system.

**Keywords** Flow assurance · Hydrates · Wax · Asphaltene · Scale

---

A. Khanna (✉) · S. Patwardhan  
Maharashtra Institute of Technology, Pune, India  
e-mail: [anchit16khanna@gmail.com](mailto:anchit16khanna@gmail.com)

© Springer Nature Singapore Pte Ltd. 2019  
K. Murali et al. (eds.), *Proceedings of the Fourth International Conference in Ocean Engineering (ICOE2018)*, Lecture Notes in Civil Engineering 22,  
[https://doi.org/10.1007/978-981-13-3119-0\\_64](https://doi.org/10.1007/978-981-13-3119-0_64)

941

## 1 Introduction

Oil and gas industry is gradually moving towards tougher and hostile environments in search for hydrocarbons. The next frontiers for the same are deepwater and ultra-deepwater reserves, which are being perused currently with great vigil. Besides problems in drilling, exploration and data acquisition in such harsh and inhospitable conditions, continuous and uninterrupted production of fluids from subsea wells to the shore is a huge challenge.

As the name suggests, flow assurance is the discipline where studies are done to assure uninterrupted flow from the reservoir sandface to the processing facility. Guaranteeing continual flow will depend upon the studies of flow assurance issues undertaken to predict and prevent these issues in hindering with the flow. Flow assurance issues may arise from the reservoir energy at hand to the final tieback between the production facility onshore and the subsea wells.

## 2 Understanding Flow Assurance Problems

Flow assurance problems taken up here are broadly considered as solid deposits which coagulate, agglomerate or adhere to the inner surface of the flowline. These solid flow assurance issues can be identified as four major species: (i) asphaltenes, (ii) waxes, (iii) hydrates and (iv) scaling, or a combination of any/all of them.

Asphaltenes are large and heavy polar components of the crude made up of condensed aromatic and naphthenic rings, which also contain heteroatoms. They are soluble in light aromatics such as benzene and toluene but are insoluble in lighter paraffins. Asphaltenes have a tendency to form aggregates in hydrocarbon called micelles, which in turn form a colloidal solution with hydrocarbon. It views that is commonly held is that the asphaltene micelles are stabilized by resins that get adsorbed at their surface and dispersion of these stabilized colloidal form a two-phase system. Problems due to asphaltenes arise in a two-step progression: (i) precipitation from the reservoir fluid and (ii) deposition of the precipitated asphaltene particles, which causes plugging. Deposition of asphaltenes from a hydrocarbon solution is dependent on the pressure, temperature and the composition of the crude.

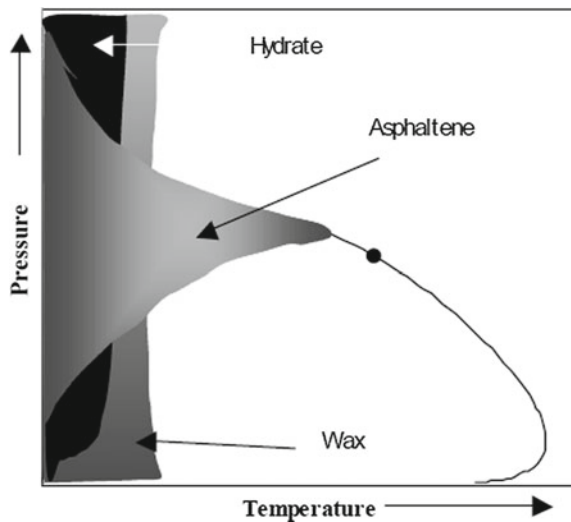
Hydrocarbon waxes are also heavy straight chained paraffins (generally C17+) which when subjected to lower temperatures precipitate out of the solution. Heavier hydrocarbon can be divided into normal (undersaturates like n-paraffins/alkanes) and non-normal (saturates like alkenes/alkynes/cyclic compounds, etc.) components. It is widely believed that only the normal fraction of the crude contributes to wax formation. Wax deposition, just as asphaltene precipitation, is a two-phase concern: (i) nucleation and (ii) crystal growth. Wax appearance temperature (WAT) is the point where the first wax molecules start to precipitate and with further decrease in temperature more and more wax nucleates and start coagulating on the flowline

walls. Further decreasing the temperature, one will encounter the Pour Point (PP) where the fluids viscosity increases exponentially and the fluid ceases to flow.

Natural gas hydrates form under operating condition of low temperatures and high pressures where there is ample supply of free water and gasses like methane, ethane, nitrogen, carbon dioxide, etc. Hydrates are formed when water freezes into a specific lattice called a clathrate structure where there are cavities formed which are occupied by the gas molecules. Microscopic particles of hydrate are formed in suitable pressure and temperature conditions, called gas hydrate stability zone (GHSZ). These particles have very high affinity to adhere to each other and agglomerate to form hydrate plugs which block the flowline. These hydrate plugs do not necessarily form at the point where hydrates start to form, but can be formed downstream as the hydrate slurry is transported with the flow.

Scales are inorganic salts carried by the produced or injected water and are precipitated due to changes in pressure and temperature on different deposition sites along the downstream like valves, pumps, flowlines, etc. If left unchecked, it may start limiting production, finally culminating to complete abandonment of the flow stream. Few common oilfield scales are calcite ( $\text{CaCO}_3$ ), barite ( $\text{BaSO}_4$ ) and celestite ( $\text{SrSO}_4$ ). A general, integrated thermodynamic phase behaviour profile can be seen in Fig. 1. These boundaries represent the pressure and temperature conditions needed for the stability of each flow assurance issue. As understood from the figure, asphaltene stability is a primary function of pressure, whereas the stability of wax and hydrate depend predominantly on the temperature. Each production fluid would have thermodynamic phase boundaries of its own as they depend upon the composition of the produced fluid. Production contingency plans ideally try to omit entering phase transition along flow paths, thus eliminating any risk of solid deposition.

**Fig. 1** Thermodynamic phase boundaries of solids [9]



### 3 Mitigation Methods

#### 3.1 *Early Solutions*

Initially, when it was found out that there are flow assurance problems lurking around the production in a field, it was too late to apply any preventive measures. Instead of focusing on tackling the problem by attacking it at its roots, emphasis was given to remediation of the problem once it occurred.

Asphaltene precipitation could not be predicted impeccably. The pressure in the flowline at which asphaltene starts to precipitate, the asphaltene onset pressure (AOP) could not be foretold. Pigging was the first line of defence followed by use solvents that would subvert the precipitation of asphaltene. With time, as the pressure profile of the system would change with production, the asphaltene problem would rise again.

Wax deposition and coagulation had a similar issue. WAT was seen as the defining parameter to be predicted. But as the temperature profile in the flowlines or the composition of the multiphase fluid flowing in it would change, it resulted in the WAT changing. Pigging and the use of insulation were the first resolutions.

High pressures in the flowlines and low temperatures at the seabed initiated formations of hydrate plugs in the flowline, as most lines had multiphase flow; i.e. water and gas were readily available for gas hydrate formation. These plugs were dissociated by depressurizing or heating, for which the production from the flowline was completely halted. Dissociation of these hydrate plugs was a huge challenge as it is difficult to control the pressure and temperature of a subsea pipeline. Brute force methods like heating the pipeline using different orientations like pipe-in-pipe or electrical heating. Insulations were used to prohibit the temperature to lower into the GHSZ which is expensive and limited by how much power can be generated on a platform. With time, the change in temperature profile caused hydrate plugs to be formed in the tubing of the well itself [15].

Scrapping and usage of anti-scaling agents or scale inhibitors had been used in the industry for a long time but the point of their injection into the flowline varies with each system.

Most of the flow assurance problems encountered in the early developed fields were due to lack of better understanding of the problem and treating each one separately. An integrated approach was required to culminate the available knowledge in a strategy that is laced with improved predictions, prevent better and improves itself with time.

#### 3.2 *Present Day*

Not all flow assurance problems are present in full intensity at every field or production facility. Each field and its parameters are to be understood first, followed

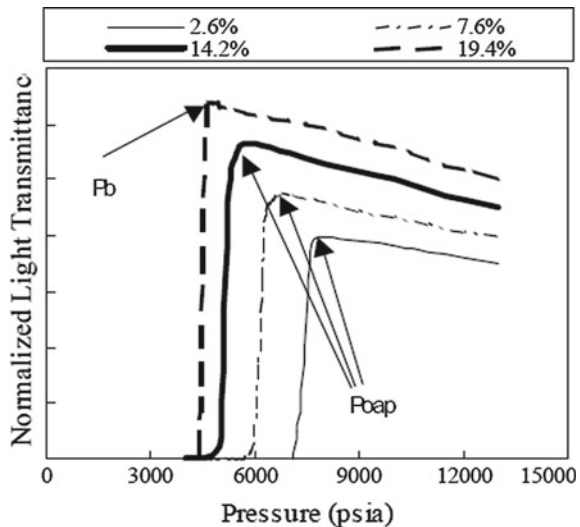
by prediction of the problems that the system may encounter. A case by case study makes it clear that the strategy we use from the pre-development phase to the operation phase defines the stability in flow assurance.

Predicting asphaltene deposition is done on the basis of different laboratory analysis's which mainly depended upon the asphaltene content in the oil. Some of the studies done on oil samples incorporated de-Boer plot [24] and SARA [8] analysis. Another laboratory technique to find the AOP (asphaltene onset pressure) is through a high-pressure microscope. Light transmittance is measured through a sample undergoing isothermal depressurization using an infrared solid detection system (SDS) [12]. A sudden drop in transmittance signifies the asphaltene onset pressure. While designing the flowlines, the engineers must make sure that the pressure in the flowlines should not drop below the AOP [17].

Figure 2 shows how the contamination of produced fluid samples from the bottomhole by the oil-based drilling mud will intervene with the AOP data. Increase in the w/w % of OBM contaminate shows a depression in AOP. Thus, the samples that get contaminated with OBM distillate would not give the best asphaltene estimation and should be discarded [9].

Models pertaining to the problem of wax are related to thermodynamics of wax precipitation. Differential scanning calorimeter (DSC) can be used to find WAT values against a small wax deposition percentage of 0.3%. Wax content (% weight of wax deposited in dead oil w.r.t. the total crude) in a specified crude oil that can deposit, also needs an accurate estimation to formulate mitigation measures. Besides an accurate thermodynamic model, wax prediction calculations require a kinetic model to estimate the rate of wax deposition. The thermo-hydraulics profiles showing the steady-state flow can be plotted against the wax phase envelope, obtained through DSC or through a software modelling of the wax through the n-paraffin components

**Fig. 2** Normalized light transmittance as a function of base oil contamination (Poap-pressure for onset of asphaltene precipitation) [9]



of the crude. A cold finger test is then taken up to find the wax deposition likelihood and the findings are compared with the laboratory data for crudes from other fields which have been previously studied for their wax deposition behaviour [7, 17].

Hydrate formation concerns rise due to low seabed temperatures, where flow-lines laid contain multiphase fluid in them. Compared to other flow assurance problems, hydrates are novel, often form and block pipes at a rapid rate and take a long time to remediate. Multiple different techniques have been developed and successfully applied in the fields. There are brute force methods of heating and insulating the pipeline. The chemical approach is to pump thermodynamic inhibitors such as methanol or mono-ethylene glycol (MEG).

An example of methanol injection strategy in use is at Terra Nova, in the Jeanne d'Arc basin, Canada. Here 2 pumps delivering 5 m<sup>3</sup>/h are used for injecting methanol as the hydrate inhibitor, at a single injection point lying between the wing and the master valve in the Christmas tree. If an unplanned shutdown takes place, the depressurization facilities are not readily available to depressurize the line and shift the system out of the hydrate stability zone. In that case, an option of bull-heading methanol is provided at the subsea 'cold spots', i.e. exposed sections of flexible pipe, the flexible riser, the host manifold piping where the riser connects, the Christmas tree flow-loop piping and any traversing subsea jumpers (found out through dynamic modelling), is available. The situation to bullhead methanol arises due to an unintentional shutdown of the system and provides the operators time to depressurize the system [16].

MEG regeneration systems are used in Albocora field in Campos basin, Brazil [4, 5]. Similar gas hydrate prevention strategy is used at the Ormen Lange field, Norway which is a predominantly gas field. Continuous MEG injection is carried out at individual wellheads. MEG distribution is designed to counter the maximum expected formation water and condensed water produced by individual well based on water production predictions for each well [3, 19].

The major issue with chemical inhibition using methanol or MEG is that very high volumes can be required—sometimes as much as a one-to-one ratio—of the produced formation fluid. Using methanol is almost always a once-through system—you inject it—it comes back to the platform, you process the water and it's disposed appropriately. Methanol also has the significant problem that a certain amount goes to the oil and refineries have a tolerance limit of about 25–50 part per million. For glycol systems, the injection rate is pretty close to the same but when that water comes back with MEG you then have a regeneration system where you boil off the water and you reclaim the MEG, that has a massive CAPEX cost to it, and MEG systems can be problematic with salty water produced from formations.

Scaling is a concern not exclusively found in deepwater but is a concern in onshore production facilities. Jubarte field in the Campos basin, Brazil is an example where scaling was the major hindrance in flow assurance. Inorganic scale deposition was seen on the impeller of the ESP due to accelerated kinetics of sulphate precipitation and stable oil-in-water emulsions were formed due to agitation by the pump. A multipurpose chemical was devised and injected continuously through an umbilical



before the pump which acted as a demulsifier as well as a scale inhibitor. ESP impeller and diffuser were also coated with Teflon to reduce roughness and make scale nucleation difficult [6].

## 4 New Modelling Efforts

As time has passed, our knowledge and understanding of each of the flow assurance problem have grown exponentially. Research in each of the specified problems, its development to its inhibition and eradication, has given rise to a different perspective on each of them.

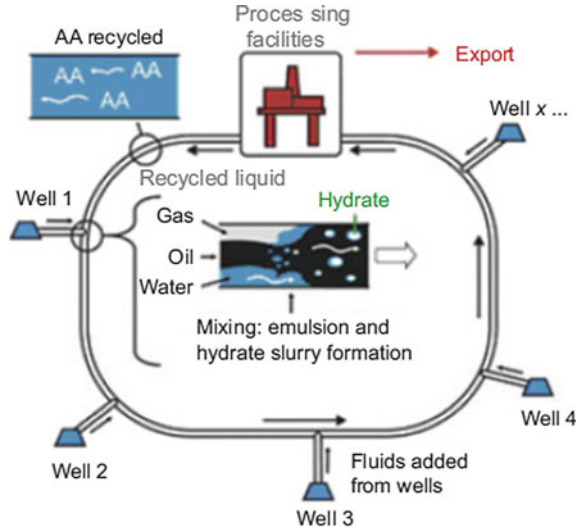
Flow assurance has been defined by a strategy called  $PI^3$  or  $\pi^3$ . This strategy helps us concentrate on the prime issues of the flow assurance discipline. '**Proficiencies**' of the people working in a specialized discipline at an organization are entrusted to provide the best possible solutions to tackle any challenge. Flow assurance is not a subject which can be addressed as one but is an agglomeration of multiple smaller disciplines (multidisciplinary) working together as an '**Integration**' to answer the complete picture of assuring flow. Once the proficiencies are integrated, '**Implementation**' of the strategy that has been drafted is the next priority to ensure smooth and successful operations. '**Improvements**' to the operating conditions and the strategy with time should be introduced based on the field experiences, and these should also be extended to other current as well as future installations as learnings [2].

Novel and innovative technologies to prevent hydrate plug formations are also on the rise. We had earlier seen how hydrate formation in the first place is prevented and thus that subsequently prevents any hydrate plug formation. The technologies termed as cold dry flow and cold wet flow deliberately favour formation of hydrate formation but inhibit their agglomeration. Agglomeration of the hydrate particles is what forms large hydrate plugs in the flowlines which are difficult to dissociate (depressurization or heating) and causes long downtimes. In dry cold-flow scheme, deliberate efforts have been made to convert all free water being produced to gas hydrates and create a multiphase flow regime with gas, oil and hydrate particles. Whereas in a wet cold-flow scheme, all free gas is to be eliminated to form a multiphase slurry with free water, oil and hydrate particles as its components. Excessive water from the sea may be added to convert all free gas to hydrate particles [1–11] (Fig. 3).

Emphasis in these approaches is given to not letting the hydrate particles agglomerate and for a hydrate plug to block the flow line. Anti-agglomeration (AAs) additives are to be added at a juncture before any hydrate particles are consciously allowed to form. This juncture could be deduced by a cross plot between the temperature profile of the flowline and the GHSZ [11].

Other than anti-agglomerates, Low dosage hydrate inhibitors (LDHIs) also comprise of kinetic hydrate inhibitors (KHIs). These inhibitors, as the name suggests, decrease the volume of injected fluid to less than 3% of the total amount of water produced which reduces the CAPEX. KHIs are primarily utilized to retard the for-

**Fig. 3** Illustration of wet cold-flow (HYDRAFLOW) pipeline loop concept [1]



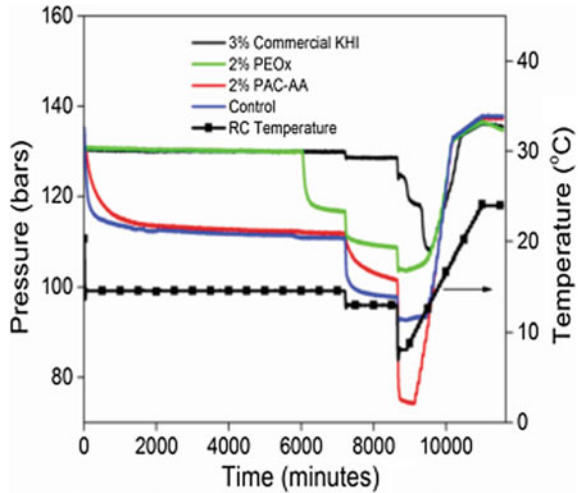
mation of clathrate hydrates enough, so the fluid reaches storage without causing blockage. The most common of which is poly-vinyl-caprolactam (PVCap).

KHIs are nothing but polymers and copolymers (or a mix thereof). A novel KHI was tested using the Rocking cell (RC-5) for the purpose of comparison with other conventionally used KHI monomers like polyacrylamide-co-acrylic acid (PAC-AA) and poly(ethyl oxazoline) (PEOx). The RC-5 consists of five Hastelloy cells capable of operating under high pressure (maximum 200 bar) and sour gas conditions and are immersed in one temperature controlled bath. It was deduced that the KHI should work at sub-cooling temperatures of 5–10.5 °C by studying the synthetic natural gas clathrate three-phase equilibrium diagram.

The results of the RC-5 analysis (Fig. 4) showed that the new commercial KHI, in a concentration of 3% of the total produced water, had performed much better than the 2 conventional KHIs currently used in the industry. The drop in pressure is indicative of the amount of the hydrates being formed and its slope signifies the rate at which they are formed. It was also visible that PEOx performed better than the PAC-AA, which could not prevent large amount of hydrates from forming at the sub-cooling temperature of 12 °C, even more than the control (brine water) for the experiment [14].

Perspectives from other disciplines have helped us understand the nature and extent of the problem that could be encountered. In Kashagan carbonate field, a study of the geology, geological history gave path to revelations about where asphaltene-rich oil can be encountered that could cause depositional problems along flowlines. Conventional asphaltene risk assessment methods like the de-Boer plot (Fig. 5) and the SARA (Fig. 6) analysis, the two approaches often used to quickly identify asphaltene potential risk, showed disagreement. Even the most critical parameter to understand asphaltene risk, the AOP analysis showed conflicted results.

**Fig. 4** Performance evaluation of commercial KHIs, including PEOx and PAC-AA [14]



Explanation of the AOP data through some conventional approaches like relation between asphaltene gravitational gradients and structural depth [13, 23] and correlation of asphaltene problem with individual reservoir/horizon [20] was also ambiguous.

A comparative study with Tengiz field having a similar geology/geohistory showed how multiple phases of migration might cause bitumen precipitation along migration paths due to depressurization. This assertion was supported by the total

**Fig. 5** Asphaltene precipitation potential risk review by de-Boer plot [21]

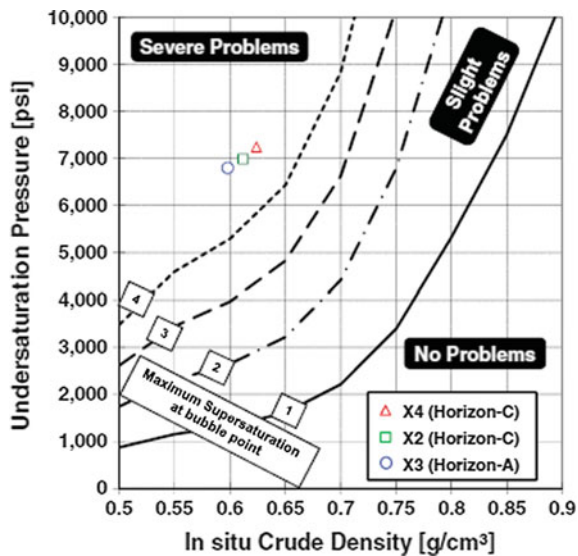
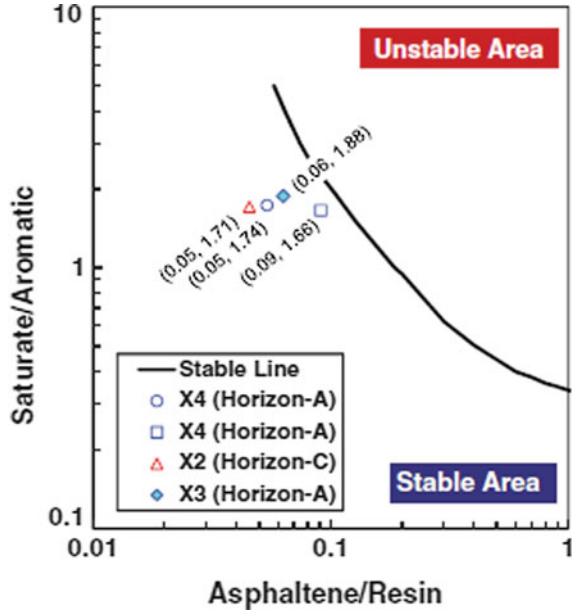
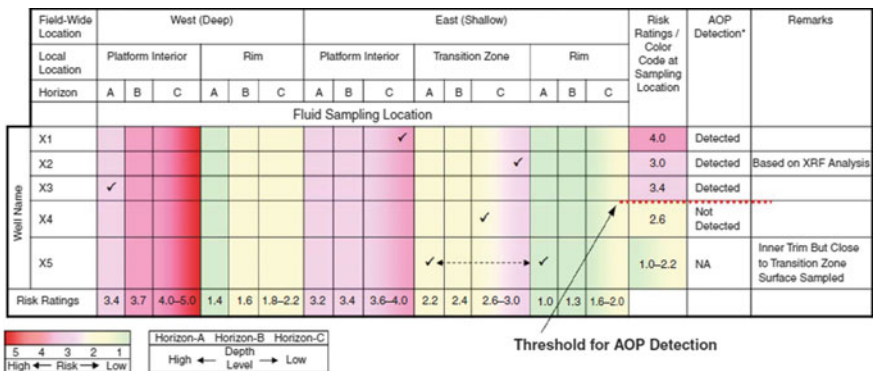


**Fig. 6** Saturate/aromatic versus asphaltene/resin plot [21]



organic carbon (TOC) and the AOP data. An asphaltene risk profile was generated for the data gathered and the chances of encountering asphaltene-rich oil were risk rated on a scale of 1–5, with 1 being lowest risk and 5 being highest risk (Fig. 7) [21].

Later this risk profile was updated to take into consideration the geological heterogeneity and the temperatures encountered in the flow line which were considerably



NA : not available because of AOP measurement cancelled.  
 \* measured at reservoir temperature

**Fig. 7** Matrix of asphaltene potential risk assumption versus AOP detection results [21]

Well Name	Risk Ratings / Color code at Sampling Location	AOP Detection			
		at reservoir temperature	at 80°C	at 65°C	at 55°C
X1	4.0	D	n/a	n/a	n/a
X3	3.4	D	n/a	n/a	n/a
X2	3.0	D	n/a	n/a	n/a
Y2	2.8	ND	n/a	D	D
X4	2.6	ND	D	n/a	n/a
X5	1.0 - 2.2	C	C	C	C

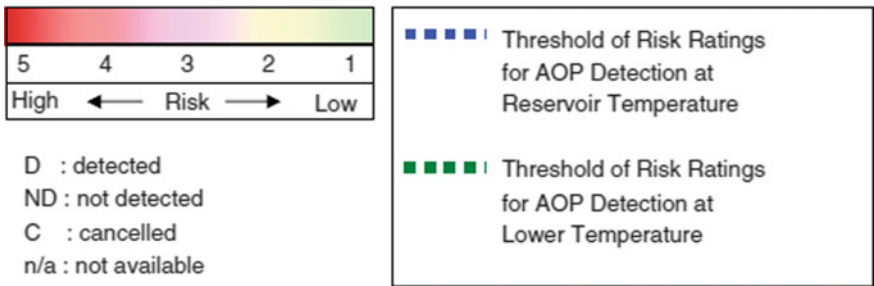


**Fig. 8** Updated matrix of asphaltene potential risk assumption versus AOP detection (sorted by risk ratings) [22]

less than the reservoir temperatures. AOP data of another well Y2 was also added to the updated matrix, which manifested the working of the risk profile (Fig. 8) [21].

Ways we do insulation and the types of insulating materials for the flowline has also advanced leaps and bounds with research. Thermally insulating water-based fluids have come up as a new technology for deepwater flow assurance management to prevent thermal loss in the wellbore (tubing) itself. These insulating packer fluids diminish the heat loss between the produced fluid and the casing-tubing annulus in a wellbore, thus reducing chance of wax or hydrate deposition in the tubing. They have demonstrated advantages over other convention thermal insulation methods like application of silicate foam, steam injection, usage of viscous oil as insulating fluid, the pressurization of annulus with inert gas, or the vacuum insulated tubing (VIT). Understanding impact of fluid viscosity and intrinsic thermal conductivity on

effective insulation and long-term thermal stability of insulation fluid at downhole temperatures is a critical benchmark for qualifying insulation fluid design [10, 18].

Figure 9 shows a temperature profile simulation performed for a well in the Gulf of Mexico (GOM) for the distance of the reservoir to the platform. Insulation gelled water-based fluid was put into the annulus up to 4,000, 10,000 and 20,000 ft below the mudline and the temperature of the produced fluid was simulated.

### 5 Conclusions

1. A multidisciplinary approach. Flow assurance strategy has to encompass multiple disciplines working together. No single discipline is sufficient to define such varied problems.
2. Try and look for answers in unorthodox places. From geological survey to the final production at the facility, any component or finding may lead to the solution of a flow assurance problem.
3. Need for better models for predicting. Presently available models provide highly ambiguous inferences because of no/small integration with other disciplines. A cohesive model between different branches would provide improved insight and would help predict more accurately.

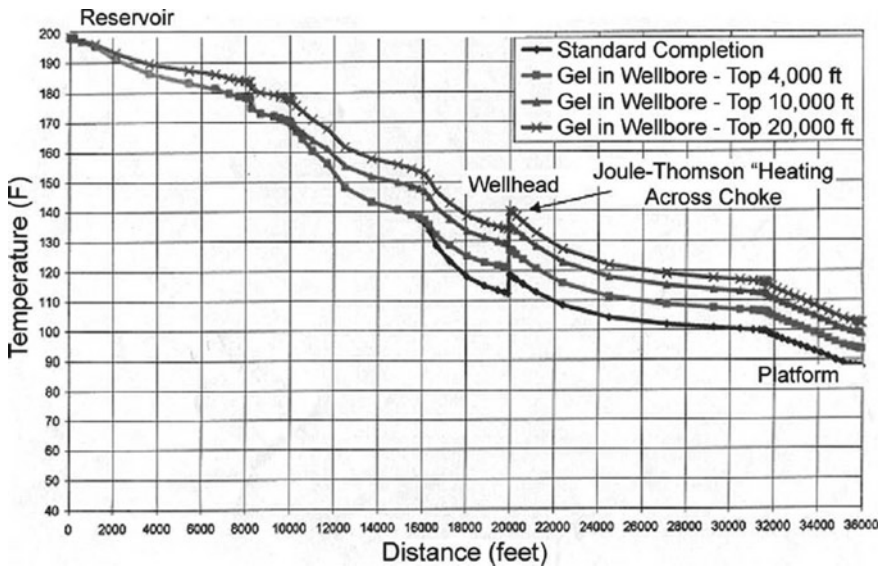


Fig. 9 Wellhead and surface temperature simulation with and without insulation packer fluid for a GOM deepwater well [18]

4. Prevention is better than cure. The pre-development phase should be used to design a strategy that would focus on prevention of the problem rather than dealing with it after it has occurred.
5. Implementation and improvements should stand the test of time. Contingency plans should be in place, ready to be deployed if one or the other thing goes as unplanned.

## 6 Future Recommendations

1. KHIs for gas fields rich in hydrogen sulphide ( $H_2S$ ) and carbon dioxide ( $CO_2$ ) that are flowing under high sub-cooling temperature need to be developed. Effect on their performance with change in salinity of the produced water needs to be investigated.
2. Investigating the performance of combinations of KIIs and MEG, and its viability as a hydrate inhibition mixture.
3. Modelling of suspected nucleation sites, where agglomeration of hydrate particles in the slurry could take place, in wet cold-flow and dry cold-flow concepts.
4. Modelling and prediction of asphaltene precipitation on the basis of geological timeline and geohistory for fields where de-Boer plot, SARA analysis and AOP data does not converge to provide an answer.

## References

1. Azarinezhad R, Chapoy A, Anderson R, Tohidi B (2009) A wet cold-flow technology for tackling offshore flow-assurance problems. Paper OTC 19485 presented at offshore technology conference 2009, Houston, Texas, USA, 4–7 May 2009
2. Brown LD (2002) Flow assurance: a  $\pi^3$  discipline. Paper OTC 14010 presented at offshore technology conference 2002, Houston, Texas, USA, 6–9 May 2002
3. Brustad S, Loken KP, Waalmann JG (2002) Hydrate prevention using MEG instead of MeOH: impact of experience from major Norwegian developments on technology selection for injection and recovery of MEG. Paper OTC 17355 presented at offshore technology conference 2002, Houston, Texas, USA, 2–5 May 2005
4. Camargo RMT, Gonçalves MAL, Montesanti JRT, Cardoso ABR, Minami K (2004) A perspective view of flow assurance in deepwater fields in Brazil. Paper OTC 16687 presented at offshore technology conference 2004, Houston, Texas, USA, 3–6 May 2004
5. Cardoso CB, Alves IN, Ribeiro GS (2003) Management of flow assurance constraints. Paper OTC 15222 presented at offshore technology conference, Houston, Texas, USA, 5–8 May 2003
6. Colodette G, Pereira CAG, Siqueira CAM, Ribeiro GASM, Rodrigues R, de Matos JS, Ribeiro MP (2007) Flow assurance field solutions (Keynote). Paper SPE 117174 presented at offshore technology conference 2007, Houston, Texas, USA, April 30–May 3 2007
7. Coutinho JAP, Edmonds B, Moorwood T, Szczepanski R, Zhang X (2002) Reliable wax prediction for flow assurance. Paper SPE 78324 presented at 13th SPE European petroleum conference, Aberdeen, Scotland, U.K., 29–31 Oct 2002

8. Fan T, Wang J, Buckley JS (2002) Evaluating crude oils by SARA analysis. Paper SPE 75228 presented at SPE/DOE improved oil recovery symposium, Tulsa, Oklahoma, USA, 13–17 Apr 2002
9. Joshi NB, Muhammad M, Creek J, McFadden J (2003) Flow assurance: a challenging path to well completions and productivity. Paper OTC 15185 presented at offshore technology conference, Houston, Texas, USA, 5–8 May 2003
10. Lively G (2002) Flow assurance begins with downhole insulation. Paper OTC 14118 presented at offshore technology conference, Houston, Texas, USA, 6–9 May 2002
11. Lv X, Gong J, Li W, Shi B, Yu D, Wu H (2013) Experimental study on natural-gas-hydrate-slurry flow. Paper SPE 158597 published in SPE J 19(02)
12. MacMillan DJ, Tackett JE Jr, Jessee MA, Monger-McClure TG (1995) A unified approach to asphaltene precipitation: laboratory measurement and modeling. Paper SPE 28990 published in J Pet Technol 47(09)
13. Mullins OC, Elshahawi H, Flannery M, o'Keefe M, Vannuffelen S (2009) The impact of reservoir fluid compositional variation and valid sample acquisition on flow assurance evaluation. Paper OTC 20204 presented at offshore technology conference, Houston, Texas, USA, 4–7 May 2009
14. Rashed MA, Elanany MS, Majnoui KA, Jabran AA et al (2015) Kinetic hydrate inhibitors for natural gas fields: rational design and experimental development. Published in Saudi Aramco J Technol Fall
15. Sloan ED, Koh CA (2007) Clathrate hydrates of natural gases, 3rd edn. Taylor & Francis Group, Boca Raton, London, CRC Press, New York
16. Stephens P, Sheorey U, Isenor R, Ewida A (2000) Terra Nova—the flow assurance challenge. Paper OTC 11915 presented at offshore technology conference, Houston, Texas, USA, 1–4 May 2000
17. Tagore A, Utgard MW, Ramachandran K, Alwazzan AT (2008) Fluid characterization: impact on deepwater field development. Paper SPE 115777 presented at SPE annual technical conference and exhibition in Denver, Colorado, USA 21–24 Sept 2008
18. Wang X, Qu Q, Javora P, Percy R (2006) New trends in oilfield flow-assurance management: a review of thermal insulating fluids. Paper SPE 103829 presented at SPE international oil & gas conference and exhibition, Beijing, China, 5–7 Dec 2006
19. Wilson A, Overaa SJ, Holm H (2004) Ormen Lange—flow assurance challenges. Paper OTC 165557 presented at offshore technology conference, Houston, Texas, USA, 3–6 May 2004
20. Yonebayashi H, Masuzawa T, Dabbouk CA, Urasaki D (2009) Ready for gas injection: asphaltene risk evaluation by mathematical modeling of asphaltene precipitation envelope (APE) with integration of all laboratory deliverables. Paper SPE 125643 presented at SPE/EAGE reservoir characterization and simulation conference, Abu Dhabi, UAE, 19–21 Oct 2009
21. Yonebayashi H, Tosic S, O'Brien DR (2012) Geology and geohistory contribute to flow assurance. Paper SPE 154585 presented at EAGE annual conference and exhibition, Copenhagen, Denmark, 4–7 June 2012
22. Yonebayashi H, Tosic S (2013) Geology and geohistory contribute to flow assurance, part II: asphaltene risk evaluation incorporation geological heterogeneity and covering all operating temperatures. Paper SPE 164877 presented at EAGE annual conference and exhibition, London, England, 10–13 June 2013
23. Zuo JY, Freed D, Mullins OC, Zhang D (2010) Paper SPE 133656 presented at SPE annual technical conference and exhibition in Florence, Italy, 19–22 Sept 2010
24. de Boer RB, Leerlooyer K, Eigner MRP, van Bergen ARD (1995) Screening of crude oils for asphalt precipitation: theory, practice, and the selection of inhibitors. Paper SPE 24987 published in SPE J 10(01)



# Coupled Flow and Geomechanics Model for CO<sub>2</sub> Storage in Tight Gas Reservoir



Awez Hanegaonkar, Tapan Kidambi and G. Suresh Kumar

**Abstract** The process of injection and withdrawal from tight gas reservoirs is a multiphysics and multicomponent problem. The aim of the present work is to capture the physics associated with the injection of CO<sub>2</sub> into tight shales, and assess and mitigate the risks associated with reservoir overpressure. The overpressure caused by CO<sub>2</sub> injection usually triggers the onset of formation–deformation, which inadvertently affects the state of the stress in the target geological formations and its surroundings, the monitoring of which is critical to understand the risks in conjunction with CO<sub>2</sub> storage. In the present work, a novel fully coupled fully implicit flow and geomechanics simulator is introduced to describe the physics in conjunction with an extended injection phase of CO<sub>2</sub>. The developed model solves for pressure saturation and porosity and permeability changes considering a multicomponent system while principally focusing on the adsorption and diffusion of CO<sub>2</sub> and stress-dependent reservoir deformation employing cell-centred finite volume method. It is envisaged that the injection of CO<sub>2</sub>, while with the primary purpose of storage, will parallelly enhance the recovery from shale gas due to lateral sweep effects. Based on these mechanisms, for the case study of a tight gas field, the applicability of the simulation model is tested for formations with varied rock and fluid moduli in a 20-year simulation period.

**Keywords** CO<sub>2</sub> storage · Reservoir simulation · Fluid flow and geomechanics  
Multiphase flow · Tight gas reservoir

## 1 Introduction

Sound understanding of the flow of a fluid through the rock formation is necessary in characterising various subsurface applications such as production forecasting and

---

A. Hanegaonkar (✉) · T. Kidambi · G. Suresh Kumar  
Department of Ocean Engineering, Indian Institute of Technology Madras,  
Chennai 600036, India  
e-mail: [awez.hanegaonkar@gmail.com](mailto:awez.hanegaonkar@gmail.com)

© Springer Nature Singapore Pte Ltd. 2019  
K. Murali et al. (eds.), *Proceedings of the Fourth International Conference in Ocean Engineering (ICOE2018)*, Lecture Notes in Civil Engineering 22,  
[https://doi.org/10.1007/978-981-13-3119-0\\_65](https://doi.org/10.1007/978-981-13-3119-0_65)

955

reservoir management. Characterisation study of reservoir by field test and experiment is a difficult task. Additionally, formation under study has very high temperature and pressure conditions such that associated risks are high. Capturing the physics associated with the development of unconventional resources and transport through these complex formations numerically has gained pace in the recent scenario in order to meet the growing energy demand. According to [1], models describing the multiphysics associated with the deformable porous media are fundamentally based on conservation of mass and momentum, energy balance, theory of poroelasticity and associated in situ stresses. Considering these difficulties, theoretical and numerical studies of coupled flow and geomechanical processes like natural gas recovery and CO<sub>2</sub> geosequestration become a research focus on the present study. Geosequestration considered to be the most promising of all prevailing solutions to mitigate greenhouse gas emissions into the atmosphere [2–5]. From coal gas study, it has been revealed that CO<sub>2</sub> is adsorbed by displacing methane at a ratio of two or more as it has a greater affinity to the reservoir [6–8]. In analogy with the coal gas, the shale formation also behaves similarly and releases methane in the presence of adsorbing CO<sub>2</sub>. Hence, the black shale acts as an excellent storage site for CO<sub>2</sub>, serves the dual purpose of storage and enhances gas production [9, 10]. Thus, in summary, CO<sub>2</sub> injection can be thought of as meeting a twofold objective. Firstly, CO<sub>2</sub> will facilitate and enhance gas production from these tight formations, and secondly, production will provide a greater volume for the storage of CO<sub>2</sub> in the same formation. It is due to these obvious advantages that there has been a tremendous interest in CO<sub>2</sub> storage in shale reservoirs [11]. It is important to study geomechanical effect of withdrawal and injection into the shale formation so as to successfully exploit the hydrocarbon resources. Injection of CO<sub>2</sub> causes reservoir over pressurisation and subsequent deformation of the formation studied by Martinez et al. [12], Birkholzer et al. [13], Person et al. [14], Kim et al. [15]. The present work provides the efficient use of subsurface resources and its development linking the geomechanics to fluid flow and captures the complex physics associated with the natural gas (CH<sub>4</sub>) production and injection of carbon dioxide CO<sub>2</sub> using numerical simulation.

## 2 Mathematical Model and Governing Equations

The pressure equation used in present study to describe multiphase fluid flow through deformable porous media is formulated based upon the model suggested by Lewis and Schrefler [16], Albinali et al. [17]. This model is modified in the present numerical study so as to incorporate the molecular diffusion, adsorption/desorption, and Knudson permeability correction as shown in Eq. 1. Water-phase pressure  $P_w$ , CO<sub>2</sub>-phase pressure and solid displacement field are considered as the primary state variables to describe the state of the material. The rock formation which is stress sensitive shows noticeable geomechanical effect [18]. In order to capture the response to such formation, it is important to couple the flow and geomechanics equation at each time step [19]. Equation 1 defines the general nonlinear equation of transient gas flow

in shale reservoir coupled between the rock deformation and fluid flow. The variation in porosity is represented by the function of: (a) the volumetrically weighted fluid pressure  $P_g$  and (b) the matrix volumetric deformation. The Biot coefficient  $\alpha_p$  is indicative of significant lateral effects and thus is imperative for porosity variation, with the lower values of  $\alpha_p$  indicating that the lateral stresses are much more dominant.

$$\begin{aligned} \nabla \cdot \left[ k_m \lambda_t (\nabla P_{gm} - (\gamma_w f_w + \gamma_g f_g) \nabla D - f_w \nabla P_{cwg}) + \frac{\delta}{\tau} D c_g S_g \nabla P_{gm} \right] - T_{mf} \\ = \phi_m c_t \frac{\partial P_{gm}}{\partial t} + \frac{\partial(1 - \phi) \rho_{ad}}{\partial t} - \alpha_p \frac{\partial}{\partial t} (\nabla \cdot u) \end{aligned} \tag{1}$$

In Eq. 1,  $k$  is the permeability of the reservoir,  $\lambda_t$  is the total mobility of fluid phases,  $f_i$  is the fractional phase of each phase with ( $i = g; w$  for gas and water phase),  $P_{cwg}$  is the capillary pressure between the phases,  $\gamma_\phi$  is the phase gravity for different phases,  $D$  is the reference depth,  $q_t$  is the net production rate,  $\alpha_p$  is the Biot poroelastic constant,  $\phi$  is the porosity of reservoir,  $C_t$  is the total compressibility of the system (both solid and fluid),  $\delta$  is the constrictivity factor,  $\tau$  is the tortuosity,  $D_o$  is the free diffusion coefficient,  $c_g$  is the gas compressibility,  $S_g$  is the gas saturation, and  $\rho_a$  is the adsorbed gas density. In multiphase, the flow velocity follows the conventional Darcy law and Darcy velocity for estimating the flow rates as

$$v_\phi = \frac{k k_{r\phi} (\nabla P_\phi - \rho_\phi g \nabla D)}{\mu_\phi} \tag{2}$$

where  $\mu_\phi$  is the phase viscosity,  $P_\phi$  is the phase pressure, and  $k_{r\phi}$  is the relative permeability of phase  $\phi$ .

The global rock displacement equation is derived from Biot’s theory and includes the shear modulus  $G$  and Lames constant as calculated from the Young modulus.

The resulting partial differential equation is

$$\begin{aligned} G \nabla^2 u + (G + \lambda) \nabla (\nabla \cdot u) + (\nabla \sigma_v - \gamma_b \nabla D) \\ = -\alpha_p [\nabla P_{gm} - (\gamma_w f_w + \gamma_g f_g) \nabla D] + \alpha_p f_w \nabla P_{cwg} + \rho_b \frac{\partial^2 u}{\partial t^2} \end{aligned} \tag{3}$$

where  $\lambda$  is Lames constant and  $G$  is shear modulus. In the global solid deformation equation,  $u$  is solid displacement and  $P_g$  is pore pressure. Equations 1 and 3 represent the coupled set of governing equation. Equation 1 is coupled to Eq. 3 by the rate of change of solid deformation  $u$ .

The saturation equation in multiphase flow is governed by mass conservation equation combining of the Darcy equation and conservation equation, and incorporating production/injection terms results into the following flow equation as shown below

$$\nabla [k_m \lambda_w (\nabla P_{gm} - \gamma_w \nabla D - \nabla P_{cwg})] = \phi_m \left[ (C_w + C_\phi) S_{wm} \frac{\partial P_{gm}}{\partial t} + \frac{\partial S_{wm}}{\partial t} \right] \quad (4)$$

In Eq. 4,  $q_w$  represents the net outflow of water from the reservoir, the terms  $C_w$  and  $C_\phi$  correspond to the water and rock compressibilities, respectively, and  $\lambda_\phi$  indicates the phase mobility of each fluid phase. This term is updated depending upon the relative permeability between the fluid phases and the viscosity ( $\mu$ ). When two phases coexist, then there will be capillary pressure. In order to incorporate relative permeability and capillary pressure, we use the modified Brooks–Corey model by Brooks and Corey [20]. Additionally to account for the porosity and permeability variations, functions of initial porosity, elastic moduli, sorption isotherm parameters and pressure change, we use the model proposed by Palmer and Mansoori [21]; these relations are given as in Eqs. 5 and 6.

$$\frac{\phi}{\phi_o} = (p - p_0) \frac{c_\phi}{\phi_o} + \frac{e_v}{\phi_o} \left( \frac{2v}{1 - v} \right) \left( \frac{P}{P + P_l} - \frac{P_o}{P_o + P_l} \right) \quad (5)$$

$$\frac{k}{k_o} = \left( \frac{\phi}{\phi_o} \right)^3 \quad (6)$$

With  $v$  representing the Poisson ratio of the formation rock,  $c_\phi$  is the pore compressibility, and  $P$  and  $P_o$  are the final and initial pore pressures, respectively. The term  $e_v$  is the incremental strain on the rock due to pressure variation, and  $P_l$  is the Langmuir sorption isotherm pressure by Langmuir [22]. The physical domain of the study area is shown below. The injection and production well are placed as shown in Fig. 1.

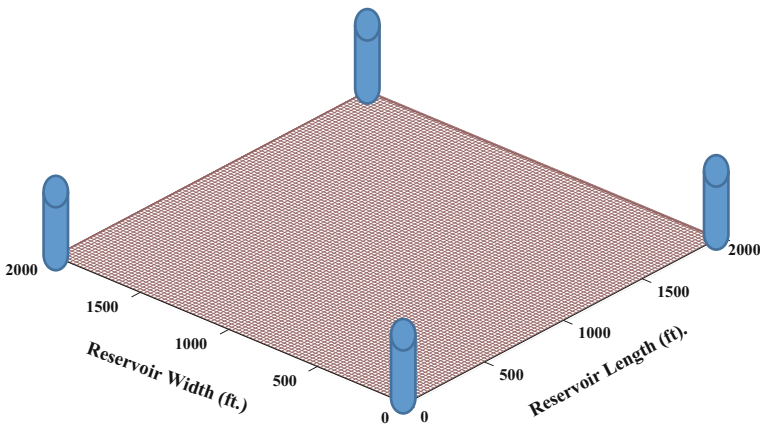


**Fig. 1** Model geometry and well locations

### 3 Initial Conditions and Boundary Conditions

During the solution procedure, initial and boundary conditions are considered. Pressure gradient in the flow equation is replaced by the potential gradient so as to incorporate gravity effect. Initially, no flow and no displacement are applied boundaries. Net flow rate  $q_{\text{total}}$  is applied at the place of injection or production well nodes in the form of source boundary. Initial conditions are as follows.

Initial conditions for saturation, deformation and pressure are, respectively,

$$\begin{aligned} S(x, y, 0) &= S_0 \\ u(x, y, 0) &= 0 \\ w(x, y, 0) &= 0 \\ P(x, y, 0) &= P_0 \end{aligned}$$

Boundary condition incorporated in the present study are shown below, which are no flow and no deformation conditions respectively,

$$\begin{aligned} \nabla P_g - (\gamma_w f_w + \gamma_g f_g) \nabla D - f_w \nabla P_{cwg} &= 0 \\ w(x, y, z, t) = 0; \quad u(x, y, z, t) &= 0 \end{aligned}$$

The study area primarily focuses on the Jurassic and lower-to-middle Cretaceous interval of the shales of the Gotnia basin in the Persian Gulf, which have been identified as potential storage sites for CO<sub>2</sub> sequestration. For a greater understanding of the local geological setting, the readers are referred to the other literature (most notably the work of [23–25]). The study area has the section of the Sargelu Formations of the Gotnia basin in the Persian Gulf. An additional point of interest is the presence of the Gotnia Salt Formation, which acts as a regional seal and prevents vertical migration of CO<sub>2</sub>. This makes an excellent case for studying these Jurassic carbonate sequences for CO<sub>2</sub> sequestration.

The rock mechanical and reservoir fluid properties pertaining to these formations are provided in Table 1. The initial and boundary conditions are defined to provide the physical boundaries, and properties are assigned to each grid block as shown in Figs. 1 and 2. For the base case simulation, we model a tight gas reservoir (2000 ft × 2000 ft) in the  $x$ - and  $y$ -planes, respectively. This study area is divided into 100-150-1 grid cells separately in the  $x$ -,  $y$ - and  $z$ -directions, respectively. The grid blocks in the  $x$ - and  $y$ -directions are 20 ft in length and width. The pay zone thickness is (grid block in the  $z$ -direction) 30 ft. The initial pore pressure at the Zone 2 reservoir level was measured at 12406 psi (85 MPa) from a pore pressure gradient of 0.823 psi/ft (18 kPa/m). The individual simulation runs start from equilibrium at a depth of 13,400 ft (4100 m); in the injection well, the pressure is 11,000 psi (76 MPa) considering a constant reservoir temperature of 106 °C. Rock compressibility is found to be approximately  $1:096 \times 10^7 \text{ psi}^{-1}$  for formation under study. The shale from zone of interest (from Table 1)

**Table 1** Input data and formation properties for the formations studied

Property	Zone 2		
Bulk modulus (psi)	1.0e7		
Burial depth (ft)	14260		
Young's modulus (psi)	1e7		
Bulk Poisson's ratio	0.22		
Formation permeability (mD)	0.04		
Porosity	0.05		
Reservoir fluid viscosity (cP)	H <sub>2</sub> O = 0.7	CH <sub>4</sub> = 0.045	CO <sub>2</sub> = 0.12
Initial reservoir pressure (psi)	12,406		
Biot coefficient ( $\alpha$ )	0.9		
Wellbore radius (in.)	9.25		
Initial water saturation	0.39		
Minimum horizontal stress (psi)	15590		
Maximum horizontal stress (psi)	17507		
Unconfined compressive strength (psi)	17175		
Isotherm data	CO <sub>2</sub>	CH <sub>4</sub>	
Langmuir pressure (psi)	850	1914	
Langmuir volume (scf/lb)	0.09	0.07626	
Bulk diffusion coefficients (ft <sup>2</sup> /d)	0.5639	0.0078	
Density (lb/ft <sup>3</sup> ) (reservoir condition)	48.4	16.60	
Viscosity (cP)	0.12	0.0447	
$\rho_{gsc}$ (density at standard condition)	0.1167	0.0447	
Critical point	$T_c(R) = 547.6$ $P_c(\text{psi}) = 1071.8$	$T_c(R) = 343.08$ $P_c(\text{psi}) = 667.174$	

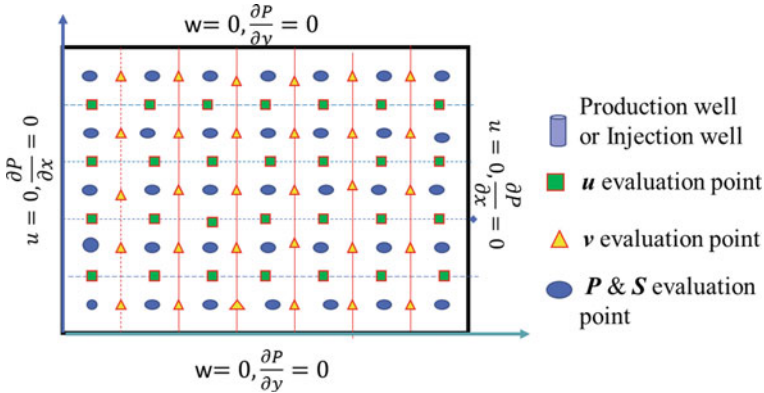


Fig. 2 Discretised domain with primary variable evaluation points

was selected as the base case with a 5% total porosity, a permeability of 0.04 mD with a cumulative injection of 4.36 MSCF of CO<sub>2</sub> and a water saturation of 39%.

### 4 Validation of the Model

In the case study of the reservoir formation in Persian Gulf, numerical model study is performed in the production process by coupling flow and geomechanics. The pressure reduction during production phase is discussed. From the results of present numerical code and results of ECLIPSE, we found the reasonable agreement as shown in Fig. 3. This shows the validity of our numerical code and shows the potential to apply and study in the real-field scenario.

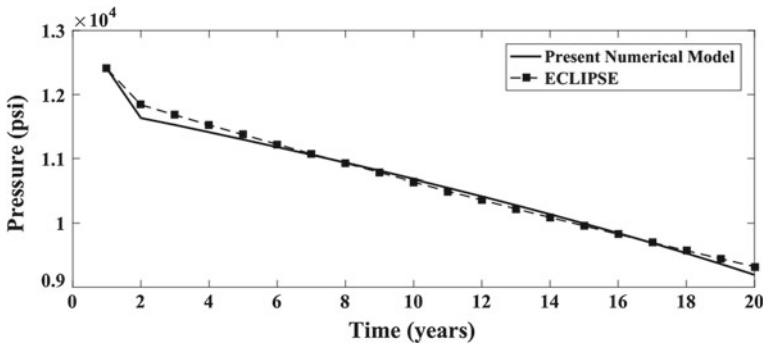
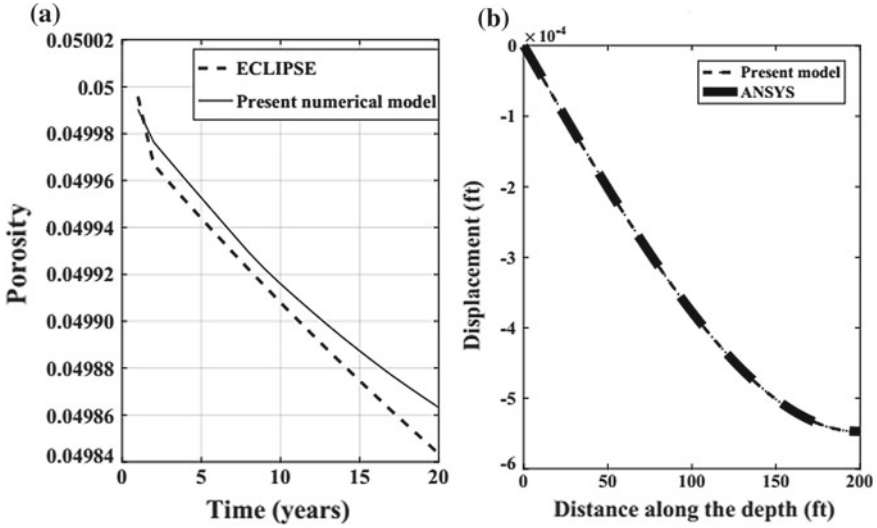


Fig. 3 Pressure variation with time by present model and ECLIPSE



**Fig. 4** Comparison of **a** porosity variation of present model and ECLIPSE and **b** displacement variation of present model and ANSYS

Figure 4a shows average porosities calculated by present numerical simulator and ECLIPSE. Again, the agreement between present code and ECLIPSE is shown. Since ECLIPSE does not solve for displacements, the validation of the displacement is done using the ANSYS Mechanical APDL solver. As can be seen from Fig. 4b, the results confirm that the present work is indeed comparable to convention solvers that use finite element for solving displacements as a very good match between the displacements computed by the two methods can be seen. The relative error percentage is less than 0.1% for all computed values of displacement between ANSYS and the developed model.

### 5 Result and Discussion

In the present study, a case study is performed on the tight gas formation of Persian Gulf. The result of the simulation for the formation under study is presented in this section. During the primary production of  $CH_4$  from the four corner wells simulated for the period of 20 years as shown in Fig. 5 and it is observed that there is significant drop in initial reservoir pressure which is governed by diffusive mass fluxes arising from high pressure gradients. From Fig. 5, it is clear that pressure is depleted from the initial pressure 12,406–9000 psi which is almost around 3500 psi for a 20-year production period. Also, the maximum variation in pressure is seen near the vicinity of the wells.



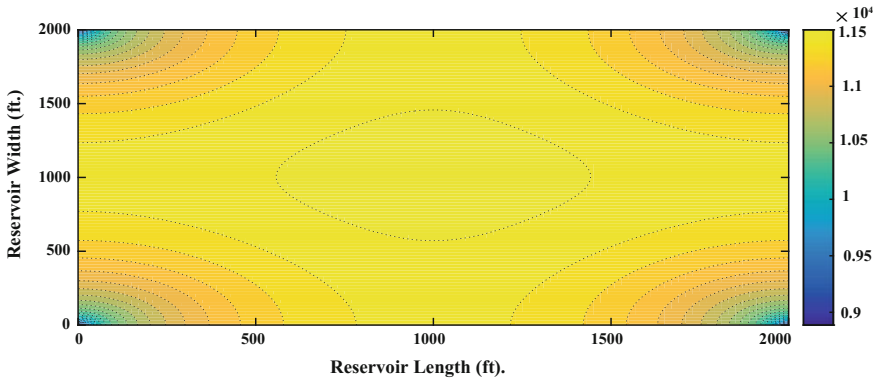


Fig. 5 Pressure profile for formation due to 20 years of continuous CH<sub>4</sub> production

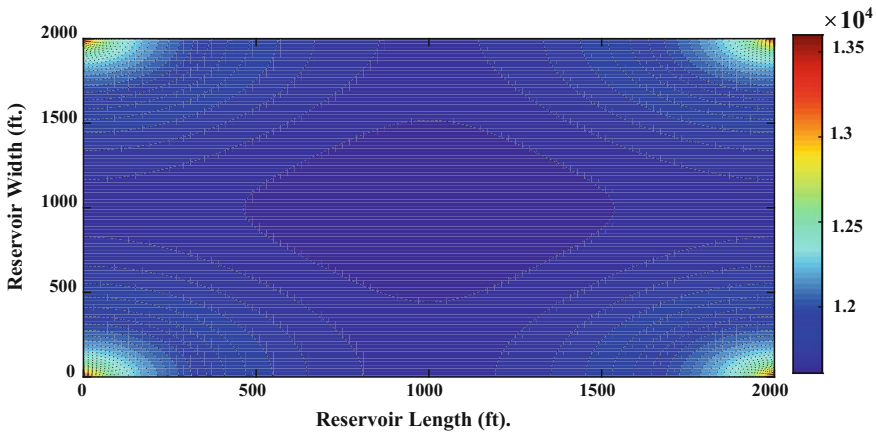


Fig. 6 Pressure profile for formation after 40 years of continuous CO<sub>2</sub> injection

After the primary production of CH<sub>4</sub>, these four corner production wells are converted into injection wells. Figure 6 shows the spatial variation of pressure after the depleted shale formation due to 40 years of continuous CO<sub>2</sub> injection. As CO<sub>2</sub> is started injecting into reservoir, the pressure starts getting build up and is almost levelling reservoir initial pressure. It is clear from Fig. 6 that maximum pressure at the injection well is around 13,500 psi which is almost 1000 psi more than the initial reservoir pressure; in addition to that, maximum pressure is less than the fracturing pressure and strength of the rock. In order to avoid the injection-induced fracturing, the injection pressure should be lower than the fracturing pressure; hence, in the present study, it is lower than the fracturing pressure.

We simulate the displacements using a pore volume-coupling approach with the mechanical properties presented in Table 1. The UCS and Young’s modulus values, of 14390 psi (98.82 MPa) and 9.84e6 psi (6.2 GPa), are used, respectively, for the

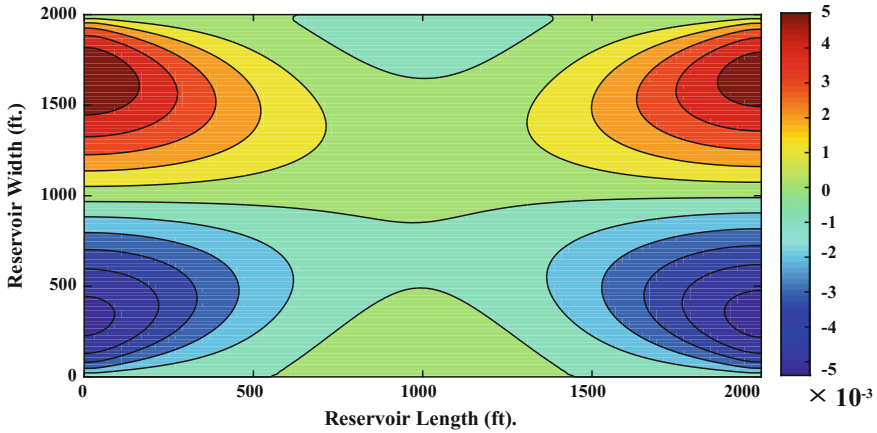


Fig. 7 Displacement profile for formation after 20 years of continuous CO<sub>2</sub> injection

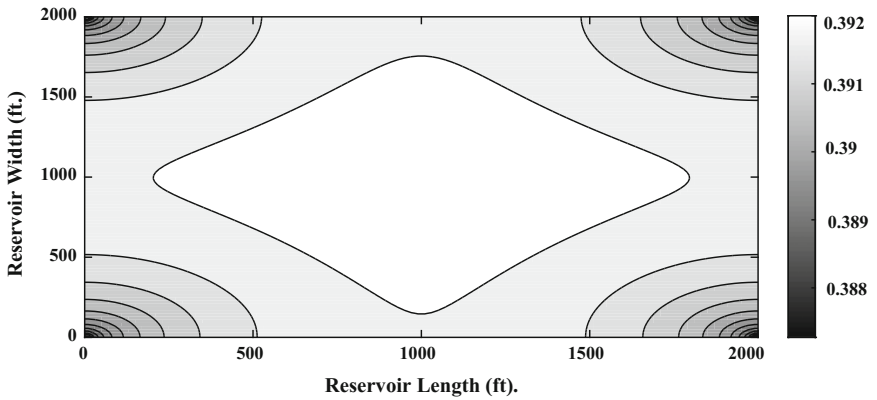
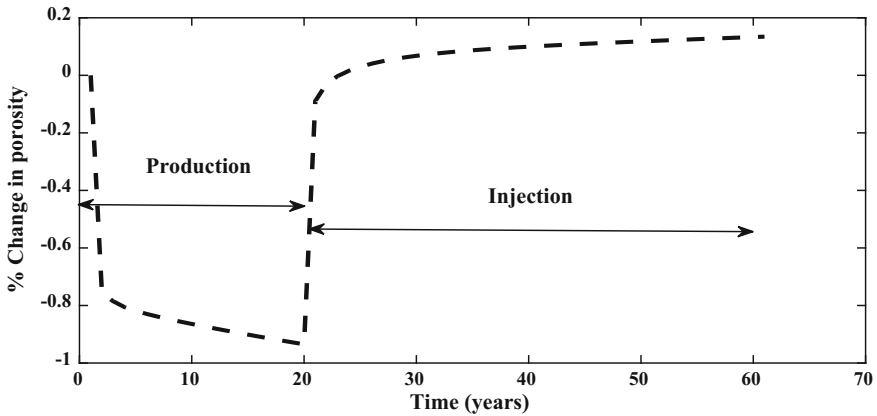


Fig. 8 Displacement profile for formation after 40 years of continuous CO<sub>2</sub> injection

formation under study. Figure 7 displays the evolution of corresponding deformation at the end of 40 years of CO<sub>2</sub> injection.

Due to CO<sub>2</sub> injection and production operations, fluid pressure in the reservoir varies dynamically, as a consequence of which the mean effective stress varies. This produces an expansion/contraction of the pore volume.

We model the domain with closed impermeable boundaries to prevent water influx. In the plot as shown in Fig. 8 for 40 years, as the injection process begins, the gas phase migrates laterally away from the wells which results in water displacement. The overall water saturation change is marginal with an overall change of 2.8%. During the injection process, there is a 0.58% decrease in the water saturation, a change mainly noticeable at the injection wells and a similar 2.1% increment can be seen at the production wells.



◀Fig. 9 Plot showing the percentage change in porosity for injection and production period

Figure 9 shows the porosity evolution of the formation as measured after each 20-year cycle. As in the case of displacements, the formations initially experience mechanical compaction due solely to the effect of confining pressure (injected pore volume = 0). Porosity progressively decreases by 0.9% (at 60 MPa, ~8700 psi) as pressure decreases (from Fig. 3). As injection initiates, the formation undergoes expansion causing porosity to increase. Figure 8 also shows that porosity variations due to geomechanical effects resulting in a net porosity increase after CO<sub>2</sub> flooding by 0.13% in the entire domain.

## 6 Conclusion and Future Work

In the present study spatial and temporal variation of the reservoir key parameters such as mechanical deformation of rock, pressure, porosity and saturation were studied. A fully coupled flow and geomechanics simulator are developed for addressing the effects of hydrocarbon production from a shale gas reservoir. Overall, there is 2% improvement in porosity and permeability. Max porosity is 0.0502, and Min porosity is 0.000494. The variation in porosity and permeability is found nonlinear. Max pore pressure change during production is around 3200 psi and during injection is 900 psi compared with initial reservoir pressure. Additionally, the effects of CO<sub>2</sub> injection on enhancing production and simultaneous storage are also explored in terms of variations in pore pressure, permeability and porosity variations. Geomechanical deformation which contributes significantly to deformation and alters flow properties is also presented.

Future work based on the work presented here will incorporate an extended Langmuir isotherm, nonisothermal effects and chemical interactions of CO<sub>2</sub> with the host rocks.

## References

1. Pettersen Ø (2008) Using relations between stress and fluid pressure for improved compaction modelling in flow simulation and increased efficiency in coupled rock mechanics simulation. *Pet Geosci* 14(4):399–409
2. Leung Dennis YC, Giorgio C, Mercedes MMV (2014) An overview of current status of carbon dioxide capture and storage technologies. *Renew Sustain Energy Rev* 39:426–443. <https://doi.org/10.1016/j.rser.2014.07.093>
3. Bachu S, Adams JJ (2003) Sequestration of CO<sub>2</sub> in geological media in response to climate change: capacity of deep saline aquifers to sequester CO<sub>2</sub> in solution. *Energy Convers Manage* 44(20):3151–3175. [https://doi.org/10.1016/S0196-8904\(03\)00101-8](https://doi.org/10.1016/S0196-8904(03)00101-8)
4. Celia MA, Nordbotten JM (2009) Practical modeling approaches for geological storage of carbon dioxide. *Ground Water* 47(5):627–638
5. Van der Zwaan B, Smekens K (2009) CO<sub>2</sub> capture and storage with leakage in an energy-climate model. *Environ Model Assess* 14(2):135–148
6. Guo M, Lu X, Nielsen CP, McElroy MB, Shi W, Chen Y, Xu Y (2016) Prospects for shale gas production in china: implications for water demand. *Renew Sustain Energy Rev* 66:742–750
7. Cipolla CL, Lolon EP, Erdle JC, Rubin B et al (2010) Reservoir modeling in shalegas reservoirs. *SPE Reservoir Eval Eng* 13(04):638–653
8. Godec M, Koperna G, Petrusak R, Oudinot A (2013) Potential for enhanced gas recovery and CO<sub>2</sub> storage in the marcellus shale in the eastern united states. *Int J Coal Geol* 118:95–104
9. Nuttall BC, Drahovzal JA, Eble CF (2005). Analysis of devonian black shales in kentucky for potential carbon dioxide sequestration and enhanced natural gas production. Report Kentucky Geological Survey/University of Kentucky (DE-FC26-02NT41442)
10. Schepers KC, Nuttall BC, Oudinot AY, Gonzalez RJ et al (2009). Reservoir modeling and simulation of the devonian gas shale of eastern kentucky for enhanced gas recovery and CO<sub>2</sub> storage. In SPE International Conference on CO<sub>2</sub> Capture, Storage, and Utilization. Society of Petroleum Engineers
11. Kang SM, Fathi E, Ambrose RJ, Akkutlu IY, Sigal RF et al (2011) Carbon dioxide storage capacity of organic-rich shales. *SPE J* 16(04):842–855
12. Martinez MJ, Newell P, Bishop JE, Turner DZ (2013) Coupled multiphase flow and geomechanics model for analysis of joint reactivation during CO<sub>2</sub> sequestration operations. *Int J Greenhouse Gas Control* 17:148–160. <https://doi.org/10.1016/j.ijggc.2013.05.008>
13. Birkholzer Jens T, Zhou Quanlin, Tsang Chin-Fu (2009) Large-scale impact of CO<sub>2</sub> storage in deep saline aquifers: a sensitivity study on pressure response in stratified systems. *Int J Greenhouse Gas Control* 3(2):181–194. <https://doi.org/10.1016/j.ijggc.2008.08.002>
14. Person M, Banerjee A, Rupp J, Medina C, Lichtner P, Gable C, Pawar R, Celia M, McIntosh J, Bense V (2010) Assessment of basin-scale hydrologic impacts of CO<sub>2</sub> sequestration, Illinois basin. *Int J Greenhouse Gas Control* 4(5):840–854
15. Kim TH, Cho J, Lee KS (2017) Evaluation of CO<sub>2</sub> injection in shale gas reservoirs with multi-component transport and geomechanical effects, *Appl Energy* 190, 1195–1206, ISSN 0306-2619, <http://dx.doi.org/10.1016/j.apenergy.2017.01.047>
16. Lewis RW, Schrefler BA (1998) The finite element method in the static and dynamic deformation and consolidation of porous media. Wiley, New York
17. Albinali A, Kazemi H, Alghamdi B et al (2011) Geomechanics and fluid flow modelling using finite-difference method

18. Longuemare P, Mainguy M, Lemonnier P, Onaisi A, Gérard C, Koutsabeloulis N (2002) Geomechanics in reservoir simulation: overview of coupling methods and field case study. *Oil Gas Sci Technol* 57(5):471–483
19. Minkoff SE, Stone CM, Bryant S, Peszynska M, Wheeler MF (2003) Coupled fluid flow and geomechanical deformation modeling. *J Petrol Sci Eng* 38(1):37–56
20. Brooks RH, Corey AT (1966) Properties of porous media affecting fluid flow. *J Irrig Drainage Div ASCE* 92(IR2):61–88
21. Palmer I, Mansoori J (1998) How permeability depends on stress and pore pressure in coalbeds: a new model. *SPE Reserv Eng* 1(6):539–543
22. Langmuir I (1916) The evaporation, condensation and reflection of molecules and the mechanism of adsorption. *Phys Rev Lett*. <https://doi.org/10.1103/Physrev.8.149>
23. Carman G (1996) Structural elements of onshore Kuwait GeoArabia, pp 239–266
24. Neele F, Vandeweyer V, Mayyan H, Sharma SR, Kamal D (2017) Options for CO<sub>2</sub> sequestration in Kuwait. In: *Energy Procedia, 13th International Conference on Greenhouse Gas Control Technologies, GHGT-13*, 14–18 Nov 2016, Lausanne, Switzerland
25. Kidambi T, Kumar GS (2016) Mechanical earth modeling for a vertical well drilled in a naturally fractured tight carbonate gas reservoir in the Persian Gulf. *J Pet Sci Eng* 141:38–51. <https://doi.org/10.1016/j.petrol.2016.01.003>

# RETRACTED CHAPTER: Effect of Nanocellulose as an Additive in Cement



Vignesh Shenoy, Sanjay Joshi and Mikhil Dange

**Abstract** Deep-water reservoirs have high formation pressure, and the fracture pressure is very close to formation pressure. During cementation, pressure has to be balanced within a small range. So, cementing a long section of casing becomes difficult. To increase economic benefit of the project, it is imperative that cementation is carried out in the least possible time, i.e. with least setting time and low weight of cementation wherever applicable. Keeping these in mind, efforts were made to increase the mechanical properties of the cement by using nanocellulose. Experiments have shown that considerable improvement in cement properties was achieved.

**Keywords** Nanotechnology · Nanocellulose · Lightweight cement

## 1 Introduction

Cementing is the process of mixing slurry of cement, cement additives and water and pumping it down. It helps in holding the casing in its place. To zonal isolation and holding the casing in place, the cement should have a high compressive strength. Even, tensile strength is equally important which is also proportional to compressive strength. Conventional 15.8 ppg cements have no issue in terms of strength, but lightweight cements around 12 ppg have low compressive strength. So, we have

---

The original version of this chapter was retracted: The retraction note to this chapter is available at [https://doi.org/10.1007/978-981-13-3119-0\\_74](https://doi.org/10.1007/978-981-13-3119-0_74)

---

V. Shenoy (✉)  
M.E. Petroleum, M.I.T, Pune, Maharashtra, India  
e-mail: [shenoyvignesh41@gmail.com](mailto:shenoyvignesh41@gmail.com)

S. Joshi  
Petroleum Department, M.I.T, Pune, Maharashtra, India

M. Dange  
Technical Professional-Cementing, Halliburton, Mumbai, India

© Springer Nature Singapore Pte Ltd. 2019, corrected publication 2022  
K. Murali et al. (eds.), *Proceedings of the Fourth International Conference in Ocean Engineering (ICOE2018)*, Lecture Notes in Civil Engineering 22,  
[https://doi.org/10.1007/978-981-13-3119-0\\_66](https://doi.org/10.1007/978-981-13-3119-0_66)

worked on to see whether nanocellulose, one of the strongest and cheapest available nanomaterials, helps to increase the strength of lightweight cement.

Cellulose is the most abundant biomaterial available in nature. It is a polymer with cellobiose unit as the smallest repeating unit. Degree of polymerization may go to 1000 in case of wood cellulose. The structure of nanocellulose is stronger than steel, and the strength-to-weight ratio of nanocellulose is 8 times compared to steel [1]. NCS (Nano cellulose in suspension with 7% concentration) helps to increase the compressive strength of the cement with changing the density of the cement slurry, due to its specific weight of 1.06 and high water content, water can be replaced by NCS to a small extent. NCS being viscous in nature cannot be used more than 5% (i.e. 0.35% nanocellulose and 3.7% water) BWOC (by weight of cement).

NCS is prepared by acid hydrolysis of cellulose (in this case from cotton) (Fig. 1).

### 1.1 Properties of NCS

1. Width = 5–20 nm and length in micrometres
2. Long fibre-like structures
3. Viscous
4. Acid hydrolysis gives short fibres (100–1000 nm in length)
5. Fibres are entangled at microscopic level
6. Tensile strength is 7.5–7.7 GPa
7. Strain up to 12%
8. Strength/weight ratio is 8 times that of steel
9. Impermeable to gas

Initially, effects of NCS were compared with neat cement for density of 15.8 pp. Five percentage is the maximum permissible after which the mixability of the slurry is very low. Increase in compressive strength with increase in NCS was seen, whereas in case of 12 pp cement decrease in strength was seen with increase in NCS and an excess of water was found in cube mould which indicated unstable slurry. So, 3% aquagel (bentonite substitute) was added to stabilize slurry. Even after stabilizing, compressive strength went on decreasing.

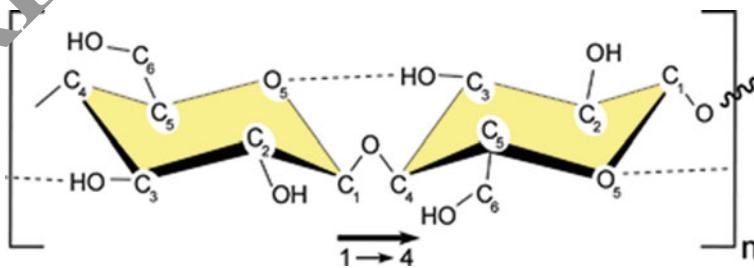


Fig. 1 Cellulose schematic. Adapted from Ref. [2]

## 1.2 Objective

- To check the effect of nanocellulose on conventional cement.
- Design slurry for 12 ppg cement.
- Get a stable 12 ppg cement (no settling and uniform density).
- Check the properties of this cement, i.e. compressive strength, tensile strength, plastic viscosity and yield point.

## 1.3 Methodology

- Prepare specimen for 15.8 ppg and 12 ppg cement by varying the proportion of nanocellulose in aqueous suspension (NCS, i.e. 7% concentration of nanocellulose in aqueous solution).
- Check the mechanical properties of conventional 15.8 ppg cement by taking NCS in proportion of 0, 2, 4, 5% BWOC.
- If positive, check the mechanical properties for 12 ppg neat cement with NCS in proportion of 0, 5, 10, 20% BWOC.

## 2 Experiments Conducted

### 2.1 Rheology Using Viscometer

Rheology refers to the deformation and flow behaviour of all forms of matter. Certain rheologic measurements made on fluids, such as viscosity, gel strength, help determine how this fluid will flow under a variety of different conditions. This information is important in the design of circulating systems required to accomplish certain desired objectives in drilling operations (Fig. 2).

**Viscosity:** Viscosity is defined as the resistance of a fluid to flow and is measured as the ratio of the shearing stress to the rate of shearing strain.

**Yield Point:** This is the measure of the electro-chemical or attractive forces in the mud under flow (dynamic) conditions. These forces depend on (1) surface properties of the mud solids, (2) volume concentrations of the solids and (3) electrical environment of the solids.

#### 2.1.1 Test Equipment

The Fann viscometer is a coaxial cylindrical rotational viscometer, used to determine single or multi-point viscosities. It has fixed speeds of 3, 6, 100, 200, 300 and 600 RPM that are switch selectable with the RPM knob.





Fig. 2 Fann viscometer

## 2.2 Hydraulic Compressive Strength Testing

Compressive strength is one of the main properties of cement which helps to avoid the collision of the casing in well. We have used the hydraulic compression machine to test the compressive strength of the cement (Fig. 3).

**Fig. 3** Chandler compressive strength testing machine



### 2.3 B.P. Settling Test

The B.P. Setting Tube is used to test the settling characteristics of a well cement. The cement slurry is poured into the tube and then cured in a consistometer or water bath. After the cement has cured, the column is then cut into six pieces (named T, A, B1, B2, C and B) and the density of each piece is measured using Archimedes principle (Fig. 4).

### 2.4 Brazilian Tensile Strength Test

The tensile strength of concrete is one of the basic and important properties. Splitting tensile strength test on concrete cylinder is a method to determine the tensile strength of concrete (Fig. 5).

Fig. 4 B.P. settling mould and sample

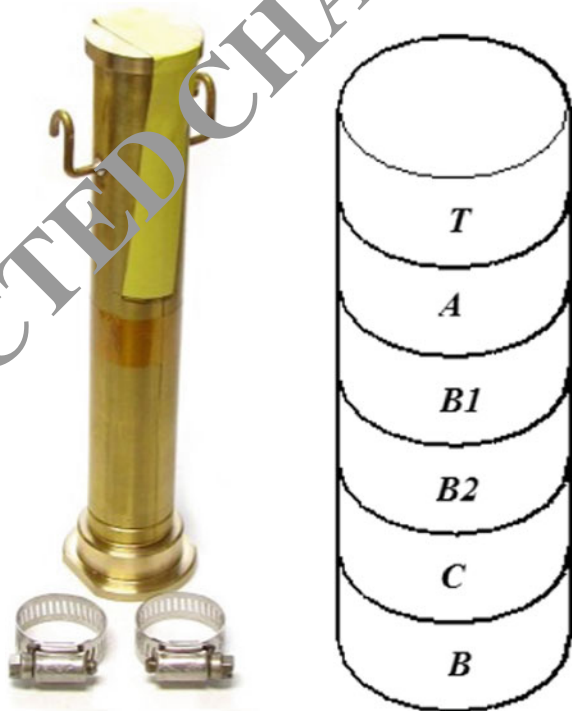




Fig. 5 Split tensile strength machine

#### 2.4.1 Sampling of Concrete Cylinders

The cylinder mould shall be of metal, 3 mm, thick. Each mould is capable of being opened longitudinally to facilitate the removal of the specimen and is provided with a means of keeping it closed while in use. The mean internal diameter of the mould is  $15 \text{ cm} \pm 0.2 \text{ m}$ , and the height is  $30 \pm 0.1 \text{ cm}$ . Each mould is provided with a metal base plate mould, and base plate should be coated with a thin film of mould oil before use, in order to prevent adhesion of concrete.

### 3 Calculation

#### 3.1 Data

Specific weight of cement ( $W_C$ ) = 3.15

Volume occupied by 1 gm ( $V_C$ ) = 0.31746 ml

Specific weight of water ( $W_W$ ) = 1.00

Volume occupied by 1 gm ( $V_W$ ) = 1.00000 ml

Specific weight of NCS ( $W_N$ ) = 1.06

Volume occupied by 1 gm ( $V_N$ ) = 0.943396 ml

Specific weight of friction reducer ( $W_F$ ) = 1.17

Volume occupied by 1 gm ( $V_F$ ) = 0.8547 ml

Specific weight of bentonite ( $W_B$ ) = 2.65  
 Volume occupied by 1 gm ( $V_B$ ) = 0.37736 ml

We take all the chemicals in their required quantities as the % BWOC (by weight of cement) except water as we need constant density. Increase and decrease in water % help to maintain the required density of the slurry. So, we take all components and then calculate the quantity of water required to get the required slurry density.

### 3.2 Steps for Calculations

1. Take the weight in % BWOC of all chemicals except water (note weight and volume of water are same, and let it be “x” for calculations).
2. Find the corresponding volume for each chemical by multiplying the volume occupied by each or by dividing its specific weight.
3. Add all weights including weight of water as “x”: let it be ( $W + x$ ).
4. Add all volumes including volume of water as “x”: let it be ( $V + x$ ).
5. Select the density of slurry in  $g/cm^3$ : let it be  $y$ .
6. Calculate  $x$  using formula:

$$\frac{W + x}{V + x} = y$$

7. For 15.8 ppg:  $y = 1.89325 g/cm^3$ .
8. For 12 ppg:  $y = 1.4379 g/cm^3$ .
9. We add all volumes of chemical as  $=V + x$  and divide 600 ml by ( $V + x$ ), to get a multiplication factor to increase the quantity of chemicals to get a final volume of slurry as 600 ml, which is the standard for blending at 12,000 rpm.

All the calculated values are shown in Table 1.

## 4 Results and Discussion

Initially, the maximum amount of NCS that can be used was found out by mixing the cement with NCS in varying proportion of 2, 5 and 10%. It was found out that 5% BWOC is the maximum that can be used as an additive due to high viscosity of the cement. Experiments were conducted to check the effect of NCS on the compressive strength and thickening time of conventional 15.8 ppg cement. Results being positive, efforts were made to use NCS as add mixture for lightweight cements, i.e. 12 ppg, and see the effects on its strength. Four samples for 12 ppg neat cement were prepared by varying NCS as 0, 5, 10 and 20%. Due to excessive water, NCS can be used more than 5% in light cements. Initially, slurry was unstable and 25% water was seen in the cube after curing. So to stabilize the slurry, bentonite was added 3% BWOC, which

**Table 1** Concentration of constituents in each sample

Sample name	15.8 ppg slurry				12 ppg slurry (without bentonite)				12 ppg slurry (with bentonite)			
	15.8A	15.8B	15.8C	15.8D	12A	12B	12C	12D	12BA	12BB	12BC	12BD
Class G cement (% BWOC)	100	100	100	100	100	100	100	100	100	100	100	100
Friction Reducer (% BWOC)	0.3	0.3	0.3	0.3	0	0	0	0	0	0	0	0
Nanocellulose (% BWOC)	0	2	4	5	0	5	10	20	0	5	10	20
Bentonite (% BWOC)	0	0	0	0	0	0	0	0	3	3	3	3
Water (% BWOC)	44.5	42.7	40.9	40.1	124.1	120.1	116	108	123.9	123.2	119.1	110

helps to get uniform slurry with no excess water in cubes. Addition of bentonite decreased the overall strength of all samples.

### 4.1 Result of 15.8 ppg Cement

#### 4.1.1 Compressive Strength

For finding the compressive strength, two cubes were set at 170 °F for 24 h for each sample. Then, it was crushed in hydraulic machine and the force utilized to break the sample was noted. Compressive strength for neat cement was found to be 2450 and 3250 psi, 3450 and 3875 psi for cement samples with 2, 4 and 5% NCS concentration. So, from Fig. 6, we can see a linear increase in the strength of cement with increase in percentage of the NCS, and this may be due to the size and shape of NCS. Being a nanosized particle, it fills in the pores in the sample which improves the structure at molecular level. And cellulose being fibre-like structure provides better bonding in the particles. Also, from Fig. 6, an increase in compressive strength by 50% is seen on addition of NCS in concentration of 5% BWOC (Tab. 2).

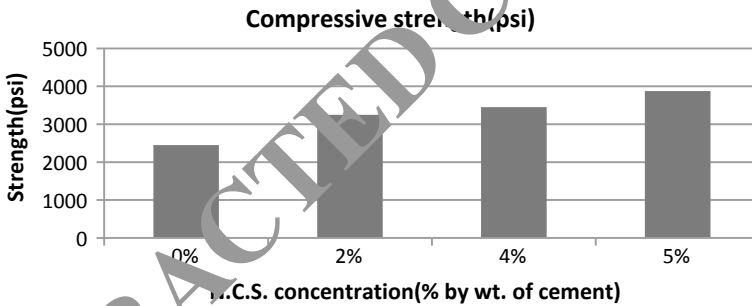


Fig. 6 Compressive strength versus NCS concentration

Table 2 Viscometer reading for 15.8 ppg cement

RFM	3	6	100	200	300	600
0% NCS	8	14	32	45	60	
	10	14	29	45		100
2% NCS	17	20	30	60	70	
	20	25	30	60		105
4% NCS	20	25	47	65	82	
	20	25	47	63		127
5% NCS	30	36	62	78	93	
	30	37	60	77		139

### 4.1.2 Rheology

From Fig. 7a, we can see an increase in plastic viscosity and yield point (Fig. 7b) with increase in NCS concentration, with highest value as 61.34 cp and 36.86 lb/100 ft<sup>2</sup> as plastic viscosity and yield point, respectively, which was even higher without the use of friction reducer. So, we cannot use more than 5% of NCS. Increase in viscosity creates problem while pumping the cement down the hole.

## 4.2 Result of 12 ppg (Without Bentonite) Cement

### 4.2.1 Compressive Strength (psi)

In case of this 12 ppg cement, huge settling was seen due to excess of water added to lower the density. Hence, the compressive strength goes on decreasing with increase in NCS content (Fig. 8). With the NCS content of 20%, the compressive strength is nearly half that of the neat cement. So, we have to stabilize the cement for proper results.

### 4.2.2 Rheology

Nanocellulose being high viscous in nature, it increases the viscosity of the cement as well as the yield point is increased. So we can see from the graph (Fig. 9a) both viscosity and yield point (Fig. 9b) go on increasing for this 12 ppg cement as well as for 15.8 ppg cement (Table 3).

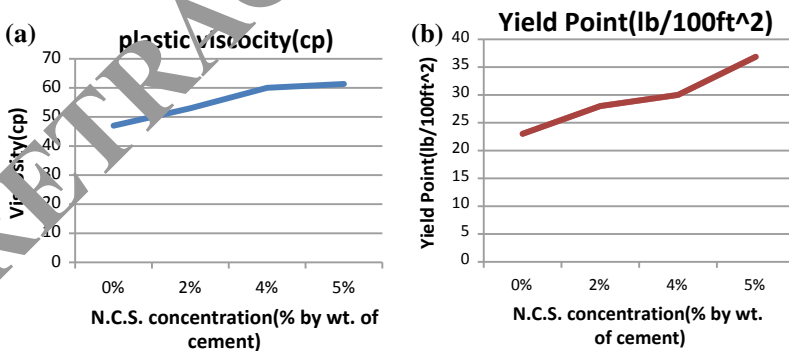


Fig. 7 a Plastic viscosity and b yield point



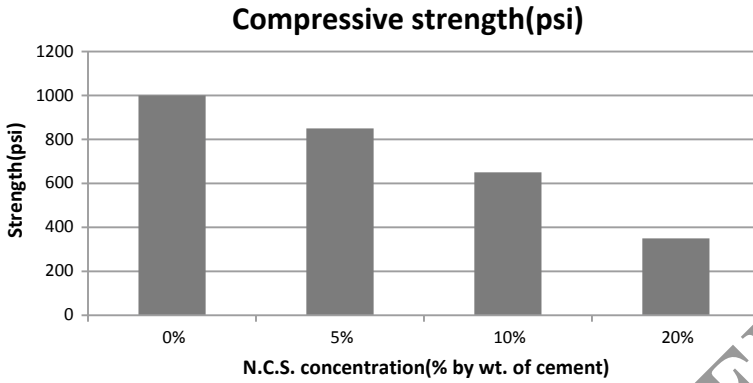


Fig. 8 Compressive strength versus NCS concentration

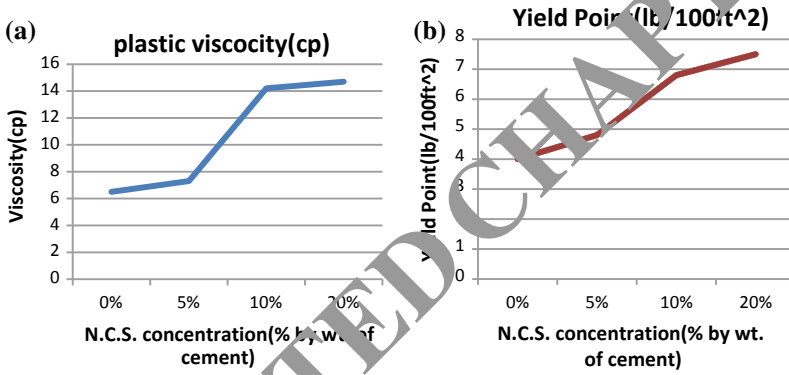


Fig. 9 a Plastic viscosity and b yield point

Table 3 Viscometer readings for 12 ppg (without bentonite) cement

RPM	3	6	100	200	300	600
0% NCS	3	4	7	9	10	
	3	4	7	9		23
5% NCS	4	5	8	10	11	
	3	4	8	10		25
10% NCS	4	6	13	16	20	
	5	8	14	16		28
20% NCS	5	6	15	17	20	
	6	7	15	19		33

### 4.3 Results of 12 ppg Stable Slurry

The previous slurry was highly unstable, and a lot of settling was there which leads to decrease in compressive strength of the cement with increase in NCS. So to stabilize this cement, we added 3% BWOC bentonite and B.P. settling test was done as shown.

#### 4.3.1 B.P. Settling Test

The samples are cut into six pieces as shown in Fig. 4. And the pieces are named as T, A, B1, B2, C and B.

From B.P. settling test results (Table 4), we can see that the density is nearly uniform throughout the sample. With least density of 11.75 ppg and highest 12.15 ppg which indicates stable slurry.

#### 4.3.2 Compressive Strength (psi)

This stable slurry has good compressive strength (Fig. 9) compared to previous slurry (Fig. 8). The compressive strength is changing very less compared to the increase in NCS. Compressive strength decreases with increase in NCS till 10% but increased at 20%. Overall, the decrease in compressive strength is due to bentonite. But, bentonite is must for getting stable slurry or the slurry will not have uniform density and huge settling will take place.

#### 4.3.3 Rheology

In case of stable slurry, plastic viscosity increases as other slurries (Fig. 11a), but here yield point (Fig. 11b) goes on decreasing with increase in NCS (Table 5).

**Table 4** B.P. settling test results

Piece	Weight in air (g)	Weight in water (g)	Density (ppg)
T	16.45	11.40	12.02
A	22.08	15.21	12.09
B	18.61	13.00	11.93
B2	20.46	14.45	11.79
C	18.72	13.27	11.75
B	20.83	14.28	12.15

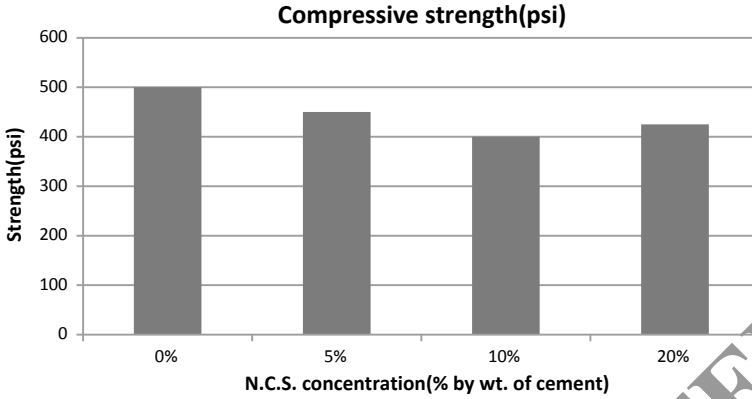


Fig. 10 Compressive strength versus NCS concentration

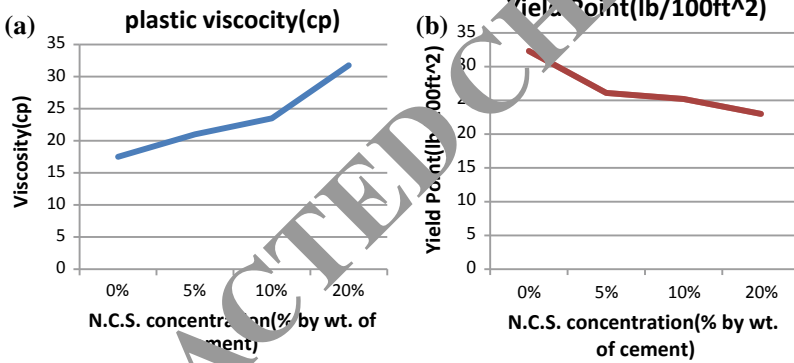


Fig. 11 a Plastic viscosity and b yield point

Table 5 Viscosity meter reading for 12 pp (with bentonite) cement

RPM	3	6	100	200	300	600
0% NCS	24	32	35	41	46	
	29	35	39	43		59
2% NCS	19	27	35	40	44	
	22	29	35	40		57
4% NCS	11	19	27	31	35	
	15	21	26	30		39
5% NCS	14	20	40	46	50	
	18	27	38	43		55

## 5 Conclusion

The results for 15.8 ppg cement showed increase in compressive strength of cement with the increase in NCS. But for 12 ppg slurry both stable and unstable, there was decrease in mechanical properties. So, NCS has been ineffective in increasing the mechanical properties of cement for low density. But considering the results of 15.8 ppg cement and the fact that nanocellulose has very high tensile strength, which is 8 times compared to steel in terms of strength-to-weight ratio, we can say that they have good scope in increasing the mechanical properties. Some more work is needed regarding this to properly utilize this material. Also, this can be used in case where we have to increase the viscosity in slurry without affecting other properties, e.g. case of ultralight cement. In ultralight cement (around 10 ppg), micro spheres are used as add mixture to get required strength. But due to low density of micro spheres and high density of cement, there is settling of cement and microsphere floats on the top, which gives us unstable cement which cannot be used. NCS particles are suspended freely in water which helps in suspension of microsphere. We can even use bentonite for same, but bentonite decreases compressive strength so NCS is a better option for this case.

## References

1. Mazlan D, Mddin MF, Tokoro C, Ibrahim IS (2016) Cellulose nanocrystals addition effects on cement Mortar matrix properties. *Int J Adv Mech Civil Eng* 3(1). ISSN 2394-2827
2. Hubbe MA, Rojas OJ, Lucia LA, Sain M. (2008) Cellulosic nanocomposites: a review. *BioResources* 3:929–980

# Analyzing the Physical and Chemical Properties of Water Column Nutrients and Sediments Along Southeast Coast of India



G. Annalakshmi and S. Sakthivel Murugan

**Abstract** The acoustic signal transmission in underwater is strongly affected by the interaction of sea-bottom sediments. The geo-properties like mean grain size, porosity, grain density of marine sediments affect the sound propagation. These properties vary from location to locations; this is dependent on depositional characteristics of the particular location. This paper presents a study on the sediment characteristics deposited along the coastal region of Tamil Nadu in the Bay of Bengal. The sediment samples were collected at four different locations like Chennai, Mahabalipuram, Cuddalore, and Kalpakkam. The sub-bottom sediment characteristics like mean, skewness, kurtosis, and sorting were analyzed using GRADISTAT program. Wide variations in mean size indicate the different energy conditions at different locations. The variation in sorting indicates the continuous addition of sand, medium sand, clay, and mud in varying proportion at different locations. The positive skewed value of sediment in particular location indicates low wave activity and longshore current. Analysis of heavy metal concentration (Fe, Zn, Cd, Pb, Cr, Ni, and Cu) and water column nutrients (nitrate, nitrite, phosphate, silicate, and urea) was analyzed to understand the physical and chemical concentration of study location. Sediment deposition and ocean current play an important role to describe the geo-properties of the particular location. Location-specific geo-inversion studies are crucial for marine activities, and data can be attained from geophysical and chemical properties.

**Keywords** Sediment analysis · Water nutrient · Trace metal · CTD measurement

---

G. Annalakshmi (✉) · S. Sakthivel Murugan  
SSN College of Engineering, Chennai, India  
e-mail: [anumevlsi@gmail.com](mailto:anumevlsi@gmail.com)

S. Sakthivel Murugan  
e-mail: [sakthivels@ssn.edu.in](mailto:sakthivels@ssn.edu.in)

© Springer Nature Singapore Pte Ltd. 2019  
K. Murali et al. (eds.), *Proceedings of the Fourth International Conference in Ocean Engineering (ICOE2018)*, Lecture Notes in Civil Engineering 22,  
[https://doi.org/10.1007/978-981-13-3119-0\\_67](https://doi.org/10.1007/978-981-13-3119-0_67)

## 1 Introduction

Almost 70% of the earth's surface is covered by marine ecosystem. The properties of the ocean such as sediment-seabed interaction, water column variability strongly influence the acoustic signal transmission. The erosion, deposition of sediment particles, is partly controlled by the chemical and physical properties of the sediment and water column properties of the particular location. The shallow water acoustics communications are largely determined by the seafloor characteristics. The nutrient variation in the sea water affects the sound propagation through the under water [1]. The interaction of biological and hydrodynamic processes mainly controls the physical and chemical properties of oceanic sediments, [2]. In order to forecast the geophysical involvement in the underwater signal transmission, the geo-property models of the real seafloor are required, which further require the physical details such as grain size, sediment type, compressional, shear wave velocities [3]. The geotechnical properties of the seafloor can be understood by using the information gathered from the sediment attenuation. Likewise to study the effect of sound propagation in the marine sediment, the information of variations of attenuation with frequency can be used. The geo-characteristics of a particular location can be described using the sediment statistical parameters like particle size, mean, sorting, kurtosis, and skewness [4]. The sediment composition depends on tides, wind, and ocean current. The grain size classifications are used to separate high and moderate energy environments [5]. The spatial and temporal properties of the seafloor are determined by the sediment deposition, which can be limited by factors like environment and sediment deposition in a particular location [6]. The sound propagation in the water column is largely affected by the variations in the water column parameters, and sound interacts with the sea bottom [7]. Density, sound speed, attenuation, and reverberation in marine sediment are important in geoacoustic parameters that affect the acoustic propagation in seafloor. The sound interaction in seabed is more complex than the sea surface. [8]. The bottom properties composition varies from soft mud to hard rock. When the acoustic signal is transmitted to the sea bottom, it is scattered and reflected back by sub-bottom. The loss in the signal can be easily predicted in seafloor when compared to sea bottom. Ocean acidification also plays an important role in determining the communication in marine environment [9]. Phase speed depends on the geo-properties of sediment such as grain size, density, porosity, and depth [10]. Sound interaction between oceans is essential for the sonar system to detect the buried objects. The scattering of the absorbent sand is mostly affected in the mid-frequency region where the speed of sound changes from low to high [11]. When the metal concentration in sediment is high compared to the water column nutrients, it generates a problem in coastal region due to their bioaccumulation and harmfulness [12]. It is important to know the environmental quality in particular locations; hence, the geophysical and chemical compositions in sediments and water column nutrients are analyzed. The sources of pollutions are anthropogenic and natural properties. Industries are the major source of pollutant in the marine coastal area. Anthropogenic discharge from the nearby area increases the concentration of

metals in the ocean [13]. Analyzing the metal concentration in sediments delivers the valuable information about metal concentration, contamination index, and pollution level of metal in sediments [14]. Geoacoustic properties of marine sediment generally have larger variations in depth near the water-sediment boundary due to various mechanisms including pressure porosity. Marine sediments concentration often changes the properties of geoacoustic in sedimentary layer [15].

## 2 Sediment Collection Method and Analysis Channel

Sediment samples were collected from Chennai, Kalpakkam, Mahabalipuram, and Cuddalore at different depths using coastal research vessel Sagar Purvi. The sediment samples were collected using Van Veen Grab. Figure 1 shows the deployment and retrieval of Van Veen Grab.

The collected sediment samples are washed in floating water and then dried at 80 °C for 48 h using hot air oven as shown in Fig. 2a. After drying the samples, 100 g is measured and placed in the sieve shaker as shown in Fig. 2b, c, which has the eight sieve sizes like 63, 90, 125, 180, 212, 250, 355 and 500  $\mu\text{m}$ . Particle size refers to the size of the particles in sediment. The statistical parameters such as mean, skewness, sorting, and kurtosis were computed using GRADISTAT grain size distribution and statistical package.

Sediment sample collected locations details are shown in Table 1. The grain size analysis of the particular location is important to understand the various depositional characteristics of the particular environment. These statistical parameters are used to describe the sediment particle size properties such as mean, skewness, kurtosis, and sorting. A well-sorted sediment is one in which the grains are all about the same size. In difference, poorly sorted sediment includes mixture of small, large, and intermediate grain sizes. In general, the mean is denoted by  $\phi$  and grain size value of the sediment varies from 0.157 to 2.140  $\phi$ . It is noted that the grain size of the study location varies from fine to medium sand. The larger value of  $\phi$  indicates the

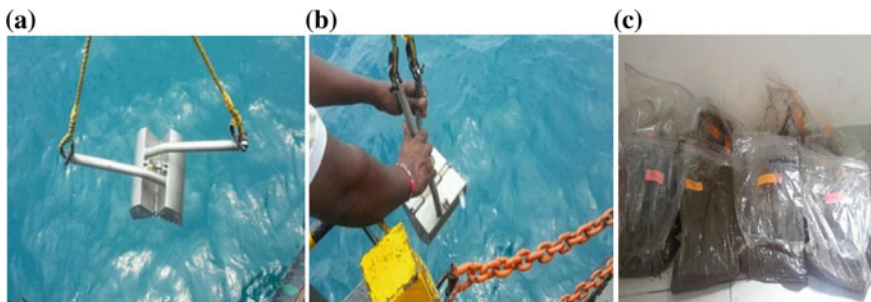


**Fig. 1** a Van Veen Grab deployment, b Van Veen retrieval, c sediment sample collected

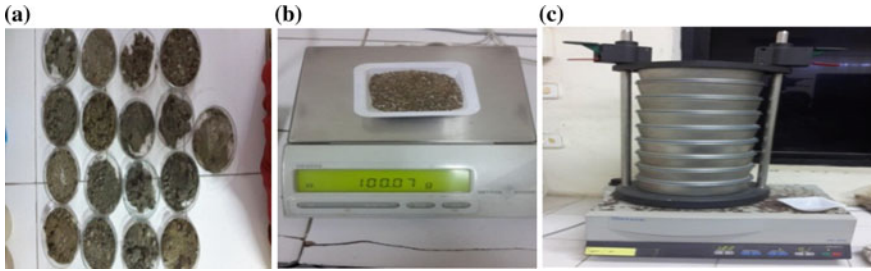


**Fig. 2** a Collection of dried sample, b 100 g of dried sample, c sieve shaker machine

energy-level variations of deposition medium. The sorting measures the difference in kinetic energy of the sediment deposition. This value ranges from 0.4 to 1.8  $\phi$ . The sorting values of sediment are continuously varied due to addition of sand during deposition. The sorting decreases with increasing the value of the sediment composition. The peakedness of the sediment distribution is measured by skewness. The skewness values range from  $-0.12$  to  $2.5 \phi$  with an average value of  $3.25 \phi$ . The negative value of the skewness represents the higher energy environment, whereas the low-energy environment is represented by positive energy. The normality distribution of the sediment is measured by kurtosis. Compare to all other statistical parameters, it is observed that kurtosis value is dominant because of the higher energy environment. The spatial property of the sediment helps to identify the current environment condition.

Comparisons on statistical parameters of the sediment collected were shown in Fig. 3. The spatial property of the sediment helps to identify the current environment condition. These methods are commonly used to simplify the comparisons among the samples and qualify the observed difference. From the analysis, percentage of sand and medium sand concentration is high compared to other types of soil. Figure 4 shows the composition of various types of soils present in various samples used for the analysis.

### 3 Sound Velocity Measurement in Seawater Using CTD Data

The sound velocity measurement in ocean is one of the important problems in hydrographic survey. The acoustic signal that travels in water column depends on the parameters like sound velocity, density, and viscosity [16]. The value of the sound velocity depends on the physical properties of ocean also it is essential to have accurate knowledge of the velocity of sound. The seawater nutrients vary as a function of temperature, depth, pressure, and salinity [17]. The speed of the sound in water column impacts the propagation of acoustic signal in the seawater column. Pressure



**Table 1** Sediment sample collected locations

S. No.	Locations	Latitude and longitude	Depth (m)
1	Chennai	N 13°15.30'' E 80°20.59''	16
		N 13°05.68'' E 80°19.92''	Trial(1)-30
			Trial(2)-30
2	Kalpakkam	N 12°38.51'' E 80°15.76''	Trial(1)-26
			Trial(2)-26
3	Mahabalipuram	N 12°38.51'' E 80°15.76''	Trial(1)-23
			Trial(2)- 23
			26
4	Cuddalore	N 11°46.55'' E 79°52.64''	25
		N 11°50.65'' E 79°58.74''	40
		N 11°48.47'' E 79°55.54''	30
		N 11°62.65'' E 79°62.74''	60

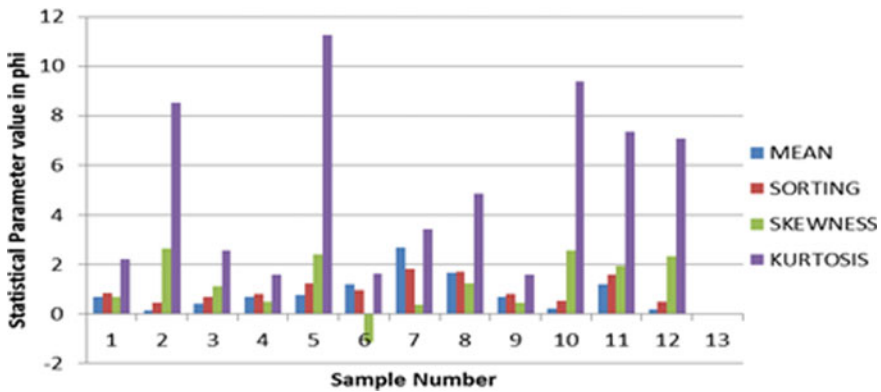


**Fig. 3** Comparison charts of statistical parameters

plays a main role in deep sea; as depth increases pressure also increases [18]. The sound velocity measurement in ocean is one of the important factors. The sound velocity profile of the water column gives valuable information about ocean properties. Sound velocity values in the sea generally range from 1500 m/s. Sound signal travels faster in ocean when temperature, salinity, and pressure values are high. The sound speed computation-based data like temperature, salinity, density were mea-

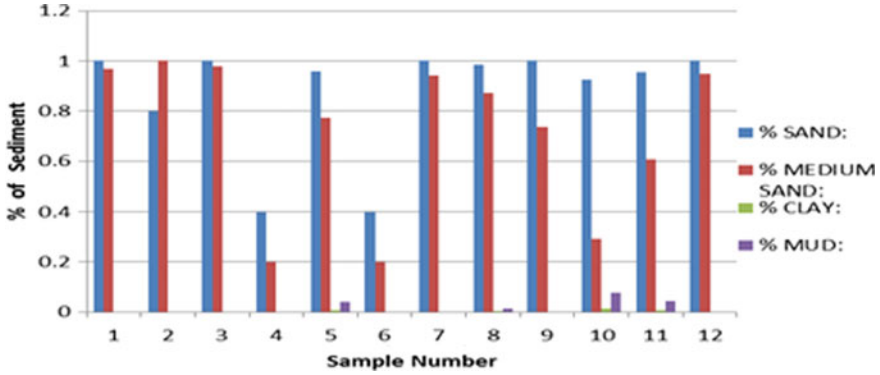


Fig. 4 Composition of various types of soil for various sediments

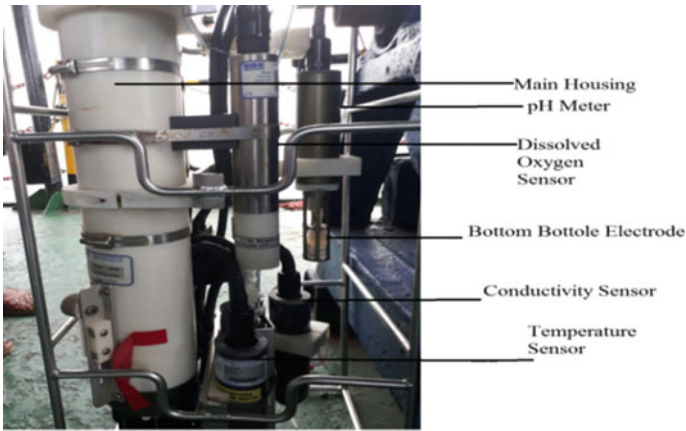


Fig. 5 SBE 25 CTD

sured in the above-mentioned location using SBE 25 plus sealogger CTD during August 2017 at the Bay of Bengal using ship CRV Sagar Purvi. Figure 5 given below shows the image of SBE 25 CTD.

Sound speed of the signal varies with respect to seawater characteristics. For the above-mentioned locations, sound speed varies between minimum and maximum of 1445–1550 m/s. The sound speed of the signal is derived from empirical formula which uses the value of salinity, pressure, and temperature. Figure 6 given below shows the CTD plots of different locations.

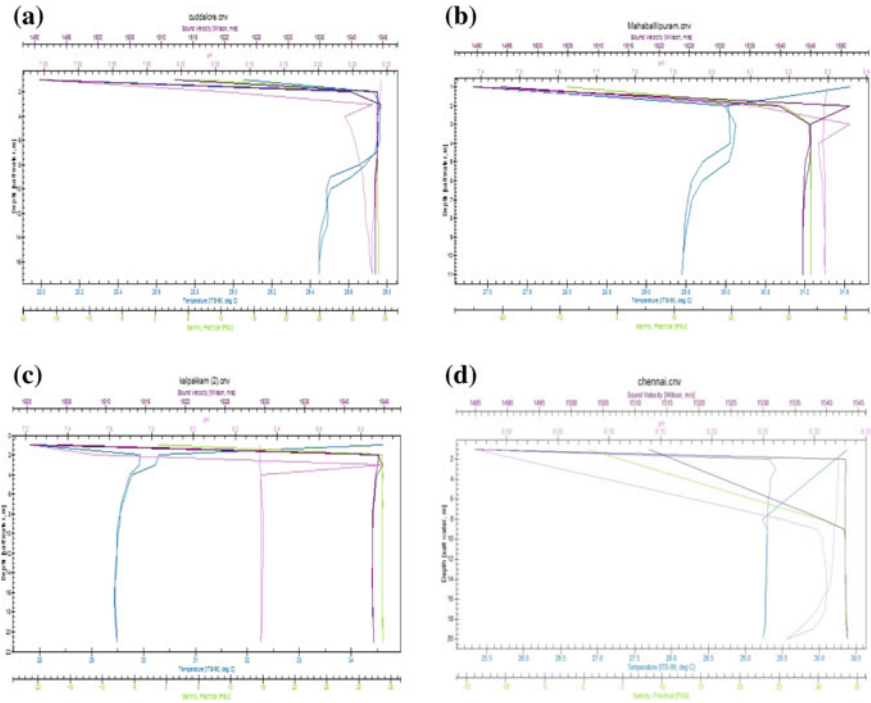


Fig. 6 CTD plots of different location **a** Cuddalore, **b** Mahabalipuram, **c** Kalpakkam, and **d** Chennai

### 4 Seawater Nutrient Analysis

The samples are collected along the coastal region of Tamil Nadu. To measure accurate chemical composition of seawater, samples are collected with almost care using 5 L Niskin water samplers. After collecting, samples are stored in freezer. Before the laboratory testing, the samples are filtered using 0.45  $\mu\text{m}$  filter papers. After that samples are analyzed using AutoAnalyzer in ICMAM laboratory. Figure 7 shows the processing steps of water sample.

Phosphate concentrations increase with depth, as remineralization of sinking particulate matter returns dissolved nutrients to the water column [19]. The phosphate concentration is high in water column due to mixing of sediment like mud. The distribution characteristic of the sediment depends on the environment condition. The higher concentration of nitrate is observed in water column due to the presence of organic matter in the ocean. Nitrate is the highest pollution indicator in ocean. The nitrate concentration in the water column is increased due to wastage discharges, rocks in the sediments, and freshwater inflow. The concentration of nitrite is increased due to seasonal variations, phytoplankton, and oxidation of ammonia [20]. The lower concentration is observed in Cuddalore (0.129  $\mu\text{mol/L}$ ). Silicate is an essential nutrient to control marine productivity. Silicate concentration may

vary due to mixing of sediments in seawater. Silicate concentration depends on land properties which has higher concentration in rainy season. Urea is getting attention in phytoplankton physiology and ecology. The higher concentration of urea affects the biological activity. The concentration of nutrient level is shown in Fig. 8.

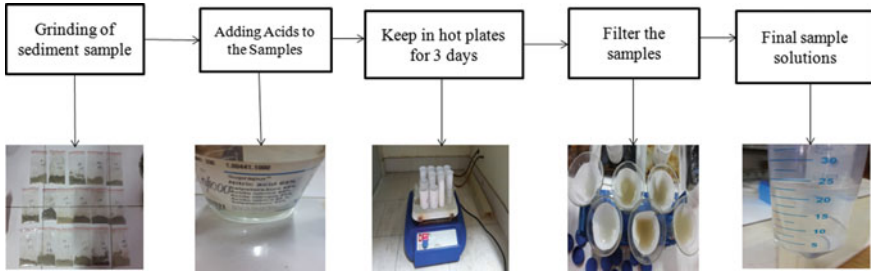


Fig. 7 Procedure to test water sample

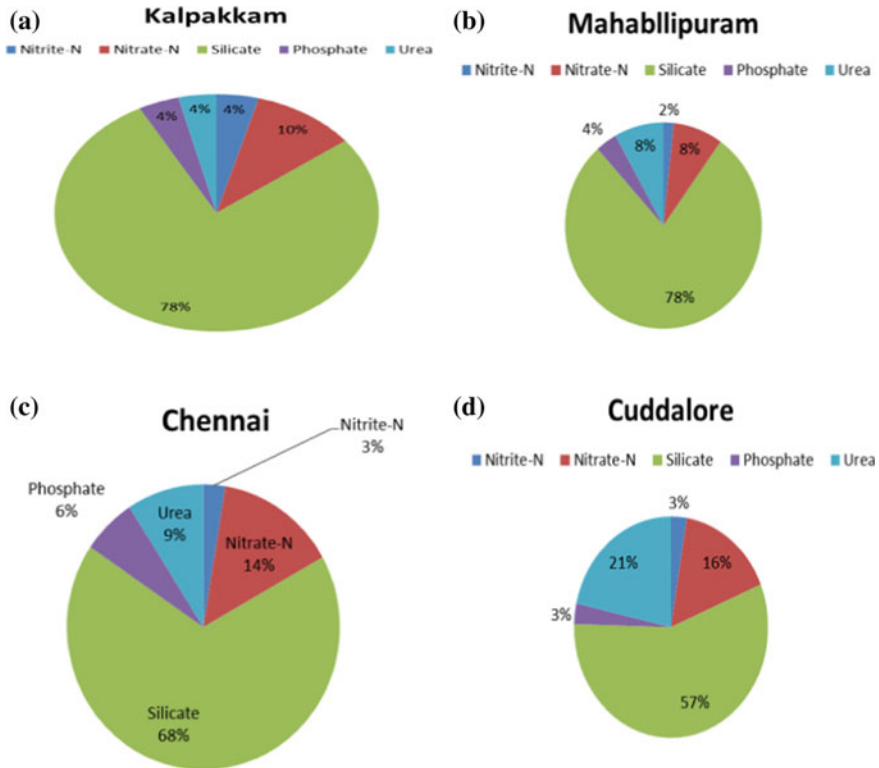
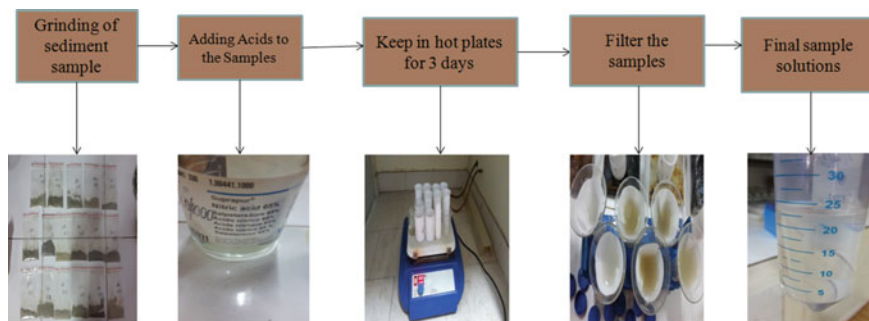


Fig. 8 Concentration of nutrient in a Kalpakkam, b Mahabalipuram, c Cuddalore, and d Chennai

## 5 Determination of Heavy Metal

In recent years, heavy metal deposition in the ocean environment has become a worldwide problem. The metal concentration in marine sediment is used to measure the pollution level of marine ecosystems. Awareness of the metal distribution in water column and sediment is needed because when the metal is introduced into the ocean water column, it is transported and deposited in marine bottom sediments [21]. Heavy metal distribution in the ocean sediments is controlled by the natural sources of the environment, different soil particles, and sizes. A biological activity along with the ocean pH level plays a vital role in controlling the heavy metal reaction in marine sediments. Various chemical processes in the ocean can also influence the metal concentration in marine sediments [22]. The sediment samples were collected along coastal region of Tamil Nadu. In collected samples, dust particles are removed through sieve analysis. Earlier to the analysis about 20 g of samples were dried in the oven at 80 °C for 24 hours. The samples are grained to make it as fine powder; from the grained powder 0.5 gm is taken in beaker and Nitric acid is added, then solutions are kept in the hot plate for three days to get white diluted sediment sample and then add 20 ml of Nitric acid to the sediment sample. Follow these samples were filtered through filter paper and make it as 25 ml of final solution for the analysis. The trace metal analysis carried in ICMAM trace metal lab using Atomic Absorption Spectrometer. The procedures details are shown in the below Fig. 9.

Copper is an essential element for ocean environment within the acceptance level [23]. Copper (Cu) creates severe problem in the ocean environment beyond acceptance limit of 35  $\mu\text{g/g}$ . Cu reacts with fine particles of marine sediments like clay and silt because of its higher ionic and absorption characteristics. The higher concentration is observed in Mahabalipuram, and lower concentration is observed in Cuddalore. The sources of copper are corrosion products, anthropogenic sources, industrial metals, and mining waste. The higher concentrations of nickel are produced by anthropogenic deposition from the fossil fuels. Cadmium (Cd) is highly toxic to plants and animals that are present in the sea, which the main anthropogenic



**Fig. 9** Steps to make liquid sediment sample

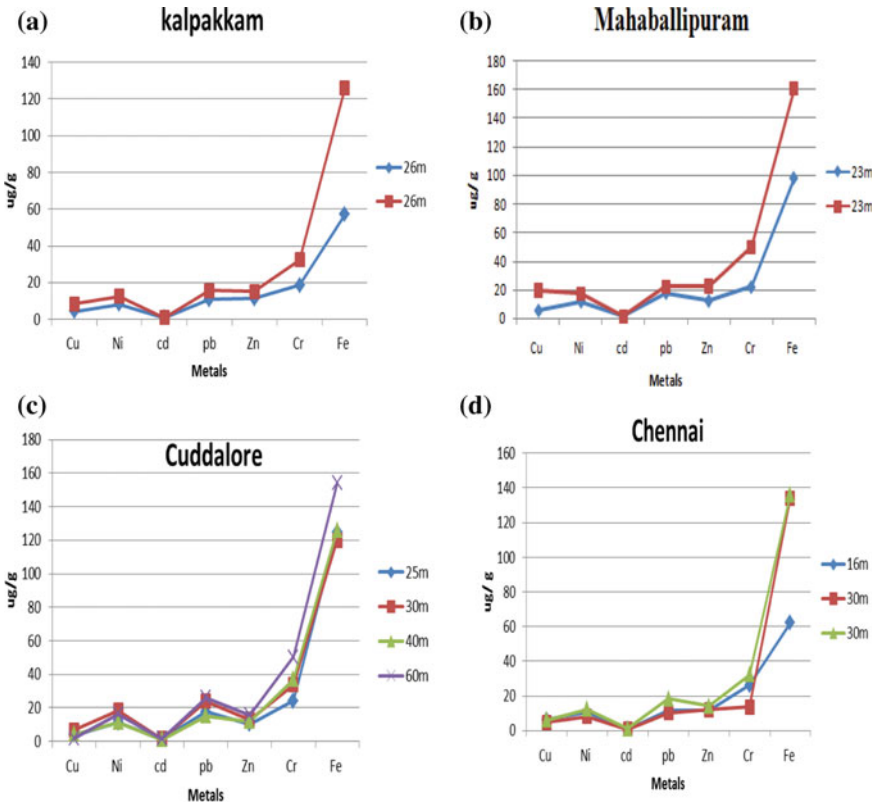


Fig. 10 Metal concentration in a Kalpakkam, b Mahabalipuram, c Cuddalore, and d Chennai

sources relate to industries wastage, mine wastes, sewage mud discharges. Contamination of chromium (Cr) is higher in sediment sample compared to world average value. The concentration of chromium is increased in the environment due to leaving of wastes in the sea. Increasing percentage of fine material increases the iron concentration in the sediment. Iron reduction in sediment samples plays a dynamic role in biogeochemical cycle. Figure 10 shows the metal concentration in Kalpakkam, Mahabalipuram, Cuddalore, and Chennai.

## 6 Conclusion

Physical characteristics of marine sediment and water column nutrients were analyzed along the coastal region of Tamil Nadu. Grain size analysis of sediment samples collected at different locations shows that in more number of samples, sand and medium sand are dominant. Mean value represents the dominance of medium sand

with dominant well-sorted character due to continuous action of waves. Most of the sediment samples are positively skewed. It is observed that increasing depth increases the chemical relation in the seawater. Sound speed profile of all the locations was plotted as a function of depth. Iron has the higher concentration compared to others due to higher sediment transport. Location-specific geo-inversion studies are crucial for marine activities, and data can be attained from geophysical and chemical properties.

**Acknowledgements** The authors thank the Vessel Management Cell and ICMAM Teams of National Institute of Ocean Technology (NIOT) for supporting this study by providing the vessel Sagar Purvi for sample collection and Dr. P. Madheswaran, Project Directorate, and his team for providing facilities in ICMAM Laboratory to carry out the study successfully.

## References

1. Hassan BA (1993) Oceanographic variability in shallow-water acoustics and the dual role of the sea bottom. *IEEE J Ocean Eng* 18(1):31
2. Richardson MD, Young DK, Briggs KB (1983) Effects of hydrodynamic and biological processes on sediment geoaoustic properties in Long Island sound, USA. *Mar Geol* 52:120
3. Hamilton EL (1980) Geo acoustic modeling of the sea floor. *J Acoust Soc Am* 68:1313
4. Leblanc LR, Panda S, Schock SG (1992) Sonar attenuation modelling for classification of marine sediments. *J Acoust Soc Am* 91(1)
5. Davis A, Haynes R, Bennell J, Huws (2002) Surficial seabed sediment properties derived from seismic profiler responses. *Mar Geol* 182:209–223
6. Schlebaum W, Schraa G, van Riemsdijk WH (1999) Influence of nonlinear sorption kinetics on the slow-desorbing organic contaminant fraction in soil. *Environ Sci Technol* 33:1413–1417
7. Hamilton EL (1980) Geoaoustic modelling of the sea floor. *J Acoust Soc Am* 68:1313–1318
8. Del Grosso VA (1974) New equation for the speed of sound in natural waters (with comparisons to other equations). *J Acoust Soc* 56:1084
9. Buckingham MJ (2005) Compressional and shear wave properties of marine sediments: comparisons between theory and data. *J Acoust Soc Am* 1:137–152
10. Gazioglu C, Edip Muftuoglu A, Demir V, Aksu A, Okutan V (2015) Connection between ocean acidification and sound propagation. *Int J Environ Geoinform* 2:16–26
11. Buckingham MJ (2005) Compressional and shear wave properties of marine sediments: comparisons between theory and data. *J Acoust Soc Am* 117(1):137–152
12. Maguera A, Bovio E, Fox WLJ, Schmidt H (2000) In situ estimation of sediment sound speed and critical angle. *J Acoust Soc Am* 3:987–996
13. Raknuzzamana M, Kawser Ahmedc Md, Saiful Islamd Md, Habibullah-Al-Mamuna Md, Tokumuraa M, Sekinea M, Masunagaa S (2016) Assessment of trace metals in surface water and sediment collected from polluted coastal areas of Bangladesh. *J Water Environ Technol* 14(4):247–259
14. Kljakovicgaspic Z, Bogner D, Ujevic I (2009) Trace metals (Cd, Pb, Cu, Zn and Ni) in sediment of the submarine pit Dragon ear (Soline Bay, Rogoznica, Croatia). *Environ Geol (Springer)* 58:751
15. Hu J, Huang X, Zhang Y, Li C, Qin F (2010) Chemical speciation of trace metals in superficial sediment from Lake Hongfeng, China. In: Second international symposium on aqua science, water resource, and low carbon energy. AIP conference proceedings, vol 1251, pp 404–407
16. Onjefu SA, Kgabi NA, Taole SH (2016) Heavy metal seasonal distribution in shore sediment samples along the coastline of Erongo region, Western Namibia. *Eur J Sci Res* 139(1):49–63

17. Suresh Gandhi M, Raja M (2014) Heavy mineral distribution and geochemical studies of coastal sediments between Besant Nagar and Marakkanam, Tamil Nadu, India. *J Radiat Res Appl Sci* 7
18. Natesan U, Ranga Rama Seshan B (2010) Vertical profile of heavy metal concentrations in core sediments of Buckingham canal, Ennore. *Indian J Geo Mar Sci* 40:83–97
19. Patey MD, Rijkenberg MJA, Statham PJ, Stinchcombe MC, Achterberg EP, Mowlem M (2008) Determination of nitrate and phosphate in seawater at nano molar concentrations. *Trends Anal Chem* 27(2)
20. Dhinamala K, Pushpalatha M, Samuel T, Raveen R (2015) Seasonal variations of nutrients in Pulicat Lake, Tamil Nadu, India. *Int J Fish Aquat Stud* 3:264–267
21. Oulad-Abdellah MK, García-Vargas M, Moreno C (2012) Analysis of heavy metals in sediments from Northern Moroccan coast using simple and low-cost methodology. *Open Environ Pollut Toxicol J* 3(Suppl 1-M6):47–54
22. Manikannan R, Asokan S, Hameed A, Ali MS (2011) Seasonal variations of physico-chemical properties of the Great Vedaranyam swamp, Point Calimere wildlife sanctuary, south-east coast of India. *Afr J Environ Sci Technol* 5(9):673–681
23. Ramamohan Rao T, Shanmukha Rao C, Sanyasi Rao K (1982) Textural analysis and mineralogy of the black sand deposits of Visakhapatnam-Bhimunipatnam Coast, Andhra Pradesh, India. *J Geo Soc India* 23:284–289



# Modeling Investigations on Sorption of Petroleum Hydrocarbons to Clay Minerals in a Saturated Porous Aquifer



Renu Valsala and Suresh Kumar Govindarajan

**Abstract** Clay minerals present within the groundwater aquifers is found to influence the migration of hazardous solutes like radionuclides and petroleum hydrocarbons. The presence of clay minerals within the aquifers is observed to either enhance or retard the movement of contaminants within the aquifer. The influence of these clay minerals on the contaminant migration depends upon the hydrologic conditions existing within the aquifer, nature of contaminants, kind of clay minerals, etc. Previous research studies have illustrated the significance of clay minerals on the migration of petroleum hydrocarbons (PHC) within the aquifers. Sorption of petroleum hydrocarbons on aquifer grains and colloid particles is a significant factor in deciding the mitigation rate of hydrocarbons. The primary objective of the present study is to numerically investigate the clay-associated transport of petroleum hydrocarbons within a saturated aquifer. The current modeling algorithm can be adapted to model the colloid-facilitated transport of other multicomponent contaminants within the fracture. The modeling algorithm is solved using a C++ program. In the present paper, simulation results for the concentration distribution of clay mineral and PHC within the aquifer are presented. Sensitivity of clay attachment and detachment rates on the concentration distribution of PHC and clay minerals are also analyzed.

**Keywords** Petroleum hydrocarbons · Sorption · Clay minerals  
Saturated porous aquifer

---

R. Valsala (✉)

Department of Ocean Engineering, IIT-Madras, Chennai 600036, India

e-mail: [renuvalsala@gmail.com](mailto:renuvalsala@gmail.com)

S. K. Govindarajan

Petroleum Engineering Program, Department of Ocean Engineering, IIT-Madras, Chennai 600036, India

e-mail: [gskumar@iitm.ac.in](mailto:gskumar@iitm.ac.in)

© Springer Nature Singapore Pte Ltd. 2019

K. Murali et al. (eds.), *Proceedings of the Fourth International Conference in Ocean Engineering (ICOE2018)*, Lecture Notes in Civil Engineering 22,

[https://doi.org/10.1007/978-981-13-3119-0\\_68](https://doi.org/10.1007/978-981-13-3119-0_68)

## 1 Introduction

A significant amount of research has been carried out in the past to investigate the colloid-associated transport of contaminants within the aquifers [7, 9, 12]. Inorganic colloids present within the aquifers in the form of clay minerals are found to considerably influence the transport of contaminants within the aquifers [8, 10]. Among various colloids, clay minerals are one of the most commonly found colloids within the aquifers. Hence, the influence of clay minerals has to be considered while modeling the contaminant transport within the aquifers. Depending upon the interaction between the clay minerals and the contaminants, the presence of clay minerals may either enhance or retard the contaminant migration within the aquifers. Attachment and detachment rates of contaminants on the surfaces of clay minerals are critical factors in deciding this interaction.

The past research investigations have shown that the transport of petroleum hydrocarbons within the aquifers is considerably affected by the presence of clay minerals within the aquifers [1, 5, 6]. Many researchers have investigated the sorption of hydrocarbons on the surface of clay minerals [4]. Carmody et al. [3] has shown that the organic clays are more efficient to remove hydrocarbons within aquifers due to its high hydrocarbon sorption capacity and high retention capacity of hydrocarbons. Zhang et al. [14] carried out experimental investigations to analyze the sorption of hydrocarbons on various clay minerals. They showed that the adsorption characteristics of petroleum hydrocarbons clay minerals are influenced by the pore parameters in clay minerals and on experimental pressure. Wu et al. [13] carried out preliminary investigations to analyze the influence of dissolved organic matter on the sorption of pyrene on clay minerals. They have concluded that the sorption isotherms governing the attachment of pyrene on montmorillonite and kaolinite complexes are different. This suggests that the sorption of hydrocarbons on clay minerals is influenced by the crystal structure of clay minerals. Simpson and Bowman [11] carried out to investigate the sorption of BTEX within a surfactant-modified zeolite, and they concluded that the sorption of dissolved BTEX is kinetic controlled and site-specific.

Research investigations carried out in the past suggest that the mechanisms governing the sorption of petroleum hydrocarbons on clay minerals vary considerably with physical and chemical characteristics of clay minerals, sorption characteristics, concentration of petroleum hydrocarbons, and on the hydrogeological conditions, etc. Hence, a generalized model is required to investigate the influence of various sorption processes on the movement of petroleum hydrocarbons within an aquifer. This study presents a numerical model to simulate the transport of petroleum hydrocarbons within an aquifer with clay minerals. The developed model can be coupled with a multicomponent dissolution model to investigate the cotransport of clay minerals and multicomponent petroleum hydrocarbons within the aquifer. The present model can be adapted to study the equilibrium and nonequilibrium sorption of hydrocarbons on clay minerals and aquifer material.

## 2 Physical System and Governing Equation

Clay minerals present within the aquifers is supposed to be present in suspended form and sorbed form. Petroleum hydrocarbons are considered to be present in dissolved form, sorbed onto the aquifer grains, sorbed onto the mobile clay minerals, and sorbed onto the immobile clay minerals. In order to model the clay-associated transport of petroleum hydrocarbons, equations governing the transport of these six constituents have to be solved. Among the six components, two components are in mobile phase, and other four are in immobile phase.

Transport of these constituents within a saturated aquifer can be represented using the equations provided in Bekhit and Hassan [2]. The equation governing the transport of suspended clay mineral within the aquifer can be represented as provided in Eq. (1) (Fig. 1).

$$\frac{\partial C_{cl}}{\partial t} = D_c \frac{\partial^2 C_{cl}}{\partial x^2} - V_c \frac{\partial C_{cl}}{\partial x} - K^a C_{cl} + \frac{K^d}{\theta} S_{cl} \tag{1}$$

where  $C_{cl}$  provides the concentration of clay in porous media [ $ML^{-3}$ ];  $D_c$  provides the dispersion coefficient [ $L^2T^{-1}$ ];  $V_c$  provides the velocity of colloid [ $LT^{-1}$ ];  $K^a$  provides the attachment rate of colloids on aquifer grains [ $T^{-1}$ ];  $K^d$  provides the

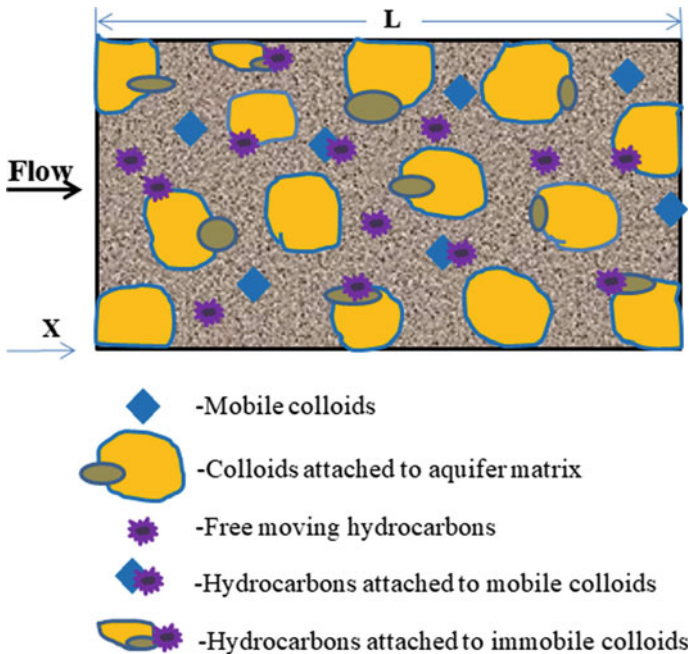


Fig. 1 Schematic representation of physical system considered for analysis

detachment rate of colloids from aquifer grains [ $T^{-1}$ ];  $\theta$  provides the porosity of aquifer; and  $S_{cl}$  provides the concentration of colloids adsorbed on the aquifer grains [ $ML^{-3}$ ], and it can be represented as provided in Eq. (2).

In Eq. (1), the third term on the R.H.S represents the attachment rate of colloids on aquifer grains and fourth term on the R.H.S represents the detachment rate of colloids from the aquifer grains. The transient equation governing the rate of change of sorbed colloid concentration within the aquifer is presented in Eq. (2).

$$\frac{1}{\theta} \frac{\partial S_{cl}}{\partial t} = K^a C_{cl} - \frac{K^d}{\theta} S_{cl} \tag{2}$$

Mass balance equation for the transport of dissolved hydrocarbon within the aquifer can be provided as given in Eq. (3).

$$\begin{aligned} \frac{\partial(\theta R_i C_i)}{\partial t} = & \theta D_i \frac{\partial^2 C_i}{\partial x^2} - \theta V \frac{\partial C_i}{\partial x} - K_i^a \theta C_i - K_{C_{m,i}}^a \theta C_{cl} \sigma_{C_{m,i}} \\ & - K_{C_{m,i}}^a S_{cl} \sigma_{C_{m,i}} + K_i^d S_i + K_{C_{m,i}}^d \theta C_i + K_{C_{m,i}}^d \theta C_i \end{aligned} \tag{3}$$

where  $R_i$  provides the retardation factor for dissolved phase hydrocarbon due to equilibrium sorption;  $D_i$  provides the dispersion coefficient of aqueous phase hydrocarbon;  $V$  provides the groundwater flow velocity.

In Eq. (3),  $K_i^a$  provides the attachment rate of hydrocarbons on aquifer matrix [ $T^{-1}$ ];  $K_{C_{m,i}}^a$  provides the attachment rate of hydrocarbons on mobile colloids [ $T^{-1}$ ];  $K_{C_{im,i}}^a$  provides the attachment rate of hydrocarbons on immobile colloids [ $T^{-1}$ ];  $K_i^d$  provides the detachment rate of hydrocarbon from the aquifer matrix [ $ML^{-3}$ ];  $K_{C_{m,i}}^d$  provides the detachment rate of hydrocarbon from mobile colloids [ $ML^{-3}$ ];  $K_{C_{im,i}}^d$  provides the detachment rate of hydrocarbon from immobile colloids [ $ML^{-3}$ ].

The transient transport equation governing the contaminant concentration adsorbed on aquifer is provided in Eq. (4).

$$\frac{1}{\theta} \frac{\partial S_i}{\partial t} = K_i^a C_i - \frac{K_i^d}{\theta} S_i \tag{4}$$

The transient equation governing the transport of contaminants attached on mobile colloids within the aquifer is provided in Eq. (5).

$$\begin{aligned} \frac{\partial(\theta C_{cl} \sigma_{C_{m,i}})}{\partial t} = & D_C \frac{\partial^2(\theta C_{cl} \sigma_{C_{m,i}})}{\partial x^2} - V_C \frac{\partial(\theta C_{cl} \sigma_{C_{m,i}})}{\partial x} \\ & + K_{C_{m,i}}^d \theta C_i + K_{C_{im,i}}^{C_m} S_{cl} \sigma_{C_{m,i}} - \theta C_{cl} \sigma_{C_{m,i}} \left( K_{C_{m,i}}^a + K_{C_{m,i}}^{C_{im}} \right) \end{aligned} \tag{5}$$

where  $\sigma_{C_{m,i}}$  provides the fraction of contaminants attached on mobile colloids;  $K_{C_{m,i}}^{C_{im}}$  provides the rate of contaminant detached from mobile colloids and attached to immobile colloids;  $K_{C_{im,i}}^{C_m}$  provides the rate of contaminant detached from immobile

cobile colloids and attached to mobile colloids; and  $\sigma_{C_{im},i}$  provides the fraction of contaminants attached to immobile colloids.

The equation governing the transport of contaminants attached on immobile colloids within the aquifer is provided in Eq. (6).

$$\frac{\partial(S_{cl}\sigma_{C_{im},i})}{\partial t} = K_{C_{im},i}^d C_i + K_{C_{m},i}^{C_{im}} \theta C_{cl}\sigma_{C_{m},i} - (K_{C_{im},i}^{C_m} + K_{C_{im},i}^a) S_{cl}\sigma_{C_{im},i} \quad (6)$$

### 3 Numerical Modeling

In order to model the cotransport of colloids and clay minerals within the saturated aquifer, coupled Eqs. (1)–(6) are solved in each time step. The algorithm adopted to solve the transport equations is presented in Fig. 2.

This algorithm can be used to model the transport of multicomponent petroleum hydrocarbons within the aquifer. In Fig. 2,  $n$  represent the index of petroleum hydrocarbon and  $N$  represents the total number of petroleum hydrocarbons considered in the analysis.

Transport Eqs. (1)–(6) are solved with respect to the boundary conditions of colloids and petroleum hydrocarbons provided in Eqs. (7) and (8). Multicomponent dissolution can be coupled with the transport model to analyze the cotransport of petroleum hydrocarbons and clay minerals within the aquifer. The transient dissolution rate of hydrocarbons can be incorporated by adopting a time-varying boundary condition at the left boundary of the aquifer.

$$C_{cl}(x = 0, t) = 0; \quad \frac{\partial C_{cl}}{\partial x}(x = L, t) = 0 \quad (7)$$

$$C_i(x = 0, t) = C_i(t); \quad \frac{\partial C_i}{\partial x}(x = L, t) = 0 \quad (8)$$

Initial conditions adopted for solving Eqs. (9) and (10).

$$C_{cl}(x, t = 0) = C_{cl,0} \quad (9)$$

$$C_i(x, t = 0) = 0 \quad (10)$$

### 4 Results and Discussions

In this section, simulated breakthrough curves for dissolved petroleum hydrocarbon and clay mineral within the aquifer is presented. Base-case parameters adopted for simulation are shown in Table 1.

Figure 3 presents the breakthrough concentration (BTC) obtained after a simulation period of 50 days. Figure 3a shows the concentration profiles of suspended and

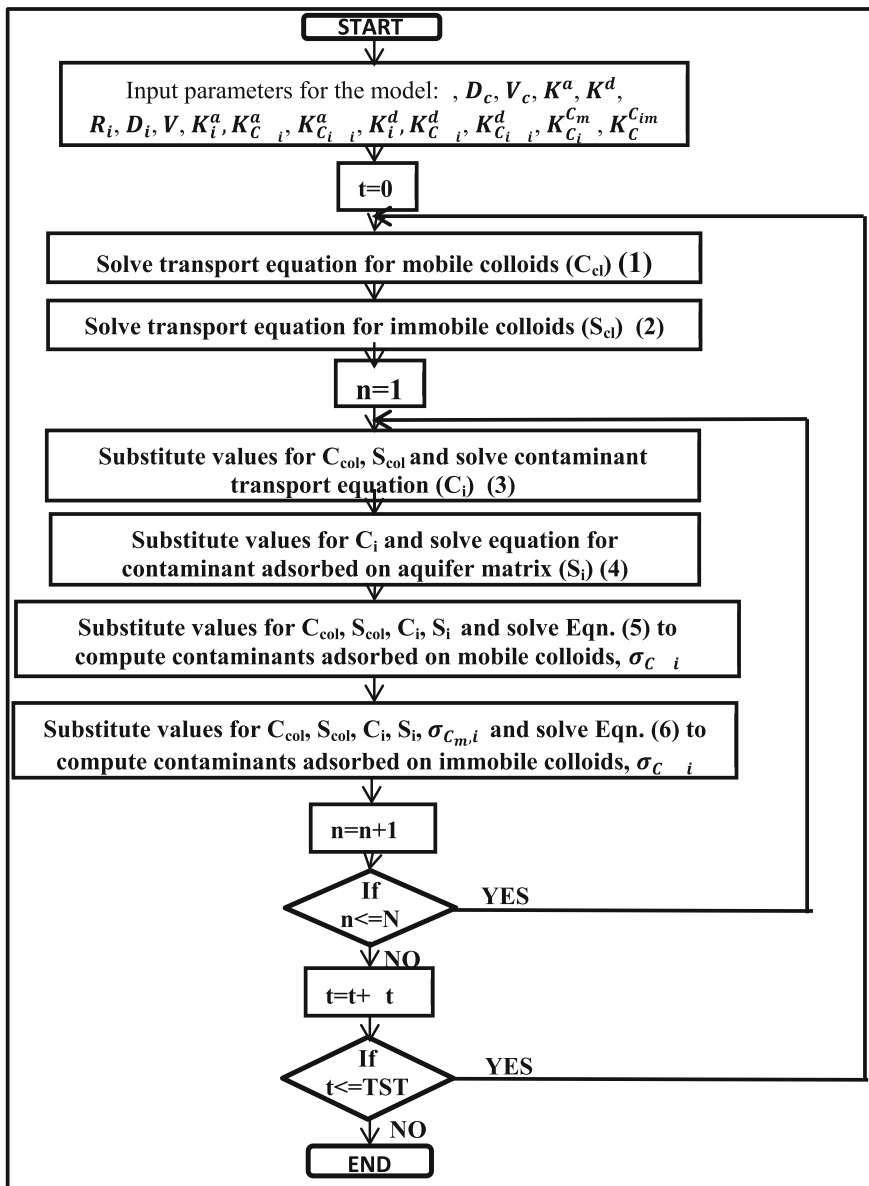


Fig. 2 Algorithm adopted to solve colloid-associated transport of multicomponent hydrocarbons

sorbed clays within the aquifers. The initial concentration of clay minerals within the aquifer is considered to be 1 mg/L. It is seen from Fig. 3a that the concentration of suspended clay mineral and the concentration of clay mineral sorbed onto the aquifer grains attains a constant value at a distance of 5 m away from the aquifer inlet. Clay

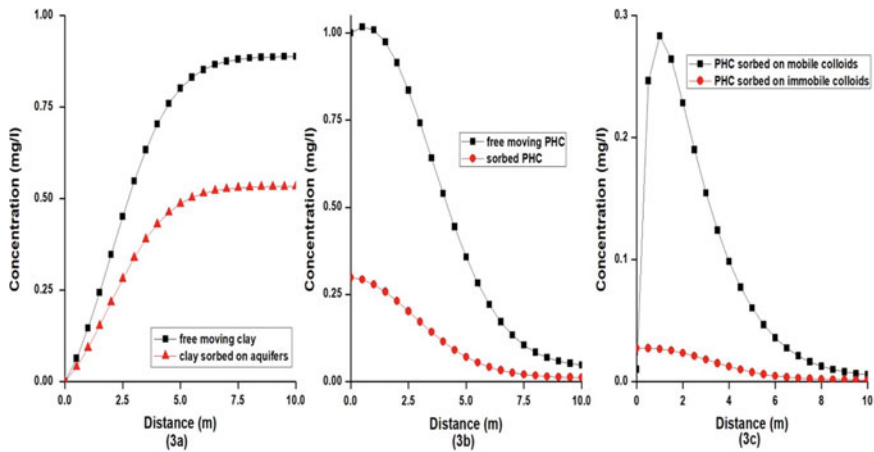
**Table 1** Base parameters adopted in the simulation study

Parameter	Value
Ground water flow velocity, $V$ (m/d)	0.1
Longitudinal dispersion coefficient, $D_C, D_i$ ( $m^2/d$ )	0.1
Clay attachment rate on aquifers, $K^a$ ( $d^{-1}$ )	1.0
Clay detachment rate from aquifers, $K^d$ ( $d^{-1}$ )	0.5
Attachment rate of PHC on aquifer, $K_i^a$ ( $d^{-1}$ )	0.1
Detachment rate of PHC from aquifer, $K_i^d$ ( $d^{-1}$ )	0.1
Attachment rate of PHC on mobile clay, $K_{C_m,i}^a$ ( $d^{-1}$ )	0.1
Detachment rate of PHC from mobile clay, $K_{C_m,i}^d$ ( $d^{-1}$ )	0.01
Attachment rate of PHC on immobile clay, $K_{C_{im},i}^a$ ( $d^{-1}$ )	0.1
Detachment rate of PHC from immobile clay, $K_{C_{im},i}^d$ ( $d^{-1}$ )	0.01
PHC attached from mobile clay to immobile clay surface, $K_{C_m,i}^{C_{im}}$ ( $d^{-1}$ )	0.01
PHC attached from immobile clay to mobile clay surface, $K_{C_{im},i}^{C_m}$ ( $d^{-1}$ )	0.01

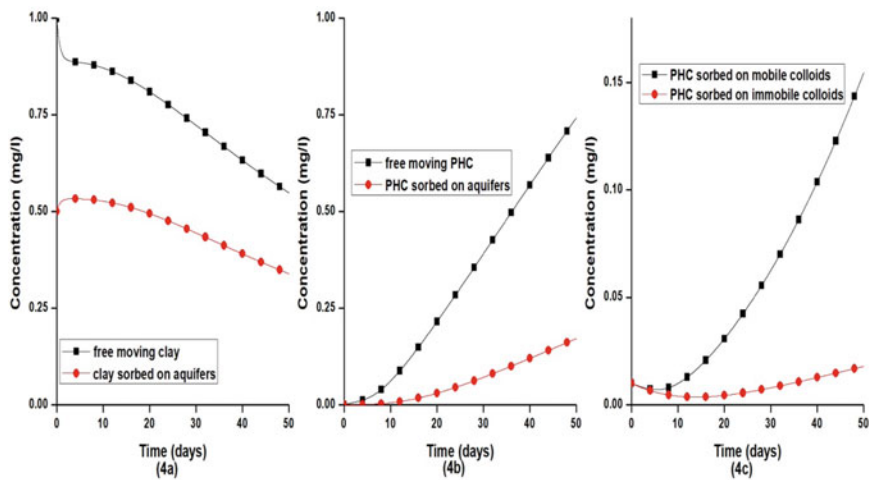
concentration sorbed onto aquifer material is found to be approximately 60% of suspended clay minerals. Figure 3b presents the concentration of free-moving and sorbed PHC within the aquifer, and Fig. 3c shows the concentration of PHC adsorbed on mobile and immobile clay minerals within the aquifer. It can be observed from Fig. 3b that the sorbed concentration of PHC is significantly less than the free-moving PHC within the aquifer as anticipated. Results presented in Fig. 3c also suggest that the PHC adsorbed on suspended clay mineral reaches the peak concentration at approximately 2 m from the aquifer inlet. The concentration of PHC adsorbed on immobile colloids is more near to the aquifer inlet and reduces after that. It is observed from Fig. 3c that the concentration of PHC adsorbed on mobile clay minerals is significantly higher than that adsorbed on immobile clay minerals.

Figure 4 provides the temporal variation of clay and PHC concentration at a distance of 3 m away from the aquifer inlet. Figure 4a shows the temporal variation of suspended and sorbed clay within the aquifer. It is seen from Fig. 4a that the suspended clay concentration within the aquifer is reducing at a higher rate with time. Figure 4b shows the temporal variation of dissolved PHC and PHC adsorbed on aquifers, and Fig. 4c presents the temporal variation of PHC sorbed on mobile and immobile clay minerals within the aquifers. The concentration of PHC adsorbed on the aquifer grains after 50 days is found to be one-third of the dissolved concentration, and the concentration of PHC adsorbed on mobile clay minerals is seen to be one-fifth of the dissolved PHC concentration.

Figure 5 provides the temporal variation of clay and PHC concentration at 3 m for different attachment rate of clay minerals on aquifer grains ( $k_1$ ). The value of  $k_1$  is considered to vary from 1 to 4  $day^{-1}$ . Figure 5a provides the concentration variation



**Fig. 3** Concentration breakthrough profiles of petroleum hydrocarbon and clay mineral obtained after 50 days



**Fig. 4** Concentration profiles of petroleum hydrocarbon and clay mineral at 3 m from the inlet

of suspended clay minerals within the aquifer; Fig. 5b provides the concentration variation of sorbed clay minerals with time, and Fig. 5c shows the concentration variation of PHC within the aquifer. As anticipated, the concentration of suspended clay mineral along the aquifer is found to be more for small  $k_1$  value. In case of low  $k_1$  value, suspended clay mineral within the aquifer is found to have more variation with time. From Fig. 5b, it can also be noted that the temporal variation of sorbed clay mineral also is varying more with time in case of low  $k_1$  value. Further, it can be noted from Fig. 5c that the dissolved concentration of PHC is only slightly ranging



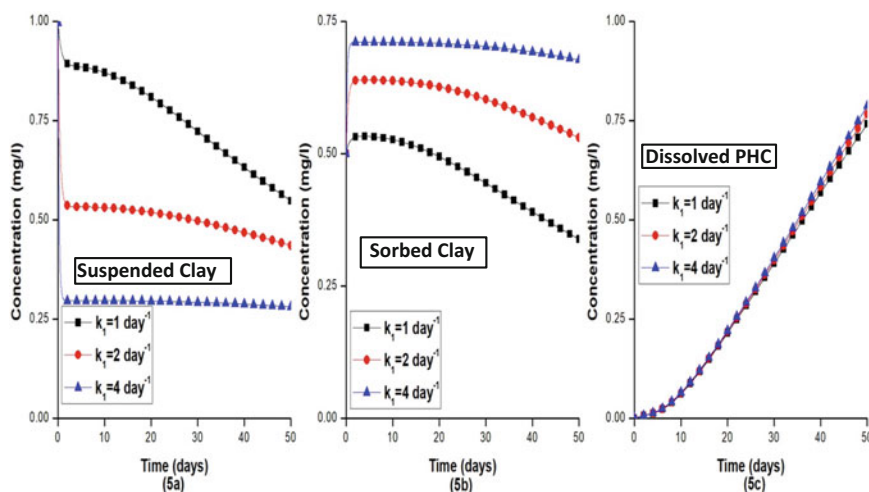


**Fig. 5** Concentration profiles at 3 m for varying attachment rate of clay minerals

with different  $k_1$  value. However, it can be observed from Fig. 5 that the influence of  $k_1$  value on dissolved PHC concentration is increasing with time.

Figure 6 provides the temporal variation of clay mineral and PHC concentration for clay detachment rate varying over one order of magnitude ( $k_2 = 0.05$  to  $0.5 \text{ day}^{-1}$ ). Figure 6a provides the temporal variation of suspended clay mineral; Fig. 6b provides the temporal variation of the clay mineral submitted on aquifer grains, and Fig. 6c provides the temporal variation of dissolved PHC. From Fig. 6, it can be noted that the concentration of suspended and sorbed clay mineral attains a constant value approximately after a simulation period of 5 days in case of low detachment rate of the clay mineral. However, in case of high clay attachment rate ( $k_2 = 0.5 \text{ day}^{-1}$ ), temporal variation in the concentration of the suspended and sorbed clay mineral is found to be high. Influence of clay detachment rate on the concentration distribution of dissolved PHC is found to increase with time. Dissolved PHC concentration is found to reduce with increment in the detachment rate of the clay mineral.

## 5 Conclusions

The developed model can be adopted for investigating the influence of clay minerals on the migration of dissolved PHC within an aquifer. The present model can be utilized for modeling the transport of multicomponent clay minerals. This model

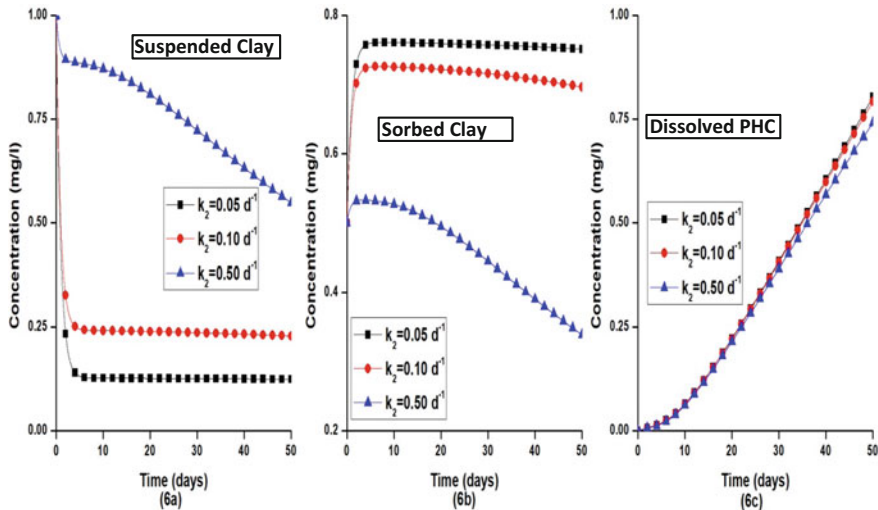


**Fig. 6** Concentration profiles at 3 m for varying detachment rate of clay minerals

can also incorporate the equilibrium and nonequilibrium sorption scenarios existing within the aquifer. The sensitivity of different sorption scenarios and sorption parameters on the migration of dissolved PHC and the mass partitioning of dissolved PHC within the aquifer can be investigated.

## References

1. Anderson MA (2000) Removal of MTBE and other organic contaminants from water by sorption to high silica zeolites. *Environ Sci Technol* 34:725–727
2. Bekhit HM, Hassan AE (2005) Two-dimensional modeling of contaminant transport in porous media in the presence of colloids. *Adv Water Resour* 28:1320–1335
3. Carmody O, Frost R, Xi Y, Kokot S (2007) Adsorption of hydrocarbons on organo-clays—implications for oil spill remediation. *J Colloid Interface Sci* 305(1):17–24
4. Chen H, Chen S, Quan X, Zhao Y, Zhao H (2008) Solubility and sorption of petroleum hydrocarbons in water and cosolvent systems. *J Environ Sci* 20(10):1177–1182
5. Chung SG, Kim DJ, Choi JW, Lee SH (2012) Processes affecting fate of toluene during transport through quartz sand. *Environ Prog Sustain Energy* 31:318–324. <https://doi.org/10.1002/ep.10550>
6. Li Y, Gupta G (1994) Adsorption/desorption of hydrocarbons on clay minerals. *Chemosphere* 28:627–638
7. Ren J, Packman AI (2004) Modeling of simultaneous exchange of colloids and sorbing contaminants between streams and streambeds. *Environ Sci Technol* 38:2901–2911
8. Saiers JE, Hornberger GM (1996) The role of colloidal kaolinite in the transport of cesium through laboratory sand columns. *Water Resour Res* 32(1):33–41. <https://doi.org/10.1029/95WR03096>
9. Sen TM, Mahajan SP, Khilar KC (2002) Colloid-associated contaminant transport in porous media: 1. *Exp Stud AIChE J* 48:2366–2374

10. Shackelford CD (1993) Contaminant transport. Geotechnical practice for waste disposal. Chapman & Hall, London, pp 33–65
11. Simpson JA, Bowman RB (2009) Nonequilibrium sorption and transport of volatile petroleum hydrocarbons in surfactant-modified zeolite. *J Contam Hydrol* 108(1–2):1–11
12. Totsche KU, Knabner P, Kogel-Knabner I (1996) The modeling of reactive solute transport with sorption to mobile and immobile sorbents, 2. Model discussion and numerical simulation. *Water Resour Res* 32(6):1623–1634
13. Wu P, Wen Y, Xiang Y et al (2015) Sorption of pyrene by clay minerals coated with dissolved organic matter (DOM) from landfill leachate. *J Chem* <https://doi.org/10.1155/2015/734610>
14. Zhang J, Lu S, Li J, Zhang P, Xue H, Zhao X, Xie L (2017) Adsorption properties of hydrocarbons (n-decane, methyl cyclohexane and toluene) on clay minerals: an experimental study. *Energies* 10:1586. <https://doi.org/10.3390/en10101586>

# Experimental and Numerical Investigations on In Situ Chemical Oxidation Model for Groundwater Contaminated with Petroleum Hydrocarbons



Natarajan Aarthi, Duraisamy Ashwin, Subbaiyan Gokulprasath, Mangottiri Vasudevan, Narayanan Natarajan and Govindarajan Suresh Kumar

**Abstract** The subsurface contamination by petroleum hydrocarbons (PHC) from leaking underground storage tanks, pipelines and refilling stations is one of the serious issues directly affecting the quality of groundwater. Application of advanced oxidation process (AOP) has been favoured for the remediation of petroleum contaminated sites due to the spontaneous redox reactions mediated by a strong activating agent. In this study, we propose a methodology for efficient injection of reagents by using two concentric PTFE tubes in a sand box model for simulating the groundwater flow, contaminant transport and in situ chemical oxidation (ISCO) using Fenton's reagents (hydrogen peroxide and zero-valent iron particles). This injection method has proved to maximize the interaction of chemicals resulting in complete oxidation of petroleum compounds. An attempt has also been made to numerically simulate the mass transfer and transport of petroleum hydrocarbons incorporating the impact of spontaneous mass transfer by means of numerical methods. It is expected to have significant difference in interface mass transfer between free phase (oil) and water leading to increased exposure of residual oil phase, thereby enhancing the complete mass removal. The presence of soil organic matter (SOM) is found to be enhancing the activity of Fenton's reagents as well as increasing the adsorption of hydrophobic organic compounds.

**Keywords** Chemical oxidation · Fenton's reagents · Groundwater Numerical model · Petroleum hydrocarbons · Remediation

---

N. Aarthi · D. Ashwin · S. Gokulprasath · M. Vasudevan (✉)  
Department of Civil Engineering, Bannari Amman Institute of Technology, Sathyamangalam,  
Erode 638401, Tamil Nadu, India  
e-mail: [devamv@gmail.com](mailto:devamv@gmail.com)

N. Natarajan  
Department of Civil Engineering, Dr. Mahalingam College of Engineering and Technology,  
Pollachi 642003, Tamil Nadu, India

G. Suresh Kumar  
Department of Ocean Engineering, Indian Institute of Technology Madras,  
Chennai 600036, India

© Springer Nature Singapore Pte Ltd. 2019  
K. Murali et al. (eds.), *Proceedings of the Fourth International Conference in Ocean Engineering (ICOE2018)*, Lecture Notes in Civil Engineering 22,  
[https://doi.org/10.1007/978-981-13-3119-0\\_69](https://doi.org/10.1007/978-981-13-3119-0_69)

## 1 Introduction

Groundwater is inherently prone to various contaminants such as volatile and non-volatile organic compounds, heavy metals, bacteriological and radio-active compounds present in the subsurface. Considering the immensity and volume of groundwater contamination through point sources such as leaking underground storage tanks (LUST) and corroding pipelines, volatile organic compounds (VOC) have been identified to be posing highest environmental risk in the emerging socio-economic scenario. The most common contaminants constituting petroleum hydrocarbons (PHC) are benzene, toluene, ethylbenzene, xylene, methyl ter-butyl ether and poly-aromatic hydrocarbons, which are infamous for their carcinogenic and hazardous characteristics [1–3]. Based on the prevailing hydro-geochemistry of the subsurface, they can exist either as a separate phase (free liquid phase in the saturated aquifer or vapour phase in the vadose zone), dissolved phase in groundwater or in the adsorbed phase with the formation matrix.

### 1.1 Strategies for In Situ Remediation

Since the inherent complexity of subsurface is yet not completely revealed, most of the in situ remediation techniques failed to report efficient removal of these priority compounds. In order to elucidate a sustainable remediation plan, synergistic application of various in situ technologies such as chemical oxidation, multiphase extraction and enhanced bioremediation need to be scientifically designed. The direct removal of free or floating phase of PHC can be effectively removed by in situ chemical oxidation (ISCO) method where chemical in liquid or gaseous form is injected to the subsurface [4]. ISCO technologies are targeted to mitigate PHCs existing in all physical forms in the subsurface, i.e. as dissolved, sorbed, mobile or residual light non-aqueous phase liquid (LNAPL). However, bioremediation can be achieved only by converting the chemicals into dissolved phase in order to cater the biochemical reaction pathway for selective micro-organisms.

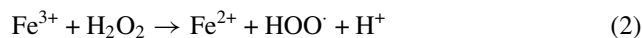
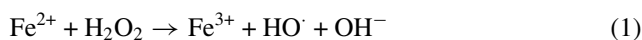
### 1.2 ISCO Technology

The basic technology of ISCO constitutes injection of oxidants (readily reducing chemicals) as well as catalysts (non-reactive, accelerating compounds) directly into the contaminant plume causing instantaneous chemical oxidation of PHCs resulting in production of innocuous substances (carbon dioxide and water) as end products [5]. This is affected by the simultaneous electron exchange between carbon in the organic compound and oxygen (or other oxidants). The key issue determining the

success of ISCO process, therefore, is the extent of direct contact achieved between the injected oxidants and subsurface contaminant.

### 1.3 ISCO Process

The common oxidants that effectively destroy petroleum hydrocarbons (Table 1) include hydrogen peroxide, Fenton's solution (hydrogen peroxide with an iron catalyst), proprietary modified Fenton's solutions, sodium persulfate, ozone or a combination of these [6, 7, 8]. The reaction of iron-catalyzed peroxide oxidation at pH of 2.5–3.5 is called a Fenton's reaction, named after its founder, H. J. H. Fenton in 1890s. Ferric ions ( $\text{Fe}^{3+}$ ) are produced (oxidized from  $\text{Fe}^{2+}$ ) during the reactions, which can be reconverted back to  $\text{Fe}^{2+}$  (if kept in the same solution) to produce hydroxyl radical and thus can continue further reactions.



In situ chemical oxidation offers the specific advantages of being rapid, aggressive and insensitive to contaminant characteristics and concentrations. However, selection of proper technology for in situ chemical treatment of contaminants at a specific site relies on careful site characterization and screening tests [4, 9]. The successful application of a particular in situ chemical treatment technique requires effective chemical reaction of the introduced chemical (oxidant) with contaminants at a proper rate and to an appropriate extent, along with effective delivery of the reagents throughout the subsurface zone to be treated.

**Table 1** Comparative strength of chemical oxidants in use for groundwater remediation

Oxidant	Standard oxidation potential (volts)	Relative oxidant strength (chlorine = 1)
Hydroxyl radical ( $\cdot\text{OH}$ )	2.8	2.0
Sulphate radical ( $\cdot\text{SO}_4^-$ )	2.5	1.8
Ozone ( $\text{O}_3$ )	2.1	1.5
Sodium persulfate ( $\text{Na}_2\text{S}_2\text{O}_8^{2-}$ )	2.0	1.5
Hydrogen peroxide ( $\text{H}_2\text{O}_2$ )	1.8	1.3
Oxygen ( $\text{O}_2$ )	1.2	0.9

## 2 Materials and Methods

### 2.1 *Strategies for Efficient Oxidant Delivery*

As mentioned above, the successful application of ISCO depends on many parameters that affect the delivery efficiency of oxidants in the soil, such as the spacing and location of injection points, volume and concentration of the oxidant (oxidant dose), the mechanism of oxidant delivery, as well as application frequency. Fenton's systems are commonly delivered via batch addition that consists of gravity or pressurized delivery utilizing a mobile injection unit with specialized pumping equipment and injection points, or by a pressurized continuous-feed system manifolded to injection points throughout the plume [10]. This type of injection is usually completed by delivering the oxidant to the deepest injection interval and moving upwards. Theoretically, the volume of oxidant necessary to achieve the desired remediation can be equated to the available pore space (porosity) since it can easily displace the liquid or gas within the pore spaces. However, in reality, the volume of oxidant injected depends on the contaminant mass distribution and prevailing heterogeneity throughout the contaminant plume [11].

### 2.2 *Experimental Set-up*

In this study, we propose a methodology for in situ decontamination of PHC-contaminated groundwater by direct extraction and simultaneous injection (DESI) using advanced oxidation with Fenton's reagent and stabilized zero-valent iron particles. The geo-cleansing process uses hydrogen peroxide ( $H_2O_2$ ) and iron salts where the effectiveness of  $H_2O_2$  is improved by iron through generation of highly reactive hydroxyl radicals [10, 8]. In order to make this reaction efficient, we propose a double polytetrafluoroethylene (PTFE) tube system with equally spaced holes separated by nylon membrane which carry the stabilized iron particles. The injection system using finite volume syringe necessitated the entry pressure for the reagents to reach the contaminated zone, thereby initiating the chemical oxidation which can result in the complete mineralization of petroleum hydrocarbons. Further, this system is highly suitable for multiphase extraction from the water table (from a mixture of oil and water), vapour extraction from the vadose zone as well as injection of microbial solution and surfactant solution to the groundwater for enhancing in situ bioremediation.

The design of the treatment system, including the number of injectors and volume of  $H_2O_2$  and catalyst solution, is based on the source volume predicted from site-specific characterization data to ensure sufficient mass of oxidant to be delivered to treat the contaminate through the calculated number of injection locations (Fig. 1). In the preliminary studies, we have attempted to optimize the amount of chemicals to be added as well as the spacing and locations of injection wells to trap the contaminant

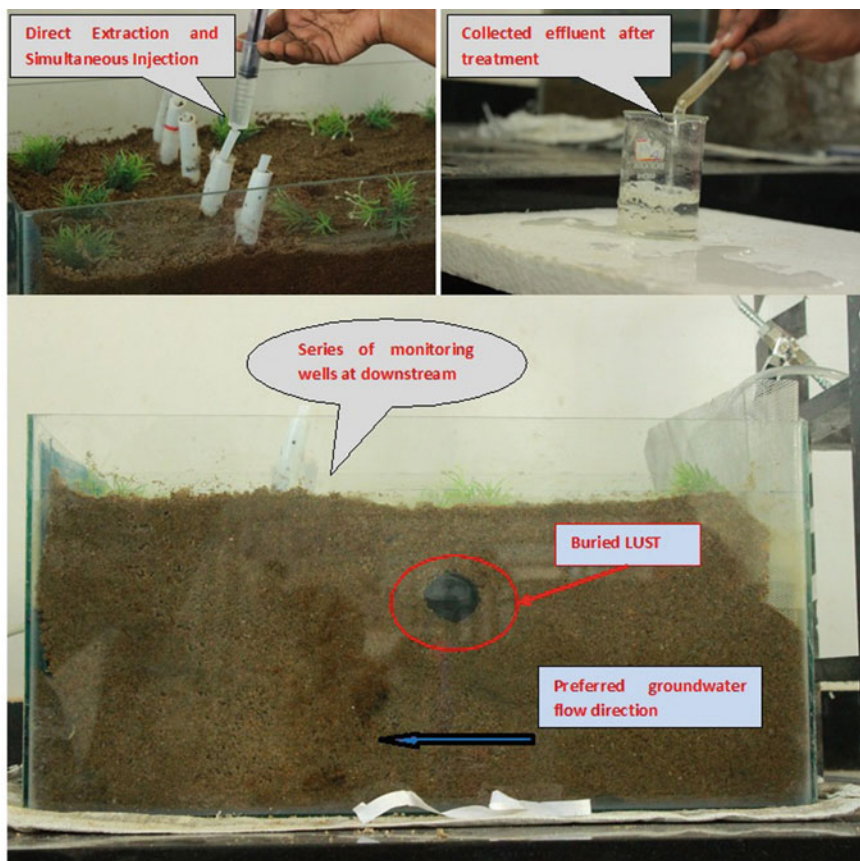


**Fig. 1** Glass box ( $0.6 \text{ m} \times 0.3 \text{ m} \times 0.3 \text{ m}$ ); sand (fineness modulus 0.2 mm); inflow rate (1.07 mL/s); expected groundwater flow velocity (1.0 m/day); PTFE tubes (1/8" and 1/4" dia.); zero-valent iron powder (0.2 mm dia.) and hydrogen peroxide (0.1 N)

plume near the source zone (Table 2). The effluent from this process is checked for efficiency, and the by-products from the reaction are non-toxic at the levels produced.

### 2.3 Numerical Model

The transport of organic contaminants originating from NAPL under conditions of residual saturation in the soil pores is, however, quite different and complicated from that of pooled NAPL because of the mass transfer limitations at the interface. Even though the conceptual approach could explain the tailing phenomena



**Table 2** Details of experimental conditions

<i>Batch experimental conditions</i>	
Amount of petrol mixed	0.5 mL in 100 mL
Amount of ZVI required	20 g/L
Amount of hydrogen peroxide required	60 ml/L
<i>Box experimental conditions</i>	
Average flow velocity	1 m/day
Average flow rate	1.07 mL/s

in concentration, the application of the chemical oxidation effect on the overall transport of total petroleum hydrocarbons (TPH) is limited due to the difficulties in understanding the chemical mass balance and rate of contaminant mass transfer.

The governing equation for the contaminant transport based on the law of conservation of mass in the mobile aqueous phase by taking into account the coupled effects of rate-limited dissolution, rate-limited sorption, biodegradation and first order mass transfer between mobile and immobile domains is given as [12–14]:

$$\text{Ret} \frac{\partial C_a}{\partial t} = D \frac{\partial^2 C_a}{\partial x^2} - v \frac{\partial C_a}{\partial x} + K_{nw}(C_{sat} - C_a) - k_m[(1 - f_r)f(C_a) - S] \quad (3)$$

where Ret is the retardation factor (–);  $C_a$  is the aqueous phase concentration of TPH ( $\text{g}/\text{m}^3$ );  $D$  is the longitudinal dispersion coefficient ( $\text{m}^2/\text{day}$ );  $v$  is the pore velocity ( $\text{m}/\text{day}$ );  $K_{nw}$  represents the lumped mass transfer coefficient for transient dissolution from non-aqueous phase to aqueous phase ( $\text{day}^{-1}$ );  $C_{sat}$  is the saturation concentration of the contaminant at equilibrium in the aqueous phase ( $\text{g}/\text{m}^3$ ).  $K_m$  is the sorption mass transfer rate coefficient ( $\text{day}^{-1}$ );  $f_r$  is the fraction of kinetic sorption (–);  $S$  is the sorbed phase concentration ( $\text{g}/\text{m}^3$ );  $t$  is the time (day) and  $x$  is the dimension of length (m).

After solving this equation (Eq. 3), we have to update sorbed phase equation (Eq. 4).

$$\frac{\rho_b}{\phi} \frac{\partial S}{\partial t} = (1 - f_r)k_m(C_a - S/k_d) + f_r k_d C_a \quad (4)$$

Now, in advanced oxidation process, corresponding to each mole of Fenton's reagent added, one more of hydroxyl radical will be released, which will react with one mole of TPH. So we can add an equation for the simple advection-dispersion transport of Fenton's reagent ( $C_F$ ) (Eq. 5).

$$R \frac{\partial C_F}{\partial t} = D \frac{\partial^2 C_F}{\partial x^2} - v \frac{\partial C_F}{\partial x} - K_{f\_or} C_F \quad (5)$$

where  $K_{f\_or}$  is the oxidation rate constant ( $\text{mg}/\text{L}/\text{day}$ ). This effect can be directly connected to the remaining residual ( $S_n$  (Eq. 6)).

$$\frac{dS_n}{dt} = \frac{-K_{nw}(C_{sat} - C_a) - K_{f\_or}K_{st}C_a}{\phi\rho_n} \tag{6}$$

where  $K_{st}$  is stoichiometric constant for the oxidation process. The spatial discretization of the advection-dominated transport equation in the mobile domain is done by fully implicit scheme while the dispersion term is discretized by semi-implicit (Crank-Nicholson) scheme.

### 3 Results and Discussion

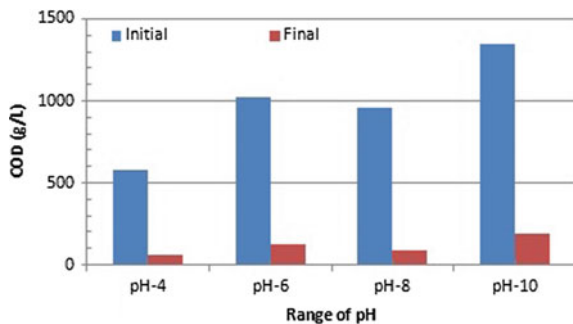
#### 3.1 Experimental Demonstration

The experimental set-up was used to demonstrate the feasibility of DESI system for TPH remediation from contaminated groundwater. It was observed that use of double layers of PTFE tube in different diameters allow simultaneous injection of the reagents in measured quantity. Destabilization of ZVI using a mixture of organic and inorganic porous media serve as additional precursors for enhancing the remediation efficiency. The consumption of reagents and evolution of by-products can be correlated to the source strength (Fig. 2). Thus, it can serve as a screening test for finding suspected leaks. It is cost-effective and easy for installation and maintenance.

#### 3.2 Variations in TPH Distribution

Figure 3 indicates the variation in TPH concentration over the length of domain. It is observed that when sorption rate constant is increased by two orders, the concentration profile takes high peak early at the initial part of the domain. However, the reduction in concentration is marginal when rate is increased beyond the normal

**Fig. 2** Reduction in contaminant concentration (in terms of COD) for different pH ranges of Fenton’s reagent application



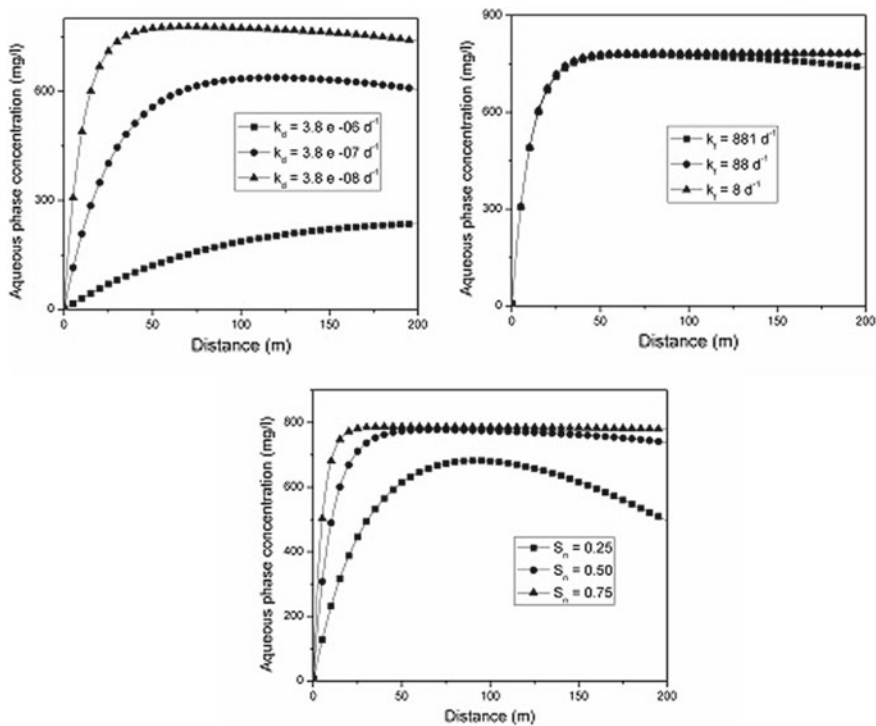


**Fig. 3** Variation in concentration for TPH for different values of  $K_d$ ,  $K_f$  and  $S_n$

range. This can be expected for the case of residual NAPL source where sorption to soil particles cannot be neglected while evaluating mass transfer effects.

### 3.3 Variations in Fenton’s Reagent Distribution

Figure 4 shows the variation in concentration of Fenton’s reagent over the length of domain during the active oxidation stage. It is important to understand the fate of dissolved contaminant concentration at the downstream of the plume to identify the removal efficiency of the applied treatment system. Generally, the rate-limiting steps in dissolved phase transport are desorption and degradation [15]. However, in case of ISCO system, the diffusion and dispersion of the contaminants in the prevailing zone will determine the extent of direct contact with the applied oxidant, and in effect, the removal efficiency.

It can be clearly observed that sorption onto soil particles is highly inhibitory to the effectiveness of these chemicals. However, as the oxidation rate increases, there is marginal change in the concentration profile. This can be explained based on the

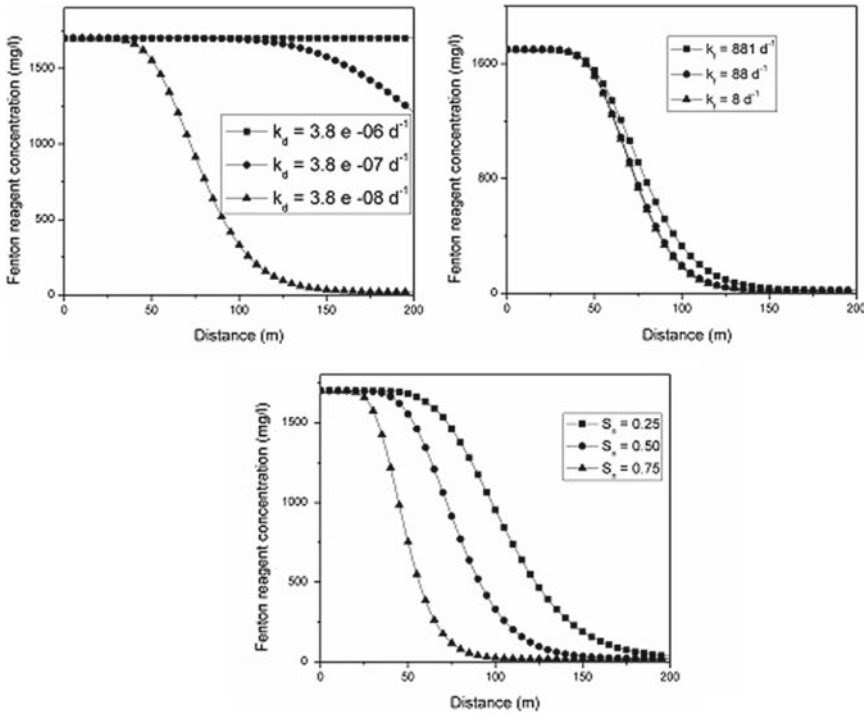


**Fig. 4** Variation in concentration for Fenton’s reagent for different values of  $K_d$ ,  $K_f$  and  $S_n$

delay in response from residual sources as compared with pooled NAPL sources. However, as  $S_n$  is increased, the reaction seems to be culminated fast, owing to the similarity with pooled NAPL sources.

### 3.4 Variations in Residual NAPL Saturation

It can be observed from Fig. 5 that variation in  $S_n$  is evenly distributed within the length of source zone. For higher  $K_d$  values, mild slope of response graph indicate the delayed desorption from soil pores. It is linearly proportional to the strength of residual source initially present. However, the variation in oxidation process drastically reduces the NAPL source strength considerably. This is due to the instantaneous oxidation available at the exposed NAPL-water interface from the highly saturated zones.

The comparison of these plots indicates the significance of understanding the mechanism of NAPL migration and transport in selecting suitable site remediation scheme. In other words, understanding the combined effect of porosity (in turn,

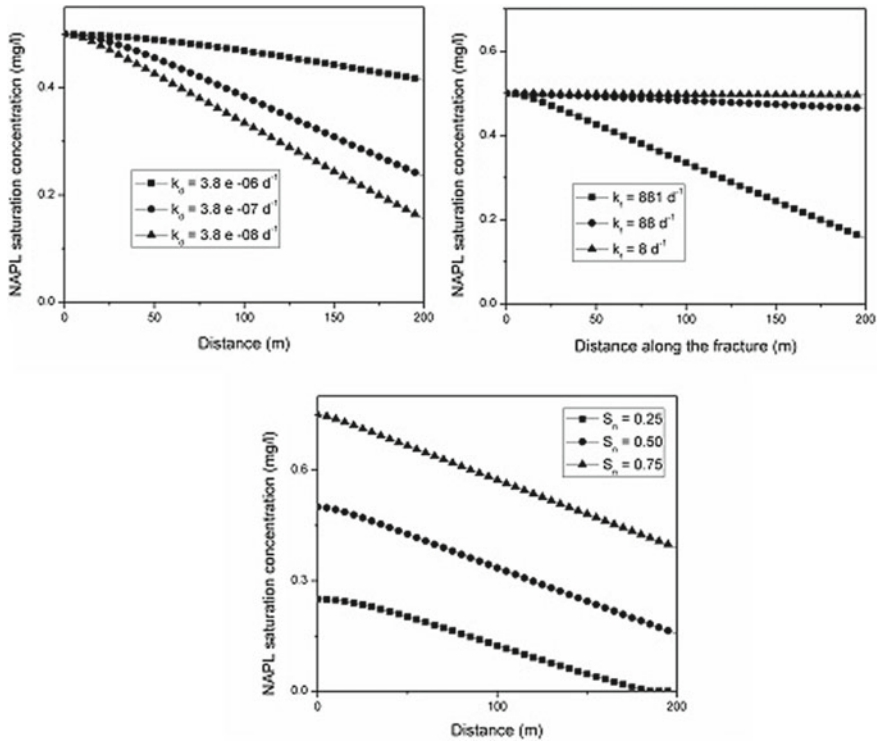


**Fig. 5** Variation in concentration for residual NAPL saturation for different values of  $K_d$ ,  $K_f$  and  $S_n$

residual saturation), chemical oxidation rate and sorption and dissolution rates can complement us with a realistic overview of the success of ISCO system for PHC removal. However, as the reaction is assumed to be of spontaneous nature, temporal variation of concentration at various locations of the plume is not intended in this study.

### 4 Conclusions

Application of advanced oxidation process (AOP) has been favoured for the remediation of petroleum contaminated sites due to the spontaneous redox reactions mediated by a strong activating agent. In this study, we propose a methodology for efficient injection of reagents by using two concentric PTFE tubes in a sandbox model for simulating the groundwater flow, contaminant transport and ISCO using Fenton’s reagents. An attempt has also been made to numerically simulate the mass transfer and transport of petroleum hydrocarbons incorporating the impact of spontaneous

mass transfer by means of numerical methods. It is observed that selection of mass transfer parameters is significant in tracking the variation of concentration profile.

## References

1. Kong SH, Watts RJ, Choi JH (1998) Treatment of petroleum-contaminated soils using iron mineral catalyzed hydrogen peroxide. *Chemosphere* 37(8):1473–1482
2. Bamforth SM, Singleton I (2005) Bioremediation of polycyclic aromatic hydrocarbons: current knowledge and future directions. *J Chem Technol Biotechnol* 80(7):723–736
3. Vasudevan M, Johnston CD, Bastow TP, Lekmine G, Rayner JL, Nambi IM, Suresh Kumar G, Ravi Krishna R, Davis GB (2016) Effect of compositional heterogeneity on dissolution of non-ideal LNAPL mixtures. *J Contam Hydrol* 194:10–16
4. Choi H, Lim HN, Kim J, Hwang TM, Kang JW (2002) Transport characteristics of gas phase ozone in unsaturated porous media for in-situ chemical oxidation. *J Contam Hydrol* 57(1):81–98
5. Kim J, Choi H (2002) Modeling in situ ozonation for the remediation of nonvolatile PAH-contaminated unsaturated soils. *J Contam Hydrol* 55(3):261–285
6. Yen CH, Chen KF, Kao CM, Liang SH, Chen TY (2011) Application of persulfate to remediate petroleum hydrocarbon-contaminated soil: feasibility and comparison with common oxidants. *J Hazard Mater* 186(2):2097–2102
7. Shafieiyoun S, Ebadi T, Nikazar M (2012) Treatment of landfill leachate by Fenton process with nano sized zero valent iron particles. *Int J Environ Res* 6(1):119–128
8. Petala E, Dimos K, Douvalis A, Bakas T, Tucek J, Zbořil R, Karakassides MA (2013) Nanoscale zero-valent iron supported on mesoporous silica: characterization and reactivity for Cr (VI) removal from aqueous solution. *J Hazard Mater* 261:295–306
9. Ferrarese E, Andreottola G, Oprea IA (2008) Remediation of PAH-contaminated sediments by chemical oxidation. *J Hazard Mater* 152(1):128–139
10. Shafieiyoun S, Ebadi T, Nikazar M (2011) Organic load removal of landfill leachate by fenton process using nano sized zero valent iron particles. In: *Proceedings of international conference on environmental science and technology (ICEST 2011)*
11. Vasudevan M, Suresh Kumar G, Nambi IM (2016) Scenario-based modeling of mass transfer mechanisms at a petroleum contaminated field site-numerical implications. *J Environ Manage* 175:9–19
12. Kartha SA, Srivastava R (2008) Effect of immobile water content on contaminant transport in unsaturated zone. *J Hydro-Environ Res* 1(3):206–215
13. Feehley CE, Zheng C, Molz FJ (2000) A dual-domain mass transfer approach for modeling solute transport in heterogeneous aquifers: application to the macrodispersion experiment (MADE) site. *Water Resour Res* 36(9):2501–2515
14. Vasudevan M, Suresh Kumar G, Nambi IM (2014) Numerical modeling of multicomponent LNAPL dissolution kinetics at residual saturation in a saturated subsurface system. *Sadhana* 39(part 6):1387–1408
15. Natarajan N, Suresh Kumar G (2011) Numerical modeling of bacterial facilitated contaminant transport in fractured porous media. *Colloids Surf A* 387:104–112

# Numerical Modelling on Enhanced Mobility of Petroleum Hydrocarbon in Saturated Porous Media



M. Berlin and G. Suresh Kumar

**Abstract** Petroleum contamination in groundwater is a widespread and well-known global environmental problem, mainly due to the leaking of aged pipelines or storage tank. The in situ treatment of petroleum hydrocarbons is relatively difficult to perform especially during pump-and-treat technique due to the trapped low-soluble hydrocarbons in the soil pores. The solubility enhancement and improved bioavailability of the small solvable portions in the petroleum products such as polycyclic aromatic hydrocarbon (PAH) can be performed by surfactants. This study aims to understand the enhanced mobility on PAH (phenanthrene) with the availability of surfactants and the associated physicochemical interactions in the saturated porous media. A 1D model is established in this regard to study the impact of surfactant on PAH enhanced solubility and subsequent transport in the saturated porous system. The hydraulic properties of soil, equilibrium partitioning and all reactions on the fate and movement of PAH are carefully included in this work. The results show that a considerable increase in the aqueous phase PAH concentration during the availability of surfactant (Triton N-101). In addition, the influence of partitioning between aqueous and solid phase, biodegradation, oxygen mass transfer are showing substantial variation on PAH transport in the saturated zone. The developed numerical model can be efficiently useful for the prediction of low-soluble organic fraction during the in situ remediation of petroleum hydrocarbon contamination.

**Keywords** Numerical model · Saturated porous media · Surfactant · Transport Polycyclic aromatic hydrocarbon

---

M. Berlin (✉)

Department of Civil Engineering, National Institute of Technology Arunachal Pradesh, Yupia 791112, Arunachal Pradesh, India  
e-mail: [berlin1982@gmail.com](mailto:berlin1982@gmail.com)

G. Suresh Kumar

Department of Ocean Engineering, Indian Institute of Technology Madras, Chennai 600036, India  
e-mail: [gskumar@iitm.ac.in](mailto:gskumar@iitm.ac.in)

© Springer Nature Singapore Pte Ltd. 2019

K. Murali et al. (eds.), *Proceedings of the Fourth International Conference in Ocean Engineering (ICOE2018)*, Lecture Notes in Civil Engineering 22,  
[https://doi.org/10.1007/978-981-13-3119-0\\_70](https://doi.org/10.1007/978-981-13-3119-0_70)

1021

## 1 Introduction

Petroleum contamination in soil due to various activities such as leaking of aged pipelines and storage tank and spillage from accidents [1, 2] is a well-known global environmental problem. Light non-aqueous-phase liquids (LNAPLs) which have densities less than that of water and dense non-aqueous-phase liquids (DNAPLs) which have densities greater than that of water [3] are the two broad classifications of petroleum hydrocarbons. Polycyclic aromatic hydrocarbons (PAHs) belong to DNAPL with hydrogen atoms and more than one bonded aromatic rings of carbon [4]. They are free into the environment mainly through fossil fuel fiery, partial burning of carbon-based substance, volcanoes, forest fires and petroleum leaks [5, 6]. The previous surveys have revealed that vehicular release is a major cause of PAHs in metropolitan areas [7–9]. Several PAHs are identified as human hazards [10], and their perseverance in the atmosphere is a serious well-being threat.

The harshness of PAH contamination in soil is comparatively less [11], but the consequences to the environment and its impact on the human health are more crucial [12, 13]. The drinking water bodies such as surface water and groundwater can get contaminated due to PAHs [14]. The groundwater is extensively contaminated by PAHs in many parts of world including India [15–17].

Generally, PAHs in subsurface may endure several physico-chemical and microbial exercises. Some studies revealed that the PAH can be degraded by bacterial activity when suitable environmental conditions are present [18, 19]. Further, PAHs have found to be a good sorption capacity with soil [20]. The transport of dissolved PAH is another important process in porous media. The soil column experiments proved the transport ability of PAH along with dissolved organic matter [21]. The sand column experiment performed by Jenkins and Lion [22] shows that the migration of PAHs especially phenanthrene in porous media is a common phenomenon along with bacteria. Soleimani et al. [23] have also confirmed that PAH compounds (naphthalene, phenanthrene, pyrene and anthracene) have the transport potential in the soil under saturated conditions. Hence, phenanthrene has good mobility in porous media, and eventually, this will exist in groundwater.

Many researchers have studied that surfactants are influencing the solubility of PAHs in porous media [24, 25]. In particular, PAH solubility is enhanced by surfactants including biosurfactants [26, 27]. However, the mathematical modelling of enhanced movement of PAH due to surfactant has yet to be addressed. Since modelling is a good tool to predict the concentration in the porous media, one has to develop the appropriate model for future prediction with various complexities. Considering this, the objective of the current study is to establish a 1D mathematical model to estimate the enhanced solubility and mobility of PAH in the saturated porous media along with the combined reactions. This work has also included various surfactants on the enhanced mobility of PAH in the saturated zone.



## 2 Mathematical Model

The physical, chemical and biological processes are considered in the transport model of dissolved PAH in saturated porous media. The surfactant-enriched degradation due to bacteria is emphasised through Monod kinetics with the addition of surfactant [28–31]. The complete transport of dissolved PAH is shown in Eq. (1).

$$R \frac{\partial C}{\partial t} = \frac{\partial}{\partial z} \left( D \frac{\partial C}{\partial z} \right) - v \frac{\partial C}{\partial z} - \frac{\mu_{\max}}{Y} \left[ M + \frac{\rho_s M_s}{\theta_m} \right] \left[ \frac{C + f C_{\text{mic}}}{K_c + C + f C_{\text{mic}} + \frac{C^2}{K_i}} \right] \left[ \frac{O_2}{K_0 + O_2} \right] \quad (1)$$

The microbe is expected to be movable in the water and is exposed to development and deterioration with other attachment or detachment to the soil [28, 32, 33], and the transport model for the movable microbe is shown by Eq. (2).

$$\begin{aligned} \frac{\partial M}{\partial t} = & \frac{\partial}{\partial z} \left( D \frac{\partial M}{\partial z} \right) - v \frac{\partial M}{\partial z} - k_a M + k_d \frac{\rho_s}{\theta_m} M_s \\ & + \mu_{\max} M \left[ \frac{C + f C_{\text{mic}}}{K_c + C + f C_{\text{mic}} + \frac{C^2}{K_i}} \right] \left[ \frac{O_2}{K_0 + O_2} \right] - k_{\text{dec}} M \end{aligned} \quad (2)$$

Likewise, the share of the adsorbed bacteria on the soil is immobile, which is imperilled to adsorption, desorption and other important processes [28, 32] as given in Eq. (3)

$$\frac{\partial M_s}{\partial t} = k_{\text{att}} \frac{\theta_m}{\rho_s} M - k_{\text{det}} M_s + \mu_{\max} M_s \left[ \frac{C + f C_{\text{mic}}}{K_c + C + f C_{\text{mic}} + \frac{C^2}{K_i}} \right] \left[ \frac{O_2}{K_0 + O_2} \right] - k_{\text{dec}} M_s \quad (3)$$

Since the bacteria utilise large amount of dissolved oxygen during the degradation, the transport of the dissolved oxygen is considered [28, 34] and shown in Eq. (4).

$$\frac{\partial O_2}{\partial t} = \frac{\partial}{\partial z} \left( D \frac{\partial O_2}{\partial z} \right) - v \frac{\partial O_2}{\partial z} - \frac{\mu_{\max}}{Y} F \left[ M + \frac{\rho_s}{\theta_m} M_s \right] \left[ \frac{C + f C_{\text{mic}}}{K_c + C + f C_{\text{mic}} + \frac{C^2}{K_i}} \right] \left[ \frac{O_2}{K_0 + O_2} \right] \quad (4)$$

where  $C$ : dissolved PAH concentration in water (ppm),  $M$ : concentration of bacteria in the water (ppm),  $z$ : distance (cm),  $M_s$ : adsorbed bacteria on the solid (mg/g),  $O_2$ : concentration of oxygen in aqueous phase,  $D$ : longitudinal dispersion coefficient,  $V$ : pore water velocity ( $\text{ms}^{-1}$ ) (where  $V = q/\theta$ ),  $q$ : Darcy velocity ( $\text{ms}^{-1}$ ),  $\theta$ : porosity,  $\rho_s$ : soil bulk density (ppm),  $R$ : retardation of PAH,  $\mu_{\max}$ : maximum specific growth rate of bacteria ( $\text{s}^{-1}$ ),  $K_c$ : half saturation constant of PAH (mg/L),  $K_d$ : distribution coefficient of PAH (l/mg),  $K_{\text{att}}$ : bacterial attachment rate coefficient ( $\text{s}^{-1}$ ),  $K_{\text{det}}$ : bacterial detachment rate coefficient ( $\text{s}^{-1}$ ),  $k_{\text{dec}}$ : bacterial death rate coefficient ( $\text{s}^{-1}$ ),  $f$ : oxygen use coefficient,  $K_i$ : Haldane inhibition constant (mg/L),  $K_0$ : half saturation constant of oxygen (mg/L).

The surfactant transport in porous media can be written in Eq. (5):

$$R \frac{\partial S}{\partial t} = \frac{\partial}{\partial z} \left( D \frac{\partial S}{\partial z} \right) - v \frac{\partial S}{\partial z} \quad (5)$$

**Table 1** Initial and boundary conditions

Particulars	Initial condition	Boundary conditions
PAH	0 ppm	Left boundary = 1.27 ppm Right boundary = zero flux
Biomass	In aqueous phase = 0 ppm In attached phase = 0 ppm	Left boundary = 1.86 ppm Right boundary = zero flux
Dissolved oxygen	3 ppm	Left boundary = 11.29 ppm Right boundary = zero flux
Surfactant (Triton N-101)	0 ppm	Left boundary = 283.5 ppm Right boundary = zero flux

The PAH solubilisation by surfactant can be stated in Eqs. (6)–(7) [35]:

$$C_{mic} = S_{mc}k_{mc}C \tag{6}$$

$$S_{mc} = \begin{cases} S - CMC & \text{for } S > CMC \\ 0 & \text{for } S < CMC \end{cases} \tag{7}$$

where  $S$ : surfactant concentration (mg/L),  $C_{mic}$ : PAH partitioned into micelles (mg/L),  $S_{mc}$ : surfactant in micellar form (mg/L),  $CMC$ : critical micelle concentration (mg/L),  $k_{mc}$ : partition coefficient of PAH between the micellar and aqueous phases (l/mg),  $f$ : bioavailable fraction of the micelle bound contaminant ( $C_{mic}$ ).

### 3 Solution Technique

The systems of equation defining dissolved oxygen, bacteria, PAH and surfactant are resolved mathematically by fully implicit finite difference system [36, 37]. The spatial derivatives are calculated using fully implicit scheme. The set of algebraic equations arrived from the discretised differential equation using Taylor series and the Thomas algorithm is used to solve the algebraic equations. The second-order central difference scheme is assumed to discretise the diffusion component, while the advection module is discretised with first-order upwind pattern. The initial and boundary conditions for various models are labelled in Table 1.

### 4 Results and Discussions

The present basic multispecies transport equation except biodegradation is validated by comparing the existing available analytical result for groundwater system provided

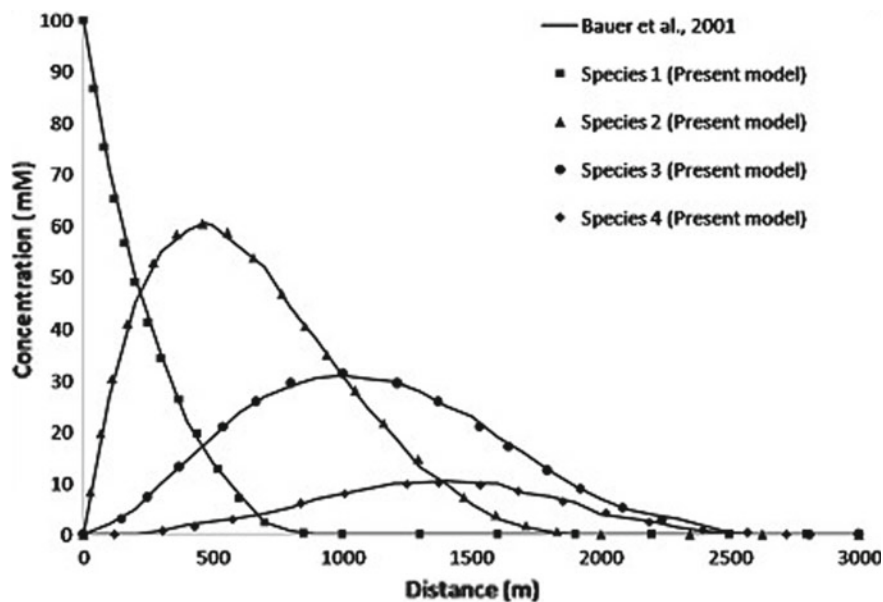


Fig. 1 Validation of contaminant transport equation in saturated soil with the literature data [38]

by Bauer et al. [38]. The simulated responses are in excellent match with published data [38] (Fig. 1).

In the current study, the PAH transport in saturated porous media is analysed during the availability and non-availability of surfactant. The biokinetic parameters along with transport of PAH are given in Table 2. The properties of various surfactants are presented in Table 3.

Figure 2 shows the disparity of PAH availability during the availability and non-availability of surfactant. The result illustrates that the concentration of PAH is observed relatively very low (1.28 mg/l) when there is non-availability of surfactant at the soil surface. However, the concentration of PAH is elevated up to 11.6 ppm when the surfactant (TN-101) is available. This considerable increase in the concentration is influenced due to the availability of surfactant, which increases the solubility of PAH [35]. Further, the results propose that the concentration becomes zero at 250, 450 and 850 cm distances from maximum concentration (approximately 1.27 mg/l) at source when the absence of surfactant during 0.5, 1 and 2 years, respectively. This distance of migration is due to the corresponding Darcy velocity and porosity of the saturated porous media. In the case of existence of surfactant, the concentration profile follows nearly similar trend except in rise in concentration (approximately 11.5 mg/l) due to the enhanced solubility. This enriched solubility by surfactant can aid to improve the elimination and conveyance of PAH from the PAH-contaminated soil domain. Conversely, the enhanced solubility can increase the availability of PAH in the water phase, which can spread near vicinity of source in the aquifer during

**Table 2** Properties used for PAH transport

Parameter	Value	Reference
$\theta$	0.381	[39]
$\rho_b$	$1.6 \times 10^6$	[40]
$D_m$	$6.6 \times 10^{-6}$	[41]
$\lambda_L$	0.5	[40]
$K_d$	$1.63 \times 10^{-4}$	[41]
$\mu_{\max}$	$3.056 \times 10^{-7}$	[35]
$K_c$	0.09	[35]
$Y$	0.39	[35]
$K_{\text{att}}$	$1.20 \times 10^{-3}$	[42]
$K_{\text{det}}$	$1.20 \times 10^{-4}$	[42]
$K_{\text{dec}}$	$6.5 \times 10^{-5}$	[43]
$f$	2.15	[44]
$K_i$	1.754	[45]
$K_0$	0.2	[46]

**Table 3** Surfactant properties [35]

Surfactant	$K_{\text{mc}}$	CMC
Triton N-101 (TN-101)	0.0362	63
Triton X-100 (TX-100)	0.0256	43
Brij-35 (B-35)	0.0144	40
Brij-30 (B-30)	0.0167	10

early time and further can contaminate the more area in the groundwater system during the later time interval.

Figure 3 shows the impact of different surfactants on the PAH solubility after one year in the saturated porous media. The concentration of surfactant is directly influenced by the adsorption rate of PAH between the micellar and water phases ( $k_{\text{mc}}$ ). The higher values of  $k_{\text{mc}}$  produce more aqueous-phase surfactant from micellar and eventually increase the solubility of PAH from solid phase to aqueous phase. The  $k_{\text{mc}}$  values are increasing in trend from Brij—35 (0.0144), Brij—30 (0.0167), Triton X—100 (0.0256) along with Triton N—101 (0.0362). Hence, the concentration of PAH increases 6, 7.6, 9.7 and 12.2 ppm for Brij—35, Brij—30, Triton X—100 and Triton N—101, respectively. Even though the critical micelle concentrations are not increasing in the same order, the effect of  $k_{\text{mc}}$  is suppressing the influence of critical micelle concentrations. Among four surfactants considered in this study, Triton N—101 is found to be the highest and Brij—35 is the lowest solubilising surfactant compared to others. It can be concluded from Fig. 3 that Triton N—101 can be used as most inspired surfactant on PAH solubilisation and further migration in the saturated porous media.

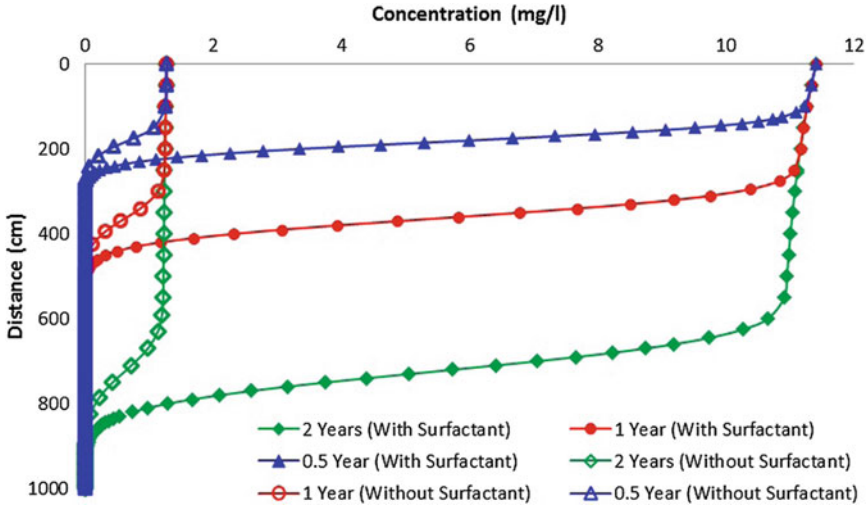


Fig. 2 Change in PAH concentration during the existence and absenteeism of surfactant at different durations

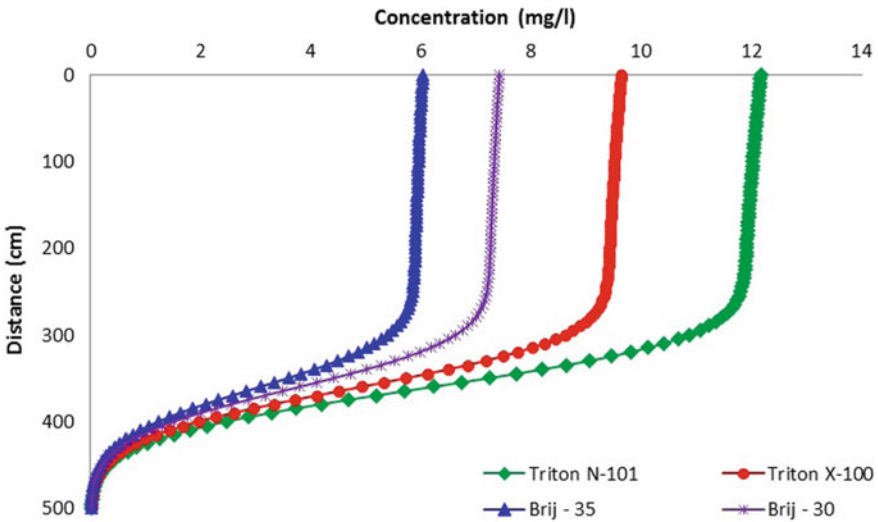


Fig. 3 Change in PAH due to various surfactants after 1 year

Figure 4 shows the influence of increase in availability of surfactant on PAH concentration after one year. It is confirmed that the rise in availability of surfactant directly triggers the PAH concentration. The PAH concentrations are observed as 1.27, 2.97, 7.57 and 12.17 mg/l when the applied Triton N—101 concentrations are 0, 100, 200 and 300 mg/l, respectively. Since all other prevailing conditions are same, the increase in concentration of PAH due to the enhanced solubility by the surfactant

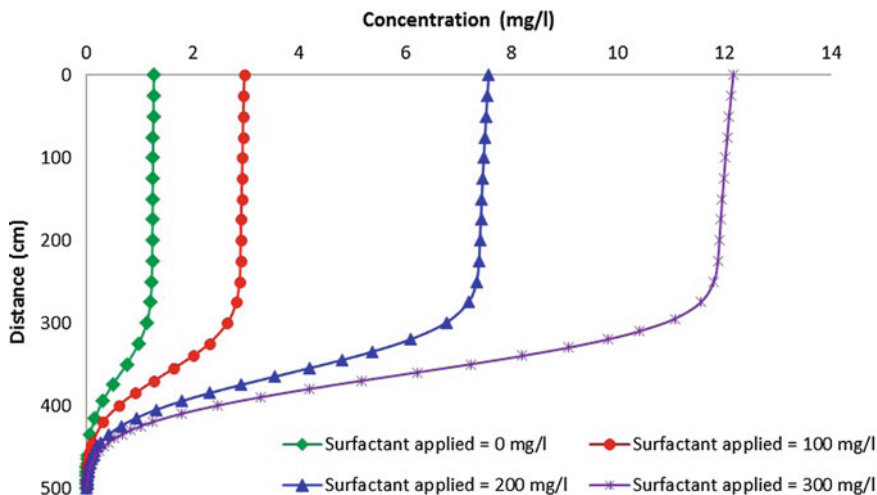


Fig. 4 Sensitivity analysis of surfactant concentration on PAH concentration after 1 year

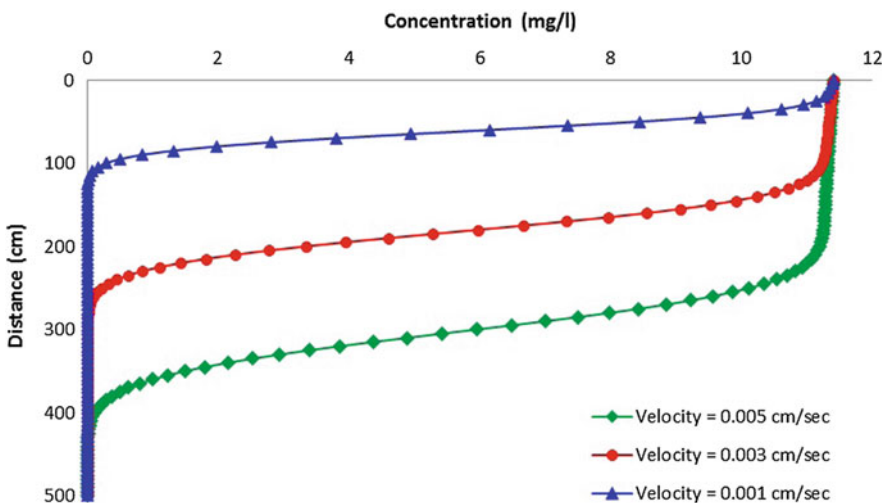


Fig. 5 Comparison of Darcy velocity on PAH variation after 0.5 year

is not prompting on the spread of migration. Similarly, Fig. 5 provides the effect of Darcy’s velocity on PAH movement in the groundwater system. The concentration of PAH becomes zero after 120 cm distance from its maximum concentration (approximately 11.4 mg/l) during the Darcy velocity of 0.001 cm/s. Further, the length of migration is increased up to 270 and 400 cm for the Darcy velocity of 0.003 and 0.005 cm/s, respectively. It is understood that the Darcy velocity plays a vital role on PAH migration due to the advective and dispersive processes. Hence, it can be con-

cluded from Figs. 4 and 5 that the different concentrations of surfactant can directly influence (increase/decrease) the magnitude of PAH concentration by changing the solubility and Darcy's velocity can directly influence (increase/decrease) the migration.

## 5 Conclusions

In the current work, a mathematical model is established to define the movement of PAH in groundwater system with and without surfactant. The developed model includes linear partitioning of PAH, microbial reactions, bacterial transport, dissolved oxygen migration along with the transport of PAH. The specific conclusions were given below:

1. The movement of PAH is directly influenced due to the saturated hydraulic variables such as Darcy velocity and porosity of the medium.
2. PAH concentration is increased up to 11.6 ppm during the availability of surfactant (TN-101) which is approximately ten times its magnitude (1.28 ppm) during unavailability of surfactant.
3. TN-101 surfactant is certainly inducing the solubility of PAH compared with TX-100, B-35 and B-30. Further, it is also observed that the solubility of PAH is subject to the type and amount of surfactant available.
4. The length of migration of PAH is independent of the surfactant properties, but depends on the physico-biogeochemical properties of the groundwater system.

Over all, the surfactant-induced solubility of PAH and its associated transport in saturated porous media can be used for future prediction.

## References

1. Che MD (2002) Conservative cost estimate including investigation and monitoring expenses. In: Soil and groundwater remediation conference, Taipei
2. Rayner JL, Snape I, Walworth JL, Harvey PM, Ferguson SH (2007) Petroleum-hydrocarbon contamination and remediation by microbioventing at sub-Antarctic Macquarie Island. *Cold Regions Sci Technol* 48:139–153
3. Sulaymon AH, Gzar HA (2011) Experimental investigation and numerical modeling of light nonaqueous phase liquid dissolution and transport in a saturated zone of the soil. *J Hazard Mater* 186:1601–1614
4. Agarwal T (2009) Concentration level, pattern and toxic potential of PAHs in traffic soil of Delhi, India. *J Hazard Mater* 171:894–900
5. Wilcke W (2000) Polycyclic aromatic hydrocarbons (PAHs) in soil—a review. *J Plant Nutrit Soil Sci* 163:229–248
6. Tian W, Wang L, Li D, Li F (2014) Leachability of phenanthrene from soil under acid rain and its relationship with dissolved organic matter. *Environ Earth Sci*

7. Rogge WF, Hildemann LM, Mazurek MA (1993) Sources of the fine organic aerosol 2. Road dust, tire debris, organometallic brake lining dust: roads as sources and sinks. *Environ Sci Technol* 27:636–651
8. Okuda T, Kumata H, Naraoka H (2002) Origin of atmospheric polycyclic aromatic hydrocarbons (PAHs) in Chinese cities solved by compound-specific stable carbon isotopic analyses. *Organ Geochem* 33:1737–1745
9. Singh DP, Gadi R, Mandal TK (2012) Levels, sources, and toxic potential of polycyclic aromatic hydrocarbons in urban soil of Delhi, India. *Hum Ecol Risk Assess* 18:393–411
10. Shaw GR, Connell DW (1994) Prediction and monitoring of the carcinogenicity of polycyclic aromatic compounds (PACs). *Rev Environ Contaminat Toxicol* 135:1–62
11. Jones KC, Stratford JA, Waterhouse KS, Vogt NB (1989) Organic contaminants in Welsh soils: polynuclear aromatic hydrocarbons. *Environ Sci Technol* 23:540–550
12. EPA (1990) Code of federal regulations. [http://www.access.gpo.gov/nara/cfr/waisidx\\_06/40cfr180\\_06.html](http://www.access.gpo.gov/nara/cfr/waisidx_06/40cfr180_06.html)
13. FAO (2008) Food and agriculture organization of the United Nations. [http://www.codexalimentarius.net/mrls/pestdes/jsp/pest\\_q-e.jsp](http://www.codexalimentarius.net/mrls/pestdes/jsp/pest_q-e.jsp)
14. Gustafson DI (1989) Groundwater ubiquity score: a simple method for assessing pesticide leachability. *Environ Toxicol Chem* 8:339–357
15. Ogbuagu DH, Okoli CG, Gilbert CL, Madu S (2011) Determination of the contamination of groundwater sources in Okrika mainland with polynuclear aromatic hydrocarbons (PAHs). *Br J Environ Climate Change* 1(3):90–102
16. Hockenreiner M, Neugebauer H, Elango L (2013) Ex situ bioremediation method for the treatment of groundwater contaminated with PAHs. *Int J Environ Sci Technol*
17. Brindha K, Elango L (2014) PAHs contamination in groundwater from a part of metropolitan city, India: a study based on sampling over a 10-year period. *Environ Earth Sci* 71:5113–5120
18. Estrada JM, Allieri MAA, Alvarez PJJ, Vazquez RR (2006) Phenanthrene removal by *Penicillium frequentans* grown on solid state culture: effect of oxygen concentration. *Environ Technol* 27:1073–1080
19. Chen JL, Wong MH, Wong YS, Tam NFY (2011) Modeling sorption and biodegradation of phenanthrene in mangrove sediment slurry. *J Hazard Mater* 190:409–415
20. Amellal S, Boivin A, Ganier CP, Schiavon M (2006) High sorption of phenanthrene in agricultural soils. *Agron Sustain Dev* 26:99–106
21. Magee BR, Lion LW, Lemley AT (1991) Transport of dissolved organic macromolecules and their effect on the transport of phenanthrene in porous media. *Environ Sci Technol* 25:323–331
22. Jenkins MB, Lion LW (1993) Mobile bacteria and transport of polynuclear aromatic hydrocarbons in porous media. *Appl Environ, Microbio* 59(10):3306–3313
23. Soleimani M, Afyuni M, Charkhabi AH (2013) Transport of polycyclic aromatic hydrocarbons in a calcareous wetland soil. *Caspian J Env Sci* 11(2):131–140
24. Chong ZY, Liao XY, Yan XL, Sun L, Zhao D, Liang T (2014) Enhanced desorption of PAHs from manufactured gas plant soils using different types of surfactants. *Pedosphere* 24(2):209–219
25. Yu H, Huang GH, Xiao H, Wang L, Chen W (2014) Combined effects of DOM and biosurfactant enhanced biodegradation of polycyclic aromatic hydrocarbons (PAHs) in soil–water systems. *Environ Sci Pollut*
26. Shin KH, Kim KW, Seagren EA (2004) Combined effects of pH and biosurfactant addition on solubilization and biodegradation of phenanthrene. *Appl Microbiol Biotechnol* 65(3):336–343
27. Fang J, Shan X, Wen B, Huang R (2013) Mobility of TX100 suspended multiwalled carbon nanotubes (MWCNTs) and the facilitated transport of phenanthrene in real soil columns. *Geoderma* 207–208:1–7
28. Choi JW, Kim SB, Ha HC, Kim DJ (2005) Analysis of benzene transport in a two dimensional aquifer model. *Hydrol Process* 19:2481–2489
29. Berlin M, Suresh Kumar G, Nambi IM (2015) Numerical modelling on fate and transport of petroleum hydrocarbons in an unsaturated sub-surface system for varying source scenario. *J Earth Syst Sci* 124(3):665–674



30. Berlin M, Suresh Kumar G, Nambi IM (2014) Numerical modeling on transport of nitrogen from wastewater and fertilizer applied on paddy fields. *Ecol Model* 278:85–99
31. Natarajan N, Suresh Kumar G (2011) Numerical modelling of bacteria facilitated contaminant transport in fractured porous media. *Colloids and surfaces A: physico. Eng Aspects* 387:104–112
32. Berlin M, Suresh Kumar G, Nambi IM (2014) Numerical modeling of biological clogging on transport of nitrate in an unsaturated porous media. *Environ Earth Sci* 73(7):3285–3298
33. Berlin M, Suresh Kumar G, Nambi IM (2014) Numerical modeling on the effect of dissolved oxygen on nitrogen transformation and transport in an unsaturated porous system. *Environ Model Assess* 19(4):283–299
34. Guha S, Jaffe PR (1996) Biodegradation kinetics of phenanthrene partitioned into the micellar phase of nonionic surfactants. *Environ Sci Technol* 30:605–611
35. Clement TP, Hooker BS, Skeen RS (1996) Macroscopic models for predicting changes in saturated porous media properties caused by microbial growth. *Ground Water* 34(5):934–942
36. Meerschaerta MM, Tadjeran C (2006) Finite difference approximations for two-sided space-fractional partial differential equations. *Appl Numer Math* 56:80–90
37. Van Dam JC, Feddes RA (2000) Numerical simulation of infiltration, evaporation and shallow groundwater levels with the Richards equation. *J Hydrol* 233:72–85
38. Bauer P, Attinger S, Kinzelbach W (2001) Transport of a decay chain in homogeneous porous media: analytical solution. *J Contam Hydrol* 49:217–239
39. Mitchell RJ, Mayer AS (1998) A numerical model for transient hysteretic flow and solution transport in unsaturated porous media. *J Contam Hydrol* 50:243–264
40. Lee MS, Lee KK, Hyun Y, Clement TP, Hamilton D (2006) Nitrogen transformation and transport modeling in groundwater aquifers. *Ecol Model* 192:143–159
41. Rehman MM, Liedl R, Grathwohl P (2004) Sorption kinetics during macropore transport of organic contaminants in soils: laboratory experiments and analytical modeling. *Water Resour Res* 40:W01503
42. Hendry MJ, Lawrence JR, Maloszewski P (1999) Effects of velocity on the transport of two bacteria through saturated sand. *Ground Water* 37:103–112
43. Guha S, Peters CA, Jaffe PR (1999) Multisubstrate biodegradation kinetics of naphthalene, phenanthrene, and pyrene mixtures. *Biotechnol Bioeng* 65(5):491–499
44. Chen YM, Abriola LM, Alvarez PJJ, Anid PJ, Vogel TM (1992) Modeling transport and biodegradation of benzene and toluene in sandy aquifer material: comparisons with experimental measurements. *Water Resour Res* 28:1833–1847
45. Moscoso F, Deive FJ, Longo MA, Sanroman MA (2012) Technoeconomic assessment of phenanthrene degradation by *Pseudomonas stutzeri* CECT 930 in a batch bioreactor. *Bioresour Technol* 104:81–89
46. Kinzelbach W, Schafer W, Herzer J (1991) Numerical modeling of natural and enhanced denitrification processes in aquifers. *Water Resour Res* 27:1123–1139

# Mathematical Modelling and Analysis of Nano-dust Explosion



Adnan Deshmukh , Samarth Patwardhan , Nilesh Sakpal ,  
Akshay Agwan  and Sagar Wakale 

**Abstract** Dust is common in process industries that manufacture, store and handle particulate material. More than half of dusts processed in industries are combustible. Explosive dust clouds can be generated from most organic materials, many metals and even some non-metallic inorganic materials. Studies have reported techniques to control explosions occurring in coal mines and other process industries and such occurrences in varied locations due to different types of dusts, point to the fact that this issue needs further investigation. Industrial practices in India are similar to developed countries but information relevant to dust explosion occurring in India is almost negligible as the type of explosion remains uninvestigated. Further, use of nanoparticles and nano-dusts in upstream oil and gas industry is increasing significantly. Under conducive conditions, storage, transport and pumping down nanoparticles downhole can be considered to be potentially vulnerable situations, leading to explosions with catastrophic consequences, not only financial but including human loss. It is difficult to eliminate dust explosion, but it can be mitigated using different methods. Such events can be prevented if technical safety parameters of dust are known. One of the important measures is the determination of worst case explosion overpressure and provision of blast resistant walls or structural components. This work investigates the dust explosion characteristics of nano-dusts, by taking into account the settings and the circumstances in which the dust is being accumulated. In order to study these changing characteristics of dust particles from an explosion as well as a technical

---

A. Deshmukh (✉) · S. Patwardhan  
Maharashtra Institute of Technology, Pune, India  
e-mail: [adnandeshmukh66@gmail.com](mailto:adnandeshmukh66@gmail.com)

S. Patwardhan  
e-mail: [samarth.patwardhan@mitpune.edu.in](mailto:samarth.patwardhan@mitpune.edu.in)

N. Sakpal · A. Agwan · S. Wakale  
Techniche Pvt. Ltd., Pune, India  
e-mail: [nilesh.sakpal@techniche-engg.com](mailto:nilesh.sakpal@techniche-engg.com)

A. Agwan  
e-mail: [akshay.agwan@techniche-engg.com](mailto:akshay.agwan@techniche-engg.com)

S. Wakale  
e-mail: [sagar.wakale@techniche-engg.com](mailto:sagar.wakale@techniche-engg.com)

© Springer Nature Singapore Pte Ltd. 2019  
K. Murali et al. (eds.), *Proceedings of the Fourth International Conference in Ocean Engineering (ICOE2018)*, Lecture Notes in Civil Engineering 22,  
[https://doi.org/10.1007/978-981-13-3119-0\\_71](https://doi.org/10.1007/978-981-13-3119-0_71)

safety perspective, a mathematical model is developed to determine a practical solution for screening in terms of an equation and demonstrate that the equation is doing fair against the experimental data. Various types of nano-dusts and their explosions are simulated using the constructed model. A sensitivity analysis for all the relevant critical parameters is undertaken with this model, after it has been validated with experimental data. The model represents explosions carried out using both micro-powders as well as nano-powders, which can assist the end-user in estimating the approximate value of overpressure and thus, in turn would largely govern further handling and analysis.

**Keywords** Nano-dusts · HSE · Explosive dusts · Mathematical model

## 1 Introduction

On 7 February 2008, the eyes of the world were opened to the hazards of combustible dust when the Imperial Sugar refinery, located in Port Wentworth, GA exploded [1]. The blast killed 14 people and injured 36 others. In 1803, it was found [2] that the coal dust in passageways had burned and caused the flame to propagate, leading to accidents in the coal mine. In 1800s, many more published works [3] report explosions because of coal dust even though there was no fire damp. A dust explosion gets initiated by the rapid combustion of fine combustible particulates in air. Due to this, there is liberation of gaseous products with a significant pressure rise; this pressure rise destructs plant, property and lives of people. Smaller the particle size, more rapid and intense burning will take place, till a stage is reached when particles become much finer and they join to form nugget (smaller particles form bigger ones). The ignited combustible dust cloud would only cause a flash fire if dust cloud is unconfined, but if the ignited dust cloud is confined, the gases released (heat generated) by combustion of cloud may result in rapid development of pressure and would eventually result in an explosion. Conditions required for a dust explosion to occur are the presence of an oxidant, a combustible dust cloud, presence of oxygen, confinement area and an ignition source to trigger the dust cloud. The oxygen required for the explosion is supplied by air.

The flame or spark that triggers a dust explosion can be produced by blowtorch, static electricity, electric spark, friction or any open flame [4]. Dust composed of sugar, cotton, coal, flour, starch, grain, combustible metallic dust or other organic materials are highly explosive. Certain metallic dusts like magnesium, aluminium dust are also explosive. Seventy per cent of working dusts in industries are combustible. Grain elevators, size reducer, packing dust, conveying manual or mechanical cyclones, electrostatic precipitator, settling chambers, classifying operations mixing and blending operation storage, filter scrubbers, bag unloading stations, unloaders are mainly subject to dust explosions (where there is a chance of dust collection there will be a chance of dust explosion). Dust explosion is effected by particle size (finer the particle size, more the chances of explosion), dust concentration (between lower

explosive limit and upper explosive limit), oxidant concentration (more percentage of oxidant or gases more will be possibility of explosion), ignition temperature, turbulence of dust cloud.

An event of dust explosion is observed to happen in two distinct stages, primary dust explosion and secondary dust explosion. Primary dust explosion occurs inside a confined area such as silo, hopper, etc. These are generally controlled by pressure relief ducts. Secondary dust explosions get initiated by primary explosions. When waves of primary dust explosion move, they will disturb the settled dust layer and form another dust cloud that will explode. It is not possible to eliminate the explosions, but there are certain methods to prevent such explosions. These are elimination of ignition sources, providing pressure relief vent holes in the design, inerting the dust, static electrification of powder during pneumatic transport, magnetizing surfactants, etc. [5]. It is also possible to prevent dust explosion if characteristics of dust like minimum ignition energy required for explosion, minimum and maximum dust concentration required for explosion are known.

## 2 Background

When very fine dust gets suspended in air and is ignited by a heating element or sparked, it will lead to a dust explosion. A dust explosion will cause rapid burning and due to this rapid burning, there is release of gases with a huge pressure rise of explosive force that will cause damage of property, plant and people's lives. The formation of cloud would be due to cohesive forces between the dust particles. Initially, one particle of dust will ignite and after that a chain will start that will ignite the whole cloud. Dust cloud will be ignited by heating element such as spark, electric motor, heating operation, etc. [6]. Sometimes dust clouds will also be ignited by electrostatic charge that is produced by friction between the particles (Fig. 1).



**Fig. 1** Burning at the welded joint and dust explosion in pipe [7]

## 2.1 Mechanism of Dust Explosion

Surface area of dust is very large as compared to their mass. Burning will occur on the surface of the dust where it reacts with oxygen. For 1.0 kg of a material of spherical shape with density and surface area of  $1.0 \text{ g/cm}^3$  and  $0.3 \text{ m}^2$  respectively, is crushed into spheres of  $50 \text{ }\mu\text{m}$  diameter then this leads to a surface area increase to  $60 \text{ m}^2$ . This large amount of increased surface area of dust allows the material to burn much faster.

## 2.2 Conditions for Dust Explosion

For dust explosion to occur certain conditions are required to be fulfilled; without which dust explosion cannot occur. These conditions are represented in Fig. 2.

These conditions are listed as follows:

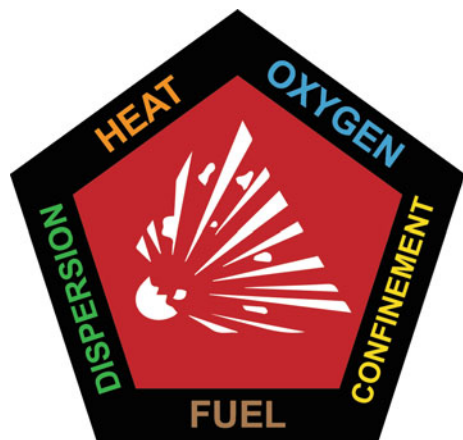
- The dust which will form a cloud must be combustible.
- Finer the dust will be, greater will be the chance of explosion.
- Dust per unit volume must be in explosive concentration.
- Supply of oxygen must be there.
- Without ignition source, no explosion takes place.

## 2.3 Dust Cloud Formation in Environment

Dust cloud formation process is given in the following steps:

Inter-particle forces between dust particles (cohesion).

**Fig. 2** Explosion pentagon  
[7]



Entrainment of particles when shock wave passing across deposit surface.  
Transport of dust particles in turbulent gas flow.

### 2.4 Stages of Dust Explosions

Primary explosion:

When combustible dust forms a cloud and comes in contact with a heating element, it leads to an explosion. The dust explosion mainly occurs in tray drier, rotary driers, dust fired heaters, spray driers, settling chamber, size reduction, pneumatic separation equipment, mills, mixers, cyclone separators, filters, silos and pneumatic transport system.

Secondary explosion:

After primary explosion, when blast waves travel in turn disturbing the settling dust which again forms a cloud of the same dust. Settling dust has very little thickness, but it is quite dangerous when it forms a cloud. So explosion caused by this settling dust cloud is called secondary explosion.

Number of accidents has taken place due to coal and wood dust is shown in Fig. 3. From study [7], it has been found that more number of accidents have occurred in silo and hopper. In this area, wood and wood products are more hazardous than coal dust.

$K_{st}$ , the dust deflagration index, measures the relative explosion severity compared to other dusts. The larger the value for  $K_{st}$ , the more severe the explosion.  $K_{st}$  provides

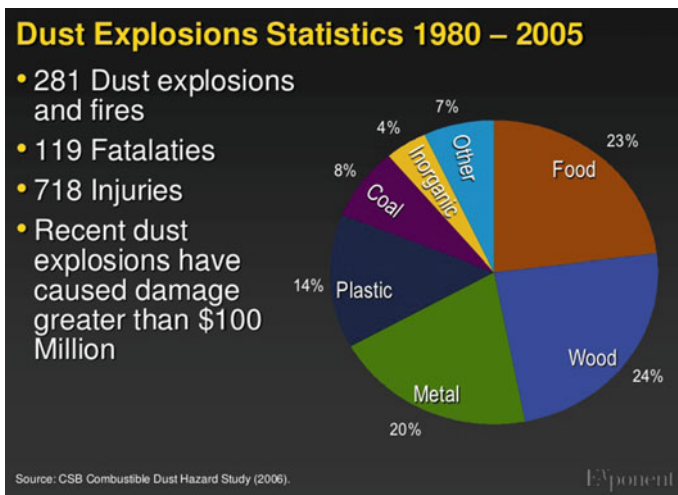


Fig. 3 Explosion statistics [1]

**Table 1** Characteristics of dust according to  $K_{st}$  [8]

Explosion classes	$K_{st}$	Characteristics
St0	–	Non-explosible
St1	$0 < K_{st} \leq 200$	Weak to moderate
St2	$200 < K_{st} \leq 300$	Strong explosion
St3	$K_{st} > 300$	Extremely explosible

**Table 2** Pressure, concentration and  $\pi$  values [9]

$P$	$\rho$	$\pi_1$	$\pi_2$	$\pi_3$	$\pi_4$
1.53E+05	0.144	4.26E–02	1.42E–05	1	1.08E+07
1.87E+05	0.1625	5.85E–02	1.81E–05	1	9.60E+06
2.40E+05	0.195	9.04E–02	2.60E–05	1	8.00E+06
2.96E+05	0.2368	1.35E–01	3.84E–05	1	6.59E+06
3.47E+05	0.297	1.99E–01	6.04E–05	1	5.25E+06
3.93E+05	0.376	2.85E–01	9.67E–05	1	4.15E+06
4.52E+05	0.5573	4.86E–01	2.13E–04	1	2.80E+06
4.80E+05	0.7337	6.80E–01	3.68E–04	1	2.13E+06
4.73E+05	0.8452	7.71E–01	4.89E–04	1	1.85E+06
4.45E+05	1.0031	8.61E–01	6.88E–04	1	1.55E+06
4.27E+05	1.11455	9.18E–01	8.50E–04	1	1.40E+06
3.91E+05	1.3096	9.88E–01	1.17E–03	1	1.19E+06
3.70E+05	1.4349	1.03E+00	1.41E–03	1	1.09E+06

the best “single number” estimate of the anticipated behaviour of a dust deflagration. Table 2 gives the characteristics of dust according to  $K_{st}$  (Table 1).

## 2.5 Determination of MIT (Minimum Ignition Temperature) of Coal Dust Cloud

Coal dust particle size (250–500  $\mu\text{m}$ ), (150–250  $\mu\text{m}$ ), (75–150  $\mu\text{m}$ ), (48–75  $\mu\text{m}$ ), (25–48  $\mu\text{m}$ ) were tested, [3], respectively at the environment temperature ( $293 \pm 5$ ) K and the pressure of powder was 0.8 MPa. MIT was determined by changing dust concentration of coal (Fig. 4).

Coal dust was sprayed into the storage tank at pressure of 2 MPa and temperature of ( $295 \pm 5$ ) K. To ignite the dust, 10 kJ of energy was supplied at the centre of the tank by chemical igniters. Maximum pressure and temperature were recorded with the help of pressure and temperature sensors. Lower explosive limit and maximum explosive limit was found at different dust concentrations.

It has been analysed from Fig. 5a that explosion pressure is constant during initial dust concentration but after 20  $\text{g}/\text{m}^3$  explosion pressure rises with an increase in dust

**Table 3** Value of  $K$  and  $n$  after regression

	Coefficients	Standard error	$t$ stat	$P$ -value
Intercept	2.12033205	0.130364075	16.2647	1.74E-10
X variable 1	0.68781448	0.034622149	19.86631	1.18E-11
X variable 2	0	0	65535	8.65E-11
X variable 3	0	0	65535	0.04

$K = 10^{2.12033205}$ ,  $n_1 = 0.68781448$ ,  $n_2 = 0$ ,  $n_3 = 0$

concentration. In Fig. 5b, explosion pressure first increase up to approx 0.45 MPa then decreases and becomes minimum at concentration more than 1000 g/m<sup>3</sup>.

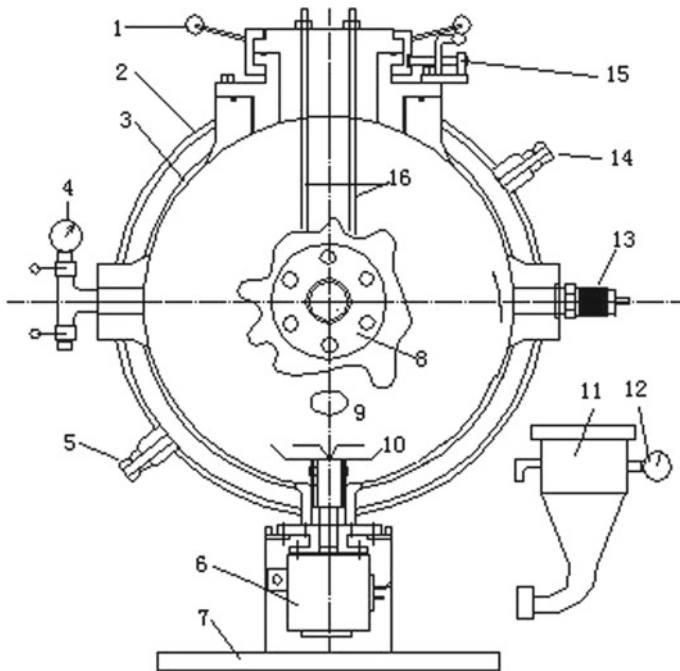


**Fig. 4** Schematic of 20 L sphere vessel dust explosion experiment [3]. 1—Operating handle; 2—the outer wall; 3—the inner wall; 4—vacuum table; 5—cooling water inlet; 6—fast opening valve; 7—base; 8—observation window; 9—inlet; 10—dust dispersed valve; 11—gas chamber ;12—electric contact pressure gauge; 13—pressure sensor; 14—cooling water outer; 15—security lock



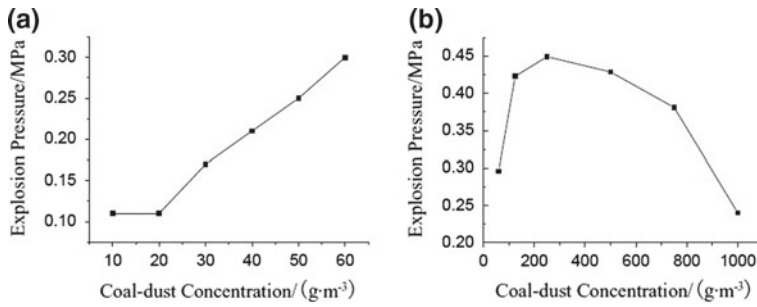


Fig. 5 a, b Experimental results of dust explosion in 20 L sphere [3]

Table 4 Validation of mathematical model

Concentration (kg/m <sup>3</sup> )	Explosion pressure (bar)	
	Experimental	Calculated
0.144	1.53E+05	217570
0.1625	1.87E+05	230056
0.195	2.40E+05	245946
0.2368	2.96E+05	264837
0.297	3.47E+05	288335
0.376	3.93E+05	314808
0.5573	4.52E+05	365618
0.6084	4.65E+05	373913
0.7337	4.80E+05	398440
0.8452	4.73E+05	426977
0.8824	4.68E+05	433945
0.9381	4.57E+05	443828
1.0031	4.45E+05	454994
1.11455	4.27E+05	473600
1.3096	3.91E+05	502130.4
1.4349	3.70E+05	521036

### 3 Model Description

Parameters like concentration of dust, initial temperature, viscosity of fluid, diameter of particle, specific heat of fluid, time and turbulence; directly or indirectly affect the explosion pressure. In this work, a mathematical model was created, which includes all the above-mentioned parameters, as a function of pressure.

$$\text{Explosion Pressure, } P = f(\rho, T_i, \mu, d_p, C_p, t, R_e)$$

**Table 5** Pressure, concentration and  $\pi$  values [9]

$P$	$\rho$	$\pi_1$	$\pi_2$	$\pi_3$	$\pi_4$
46,000	0.007189	1.12E-03	6.23E-08	1	1.24E+08
74,000	0.01977	4.97E-03	4.71E-07	1	451,04,933
104,000	0.023963	8.47E-03	6.92E-07	1	37,212,558
136,000	0.028756	1.33E-02	9.96E-07	1	310,10,034
173,000	0.036244	2.13E-02	1.58E-06	1	24,603,370
198,000	0.041636	2.80E-02	2.09E-06	1	21,417,152
221,000	0.046429	3.49E-02	2.60E-06	1	19,206,197
271,000	0.054516	5.02E-02	3.58E-06	1	16,357,116
289,000	0.057512	5.65E-02	3.98E-06	1	15,505,017

Since, the Buckingham  $\pi$  theorem provides a method for computing sets of dimensionless parameters from given variables, even if the form of the equation remains unknown.

By using Buckingham  $\pi$  Theorem:

$$\pi_1 = K(\pi_2)^{n_1}(\pi_3)^{n_2}(\pi_4)^{n_3} \tag{1}$$

$$\begin{aligned} \pi_1 &= P \cdot \rho \left(\frac{d_p}{\mu}\right)^2 \\ \pi_2 &= C_p \cdot \rho^2 \cdot T_E \left(\frac{d_p}{\mu}\right)^2 \\ \pi_3 &= R_e \\ \pi_4 &= \frac{t \cdot \mu}{\rho \cdot d_p^2} \end{aligned}$$

where

- $P$  Pressure (Pa)
- $\rho$  Dust concentration (kg/m<sup>3</sup>)
- $T_i$  Initial temperature = 293 K
- $\mu$  Viscosity =  $1.98 \times 10^{-2}$  kg/(s m)
- $d_p$  Diametre of particle (m)
- $C_p$  Specific heat = 1.21
- $t$  time = 60 ms

Table 6 gives the  $\pi_1, \pi_2, \pi_3, \pi_4$  terms for 27.6  $\mu\text{m}$  coal particle.

From Table 3, the values of  $K$  and  $n$  are calculated by regression, which are values of the intercept and variables, respectively. In other words,  $K$  is the  $Y$ -intercept and  $n_1, n_2, n_3$  are the slopes of the line  $Y = Nx + C$  (Table 4).

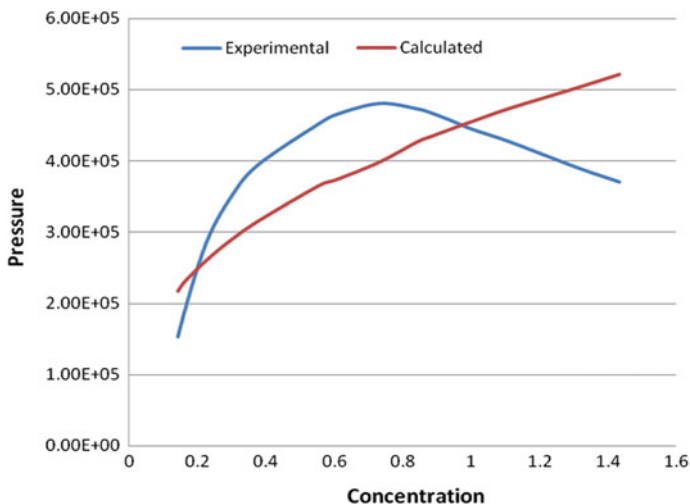


Fig. 6 Results of model validation with experimental data for 27.6 μm coal

In Fig. 6 it is observed that there is a decrease in the experimental data after certain concentration, whereas the calculated data shows a constant increment in pressure along with concentration. The reason for this difference is that there were only three  $\pi$  terms used in calculating the experimental data ( ) while the other data is calculated by using four  $\pi$  terms (Table 5).

Table 3 gives the  $\pi_1, \pi_2, \pi_3, \pi_4$  terms for 36.5 μm coal particle (Fig. 5):

From Table 6, the values of  $K$  and  $n$  are calculated by regression, which are values of the intercept and variables, respectively. In other words,  $K$  is the  $Y$ -intercept, and  $n_1, n_2, n_3$  are the slopes of the line  $Y = Nx + C$  (Table 7).

Based on the results of mathematical model reported above, an analysis was carried out to check the conformity with the experimental data and to determine the % error denoting the deviations from experimental values.

Similarly, mathematical models were built for other dust particles such as Mg and Al which gave similar results to 36.5 μm coal particles with the same values of  $K, n_1, n_2, n_3$  and hence, its code stands true for all these dusts.

Table 6 Value of  $K$  and  $n$  after regression

Coefficients		Standard error	$t$ stat	$P$ -value
Intercept	4.11810	0.2142318	19.222670	3.16084E-09
X variable 1	0.99958	0.0356992	28.000221	7.83891E-11
X variable 2	0	0	65535	0.085861
X variable 3	0	0	65535	8.18E-21

$K = 10^{4.118108984}, n_1 = 0.999585819, n_2 = 0, n_3 = 0$

**Table 7** Validation of mathematical model

Concentration (kg/m <sup>3</sup> )	Explosion pressure (bar)	
	Experimental	Calculated
0.007189	46,000	3.36E+04
0.01977	74,000	9.24E+04
0.023963	104,000	1.12E+05
0.028756	136,000	1.34E+05
0.036244	173,000	1.69E+05
0.041636	198,000	1.95E+05
0.046429	221,000	2.17E+05
0.054516	271,000	2.50E+05
0.057512	289,000	2.68E+05

## 4 Results and Discussion

As shown in above Fig. 7, the % error 9.453% which is well within acceptable limits. The smaller error confirms the applicability of equation for using as an empirical correlation for estimation of initial guess for any facility which would be related with generation, accumulation and settling of dust having properties similar to coal. Although the equation is validated for particles with size in the range of microns, the same can be effectively used for nano-sized particles. It is reported in the literature [10] that with a reduction in particle size, the minimum ignition energy (MIE) required for explosion greatly reduces. For aluminium dusts, the transition of particle size from micro to nano would be responsible for the value of MIE being reduced by 65% [11]. It means that the nano-sized cloud would burn for any flame or spark with having a very low value of MIE, while a micro-sized dust would need a significant value of MIE producing approximately same value of explosion overpressure (Fig. 8).

## 5 Conclusion

The empirical correlation mentioned in this paper, can be used as screening tool on the basis of which a designer or an engineer can determine if any dedicated analysis, such as computational fluid dynamics-based analysis, should be used to determine actual value of explosion overpressure and its profile with respect to time and space which can in turn govern in approach used for detailed engineering. In the current scenario, very little guidance is available on determination of the value of explosion overpressure. The tools available are either too costly or require a very high degree of expertise in mathematics or modelling, because of which the decision-makers are sceptical about investing in any such analysis which would incur additional

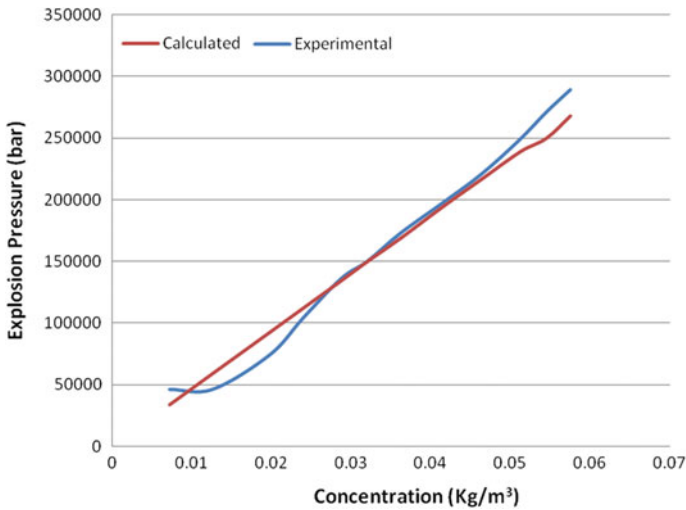


Fig. 7 Results of model validation with experimental data

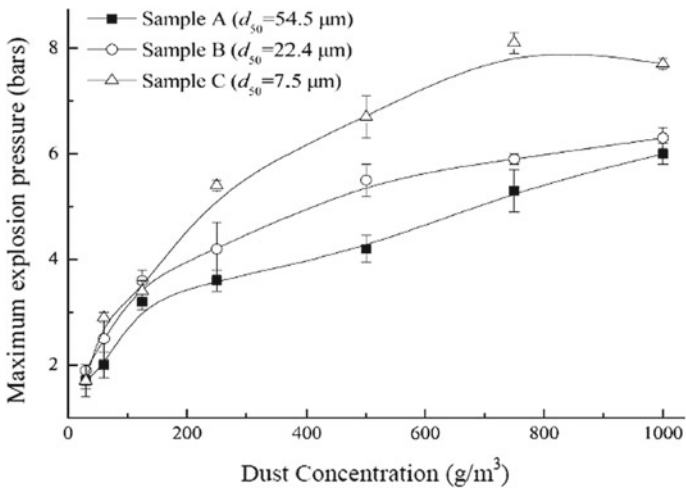


Fig. 8 Relation between dust concentration and explosion pressure [3]

costs and which might conclude that the particular dust is not responsible for any severe damage. The use of this equation can help the decision-makers to estimate the approximate value of overpressure and thus in turn would largely govern the further analysis, especially in developing country like India.

In addition to the equation, review of the literature also suggests some preliminary measures which can be effectively used to avoid dust explosion, such as removal of all sources that will ignite dust like naked flames, smoking, electricity spark, gas cutting,

welding, etc., i.e. carrying out electrical hazardous area classification as per industry standard guidelines like NFPA 499, etc. Another measure which can be effective, especially for nano-sized particles is provision of earthing of all equipment to prevent from static electrical charges having very low MIE. Inerting of dust collected in any enclosure can also be an effective mean to reduce possibility of explosion by removing/replacing the oxygen available.

## 6 Way Forward

The reported equation is derived from the experimental properties of coal dust. A similar set of experiments can be carried out to measure the explosion overpressure associated other materials like aluminium, magnesium, zinc, chromium, organic dust, etc. and consequently developing equations for each of the species being analysed. The set of equations obtained can be further reviewed to devise a more generalized equation which can be applied to any dust including the one whose properties are unknown such as mixture of dust particles of different materials. The experimental set-up can be indigenously prepared and used for determination of properties of dust particles of unknown or mixed origin. Another application of the experimental data generated can be to prepare a CFD-based model for modelling of the dust explosion in a sophisticated manner and to provide a cost-effective solution to decision-makers in India. The use of cost-effective alternative would promote the awareness about the hazards of said phenomenon and would ensure a greater level of sense of security and safety in the minds of the operator.

**Acknowledgements** This research was supported by Techniche Pvt. Ltd. India. We thank our colleagues from MIT, Pune who provided insight and expertise that greatly supported the research.


## References

1. Li Y, Xu H, Wang X (2013) Experimental study on the influence of initial pressure on explosion of methane—coal dust mixtures. *Procedia Eng* 62:980–984
2. Mallick SS, Barman S, Harpreet Singh (2015) *Int J Sci Eng Res* 6(4):351. ISSN 2229-5518
3. Weiguo CAO, Huang L, Zhang J, Xu S, Qiu S, Pan F (2012) Research on characteristics parameters of coal dust explosion. *Procedia Eng* 45:442–447
4. Manju Mittal (2014) Explosion characteristics of micron and nano magnesium powder. *J Loss Prev Process Ind* 27:55–64
5. Dufaud O, Traore M, Perrin L, Chazelet S, Thomas D (2010) Experimental investigation and modeling of aluminum dusts explosions in 20 L sphere. *J Loss Prev Process Ind* 23, 226–236
6. HSL/2004/12 J:\xcontrol\reports\2004\ec\_04\_03\ec\_04\_03.doc.-Explosion Parameters such as LEL, MEC, MIE, etc
7. Abbasi T, Abbasi SA (2006) Dust explosion—cases, cause, consequences and control. Center of pollution control and energy technology
8. Peter W (2005) Dust explosion characteristics. Mechanical Engineering, University of Wollongong

9. Kuai N, Li J, Chen Z, Huang W, J Yuan, Xu W (2011) Experiment-based investigations of magnesium dust explosion characteristics. *J Loss Prev Process Ind* 24:302–313
10. IChemE Symposium Series NO. 155 Hazards XXI # 2009 Crown Copyright -Explosion properties of nanopowders and 20L Sphere Vessel
11. Dufaud O, Vignes A, Henry F, Perrin L, Bouillard J (2014) Ignition and explosion of nanopowders: something new under the dust

# Environmental Challenges and Opportunities in Marine Engine Heavy Fuel Oil Combustion



Abdul Gani Abdul Jameel , Abdulrahman Alkhateeb, Selvedin Telalović, Ayman M. Elbaz, William L. Roberts and S. Mani Sarathy

**Abstract** Heavy fuel oil (HFO) has been used as fuel to propel marine engines for over half a century. HFO combustion results in the release of particulate matter like smoke, cenospheres, and ash, and the high sulfur content in HFO results in sulfur dioxide emissions. The use of HFO has resulted in deleterious effects on the environment and on human health. As a result, the International Maritime Organization (IMO) has placed a complete ban on its use on ships in the Antarctic waters to preserve the ecosystem from harm; by 2020, this regulation could be extended to the rest of the world. In the present work, the environmental challenges associated with HFO combustion in the form of gaseous emissions like CO<sub>2</sub>, CO, SO<sub>2</sub>, and NO were analyzed using TGA-FTIR technique. Particulate emission like cenosphere formation during HFO combustion was also studied by employing HFO droplet combustion experiments. The influence of asphaltenes, which are notorious for negatively impacting HFO combustion and are responsible for cenosphere formation, was also studied. Strategies like desulfurization, asphaltene removal, and gasification were proposed to help reduce the environmental impact of ships powered by HFO.

**Keywords** Heavy fuel oil · Sulfur dioxide · Cenospheres · Asphaltenes

## 1 Introduction

HFOs have been used as fuel to propel marine engines since the early 1960s. Despite being highly viscous and dirty, HFOs have found use in the marine industry because they are inexpensive. The shipping industry uses nearly 240 Mt of HFO every year [1].

---

A. G. Abdul Jameel (✉) · A. Alkhateeb · A. M. Elbaz · W. L. Roberts · S. M. Sarathy  
Clean Combustion Research Centre (CCRC), King Abdullah University of Science and  
Technology (KAUST), Thuwal 23955-6900, Saudi Arabia  
e-mail: [abdulgani.abduljameel@kaust.edu.sa](mailto:abdulgani.abduljameel@kaust.edu.sa)

S. Telalović  
Catalysis Centre, King Abdullah University of Science and Technology (KAUST), Thuwal  
23955-6900, Saudi Arabia

© Springer Nature Singapore Pte Ltd. 2019  
K. Murali et al. (eds.), *Proceedings of the Fourth International Conference in Ocean  
Engineering (ICOE2018)*, Lecture Notes in Civil Engineering 22,  
[https://doi.org/10.1007/978-981-13-3119-0\\_72](https://doi.org/10.1007/978-981-13-3119-0_72)

1047



High sulfur content (up to 4.5% by mass) in HFO is responsible for the sulfur dioxide emissions [2]. Particulate matters like smoke, cenospheres, and ash are produced due to HFO combustion. The International Maritime Organization (IMO) has stated, starting from 2015, that marine fuels should possess less than 0.1% of sulfur on ships sailing in the North Sea, English Channel, and the Baltics to mitigate the harmful effects of HFO on the environment and on human health [3]. This has resulted in a worldwide demand of 40 Mt/y of low sulfur fuels [4]. By 2020, there are plans to extend this regulation to the rest of the world. In 2011, the IMO placed a complete ban on the use of HFO on ships sailing in the Antarctic waters to preserve the ecosystem from harm [3]. This means that if HFOs are to be employed by the marine industry in the future, then they need to become more eco-friendly; otherwise, this could signal the end of their use.

## 2 HFO Characterization

The properties of HFO depend on the composition of the parent crude and the conditions in which it was processed. Lighter solvents may be added to HFO based on refinery availability to reduce the viscosity of HFO and enable its easier flow. The present sample of HFO was sourced from a refinery in Saudi Arabia, and its physical and chemical properties are presented in Table 1. HFO has a high viscosity of 746.5 ( $10^{-6}$  m<sup>2</sup>/s) at 313 K, which is a thousand time larger than the viscosity of water. HFO is usually preheated to reduce its viscosity before being atomized and burned in boilers or in marine engines. The sample contains 2.39 mass% of sulfur which acts as a potential source of SO<sub>2</sub> emissions when burned. The proximate analysis of HFO was performed using the thermogravimetric analysis (TGA) method by Karetepe and Küçükbayrak [5]. The sample contains very less (<1 mass%) of moisture and ash content and has a very high quantity (84.79 mass%) of volatile matter. The fuel has a high aromatic content of nearly 37 mass% as shown in our previous works [3, 6, 7].

## 3 Environmental Challenges

### 3.1 Gaseous Emissions

The gaseous pollutants evolved during HFO combustion were analyzed using TGA-FTIR apparatus. When the FTIR technique is complemented with a TG apparatus, useful information can be obtained about the composition of the evolved gases. A number of typical compounds can be identified by their characteristic absorbance bands. The HFO sample was heated in the presence of air at three different heating rates and pollutant gases. The pollutant gases analyzed are shown in Fig. 1.

**Table 1** Physical and chemical properties of HFO

Property	Unit	Value	Method
Density (at 288 K)	kg/m <sup>3</sup>	968	ASTM D4052-11
Specific gravity (at 288 K)	No units	0.967	ASTM D4052-11
Kinematic viscosity (at 313 K)	10 <sup>-6</sup> m <sup>2</sup> /s	746.5	ASTM D445-12
Enthalpy of combustion (at 298 K)	MJ/mol	31.35	ASTM D4868
Asphaltene content	mass%	8.2	IP 143
<i>Ultimate analysis</i>			
Carbon	mass%	84.35	EPA 440
Hydrogen	mass%	10.65	EPA 440
Oxygen	mass%	2.29	EPA 440
Nitrogen	mass%	0.31	EPA 440
Sulfur	mass%	2.39	ASTM D4294-10
<i>Proximate analysis</i>			
Moisture	mass%	0.81	
Ash content	mass%	0.55	
Volatile matter	mass%	84.79	
Fixed carbon	mass%	13.85	

CO<sub>2</sub> is a greenhouse gas and responsible for most of the global warming in the atmosphere [8]. It is also responsible for other environmental hazards like ocean acidification due to its propensity to dissolve in water forming carbonic acid. CO is a temporary atmospheric pollutant that is responsible (along with aldehydes) for the reactions that lead to the formation of photochemical smog. It also plays a major role in the formation of tropospheric ozone which is a pollutant. CO is a toxic gas and when inhaled in high concentrations (>1000 ppm) can lead to unconsciousness and continued exposure could be lethal. NO is a pollutant gas that is formed at high temperatures by the reaction of nitrogen with oxygen and also with hydrocarbons during combustion reactions. NO also takes part in depletion of the ozone layer which is necessary to filter the harmful UV rays from the sun. SO<sub>2</sub> is one of the major air pollutants due to its harmful effects on human life. It is an irritant of the respiratory passages, and its concentration in the atmosphere has a negative impact on the various plant communities and wildlife habitat and acts as a precursor to atmospheric particulates and acid rain.

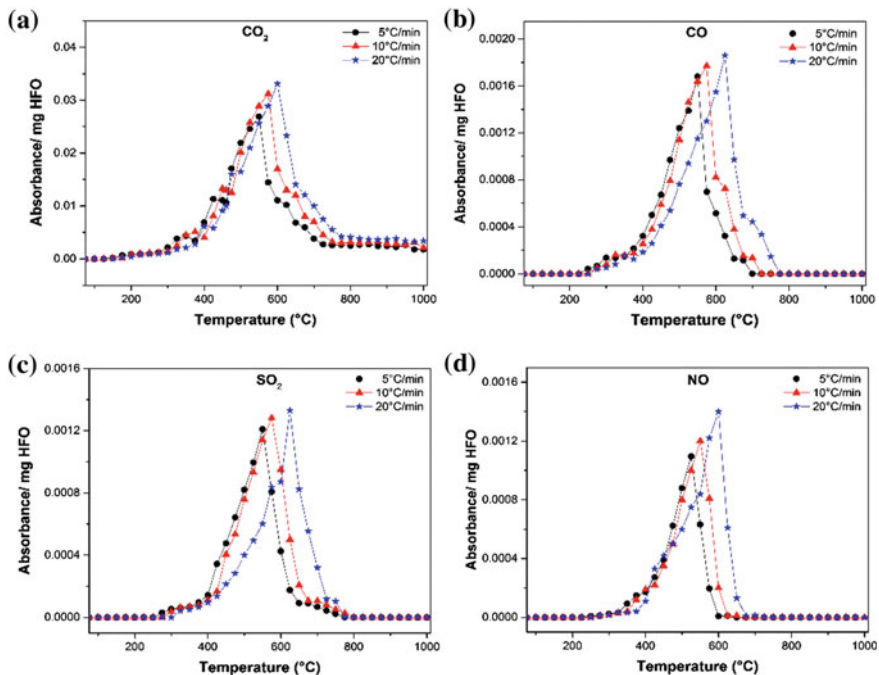


**Fig. 1** Evolution of pollutant gases during HFO combustion at heating rates of 5, 10, and 20 °C/min. **a** CO<sub>2</sub>, **b** CO, **c** SO<sub>2</sub>, and **d** NO

### 3.2 Particulate Emissions

HFO combustion leads to the emission of particulate matters like cenospheres, ash, and smoke [9]. These particulate matters have been shown to reduce visibility in many coastal areas and are carried over long distances by wind. They have damaged aquatic ecosystems, altered the nutrient balance in large river basins besides having a detrimental effect on human health in the form of bronchitis, asthma, and other respiratory problems. HFO contains asphaltenes, which are high molecular weight aromatics with largely unknown chemical identity. They are defined as the content of the fuel insoluble in n-heptane and usually range between 2.6 and 12 mass%. They are generally considered as a precursor to the formation of particulate emissions like cenospheres, ash, and smoke and are difficult to burn. Unlike fly ash, cenospheres are mostly hollow spheres, light in weight, and carbonaceous, which are formed during droplet combustion at temperatures lower than that of soot formation [10]. Their formation is known to depend more on the asphaltene chemistry than asphaltene quantity in the HFO [9]. Figure 2 shows the SEM image of two different cenosphere particles obtained during the droplet combustion of HFO. It is highly carbonaceous and has a porous morphology.

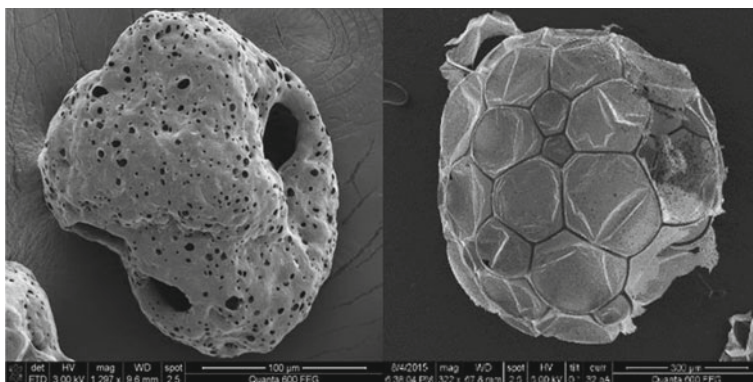


**Fig. 2** SEM image of two different cenosphere particles obtained during HFO combustion

## 4 Strategies to Reduce Environmental Impact

### 4.1 Desulfurization

The  $\text{SO}_2$  emissions from HFO combustion are primarily due to the sulfur content of the fuel. Reducing the sulfur in HFO will ultimately result in a reduction of  $\text{SO}_2$  emissions. A number of techniques have been reported in the literature like hydro-desulfurization (HDS) [11], where the bond between C and S is broken by hydrogenolysis which results in the formation of  $\text{H}_2\text{S}$  gas and sulfur-reduced HFO. Another method is oxidative desulfurization (ODS) [12] in which hydroxyl radicals are produced from catalyzed hydrogen peroxide. These radicals then react with the sulfur in HFO to form sulfones and/or sulfoxides which are removed by using a polar solvent. These desulfurization techniques can reduce up to 70% of sulfur in the fuel which will reduce  $\text{SO}_2$  emissions [13].

### 4.2 Asphaltene Removal

As discussed above, asphaltene content in HFO is directly related to the formation of particulate matter like cenospheres. Also, they are responsible for the high viscosity and difficult to burn nature of HFO [14]. Removal of asphaltenes from HFO by *n*-heptane solvent extraction thus sounds advantageous to facilitate easier combustion while reducing the emissions of particulate matter. A suspended droplet of HFO with varying levels of asphaltene content, namely 0, 8, and 16% by mass, was burnt to analyze its combustion characteristics. Figure 3 shows the temperature history of the HFO droplets, and Fig. 4 shows the combustion of the HFO droplets.

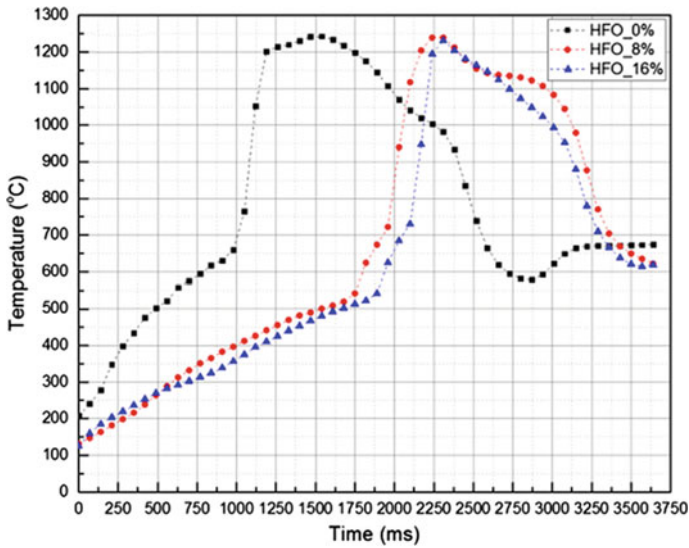


Fig. 3 Temperature history of combustion of HFO droplets with varying asphaltene contents

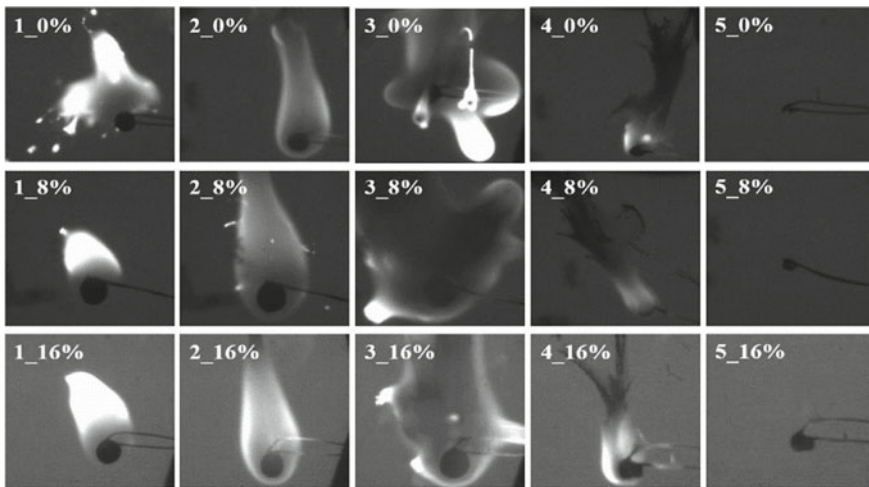


Fig. 4 Combustion of HFO droplets with varying asphaltene contents

It can be seen from Fig. 3 that the ignition delay time (IDT) decreases with decreasing asphaltene content in HFO. The droplet with 0% asphaltene content requires lesser time to reach the critical ignition temperature compared to droplets containing 8 and 16% of asphaltenes. From Fig. 4, it can be observed that droplets containing 0% asphaltenes burn more rapidly compared to the droplets with higher asphaltene contents. Also, a higher cenosphere formation was recorded when the asphaltene

content was high. This shows that asphaltene removal can be employed to reduce the environmental effects of HFO combustion.

### 4.3 Gasification

Gasification is an environmentally friendly process of converting HFO into clean combustible gases ( $H_2$  and  $CO$ ) called syngas. By gasification, an inexpensive low-grade fuel is converted into a valuable and eco-friendly fuel which is easier to burn compared to a viscous, semisolid fuel such as HFO. The composition of the syngas obtained is dependent on the HFO feedstock, gasification method, and conditions like temperature and pressure inside the gasifier. The asphaltenes separated from HFO can also be gasified to yield syngas [15].

The schematic of HFO gasification process employed by Meratizaman et al. is shown in Fig. 5. HFO entering into the gasifier is first preheated to reduce its viscosity and increase its flow properties. Gasification is the partial oxidation of the fuel in the presence of  $O_2$  which is separated from air using an air separation unit. Steam is added into the gasifier to convert  $CO_2$  into  $H_2$  as per the water–gas shift reaction. The hot syngas produced is taken to the heat recovery steam generator (HRSG) which recovers the extra heat in the syngas to produce steam, which is fed to the gasifier. The heat in the untreated syngas is also used to preheat the HFO inlet, followed by an acid removal system that gives clean syngas. This syngas can then be used as fuel to propel marine engines [17]. Gasification is an ideal way to prevent particulate emissions from HFO and reduce significant volumes of sulfur dioxide emissions [18].

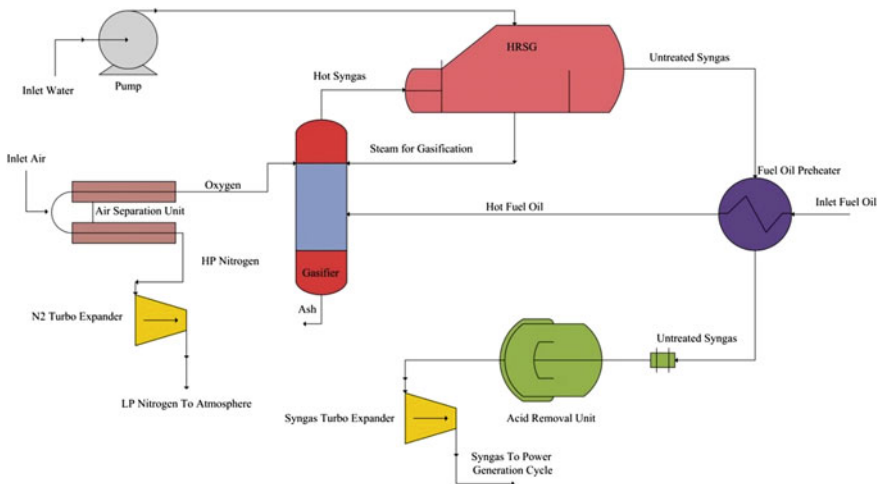


Fig. 5 Schematic of HFO gasification by Meratizaman et al. [16]

## 5 Summary and Conclusion

Burning HFO in marine engines as a fuel results in the destruction of the marine ecosystems due to the emissions of pollutant gases like sulfur dioxide and particulate matters like cenospheres, ash, and smoke. HFO is an inexpensive fuel, and various strategies were discussed that would reduce its environmental impact so that it can be continued to be used as a fuel. Removing the sulfur bound to the fuel via desulfurization techniques helps to significantly reduce the sulfur dioxide emissions. The asphaltenes present in HFO are responsible for the emissions of particulate matter, and its separation from the fuel reduces the emissions. HFO gasification is another important technique in which the fuel can be upgraded into a valuable gaseous fuel, thus making it an eco-friendly fuel.

**Acknowledgements** Research reported in this publication was supported by Saudi Electric Company (SEC) and by competitive research funding from King Abdullah University of Science and Technology (KAUST). The authors acknowledge support from the Clean Combustion Research Center under the Future Fuels research program.

## References

1. U.S. EIA (2016) The International Energy Outlook 2016, pp 1–279
2. Elbaz AM, Gani A, Hourani N, Emwas A-H, Sarathy SM, Roberts WL (2015) TG/DTG, FT-ICR mass spectrometry, and NMR spectroscopy study of heavy fuel oil. *Energy Fuels* 29:7825–7835. <https://doi.org/10.1021/acs.energyfuels.5b01739>
3. Abdul Jameel AG, Elbaz AM, Emwas A-H, Roberts WL, Sarathy SM (2016) Calculation of average molecular parameters, functional groups, and a surrogate molecule for heavy fuel oils using <sup>1</sup>H and <sup>13</sup>C nuclear magnetic resonance spectroscopy. *Energy Fuels* 30:3894–3905. <https://doi.org/10.1021/acs.energyfuels.6b00303>
4. World Energy Council: Global Transport Scenarios 2050, pp 1–72
5. Karatepe N, Küçükbayrak S (1993) Proximate analysis of some Turkish lignites by thermogravimetry. *Thermochim Acta* 213:147–150. [https://doi.org/10.1016/0040-6031\(93\)80012-Y](https://doi.org/10.1016/0040-6031(93)80012-Y)
6. Abdul Jameel AG, Han Y, Brignoli O, Telalović S, Elbaz AM, Im HG, Roberts WL, Sarathy SM (2017) Heavy fuel oil pyrolysis and combustion: kinetics and evolved gases investigated by TGA-FTIR. *J Anal Appl Pyrolysis* 127:183–195. <https://doi.org/10.1016/j.jaap.2017.08.008>
7. Abdul Jameel AG, Naser N, Emwas A-H, Dooley S, Sarathy SM (2016) Predicting fuel ignition quality using <sup>1</sup>H NMR spectroscopy and multiple linear regression. *Energy Fuels* 30:9819–9835. <https://doi.org/10.1021/acs.energyfuels.6b01690>
8. Treatment of tannery effluent using a rotating disc electrochemical reactor. *Water Environ Res* 1–2. <https://doi.org/10.2175/106143016x14609975746046>
9. Bomo N, Lahaye J, Prado G, Claus G (1985) Formation of cenospheres during pyrolysis of residual fuel oils. *Symp Combust* 20:903–911. [https://doi.org/10.1016/S0082-0784\(85\)80579-8](https://doi.org/10.1016/S0082-0784(85)80579-8)
10. Bartle KD, Jones JM, Lea-Langton AR, Pourkashanian M, Ross AB, Thillaimuthu JS, Waller PR, Williams A (2013) The combustion of droplets of high-asphaltene heavy oils. *Fuel* 103:835–842. <https://doi.org/10.1016/j.fuel.2012.07.004>
11. Levy A, Merryman EL, Reid WT (1970) Mechanisms of formation of sulfur oxides in combustion. *Environ Sci Technol* 4:653–662. <https://doi.org/10.1021/es60043a005>

12. De Filippis P, Scarsella M (2003) Oxidative desulfurization: oxidation reactivity of sulfur compounds in different organic matrixes. *Energy Fuels* 17:1452–1455. <https://doi.org/10.1021/ef0202539>
13. Farshi A, Shiralizadeh P (2015) Sulfur reduction of heavy fuel oil by oxidative desulfurization (ODS) method. *Pet Coal* 57:295–302
14. Hasan SW, Ghannam MT, Esmail N (2010) Heavy crude oil viscosity reduction and rheology for pipeline transportation. *Fuel* 89:1095–1100. <https://doi.org/10.1016/j.fuel.2009.12.021>
15. Vaezi M, Passandideh-Fard M, Moghiman M, Charmchi M (2011) Gasification of heavy fuel oils: a thermochemical equilibrium approach. *Fuel* 90:878–885. <https://doi.org/10.1016/j.fuel.2010.10.011>
16. Meratizaman M, Monadzadeh S, Pourali O, Amidpour M (2015) High efficient-low emission power production from low BTU gas extracted from heavy fuel oil gasification, introduction of IGCC-SOFC process. *J Nat Gas Sci Eng* 23:1–15. <https://doi.org/10.1016/j.jngse.2015.01.023>
17. Bates RP, Dölle K (2017) Syngas use in internal combustion engines—a review. *Int J Innov Res Multidiscip Field* 10:1–8. <https://doi.org/10.9734/air/2017/32896>
18. Ghassemi H, Beheshti SM, Shahsavan-Markadeh R (2015) Mathematical modeling of extra-heavy oil gasification at different fuel water contents. *Fuel* 162:258–263. <https://doi.org/10.1016/j.fuel.2015.09.018>



# Exergy Analysis of Auxiliary Boiler for Marine Application



Jitendra Singh Pal, S. N. Sapali and T. R. Anil

**Abstract** Low-pressure auxiliary boiler is used for generating steam for the purpose of fuel oil heating, tank cleaning, lubricating oil purification, operation of cargo pump, power generation and air conditioning in commercial marine vessels. The thermal performance of these auxiliary boilers is very poor. The present study investigates the auxiliary boiler of capacity 400 kg/h at 10.5 kg/cm<sup>2</sup> installed in training ship at Tolani Maritime Institute, Pune. The parametric analysis of the auxiliary boiler for first and second law of thermodynamic efficiency calculation, exergy efficiency and numerical analysis on pressure jet burner is carried out. This study is aimed to enhance the energy saving in auxiliary boiler on-board ship. The light diesel oil is used as a fuel in this study. The reverse flame from the jet burner is heating the water tubes, which generates wet steam. The flue gases leaving the boiler will pass through economizer where feed water temperature raises to saturated level. Existing condition of this boiler is assessed by rate of fuel consumption per day at steam pressure 10.5 kg/cm<sup>2</sup> and irreversibility at its various parts and proposes various remedial actions to overcome these losses. Computation fluid analysis of combustion reveals that the improper air circulation leads to less heat transfer at water tubes and complete oxidation of hydrocarbon.

**Keywords** Auxiliary boiler · Light diesel oil · Irreversibility · Waste heat recovery Preheating of air

---

J. S. Pal (✉)

Tolani Maritime Institute, Pune, India  
e-mail: [jitendrasinghpal2011@gmail.com](mailto:jitendrasinghpal2011@gmail.com)

S. N. Sapali

Collage of Engineering, Pune, India  
e-mail: [sns.mech@coep.ac.in](mailto:sns.mech@coep.ac.in)

T. R. Anil

Gogte Institute of Technology, Belagavi, India  
e-mail: [tranil@git.edu](mailto:tranil@git.edu)

© Springer Nature Singapore Pte Ltd. 2019

K. Murali et al. (eds.), *Proceedings of the Fourth International Conference in Ocean Engineering (ICOE2018)*, Lecture Notes in Civil Engineering 22,  
[https://doi.org/10.1007/978-981-13-3119-0\\_73](https://doi.org/10.1007/978-981-13-3119-0_73)

1057

## 1 Introduction

The new International Maritime Organization rules on emission limits in shipping are creating opportunities for introducing new alternatives to the boiler and fuel choice. In current ships with auxiliary boiler, half of the fuel is used to generate steam and other half is lost to the sea as waste heat or irreversibility. Therefore, it is required to identify the sources of thermodynamic irreversibility like heat transfer that leaks directly through the boiler parts, heat transfer across the finite temperature gradients and the internal thermal resistance. In this study, the auxiliary boiler is a once through, three pass, water tube with reverse flame technology. The special feature is unique coil design, optimizer–economizer and cyclonic separator (Fig. 1).

## 2 Literature Review

Moran [1] gives the definition and second-law efficiencies for efficient energy use. According to him, the availability is the maximum work that can be extracted from the combined system of control mass and environment as the control mass passes from a given state to the dead state. Availability, symbolized by  $A$ , is an extensive property calculated by



**Fig. 1** Rx4 Auxiliary boiler

$$A = (E - U_O) + P_O(V - V_O) - T_O(S - S_O) \quad (1)$$

where  $E (=U + KE + PE)$ ,  $V$  and  $S$  denote, respectively, the energy, volume and entropy of the control mass at the given state, and  $U_O$ ,  $V_O$  and  $S_O$  are the same properties when the control mass is at rest at the dead state.

The second-law efficiency  $\epsilon$  is a ratio of availability out in product to availability in. Another class of second-law efficiencies is composed of task efficiencies. Task efficiency is the ratio of the theoretical minimum input required by the first and second laws to accomplish some task to the actual input for a particular means.

$$\epsilon = \Delta A / WE = \text{Availability} / \text{Energy amount} \quad (2)$$

In Som and Datta [2], they presented paper to make a comprehensive review pertaining to fundamental studies on thermodynamics irreversibility and exergy analysis in the process of combustion of gaseous, liquid and solid approaches of exergy analysis and the results arrived by different research works in the boiler.

Kotas [3] explained that the irreversibility inherent in the adiabatic combustion process corresponds to a large proportion of the original exergy of the fuel. To reduce this irreversibility, a reduction in the rate of increase in entropy is required, which is always associated with an increase in the maximum temperature of the products and it can be achieved by isochoric combustion, oxygen enrichment and preheating of the reactants.

In Zaili et al. [4], they studied on the losses identification and studied the influences of thermodynamic perfection of boiler, did exergy analysis of model WGZ220/6.81 type alkali recovery boiler and developed software by use of Microsoft Visual Basic 6.0.

Ohijeagbon et al. [5] studied the performance variables and potential for energy saving in oil-fired industrial steam boiler. Operational parameter of steam boiler using low pour fuel oil (LPFO) and diesel was used to determine thermodynamic properties of material streams and exergetic parameters. By going through these papers, it was concluded that less work is carried out to identify the processes where loss of availability occurs. There is less research done on the analysis of thermodynamic parameters of the exergy destruction and losses from on-board propulsion and steam generation machine.

### 3 Construction and Working

In the furnace section of the boiler of a membrane coil, fuel is burnt. This coil is housed in a jacket assembly consisting of inner jacket and outer jacket. Pressure jet burner is mounted on the top cover of the outer jacket. Apart from the main boiler section, economizer and heat optimizer are provided before the feed water pump. Economizer is a jacket and tube heat exchanger, and optimizer is tube in tube-type heat exchanger. The necessary fuel-handling system is also provided along with the

boiler. Fuel is burnt in the membrane coil by the pressure jet burner using the air from combustion air fan. At the outlet of the boiler, the flue gas is exhausted through the economizer to recover further heat from the flue gas. This boiler is working on light diesel oil (LDO), which is supplied by a gear pump having an output capacity of 2000 l/h against 50 psi delivery pressure. One mesh-type filter of  $80 \times 80$  mesh is provided just at the outlet of the main storage tank.

## 4 Thermal Analysis of Auxiliary Boiler

### 4.1 First Law Analysis of Auxiliary Boiler

The fuel consumption for various ship processes is received as a function of the monthly running hours. This analysis can be called the “first law analysis” which is useful to study the quantities of different energy and conservation of energy.

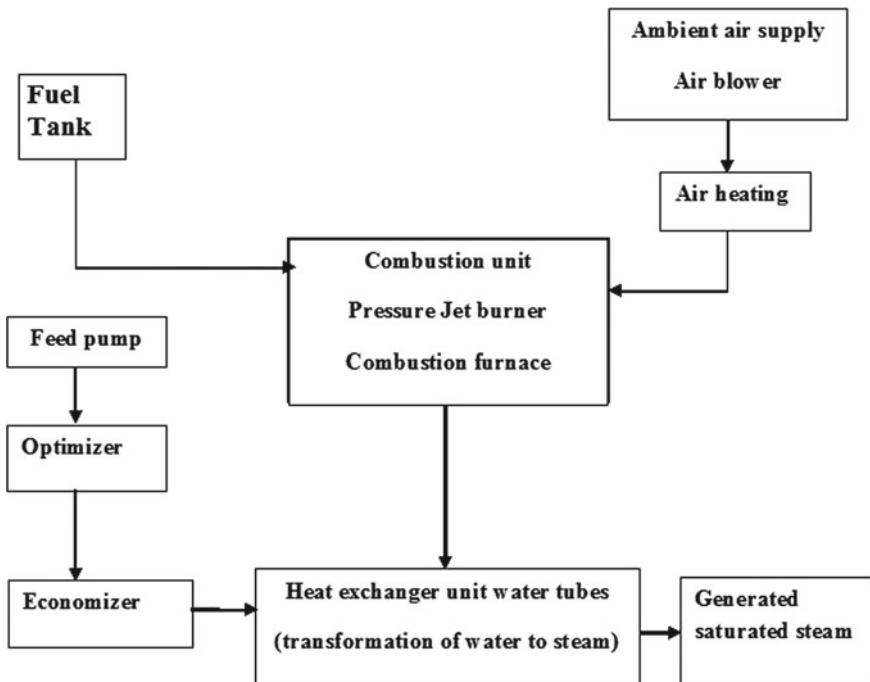
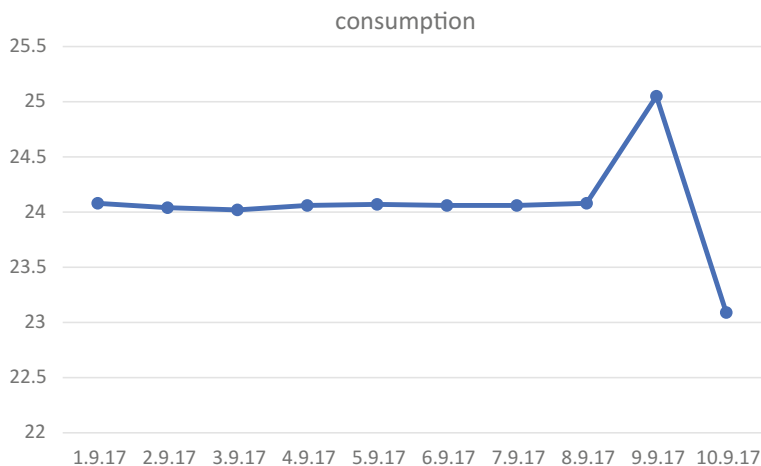


Fig. 2 Fluid flow in auxiliary boiler



**Graph 1** Detail of fuel consumption of auxiliary boiler

**Table 1** Details of auxiliary boiler

S. No.	Cardinals	Specification	Description
01	Model	RXA 4	10.54 kg/cm <sup>2</sup>
02	Capacity	Evaporation	400 kg/h
03	Efficiency	Oil	87.5%
04	Burner	Oil	Pressure jet
06	Weight	Dry	1100 kg
07	Fuel	Oil	Light diesel oil

**Table 2** Fuel consumption of auxiliary boiler

Fuel consumption		
S. No.	Date	Consumption
1	1.9.17	24.08
2	2.9.17	24.04
3	3.9.17	24.02
4	4.9.17	24.06
5	5.9.17	24.07
6	6.9.17	24.06
7	7.9.17	24.06
8	8.9.17	24.08
9	9.9.17	25.05
10	10.9.17	23.09

It is not possible to identify the irreversibility in the components through first law analysis and subsequently to identify the potential components to be identified for the performance improvement. In this study for exergy analysis, the reference point of temperature and pressure of all fluids studied is taken as  $T_O = 20\text{ }^\circ\text{C}$  and  $P_O = 1.0\text{ Atm}$  (Fig. 2; Tables 1 and 2).

The reference state of water and fuel oil is liquid state, and flue gas, steam and air are in gaseous state. For a liquid fuel at  $T_O$  and  $P_O$ , the chemical exergy is maximum theoretical work that could be obtained through reaction with oxygen in the boiler furnace. It is found by analysing the Graph 1 that fuel consumption is 24.04 kg/h for this auxiliary boiler. This analysis states that the fuel consumption is high due to heat loss at its various parts and high-temperature gradient. In process of fully thermal analysis of this boiler system, exergy analysis method is worthy of our consideration.

## 4.2 Second Law Analysis of Auxiliary Boiler

The thermal analysis of the auxiliary boiler is analysed by heat transfer, chemical energy of fuel, feed water and air compared with products formed during combustion and steam generation. This analysis is also referred to as second law analysis. Most boilers are designed and operated at high efficiencies, like the auxiliary boiler of training ship Prabhu Vidya with a thermal efficiency of 87.5%.

For effective mapping, we have to know how much heat is radiated from individual components of the auxiliary boiler. The remote heat system measurement is capable of collecting and storing a large number of data in a simple, flexible and effective way. Introducing an energy-based efficiency in Eq. (3) and data shown in Graph 2, the  $\text{€}/n = \text{task efficiency/energy efficiency}$  is calculated and shown in Table 3. The parameter taken as per Fig. 1 is  $T_s = 1850\text{ }^\circ\text{C}$ ,  $T_o = 250\text{ }^\circ\text{C}$ .

$$\text{Task efficiency} = n(1 - T_O/T_U)/(1 - T_O/T_S) \quad (3)$$

Table 3 shows that when the combustion species temperature is achieved by burning light diesel fuel, there is a significant destruction of availability associated with the combustion process.

**Table 3** Parameter of auxiliary boiler at various load

Load on aux. boiler (%)	$T_U$ exhaust temperature, centigrade	$\text{€}/n = \text{Task efficiency/energy efficiency}$
25	350	0.94
35	400	0.95
45	450	0.96
55	500	0.97

### 4.3 Evaluation of Losses Generated by Auxiliary Boiler

The evaluation of losses generated by auxiliary engine is carried out through experimentation at training ship Prabhu Vidya’s auxiliary engine. The irreversibility to be studied is

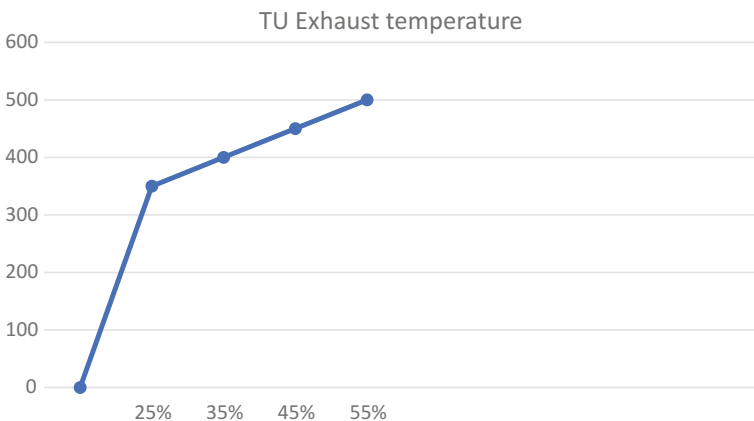
- (1) Isochoric combustion which involves changing the character of the process. Isochors on a T-S diagram are steeper than isobars.
- (2) O<sub>2</sub> enrichment of the reactants reduces nitrogen dilution which leads to reduction of the heat capacity of the reactants and products.
- (3) Preheating of air in the casing of the boiler.
- (4) A very high temperature difference in the combustion process will cause heat losses.
- (5) Some incomplete combustion of diesel fuel.
- (6) The exhaust gases such as CO<sub>2</sub>, H<sub>2</sub>O, CO, NO, SO<sub>2</sub> and N<sub>2</sub> discharged to atmosphere; Table 4).

### 4.4 Calculation of Irreversibility in a Pressure Jet Burner

Diesel fuel oil C<sub>8</sub>H<sub>18</sub> (Gaseous octane) is oxidized through the pressure jet burner in this boiler at a pressure of 4.033 kg/cm<sup>2</sup>. Diesel fuel temperature is 250 °C, and air enters at 437 °C. The exhaust gases leave the furnace at 827 °C at adiabatic condition.

We have:

$$H_g \text{ (Total enthalpy of reactants)} = H_p \text{ (Total enthalpy of products)} \quad (4)$$

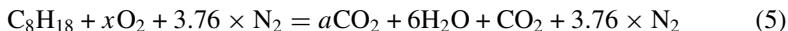


**Graph 2** Auxiliary boiler exhaust temperature increases with load

**Table 4** Thermodynamic properties of diesel fuel of auxiliary boiler

Cardinals	Diesel oil	
	kmol/kmol fuel	kg/kg fuel
C	$X = 10.8$	$C = 0.874$
H	$Y = 18.7$	$h = 0.126$
O	$Z = 0$	$O = 0$
Molar mass	148.3 kg fuel/kmol fuel	
$h_f^0 C_8H_{18}$	-208,450	
$h_{710 \text{ air}}$	713.27	
$h_{298 \text{ air}}$	298.19	
$S^0 C_8H_{18}$	466.73	
$S C_8H_{18}$	455.20 kJ/kg mol K	
$S \text{ Air}$	208.31 kJ/kg mol K	
$S_g$	78 113 kJ/K	

The combustion reaction for 1 mol of fuel is written as



For stoichiometric combustion  $x = 12.5$ , so the per cent theoretical air is  $78.32/12.5 = 626\%$ . The air/fuel ratio is thus 94.74 kg air/kg fuel.

The total entropy of the reactants is  $S_R = 78,113 \text{ kJ/K}$ .

The change in availability is

$$\Delta B = -T_O(S_P - S_R) \tag{6}$$

The total entropy of the products is thus 86,402 kJ/K.

Then form Eq. (6)  $\Delta B = -2,470,122 \text{ kJ}$

The maximum work output is the negative of this quantity, or

$$W_{\max} = +2,470,122 \text{ kJ}$$

The actual work output is zero, so the irreversibility is

$$I = W_{\max} - W_{\text{ACT}} \tag{7}$$

$I = +247,012 \text{ 2kJ/kg mol fuel I (Irreversibility) (Table 5)}$ .



**Table 5** Irreversibility generation and its remedial action in boiler

S.	Components	Irreversibility generation	Remedial action
01	Cascade tank	Temperature difference of cold feed water and hot condensate water	Preheating of feed water to be carried out and use of baffles
02	Economizer and optimizer	Temperature difference, non-uniform gradient, pressure drop and low heat transfer	Use as low as possible driving force. Use as uniform gradients of temperature
03	Steam condenser	Fouling Air in system	Use of backwashing to remove scale on tubes Purging to be followed
04	System valves	Pressure drop and cavitation	Fully opened or shut the valves
05	Furnace	A chemical reaction for oxidation of the light diesel oil	Preheating of air. Mix air and fuel as uniformly as possible

## 5 Numerical Analysis of Auxiliary Boiler Burner

Numerical analysis of auxiliary boiler nozzle is carried out and compared for the exergy losses. This numerical analysis is carried out in pressure jet burner with 03-mm-diameter hole. The mesh is generated with ANSYS software code 18.1. The numerical model of the burner is studied by two-step chemical reaction, and the property value is based on temperature gradients, mass fraction and species concentration. The boundary condition is given as follows (Figs. 3, 4 and 5; Table 6).

**Table 6** Boundary condition

S. No.	Cardinals	Value
1	Preheated air	1.5 kg/cm <sup>2</sup> and 45 °C
2	Fuel	15 kg/cm <sup>2</sup>
3	Water	80 °C
4	Fuel velocity	150 mm/s

**Fig. 3** Rx4 auxiliary boiler burner

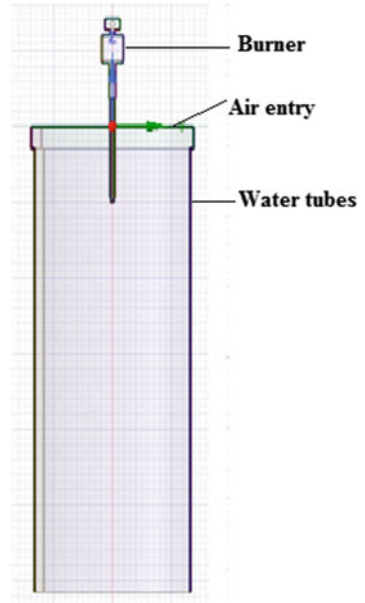


**Fig. 4** Rx4 auxiliary boiler pressure jet burner and nozzle

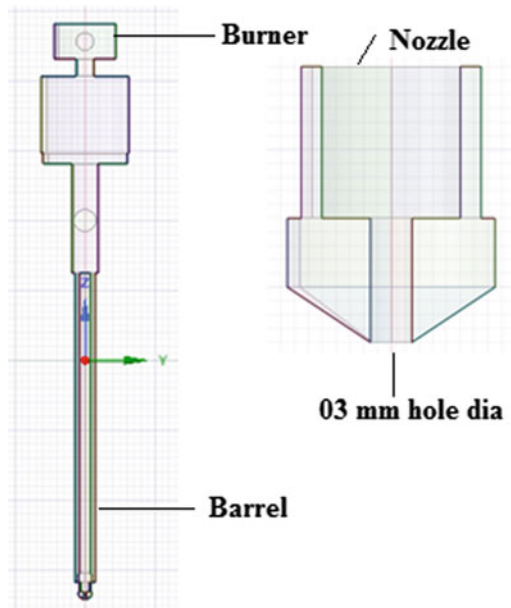
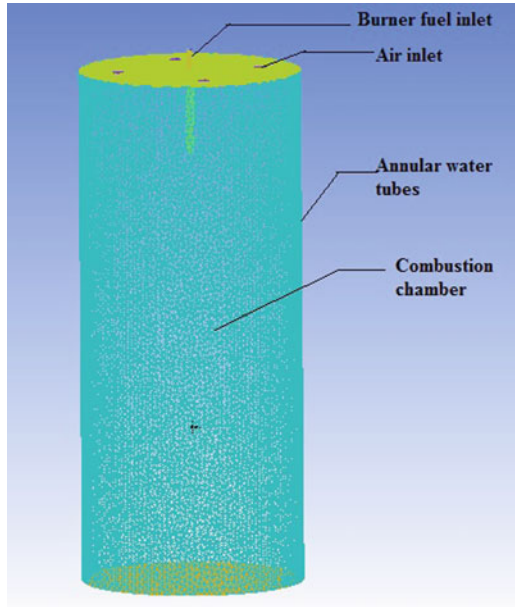


**Fig. 5** Meshing of pressure jet burner of the auxiliary boiler



### **5.1 Validation of CFD Results with Experimental Results**

Figure 6 shows the incomplete oxidation of  $\text{CO}_2$  in the nozzle of the burner. As in annular space of water tubes, the incomplete distribution of temperature gradient can be visualized in the ZY-plane of Fig. 7. Velocity contour of combustion product reveals that it is concentrated at the centre of the combustion chamber. Distribution of mass fraction of  $\text{C}_8\text{H}_{18}$  diesel fuel is seen on the tip of the burner nozzle in Fig. 7. Figure 10 shows the whirling of air distribution in the combustion chamber. Graph 3 shows the turbulence of transport species with respect to time step (Figs. 8 and 9).

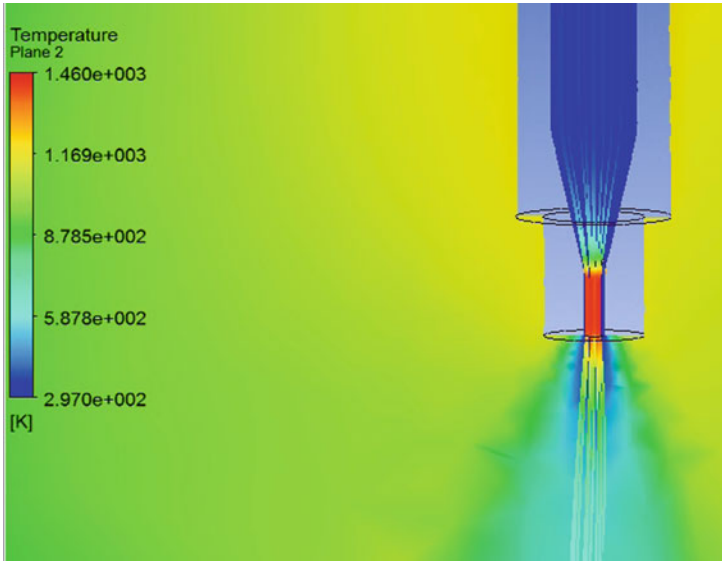


Fig. 6 Temperature of combustion space of the auxiliary boiler

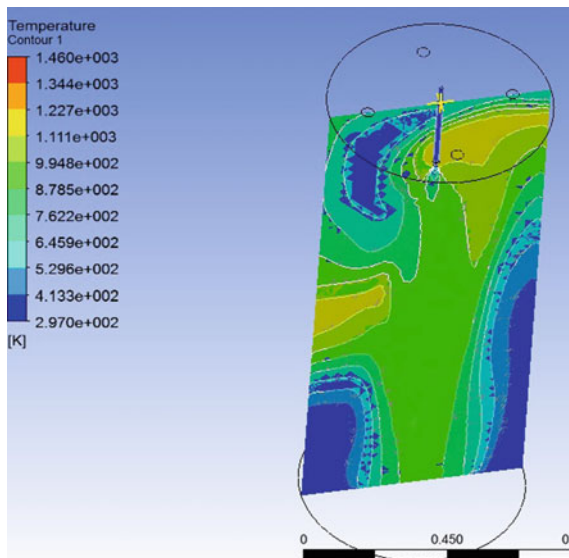


Fig. 7 Temperature of combustion space of the auxiliary boiler in YZ-plane

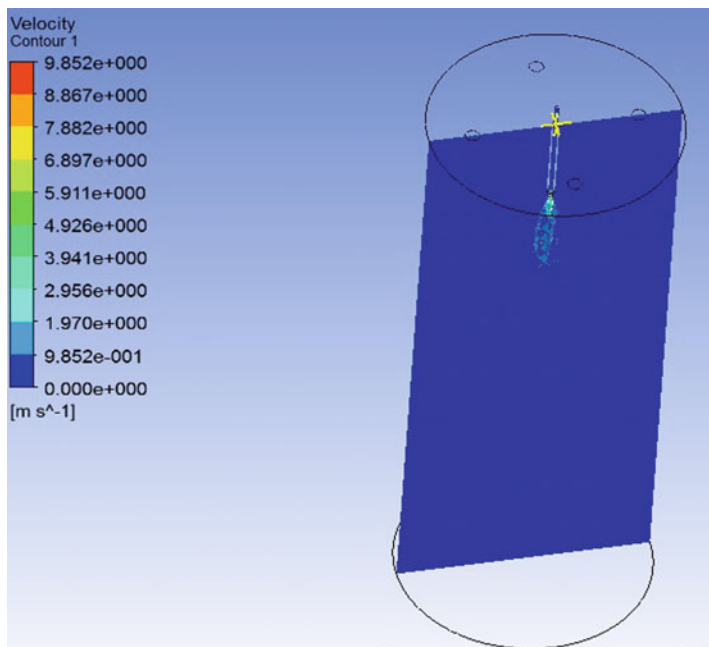


Fig. 8 Velocity contour of velocity through the nozzle

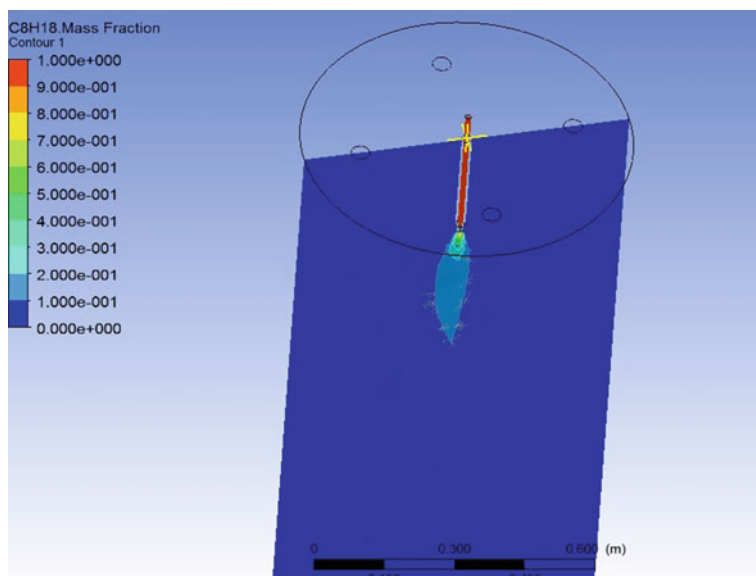


Fig. 9 Mass fraction contour in YZ-plane of burner of auxiliary boiler

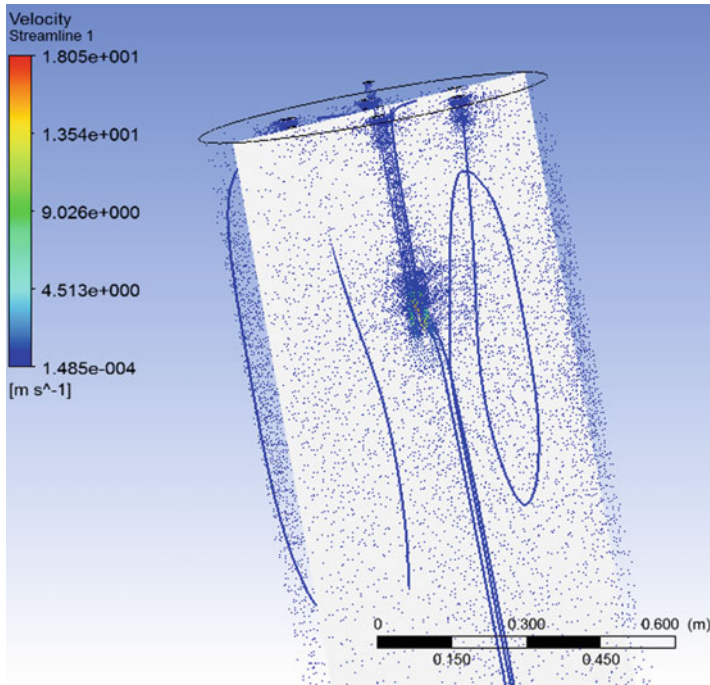
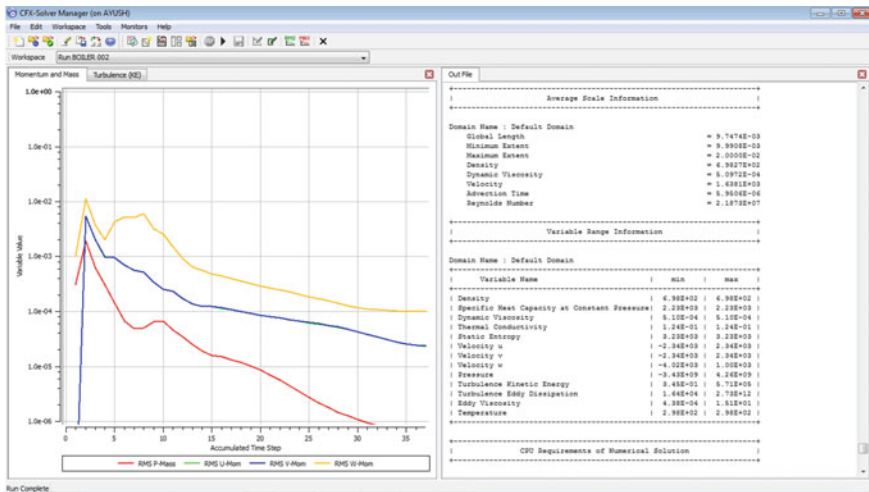


Fig. 10 Streamline in YZ-plane of burner of auxiliary boiler



Graph 3 Result and graph generation

## 6 Conclusion

The study is carried out on the auxiliary boiler for first and second law of thermodynamic efficiency calculation, exergy efficiency and numerical analysis aiming for most efficient method of available energy enhancing. The study suggests 15% better optimization than the existing system, and more rational operation of the installation is achieved by exergy addition, exergy losses and exergy consumption on the measured operating data and the thermodynamic state of the plant components. This analysis of the auxiliary boiler will contribute to an enhanced understanding, a superior design and a more rigorous evolution of steam system of the commercial vessels and leads to another methodology for tackling the energy problem. Hence, it is desirable to incorporate this system for future vessels as well as vessels currently in operation for better safety and improved working conditions of the seafarers. The major observations relating to the reduction of irreversibility in auxiliary boiler are as follows:

- (a) The efficiency of auxiliary boiler increases with increase in load, maximum at 55%.
- (b) The total entropy of the products is 86,402 kJ/K, which can be reduced by preheating the air.
- (c) The task efficiency/energy efficiency of this auxiliary is 97%, and maximum work output is 247,012 kJ/kg mol fuel.
- (d) The analysis of this auxiliary boilers shows that the chemical reaction and physical transport processes are the sources of irreversibility in combustion, which can be decreased by the air circulation.

**Acknowledgements** This research is supported by Tolani Maritime Institute, Induri (India). Authors express their sincere gratitude for their support. Moreover, authors express warm gratitude towards Dr. Sanjeet Kanungo (Vice Principal of Tolani Maritime Institute, Induri) for his invaluable inputs during the investigation of this auxiliary boiler.

## References

1. Michael J (1982) Moran, availability analysis: a guide to efficient energy use. Prentice hall, Inc., Englewood cliffs
2. Som SK, Datta A (2007) Thermodynamic irreversibility and exergy balance in combustion process. *Prog Energy Combust Sci* 34:351–376
3. Kotas TJ (2012) The exergy method of thermal plant analysis. Exergon Publishing Company UK Ltd., London. ISBN: 978-1-908341-89-1
4. Zhao Z, Yuan Z, Cui Q, Yan N (2010) Exergy analysis of an WGZ220/6.8-1 type alkali recovery boiler. *Mod Appl Sci* 4(2):23–29
5. Ohijeagbon IO, Waheed MA, Jekayinfa SO, Lasode OA (2014) Exergetic modelling of oil-fired steam boilers. *Niger J Technol (NIJOTECH)* 33(4):523–536

# Retraction Note to: Effect of Nanocellulose as an Additive in Cement



Vignesh Shenoy, Sanjay Joshi, and Mikhil Dange

**Retraction Note to:**  
**Chapter “Effect of Nanocellulose as an Additive in Cement”**  
**in: K. Murali et al. (eds.), *Proceedings of the Fourth International Conference in Ocean Engineering (ICOE2018)*, Lecture Notes in Civil Engineering 22,**  
[https://doi.org/10.1007/978-981-13-3119-0\\_66](https://doi.org/10.1007/978-981-13-3119-0_66)

Retraction Note to: Shenoy V., Joshi S., Dange M. (2019) Effect of Nanocellulose as an Additive in Cement In: Murali K., Sriram V., Samad A., Saha N. (eds) Proceedings of the Fourth International Conference in Ocean Engineering (ICOE2018). Lecture Notes in Civil Engineering, vol 22. Springer, Singapore. [https://doi.org/10.1007/978-981-13-3119-0\\_66](https://doi.org/10.1007/978-981-13-3119-0_66)

The corresponding author has retracted this chapter because, following publication, the authors became aware that they did not have permission to publish the data. All authors agree to this retraction.

---

The retracted version of this chapter can be found at  
[https://doi.org/10.1007/978-981-13-3119-0\\_66](https://doi.org/10.1007/978-981-13-3119-0_66)

© Springer Nature Singapore Pte Ltd. 2021  
K. Murali et al. (eds.), *Proceedings of the Fourth International Conference in Ocean Engineering (ICOE2018)*, Lecture Notes in Civil Engineering 22,  
[https://doi.org/10.1007/978-981-13-3119-0\\_74](https://doi.org/10.1007/978-981-13-3119-0_74)